AD-A264 177

0

AGARD-CP-527

AGARD-CP-527

AGARD

ADVISORY GROUP FOR AEROSPACE RESEARCH & DEVELOPMENT
7 RUE ANCELLE 92200 NEUILLY SUR SEINE FRANCE

AGARD CONFERENCE PROCEEDINGS 527

Heat Transfer and Cooling in Gas Turbines

(Le Transfert Thermique et le Refroidissement dans les Turbines à Gaz)

DTIC
ELECTE
APR 27 1993
S E D

Papers presented at the Propulsion and Energetics Panel 80th Symposium held in Antalya, Turkey, 12th—16th October 1992.

93-08810

495P8

[illegible] 4 2 035

NORTH ATLANTIC TREATY ORGANIZATION

DISTRIBUTION STATEMENT
Approved for public release;
Distribution Unlimited

Published February 1993

Distribution and Availability on Back Cover

AGARD-CP-527

AGARD

ADVISORY GROUP FOR AEROSPACE RESEARCH & DEVELOPMENT

7 RUE ANCELLE 92200 NEUILLY SUR SEINE FRANCE

AGARD CONFERENCE PROCEEDINGS 527

Heat Transfer and Cooling in Gas Turbines

(Le Transfert Thermique et le Refroidissement dans les Turbines à Gaz)

Accesion For
NTIS CRA&I ☒
DTIC TAB ☐
Unannounced ☐
Justification
By
Distribution /
Availability Codes
Dist | Avail and / or Special
A-1

Papers presented at the Propulsion and Energetics Panel 80th Symposium held in Antalya, Turkey 12th—16th October 1992.

North Atlantic Treaty Organization
Organisation du Traité de l'Atlantique Nord

93-07888

93 4 14 145

The Mission of AGARD

According to its Charter, the mission of AGARD is to bring together the leading personalities of the NATO nations in the fields of science and technology relating to aerospace for the following purposes:

- Recommending effective ways for the member nations to use their research and development capabilities for the common benefit of the NATO community;
- Providing scientific and technical advice and assistance to the Military Committee in the field of aerospace research and development (with particular regard to its military application);
- Continuously stimulating advances in the aerospace sciences relevant to strengthening the common defence posture;
- Improving the co-operation among member nations in aerospace research and development;
- Exchange of scientific and technical information;
- Providing assistance to member nations for the purpose of increasing their scientific and technical potential;
- Rendering scientific and technical assistance, as requested, to other NATO bodies and to member nations in connection with research and development problems in the aerospace field.

The highest authority within AGARD is the National Delegates Board consisting of officially appointed senior representatives from each member nation. The mission of AGARD is carried out through the Panels which are composed of experts appointed by the National Delegates. the Consultant and Exchange Programme and the Aerospace Applications Studies Programme. The results of AGARD work are reported to the member nations and the NATO Authorities through the AGARD series of publications of which this is one.

Participation in AGARD activities is by invitation only and is normally limited to citizens of the NATO nations.

The content of this publication has been reproduced
directly from material supplied by AGARD or the authors.

Published February 1993

Copyright © AGARD 1993
All Rights Reserved

ISBN 92-835-0701-0

SPS

Printed by Specialised Printing Services Limited
40 Chigwell Lane, Loughton, Essex IG10 3TZ

Recent Publications of the Propulsion and Energetics Panel

CONFERENCE PROCEEDINGS (CP)

Heat Transfer and Cooling in Gas Turbines
AGARD CP 390, September 1985

Smokeless Propellants
AGARD CP 391, January 1986

Interior Ballistics of Guns
AGARD CP 392, January 1986

Advanced Instrumentation for Aero Engine Components
AGARD CP 399, November 1986

Engine Response to Distorted Inflow Conditions
AGARD CP 400, March 1987

Transonic and Supersonic Phenomena in Turbomachines
AGARD CP 401, March 1987

Advanced Technology for Aero Engine Components
AGARD CP 421, September 1987

Combustion and Fuels in Gas Turbine Engines
AGARD CP 422, June 1988

Engine Condition Monitoring — Technology and Experience
AGARD CP 448, October 1988

Application of Advanced Material for Turbomachinery and Rocket Propulsion
AGARD CP 449, March 1989

Combustion Instabilities in Liquid-Fuelled Propulsion Systems
AGARD CP 450, April 1989

Aircraft Fire Safety
AGARD CP 467, October 1989

Unsteady Aerodynamic Phenomena in Turbomachines
AGARD CP 468, February 1990

Secondary Flows in Turbomachines
AGARD CP 469, February 1990

Hypersonic Combined Cycle Propulsion
AGARD CP 479, December 1990

Low Temperature Environment Operations of Turboengines (Design and User's Problems)
AGARD CP 480, May 1991

CFD Techniques for Propulsion Applications
AGARD CP 510, February 1992

Insensitive Munitions
AGARD CP 511, July 1992

Combat Aircraft Noise
AGARD CP 512, April 1992

Airbreathing Propulsion for Missiles and Projectiles
AGARD CP 526, September 1992

Heat Transfer and Cooling in Gas Turbines
AGARD CP 527, February 1993

ADVISORY REPORTS (AR)

Suitable Averaging Techniques in Non-Uniform Internal Flows *(Results of Working Group 14)*
AGARD AR 182 (in English and French), June/August 1983

Producibility and Cost Studies of Aviation Kerosines *(Results of Working Group 16)*
AGARD AR 227, June 1985

Performance of Rocket Motors with Metallized Propellants *(Results of Working Group 17)*
AGARD AR 230, September 1986

Recommended Practices for Measurement of Gas Path Pressures and Temperatures for Performance Assessment of Aircraft Turbine Engines and Components *(Results of Working Group 19)*
AGARD AR 245, June 1990

The Uniform Engine Test Programme *(Results of Working Group 15)*
AGARD AR 248, February 1990

Test Cases for Computation of Internal Flows in Aero Engine Components *(Results of Working Group 18)*
AGARD AR 275, July 1990

Test Cases for Engine Life Assessment Technology *(Results of Working Group 20)*
AGARD AR 308, September 1992

Terminology and Assessment Methods of Solid Propellant Rocket Exhaust Signatures *(Results of Working Group 21)*
AGARD AR 287, February 1993

LECTURE SERIES (LS)

Ramjet and Ramrocket Propulsion Systems for Missiles
AGARD LS 136, September 1984

3-D Computation Techniques Applied to Internal Flows in Propulsion Systems
AGARD LS 140, June 1985

Engine Airframe Integration for Rotorcraft
AGARD LS 148, June 1986

Design Methods Used in Solid Rocket Motors
AGARD LS 150, April 1987
AGARD LS 150 (Revised), April 1988

Blading Design for Axial Turbomachines
AGARD LS 167, June 1989

Comparative Engine Performance Measurements
AGARD LS 169, May 1990

Combustion of Solid Propellants
AGARD LS 180, July 1991

Steady and Transient Performance Prediction of Gas Turbine Engines
AGARD LS 183, May 1992

AGARDOGRAPHS (AG)

Measurement Uncertainty within the Uniform Engine Test Programme
AGARD AG 307, May 1989

Hazard Studies for Solid Propellant Rocket Motors
AGARD AG 316, September 1990

Advanced Methods for Cascade Testing
AGARD AG 328 (to be published in 1993)

REPORTS (R)

Application of Modified Loss and Deviation Correlations to Transonic Axial Compressors
AGARD R 745, November 1987

Rotorcraft Drivetrain Life Safety and Reliability
AGARD R 775, June 1990

Theme

Heat transfer and cooling in gas turbine engines are still key factors to achieve high performance, increased life and improved reliability. Any progress in this field will lead to a reduction of maintenance cost and fuel consumption.

The purpose of this Symposium was to bring together experts from industry, research establishments and universities to discuss fundamental and applied heat transfer problems relevant to gas turbines, to exchange practical experience gained and to review the state of the art.

The Symposium focused on turbine blade cooling (both external and internal heat transfer); heat transfer in combustors, to disks, in labyrinth seals, and in shafts; measurement techniques and prediction methods; as well as interactions.

Thème

Le transfert thermique et le refroidissement continuent à jouer un rôle clé dans l'obtention de meilleures performances, l'augmentation de la durée de vie et l'amélioration de la fiabilité des turbines à gaz. Tout progrès réalisé dans ce domaine permettra de réduire les coûts de maintenance et de diminuer la consommation de carburant.

L'objet du Symposium était de rassembler des spécialistes de l'industrie, des établissements de recherche et des universités pour discuter des problèmes fondamentaux et d'application en transfert thermique dans les turbines à gaz. La réunion a fourni l'occasion pour un échange d'expérience pratique et l'examen de l'état de l'art dans ce domaine.

Le Symposium a traité du refroidissement des aubes de turbine (le transfert thermique interne et externe), du transfert thermique dans les chambres de combustion, les disques, les presse-garnitures à labyrinthe et les arbres, ainsi que des méthodes de prévision et des techniques de mesure et les interactions qui en résultent.

Propulsion and Energetics Panel

Chairman: Prof. Dr Ahmet Üçer
Middle East Technical University
O D T Ü
Makina Müh. Bölümü
Ankara
Turkey

Deputy Chairman: Mr Robert E. Henderson
Acting Chief
Advanced Propulsion Division
WL/POT
Wright Patterson Air Force Base
Ohio 45433-6563
United States

PROGRAMME COMMITTEE

Professor Dr Dietmar K. Hennecke
(Chairman)
Fachgebiet Flugantriebe
Technische Hochschule Darmstadt
Petersenstrasse 30
W-6100 Darmstadt, Germany

Dr Robert Bill
US Army Propulsion Directorate
NASA Lewis Research Center
Mail Stop 77-12
21000 Brookpark Road
Cleveland, Ohio 44135
United States

Professor Frans Breugelmans
Head, Turbomachinery Dept,
Assistant Director
von Kármán Institute for
Fluid Dynamics
72 Chaussée de Waterloo
1640 Rhode St Genèse, Belgium

M. le Professeur Jacques Chauvin
Laboratoire d'Energetique et de
Mécanique des Fluides
Internes (LEMFI)
Campus Universitaire
Bt 502
91405 Orsay Cedex, France

Mr David P. Kenny
Director, Analytical Engineering
Pratt and Whitney Canada, Inc.
1000 Marie-Victorin
Longueuil, Quebec, Canada

Professor Jose J. Salva Monfort
Escuela Tecnica Superior de
Ingenieros Aeronauticos
Plaza Cardenal Cisneros 3
28040 Madrid, Spain

Ing. Claudio Vinci
FIAT Aviazione s.p.a.
Progettazione
Corso Ferrucci 112
10138 Torino, Italy

Mr William W. Wagner
Technical Director (Code 07)
Naval Air Propulsion Center
P.O. Box 7176
Trenton, New Jersey 08628-0176
United States

Mr David Way
Superintendent, Turbomachinery
Propulsion Department
Defence Research Agency
(Aerospace Division) RAE
Pyestock, Farnborough,
Hants GU14 0LS
United Kingdom

HOST NATION COORDINATOR

Professor Dr Ahmet Üçer

PANEL EXECUTIVE OFFICE

Mail from Europe:
AGARD—OTAN
Attn: PEP Executive
7, rue Ancelle
F-92200 Neuilly-sur-Seine
France

Mail from US and Canada:
AGARD—NATO
Attn: PEP Executive
Unit 21551
APO AE 09777

Tel: 33(1)47 38 57 85
Telex: 610176F
Telefax: 33 (1) 47 38 57 99

ACKNOWLEDGEMENT

The Propulsion and Energetics Panel wishes to express its thanks to the National Authorities from Turkey for the invitation to hold this meeting in Antalya, Turkey, and for the facilities and personnel which made this meeting possible.

Contents

Page

Recent Publications of PEP iii

Theme/Thème v

Propulsion and Energetics Panel vi

Reference

Technical Evaluation Report T
by R.E. Mayle

Keynote Address: Unsteady, Multimode Transition in Gas Turbine Engines K
by R.E. Mayle

SESSION I – TURBINE BLADES: EXTERNAL HEAT TRANSFER

Heat Transfer and Aerodynamics of a 3D Design Nozzle Guide Vane Tested in the Pyestock Isentropic Light Piston Facility 1
by K.S. Chana

Vortex Structure and Mass Transfer Near the Base of a Cylinder and a Turbine Blade 2
by M.Y. Jabbari and R.J. Goldstein

Thermal Effects of a Coolant Film along the Suction Side of a High Pressure Turbine Nozzle Guide Vane 3
by T. Arts and I. Lapidus

Etude Expérimentale du Transfert de Chaleur près d'une Paroi Plane Chauffée en Présence d'Injections Multiples 4
par E. Foucault, P. Deniboire, J.-L. Bousgarbiès et J.J. Vullierme

The Influence of Non-Uniform Spanwise Inlet Temperature on Turbine Rotor Heat Transfer 5
by G.R. Guenette, G. Pappas and A.H. Epstein

Determination of Surface Heat Transfer and Film Cooling Effectiveness in Unsteady Wake Flow Conditions 6
by M. Sautner, S. Clouser and J.C. Han

Measurement of Turbulent Spots and Intermittency Modelling at Gas Turbine Conditions 7
by J.P. Clark, J.E. LaGraff, P.J. Magari and T.V. Jones

Heat Transfer in High Turbulence Flows – a 2D Planar Wall Jet 8
by R.B. Rivir, W.T. Troha, W.A. Eckerle and W.J. Schmoll

Heat Transfer with Moderate Free Stream Turbulence 9
by S.N.B. Murthy

SESSION II – TURBINE BLADES: INTERNAL HEAT TRANSFER

Echanges Thermiques dans les Canaux de Refroidissement des Aubes de Turbine 10
par Y. Servouze et A. Ristori

The Effect of Orthogonal-Mode Rotation on Forced Convection in a Circular-Sectioned Tube Fitted with Full Circumferential Transverse Ribs 11
by W.D. Morris and R. Salemi

Reference

Turbulent Flow and Heat Transfer in Idealized Blade Cooling Passages 12
by T. Bo and B.E. Launder

Cooling Geometry Optimization using Liquid Crystal Technique 13
by G. Lodigiani, A. Trovati, L. Paci and P. Pirrelli

Fundamental Studies of Impingement Cooling Thermal Boundary Conditions 14
by M.G. Lucas, P.T. Ireland, Z. Wang, T.V. Jones and W.J. Pearce

Prediction of Jet Impingement Cooling Scheme Characteristics (Airfoil Leading Edge Application) 15*
by A. Riahi, H.J. Saabas and W. Abdel-Messeh

SESSION III – MEASUREMENT TECHNIQUES

An L2F-Measurement Device with Image Rotator Prism for Flow Velocity Analysis in Rotating Coolant Channels 16
by M. Beversdorff, O. Hein and R. Schodl

Local Heat Transfer Measurement with Liquid Crystals on Rotating Surfaces including Non-axisymmetric Cases 17
by D.E. Metzger and Y.K. Kim

Paper 18 withdrawn

The Swollen Polymer Technique and its Use for Heat Transfer Investigations on Film Cooled Surfaces 19
by N. Hay, D. Lampard and N. McLeod

The USAF Advanced Turbine Aerothermal Research Rig (ATARR) 20
by C.W. Haldeman Jr, M.G. Dunn. C.D. MacArthur and C.G. Murawski

SESSION IV – ROTATING DISKS, LABYRINTH SEALS AND SHAFTS

Transient Thermal Behaviour of a Compressor Rotor with Axial Cooling Air Flow and Co-Rotating or Contra-Rotating Shaft 21
by C. Burkhardt, A. Mayer and E. Reile

Calculs Aérothermiques d'Ecoulements dans des Cavités Interdisques de Turbines 22
par D. Dutoya et Ph. Poncelin de Raucourt

Study of Flow Structure in Rotating Cavities: Numerical Predictions of Laminar and Turbulent, Steady and Unsteady Flows 23
by P. Maubert et al.

Modelling Thermal Behaviour of Turbomachinery Discs and Casings 24
by R.D. Monico and J.W. Chew

Flow and Heat Transfer between Gas-Turbine Discs 25
by X. Gan, M. Kilic and J.M. Owen

Heat Transfer and Leakage in High-Speed Rotating Stepped Labyrinth Seals 26
by W. Waschka, S. Wittig, S. Kim and Th. Scherer

Fluid Flow and Heat Transfer in the Entrance Region of an Annulus between Independently Rotating Tubes with a Turbulent Axial Flow 27
by H. Pfitzer, T. Rothe and H. Beer

---

* Paper available and distributed but not presented at the Symposium.

Reference

SESSION V – COMBUSTORS

Paper 28 withdrawn

The Effect of Main Stream Flow Angle on Flame Tube Film Cooling 29
by H. Klinger and D.K. Hennecke

Impingement/Effusion Cooling 30
by G.E. Andrews et al.

Evaluation of Multi-Dimensional Flux Models for Radiative Transfer in Cylindrical Combustion Chambers 31
by N. Selçuk

Calculs d'Ecoulements Turbulents Réactifs dans les Foyers Aéronautiques 32
par P. Caillau et F. Dupoirieux

SESSION VI – DESIGN, INTERACTIONS

Aero-thermal Design of a Cooled Transonic NGV and Comparison with Experimental Results 33
by S. Colantuoni, A. Colella, L. Di Nola, D. Carbone and D. Marotta

Paper 34 withdrawn

The Aerodynamic Effect of Coolant Ejection in the Leading Edge Region of a Film-cooled Turbine Blade 35
by A. Beeck, L. Fottner, E. Benz and S. Wittig

On the Development of a Film Cooling Layer 36
by F. López Peña and T. Arts

Paper 37 withdrawn

SESSION VII – PREDICTION METHODS

Paper 38 withdrawn

Modelisation d'un Ecoulement Turbulent en Presence de Jets Parietaux Discrets de Refroidissement 39
par J.M. Maurice, F. Leboeuf et P. Kulisa

Coupling of 3D-Navier-Stokes External Flow Calculations and Internal 3D-Heat Conduction Calculations for Cooled Turbine Blades 40
by A. Heselhaus, D.T. Vogel and H. Krain

A Navier Stokes Solver with Different Turbulent Models Applied to Film-Cooled Turbine Cascades 41
by F. Bassi, S. Rebay, M. Savini, S. Colantuoni and G. Santoriello

Navier-Stokes Analysis of Three-Dimensional Flow and Heat Transfer inside Turbine Blade Rows 42
by C. Hah

Cooling Predictions in Turbofan Engine Components 43
by A. Matesanz, R. Rebolo, A. Viedma and M. Rodriguez

Technical Evaluation Report

by

Robert E. Mayle
Rensselaer Polytechnic Institute
Troy, New York 12180
United States

It is always good to participate in such a symposium where all of those attending have a common interest and objective. Somehow it gives me a feeling of compatriotism, creativity and accomplishment. It is even better when the nearly one hundred and forty of us attending not only come from multifarious nations, but also from industry, universities and various government agencies. This sort of meeting provides the best in diversity of approaches to our common problem and the best chance for the diffusion of our ideas. As we have experienced this week, the outcome was not only forty presentations which covered most aspects of gas turbine heat transfer and cooling, but lively discussions and a comradery. In addition, I had some impressions. Some arose from what I have heard this week, some were reflections of what I have experienced during my twenty-some years as an active researcher in the gas turbine heat transfer community, and some involved what I foresee concerning research and development in the field of gas turbine heat transfer. Now I wish to share them with you.

During this Symposium, the 80th Symposium of the Propulsion and Energetics Panel of AGARD, the common interest has been "Heat Transfer and Cooling in Gas Turbines" and the common objective has been to improve gas turbine durability and performance. Seven years ago, the Propulsion and Energetics Panel held a similar symposium (see AGARD CP 390), and the interest and objective were the same. What has changed? From the standpoint of fundamental understanding, not much. Progress in fundamental understanding is slow, as I will now illustrate with a story. About twenty years ago when I started my career in the field of gas turbine heat transfer, my supervisor told me, contrary to my belief, that the laminar-turbulent transition problem had been solved and that I should work on the much more relevant problem of film cooling. So I begun my work in film cooling and today, in spite of my efforts then and those of many others since, we still cannot predict heat transfer downstream of an arbitrary film cooling scheme because the fundamental problem of film cooling remains unsolved. The story does not end here and, in fact, closes at the beginning. About four years ago I began working on the transition problem again, although I was interested in its unsteady aspects, and was surprised to learn how little our fundamental understanding of transition had changed in twenty years. Indeed, it really hasn't changed much since 1951 when Emmons discovered the formation of turbulent spots in a laminar boundary layer.

So what has changed? From the fundamental standpoint, not much. From the standpoint of a gas turbine design engineer, however, a lot. Since the last symposium, there has been an increasing flow of data from a wide variety of experiments pertaining to gas turbine heat transfer, much of which is well documented. This has provided the designer with a continuing update of his or her data base. Some of these data were obtained in full-scale turbine test facilities using advanced data acquisition systems, and some were obtained in large scale test facilities operated according to the fluid mechanic similarity principles. Each type of facility is needed, although I favor the large scale type because of their simplicity and the chance of obtaining more detailed data. In addition, there have been significant advances in numerical methods of analysis and experimental techniques which together will provide the foundation of our future gas turbine design systems. So the changes depend upon our standpoint and needs, even though the primary interest and objective of our community have remained the same.

This Symposium covered most aspects of heat transfer and cooling in gas turbines. This may be seen from the titles of the sessions themselves, namely,

- Turbine Blades — External Heat Transfer
- Turbine Blades — Internal Heat Transfer
- Measurement Techniques
- Rotating Disks, Labyrinth Seals and Shafts
- Combustors
- Design, Interactions
- Prediction Methods.

After reviewing the papers presented in these sessions, not including the Keynote Address, I would say about eighteen concerned increasing our data base, ten concerned numerical methods of analysis, five concerned measurement techniques, five concerned full-scale engine simulation tests for the purpose of design substantiation, and only one concerned a fundamental question regarding gas turbine heat transfer. Except for a few which addressed specific design issues, most contain some element of research, some element of "newness". Coming back to the point I made earlier, and considering the numbers above, it should not surprise anyone that a lot has changed from a designer's standpoint while not much has changed from the fundamental standpoint. Now I wish to discuss some of the advances I think we have made in the last seven years, and, in so doing, I will also try to indicate their future impact on gas turbine heat transfer and cooling design.

In recent years, the most significant advances have been in the areas of unsteady flow, transitional flow, and rotational flow, and in applications of the experimental liquid crystal technique and the computational fluid dynamic methods. Since I am personally involved in two of these areas, namely, unsteady and transitional flow, I will start with them.

I strongly believe that the largest improvements of durability and efficiency in future gas turbine engines depend upon our understanding of, and our ability to predict the highly unsteady and three-dimensional flows which occur within these engines. In addition, I truly believe that the last frontier in gas turbine technology is understanding and either actively or passively controlling these flows. The recent advances in this area have been swift. About seven years ago we just started to digest the first truly unsteady heat transfer and aerodynamic results, and now we already have simple, but useful unsteady flow models for transition and complex, but practical unsteady, three-dimensional computer programs. The advances being made in this area have been fundamental as well as practical. Today, Dr Hah[1] described his unsteady, three-dimensional computer program and told us that the time-averaged aerodynamic loss associated with these flows is not equal to the loss predicted by a steady flow calculation using the time-averaged inlet flow conditions. Earlier this week, I described a simple model for unsteady, multimode transition and showed even for two-dimensional flow that the time-averaged heat load on a cooled turbine airfoil cannot be calculated using a steady flow analysis with time-averaged inlet flow conditions. In other words, correct predictions of either the aerodynamic losses or blade heat transfer require unsteady flow considerations. In addition, Dr Epstein described the three-dimensional effects of a non-uniform inlet temperature profile on turbine blade heat transfer. Presently, our design systems either neglect these unsteady, three-dimensional effects or incorrectly attempt to take them into account by using time- and circumferentially-averaged inlet conditions. We should be working hard toward replacing these systems with their unsteady, three-dimensional counterparts and using the new systems to design three-dimensionally-tailored cooled airfoils having lower aerodynamic losses which can operate at higher inlet temperatures.

Coming back to the story I related earlier, laminar-turbulent transition has been a problem for many years and is, since most flows in a gas turbine are transitional, still an important problem to solve. Fortunately, there have been significant advances here too. As explained in my recent review paper[2] on the subject, the advances have not been in "fixing up" old two-dimensional, steady-flow models of the phenomenon, but in accepting and using the turbulent spot ideas of Emmons. Mr Clark showed us very clearly this week that these ideas provide an accurate description of transitional flow. The new ideas also allow us to solve the unsteady transitional flow problems such as those discussed in my presentation. All of the advances here are very recent, and can be attributed solely to a revolution in our thinking more than anything else. Presently, however, most design systems still use the old methods for calculating transitional flows. We should be working towards incorporating the new thinking into these design systems and obtaining data to clarify some of the missing details in the new models.

The work in rotational flow with heat transfer can usually be divided into three areas; flow in disk cavities, flow through labyrinth seal passages, and flow in airfoil cooling passages. Advances in all of these areas have mainly been associated with acquiring more information about these flows, which, in turn, has helped to dispel some of the "mysticism" surrounding (no pun intended) them. The more common experiments involve rather sophisticated rotating test models and data acquisition systems such as that described by Prof. Morris. A conceptionally simpler rotating test facility using the liquid crystal measurement technique was described by Prof. Metzger. While interest in rotating flows and the heat transfer associated with them is relatively recent, research and advances have generally followed the increase in turbine inlet temperatures and coincided with the designer's need. Calculation methods, such as those described separately by Professor Owen and Professor Launder, have also been developed to handle these complicated flows. Presently, however, most design systems use correlations to predict the effects of rotation on turbine heat transfer. Here, we should continue to develop practical computational methods for these flows, particularly methods which can handle rotational flows in complex airfoil cooling passages.

Following up on this statement, it is now clear that computational fluid dynamic and heat transfer programs have now been developed to a point where they become more attractive to use as a design tool. Euler solvers are now commonly used by aerodynamicists and Navier-Stokes solvers are quickly being introduced. Before these programs can become a mainstay of the heat transfer design system, however, they must become more accurate. The comparisons between calculated and experimental results shown separately by Dr Chana and Dr Rivir[3] just aren't good enough yet for heat transfer design purposes. Nevertheless, it is now practical to consider a design methodology which uses computational fluid dynamic and heat transfer programs, together with liquid-crystal-type experiments to "quick check" the design and subsequently modify it accordingly. As shown by Dr Pirrelli, this method appears most suitable for designing turbine blade cooling flow systems where the geometry of the passages and the flows within them are so complex that our correlation laden design programs are only approximate anyway. This is the direction of the future, both for internal and external flows, and we should be pursuing it vigorously.

In conclusion, there have been many changes. There have been many advances, and if we are as successful in the next seven years as we have been in the last, the next symposium will be well worth attending. It has been a pleasure to participate in this Symposium. The presentations and discussions have been very good and stimulating. Now I wish to close by thanking the Propulsion and Energetics Panel and all those who participated in the Symposium. It has been a very worthwhile experience.

---

[1] The authors named in this report are those who presented their papers. They may not be the paper's first author.

[2] "The Role of Laminar-Turbulent Transition in Gas Turbine Engines," J. Turbomachinery, Vol. 113, 1991, pp. 509-537.

[3] Dr Rivir presented the paper authored by Haldeman, Dunn, MacArthur and Murawski.

Keynote Address

UNSTEADY, MULTIMODE TRANSITION IN GAS TURBINE ENGINES

Robert E. Mayle
Rensselaer Polytechnic Institute
Troy, New York 12180
USA

Abstract

A theory for unsteady, multimode transition on gas turbine airfoils is presented. The theory, which provides a correction to the Mayle-Dullenkopf multimode model, considers a more physically correct viewpoint by taking into account the periodic disturbance caused by both the wake-induced turbulent strips and the "becalmed" flow following them. In addition, a comparison of the theory with data is provided, which shows excellent agreement, and results illustrating the effects of transition onset distance and wake-passing Strouhal number on multimode transition are presented.

List of Symbols

a	production rate of turbulent strips
c	airfoil chord
n	production rate of turbulent spots per unit distance in the spanwise direction
Nu	Nusselt number
Re	Reynolds number
S	Strouhal number
t	time
U_∞	free-stream velocity
x	surface coordinate in stream-wise direction
x_{tn}	onset of the wake-disturbed normal transition
x_{tw}	onset of the wake-induced transition

Greek

γ	intermittency
$\tilde{\gamma}$	time-averaged intermittency
ν	kinematic viscosity
σ	Emmons' spot propagation parameter
τ	wake-passing period
ω	wake-passing frequency

Subscripts

L	laminar
n	normal transition mode
T	turbulent
w	wake induced transition mode

Introduction

In the past, laminar-to-turbulent boundary layer transition on gas turbine airfoils was considered to be a "steady" event, or at least a statistically steady event, and was calculated as such. During the past decade or so, however, experimental evidence began to appear which showed otherwise and now, after numerous experiments (Pfeil and Herbst, 1979, Herbst, 1980, Pfeil et al.,1983, Hodson, 1984, Schröder, 1985, 1989, 1990, Ashworth et al., 1985, Doorly et al., 1985a, b and c, 1988, Dring et al., 1986, Dunn et al., 1986, Wittig et al., 1988, LaGraff et al., 1989, Dong and Cumpsty, 1989a and b, Mayle and Dullenkopf, 1989, 1990, Liu and Rodi, 1989, Dullenkopf, et al., 1991, Orth, 1991, and Dullenkopf, 1992), it is generally accepted that transition on gas turbine airfoils is unsteady and that the unsteady passing of wakes from the previous airfoil row (see Fig.1) has the greatest effect. In particular, it is now recognized that the wakes themselves produce nearly two-dimensional, spanwise-oriented, turbulent strips which periodically propagate and grow along the airfoil surface, as shown in the lower portion of Fig. 2, such that the affected flow is part of the time laminar and part of the time turbulent. This transition is called "wake-induced transition" and was, until recently, considered to be the main unsteady effect of the wake on the flow. The fraction of time the flow is turbulent is defined as the intermittency, γ. For laminar flow $\gamma = 0$, while for turbulent flow $\gamma = 1$. For transitional flow, of course, γ lies between zero and unity. Several intermittency distributions for wake-induced transition are shown in the upper portion of Fig. 2. In this figure, the onset of wake-induced transition is presumed to occur at the streamwise position x_{tw}.

Some of the same experiments (Pfeil and Herbst, 1979, Herbst, 1980, Pfeil et al., 1983, Wittig et al., 1988, Mayle and Dullenkopf, 1989, 1990, Dullenkopf, et al., 1991, Schröder, 1985, 1989, 1990, and Dong and Cumpsty, 1989a and b), however, also revealed that transition by any other mode can occur between the passing turbulent strips. In each case, the transition taking place between the strips was a periodically disturbed version of that which would have occurred there if the mainstream flow had been steady. For this reason, and in the following, this transition will be referred to as the "wake-disturbed" transition. A typical intermittency distribution for a transition which would occur if the mainstream flow was steady is shown in Fig. 3. In this figure, the onset of transition is presumed to occur at the streamwise position x_{tn} and is caused by a random production of turbulent spots as first described by Emmons (1951). An interesting consequence of a combined unsteady, wake-induced and wake-disturbed transitional flow is that multiple regions of laminar and turbulent flow can occur simultaneously on the same surface. That is, an instantaneous snapshot of the flow over a gas-turbine airfoil, say, may show a laminar boundary layer near the leading edge, a wake-induced turbulent strip farther downstream, followed by a second region of laminar flow, and another transition to turbulent flow by any one of the usual modes, be it natural, bypass, or separated-flow transition. This multiple transitional behavior is called "unsteady, multimode transition" or simply "multimode transition" (Mayle, 1991).

To this author's knowledge the first evidence of multimode transition was presented by Pfeil and Herbst (1979) and later described in a series of articles by Herbst (1980), Pfeil et al. (1983), and Schröder (1985). They measured the steady and unsteady velocity components in a flow along a flat plate positioned downstream of a rotating cylinder of circular spokes aligned parallel to the leading edge of the plate. Besides discovering that the wakes produce turbulent strips and correctly describing the wake-induced transition process, they discovered that a periodically unsteady transition could occur between the strips. In this regard, they were the first to establish the basic features of the multimode transition process as we know them today. Later, Wittig et al. (1988) measured the time-averaged heat transfer on a gas turbine airfoil in an unsteady wake-disturbed incident flow which clearly showed multimode transitional behavior. These measurements were obtained for wake-passing Strouhal numbers less than four and indicated that one could easily treat the wake-disturbed transitional portion of the flow as steady. Later measurements obtained by Dullenkopf et al. (1991) and Dullenkopf (1992) for higher Strouhal numbers, however, showed that this is not always the case. About the same time, Dong and

Cumpsty (1989a and b) presented their measurements on the unsteady interaction between wake-induced turbulent strips and a separated-flow transition bubble. In these papers, where velocity measurements on a compressor blade in an unsteady wake-disturbed incident flow are reported, it is clearly shown that laminar separation was suppressed as the strips passed over the separation location. In fact, for certain conditions, it was found[1] that the wake flow prevented both separation and transition from occurring at all, such that the flow between the turbulent strips remained laminar all the way to the airfoil's trailing edge.

In developing their theory for wake-induced transition, Mayle and Dullenkopf (1989) also presented a model for unsteady, multimode transition. Based on the results of Wittig, et al., 1988, which indicated little interaction, and Emmons' (1951) turbulent spot transition theory, they obtained an expression for the time-averaged intermittency of a multimode transitional flow by assuming that the downstream transition was undisturbed by the wake-induced turbulent strips except to the extent that the areas covered by the strips were always turbulent. Specifically, this was done by considering the production of turbulent strips and spots to be independent of one another and the downstream transition to be steady. As shown in their original paper, the agreement between this model and measurements for small Strouhal numbers was excellent. As shown recently (see Dullenkopf and Mayle, 1992, Fig. 2), however, their model fails to predict the correct behavior for higher wake-passing frequencies. In addition, the theory is incapable of predicting either an extended laminar or wake-disturbed transitional flow region such as observed by Dong and Cumpsty.

The present paper is an effort to correct these shortcomings. In the following, the idea of a "becalmed" flow will first be introduced and its effect on wake-disturbed transition described. Then the Mayle-Dullenkopf multimode transition result will be outlined and a new theory introduced which accounts for the effect of the becalmed flow. This is followed by a comparison of the new theory with data. Finally, the results of several parametric studies for multimode transition are presented.

The "Becalmed" Flow

As shown by Schubauer and Klebanoff (1955) the flow directly following a turbulent spot is laminar and stable with regard to any disturbances impressed upon it. Although not "calm," the flow within this region has been called "becalmed." While the reason for this behavior is not yet known, the implication in terms of transition is clear; turbulent spots can not be produced at any position on the surface covered by this stable flow. Recent measurements by Orth (1991) show that a similar becalmed flow also follows a turbulent strip. Therefore, in multimode transition where wake-induced turbulent strips pass through another transition region, both the disturbance of the strips and the stability of the flow following them must be taken into account.

Considering the effect of the becalmed flow on a boundary layer in multimode transition, an instantaneous view of the boundary layer and its intermittency distribution may appear something like that shown in Fig. 4. In this figure, the flow upstream of x_{tw} is supposed fully laminar, while that far downstream is expected to be fully turbulent. At the instant shown, the first turbulent strip has yet to interact with the transition occurring downstream, while the second strip, together with its attendant becalmed flow, lies within it. Since the becalmed flow prevents any turbulent spots from forming where they would normally form, a completely laminar "strip" follows the turbulent strip as it propagates through the wake-disturbed region of transition. Unlike the turbulent strips, however, and as will be seen later, these laminar strips decrease in length as they propagate downstream.

The various laminar, turbulent, laminar becalmed, and transitional flow regimes corresponding to the flow just described are shown in the distance-time diagram of Fig. 5. Cuts parallel to the x axis describe the instantaneous state of flow on the surface, while vertical cuts describe the unsteady behavior of the flow at a fixed position on the surface. The instantaneous state represented by the dashed line in this figure corresponds to that shown in Fig. 4. The dark gray areas in Fig. 5 represent the turbulent flow regions caused by the wakes, i.e., turbulent strips. Their period corresponds to the wake-passing period τ. Measurements show that these strips are nearly two-dimensional and travel at an average velocity equal to about 0.7 U_∞, which is slower than the wake. The velocities of the leading and trailing edges of these strips are presented in Table 1, together with data previously gathered on turbulent spots. Their growth rate is given by (U_{le} -U_{te}). Hence, turbulent strips and spots propagate and grow at about the same rate. Furthermore, as shown by Orth (1991), the rate is independent of whether or not the flow is accelerating or decelerating. This latter observation confirms the assumption made by Chen and Thyson (1971) in their transition model. Since turbulent strips and spots simply convect with the flow, it is always possible to represent their boundaries by straight lines in

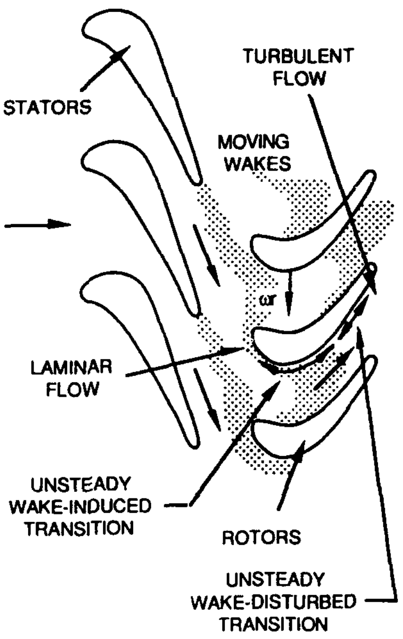
STATORS
TURBULENT FLOW
MOVING WAKES
U
ωr
LAMINAR FLOW
UNSTEADY WAKE-INDUCED TRANSITION
ROTORS
UNSTEADY WAKE-DISTURBED TRANSITION

Figure 1. Unsteady flow in a turbine passage with multimode transition.

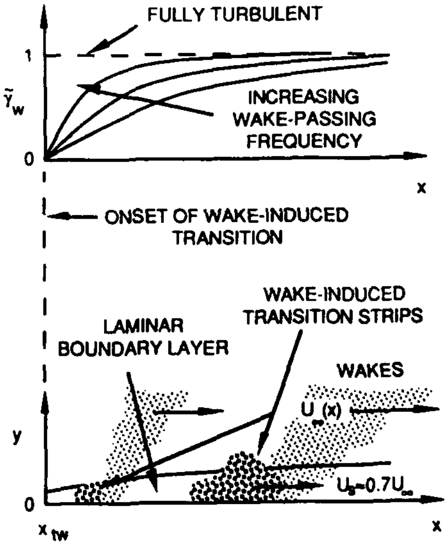

Figure 2. Wake-induced transition on a surface and time-averaged intermittency.

---

[1] N. Cumpsty, 1992, private communication.

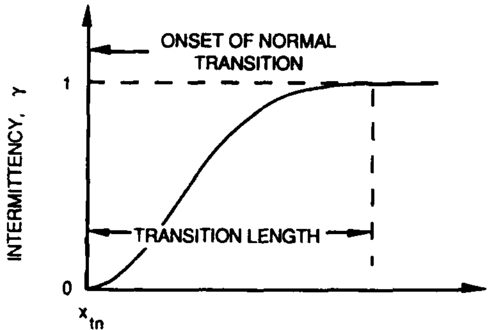

Figure 3. Intermittency distributions for a normal transition in steady flow.

an x-t plot, even if the free-stream velocity varies. This may be done by using a transformed streamwise coordinate $x = U_\infty \int dx'/U(x')$. Figure 5 has been drawn with this in mind.

Table 1

Reference	Type	U_{le}/U_∞	U_{te}/U_∞
Orth (dp/dx = 0, > 0, and <0)	Strips	0.88	0.5
Schubauer & Klebanoff (dp/dx=0)	Spots	0.88	0.5
Wynanski et al. (dp/dx=0)	Spots	0.89	0.5

The white areas in the figure represent the laminar portions of the flow on the surface. They have been separated into two regions, however, in order to distinguish the laminar becalmed flow from the remaining laminar flow. The line separating these regions represents the trailing edge of the becalmed flow. Schubauer and Klebanoff measured a trailing edge velocity equal to the Tollmien-Schlichting wave speed. In their case, the speed was $0.29U_\infty$. Orth's data indicates a similar situation exists for turbulent strips. From his data, the trailing edge velocity of the becalmed flow is estimated to lie between $0.30U_\infty$ and $0.38U_\infty$. The latter value nearly corresponds to the Tollmien-Schlichting wave speed for the critical Reynolds number of instability, while the former nearly corresponds to that found by Schubauer and Klebanoff. These facts strongly suggest that the size of the becalmed region is connected to the Tollmien-Schlichting wave speed. If true, then the trailing edge velocity of the becalmed flow will vary slightly with streamwise distance as the boundary layer grows, however, there are not enough data available to prove it. Neglecting this variation and using the average of the above values, the trailing edge velocity of the becalmed flow will be about $0.34U_\infty$. From this and the values given previously for the turbulent strip velocities, it is easy to calculate that the ratio between the residence time of the becalmed flow over a point on the surface and the residence time of the turbulent strip itself is about unity.

The light gray areas in Fig. 5 represent the transitional flow occurring between the turbulent strips and becalmed flow. It should be shaded light to dark from left to right indicating the laminar-to-turbulent transition as shown in Fig. 3. This may be either a natural, bypass, or separated-flow transition. Since the turbulent spots which cause this transition are produced only at x_{tn} and only after the becalmed flow has passed, transition can only occur within the skewed triangular portion shown. The interval of time, τ_n, during which spots can be produced is easily determined from geometry to be

$$\frac{\tau_n}{\tau} = 1 - \frac{\tau_w}{\tau} - \frac{(x_{tn}-x_{tw})}{\tau}\left(\frac{1}{(U_{te})_b} - \frac{1}{U_{le}}\right); \quad (x_{tn} \geq x_{tw}) \qquad (1)$$

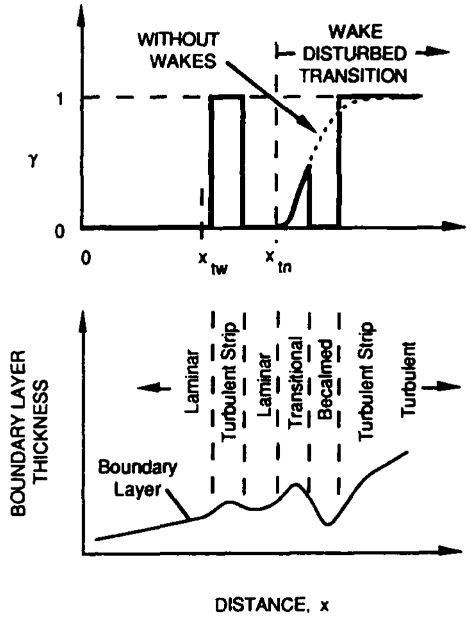

Figure 4. An instantaneous view of a multimode transitional flow.

where τ_w is the interval of time during which turbulent strips are produced by the wake at x_{tw}, and $(U_{te})_b$ is the trailing edge velocity of the becalmed region. Using $(U_{te})_b \approx 0.34U_\infty$ and $Ule = 0.88U_\infty$, this expression becomes

$$\tau_n = \tau - \tau_w - 1.80(x_{tn} - x_{tw})/U_\infty \qquad (2)$$

The maximum distance downstream at which transition by any other mode can begin is, therefore, $x_{tn\,max} = x_{tw} + 0.55(\tau - \tau_w)U_\infty$. Introducing the wake-passing Strouhal number, $S = \omega c/U_\infty$, where ω is the wake-passing frequency, this condition may be rewritten as

$$\frac{\Delta x_{tn\,max}}{c} = \frac{x_{tn\,max} - x_{tw}}{c} = 0.55\left(\frac{2\pi}{S} - \frac{U_\infty \tau_w}{c}\right) \qquad (3)$$

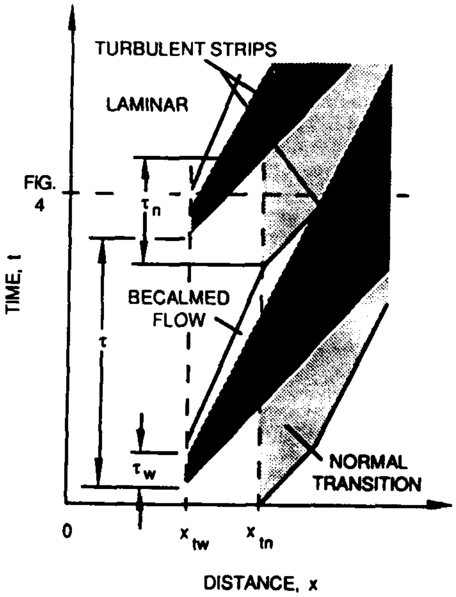

Figure 5. Multimode transition in the x-t plane.

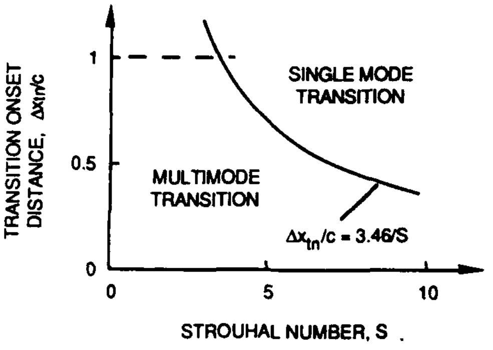

Figure 6. Topology diagram for single and multimode transition, $\tau_{tw} = 0$.

This relation is plotted in Fig. 6 for $\tau_w = 0$. If the distance between the onset of transition for an undisturbed incident flow and wake-induced transition is greater than this, then transition cannot occur between the strips, and only wake-induced transition will occur. For $\Delta x_{tn} < \Delta x_{tn\ max}$, however, a multimode transition will occur. The problem now is to determine the time-averaged intermittency for multimode transition.

A Multimode-Transition Intermittency Model

The time-averaged[2] intermittency $\tilde{\gamma}_w$ for wake-induced transition was obtained by Mayle and Dullenkopf (1989) and is given by

$$\tilde{\gamma}_w(x) = 1 - \exp\left[-4a\tan\alpha\left(\frac{\tau_w}{\tau}\right)\left(\frac{x - x_{tw}}{U_s}\right)\right]; \quad (x \geq x_{tw}) \qquad (4)$$

where "a" is the production rate of turbulent strips, α is one-half of their growth angle in the x-t plane ($\alpha \approx 7.4°$), and U_s is their average propagation velocity ($U_s \approx 0.7U_\infty$). A sketch of this expression showing the effect of increasing wake-passing frequencies (decreasing τ) was given in the upper portion of Fig. 2. To obtain eq. (4), Mayle and Dullenkopf assumed that the wakes turned the production of turbulent strips on and off as they passed over the location x_{tw}. Their assumed production rate distribution is shown in Fig. 7. Later (1990), for typical gas turbine flows, they found eq. (4) could be replaced by a much simpler expression, viz.,

$$\tilde{\gamma}_w(x) = 1 - \exp\left[-1.9\left(\frac{x - x_{tw}}{U_\infty \tau}\right)\right]; \quad (x \geq x_{tw}) \qquad (5)$$

A plot of this expression and its comparison to some experimental results are provided in Fig. 8. The agreement is seen to be excellent even though, as it turns out, the value of $a\tau_w$ is much larger than that for which eq.(4) was derived.

An expression for the time-averaged intermittency for either natural or by-pass transition, assuming all turbulent spots are randomly produced at x_{tn} was given by Dhawan and Narasimha (1958), viz.,

$$\tilde{\gamma}_n(x) = 1 - \exp\left[-\left(\frac{n\sigma}{U_\infty}\right)(x - x_{tn})^2\right]; \quad (x \geq x_{tn}) \qquad (6)$$

In this expression, n is the turbulent spot production rate per unit distance in the spanwise direction and σ is Emmons' dimensionless spot propagation parameter[3] which depends on the shape and velocity of the spot. A sketch of this expression was given in Fig. 3. Comparisons of eq. (6) to experimental results may be found in the original paper by Dhawan and Narasimha, among many others (see Mayle's 1991 review). The agreement is found to be excellent.

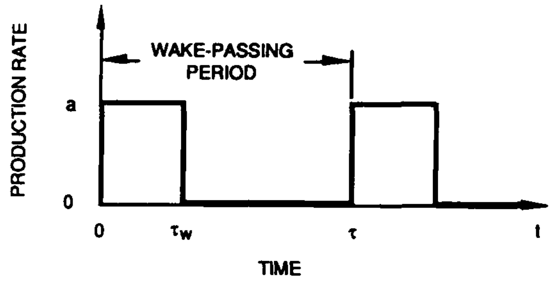

Figure 7. Wake-induced production function for turbulent strips.

The multimode model proposed by Mayle and Dullenkopf uses eq. (5) for the wake-induced intermittency and eq. (6) for the wake-disturbed intermittency, together with a superposition model which provides the fraction of time the flow is turbulent when both transition processes occur simultaneously, viz.,

$$\tilde{\gamma}(x) = 1 - (1 - \tilde{\gamma}_n)(1 - \tilde{\gamma}_w) \qquad (7)$$

The present theory attempts to correct their result by modifying eq. (6) to account for the periodic passing of the turbulent strips and their becalmed regions of flow.

Since turbulent spots cannot be produced at x_{tn} when either a turbulent strip or its attendant becalmed flow is directly above, it is assumed that the production of turbulent spots at x_{tn} will be as shown in Fig. 9. This production function may be substituted directly into Emmons' general intermittency expression and time-averaged similar to that done by Mayle and Dullenkopf (see Appendix, 1989) to obtain the time-averaged intermittency distribution for wake-induced transition. Although the analysis is not simple, it can be shown that for small values of $n\sigma U_\infty \tau^2$ the solution is

$$\tilde{\gamma}_n(x) = 1 - \exp\left[-\left(\frac{n\sigma}{U_\infty}\right)\left(\frac{\tau_n}{\tau}\right)(x - x_{tn})^2\right]; \quad (x \geq x_{tn}) \qquad (8)$$

The restriction on $n\sigma U_\infty \tau^2$ implies that the dimensionless production rate $n\sigma v^2/U_\infty^3$ for typical mid-sized gas turbines should be less than $(10)^{-9}$. This implies that the free-stream turbulence level should be less than eight percent (see Mayle, Fig. 9, 1991). Since this restriction is quite reasonable for gas turbine flows, it would appear that eq. (8) will provide a good approximation for the time-averaged intermittency distribution in the wake-disturbed transition regime on a turbine airfoil.

With this, the present method for predicting the time-averaged intermittency in multimode transitional flows is to use eqs. (7),

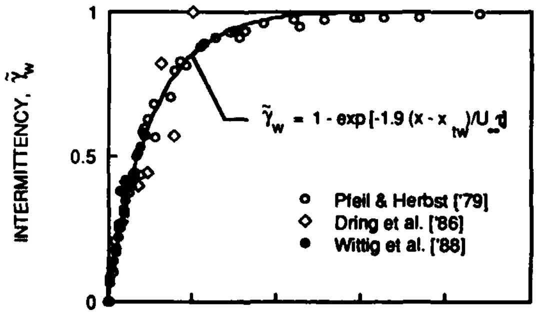

Figure 8. A comparison of wake-induced transition theory with experiment.

---

[2] Averaged over one wake-passing period

[3] See Emmons (1951)

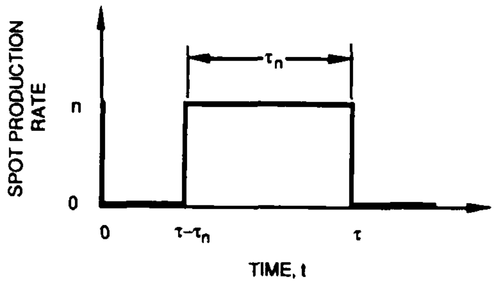

Figure 9. Production function for turbulent spots when disturbed by wakes.

(5) and (8), with τ_n obtained from eq. (2). The quantities $n\sigma$, x_{tw}, and x_{tn} may be obtained from correlations presented by Mayle (1991). A simple, but good, method for obtaining the Nusselt number distribution (or the distribution of any boundary layer quantity) is to use Emmons' superposition model, viz.,

$$Nu(x) = (1 - \bar{\gamma})\, Nu_L(x) + \bar{\gamma}\, Nu_T(x) \qquad (9)$$

where Nu_L and Nu_T are the Nusselt numbers for fully-laminar and fully-turbulent flow on the surface. When using this expression, however, and as shown by Dhawan and Narasimha, the fully-turbulent boundary layer must be considered to start from the onset of transition. For other boundary layer quantities, such as the energy thickness, one substitutes the corresponding quantities for Nu, Nu_L, and Nu_T into eq. (9).

A Comparison of the Theory with Data

The only data available with which this theory can be compared are the heat transfer measurements presented by Dullenkopf, et al. (1991). The measurements were obtained on an airfoil in a full-scale, stationary cascade, with an unsteady wake generator of rotating bars placed upstream. The apparatus and experimental technique have been completely described by Wittig et al. (1988) where some preliminary results were given. All of the results may be found in Dullenkopfs dissertation. Measurements without bars were also obtained both with and without an upstream turbulence grid. For the data shown below, the inlet flow velocity was 80 m/s and the angular velocity of the rotating bars was 262 radians/s. The different wake-passing frequencies were obtained by rotating a different number of bars. The airfoil chord was 82 mm.

For each test, the time-averaged intermittency data was evaluated using the measured Nusselt numbers and eq. (9), viz.,

$$\bar{\gamma}(x) = \frac{Nu(x) - Nu_L(x)}{Nu(x)_T - Nu_L(x)}$$

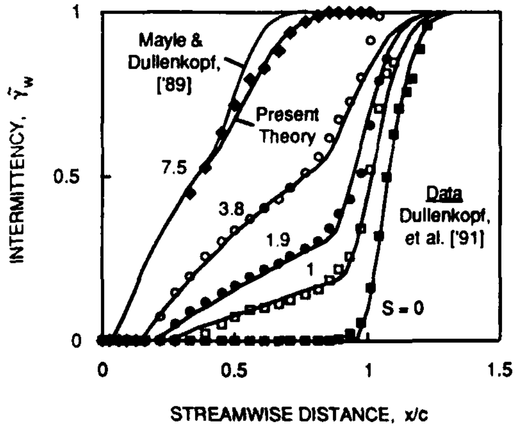

Figure 10. Comparison of multimode transition theory with data.

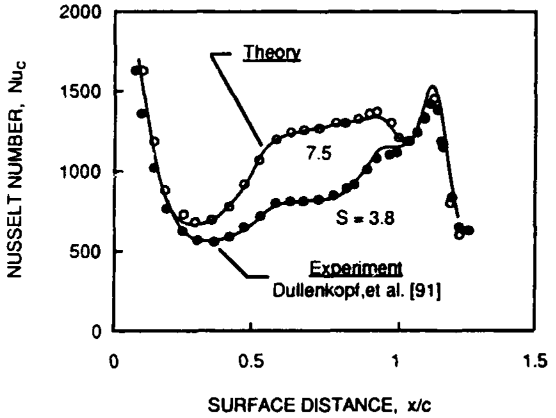

Figure 11. Airfoil heat transfer data and predictions.

and compared to the theory calculated as explained above. The values of Nu_T and Nu_L were obtained from the data taken without bars and with the turbulence grid in and out, respectively. The values of x_{tw} were obtained by a best fit to the wake-induced portion of the data, while the x_{tn} values were obtained by a best fit to the wake-disturbed portion. The latter values correspond closely to those which would be predicted using the free-stream turbulence of the incident flow between the wakes and the correlations presented by Mayle (Figs. 10 and 15, 1991). While similar correlations do not exist for x_{tw}, all the values obtained by fitting the data were found to lie near the minimum pressure region on the airfoil. This corresponds to Mayle's rule of thumb (see discussion on pp. 522 and 523, 1991). The value of $n\sigma$ was obtained by fitting the transition data obtained on the airfoil for a steady incident flow, undisturbed by wakes, and with no grid.

The results for the suction side of the airfoil are shown in Fig. 10. (See Dullenkopf and Mayle, 1992, for a discussion on the effect of the wakes on the pressure side of the airfoil.) In this figure, the wake-passing Strouhal numbers are based on the inlet velocity. A typical Strouhal number for a mid-sized gas turbine is about four. Each data set represents an average of four to five test runs with a scatter of less than five percent. The theoretical values of the time-averaged intermittency were calculated from eqs. (5), (7), (8) and (2), with $\tau_w = 0$. The agreement between data and theory is excellent, even for the highest Strouhal number where the effect of the turbulent strips and becalmed flow on the downstream transition is the largest. For this case, the intermittency calculated using the original Mayle-Dullenkopf multimode model is also shown and predicts a shorter transition to fully turbulent flow. The difference between these two predictions is the result of taking into account the becalmed flow. The differences for the lower Strouhal numbers are much smaller and are not shown for clarity.

The results shown in Fig. 10 for the two highest Strouhal numbers are presented as Nusselt number distributions in Fig. 11. The data is that measured directly, while the theoretical values were calculated using eqs. (5), (7), (8), (2) and (9). The agreement is excellent.

Some Calculations

While the above comparisons provide a typical example of multimode transition, the effects of onset location and wake Strouhal number on the overall behavior are not so obvious. These effects are shown in Figs. 12 and 13 where calculated time-averaged intermittency distributions are plotted against the streamwise distance measured from the onset of wake-induced transition. In each of these figures, $\bar{\gamma}$ has been calculated using eqs. (2), (5), (7) and (8) with $\tau_w = 0$ and $n\sigma c^2/U_\infty = 1$.

The effect of distance between the onset of wake-induced transition and the onset of wake-disturbed transition is shown in Fig. 12 where $\Delta x_{tn}/c = (x_{tn} - x_{tw})/c$. In general, the position where each curve leaves the wake-induced transition curve divides the

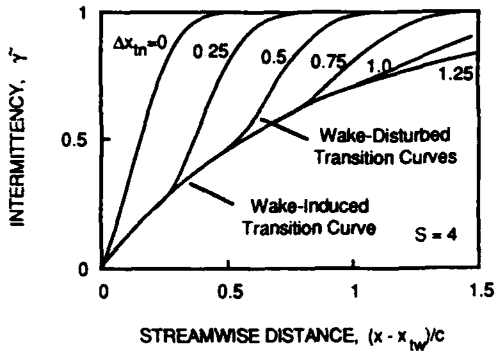

Figure 12. Effect of transition onset distance on the time-averaged intermittency for multimode transition.

flow into two regimes. Upstream of this position, the flow is dominated by the wake-induced transition process, while downstream it is dominated by the wake-disturbed process. In Fig. 12, it is obvious that as the distance between the two transition onset locations increases, more of the flow over the surface is dominated by the wake-induced transition process. Not so obvious is the effect of the becalmed flow. This effect may be seen by comparing the length of the wake-disturbed transition region for different values of $\Delta x_{tn}/c$. For larger $\Delta x_{tn}/c$, the effect of the becalmed flow is to decrease the time during which turbulent spots can be produced, therefore delaying transition to fully turbulent flow.

The effect of Strouhal number on multimode transition is shown in Figs. 13a and b where calculations for Strouhal numbers S = 2, 4 and 8 are presented. Here the effect of the becalmed flow is more obvious. As the Strouhal number increases, the time during which turbulent spots can be produced between the strips decreases, again delaying transition to fully turbulent flow. As pointed out earlier, and as shown in Fig. 6, it is possible for large values of either S or $\Delta x_{tn}/c$ that no transition will occur between the turbulent strips. The condition for this to occur is given by eq. (3).

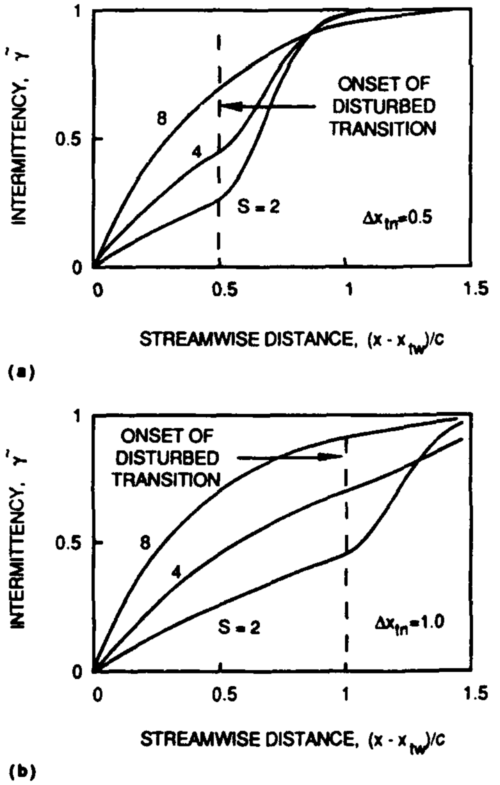

Figure 13. Effect of wake Strouhal number on multimode transition; (a) Δx_{tn} = 0.5, (b) Δx_{tn} = 1.0.

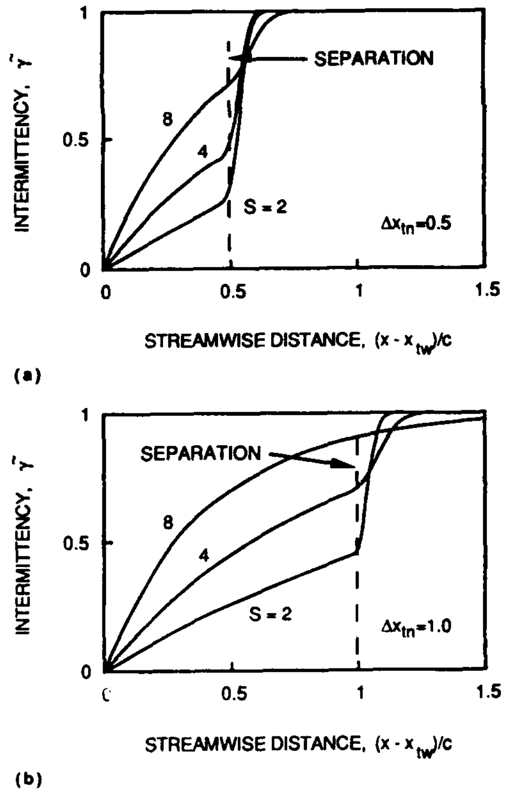

Figure 14. Effect of wake Strouhal number on multimode transition with separated-flow transition; (a) Δx_{tn} = 0.5, (b) Δx_{tn} = 1.0.

Since the behavior for large values of S and $\Delta x_{tn}/c$ is similar to that observed by Dong and Cumpsty, a calculation was performed using a simple model for separated-flow transition. The model, although strictly hypothetical, is based on the separated-flow transition model presented by Mayle (1991) which presumes a similarity between separated-flow and attached-flow transition. The implication is that separated-flow transition may be treated as a short attached-flow transition when calculating the intermittency distribution. Arbitrarily assuming $n\sigma c^2/U_\infty$ = 0.1, which provides a short transition length, time-averaged intermittency distributions were calculated using eqs. (2), (5), (7) and (8). The results of these calculations are shown in Figs. 14a and b for several "separated-flow" multimode transition situations where "separation" was assumed to occur at Δx_{tn}. The trend, which clearly shows a delay in transition to the fully turbulent state, may explain the observations of Dong and Cumpsty. Again, the effect is caused by the periodic passing of the wake-induced turbulent strips and becalmed flow. In this case, however, it is physically attributed to the fact that neither separation nor transition can occur when the strips and the becalmed flow pass over the separation point.

Conclusions

A model for multimode transition which correctly predicts experimental results for high as well as for low wake-passing frequency was developed by accounting for the effects of the becalmed flow following the wake-induced turbulent strips. The model also predicts that transition to the fully turbulent state will be delayed by the unsteady effect of passing wakes. This effect, which has been observed experimentally, depends on both the wake-passing Strouhal number and the distance between the onset of wake-induced transition and the onset of wake-disturbed transition. For larger values of both, it was shown that multimode transition cannot occur. A criterion for this situation was also provided.

References

Ashworth, D.A., LaGraff, J.E., Schultz, D.L., and Grindrod, K.J., 1985, "Unsteady Aerodynamic and Heat Transfer Processes in a Transonic Turbine Stage," J. Engng. for Gas Turbines and Power, 107, pp. 1022-1030.

Chen, K.K., and Thyson, N.A., 1971, "Extension of Emmons' Spot Theory to Flows on Blunt Bodies," AIAA Journal, 9, pp. 821-825.

Dhawan, S., and Narasimha, R., 1958, "Some Properties of Boundary Layer Flow during Transition from Laminar to Turbulent Motion," J. Fluid Mech., 3, pp. 418-436.

Dong, Y., and Cumpsty, N.A., 1989a, "Compressor Blade Boundary Layers: Part 1 - Test Facility and Measurements with No Incident Wakes," ASME Paper 89-GT-50.

Dong, Y., and Cumpsty, N.A., 1989b, "Compressor Blade Boundary Layers: Part 2 - Measurements with Incident Wakes," ASME Paper 89-GT-51.

Doorly, D.J., and Oldfield, M.L.G., 1985a, "Simulation of the Effects of Shock Wave Passing on a Turbine Rotor Blade," J. Engng. for Gas Turbines and Power, 107, pp. 998-1006.

Doorly, D.J., and Oldfield, M.L.G., 1985b, "Simulation of Wake Passing in a Stationary Turbine Rotor Cascade," J. Propulsion and Power, 1, pp. 316-318.

Doorly, D.J., Oldfield, M.L.G., and Scrivener, C.T.J., 1985c, "Wake-Passing in a Turbine Rotor Cascade," Heat Transfer and Cooling in Gas Turbines, AGARD-CP-390, pp. 7-1 to 7-18.

Dring, R.P., Blair, M.F., Joslyn, H.D., Power, G.D., and Verdon, J.M., 1986, "The Effects of Inlet Turbulence and Rotor/Stator Interactions on the Aerodynamics and Heat Transfer of a Large-Scale Rotating Turbine Model," NASA CR 4079.

Dullenkopf, K., Schulz, A., and Wittig, S., 1991, "The Effect of Incident Wake Conditions on the Mean Heat Transfer on an Airfoil," J. Turbomachinery, 113, pp. 412-418.

Dullenkopf, K., and Mayle, R.E., 1992, "The Effects of Incident Turbulence and Moving Wakes on Laminar Heat Transfer in Gas Turbines," ASME Paper No. 92-GT-377.

Dullenkopf, K., 1992, "Untersuchungen zum Einfluß periodisch instationärer Nachlaufströmungen auf den Wärmeübergang konvektiv gekühlter Gasturbinenschaufeln," Dr.-Ing. Dissertation, Universität Karlsruhe, Karlsruhe.

Dunn, M.G., George, W.K., Rae, W.J., Woodward, S.H., Moller, J.C., and Seymour, P.J., 1986, "Heat-Flux Measurements for the Rotor of a Full-Stage Turbine: Part II - Description of Analysis Technique and Typical Time-Resolved Measurements," J. Turbomachinery, Vol. 108, 1, pp. 98-107.

Emmons, H.W., 1951, "The Laminar-Turbulent Transition in a Boundary Layer - Part I," J. Aero. Sci., Vol. 18, pp. 490-498.

Herbst, R., 1980, "Entwicklung von Grenzschichten bei instationärer Zuströmung," Dr.-Ing. Dissertation, Technische Hochschule Darmstadt, Darmstadt.

Hodson, H.P., 1984, "Boundary Layer and Loss Measurements on the Rotor of an Axial-Flow Turbine," J. Engng. for Gas Turbines and Power, Vol. 106, pp. 391-399.

LaGraff, J.E., Ashworth, D.A., and Schultz, D.L., 1989, "Measurement and Modeling of the Gas Turbine Blade Transition Process as Disturbed by Wakes," J. Turbomachinery, 111, pp. 315-322.

Liu, X., and Rodi, W., 1989, "Measurements of Unsteady Flow Over and Heat Transfer from a Flat Plate," ASME-Paper 89-GT-2.

Mayle, R.E., 1991, "The Role of Laminar-Turbulent Transition in Gas Turbine Engines," 1991 ASME International Gas Turbine Institute Scholar Award Paper, J. Turbomachinery, 113, pp. 509-537.

Mayle, R.E. and Dullenkopf, K., 1989, "A Theory for Wake-Induced Transition," J. Turbomachinery, 112, pp. 188-195.

Mayle, R.E. and Dullenkopf, K., 1990, "More on the Turbulent-Strip Theory for Wake-Induced Transition," ASME Paper 90-GT-137.

Orth, U., 1991, "Untersuchung des Umschlagvorganges von Platten- und Zylindergrenzschichten bei ungestörter und stationär oder periodisch gestörter Zuströmung," Dr.-Ing. Dissertation, Technische Hochschule Darmstadt, Darmstadt.

Pfeil, H., and Herbst, R., 1979, "Transition Procedure of Instationary Boundary Layers," ASME-Paper No. 79-GT-128.

Pfeil, H., Herbst, R., and Schröder, T., 1983, "Investigation of the Laminar-Turbulent Transition of Boundary Layers Disturbed by Wakes," J. Engng. for Power, 105, pp. 130-137.

Schröder, T., 1985, "Entwicklung des instationären Nachlaufs hinter quer zur Strömungsrichtung bewegten Zylindern und dessen Einfluß auf das Umschlagverhalten von ebenen Grenzschichten stromabwärts angeordneter Versuchskörper," Dr.-Ing. Dissertation, Technische Hochschule Darmstadt, Darmstadt.

Schröder, T., 1989, "Measurements with Hot-Film Probes and Surface-Mounted Hot-Film Gauges in a Multistage Low-Pressure Turbine," 1989 European Propulsion Forum, Bath, UK, 15, pp.1-27.

Schröder, T., 1990, oral presentation, 1990 Turbo Expo Congress, Brussels.

Schubauer, G.B., and Klebanoff, P.S., 1955, "Contributions on the Mechanics of the Boundary-Layer Transition," NACA TN 3489.

Wittig, S., Schulz, A., Dullenkopf, K., and Fairbank, J., 1988, "Effects of Free-Stream Turbulence and Wake Characteristics on the Heat Transfer Along a Cooled Gas Turbine Blade," ASME Paper 88-GT-179.

Wygnanski, I., Sokolov, M., and Friedman, D., 1976, "On a Turbulent Spot in a Laminar Boundary Layer," J. Fluid Mech., 78, 4, pp. 785-819.

HEAT TRANSFER AND AERODYNAMICS OF A 3D DESIGN NOZZLE GUIDE VANE TESTED IN THE PYESTOCK ISENTROPIC LIGHT PISTON FACILITY

Mr. K.S. Chana
Defence Research Agency
Aerodynamics & Propulsion Department
Pyestock, Farnborough,
Hampshire. GU14 0LS
United Kingdom.

ABSTRACT

In HP turbines, predictions of the heat transfer to the blade and endwalls is particularly important for an accurate assessment of turbine component life. On the endwalls, there are often complex 3D (secondary) flows present which make predictions of heat transfer particularly difficult.

A detailed investigation of this area has been carried out on a fully annular cascade of highly 3D nozzle guide vanes. Measurements were made on the vane and endwalls to determine heat transfer and aerodynamic characteristics. Testing was conducted in a short duration Isentropic Light Piston test facility, at engine representative Reynolds number, Mach number and gas-to-wall temperature ratio. Interpreted test data are compared with computations obtained at test conditions.

1. INTRODUCTION

In order to increase thrust-to-weight ratio and achieve maximum cycle efficiencies with gas turbine engines it is necessary to raise the cycle temperatures to the maximum, within the constraints of structural integrity. Thus the need to understand in detail and predict accurately the heat transfer distributions for high pressure turbines becomes an important factor. The presence of complex highly three-dimensional secondary flows within the turbine passage makes the turbine designer's task very difficult.

Several different investigations of nozzle guide vane (NGV) aerofoil and endwall heat transfer behaviour have been reported in the literature. The work of York et al (1983), Gladden et al, (1988) and Boyle et al (1989), concentrated on two-dimensional cascade measurements, and although general features of the flow were modelled radial pressure gradients were not. Granziani et al (1979), and Gaugler and Russell (1983), correlated detailed heat transfer measurements with secondary flow patterns. This work was not representative of engine operating conditions in terms of Reynolds number, Mach number and gas-to-wall temperature ratio. More recent work by Harasgama et al, (1990), and Harvey et al, (1990), have shown detailed information on the pattern of heat transfer within a NGV passage. However, these NGV designs incorporated relatively few three-dimensional features.

A highly three-dimensional nozzle guide vane has been designed and tested at DRA Pyestock. The prime objective was to produce a challenging three-dimensional design which would act as a stimulus for aerodynamic and thermodynamic research. Fully three-dimensional flow calculation methods were employed in the design of the variable-lean nozzle guide vane. Figure 1 shows the details of the vane and the computational grid used.

The purpose of this paper is to describe heat flux and pressure measurements obtained from a set of NGV's using the Isentropic Light Piston Facility (ILPF) a short duration heat transfer tunnel. The NGV annular ring was tested over a range of Reynolds number, Mach number and gas-to-wall temperature ratios, representative of engine conditions. The detailed measurements are compared with theoretical flow and heat transfer predictions.

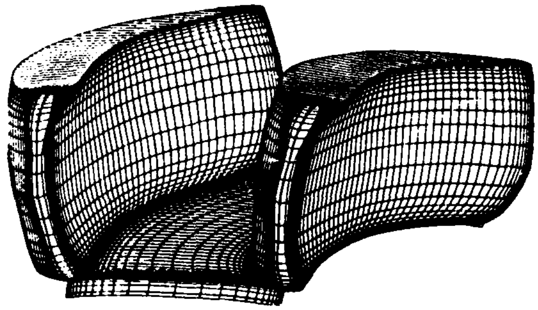

Figure 1. HTDU 4X vane and computational grid

2 DESIGN DETAILS

2.1 Duty

The aerodynamic design of the high pressure turbine was targeted for a future engine of advanced military duty. The turbine has been designated the High Temperature Demonstrator Unit (HTDU) 4X. It has the following overall design parameters.

Stator outlet temperature (SOT)	2066.1K
Specific work capacity (CpΔT/T)	179.6 J/Kg K
Stage loading factor $\Delta H/U^2$	2.002
Stage pressure ratio	2.416
Flow function Va/U^2	0.625
NGV flow function $w\sqrt{T}/P$	1.06×10^{-3} Kg√K m^2/SN

Mean rotor hub/tip ratio	0.87
Number of NGVs	27
Number of rotor blades	56

2.2 Overall Design Objectives

The HTDU 4X NGV was designed to take account of three-dimensional aerodynamic effects. Full three-dimensional inviscid time marching flow calculation methods such as those developed by Denton (1982), provide the scope for a better understanding of the aerodynamics in complex three-dimensional blade passages. Such tools have been used to design the HTDU 4X blading in order to control the flow in a particular manner and hence achieve high efficiency. The design criteria set for HTDU 4X were:-

i Maximise space/chord ratios without penalising aerodynamic performance by controlling the aerodynamic lift across the span of the blade.

ii Control of secondary flows and deleterious pressure gradients within the blading to achieve lower losses.

Item (i) should result in significant advantage in terms of reduced aerofoil numbers, lower weight and reduced cooling flow and therefore be of direct benefit to military engines operating at high SOT. In the case of (ii) there is a significant amount of research (Horton et al, 1991), which demonstrates that endwall profiling can be very effective in reducing endwall secondary flows, and the strength of the passage vortices which contribute significantly to the overall turbine losses. An undesirable migration of endwall boundary layer flows on to the aerofoil can be controlled by correct optimisation of the three-dimensional geometry. The inclusion of such features should facilitate achievement of high target efficiencies.

Although designed with the Denton code this paper presents comparisons of experimental data with predictions from the three-dimensional Dawes Navier-Stokes code (Dawes, 1986).

2.3 HTDU 4X NGV Design Details

The following design concepts were applied:-

i Spanwise control of aerodynamic lift.

ii Variable-lean of the NGV trailing edge.

iii Control of aerofoil pressure surface diffusion.

The principle of spanwise graduation of aerodynamic lift to maximise space/chord ratio without penalising aerodynamic performance is achieved by the variation in loading from hub to tip. The tip is forward loaded and the hub rearward. In the hub regions, where exit Mach numbers are highest aerodynamic lift is deliberately restrained to moderate levels. In the centre and outer span regions, where exit and peak surface Mach number levels are lower, higher levels of loading can be tolerated. This provides the potential for increasing aerodynamic lift but at the expense of some risk of boundary layer thickening or separation on the back surface, with accompanying increase in profile loss. The diffusion on the back surface must be controlled to avoid this happening.

Variable-lean is applied to the NGV through compound tangential and axial lean on the trailing edge. The purpose of this three-dimensional geometry is to control (i) secondary flows in the passage, (ii) the aerodynamic loading on aerofoil sections close to the endwalls, (iii) the migration of boundary layers on the aerofoil surfaces.

Control of aerofoil pressure surface diffusion involves the concept of designing the aerofoil pressure surfaces for minimum forward pressure surface diffusion adjacent to endwalls. This principle has been applied successfully to previous research turbines. The method involves thickening up the forward pressure surface of the aerofoil close to the endwalls so that velocities are increased in this region.

There is no doubt that the HTDU 4X NGV is an adventurous design in that it embodies to an extreme degree design concepts which are believed to be sound in principle but have yet to be clearly demonstrated. The present tests have enabled some of these concepts to be assessed.

3 EXPERIMENTAL FACILITY

The tests were performed in the DRA Pyestock ILPF. This is a short duration transient rig, designed to allow high quality heat transfer and aerodynamic measurements to be taken for a full-size annular cascade of turbine vanes. The use of this technique for turbomachinery measurements was pioneered by Schultz et al, (1973), The Pyestock facility is described by Brooks et al, (1985). A schematic view of the ILPF is shown in Figure 2.

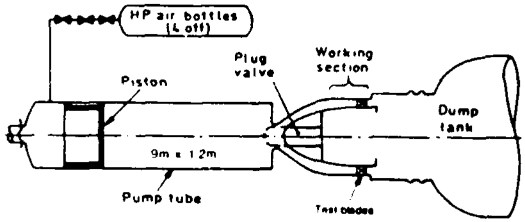

Figure 2. The Isentropic Light Piston Facility

A light free piston is forced along a tube by high pressure air. The action of the piston compresses and thereby heats the air ahead of it. When a predetermined level of pressure is reached a fast acting valve opens allowing the heated air to flow through the working section and into a dump tank. This gives steady state operating conditions for the duration of the run, which can be varied from about 0.5 to 1.0 sec depending on the rise in air temperature required. The test conditions can be matched to engine values of both Reynolds number and Mach number. Engine values of gas-to-wall temperature ratio are also matched. A major extension of the facility, to enable heat transfer data to be taken from a rotating rotor mounted downstream of the nozzle row, has been designed and manufactured and is currently being commissioned.

For heat transfer measurements the NGVs are manufactured from machinable glass ceramic (Corning Macor)[1] which has a low thermal diffusivity, on which are painted thin film gauges. The rapid change in surface temperature during an ILPF run is converted to heat transfer rate by an electrical analogue circuit which solves the one-dimensional transient heat conduction equation (Oldfield et al, 1984). The output signal is then digitised and recorded on a mini computer. The present tests included thin film gauges at 10%, 20%, 40%, 60%, 80% and 90% spanwise locations with 12 on the suction side and 10 on the pressure side at each spanwise location. There were 82 gauges on the inner wall and 76 gauges on the outer wall. With this level of instrumentation it was possible to obtain an accurate distribution of vane surface and endwall heat transfer. Accuracy of the present heat transfer data is within ±5%. Figure 3 shows vanes instrumented with thin films.

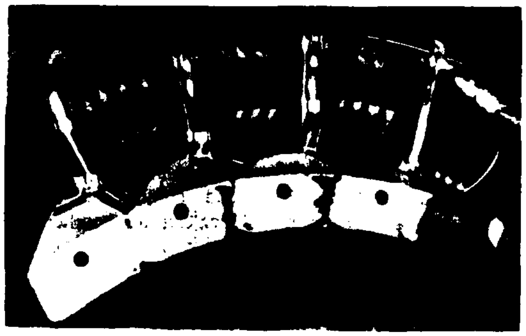

Figure 3. Vanes instrumented with thin films

The distribution of static pressure on the NGVs was measured using surface tappings, and the inlet total pressure was determined using 3 inlet probes, positioned at 120° intervals circumferentially. The pressure signals were recorded using a fast acting Scanivalve[2] ZOC (Zero, Operate, Calibrate) system. The NGVs were fitted with tappings at 5%, 10%, 20%, 40%, 60%, 80%, 90% and 95% span with 14 on the suction side and 11 on the pressure side, at each spanwise location. The inner platform was instrumented with 83 pressure tappings and the outer platform contained 77 pressure tappings. The overall accuracy for the aerodynamic results is such that the isentropic Mach numbers calculated from the measured static pressures are accurate to within ± 0.1% for transonic flow conditions. At low flow velocities the error is significantly larger, representing about 10% at 0.1 Mach number due to the smaller difference between the total and static pressures. All tests were performed with a turbulence grid at 4.5 axial chords upstream of the NGVs, giving an inlet turbulence level of 6.5%. Table 1 shows details of the NGV operating conditions.

4 AERODYNAMIC RESULTS

4.1 Surface Aerodynamics

Mach number distributions at 60% span for three Mach number conditions are shown in Figure 4. The measured Reynolds number has been kept constant for these results. The pressure side aerodynamics are little influenced by changes in exit Mach number. The suction side results are similar for all three conditions during the initial acceleration from the leading edge to approximately 20% axial chord. The below design and design Mach number condition show diffusion once the initial acceleration peak has been reached, whereas the above design condition continues to accelerate further before diffusion takes place at approximately 85% axial chord.

TABLE 1. TEST OPERATING CONDITIONS

	Re.D: M. –	Re.D: M.D	Re.D: M +	Re-: M.D	Re.D: M.D	Re+: M.D
EXIT MACH NUMBER	0.75	0.88	1.10	0.88	0.88	0.88
EXIT REYNOLDS NUMBER	2.96E6	2.96E6	2.96E6	1.48E2	2.96E6	4.44E6
GAS-TO-WALL TEMP. RATIO	1.5	1.5	1.5	1.5	1.5	1.5
INLET TURBULENCE	6.5%	6.5%	6.5%	6.5%	6.5%	6.5%

Measured and predicted Mach number distributions at 60% span at the design condition are shown in Figure 5. As can be seen the Dawes code (Dawes, 1986) does not predict the suction side diffusion very well. Possible reasons for this could be inadequate modelling of the trailing edge geometry, differences between the modelled and true downstream annulus duct and the lack of grid resolution. The grid used for this prediction is 74 axial, 25 radial and 25 tangential points on a sheared H grid. The discrepancies near the leading edge on the pressure side are attributed to experimental error. The total to static pressure differences are small in this region, thus the error in isentropic Mach number becomes more significant. The remainder of the pressure surface is very well modelled.

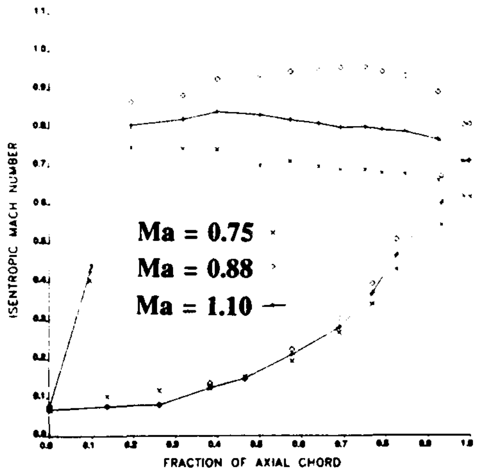

Figure 4. 60% span Mach number variation

Measured and predicted suction side isentropic Mach number distributions for three exit Mach number conditions are shown in Figure 6. Mach numbers at the vane root are higher than the tip, as required by radial equilibrium. The distributions indicate a significant change in aerodynamics as the exit Mach number is increased from the below design condition to design and above design. The predictions show similar features to the experimental results. The initial rapid acceleration is predicted well in all three cases, with some differences towards the tip.

---

[1] Corning Macor Trademark of Corning Macor Glass, Corning, USA

[2] Scanivalve - Trademark of Scanivalve Corp, San Diego, USA

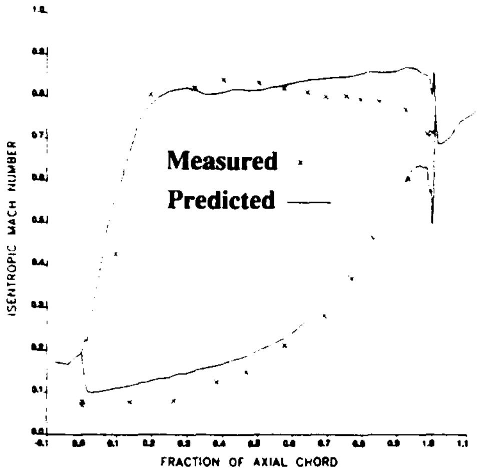

Figure 5. Vane surface Mach number distribution at 60% span.

However, this region has highly 3D geometry and is of particular difficulty for instrumenting static tappings. It is possible that some tappings may not be normal to the local surface. The vanes are manufactured by the use of a computer numerically controlled machine and are then hand finished to achieve a smooth surface particularly at the leading edge, at the junction between endwalls and the vane and at the trailing edge. This final finishing process may have introduced small local differences in these areas.

Discrepancies towards the trailing edge of the vane vary depending on the Mach number condition. For the below design case the prediction compares very well with a few small differences near the trailing edge between 40% and 60% span. As previously discussed, the design and above design conditions show much less agreement with the prediction once the initial acceleration peak is reached. The experimental results show mainly diffusion but the prediction indicates a further acceleration.

The measured pressure side isentropic Mach number for the design condition is shown in Figure 7 together with a prediction. The prediction compares very well with the computed results. This was also true of the below and above design Mach number condition.

Hub and casing Mach number distributions for measured and predicted results are shown in Figure 8a and 8b. The hub Mach numbers exceed those on the casing due to the radial equilibrium criteria. When operating at the high Mach number condition the hub platform shows a trailing edge shock impinging on the suction surface. The comparison between measured and computed results shows very good agreement, for both hub and casing platforms. These results obviously validate the 3D Navier-Stokes code as a fast and relatively accurate method for the aerodynamic design of turbine NGVs. However, the suction side prediction towards the trailing edge could be improved further and warrants more investigation.

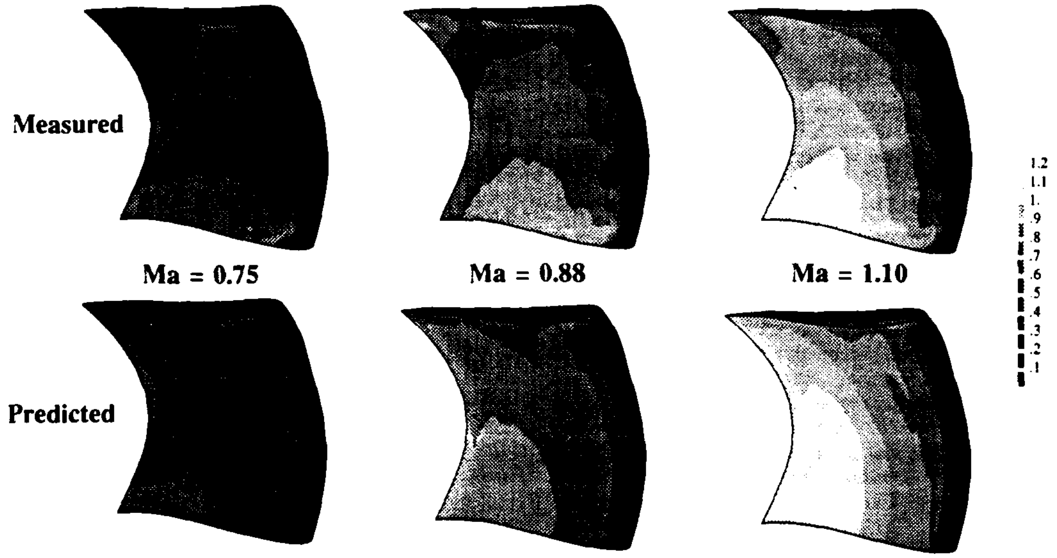

Figure 6. Comparison of measured and predicted suction surface Mach no

4.2 Exit Area Traversing

The total pressure trace obtained from the centre hole of the three hole probe together with a 3D flow (Dawes, 1986) prediction are shown in Figure 9. A small amount of digital smoothing has been applied to the measured data to remove high frequency noise. The application of 3 hole probes in the ILPF has been described by Harasgama and Chana (1990).

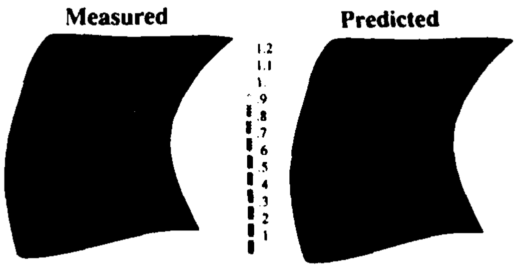

Figure 7. Comparison of measured and predicted pressure surface Mach no

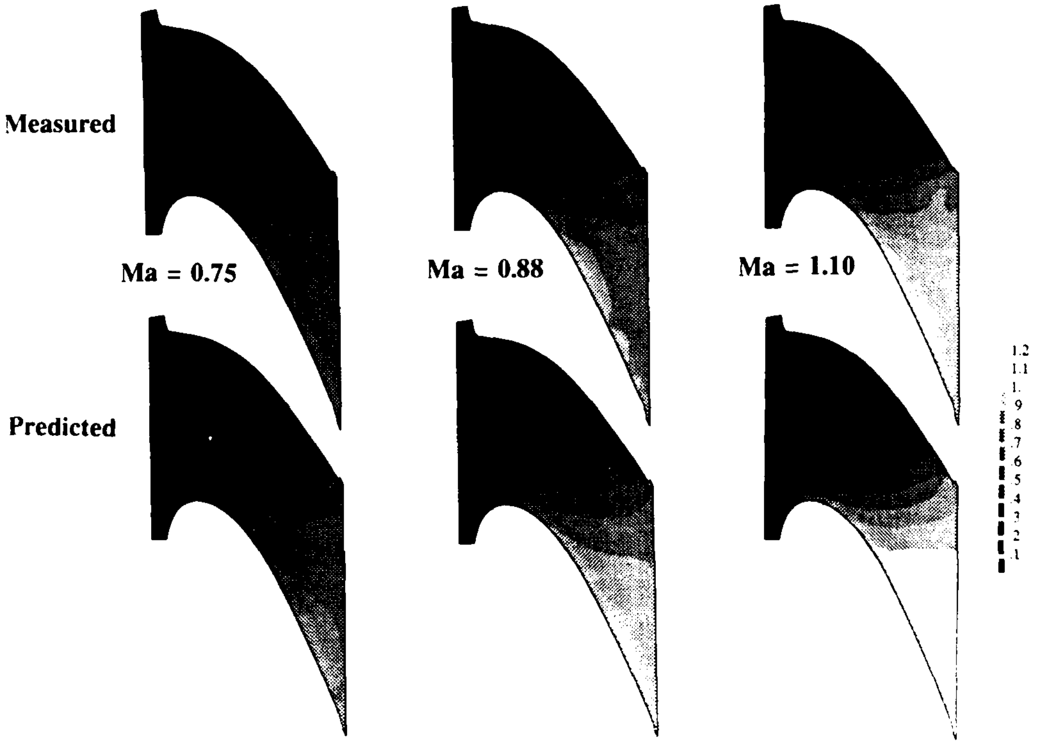

Figure 8a. Measured and predicted hub Mach number distribution

Individual experimental sweeps, after processing, have been combined to form the complete area traverse. The traverse was carried out at approximately 5% axial chord downstream of the trailing edge. The measured profile wakes can be clearly seen, at mid-height the wake is considerably wider than that near the endwalls. The wake is wider due to the trailing edge stacking; the probe tip is thus further from the trailing edge at mid-height than near the root and tip. The measured data also show areas of significant total pressure loss, these correspond to the horse-shoe vortex as seen in Figure 12a. The Navier-Stokes prediction also shows wider wakes at mid-height than near the endwalls and compares very well, although the areas of much larger loss created by the horse-shoe vortex are not predicted at all.

5 HEAT TRANSFER RESULTS

Nusselt number distributions on the vane aerofoil surface at 60% span for 5 running conditions are shown in Figure 10. As can be seen the Nusselt number increases as Reynolds number is increased, on both suction and pressure side. The variation of heat transfer with Mach number is also shown on Figure 10. In this case Nusselt number decreases with increasing Mach number. This is due to the shear stress in the boundary layer decreasing as the flow velocity increases. These results are in agreement with the work of previous authors (Jones et al, 1989).

Contours of Nusselt number overlaid onto a 3D view of the NGV suction side are presented in Figure 11. It can be seen that there is a significant effect of the secondary flow on the heat transfer distributions. The effect is seen to be more pronounced at the tip than the hub. The mid-span Nusselt numbers towards the trailing edge are consistently higher than near the endwalls, for all operating conditions. This is due to endwall boundary layer migration onto the vane suction side resulting from secondary flow in the vane passage. Flow visualisation performed on the endwall and vane surface in the ILPC (Figure 12a and 12b) indicate that the secondary flow is stronger near the casing than at the hub. This effect is well predicted by the Dawes (1986) flow solver as can be seen in Figure 13. The hub secondary flow appears on the suction surface later than the casing and does not migrate along the span to the same extent. The prediction shows this effect but to somewhat lesser extent than indicated by the flow visualisation.

Increasing Reynolds number causes the Nusselt number over the entire vane surface to increase, whilst on the suction surface the reverse occurs for increasing Mach number. The pressure side Nusselt number distributions did not vary significantly with the Mach number changes and there is very little spanwise variation, see Figure 14.

Endwall heat transfer is affected by the inlet boundary layer, vane aerodynamic loading and the geometry of the vane passage. The tests have shown that there are some differences in the inner and outer wall Nusselt numbers both in magnitude and distribution. Figure 15 shows hub Nusselt numbers for all conditions. As the Reynolds number is increased the region of highest heat transfer becomes concentrated at the pressure side trailing edge.

The inlet endwall boundary layer stagnates at the vane leading edge and forms a horseshoe vortex. The two legs of this vortex, on the pressure and suction sides, proceed into the two adjacent passages. The pressure side leg is swept across the endwall by the

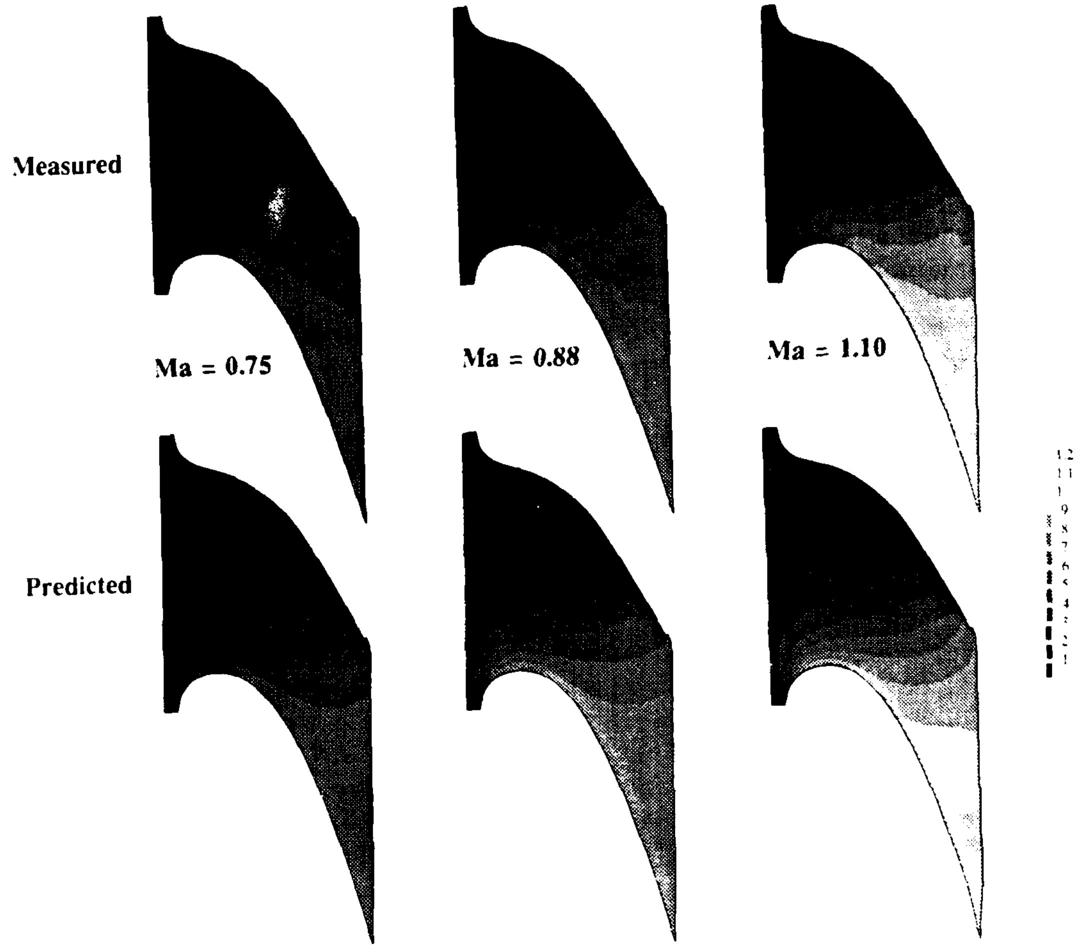

Figure 8b. Measured and predicted casing Mach number distribution

passage secondary vortex to the suction side and then up the vane suction surface. This causes the boundary layer to be stripped off the endwall and convected to the suction side of the passage and then up the suction surface of the vane. A new thin highly skewed boundary layer thus forms behind the separation line, which results in high heat transfer in this region (Chana, 1992). Low values of heat transfer are evident close to the suction side of the passage after approximately 50% axial chord. This is generated by the low energy fluid migrating across from the pressure side trailing edge region. Outer

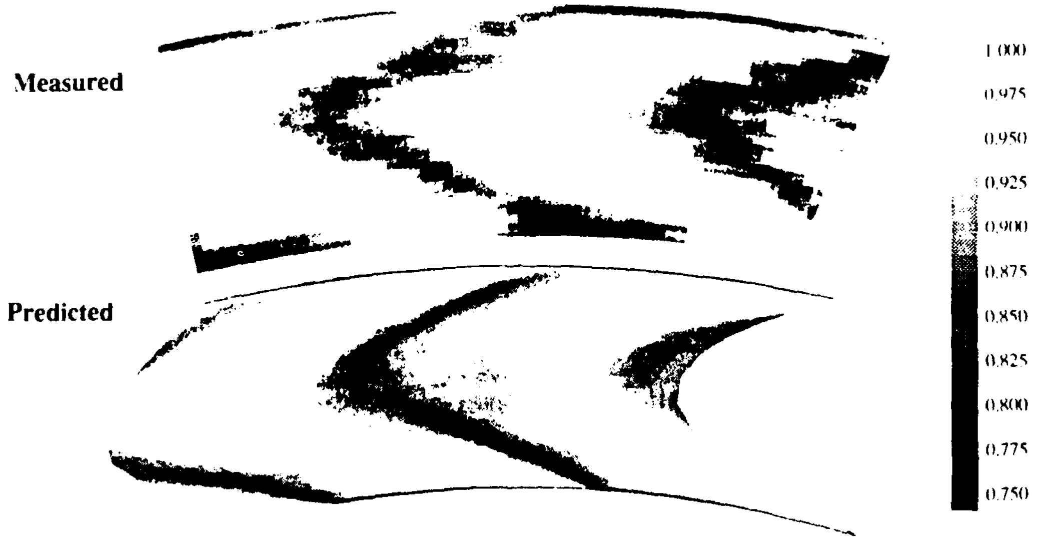

Figure 9. Measured and predicted total pressure contours 105% axial chord

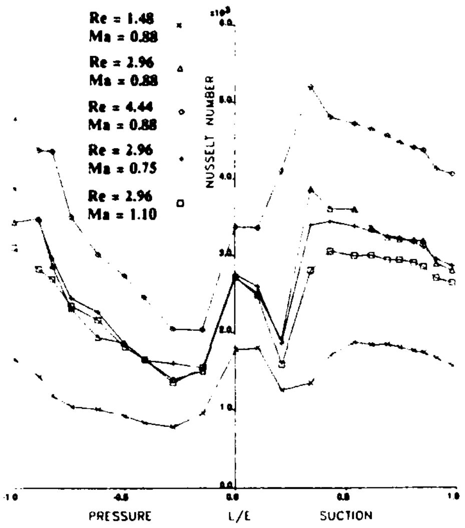

Figure 10. Variation of Nusselt number for all conditions

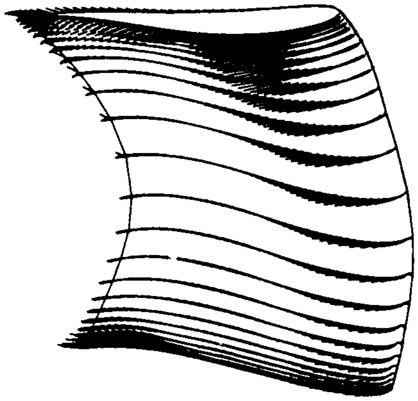

Figure 13. Predicted flow vectors

endwall Nusselt numbers show a similar trend (Figure 16), although the distributions show lower heat transfer near the suction surface indicating a greater migration of the endwall boundary layer from the pressure side towards the suction side.

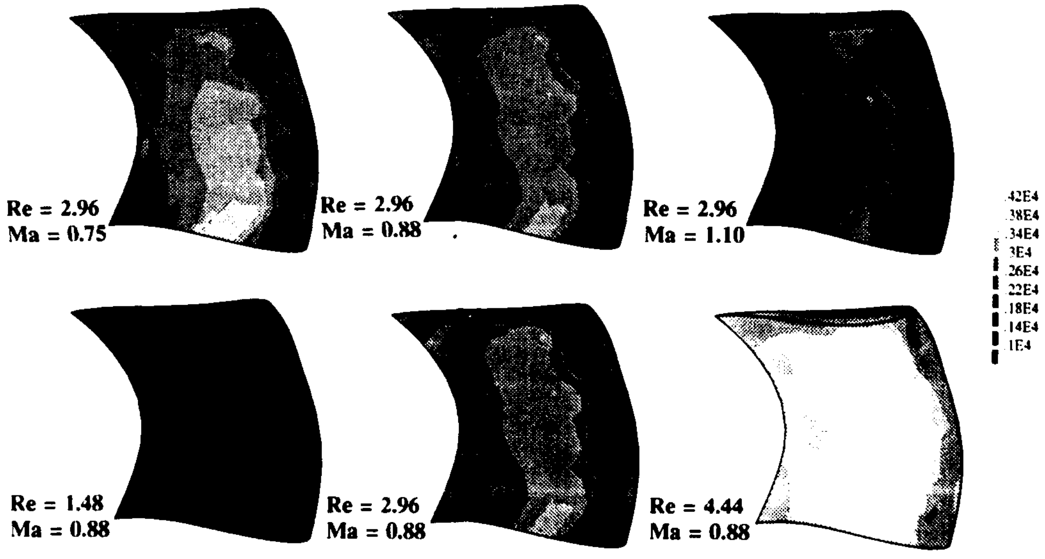

Figure 11. Suction side Nusselt number distribution

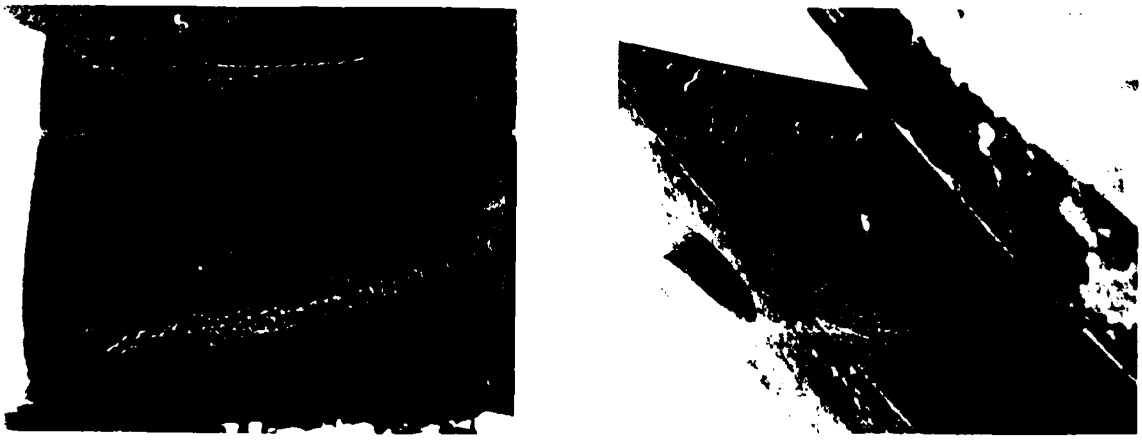

(a) Figure 12. Suction side flow visualisation (b)

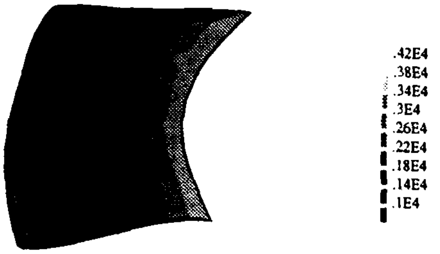

Figure 14. Pressure side Nusselt number distribution

An attempt has been made to compute the Nusselt number distribution to the vane at 60% span. Figure 17 shows measured and predicted aerofoil Nusselt numbers. The predictions were performed using versions of the Stancool and Texstan boundary layer codes (Crawford and Kays, 1976). The codes were run using the predicted pressure distribution from 3D Dawes. Two-dimensional calculations were performed along grid lines on the vane surfaces; no allowance for surface curvature was included. The grid lines in this region follow the stream lines very closely. The inlet turbulence was set at 6.5%. The Prandtl mixing length model was used with Van Driest damping in the near wall region.

The Texstan computation was started close to the leading edge from a specified boundary layer dimension. In the case of Stancool an initial distance from the stagnation point was specified. It was found that the subsequent turbulent boundary layer development was only weakly dependent on the initial laminar region. Transition location was determined by the correlation of Abu-Ghannam and Shaw (1980) in the case of Stancool computations and a transition Reynolds number of 200 was specified for Texstan. It will be seen that transition is quite well predicted using both approaches. The heat transfer levels are in error by around 30% in the worst case, for the pressure side, but the errors are more typically 10%. The pressure surface results from Texstan show good agreement. The discrepancies towards the trailing edge are probably due to irregularities in the trailing edge predicted pressure distribution from Dawes, as discussed in Section 4. On the suction surface Texstan performed less well with a large over-shoot but then approached the experimental results. Stancool predicted the suction side Nusselt number distribution reasonably well but substantially under predicted on the pressure side. Stancool results with the transition location determined by a Reynolds number of 200 predicted slightly later transition and gave slightly better results.

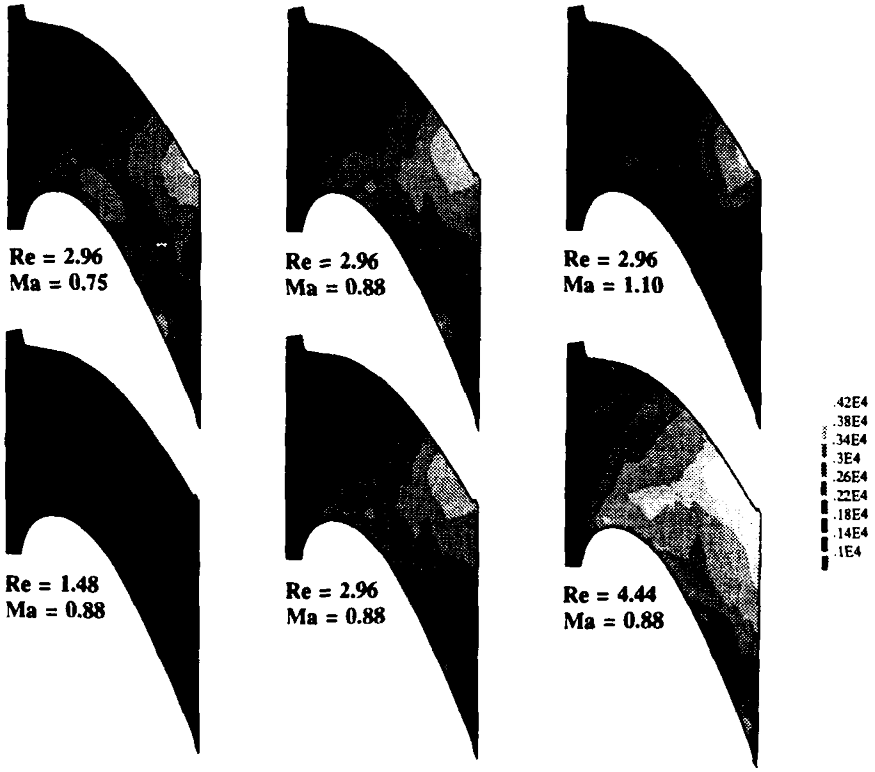

Figure 15. Hub Nusselt number distributions

The Texstan code used was an earlier release and did not include many of the features of the more mature Stancool code. Many refinements to the predictions remain to be explored. These include smoothing of the imposed free stream velocity distribution, curvature specification and introduction of turbulent transport equations.

CONCLUSIONS

A highly 3-dimensional nozzle guide vane has been successfully designed and tested at engine representative conditions.

Three sets of aerodynamic measurements have been taken at different Mach number conditions. The results indicate the vane is generally operating as

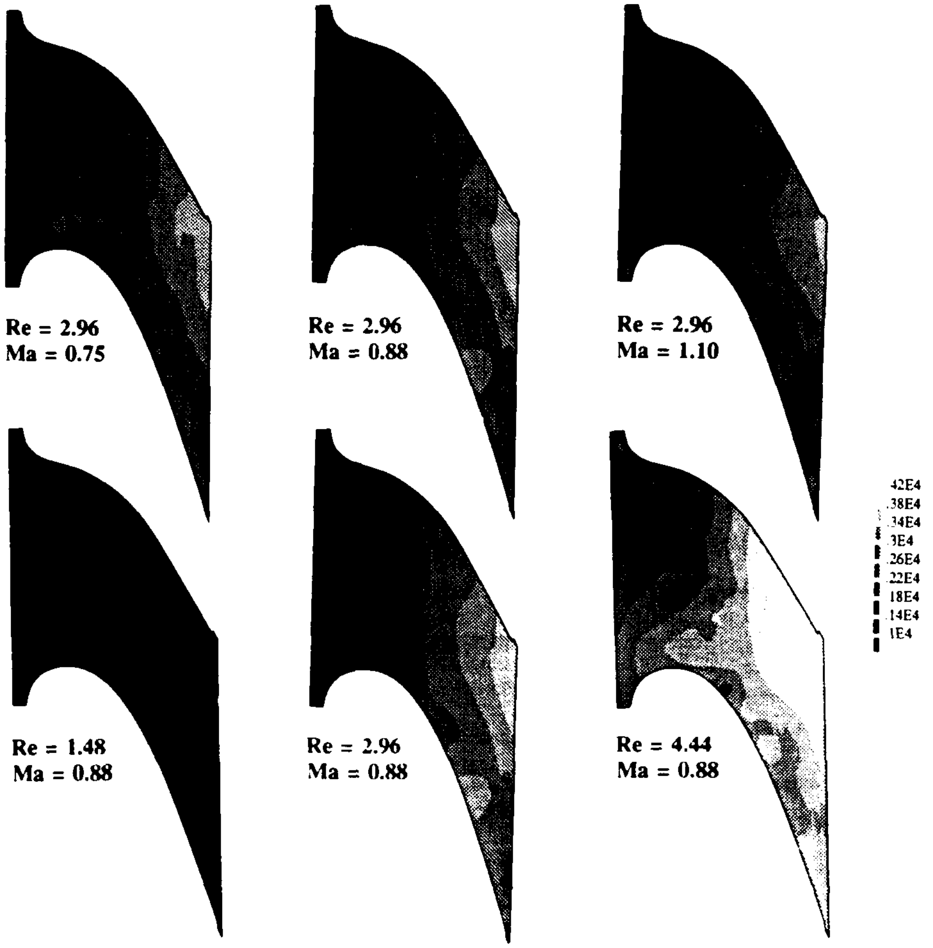

Figure 16. Casing Nusselt number distributions

designed with some unexpected behaviour towards the suction side trailing edge. This warrants further investigation. The flow visualisation of endwall cross flow indicated the presence of secondary flows and ties in with measured heat transfer patterns. Regions of high heat transfer found in other designs previously (Harasgama, 1990) in the endwall mid passage region have been reduced in area and confined to the trailing edge region. Variation of the Nusselt number with changes in Reynolds number are consistent with classical flat plate analogy. The effect of Mach number variation on Nusselt number confirms results reported by other authors.

All the measurements and predictions indicate that the secondary flows present are strongest near the casing. The downstream area traversing technique has produced good results, and these compare well with those predicted using the 3D Dawes Navier Stokes solver. However the computations made so far show no evidence of the endwall horse-shoe vortices.

Boundary layer heat transfer calculations at 60% span on the vane surfaces are promising. Transition was well predicted using either a Reynolds number of 200 or the correlation of Abu-Ghannam and Shaw. Predicted heat transfer levels are in error by typically 10% with a worse case error of 30%. Further work is obviously required to resolve inconsistencies and refine the results.

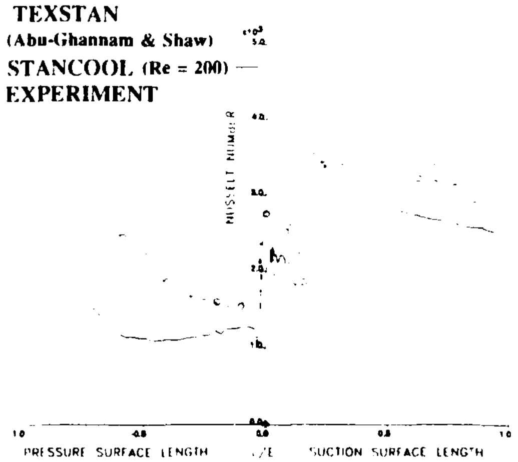

Figure 17. Predicted and measured aerofoil Nusselt number at 60% span

ACKNOWLEDGEMENTS

The author would like to thank Dr R Jackson and Mr G C Horton for their contributions to the work described in this paper.

NOMENCLATURE

Cp - Specific heat at constant pressure
ΔH - Enthalpy change
Mn - Isentropic Mach number
Re - Reynolds number based on true chord
P - Total pressure
T - Total temperature
ΔT - Temperature change
Va - Axial Velocity
U - Mean Blade Speed

REFERENCES

Gaugler, R.E.
Russell, L.M.
"Comparison of visualised turbine endwall secondary flows and measured heat transfer patterns" NASA Technical memorandum - TM 83016, 1983

York, R.E.
Hylton, L.D.
Mihelc, M.S.
"An experimental investigation of endwall heat transfer and aerodynamics in a linear vane cascade" ASME Paper 83-GT-52, 1983

Honon, G.C.
Harasgama, S.P.
Chana, K.S.
"Predictions and measurements of three-dimensional viscous flow in a transonic turbine nozzle guide vane" AGARD CPP Paper 19, 1991

Harasgama, S.P.
Chana, K.S.
"Turbine nozzle guide vane exit area traversing in a short duration light piston test facility" 10th International Symposium Measuring Techniques for transonic and supersonic flows in cascades and turbomachines, 1990

Granziani, R.A.
Blair, M.F.
Taylor, J.R.
Mayle, R.E.
"An experimental study of endwall and airfoil surface heat transfer in a large scale turbine blade cascade" ASME Paper 79-GT-99

York, R.E
Hylton, L.D.
Mihelc, M.S.
Turner, E.R.
"Experimental investigations of turbine endwall heat transfer" Final reports I-III. Aero Propulsion Labs, Wright Patterson Air Force Base, AFWAL TR-81-2077, 1981

Schultz, D.L.
Jones, T.V.
"Heat transfer measurements in short duration hypersonic facilities" AGARD-AG-165, 1973

Dawes W.N.
"A numerical method for the analysis of three-dimensional viscous compressible flow in a turbine cascade: application to secondary flow development in a cascade with and without dihedral" ASME Paper 86-GT-145, 1986

Crawford, M.E.
Kays, W.M.
"STAN5 a program for numerical computation of two dimensional internal and external boundary layers" NASA-CR 2742, 1976

Oldfield, M.L.G.
Burd, H.J.
Doe, N.C.
"Design of wide bandwidth analogue circuits for heat transfer instrumentation in a transient tunnel" 16th Symposium of ICHMT, Hemisphere Publication, Dubrovnik, 1984

Brooks, A.J.
Colbourne, D.E.
Wedlake, E.T.
Jones, T.V.
Oldfield, M.L.G.
Schultz, D.L.
Loftus, P.J.
"The isentropic light piston cascade at RAE Pyestock" AGARD-CP-390, 1985

Gladden, H.J.
Simoneau, R.J.
"Review and assessment of the database and numerical modelling for turbine heat transfer" 33rd ASME International Gas Turbine Congress, 1988

Harasgama, S.P.
Wedlake, E.T.
"Heat transfer and aerodynamics of a high rim speed turbine nozzle guide vane treated in the RAE isentropic light piston cascade (ILPC)" ASME Paper 90-GT-41

Chana, K.S.
"Heat transfer and aerodynamics of a high rim speed turbine nozzle guide vane with profiled endwalls" ASME Paper 92-GT-243

Harvey, N.W.
Jones, T.V.
"Measured and calculation of endwall heat transfer and aerodynamics on a nozzle guide vane in annular cascade" ASME Paper 90-GT-301

Jones, T.V.
Harvey, N.W.
Ireland, P.T.
Wang, Z.
"Detailed heat transfer measurements in nozzle guide vane passages in linear and annular cascades in the presence of secondary flows" AGARD Luxembourg, 1989

Abu-Ghannam, B J.
Shaw, R.
"Natural transition of boundary layers. The effects of turbulence, pressure, and flow history". J Mech Engr. Science Vol 22, No 5, 1980.

Discussion

QUESTION 1:

DISCUSSOR: T. Arts, von Karman Institute

Did you measure the inlet pressure and temperature profiles and did you take them into account in your predictions?

AUTHOR'S REPLY:

The boundary layer thickness has been measured. It is very small and has been taken into account in the Navier-Stokes calculations. The temperature profile is almost linear. The calculation, however, does not take this into account.

QUESTION 2:

DISCUSSOR: C. Hah, NASA Lewis Research Center

What type of transition model was used for the full three-dimensional flow and heat transfer calculation?

AUTHOR'S REPLY:

For the full three-dimensional calculation the start and end of transition was specified. For the two-dimensional boundary layer calculation a transition momentum thickness Reynolds number of 200 and the correlation of Abu-Ghannam and Shaw were both used.

Vortex Structure and Mass Transfer Near the Base of a Cylinder and a Turbine Blade

M.Y. Jabbari and R.J. Goldstein

Mechanical Engineering Department
University of Minnesota
111 Church Street SE
Minneapolis, MN 55455
USA

SUMMARY

Results of naphthalene sublimation measurements and flow visualization studies near the base of round and a square cylinders mounted on a flat plate are compared with similar measurements in the endwall region of a turbine blade. Differences and similarities of the flow and mass transfer are discussed. Samples of mass transfer distribution and visualization results in the region are provided. Supported by the sublimation and the flow visualization results models for the vortex structure in the flow are suggested.

NOMENCLATURE

C	Blade chord length
D	Diameter of round or side of square cylinders
D_f	Diffusion coefficient of napthalene
h_m	Mass transfer coefficient
Re	Reynolds number(UC/ν or UD/ν)
Sh	Sherwood Number ($h_m C/D_f$ or $h_m D/D_f$)
S_s	Curvilinear distance along the suction side (Fig. 5)
St_m	Mass transfer Stanton number (h_m/U)
St_0	Mass transfer Stanton number in the absence of protrusion
U	Upstream velocity
X,Y,Z	Coordinate system
δ_1	Boundary layer displacement thickness
ν	Kinematic viscosity of air

INTRODUCTION

Knowledge of flow and temperature fields near the junction of a body attached to a surface is required in a number of systems. Junctions of blades to hub in turbomachinery, flat fins to pipe or pin fins to plate in heat exchangers, and wings to body in air planes, are only few examples where the knowledge is useful.

Investigation of the flow field near such junctions are reported by many authors. References (1-4) contain results of flow measurement near the junction of a round cylinder mounted on a flat plate, and references (5-8) provide information on the flow near the base of a turbine blade. These investigations indicate that the flow boundary layer separates ahead of the projected body and a system of interacting vortices are formed. The largest of these vortices, commonly called horseshoe vortex, is the one that is most mentioned in the literature. Smaller vortices (a corner vortex and sometimes pairs of counter rotating vortices) are also reported. The important parameters that influence the vortex structure have been determined to be the flow Reynolds number (based on the protrusion's dimension), the thickness of the boundary layer, and the size and the shape (bluntness) of the protrusion. The flow is found to be unsteady.

In front of an upright cylinder mounted on a flat plate, different numbers of vortices (Ref 4) with varying strengths (Ref 9) are reported. The observed numbers of vortice, besides being influenced by geometrical dimensions and flow conditions, appears to have been affected by the observation technique and the size and the speed of response of the sensor employed. A similar situation, enhanced in complexity by the blade shape, the flow incidence angle, and the cross flow in the passage, prevails in studies of flow near the base of a turbine blade.

Many studies, e.g. references (9-24), have reported heat or mass transfer measurements near the junction of a protruding object. These, in addition to providing knowledge needed for thermal design applications, often contribute to understanding of the prevailing near-surface flow structure. For example, a sharp local maximum in heat transfer (if detected) can indicate a down-wash region of a vortex or the reattachment region of a separated flow. Conversely, a local minimum points to a vortex up-wash region or a detachment of the flow. The extrema are particularly useful when a vortex (or a separated region) is very small (and close to the wall) so that other means of detection fail to indicate it.

Conventional heat transfer measurements (wall temperature and wall heat flux measurements), due to finite conductivity of wall materials, are generally not capable of showing the effects of very small fluctuating vortices (or separated regions). In contrast, the naphthalene sublimation measurements, if carried out locally over fine enough grids, can easily pick-up the sharp local variations in mass transfer though these are integrated over time. In the following, mass transfer results measured at the base of protruding cylinders and a turbine blade are reviewed and some important inferences drawn from them are discussed.

Measurement technique and procedure

Most of the results to be discussed in the next section are obtained using naphthalene sublimation; a mass transfer process employed to measure the mass (analogous to heat) transfer coefficient. In this technique, the surface upon which heat transfer distribution is sought is covered (usually by casting) with a thin layer of naphthalene. The surface is then exposed to the flow of air where some of the naphthalene will sublime and enter the flow. The rate of sublimation, and consequently the mass (heat) transfer coefficient, can be determined by measuring the exposure time and the local depth of the sublimation. The sublimation depth is obtained from accurate measurement of the naphthalene's surface profile, relative to a datum, before and after its model's exposure to the flow. The strength of this measurement technique is in that it is non-intrusive and has high resolution (better than 0.025 mm in locating the sensor and 0.000025mm in measuring the sublimation depth). Thus, it is capable of detecting sharp local gradients. Further details of the procedure and the instrumentation can be found in references (9 and 12). Improvement of the system and an analysis of its precision are covered in (Ref 24 and 25). An important feature of the improved system is that it combines a rotating table and a three dimensionally moving depth gauge (LVDT) holder, Fig. 1, which enables scanning of arbitrary cylindrical surfaces for surface profile determination.

In discussing the mass transfer measurements reference will be made to results of flow visualization studies. The visualizations results are obtained by spreading a thin layer of a mixture of light oil and lampblack powder on a surface of interest. The shear force from the flow, moves the lampblack particles in the oil leaving a trace behind which indicates the direction, and qualitatively the magnitude, of the forces on the surface. In an up-wash region of a vortex, where low momentum fluid from opposing sides come together, the lampblack accumulates (here mass transfer might be a local minimum). In contrast, in a down-wash region of a vortex the lampblack is dispersed to the sides leaving a bare surface (here a local maximum in mass transfer might be expected). Extreme care must be exercised in interpreting the visualization results, particularly, when small fluctuating vortices are involved.

Discussion

Mass transfer measurements on a plate near its junction with a circular cylinder and on a circular cylinder near its junction with a plate are reported in (Ref 12) and (Ref 13), respectively. Local maximum and minimum in mass transfer are observed which are attributed to the action of vortices in the flow. Based on this measurement and the results obtained by others, a model of vortices is presented in Fig. 2. The model includes a large horseshoe vortex (V1) a corner vortex (V2) and a smaller vortex (V3) above the corner vortex. Later measurements (Ref 9, 15) support the model and show that the vortex above the corner- vortex (V3) becomes weaker and possibly disappears at lower Reynolds numbers. A photograph taken, by authors of ref. (Ref 15), from a naphthalene covered cylinder is presented in Fig. 2 as a visible evidence for the vortex system. The cylinder has been over exposed to air flow (an exposure time of several hours versus 30-45 minutes for a normal mass transfer measurement) so that the depth of the sublimed naphthalene rendered by vortices could be more easily visualized. The photograph clearly shows action of the vortices that have produced the considerable change in the surface profile. A more complete vortex structure, however, is deduced from the mass transfer distribution for which the change of surface profile is only in the hundredths (or at the most one tenth) of a millimeter. The photograph reveals the multiplicity of the vortices that form in the region (a smaller vortex, V4, or its effect as will be presented shortly seems not to have survived the change of the surface profile).

Mass transfer distributions near the base of a square cylinder mounted perpendicularly on a plate (Ref 16,17) shows repeated local maxima and minima in Sherwood number, both on the cylinder and the endwall. These together with re-evaluation of the earlier results, suggest a modified model of vortex system as shown in Fig. 3. This flow structure resembles that offered in Fig. 2, exception being inclusion of vortices V4, V5, and V6. Introduction of vortex V4 makes the up-wash/down-wash regions correspond to the minimum/maximum in the measured wall mass transfer and the rotation between vortices V2 and V3 compatible. This newer model represents measurements on both square and round cylinders. The function of the weaker vortex V4, in separating vortices V2 and V3, seems to have been substituted by the ridge between the adjacent trenches on the photograph shown in Fig. 2. The replacement, perhaps, has been a gradual take over caused by the change in surface profile. The counter-rotating pair of vortices V5,V6 is added upstream and under vortex V1 for similar reasons; to match mass transfer variations and make rotations compatible. Presence of this pair has been observed by Baker (Ref 1) and are also evident in mass transfer data (Ref 15, 16). Note that incompatibility in direction of rotation between V4 and a stretch of V2 above it makes the arrangement unstable. Consequently, the arrangement frequently breaks down and forms again. Similar unstable behavior, perhaps caused by the inherent instability due to opposite rotation of V5 and a stretch of V1 is observed in a preliminary fog (smoke) visualization study. Also noticeable is the resemblance in structure between proposed vortex groups V2, V3, V4 and V1, V5, V6. The resemblance is well justified because the turned flow along the cylinder faces an obstacle (the endwall) the same way that the original flow along the endwall faces the cylinder.

If the rate of mass transfer is a measure of the intensity of a vortex, then the ratio of local peak rendered by vortex V2 on cylinder to that on endwall should be close to unity. This ratio is about 0.90 (cf Fig. 3) for a square cylinder and 0.87 [15] for a circular cylinder (in reality the peak on the cylinder is caused jointly by V2 and V4 and on the endwall by V1 and V2 which indicates that vortices V1 and V4 may have similar contribution in carring mass away from the wall). The ratio of the peak mass transfer caused by the (V5,V6) vortex pair to that caused by (V1,V2) is approximately 0.7 for the square cylinder (cf. Fig. 3) and 0.4 for the round cylinder (Ref 15), indicating a relatively stronger (V5,V6) pair in front of the square cylinder. For the same cylinder sizes (25.4 mm), and about the same boundary layer displacement thicknesses (2.474 mm vs 2.388 mm), this relative higher strength is despite lower Reynolds number (18800 vs 30060), for the square cylinder. The reason is attributed to the difference in bluntness of the cylinders; the abrupt obstruction of flow by square cylinder versus a more gentle and gradual obstruction by the round cylinder.

The effect of the flow angle (angle between upstream velocity and normal to the surface facing the flow) on mass transfer from a square cylinder and its base plate is discussed in reference (Ref 17). Figure 4, as an example, shows mass transfer distribution on the base plate (endwall) when the flow angle is 20 deg. For comparison a lampblack visualization of the surface flow is also included. A horseshoe vortex system forms in front of a side which has flow angle less than or equal to 45 deg. For the side with flow angle greater than 45 deg., no clear signs of vortex formation is observed.

A horseshoe vortex forms ahead of the leading edge of a turbine blade at its junction with an endwall. Although the blade's leading edge may be well-rounded, the flow will sense a blunt body with a shape depending on the blade profile and the flow incidence angle. The vortex system, therefore, will be expected to be influenced by the flow angle, the shape of the blade, the presence of neighboring blades, and the blades arrangement (solidity ratio). From mass transfer measurements on the endwall (Ref 23), and on the blade (Ref 24), in a specific turbine cascade the vortex structure that is shown in Fig. 5 is inferred. Distribution of mass transfer near the blade's stagnation line (Ref 26) agrees well with the measurements reported along the stagnation line of a circular cylinder (Ref 9) at a comparable flow Reynolds number (about 12000 based on the blade's leading edge diameter). Thus vortices shown in Fig. 5 are similar to those expected in front of a blunt cylinder though at a lower Reynolds number; as the equivalent of V3 and V4 (cf Fig. 3) are not present while the pair V5,V6 which reflects the bluntness of the blade are included.

Effects of neighboring blades on the leading edge vortices are evident in Fig. 6. (Ref 27), showing lampblack visualization of the surface flow between adjacent blades. Several regions of flow having different origins or characeter are distinct and labeled in the adjacent sketch. The labeling is in accordance with the vortex (see identification in Fig 5) or the flow that washes the region. The footprint of vortex V2 can not be clearly seen in this visualization; therfore, it is not marked. Boundaries of the labeled regions are the approximate location of the up-wash/down-wash line of the vortex. The intersection of the leading-edge-stagnation-plane and the endwall is marked DL (dividing line). The near-surface-flow contained between adjacent dividing lines will eventually pass through the passage. In contrast to the case of a single cylinder, extension of the legs of vortices around the blade's leading edge is influenced by the neighboring blade. The cross flow in the passage diverts the near-endwall-flow of the entrance region (regions V1, V5, V6, ...) to cross over to the suction side of the blade A. It also seems to contribute to earlier detachment of the pressure-side-leg of the horseshoe vortex (V1) from the pressure side of the blade B. The suction-side-legs of vortices V1, V2 (not shown), V5, and V6 of the blade A are pushed to converge and remain attached to its suction side. They (the suction side legs) are eventually forced to rise along the suction surface and move away from the endwall. The remnants of the suction-side-legs of vortices from blade A (specifically V5 and V6), the diverted upstream flow, and the pressure-side-legs of vortices from blade B, approach the suction surface at a flow angle less than about 45 deg.; a condition seemingly required for formation of a new horseshoe vortex system (see earlier paragraph on the effects of flow angle). This condition and the interaction of the various flow stream in this area create a new vortex system part of which lays over a strip along the junction of suction side and the endwall (Ref 27). The result is a region, extending to near the trailing edge, covered with many interacting vortices (Fig. 6). Figure 7 shows a representative mass transfer distribution on the suction-side and the endwall in this region with its multiple local maxima and minima.

Acknowledgments

The financial support for this study by the Air Force Office of Scientific Research is gratefully acknowledged.

REFERENCES

1. Baker, C.J., "The Turbulent Horseshoe Vortex," Journal of Wind Engineering and Industrial Aerodynamics, Vol. 6, 1980, PP 9-23.
2. Dargahi, B., "The Turbulent Flow Field Around a Circular Cylinder," Experiments in Fluids, Vol. 8, 1989, PP 1-12.
3. Angui, J., Andreopoulos, J.,, "Experimental Investigation of a Three-Dimensional Boundary Layer Flow in the Vicinity of an Upright Wall Mounted Cylinder,", 1990, AIAA 90-1545.
4. Pierce, F.J., Tree, I.K., "The Mean Flow Structure on the Symmetry Plane of a Turbulent Junction Vortex," Journal of Fluids Engineering, Vol. 112, 1990, PP 16-21.
5. Sieverding, C.H., "Recent Progress in the Understanding of Basic Aspects of Secondary Flows in Turbine Blade Passages,"Journal of Engineering for Gas Turbines and Power, Vol. 107, 1985, PP 248-257.
6. Sonoda, T., "Experimental Investigation on Spatial Development of Steamwise Vortices in a Turbine Inlet Guide Vane Cascade," , 1985, ASME 85-GT-20.
7. Jilek, J., "An Experimental Investigation of the Three-Dimensional Flow Within Large Scale Turbine Cascades," ,1986, ASME 86-GT-170.
8. Hazarika, B.K., Raj, R., Boldman, D.R., "Three-Dimensional Fluid Flow Phenomena in the Blade Endwall Corner Region,", 1986, ASME Paper 86-GT-179.
9. Karni, J. and Goldstein, R.J., "Endwall Effects on Local Mass Transfer from a Cylinder in Crossflow", Proceedings of the 2nd International Symposium on Refined Flow Modeling and

Turbulence Measurement, Vol. I, K4; 1985, 1-33

10. Blair, M.F., "Heat Transfer in the Vicinity of a Large-Scale Obstruction in a Turbulent Boundary Layer," J. Propulsion, Vol. 1, 1984, PP 158-160.

11. Hinckel, J.N. and Nagamatsu, H.T.,, "Heat transfer in the stagnation region of the junction of a circular cylinder perpendicular to a flat plate," Int. J. Heat and Mass Transfer, Vol. 29, 1986, PP 999-1005.

12. Goldstein, R.J., Chyu, M.K., Hain, R.C., "Measurement of Local Mass Transfer on a Surface in the Region of the Base of a Protruding Cylinder with a Computer-Controlled Data Acquisition System," International Journal of Heat and Mass Transfer, Vol. 28, 1985, PP 977-985.

13. Goldstein, R.J., Karni, J., "The Effect of a Wall Boundary Layer on Local Mass Transfer From a Cylinder in Crossflow," J. Heat Transfer, Vol. 106, 1984, PP 260-267.

14. Van Dresar, N. and Mayle, R. E. "Convection at the base of a cylinder with a horseshoe vortex," Proc. 8th Int. Heat Transfer Conf., Vol. 3, 1986, PP 1121-1126.

15. Goldstein, R.J., Karni, J, and Zhu, Y., "Effect of Boundary Conditions on Mass Transfer Near the Base of a Cylinder in Crossflow," J. Heat Transfer, Vol. 112 (2), 1990, PP 501-504.

16. Goldstein, R.J., Yoo, S.Y., and Chung, M.K., "Mass Transfer from a Square Cylinder and It's Endwall in Crossflow," Int. J. of Heat and Mass Transfer, Vol. 33, No. 1, 1990, PP 1-18.

17. Yoo, S.Y., Goldstein, R.J., and Chung, M.K., "Effects of Angle of Attack on Mass Transfer From a Square Cylinder and Its Base Plate," To appear in the Int. J. of Heat and Mass Transfer. 1992

18. Graziani, R.A., Blair, M.F., Taylor, J.R., Mayle, R.E., "An Experimental Study of Endwall and Airfoil Surface Heat Transfer in a Large Scale Turbine Cascade," Journal of Engineering for Power, Vol. 102, 1980, PP 257-267.

19. Gaugler, R.E., Russell, L.M., "Comparison of Visualized Turbine Endwall Secondary Flows and Measured Heat Transfer Patterns,", 1983, ASME 83-GT-83.

20. Hippensteele, S.A., Russell, L.M., Torres, F.J., "Local Heat-Transfer Measurements on a Large Scale-Model Turbine Blade Airfoil Using a Composite of a Heater Element and Liquid Crystals,". 1985, ASME 85-GT-59.

21. Hippensteele, S.A., Russell, L.M., Torres, F.J., "Use of a Liquid-Crystal, Heater-

Element Composite for Quantitative, High-Resolution Heat Transfer Coefficients on a Turbine Airfoil, Including Turbulence and Surface Roughness Effects,", 1987, NASA Technical Memorandum 87355.

22. Hippensteele, S.A., Russell, L.M., "High-Resolution Liquid-Crystal Heat-Transfer Measurements on the Endwall of a Turbine Passage with Variations in Reynolds Number," Proceedings of the 1988 National Heat Transfer Conference, ASME publication HTD-96, 1988, Vol. 3, PP 443-453.

23. Goldstein, R.J., Spores, R.A., "Turbulent Transport on the Endwall in the Region Between Adjacent Turbine Blades,"Journal of Heat Transfer, Vol. 110, 1988, PP 862-869.

24. Chen, P.H., Goldstein, R.J., "Convective Transport Phenomena on the Suction Surface of a Turbine Blade Including the Influence of Secondary Flows Near the Endwall,", 1991, ASME Paper 91-GT-35.

25. Hain, R.C., Wang, H.P., Chen, P.H., Goldstein, R.J., "A microcomputer-controlled data acquisition system for naphthalene Conf., Sao Paulo, Brazil, Dec. 1991.

26. Chen, P.H., "Measurement of local mass transfer from a gas turbine blades," Ph.D. Thesis, University of Minnesota, 1988.

27. Jabbari, M.Y., Goldstein, R.J., Marston, K.C., and Eckert, E.R.G. "Three Dimensional Flow at the Junction Between a Turbine Blade and End-Wall," Warme-und Stoffubertragung (Thermo-and Fluid Dynamics), Vol. 27, 1992, PP 51-59.

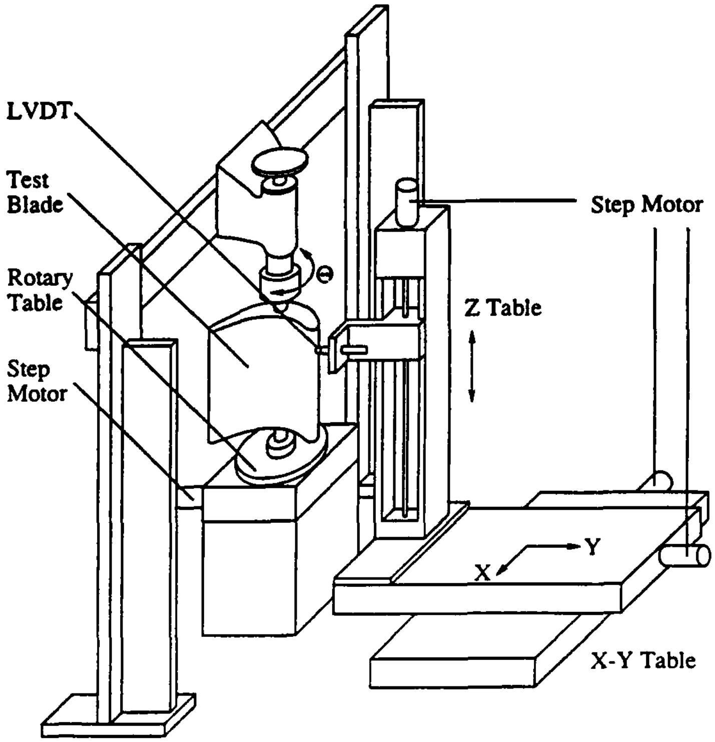
LVDT
Test Blade
Rotary Table
Step Motor
Step Motor
Z Table
X
Y
X-Y Table
Θ

Figure 1- Surface profile measurement system

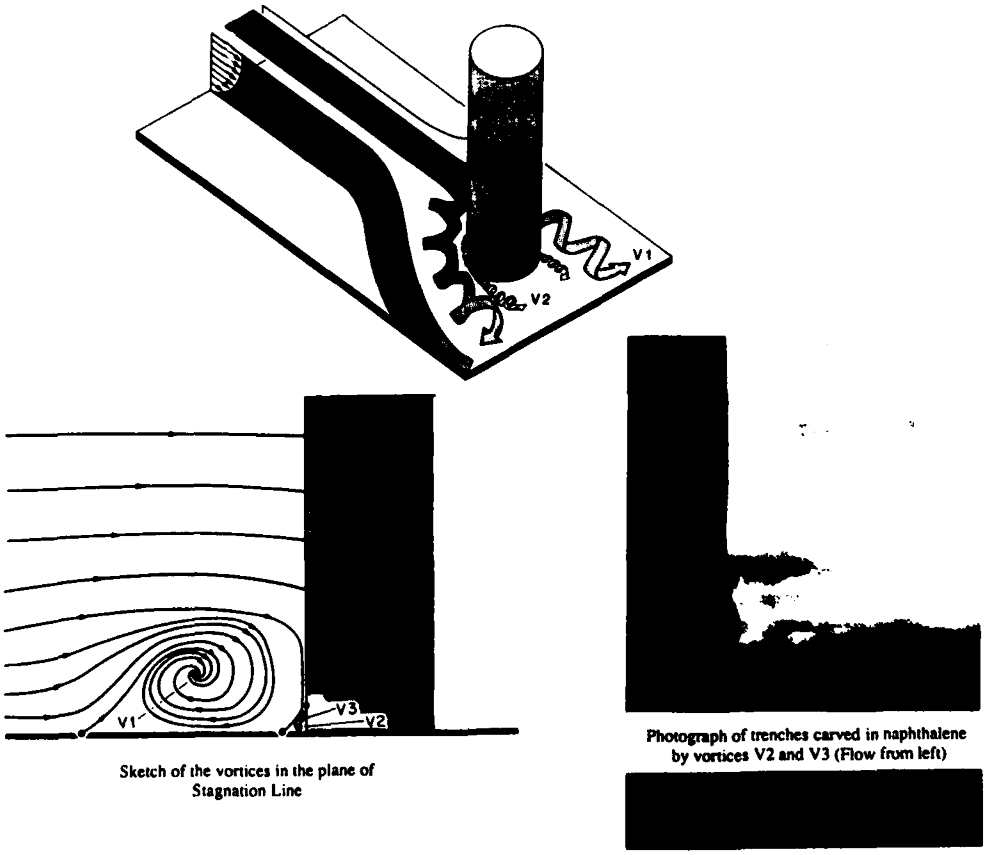
V1
V2
a
V1
V3
V2

Sketch of the vortices in the plane of Stagnation Line

Photograph of trenches carved in naphthalene by vortices V2 and V3 (Flow from left)

Figure 2- The vortex system and photograph of its effect near the base of a round cylinder (Refs. 9 and 15)

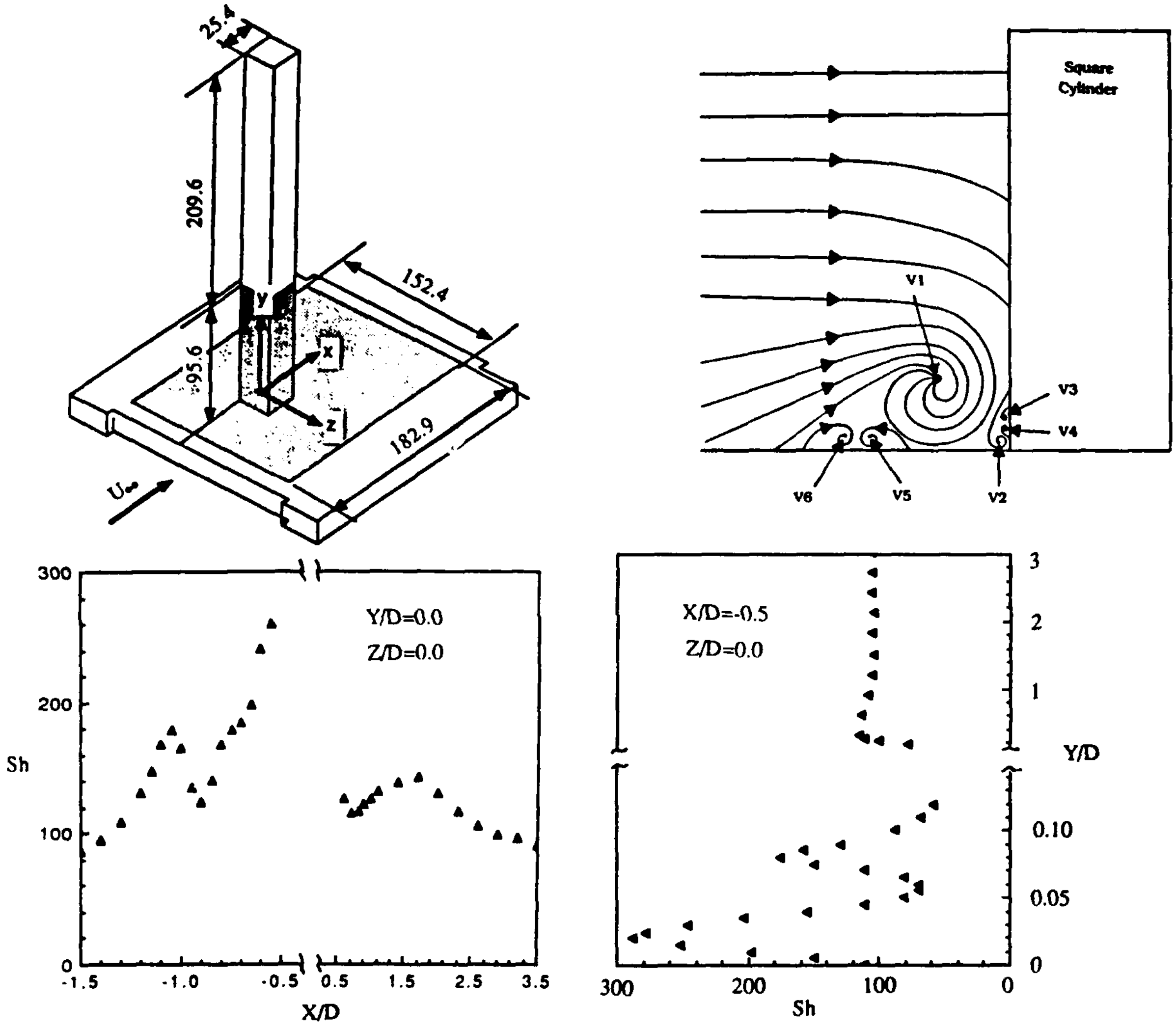

Mass transfer on the plate

Mass transfer on the cylinder

Figure 3- Mass transfer distribution (Ref. 16) and the vortex system near the base of a square cylinder

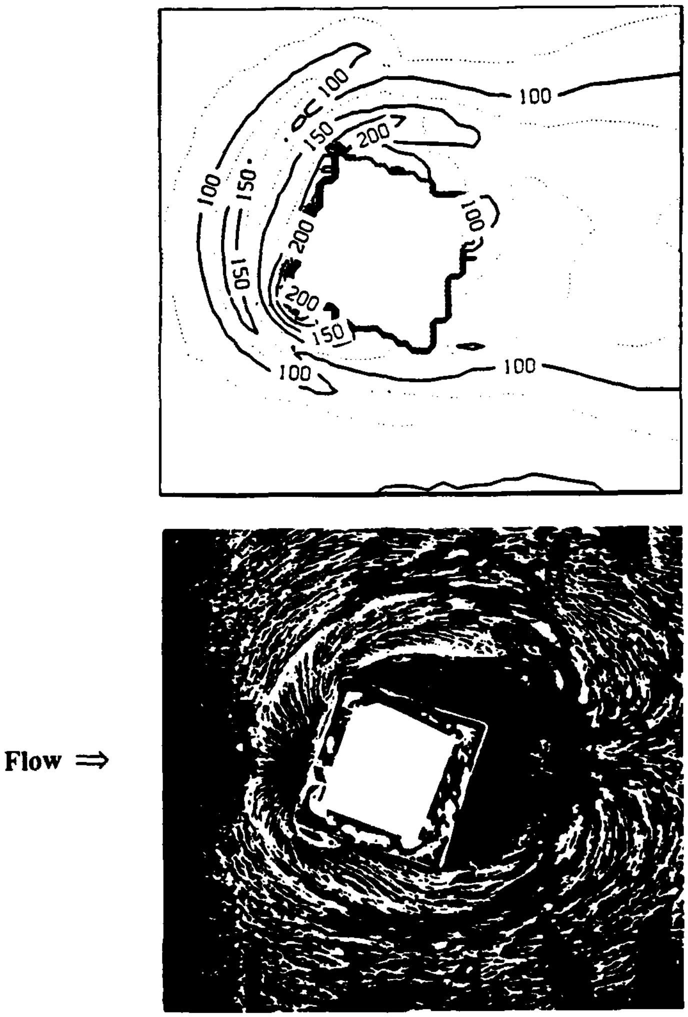

Figure 4- Mass transfer distribution and visualization of flow on the endwall of a square cylinder, flow angle 20 deg. (Ref. 17)

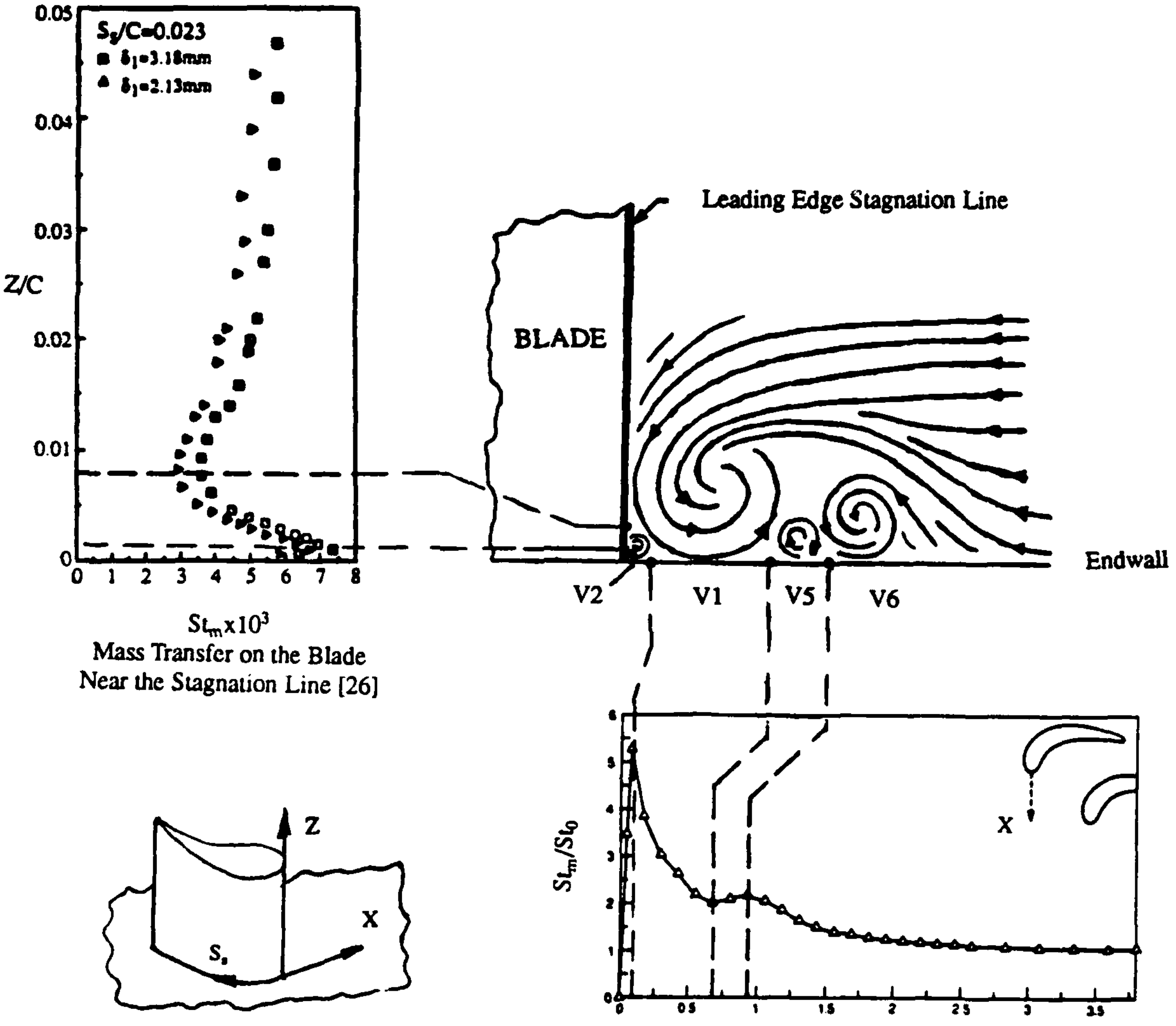

Mass Transfer on the Blade
Near the Stagnation Line [26]

Mass Transfer on the Endwall Upstream
of the Stagnation Line [23]

Figure 5- The vortex system and the mass transfer in the leading edge stagnation plane of a turbine blade

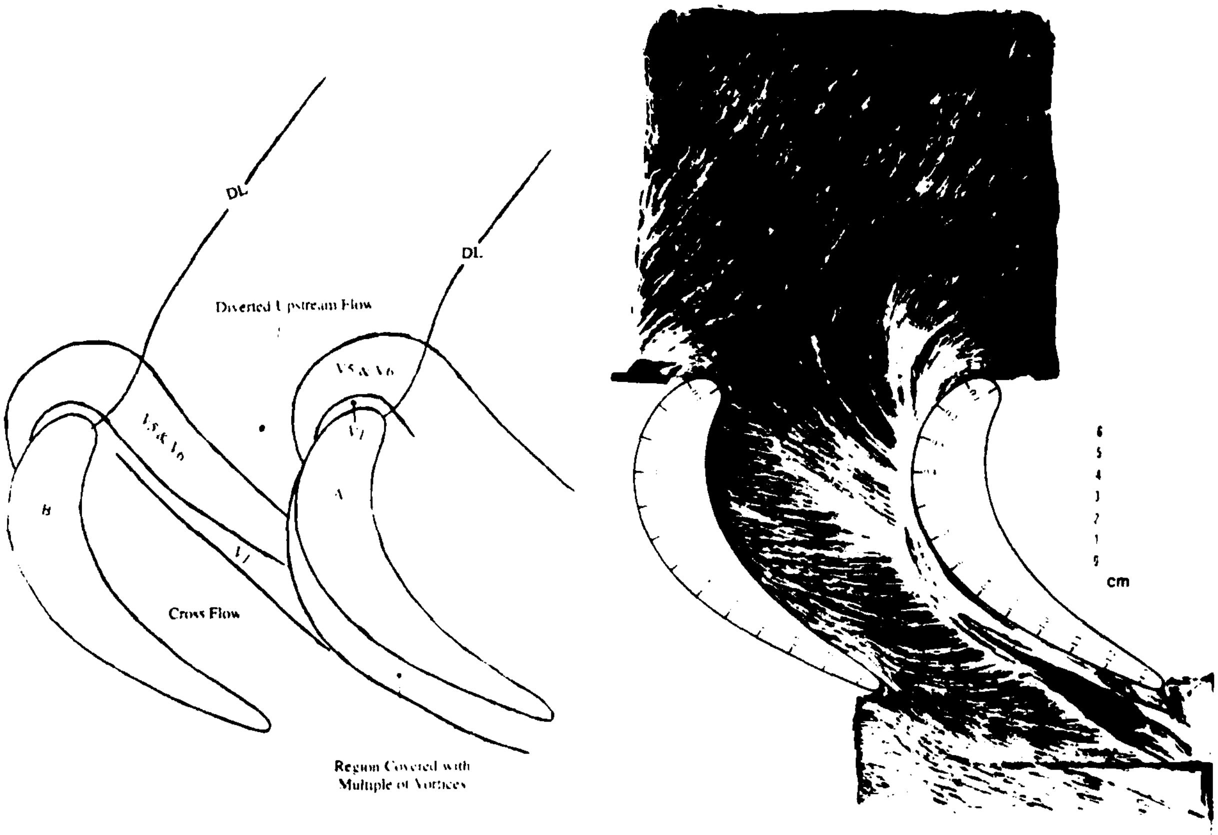
DL
DL
Diverted Upstream Flow
V5 & V6
V5 & V6
V7
V7
B
A
Cross Flow
Region Covered with
Multiple of Vortices
6
5
4
3
2
1
0
cm

Figure 6- Visualization of flow on the endwall of the passage between adjacent turbine blades (Ref. 27)

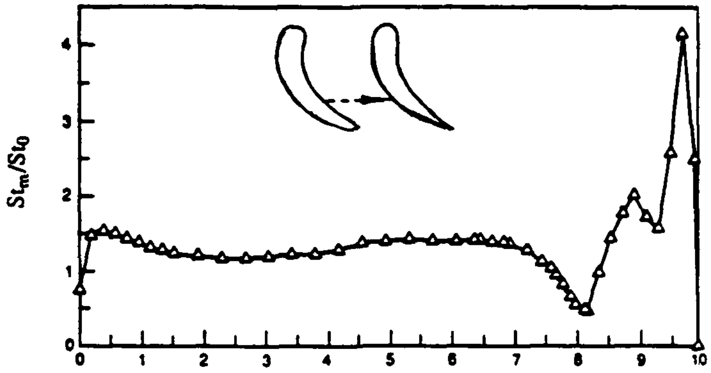

Distance Across the Passage (cm)
Mass Transfer Distribution on the Endwall [23]

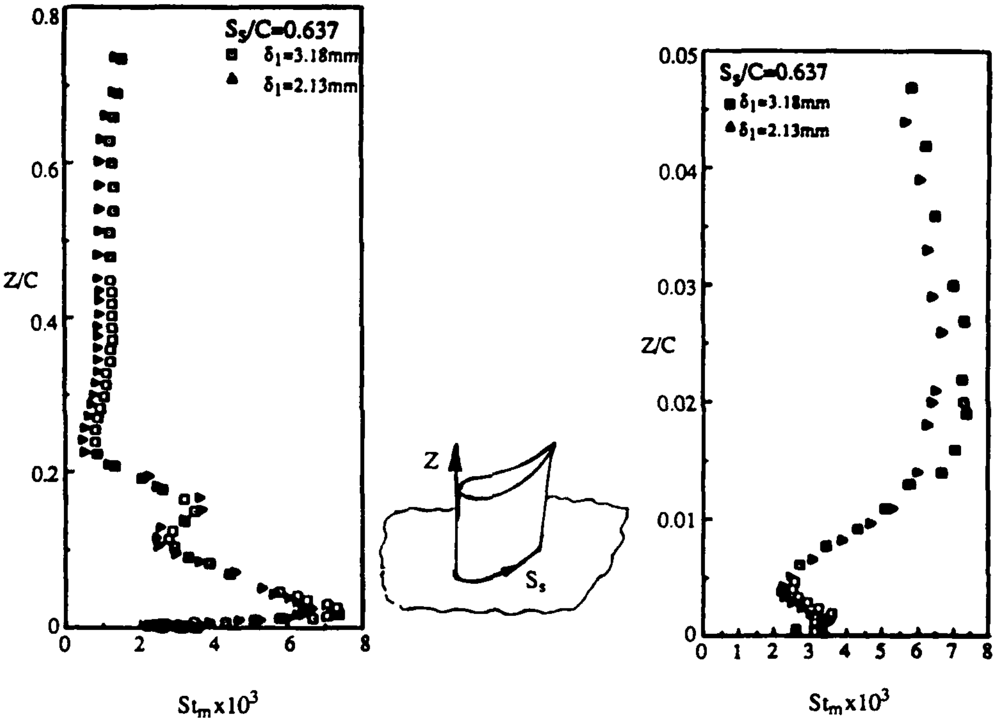

Mass Transfer Distribution on the Suction-Side [24]

Mass Transfer Distribution on the Suction-Side [24]
(Blown-up of the Near Endwall Region)

Figure 7- Mass transfer distribution in the junction region of suction side and the endwall

Discussion

QUESTION 1:

DISCUSSOR: A. Heselhaus, Institut fur Antriebstechnik

Were the endwalls also coated with naphthalene when the mass transfer measurements on the blade surface were made, and were the blade surfaces naphthalene-coated for the endwall measurements.

AUTHOR'S REPLY:

The case of both endwall and cylinder coated with naphthalene has been studies and published (Ref. 15). The effect as I recall is slight reduction in local maximum mass transfer on the cylinder.

THERMAL EFFECTS OF A COOLANT FILM ALONG THE SUCTION SIDE OF A HIGH PRESSURE TURBINE NOZZLE GUIDE VANE

by

T. Arts
von Kármán Institute for Fluid Dynamics
72 Chaussée de Waterloo
1640 Rhode Saint Genèse
Belgium

I. Lapidus
SNECMA, Centre de Villaroche
France

ABSTRACT

The purpose of the paper is to try to describe some of the influences on external convective heat transfer of a coolant film whose position varies along the suction side of a high pressure turbine nozzle guide vane. The measurements were performed in the short duration Isentropic Light Piston Compression Tube facility CT-2 of the von Karman Institute. The effects of external and internal flow are considered in terms of Mach number, Reynolds number, freestream turbulence intensity, blowing rate and coolant to freestream temperature ratio. The way to evaluate those results in terms of heat transfer coefficient is finally discussed.

LIST OF SYMBOLS

d	cooling hole diameter
h	heat transfer coefficient
h_o	heat transfer coefficient without cooling
m	blowing rate
M	Mach number
Re	Reynolds number
s	non dimensional wetted length
Tu	freestream turbulence intensity

Subscripts

o	total condition
1	inlet condition
2	exit condition
∞	upstream condition
c	coolant condition
is	isentropic condition

1. INTRODUCTION

The strong interest devoted to the convective heat transfer phenomena existing in the first stages of a modern high pressure gas turbine is motivated by the important thermal loads observed in this severe environment. An efficient cooling of the blades and the endwalls is most often required to prevent an early degradation. Film cooling is one of the techniques applied for this purpose. Considering the complexity of the flow developing in modern aero-engines, an experimental approach in conditions and with models representative of reality is absolutely necessary. A large number of research programmes have therefore been undertaken over the 25 last years to investigate numerous aspects of the film cooling technique.

A lot of parameters have to be considered to correctly simulate the geometry and the flow conditions encountered in modern turbines : airfoil geometry, coolant emission location and geometry, gas to wall temperature ratio, blade loading, freestream Reynolds number, freestream turbulence intensity, secondary flows, coolant to freestream mass weight ratio and temperature ratio, etc...

Many experimental investigations have been presented on the fundamental aspects of film cooling. Their objective was to understand and to eventually model the thermal and aerodynamic characteristics of a coolant film. Typical examples of this type of research were published by Goldstein [1], Teekaram et al. [2] and Sinha et al. [3]. Some of the available measurements on film cooled turbine cascade models were presented by Lander et al. [4], Nicolas & Le Meur [5], Ito et al. [6], Daniels [7], Dring et al. [8], Horton et al. [9], Camci & Arts [10], Nirmalan & Hylton [11], Arts & Bourguignon [12]. A large number of these heat transfer data, presented either in terms of heat transfer coefficient or in terms of adiabatic effectiveness, are however difficult to use as such for modern cooled gas turbine design because of the limited range of test conditions considered in some of these investigations.

Over the last 10 years, SNECMA and the von Karman Institute have been conducting a systematic research programme on the aerodynamic and thermal performances of uncooled and cooled two-dimensional vanes and blades. The main objective of these investigations is to develop and to verify accurate and reliable calculation methods under the presence of film cooling; a second objective is to possibly identify relatively simple correlations, taking into account the freestream and flow parameters, to be eventually used during the design procedure of new blades. The selection of the different airfoil geometries and cooling configurations did not especially depend upon the fact that these profiles eventually were or were not used in an existing engine. The tested models were rather considered as general demonstrator test cases, representative of modern aerodynamic design.

The more specific objective of the present paper is to describe one of the investigated topics, namely to quantify the influence on convective heat transfer of a coolant film whose emission position varies along the suction surface of a high pressure turbine nozzle guide vane. The effects of both external and internal flows are considered in terms of Mach and Reynolds number, freestream turbulence intensity, blowing ratio and coolant to freestream temperature ratio. A discussion of the heat transfer characteristics along the pressure side of the same airfoil has been presented in an earlier publication [12].

2. EXPERIMENTAL APPARATUS

2.1. Wind tunnel

This experimental investigation was performed in the von Karman Institute Isentropic Light Piston Compression Tube Facility CT-2. The basic principles of this type of short duration wind tunnel were established about 20 years ago by Jones and Schultz [13]. Its operation is based on the isentropic compression in a large cylinder of a test gas, usually air, by means of a light weight piston. A volume of gas at well defined total pressure and temperature is generated in this way. The flow is then admitted in the test section by opening a fast acting slide valve isolating the compression cylinder from the test section. Constant freestream conditions are maintained for about 0.5 s. The flow is dumped in a large reservoir, sealed from atmosphere and eventually separated from the test section by a sonic throat in order to maintain constant aerodynamic conditions downstream of the test section.

The definite advantage of this type of wind tunnel is to provide at relatively low cost an exact similitude in terms of Mach number as well as gas to wall and gas to coolant temperature ratios with respect to the values currently observed in modern aero-engines. Further details about the VKI CT-2 facility were presented by Richards [14] and Camci [15].

2.2. Test model

The measurements described in the present paper were carried out along a film cooled nozzle guide vane mounted in a linear cascade configuration. This cascade consisted of 5 blades (4 passages). The central blade was instrumented either for static pressure or for convective heat transfer measurements (Fig. 1).

Eight independent cooling locations were considered on four different interchangeable models: 4 were located on the suction side and 4 on the pressure side (one pair on each model). Each of these emission sites consisted of two staggered rows of 30 cylindrical holes (d=0.5 mm). As in many other previous investigations, the row and hole spacing were both equal to 3 hole diameters and the upstream row was angled at 50° with respect to the blade surface. The downstream row axis was parallel to the upstream one.

As mentioned in the introduction, only the measurements along the suction surface will be considered in the present investigation. Along this surface, the 4 emission sites were respectively located at 3.9% (E1), 11.1% (E2), 20.9% (E3) and 30.1% (E4) of the suction side wetted length. These locations were selected to obtain a maximum of information on the coolant film. They do not necessarily duplicate the exact cooling configurations observed in a real engine.

Velocity distributions were only measured for the uncooled configuration. The instrumented profile was equipped with 28 static pressure tappings. The four different cooled blades for convective heat transfer measurements were made of Macor glass ceramic. They were instrumented by means of 45 platinum thin film gauges (Fig. 2). The coolant was independently supplied to each cooling site through a cylindrical cavity extending along the blade height, by means of a regenerative type cryogenic heat exchanger to simulate different coolant to freestream temperature ratios.

The cascade model was finally equipped with the necessary instrumentation (pressure and temperature probes) to record the upstream total pressure and temperature as well as the freestream turbulence intensity, the downstream static pressure distribution across at least two passages and the coolant flow characteristics.

2.3. Measurement techniques

Local wall static pressure and upstream total pressure measurements provided the isentropic Mach number distribution around the blade. A transient measurement technique, described by Schultz and Jones [16], was used to determine local wall heat fluxes. The convective heat transfer coefficient h used in this paper is defined as the ratio of the measured wall heat flux and the difference between the upstream freestream and the local wall temperatures. It is important to remark that the present heat transfer measurements provide a spanwise averaged information as the different thin films were about 20 mm long. The coolant mass flow was measured by means of a choked orifice and miniature total pressure and temperature probes continuously provided the coolant characteristics at the inlet and the exit of the plenum cavity.

The uncertainty on the measured quantities has been discussed in earlier publications [10, 12, 15]. Repeatability was found to be very good, as well for repeated measurements on a given model as for similar measurements (zero coolant mass flow) repeated on different models.

2.4. Test conditions

The test programme was conducted according to the following matrix :

$Re_{2,is}$	$M_{2,is}$	Tu_∞
2.25 10^6	1.10	1-4-6 %
2.25 10^6	0.85 - 1.25	4 %
1.50 10^6	1.10	4 %
3.0 10^6	1.10	4 %

For each test condition, 5 to 7 values of the blowing rate and 3 values of the coolant to freestream temperature ratio were considered.

3. BLADE VELOCITY DISTRIBUTION

The isentropic Mach number distributions were experimentally determined along the blade profile for different loadings. These measurements were performed at zero coolant mass flow. Typical results are presented in Figs. 3 ($M_{2,is}$ =1.10) and 4 ($M_{2,is}$=0.85); the isentropic Mach number distributions are plotted in function of the relative suction and pressure side wetted lengths. They are also compared to a numerical prediction, obtained from a two-dimensional Euler solver developed at VKI [17]. The agreement between measured and calculated values is quite good.

A velocity peak is clearly observed around 10% of the pressure side wetted length. As demonstrated in an earlier publication [12], it is responsible for the existence of a small recirculation bubble in this region. A shock is identified along the suction side ($s\simeq0.50$) at nominal conditions

($M_{2,is}$=1.10). The change in acceleration along the front part of the blade (s≃0.26) has to be kept in mind for the interpretation of the heat transfer results.

4. HEAT TRANSFER WITHOUT FILM COOLING

In order to establish a base line for our measurements, the influence of the most important freestream parameters (Mach and Reynolds numbers, turbulence intensity) was first investigated on an uncooled, smooth profile without any film cooling holes present. These results are presented as heat transfer coefficient evolutions, plotted in function of the relative suction side wetted length.

The influence of blade loading will first be discussed as it seems to be the main parameter affecting the onset of transition (Fig. 5). At nominal Mach number ($M_{2,is}$=1.10), transition starts at s≃0.26; this is shown by the random appearance of turbulent bursts when looking at the time history of the local heat flux signals. This position corresponds to the first change in velocity gradient observed in Fig. 3. As the flow reaccelerates further downstream, the complete transition process is delayed, and even stabilized until s≃0.50, which is the position at which the shock wave is observed. A fully turbulent boundary layer is then established. The transitional nature of the boundary layer between s≃0.26 and s≃0.50 is farther demonstrated by the almost constant level of the heat transfer coefficient : a laminar behaviour would show a definite decrease of the latter. It finally seems that a small separation bubble appears just upstream of the shock wave. This is shown by a decrease in heat flux measured by the last gauge before the impingement point of the shock on the suction surface. A better evidence of this phenomenon is observed at lower Reynolds number (Fig. 6).

A similar discussion can be made for $M_{2,is}$=1.25. The only difference is a slightly later establishment of the fully turbulent boundary layer. This is consistent with a small shift to the right of the velocity peak when the nozzle works at higher loading. For $M_{2,is}$=0.85, the maximum velocity peak is shifted to the left (s≃0.43), (Fig. 4). This results in a shorter transition length. A higher level of heat transfer is also, as expected, measured along the turbulent part of the boundary layer.

The influence of freestream Reynolds number is presented in Fig. 6. A first overall effect is observed on the mean level of the heat transfer coefficient. For the nominal (2.25 10^6) and highest (3.0 10^6) values of $Re_{2,is}$, the onset of transition is again observed at s≃0.26, whereas the boundary layer seems to remain laminar until the shock for the lowest value (1.5 10^6) of $Re_{2,is}$. For the highest Reynolds number value, the effects of transition result in a very quick increase of the heat transfer coefficient and a short transition length : the heat load on the blade is much more important.

The influence of turbulence intensity is shown in Fig. 7. As expected, its main effect is observed in the stagnation region and along the laminar portion of the boundary layer. It does not have any influence on the onset of transition. A definite effect is nevertheless observed along the transitional part of the boundary layer, especially at the highest turbulence intensity (Tu_∞=6%).

Tests were finally performed to verify the influence of the existence of the cooling holes on boundary layer transition. In order to avoid any undesirable film cooling effects due e.g. to recirculation between the two rows of holes, the plenum cavities were filled as carefully as possible with rubber seals. The results are presented in Fig. 8, and compared to the heat transfer distribution measured along the smooth blade. A definite effect is observed. It appears that the transition is now always triggered by the presence of the rows of holes; its onset indeed corresponds to their position. The only exception is configuration E1, where the acceleration seems to be high enough to maintain a laminar boundary layer.

5. HEAT TRANSFER WITH FILM COOLING

More than 500 heat transfer distributions were obtained for the different cooling configurations by varying both freestream and coolant conditions. Some typical examples of the information obtained from this test programme will be presented in terms of h/h_o distributions. The base line reference cases correspond to the heat transfer distributions measured along the four different profiles (E1, E2, E3, E4) equipped with cooling holes but with zero cooling mass flow (Fig. 8).

5.1. Discharge coefficient

The discharge coefficient evolutions corresponding to the four injection configurations are presented in Fig. 9 as a function of coolant to freestream pressure ratio. These tests were made for three different coolant to freestream temperature ratios. Depending upon configuration and pressure ratio, the discharge coefficient values range between 0.4 and 0.8. These tests were carried out for different freestream Reynolds numbers.

5.2. Effect of cooling flow on transition (configuration E1)

The cooling flow has a direct influence on the transition process of the suction side boundary layer when considering configuration E1. Figure 10 shows the measurement results obtained for two extreme values of the blowing rate at a relatively low coolant to freestream temperature ratio (T_{oc}/T_{01}=0.626). The measurements were performed at nominal values of $M_{2,is}$(1.10), $Re_{2,is}$ (2.25 10^6) and Tu_∞ (4%). One remarks that for the lowest value of the blowing rate (m=0.454), a relatively good protection of the blade surface is ensured just downstream of the emission location whereas higher values of the heat transfer coefficient are measured for the highest value of the blowing rate (m=1.708). It seems that the higher momentum of the coolant film induces higher local turbulence and leads to an increase of the heat transfer coefficient. One also observes that the "plateau" region identified at zero blowing rate between s≃0.25 and s≃0.50 does not exist anymore. The heat transfer coefficient increases from the onset of transition. This behaviour is somewhat similar to the one observed at zero cooling flow and highest freestream turbulence (Fig. 7). The negative effect of the coolant film, destabilizing the boundary layer and providing very little efficiency in the transition region is clearly demonstrated here. It also stresses the importance of accurate transition modeling when trying to predict this type of flow. Farther downstream, however, after the establishment of a fully turbulent boundary layer, the positive effect of the coolant film is again demonstrated.

5.3. Effect of coolant temperature

The effect of coolant temperature is demonstrated on configuration E3 (Fig. 11). The measurements were performed at nominal freestream conditions ($M_{2,is}$=1.10, $Re_{2,is}$=2.25 10^6, Tu_∞=4%), for an intermediate value of the blowing rate (m≃0.470) and for three different values of the coolant to freestream temperature ratio (T_∞/T_{01}=0.617, 0.689 and 0.769).

The results presented in figure 11 show, as expected, the decrease of heat transfer coefficient with coolant temperature. The most important differences are observed just downstream of the emission location. At constant blowing rate, increasing the coolant temperature will decrease the coolant density and increase its velocity as well as its momentum. This explains the almost monotonic increase of h/h_o at low values of T_{oc}/T_{01} compared to the decreasing/increasing behaviour at higher values of this temperature ratio. This effect was already reported earlier [Ref. 10].

The impingement of the shock wave on the suction side is still observed. Finally, it seems that, close to the trailing edge, the coolant effect is rather small when lowering the coolant temperature below a certain limit. This would lead to a sharper heat transfer coefficient increase along the suction side length when dealing, at least at this value of the blowing rate, with lower coolant temperatures.

5.4. Effect of blowing rate

The effect of blowing rate is demonstrated on configurations E1, E2 and E4 (Figs. 12 a,b,c). These measurements were again performed at nominal freestream conditions ($M_{2,is}$=1.10, $Re_{2,is}$=2.25 10^6, Tu_∞=4%) and for a relatively low coolant to freestream temperature ratio (T_{oc}/T_{01} ≃0.620). The non dimensionalized heat transfer coefficient evolution has been plotted in function of the blowing ratio at four distinct locations, respectively at 2, 10, 50 cooling hole diameters downstream of the emission location and just upstream of the trailing edge (last measurement point).

Let us first consider configuration E1 (Fig. 12a). Just downstream of the cooling holes (2 diameters), the heat transfer coefficient regularly increases with the blowing ratio. For values of m larger than 0.8, the heat transfer level with coolant emission is even more important than without. This effect is due to the high perturbating effect of the jets at the largest value of the blowing rate. Farther downstream (10 diameters) the optimum value of m seems to be around 0.8; a regular increase of h/h_o is observed for larger values. A very strong increase of h/h_o is detected 50 diameters downstream of the cooling holes. It is due to a different transition mechanism, as explained in section 5.2. Close to the trailing edge, an almost monotonic decrease of h/h_o is measured.

Similar conclusions can be drawn when looking at the results obtained for configuration E2 (Fig. 12b). The major difference however is that the non dimensionalized heat transfer coefficient value always remains below 1. Very good performances of the coolant film are observed along the suction side, even if they deteriorate somewhat close to the injection holes (2 and 10 diameters) when increasing the blowing rate. An optimum value of the latter would be of the order of 0.65 ... 0.75 for the present configuration.

If one finally considers configuration E4 (Fig. 12c), it appears that only the region just downstream of the cooling holes is negatively affected by the highest blowing rates. Farther downstream, the non dimensionalized heat transfer coefficient continuously decreases with increasing values of m. A h/h_o value equal to 0.55 is even measured in the trailing edge region for the highest blowing rate. The optimal value of m would here be of the order of 0.75 ... 0.85.

5.5. Effect of Reynolds number

The effect of Reynolds number on configuration E2 is presented in figures 13 a,b,c. The measurements were performed at nominal Mach number ($M_{2,is}$=1.10) and freestream turbulence intensity (Tu∞=4%) and for a low coolant to freestream temperature ratio (T_{oc}/T_{01} ≃0.62). The non dimensionalized heat transfer coefficient is plotted in function of the blowing ratio at three different locations, respectively 2, 10 and 50 cooling hole diameters downstream of the emission location.

By comparing the results obtained for the three considered Reynolds numbers, a definite difference appears between the lowest (1.5 10^6) and the two highest (2.25 10^6 and 3.0 10^6) values. Small differences are measured in the latter case whereas much higher heat transfer coefficients are identified for $Re_{2,is}$=1.50 10^6. This is due to the nature of the boundary layer. At this low Reynolds number, it is in a laminar state without cooling and in a highly transitional state with cooling. Especially at 50 diameters downstream of the emission location (Fig. 13 c) the detrimental effect on h/h_o of this early transition is somewhat compensated by the coolant layer as the blowing ratio increases. The same effect was observed along the pressure side of this airfoil [Ref. 12].

6. SUMMARY - CONCLUSIONS

Experimental results have been obtained from a systematic research program on external convective heat transfer measurements with film cooling along the suction side of a high pressure turbine nozzle guide vane. The major effects of the different main and coolant flow parameters on the heat transfer coefficient have been identified.

A better thermal protection is obtained for all configurations when the blowing ratio is increased, except :

- in the near hole region (up to 10-15 cooling hole diameters downstream of the emission site);

- in the transitional region, where the coolant film induces an earlier and more abrupt transition to the turbulent status of the boundary layer.

The present investigation not only demonstrates the heat transfer coefficient variations due to geometrical and aerothermal modifications but also emphasizes the boundary layer perturbation due to the coolant layers. It also stresses the importance of an accurate transition and turbulence modeling when trying to numerically predict this type of flow.

Acknowledgments

The authors wish to thank SNECMA for the financial support and the permission to publish the paper and the technical personnel of the VKI Turbomachinery

Department for the assistance throughout the testing program.

REFERENCES

1. Goldstein, R.J.: Film Cooling. Advances in Heat Transfer, Vol. 7, Academic Press, 1971, pp 321-379.

2. Teekaram, A.J.H.; Forth, C.J.P.; Jones, T.V.: Film cooling in the presence of mainstream pressure gradients. ASME Paper 90-GT-334, 1990.

3. Sinha, A.K.; Bogard, D.G.; Crawford, M.E.: Film cooling effectiveness downstream of a single row of holes with variable density ratio. ASME Paper 90-GT-43, 1990.

4. Lander, R.D.; Fish, R.W.; Suo, M.: External heat transfer distribution on film cooled turbine vanes. J. of Aircraft, Vol. 9, No 10, 1972, pp 707-714.

5. Nicolas, J. & Le Meur, A.: Curvature effects on a turbine blade cooling film. ASME Paper 74-GT-156, 1974.

6. Ito, S.; Goldstein, R.J.; Eckert, E.R.G.: Film cooling of a gas turbine blade. J. of Engineering for Gas Turbine and Power, Vol. 100, 1978, pp 476-481.

7. Daniels, L.C.: Film cooling of gas turbine blades. PhD Thesis, University of Oxford, UK, 1979.

8. Dring, R.P.; Blair, M.F.; Joslyn, H.D.: An experimental investigation of film cooling on a turbine rotor blade. J. of Engineering for Gas Turbine and Power, Vol. 102, No 1, 1980, pp 81-87.

9. Horton, F.G.; Schultz, D.L.; Forest, A.E.: Heat transfer measurements with film cooling on a turbine blade profile in cascade. ASME Paper 85-GT-117, 1985.

10. Camci, C. & Arts, T.: Short duration measurements and numerical simulation of heat transfer along the suction side of a film cooled gas turbine blade. J. of Engineering for Gas Turbine and Power, Vol. 107, No 4, 1985, pp 991-997.

11. Nirmalan, V. & Hylton, L.D.: An experimental study of turbine vane heat transfer with leading edge and downstream film cooling. ASME paper 89-GT-69, 1989.

12. Arts, T. & Bourguignon, A.E.: Behaviour of a two rows of holes coolant film along the pressure side of a high pressure nozzle guide vane. ASME Paper 89-GT-186, 1989. J. of Turbomachinery, Vol. 112, No 3, 1990, p 512.

13. Jones, T.V.; Schultz, D.L.; Hendley, A.D.: On the flow in an isentropic free piston tunnel. ARC R&M 3731, 1973.

14. Richards, B.E.: Heat transfer measurements related to hot turbine components in the von Karman Institute Hot Cascade Tunnel. 'Testing and Measurement Techniques in Heat Transfer and Combustion' AGARD CP 281, Paper 6, 1980.

15. Camci, C.: An experimental and theoretical heat transfer investigation of film cooling on a high pressure gas turbine blade. PhD Thesis, Katholieke Universiteit Leuven, Belgium, 1985.

16. Schultz, D.L. & Jones, T.V.: Heat transfer measurements in short duration hypersonic facilities. AGARDograph 165, 1973.

17. Arts, T.: Etude de l'écoulement tridimensionnel complet dans un étage de turbine transsonique. PhD Thesis, Université Catholique de Louvain, Belgium, 1982.

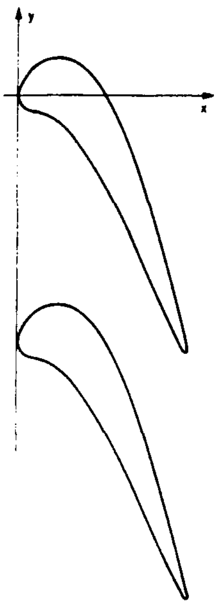

Fig.1 - Cascade model

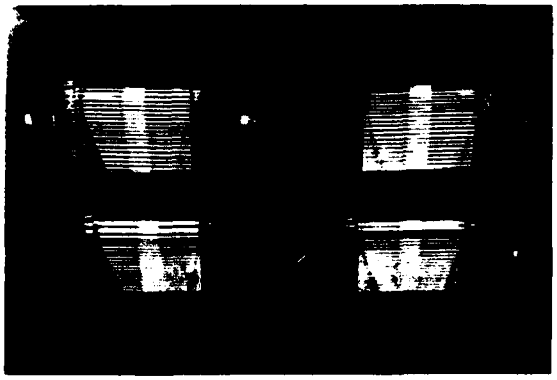

Fig.2 - Heat transfer models

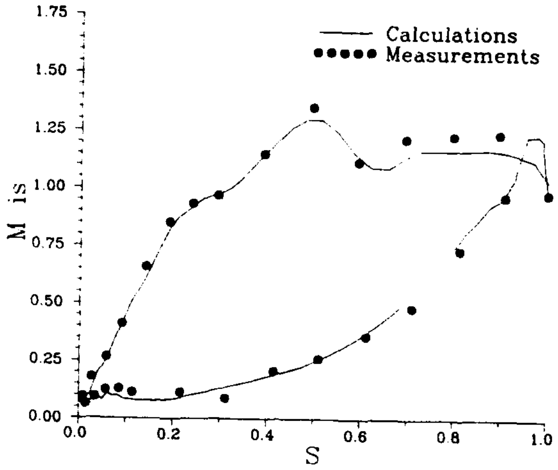

Fig.3 - Blade velocity distribution ($M_{2,is} = 1.10$)

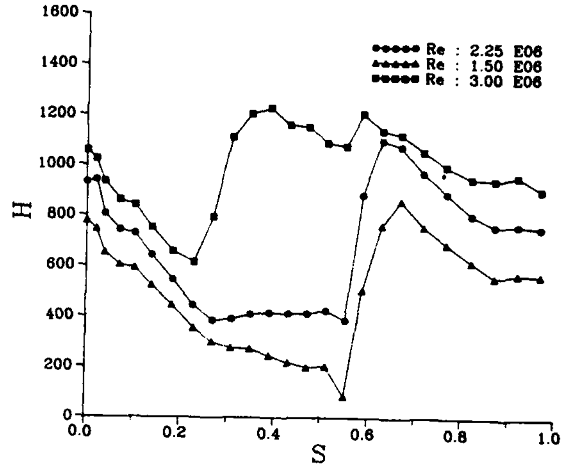

Fig.6 - Heat transfer without film cooling
Influence of Reynolds number

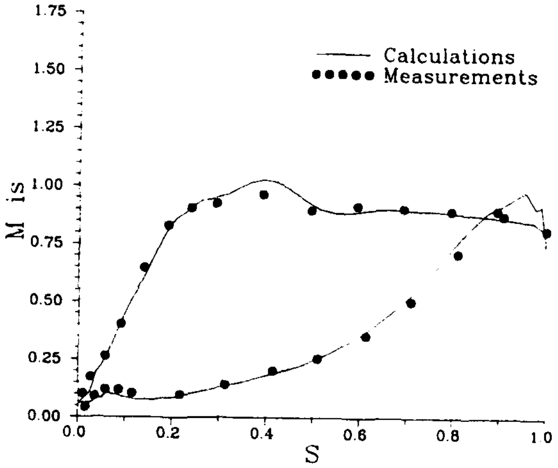

Fig.4 - Blade velocity distribution ($M_{2,is} = 0.85$)

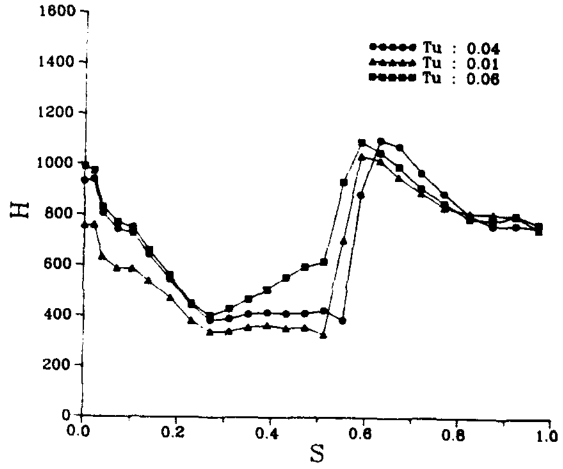

Fig.7 - Heat transfer without film cooling
Influence of freestream turbulence intensity

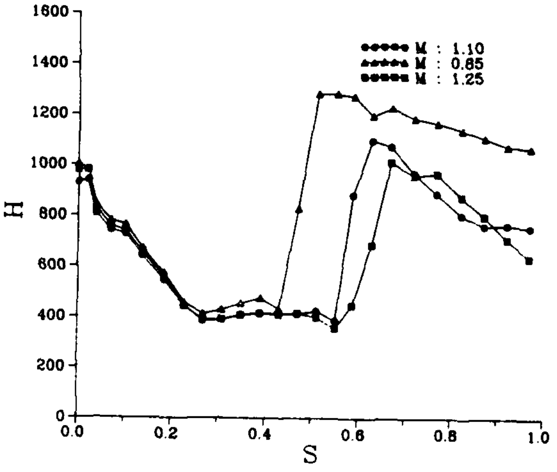

Fig.5 - Heat transfer without film cooling
Influence of blade loading

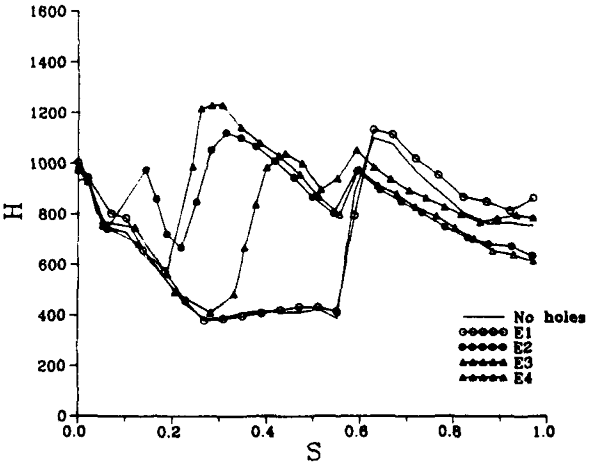

Fig.8 - Heat transfer without film cooling
Influence of the existence of the cooling holes

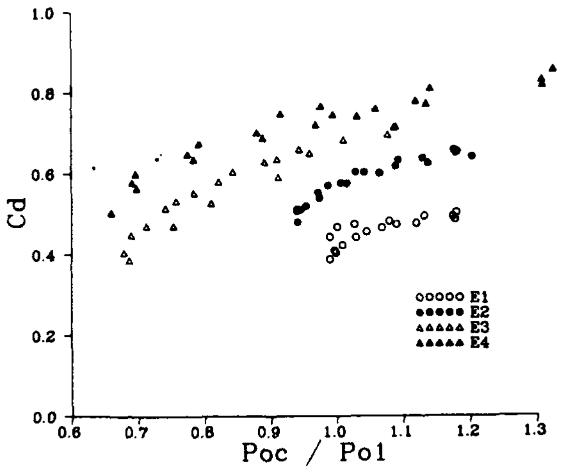

Fig.9 - Discharge coefficients

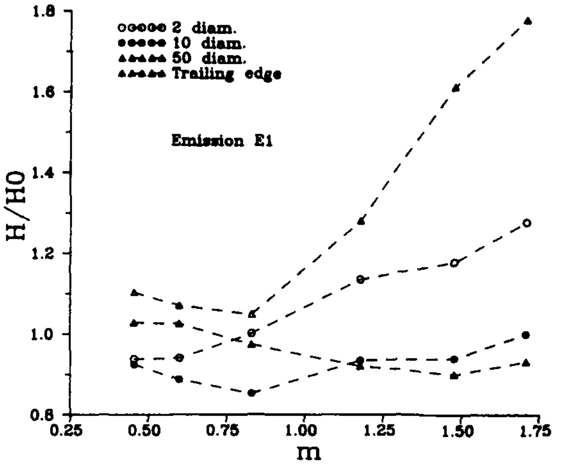

Fig.12a - Effect of blowing rate (E1)

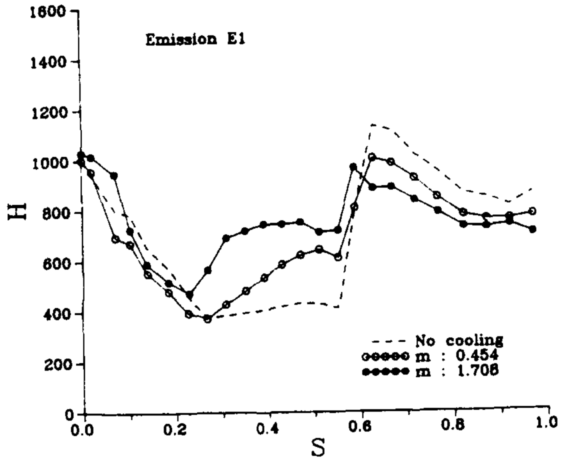

Fig.10 - Effect of cooling on transition (E1)

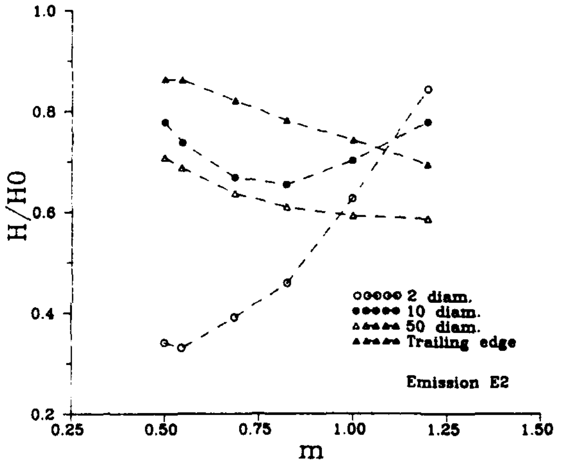

Fig.12b - Effect of blowing rate (E2)

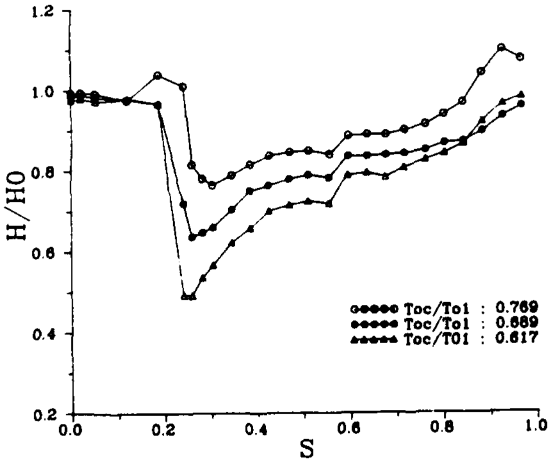

Fig.11 - Effect of coolant temperature (E3)

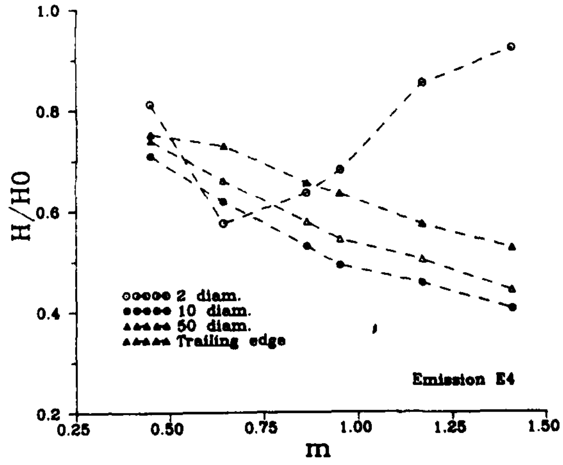

Fig.12c - Effect of blowing rate (E4)

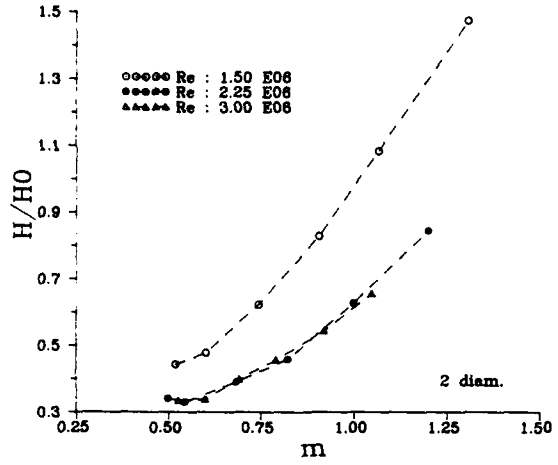

Fig.13a - Effect of Reynolds number (E2)

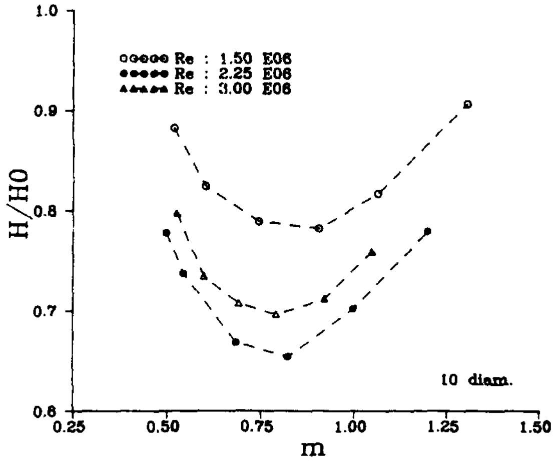

Fig.13b - Effect of Reynolds number (E2)

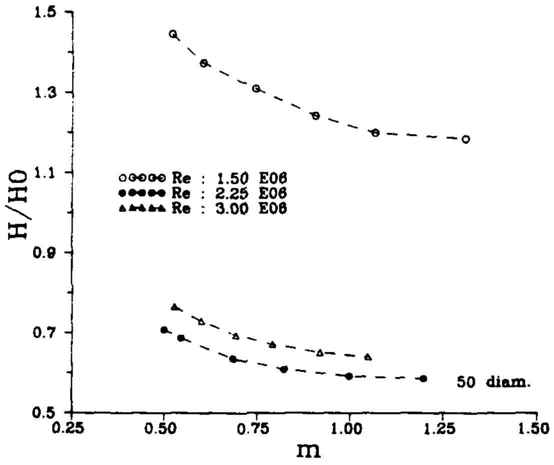

Fig.13c - Effect of Reynolds number (E2)

Discussion

QUESTION 1:

DISCUSSOR: P. Harasgama, ABB

Have you assessed the effect of blowing rate on the actual heat flux and compared this with the uncooled heat flux in the laminar regime?

AUTHOR'S REPLY:

No, we did not. Comparisons were done based on the heat transfer coefficient only.

QUESTION 2

DISCUSSOR: P. Harasgama, ABB

Did you perform experiments with more than one row of cooling holes (i.e., 2, 3 or 4) operating simultaneously?

AUTHOR'S REPLY:

Those configurations were not considered in the present program. The program only focused on individual configurations.

ETUDE EXPERIMENTALE DU TRANSFERT DE CHALEUR PRES D'UNE PAROI PLANE CHAUFFEE EN PRESENCE D'INJECTIONS MULTIPLES (ECOULEMENT SUBSONIQUE).

E. Foucault
P. Deniboire
J-L. Bousgarbiès
Laboratoire d'Etudes Aérodynamiques (URA 191)
40 Avenue du recteur Pineau
86022 Poitiers CEDEX France

J-J. Vullierme
E. Dorignac
Laboratoire d'Etudes Thermiques (URA 1403)
ENSMA rue Guillaume VII
86034 Poitiers France

1. RESUME :

L'article présente les résultats d'une étude expérimentale détaillée des champs aérodynamique et thermique au sein de la couche-limite d'une paroi plane chauffée en présence d'injections localisées d'air chaud. Pour deux valeurs du rapport des vitesses jets/écoulement principal (0,6 et 1,6) les trois composantes du vecteur vitesse et la température locale de l'écoulement sont mesurées en de nombreuses positions, respectivement par anémométrie LASER Doppler à l'aide d'une sonde fil froid. Une carte de la température de la paroi plane est obtenue au moyen d'une caméra infra-rouge. Les résultats montrent l'aspect fortement tridimensionnel de l'écoulement en aval des jets qui est dominé par la présence de structures tourbillonnaires. Ces dernières génèrent des zones de forts taux de turbulence et ont une grande influence sur le champ de température dans le sillage des jets. Pour le plus grand des deux rapports de vitesses considérés, l'écoulement transversal pénètre sous les jets en aval des orifices d'injection et s'oppose ainsi au transfert de chaleur.

2. INTRODUCTION :

L'augmentation du rendement des moteurs d'avion est en partie rendue possible grâce à un accroissement de la température des gaz à l'entrée de la turbine. Cependant cette température élevée a un effet néfaste sur la bonne tenue mécanique et la longévité des aubes de la turbine, aussi est-il nécessaire de refroidir leurs parois placées dans l'écoulement d'air surchauffé. Ce refroidissement est en partie assuré par une circulation d'air frais à l'intérieur de l'aube et également par l'émission d'un film d'air frais en surface, grâce à des injections localisées à travers la paroi.

L'objectif assigné au film de refroidissement est l'obtention d'une protection thermique de la paroi efficace, sans pour autant affecter les performances aérodynamiques de la turbine d'une manière trop pénalisante. Pour parvenir à un tel compromis il est nécessaire d'appréhender de manière complète et détaillée les nombreux phénomènes aérothermiques, souvent très complexes, qui apparaissent dans une couche-limite en présence d'injections discrètes d'air frais.

De nombreux travaux ont déjà été consacrés à l'étude de l'écoulement généré par un ou plusieurs jets débouchant au sein d'un écoulement transversal. Les premiers d'entre eux avaient pour objectif la prévision de la trajectoire de l'axe du jet en supposant que la distribution de vitesse moyenne vérifie une loi affine - cf : Keffer et Baines (1963) Chassaing & al. (1974) -. Cependant des expériences ont très rapidement révélé la présence de structures tourbillonnaires dont certaines dominent l'écoulement en aval de l'injection et ont une influence directe sur la forme de la section droite du jet - cf : Kamotani et Grebber (1972); Fearn et Weston (1974); Moussa & al. (1977) -. Des méthodes numériques, tenant compte de l'existence de ces tourbillons, ont alors été développées par Le Grivès (1978), Jones et Mc Guirk (1979), Broadwell et Breidenthal (1984) et Kulisa & al. (1990).

L'amélioration des modèles numériques qui, grâce à la puissance croissante des moyens de calcul deviennent de plus en plus sophistiqués, exige des mesures expérimentales plus complètes et précises, aussi bien pour la validation du code que pour mieux appréhender les phénomènes. Une étude détaillée du champ de vitesse a été réalisée par Crabb & al. (1981) puis par Andréopoulos et Rodi (1984), dans le cas d'un jet unique débouchant perpendiculairement dans un écoulement transversal. Le cas d'une rangée de jets inclinés a récemment été étudiée par Pietrzyk & al. (1988). Ils se sont intéressés à l'influence du taux d'injection sur les vitesses moyennes et leurs fluctuations et donnent des cartes de ces grandeurs dans le plan vertical du jet. Dans une étude récente Chen et Hwang (1991) ont considéré successivement le cas d'une rangée puis de deux rangées de jets chauds injectés perpendiculairement dans un écoulement transversal froid. Ils ont obtenus des profils de température et de vitesse longitudinale moyennes et fluctuantes dans le plan médian vertical de la section d'essais pour de grandes valeurs du taux d'injection.

Les résultats de la présente étude concernent le cas d'une rangée de jets chauds débouchant au sein de la couche-limite d'une paroi plane chauffée placée dans un écoulement transversal froid. Les injections sont assurées par l'intermédiaire de cinq tubes longs et inclinés. L'objectif de ce travail est d'obtenir, sur la même installation, un ensemble de résultats concernant à la fois les distributions de vitesse et de température, dans plusieurs plans parallèles à la direction de l'écoulement principal. Les expériences sont réalisées en liaison avec l'équipe de F. Lebœuf à L'Ecole Centrale de Lyon, qui développe un modèle de calcul de film de refroidissement. La mise au point de ce code et sa validation exige de disposer d'une base de données expérimentales aérothermiques rendant compte du caractère fortement tridimensionnel de l'écoulement. L'allure de sa structure est, dans un premier temps, déduite de visualisations par tomographie LASER. Des mesures de vitesses sont effectuées par ADL et la température locale, au sein de l'écoulement, est relevée par une sonde à fil froid. Une caméra infra-rouge permet de connaître la température à la surface de la paroi plane.

3. DISPOSITIF D'ESSAIS :

Les expériences ont été effectuées dans une soufflerie subsonique de type Eiffel, dont la veine d'essais (section droite rectangulaire de 1000 mm de long sur 300 mm de large et 400 mm de haut) est placée à l'aval d'un convergent de rapport de contraction 4/1. Le plancher de cette veine constitue la paroi plane à travers laquelle ont été aménagés les orifices d'injection.

L'air est injecté dans la couche-limite de cette paroi par une série de cinq trous (Fig. 1). Les injections sont assurées par cinq tubes de sections droites circulaires (diamètre d = 5 mm, longueur 20 d), inclinés d'un angle de 45° par rapport à la direction de l'écoulement principal. Elles sont régulièrement espacées suivant l'envergure (distance 3 d) et l'abscisse d'injection est située à une distance de 100 d de l'entrée de la veine d'essais.

Les jets sont chauffés à une température de l'ordre de 60°C, alors que l'écoulement principal est à la température ambiante. Le plancher de la veine est maintenu à une température constante grâce à une circulation d'eau thermostatée. Pour les expériences rapportées par la suite, la température de paroi a été fixée à 60°C.

Le plancher de la veine est constitué d'un "sandwich" formé par une plaque de PVC en contact avec l'écoulement, et par une plaque inférieure en cuivre. Celle-ci est maintenue à une température constante par une circulation d'eau chaude thermostatée. Pour les expériences rapportées ici, la température de ce radiateur a été fixée à 60°C et est contrôlées au moyen de thermocouples implantés à 0,8 mm au dessous de la face supérieure de la plaque en PVC. Ces derniers permettent de mesurer la distribution de température dans la paroi plane à une profondeur connue (y = 0,8 mm).

Les cartes de température de surface ont été relevées au moyen d'une caméra infra-rouge placée au dessus de la veine d'essais. La paroi supérieure de cette veine est formée de plaques permutables. Sur l'une d'elles un orifice circulaire a été ménagé afin de permettre le passage de l'objectif de la caméra lors des essais.

Les tomographies de l'écoulement suivant 3 directions orthogonales, sont réalisées avec la technique classique de la nappe lumineuse obtenue à partir d'un faisceau LASER et d'un jeu de lentilles cylindriques et sphériques. L'écoulement est ensemencé au moyen d'un aérosol d'huile végétale mélangé à

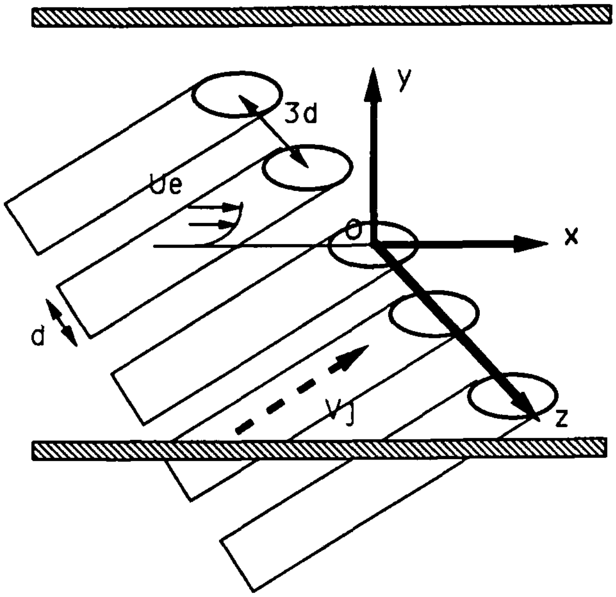

Fig. 1 : schéma et système de coordonnées

l'air des jets. Les images des visualisations sont enregistrées par vidéo ou photographie. Dans le premier cas la restitution fait appel à un traitement numérique des images.

Les mesures de la vitesse locale instantannée ont été réalisées à l'aide d'une chaîne deux composantes comportant deux compteurs de périodes et deux décaleurs de fréquences DANTEC. Les valeurs des composantes normale (v) et transversale (w) de la vitesse ne peuvent être obtenues que si le volume de mesure est parallèle à la direction de l'écoulement principal. Cette disposition est obtenue en plaçant un miroir plan orienté à 45° dans la partie aval de la veine d'essais. Les trois faisceaux LASER pénètrent toujours dans la veine perpendiculairement mais, après réflexion sur le miroir, leur volume d'intersection se trouve placé dans la direction de l'écoulement principal (cf: Fig. 2). Un aérosol d'huile végétale permet d'ensemencer les jets ainsi que l'écoulement principal en particules.

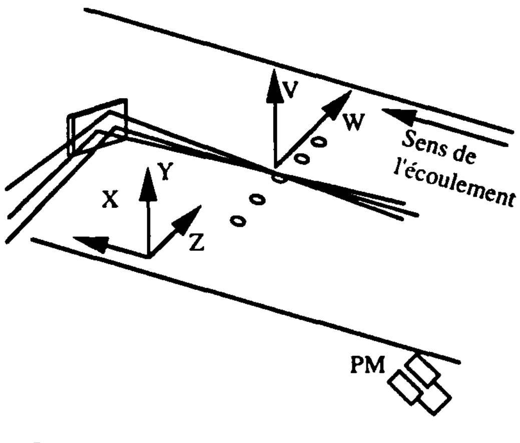

Fig. 2 : schéma du dispositif de mesure des composantes v et w

La température locale a été mesurée, simultanément à la vitesse, à l'aide d'une sonde fil froid (Ø = 5 µm, l = 0,5 mm), placée immédiatement à l'aval du volume de mesure de la chaîne ADL. Les compteurs de cette chaîne, ainsi que le pont de mesure de température sont reliés à une carte d'acquisition de données implantée dans un micro-ordinateur de type compatible-PC. Ce dispositif permet la mesure simultannée des valeurs instantannées des deux composantes de la vitesse (u,v ou v,w) et de la température. Il est ainsi possible de calculer les tensions de Reynolds et les flux de diffusion turbulente de chaleur. Les différentes quantités moyennes présentées dans cet article ont été calculées à partir d'échantillons composés de 1000 valeurs instantannées.

4. RESULTATS :

Le domaine exploré est défini par $-1 \leq x^* \leq 10$; $y^* \leq 6$ et $-1,5 \leq z^* \leq 1,5$. Le système de coordonnées est centré au point d'intersection de la paroi plane et de l'axe du jet central (cf: Fig. 1). Les coordonnées réduites x^*, y^* et z^* sont déduites des valeurs dimensionnelles en prenant le diamètre du tube d'injection comme échelle de longueur.

Les expériences ont été réalisées pour des valeurs du taux d'injection successivement égales à 0,6 et 1,6; ce paramètre étant défini comme le rapport $r = \rho_j v_j / \rho_e u_e$ avec ρ_j et v_j désignant respectivement la masse volumique de l'air injecté (à la température T_j) et sa vitesse moyenne, tandis que ρ_e et u_e représentent la masse volumique et la vitesse de l'écoulement transversal à l'extérieur de la couche-limite.

4.1. Vitesses moyennes :

les figures 3, 4, 5, et 6 donnent quelques exemples de profils de la projection du vecteur vitesse moyenne dans des plans parallèles à la direction de l'écoulement moyen ($z^* = c^{te}$). Les deux premières figures correspondent à la distribution de vitesse enregistrée dans le plan médian ($z^* = 0$) pour chacun des deux rapports d'injection étudiés. Pour le plus grand d'entre eux ($r = 1,6$) la présence du jet se traduit par un ralentissement des couches de fluide proches de la paroi (cf: profil enregistré à $x^* = -1$). Ce phénomène n'est plus perceptible lorsque, à la même abscisse, le taux d'injection est ramené à 0,6. On obtient alors un profil identique à celui enregistré en dehors de la zone d'influence des jets ($z^* = 20$) pour la même abscisse, où une traversée de référence a été réalisée. Le profil mesuré dans le plan $z^* = 2,5$ pour $r = 1,6$ (Fig. 4) est également semblable à ce profil de référence, alors qu'en $z^* = 0,4$ (Fig. 3) l'effet de ralentissement est encore notable.

Les mesures réalisées à la verticale de l'orifice d'injection, montrent que le débit de fluide provenant du jet est plus important dans la moitié aval de la section de sortie, la déviation étant plus grande lorsque r diminue. Cette observation est en accord avec celle effectuée par Andréopoulos et Rodi (1984) dans le cas d'un jet transversal alimenté par un tube long (rapport longueur/diamètre = 12, valeur voisine de celle choisie dans la présente étude), débouchant perpendiculairement au sein d'un courant transversal. Dans le cas d'un tube incliné à 35°, mais plus court (rapport longueur/ diamètre égal à 3,5), Pietrzyk et al. (1988) observent une déformation plus faible du jet par l'écoulement principal. Il faut par ailleurs noter que l'épaisseur de la couche-limite de l'écoulement principal n'est que 0,4 d dans leur dispositif, contre 1,5 d dans le cas de la presente étude.

En aval de l'injection (Fig. 3 et 4) et au voisinage de la paroi plane, la zone de sillage est très différente suivant la valeur du taux d'injection. Pour le plus grand d'entre eux ($r = 1,6$) on remarque un effet de blocage de l'écoulement transversal par le fluide du jet qui s'observe nettement sur les profils tracés Fig. 4 entre $x^* = 1$ et 3. Dans cette région la vitesse des couches fluides proches de la paroi ($y^* \leq 0,2$) est bien plus faible que celle mesurée lorsque le rapport des vitesses est moins important (eg : $r = 0,6$; Fig. 3). Ce ralentissement n'est pas seulement observé dans le plan de symétrie du jet ($z^* = 0$), mais également de part et d'autre de celui-ci sur une largeur d'environ 1 d. Il faut par ailleur noter qu'aucun écoulement retour n'est mis en évidence dans ce sillage, contrairement à ce qui a été observé par Pietrzyk et al. dans le cas d'un tube d'injection court. L'idée émise par ces auteurs, selon laquelle la géométrie du dispositif d'amenée du fluide a une très forte influence sur l'écoulement dans la section de sortie du jet et immédiatement en aval, se trouve ainsi renforcée.

La figure 6 met en évidence une autre particularité de l'écoulement obtenu lorsque le taux d'injection est de 1,6. Dans ce plan $z^* = 1,5$, situé à égale distance de deux jets, on remarque la très nette déviation de l'écoulement transversal vers la paroi plane. Cette déclinaison se manifeste dès que le fluide de la couche-limite approche les orifices d'injection. L'épaisseur de la couche affectée par ce phénomène croît avec l'abscisse, elle est d'environ 0,7 d à l'origine (ie : $x^* = 0$) et de 2,6 d à $x^* = 10$. Dans la région ainsi définie, la composante normale du vecteur vitesse prend des valeurs négatives. Cette particularité de l'écoulement trouve son origine dans la présence d'une paire de tourbillons contra-rotatifs situés de part et d'autre du jet. L'existence de cette structure tourbillonnaire est bien connue dans le cas des jets perpendiculaires depuis les travaux de Moussa et al. confirmés par ceux de Kamotani et Greber (1972), puis de Crabb et al. (1981) et l'étude détaillée d'Andréopoulos et Rodi (1984). La présence de ces tourbillons jumeaux dans le cas des jets inclinés étudié ici, se retrouve sur les cartes des vecteurs vitesse obtenues dans les plans transversaux $x^* = c^{te}$ dont un exemple est présenté Fig. 7. Ces profils, déduits des vitesses normale et transversale mesurées dans le plan $x^* = 2$, confirment l'existence de deux tourbillons contra-rotatifs d'axes sensiblement perpendiculaires au plan de la figure. Cette configuration du champ des vitesses dans un plan transversal est tout à fait semblable à celle observée dans le cas d'une injection normale (Réf. [17] et [1]). Une des conséquences de la présence des tourbillons est l'entraînement de fluide, situé initialement dans les parties hautes de la couche-limite, vers la paroi plane. Ce mouvement descendant est localisé de part et d'autre du plan $z^* = 1,5$. La portion de fluide de l'écoulement transversal ainsi déviée, se trouve incorporée dans l'enroulement et se glisse sous le jet. La présence de ce mouvement entrant

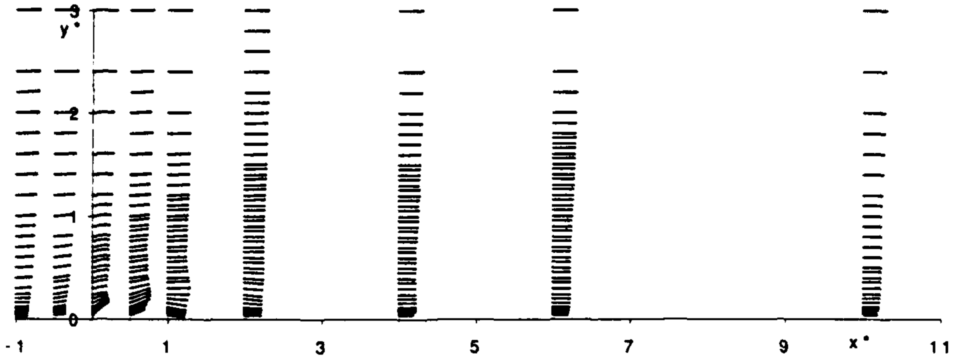

Fig. 3 : Profils de la vitesse moyenne réduite dans le plan z* = 0 pour r = 0,6

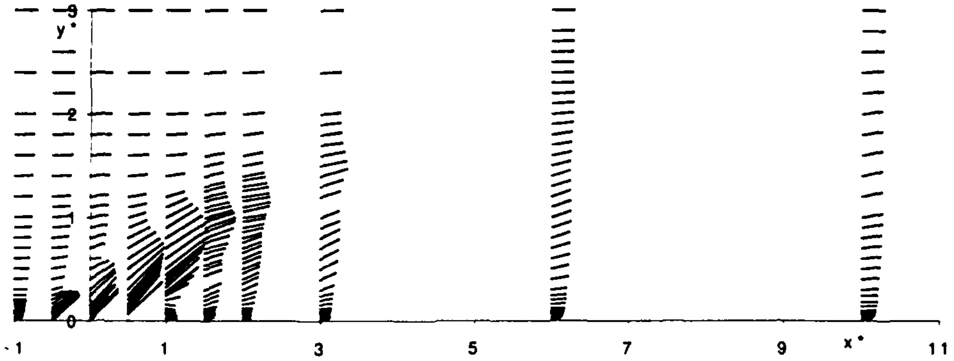

Fig. 4 : Profils de la vitesse moyenne réduite dans le plan z* = 0 pour r = 1,6

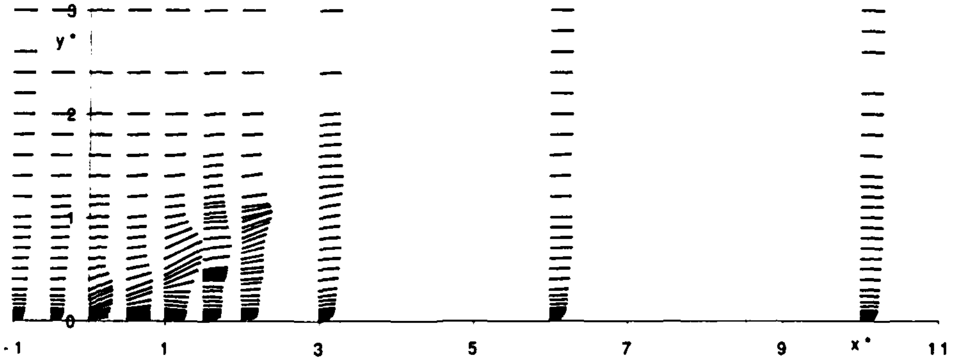

Fig. 5 : Profils de la vitesse moyenne réduite dans le plan z* = 0,4 pour r = 1,6

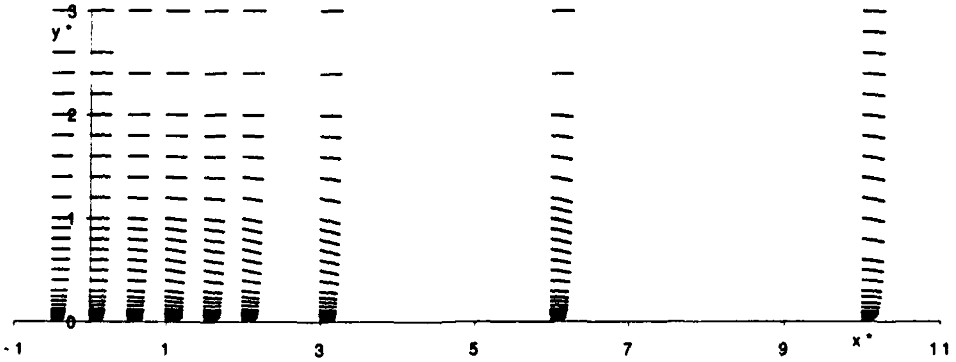

Fig. 6 : Profils de la vitesse moyenne réduite dans le plan z* = 1,5 pour r = 1,6

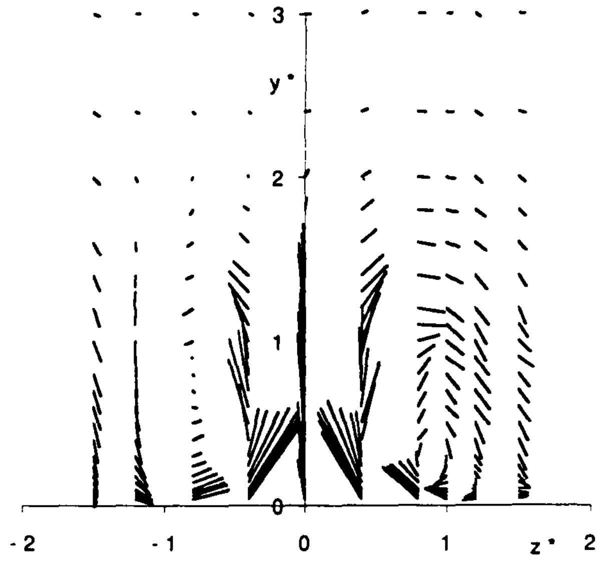

Fig. 7 : Profils de la vitesse moyenne réduite dans le plan $x^* = 2$ pour $r = 1,6$

vers le plan $z^* = 0$ est confirmée par la vue en coupe de l'écoulement, obtenue par tomographie LASER, pour la même valeur du taux d'injection ($r = 1,6$). Le cliché présenté Fig.8 est une image numérisée extraite d'une séquence vidéo également enregistrée dans le plan $x^* = 2$. On peut observer la trace du jet central et de ses voisins de gauche et de droite, et constater, sous chacun d'eux, la présence de fluide non ensemencé, c'est à dire provenant de la couche-limite transversale et non du jet. La frontière amont du jet, est étirée sous l'influence combinée des deux tourbillons et de la courbure provoquée par l'écoulement principal, tandis que la partie aval se trouve au contraire comprimée. Il s'ensuit une déformation rapide de la section droite du jet qui prend l'allure d'un "haricot". Cette forme rappelle celle des surfaces isobares obtenues dans le cas d'un jet unique débouchant perpendiculairement (Réf.[19]).

4.2. Température moyenne :

L'évolution, en fonction de l'abscisse x^*, des profils de température dans le plan de symétrie du jet central ($z^* = 0$) est présentée sur la figure 9. La température réduite utilisée est définie par $T^* = (Tm-Te)/(Tj-Te)$, où Tm désigne la température moyenne locale mesurée au fil froid, tandis que Te et Tj représentent respectivement la température de l'écoulement transversal hors couche-limite et la température de l'air injecté. Dès l'aval de l'orifice d'injection ($x^* = 1$), les profils présentent un maximum qui s'élargit au fur et à mesure que x^* augmente, alors que son intensité va en diminuant. L'ordonnée y^* de ce maximum est toujours légèrement supérieure à celle correspondant au maximum de vitesse du profil tracé Fig. 4. Cette non coïncidence locale des profils de température et de vitesse a déjà été notée par Kamotani et Greber (1972) et a également été observée par Crabb & al. (1981) en comparant les champs de vitesse et de concentration dans le cas d'un jet ensemencé d'hélium.

De part et d'autre du plan $z^* = 0$, les profils de température moyenne mesurés dans le sillage proche du jet ($1 \le x^* \le 4$) présentent deux maximums comme l'indiquent les courbes de la figure 10 (plan $z^* = 0,4$). Au delà de $x^* = 4$, au contraire, les profils sont semblables à ceux obtenus dans le plan $z^* = 0$, mais la position du maximum de température est plus proche de la paroi lorsqu'on s'écarte du plan de symétrie du jet. Plus généralement, la déformation du champ de vitesse à travers une section droite du jet, signalée précédemment, se répercute au niveau de la distribution de température. Ce phénomène peut être observé sur les traces des surfaces isothermes dans le plan transversal $x^* = 2$ présenté Fig 11. Tous les contours jusqu'à l'isotherme $T^* = 0,2$ ont la forme caractéristique de haricot mise en évidence sur les vues en coupe lors des visualisations. De l'air frais, provenant de l'écoulement transversal, est entraîné sous celui du jet, au sein de l'enroulement créé par les tourbillons contra-rotatifs, puis remonte sous le jet au niveau du plan de symétrie (ici $z^* = 0$). Il s'agit là d'un phénomène néfaste pour l'obtention d'un film de refroidissement qui, en principe, doit former une couche protectrice entre la paroi et l'écoulement transversal. Les distributions de température de paroi, présentées Fig. 11 & 12, montrent que dans le sillage proche du jet, il existe une couche protectrice lorsque le taux d'injection est petit ($r = 0,6$) mais qu'elle disparaît pour un taux plus élevé ($r = 1,6$). Ces cartes ont été obtenues au moyen d'une caméra infra-rouge étalonnée à l'aide des thermocouples implantés dans la paroi plane (cf : E. Dorignac - J-J. Vullierme). On peut observer, pour $r = 0,6$ une température réduite dans le sillage des jets bien supérieure à celle régnant sur les parties de plaque situées entre des jets voisins. Lorsque $r = 1,6$ au contraire, la température de la plaque présente un minimum derrière chaque jet. L'addition des informations obtenues par la techniques du fil froid et la caméra infra-rouge (Réf. [7]) montrent alors que les profils de température à la verticale de ces régions passent par une valeur minimum qui s'approche de celle de l'air extérieur à la couche-limite. La distance de ce minimum à la paroi est très petite (ie : inférieure à 0,06 d).

La présence d'une poche d'air frais issu de la région externe de l'écoulement transversal, peut également être observée sur le réseau d'isothermes présenté Fig. 14. Il s'agit des températures réduites mesurées dans le plan de symétrie du jet central ($z^* = 0$) pour un taux d'injection de 1,6. On peut observer que la ligne $T^* = 0,2$ située immédiatement derrière le jet, se referme sur la paroi à $x^* = 3,6$ délimitant ainsi une zone occupée par du fluide dont la température est inférieure à celle de la paroi. Ce réseau de courbes montre par ailleurs que, pour le rapport de vitesses considéré, le jet n'est que faiblement dévié par l'écoulement transversal puisqu'une partie du fluide chaud émerge à la frontière de la couche-limite. L'isotherme $T^* = 0,5$ atteint la cote $y^* = 1,5$ et la surface délimitée par $T^* = 0,3$ (qui peut être considérée comme la zone où l'influence thermique du jet est perçue de manière encore sensible) s'élève jusqu'à $y^* = 2$ et s'étend dans la direction de l'écoulement transversal jusqu'à environ 8 diamètres en aval de l'injection.

4.3. Fluctuations de vitesse :

De manière générale les valeurs des fluctuations de vitesse sont maximales dans les zones où les profils des valeurs moyennes présentent les plus forts gradients, c'est à dire dans les régions frontières entre le fluide du jet et de la couche-limite transversale. Les contours d'iso-taux de turbulence mesurés dans le plan $z^* = 0$ pour $r = 1,6$ (cf : Fig. 15) illustrent cette propriété. Les valeurs portées sur ce graphique concernent le taux de turbulence défini par $t = \sqrt{\overline{u'^2} + \overline{u'^2}} / U_e{}^2$, u' et v' désignant les fluctuations de vitesses longitudinale et normale. La zone où l'on trouve les plus grandes valeurs de t sont situées le long de la frontière supérieure du jet, immédiatement après sa sortie, c'est à dire là où les profils de vitesse mesurés dans le plan $z^* = 0$ (Fig. 4) présentent les variations les plus fortes suivant y^*. On note également de fortes fluctuations de vitesse juste derrière l'orifice d'injection, lieu où les mesures de température ont révélé la présence d'une poche d'air frais. Pietrzyk & al. (1988) ont observé le même phénomène et l'attribuent à l'existence d'une zone décollée avec la présence d'un écoulement retour au voisinage de la paroi plane. Ce type d'écoulement n'a pas été observé ici mais dans la région concernée le vecteur vitesse varie fortement en direction et en intensité comme le montre par exemple le profil mesuré à $x^* = 1$ (cf : Fig.4). La présence de cette zone de cisaillement entre le fluide du jet et le fluide de la couche-limite pénètrant dessous, génère les fortes fluctuations observées. Leur niveau maximum de 35 % est supérieur à celui mesuré par Pietrzyk & al. (26 %) mais pour un angle d'incidence de seulement 35°. Jubran et Brown trouvent une valeur de 30 % dans le cas d'une double rangée de jets inclinés de 30°, alors que dans les expériences conduites par Chen et Hwang (1991), le taux de fluctuation de la seule composante longitudinale atteint 40 %. Dans ce dernier cas les jets sont normaux à l'écoulement transversal et le taux d'injection particulièrement élevé ($r = 4,6$).

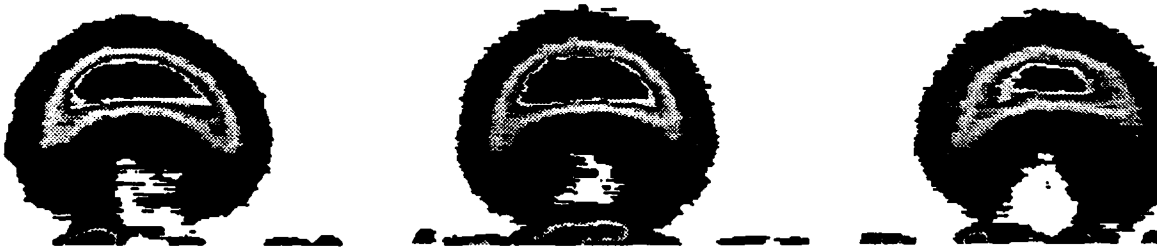

Fig. 8 : vue en coupe de l'écoulement dans le plan $x^* = 2$ pour $r = 1,6$

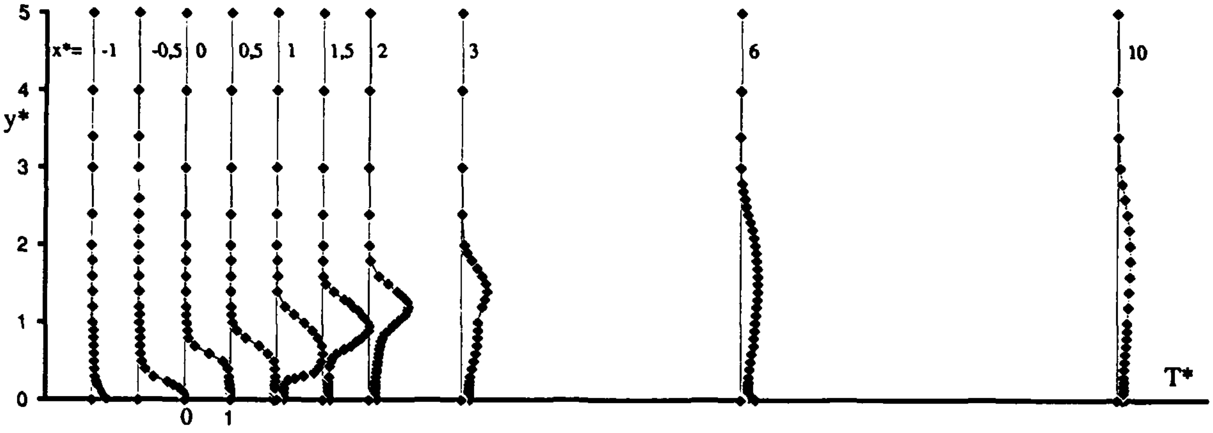

Fig. 9 : profils de la température réduite dans le plan $z^* = 0$ pour $r = 1,6$

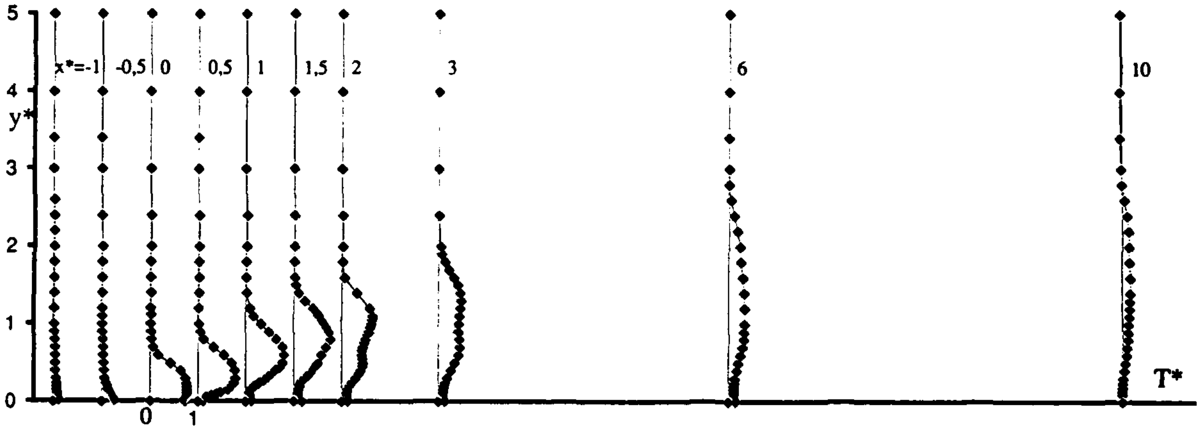

Fig. 10 : profils de la température réduite dans le plan $z^* = 0,4$ pour $r = 1,6$

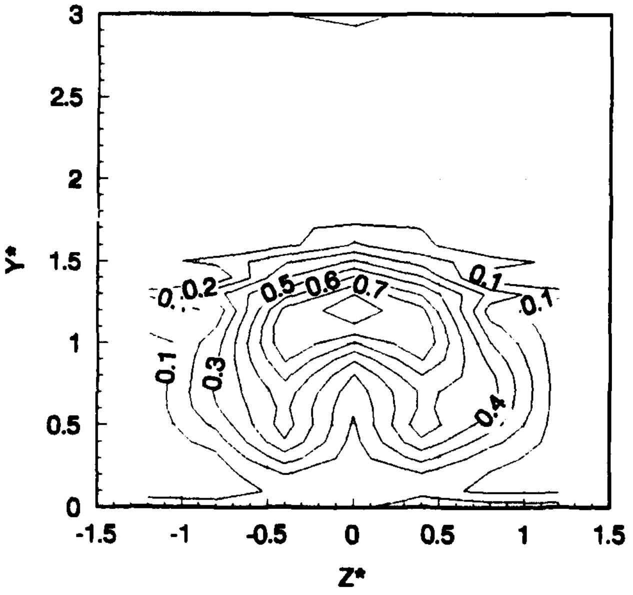

Fig. 11 : isothermes dans le plan $x^* = 2$ pour $r = 1,6$

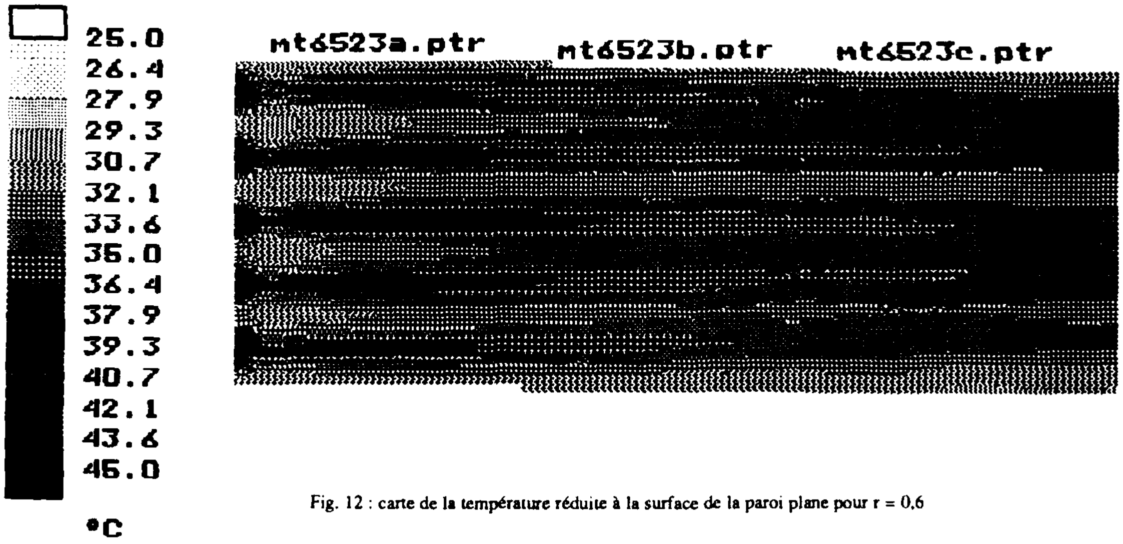

Fig. 12 : carte de la température réduite à la surface de la paroi plane pour r = 0,6

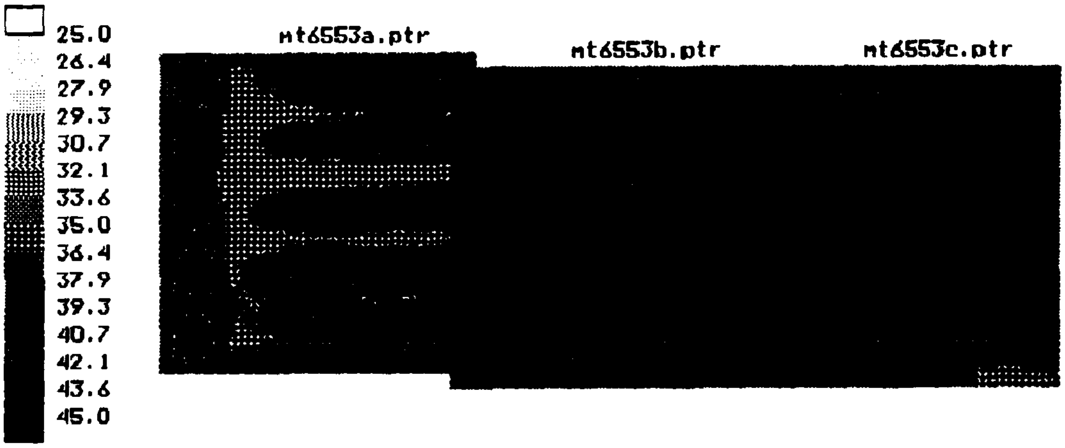

Fig. 13 : carte de la température réduite à la surface de la paroi plane pour r = 1,6

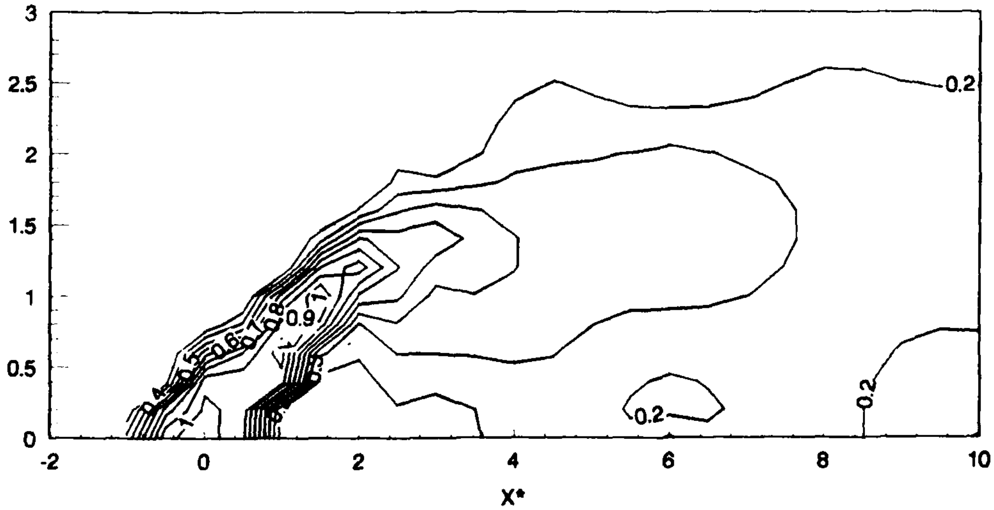

Fig. 14 : isothermes dans le plan z* = 0 pour r = 1,6

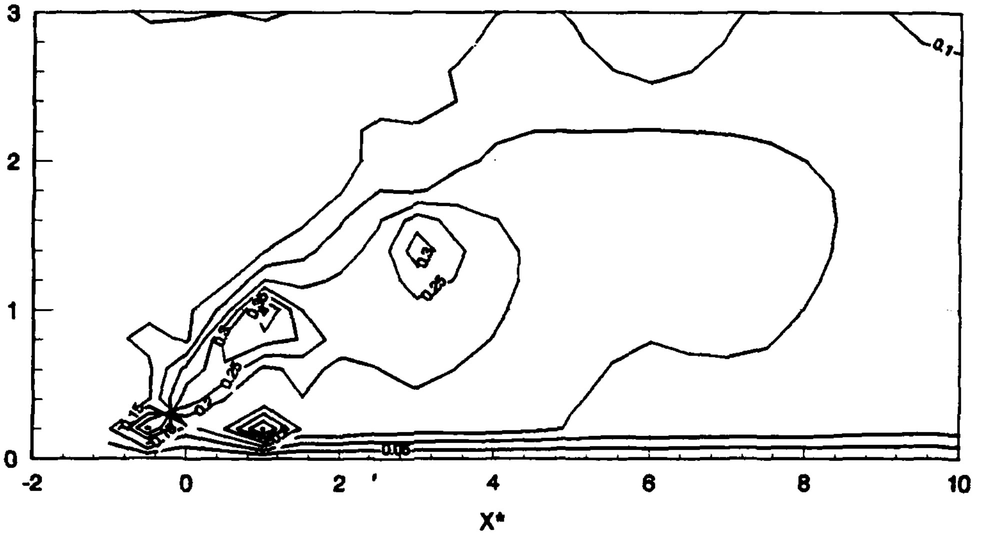

Fig. 15 : contours iso-taux de fluctuation de vitesse dans le plan $z^* = 0$ pour $r = 1,6$

Pour la plus grande valeur du taux d'injection étudié ($r = 1,6$), la tension de cisaillement $u'v'/U_e^2$ est maximale à la frontière supérieure du jet et de la couche-limite, comme le montrent les profils de figure 16. A partir du centre de l'orifice d'injection, on observe l'apparition d'un pic secondaire dont l'intensité augmente d'abord avec l'abscisse jusqu'à $x^* = 1$ puis décroît très rapidement au delà. Pour $x^* = 1$ les deux pics correspondent sensiblement à la même valeur $\approx 0,009$ qui est proche de celle mesurée par Pietrzyk & al. : 0,007.

4.4. Fluctuations de température

Les profils du taux de fluctuation de température (quantité calculée par rapport à la température moyenne locale) présentent dans tous les cas un maximum à la frontière supérieure du jet. Les courbes montrées Fig. 17 & 18 correspondent aux mesures effectuées respectivement dans les plans $z^* = 0$ et 1,4 pour le plus grand des taux d'injection étudiés ($r = 1,6$). Un premier pic de fluctuation est présent dès l'amont du jet ($x^* = -0,5$) et est encore nettement perceptible dans le plan de mesure le plus éloigné choisi pour notre étude ($x^* = 10$). L'intensité de ce maximum croît d'abord avec l'abscisse, passe par un sommet à $x^* = 1,5$ puis commence à diminuer lentement lorsqu'on s'éloigne vers l'aval. Son ordonnée, qui coïncide avec celle du point d'inflexion du profil de température moyenne correspondant (cf : Fig. 9 & 10), croît avec l'abscisse.

Un second maximum apparaît sur les profils de fluctuations mesurés dans le sillage de chaque jet, juste à l'aval de l'orifice d'injection ($x^* = 1$). Si l'on considère les profils obtenus dans le plan $z^* = 0$ (Fig. 17), on remarque une évolution, en fonction de la distance au point d'injection, de l'intensité du maximum secondaire semblable à celle du pic principal. Après une première étape de croissance elle passe par un maximum à $x^* = 1,5$ puis décroît, rapidement cette fois. La position du maximum secondaire, qui correspond également au gradient maximum de la température moyenne au même point, s'écarte également de la paroi lorsque l'abscisse croît. Il s'en éloigne cependant plus rapidement que le pic principal, et à $x^* = 3$, où son intensité a fortement diminué, les deux pics tendent à se confondre. Ce résultat est atteint plus loin vers l'aval et l'on voit alors apparaître un troisième maximum de fluctuation de température, situé approximativement à la cote $y^* = 0,5$ qui correspond encore à un changement de pente du profil de vitesse moyenne à cette abscisse. Ensuite, ce troisième pic s'estompe en s'élargissant, lorsque l'on progresse vers l'aval.

L'existence et l'évolution de ces divers pics peuvent être reliées à la forme caractéristique, dite en "haricot", de la section droite du jet, telle que la mettent en évidence les vues en coupe de l'écoulement. Observons, par exemple, la frontière inférieure de cette forme en "haricot" (limite entre les zones noire et grise) du jet central représenté sur la figure 8, enregistrée à $x^* = 2$. Dans le plan de symétrie du jet ($z^* = 0$), la cote de la frontière ($y^* \approx 0,9$) est la même que celle du pic secondaire du profil de fluctuation de température relatif à la même abscisse (cf : Fig. 17). Cette frontière de forme concave paraît donc bien être le siège de ces fluctuations de température importantes. La vue en coupe de la figure 8 permet également d'avancer une explication à la présence d'un troisième extremum sur certains des profils des figures 17 & 18. Il semble en effet correspondre au contact du fluide chaud, entraîné vers le plan de symétrie par les deux tourbillons contra-rotatifs, avec la poche de fluide froid qui subsiste entre ces deux structures (cf : la zone blanche sur la figure 8). Si l'on s'éloigne du plan de symétrie du jet pour se rapprocher de l'axe de rotation de l'un des deux tourbillons contra-rotatifs (eg : le plan $z^* = 0,4$; Fig. 18), l'intensité du troisième extremum de fluctuation de température augmente. Sa présence peut même être détectée dès la sortie du jet (eg : profil mesuré en $x^* = 0,5$) ce qui confirme la naissance des tourbillons contra-rotatifs à cet endroit.

La figure 17 ($z^* = 0$) montre également que le maximum de fluctuation de température intermédiaire, disparaît des profils au delà de $x^* = 3$. Cette abscisse est voisine de celle où l'isotherme $T^* = 0,2$ (cf : Fig. 14) rejoint la paroi plane, ce qui montre la disparition à partir de ce point de la trace de fluide froid sous le jet.

5. COMPARAISON AVEC LES SIMULATIONS NUMERIQUES :

Comme cela a déjà été indiqué dans l'introduction, un des objectifs de cette étude était la constitution d'une base de données expérimentales destinée à tester une méthode de calcul de couche-limite turbulente en présence d'injections discrètes développée à l'ECL. Une première comparaison a été réalisée par P. Kulisa, F. Lebœuf et G. Perrin (1991) dans le cas d'un taux d'injection égal à 0,6. Du point de vue aérodynamique il existe un bon accord entre les vecteurs vitesses calculés et ceux mesurés dans le plan de symétrie $z^* = 0$. Une comparaison plus détaillée des profils de vitesse longitudinale obtenus à plusieurs abscisses, fait apparaître une surestimation des valeurs calculées. les auteurs attribuent l'écart au fait que la distribution de vitesse réelle dans la section de sortie du jet n'est certainement pas aussi uniforme que cela a été supposé dans les calculs. En revanche, l'évolution de la "trajectoire thermique" du jet (lieu de la position du maximum de température) déduite de l'étude expérimentale est bien retrouvée par le calcul. Ce dernier prédit également la présence d'un minimum sur les profils de température moyenne en aval de l'injection, résultat confirmé par l'expérience.

Des comparaisons plus détaillées, portant sur les résultats obtenus pour les deux rapports de vitesses choisis lors des essais, viennent d'être réalisées par J-M. Maurice, F. Lebœuf et P. Kulisa (1992).

6. CONCLUSION :

Des expériences concernant la couche-limite d'une paroi plane chauffée en présence d'une rangée de jets d'air chaud inclinés, ont été réalisées. Les résultats obtenus concernent à la fois les champs aérodynamique et thermique, pour deux valeurs du taux d'injection.

Le résultat principal concerne l'existence d'une région, située immédiatement en aval de chaque injection, où le transfert de chaleur entre le jet et la paroi est très faible. Cela peut constituer un inconvénient important à la mise en œuvre de la technique de refroidissement par injections localisées. Ce phénomène apparaît principalement lorsque le rapport des vitesses est supérieur à un. Il est dû à la présence d'un volume, entre le jet et la paroi, où est entraîné de l'air provenant de l'écoulement transversal. Ce mouvement entrant est généré par les deux tourbillons contra-rotatifs qui se forment dès la sortie du jet dans la couche-limite de l'écoulement transversal. Cette paire de tourbillons jumeaux, qui domine l'écoulement à l'aval de l'injection, a une influence importante sur le champ thermique, dans le sillage proche des jets. L'optimisation des conditions de transfert dans cette région passe par un approfondissement des connaissances de ces structures et des paramètres qui les gouvernent.

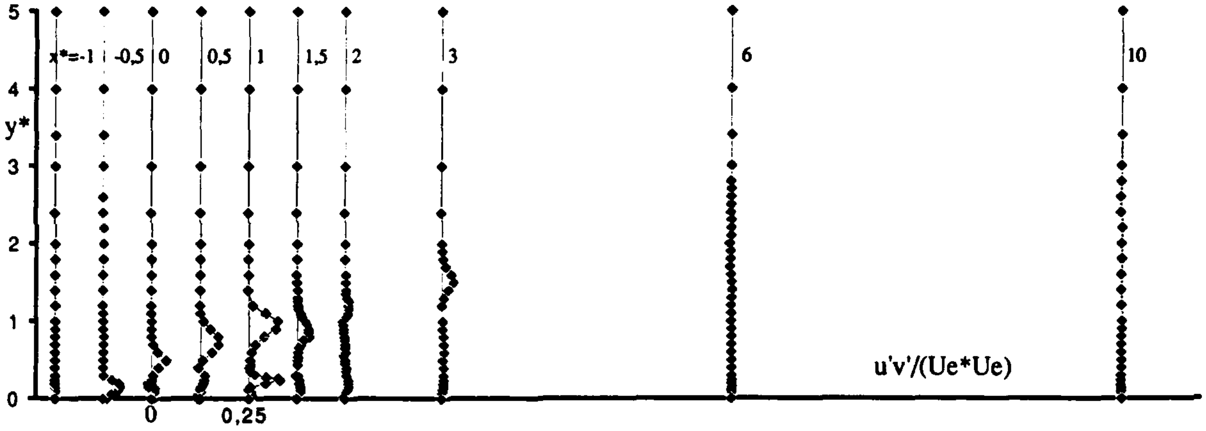

Fig. 16 : profils de tension de cisaillement dans le plan z* = 0 pour r = 1,6

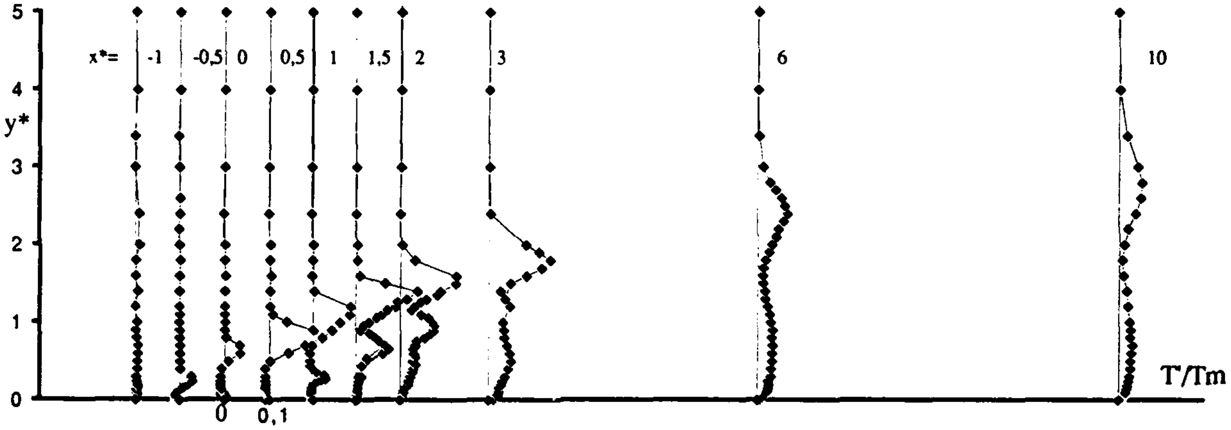

Fig. 17 : profils de taux de fluctuation de température dans le plan z* = 0 pour r = 1,6

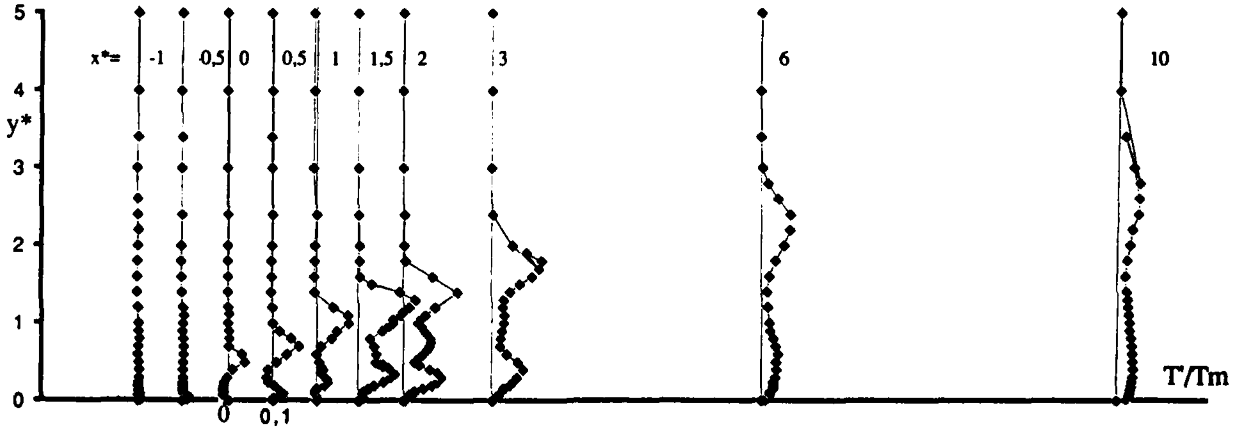

Fig. 18 : profils de taux de fluctuation de température dans le plan z* = 0,4 pour r = 1,6

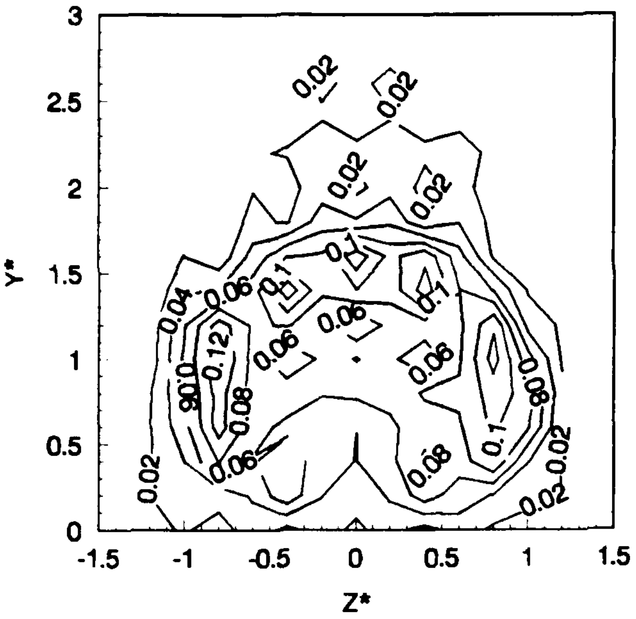

Fig. 19 : contours d'iso taux de fluctuation de température dans le plan transversal x* = 2 pour r = 1,6

Ce travail, entrepris à l'initiative de la SNECMA, a pu être réalisé grâce au support de la DRET, Direction des Recherches, Etudes et Techniques.

7. REFERENCES :

1 Andréopoulos J. - Rodi, W. : Experimental investigation of jets in a crossflow. JFM, (1984), 138, 93-127.

2 Broadwell, J.E. - Breidenthal R.E. : Structure of a transverse jet in incompressible flow. JFM, (1984), 148, 405-412.

3 Chassaing, P. - George, J. - Claria, A. - Sananes, F. : Physical characteristics of subsonic jets in a cross-stream. JFM, (1974), 62, 41-64.

4 Chen, K.S. - Hwang, J.Y. : Experimental study on the mixing of one- and dual-line heated jets with a cold crossflow in a confined channel. AIAA, (1991), 29(3), 353-360.

5 Crabb, D. - Durao, D.F.G. - Whitelaw, J.H. : A round jet normal to a cross flow. J. Fluids Engng, (1981), 103, 142-152.

6 Dorignac, E. - Vullierme, J.J. - Bousgarbiès, J.L. - Deniboire, P.: Heat transfer and film cooling following injection through inclined circular tubes of little dimension compared with the boundary layer thickness. Eurotherm 25, Pau, juillet 1991.

7 Dorignac, E. - Vullierme, J.J.: Mesure des flux convectifs sur une plaque plane en écoulement subsonique avec injection d'air chaud. Colloque de thermique SFT, Belfort, mai 1991.

8 Fearn, R. - Weston, R.P. : Vorticity associated with a jet in a cross flow. AIAA, (1974), 12(12), 1666-1671.

9 Jones, W.P. - McGuirk, J.J. : Computation of a round turbulent jet discharging into a confined cross-flow. 2nd Symposium on Turbulent Shear Flow, London, (1979). Turbulent Shear Flow 2 (Springer Verlag).

10 Jubran,B. - Brown, A. : Film cooling from two rows of holes inclined in the streamwise and spanwise directions. J. of Engineering for Gas Turbines and Power, (1985), 107, 84 -91..

11 Kamotani, Y. - Greber, I. : Experiments on a turbulent jet in a cross flow. AIAA, (1972), 10 , 1425-1429.

12 Keffer, J.F. - Baines, W.D. : The round turbulent jet in a cross-wind. JFM, (1963), 15, 481-496.

13 Kulisa, P - Lebœuf, F. - Perrin, G; : computation of a wall boundary layer with discrete jet injections. International Gas Turbine and Aeroengine Congress and exposition, Orlando, 3-6 juin 1991.

14 Kulisa, P; - Lebœuf, F. - Klinger, P. - Bernard, J.: Aerothermal boundary layer computation including strong viscous-inviscid flow interaction, ASME 90-GT-223.

15 Le Grivès, E. : Champ aérodynamique induit par un jet pénétrant dans un écoulement transversal, en régime subsonique. Journal de mécanique, (1978), 17, 23-52.

16 Maurice, J.M. - Lebœuf, F. - Kulisa, P.: Modélisation d'un écoulement turbulent en présence de jets pariétaux de refroidissement.80 th Symp. PEP, Heat transfer and cooling in gas turbines, Antalya, oct. 1992.

17 Moussa, Z.M. - Trischka, J.W. - Eskinasi, S. : The near field in the mixing of a round jet with a cross-steam. JFM, (1977), 80, 49-80.

18 Pietrzyk, J.R. - Bogard, D.G. - Crawford, M.E. : Hydrodynamic measurements of jets in crossflow for gas turbine film cooling application. ASME, (1988).

19 Sugiyama, Y. - Kawase, M. : A flow field with a jet affected by a nonuniform cross flow. Bulletin of JSME, (1985), 28(241), 1387-1395.

Discussion

QUESTION 1:

DISCUSSOR: D.T. Vogel, DLR

What is the turbulence intensity of the upstream flow?

AUTHOR'S REPLY:

The upstream boundary layer is turbulent and the free-stream turbulence level is about one percent.

QUESTION 2:

DISCUSSOR: D.T. Vogel, DLR

Did you measure the adiabatic film cooling effectiveness?

AUTHOR'S REPLY:

We did not measure the adiabatic wall temperature, but we did calculate the adiabatic film cooling effectiveness. The effectiveness was obtained from the measurement of the wall heat flux density, with the hypothesis that the heat transfer coefficient with injection is the same as that without injection. The expression for the effectiveness using this assumption is

$$\varphi = \frac{T_s(x,z) - T_e - \varphi_c(x,z)/h_c}{T_j - T_e}$$

QUESTION 3:

DISCUSSOR: N. Hay, University of Nottingham

Have you compared your results with others in the literature? And if not, do you intend to?

AUTHOR'S REPLY:

We have not found experimental results in the literature with similar test conditions ($\alpha = 45°$, $0.6 \leq r \leq 1.6$ and $\delta/d \cong 2.5$). Velocity and temperature measurements for experiments we have found are all for lower values of the ratio δ/d.

Our experimental results have been compared with numerical calculations performed in Ecole Centrale de Lyon (cf. the paper presented in this symposium by M. Maurice and Leboeuf, and Reference 13 of our paper). Indeed, the purpose of the present work was first to collect experimental data concerning velocity and temperature fields in order to develop a new computing code at the Ecole Centrale de Lyon.

QUESTION 4:

DISCUSSOR: B. Launder, UMIST

Most of the results that you presented were for the case of $r = 1.6$ which, as has been known from the data taken in the 1970's, gives poor levels of effectiveness. Why did you not give more emphasis to lower injection-velocity ratios?

AUTHOR'S REPLY:

As mentioned, the first aim of this work is to provide an extended data base in order to validate a numerical model developed at the Ecole Centrale de Lyon by F. LeBoeuf et al. (cf: paper presented at this symposium). This model applies to well defined flow and thermal conditions, particularly at large δ/d ratios. Most of the results are presented for the case of the injection rate (r) equal to 1.6, as for this value, the influence of the counter-rotating vortices on the velocity and the temperature fields are more apparent than for smaller values for which the jets are closer to the wall. As it appears on the map of the surface temperature, presented in this paper, the effectiveness is greater in the second case ($r = 0.6$), as it is well known. Moreover, the fact that the boundary layer thickness at the injection location is greater than the diameter of the jets, seems to introduce weak values for the effectiveness parameter. One of the features of this study is the chosen ratio $\delta/d \cong 2.5$, larger than the ones considered in the cases studied in the 1970's.

THE INFLUENCE OF NON-UNIFORM SPANWISE INLET TEMPERATURE ON TURBINE ROTOR HEAT TRANSFER

by

G.R. Guenette, G. Pappas[*] and A.H. Epstein
Massachusetts Institute of Technology
Gas Turbine Laboratory
60 Vassar Street
Building 31, Room 266
Cambridge, MA 02139
United States

ABSTRACT

The influence of a spanwise varying, circumferentially uniform inlet total temperature distortion was measured on a transonic turbine stage in a short duration turbine test facility. Large levels of distortion were found to increase rotor blade heat transfer, especially on the pressure surface. A three-dimensional, steady, multi-blade row, Euler code and a streamline curvature calculation were used to interpret the data but did not account for all of the heat transfer increase observed.

INTRODUCTION

Our understanding of turbine heat transfer and aerodynamics has increased considerably over the past 50 years, driven by the need for increased performance and life and aided by the evolution of new computational and experimental techniques. We are currently at the state in which we expect to do quite well in predicting turbine airfoil behavior in idealized situations such as test cascades and even rigs [1], but less well in the more complicated environment of full scale gas turbine engines.

One phenomenon characteristic of the engine environment but often absent from simpler test facilities is the spatial and temporal gas temperature non-uniformities at the turbine inflow generated by the combustor. These circumferential and radial variations in combustor exit gas temperature result from the many constraints imposed upon the combustor design and are often unwanted from the turbine point of view. We have long known that localized gas temperature variations ("hot spots" or "hot streaks") induce thermal stress and oxidation in turbine hardware and are a prime cause of shortened turbine life. More recently, Sharma and his colleagues have pointed out that turbine aerodynamic efficiency may suffer as well [2].

Non-uniformities at the turbine inlet propagate in some form through several turbine blade rows and complicate the design and analysis process. They introduce an added degree of dimensionality and demand more elaborate analysis than would be required in a machine with uniform inflow. For many years, secondary flow theory served as the primary tool [3]. Now, computational codes greatly augment our ability to analyze and understand three-dimensional, unsteady turbine flows and work has expanded in this area over the last decade. Much of the work on temperature non-uniformities in literature has been analytical or numerical. Numerical simulations have been done by Rai and Dring [4], Saxer and Giles [5], Dorney et al. [6], [7], and Harasgama [8]. There has been less experimental work published. Schwab et al. [9] reported aerodynamic measurements taken at the exit of a single-stage, warm air rig turbine with a spanwise inlet temperature profile. Butler et al. [10] performed measurements on a low speed, large scale turbine in which point injection of CO_2 was used as an analogue to a combustor hot streak. Several subsequent papers have used this data for comparison with numerical computations and analysis.

It is clear from the work to date that temperature non-uniformities can influence both turbine performance and heat transfer, and that numerical tools can be of great use in studying this problem. There remains, however, little experimental high speed turbine data in the literature which delineates these effects. The work described herein is the first part of a systematic effort to quantify the influence of thermal inhomogeneities on advanced turbine stages and to assess the manner in which turbines can be improved by accounting for such phenomena. It should be noted that total pressure non-uniformities also generate secondary flows, but that these are less of a problem in combustor outflows of interest and will not be treated here.

It is convenient for both analysis and experiment to characterize these temperature inhomogeneities into one of two categories: spanwise or radial variations in temperature which are circumferentially uniform and are thus two-dimensional at the turbine inlet, and hot spots (hot streaks) localized both radially and circumferentially which are inherently three-dimensional in nature. The radial variations stem in part from design intent of the combustor while the localized hot spots are often associated with fuel nozzle location and would be eliminated from the engine, if possible, given the design constraints (at least from the turbine designer's viewpoint). In this paper, we will consider only radial temperature variations. This approach of separating the distortion patterns into categories was adopted in an attempt to simplify the problem initially. Later efforts will expand to include hot spots as well.

---

[*] Current Address: Adroit Systems, Alexandria, VA, USA

In subsequent sections, we describe an experiment designed to measure the influence of spanwise turbine inflow temperature non-uniformities on rotor blade heat transfer, present the experimental data, describe a numerical calculation which models some aspects of the flow in the turbine, and then discuss the results of the research.

EXPERIMENTAL APPARATUS

The experiments were performed in the MIT Blowdown Turbine Tunnel [11]. This facility consists of a supply tank separated by a large diameter, fast-acting valve from the test section which, in turn, discharges to a dump tank (Fig. 1). The test section contains a 0.55 meter (22 inch) diameter test turbine stage and rotating assembly, including an eddy brake power absorber and 10 KW drive motor. The flow path upstream of the stage includes a boundary layer bleed and a combustor-like contraction.

The entire facility is initially evacuated and the supply tank and valve heated by circulating oil. The valve is then closed and the supply tank filled with an argon/Freon-12 mixture (used to reproduce the ratio of specific heats of combustor exit air). The turbine rotor is now brought up to operating speed in vacuum. To start the test, the main valve is opened and the eddy brake energized simultaneously. After a 250 ms startup transient, the corrected parameters are constant to better than 1% for 300 ms. (The corrected weight flow is held constant so long as the nozzle guide vanes are choked. The corrected speed is held constant by the eddy current brake.) The blades and tunnel walls have sufficient thermal inertia to remain at approximately constant temperature during the test time.

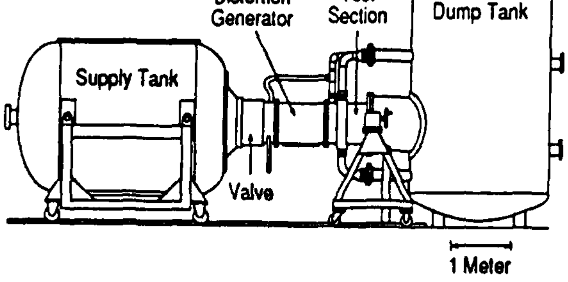

Fig. 1: MIT Blowdown Turbine Facility.

The facility has been designed to closely simulate all the non-dimensional parameters important to turbine fluid mechanics and heat transfer: Reynolds number, Mach number, Prandtl number, Rossby number, ratio of specific heats, corrected speed and weight flow, and gas-to-metal temperature ratios. The principal scaling is to reduce the initial turbine metal temperature to room temperature, while keeping the gas-to-metal temperature ratio constant. This scaling is shown in Table 1.

TABLE 1
MIT BLOWDOWN TURBINE SCALING

	Full Scale	MIT Blowdown
Fluid	Air	Ar-Fr 12
Ratio specific heats	1.28	1.28
Mean metal temperature	1118° K (1550° F)	295° K (72° F)
Metal/gas temp. ratio	0.63	0.63
Inlet total temperature	1780° K (2750° F)	478° K (400° F)
True NGV chord	8.0 cm	5.9 cm
Reynolds number*	2.7×10^6	2.7×10^6
Inlet pressure, atm	19.6	4.3
Outlet pressure, atm	4.5	1.0
Outlet total temperature	1280° K (1844° F)	343° K (160° F)
Prandtl number	0.752	0.755
Eckert number†	1.0	1.0
Design rotor speed, rpm	12,734	6,190
Mass flow, kg/sec	49.0	16.6
Power, watts	24,880,000	1,078,000
Test time	Continuous	0.3 sec

* Based on NGV chord and isentropic exit conditions

† $(\gamma-1)M^2T/\Delta T$

A temperature distortion generator was designed and fabricated for these tests. The design criteria for the generator included: 1) the generation of temperature distortions only, the total pressure field should remain uniform; 2) the capability of generating engine-like circumferentially uniform, radially (spanwise) varying temperature patterns; and 3) the capability for later retrofit to generate hot spot-like patterns about the circumference. The radial distortion desired was specified in terms of a radial temperature distortion factor, RTDF

$$\mathrm{RTDF} = \frac{T_{max} - T_{mean}}{T_{ref}} \times 100\%$$

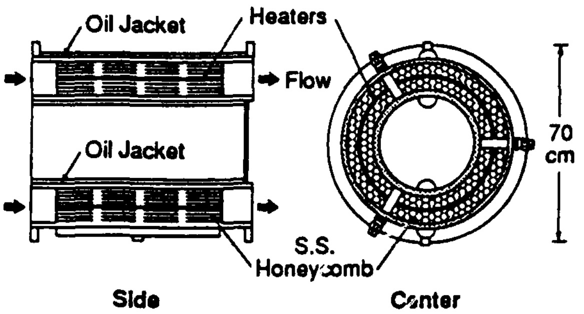

Fig. 2: Temperature distortion generator modified for simultaneous radial and circumferential patterns.

where T_{max} is the maximum total gas temperature; T_{mean} the mean average temperature over the passage height; and T_{ref} a reference temperature, nominally the combustor temperature rise. The combustor spanwise profile is assumed to be parabolic.

Designs considered included cold gas injection from the walls, liquid Freon injection, and a storage matrix heat exchanger. The latter was selected based on low pressure distortion, technical risk, and cost [12]. The generator as constructed is illustrated in Fig. 2. It consists of a 0.5 meter long honeycomb matrix heat exchanger constructed of 3 mm wide triangular channels brazed from 0.25 mm thick stainless steel sheet. The inner and outer annulus walls are cooled by circulating oil. Stainless steel sheathed electrical resistance heating wires are threaded through the matrix at mid-passage height from one end to another. Thus, the heat is injected at the center of the passage and removed at the peripheral walls, generating a spanwise temperature variation, hottest at mid-passage. In operation, the matrix is heated in vacuum for several hours preceding a test. The amplitude and shape of the temperature distortion is controlled by the current history into the heaters and monitored by thermocouples spotted about the unit.

TABLE 2
TURBINE DESIGN PARAMETERS

Turbine loading, $\Delta H/U^2$	-2.3
Total pressure ratio	4.2
Velocity ratio, C_x/U	0.63
Rotor aspect ratio	1.5
NGV exit Mach No.	1.18

During a blowdown test, the matrix acts as a high effectiveness heat exchanger. The length of the matrix is such that the thermal cooling wave within the metal, which starts at the upstream end, has not reached the discharge end of the unit during the 0.5 second test time. The result is that the gas exits the matrix at the local metal temperature, thus imposing the temperature distortion pattern set up in the metal prior to the test onto the gas. Because the heat is added at very low Mach number, no appreciable total pressure distortion is introduced in the heating process.

Aerodynamic instrumentation consisted of total pressure and temperature rakes upstream and downstream of the turbine and wall static pressure taps on the outer casing. Thin film, multi-layer, heat flux gauges were mounted about the rotor blade chord at two spanwise locations, at midspan and near the blade tip (81.5% leading edge span). These sensors directly measure heat flux to the blades from DC to 100 kHz [13]. For these tests, the raw heat flux data was low pass filtered at 30 kHz (vane-blade interaction frequency is 3.6 kHz) and ensemble-averaged over 300 blade passings for the time-resolved data, and time-averaged for DC data.

The test article was a 0.5 meter diameter, 4-to-1 pressure ratio, transonic, single-stage turbine whose design parameters are given in Table 2. Data from this geometry has been previously reported for a stage with uniform inflow [14], as a cooled stage [15], and in a cascade [16]. Figure 3 depicts the turbine installation and flow path.

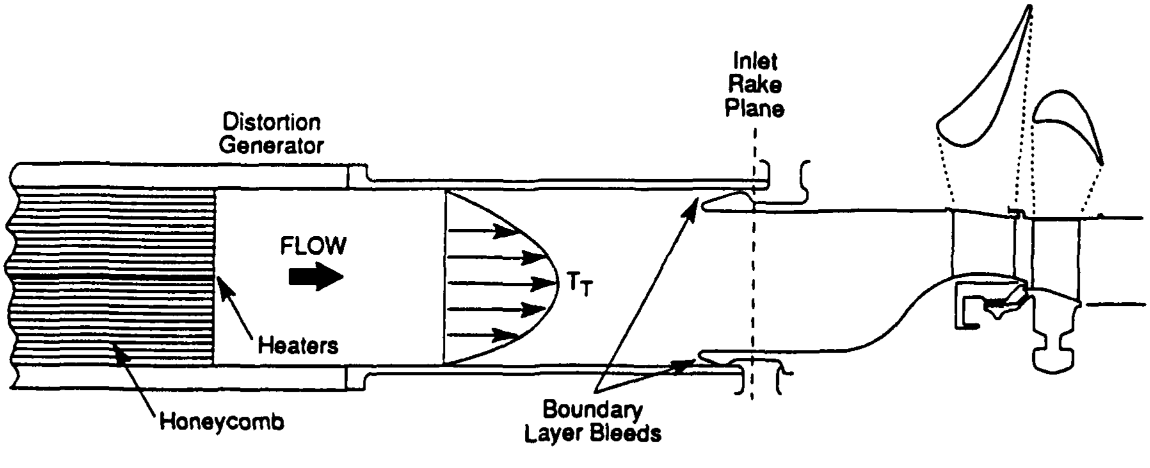

Fig. 3: Blowdown turbine rig flow path.

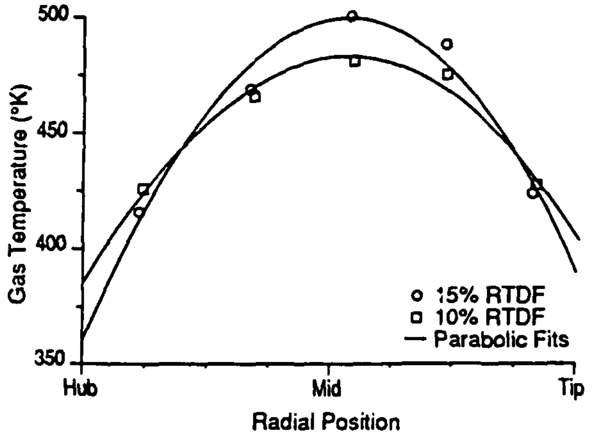

Fig. 4: Radial temperature profiles measured upstream of the turbine inlet compared with parabolic fits.

EXPERIMENTAL EXPERIENCE AND RESULTS

The distortion generator was operated so as to provide varying levels of temperature distortion at a constant level of annulus averaged enthalpy flow. Distortion levels (RTDF's) from 2% (as close to uniform as could be achieved) to 15% were studied. Gas total temperature profiles measured downstream of the distortion generator compare well with parabolic fits in Fig. 4, confirming that the generator performed as designed. Unfortunately, the generator passages were contaminated by fine ($\sim 25\ \mu m$) particles during fabrication. The particles did not flush from the unit during pretest cleaning, but were expelled gradually during the tests. This fine dust eroded the thin film heat flux gauges, especially on the pressure side of the blades (the other aerodynamic instrument was not affected). The erosion resulted in calibration drift (greatly complicating the data reduction procedure) and rapid gauge failure. Fewer working gauges remained after each test with eventually most of the gauges being destroyed. Thus, the data presented herein is rather sparse with not all measurement points being available for every test.

The integrity of the data reduction procedure was established by comparing the low distortion (2% RTDF) data at midspan with that taken earlier without the distortion generator [14], and thus with uniform inflow. Figure 5 shows these to be substantially the same except at the pressure surface trailing edge.

The measured heat flux distributions about the rotor blade at -11° incidence angle and the nominal bulk conditions listed in Table 1 are presented in dimensional form at midspan and tip locations in Figs. 6 and 7 respectively. At midspan, low levels of distortion (2%) slightly reduced the heat transfer compared to no distortion measurement. Increasing the distortion to high levels (10% and 15%) significantly enhanced the heat transfer, by about 50% on the suction surface and 70% on the pressure surface. Near the blade tip, changes in heat transfer due to temperature distortion are of similar magnitude.

Time-resolved data are presented in Fig. 8. On the pressure surface (Figs. 8a and 8b), the influence of the temperature distortion is seen as principally raising the average level of heat transfer without substantially changing the shape of the waveform. This is true near the trailing edge of the suction surface as well (Fig. 8d). On the crown of the suction surface, however (Fig. 8c), the waveform is substantially altered. At this location, the effect of temperature distortion is to increase the height of the spike that a previous unsteady 2-D numerical simulation of the undistorted flow [1] has shown to be caused by a reflected shock wave moving through the rotor passage.

NUMERICAL MODELLING OF THE FLOW

Customarily, heat transfer is treated in non-dimensional terms in the form of Nusselt number or Stanton number, in which the local heat transfer is normalized by an appropriate gas-to-wall driving temperature difference. With uniform turbine inflow, it is convenient to use the rotor relative total temperature. The proper choice of reference gas temperature is much less certain when large temperature distortions are introduced. Circumferentially uniform, spanwise distorted temperature patterns will influence the flow through two primary mechanisms. The first is the alteration of the spanwise distribution of rotor inflow angles (the velocity triangles) due to the change in reference frame going from the stationary NGV's to the rotating rotor. The second is the secondary flow generated in the rotor by the spanwise

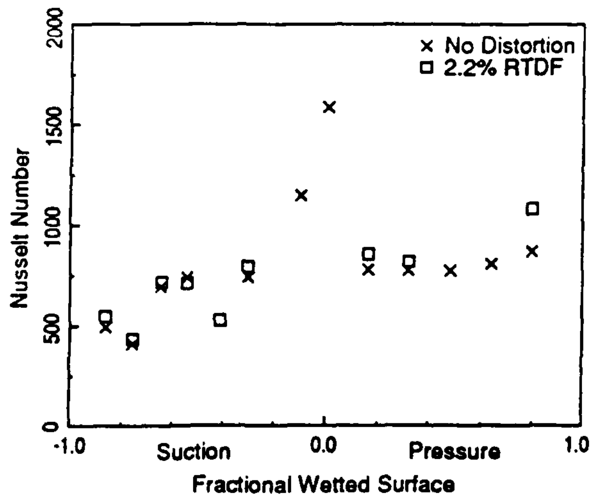

Fig. 5: Midspan rotor heat transfer taken without the distortion generator installed compared to that with the generator operated at low distortion level.

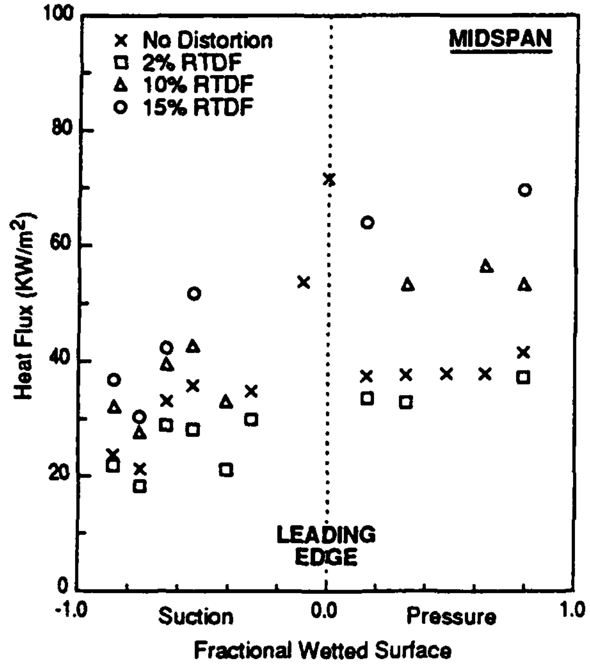

Fig. 6: Time-averaged heat flux measured at rotor midspan.

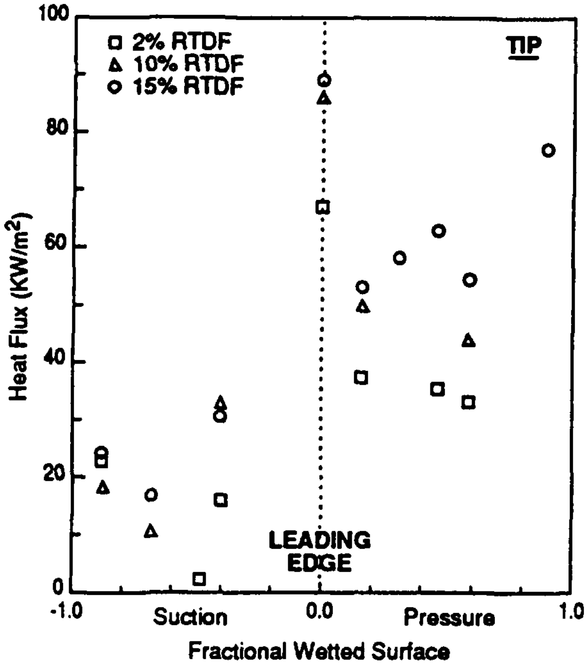

Fig. 7: Time-averaged heat flux measured at rotor tip.

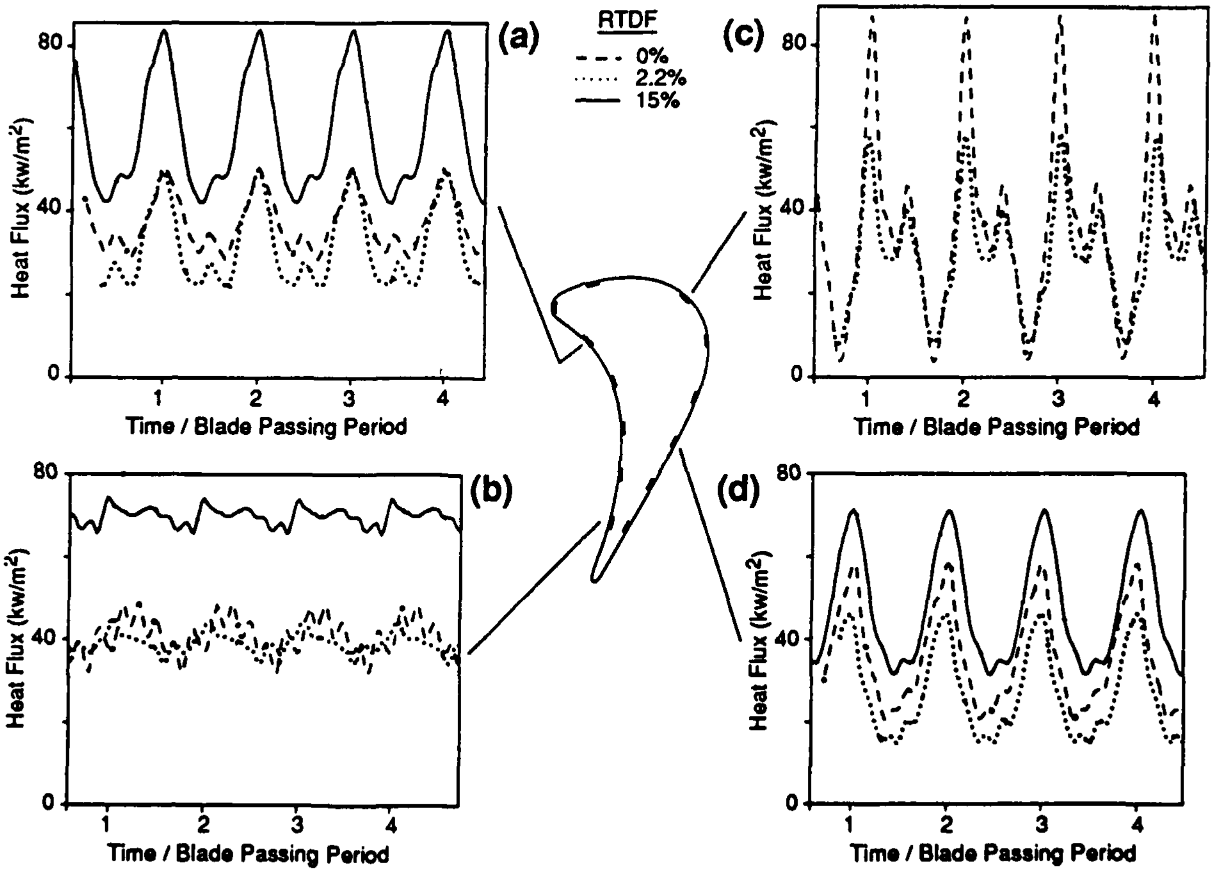

Fig. 8: Time-resolved rotor heat flux measurements at varying levels of temperature distortion.

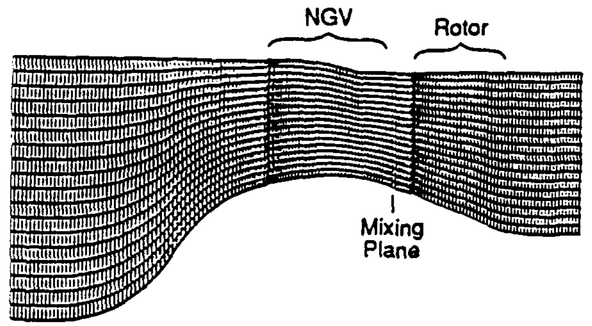

Fig. 9: Grid geometry used for 3-D Euler calculation.

pressure gradients. (Note that the temperature distortion alone will not generate secondary flows in the stationary frame NGV's; a pressure distortion is required [17], which is a motivation for designing this initial experiment with uniform inlet total pressure.) To aid in interpreting these measurements and to shed insight into the fluid mechanisms at work, we have modelled the inviscid flow in the turbine in two ways. The simplest is a streamline curvature calculation [18] which includes the axisymmetric velocity triangle effects. The next level in sophistication is to calculate the three-dimensional, steady inviscid flow within the turbine.

A 3-D, multi-blade row, steady Euler calculation of the flow in the turbine was made using Denton's MULTISTAGE code [19]. MULTISTAGE calculates the inviscid, 3-D flow in each blade row with an azimuthal averaging technique employed at the boundary (mixing plane) between the stationary and rotating blade rows. The H grid used followed the experimental geometry from the upstream rake measurement plane to about one chord downstream of the rotor. There were 162 grid points axially, 19 along the span, and 19 circumferentially. The rotor leading edges were cusped to reduce numerical errors. The 36 NGV, 61 rotor blade spacings of the experiment were preserved. The grid is illustrated in Fig. 9. The code results were checked insofar as possible by comparing with measured cascade blade static pressure distributions and by examining total pressure, temperature, and entropy changes. Details can be found in Pappas [20].

The computational results show that the inlet temperature distortion has little influence on the nozzle guide vane flow, as would be expected from Monk and Prim. Translation into the rotating frame significantly alters the flow into the rotor as can be seen in the swirl angle, and temperature and pressure distributions of Fig. 10. These result in the generation of secondary flow within the rotor passage which concentrates the hotter fluid at midspan toward the rotor pressure surface and moves it out toward the blade tip (Figs. 11 and 12). One result is to increase the driving gas temperature along the pressure surface relative to that along the suction surface. These results are quite similar to those of Saxer and Giles, who calculated the three-dimensional, steady flow within the same geometry using a different code.

USING COMPUTATIONS TO INTERPRET THE MEASUREMENTS

The primary interest here is to improve the understanding of turbine rotor heat transfer in the presence of spanwise temperature distortion. There are many questions which may be addressed, but two of direct engineering concern are whether distortion changes either (a) the

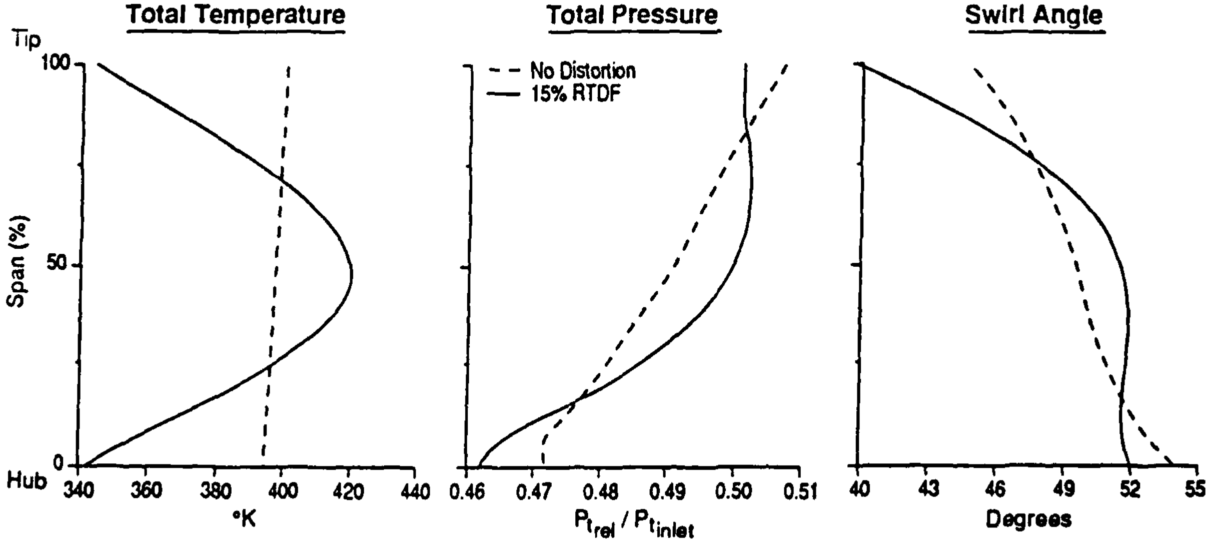

Fig. 10: Calculated influence of spanwise temperature distortion on rotor relative inflow conditions.

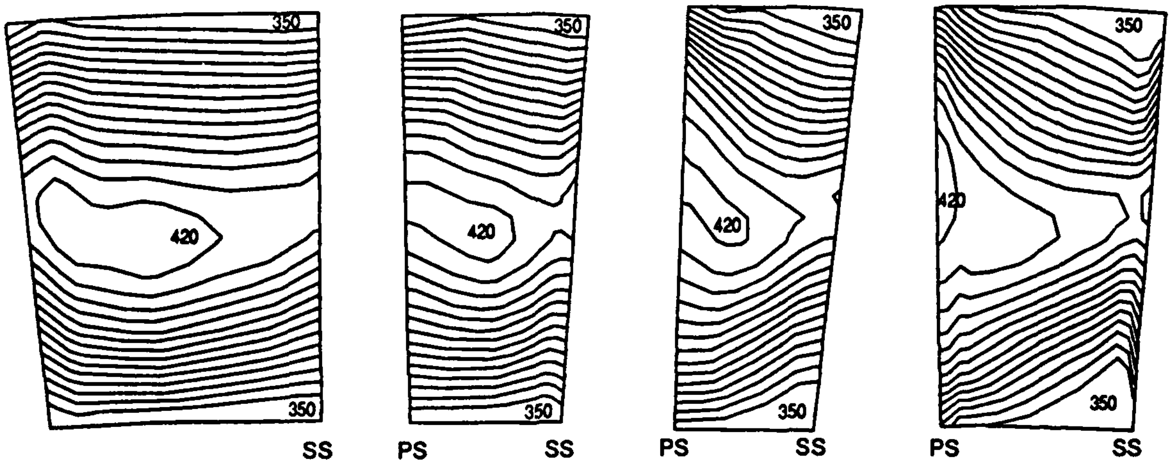

(a) Leading Edge Plane (b) 30% Axial Chord (c) 60% Axial Chord (d) Trailing Edge Plane

Fig. 11: Migration of total temperature in rotor blade passage (15% RTDF) cutting planes at axial stations from (a) leading to (d) trailing edges.

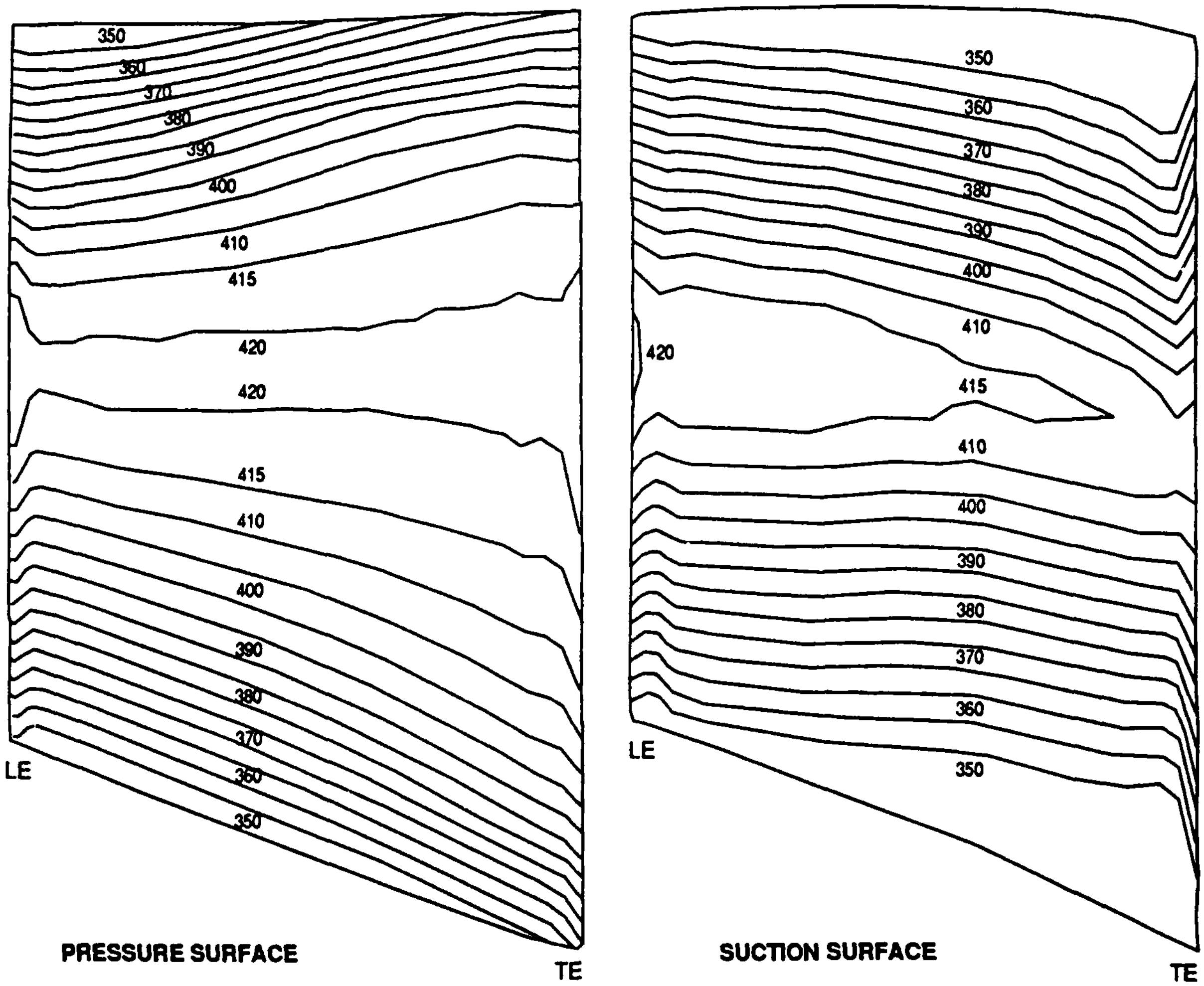

Fig. 12: Rotor blade surface total temperature (°K) contours calculated for 15% RTDF. For an undistorted inflow, the blade temperature is calculated at 400°K ±5°K.

integrated heat load blade (and thus alters the cooling requirements), or (b) the local distribution of heat flux and thus blade temperature in a manner not adequately captured by current predictive techniques (leading to blade thermal distress).

There is insufficient spatial coverage in the measurements to accurately assess the change in integrated heat load into the blade for either an equivalent inlet enthalpy flux or work extraction. The data taken (Figs. 6 and 7) show a 30-50% increase in heat flux at midspan with 15% RTDF compared to the no distortion case and 20-40% increase at the tip. No measurements at the hub are available. The inviscid calculation could be used to assess the change in driving temperature integrated over the blade surface, but a viscous calculation would be required to evaluate any heat transfer coefficient changes. Harasgama used a 3-D viscous code and a 2-D boundary layer solver to investigate the influence of a 20% RTDF on a 4-to-1 pressure ratio turbine. He found an increase of approximately 60% in heat flux near the tip of the pressure surface and 10% near the hub.

We can consider the influence of temperature distortion on the steady heat transfer to consist of two mechanisms – the alteration of the mostly inviscid core flow in the blade passage so as to change the gas-to-wall temperature difference driving the heat flux, or a change in the boundary layer with a concomitant change to the heat transfer coefficient. To assess the relative importance of the two mechanisms, we reduced the raw heat flux data into Nusselt number using as the reference gas temperature the local temperature at the heat flux sensor location as estimated by either the 3-D steady inviscid calculation or a streamline curvature procedure. If the primary influence of distortion were to alter the inviscid flow field and thus the driving temperatures, then this procedure would collapse the distorted data onto that with no distortion. For comparison, a Nusselt number using the spanwise average temperature (the same as for the no distortion measurements) was computed. The results are presented in Fig. 13 for midspan and Fig. 14 for the tip. At midspan, the streamline curvature calculation generally does a better job than the 3-D Euler, especially on the pressure surface. Near the tip, the comparison is not clearcut, and the corrections do not improve the data reduction. We infer from this that some essential elements of the fluid mechanics are not captured in the streamline curvature and 3-D, steady Euler calculations.

One phenomenon which is not modelled here is the unsteady interactions between blade rows, influencing both the potential and viscous flow. Ashworth showed how simulated NGV blade wakes can enhance rotor heat transfer on this midspan profile. Rigby et al. [21] constructed a simple model of the manner in which shock wave impingement can increase heat transfer. Abhari [1] showed how even the small geometry variations which result from normal manufacturing tolerances can cause large variations in heat transfer in a transonic turbine. The latter is directly applicable here since the temperature distortion generates relatively large flow angle variations which may significantly alter the unsteady shock wave system in the turbine. We would thus not be surprised if the changes in the unsteady flow field were an important influence in enhancing the rotor heat transfer.

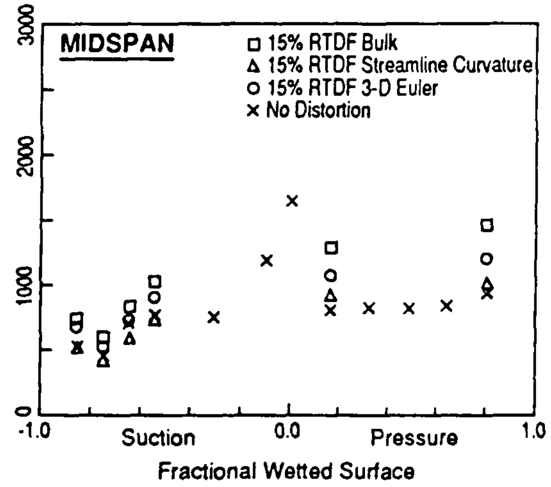

Fig. 13: Nusselt number near midspan with the reference temperature calculated as spanwise average (bulk), from streamline curvature, or from local wall temperature estimated with a 3-D, steady Euler calculation.

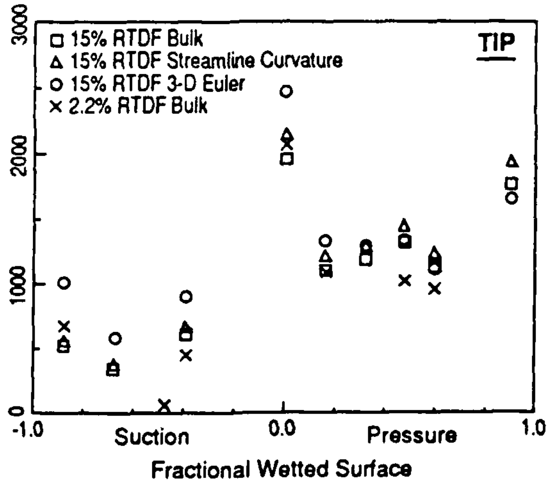

Fig. 14: Nusselt number near tip with the reference temperature calculated as spanwise average (bulk), from streamline curvature, or from local wall temperature estimated with a 3-D, steady Euler calculation.

SUMMARY AND CONCLUSIONS

An experiment has been constructed to measure the influence of spanwise varying, circumferentially uniform total temperature distortion on turbine rotor heat transfer. The first data from this experiment shows that temperature distortion increases both tip and midspan rotor heat transfer, especially on the pressure surface. Both a 3-D, steady, Euler, multi-stage code and a streamline curvature calculation were used to interpret the data. These calculations did not account for all of the increased heat transfer observed.

This is very much work in progress. We are in the process of re-instrumenting the turbine rotor for improved spatial coverage of the heat flux sensors, and adding sufficient aerodynamic instrumentation to assess aeroperformance changes. Both spanwise and circumferential distortions will be investigated experimentally. New computational tools will be brought to bear, including a 3-D, unsteady, multi-blade row code. Overall, turbine temperature distortion is a problem for which the tools are in hand and we hope to make considerable progress in the coming years.

ACKNOWLEDGEMENTS

We would like to thank Professor J. Denton for the use of his code and his technical assistance, and Dr. R.J.G. Norton for the stream curvature calculations and his advice. We thank D. Park for preparation of the manuscript. This work was supported by Rolls-Royce Inc., Mr. A. Veninger, technical monitor, and the US Air Force Research in Aero Propulsion Technology (AFRAPT) program which provided fellowship support.

REFERENCES

1. Abhari, R.S., Guenette, G.R., Epstein, A.H., Giles, M.B., "Comparison of Time-Resolved Measurements and Numerical Calculations," ASME 91-GT-268, 1991.
2. Sharma, O.P., Pickett, G.F., Ni, R.H., "Assessment of Unsteady Flows in Turbines," ASME Paper 90-GT-150, 1990.
3. Hawthorne, W.R., "Secondary Vorticity in Stratified Compressible Fluids in Rotating Systems," CUED/A-Turbo/TR-63, University of Cambridge, Department of Engineering, 1985.
4. Rai, M.M., Dring, R.P., "Navier Stokes Anal-ysis of the Redistribution of Inlet Temperature Dis-tortions in a Turbine," AIAA Paper AIAA-87-2146, 1987.
5. Saxer, A.P., Giles, M.B., "Inlet Radial Temperature Redistribution in a Transonic Turbine Stage," AIAA Paper AIAA-90-1543, 1990.
6. Dorney, D.J., Davis, R.L., Edwards, D.E., Madavan, N.K., "Unsteady Analysis of Hot Streak Migration in a Turbine Stage," AIAA Paper AIAA-90-2354, 1990.
7. Dorney, D.J., Davis, R.L., Sharma, O.P., "Two-Dimensional Inlet Temperature Profile Attenuation in a Turbine Stage," ASME Paper 91-GT-406, 1991.
8. Harasgama, S.P., "Combustor Exit Temperature Distortion Effects on Heat Transfer and Aerodynamics Within a Rotating Turbine Blade Passage," ASME Paper 90-GT-174, 1990.
9. Schwab, J.R., Stabe, R.G., Whitney, W.J., "Analytical and Experimental Study of Flow Through an Axial Turbine Stage With a Nonuniform Inlet Radial Temperature Profile," NASA TM-83431, AIAA Paper AIAA-83-1175, 1983.
10. Butler, T.L., Sharma, O.P., Joslyn, H.D., Dring, R.P., "Redistribution of an Inlet Temperature Distortion in an Axial Flow Turbine Stage," AIAA Paper AIAA-86-1468, 1986.
11. Epstein, A.H., Guenette, G.R., Norton, R.J.G., "The MIT Blowdown Turbine Facility," ASME Paper 84-GT-116, 1984.
12. Haldeman, C.W., "An Experimental Study of Radial Temperature Profile Effects on Turbine Tip Shroud Heat Transfer," MS Thesis, Department of Aeronautics and Astronautics, Massachusetts Institute of Technology, August 1989.
13. Epstein, A.H., Guenette, G.R., Norton, R.J.G., Yuzhang, C., "High Frequency Response Heat Flux Gauge," *Rev. of Sci. Inst.*, 57, 4, 1986, pp. 639-649.
14. Guenette, G.R., Epstein, A.H., Giles, M.B., Haimes, R. and Norton, R.J.G., "Fully Scaled Tran-sonic Turbine Rotor Heat Transfer Measurements," *J. of Turbomachinery*, III, 1989, pp. 1-7.
15. Abhari, R.S., Epstein, A.H., "An Experimental Study of Film Cooling in a Rotating Transonic Turbine," ASME Paper 92-GT-201, 1992.
16. Ashworth, D.A., LaGraff, J.E., Schultz, D.L., Grindrod, K.J., "Unsteady Aerodynamics and Heat Transfer Processes in a Transonic Turbine Stage," *ASME J. of Eng. for Power*, 107, 4, 1985.
17. Munk, M., Prim, R.C., "On the Multiplicity of Steady Gas Flows Having the Same Streamline Pattern," *Proc. of the National Academy of Sciences, US*, 33, 1947.
18. Norton, R.J.G., Private Communication, 1989.
19. Denton, J., "The Calculation of Three-Dimensional Viscous Flow Through Multistage Turbomachines," *ASME J. of Turbomachinery*, 114, 1, 1992, pp. 18-26.
20. Pappas, G., "The Influence of Inlet Radial Temperature Distribution on Turbine Rotor Heat Transfer," M.S. Thesis, Department of Aeronautics and Astronautics, Massachusetts Institute of Technology, 1990.
21. Rigby, M.J., Johnson, A.B., Oldfield, M.L.G., Jones, T.V., "Temperature Scaling of Turbine Blade Heat Transfer With and Without Shock Wave Passing," 9th International Symposium on Air Breathing Engines, Athens, Greece, 1989.

Discussion

QUESTION 1:

DISCUSSOR: F. LeBoeuf, Ecole Centrale de Lyon

As vorticity may be enhanced by gradients of density and static pressure, the three-dimensional consequences of the present inlet temperature distortion could be obtained by comparing the static pressure fields, with and without distortion of T_0, in the plane between the stator and rotor. Do you have any experimental or numerical results that would illuminate this point?

AUTHOR'S REPLY:

With the complete stage geometry (rotor plus stator), we measure the wall static pressure only on the inner and outer annulus walls in the middle of the nozzle guide vane passage at the nozzle guide vane trailing edge plane. This is due to the close spacing between the rotor and stator (3mm). We can measure the pressure distribution at the nozzle guide vane exit with the rotor removed. Also we believe that three-dimensional calculations should do a good job of calculating the flow through the nozzle guide vane with temperature distortion.

QUESTION 2:

DISCUSSOR: G. Andrews, University of Leeds

In practice the real situation is more complex than the simple parabolic temperature profile you have used. The radial profile is skewed toward the hub for blade stress reasons. Also there is likely to be a strong velocity, hence, total pressure profile as well as a temperature profile. Typical radial temperature distortion factor values are around 8% and your 15% value seems unrealistic. However, the greatest temperature variations are in the circumferential direction where distortion factors can be typically 25%. How are these additional non-uniformities likely to influence the heat transfer?

AUTHOR'S REPLY:

Our intent in the design of this experiment was to build a realistic turbine inflow in steps of relatively simple elements, of which the parabolic profile is the first. We are currently looking at circumferential distortions as well as variable levels of inlet turbulence. Total pressure distortions can be added later with relatively little effort should it be desired. As far as the radial temperature distortion factor reported herein is concerned, the inlet profile is somewhat skewed toward the hub as examination of Figure 4 will show. The 15% radial temperature distortion factor was one of the largest of several studied in the range of 2% to 20%. Also, while 8% is a typical design intent, values of 15% or greater have been observed in practice.

DETERMINATION OF SURFACE HEAT TRANSFER AND FILM COOLING EFFECTIVENESS IN UNSTEADY WAKE FLOW CONDITIONS

M. Sautner
S. Clouser
Naval Air Warfare Center
Aircraft Division
Trenton, New Jersey 08628

J.C. Han
Turbine Heat Transfer Laboratory
Department of Mechanical Engineering
Texas A&M University
College Station, Texas 77843

SUMMARY:

The effect of unsteady wake flows on blade heat transfer and film cooling effectiveness was experimentally determined by using a spoked-wheel type wake generator. The experiments were performed with a five airfoil linear cascade at the Texas A&M University low speed wind tunnel facility. The mainstream Reynolds number based on airfoil chord length was about 3 x 10^5. The wake Strouhal number was varied between 0 and 0.4 by changing the rotating wake passing frequency. A hot wire anemometer system was located at the cascade inlet to detect the instantaneous velocity, phase-averaged mean velocity, and turbulence intensity induced by the passing wake. A pressure tap instrumented blade was used to measure the surface static pressure distributions and compared well with predicted velocity distributions in the cascade. An instrumented blade without film holes equipped with a thin foil thermocouple was used to determine the surface heat transfer coefficient distributions. The results show that the periodically passing wake promotes earlier boundary layer transition, causing much higher heat transfer on the suction surface. The passing wake also significantly enhances the heat transfer on the pressure surface. The other thin foil thermocouple instrumented blade contained several rows of film cooling holes at the stagnation region and on both the suction and pressure surfaces, and was employed to determine the film cooling effectiveness distributions. The results show that the strong passing wake interacts with the film layer and causes a relatively lower film effectiveness on both the suction and pressure surfaces for all three blowing ratios studied ($M = 0.4$, 0.8 and 1.2).

LIST OF SYMBOLS:

C	airfoil chord
d	rotating rod diameter
h	heat transfer coefficient
H	blade radial (spanwise) length
K	thermal conductivity of air
M	blowing ratio, $(\rho V)_c/(\rho V)_\infty$
n	rotating rod number
Nu	Nusselt number based on blade chord, hC/K
q''	net surface convection heat flux
q''_{gen}	foil generated surface heat flux
q''_{loss}	surface heat flux loss
Re	Reynolds number based on blade chord, V_1C/ν
S	Strouhal number, $2\pi wdn/(60V_1)$
Tu	turbulence intensity
V	local mainstream velocity in the cascade
V_1	mainstream velocity at the inlet of the cascade
V_2	mainstream velocity at the exit of the cascade
X	blade surface coordinate in streamwise direction
Y	blade radial coordinate in spanwise direction
w	rotating rod speed, rpm

$(\rho V)_c$	local injection coolant mass flux
$(\rho V)_\infty$	local mainstream mass flux
η	film cooling effectiveness
T_c	injection coolant flow temperature
T_w	blade surface temperature
T_{aw}	adiabatic blade surface temperature
T_∞	mainstream air flow temperature at the inlet
ν	kinematic viscosity of air

INTRODUCTION:

Technology development efforts for advanced military aircraft gas turbine engines are directed towards the goal of doubling current propulsion system capability by around the turn of the century, while concurrently effecting significant improvements in life, reliability and maintainability. The two dominant figures of merit for measuring propulsion system capability are engine thrust to weight ratio (Fn/Wt) and specific fuel consumption (SFC). Obviously, to achieve a 100 percent increase in thrust to weight ratio relative to current production engines will require revolutionary advances in turbine engine technology in the years ahead.

One of the major contributing gas turbine components in providing increased engine thrust is the turbine system. The performance of gas turbine engines is strongly influenced by turbine rotor inlet temperature. This is dramatically illustrated in Figure 1, which plots specific core power production (which can be related to specific thrust) as a function of turbine rotor inlet temperature. The engines tend to track fairly close to the ideal performance line, which represents cycle power output with 100% efficient turbines with no leakage or cooling flows. Clearly, increasing hot section temperatures is one of the key ingredients to realizing quantum jumps in gas turbine engine performance.

Modern gas turbines are designed to run at high turbine inlet temperatures well in excess of current metal temperature limits. In addition to improved temperature capability materials and coatings, highly sophisticated cooling techniques such as augmented internal cooling and external film cooling have to be employed in order to maintain acceptable life and operational requirements under such extreme heat load conditions. In order to design systems that will most efficiently cool turbine flow path components, it is necessary to better comprehend the detailed flow physics within the turbine itself. There is a great need to increase the understanding of heat transfer within this unsteady, highly complex flow field. Current turbine designs are characterized by an inability to accurately predict heat transfer coefficients. This results in non-optimized designs using inordinate amounts of cooling air, which ultimately causes significant penalties to the cycle in terms of thrust and SFC. One of the aspects of the turbine flow field that has received considerable attention recently is the effect of unsteady wakes caused by the passing of the upstream airfoil row on the downstream blade row. This investigation focuses on the measurement of the surface heat transfer coefficient and film cooling effectiveness on a model turbine blade under incident unsteady wake conditions.

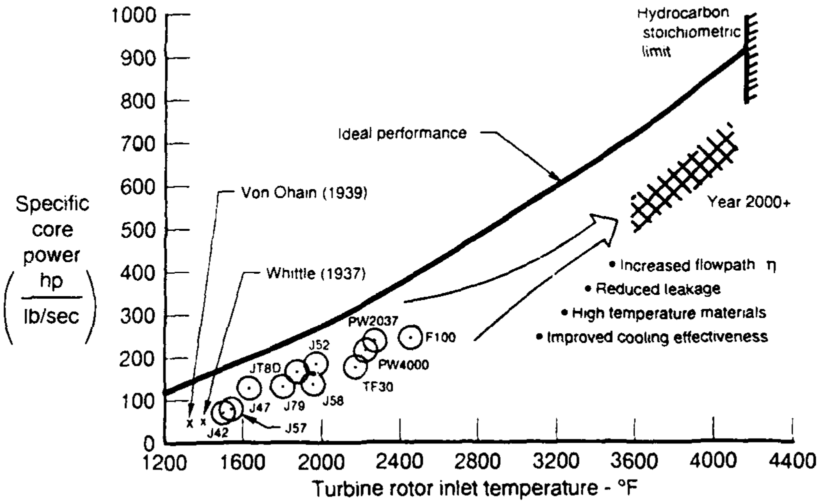

AVP370533E 910204

Figure 1
Increased Turbine Temperature Dramatically Improves Cycle Power Output (Courtesy of Pratt & Whitney)

There have been many studies on the effects of unsteady wake caused by the passing of the upstream airfoil row on the surface heat transfer coefficient of the downstream blade row. Many published results have investigated the interaction between the wake flow and the suction side boundary layer on a turbine blade. It is well known that the unsteady wake impact causes an increased heat transfer in the stagnation region and an early laminar-turbulent boundary layer transition. This wake-induced earlier transition covers a longer streamwise length on the suction surface of a turbine blade. These zones of transition form a higher heat transfer and a growing region of turbulent flow. Experiments have been conducted in turbines (Dunn et al., 1986a, 1986b, 1988, 1992; Blair et al., 1989; Blair, 1992; Abhari et al., 1991, 1992) or in laboratory simulations (Doorly et al., 1988; Priddy and Bayley, 1988; O'Brien and Capp et al., 1989; Wittig et al., 1986, 1988; Liu and Rodi, 1989, 1992; Dullenkopf et al., 1990, 1992). A squirrel cage type wake generator was used in laboratory simulations by Priddy and Bayley and Liu and Rodi; a spoked wheel type generator was employed by Doorly et al., O'Brien and Capp, Wittig et al., and Dullenkopf et al. Some investigators (Dunn et al., Doorly et al., and Abhari et al.) used fast response sensors to detect the real time variation on the blade surface heat transfer induced by the unsteady wake, while other researchers (Dullenkopf it al., Wittig et al., Liu and Rodi, and Blair et al.) employed the standard method to obtain the mean (time-average) heat transfer on an airfoil in unsteady wake conditions. Mayle and Dullenkopf (1990, 1991) recently developed a theory to incorporate unsteady effects into a steady-flow analysis by introducing a time-averaged intermittency factor. They showed that the time-average heat transfer distribution on the airfoil surface can be obtained from the predicted time-averaged intermittency factor and the laminar and turbulent heat transfer distributions as calculated from steady-flow conditions. They also found that the theory agrees with the measurement of the time-averaged heat transfer coefficient on the suction surface of a turbine blade in a spoked wheel generated wake flow condition.

Most of the previous studies are limited to the effect of the unsteady wake on the surface heat transfer of a turbine blade with no film cooling conditions. However, film cooled turbine blades are common in advanced gas turbine engines. In film cooling, relatively cool air is injected onto the blade surface to form a protective layer between the surface and hot mainstream gases. Most film cooling studies do not incorporate wake flow conditions (for example; Nirmalan and Hylton, 1989 Camci and Arts, 1990).

This study focuses on the effect on unsteady wake on the heat transfer coefficient and film cooling effectiveness distributions on a model turbine blade. The unsteady wake caused by the upstream blade row may interact with the cooling film ejected from the surface of the downstream blade row. It is of interest whether this wake jet interaction may penetrate into the film layer and change the heat transfer coefficient and film effectiveness distributions on the blade surface. For this study, a five-blade cascade (including the instrumented middle blade) was installed in a low speed wind tunnel at the Turbine Heat Transfer Laboratory of Texas A&M University. The upstream unsteady wake is produced by a spoked wheel type wake generator similar to those used by O'Brien and Capp, Dullenkopf et al., and Wittig et al. The standard thin foil thermocouple technique is used to determine the mean (time-averaged) heat transfer coefficient and film effectiveness on the instrumented model blade. This thin foil thermocouple method has also been employed to determine the leading edge heat transfer coefficient and film effectiveness distributions under high mainstream turbulence conditions (Mehendale et al., 1991; Ou and Han, 1991). The main objectives of this investigation are: (a) to determine the blade heat transfer coefficient distributions on the suction and pressure surfaces both with and without film holes at unsteady wake conditions, and (b) to determine the blade film cooling effectiveness distributions on the suction and pressure surfaces in unsteady wake conditions.

TEST APPARATUS:

Low Speed Wind Tunnel: The cascade setup and instrumentation layout are illustrated in Figures 2 and 3. The wind tunnel consists of an inlet nozzle, a wake generator, a test section, an exhaust duct, and a suction blower. A five airfoil cascade is installed inside the test section downstream of the wake generator. The wind tunnel has been modified to accommodate the 107.49° turning in the cascade. The spoked wheel wake generator has sixteen rotating rods (0.63 cm in diameter). A casing has been installed around the rotating spoked wheel to prevent leakage flow and to protect the system.

Cascade Design and Analysis: The cascade is designed to accommodate the low speed wind tunnel facility with an inlet air speed of approximately 20 m/s, or Mach No. 0.05. The airfoil configuration will produce a velocity ratio distribution similar to that of a typical advanced high pressure turbine blade. The computer software used in the airfoil design and analysis were performed within General Electric Aircraft Engines. The selected blade has 107.49° of turning, with relative flow angles of 35° and -72.49° at the blade inlet and exit, respectively. The 5X cascade is made of high quality

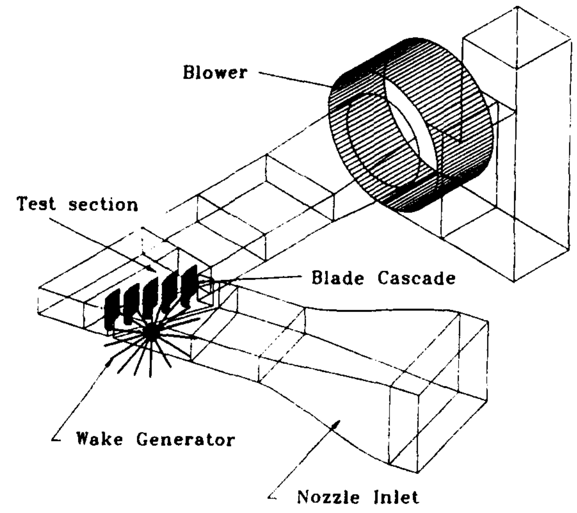
Blower
Test section
Blade Cascade
Wake Generator
Nozzle Inlet

Figure 2: Experimental Apparatus

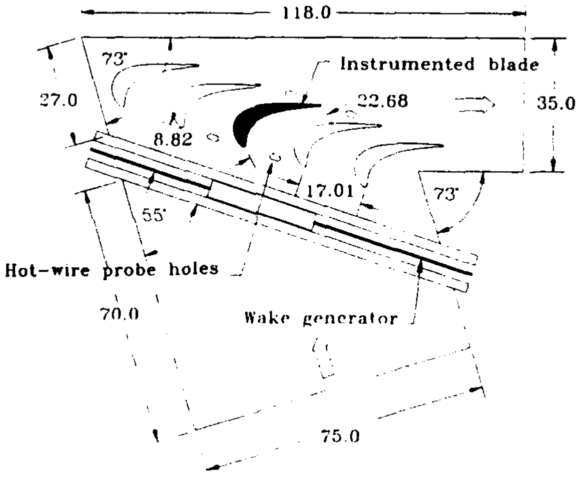
118.0
73°
Instrumented blade
27.0
22.68
35.0
8.82
17.01
73°
55°
Hot-wire probe holes
70.0
Wake generator
75.0

Figure 3: Test section and Instrumentation Layout (cm)

wood and has a chord length of 22.68 cm, a radial span of 25.2 cm, and a blade spacing of 17.01 cm. The center blade is instrumented and can be replaced for pressure, heat transfer, or film cooling experiments. Two slots are located near the blade leading edge and the middle of flow passages to measure flow velocities, wake profiles, turbulence fluctuations, and to check the flow periodicity between two adjacent flow passages. The distance between the rod and blade inlet is 8.82 cm.

Rotating Wake Simulation: The wake simulation was accomplished by means of the rotating spoked wheel shown in Figure 4. The wake Strouhal number (S) is used to simulate the unsteady wake flow characteristics of modern gas turbines (O'Brien and Capp, 1989) and is defined as:

$$S=\frac{2\pi\omega dn}{60V_1}$$

where ω is the rotating rod revolutionary speed (rpm), d is the rotating rod diameter (m), n is the number of rotating rods, and V_1 is the mainstream flow velocity at the inlet of the cascade (m/s). A wider range of Strouhal numbers can be tested in this program by varying the rod rotating speed, rod number, rod diameter and inlet flow velocity. In this paper, however, the Strouhal number ranges from 0 to 0.4 by varying the rod rotating speed (ω = 0 to 765 rpm) for a fixed value rod diameter (d = 0.63 cm), rod number (n=16), and flow inlet velocity (V_1 = 20 m/s). The Reynolds number (Re) is defined as:

$$Re=\frac{V_1 C}{\upsilon}$$

where V_1 is the mainstream flow velocity at the inlet of the cascade, C is the airfoil chord, and υ is air kinematic viscosity. As previously mentioned, the inlet flow velocity is 20 m/s and the airfoil chord is 22.68 cm. Therefore, the Reynolds number is approximately 3 x 10^5.

INSTRUMENTATION AND DATA ANALYSIS:

Hot Wire Instrumentation: A calibrated single hot wire anemometer TSI IFA 100 is used to measure the unsteady (instantaneous) velocity profile of the passing wake. The hot wire anemometer is connected to an IBM PC through a 100 KHZ A/D converter in order to get sufficient sampling data for analysis. The anemometer also is connected to a NICOLET 446A Spectrum Analyzer that displays the instantaneous wake profile and frequency distribution. The hot wire sensor is located at 8.82 cm downstream from the rotating rod. The connection of the hot wire system is depicted in Figure 5. The mean velocity and turbulent intensity are time dependent and periodic and, because of the periodic nature of the wake passing and shedding, the analysis of the unsteady random signal indicates that its behavior cannot be characterized by the time mean average only. In order to get the time dependent periodic mean velocity and turbulent intensity of the wake flow, the phase-averaged (or ensemble-averaged) method suggested by O'Brien and Capp (1989) and Dullenkopf et al. (1990) is adapted. The phase-averaged mean velocity is obtained by dividing each rod-passing period into a certain number of bins and entering data from the selected number of the period into each bin. The phase-averaged mean velocity for each bin is then simply the sum of all the entering data for that bin divided by the selected number of the period. The phase-averaged turbulent intensity of the wake flow is obtained in a similar way. In this paper, digital sampling rates up to 100 KHZ are obtained depending on rod-passing frequency such that approximately 100 rod-passing periods and 150 samples per period are included in each digital record.

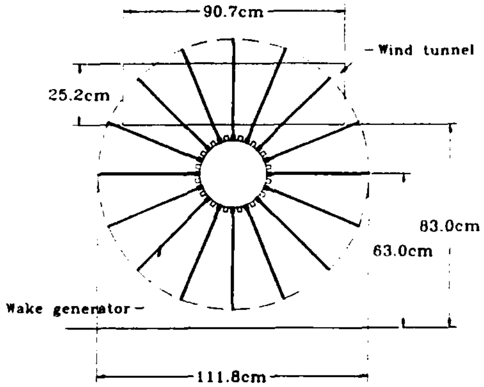

Figure 4: Wake Flow Generator

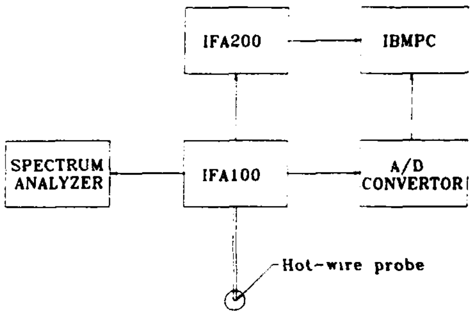

Figure 5: Hot Wire Instrumentation

Pressure Tap Blade Instrumentation: Figure 6a shows the schematic of the instrumented blade for static pressure measurement. The pressure tap blade is also made of high quality wood with a smooth surface. There are 26 pressure taps located in the midspan of the blade: one on the stagnation point, 11 on the pressure side, and 14 on the suction side. The taps are connected to the pressure transducers and interfaced to the IBM PC for the blade surface velocity calculations.

Heat Transfer Blade Instrumentation: Figure 6b shows a sketch of the instrumented blade for heat transfer measurements. Again, the blade is made of wood with a smooth surface. 26 foil strips are vertically cemented on the outer surface of the test model. Each strip of foil is 25.4 cm long, 2 cm wide, and 0.378 mm thick. A gap of 0.8 mm separates any two foils. These gaps are filled with wood filler and made flush with the foil surface for electrical insulation. All foils are connected in series by copper bus bars. The heated foils produce a nearly constant heat flux for the heat transfer test. The 36 gage copper-constantan thermocouples are soldered on the underside of the foils with 12 rows on the pressure side and 15 rows on the suction side. Each row contains 4 thermocouples around the midspan region of the blade. All thermocouples are connected to a Fluke 2280A data logger interfaced with an IBM PC. The voltage and current input through the foils are measured by digital multimeters. The local heat transfer coefficient (h) is calculated as:

$$h=\frac{q''}{T_w-T_{aw}}=\frac{q''_{gen}-q''_{loss}}{T_w-T_{aw}}$$

where q'' is the net convective heat flux from the foil surface, q''_{gen} is the generated surface heat flux from voltage-current measurements, q''_{loss} is the heat loss, T_w is the local steady foil temperature, and T_{aw} is the local adiabatic wall temperature. Loss tests were

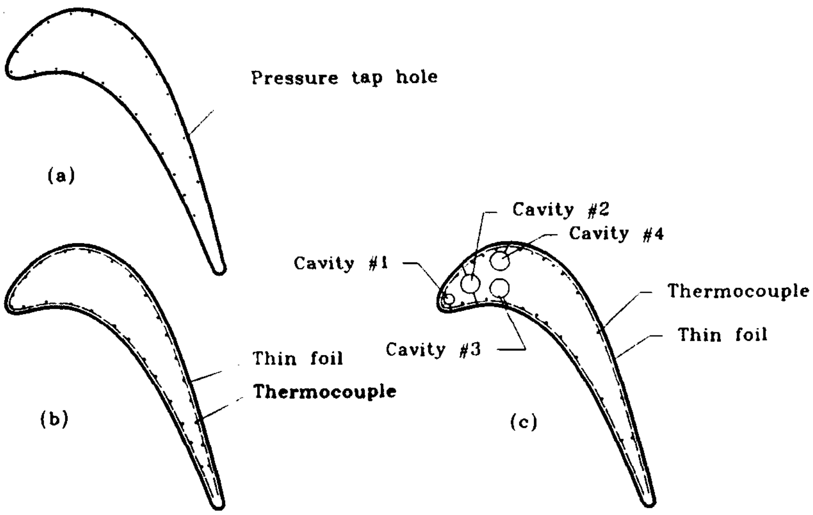

Figure 6: Sketches of Test Blade. (a) Pressure Tap Blade, (b) Heat Transfer Blade, (c) Film Cooling Blade

performed to determine the heat losses from the test model for a no flow (ie; no convection) condition. The relationship between the heat losses and foil temperature was established. T_w was about 40-50°C and T_{aw} about 25°C for the heat transfer test. The local heat transfer coefficient was then converted into the local Nusselt number (Nu = hC/K) based on the blade chord (C) and air thermal conductivity (K).

Film Cooling Blade Instrumentation: Figure 6c shows the schematic of the instrumented blade for the film cooling experiment. This blade is also fabricated of the same high quality wood. The first cavity has three rows of film holes with one row each on the stagnation line, suction side and pressure side. The second cavity has one row of film holes on the suction side and one row on the pressure side. The third cavity has one row of film holes on the pressure side while the fourth cavity has one row on the suction side. Each row has 8 to 10 film holes depending on the location. Most of the film holes have a compound angle (both radial and tangential components) relative to the mainstream flow (blade curvature). The detailed configurations of the film holes (diameter, length, spacing, angle) for this 5X model blade are specified by General Electric Aircraft Engines. Each cavity has individually controlled injecting flow rates. The local blowing ratio was determined by knowing the local mainstream velocity measured from the pressure tap blade.

The previously mentioned thin foil thermocouple method for the heat transfer blade is also employed here for the film cooling blade, except that the thin foils do not cover the film holes. The previously established equation for heat transfer coefficient can also be used to determine the local heat transfer coefficient with film injection by powering the thin foils and measuring surface temperatures. The injectant temperatures are kept at the same temperature as the mainstream flow for the heat transfer with film injection test. For the film cooling effectiveness test, the injectant (nitrogen gas) temperatures are about 15°C lower than the mainstream flow (the density ratio is about 1.05). The power does not turn on through the thin foils during this test. Therefore, the local adiabatic film cooling effectiveness (η) is determined as:

$$\eta = \frac{T_{aw} - T_\infty}{T_C - T_\infty}$$

where T_{aw} is the local adiabatic wall temperature, T_C is the coolant (nitrogen gas) temperature measured by thermocouples at the inlet of each cavity, and T_∞ is the mainstream temperature. An uncertainty analysis based on the method of Kline and McClintock (1953) was carried out for both the heat transfer coefficient and film effectiveness. The uncertainty of the heat transfer coefficient is about 5% whereas the uncertainty of the film cooling effectiveness is about 10%. Note that the above mentioned thin foil thermocouple technique is the same as that used by Mehendale et al. (1991) and Ou and Han (1991).

RESULTS AND DISCUSSION:

Aerodynamics Test: The periodicity of the velocity profiles between adjacent flow paths has been measured and confirmed.

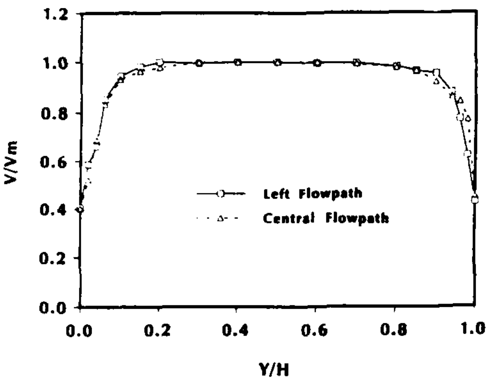

Figure 7: Inlet Velocity Profiles with No Wake Condition for Re = 300,000

The radial velocity profile is non-dimensionalized as V/V_m, where V_m is the pitchline velocity. Figure 7 shows the velocity profiles in the radial direction for a Reynolds number of 3×10^5 at the inlet of the central flow path and at the inlet of an adjacent flow path. The results indicate that the inlet velocity profile is essentially uniform between 25% and 75% span. The periodicity of velocity profiles between adjacent flow paths is excellent. The pressure tap airfoil provided the distribution of surface static pressures, which were used to calculate the velocity distribution around the airfoil. Figure 8 shows the distribution of velocity ratio (V/V_2) between local and exit velocity. The solid line in Figure 8 is the pre-test prediction. The velocity on the pressure side surface is an excellent match. The measured velocity on the suction side surface is higher than the predicted value, but nonetheless representative of typical velocity distributions for advanced high pressure turbine blades.

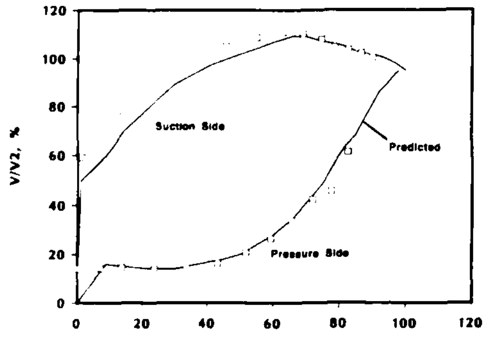

Figure 8: Velocity Distribution on the Pressure Tap Blade Model with No Wake Condition for Re = 300,000

Wake Flow Measurement: The hot wire probe was located near the blade leading edge and in the middle of flow passages to measure the instantaneous velocities in unsteady wake flow conditions. Figure 9 shows a typical instantaneous velocity profile, a phase-averaged mean velocity profile, and a phase averaged turbulent intensity profile for S = 0.1 and Re = 3×10^5. The instantaneous velocity profile shows the periodic unsteady fluctuations caused by the upstream passing wake, while the phase-averaged profile shows the time dependent mean velocity defect caused by the upstream passing wake. The phase-averaged turbulent intensity reaches 20% inside the wake, whereas the time-averaged turbulence intensity is about 7%. The background turbulence intensity is only about 0.75% for the case of no rotating rods in the wind tunnel.

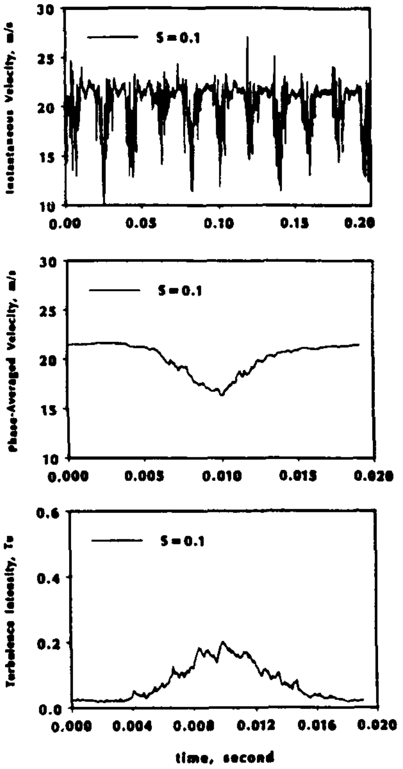

Figure 9: Typical Wake Flow Profile for S = 0.1, Re = 300,000

Heat Transfer Test: Figure 10 shows the spanwise averaged Nusselt number (Nu = hC/K) distributions on the blade surface with no film holes in several wake conditions. Test results for the steady mainstream flow condition (ie; with no rotating rods, turbulence intensity Tu = 0.5%, S = 0) are also included for comparison. The conditions are: Re = 3×10^5, V_1 = 20 m/s, n = 16, d = 0.63cm, S = 0.05, 0.1, 0.2 and 0.4 (corresponding to ω = 96, 192, 384 and 765 rpm). The results for the no wake flow case show that the suction surface Nusselt number decreases with increasing streamwise distance from the blade stagnation line, and then increases sharply due to transition into turbulent flow at 80% blade chord distance (x/C = 0.8). The

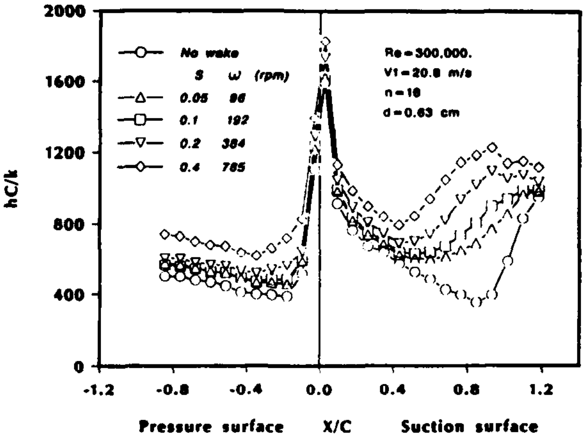

Figure 10: Effect of Unsteady Wake on the Local Heat Transfer Coefficient Distribution with No Film Holes

pressure surface Nusselt number decreases sharply with increasing streamwise distance from the leading edge of the blade and, due to strong acceleration, starts to gradually increase at about 20% blade chord distance. The general trends of the results for the wake flow cases are: (1) the Nusselt number on both the suction and pressure surfaces increases with increasing Strouhal number due to higher wake passing frequency; (2) the passing wake has more impact on the suction surface heat transfer than on the pressure surface heat transfer, ie; there is greater augmentation of the suction surface Nusselt numbers than the pressure surface in wake flow conditions; (3) the suction surface boundary layer transition starts earlier but requires a longer distance to become fully turbulent under wake flow conditions; (4) the wake not only effects the suction surface boundary layer transition but also disturbs the laminar type boundary layer from the blade leading edge to transition, thereby enhancing its heat transfer; (5) the suction side Nusselt number increases about 15% at the blade leading edge and about 3 times at 80% blade chord length when the wake passing Strouhal number changes from zero (no wake) to 0.4 (strong wake); and (6) the pressure side Nusselt number increases somewhere between 30-100%, with the smallest increment near the blade leading edge and the largest increment near 20% blade chord length, when wake Strouhal number varies from 0 to 0.4. The general observations of the passing wake impact on the blade surface heat transfer, as shown in Figure 10, agree with those presented and discussed in previous investigations (for example: Dullenkopf et al., 1990; Mayle 1991).

Figure 11 shows the spanwise averaged Nusselt number distributions on the film cooled blade surface under various intensity wake flow conditions. The results shown are for a constant blowing ratio of M = 1.2. The line indicated by squares represents the no film cooling condition. It is included for comparison

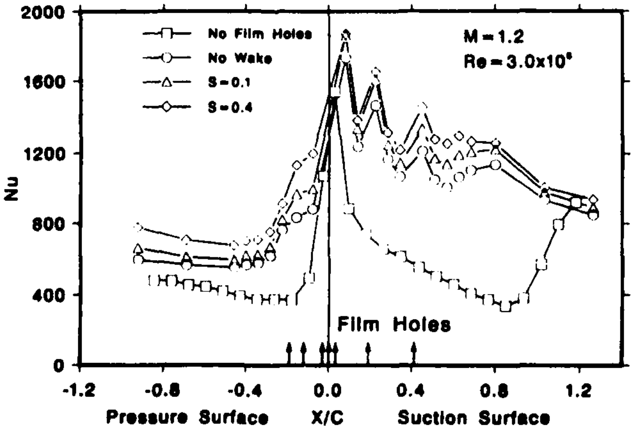

Figure 11: Effect of Unsteady Wake on Nusselt number with Air Injection for M = 1.2 and Re = 300,000

purposes, and is the same characteristic shown by circles in Figure 10. The arrows at the bottom of the figure represent the location of film rows along the blade surface. The results of the test indicate the following: (1) The introduction of film cooling alone results in a significant heat transfer augmentation, especially along the blade suction surface; and (2) the addition of upstream wakes on the film cooled blade causes up to a 20% increase in heat transfer coefficient on the suction surface and as much as a 60% increase along the pressure surface between no wake (S = 0) and strong wake (S = 0.4) conditions. The results of this particular experiment is significant when compared to the no film holes blade experiment shown in Figure 10. In particular, comparison of the suction surface heat transfer augmentation due to wake flow for the film cooled and non-film cooled blades is most interesting. When no film holes are present, the addition of wakes results in a 3X magnitude heat transfer increase; when film cooling of the blade is present, the addition of strong upstream wakes only increases the heat transfer coefficient by 20%. The implications are that the film cooling holes are the dominant factor in inducing boundary layer transition and heat transfer augmentation along the turbine blade surface, and the independently measured impacts of film cooling injection and wake flow on blade surface heat transfer are not additive.

Film Cooling Test: Figures 12-14 show the effect of passing wake on the spanwise averaged film cooling

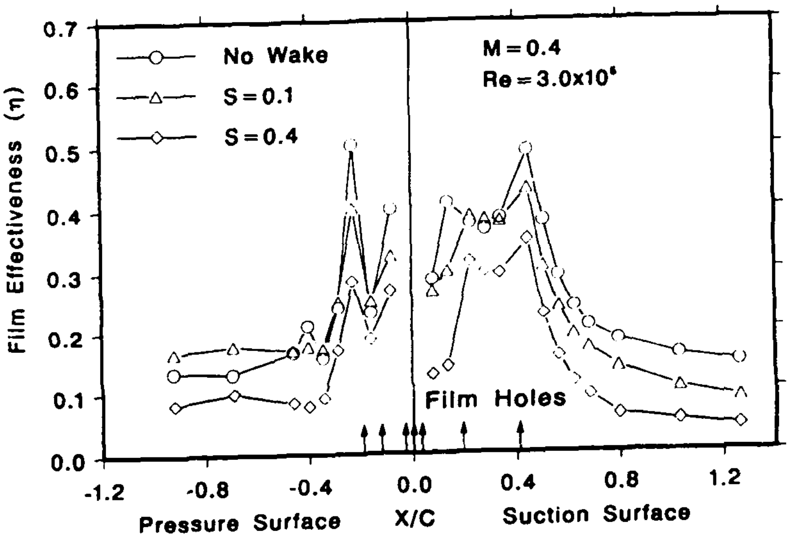

Figure 12: Effect of Unsteady Wake on Film Cooling Effectiveness Distribution for M = 0.4 and Re= 300,000

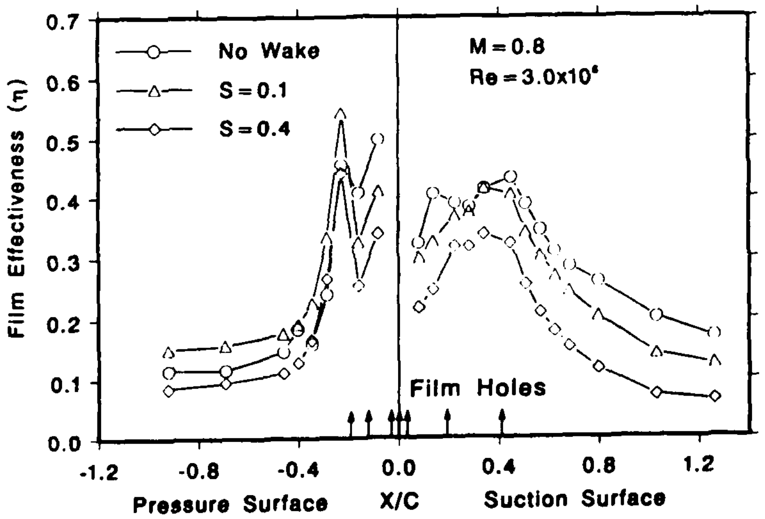

Figure 13: Effect of Unsteady Wake on Film Cooling Effectiveness Distribution for M = 0.8 and Re = 300,000

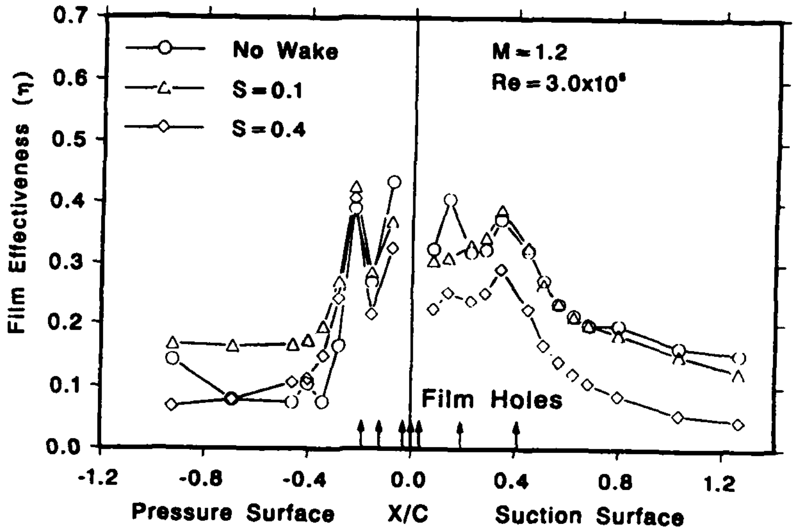

Figure 14: Effect of Unsteady Wake on Film Cooling Effectiveness Distribution for M = 1.2 and Re = 300,000

effectiveness distributions on the blade surface at Re = 3 x 10^5 for three blowing ratios (M = 0.4, 0.8, 1.2). The results in each blowing ratio are presented for zero wake (S = 0), medium wake (S = 0.1), and strong wake (S = 0.4) conditions. Again, note that the arrows represent locations of the film row holes on the blade surface and also that there are no thermocouples near the blade leading edge although it has three row of film cooling holes. The general observations of the results are: (1) both suction and pressure surface film effectiveness decreases with an increasing Strouhal number due to higher wake passing frequency; (2) the passing wake impact on the pressure side effectiveness is comparable with that on the suction side, (3) the film effectiveness distributions are similar with and without wake flow conditions although the passing wake reduces film effectiveness; (4) film effectiveness is generally higher just downstream of the film row holes and lowest near the blade trailing surface (η = 10%) due to film dilution (mixing) with the mainstream flow; and (5) the ability of the passing wake to destroy the film coverage does not seem to depend on blowing ratios between 0.4 and 1.2.

CONCLUDING REMARKS:

The influence of the upstream passing wake on the blade surface heat transfer coefficient and film cooling effectiveness distributions has been performed in a linear turbine cascade by using spoked wheel type rotating rods as wake generators. The periodic nature of instantaneous velocity, phase-averaged mean velocity and high turbulence intensity caused by unsteady passing wake has been detected by a fixed hot wire anemometer at the cascade inlet. The results show strong effects from the unsteady wake on the suction surface boundary layer transition and heat transfer. The strong wake also significantly increases the pressure surface heat transfer as a function of the wake passing frequency (Strouhal number). This confirms the observations of previous investigators. However, these experiments also provide the interesting result that wake effects on surface heat transfer are not nearly as significant when film cooling holes are present, and wake effects and film cooling effects on heat transfer are not additive. It appears that film cooling, and not unsteady wakes, are the dominant factor in early boundary layer transition and heat transfer augmentation. The results also demonstrate that the strong unsteady wakes greatly reduce the film cooling effectiveness on both pressure and suction surfaces over a range of blowing ratios.

This paper represents the first results of an ongoing Unique Turbine Cooling Studies project sponsored by the Naval Air Warfare Center, Aircraft Division, Trenton through General Electric Aircraft Engines. Parametric investigations on the effect of varying wake Strouhal numbers and mainstream Reynolds numbers on blade film cooling and heat transfer are underway.

Numerous opportunities exist for future work utilizing this unique facility. Future studies could consider phenomena such as mainstream turbulence effects, different blowing ratios/Reynolds number, or conduct parametric evaluations of various cooling configurations, film hole shapes, etc.

ACKNOWLEDGEMENT:

The authors are indebted to Dr. C. Pang Lee, project manager for General Electric Aircraft Engines, for his performance of the cascade design and analysis, as well as his helpful discussions throughout the project investigation. The authors also wish to thank Mr. Andrew Rutherford of the Naval Air Warfare Center for his valuable insight and comments on this study effort.

REFERENCES:

Abhari, R.S., Guenette, G.R., Epstein, A.H., and Giles, M.B., 1991, "Comparison of Time-Resolved Measurements and Numerical Calculations," ASME Paper No. 91-GT-268.

Abhari, R.S. and Epstein, A.H., 1992, "An Experimental Study of Film Cooling in a Rotating Transonic Turbine," ASME Paper No. 92-GT-201.

Blair, M.F., Dring, R.P., and Joslyn, H.D., 1989, "The Effects of Turbulence and Stator/Rotor Interactions on Turbine Heat Transfer: Parts I and II," ASME Journal of Turbomachinery, Vol. 111, pp. 87-103.

Blair, M.F., 1992, :An Experimental Study of Heat Transfer in a Large-Scale Turbine Rotor Passage," ASME Paper No. 92-GT-195.

Camci, C. and Arts, T., 1990, "An Experimental Convective Heat Transfer Investigation Around a Film-Cooled Gas Turbine Blade,: ASME Journal of Turbomachinery, Vol. 110, pp. 27-37.

Dunn, M.G., 1986a, "Heat Flux Measurements for the Rotor of a Full Stage Turbine: Part I - Time Averaged Results," ASME Paper No. 86-GT-77.

Dunn, M.G., George, W.K., Rae, W.J. Woodward, S.H., Moller, J.C., and Seymour, J.P., 1986b, "Heat Flux Measurements for the Rotor of a Full-Stage Turbine: Part II - Description of Analysis Technique and Typical Time-Resolved Measurements," ASME Paper No. 86-GT-78.

Dunn, M.G., Seymour, P.J., Woodward, S.H., George, W.K., and Chupp, R.E., 1988, "Phase-Resolved Heat Flux Measurements On the Blade of a Full-Scale Rotating Turbine," ASME Paper No. 88-GT-173.

Dunn, M.G., Kim, J., Civinskas, K.C., and Boyle, R.J., 1992, "Time Averaged Heat Transfer and Pressure Measurements and Comparison With Prediction for a Two Stage Turbine," ASME Paper No. 92-GT-194.

Dullenkopf, K., Schulz, A., and Wittig, S., 1990, "The Effect of Incident Wake on the Mean Heat Transfer of an Airfoil," ASME Paper No. 90-GT-121.

Dullenkopf, K. and Mayle, R.E., 1992, "The Effect of Incident Turbulence and Moving Wakes on Laminar Heat Transfer in Gas Turbines," ASME Paper No. 92-GT-377.

Kline, S.J. and McClintock, F.A., 1953, "Describing Uncertainties in Single-Sample Experiments," Mechanical Engineering, Vol. 75, pp. 3-8.

Liu, X. and Rodi, W., 1989, "Measurements of Unsteady Flow and Heat Transfer In a Linear Turbine Cascade," ASME Paper No. 89-GT-323.

Liu, X. and Rodi, W., 1992, "Measurements of Unsteady Flow Over and Heat Transfer from a Flat Plate,"ASME Paper No. 89-GT-2.

Mayle, R.E. and Dullenkopf, K., 1990, "A Theory for Wake-Induced Transition," ASME Journal of Turbomachinery," Vol. 113, pp. 509-537.

Mehendale, A.B., Han, J.C., and Ou, S., 1991,"Influence of High Mainstream Turbulence on Leading Edge Heat Transfer," ASME Journal of Heat Transfer, Vol. 113, pp. 843-850.

Nirmalan, V. and Hylton, L.O., 1989, "An Experimental Study of Turbine Vane Heat Transfer with Leading Edge and Downstream Film Cooling," ASME Paper No. 89-GT-69.

O'Brien, J.E. and Capp, S.P., 1989, "Two-Component Phase-Averaged Turbulence Statistics Downstream of a Rotating Spoked-Wheel Wake Generator," ASME Journal of Turbomachinery, Vol. 111, pp. 475-482.

Ou, S., and Han, J.C., 1991, :Influence of Mainstream Turbulence on Leading Edge Film Cooling Heat Transfer Through Two Rows of Inclined Film Slots," ASME Paper No. 91-GT-254.

Priddy, W.J. and Bayley, F.J., 1988, "Turbulence Measurements in Turbine Blade Passages and Implications for Heat Transfer," ASME Journal of Turbomachinery, Vol. 110, pp. 73-79.

Wittig, S., Dullenkopf, K., Schulz, A., and Hestermann, R., 1986, "Laser-Doppler Studies of the Wake-Effected Flow Field in a Turbine Cascade," ASME Paper No. 86-GT-160.

Wittig, S., Schulz, A., Dullenkopf, K., and Fairbank, J., 1988, "Effects of Free-Stream Turbulence and Wake Characteristics on the Heat Transfer Along a Cooled Gas Turbine Blade," ASME Paper No 88-GT-179.

Discussion

QUESTION 1:

DISCUSSOR: P. Harasgama, ABB

Do you intend to extend this work to engine representative conditions, such as high Mach number and Reynolds number?

AUTHOR'S REPLY:

While certainly desirable, increasing our Mach and Reynolds number capabilities at this point would require a facility modification. Bear in mind this is a relatively large wind tunnel. Generally speaking our objective for future work is to incrementally modify the cascade facility in order to approach a more realistic engine environment. Modifications currently being considered include provisions for freestream turbulence, incorporation of additional secondary flows, and coolant to freestream density effects, as well as enhanced Mach/Reynolds number capability.

QUESTION 2:

DISCUSSOR: N. Hay, University of Nottingham

You mention various shapes and geometries of holes. Can you tell us what shapes and geometries?

AUTHOR'S REPLY:

Most of the holes feature a compound angle discharge, which is a combination of angles in the radial and axial directions. The specific geometries of the film holes are company proprietary in some cases. So, although we cannot provide detailed specifications, we should be able to share the available data from the tests, if such information would be useful to you.

QUESTION 3:

DISCUSSOR: R.E. Mayle, Rensselaer Polytechnic Institute

There are some recent results by Abhari and Epstein showing that the large pressure fluctuations caused by the wakes from the upstream airfoils affect the flow leaving the cooling holes. Did you measure any pressure fluctuations and did you see any effects on the coolant flow which subsequently would change the film cooling?

AUTHOR'S REPLY:

At this point we did not measure that. The only pressure measurements we were able to take were on the blade that did not have film holes in it. That would certainly be an area that would be good to explore.

Measurement of Turbulent Spots and Intermittency Modelling at Gas-Turbine Conditions

J.P. Clark, Oxford University
Dept. of Engineering Science, Osney Laboratory
Oxford, OX1 3PJ, United Kingdom

J.E. LaGraff, Syracuse University, Syracuse, N.Y., U.S.A.
P.J. Magari and **T.V. Jones**, Oxford University, Oxford, U.K.

SUMMARY

Measurements have been made of instantaneous heat-transfer rates to a flat-plate surface under a transitional boundary layer. The thin-film surface instrumentation used in the study was capable of time-resolving the effects of changes in the heat-transfer rate within an accuracy of 10μs. The tests were conducted in the Oxford University 6 inch Isentropic Light-Piston Tunnel (ILPT) under simulated gas-turbine Reynolds numbers, Mach numbers, gas-to-wall temperature ratios, and pressure gradients.

The ability to observe and track the end stage of the transition process (i.e. turbulent spots) in a laminar boundary layer undergoing transition allowed turbulent-spot convection speeds and spreading angles to be estimated. In these tests, the important fluid-dynamic parameters of Mach number, Reynolds number, and streamwise pressure gradient were varied independently over a wide range of values characteristic of those encountered in the turbine environment.

Using quantitative values of the measured turbulent-spot characteristics, a simple time-marching code was developed based on Emmons' turbulent-spot theory to estimate the intermittency. This work was sponsored by the United States Air Force Office of Scientific Research under grant numbers 89-0427 and F49620-92-J-0079 with Major Daniel Fant acting as technical monitor.

LIST OF SYMBOLS

f_l	turbulent-spot leading-edge convection rate (as a fraction of the freestream velocity)
f_t	turbulent-spot trailing-edge convection rate (as a fraction of the freestream velocity)
g	turbulent-spot source-rate-density function
K	acceleration parameter $[K=(\nu/U_\infty^2)dU_\infty/dx]$
l	thin-film-gauge length in cross-stream direction (mm)
M_∞	freestream Mach number
n	turbulent-spot generation rate (s^{-1} m^{-1})
P	freestream static pressure (N/m^2)
P_o	total pressure (N/m^2)
q	heat flux (kW/m^2)
Re_ν	freestream unit Reynolds number at the working-section inlet (m^{-1})
s	distance along the suction surface of a turbine blade (m)
T_o	total temperature (K)
T_w	wall temperature (K)
Tu	freestream turbulence intensity $[u'/U_\infty]$
t_{NT}	amount of time an unsteady heat-transfer signal is non-turbulent (s)
t_T	amount of time an unsteady heat-transfer signal is turbulent (s)
U_{le}	turbulent-spot leading-edge velocity (m/s)
U_m	turbulent-spot mean convection velocity (m/s)
U_{te}	turbulent-spot trailing-edge velocity (m/s)
U_∞	freestream velocity (m/s)
U_{inf}	freestream velocity (m/s)
w	thin-film gauge width in streamwise direction (mm)
x	distance from the leading edge of the flat plate (m)
x_t	distance from the leading edge of the flat plate to the point of transition onset (m)
x_0	turbulent-spot origin (m)
z	distance of gauge centerline from the centerline of the flat plate (mm)
α	turbulent-spot spreading angle (degrees)
γ	intermittency $(t_T/(t_T+t_{NT}))$
ν	kinematic viscosity (m^2/s)
σ	Emmons' non-dimensional turbulent-spot propagation parameter $[\sigma = \tan\alpha\,(f_t^{-1} - f_l^{-1})]$

INTRODUCTION

Much of the boundary layer on the suction surface of a gas-turbine blade can be transitional. Consequently, knowledge of the location and extent of the transition zone is essential for proper cooling design. Without such information, gross errors can be made in estimating the total heating-load on the blades.

The transition process associated with gas turbines is influenced by a variety of mechanisms. These include freestream turbulence, pressure gradient, surface curvature, compressibility, and the periodic passage of wakes and shocks from upstream nozzle-guide-vanes. A comprehensive review of the above effects on the transition process in gas turbines is given by Mayle (Ref. 1). Previously at Oxford, much research has been devoted to the study of transition on the suction surfaces of gas-turbine blades in a two-dimensional cascade. In 1983, Doorly (Ref. 2) studied the effect of simulated nozzle-guide-vane wakes and shocks on the transition region. Following his work, LaGraff et al. (Ref. 3) and Ashworth et al. (Ref. 4) studied the combined effects of freestream turbulence and wake passage on transition.

A major finding of the experiments described above is that the transition region on a gas-turbine blade is "multimoded" (after Mayle [Ref. 1]). This means that at any given time, transition to turbulence on the suction surface of a blade can arise at multiple locations for different reasons. This process is illustrated in Figure 1, which is a typical result of the work of LaGraff et al. (Ref. 3). Clearly, the boundary layer is undergoing transition caused by two distinct phenomena. First, the wake impinging on the blade has brought about bypass transition to turbulence. This region convects downstream in the form of a "turbulent strip" (after Mayle and Dullenkopf [Ref. 5]). Second, between the wake-induced turbulent strips, a region of "natural" transition can be observed. The results depicted in the figure are influenced by many factors. Therefore, a more fundamental experimental program has been undertaken to study the effects of certain parameters in isolation. In this study, transition experiments were performed on a flat plate instrumented with thin-film heat-transfer gauges. Effects of pressure gradient and compressibility have been determined separately at turbine-representative Reynolds numbers and gas-to-wall temperature ratios.

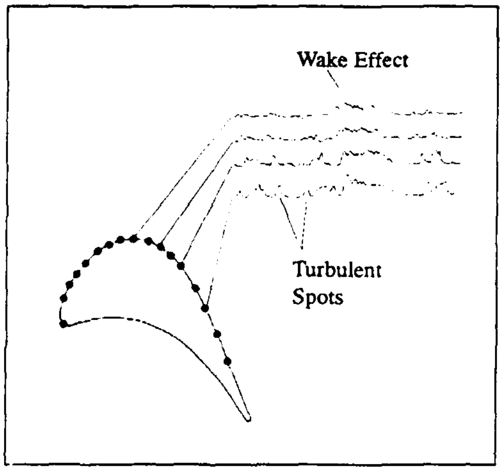

Figure 1 - Typical results from the work of LaGraff et al. (Ref. 3) illustrating "multimoded" transition.

The parameter which best describes the state of the boundary layer during the transition to turbulence is the intermittency. The variation of intermittency through the transition zone is dictated by the rate and distribution of turbulent-spot generation, spot convection velocity, and lateral spreading. As a result, detailed measurements of turbulent-spot parameters could lead directly to a model for the variation of intermittency through the transitional boundary layer. In this study, a time-marching code was developed after that of Ashworth and LaGraff (Ref. 6), which makes use of the Emmons transition model (Ref. 7) in conjunction with the concept of concentrated breakdown as put forward by Narasimha (Ref. 8). This allowed the authors to generate computer-simulated unsteady heat-transfer traces for comparison with time-resolved measurements. It also enabled the authors to utilize preliminary experimental results to determine the optimal gauge layout for accurate extraction of the turbulent-spot parameters from unsteady heat-transfer traces. In addition, it is hoped that this simple model, in conjunction with the detailed measurements of turbulent-spot characteristics being made in this study, will yield a generalized model for the variation of intermittency through the transition zone on gas-turbine blades. Such a model could be easily "patched" into time-marching schemes already used in the design process for the prediction of laminar- and turbulent-boundary-layer heat transfer to gas-turbine blades. The only design variable unspecified would be the starting point of transition.

DESCRIPTION OF FACILITY AND EXPERIMENTAL TECHNIQUE

The experiments were conducted in a short-duration piston-driven facility known as an Isentropic Light-Piston Tunnel (ILPT). The Oxford University 6" ILPT is shown schematically in Figure 2 and is described completely in Jones et al. (Ref. 9). The device consists of a high-pressure reservoir which can be vented via several fast-acting ball valves into a relatively low-pressure tube fitted with a light-weight piston. At the initiation of a run, the stroke of the piston begins at the reservoir end of the tube. The piston is propelled towards the test section by venting the high-pressure reservoir into the region behind it. As the piston travels down the bore of the tube, the gas ahead of it is compressed (and hence its temperature is increased) since the test section is sealed from the dump tank by a fast-acting gate valve. The compression process is relatively slow since the piston velocity is much less than the local acoustic speed. Therefore, if heat transfer from the hot test-gas to the walls of the tube is neglected, the compression can be assumed to be isentropic. When the desired operating conditions are achieved, the gate valve is opened and the hot test-gas washes through the test section.

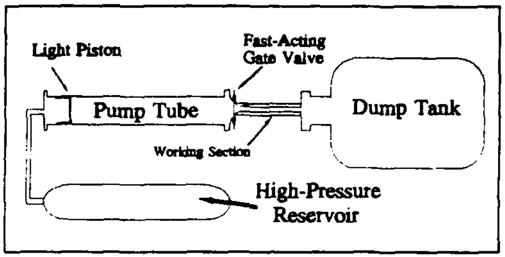

Figure 2 - Schematic of the Isentropic Light-Piston Tunnel.

One of the primary advantages of this type of facility is that the freestream Mach number, Reynolds number, and gas-to-wall temperature ratio can be controlled independently. Also, since the temperature of the test gas can be elevated significantly above that of a model placed in the working-section region, heat transfer will occur naturally between the flow and the model surface. This makes it possible to use thin-film heat-transfer gauges to monitor the surface heat-flux. A full description of this technique can be found in Schultz and Jones (Ref. 10).In the present study, a flat-plate model, densely populated with platinum thin-film heat-transfer gauges, was fitted in the ILPT test-section as shown schematically in Figure 3, which is the subsonic configuration. The dimensions of the thin-film gauges are listed in Appendix A. For the supersonic tests, the nozzle throat was placed upstream of the instrumented section of the plate and just downstream of the leading edge to avoid the problems associated with a supersonic leading-edge. The freestream pressure gradients tested were qualitatively consistent with those encountered on a typical turbine-blade suction surface (see Figure 4) and similar in severity to those seen in the cascade tests of LaGraff et al. (Ref. 3). The freestream pressure gradients, which are depicted in Figure 5, were effected by varying the contour of the test-section wall opposite the flat plate.

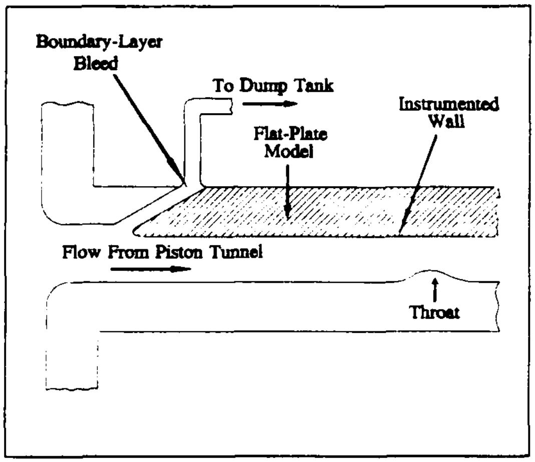

Figure 3 - Schematic of the **ILPT** test section fitted with an instrumented flat plate.

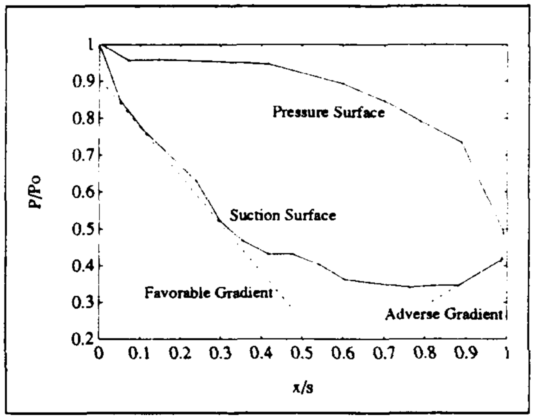

Figure 4 - The pressure distribution around a typical turbine blade (from Ref. 11).

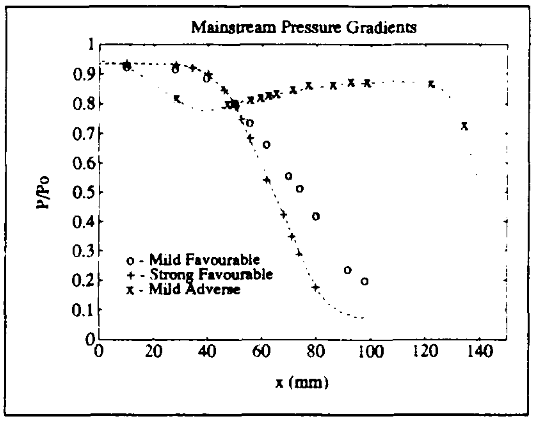

Figure 5 - Freestream pressure gradients.

The use of thin-film gauges for the measurement of steady and unsteady heat-transfer rates is described fully by Schultz and Jones in Ref. 10. The thin-film gauges used in this study were operated at a constant current, and the signals from the gauges were processed through electrical analogs of the one-dimensional unsteady heat-conduction equation. The analogs used are based on the design of Oldfield, et al. (Ref. 12) and have a nominal bandwidth of 0.1-100kHz. High-speed data-acquisition channels are available to monitor 16 thin-film signals simultaneously. Each channel has a maximum data-rate of 1MHz and a storage capacity of 64Kb.

This study was conducted using a model made of Macor with thin films produced via a hand-painting-and-firing technique (see Schultz and Jones [Ref. 10]). The disadvantage of this production technique is that it is difficult to produce very small and/or complicated gauge/lead patterns. As such, a new gauge production-technique is being developed whereby the gauge and lead patterns are photo-resistance etched on a thin sheet of polymer which has a layer of vapor-deposited metal on the surface. The technique is similar to that utilized in the production of printed-circuit boards. The polymer sheet can then be bonded to a perspex model, and wire leads can be soldered directly to the model surface. Complicated gauge/lead patterns are relatively simple to realize, and gauges have been produced with streamwise extents of 25μm and spanwise extents of 100μm via the technique. Future studies will incorporate results from this type of gauge (see Ref. 13).

ANALYSIS TECHNIQUES

As previously mentioned, the variation of intermittency through the transition zone is dictated by the rates of turbulent-spot generation, convection, and lateral spreading. This is apparent from the equation of Narasimha (Ref. 8)

$$\gamma(x)=1-e^{\left\{\frac{-(x-x_t)^2\, n\sigma}{U_\infty}\right\}} \tag{1}$$

which results from the application of Emmons' transition model with the assumption of concentrated breakdown to a flat plate, constant-pressure flow. In Equation 1, x_t is the location of breakdown, n is the number of turbulent spots formed there per unit time and spanwise distance, U_∞ is the freestream velocity, and x is a location on the surface further downstream than x_t. σ is Emmons' non-dimensional spot propagation parameter, which takes into account the convection velocity of the spots and their rate of lateral spreading.

A more general relation for the variation of intermittency through the transition zone, which was given by Ashworth and LaGraff (Ref. 6), is seen in Equation 2. In the

$$\gamma(x) = 1 - \exp\left\{ -\int_0^x g(x_0) \left[\int_{x_0}^x \tan(\alpha(x))\,dx\right] \left[\int_{x_0}^x (f_t^{-1}-f_l^{-1})\frac{dx}{U_\infty(x)}\right] dx_0 \right\} \tag{2}$$

equation, x_0 is the turbulent-spot origin along the surface of the plate, U_∞ is the freestream velocity, $g(x_0)$ is the source-rate-density function for turbulent-spot formation, α is the spot spreading angle, and f_l and f_t are the spot leading- and trailing-edge convection velocities as fractions of the freestream celerity, respectively. In effect, it is this equation which is embodied in the time-marching code. Thus it is possible to make allowances for non-constant freestream velocity and spot growth parameters in the model. Also, provision has been made for the incorporation of a more general source-rate-density function than the Dirac delta strictly implied by Narasimha's concept of concentrated breakdown. The source-rate function here can be assumed to vary around the starting point of transition in a Gaussian sense. In this study, turbulent-spot parameters are determined experimentally and then input to the time-marching scheme. Turbulent-spot convection and generation rates are extracted from unsteady heat-transfer traces with the aid of a digital intermittency-detector. The lateral-spreading rate is calculated from estimates of the rate-of-change of thin-film-gauge coverage with distance along the flat-plate model surface.

Intermittency detectors, either analog or digital, have been utilized for a number of years in the analysis of hot-wire signals. A comprehensive review of the technique was given by Hedley and Keffer (Ref. 14). In essence, a raw signal is transformed in such a way that a decision for or against the presence of turbulence at the sensor can be rationally made. Typically, the signal is differentiated and squared to emphasize the high-frequency components. The purpose behind the signal transformation employed by an intermittency detector is to significantly reduce the probability of making an incorrect turbulent/non-turbulent decision over that which would occur if the signal level alone were used as an indicator of turbulent activity. Full details of the method used in this study can be found in Clark et al. (Ref. 13).

The results of the intermittency detection process can be used to determine a number of turbulent-spot parameters. Firstly, the variation of intermittency through the transition zone can be determined. Secondly, it is possible to use the results as a simple turbulent-spot counter, thus yielding the turbulent-spot generation rate. Finally, the intermittency can be separated into two more signals; the first consisting of the leading-edge passage times and the second made up of the trailing-edge times. The leading- and trailing-edge signals from adjacent gauges can then be cross-correlated to determine the convection rates of the leading and trailing edges of the turbulent spots in the streamwise direction.

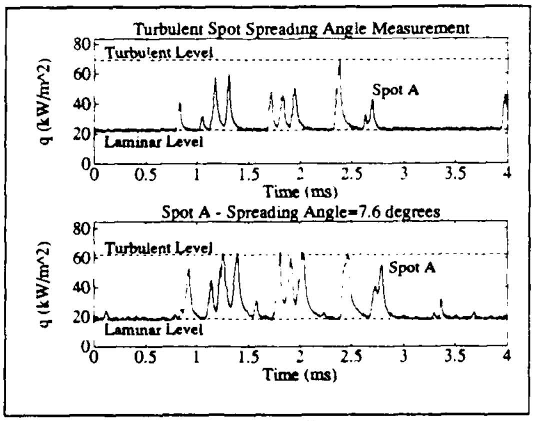

Figure 6- Turbulent-spot spreading-angle measurement. The streamwise distance between the gauges is 11.95 mm.

The heat-transfer rate measured by a thin-film gauge is an average of the heat-transfer distribution over the sensing area of the gauge. Consequently, it is possible to make estimates of turbulent-spot lateral growth from the rate-of-change of thin-film-gauge coverage with distance along the model surface. Figure 6 is an illustration of this process. It can be seen that the turbulent spot labeled A in the figure brings the instantaneous heat flux to a value somewhere between the laminar and fully-turbulent levels as indicated on the upper trace of Figure 6. This is because only a fraction of the total gauge length is covered by the spot. However, as the spot travels downstream it is continually growing in the cross-stream direction. As a result, the spot covers a greater percentage of the trace plotted in the bottom half of the figure. Knowing the gauge locations on the plate, it is possible to determine the position of the lateral edge of the turbulent spot over each gauge. The turbulent-spot spreading angle can then be determined from simple geometry.

EXPERIMENTAL RESULTS

Figure 7 is a set of unsteady heat-transfer traces taken at Mach 0.55 in constant-pressure flow. The traces seen in the figure are typical of those recorded during a single run. Clearly, turbulent spots can be seen to propagate along the model surface in the streamwise direction. In any given run, as many as 16 heat-transfer traces like those seen in the figure are recorded. This data is then analyzed as described in the previous section.

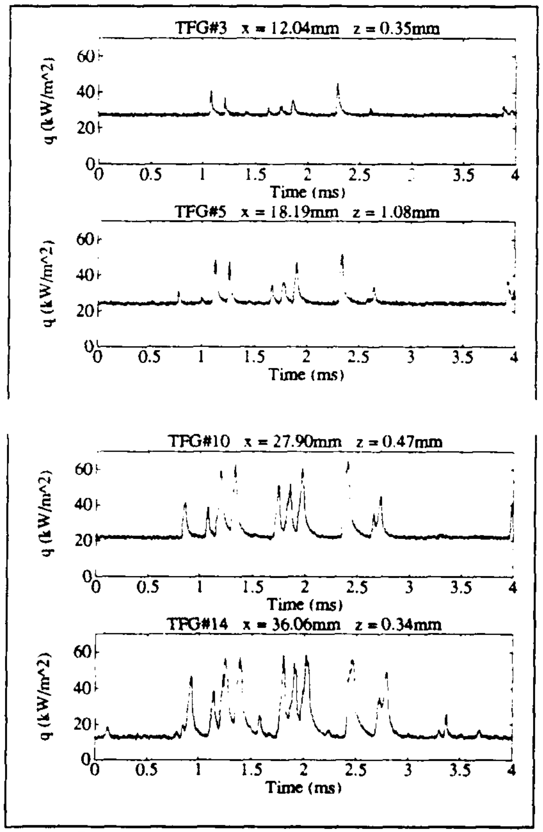

Figure 7- Unsteady heat-transfer traces (M_∞=0.55, zero pressure gradient, Re_u=7.5x10^{-6}, T_o/T_w=1.4, Tu=0.1%).

Figure 8 is a plot of turbulent-spot trajectories resulting from the application of the procedure described above to the unsteady heat-transfer traces of Figure 7. The conditions of the run are zero pressure gradient, a gas-to-wall temperature ratio of 1.4, and a freestream Mach number of 0.55. Three trajectories are shown, and the values of percentage freestream velocity associated with each line are indicated. The "mean" trajectory was determined from cross-correlating the raw signals as described in Clark et al. (Ref. 15). Figure 9 is a plot of the spot trajectories for the same conditions as those above except that the freestream Mach number is 1.86. Interestingly, the leading-edge, trailing-edge, and 'mean' convection rates are nearly the same fraction of the freestream velocity for the Mach 0.55 and 1.86 cases. Also, the results agree very well with those of Schubauer and Klebanoff (Ref. 16) for artificially-generated turbulent-spot leading- and trailing-edge convection velocities at incompressible conditions. It should be noted that this marks the first time that these parameters have been determined in "natural" transition at subsonic compressible and supersonic Mach numbers.

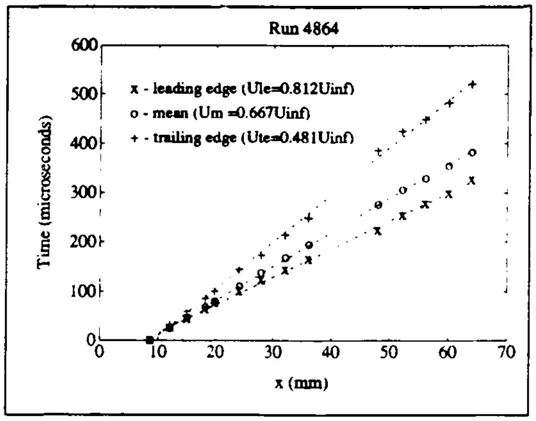

Figure 8 - Turbulent-spot leading-edge, trailing-edge, and "mean" trajectories for M_∞=0.55, zero pressure gradient, Re_u=7.5x10^6/m, T_o/T_w=1.4, and Tu=0.1%.

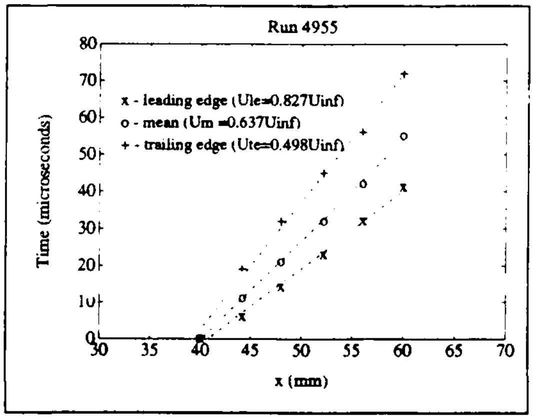

Figure 9 - Turbulent-spot leading-edge, trailing-edge, and "mean" trajectories for M_∞=1.86, zero pressure gradient, Re_u=23.6x10^6/m, T_r/T_w=1.4, and Tu=0.1%

There are some differences between the spot trajectories measured in zero and non-zero pressure gradients. Figure 10 is a set of turbulent-spot trajectories for the mild-favorable pressure gradient case depicted in Figure 5, and Figure 11 is a plot of the variation of leading-edge, trailing-edge, and "mean" convection velocities with distance along the model surface for the same case. For comparison, the variation of freestream velocity with distance is also illustrated. It is evident that, over the region of constant streamwise pressure gradient indicated in the figure, the leading-edge velocity is a roughly constant fraction of the freestream velocity, while the trailing-edge and "mean" convection rates are not. Wygnanski (Ref. 17) found that neither the leading- nor the trailing-edge velocity scales directly with that of the freestream in a favorable pressure gradient. In addition, he concluded that a turbulent spot which is formed in a zero pressure gradient has "memory" of its conditions at formation and is unaffected by subsequent increases in freestream velocity. No evidence of the latter effect is manifest in the results of this experiment. This perhaps points to the dangers of relying on turbulent-spot information extracted from experiments performed with artificially-generated spots in otherwise laminar boundary layers for the design of gas turbines.

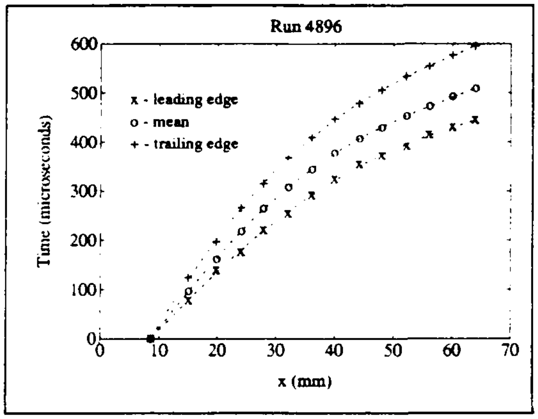

Figure 10- Turbulent-spot leading-edge, trailing-edge, and "mean" trajectories for the Mild-Favorable Pressure Gradient, Re_u=8x10^6, Tu=0.1% (0.3≤M_∞≤0.9 over the range indicated by the plot).

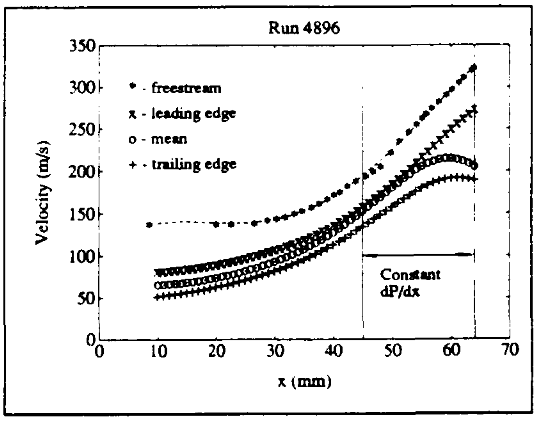

Figure 11- Turbulent-spot leading-edge, trailing-edge, and "mean" velocities compared with freestream velocity for the Mild-Favorable Pressure gradient, Re_u=8.9x10^6, Tu=0.1% (0.3≤M_∞≤0.9 over the range indicated by the plot).

This is further emphasized in Figure 12, which is a plot of the ratio of spot velocities to the freestream celerity versus distance along the flat-plate-model surface. The plot focuses on the region of constant pressure gradient (as seen in Figure 11). The variation of the acceleration parameter, K, over the same distance is indicated in Figure 13. It is clear that the velocity of the trailing-edge is much closer to that of the leading-edge at higher values of K. Also, as K decreases, the trailing-edge velocity of the spot begins to approach the value it normally takes under zero pressure gradient. Moreover, it would seem that at larger values of K the turbulent-spot grows more slowly in the streamwise direction than it normally would under a zero pressure gradient.

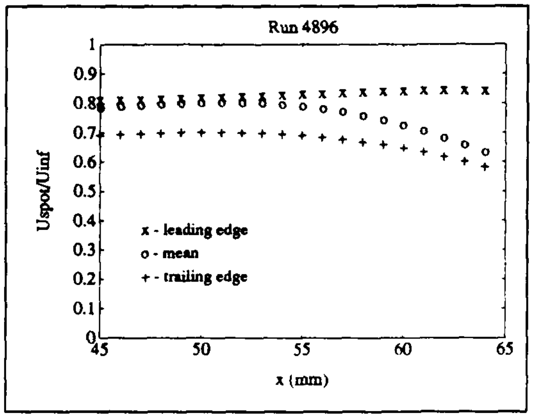

Figure 12- Turbulent-spot leading-edge, trailing-edge, and "mean" velocities normalized by freestream velocity for the Mild-Favorable Pressure gradient, Re_u=8.9x10^6, Tu=0.1%.

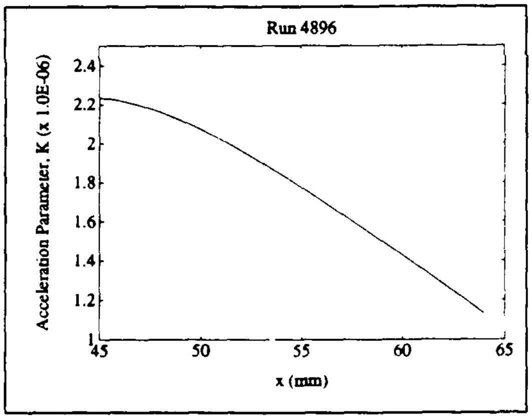

Figure 13- Variation of acceleration parameter with distance along the flat-plate-model surface for the constant dP/dx region of the working section.

Some preliminary results of turbulent-spot spreading angle under various conditions are presented in Table 1. It can be seen that, as expected, the lateral growth of turbulent spots is greatly inhibited by a favorable pressure gradient and augmented by an adverse one. This is in general agreement with estimates of the effect of pressure gradient from artificial-spot studies, and it supports the conclusion of Gad-el-Hak et al. (Ref. 18) that spots spread laterally by the local destabilization of the laminar boundary layer at their edges. Also, the value of 7.6° given for the spreading angle at zero pressure gradient and Mach 0.55 is significantly lower than that generally accepted at incompressible Mach numbers (10-11°). This supports the theoretical prediction of Doorly and Smith (Ref. 19) that the spreading angle of a turbulent spot decreases monotonically as freestream Mach number increases.

Pressure Gradient	Spreading Angle
Zero, M_∞=0.55	7.6°
Mild favorable	2.8°
Strong Favorable	1.2°
Mild Adverse	15.0°

Table 1 - Estimates of turbulent-spot spreading angles under various conditions.

Figure 14 is a plot of the variation of intermittency with distance along the flat-plate model surface for various pressure gradients. All three curves represent data gathered at an inlet unit Reynolds number of 6x10^6 per meter and a gas-to-wall temperature ratio of 1.4. It can be seen that an adverse pressure gradient leads to a decrease in the length of the transition zone as compared to the zero pressure gradient case, while the opposite is true of a favorable pressure gradient. Indeed, in the case of the favorable pressure gradient, the intermittency changes only slightly over the measurement interval represented in the figure. These results are also in agreement with those presented in Table 1.

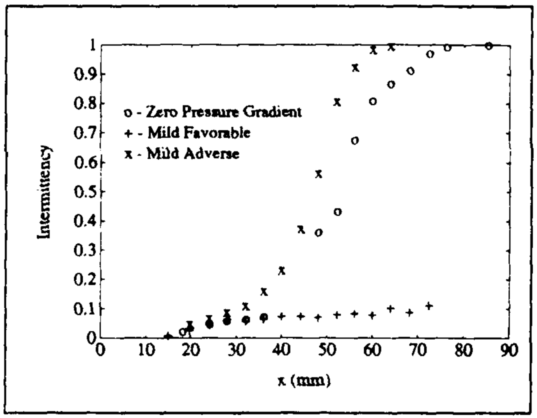

Figure 14- Intermittency distributions for three freestream-pressure-gradient conditions.

MODELLING RESULTS

At present, the time-marching code has been used primarily for the validation of the analysis techniques developed in the study. The following two figures are an example of this procedure. Figure 15 is a plot of unsteady heat-transfer traces which resulted from the application of the time-marching intermittency model at Mach 0.55 in a zero pressure gradient. The leading- and trailing-edge propagation rates of the turbulent spots input to the model were the same values determined experimentally under these conditions (see Figure 8). Figure 16 is a plot of the leading- and trailing-edge trajectories calculated for the traces of Figure 15. For comparison, the input values are indicated on the plot as well. It is clear that the results correspond well with the known input values, especially in the case of the trailing-edge trajectory. The leading-edge convection rate is only 7% different from the known input. This slight discrepancy is not due to a lack of sensitivity in the analysis technique, however. Instead, it is a result of the gauge length input to the time-marching scheme and the effect this subsequently has on the character of the unsteady heat-transfer signals.

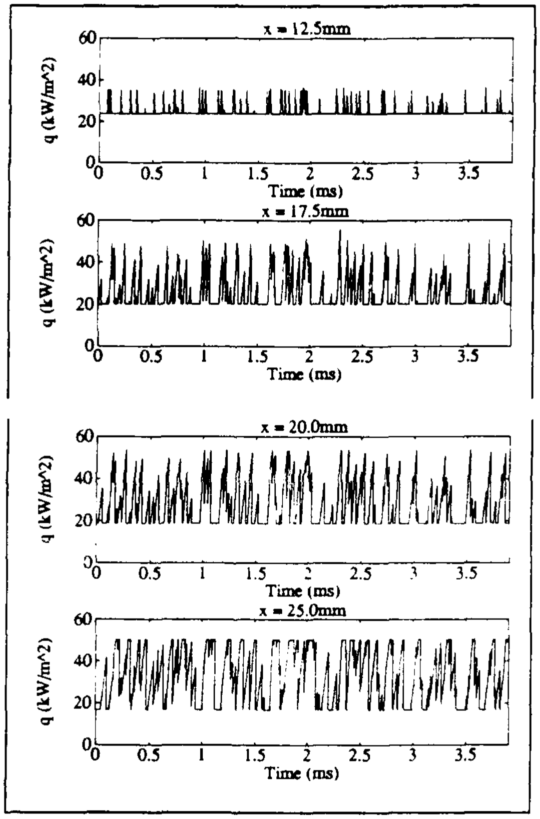

Figure 15- Unsteady heat-transfer traces which resulted from the application of the time-marching model at M_∞=0.55, zero pressure gradient, To/Tw=1.4, and Re_u=6x10^6/m (gauge length = 2.5mm).

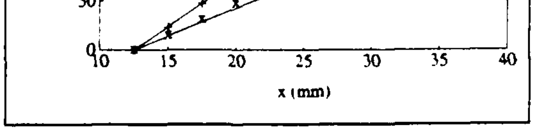

Figure 16- Turbulent-spot trajectories calculated for the traces of Figure 15 (l=2.5mm).

Figure 17 is a plot of similar results to those in Figure 16. The only difference in the inputs to the time-marching scheme between the two cases is the length of the thin-film gauges. Also, all inputs to the data analysis algorithm are identical to those used to generate the data plotted in Figure 16. Clearly, more accurate results of spot leading-edge convection rates are obtained when thin-film gauges which have smaller lengths in the cross-stream direction are used. This is one example of the usefulness of the time-marching code for the optimization of thin-film sensor arrays. At this point, it is worth noting that the results for turbulent-spot leading-edge velocity plotted in Figures 8 and 9 are roughly 7% different from the accepted low-speed value of $0.88U_\infty$, and that the average length of the thin films used in this study is roughly 3mm.

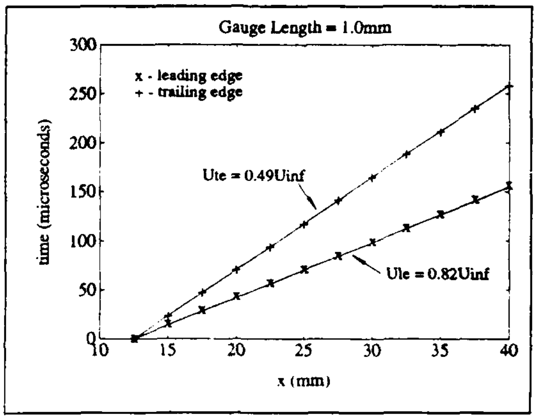

Figure 17- Turbulent-spot trajectories calculated at the same conditions as Figure 16, except that l=1.0mm.

CONCLUSIONS

Turbulent spots have been tracked in a boundary layer undergoing natural transition at gas-turbine-representative conditions. The separate effects of pressure gradient and compressibility on the growth characteristics of turbulent spots have been assessed. For the first time, turbulent-spot leading- and trailing-edge convection velocities have been extracted from natural transition data at compressible conditions. It was observed that in a zero pressure gradient, the spot leading and trailing edges propagated at essentially the same fraction of the freestream velocity observed by other researchers at incompressible conditions. Favorable pressure gradients were found to have little effect on the convection rate of the spot leading edges, which was found to be roughly the same fraction of freestream velocity seen in zero pressure gradient. By contrast, it was observed that the velocity of turbulent-spot trailing-edge propagation does not scale directly with that of the freestream.

It is also possible to make estimates of the growth rates of turbulent spots from the results of these experiments. Preliminary results of turbulent-spot spreading angles presented in this paper indicate that the lateral growth of turbulent spots is greatly affected by mainstream pressure gradients. In addition, it was also shown that the streamwise growth of turbulent spots can be affected by a favorable pressure gradient. At large values of the acceleration parameter, K, the trailing-edges of turbulent spots appear to propagate as much as 40% faster than under zero-pressure-gradient conditions, implying a significant reduction of spot growth in the streamwise direction.

ACKNOWLEDGEMENTS

Special thanks must go to Trevor Godfrey for his assistance in designing the working section of the tunnel and technical support throughout the study. Also, the advice of Dr. David Ashworth, of Rolls-Royce, plc., during the experimental program, the modelling effort, and the preparation of this manuscript is gratefully acknowledged. Special thanks also to S.R. Smelser for help in the production of some of the figures in this report. The work herein was supported by the United States Air Force Office of Scientific Research under grant numbers F49620-92-J-0079 and 89-0427, with Major Daniel Fant acting as technical monitor.

REFERENCES

1. Mayle, R.E., "The Role of Laminar-Turbulent Transition in Gas-Turbine Engines", ASME Journal of Turbomachinery, *113*, October 1991, pp. 509-537.

2. Doorly, D.J., "A Study of the Effect of Wake Passing on Turbine Blades", D.Phil. Thesis, University of Oxford, United Kingdom, 1983.

3. LaGraff, J.E., Ashworth, D.A., and Schultz, D.L., "Measurement and Modelling of the Gas-Turbine-Blade Transition Process as Disturbed by Wakes", ASME Journal of Turbomachinery, *111*, July 1989, pp. 315-322.

4. Ashworth, D.A., LaGraff, J.E., and Schultz, D.L., "Unsteady Interaction Effects on a Transitional Turbine Blade Boundary Layer , ASME Journal of Turbomachinery, *111*, April 1989, pp. 162-168.

5. Mayle, R.E. and Dullenkopf, K., "A Theory for Wake-Induced Transition", ASME Journal of Turbomachinery, *112*, 1990, pp. 188-195.

6. Ashworth, D.A. and LaGraff, J.E., "Measurement and Modelling of Turbulent-Spot Growth on a Gas-Turbine Blade", AIAA Paper No. 89-0328, 1989.

7. Emmons, H.W., "The Laminar-Turbulent Transition in a Boundary Layer - Part 1", Journal of the Aeronautical Sciences, *18*, 1951, pp. 490-498.

8. Narasimha, R., "On the Distribution of Intermittency in the Transition Region of a Boundary Layer", Journal of the Aeronautical Sciences, *24*, 1957, pp. 711-712.

9. Jones, T.V., Schultz, D.L., and Hendley, A.D., "On the Flow in an Isentropic Light-Piston Tunnel, ARC 34217, 1973.

10. Schultz, D.L. and Jones, T.V., "Heat Transfer Measurements in Short-Duration Hypersonic Facilities", NATO AGARDOGRAPH 165, 1973.

11. Teekaram, A.J.H., "Film-Cooling in the Presence of Mainstream Pressure Gradients and Foreign-Gas Injection", D.Phil. Thesis, University of Oxford, U.K., 1989.

12. Oldfield, M.L.G., Burd, H.J., and Doe, N.G., "Design of Wide-Bandwidth Analogue Circuits for Heat_Transfer Instrumentation in Transient Tunnels", 16th Symposium of ICHMT, Dubrovnik, Hemisphere Publications, 1982.

13. Clark, J.P., Magari, P.J., Jones, T.V., and LaGraff, J.E., "Turbulent-Spot Growth and Dynamics at Compressible and Incompressible Conditions," to be presented at the 31st AIAA Aerospace Sciences Meeting, Reno, Nevada, 1993.

14. Hedley, T.B. and Keffer, J.F., "Turbulent/Non-Turbulent Decisions in an Intermittent Flow", Journal of Fluid Mechanics, *64*, 1974, pp. 645-678.

15. Clark, J.P., Jones, T.V., Ashworth, D.A., and LaGraff, J.E., "Turbulent-Spot Development in a Mach 0.55 Flow", Proceedings of the Royal Aeronautical Society Boundary-Layer Transition and Control Conference, April 1991, Cambridge, U.K., Paper 21.

16. Schubauer, G.B. and Klebanoff, P.S., "Contributions on the Mechanics of Boundary-Layer Transition", NACA TN-3489, 1955.

17. Wygnanski, I., "The Effects of Reynolds Number and Pressure Gradients on the Transitional Spot in a Laminar Boundary Layer", Lecture Notes in Physics, *136*, 1981, pp. 304-322.

18. Gad-el-Hak, M., Blackwelder, R.F., and Riley, J.J., "On the Growth of Turbulent Regions in Laminar Boundary Layers", Journal of Fluid Mechanics, *110*, 1981, pp. 73-95.

19. Doorly, D.J. and Smith, F.T., "Initial-Value Problems for Spot Disturbances in Incompressible and Compressible Boundary Layers", Journal of Engineering Mathematics, *26*, 1992.

APPENDIX A - Thin-film gauge dimensions.

TFG#	x (mm)	z (mm)	l (mm)	w (mm)
1	1.73	0.105	2.81	0.48
2	8.63	0.340	2.82	0.49
3	12.04	0.350	3.10	0.42
4	15.01	0.485	3.07	0.57
5	18.19	1.075	3.57	0.61
6	19.81	1.005	4.03	0.44
7	21.96	3.250	2.46	0.41
8	24.11	0.630	3.50	0.48
9	26.36	-2.295	2.29	0.49
10	27.90	0.470	4.00	0.45
11	30.02	3.315	3.11	0.46
12	32.07	0.535	3.17	0.55
13	34.02	-2.400	3.02	0.55

TFG#	x (mm)	z (mm)	l (mm)	w (mm)
14	36.06	0.340	3.38	0.46
15	38.02	2.485	3.23	0.58
16	39.93	0.475	3.59	0.41
17	42.34	-2.640	3.42	0.42
18	44.18	0.190	3.02	0.51
19	46.15	1.730	3.46	0.52
20	48.00	0.845	3.11	0.46
21	49.96	-1.740	2.90	0.45
22	52.18	0.150	2.94	0.46
23	54.04	2.790	2.10	0.43
24	56.04	0.480	3.28	0.45
25	58.00	-2.165	2.91	0.47
26	60.00	0.310	3.12	0.49
27	62.16	3.110	3.22	0.46
28	63.95	0.100	2.84	0.42
29	66.34	-2.495	2.57	0.48
30	68.25	0.200	2.72	0.48
31	70.00	2.975	2.51	0.35
32	72.46	0.020	3.80	0.47
33	74.37	-2.540	2.58	0.45
34	76.28	0.520	3.42	0.52
35	79.84	0.350	3.36	0.38
36	85.17	0.290	3.60	0.50
37	90.17	0.290	3.20	0.52
38	95.15	0.130	3.24	0.46
39	100.00	0.020	3.46	0.52

Discussion

QUESTION 1:

DISCUSSOR: H.B. Weyer, ABB

How did you define leading and trailing edges of the spots and did you use a cross-correlation of the data to analyze downstream movement of the spots?

AUTHOR'S REPLY:

If a cross-correlation analysis is applied to unsteady heat-flux traces from two locations on the flat-plate surface, a peak in the cross-correlation coefficient is obtained at some time lag, Δt. In this study the Δt corresponding to the peak is said to be the "average" time it takes a turbulent spot to convect from one thin-film gauge to the next. Performing such an analysis from gauge to gauge along the model surface allows one to construct a "mean" turbulent spot trajectory through the transition zone. Differentiating such a trajectory with respect to time yields the "mean" convection rate of the turbulent spots.

It is desirable to determine the convection rates of the spot leading and trailing edges as well as the "mean" celerity of the spots. In this study, turbulent spot leading- and trailing-edge velocities are extracted from unsteady heat-flux traces with the aid of a digital intermittency detector.

Intermittency detectors, whether analog or digital, have been used for a number of years in the analysis of hot-wire signals. A comprehensive review of the technique was given by Hedley and Keffer (Ref 1). An intermittency detector is in essence a signal processor which is used to significantly reduce the probability of making an incorrect turbulent/non-turbulent decision over that which would occur if , for example, the signal level alone were used as an indicator of turbulent activity at the sensor.

The process by which turbulent/non-turbulent decisions are made in this study is illustrated in Figure 1. The top-trace in Figure 1 is the raw heat-flux signal $\dot{q}(t)$. The second trace from the top is , after Hedley and Keffer, the detector function which is defined as

$$D_i = m\left(\dot{q}_i'\right)^2 \tag{1}$$

where m is the signal magnitude, given by

$$m = \frac{\dot{q}_i - \dot{q}_{min}}{\dot{q}_{max} - \dot{q}_{min}} \tag{2}$$

The first derivative of the instantaneous heat flux is found by the central difference equation

$$\dot{q}_i' = \frac{\dot{q}_{i+1} + \dot{q}_{i-1}}{2h} \tag{3}$$

where h is the sampling period. The third trace from the top is the criterion function. It is an essentially-weighted centered-moving-average of the detector function, and can be represented by

$$C_i = \frac{h^2}{1 + (\tau_s/h)} \sum_{j=i-(\tau_s/2h)}^{j=i+(\tau_s/2h)} w_j D_j \tag{4}$$

where w_j is the weighting factor, defined by

$$w_j = e^{-\left\{[0.625/(\tau_s/h)]\ |j-i|\right\}} \tag{5}$$

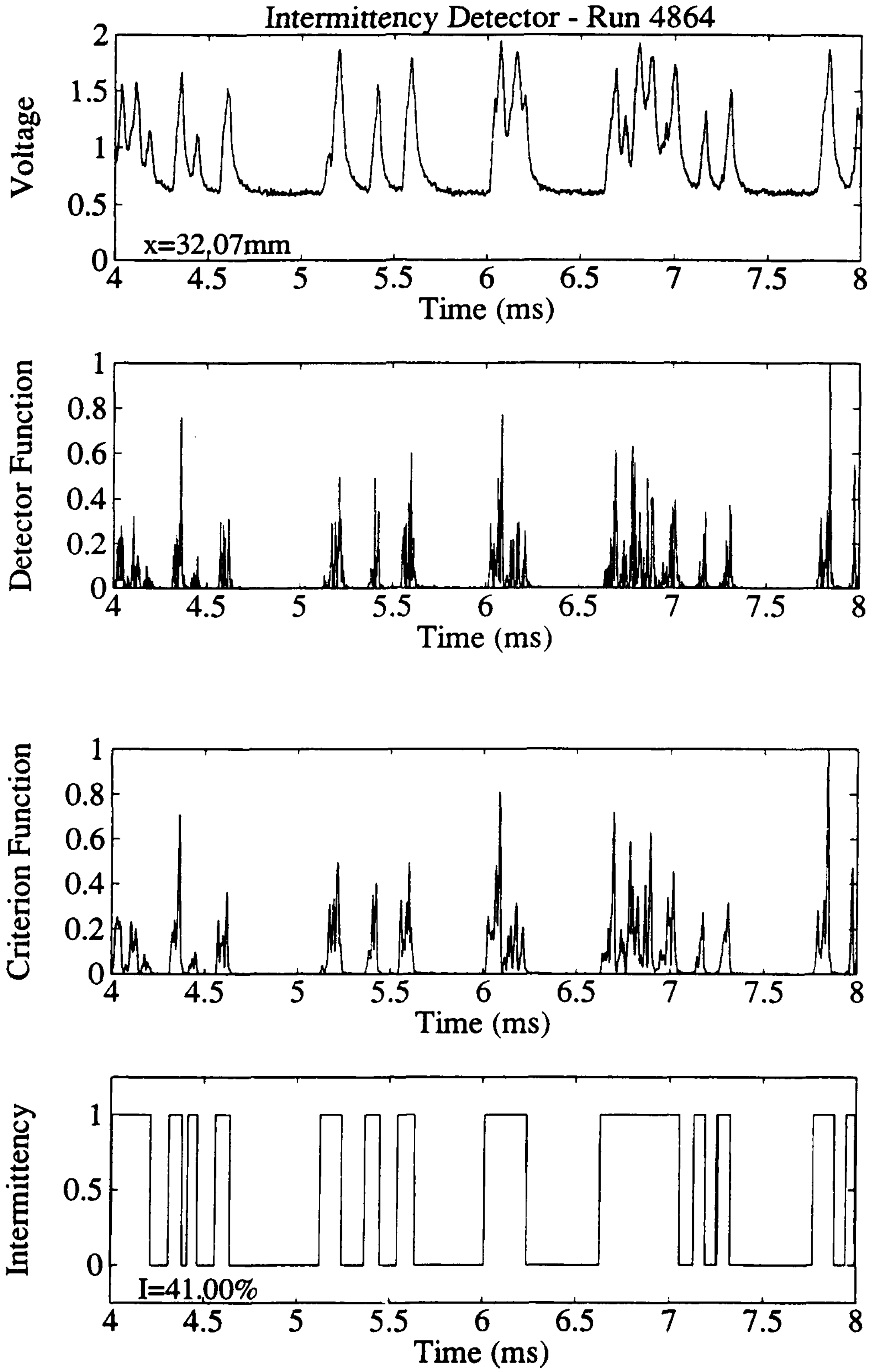

Figure 1 The intermittency detection process.

and τ_s is the smoothing period. The smoothing period was in this case chosen to be 10 μs. This ensured that the smallest detectable turbulent spots were included in the analysis. The intermittency signal, which is obtained by setting an appropriate threshold for the criterion function.

Once the intermittency signal has been calculated for more than one heat-flux trace on the model surface it is then a straightforward procedure to find the convection times of the spot leading- and trailing-edges. The intermittency signal shown in Figure 1 can readily be separated into two more signals. The first signal would be composed of the locations in time of the spot leading edges over the thin-film gauge, while the second would contain the same for the trailing edges. A cross-correlation of the leading edge signals from two gauges along the model surface yields the convection time of the spot leading edges from one gauge to the next. The results of such a cross-correlation analysis performed on the leading- and trailing-edge signals from two gauges are shown in Figure 2. Again, performing such an analysis from gauge to gauge along the model surface yields the the trajectories of the spot leading and trailing edges through the transition zone.

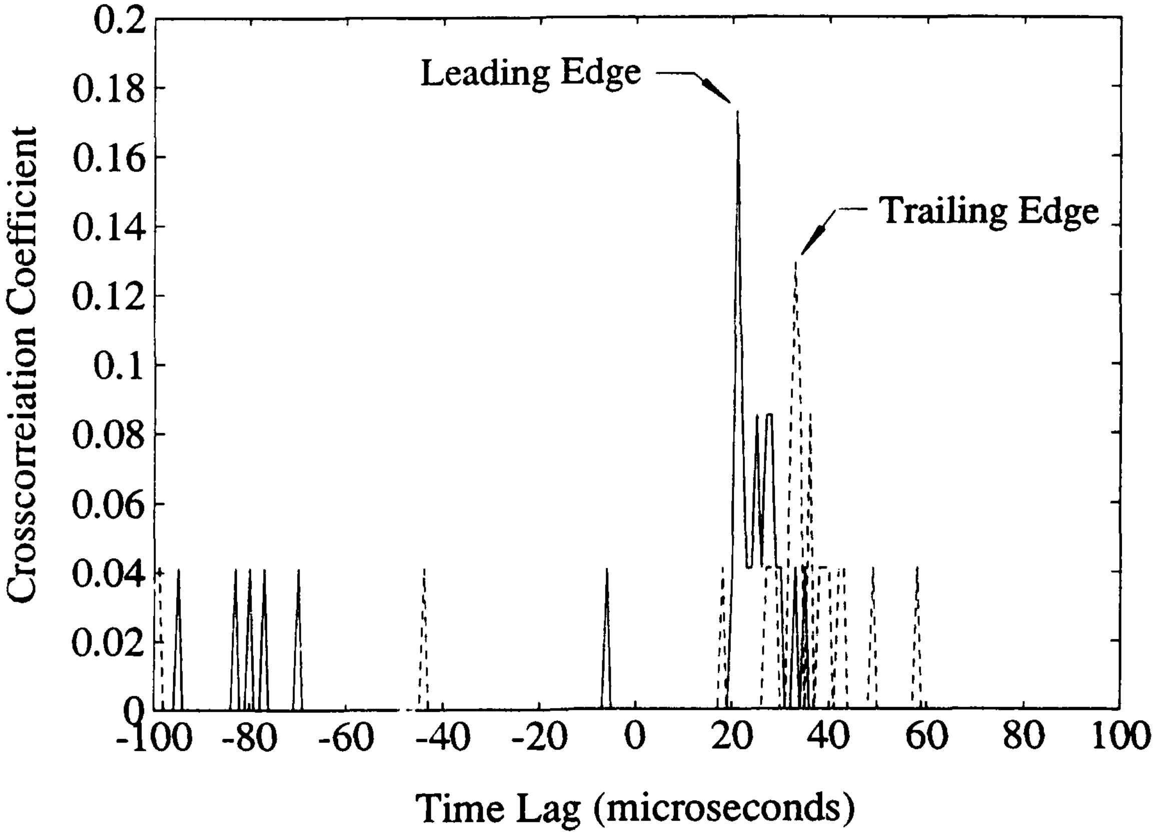

Figure 2 Results of a cross-correlation analysis applied to leading- and trailing-edge signals from two locations along the flat-plate surface.

Reference

1. Hedley, T.B. and Keffer, J.F., "Turbulent/Non-turbulent Decisions in an Intermittent Flow," Journal of Fluid Mechanics, Vol. 64, 1974, pp. 645-678.

List of Symbols

C : criterion function
D : detector function
h : sampling period

i,j : symbols used to indicate the value of a function at a certain time
m : signal magnitude
$\dot{q}$: unsteady heat-flux
$\dot{q}_{max}$: maximum heat-flux measured at a given sensor location
$\dot{q}_{min}$: minimum heat-flux measured at a given sensor location
t : time
W : weighting factor
τ_s : smoothing period

QUESTION 2:
DISCUSSOR: B. Launder, UMIST

Your data show a substantial dependence of the downstream growth of intermittency on the prevailing pressure gradient. Would you care to comment on the implications of your results for Prof. Mayle's strategy? As I understood his model, it did not include pressure gradient influences once the transition had been initiated.

AUTHOR'S REPLY:

Figure 14 of our paper does indeed show a strong dependence of transition length on the mainstream pressure gradient. This is a manifestation of other results presented in the paper that indicate the spanwise and streamwise growth rates of individual turbulent spots are dependent on the prevailing pressure gradient. It has been shown here that the trailing edge of a turbulent spot propagates at a rate much closer to that of the leading edge of the spot at high positive values of the acceleration parameter, K. This makes sense intuitively when one keeps in mind that a boundary layer relaminarizes at sufficiently high values of the acceleration parameter and has particular relevance to Prof. Mayle's model for wake-disturbed transition.

The physical assumption behind Prof. Mayle's model is that an impinging wake causes the production of a series of turbulent spots which quickly coalesce into a "turbulent strip." This "turbulent strip" then propagates downstream in a manner equivalent to that of an individual turbulent spot. His theory, as embodied by equation 8 of his paper, assumes that the non-dimensional spot-propagation parameter, σ, is constant along a gas-turbine-blade suction surface and equal to the value it takes under low speed, zero pressure gradient conditions. Since σ is a function of the rates of spot propagation in the spanwise and streamwise directions, it follows from my results that σ should be neither constant nor equal to its low speed, zero pressure gradient value on a gas-turbine blade. Moreover, equation 8 of Prof. Mayle's paper should be strictly valid only if U_∞ is constant.

There is some evidence that the trailing-edge convection velocity of a wake-induced turbulent strip approaches that of its leading-edge on a gas-turbine blade from the experiments of LaGraff et al. (1989), Hodson (1984), and Orth (1992). Prof. Mayle's model, which seems to be a good first approximation for describing wake-disturbed transition, would need some modification to account for the effect of pressure gradient on spot propagation to achieve maximum utility for the gas-turbine blade designer. If such modifications are made to Prof. Mayle's model, it is doubtful that such a simple relation as his equation 8 would be derivable. Possibly an integral relation, or indeed a simple time-marching model like that under development at Oxford would be more appropriate.

DISCUSSOR: R.E. Mayle, Rensselaer Polytechnic Institute

I would like to make a point of clarification regarding Professor Launder's question. The model that I propose does take into account the effects of pressure gradient or acceleration on both growth and propagation rates. The model is based on the Chen-Thyson thinking which assumes that the spot propagation rates are directly proportional to the local free-stream velocity. An implication of this model is also that the spots grow inversely proportional to the local velocity. That is, as the flow accelerates the spots grow less. Granted, the model is simple, and probably a first cut as to what is happening, but so far it seems to work.

AUTHOR:

Yes, I agree that it is a very useful first cut and because it does correspond so well to the experimental data perhaps the refinement I have presented really isn't necessary; it may be purely academic.

R.E. Mayle:

I wouldn't say that it's not necessary. Your measurements, besides those made earlier by Narasimha, are the only data available on spot propagation and growth in accelerating flows. I think this kind of information is necessary if we are ever going to understand the transition process.

HEAT TRANSFER IN HIGH TURBULENCE FLOWS - A 2D PLANAR WALL JET

R. B. Rivir
W. T. Troha
Aero Propulsion and Power Directorate, Wright Laboratories
Wright Patterson Air Force Base, Ohio, 45433-6563

W. A. Eckerle
Cummins Engine Company Inc.
Columbus, Indiana

W. J. Schmoll
University of Dayton Research Institute
Dayton, Ohio

SUMMARY

The accurate prediction of turbine heat transfer remains beyond our current capabilities. To investigate this condition, non conventional turbulence generation techniques have been employed to explore the impact of high turbulence or unsteadiness on heat transfer. The heat transfer from a 2D planar wall jet will be compared with an axi-symmetric wall jet with twice the turbulence scale and more turbulent kinetic energy - with an increased heat transfer shown by the planar configuration. The resulting comparisons of wall jet augmented heat transfer to engine turbine blade heat transfer is quite favorable.

LIST OF SYMBOLS

A	constant
C_p	specific heat at constant pressure, W-s/kg-°C
h	heat transfer coefficient, W/m^2-°C
h´	nozzle height, cm
l	nozzle length, cm
Pr	Prandtl number = $\mu C_p/k$
$R_{ex'}$	Reynolds number = $\rho Ux/\mu$, $\rho U\theta/\mu$
S_t	Stanton number = $h/(U\rho C_p)$
S_{to}	Stanton number for fully turbulent flat plate
T_u	x component of turbulence intensity = u'/U
U	local x mean velocity, m/s
U_{max}	maximum mean x velocity, m/s
u´	rms fluctuating component of x velocity, m/s
u^+	non dimensional velocity defined by equation 1
V	local y mean velocity, m/s
v´	rms fluctuating component of y velocity, m/s
W	local w mean velocity, m/s
w´	rms fluctuating component of w velocity, m/s
w	span location from jet centerline, cm
x	distance from wall jet nozzle exit, cm
Y_{max}	y distance from wall to U_{max}, cm
y	y distance from wall, cm
y^+	non dimensional distance from wall, equation 1
δ	boundary layer thickness, cm
Λ	integral scale of turbulence, cm
θ	momentum thickness, cm

1. INTRODUCTION

The near wall turbulence level for a fully turbulent flat plate boundary layer is typically 10-12% in the flow direction after the boundary layer has developed some age. This maximum occurs in buffer or transition region between the linear and the log law of the wall regions of the boundary layer. The turbulence then falls off to the free stream value. Film cooling flows exhibit similar characteristics with a maximum of 15-20% occurring farther away from the wall (Rivir et al. 1987) in the profile, as the blowing ratio increases, and then decays to the free stream value. Until very recently heat transfer and film cooling data for turbine designs were obtained with very low values of free stream turbulence (0.5-2%). The entering free stream turbulence level for a turbine rotor, although not comprehensively documented under engine conditions, has been measured by Binder et al. (1985) for cold flow due to the stator wakes. The level of turbulence was shown to approach 20% on the pressure surface and 10% on the suction surface. The issue to be addressed is what happens to the heat transfer when there is a 10-20% unsteadiness level in the free stream which then interacts with the naturally occurring wall or film cooling generated levels of 10-20%.

Under estimating the turbine blade surface temperature by 10% can result in a significant loss in lifetime for that component. This kind of accuracy in heat transfer can only be approached for very simple, well behaved, 2D boundary layers. Current heat transfer data bases for turbine blades and vanes are obtained from experiments which include flat plates, linear cascades, large scale rotating cascades, light piston tubes, blow down tunnels, shock tubes, and engines. The fully turbulent flat plate boundary layer can be accurately (with in a few %) predicted by the empirical relationship of Kays and Crawford (1980), or 2D boundary layer codes such as STAN5 or Texstan, which have evolved from the Patankar Spaulding formulation. These codes typically invoke mixing length, $\kappa\varepsilon$, or other forms of turbulence models. When the free stream turbulence levels were increased to 4-6% by the use of up stream grids, systematic increases up to 10% above the predicted fully turbulent values of heat transfer were observed by Blair (1981). The addition of pressure gradient or acceleration combined with the 4-6% turbulence resulted in a further underestimate in the prediction of the heat transfer of 2D boundary layer codes, such as STAN5, by 30% (MacArthur 1985), as illustrated in Figure 1. Transition length from laminar to turbulent heat transfer is also slightly under predicted in length with Reynolds number by these 2D codes, again as illustrated in Figure 1.

In linear cascades, heat transfer measurements predicted with similar 2D codes show that transition and transition length are poorly predicted on both suction and pressure surfaces. In addition the absolute level of heat transfer on the pressure surface was under estimated by 50%. Figure 2 from Wittig et al. (1985) has been annotated to indicate the typical discrepancies with calculated values of heat transfer for the linear cascades. This is a combustion driven tunnel which uses grid generated turbulence to simulate wakes of the up stream stator. These calculations use a low Reynolds number $\kappa\varepsilon$ turbulence model which is known to over predict heat transfer for some cases. Consigny and Richards (1982) tend to show the resulting VKI linear cascade effort heat transfer results, along with many others, to be bounded between the fully turbulent flat plate and the laminar flat plate case - based on the chord and the cascade exit Reynolds number. Locally these heat transfer measurements can exceed the fully turbulent flat plate values as indicated by Arts et al. (1992) in the same facility. The heat transfer in linear cascades is reasonably well predicted by the simple laminar and fully turbulent flat plate for many but not all cases. The additional complexity of an annular cascade does not appreciably affect the heat transfer prediction discrepancies.

The next level of complexity, addition of rotation and upstream stators, becomes more difficult to predict and explain the observed heat transfer due to the interaction of several unsteady flows are added to low levels of up stream turbulence. These experiments include transient experiments such as shock tubes (Calspan) and light piston tubes (MIT, Oxford, and RAE Pystock). Bayley and Priddy(1981) showed an increase of 2 to 4 times over steady state heat transfer values when a rotating bar investigated frequency effect (at a constant scale of turbulence) on the steady heat transfer value in a linear cascade. Rae et al., 1986 (Calspan) presents predictions for both a 2D and a 3D vane/rotor combination with an inlet turbulence of 5% of an unknown length scale. The 3D case is particularly difficult to rationalize with a 100% discrepancy on the vane surfaces and near experimental values on the rotor. In a low speed, large scale, multi-stage experiment, Sharma, et al. (1992) has observed excellent predictions of heat transfer on the rotor and then a large under prediction on the 2nd stator. This observation exceeds the fully turbulent flat plate value of heat transfer, as illustrated in Figure 3. Additional unpredicted behavior that is not captured by 2D or 3D Euler or Navier Stokes solvers are observed at the stagnation point as well as on the pressure and suction surfaces. Transition and transition length again are not predictable. There are numerous cases where the heat transfer exceeds the steady flow fully turbulent flat plate values such as Blair (1981), Bayley and Priddy (1981), Wittig et al. (1985), Rae, et al. (1986), and Sharma et al. (1992).

The examination of engine data, which now includes the combustor upstream, shows observed increases over the fully turbulent flat plate from over 3 times on the pressure and stagnation surfaces to 2 times on the suction surfaces, as shown in figure 4. Non steady Navier-Stokes calculations are now being made for these flows including the effects of the stator on the rotor for multi-stage geometries. Although these calculations show improvements they fail to come close to engine results. It is these cases which exhibit heat transfer above the fully turbulent flat plate predictions which are of interest for the non conventional turbulence or unsteady flow evaluation.

There have been several efforts underway to explore non conventional turbulence generators, and to establish the relationships between heat transfer, turbulence, turbulence length scale and the higher levels of heat transfer that occur in the actual engine. These turbulence generators have included free jets, wall jets, jets in cross flow, rotating bars, moving walls with grids, and blown grids. Grid generated turbulence has been able to produce only 6-8% levels in the final period of decay at scale sizes comparable to the boundary layer thickness or the blade passage size. In addition to the axial turbulence level, the appropriate nonisotropic turbulence decay rate (du'/dx) and turbulence scales (Λ/δ) are issues which have not been satisfactorily resolved in attempts to simulate the unsteady effects in the turbine hot section. A number of non conventional turbulence generators have been investigated over the years to achieve high turbulence levels at appropriate scales. In 1985, Maciejewski, Moffat, Han, and Rivir began looking at the importance of higher free stream turbulence levels. These turbulence levels were comparable or greater than the near wall levels. Moffat and Maciejewski investigated turbulence levels of 26-48% at Reynolds numbers of $2\text{-}5\times10^4$ with a flat plate in a free axi-symmetric jet. This represented an augmentation of the fully turbulent flat plate heat transfer of 350%. Han, Rivir and later others (MacMullin et al. 1986) investigated turbulence levels of 2-20% with axi-symmetric and planar wall jets at Reynolds numbers of 1×10^5 to 8×10^6. The resulting heat transfer was observed to be up to 200% of the fully turbulent flat plate. McCarthy (1989) used a box with one wall a constant heat flux surface and the same 2D planar free jet which had been used in the wall jet studies. This resulted in an augmentation of 20 - 60% in the heat transfer. Young et al. (1991) used blown grids to generate turbulence levels of 5-20%. Ames (1990) used wall jets and jets in cross flow to simulate a combustor at turbulence levels of 5-20%. This resulted in a 30% augmentation in heat transfer over the fully turbulent level. The results of these efforts are compared in Figure 5. The heat transfer results have been shown to be similar to engine results even though the simulations provided by these alternate sources are not direct. Figure 4 shows the axi-symmetric and planar wall jet heat transfer results in engine coordinates.

2. DESCRIPTION OF THE 2D WALL JET EXPERIMENT

This effort presents three component LV measurements and begins to address the scale effect for a non conventional turbulence generator with a planar wall jet. An axi-symmetric wall jet which was used previously for high turbulence heat transfer investigations is described in MacMullin et al. (1987).

The same constant heat flux heat transfer surface was employed as described in the 1987 work with new foil and thermocouples. The axi-symmetric 20.32 cm ASME nozzle was replaced with a short radius ASME planar nozzle; 6.67 by 49.53 cm (l/h´=7.43) with a 0.64 cm lip thickness. In the settling chamber a 20/1 length to diameter flow straightener, with 75 mesh screens on either side, was added to reduce the exit core flow axial turbulence level from 5% in the 1987 work to 2%. A three component TSI off axis LV and traverse have been employed to obtain velocity, turbulence, and Reynolds stress profiles in the present work. A half angle of 15 degrees was required between component beams for other experiments with limited optical access. This reduces the accuracy of all components slightly over the recommended 20 degree half angle. The LV beam position accuracy was ±.00025 cm. The optics used produced a measurement ellipsoid of 25 microns diameter by 3 mm in length in the span wise direction. The axial turbulence scales are the order of several cm and the vertical scales the order of mm in the near wall regions. Nearly all the turbulent energy is below 3,000 Hertz for these flows, so the spatial resolution of the measurement volume is quite good except for the span wise direction. The LV measurements were made with-in a nominal coincidence window of 10 micro seconds. A small (10 degree) angle to the heat transfer surface was employed to allow wall measurements to be obtained. The LV axial and vertical mean and turbulent measurements were checked against single element hot wire measurements in the axi-symmetric wall jet and in the TSI 0.64 cm diameter calibration jet. The mean velocities agreed quite well. The u´ measurement in the calibrator free jet fell with in ±0.5 to 1% of the hot wire up to turbulence intensities of 10%, and were lower than the hot wire by 2% for turbulence intensities of 10 to 20%.

Single element hot wire measurements were employed to obtain the axial and vertical turbulence scales using a HP 3562 dynamic signal analyzer which provided the frequency spectrum and then inverted the spectrum with a FFT to provide the auto correlation function which was normalized and multiplied by the local mean velocity to provide the integral scale. This technique was compared against a direct auto correlation which was used in our 1987 axi-symmetric wall jet work and the 32,000 sample spectrum, an FFT, and an auto correlation calculation of Ames (1990) with favorable results - all three measurements gave the same value within 30% at the same time on the same flow. The vertical scale was obtained by rotating the single element wire to the span wise direction, with out moving the traverse, and repeating the measurement. The vertical scale measurement is sensitive to both the vertical and the span wise components. The vertical scale implication then needs to be considered to be representative of both near the wall rather than the vertical component alone. The measurements presented in this paper will be for the short radius ASME planar nozzle.

Heat transfer measurements were made at 7 stations with the same techniqueues described in MacMullin et al. (1987) axi-symmetric wall jet work. The x/h´ locations for the planar wall jet measurements become 7.69, 15.24, 26.28, 30.10, 37.48, 44.95 , and 52.95.

3. PLANAR WALL JET RESULTS

The original purpose of this planar wall jet effort was to provide a 2D flow with a smaller scale at the same x Reynolds numbers as the axial wall jet. Although the width to height dimension of this wall jet (7.43) make it a marginal 2D source by planar wall jet standards (Launder and Rodi,1981), there are two significant observations applicable to all planar wall jet measurements which should be made. The Reynolds number of this wall jet was chosen to provide heat transfer measurements in the x Reynolds number range for turbine blades. This places these measurements an order of magnitude above wall jet studies in the literature. The velocity profiles for these measurements (and also those of the axi-symmetric wall jet) are all locally similar in velocity profiles for all reported heat transfer and velocity profiles. These centerline velocity profiles give an axial jet decay which approaches that of Wygnasiki et al. (1991) at his highest Reynolds number flow of 19,000. These measurements then imply a high Reynolds number limit for wall jet spread which is independent of wall jet pressure ratio for this intermediate range of x/h´. Secondly, these mean velocity profiles have been analyzed in law of the wall coordinates by Narayanan et al. 1992) with the assumption of a constant Karman constant in the law of the wall relation:

$$u^+ = A + 2.44 \ln y^+ \qquad (1)$$

This relation was shown to be valid for all fully developed planar wall jets with the constant A dependent only on the axial turbulence in a simple linear relationship. This same relationship was also observed to be valid for a turbulent flat plate boundary layer when the maximum near wall axial turbulence intensity is used for the turbulence intensity. The LV wall jet profiles presented in this paper were used to obtain this result.

The center line velocity and velocity fluctuation profiles are presented in Figures 7 and 8 at each heat transfer measurement station. The velocity profiles are locally similar as previously pointed out, but are otherwise as one would expect for a planar wall jet. The rms fluctuations are nearly constant across the wall layer in the axial direction. This contrasts to profiles at much larger x/h´ locations normally quoted by planar wall jet efforts in which the shear layer has eroded the wall layer. A law of the wall plot at x/h´ = 52.95 is shown in figure 9, where the log region extending over a 1,000. This extremely large log region made an accurate assessment of the constants in the law of the wall region in contrast to regions of 50-100 in other planar wall jet studies. The span wise distribution of x hot wire measured velocities and rms velocities are shown in Figure 10.

The normalized Reynolds stresses $u'v'$, $v'w'$, $u'w'$, u'^2, v'^2, and w'^2, are shown in Figure 11. The u´ and v´ components are well behaved, however the span wise components of w´ all take on very large values as the wall is approached. The span wise components were shown to be very significant contributors to increases in shear stress in Johnson and Johnston (1989), and increases are to be expected - particularly for a free boundary. We are currently attempting to check the span wise wall shear directly. A few of the last two near wall w´ component data points have been omitted until further checks can be performed. The u´v´ component is initially negative and then goes through 0 at about 60% of y_{max}. It then goes and remains positive as observed in other planar wall jets (Launder and Rodi,1981) investigations.

The integral turbulence scales on the wall jet centerline, for axial scales and for the lateral or vertical scales at y_{max} are shown in Figure 13. A boundary layer traverse of the axial scale is shown at x/h´ = 26.28 in Figure 14.

The scale is sensitive to the mean velocity and the facility compressor operation which results in mean velocity fluctuations of 2%. Four to six scale measurements were made for each data point for both span and centerline profiles to assure reproducibility in the scale measurements.

Moffat and Maciejewski (1989) have observed a linear relationship of h, the heat transfer coefficient, with u´. These observations were also made in this investigation, with the addition that a family of these relationships, not just a single one were observed. This leads to the conclusion that other functional relationships are involved in the relationship for h. The ratio of turbulence scale to boundary layer thickness has been suggested by several investigators with a functional dependence proposed by Simonich and Bradshaw (1978), and this later modified by Blair (1981) for 2D flat plate boundary layers such that:

$$S_t\text{-}S_{to}/S_{to} = T_u * \alpha * \beta \qquad (2)$$

$$\alpha = (\Lambda/\delta + 2)$$

$$\beta = (3e^{-Re}\theta^{/400} + 1)$$

where S_t is the local x Stanton number and S_{to} is the fully turbulent local Stanton number from the Kays and Crawford relationship. The heat transfer at a 20% turbulence level is shown in Figure 15. The planar jet shows similar behavior to the axi-symmetric wall jet heat transfer, but is slightly higher at similar turbulence intensities. Figure 4 shows schematic wall jet heat transfer superimposed on engine data, indicating similar levels of heat transfer and dependence with Reynolds number.

The scale size ratio of y_{max} 3D / y_{max} planar is 2. Scales have also been measured for the axi-symmetric 3D jet, and this is considered a reasonable comparison of the two scales. The normalized turbulent kinetic energy of the 3D wall jet is .075, and for the planar wall jet (3 component LV measurements) is .053 at a x/D, x/h´ of 8.63 and 7.8, respectively. The normalized heat transfer and scale dependence of equation 2 is shown in Figure 16. Here we see an increased heat transfer for the planar wall jet even though it has less turbulent kinetic energy at similar Reynolds numbers. The lack of collapse of the data would indicate that the functional dependence is not the appropriate relationship.

4. SUMMARY

There remains a very strong need to characterize the inlet flow to the turbine quantitatively in terms of three components of spatial and temporal velocities, the magnitudes of spatial and temporal temperature gradients, as well as the decay characteristics of these fluctuations. Typical gas turbine combustor flows are far from classical isotropic turbulence. The non conventional turbulence sources, as well as 3D Navier Stokes solvers are showing magnitudes of some effects such as T_u and scale but simulations and computations clearly require additional definition.

REFERENCES

1. Ames F. E., "Heat transfer with High Intensity, Large Scale Turbulence: The Flat Plate Turbulent Boundary Layer and the Cylindrical Stagnation Point," Ph.D. Dissertation, Department of Mechanical Engineering, Stanford University, Nov 1990.

2. Arts, T. and Lambert de Rouvroit, M., "Aero-Thermal Performance of a Two-Dimensional Highly Loaded Transonic Turbine Nozzle Guide Vane: A Test Case for Inviscid and Viscous Flow Computations," Journal of Turbomachinery, Vol. 114, pp. 147-154, January 1992.

3. Bayley, F.J. and Priddy, W.J., "Effects of Free-Stream Turbulence Intensity and Frequency on Heat Transfer to Turbine Blading," ASME Journal of Engineering for Power, Vol. 103, pp. 60-64, January 1981.

4. Binder, A., Forster, W., Kruse, H., and Rogge, H., "An Experimental Investigation Into the Effects of Wake on the Unsteady Turbine Rotor Flow," ASME Journal of Engineering for Gas Turbines and Power, Vol. 107, pp. 458-466, 1985.

5. Blair, M.F. and Werle, M.J., "Combined Influence of Free-Stream Turbulence and Favorable Pressure Gradients on Boundary Layer Transition and Heat Transfer," United Technologies Research Center, Report No. R81-914388-17, March 1981.

6. Consigny, H. and Richards, B.E., "Short Duration Measurements of Heat-Transfer Rate to a Gas Turbine Rotor Blade," ASME Journal of Engineering for Power, Vol. 104, pp. 542-551, July 1982.

7. Johnson P.L. and Johnston, J.P., "The Effects of Grid Generated Turbulence on Flat and Concave Turbulent Boundary Layers," Department of Mechanical Engineering, Stanford University, Report No. 14053, November 1989.

8. Kays, W.M. and Crawford, M.E., "Convective Heat and Mass Transfer", 2nd ed., McGraw-Hill, New York, p. 172, 1980.

9. Launder, B.E. and Rodi, W., "The Turbulent Wall Jet," Progress in Aerospace Science, Vol. 19, pp. 81-128, 1981.

10. Launder, B.E. and Rodi, W., "The Turbulent Wall Jet - Measurements and Modeling," Annual Review of Fluid Mechanics, pp. 429-458, 1983.

11. MacArthur, C.D., "Prediction of Free Stream Turbulence Effects on Boundary Layer Heat Transfer - An Evaluation of the Heat Transfer Code STAN5," Final Report on Contract F49620-82-0035, September 1983.

12. MacMullin, R., Elrod, W. and Rivir, R., "Free-Stream Turbulence From a Circular Wall Jet on a Flat Plate Heat Transfer and Boundary Layer Flow," ASME Journal of Turbomachinery, Vol 111, pp. 78-86, January 1989.

13. McCarthy, J.W., "The Effects of Free Stream Turbulence from a Slot Jet on Flat Plate Heat Transfer," Thesis Department of Mechanical Engineering, University of Dayton, July 1989.

14. Moffat, R. and Maciejewski, P.K., "Heat Transfer With Very High Free-Stream Turbulence," NASA Grant NAG3-522, Proceedings of the 1985 Turbine Engine Hot Section Technology Conference (NASA Conference Publication 2405), pp. 203-215.

15. Narayanan, M.A.B., Rivir, R. and MacArthur C.D., "Effect of High Turbulence on Wall Shear and Heat Transfer", Presented to Fifth Asian Congress of Fluid Mechanics, Asian Fluid Mechanics Committee, August 1992.

16. Rae, W.J., Taulbee, D.B., Civinskas, K.C., and Dunn, M.G., "Turbine-Stage Heat Transfer: Comparison of Short-Duration Measurements with State-of-the-Art Prediction," AIAA Paper 86-1465, AIAA/ASME/SAE/ASEE 22nd Joint Propulsion Conference, Huntsville, Alabama, June 1986.

17. Rivir, R.B., Roqumore, W.M. and McCarthy, J.W., "Visualization of Film Cooling Flows Using Laser Sheet Light," AIAA Paper 87-1914, AIAA/SAE/ASME/ASEE 23rd Joint Propulsion Conference, San Diego, CA, July 1987.

18. Sharma, O.P., Pickett, G.F. and Ni, R.H., "Assessment of Unsteady Flows in Turbines", Journal of Turbomachinery, Vol. 114, pp. 79-90, January 1992.

19. Simonich, J.C. and Bradshaw P., "Effect of Free-Stream Turbulence on Heat Transfer Through a Turbulent Boundary Layer," ASME Journal of Heat Transfer, Vol. 100, pp. 671-677.

20. Wittig, S., Schulz, A. Bauer, H.J. and Sill, K.H., "Effects of Wakes on the Heat Transfer in Gas Turbine Cascades," AGARD, CP-390, 1985.

21. Wygnanski, I., Katz, Y. and Horev, E., "On the Applicability of Various Scaling Laws to the Turbulent Wall Jet," Journal of Fluid Mechanics, Vol. 234, pp. 669-690, 1992.

22. Young, C.D., Han, J.C. Huang, Y., and Rivir, R. B., "Influence of Jet-Grid Turbulence on Flat Plate Turbulent Boundary Layer Flow and Heat Transfer," 3rd ASME-JSME Thermal Engineering Joint Conference, Reno, Nevada, March 1991.

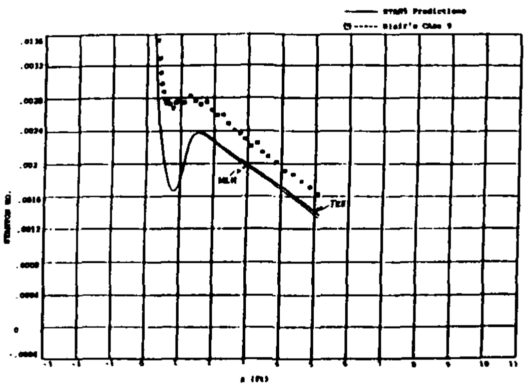

Figure 1. STAN5 calculation of flat plate Tu=4% a=7.5x10^5 (MacArthur, 1983)(Blair, 1981)

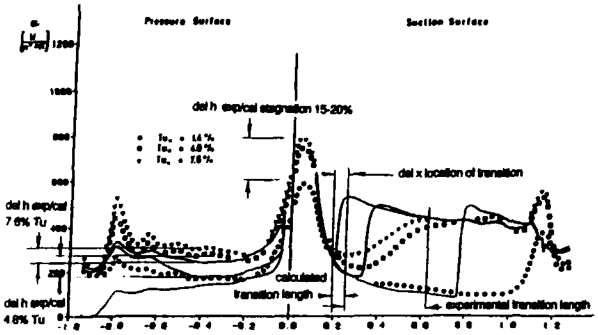

Figure 2. Linear cascade comparison of experimental calculations (Wittig, 1985)

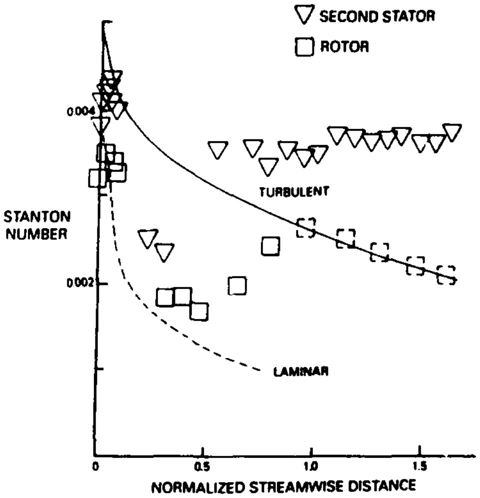

Figure 3. Large scale multi-stage rotating cascade comparison of experiment to fully turbulent flow (Sharma, et al., 1992)

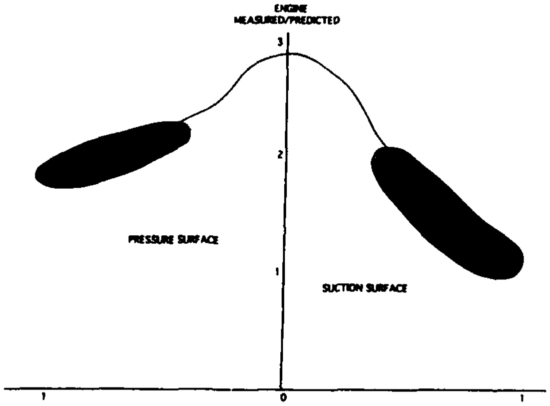

Figure 4. The measured/predicted heat transfer for turbine engine blades and vanes

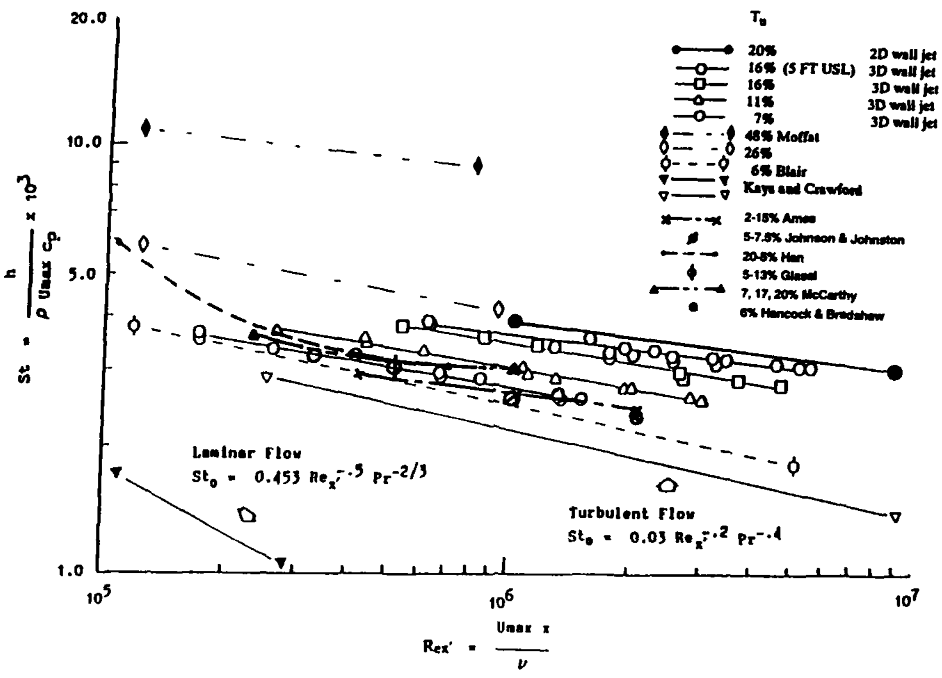

Figure 5. Heat transfer characteristics for non standard turbulence generators

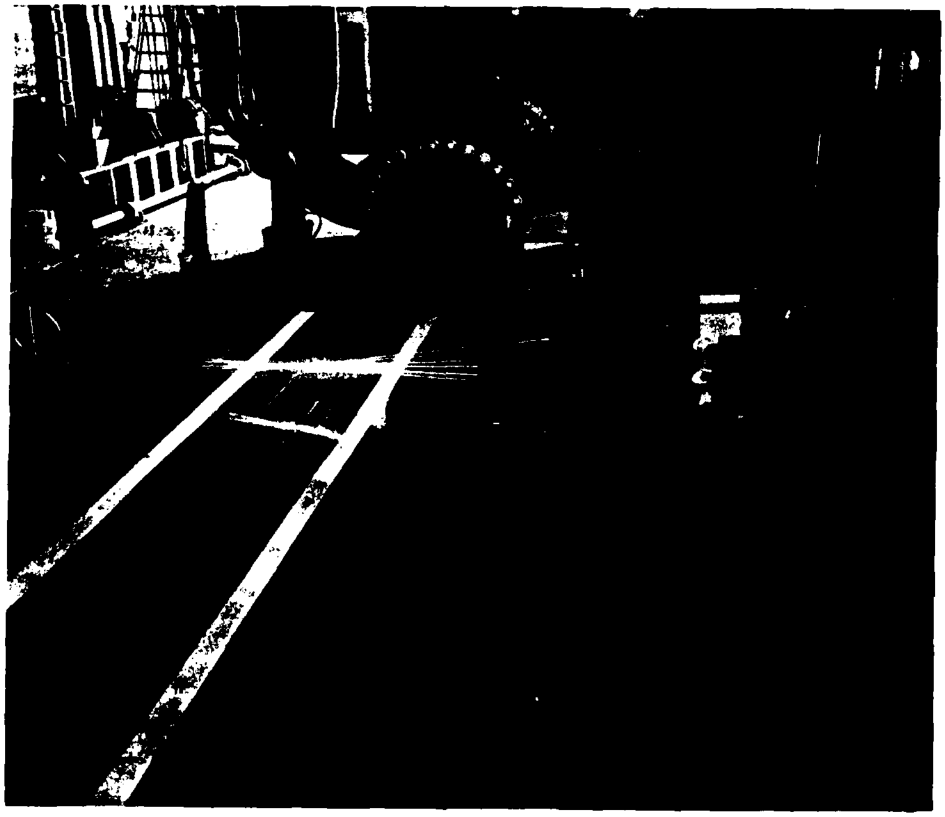

Figure 6. 2D wall jet

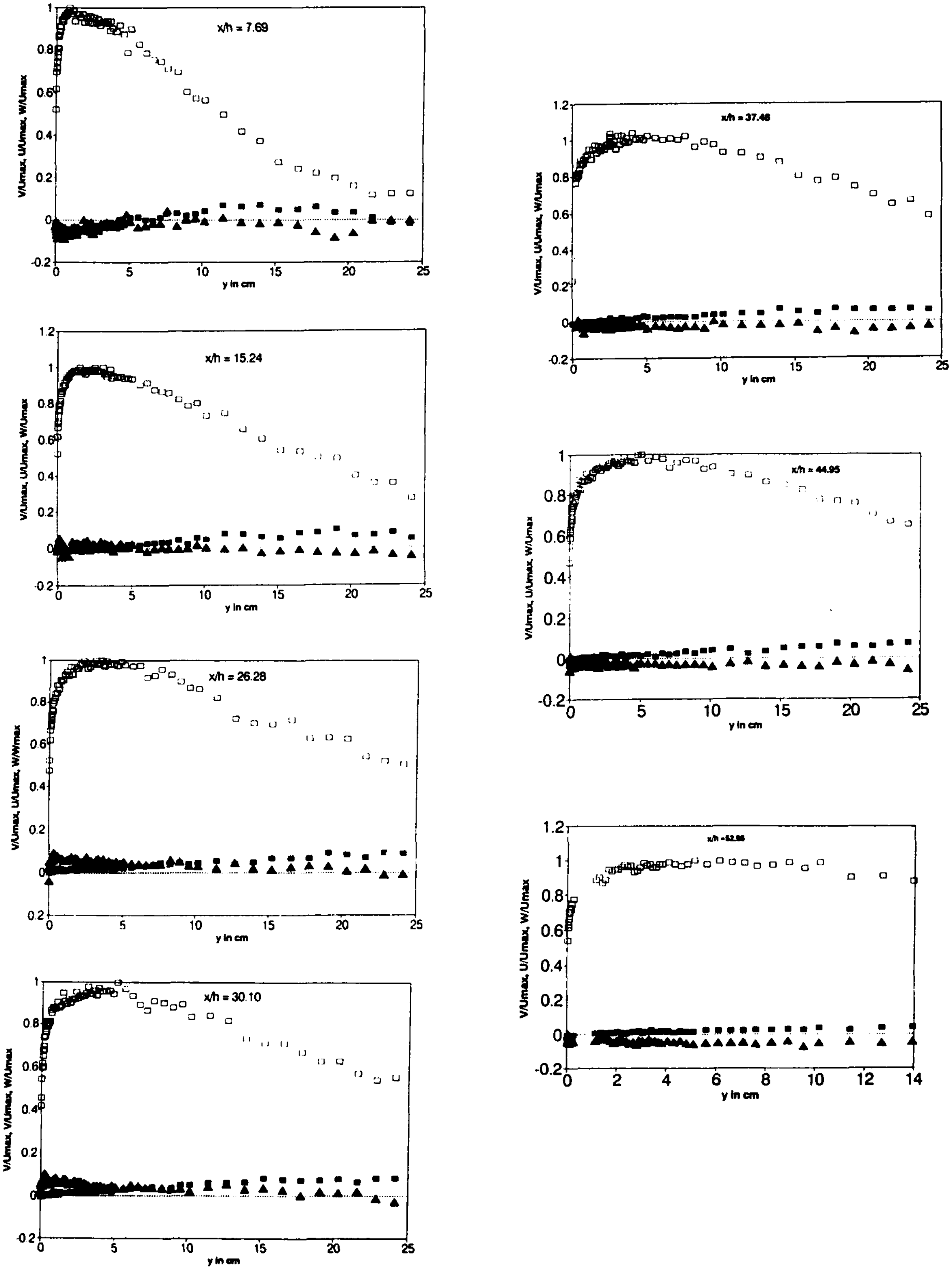

Figure 7. LV mean velocity profiles

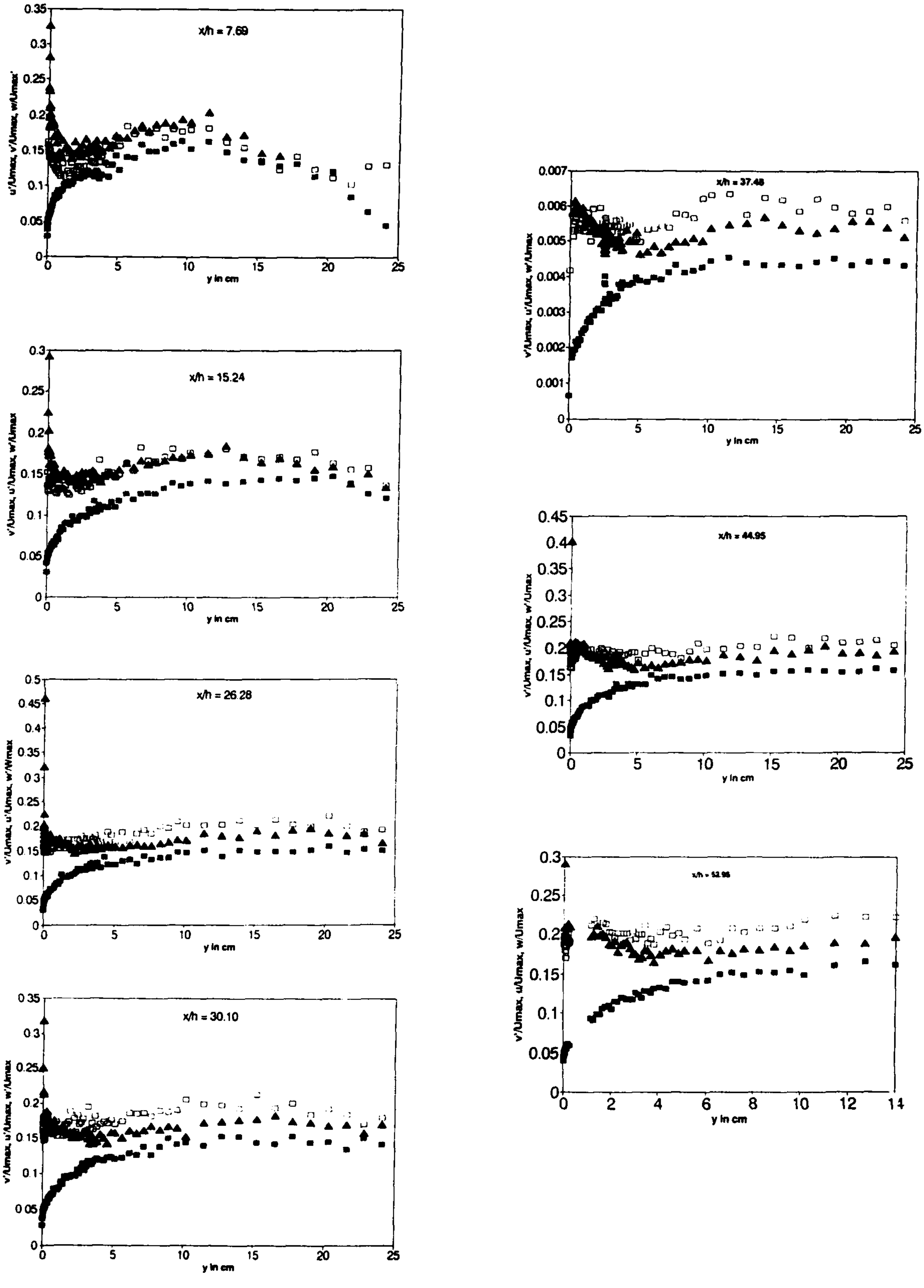

Figure 8. LV rms velocity profiles

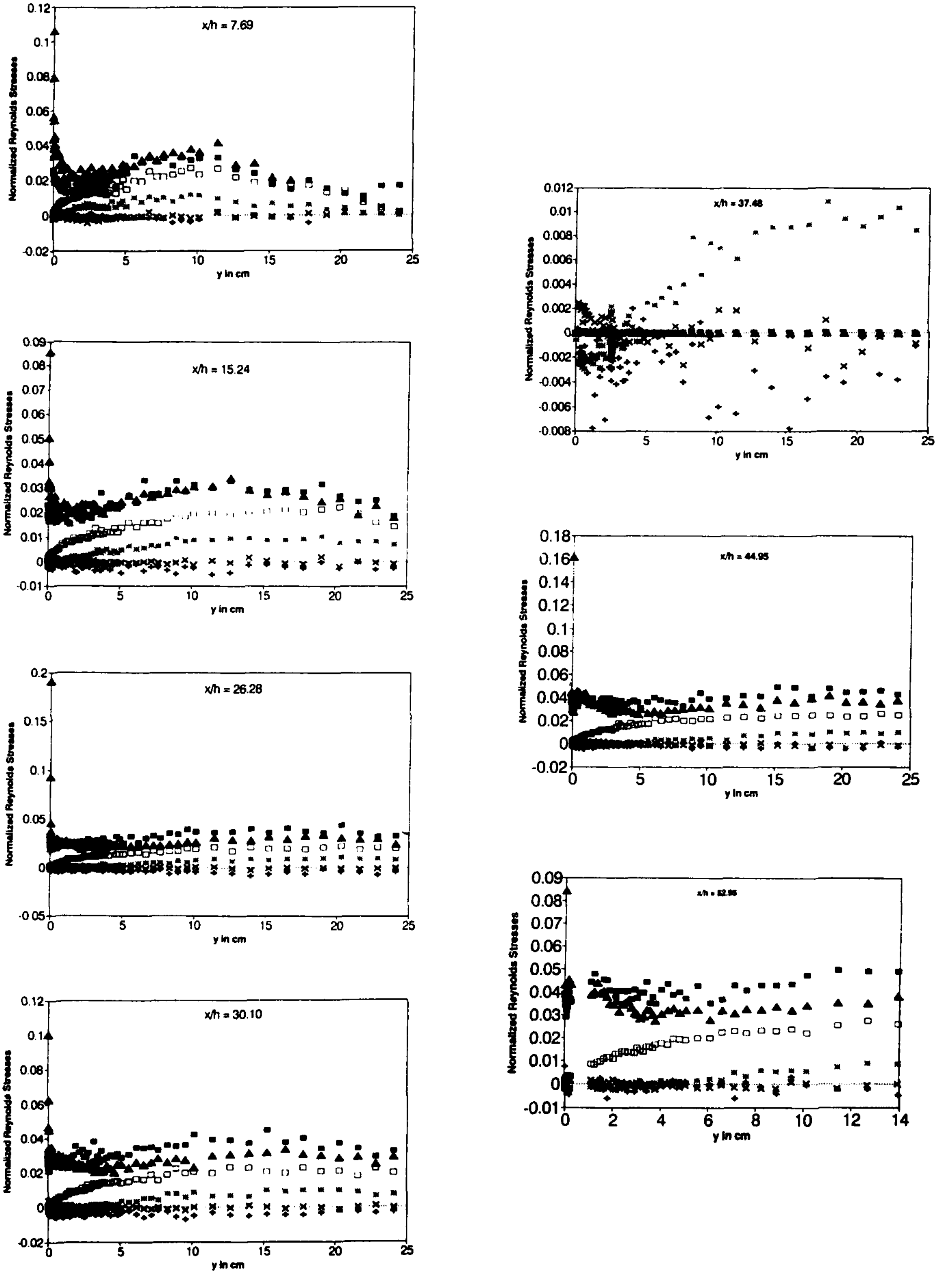

Figure 9. LV normalized Reynolds stress profiles

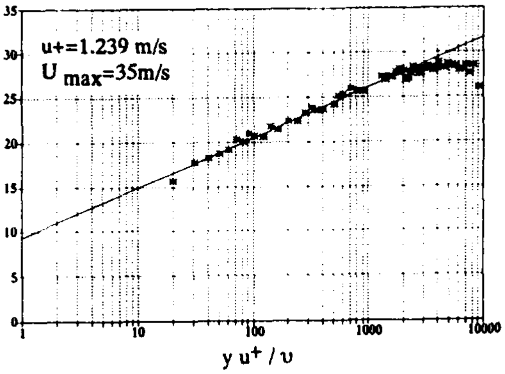

Figure 10. LV velocity profile at 353 cm, Tu -20%

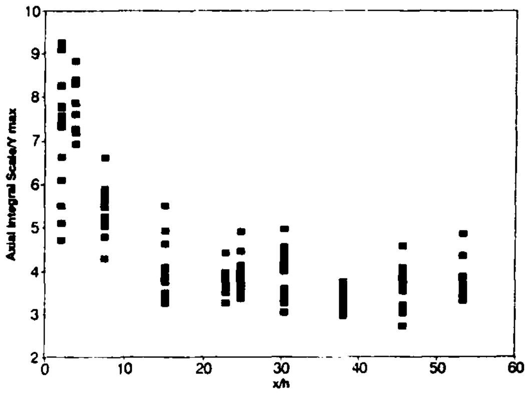

Figure 12. Axial integral scale

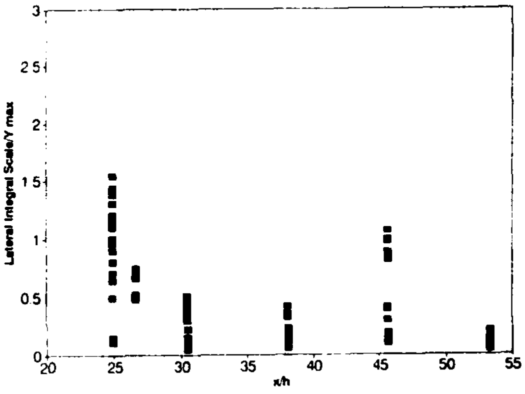

Figure 13. Lateral/vertical integral scale

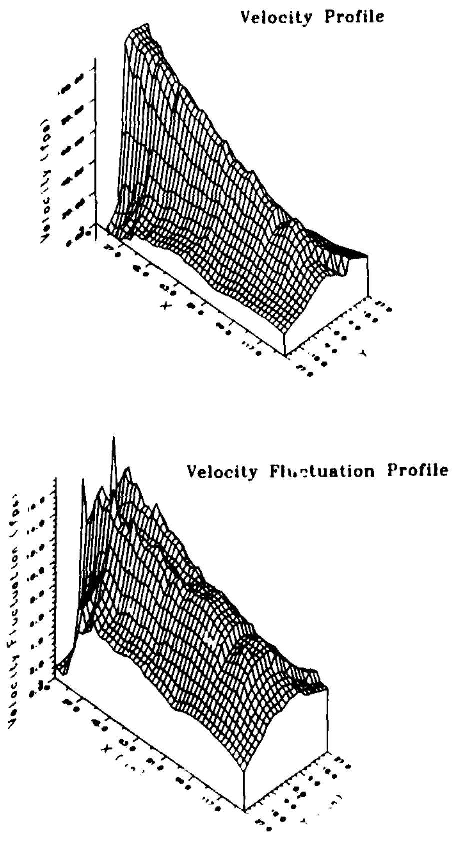

Figure 11. Span hot wire measurements of velocity and rms velocity

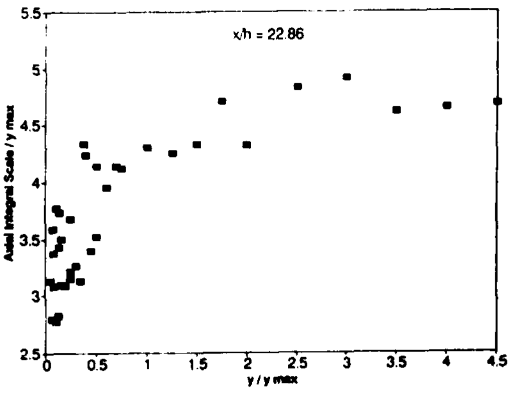

Figure 14. Axial scale distribution through the boundary layer

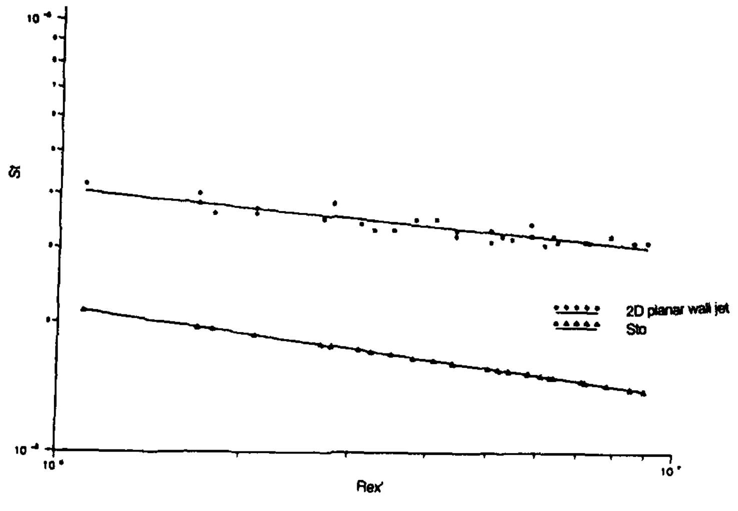

Figure 15. 2D wall jet heat transfer at Tu=20%

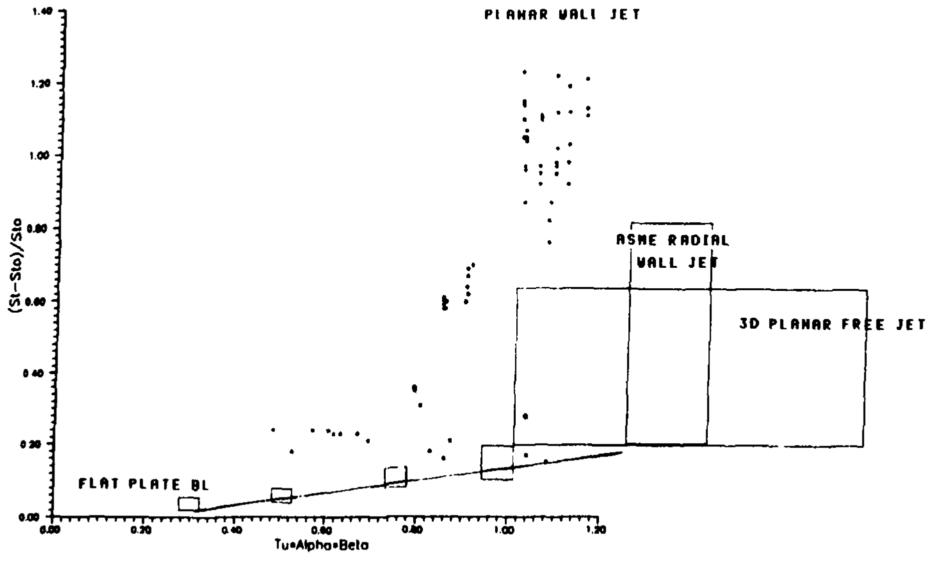

Figure 16. Comparison of 2D wall jet, 3D wall jet, and free jet

Discussion

QUESTION 1:

DISCUSSOR: B. LAUNDER, UMIST

What length scale in the wall jet did you take as relevant to the boundary layer? Was it the distance to the maximum velocity surface?

AUTHOR'S REPLY:

Yes, the comparisons in Figures 12 through 14 reference the length scales to the distance, Y_{max}, which is the distance to the maximum velocity. The same is done in Figure 16 which compares the wall jet heat transfer results to Simonich and Bradshaw's boundary layer correlation. We know that other reference lengths are more appropriate than Y_{max}. We found the enthalpy thickness to be a better choice for the wall jet and it would probably also be a better choice for the boundary layer as well.

HEAT TRANSFER WITH MODERATE FREE STREAM TURBULENCE

S.N.B. Murthy
1003 Chaffee Hall
School of Mechanical Engineering
Purdue University
West Lafayette, IN 47907-1003 USA

ABSTRACT

Turbulence in turbine flows of gas turbine engines is generally inhomogeneous and is also characterized by wide ranges of intensity and scale. The interaction between FST and boundary layer turbulence (BLT) is complicated in all but the case of low values of both intensity and scale. In a recent investigation, an attempt has been made to establish the effect of homogeneous FST on wall friction (when there is no heat transfer) in the relatively simple case of flat plate, zero pressure gradient boundary layer. In the current paper the method has been extended for the prediction of heat transfer in the same flowfield. In any problem involving heat and momentum transport, it is common to introduce some type of similarity between the two transport processes. The current method is based on the application of a similarity rule governing the spectra of turbulence intensity and temperature variance. The principal outcome is a method of establishing heat transfer in a given flowfield for which experimental data are available under cold flow conditions and have been verified with the model prediction scheme.

Introduction

Heat transfer to turbine blades is affected directly by the combustor exit conditions in a gas turbine engine. The output of a gas turbine combustor is invariably inhomogeneous. The scale and intensity of events in the flowfield raise several questions in the description and modelling of the flow features. In the context of turbulent flows, it is necessary to include at least the following characteristics: (a) inhomogeneity in intensity and scale; (b) gaps in the spectrum of flow properties; and (c) time-dependence. If a more general description is undertaken based on an unsteady, inhomogeneous, and randomly distributed vortex flowfield, the removal from consideration of structure and coherence in the flow field leads to unmanageable complexities. There is a growing recognition, however, that the combustor flowfield requires a new basis of description (References 1 - 2). Nevertheless, for purposes of determining heat transfer in the turbine blades exposed to combustion products, some form of a turbulent flow model seems indicated for purposes of practical predictions, if not for advances in phenomenological understanding, for example References 3 - 8.

Heat transfer in turbine blades is traditionally examined in three regimes: (i) the stagnation region, (ii) the blade surface, and (iii) the trailing edge region. The nature of the boundary layer is significant in all cases. Over the blade surface, the boundary layer or, better, region may be laminar, transitional, or turbulent, even when the main flow is variously complex. The region affected by the no-slip condition at the wall in the case of a uniform, laminar main flow, with no external pressure gradient, is only a function of the Reynolds number, the difference, if any, between the temperature of the main flow and that of the boundary wall, and the difference in diffusivity of momentum and heat in the fluid. When the main flow has any type of complexity, there arise both a change in the thickness of the affected region as well as in the processes therein, except when the main flow complexity involves time and length scales that are small like those of the laminar flow processes in a boundary layer. Thus when the main flow is turbulent, there must be an interactive effect on the boundary region, with respect to the resulting skin friction, and also heat transfer when conditions admit.

A flowfield that is reasonably unambiguous can be visualized in the problem of heat transfer as follows: A reasonably high Reynolds number, turbulent main flow over a wall with a turbulent boundary region, and a modest difference in temperature between the main flow and the wall. The interaction between the main flow and the boundary region should be a function of Re, Tu, L_ϵ/δ_t, and T_w/T; here, L_ϵ is the dissipation length scale in the main flow, δ_t, the thickness of the turbulent boundary layer under the same conditions but without main flow turbulence, and $(\ )_w$, the wall value; all other symbols are standard.

It has been pointed out, for example in Reference 9, that, while the result of the interaction between the main flow turbulence and the boundary region turbulence is unambiguous in the case of skin friction coefficient, there can be considerable ambiguity in regard to heat transfer. The skin friction coefficient, on one hand, invariably increases when the main flow is turbulent. On the other hand there may be an increase or decrease of Stanton number with no discernible relationship of the changes to the main parameters of the flowfield. One of the chief difficulties in such cases is the lack of adequate experimental data, since in all cases there is undoubtedly a set of complex interactions, and those have yet to be established.

Attempts have been made by several investigators on correlating experimental data on heat transfer in terms of a parameter including turbulence scale and intensity (References 5, 7 and 10). However, they have not been successful in elucidating physical effects, and therefore, the suggested parameter has not been universally applicable.

There has also been an attempt, although in the absence of free stream turbulence, to develop a boundary layer model based on turbulent boundary layer structure considerations, and then invoking an analogy between momentum and heat transport (Reference 11). However, no data or models are available for the changes in bursts and quiescent periods when the main flow is turbulent with given values of intensity and scale.

One of the techniques developed for examining boundary layer structural changes as a function of main flow turbulence parameters provides the extent and intermittency of penetration of outer fluid into the boundary region, and also boundary layer intermittency at the outer edge (References 12 - 13). These experiments have not been repeated in the case of heat transfer studies. Thus it is not clear if the ambiguous changes of Stanton numbers in different cases are due, in part, to physical penetration characteristics of the outer fluid and thus, to turbulence scales therein.

Heat Transport Measurement and Theory

If a direct and simple analogy between momentum and heat transport in the form of a value for turbulent Prandtl number is to be avoided, it is still necessary to introduce some type of relation between the two transports since a total of four time scales (two related to each of dissipation and production) are involved, even in the absence of FST, and there is no direct connection between them. In the presence of FST, one must, in fact, recognize six time scales.

One possible approach to calculating heat transfer is to relate stress and heat transport to intensity of velocity and temperature fluctuations (rather than to gradients of mean quantities), as in Reference 14. Such an assumption leads to a finite velocity of transport (see also Reference 15), but, somewhat more significantly in the context of the model to be developed later, to a possible consideration of the relation between local spectra of turbulence intensity and temperature variance (References 16 - 18).

In the problem of heat transfer in turbine blades, the flow is nonisotropic and inhomogeneous, and also, subjected to shear and pressure gradients. Thus, the temperature spectrum, F_θ, and the kinetic energy spectrum, F_q, may not be simply related except in parts of a boundary layer and over selected frequency ranges. In other words, the type of flowfield and the initial and boundary conditions affect the details of the nature and extent of the analogy between F_θ and F_q. Another important factor pointed out in References 16 - 17 is that, considering the overall spectral range of frequencies, the analogy between the two spectra must be based on $\overline{q^2}$, rather than on $\overline{u_i^2}$ or $\overline{u_j^2}$ except over selected frequency ranges.

Measurements in turbulent boundary layers, reported in References 16 - 17, verify the foregoing. However, there are no detailed data in the presence of main flow turbulence. In addition to the magnitude of effort involved in generating such data, there are also important questions related to the method utilized for generating a flow with desired levels of Reynolds number, and intensity and scale of turbulent fluctuations.

Skin Friction and Heat Transfer Correlations

Several attempts at correlating skin friction and heat transfer coefficients and also, the Reynolds analogy factor, R, equal to $St/(C_f/2)$, have been discussed in Reference 10. In summary, while measured skin friction values can be correlated by a combination of factors, namely $\left[\sqrt{\overline{u_e^2}}/U_e\right]$ and $\left(L_\epsilon/\delta_t\right)$, heat transfer coefficients do not seem to lend themselves to a similar procedure. Here $(\ )_e$ denotes the main stream. Experimental data do indicate a distinct influence of the intensity and the length scale of main stream turbulence. However attempts at modifying the C_f - correlations for correlating St and R have remained unsuccessful.

Possibilities for Numerical Experiments

In view of the foregoing, there is some scope for undertaking numerical experiments for establishing the nature of interactions between the main flow turbulence and boundary region turbulence. The numerical experiments must include two considerations: (i) the extent of changes in boundary region turbulence, and (ii) the relation between momentum and heat transports. A direct simulation of Navier-Stokes equations and heat transfer equations (Reference 19) will obviously remove the necessity for separating the two issues, but such work is dependent upon computer capability. In the foreseeable future, the separation of the two issues provides an opening for advances.

In the preceding, the wall-affected region has been referred to as the boundary wall region, rather than as the boundary layer region. The reason for this distinction is that a boundary layer has a classical definition. For example, a log law-governed region is expected in a boundary layer. However, in the presence of main flow turbulence, the existence of a log law region has to be imposed as an additional constraint before a boundary layer type solution is obtained uniquely among all of the possible solutions (Reference 20).

Problem Addressed

In the current investigation, a beginning has been made on establishing the influence of free stream turbulence (FST) on a turbulent boundary layer (TBL) in the context of heat transfer between the fluid and the boundary wall.

A simple case is chosen of a turbulent boundary layer beneath an incompressible, turbulent flow past a flat plate with no imposed pressure gradient (Fig. 1). The main flow is assumed to be moderately turbulent, as depicted in Fig. 2. The turbulence is assumed to be homogeneous in the first instance, and the consequences of relaxing this assumption are discussed in a later section. The boundary wall is assumed to be isothermal at a temperature below that of the fluid.

The objective is to set up a model for the flowfield, that takes into account (a) the interactions between the external and the boundary region flows, and (b) the heat transfer, such that the free stream turbulence characteristics can be treated parametrically. The turbulence characteristics are Tu, the velocity and temperature spectra, and L_ϵ/δ_t; the Reynolds number is assumed to be high.

Basis of the Model

The modelling is carried out in two parts: (i) turbulence representation, and (ii) similarity between heat and momentum transport.

Turbulence Representation

The problem of predicting the development of a TBL continues to be challenging, for example as in Reference 21. When FST is present, the complexity involved is the interaction of a random vortex fields with one that has a characteristic structure in a random field. It is clear that a method akin to large eddy simulation (LES) is probably required in order to account fully for the random vorticity field interactions.

Meanwhile, the rational representation of turbulence suggested by Lumley (Refs. 22 - 23) as a means of examining eddy-mean shear and eddy-eddy interactions, has been chosen here for application. Some experience is available with its application to boundary layer flows (Refs. 24 - 26). The rational representation has been utilized to establish characteristic structures in a channel flow (Ref. 27), and also to obtain the structure of wall layer in a boundary layer (Ref. 28). The Lumley representation has been utilized here entirely at the statistical level to determine the classical structure of TBL with FST.

The basis of statistical turbulence representation is the Loeve orthogonal decomposition theorem by means of which the velocity fluctuation is expressed in the form of generalized Fourier series:

$$u_i = \sum_{n=1}^{\infty} \alpha_n \, \phi_i^{(n)}(\underline{x}\; t) \tag{1}$$

where n represents the modes, 1,2,3 ...., α_1 α_2, α_3, ... are random coefficients with units of velocity, uncorrelated with one another. $\phi_i^{(n)}$ are structure functions, which are furthermore assumed to be orthonormal. The orthogonality condition implies that none of the $\phi_i^{(n)}$ is identically zero. It follows that

$$\overline{\alpha}_n = o \tag{2.1}$$

$$\overline{\alpha_m \alpha_n} = \lambda^{(n)} \delta_{mn} \tag{2.2}$$

$$\int \phi_i(p)\, \phi_i(q)\, d\underline{x}\, dt = \delta_{pq} \tag{2.3}$$

$$\alpha_n = \int u(\underline{x},t)\, \phi_i(n)\, (\underline{x},t)\, d\, \underline{x}\, dt \tag{2.4}$$

It is assumed that α_1, α_2, α_3 .... are ordered such that

$$\lambda(1) > \lambda^{(2)} > \lambda^{(3)} > \cdots > 0.$$

Based on the randomness of α_n and the orthogonality of $\phi_i(n)$, one can write for the two-point correlation.

$$R_{ij}(\underline{x}, \underline{x}' ; t, t') = \sum_{n=1}^{\infty} \lambda^{(n)} \phi_i^{(n)} \phi_j^{(n)} \tag{3}$$

and

$$\int R_{ij}\, \phi_i(n)\, (\underline{x}', t')\, d\underline{x}'\, dt' = \lambda^{(n)} \phi_i(n)\, (\overline{x}\; t) \tag{4}$$

where $\phi_i^{(n)}$ are eigenfunctions with $\lambda^{(n)}$- as the eigenvalues. For the turbulent kinetic energy, one can then write

$$\int \frac{1}{2} \overline{u^2}\, d\underline{x}\, dt = \frac{1}{2} \sum_{n=1}^{\infty} \lambda^{(n)} \tag{5}$$

It follows that $\lambda^{(n)}$ represents the kinetic energy content of the entire flow associated with $\phi_i(n)$ or the nth mode.

The uniqueness of the decomposition is established through calculus of variations, which yields that each mode must account for the maximum of the energy available. One thus has a rational, unique representation of the velocity fluctuation in terms of a series of characteristic eddies. In a given shear flow, the eddies must interact with one another and with the mean shear during flow development. The immediate problem is partitioning of the energy among the different modes. This can be done either by recourse to experimental data or by truncating the nonlinear interactions. On the other hand, the large eddy interaction hypothesis (LEIH) involves consideration of only the first mode over the entire spectrum and its interactions with the mean shear and all of the eddies. This is obviously a strong limitation of the predictive scheme presented here.

Based on Navier-Stokes equations, (Appendix I), one can set up a dynamical equation for the first mode as follows.

$$\frac{\partial \tilde{\phi}_i^{(1)}}{\partial t} + U_j \frac{\partial \tilde{\phi}_i^{(1)}}{\partial x_j} + \frac{\partial U_i}{\partial x_j} \tilde{\phi}_j^{(1)}$$

$$+ \frac{\partial}{\partial x_j} \left\{ \sum_{p=1}^{\infty} \sum_{p=1}^{\infty} \frac{\alpha_1 \; \alpha_p \; \alpha_q}{\left[\lambda^{(1)} \; \lambda^{(p)} \; \lambda^{(q)}\right]^{1/2}} \tilde{\phi}_i^{(p)} \; \tilde{\phi}_j^{(q)} \right\}$$

$$= \frac{\partial \tilde{\pi}^{(1)}}{\partial x_i} + \nu \frac{\partial^2 \tilde{\phi}_i^{(1)}}{\partial x_j^2} \tag{6}$$

where

$$\tilde{\phi}_i^{(1)} = \sqrt{\lambda^{(1)}} \; \phi_i^{(1)} \tag{7.1}$$

$$\tilde{\pi}^{(1)} = -\frac{1}{\rho} \frac{\overline{\alpha_1 \; p}}{\sqrt{\lambda^{(1)}}} \tag{7.2}$$

and, for incompressible flow,

$$\frac{\partial^2 \tilde{\pi}^{(1)}}{\partial x_j^2} = 2 \frac{\partial U_j}{\partial x_k} \frac{\partial \tilde{\phi}_k^{(1)}}{\partial x_j} + \frac{\partial^2}{\partial x_k \, \partial x_j} \left\{ \qquad \right\} \tag{8}$$

In Eqns. (6) and (8), $\{ \quad \}$ represents the eddy-eddy interactions. It is essential to model the term. Among various possibilities, the one chosen here is as follows.

$$\sum_{p=1}^{\infty} \sum_{q=1}^{\infty} \frac{\overline{\alpha_1 \; \alpha_p \; \alpha_q}}{\left[\lambda^{(1)} \; \lambda^{(p)} \; \lambda^{(q)}\right]^{1/2}} \tilde{\phi}_i^{(p)} \; \tilde{\phi}_j^{(q)}$$

$$= \frac{\overline{\alpha_1^3}}{\left[\lambda^{(1)}\right]^{3/2}} \tilde{\phi}_i^{(1)} \; \tilde{\phi}_j^{(1)} - \nu_t \left(\frac{\partial \tilde{\phi}_i^{(1)}}{\partial x_j} + \frac{\partial \tilde{\phi}_j^{(1)}}{\partial x_i} \right) \tag{9}$$

Here the first term on the right hand side involves a coefficient in the nature of a skewness factor and the second, one resembling eddy viscosity, a type of damping factor. It may be stated at the outset that the second term with ν_t is found to be essential in numerical predictions. The skewness factor is associated with the inhomogeneity of the velocity field and the transfer of energy from regions of high intensity to regions of lower intensity. Equation (6) may then be rewritten as follows.

$$\frac{D}{Dt}\left(U_j \tilde{\phi}_i^{(1)}\right) + \frac{\partial U_i}{\partial x_j}\tilde{\phi}_j^{(1)}$$

$$= \frac{\partial}{\partial x_j} S_u \tilde{\phi}_i^{(p)} \tilde{\phi}_j^{(q)} - \nu_t \left(\frac{\partial \tilde{\phi}_i^{(1)}}{\partial x_j} + \frac{\partial \tilde{\phi}_j^{(1)}}{\partial x_i}\right)$$

$$+ \frac{\partial \tilde{\pi}^{(1)}}{\partial x_i} + \nu \frac{\partial^2 \tilde{\phi}_i^{(1)}}{\partial x_j^2} \tag{6.1}$$

where S_u is the so-called ***skewness factor***, and ν_t, the ***eddy damping favor***.

Referring the the equations for mean temperature and intensity of temperature fluctuations given in Appendix I, one can introduce a rational decomposition for temperature fluctuation in a manner similar to that for the velocity fluctuation, namely

$$\theta = \sum_{n=1}^{\infty} \beta_n \, \psi^{(n)}(\underline{x}, t) \tag{10}$$

and write the following dynamical equation.

$$\frac{\partial \tilde{\psi}^{(1)}}{\partial t} + U_j \frac{\partial \tilde{\psi}^{(1)}}{\partial x_j} + \frac{\partial U_i}{\partial x_j} \tilde{\psi}^{(1)}$$

$$+ \frac{\partial}{\partial x_j} \left\{ \sum_{p=1}^{\infty} \sum_{q=1}^{\infty} \frac{\beta_1 \, \beta_p \, \beta_q}{\left(\gamma^{(1)} \, \gamma^{(p)} \, \gamma^{(q)}\right)^{1/2}} \tilde{\psi}^{(p)} \, \tilde{\psi}^{(q)} \right\}$$

$$= \kappa \frac{\partial^2 \, \tilde{\psi}^{(1)}}{\partial \, x_j^2} \tag{11}$$

where

$$\tilde{\psi}^{(1)} = \sqrt{\gamma^{(1)}} \, \psi^{(1)} \tag{11.1}$$

and

$$\overline{\beta_m \, \beta_n} = \gamma^{(n)} \, \delta_{mn}$$

The main describing equations for the turbulence quantities u_i, π, and θ are Eqns. (6), (8), and (11). They must be solved in spectral space.

Momentum and Heat Transport

Writing the usual definition of turbulent Prandtl number in the form

$$\sigma_t = \frac{\overline{u_i u_j}}{\overline{u_j \theta}} \cdot \frac{\partial U/\partial x_j}{\partial T/\partial x_j}, \tag{12}$$

and assuming

$$\overline{u_i u_j} = k_u \overline{q}^2, \quad \text{and} \quad \overline{u_j \theta} = k_\theta \overline{\theta}^2,$$

it follows that

$$\sigma_t = \left(\frac{k_u}{k_\theta}\right) \frac{\overline{q}^2}{\overline{\theta}^2} \frac{\partial U/\partial x_j}{\partial T/\partial x_j} \tag{13}$$

or,

$$\frac{\overline{q}^2}{\overline{\theta}^2} = B^2 \left(\frac{\partial U/\partial x_j}{\partial T/\partial x_j}\right)^2, \tag{14}$$

as suggested in Reference 16, with the dimensionless parameter B^2 treated as a parameter across the boundary layer.

In the inner wall region, the use of wall functions is avoided by use of a modified spectral analogy (References 16 - 17, and 29) as follows: Based on physical structural considerations, and the available evidence for the time ratio between temperature and velocity u_i to be nearly unity in the inner layer, the analogy invoked is between F_{u_i} and F_θ.

Flowfield Description

The flowfield model is illustrated in Fig. 3 with four interactive regions: viscous layer, matching layer, outer layer, matching layer, outer layer, and free stream. It is assumed that the wall region is of the nature of a TBL beneath the main flow with FST. Accordingly the four regions are described in terms of asymptotic expansions utilizing relevant small expansions parameters (References 30 - 31). There are several problems, however, in adopting this procedure.

First, one has to account for the length scale of FST, L_ϵ: The describing equations involve no physical influence of L_ϵ. Therefore, we have proceeded as follows: a value of $\delta_{0.995}$ is chosen, and the condition is imposed that, at the location $\delta_{0.995}$, the dissipation length scale in the boundary layer be equal to L_ϵ. In other words, that solution is assumed to be the one required that ensures the equality of dissipation length scales, within the boundary layer at a particular location and the free stream.

Second, there is the requirement that the matching layer must be of the nature of a log layer. In References 4 and 7, there is considerable evidence for the existence and persistence of the log law character of the region, and also, for the transverse growth of the region with FST intensity. In Reference 21 for the case of an ordinary TBL, one without FST, it was a main objective to recover a constant stress layer in a log law-governed region. In Reference 11 the log law character of mean flow variation was prescribed in dealing with an ordinary TBL. When FST is present, it was found (Reference 20) that a number of solutions was feasible, and a unique solution could be recovered only when it was required that the matching layer be governed by a given law such as the log law. It may be pointed out that prescribing a particular type of mean flow does not specify the extent of the log law region or of any of the other regions.

Last, in the presence of thermal gradients and heat transfer, it is also necessary to match the dissipation scale for temperature at a predetermined value of $\delta^T_{0.995}$, the thermal boundary layer thickness.

Case Chosen for Numerical Experiments

The case chosen for predictions is the flowfield reported in Reference 13. That experiment included a slight heating of the boundary layer up to 3 - 4 C above ambient. However, no heat transfer measurements were intended or made. The experiments were conducted solely for establishing the combined effects of free stream turbulence intensity and scale on a turbulent boundary layer, and the data presented constitute an important benchmark set in cold flow studies with FST. Although data sets with heat transfer are available from other investigations, for example References 7 and 10, the basic cold flowfield is not fully documented, and some ambiguities exist in those sets. We have chosen the data set of Reference 13 primarily because the data set was utilized earlier in verifying, with some success, the application of the LEIH model to the FST case in Reference 20.

A test flowfield was then made up by specifying that there was a difference of 10 C between the fluid and the boundary plate, while all other conditions remained the same, and it was required to predict the heat transfer parameters under various turbulent flow conditions.

The experiments reported in Reference 13 were conducted with a wind tunnel fitted with appropriate grids for generating a variety of combinations of intensity and scale. A flat plate was set up in the wind tunnel, and the boundary region flowfield of the plate was studied, ensuring no streamwise pressure gradient in the flow. The main parameters of the flowfield and the selected conditions for predictive calculations are given in Table I and Fig. 4.

Table I

Details of the Flowfield

• Free stream velocity	- - 20 m/s
• Reθ	- - equal to or greater than 2,000
• Reδ (with no FST)	- - equal to or greater than 2E4.
• Selected cases (1) - (5)	- - Figure 4
• Maximum turbulence intensity	- - 6 per cent

It may be noted that the FST had a continuous spectrum with no gaps or peaks.

Methodology for Predictions

Under incompressible flow conditions, as in the chosen cases, the flowfield can be separated from the thermal field, and determined as in Reference 20. The mean flow equations, along with the dynamical equation for ϕ_i and the pressure fluctuation equation for π, are solved together over a calculation domain as in Fig. 5. The value of the parameters S_u and ν_t are adjusted so as to recover the experimental data for chosen turbulence parameters.

Next, in each case, the mean temperature equation and the heat transport equation are solved utilizing the spectral analogy parameter B^2 as an adjustable quantity. In view of the lack of experimental data for the chosen flowfield in respect of heat transfer parameters, the calculations have been confined to examining the effect of the value assigned to B^2 on the predicted thermal intensity and transport.

A brief outline of the computational procedure is presented in Appendix I.

Preliminary Calculations

In order to test the procedure, the standard equilibrium boundary layer case, the one equivalent to the Falkner-Skan family of laminar boundary layers, was computed for $Re\theta$ of 2,500 in the case of an adiabatic wall with air flow past it. The convergence of the solution as well as the method of choosing the values of S_u and ν_t were found satisfactory. It may be noted that, since there is no FST in this case, it is adequate to demand convergence of the solution.

Considering next a temperature difference of 10 C between the air and the plate, the heat transfer was calculated based on structural similarity. Initially two values of B^2 were tried across different parts of the boundary layer: one, B_I^2 in the inner layer, related to $\overline{u_I^2}$ and the second, B_O^2 in the outer layer, related to $\overline{q^2}$. However, values of heat transfer cited in literature could be recovered for a value of B^2 equal to 1.46. The basic requirement of an equilibrium layer - where the influence of advective processes is negligible on the balance of fluctuating quantities, and the viscous layer can be decoupled from consideration - is thus satisfied.

Predictions

Approximately 300 - 500 iterations are required in time in most cases at each point in the flowfield. The flowfield was calculated first, and then, the heat transfer, as the flowfield was incompressible. Heat transfer calculations required less than about 100 iterations.

The values of S_u and ν_T utilized in various cases are listed in Table II.

Table II

Values of S_u and ν_t

Cases	S_{ui}	S_{uj}	ν_{ti}	ν_{tj}
1	0.811	0.82	0.11	0.10
2	0.92	0.92	0.11	0.10
3	0.91	0.93	0.11	0.10
4	0.90	0.93	0.11	0.10
5	0.90	0.91	0.11	0.10

The values of B_I^2 and B_O^2 selected as parameters for calculations of heat transfer are as in Table III.

Table III

Values of B_I^2 and B_O^2 Selected

Case	B_I^2	B_O^2
1	1.5, 1.55	1.5, 1.49
2	1.5, 1.62	1.5, 1.49
3	1.5, 1.59	1.5, 1.49

It will be observed that a total of six parameters have to be chosen in order to establish the velocity and thermal fields, although ν_{ti} and ν_{tj} could be reasonable non-zero values. It may also be pointed out that the introduction of B_O^2 and B_I^2, rather than a single value of B^2, was by choice; calculations have been performed with a single value of B^2 across the entire boundary layer, as seen from Table III.

All of the predictions have been based on assuming the existence of a log law region, and matching the FST dissipation length scale with that at $\delta_{0.995}$. This is essentially a method of establishing the transverse extent of the boundary layer affected by the FST.

The calculation required in most cases CPU time about an order of magnitude less than the reported time for DNS calculations, and, therefore, still large.

Predicted Results

The predicted results are presented as follows.

Figure 6:	Mean flow velocity in cases 1 through 5.
Figure 7:	Mean temperature in cases 1 through 5.
Figure 8:	Shear stress distribution
Figure 9:	$\overline{v\theta}$ distribution
Figure 10:	Direct stress distribution
Figure 11:	$\overline{\theta^2}$ distribution, and

Figure 12: Stanton number variation.

As stated earlier, there are no experimental data to compare with. However, matching of the four regions in the transverse direction and matching the dissipation scale in the FST with that at $\delta_{0.995}$ limit the permissible values of B_1^2 and B_0^2. In fact, no predictions are presented from the calculations conducted with values of B_1^2 and B_0^2 both equal to 1.5 since they yielded unacceptable mean temperature profiles corresponding to the mean velocity profiles; the latter were generated such that they matched the experimental data. Thus, a mathematically unique method of choosing B^2 can be foreseen.

Discussion

A framework has been set up for establishing the effects of FST intensity and scale on a boundary layer when there is heat transfer between the fluid and the boundary wall under incompressible flow conditions. The framework has yielded well accepted predictions in the case of Falkner-Skan type of flows. It has also been possible to recover the experimental results in Ref. 13 utilizing the LEIH model, while recognizing that heat transfer was not a parameter in those tests. Finally, the limited spectral analogy (weighted by velocity and temperature gradients) has been utilized in the cases with heat transfer, and the nature of the results seem meaningful.

The rational representation of turbulence and the solution procedure in spectral space permit inhomogeneities and gaps in turbulence to be taken into account. The redistribution of energy cannot, however, be predicted without additional phenomenological hypotheses, such as those leading to the Eddy Damped Quasi Normal Markovin (EDQNM) approximation (Reference 32).

The framework generated is useful for output interrogation with respect to specific questions, and not for calculations for design or general heat transfer prediction. However, under incompressible flow conditions, if flowfield measurements are available, S_u and ν_t can be selected based on such data, and the thermal field determination requires only a choice of B^2. If this procedure becomes established, it can yield some savings in determining heat transfer. This can only be accomplished if the framework is suitably calibrated and verified in a number of cases.

In this connection, it is well recognized that S_u and ν_t are not directly measurable; in fact, they are only of the nature of a skewness factor and an eddy viscosity-like damping factor. Thus, it is necessary to compute some other parameter such as the probability density function (pdf) for velocity and temperature. This has been attempted in Reference 33 for velocity fluctuations in turbulent boundary layers. It is suggested that the pdf obeys a general distribution law with several parameters applying to different parts of a boundary layer. Such investigations have not been attempted with FST, or in relation to scalar properties such as temperature without or with FST. The current framework does permit a determination of the pdf of both velocity and temperature fluctuations, and thus lead to an experimental verification of the validity of the choice of S_u, ν_t, and B^2.

The limited similarity between intensity and temperature variance may be affected by complexities in flows. Adequate experimental data are not available to delineate the complexities that do not affect the similarity from those that do. Any complexity that brings about a coupling between the velocity and the thermal fields can cause a basic change in the postulated similarity.

Two important questions in the prediction procedure pertain to the postulated limited similarity between velocity and temperature spectra: (i) What is the influence of scale? And, (ii) What causes the dissimilarity in spectra? Neither of these questions can be resolved adequately at this time. It is suggested that there may be a combination of the two scales of velocity fluctuations and the two scales of temperature fluctuations that together determine the penetration, entrainment and subsequent dissipation of fluid packets, and then cause the differences in the spectra. An experiment in which the two sets of the two scales can be adjusted independently is indicated.

Acknowledgement: Parts of the initial work on this problem were supported under AFOSR Contract No. F49620-87-k-0008. Several discussions with Dr. R. Rivir and Professor P. Bradshaw have been most helpful.

REFERENCES

1. Murthy, S.N.B. and Sullivan, J.P.: Combustor Complexities: Diagnostics/Predictions, Paper presented at the NATO Advanced Study Institute on Combusting Flow Diagnostics, April 1990, Algarve, Portugal.
2. Roquemore, W.M., et al: Experimental and Theoretical Studies in a Gas-Fueled Research Combustor, AIAA 91-0639.
3. Bradshaw, P.: Effects of Free-Stream Turbulence on Turbulent Shear Layers, ARC Report No. 35648, 1974.
4. Hancock, P.E. and Bradshaw, P.: "The Structure of a Turbulent Boundary Layer Beneath a Turbulent Free Stream," 6th Symposium on Turbulent Shear Flows, Toulouse, Sept. 1987.
5. Simonich, J.C., and Bradshaw, P.: Effect of Free-Stream Turbulence on Heat Transfer Through a Turbulent Boundary Layer, J. Heat Transfer, Vol. 100, No. 4, 1978.
6. Van Fossen, Jr. G.J., and Simoneau, R.J.: A Study of the Relationship Between Free-Stream Turbulence and Stagnation Region Heat Transfer, J. Heat Transfer, Vol. 109, Feb. 1987.
7. Blair, M.F. "Influence of Free Stream Turbulence on Turbulent Boundary Layer Heat Transfer and Mean Flow Development," Parts I and II, ASME J. Heat Transfer, Vol. 105, Feb. 1983.
8. Wittig, S., et al: Effects of Wakes on the Heat Transfer in Gas Turbine Cascades, AGARD-CP-390, Paper No. 6, 1985.
9. Maciejewski, P.K., and Moffat, R.J.: The Effects of High Free-Stream Turbulence on Heat Transfer in Turbulent Boundary Layers, Paper presented at the Zaric Memorial Meeting, Dubvronik, 1988.
10. Baskaran, V., Abdellatif, O.E., and Bradshaw, P.: Effects of Free Stream Turbulence on Turbulent Boundary Layers with Convective Heat Transfer, Seventh Symposium on Turbulent Shear Flows, Stanford University, August 1989.
11. Walker, J.D.A., Scharnhorst, R.K., and Weigand, G.G.: Wall Layer Models for the Calculation of Velocity and Heat Transfer in Turbulent Boundary Layers, AIAA-86-0213, January 1986.
12. Charnay, G., Mathieu, J., and Compte-Bellot, G.: Response of a Turbulent Boundary Layer to Random Fluctuations in the External Stream, The Physics of Fluids, Vol. 19, September, 1975.
13. Hancock, P.E.: The Effect of Free Stream Turbulence on Turbulent Boundary Layers, Ph.D. Thesis, University of London, 1980.
14. Bradshaw, P., Ferris, D.H., and Atwell, N.P.: Calculation of Boundary-Layer Development Using the Turbulent Energy Equation, J. Fluid Dynamics, Vol. 28, march 1967.
15. Hong, S.K., and Murthy, S.N.B.: Effective Velocity of Transport in Curved Wall Boundary Layers, AIAA J. Vol. 24, march 1986.
16. Fulachier, L., and Dumas, R.: Spectral Analogy Between Temperature and Velocity Fluctuations in a Turbulent boundary layer, J. Fluid Mech., Vol. 76, 1976.

17. Fulachier, L., and Antonia, R.: Spectral Analogy Between Temperature and Velocity Fluctuations in Several Turbulent Flows, Int. J. Heat Mass Transfer, Vol. 27, 1984.

18. Kader, B.A., and Yaglom, A.M.: Spectra of Anisotropic Turbulent Velocity and Temperature Fluctuations in Turbulent-Wall Flows, Fluid Mechanics - Soviet Research, Vol. 16, 1987.

19. Kim, J., and Moin, P.: Transport of Passive Scalars in a Turbulent Channel Flow, Turbulent Shear Flows VI, Springer, Berlin, 1989.

20. Murthy, S.N.B., and Hong, S.K.: Turbulent Boundary Layer with Free Stream Turbulence, AIAA 90-1503, June 1990.

21. Spalart, P.R.: Direct Simulation of a Turbulent Boundary Layer up to $R\theta =$ 1,440, J. Fluid Mech., Vol. 187, 1988.

22. Lumley, J.L.: The Structure of Inhomogeneous Turbulent Flows," Atmospheric Turbulence and Radio Wave Propagation, ed. A.M. Yaglom, and V.L. Tatarsky, NAUKA, Moscow, 1967.

23. Lumley, J.L.: Coherent Structures in Turbulence, Transition and Turbulence, ed. R.E. Meyer, Academic Press, New York, 1981.

24. Hong, S.K.: Large Eddy Interactions in Curred Wall Boundary Layers, Ph.D. Thesis, Purdue University, Aug. 1983.

25. Glauser, M.N., Leib, S.J., and George, W.K.: Coherent Structures in Axisymmetric Jet Mixing Layer, Proc. 5th Symp. Turb. Shear Flow, Cornell, 1985.

26. Moin, P.: Probing Turbulence via Large Eddy Simulation, AIAA-84-0174, January, 1984.

27. Hong, S.K.: Large Eddy Interactions in a Turbulent Channel Flow, NASA Tech. Memo. 86757, Sept. 1985.

28. Aubry, N.: A Dynamical System/Coherent Structure Approach to the Fully Developed Turbulent Wall layer, Ph.D. Dissertation, Cornell University, May 1987.

29. Antonia, R.A., Krishnamoorthy, L.V. and Fulachier, L.: Correlation between the Longitudinal Velocity Fluctuation and Temperature Fluctuation in the Near-Wall Region of a Turbulent Boundary Layer, Int. J. Heat Mass Transfer, Vol. 31, 1988.

30. Yagnik, K.S.: J. Fluid Mech., Vol. 42, 1970.

31. Mellor, G.L.: The Large Reynolds Number, Asymptotic Theory of Turbulent Boundary Layers, Int. J. Engng. Sci., Vol. 10, 1972.

32. Pouqet, A., et al.: Turbulence with a Spectral Gap, The Phys. Fluids, Vol. 26, April 1983.

33. Rodi, W., Scheuerer, G.: Calculation of Turbulent Boundary Layers Under the Effect of Free Stream Turbulence, Turbulent Shear Flow conference V, Cornell University, 1985.

34. Peyret, R., and Taylor, T.D.: Computational Methods for Fluid Flow, Springer, New York, 1982.

35. Kim, Y., and Moin, P.: Application of a Fractional Method for Incompressible Navier-Stokes Equations, NASA Tech. Memo. No. 85898, March 1984.

Appendix I

The mean flow equations are written in a conservative form as follows:

$$\frac{\partial U_i}{\partial t} + \frac{\partial}{\partial x_j}\left(U_i\, U_j - \overline{u_i u_j}\right) = -\frac{\partial P}{\partial x_i} + \frac{1}{Re}\,\frac{\partial^2 U_i}{\partial x_j^2} \qquad \text{(A.1.1)}$$

$$\frac{\partial T}{\partial t} + U_j\,\frac{\partial T}{\partial x_j} = -\frac{\partial \overline{u_j \theta}}{\partial x_j} + \kappa\,\frac{\partial^2 T}{\partial x_j^2} \qquad \text{(A.1.2)}$$

The kinetic energy of velocity fluctuations and the variance of temperature fluctuations can be balanced as follows:

$$\frac{\partial}{\partial t}\left(\frac{1}{2}\overline{q^2}\right) + U_j\frac{\partial}{\partial x_j}\left(\frac{1}{2}\overline{q^2}\right) + \frac{\partial}{\partial x_j}\left(\overline{pu_j} + \frac{1}{2}\,\overline{q^2 u_j}\right)$$

$$= -\overline{u_i u_j}\,\frac{\partial U_i}{\partial x_j} + \nu\,\overline{u_i\frac{\partial^2 u_i}{\partial x_j^2}} \qquad \text{(A.1.3)}$$

and

$$\frac{\partial}{\partial t}\left(\frac{1}{2}\overline{\theta^2}\right) + U_j\frac{\partial}{\partial x_j}\left(\frac{1}{2}\overline{\theta^2}\right) + \frac{\partial}{\partial x_j}\left(\frac{1}{2}\overline{\theta^2 u_j}\right)$$

$$= -\overline{\theta u_j}\,\frac{\partial T}{\partial x_j} + \kappa\,\frac{\partial^2}{\partial x_j^2}\left(\frac{1}{2}\overline{\theta^2}\right) - \kappa\overline{\left(\frac{\partial \theta}{\partial x_j}\right)^2} \qquad \text{(A.1.4)}$$

The pressure fluctuation, p, expressed in terms of the parameter π, See Eq. (7.2), can be shown to obey the Poisson equation in incompressible flow.

$$\overline{u_i u_j} = \phi_i\ \phi_j \quad , \text{ and } \quad \overline{\theta u_j} = \beta\ \phi_j \qquad \text{(A.2)}$$

The large-eddy functions ϕ_i are governed by the dynamical equation in physical (x,y,z) space as follows.

$$\frac{\partial \phi_i}{\partial t} + \frac{\partial}{\partial x_j}\left(\phi_i\ U_j\right) + \frac{\partial}{\partial x_j}\left(\phi_i\ U_j\right) + S_u\,\frac{\partial}{\partial x_j}\left\{\phi_i\ U_j\right\}$$

$$= -\frac{\partial \pi}{\partial x_i} + (\nu + \nu_t)\frac{\partial^2 \phi_i}{\partial x_j^2} \qquad \text{(A.3)}$$

In the following, the solution procedure is illustrated only for the x-component of ϕ_i. The same procedure can be extended to other components of ϕ_i.

The flow is assumed to be homogeneous in the spanwise z-coordinate direction. One can then introduce Fourier expansions for velocity and pressure as follows.

$$\phi_i\,(x,y,z,t) = \sum_{k=-\infty}^{\infty} \hat{\phi}_i\,(x,y,k,t)\, d^{\hat{i}\,kz} \tag{A.4}$$

$$\pi\,(x,y,z,t) = \sum_{k=-\infty}^{\infty} \hat{\pi}\,(x,y,k,t)\, d^{\hat{i}\,kz} \tag{A.5}$$

where $\hat{i} \equiv \sqrt{-1}$. Applying these to Eq. (A.5), one obtains a complex equation for $\hat{\phi}_1\,(x,y,k,t)$ as shown below.

$$\begin{aligned} &\frac{\partial \hat{\phi}_1}{\partial t} + 2\,\frac{\partial}{\partial x}\left(U\,\hat{\phi}_1\right) + \frac{\partial}{\partial y}\left(V\hat{\phi}_1\right) + \frac{\partial}{\partial y}\left(U\,\hat{\phi}_2\right) \\ &\quad + \hat{i}\,k\,U\,\hat{\phi}_3 + S\cdot F\left\{\frac{\partial}{\partial x_j}(\phi_1\;\phi_j)\right\} \\ &\quad = -\,\frac{\partial \hat{\pi}}{\partial x} + (\nu + \nu_t)\left(\frac{\partial^2}{\partial x^2} + \frac{\partial^2}{\partial y^2} - k^2\right)\hat{\phi}_1 \end{aligned} \tag{A.6}$$

where the F - term is equivalent to

$$\begin{aligned} \sum_{k'=-\infty}^{\infty} \Bigg\{ &\frac{\partial}{\partial x}\left[\hat{\phi}_1(k')\hat{\phi}_1\,(k-k')\right] + \frac{\partial}{\partial y}\left[\hat{\phi}_1(k')\hat{\phi}_2(k-k')\right] \\ &+ \hat{i}\,k\,\hat{\phi}_1\,(k')\,\hat{\phi}_3\,(k-k')\Bigg\} \end{aligned}$$

Thus information between a large and a small wave number is exchanged through the convolution term. The solution for $\hat{\phi}_1$ can then be obtained at time $t = t_0 + \Delta t$ utilizing the values of mean velocities U and V which have been determined corresponding to that instant but, as stated under Numerical Procedure, with the Reynolds stresses for $t = t_0$.

The first step in solving Eq. (A.6) is to determine an intermediate function $\hat{\phi}_1^*$ from the following equation.

$$\frac{\hat{\phi}_1^* - \hat{\phi}_1^n}{\Delta t} + U\left\{\frac{\partial \hat{\phi}_1}{\partial x} + V\,\frac{\partial \hat{\phi}_1}{\partial y} + \frac{\partial U}{\partial x}\,\hat{\phi}_1 + \frac{\partial U}{\partial x}\,\hat{\phi}_2\right\}^n + \frac{1}{2}\left\{3\cdot S\cdot F\left(\phi_1\ \phi_j\right)^n - S\cdot F\left(\phi_1\ \phi_j\right)^{n-1}\right\} = \frac{1}{2}\,\frac{1+\nu_t}{Re}\left(\frac{\partial^2}{\partial x^2} + \frac{\partial^2}{\partial y^2} - k^2\right)\left(\hat{\phi}_1^* + \hat{\phi}_1^n\right) \tag{A.7}$$

It is subject to the conditions

$$\hat{\phi}_1^* = \hat{\phi}_1^{n+1} + (\Delta t)\left(\frac{\partial \hat{\pi}}{\partial x}\right)^{n+1} \approx \hat{\phi}_1^{n+1} + (\Delta t)\left(\frac{\partial \hat{\pi}}{\partial x}\right)^{n} \tag{A.8}$$

Equation (A.8) assumes that $\hat{\pi}^{n+1} \approx \hat{\pi}^n$ at the boundary and is a second-order approximation in time, O (Δt^2) (Ref. X). Introduction of $\hat{\phi}_1^*$ in the viscous term in Eq. (A.8) stabilizes the numerical solution for $\hat{\phi}_1^*$. Once $\hat{\phi}_1^*$ is solved from the elliptic equation (A.8), then pressure spectra $\hat{\pi}^{n+1}$ is obtained from

$$\frac{\partial^2 \hat{\pi}}{\partial x^2} + \frac{\partial^2 \hat{\pi}}{\partial y^2} - k^2 \hat{\pi} = \frac{1}{\Delta t}\left(\frac{\partial \phi_1^*}{\partial x} + \frac{\partial \phi_2^*}{\partial y} + \hat{i}k\ \phi_3^*\right) \tag{A.9}$$

subject to boundary conditions, namely

$$\frac{\partial \hat{\pi}^{n+1}}{\partial x} = \frac{1}{\Delta t}\left(\hat{\phi}_1^* - \hat{\phi}_1^{n+1}\right)$$

$$\frac{\partial \hat{\pi}^{n+1}}{\partial y} = \frac{1}{\Delta t}\left(\hat{\phi}_2^* - \hat{\phi}_2^{n+1}\right)$$

$$\hat{i}\,k\,\hat{\pi}^{n+1} = \frac{1}{\Delta t}\left(\hat{\phi}_3^* - \hat{\phi}_3^{n+1}\right) \tag{A.10}$$

Finally, updated values for $\hat{\phi}_1^{n+1}$ are computed directly from

$$\frac{\hat{\phi}_1^{n+1} - \hat{\phi}_1^*}{\Delta t} = -\,\frac{\partial \hat{\pi}^{n+1}}{\partial x}$$

$$\hat{\phi}_1^{n+1} = \hat{\phi}_1^* - (\Delta t)\frac{\partial \hat{\pi}^{n+1}}{\partial x}$$

The intensities and Reynolds stress components $\overline{u_i u_j}$ are then calculated from $\hat{\phi}_i$, integrating over a chosen wave number range as follows.

$$\overline{u_i u_j}\,(x,y,t) = \int_{-\infty}^{\infty} \hat{\phi}_i(x,y,k,t)\, \phi_j^*\,(x,y,k,t)\, dk \qquad (A.12)$$

where * on $\hat{\phi}_j$ denotes the complex conjugate. It is found that a set of discrete wave numbers encompassing the desired range is adequate in practice.

A similar analysis can be carried out for ψ_1.

The basic equations are solved in two groups: (i) Equations (A.1.1), (A.3), and (A.9), and (ii) Equations (A.1.3), (A.1.4), and (A.3).

The numerical method is a fractional method (Refs. 34 and 35). As indicated above, the cross-flow direction z is transformed into wave number space k. The convection terms are transformed with second order Crank-Nicolson method. A staggered grid is employed for discretization: the u-component variables are placed on the east side of the grid cell, the v-component ones are on the south-north sides, and the w-component variables and pressure are located at the cell centers. The resulting Poisson equations are solved implicitly with an elliptic procedure without resorting to an approximate factorization technique.

The mean flow equations are decoupled from the large eddy equations during integration in time by allowing the turbulent transport terms in the mean flow equations to lag by the time step Δt when the mean flow velocities are being solved at $t = (t_0 + \Delta t)$. Meanwhile the large eddy field interacting with the current mean flowfield is implicitly updated for $t = (t_0 + \Delta t)$.

In general about 300 - 500 iterations are required in time at each point in the flowfield for the chosen values of S_u and ν_T. Three sets of matching conditions are required along the transverse direction, while requiring the matching layer to be of the character of log law. Finally the calculated flowfield has to be iterated with respect to the domain boundary conditions. The solution so obtained applied to the FST of given intensity and a dissipation length scale obtained at $\delta_{0.995}$.

When it is desired to consider FST with a given length scale, the outer edge of the boundary layer region must be varied over a range of values, approximately over 1.5 to 3.0 times the given length scale.

In the second part of the solution procedure, the parameter to be chosen is B^2. If relevant experimental data are available, then B^2 can be chosen such as to recover the experimental data.

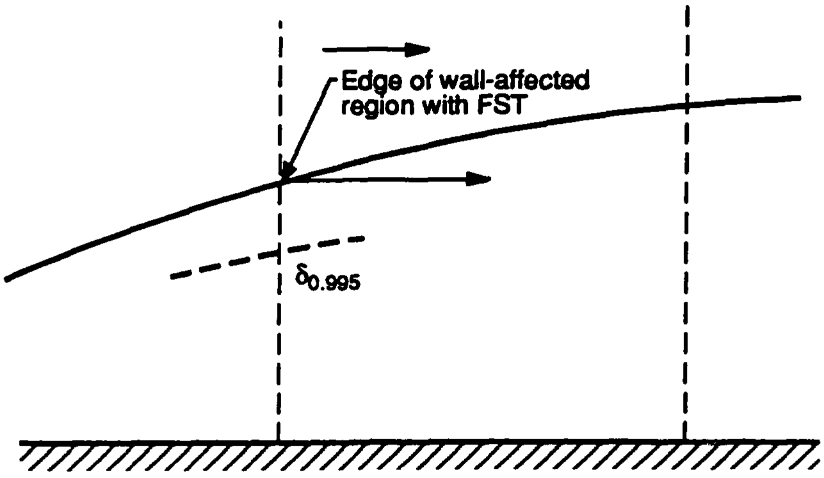
Edge of wall-affected region with FST
$\delta_{0.995}$

Figure 1. Turbulent boundary layer with free stream turbulence.

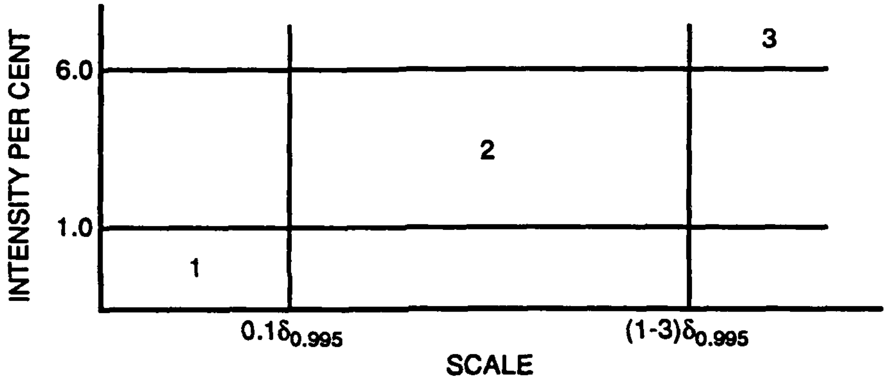

Figure 2. Free stream turbulence intensity and scale. 1. Weak turbulence; 2. moderate turbulence; and 3. large scale turbulence.

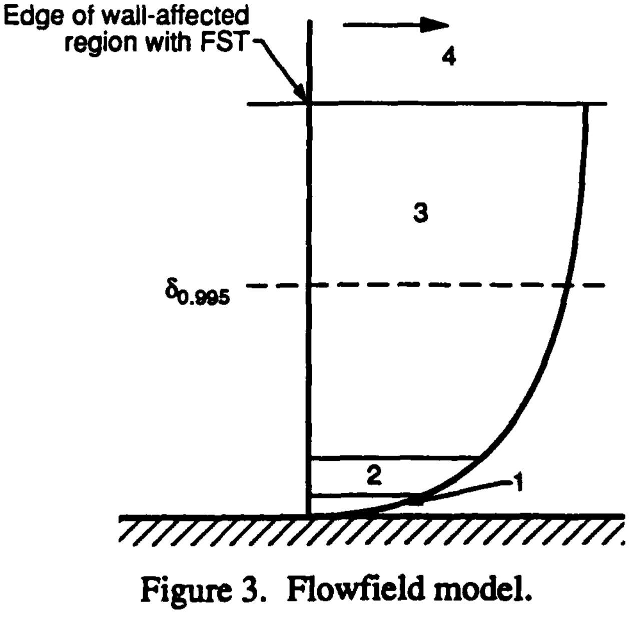
Edge of wall-affected region with FST
4
3
$\delta_{0.995}$
2
1

Figure 3. Flowfield model.

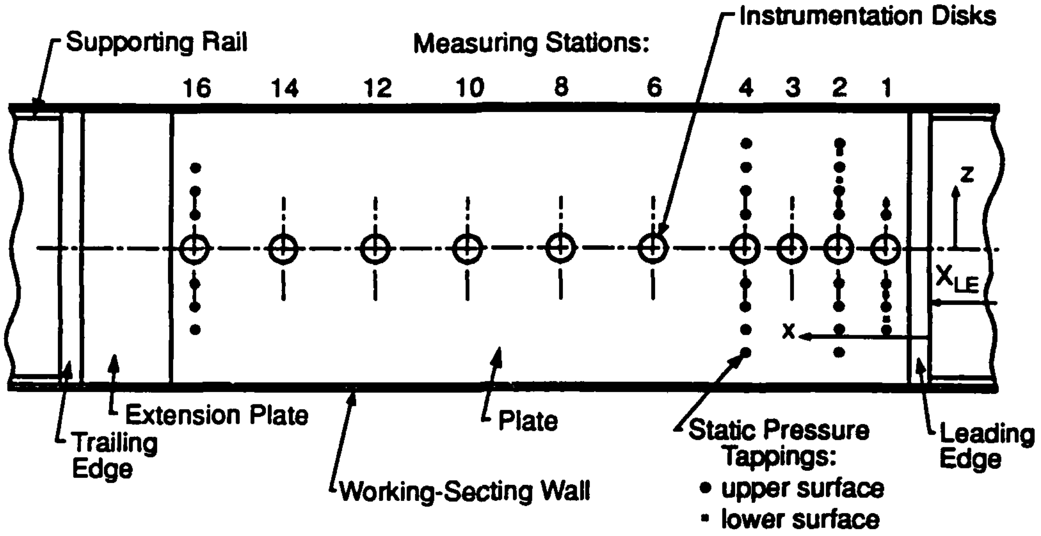
Supporting Rail
Measuring Stations:
16
14
12
10
8
6
4
3
2
1
Instrumentation Disks
z
X_{LE}
x
Extension Plate
Trailing Edge
Plate
Working-Secting Wall
Static Pressure Tappings:
• upper surface
▪ lower surface
Leading Edge

Figure 4. Selected cases:
i. Flat plate.

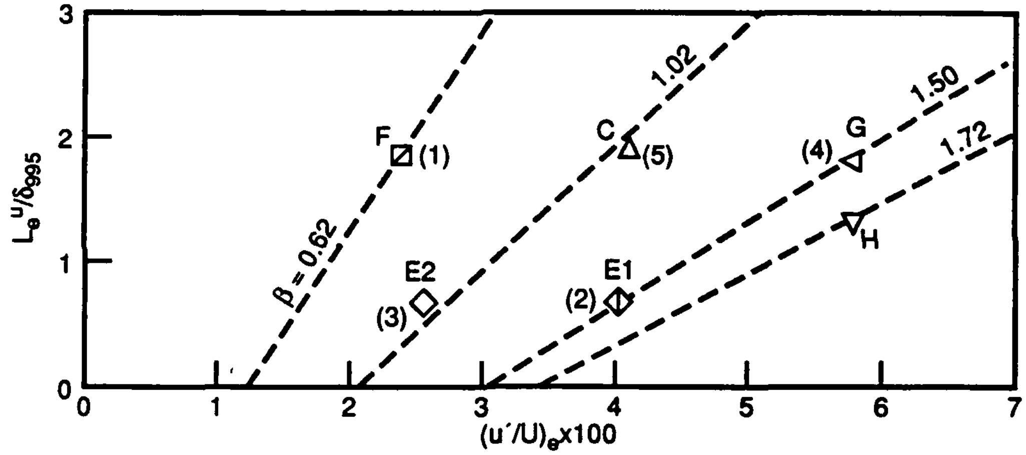

Figure 4.(continued) Selected cases:
(ii). Test cases. Bar spacing 7.2 cm for cases (1), (2), and (3), and 15.2 cm for (4) and (5).

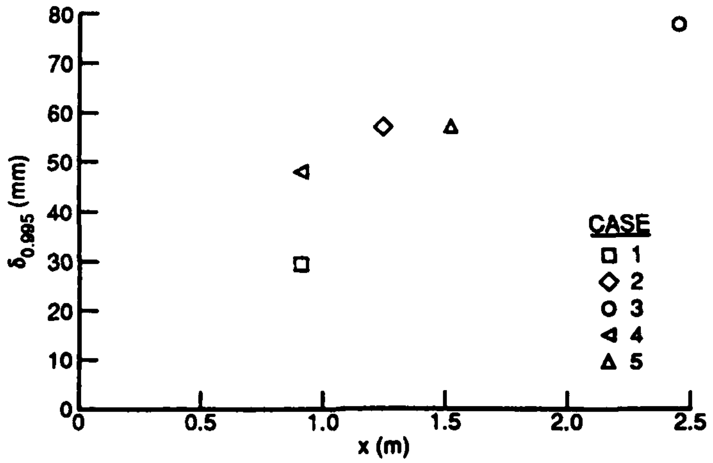

Figure 4.(continued) Selected cases:
(iii). Boundary layer thickness for different cases.

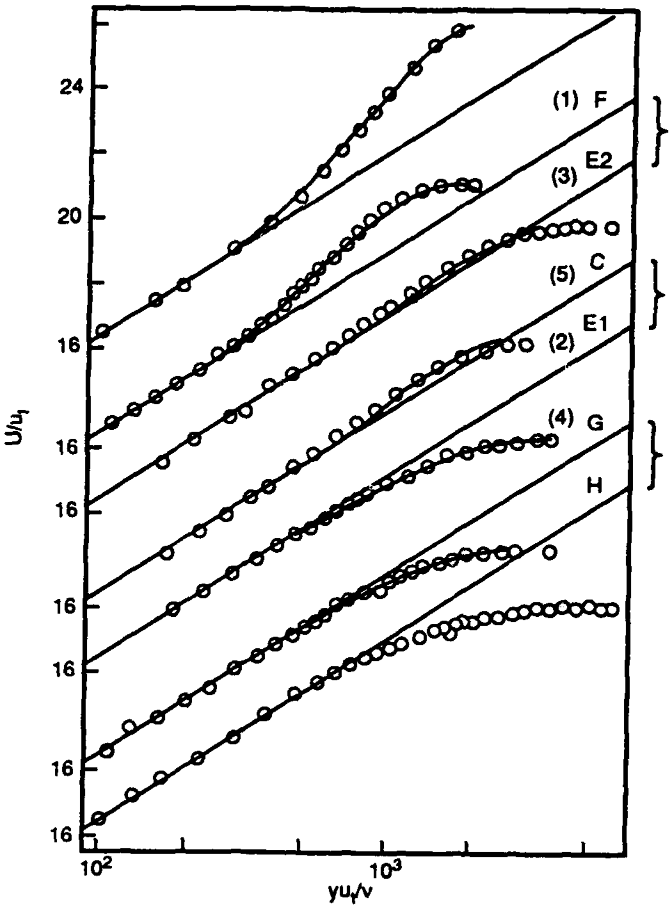

Figure 4.(continued) Selected cases:
(iv). Mean velocity profiles.

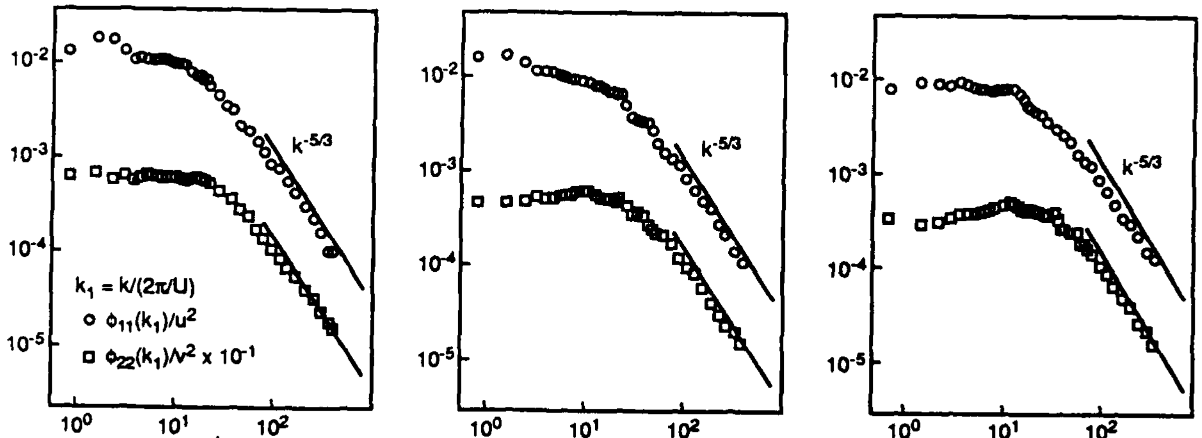

CASE 1

CASE 2

CASE 3

Figure 4.(continued) Selected cases:
(v). Examples of free-stream/spectra.

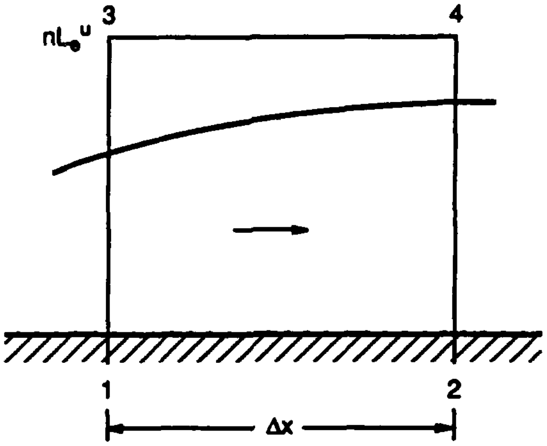
nL_e^u
3
4
1
2
Δx

Figure 5. Calculation domain.

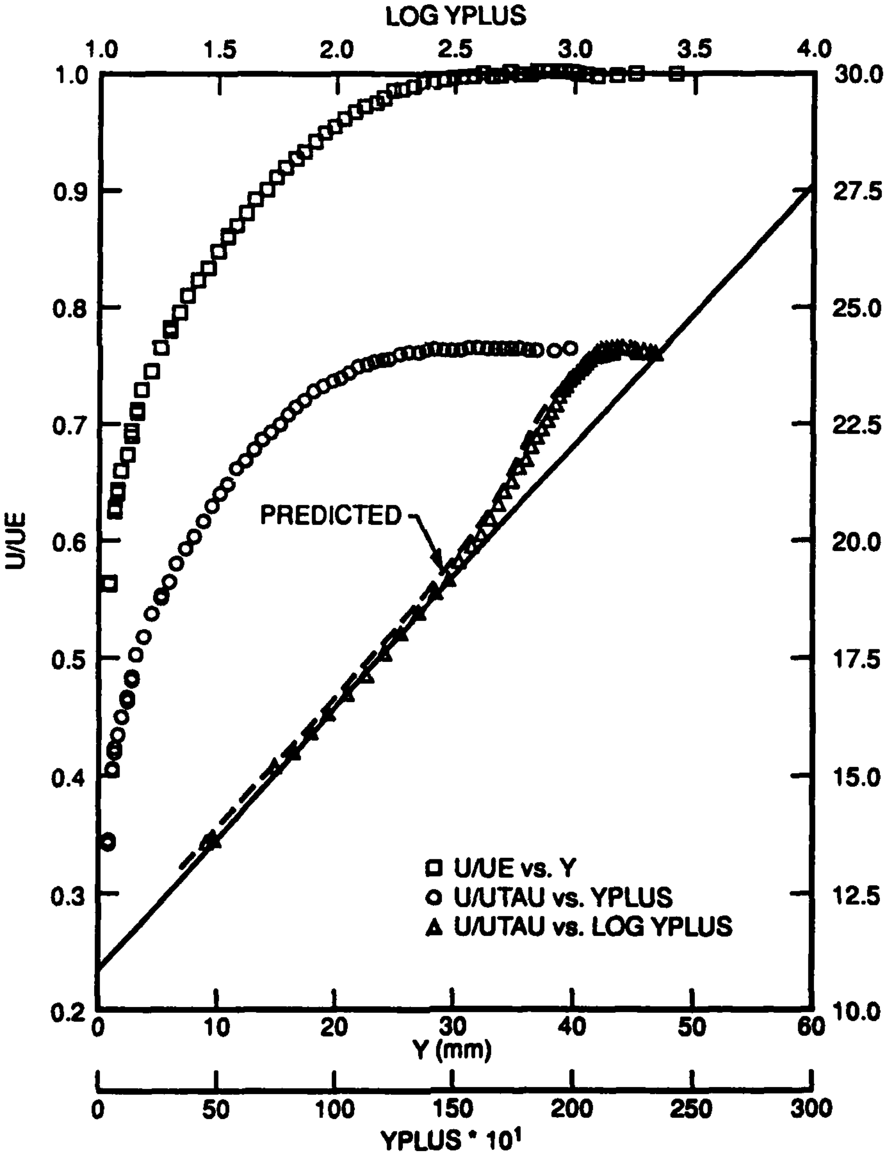

(i). Case 1

Figure 6. Mean velocity profiles.

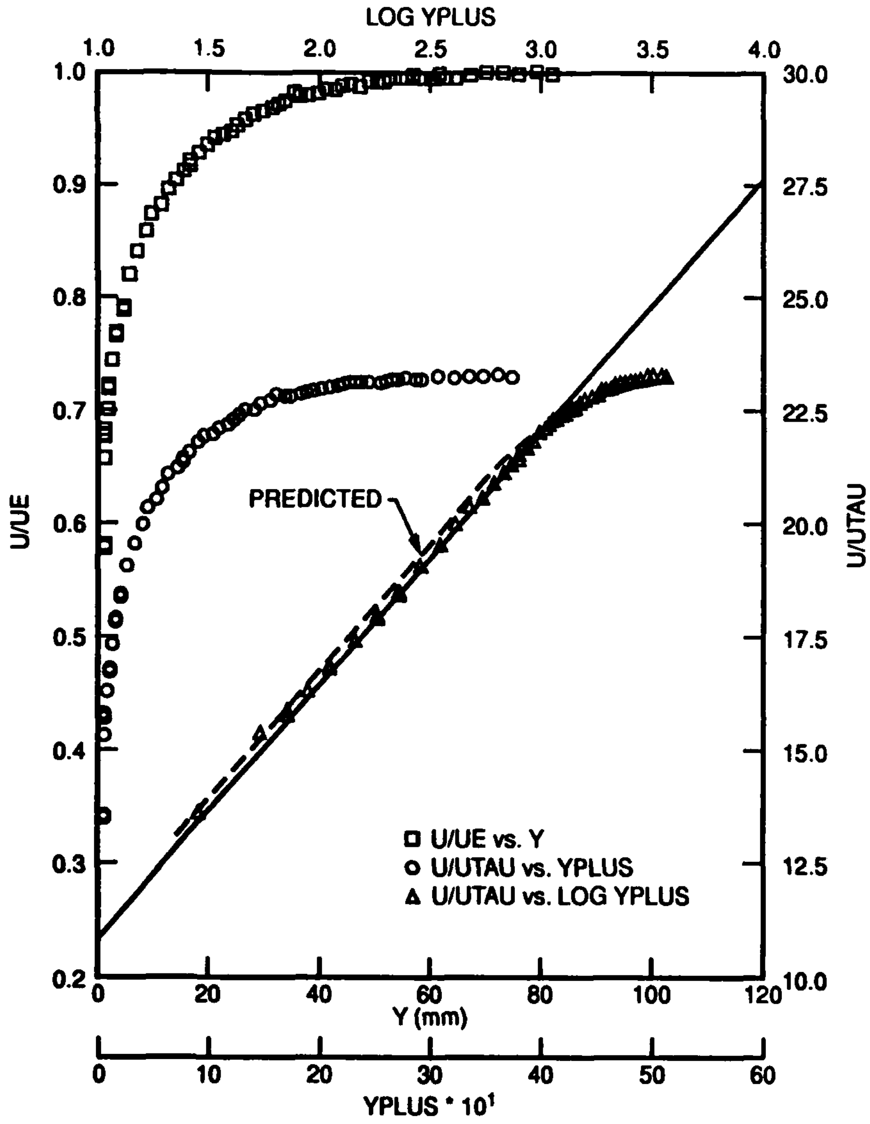

(ii). Case 2
Figure 6. Mean velocity profiles.

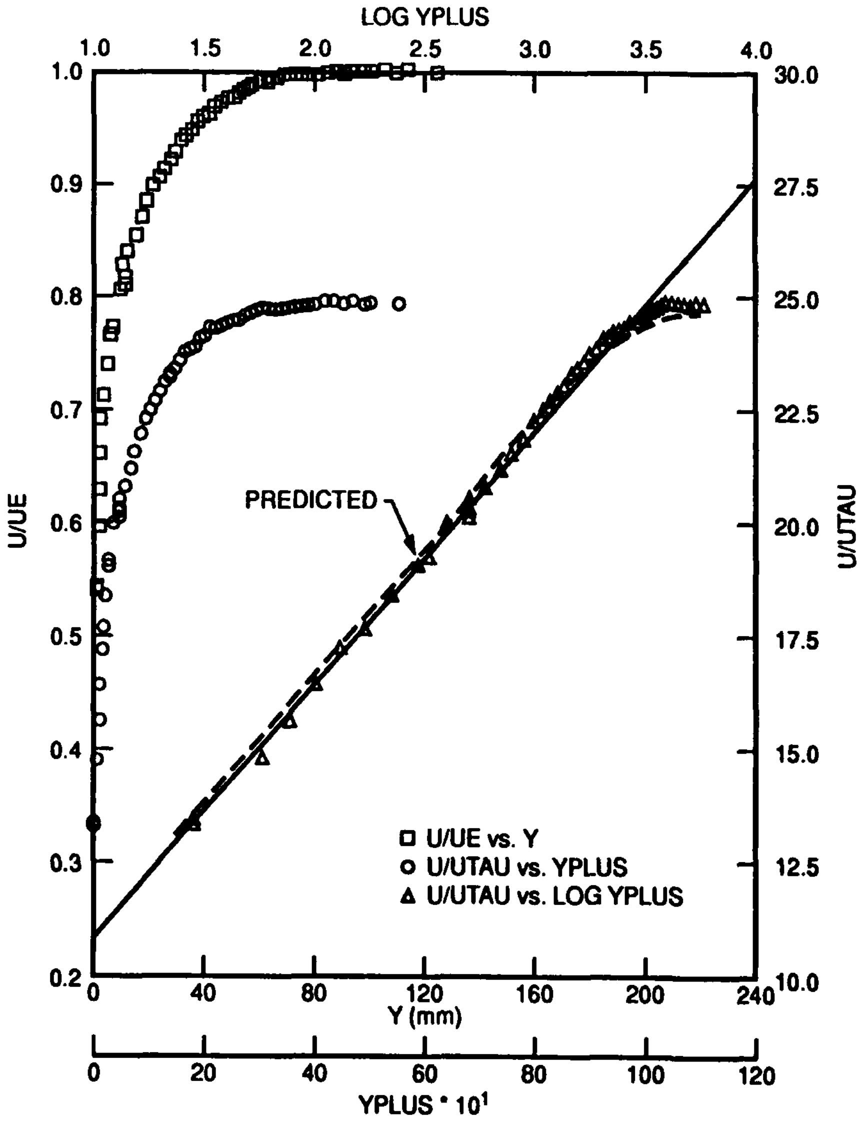

(iii). Case 3
Figure 6. Mean velocity profiles.

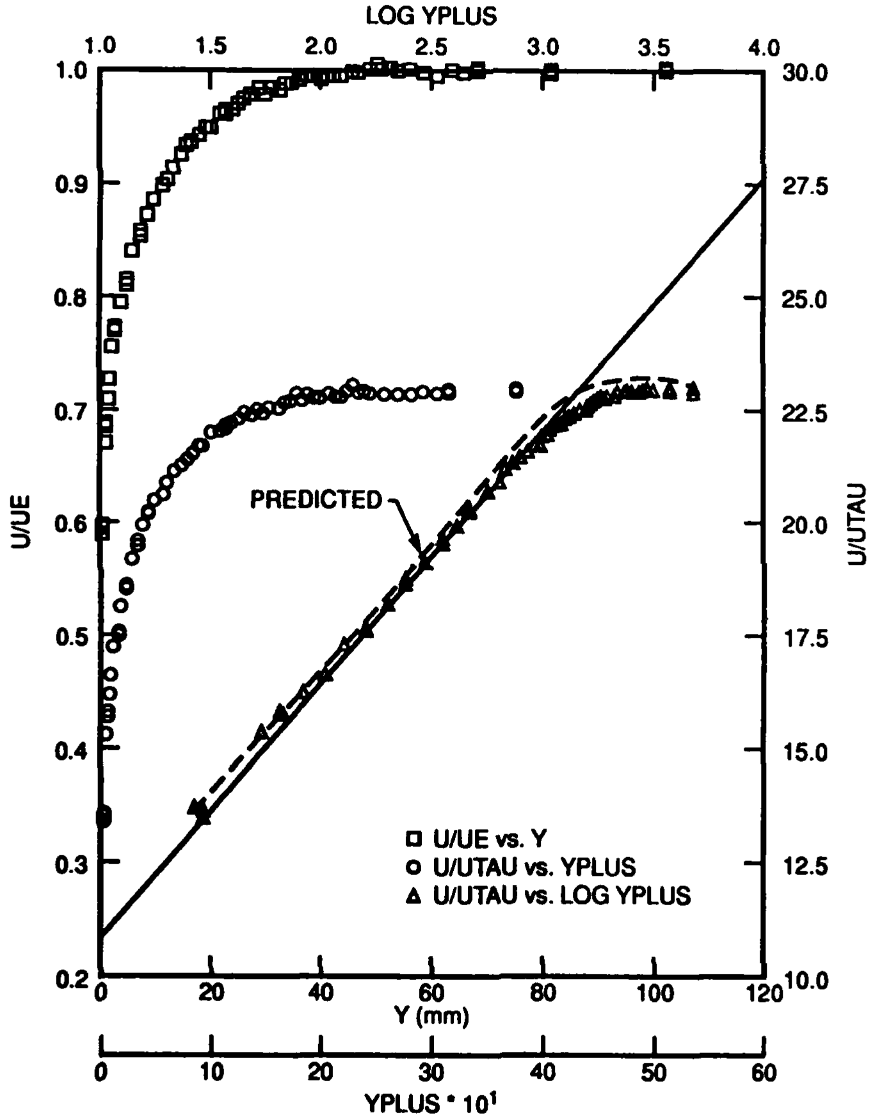

(iv). Case 4

Figure 6. Mean velocity profiles.

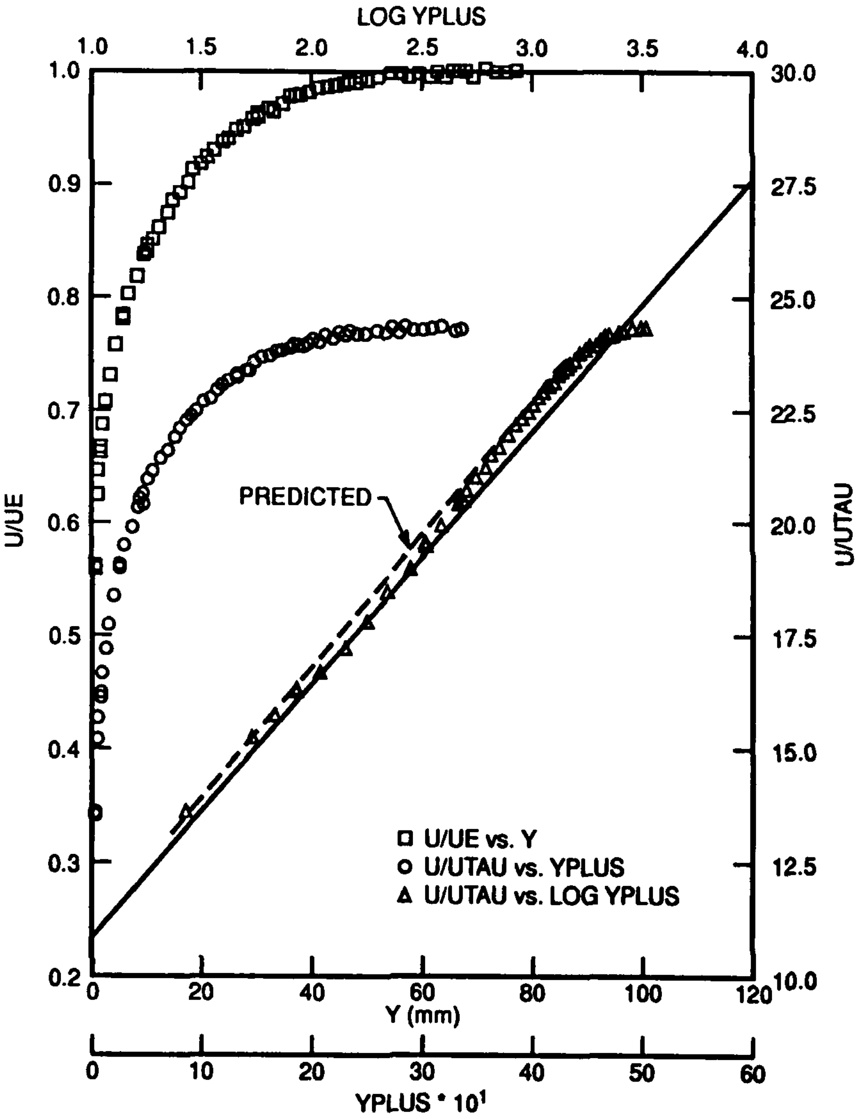

(v). Case 5

Figure 6. Mean velocity profiles.

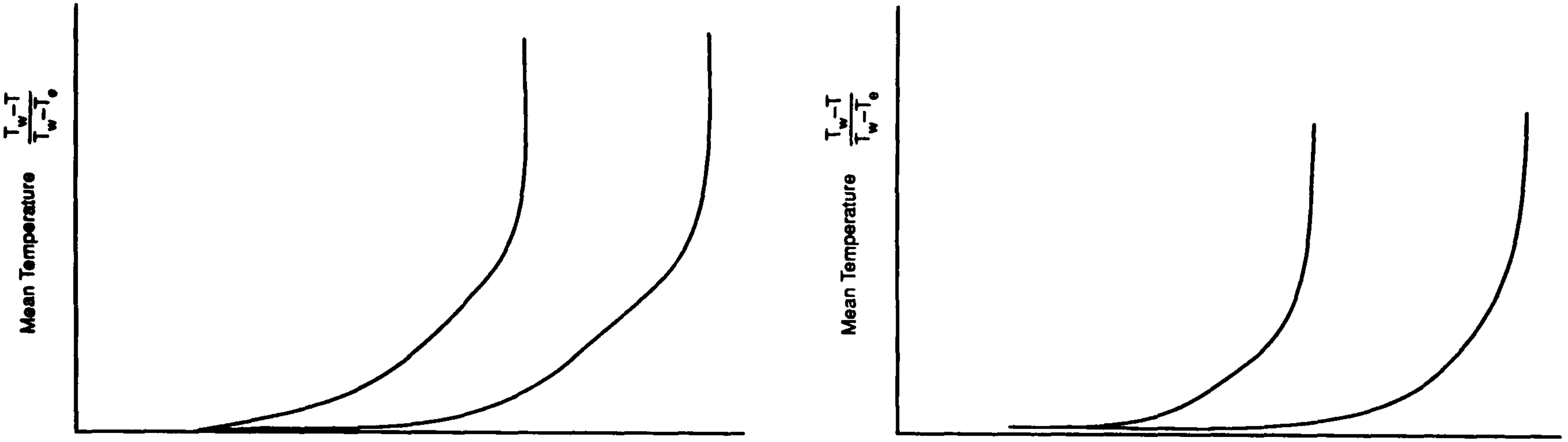

(i) Case 1.

(ii) Case 2.

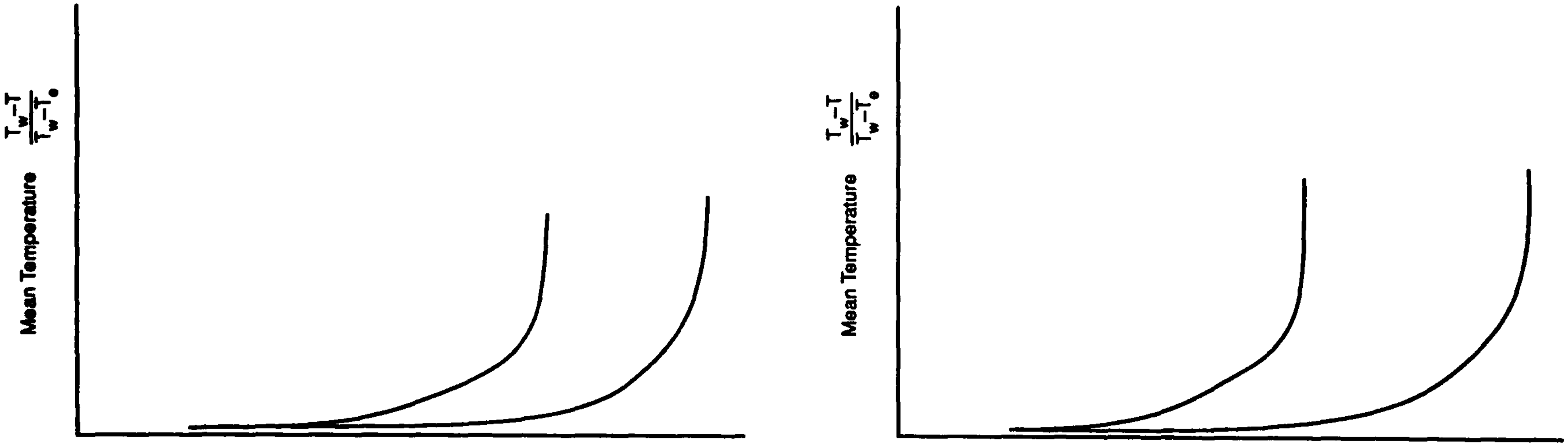

(iii) Case 3.

(iv) Case 4.

Figure 7. Mean temperature profiles.

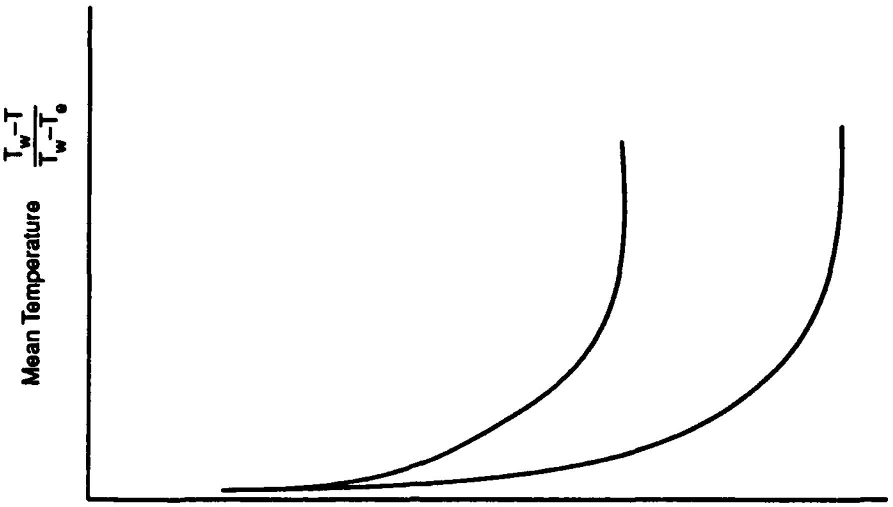

(v) Case 5.
Figure 7. Mean temperature profiles.

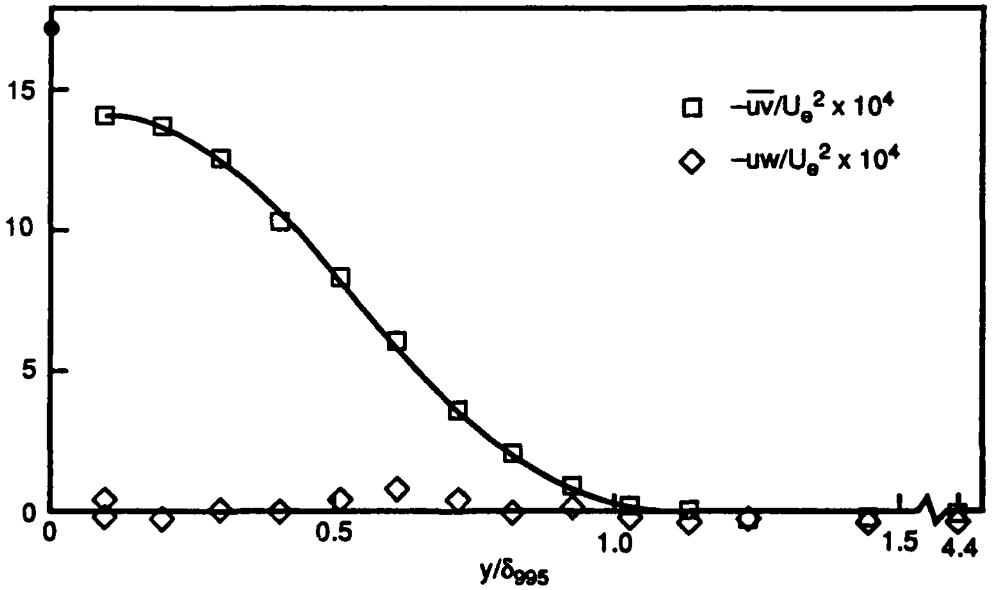

(i) Case 1.
Figure 8. Shear stress distribution.

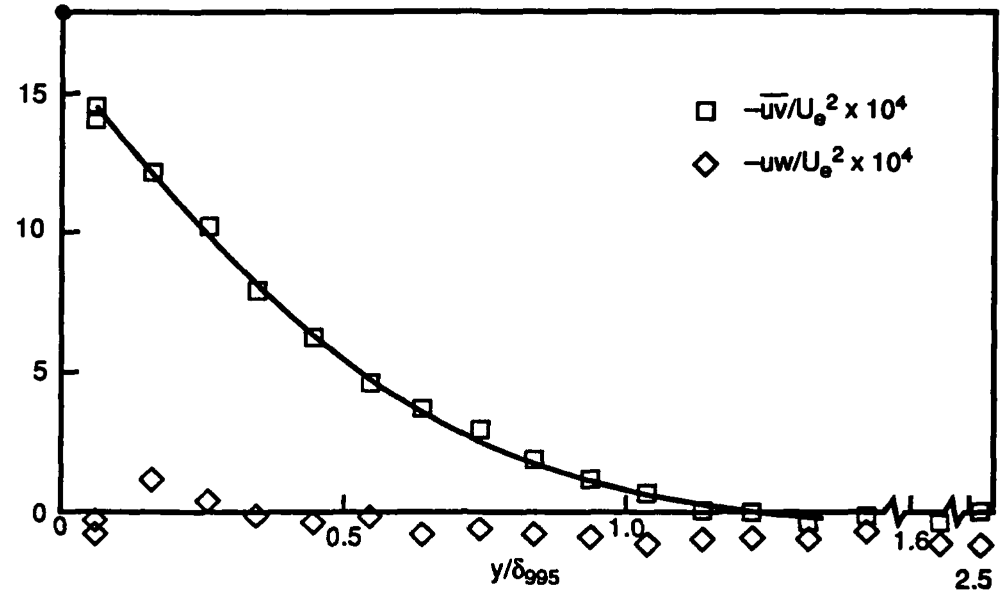

(ii) Case 2.
Figure 8. Shear stress distribution.

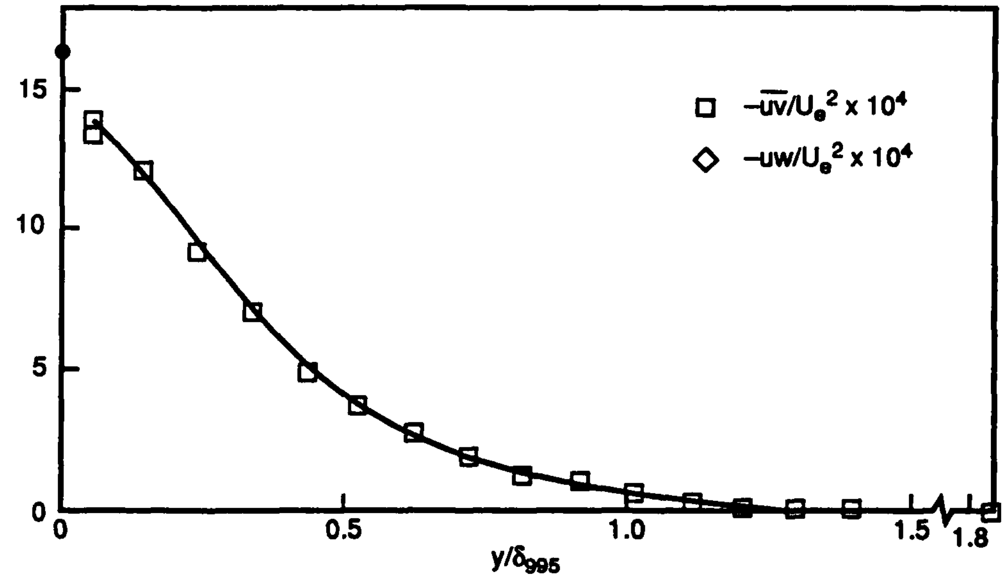

(iii) Case 3.
Figure 8. Shear stress distribution.

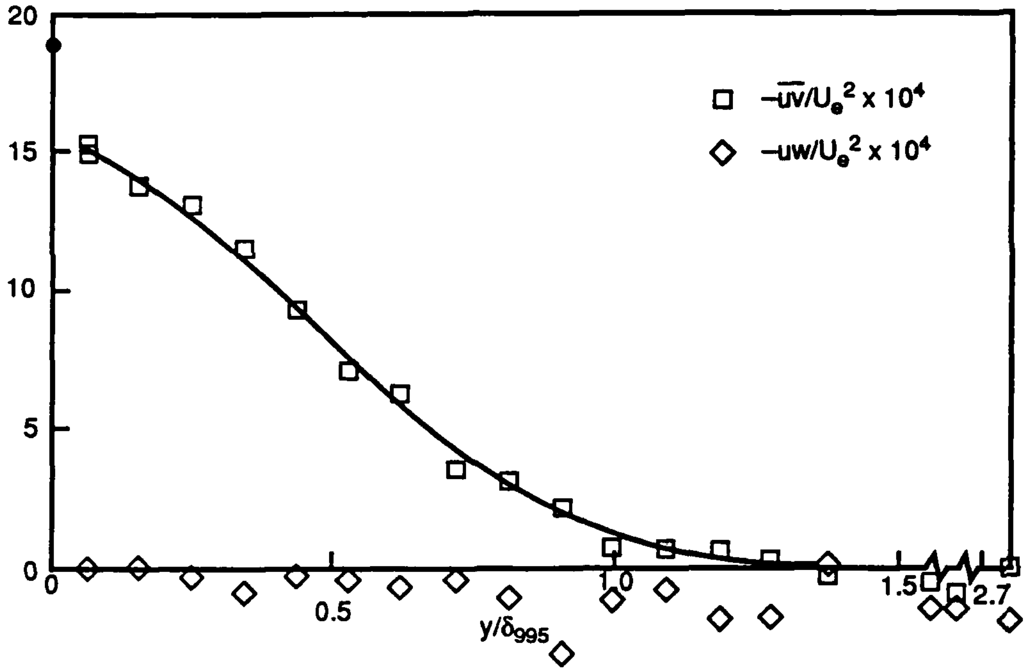

(iv) Case 4.
Figure 8. Shear stress distribution.

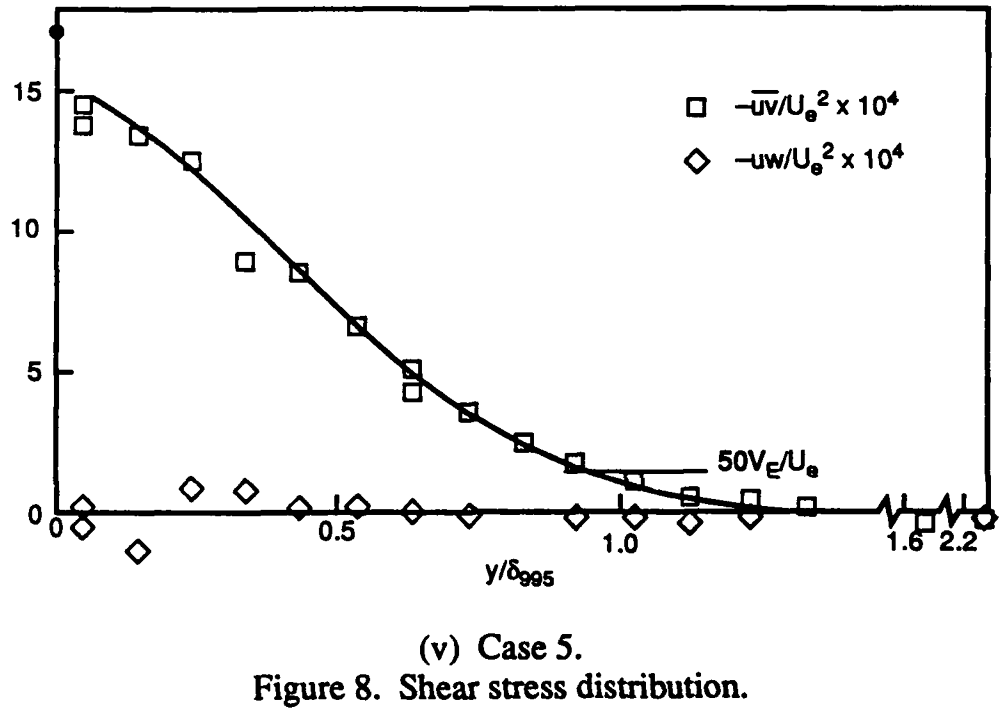

(v) Case 5.
Figure 8. Shear stress distribution.

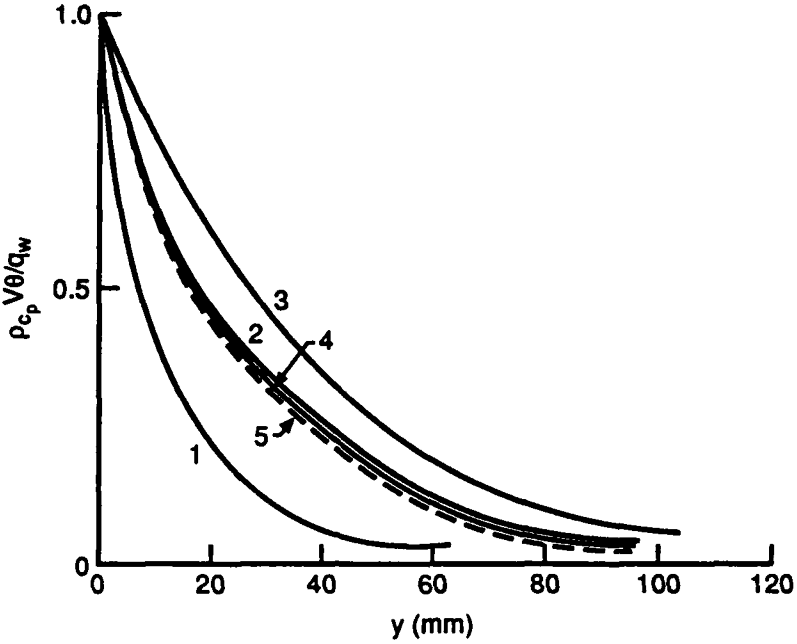

Figure 9. $\overline{V\theta}$ distribution: cases 1, 2, 3, 4, and 5.

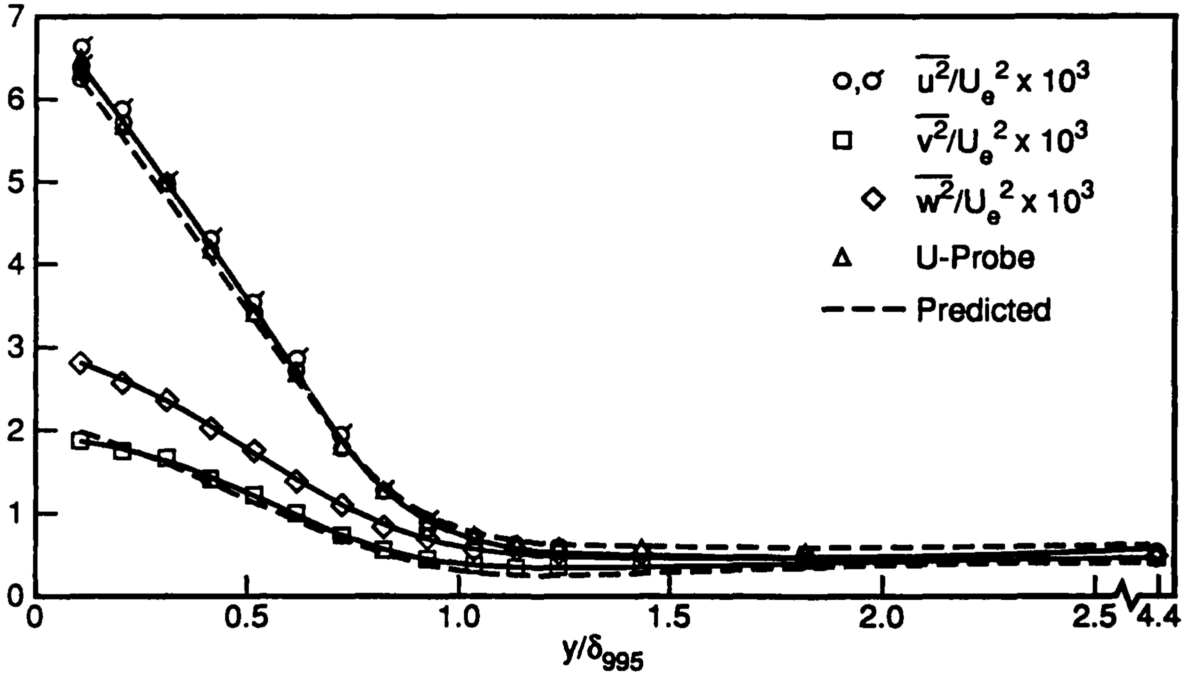

(i) Case 1.

Figure 10. Direct stress distribution.

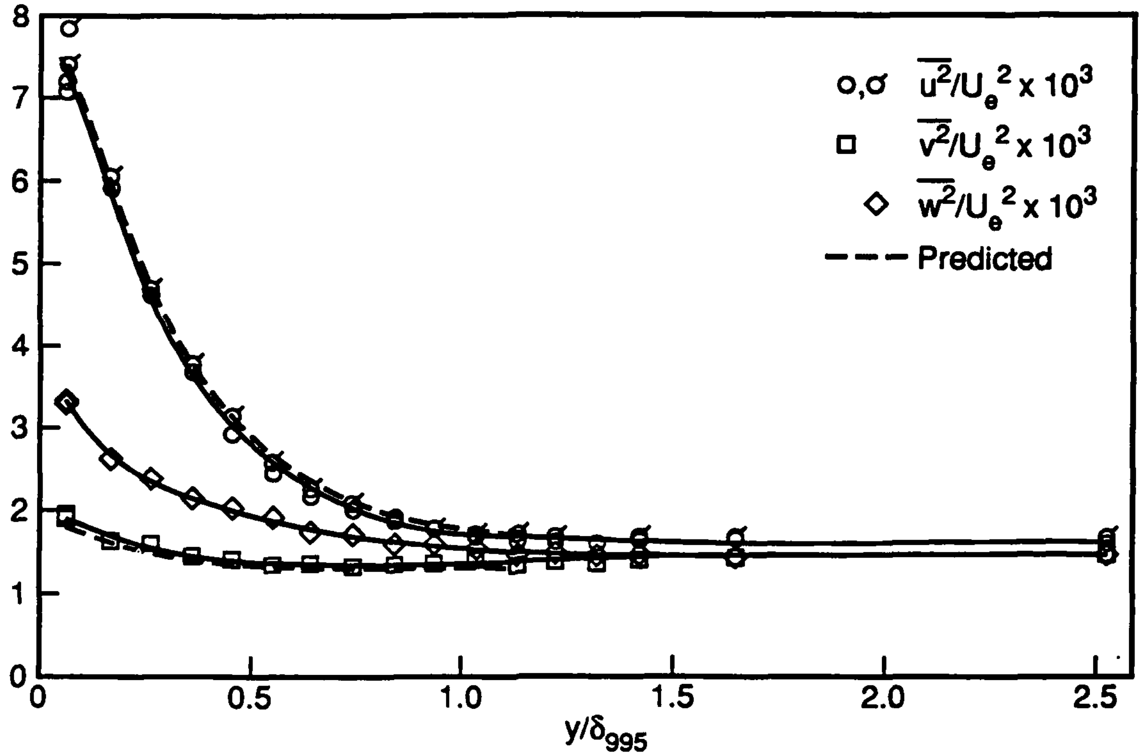

(ii) Case 2.
Figure 10. Direct stress distribution.

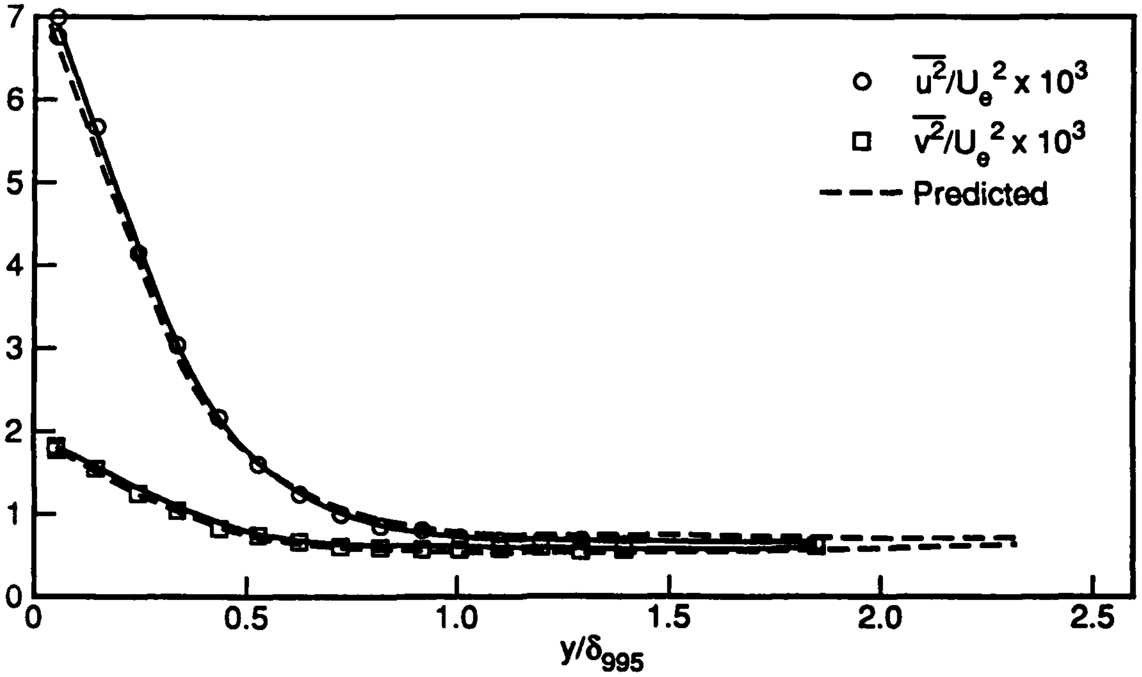

(iii) Case 3.
Figure 10. Direct stress distribution.

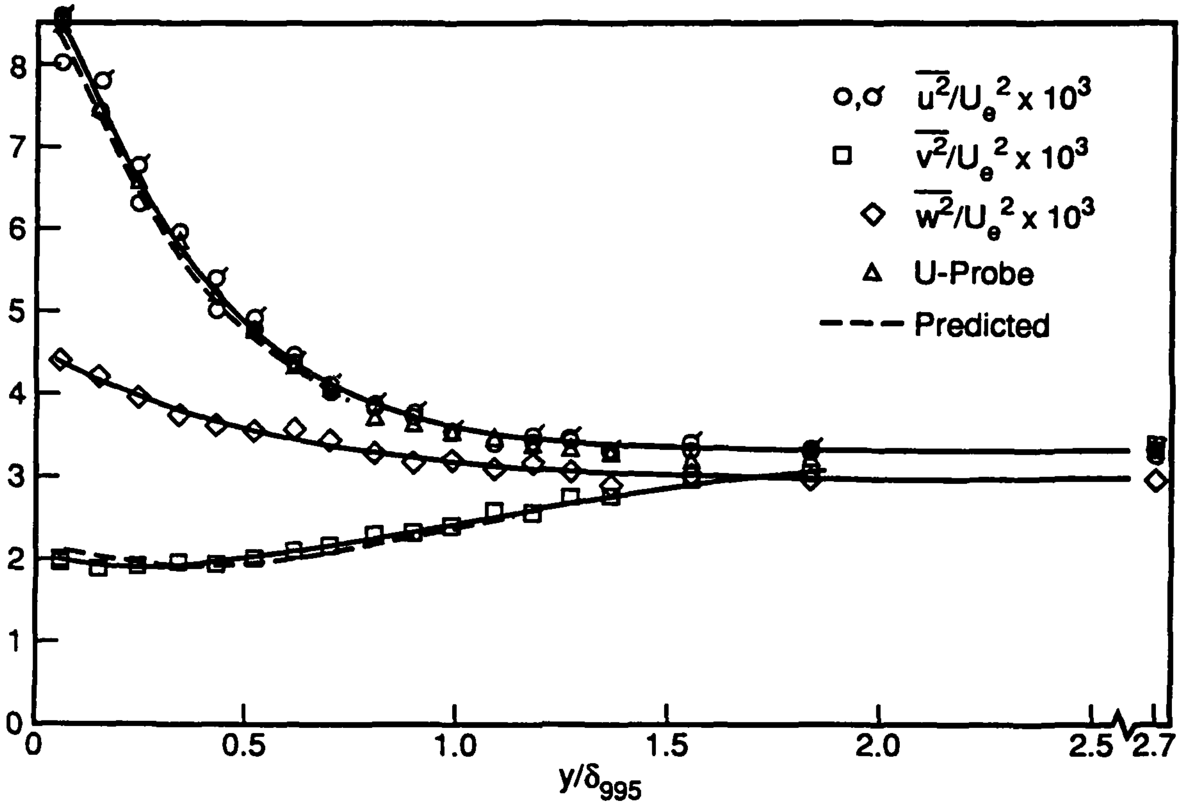

(iv) Case 4.
Figure 10. Direct stress distribution.

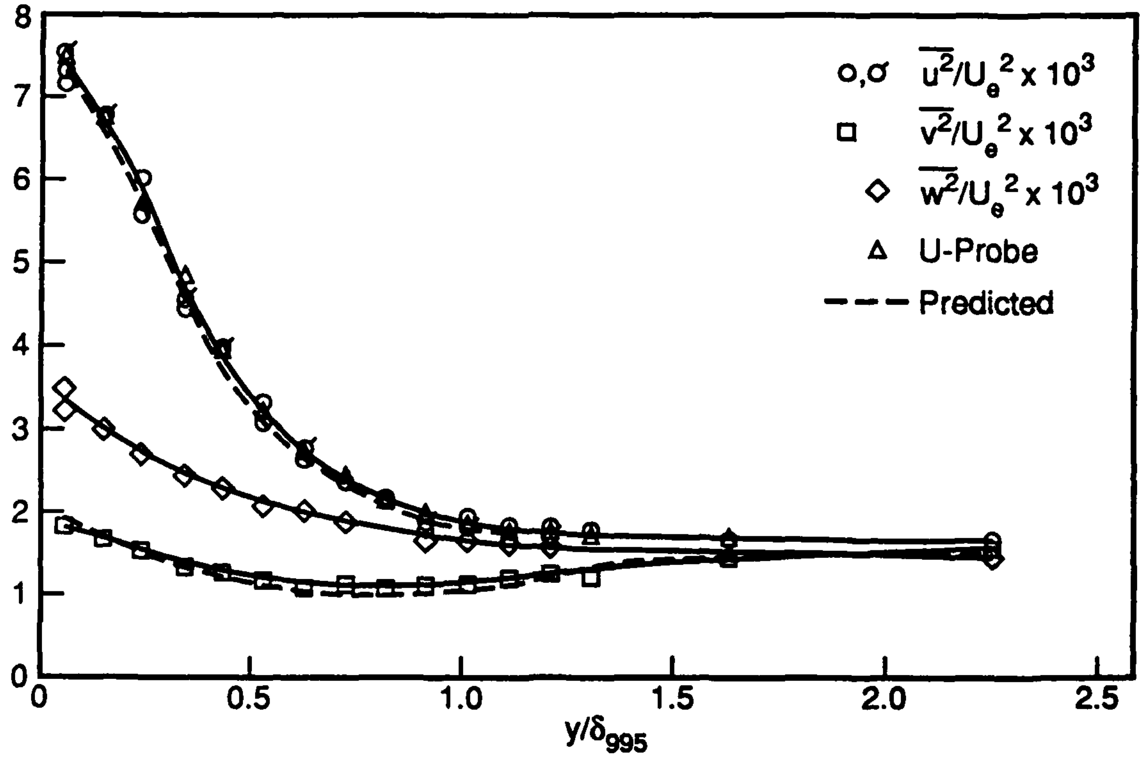

(v) Case 5.
Figure 10. Direct stress distribution.

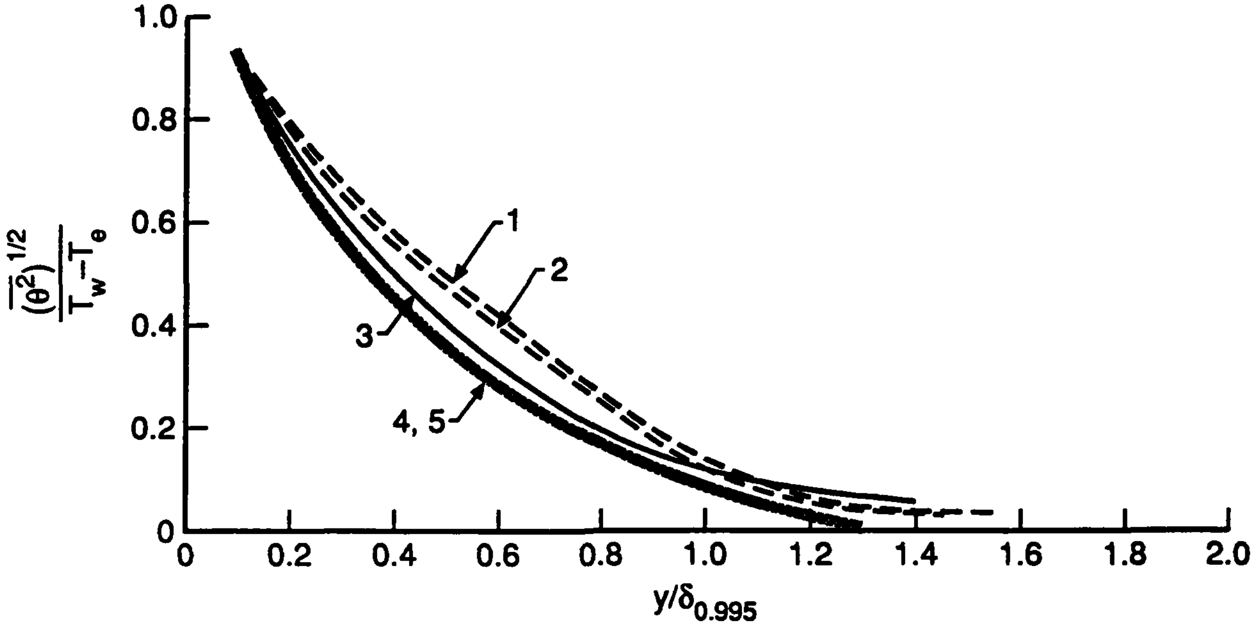

Figure 11. $\overline{\theta^2}$ distribution: cases 1, 2, 3, 4, and 5.

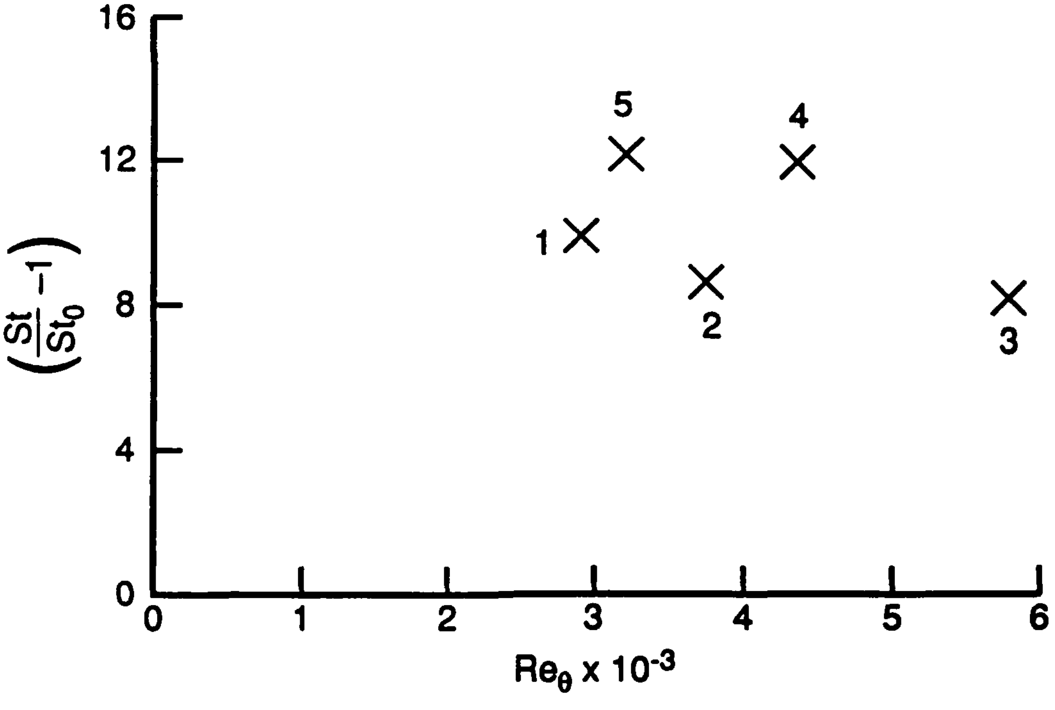

Figure 12. Stanton number distribution: cases 1, 2, 3, 4, and 5.

ECHANGES THERMIQUES DANS LES CANAUX DE REFROIDISSEMENT DES AUBES DE TURBINE

Yves SERVOUZE
Arnaud RISTORI
Office National d'Etudes et de Recherches
Aérospatiales (ONERA)
B.P. N° 72 - 92322 CHATILLON Cedex
(France)

RESUME

Afin d'optimiser les circuits de ventilation des aubes de turbine il est nécessaire de mieux connaitre les échanges thermiques qui résultent des écoulements complexes rencontrés dans les canaux de cavités internes.

La rotation, la géométrie des canaux, la présence de perturbateurs aux parois (ou promoteurs de turbulence) sont des paramètres importants dont il faut chiffrer les effets.

Dans un premier temps, l'ONERA a mené une étude expérimentale des effets de la rotation sur les échanges convectifs dans un canal lisse de section rectangulaire avec une branche centripète et une branche centrifuge. Les gammes de nombre de Reynolds et de nombre de Rossby vont respectivement de 10000 à 60000 et de 0 à 0,45. Dans ces conditions il est montré un accroissement des échanges thermiques sur la face dite de pression qui peut atteindre un facteur multiplicatif de 3. Cependant que sur la face opposée une décroissance est constatée qui peut atteindre un facteur de 0,4. Une modélisation numérique de tels écoulements a été engagée à l'aide d'un code Navier-Stokes 3D qui confirme les résultats expérimentaux.

Dans un deuxième temps, l'ONERA a lancé une étude expérimentale et de modélisation des échanges thermiques convectifs dans un canal statique de section carrée dont une des parois internes est munie de perturbateurs. La description du montage ainsi que les premiers résultats expérimentaux et numériques sont exposés.

ABSTRACT

In order to optimize the internal cooling passages of turbine blades, it is necessary to acquire a better knowledge of heat transfers which result of such complexe flows.

The geometry of the channels and the rotation are major parameters of which we study the effects.

For that purpose ONERA has conducted experimental and numerical studies in the case of a smooth rectangular channel with a centripetal arm and a centrifugal arm connected by a bend. For a flow with a Reynolds number from 10000 to 60000 and a Rossby number from 0 to 0,45 an increase of heat transfer is shown on the pressure side which can reach a rate of 3. However, a decrease is shown on the suction side which can reach a rate of 0,4. The numerical simulation with a 3D Navier-Stokes code confirms these thermical results. It gives information on secondary flows which result of Coriolis forces.

1. INTRODUCTION

Les cavités internes de ventilation des aubes de turbines aéronautiques modernes ont des formes géométriques complexes. Cette complexité résulte de contraintes technologiques mais aussi du souci d'intensifier les échanges convectifs (présence de perturbateurs aux parois, augmentation de la turbulence des écoulements internes) et donc l'efficacité du refroidissement. La rotation, par les écoulements secondaires qu'elle génère, a également un effet sur les échanges convectifs internes du fait de la modification du champ de vitesse.

Sur ces thèmes, l'ONERA conduit des études expérimentales et numériques. Les premières visent à évaluer les flux thermiques échangés sur parois lisses en présence de la rotation (expérimentation MERCI) [1], [2], et sur parois munies de perturbateurs en statique (expérimentation DELPHES) [3], [4]. Les secondes visent à développer un code Navier-Stokes 3D (code MATHILDA) apte à prévoir de tels écoulements [5]. La validation du code numérique avec les résultats expérimentaux constitue la liaison entre les deux activités.

Cet exposé, en reprenant les thèmes ci-dessus exposés, montre l'état actuel de la confrontation des résultats expérimentaux et numériques.

2. PRESENTATION DU CODE MATHILDA

Le code MATHILDA [6] permet de traiter les écoulements compressibles fortement turbulents à l'intérieur de cavités de formes complexes.

Les équations de continuité, de quantité de mouvement et d'énergie sont exprimées dans un repère galiléen lié à la géométrie ou éventuellement dans un repère mobile tournant à la vitesse angulaire Ω autour d'un axe. Dans ce cas la rothalpie ou enthalpie de rotation est introduite.
La turbulence est décrite par le modèle K-L. Les deux grandeurs K et L sont calculées en chaque point du champ grâce à deux équations de bilan. Les géométries complexes sont traitées grâce à une transformation régulière éventuellement fonction du temps qui fait passer du domaine physique (coordonnées x, y, z) au domaine de calcul. Dans l'espace ainsi transformé un maillage peut être construit par simple discrétisation (indices I, J, K des mailles). Autrement dit, on peut se représenter le réseau dans l'espace transformé comme un assemblage de domaines parallélépipédiques images de volumes élémentaires à six faces et huit sommets. Certains de ces domaines parallélépipédiques repérés par un code approprié appartiennent aux conditions aux limites: parois fixes ou mobiles, entrées et sorties de fluide. Les échanges thermiques fluide-paroi sont schématisés par des lois de paroi. Les conditions aux limites possibles sont variées: pression, température, débit par unité de surface, direction d'injection, vitesse angulaire, taux et échelle de turbulence, flux de chaleur... Le temps de calcul est suivant les cas de l'ordre de 12 à 20 μs par maille par itération et par équation sur CRAY XMP.

3. ECHANGES THERMIQUES DANS LES CANAUX STATIQUES

3.1. Présentation du montage DELPHES

Le montage DELPHES (figure 1) est une soufflerie chaude destinée à l'étude de l'influence de perturbateurs en paroi sur les échanges convectifs dans un canal rectiligne de section carrée 50x50 mm2. Le flux thermique est déduit de l'évolution temporelle de la température de surface relevée en transitoire par thermocouples et par thermographie infrarouge. L'écoulement d'air chaud est généré par une chambre de combustion à fort taux de dilution qui porte l'écoulement à une température de 550 K. Un mélangeur assure l'homogénéisation en température de l'écoulement. Une vanne bypass permet d'envoyer l'écoulement chaud vers le circuit 1 et ainsi de réaliser des transitoires thermiques. Le circuit 1 se divise en deux circuits 1a et 1b. Le circuit 1a comporte la section utile de mesure du flux thermique; le circuit 1b de décharge permet l'ajustement du débit et de la pression.

Dans ces conditions l'écoulement dans le circuit de mesure peut avoir les caractéristiques suivantes:
- température génératrice Ti= 550 K
- pression génératrice 1 bar<Pi<5 bars
- nombre de Reynolds $3,5.10^4<Re<7.10^5$
- nombre de Mach M< 0,8

La section utile de mesure du flux thermique est constituée par une plaque plane amovible de 250 mm de long, de faible épaisseur 3 mm, munie de perturbateurs de 5 mm par 5 mm espacés de 50 mm. Elle est équipée de thermocouples de masse installés en rainures. La paroi en vis à vis est constituée d'un hublot en saphir qui autorise la mesure de température de surface de la plaque par thermographie infrarouge.

Un maillage de la section médiane de la plaque est utilisé comme domaine de calcul pour un code numérique de conduction qui donne le champ thermique en fonction de conditions aux frontières. Un processus itératif qui porte sur l'ajustement du coefficient d'échange convectif plaque-écoulement permet d'identifier en tous les points de la section médiane de la plaque et en particulier aux points de mesure les évolutions temporelles de température calculées et mesurées (figure 2).

3.2. Confrontation expérience-calcul numérique

Des comparaisons de résultats issus de l'expérience et du calcul numérique MATHILDA ont été faites pour les valeurs successives du nombre de Reynolds 420000, 560000, 700000 et à la pression génératrice de 3 bars (figures 3, 4, 5). Les écarts maximum entre l'expérience et le calcul sont notés sur les sommets des perturbateurs et sont dûs à la résolution de la caméra I.R. Derrière les perturbateurs, l'accord entre l'expérience et le calcul est satisfaisant, sauf à l'aval du premier perturbateur où les profils mesurés et calculés sont inversés.

4. ECHANGES THERMIQUES DANS LES CANAUX EN ROTATION

4.1. Présentation du montage MERCI

Le montage MERCI est un banc d'essai déjà ancien qui n'est plus exploité à l'heure actuelle. Ce banc et les résultats expérimentaux obtenus ont été présentés lors de congrès ASME et AGARD [1], [2], il n'est donc pas nécessaire d'y revenir de manière détaillée seulement pour dire que les mesures sont de nature thermique. Aucune investigation de l'écoulement (champ de pression ou champ de vitesse) n'y a jamais été faite.

La maquette instrumentée en thermocouples de masse est un canal de section rectangulaire en forme d'épingle à cheveu qui tourne autour d'un axe perpendiculaire à l'axe du canal (figure 6). L'air qui circule à l'intérieur reçoit un flux thermique au contact des quatre parois chauffées extérieurement par un flux de rayonnement calibré. Un bilan thermique qui tient compte de la conduction dans les parois (en régime stabilisé aussi bien qu'en transitoire), à partir de la connaissance de la température de surface du canal (thermocouples et pyrométrie infrarouge), de la connaissance du flux de rayonnement incident, de l'évolution de la température de l'écoulement, permet de remonter au flux thermique local face par face. La figure 7 montre l'évolution de ce flux convectif dans une section transversale du canal centrifuge.

Les caractéristiques du montage sont:
- une maquette de section rectangulaire rapport des cotés a/b= 2, diamètre hydraulique 13,3mm,
- une vitesse de rotation pouvant atteindre 5000 tr/mn,
- une température de surface de 773°K,
- nombre de Reynolds 10000 à 60000,
- nombre de Rossby 0 à 0,5
- nombre de Rayleigh 90.10^5 à 150.10^6.

4.2. Confrontation expérience-calcul numérique

Des simulations numériques de la configuration MERCI ont été faites en faisant varier la vitesse de rotation du canal de 0 à 5000 tr/mn par pas de 100 tr/mn. Les autres conditions de la simulation sont:
- nombre de Reynolds Re= 25000,
- flux de chaleur pariétal imposé: $Qw= 15\ KW/M^2$,
- température d'entrée de l'air Te= 356°K,
- modèle de turbulence: K.L.,
- longueur de mélange L= 1mm,
- taux de turbulence: 1%,

Les résultats numériques obtenus sont très locaux et très riches par rapport aux résultats expérimentaux qui ne portent que sur les flux convectifs échangés dans les sections instrumentées du canal. Aussi la comparaison essentielle qui puisse être faite concerne les échanges aux parois sous la forme du nombre de Nusselt en fonction du nombre de Rossby. La figure 8 met en relief, pour le canal centrifuge, que l'action de la rotation est sous estimée par le calcul. Cependant, le comportement général est bien reproduit:
- accroissement des échanges sur la face du canal dite de "pression" avec la vitesse de rotation,
- décroissance des échanges sur la face du canal dite de "dépression" avec la vitesse de rotation.

Les observations qui peuvent être faites à propos de cette simulation à la vitesse de rotation de 5000tr/mn sont les suivantes. Le champ des pressions statiques est stratifié du fait de la rotation et on note une forte dépression dans le coté intérieur du coude (figure 9), elle apporte de fortes vitesses. Dans la partie centrifuge, les forces de Coriolis génèrent un écoulement secondaire caractérisé par la structure classique à deux tourbillons (figure 10). Ceci induit une forte distorsion du champ des vitesses débitantes (figure 10). Le coude a pour effet de détruire cette structure par l'action des forces d'inertie, il en résulte une structure à tourbillon unique à la sortie (figure 11) qui se poursuit dans le canal centripète en perdant de son intensité tout en se décentrant (figure 12).

5. CONCLUSION

L'association sur un même thême d'étude des approches expérimentale et numérique, permet d'acquérir une bonne compréhension des phénomènes physiques et d'avoir une solide base de validation.

Du point de vue expérimental il serait bénéfique de pouvoir disposer d'un canal tournant muni de perturbateurs. En canal statique il est prévu d'obtenir des résultats sur un canal qui suit un coude, tout en faisant des expérimentations à caractère plus aérodynamique.

Du point de vue numérique il est important de pousuivre le travail d'amélioration de la prévision des échanges thermiques aux parois.

REMERCIEMENTS

Les auteurs remercient la DRET pour le soutien apporté à la réalisation de ces travaux.

REFERENCES

[1] J. GUIDEZ
"Study of the convective heat in rotating coolant channel".
33rd ASME International Gas Turbine and Aeroengine Congress and Exposition, Amsterdam, 5-9 juin 1988.

[2] J. GUIDEZ & al
"Etude théorique de l'écoulement dans un canal en rotation".
AGARD Conference Proceedings n° 469.

[3] A. RISTORI & al
"Numerical simulation of flows inside internal cavities of turbine rotor blades".
Eurotherm Seminar N° 25: "Heat transfer in single phase flows", Pau, july 8-9, 1991.

[4] A. RISTORI & al
"Mesures indirectes de flux convectifs par thermographie infrarouge".
SFT "Problèmes rsdiatifs dans les domaines aéronautiques et spatiaux", Paris, 1 avril 1992.

[5] D. DUTOYA & al
"Présentation d'un code de calcul d'écoulements compressibles 3D dans des canaux et des cavités de forme complexe".
Symposium PEP/AGARD "CFD Techniques for Propulsion Applications".
San Antonio (USA), 27-31 mai 1991.

[6] M. ERRERA
"Modélisation multidimensionnelle de l'aérodynamique interne dans les moteurs diésel".
Thèse présentée à l'Université Pierre et Marie Curie, Paris 1990.

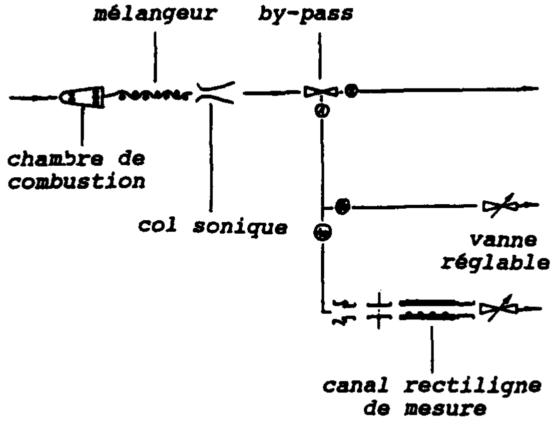
mélangeur
by-pass
chambre de combustion
col sonique
vanne réglable
canal rectiligne de mesure

Figure 1: Schéma du montage DELPHES

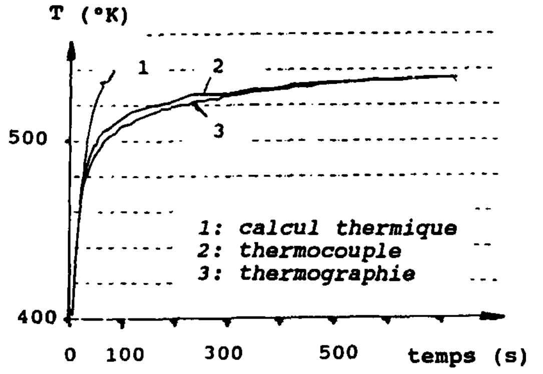

Figure 2: Evolutions temporelles de la température de paroi

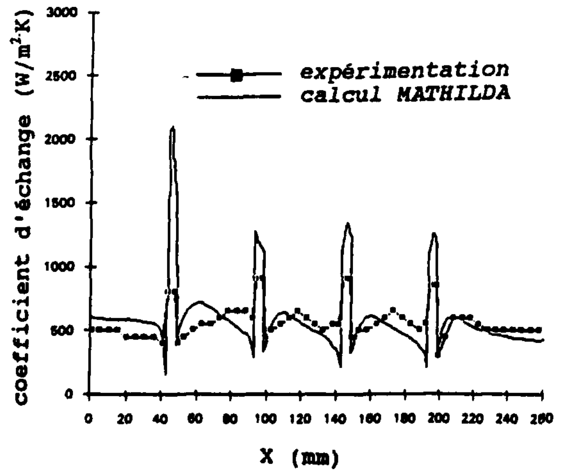

Figure 3: Coefficient d'échange convectif sur paroi avec perturbateurs *(expérience-calcul MATHILDA)*

Re= 420000, P= 3bars

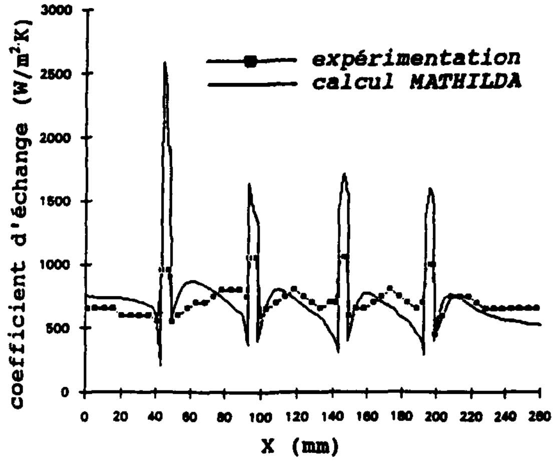

Figure 4: Coefficient d'échange convectif sur paroi avec perturbateurs *(expérience-calcul MATHILDA)*

Re= 560000, P= 3bars

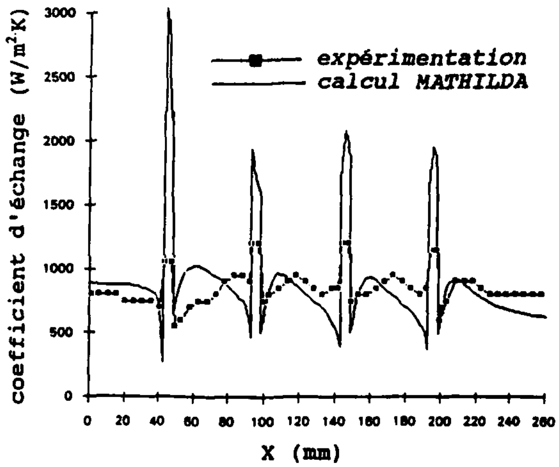

Figure 5: Coefficient d'échange convectif sur paroi avec perturbateurs *(expérience-calcul MATHILDA)*

Re= 700000, P= 3bars

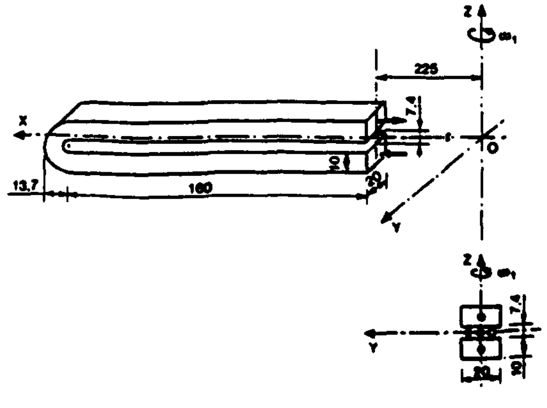
Z
ω1
225
7.4
X
O
20
13.7
160
Y
Z
ω1
7.4
Y
20
10

Figure 6: Maquette de l'expérimentation MERCI *(canal tournant)*

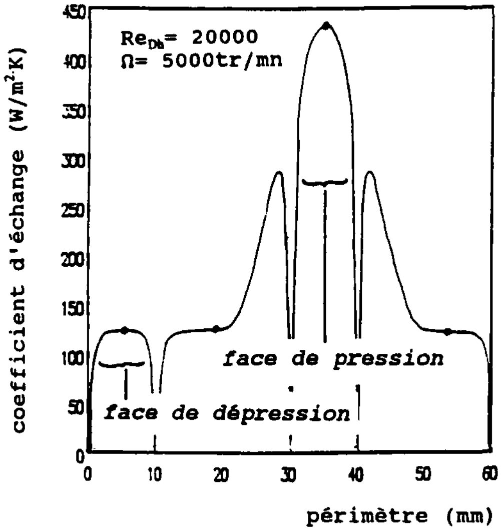

Figure 7: **Répartition expérimentale du coefficient convectif interne** ***(branche centrifuge)***

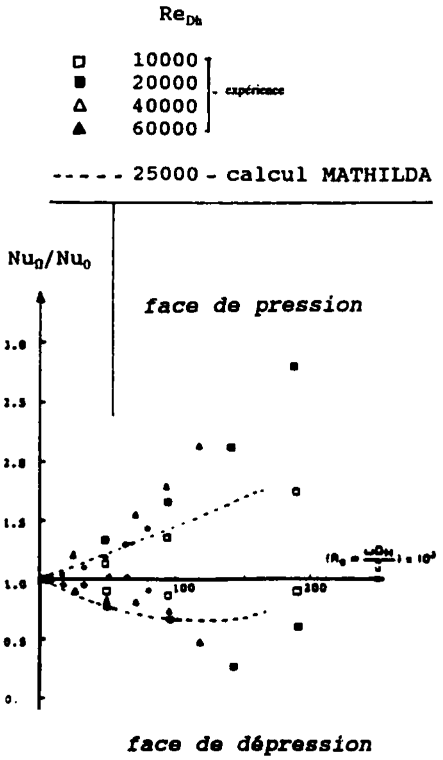

Figure 8: **Influence de la rotation sur les échanges convectifs internes** ***(expérience-calcul MATHILDA)***

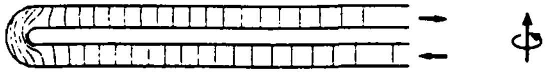

Figure 9: **Canal tournant** ***(pression statique)***

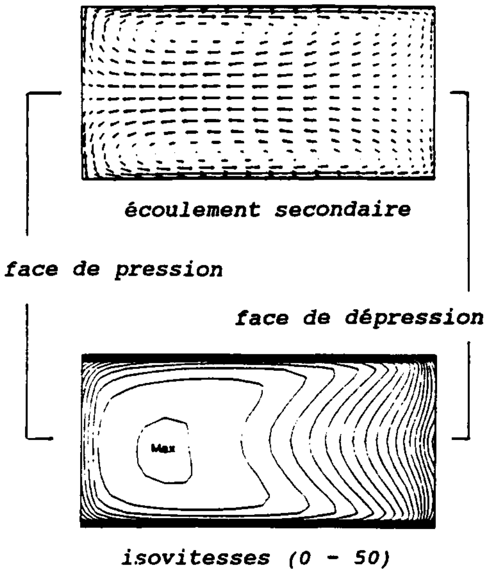
écoulement secondaire
face de pression
face de dépression
Max
isovitesses (0 - 50)

Re_{Dh}= 25000
Ω= 5000tr/mn

Figure 10: **Canal tournant** ***(branche centrifuge)***

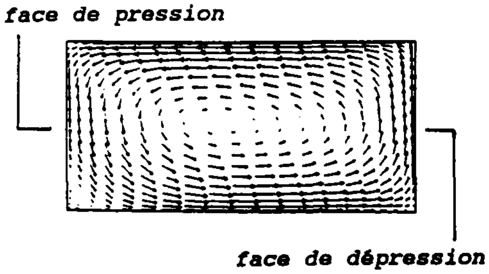
face de pression
face de dépression

Re_{Dh}= 25000
Ω= 5000tr/mn

Figure 11: **Canal tournant** ***(sortie du coude)***

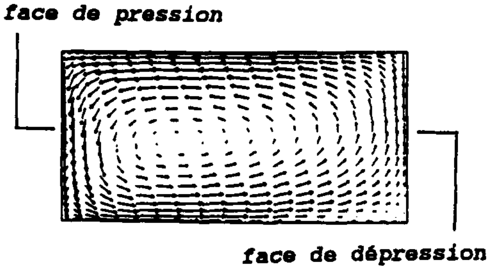

$Re_{Dh}= 25000$
$\Omega= 5000$tr/mn

Figure 12: Canal tournant
(branche centripète)

Discussion

QUESTION 1:

DISCUSSOR: B.E. Launder, UMIST

Will more details of your work be given in the final version of the paper than appear in the conference version? There are no grid details or demonstrations of grid sensitivity.

AUTHOR'S REPLY:

I presume you are referring to the results presented in Figures 10, 11, and 12. These figures were obtained from color graphic representations of the results and are given in their final form. The results, however, are presented elsewhere (see our references) and we will, of course, supply you with details if you wish.

THE EFFECT OF ORTHOGONAL-MODE ROTATION ON FORCED CONVECTION IN A CIRCULAR-SECTIONED TUBE FITTED WITH FULL CIRCUMFERENTIAL TRANSVERSE RIBS

W.D. MORRIS[*]
and
R. SALEMI[**]

[*] Professor of Mechanical Engineering
[**] Formerly Senior Research Assistant
Department of Mechanical Engineering,
University College of Swansea,
Singleton Park, Swansea, SA2 8PP, U.K.

SUMMARY

This paper presents the results of an experimental programme aimed at investigating the effect of Coriolis forces and centripetal buoyancy on forced convection in an internally finned circular tube which rotates about an axis orthogonal to the tube's central axis. This geometric arrangement typifies the internal coolant channels of gas turbine rotor blades.

It is demonstrated that, as with smooth-walled tubes, Coriolis-driven secondary flows give rise to relatively better heat transfer on the trailing edge of the tube compared with that on the leading edge. Leading edge heat transfer is shown to be significantly impaired in relation to that which occurs under non-rotating conditions.

Centripetal buoyancy is shown to improve local heat transfer on the leading and trailing edges for a given value of the through flow Reynolds number and the Rossby number.

Although duct rotation tends to improve heat transfer on the trailing edge in comparison with normal stationary duct forced convection, serious overprediction of heat transfer results from ignoring rotational effects on the leading edge. This is an important observation in the context of the design of turbine rotor blade cooling systems.

NOMENCLATURE

English Symbols

A	Coefficient
Bu	Buoyancy parameter
c_p	Constant pressure specific heat
d	Diameter of tube measured at a rib
D	Plain tube diameter
k	Thermal conductivity
H	Eccentricity at entry plane of heated tube
l	Rib land
Nu	Local Nusselt number
n	Exponent
p	Rib pitch
Pr	Prandtl number
$\dot{q}$	Heat flux
Re	Reynolds number
Ro	Rossby number
T_B	Local fluid bulk temperature
T_W	Local wall temperature
w	Mean axial velocity
z	Axial location
Z	Non-dimensionalised axial location

Greek Symbols

β	Volume expansion coefficient
ε	Eccentricity parameter
ρ	Density
μ	Absolute viscosity
ω	Angular velocity
ϕ	Functional relationship

INTRODUCTION

State of the art cooling of aero gas turbine rotor blading in the high pressure stages involves the use of internal airways which incorporate a variety of surface heat transfer augmentation devices, including combinations of fins, ribs and other artificial surface roughening aids. These internal airways permit compressor-bled cooling air to flow in a predominantly spanwise direction along the blade, in either the radially outward or inward direction, as illustrated in Figure 1. This rotating duct/flow geometry is often referred to as orthogonal-mode rotation in the technical literature and this descriptor will be adopted in the present paper. Since the coolant is constrained to flow in a channel which is rotating, it is influenced by Coriolis and centripetal inertial forces which can drastically change the relative flow field, and consequently the surface heat transfer, in comparison to the usual forced convection situation which occurs with a stationary coolant hole.

Because of its relevance to rotor blade cooling considerable interest has been shown in determining the effect of orthogonal-mode rotation on convective heat transfer in smooth-walled tubes and a variety of cross sectional shapes have been studied from both the theoretical and experimental viewpoint, see references (1) through (27) by way of example. The following salient points illustrate the main features of this class of rotary flow heat transfer situation which have arisen from these investigations and serve as necessary background to the work to be reported in the present paper.

Coriolis forces generate a strong secondary flow in planes perpendicular to the main spanwise flow direction. The resulting spiralling flow along the duct causes core region fluid to move towards the trailing or rearward edge of the duct with a return flow along the duct periphery towards the leading or forward edge, as illustrated in Figure 2 for a circular-sectioned duct.

This secondary flow tends to improve local cooling in the vicinity of the trailing edge in relation to that at the leading edge due to the washing effect of the relatively cool core fluid.

The relative impediment to heat transfer in the leading edge regions can give rise to conditions which are worse than those suggested by treating the problem by stationary duct forced convection methods. This is important from the design viewpoint since hot spots can develop as a consequence near the leading edges of the coolant channel.

When large wall to fluid temperature differences are present the Coriolis-driven flow field is modified due to centripetal buoyancy. Various workers have suggested that this mechanism can improve or impair the relative heat transfer around the periphery of the coolant channel cross sectional shape being considered. Although this additional effect is not yet fully understood, probably due to complex changes in the flow structure as a result of rotation (see Johnson et al (5) and unpublished flow visualization studies by (Morris and Claypole (28)), a recent proposal for a possible empirical correlating factor including the simultaneous effect of Coriolis forces and centripetal buoyancy has been proposed by Morris and Salemi (26). This will be discussed in greater detail later in this paper when new experimental data is presented.

An important point concerning the effect of orthogonal-mode rotation on convective heat transfer has been raised by Medwell et al (22) and Taylor et al (25), (27) and this reflects the manner in which conduction in the duct wall can smooth out the rotationally driven peripheral asymmetry in convection. These workers have demonstrated the need to treat the analysis of experimental data from a systems viewpoint which includes circumferential conduction in the duct walls. The omission of this effect could well explain discrepancies in the reported data of various researchers to date.

Although numerous smooth-walled ducts have been studied, the practically important problem of assessing the influence of orthogonal-mode rotation on convection in tubes fitted with heat transfer augmentation devices has been not received as much attention to date. Clearly numerous geometric arrangements of ribs, fins, artificial roughening, etc may be devised for blade cooling applications. Before a particular configuration is introduced into service, however, its performance must be adequately assessed and this involves time consuming and expensive research and development programmes.

In an attempt to develop a fundamental understanding of the combined effect of surface enhancement devices and orthogonal-mode rotation on ducted flow heat transfer, the present authors have selected a simple, but practical, test geometry for a detailed experimental study under laboratory conditions. The actual test geometry, illustrated in Figure 3, is comprised of a circular-sectioned tube fitted with full circumferential transverse ribs at regular downstream intervals. The geometric specification may be described in terms of the three non-dimensional groups defined in Figure 3. For this initial set of experiments the relative size of the ribs was selected to give geometrical parameters typical of those in current practical cooling system designs and the actual values used are cited below.

Pitch/plain bore diameter ratio = 2

Blockage ratio = 0.36

Land/pitch ratio = 0.1

The present paper reports the effect of the ribs on normal stationary duct forced convection in comparison with a smooth-walled circular-sectioned tube and then demonstrates the effect of orthogonal-mode rotation on the stationary ribbed configuration. Local axial distributions of heat transfer are presented for the leading and trailing edges of the test section.

APPARATUS

The test section constructional details are shown in Figure 4. The heated test section (1) had a plain tube bore diameter of 10 mm with an outer diameter of 13 mm. The rib pitch was 20 mm and each of the five ribs machined onto the inner bore had a land of 2 mm. The bore diameter measured at each rib section was 6 mm, thus creating a blockage ratio of 0.36. A plain bore heated section nominally 25 mm long preceded the first rib and an identical plain bore heated section was incorporated downstream of the final rib as shown in the figure. This test piece was machined from a solid bar of ceramic glass having a thermal conductivity of 1.3 W/m K and was held between inlet and exit insulated support bushes, (2) and (3) respectively, to give an actively heated test length of 130 mm. The support bushes and test section were enclosed in an aluminium tube (4) fitted with external "O" ring seals (5) at both ends.

Twelve Chromel/Alumel thermocouples were attached to two diametrically opposed edges of the test section at axial locations indicated in Figure 3 to permit the wall temperature to be measured along the leading and trailing edges of the section. These thermocouples were embedded in the wall of the test section so that their sensing beads were 1 mm deep measured from the outer diameter of the test section. The axial distribution of the thermocouples corresponded approximately to the centre land and mid-pitch locations with minor discrepancies to blend with a screw thread machined on the outer surface to locate the heating wire used. Chromel/Alumel thermo-couples, with their sensing beads located on the duct axis in the inlet and exit bushes, permitted the air temperature rise to be assessed.

The tube was electrically heated with Nichrome resistance wire spirally wound into the screw thread machined on the outer surface of the tube. Thermocouple and heater cables were brought from the test assembly through holes machined in the exit support bush (3). The space between the outer surface of the glass tube and the inner surface of the encapsulating sheath (4) was filled with Fiberfrax thermal insulation to minimise external heat loss from the module.

The instrumented test section was fitted into a spin rig facility so that the eccentricity, measured at the cross sectional plane where heating commenced, was 270 mm. This spin rig incorporated a drive system, an air plenum and supply system, a thermocouple instrumentation slipring and a power slipring for the electrical heater. Further details on the spin facility, including an air delivery system and data acquisition system, have been reported by the authors in reference (26). Figure 5 shows the final internal flow circuit for air delivery to the test section.

EXPERIMENTAL DETAILS AND DATA PRESENTATION

The programme of tests undertaken involved four nominal Reynolds number values in the range 15000(5000)30000. These nominal values were based on the inlet temperature of the air entering the test section. Four rotational speeds were used, namely 0, 1000, 2000 and 2700 rev/min and, for each Reynolds number/speed option, five different levels of heater power were used. A maximum wall temperature was imposed at 180°C for test section integrity reasons. At each individual test the mass flow rate was adjusted to ensure that each nominal Reynolds number value was held to within ±1%.

The power dissipated in the heater section is not entirely transferred to the fluid due to external losses and conduction along the duct wall. Duct wall conduction was minimised by using low conductivity machinable glass for the manufacture of the test section itself. A series of heat loss calibrations was undertaken to establish the external loss characteristics of the test section at all rotational speeds tested. An energy balance at each axial location where wall temperature measurements were effected permitted the associated wall value of heat flux to be calculated at those locations.

Having determined the axial variation of heat flux, the fluid bulk temperature was calculated by means of an enthalpy balance. Thus from knowledge of heat flux, wall temperature and fluid bulk temperature, the heat transfer coefficient distributions along the duct could be calculated and presented non-dimensionally in terms of a local Nusselt number on the leading and trailing edges of the duct. It should be pointed out that, when dealing with the smooth-walled tube, the measured wall temperatures were corrected to give the implied surface temperature using a straight forward one dimensional conduction correction through the tube wall. Owing to difficulties in making full surface temperature measurements over the finned surfaces, the wall temperatures used in the analysis at a ribbed location was taken to be the corrected equivalent smooth-walled value as described above. In other words a wall temperature corrected to the root of a rib was used. At mid-rib locations the smooth walled technique was still applicable.

The method of non-dimensional data presentation follows ideas presented previously by the authors, see reference (26). However in the interest of completeness this method is briefly repeated as follows.

The usual forced convection mechanism present in the tube is modified due to the presence of Coriolis forces and centripetal buoyancy. The Coriolis effects may be expressed non-dimensionally in terms of a Rossby number, Ro, defined as

$$Ro = w/\Omega D \tag{1}$$

and the centripetal buoyancy via a buoyancy parameter, Bu, defined as

$$Bu = \beta(T_W - T_B) \tag{2}$$

together with an eccentricity parameter, ε, defined as

$$\varepsilon = H/D \tag{3}$$

where all symbols are as defined in the Nomenclature section.

The net result of including these additional groups into the well known non-dimensional heat transfer relationships for forced convection in ducts is an equation, which may be applied to any circumferential location on the tube wall, having the structure

$$Nu = \phi(Re, Pr, Ro, Bu, \varepsilon, Z) \tag{4}$$

where

$$Nu = \dot{q}D/k(T_W - T_B) \quad \text{(Nusselt number)} \tag{5}$$

$$Re = \rho w D/\mu\xi \quad \text{(Reynolds number)} \tag{6}$$

$$Pr = \mu c_p/k \quad \text{(Prandtl number)} \tag{7}$$

and

$$Z = z/D \quad \text{(Downstream location)} \tag{8}$$

with all symbols again defined in the Nomenclature. Note that equation (4) by implication, in the context of the present paper, is applicable for a specified rib/tube geometry. A full description of the physical derivation of non-dimensional groups applicable to a rotating duct system is given in Morris (11)

The results of all tests undertaken were evaluated on a local basis using the non-dimensional groups described above. All property values needed were calculated at the locally prevailing bulk temperature of the fluid. A discussion of the results obtained now follow.

RESULTS AND DISCUSSION

Results obtained from a series of experiments, using the same test section constructional details and data processing procedure as described above, have already been published by the authors for the smooth-walled situation, see reference (26). This data is used here in order to demonstrate the improvement in heat transfer created by the incorporation of the ribs for the case of zero rotation. The zero rotation ribbed tube data is subsequently used for assessing the influence of rotation on the ribbed tube performance.

With ribs fitted, an examination of the raw experimental data demonstrated an immediate fundamental change in comparison to the plain tube situation. This is illustrated in Figure 6, where typically measured axial distributions of wall and fluid bulk temperature are shown. The experimental control approximated well to a uniform heat flux boundary condition. Under these circumstances the fluid bulk temperature increases linearly and, as the flow develops in a smooth-walled tube, the wall temperature tends to become parallel to the bulk fluid temperature. This tendency is clearly evident in the smooth-walled distribution shown in Figure 6a. It should be noted that the final 20% of the test section suffers an end loss effect which tends to lower the wall temperature in this region and it is customary to omit this final section from detailed analysis in forced convection experimental work. This procedure will also be adopted when derived data is analysed later for the ribbed tube situation and effectively omits the fifth rib region from our detailed analysis.

With ribs fitted, see Figure 6b, the wall temperature tended to vary cyclically in the downstream direction, with regions of relatively higher temperature occurring at the ribs themselves. This suggests that the flow field is producing higher heat transfer coefficients in the mid region between ribs, probably due to flow re-attachment downstream of each rib. Although the wall temperature was found in all cases of the ribbed tube to vary in a cyclic manner, it was also observed that the wall temperature tended to decrease in the downstream direction for rib and mid-rib locations over the first four ribs. It is important to note that there was no evidence of temperature variations between the leading and trailing edges in the absence of rotation of any substantial nature, thus confirming the expected axisymmetric heat transfer behaviour.

Figure 7 compares the axial development of local heat transfer, expressed in the form of the local Nusselt number, for the smooth and ribbed tube cases. For the reasons mentioned above it is suggested that the final section of the test section, beyond the mid-rib location between the fourth and fifth rib, is ignored from subsequent analysis. The smooth wall data follows the well known classical development where a region of high heat transfer, in the immediate entry region, asymptotes towards a fully developed or terminal Nusselt number value as the thermal boundary layer becomes progressively established.

The undulations in the wall temperature created by the ribs are reflected in the local Nusselt number distributions and this is also shown in Figure 7. Since the local heat flux is relatively uniform and the wall temperature decreases cyclically then there has to be a consequential cyclically increasing Nusselt number in the direction of flow. This tendency is clearly shown in the figure.

If the variation of Prandtl number is ignored over the fluid temperature range covered in the present work, then the local Nusselt number at a specified axial location in the duct will have the customary forced convection form

$$Nu = A\,Re^{n} \tag{9}$$

where A and n are constants. For the range of Reynolds numbers tested data obtained at rib and mid-rib locations were analysed in terms of equation (9) and the appropriate constants evaluated. The numerical results of this empirical analysis are shown in Tables 1 and 2. The following points are worthy of note.

For the ribbed locations, the exponent, n, tended to decrease as the rib number increased. Extrapolation backwards towards the inlet section preceding the first rib suggests that this exponent approaches the well established 0.8 value for smooth-walled forced convection in ducts. A similar exponent trend was found for the mid-rib locations, although the decrease in exponent was less marked. The variation of the exponent, n, is plotted against axial location in Figure 8 where the above mentioned trends are clearly shown. It is probable that, as the flow pattern establishes itself in a multi ribbed tube, these exponents will asymptote to a constant value. This has strong support from the finite element analysis of this flow geometry reported by Taylor et al (27).

Rib location	A	n
1	0.092	0.724
2	0.176	0.668
3	0.352	0.609
4	0.515	0.589

Table 1: Empirical correlations for rib locations

Midrib location	A	n
1-2	0.084	0.749
2-3	0.125	0.725
3-4	0.221	0.681

Table 2: Empirical correlations for mid-rib locations

The coefficients, A, from equation (9) are also given in Tables 1 and 2. The values tended to increase in the downstream direction with relatively lower values occurring in the midrib locations as illustrated in Figure 8.

The overall complexity of the flow field and associated heat transfer which occurs when this ribbed duct was rotated is evident from the typical wall temperature distributions shown in Figure 9. These results, which are typical for all rotating tests, clearly illustrate the circum-ferential variation in heat transfer produced due to the Coriolis-driven cross stream secondary flow. The trailing edge of the duct was consistently found to operate at a lower temperature than its leading counterpart in a similar manner to that found with the smooth-walled tube (see reference (26)). It is interesting to note also that the cyclical ripples in wall temperature, noted with the stationary ribbed duct, were still in evidence on the trailing edge but this rippling was severely suppressed on the leading edge. It is not possible to fully explain this effect with the present data but it is very likely that changes to the basic turbulent flow structure is occurring on the leading edge. This has been observed and noted in references (5) and (28) for the smooth-walled case.

Figure 10 shows the form of local Nusselt number variations calculated from the data processing technique described above and the marked relative improvement in heat transfer on the trailing edge is clearly shown. The suppression of the wall temperature ripple on the leading edge is also clearly reflected in this local Nusselt number plot. Similar trends were detected for all rotational tests undertaken.

Prior to conducting the rotational experiments, it was felt that there would be a strong possibility that the influence of centripetal buoyancy would be small in relation to the combined complexity of the presence of the ribs and the Coriolis-driven secondary flow. It was surprising therefore to note the comparative results shown in Figure 11. Here, for two Reynolds numbers and the highest rotational speed used, are shown the trends found by increasing the buoyancy parameter whilst effectively keeping the Reynolds and Rossby numbers fixed. Note that this effectively means running at progressively higher heat fluxes.

There was a systematic tendency for the heat transfer to increase with increases in the buoyancy parameter although, in the main, significant impediment to the local leading edge heat transfer was noted in comparison to the stationary tube situation. As with the smooth-walled results quoted by other workers in this field, this implies a serious potential overheat situation on the leading edge if rotational effects are ignored in the rotor blade application.

Figure 12 shows the corresponding trends found for local heat transfer on the trailing edge. Again the effect of increasing the buoyancy parameter, whilst maintaining a fixed value of Reynolds and Rossby number, was to produce progressive increases in the trailing edge heat transfer in the main. However in this case, the local heat transfer tends to be enhanced in relation to the stationary duct situation.

Thus far the general effects of rotation found with the ribbed duct have been similar in qualitative terms to those noted by other workers studying the smooth-walled situations and, in particular, the complementary study undertaken by the present authors (reference (26)). In this respect the general trends found may be summarised as follows.

Coriolis forces are still significantly affecting the ribbed duct flow field by the generation of a cross stream secondary flow which enhances local heat transfer on the trailing edge of the duct in relation to the leading edge. Although there is a tendency for a net beneficial effect of rotation on the trailing edge, serious impediment to the local heat transfer has been noted on the leading edge in comparison to what might be expected in the absence of rotation. As will be shown below, reductions in leading edge heat transfer up to approximately 25% compared to the stationary case have been detected during these exploratory experiments, particularly in the mid-fin locations. Improvements in heat transfer up to approximately 25% have been measured on the trailing edge.

In their work with the smooth-walled duct, the present authors proposed a method of correlating the combined effect of Coriolis forces and centripetal buoyancy by means of a parameter involving the quotient of the buoyancy parameter with the Rossby number. Thus by plotting the ratio of the Nusselt number obtained with rotation against that obtained without rotation but with the corresponding Reynolds number, it was possible to give a strong tendency to collapse all rotational data onto unique curves for the leading and trailing edges. The proposal also worked well for the experimental data of Wagner et al (19) obtained with a smooth-walled square sectioned duct.

This method of data presentation has also been attempted with the present data for the ribbed duct. Thus, in Figure 13 for the fin locations, are shown the plots of the Nusselt number ratios obtained with and without rotation against the combined rotational parameter, $\beta\ \Delta T/Ro$, proposed for the smoothed walled case. The data clearly shows in the main, the significant enhancements and impediments to heat transfer which can occur as a result of rotation, although the tendency to collapse data uniquely is not as good as that found with the smooth-walled ducts. This clearly reflects the total complexity of the flow field created with a rotating ribbed duct. A similar plot for the mid-fin regions is shown in Figure 14, where similar overall observations may be made.

In conclusion the following broad observations result from this investigation.

As with smooth-walled ducts, Coriolis forces are still capable of significantly modifying the flow field and the corresponding local heat transfer along the duct. The general effects are similar to smooth-walled observations in that the trailing edge heat transfer is significantly better, in relative terms, than that on the leading edge.

Significant reductions in heat transfer compared to that suggested for stationary ducts with the same coolant flow rates are likely on the leading edges of ribbed ducts. This is an important result in terms of the design of cooled rotor blades in that "hot spots" may occur in practice if rotational effects are not adequately taken into account.

Increasing the buoyancy parameter at fixed levels of the Reynolds and Rossby numbers tends to improve the heat transfer, in relative terms, on both leading and trailing edges. Although certainly not definitive, the use of the rotational parameter combining the effect of Coriolis forces and centripetal buoyancy clearly illustrates the levels of heat transfer change likely to occur as a consequence of rotation.

ACKNOWLEDGEMENTS

The authors wish to acknowledge with thanks support from the Ministry of Defence, The Science and Engineering Research Council and Rolls-Royce, plc. for these fundamental studies and, in particular the encouragement received from Dr. R. Kingcombe (M.O.D.) and Mr. W. Pearce (Rolls-Royce).

REFERENCES

1. Barua, S.N. "Secondary Flow in a Rotating Straight Pipe", Proc. Roy. Soc., A, 227, 133, 1955.

2. Mori, Y. and Nakayama, W. "Convective Heat Transfer in Rotating Radial Circular Pipes (1st Report - Laminar Region)", Int. Jnl. Heat and Mass Transfer, 11, 1027, 1968.

3. Benton, J.S. and Boyer, D. "Flow Through a Rapidly Rotating Conduit of Arbitrary Cross-Section", J. Fluid Mech., 26, Part I, 1969.

4. Ito, H. and Nanbu, K. "Flow in Rotating Straight Pipes of Circular Cross-Section", Trans., ASME, Jnl. Basic Eng., 93 (3), 383, 1971.

5. Johnston, J.P. Halleen, R.M. and Lezius, D.K. "Effects of Spanwise Rotation on the Structure of Two-dimensional Fully Developed Turbulent channel flow". J. Fluid Mechanics, Vol. 56, pp. 537-557, 1972.

6. Lokai, V.I. and Limanski, A.S."Influence of Rotation on Heat and Mass Transfer in Radial Cooling Channels of Turbine Blades", Izvestiya VUZ, Aviatsionnya Tekhika, 18, 3, 69, 1975.

7. Metzger, D.E. and Stan, R.L. "Entry Region Heat Transfer in Rotating Radial Tubes", AIAA 15th Aerospace Sciences Meeting, Los Angeles, Paper 77-189, 1977.

8. Skiadaresis, D. and Spalding, D.B."Heat Transfer in a Pipe Rotating about a Perpendicular Axis". ASME Paper 77-WA/HT-39, 1977.

9. Zysina-Molozken, L.M. Dergach, A.A. and Kogan, G.A. "Experimental Investigation of Heat Transfer in a Radially Rotating Pipe", HGEEE High Temp., 14, 988, 1977.

10. Morris, W.D. and Ayhan, T."Observations on the Influence of Rotation on Heat Transfer in the Coolant Channels of Gas Turbine Rotor Blades", Proc. Inst. Mech. Eng., 193, 21, 303, 1979.

11. Morris, W.D. "Heat Transfer in Rotating Coolant Channels", Research Studies Press, John Wiley and Sons, 1981.

12. Morris, W.D. and Ayhan, T. "Experimental Study of Turbulent Heat Transfer in a Tube which Rotates about an Orthogonal Axis", Proc. XIV ICHMT Symposium on Heat and Mass Transfer in Rotating Machinery, Dubrovnik, Yugoslavia, 30 August - 3 September, 1982.

13. Clifford, R.J. Morris, W.D. and Harasgama, S.P. "An Experimental Study of Local and Mean Heat Transfer in a Triangular Sectioned Duct Rotating in the Orthogonal Mode", Proc. ASME 29th Int. Gas Turbine Conf., Amsterdam, Netherlands, 1984, Paper No. 84-GT-142.

14. Morris, W.D. and Harasgama, S.P."Local and Mean Heat Transfer on the Leading and Trailing Surfaces of a Square Sectioned Duct Rotating in the Orthogonal Mode", Presented at Heat Transfer and Cooling in Gas Turbines, AGARD-CP-390, Bergen, Norway, 6-10 May, 1985.

15. Clifford, R.J. "Rotating Heat Transfer Investigations on a Multi-Pass Cooling Geometry", Presented at Heat Transfer and Cooling in Gas Turbines, AGARD-CP-390, Bergen, Norway, 6-10 May 1985.

16. Iskakov, K.M. and Trushin, V.A. "The Effect of Rotation on Heat Transfer in the Radial Cooling Channels of Turbine Blades", Teploenergetika, 32 (2), 52-55, 1985.

17. Wagner, J.H. Kim, J.C. and Johnson, B.V. "Rotating Heat Transfer Experiments with Turbine Airfoil Internal Passages", 31st Int. Gas Turbine Conf., Dusseldorf, FRG, June 1986, Paper 86-GT-133, 1986.

18. Morris, W.D. Harasgama, S.P. and Salemi, R. "Measurements of Turbulent Heat Transfer on the Leading and Trailing Surfaces of a Square Duct Rotating About an Orthogonal Axis". ASME Gas Turbine and Aeroengine Congress, Amsterdam, The Netherlands, June 6-9, 1988.

19. Wagner, J.H. Johnson, B.V. and Hajek, T.J. "Heat Transfer in Rotating Passages with Smooth Walls and Radial Outward Flow.", ASME Gas Turbine and Aeroengine Congress and Exposition, June 4-8, 1989, Toronto, Ontario, Canada.

20. Morris, W.D. and Ghavami-Nasr, G. "Heat Transfer Measurements in Rectangular Channels With Orthogonal Mode Rotation", ASME Gas Turbine and Aeroengine Congress and Exposition, June 11-14, 1990, Brussels, Belgium.

21. Medwell, J.O. Morris, W.D. Xia, J.Y. and Taylor, C. "An Investigation of Convective Heat Transfer in a Rotating Coolant Channel.", ASME Gas Turbine and Aeroengine Congress and Exposition, June 11-14, 1990, Brussels, Belgium.

22. Iacovides, H. and Launder, B.E."Parametric and Numerical Studies of Fully-Developed Flow and Heat Transfer in Rotating Rectangular Passages.", ASME Gas Turbine and Aeroengine Congress and Exposition, June 11-14, 1990, Brussels, Belgium.

23. Wagner, J.H. Johnson, B.V. and Kopper, F.C. "Heat Transfer in Rotating Serpentine Passages With Smooth Walls." ASME Gas Turbine and Aeroengine Congress and Exposition, June 11-14, 1990, Brussels, Belgium.

24. Taylor, C. Xia, J.Y. Medwell, J.O. and Morris, W.D. "Finite Element Modelling of Flow and Heat Transfer in Turbine Blade Cooling." Proceedings European Conference on Turbomachinery, March 19-20, 1991, London, U.K.

25. Morris, W.D. and Salemi, R. "An Attempt to Experimentally Uncouple the Effect of Coriolis and Buoyancy Forces on Heat Transfer in Smooth Circular Tubes Which Rotate in the Orthogonal Mode". ASME Gas Turbine and Aeroengine Congress and Exposition, June 1-4, 1991, Orlando, U.S.A.

26 Taylor, C. Xia, J.Y. Medwell, J.O. and Morris, W.D. "Numerical Simulation of Three Dimensional Turbulent Flow and Heat Transfer Within a Multi-Ribbed Cylindrical Duct." ASME Gas Turbine and Aeroengine Congress and Exposition, June 1-4, 1991, Orlando, U.S.A.

27. Morris, W.D. and Claypole, T.C. Unpublished Flow Visualisation Video Film, Department of Mechanical Engineering, University College of Swansea, Singleton Park, Swansea, SA2 8PP, U.K.

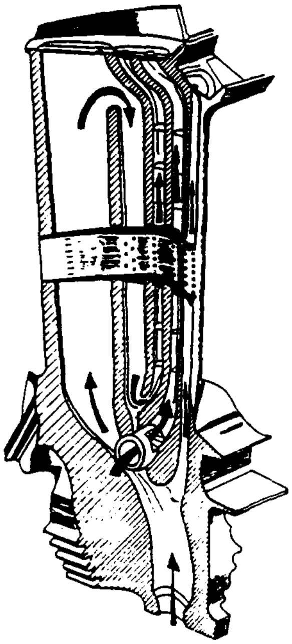

FIGURE 1 TYPICAL ROTOR BLADE COOLING CHANNEL NETWORK

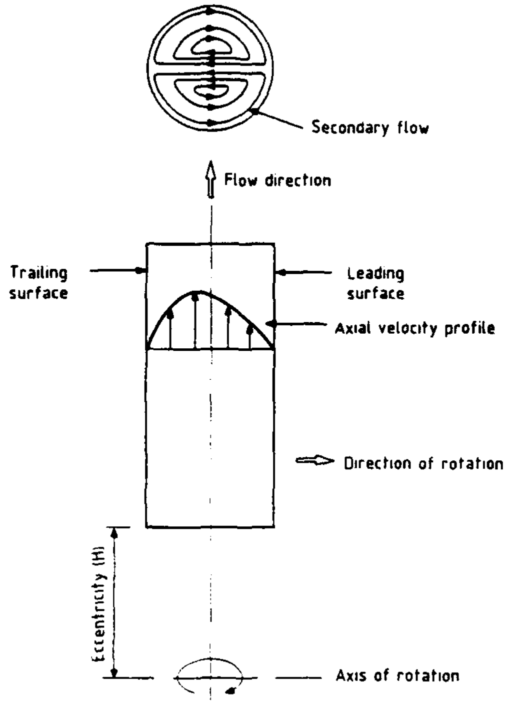
Secondary flow
Flow direction
Trailing surface
Leading surface
Axial velocity profile
Direction of rotation
Eccentricity (H)
Axis of rotation

FIGURE 2 FUNDAMENTAL FLOW GEOMETRY WITH ORTHOGONAL-MODE ROTATION

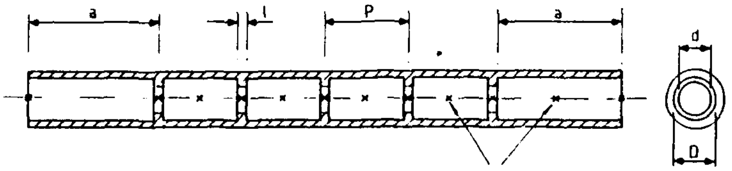
a
l
P
a
d
D
Axial positions of thermocouples

D = Plain bore diameter (10mm)
d = Bore at fin (6mm)
P = Pitch (20mm)
l = Land (2mm)
a = Inlet/exit zones (25mm)

Geometry descriptions
Pitch/plain bore diameter ratio = P/d
Blockage ratio = d^2/D^2
Land/pitch ratio = l/P

FIGURE 3 GEOMETRY OF RIBBED TUBE STUDIED

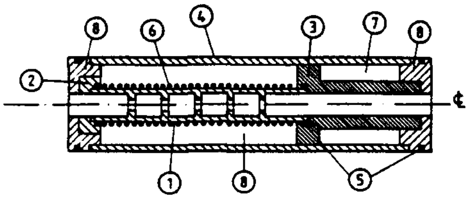
8
6
4
3
7
8
2
℄
1
8
5

1 Circular sectioned tube
2 Insulated inlet bush
3 Insulated exit bush
4 Aluminum tube
5 "O" ring seals
6 Heater coil
7 Fibrefrax insulation
8 Support

FIGURE 4 TEST SECTION CONSTRUCTION

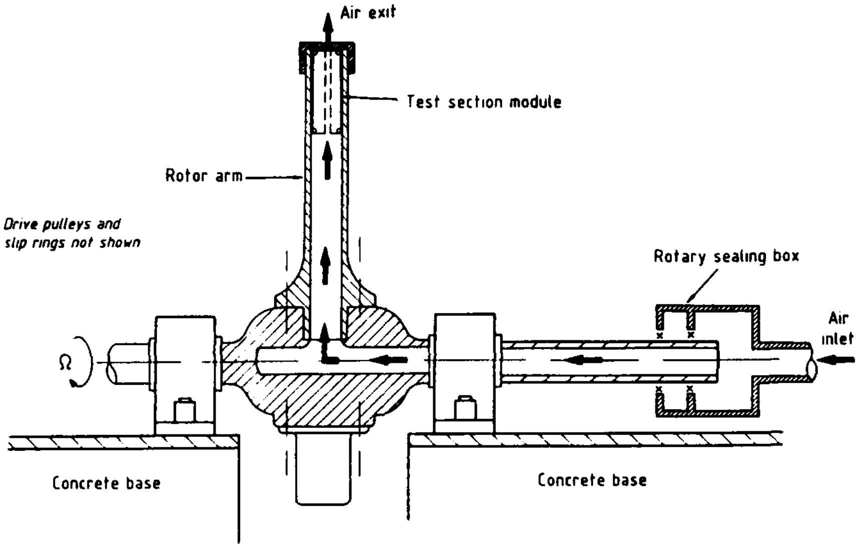
Air exit
Test section module
Rotor arm
Drive pulleys and
slip rings not shown
Rotary sealing box
Air
inlet
Ω
Concrete base
Concrete base

FIGURE 5 SCHEMATIC OF ROTATING TEST FACILITY

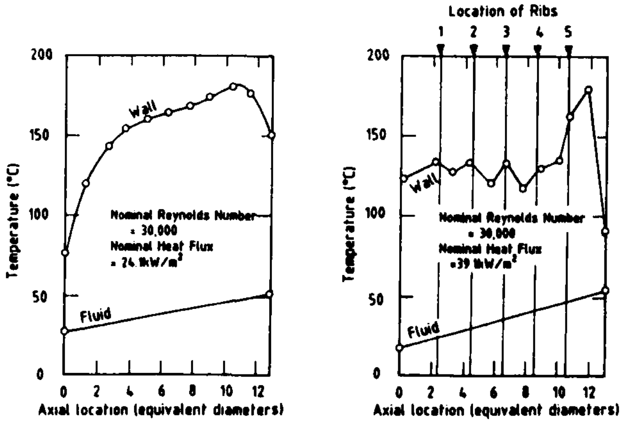

(a) Smooth-walled tube

(b) Ribbed tube

FIGURE 6 TYPICAL COMPARISON OF WALL TEMPERATURE DISTRIBUTIONS WITH FINNED AND SMOOTH-WALLED TUBES

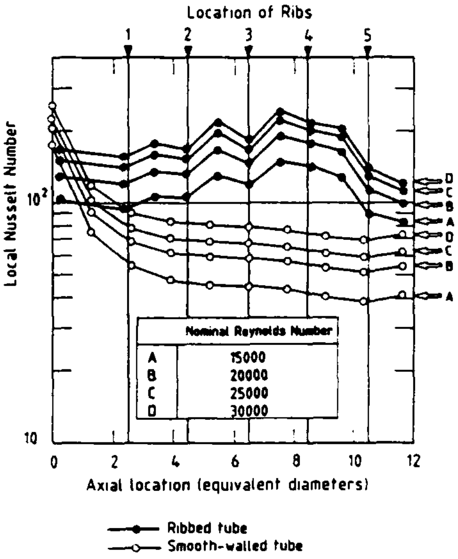

FIGURE 7 COMPARISON OF LOCAL NUSSELT NUMBER DISTRIBUTIONS FOR FINNED AND SMOOTH-WALLED TUBES

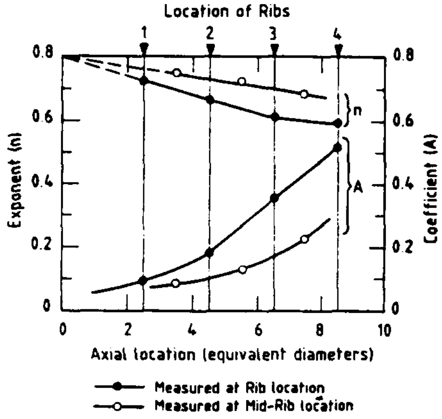

FIGURE 8 EFFECT OF RIB LOCATION ON LOCAL NUSSELT NUMBER/REYNOLDS NUMBER CORRELATIONS

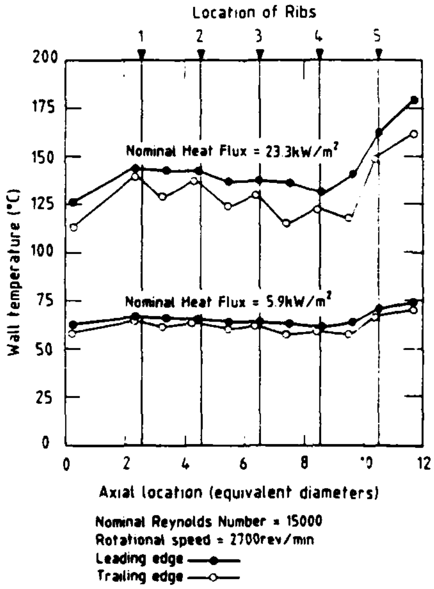

FIGURE 9 EFFECT OF ROTATION ON LEADING AND TRAILING EDGE WALL TEMPERATURE FOR FINNED TUBE

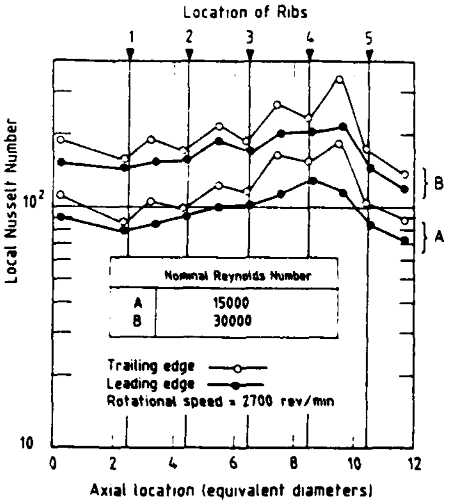

FIGURE 10 TYPICAL EFFECT OF ROTATION ON LOCAL HEAT TRANSFER OVER LEADING AND TRAILING EDGES

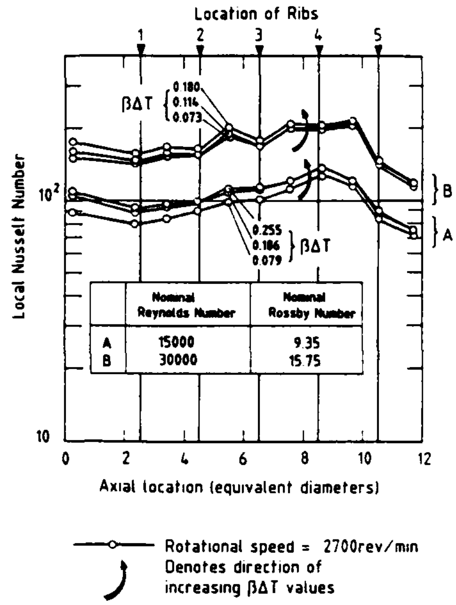

FIGURE 11 TYPICAL EFFECT OF CENTRIPETAL BUOYANCY ON LEADING EDGE LOCAL HEAT TRANSFER

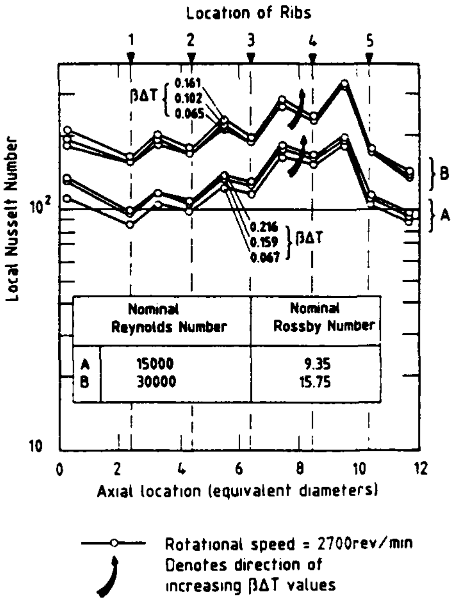

FIGURE 12 TYPICAL EFFECT OF CENTRIPETAL BUOYANCY ON TRAILING EDGE LOCAL HEAT TRANSFER

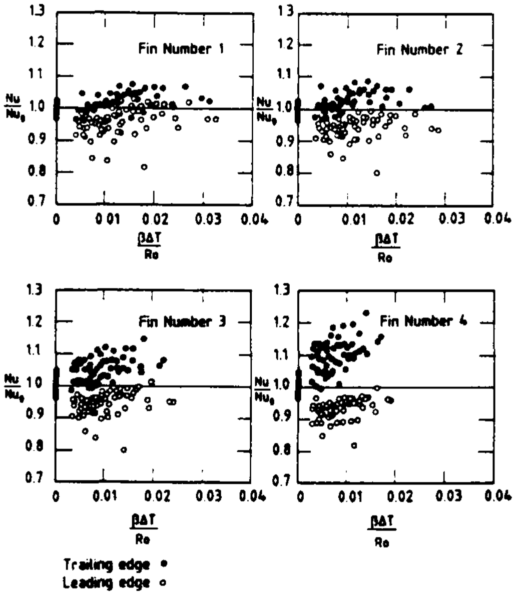

FIGURE 13 COMBINED EFFECT OF CORIOLIS FORCE AND BUOYANCY ON LEADING AND TRAILING EDGE HEAT TRANSFER AT FIN LOCATIONS

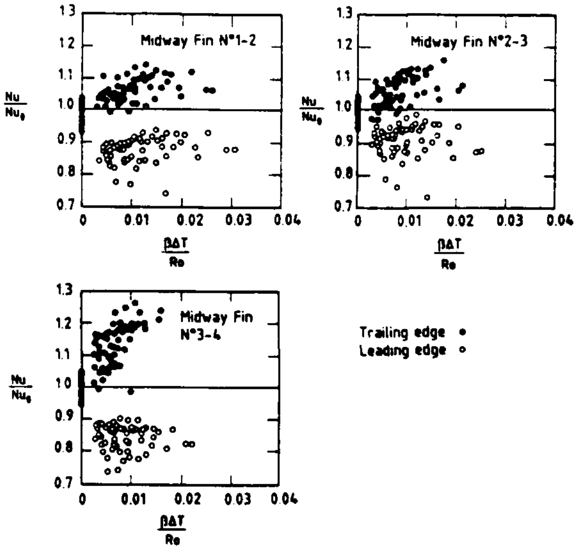

FIGURE 14 COMBINED EFFECT OF CORIOLIS FORCE AND BUOYANCY ON LEADING AND TRAILING EDGE HEAT TRANSFER AT MID-FIN LOCATIONS

Turbulent Flow and Heat Transfer in Idealized Blade Cooling Passages

T. Bo and B.E. Launder
UMIST
Manchester
U.K.

1. ABSTRACT

The paper brings together recent research at UMIST directed at the prediction of flow through tight, square-sectioned U-bends rotating in orthogonal mode. The cases of flow through rotating straight ducts and stationary U-bends are considered first to allow comparison with experimental data; finally, having demonstrated the level of accord achieved with experiment, predictions for the rotating U-bend are provided. A fairly simple turbulence model has been adopted with the usual high Reynolds number k-ε model being interfaced with a 1-equation near-wall model. To achieve, in the case of the U-bend, grid independent behaviour with the available computer core, a bounded third-order discretization of convective transport had to be applied to all dependent variables.

The agreement with the available experimental data is broadly satisfactory in the case of the rotating straight duct (the substantial modifications to the Nusselt number on the pressure and suction faces of the duct due to Coriolis and buoyant forces being well reproduced. Agreement is less complete in the case of the U-bend but even so the predicted levels of Nusselt number and the distribution of velocity downstream of the bend are broadly in line with experiment.

The results point to the desirability of incorporating second-moment closure into the bend-flow calculations as models of this type have a track record of capturing the sensitivity of the turbulent stresses to complex strains better than the eddy viscosity model adopted here.

NOMENCLATURE

D	hydraulic diameter of duct (equal to dimensions of sides)
k	turbulent kinetic energy
ℓ	turbulent length scale
Nu	Nusselt number
P	static pressure
r_c	mean radius of bend
$\overline{u_i u_j}$	Reynolds stresses
u_j	fluctuating velocity component in direction x_j
U_j	mean velocity in direction x_j
W	streamwise mean velocity
$\overline{W}$	bulk mean averaged velocity
x	direction parallel to symmetry plane
x_j	Cartesian space coordinate
y	direction normal to symmetry plane
z	direction along duct axis
ε	dissipation rate of turbulence energy
θ	turbulent temperature fluctuation
Θ	mean temperature
λ	thermal diffusivity
μ	dynamic viscosity
ν	kinematic viscosity
ν_t	turbulent kinematic viscosity
ρ	density
Ω_j	angular rotation vector

Subscript

o	value under non-rotating conditions
overbar	averaged value: time or space averaging according to context

2. INTRODUCTION

A recent contribution by Dutoya et al [1] has strikingly demonstrated the power of CFD software to reproduce the complex flow patterns that arise in a rotating, rectangular-sectioned U-bend analogous to those occurring in the cooling passages of turbine blades. Before quantitative reliance can be placed on CFD computations, however, both the adequacy of the numerical resolution and the turbulence model need to be thoroughly validated. The present article reports CFD research at UMIST directed at both these aspects of predicting internal blade cooling. The principal cases considered are a rotating square-sectioned straight duct and a stationary U-bend for both of which experimental data are available. Finally applications are presented for the case of a rotating U-bend.

Section 3 summarizes the numerical and physical models adopted in this work while applications are presented in Section 4.

3. THE MATHEMATICAL AND PHYSICAL MODEL

3.1 The Mean-Flow Equations

The Reynolds and continuity equations describing the motion of turbulent flow in an arbitrarily rotating coordinate system may be written

$$\frac{\partial}{\partial x_j}(\rho U_j U_i) = -\frac{\partial P}{\partial x_i} + \frac{\partial}{\partial x_j}\left\{\mu\left[\frac{\partial U_i}{\partial x_j} + \frac{\partial U_j}{\partial x_i}\right] - \rho\overline{u_i u_j}\right\} \tag{1}$$

$$-2\rho\epsilon_{ipj}\Omega_p U_j$$

$$-\rho\{\Omega_j x_j \Omega_i - \Omega_j x_i \Omega_j\}$$

$$\frac{\partial}{\partial x_i}(\rho U_i) = 0 \tag{2}$$

U_i being the mean velocity vector, Ω_i the coordinate rotation vector and $\overline{u_i u_j}$ the unknown Reynolds stress. The local density ρ is related to the mean temperature θ through

$$\rho = \rho_o \theta_o / \theta \tag{3}$$

and the temperature is obtained from the energy equation

$$\frac{\partial}{\partial x_j}(\rho U_j \theta) = \frac{\partial}{\partial x_j}\left\{\lambda\frac{\partial \theta}{\partial x_j} - \rho\overline{u_j\theta}\right\} \tag{4}$$

where $\overline{u_j\theta}$ is the kinematic turbulent heat flux.

3.2 The Turbulence Model

The choice of turbulence model in the present study has been a compromise between the goal of achieving physical realism and the necessity of securing convergent behaviour with good numerical accuracy. Our usual practice [2, 3] of applying high order discretization just on the mean-field variables while retaining 1st-order upwind differencing on the turbulent quantities k and ε proved to be unsatisfactory when handling the separated U-bend. However, due to the reduced stability that accompanies the adoption of higher-order discretization, we have been obliged to work within the framework of an eddy-viscosity stress-strain relation, at least for this initial study. For the rotating straight duct numerical problems are less severe and we have in this case obtained results with a more advanced turbulence model that are to be reported in detail in a forthcoming publication [4]; a brief comparison with those results is included in §4.

The principal computational results have been obtained with a hybrid eddy viscosity model in which, across the near-wall sublayer, a 1-equation model [5] is applied while the usual, high Reynolds number form of the k-ε model [6] is adopted over the core region. The details of the model are given in Table 1. In fact two forms of 1-eq scheme have been adopted - a genuine fixed-length-scale treatment and one where the slope adjusts to length scale levels in the outer region.

3.3 The Numerical Solvers

Elliptic and parabolic 3-dimensional finite-volume solvers have been employed in the present study for the U-bend and rotating straight duct computations respectively. Each is an adaptation of UMIST's semi-elliptic duct flow code SEDUCT developed by Iacovides [7] and reported in several previous publications, e.g. [2, 3]. They are based on the pressure-correction strategy of Patankar and Spalding [8] while the general program structure is that of the TEACH family of computer codes.

The parabolic solver retains the practices of the parent code [7] for discretizing convective transport: quadratic upstream interpolation [9] is applied to cross-stream velocity components and temperature while a hybrid treatment is applied to all other dependent variables with the changeover from central to upwind differencing occurring at a cell Reynolds number of 2.

More extensive adaptations have been necessary in constructing the elliptic code, details of which are reported by Bo and Iacovides [10]. The fully-elliptic treatment greatly increased storage requirements relative to the semi-elliptic code but it meant that more accurate interpolation practices could be adopted. The "streamwise" velocity component was now treated in the same way as those in the cross-stream plane. In place of the original quadratic upwind interpolation [9], a bounded version, LODA, (Local Oscillation Damping Algorithm) due to Zhu and Leschziner [11], was implemented due to its improved stability for negligible loss of accuracy.

It is generally supposed that a high-order discretization of convection in the k and ε equations is not necessary because of the presence of large source and sink terms in these equations. However, the fact that a fairly coarse mesh had inevitably to be used in these 3D elliptic computations made us decide to explore the consequences of adopting LODA on these turbulence variables also. This change introduced significant (additional) convergence difficulties which were eventually overcome, however. The results, in fact, showed a strong dependence on discretization practice as is shown briefly in Section 4 and more fully by Bo and Iacovides [10].

4. COMPUTATIONAL RESULTS

4.1 Grid-Dependence of Elliptic Computations

For the flow around the U-bend shown in Fig 1 extensive grid-dependence tests were carried out with four different meshes and four different practices regarding the use of LODA (on all variables; on none; on mean-field quantities; and on all except ε). Where LODA is not employed the usual first order HYBRID (upwind/central) scheme is adopted. Here, to indicate the degree of grid sensitivity, Figure 2 focuses on the mean axial velocity profile on the plane of symmetry three diameters downstream of the bend exit. The behaviour at this position is entirely typical. With the coarser 35 x 67 x 133 mesh when HYBRID differencing is applied to all variables the near-wall velocity on the left side (which corresponds with the inside of the bend) is nearly zero, indicating that the flow had reattached just a short distance upstream. Grid refinement to 35 x 77 x 177, where the extra thirty streamwise planes were all concentrated within the bend itself, leads to a significant increase in velocity near the inside wall, albeit well below that of the experiments.

With LODA applied to all variables except ε, the coarser grid produces a profile similar to that with HYBRID on the finer mesh. With the grid refinement, however, the velocity near the left wall appreciably increases to pass close to the measured data. Somewhat coarser meshes have been adopted with LODA on all variables. With a 35 x 67 x 103 grid (of which 50 planes lie in the 180° bend section), near-wall velocities are even higher than with the finer mesh in Fig 2b; moreover, a velocity minimum develops in the centre of the profile. When the grid is refined to 35 x 67 x 133 (with the extra streamwise planes again being placed within the bend), there is, in fact, very little change in the computed behaviour. The results of this study left little doubt that the results obtained with LODA applied to all variables were the most accurate: not only was it the only scheme not to exhibit significant change to grid refinement but grid refinement applied to the other practices produced a shift in the computed behaviour towards that obtained with LODA on all variables - though they remained some way off that limit. The fact that substantial grid-related errors remain with these other two cases is further emphasized in Fig 3: the turbulent kinetic energies are appreciably higher than when LODA is applied to all variables, particularly so for the case where LODA is applied to all variables except ε. The reason for this is easily appreciated: LODA removes second-order false diffusion but the first-order upwind differencing applied to ε does not. So ε, which is produced in regions of high turbulence energy production, leaks away by false diffusion giving appreciably too high turbulence energies partly because ε is too small and partly because the turbulent viscosity, $c_\mu k^2/\varepsilon$, becomes too high. As indicated in §2, Bo and Iacovides [10] provide a more extensive account of these grid-dependency explorations.

4.2 Developing Flow Around a Stationary U-Bend

The square section U-bend had an inlet tangent of approximately 30 hydraulic diameters and a mean bend radius r_c equal to 0.65D. A fully developed flow at a Reynolds number of 10^5 is assumed at the entry plane located 3D ahead of the curved section; these fully developed profiles were obtained from a separate computation. The use of an eddy viscosity model meant that turbulence-driven secondary flows and their modification of the axial velocity were not accounted for. However, our experience of flows around *un*separated U-bends [3] indicates that quite substantial changes in inlet conditions have an insignificant effect on the flow conditions at the bend exit. It seems probable that in this separated U-bend minor inaccuracies in inlet conditions will have an even smaller effect on the flow by the end of the bend. Computations extended to 9D downstream of the bend exit where zero-gradient values were applied to the secondary velocities, temperature and turbulence variables and the axial velocity was obtained from solving the streamwise momentum equation with a uniform streamwise pressure gradient over the duct exit plane, the magnitude of which adjusted to achieve compliance with continuity. At the wall mean velocity components and turbulence energy were set to zero while the wall heat flux was set to a uniform level. In fact the experiment adopted a transient technique to measure the heat transfer coefficient and thus the actual boundary condition corresponded neither to uniform wall temperature nor uniform wall heat flux. However, it is known that in turbulent flow there is only a very weak dependence of heat transfer coefficients on the precise thermal boundary condition.

Experimental velocity profiles have been reported [12] at distances of 1D and 3D downstream of the U-bend exit and comparisons with these results are drawn in Fig 4-7. At 1D downstream the flow is separated on the inside of the U-bend. The experiments suggest that the separated region is greatest along the plane of symmetry and diminishes along parallel traverse lines as one proceeds towards the upper wall. The computations display a velocity distribution broadly in accord with measurements though the separation does not significantly alter with distance from the symmetry plane. The predicted turbulent kinetic energy profiles in Fig 5 indicate, in accord with experiments, higher levels of k on the inside of the bend and lower on the outside. On the symmetry plane, however, measurements indicate levels in the centre nearly twice as high as the predictions, possibly the result of higher secondary flow in the experiment. In contrast, the turbulence energy level near the outer wall is overestimated by the computations. A possible cause for this could be the acceleration of fluid on the outside of the bend near the bend exit producing local thickening of the viscous sublayer and a reduction of turbulence energy generation. The level of the dimensionless streamwise pressure gradient - $\nu/\rho U_\tau^3\, dP/dz$ reaches a peak level of 3 x 10^{-2} in this region which certainly exceeds the value of 10^{-2} above which sublayer thickening occurs, Bradshaw [13].

At 3D downstream, Fig 6, the flow has reattached on the inside wall. While computations agree with experiments on this, the predictions have shown a too rapid acceleration of the flow on the inside wall as the positive (adverse) pressure gradient, present at the bend exit, becomes negative. This discrepancy points to a too low computed viscosity level near the inside wall. Support for this is provided by the fact that when the diffusive upwind scheme is applied to the ε equation, leading, as discussed above, to excessive near-wall viscosities, agreement with experiment is actually improved, Fig 2b. The computed turbulence energy at this downstream station, Figure 7, is markedly too low, particularly near the inner wall.

A factor contributing to the disagreement is the requirement that the near-wall turbulent length scale should equal that in equilibrium turbulence. Physically it is reasonable to suppose that large external levels of length scale will tend to increase near-wall values of ℓ. A repeat set of computations have thus been made in which the sublayer length scale could adjust in magnitude according to the level of ε prevailing in the fully turbulent region, see §2. The results from these computations are shown by a broken line in figures 4-7. While there are only small differences in mean velocity at 1D downstream, there are perceptible improvements in the predicted turbulence energies. At 3D downstream there are noticeable changes to the mean velocity field as well as the turbulence energy, both indicating better accord with data than obtained with the conventional 1-eq near-wall model, a result supporting the physical concept behind its introduction.

The main practical goal is to be able to predict the resultant convective heat transfer pattern within and downstream of the U-bend [14]. Fig 8 shows, in contour form, the distributions of local heat transfer coefficients on the top wall of the U-bend. The values of heat-transfer coefficient for both computation and experiment are those based on gas inlet temperature. The standard 1-equation/2-equation model captures the shape of the contours fairly well. Indeed, if the heat-transfer coefficients are averaged at any section we note in Fig 9a that the steep rise in mean heat-transfer coefficient through and downstream of the bend is very well captured. The measured heat-transfer coefficients for the inner and outer walls of the U-bend adopted gas temperatures measured 'in the vicinity of' the point on the surface. This brings a measure of uncertainty to their absolute values. The comparison of the side-averaged levels presented in Fig 9, however, serves to indicate the overall behaviour. The computed maximum level on the concave wall (Fig 9b) downstream of the bend is some 40% above the measured value. It seems likely that the strong acceleration along the wall in this region partially "laminarizes" the near-wall layer depressing the heat-transfer coefficients. For the inside wall, Fig 9c, no measurements were obtained in the bend section itself. Downstream of the bend the computed heat transfer coefficient rises more slowly than the measurements reaching a maximum value about two diameters further downstream than in the experiments. The reason for this relative displacement of the peak h's is not clear since the reattachment length is apparently predicted accurately. As is usually the case in impinging flows [15], the use of a 1-equation near-wall model leads to an underestimate of the peak heat transfer coefficient.

4.3 Rotating Straight Duct Rotating in Orthogonal Mode

The flow configuration is essentially that of the straight inlet tangent of the U-bend shown in Fig 1. For these three-dimensional parabolic computations a 35 x 67 mapped the half cross-section on one side of the symmetry plane. The hydrodynamic entry conditions that most closely corresponded to those of the experiment appeared to be that of fully-developed flow in a *stationary* duct with a uniform fluid temperature at entry. In making heat transfer comparisons, in order to minimize the effects of any inconsistencies between the numerical and the experimental entry conditions, the values of the side-averaged Nusselt number were normalized by those of the corresponding stationary duct at the same stage of thermal development. To distinguish, in the computations, the contribution made by Coriolis forces (as opposed to Coriolis and buoyant forces in combination), computations were also made with the fluid density held strictly constant - a practice that eliminates buoyant effects.

Computations have been made for rotation numbers of 0.12 and 0.24 for which conditions the Rayleigh numbers (which increase as the square of the rotation speed are 2.5 x 10^7 and 10^8). These combinations of parameter values are broadly in line with those found in gas-turbine practice.

No experimental data of the velocity-field are available but the computed axial velocity contours and secondary flow vectors at the higher rotation rate (Ro = 0.24) are presented in Figures 10 and 11, the latter for the case with density uniform. We note in Fig 10 the strong secondary flow carrying near-wall fluid to the suction side, the establishment of a weak counter-rotating secondary vortex near z/D = 6.0 and its disappearance by z/D = 9.0. It is also noted, Fig 11, that there is a considerable change produced in both the axial and secondary velocity field if density variations are suppressed. This testifies to the importance of buoyant influences at this pair of Ro/Ra values. Interestingly, with buoyant forces suppressed, the flow pattern near the pressure surface continues to change appreciably up to 30D with a second vortex forming near the pressure surface at z/D ~ 20 and growing steadily in strength for the next ten hydraulic diameters. In contrast, when buoyancy effects are included, there is little change in the flow pattern beyond z/D = 9.0. The flow field at the lower rotation number (Ro = 0.12) shows qualitatively similar behaviour to that in Fig 10 with a secondary vortex forming near the suction surface; there is no significant difference between the pattern with and without buoyancy effects.

This preliminary consideration of the velocity field is helpful in explaining features of the convective heat transfer results. Fig 12 shows, for Ro = 0.12, the development of the side-averaged Nusselt number relative to that for a non-rotating duct. The computational behaviour mimics quite accurately that of the experiments [16] with a steady augmentation of Nu on the pressure surface and a corresponding depression on the suction surface. The reason is that warmed air close to the pressure surface is continuously being drawn away, being replaced by cool, high velocity fluid, while the warmed air accumulates on the suction side. There is little change in Nusselt number when density variations are suppressed which is consistent with the velocity field being virtually unaffected.

When the rotation rate is doubled, Fig 13, the effects of rotation are stronger and, according to the experimental data, produce a rather irregular effect on the Nusselt number on the suction side. Again this behaviour is quite well captured, particularly on the pressure surface. The substantial dependence of the velocity field on whether or not buoyant terms were included is reflected in the significantly different Nusselt number developments for the two cases. Indeed, for the non-buoyant case the increase in the Nusselt number on the pressure surface beyond z/D = 20 is directly associated with the extra vortex formed near that surface. The least satisfactory feature of the predictions is that, on the suction surface, the damping of heat transport (while mimicking qualitatively the somewhat irregular variation of the experiments) is insufficient: indeed, errors in Nu are as large as 50% in places. In a continuation of the present work, the authors have found that replacing the eddy viscosity model by a more elaborate second-moment closure leads to improved agreement, particularly on the suction surface, Fig 14. The details of those computations are to be reported in a forthcoming publication [4].

4.4 Flow Through a Rotating U-Bend

The rotating flow case considered is that where the pressure face of the duct, at entry to the curved section, corresponds with the outside of the bend, Fig 1. The secondary flow due to the Coriolis force thus proceeds in the same sense as that arising from curvature. Precisely the same grid distribution was adopted as for the non-rotating bend. The prescribed inlet conditions, three diameters upstream of the bend, were those of fully developed flow in a rotating pipe. The rotation number was 0.12 and, as for the stationary U-bend, the bulk Reynolds number was 10^5. Although results have been obtained using both HYBRID and LODA treatments of convection, only the latter are reported here.

The hydrodynamic results are summarized by way of secondary flow vectors and axial velocity contours. As noted in §4.3, in fully developed flow at Ro = 0.12 a secondary eddy near the suction surface is present in rotating flow leading to the marked displacement of the axial velocity contours seen in Fig 15a. Somewhat surprisingly, as the flow develops around the bend, there is no tendency for this secondary eddy to be swamped by the clockwise circulation induced by the bend, at least not over the first half of the bend (Fig 15b). Separation occurs on the inside wall near the corner close to the 120° station (not shown). By 150° (Fig 15c) there is backflow across the complete width of the inner wall while the greatest extent of the separated region is reached between 0.5 and 1.0 diameters downstream of the bend (Fig 15d).

It is interesting to compare this behaviour with that in the non-rotating bend. At 60° (Fig 16a) the axial velocity contours are similar save that in the rotating case the end-wall boundary layers are much thinner while the secondary flow forms just a single, clockwise vortex. Separation from the inner wall occurs at about the same angular position but there are stronger three-dimensional variations in axial velocity, Fig 16(b and c) than in the rotating case.

The variation of the side averaged Nusselt numbers is presented in normalized form in Fig 17. The normalizing parameter is the Nusselt number prevailing at the same station for the non-rotating flow. Notice first that in the fully developed flow ahead of the bend, rotation raises the Nusselt on the top and pressure (outer) faces while reducing it on the inside. Passage around the bend brings the Nusselt number ratio close to unity on all surfaces by the 180° station - in other words, the mean heat transfer coefficient at bend exit is so dominated by the field created by the bend that there is little effect of the rotation.

The downstream development sees a gradual reversion to the levels prevailing upstream of the bend. Only on the outer surface does this reversion appear to be monotonic, however. Along the inner wall the normalized Nusselt number falls to about 40% of that in the non-rotating bend before beginning its recovery. The top wall also records a decline in normalized Nusselt number before starting to increase again, a process that is by no means complete by the end of the calculation domain.

5. CONCLUDING REMARKS

The paper has reported accurate numerical computations of turbulent flow and convective heat transfer in three-dimensional flows generically similar to the cooling passages of turbine blades. Overall, the simple two-layer turbulent viscosity model adopted in these studies captures the measured flow behaviour sufficiently well for it now to be used, with caution, in passage design and hot-spot diagnosis. In particular, the modification of Nusselt number by Coriolis and buoyant forces in straight ducts, producing an augmentation in Nu on the pressure face, is accurately captured. The corresponding damping on the suction surface is also reproduced though not as accurately.

Likewise, the computed velocity field downstream of a non-rotating U-bend reproduces with reasonable fidelity the measured streamwise velocity profiles downstream of the bend including the reattachment position. The broad trends of the convective heat transfer pattern are also well reproduced, though the predicted level of Nusselt number is substantially overestimated in the exit region on the concave wall, presumably because the severe acceleration there induces a thickening of the viscous sublayer. This tendency cannot be captured with the one-equation sublayer model adopted here.

For the rotating U-bend, the streamwise velocity exhibits less variation with distance from the symmetry plane than in the stationary case though the main features, such as the location of the separation and reattachment lines, are not greatly modified. Concerning heat transfer, the mixing due to the bend gradually takes over from that due to the Coriolis force so that, by the bend exit, the mean Nusselt number levels on each face are nearly the same as in the non-rotating case. Downstream of the bend, levels of Nu gradually revert to those prevailing upstream of the bend - though not monotonically. In particular, the Nusselt number on the inside of the bend decreases to only 40% of that in the non-rotating duct before rising again. This result emphasizes the limitations of using non-rotating tests to estimate heat transfer coefficients in rotating systems. The idea that the extra circulation induced by Coriolis forces will tend to increase heat transfer coefficients or, at least, not reduce them, is not borne out.

Finally, we note that, while the present eddy viscosity modelling has produced results of sufficient accuracy to guide passage design, in the future greater fidelity of predictions will certainly result from including second-moment closure treatments. Already such a model has been used for the flow developing in a straight rotating duct, a step that brought marked improvement to the predicted distribution of Nusselt number on the suction face.

6. ACKNOWLEDGEMENTS

This work has been carried out with the support of the Procurement Executive, Ministry of Defence, and Rolls-Royce plc under Brochure B1D2-125D and is published with their permission. The research has been considerably helped and stimulated by the interest and input from members of the contract monitoring team to whom we offer our appreciative thanks. Dr H. Iacovides has made a considerable contribution to the research programme. His omission from the list of authors was at his request, for personal reasons. The camera-ready version of the manuscript has been compiled with great care by Mrs J. Buckley.

Authors' names are sequenced alphabetically.

7. REFERENCES

1. Dutoya, D., Errera, M., Michard, P.J. and Ristori, A., Paper 29 in CFD Techniques for Propulsion Applications, AGARD-CP-510, 1992.
2. Iacovides, H. and Launder, B.E., Proc. 4th Int. Conf. on Num. Meth. in Lam. & Turb. Flow, 1023-1045, Swansea, 1985.
3. Iacovides, H., Launder, B.E., Loizou, P.A. and Zhao, H.H., ASME J. Fluids Eng., 112, 409-415, 1990.
4. Bo, T., Iacovides, H. and Launder, B.E., "The computation of developing turbulent flow in ducts rotating in orthogonal mode", Manuscript in preparation.
5. Wolfshtein, M., Int. J. Heat Mass Trans., 12, 301, 1969.
6. Launder, B.E. and Spalding, D.B., Comp. Meth. in Appl. Mech. & Engrg., 3, 269, 1974.
7. Iacovides, H., PhD Thesis, Faculty of Technology, University of Manchester, 1986.
8. Patankar, S.V. and Spalding, D.B., Int. J. Heat Mass Transfer, 15, 1787, 1972.
9. Leonard, B.P., Comp. Meth. in Appl. Mech. & Engrg., 19, 59, 1979.
10. Bo, T. and Iacovides, H., "Discretization of the turbulence transport equations in the prediction of flow and heat transfer through sharp U-bends", In preparation, 1992.
11. Zhu, J. and Leschziner, M.A., Comp. Meth. for Appl. Mech. Eng., 67, No. 3, 1988.
12. Hicklin, D.J., "Experimental velocity and turbulence measurements in a perspex 180° bend model using a Polytec laser anemometer", RR Report GN29335, 1988.
13. Bradshaw, P., J. Fluid Mech., 35, 387, 1969.
14. Davenport, R., "Innovative use of thermochromic liquid crystals for turbine blade internal cooling passage flow visualization and heat transfer measurements", Paper 16, Proc. Conf. on Modern Techniques and Developments in Engine and Component Testing, Royal Aero. Soc., 1989.
15. Launder, B.E., ASME J. Heat Transfer, 110, 1112-1128, 1988.
16. Wagner, J.H., Johnson, B.V. and Hajek, T.J., ASME 89-GT-272, Int. Gas Turb. Conf., Toronto, 1989.

Table 1 The Turbulence Model Adopted

$$-\left(\overline{u_i u_j} - \frac{2}{3}\,\delta_{ij}k\right) = \nu_t\left(\frac{\partial U_i}{\partial x_j} + \frac{\partial U_j}{\partial x_i}\right)$$

$$-\overline{u_i\theta} = \frac{\nu_t}{\sigma_\theta}\,\frac{\partial\Theta}{\partial x_i}$$

In fully turbulent region [6]

$$\nu_t = c_\mu \rho k^2/\varepsilon$$

$$\frac{Dk}{Dt} = \frac{\partial}{\partial x_j}\left(\left(\frac{\nu_t}{\sigma_k} + \nu\right)\frac{\partial k}{\partial x_j}\right) - \overline{u_i u_j}\,\frac{\partial U_i}{\partial x_j} - \varepsilon$$

$$\frac{D\varepsilon}{Dt} = \frac{\partial}{\partial x_j}\left(\left(\frac{\nu_t}{\sigma_\varepsilon} + \nu\right)\frac{\partial \varepsilon}{\partial x_j}\right) - c_{\varepsilon 1}\,\overline{u_i u_j}\,\frac{\partial U_i}{\partial x_j}\,\frac{\varepsilon}{k} - c_{\varepsilon 2}\,\frac{\varepsilon^2}{k}$$

$c_\mu = 0.09$; $c_{\varepsilon 1} = 1.44$; $c_{\varepsilon 2} = 1.92$; $\sigma_k = 1.0$; $\sigma_\varepsilon = 1.3$; $\sigma_\theta = 0.9$

In viscosity-affected sublayer [5]

$\nu_t = c_\mu k^{1/2}\ell_\mu$; $\sigma_\theta = 0.9$

o k from transport equation above

o $\ell_\mu = c_\ell y\,(1 - \exp - y^*/A_\mu)$; $y^* \equiv y_{min}k^{1/2}/\nu$

o $\varepsilon = k^{3/2}/\ell_\varepsilon$; $\ell_\varepsilon = c_\ell y\,(1 - \exp - y^*/A_\varepsilon)$

o $c_\mu = 0.09$; $c_\ell = 2.4$; $A_\mu = 62.5$; $A_\varepsilon = 3.80$

Modified 1-equation model (originates with this study)

$\nu_t = c_\mu k^{1/2}\ell_\mu$

o k from transport equation above

o $\ell_\mu = c_\ell' y\,[1 - \exp(\tilde{R}_t/A_\mu)]$ $\tilde{R}_t = k^2/\nu\tilde{\varepsilon}$ $\tilde{\varepsilon} = \varepsilon - 2\nu\,(\partial\sqrt{k}/\partial y)^2$

o $\varepsilon = k^{3/2}/\ell_\varepsilon$; $\ell_\varepsilon = c_\ell' y\,[1 - \exp(\tilde{R}_t/A_\varepsilon)]$

o $c_\ell' = \max[2.4, (k^{3/2}/\varepsilon y)_{interface}]$; $A_\mu = 182$; $A_\varepsilon = 11.7$

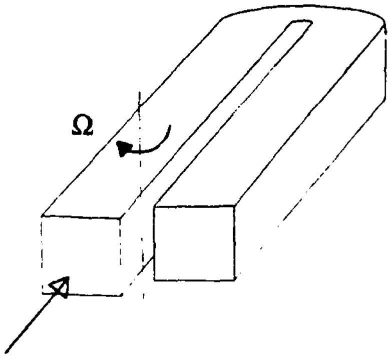

Fig 1 The flow configuration under study

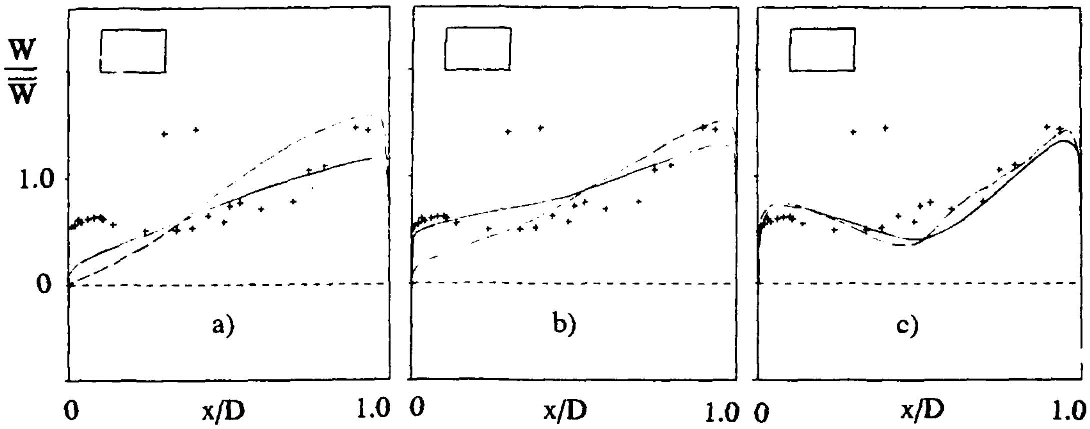

Fig 2 Grid sensitivity for different treatments of convection
a) HYBRID; b) LODA on all but ε; c) LODA
------ coarse grid; —— fine grid

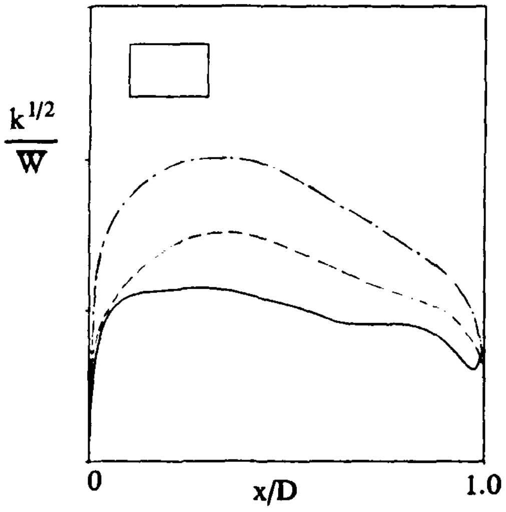

Fig 3 Effect of convection treatment on turbulent kinetic energy (with fine grid)
------ HYBRID; — - — LODA on all but ε; —— LODA

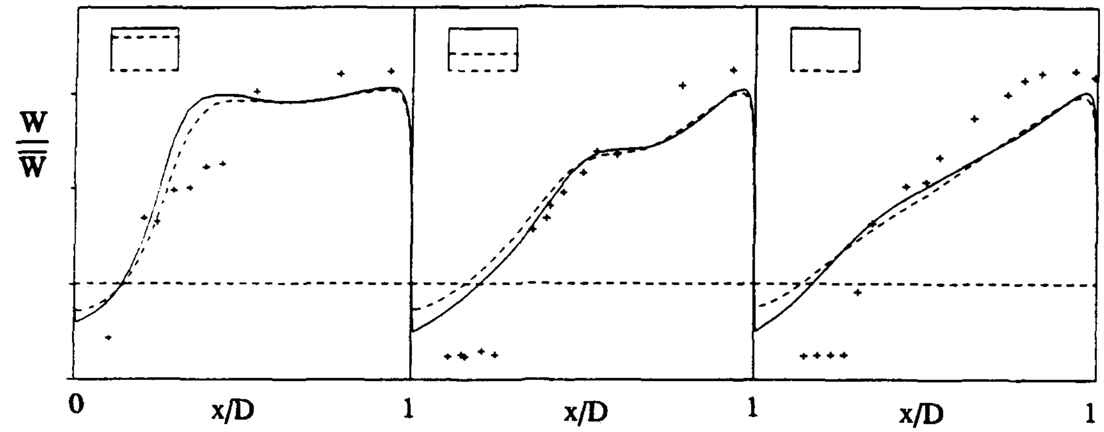

Fig 4 Streamwise mean velocity profile 1D downstream of U-bend
—— basic 1-eq; ----- modified 1-eq; ++++++ experiments, Hicklin [12]

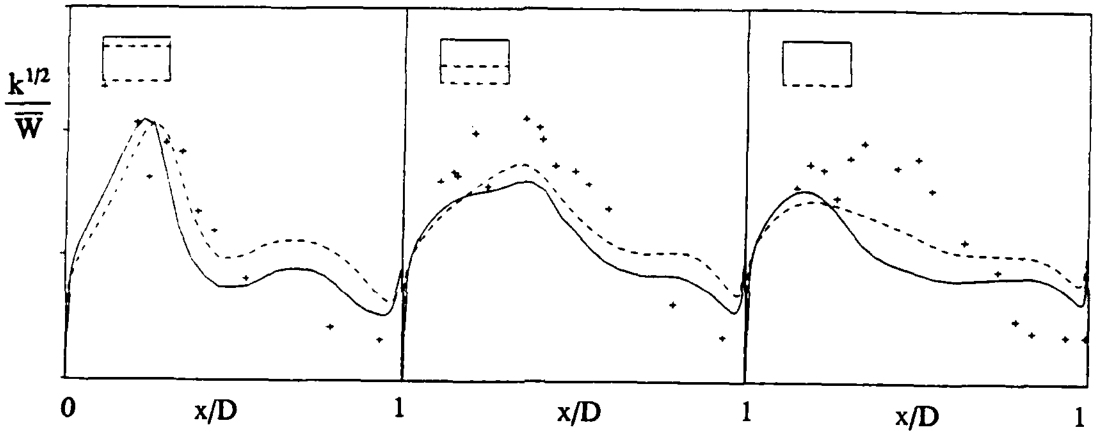

Fig 5 Profiles of $k^{1/2}$ 1D downstream of U-bend
Key as Fig 4

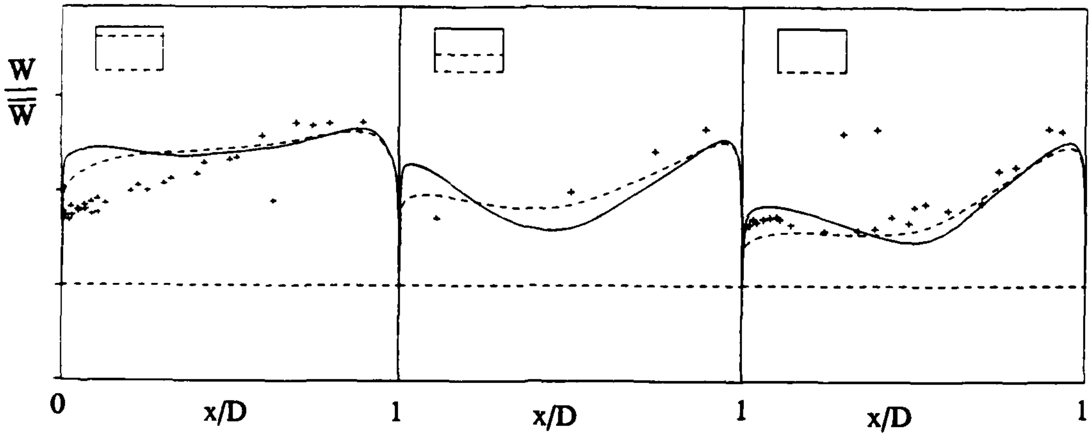

Fig 6 Streamwise mean velocity profile 3D downstream of U-bend
Key as Fig 4

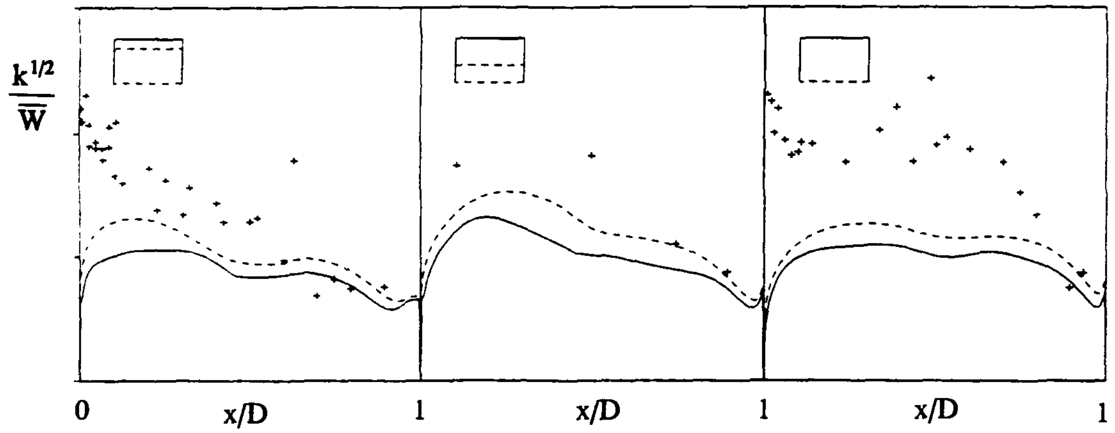

Fig 7 Profiles of $k^{1/2}$ 3D downstream of U-bend
Key as Fig 4

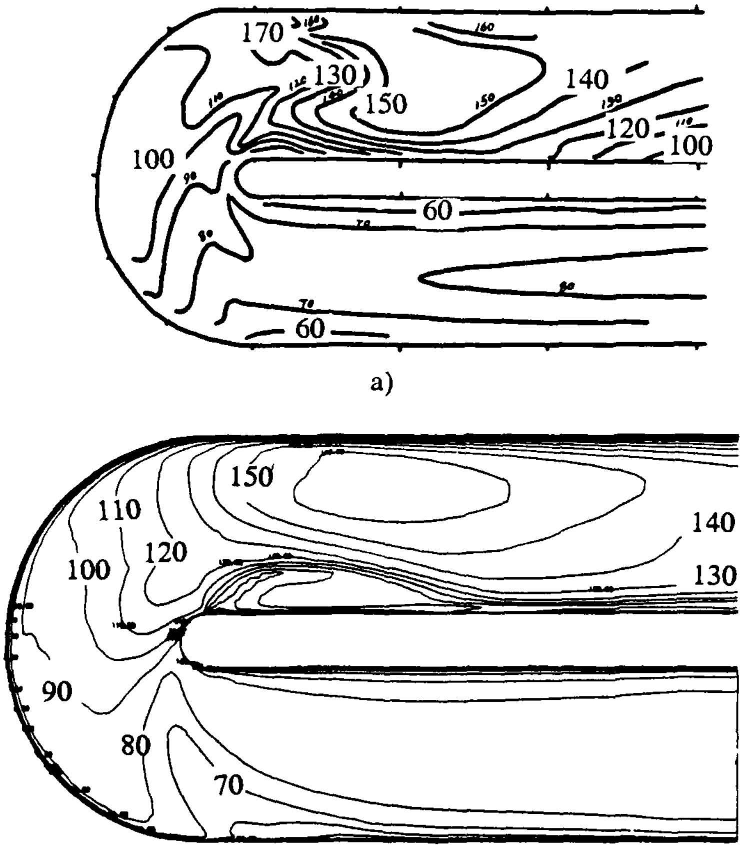

a)

b)

Fig 8 Contour plot of heat transfer coefficients on top wall (w/m^2/k)
a) experiment, Davenport [14]
b) present computations

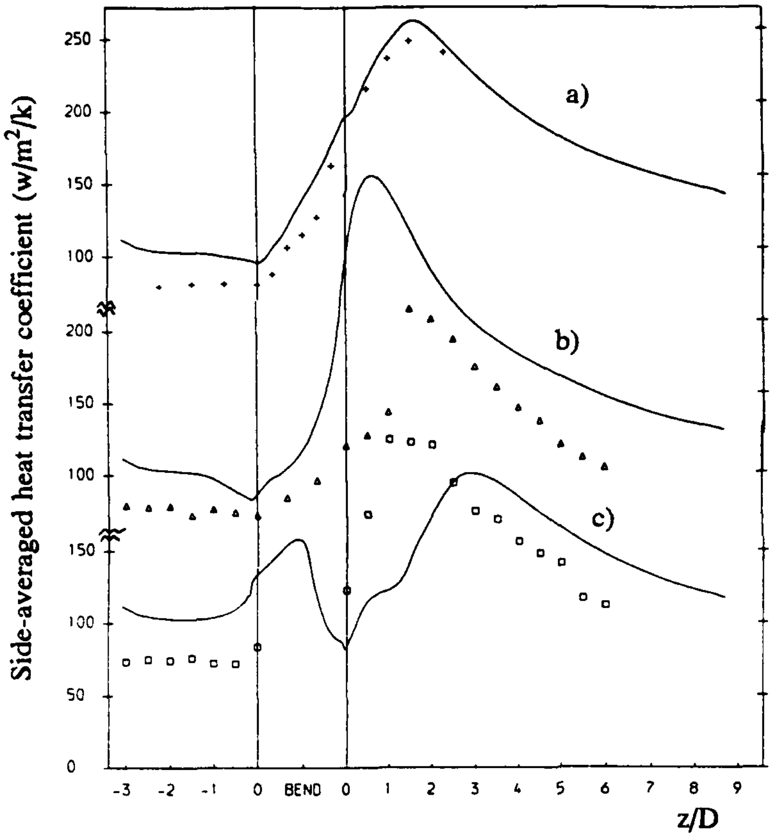

Fig 9 Development of face averaged heat transfer coefficient around U-bend
a) top wall
b) outer wall
c) inner wall

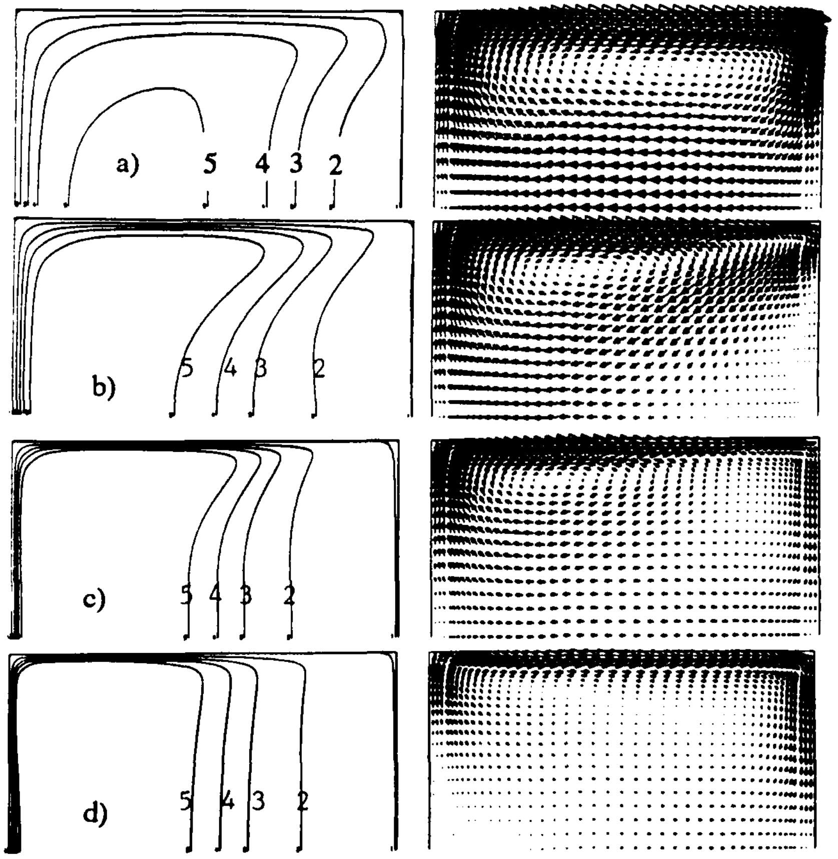

Fig 10 Development of computed axial velocity contours and secondary velocity vectors in straight rotating duct
a) 3D; b) 6D; c) 9D; d) 21D
Contour values of W/W:
1 - 0; 2 - 0.8; 3 - 1.0;
4 - 1.1; 5 - 1.2

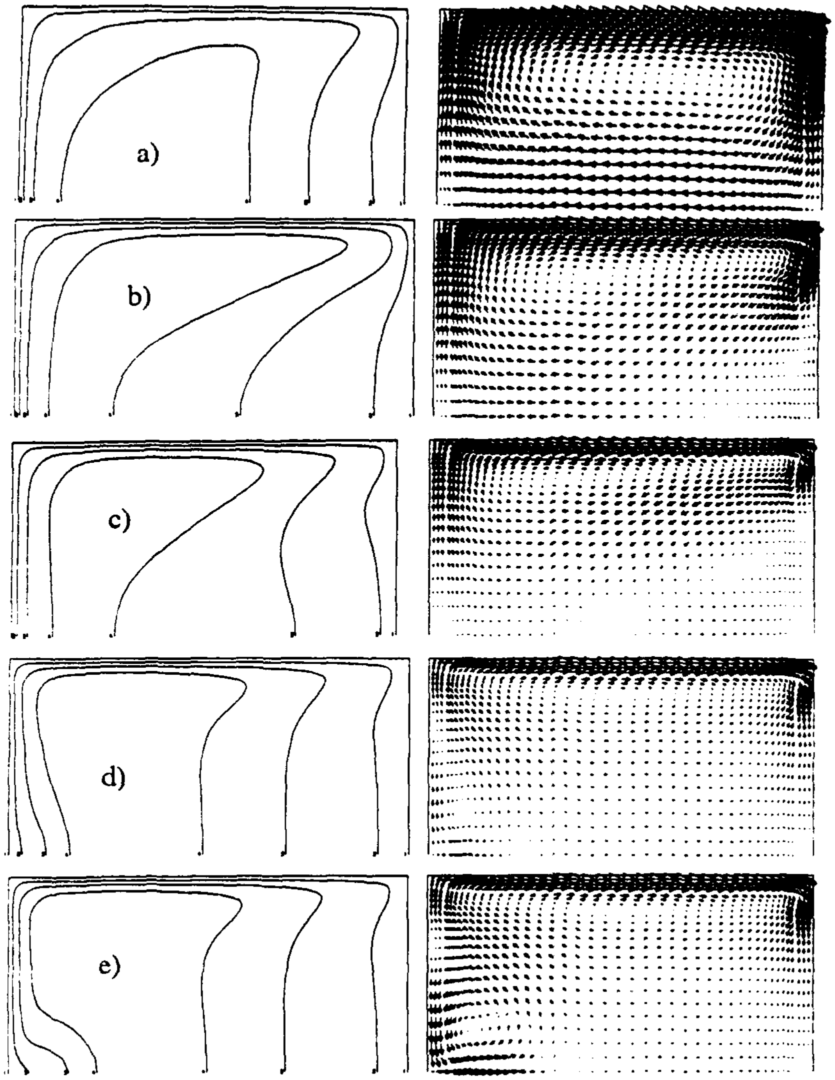

Fig 11 As Fig 10 with density constant
a) 3D; b) 6D; c) 9D;
d) 24D; e) 30D

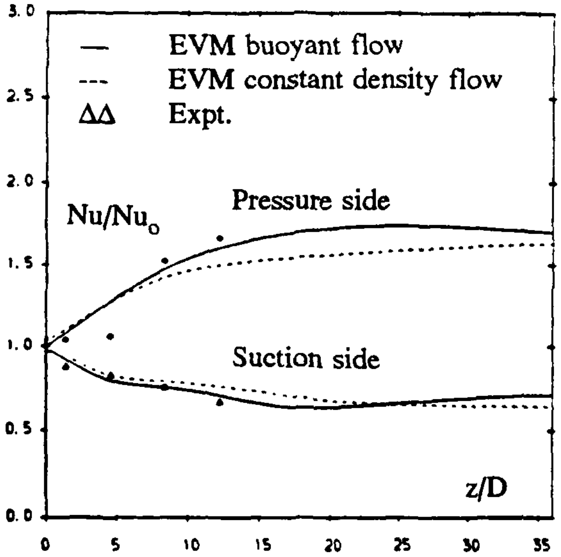

Fig 12 EVM comparisons of side-averaged Nusselt number development
Ro = 0.12

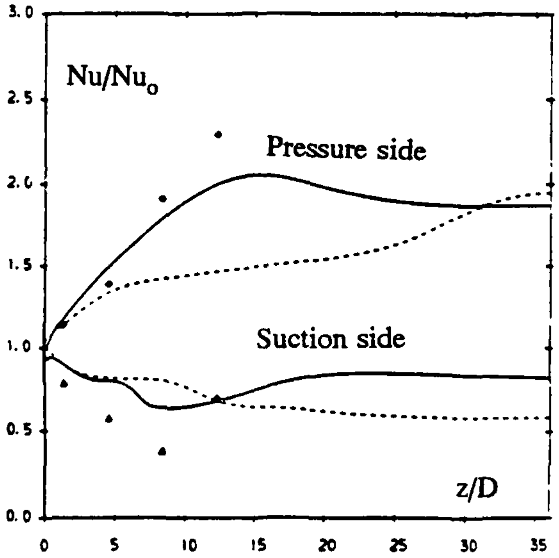

Fig 13 EVM comparisons of side-averaged Nusselt number development
Ro = 0.24

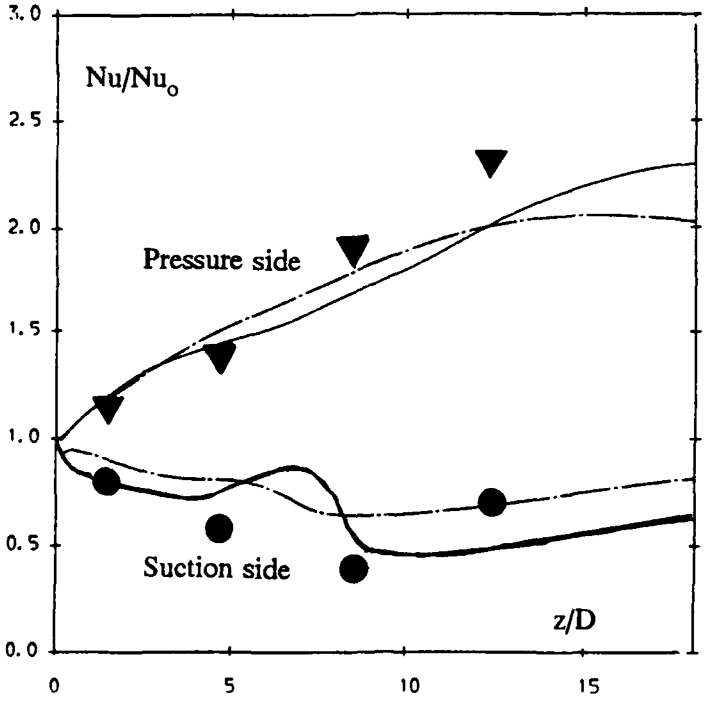

Fig 14 Comparison of ASM and EVM predictions of the Nusselt number axial development
Ro = 0.24, Ra = 10^8 (from Bo et al [4])
—— low-Re ASM; - —— -k-ε/1-eqn

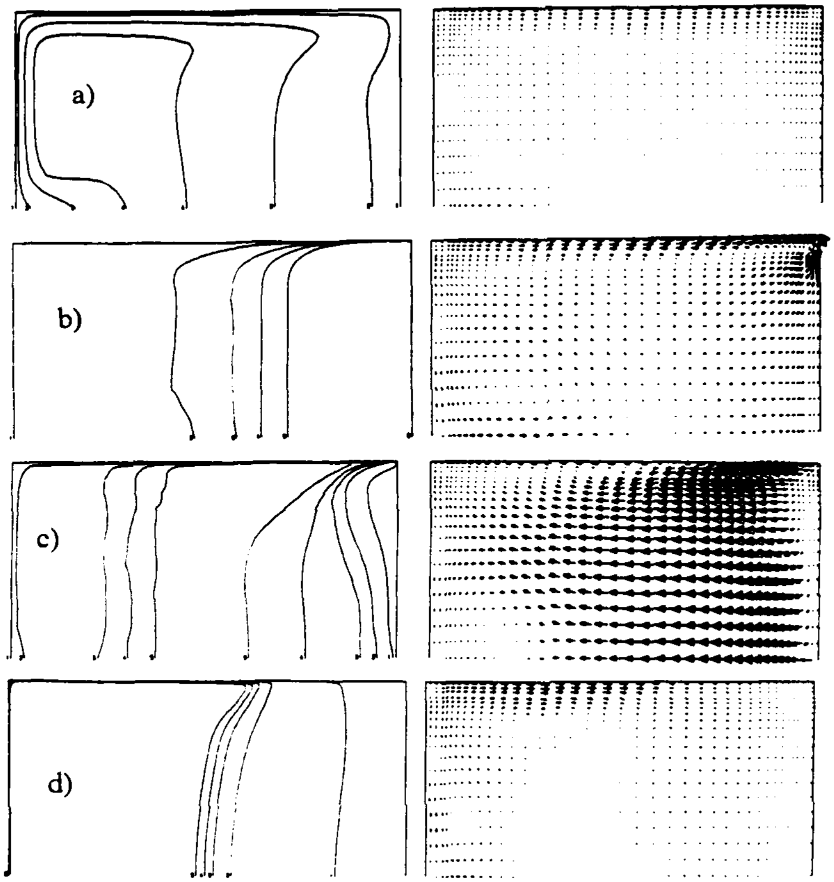

Fig 15 Development of axial velocity contours and secondary velocity vectors around rotating U-bend
a) inlet; b) 60°;
c) 150°; d) 1D downstream

Key to axial velocity contours: See Fig 10

Secondary flow vectors: an arrow length of 0.15D corresponds to a velocity magnitude of $\bar{W}$

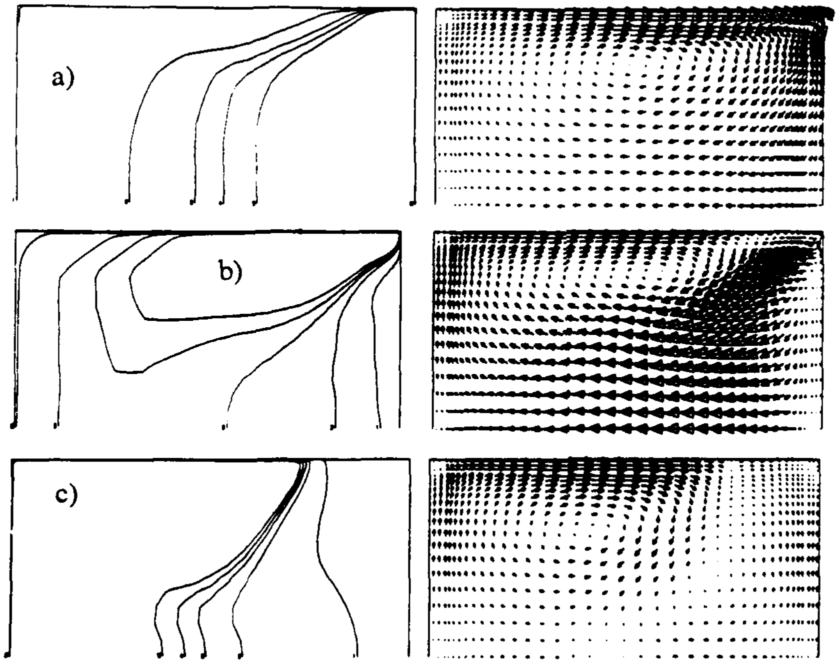

Fig 16 Development of axial velocity contours and secondary velocity vectors around stationary U-bend
a) 60°; b) 150°;
c) 1D downstream

Key as Fig 15

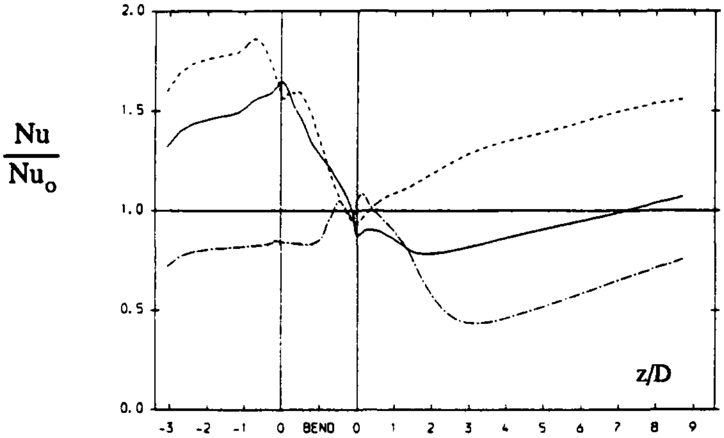

Fig 17 Distribution of relative levels of Nusselt number around rotating U-bend
—— top wall; - — - inner wall; ------ outer wall

Discussion

QUESTION 1:

DISCUSSOR: E. Benz, University of Karlsruhe

How many grid points are used to resolve the near-wall region with the one-equation turbulence model? Have you done grid independence tests for different numbers of grid points clustered in the boundary layer?

AUTHOR'S REPLY:

There are about twelve nodes in the one-equation region. We have not done grid independence tests on these flows but have done so in earlier studies of fully developed flow in rotating ducts (see Iacoirdes & Launder Numerical Heat Transfer 1988).

QUESTION 2:

DISCUSSOR: P. Harasgama, ABB

How do you treat the turbulent Prandtl number in your modified one-equation model? It is not stated in the paper.

AUTHOR'S REPLY:

As with the other models, the turbulent Prandtl number is taken as 0.9.

QUESTION 3

DISCUSSOR: W.D. Morris, University of Swansea

Have you found the need to include the effect of thermal conductivity in the tube wall when comparing heat transfer predictions with experimental data?

AUTHOR'S REPLY:

Not with the cases here reported. It's true however that if a constant wall heat flux is applied, a strong circumferential variation of temperature may lead to undetected heat leakages that, if unrecognized, will lead to spurious values of the heat transfer coefficient.

QUESTION 4:

DISCUSSOR: N. Hay, University of Nottingham

What is the penalty in computing time for using the second-moment closure instead of the k-ε equation (Ref. Fig. 14)?

AUTHOR'S REPLY:

Something like 3:1 for the parabolic computations. At least half of this is associated with the addition of the further dozen or so nodes in the buffer layer which are necessary to resolve the ε equation accurately.

QUESTION 5:

DISCUSSOR: D.T. Vogel, DLR

Why did you neglect the physical dissipation in the mathematical formulation of the energy equation? Did you use any wall functions? If so, what kind?

AUTHOR'S REPLY:

Viscous dissipation of mean kinetic energy was not included as a source term in the energy equation because, for the low speed flows with high wall heat flux considered in the study, its effect is negligible, i.e., the Eckert number is very small.

Wall functions were not used. In our early work on flows in bends we found that they led to a serious under-estimate of the secondary flow and we have accordingly abandoned them in our subsequent work.

QUESTION 6:

DISCUSSOR: F. Baron, EDF

You conclude that you expect improvement with a second-moment closure. Could you comment what part of this improvement can be expected from the fact that the Coriolis force directly influences the individual Reynolds stresses and not the turbulent kinetic energy.

AUTHOR'S REPLY:

We have separately done second-moment calculations in the rotating straight duct for the case where Coriolis forces in the turbulence equations were dropped. Their omission was not very significant. The main improvement seems to arise from the better accounting of the strain field effects on the turbulent stresses.

COOLING GEOMETRY OPTIMIZATION USING LIQUID CRYSTAL TECHNIQUE

G. Lodigiani
A. Trovati
L. Paci
Fiat Avio S.p.A.,C.so Ferrucci 112, 10138 Torino, Italy
P. Pirrelli
Elasis S.C.p.A. - Centro Ricerche Avio, V.le Arno 11, 72100 Brindisi, Italy

SUMMARY

Experimental results on the cooling performance of jet engine blading internal passages are presented. Use was made of the Liquid Crystal Transient Technique in order to obtain detailed information about heat transfer coefficients on the internal blade surfaces in presence of turbulence promoters. A peculiar behaviour of the cooling channels with turbulators was detected, which reduces the expected heat transfer effectiveness. Heat transfer experimental results, reproducing actual engine operating conditions, were employed to predict the blade metal temperature : cooling flow parameters and internal channel characteristics were therefore tuned in order to attain a suitable metal temperature distribution, and to optimize the cooling effectiveness. The outcome of experimental and calculation work was then compared to engine test blade surface temperature distribution, obtained by means of thermal paints. The comparison showed fairly good agreement, demonstrating once more the usefulness of Liquid Crystal Transient Tecnique in allowing designers to improve present blade cooling devices.

LIST OF SYMBOLS

A - Area
C_p - Specific heat
f - Friction factor
h - Heat transfer coefficient
k - Conductivity
L - Channel lenght
Pr - Prandtl number $[\mu C_p/k]$
Re - Reynolds number
St - Stanton Number $[h\,A/(W\,C_p)]$
T - Model temperature
$\overline{T}$ - Model wall temperature at melting
Ta - Ambient temperature
Tg - Gas temperature
Tm - Metal temperature
Tref- Reference temperature
$\overline{t}$ - Instant of melting
t - Time
W - Mass flow
x - Distance
α - Diffusivity $[k/(\rho\, C_p)]$
δ - Wall thickness
μ - Air viscosity
ρ - Air density

1. INTRODUCTION

The high turbine entry temperatures of modern aero engines require efficient air cooling of turbine vanes and blades. The design of such blades requires an accurate prediction of the distribution of temperature and stress within the blade, in order to evaluate the expected life in the engine environment. At this purpose the heat exchange characteristics of complex internal cooling devices must be estimated. In recent years, extensive research has been completed in order to supply designers with theoretical prediction methods. Nevertheless the available correlations are not yet sufficiently reliable when used to predict the performance of advanced cooling devices. Therefore the developement of blade cooling systems demands close interaction between theoretical and experimental work.
The experimental technique based on the use of liquid crystal paints was adopted by Fiat Avio and integrated in the industrial design process. This technique provides relevant information on heat exchange characteristics of blade cooling channels, and, what is of the utmost importance, allows the designers to check different solutions and configurations in an early phase of development, reducing the impact on the industrial manufacturing of the component.
In spite of these advantages, engine tests are still necessary. This is due both to the fact that each test at rig level reproduces only one particular aspect of the global task, and to the fact that rig experience, while more accurate than calculation, is still not able to simulate completely the phenomena occurring in the engine.

Within the paper some test results on heat exchange in blade cooling passages are first presented. Then, the use of them within the design process, leading to some modification of the initial configuration, is reported. The paper is concluded with a comparison among predicted and measured values at engine test level.

2. THE LIQUID CRYSTAL TECHNIQUE

A hot air steady flow is set up into the internal cooling passages and the surface and gas temperature transients are monitored. The model internal walls are thinly painted with liquid crystals which have the property of becoming transparent when they reach a certain melt temperature. The transient hot gas temperature is measured by means of thermocouples. In such a way it is possible to solve the Fourier heat conduction equation in the model wall and calculate the heat transfer coefficients on the surface.

The following hypotheses are made (ref. 1).

a. - the heat transfer coefficients remain constant during the coolant temperature transient;

b. - the heat transfer coefficients do not depend on the upstream wall temperature distribution;

c. - the heat conduction is one-dimensional, namely normal to the surface, and lateral conduction is negligible;

d. - the model walls are semi-infinite, namely the heat flux from the outer wall is negligible.

Accordingly, the material employed is perspex, which has low conductivity and permits visualization of the inner surface. The model walls are thick in order to approximate hypothesis c. and to better resist differential pressure loads. The melt time is short enough, minimising lateral conduction effects. Solving the Fourier equation with appropriate boundary conditions, thin-wall models might as well be used. That would entail monitoring the temperature history of the outer surface, and structural integrity problems may be encountered.

In the present practice, the Fourier one dimensional differential equation

$$\frac{\partial^2 T}{\partial x^2} = \frac{1}{\alpha} \cdot \frac{\partial T}{\partial t}$$

where x is the wall penetration coordinate, with the related boundary conditions

$$T[0,0] = T_a$$

$$-k \cdot \frac{\partial T[0,t]}{\partial x} = h \cdot \{T_g[t] - T[0,t]\}$$

$$\frac{\partial T[\delta,t]}{\partial x} = 0$$

is solved iteratively by a dedicated finite differences code once

$$T[0,\bar{t}] = \bar{T}$$

is known from the liquid crystals phase-change.

3. TEST RIG AND MODEL

A schematic layout of the rig is shown in fig. 3.1. The air is heated electrically and flowed through a by-pass line until it reaches a steady-state condition. Then it is suddenly directed to the line containing the model by means of electro-valves. Two lines exit from the model: one at tip and the other at the trailing edge. The compliance with the required test conditions, namely Reynolds and Mach numbers and inlet/outlet pressure ratios, is achieved by pre-determined valve setting. A low-pressure compressor pump drives the system, together with a vacuum-pump, the latter being used to generate the correct pressure ratios at the discharge plenum chambers. All the rig lines are instrumented with flow-meters, static pressure tappings and thermocouples.

During the test a video camera is operated to record the liquid crystals colour/phase changes on the inner surface.Once the test is over, the video recording is analysed and the phase-change instants determined.

The inner cooling passages of the blade are reproduced by an enlarged scale model. That is of the thick-wall perspex type. The flow enters the model through a plenum chamber and leaves it both at tip and through trailing-edge film cooling holes passing by plenum chambers. Thermocouples and pressure tappings are located inside the model and the plenum chambers.

The rotor blade tested model being stationary does not allow to reproduce centrifugal and Coriolis force fields generated by rotation. Moreover the heat flux in the test and the real situation are reversed. As a consequence secondary flows and buoyancy effects cannot be correctly reproduced. The only rotational effect accounted for in this test campaign was the augmented mass flow due to centrifugal forces. It was obtained by setting a higher pressure ratio in the passages.

Tested configurations

In fig. 3.2 the schematic arrangement of the cooling channels of the blades are depicted. Three adjacent cooling channels run spanwise through the blade and discharge at the tip. Also, air is discharged from film cooling holes in the trailing-edge passage. Each channel contains rib turbulators with constant pitch, height and angle to the flow. The cross-section of the leading-edge

and trailing-edge channels is almost triangular and that of the central one is square/rectangular.
Tests were executed on two configurations differing in the location and number of the turbulators. In the first configuration, called 'standard' henceforth, the ribs are placed in each channel from about 30 to 85% of the span. In the 'modified' one, ribs were removed in the hub zone in all passages and added at the tip only in the leading-edge and trailing-edge channels.

4. EXPERIMENTAL RESULTS AND CALCULATION OF BLADE COOLING SYSTEM PERFORMANCE

Due to experimental requirements, the cooling system test is subdivided in two sections : a "cold flow" one, where the model is operated without liquid crystal paint, and a "hot flow" one, where the model is operated with liquid crystal. Cooling flow fluidodynamic similarity for an operating conditionl, is achieved by maintaining the same Reynolds and Mach flow numbers for both "cold" and "hot" test. Within the assumption that the Prandtl number difference is negligible, the Stanton flow number is constant (ref. 2). In the "cold flow" test information on mass flow distribution, pressure loss - friction factors, Reynolds number evolution is gathered. In the "hot flow " test local heat transfer coefficients are measured and Stanton numbers derived.

Analytical calculations of the cooling system performance were worked out by means of a computer code (MLTCHU), resorting to various semi-empirical correlations found in literature sources. These correlations are rarely able to reproduce correctly actual cooling geometry performance, due to variation of flow parameters along the channel length. Moreover they are not able at all to estimate local values.

The results presented in the following are relevant to tests reproducing engine working conditions

Mass flow distribution

The mass flow distribution among the channels experienced during test was somewhat different from the predicted, and desired, one.

MASS FLOW DISTRIBUTION

Channel	Prediction	Measurement
1 (lead. edge)	31.5 %	34.9 %
2 (center)	34.8 %	35.2 %
3 (trail. edge)	33.7 %	29.8 %
3 tip	7.2 %	6.3 %
3 t.e.	26.5 %	23.5 %

In the first three rows the distribution among the three channels is described. The last two row reports the trailing edge channel mass flow distribution between the tip and the trailing edge holes exits. The differences between predicted and measured values are due both to errors in the prediction methods, and to the difficulty of reproducing actual engine conditions. Namely, in the experiments, it is not possible to reproduce at the trailing edge exit holes a pressure field continuously varying along the span. In addition the measured total coolant mass flow was about 12% less then the predicted one.

Reynolds number evolution

The evolution of the Reynolds number along the channel, shown in fig. 4.1 and 4.2, is a useful indication of the behaviour of heat exchange. In channels 1 (leading edge) and 2 (center blade), the Reynolds number changes because of the channel cross section variation and coolant viscosity increase, due to temperature rise : it happens to increase. In channel 3 (trailing edge), the decrease of Reynolds number is due to the decrease of mass flow exiting from trailing edge film cooling holes. The distribution of mass flow through the trailing edge holes was estimated by calculation.

Friction factor

Through the total pressure monitoring along each channel, it was possible to evaluate the evolution of the friction factor between consecutive stations :

$$f = \frac{1}{4} \cdot \Delta P_0 \cdot \frac{D}{\frac{1}{2} \cdot \bar{\rho} \cdot \bar{v}^2 \cdot l}$$

where : ΔP_0 = total pressure difference between consecutive sections
$\bar{\rho}$ = average density
$\bar{v}$ = average velocity
l = distance between stations

In fig. 4.3 and 4.4, the friction factor evolution as a function of the non-dimensional blade height is plotted. In the figures the values calculated by means of the correlations are reported, both for smooth pipe (Blasius) and for ribbed pipe (ref. 3).The friction factor shows a steep increase where the flow encounters the turbulators. In channel 1 (leading edge) it stays around the value given by the correlation for ribbed pipe, and begins to decrease where turbulators are still present. In channel 2 (center blade) it exceedes the value of the correlation for ribbed pipe, and decreases at the end of the ribbed zone. As for channel-averaged friction factors, they were found to be 5 to 20% higher than those given by the Han et Al. correlations (ref. 3).

Heat exchange

The behaviour of the coolant-blade inner passages heat exchange is depicted in fig. 4.5, 4.6 and 4.7, where the average *Stanton number* is plotted along each channel ribbed zone. The presented values of Stanton were evaluated on the basis of the measured local heat transfer coefficients. Firstly they were averaged in order to smooth out the fluctuations between consecutive ribs. It is well known how the heat transfer coefficient is doubled in the boundary layer reattachement zone, after the turbulence promoter has induced separation (ref. 4, 5). Secondly an average between the heat transfer coefficient measured on the ribbed surfaces and the coefficients relevant to smooth walls of the pipe was evaluated. These coefficients were estimated on the basis of correlations (ref. 3).

Two sets of curves are reported : the solid lines are relevant to standard configuration, the dashed ones refer to the modified configuration and will be discussed in the next paragraphs. Each set consists of three curves :

- smooth pipe correlation value (McAdams) :

$$St = 0.023 \cdot \mathrm{Re}^{-0.2} \cdot \mathrm{Pr}^{-0.6}$$

- measured values

- ribbed pipe correlation values (ref. 3) :

$$St = St(\mathrm{Re}, \frac{p}{e}, \frac{e}{D}, \beta, r)$$

where :
r = channel width/channel height
e = rib height
p = rib pitch
D = equivalent diameter
β = rib -to-flow angle

The channel ribbed zones are indicated in the figures on the lower x-axis for the standard configuration and on the upper x-axis for the modified configuration.

As for the ribbed pipe correlation, because of channel inherent problems, it was used in a approximate way. Since the cross section shapes of the channels were not exactly rectangular and continuously changing along the channel lengths, the factor r was assumed constant and equal to unity. For channel 3, the value of the rib-to-flow angle is certainly variable (and not predictable) along the span and along the channel width, because of coolant flowing through the trailing edge holes. In the correlation formula it was assumed constant. Within the limits of the use that was made of the correlation, the Stanton number measured values appear to depart gradually from the smooth pipe value where the ribbed zone starts. It almost reaches the values predicted by the ribbed pipe correlation in the middle of the ribbed zone and then starts to decrease despite the presence of ribs. The observed heat transfer evolution along the channels fairly agrees with the early decrease of the friction factor along the ribbed zone (see fig. 4.3 and 4.4).

This behaviour was compared with the studies of Han et Al. (ref. 3) where a similar behaviour was experienced in the case of a pipe with ribbed surfaces and a sudden contraction entrance. Probably it is due to peculiar boundary layer behaviour , while it separates and reattaches along the ribbed surface. These phenomena are not predictable on the bases of the currently available correlations. In addition, if the designer were to assume the values available from correlations, without taking into account these "ribbed zone extremity effects", an overestimate of the heat transfer coefficient would result. As a matter of fact the "extremity effects" sensibly lower the overall heat transfer along the channel length.

Blade metal temperature

The results of the experimental investigation on internal heat transfer coefficient were introduced in the blade design process for obtaining the metal temperature. These calculations are based on the solution of the metal conduction equation making use of boundary conditions coming from experimental results (internal surfaces heat transfer coefficients, and external hot gas temperature profile), and from CFD simulation (blade external surface heat transfer coefficients, and boundary layer evolution). The results are presented in fig.4.8, 4.9 and 4.10, where experimental thermal paint results, to be discussed in next paragraphs, are reported as well. The metal temperature in the figures is plotted against the blade non-dimesional chord for tip, mid-span and hub sections. These results showed a tip blade metal temperature too high , and, therefore, the necessity to improve the performance of the cooling system at the tip.

Thermal paint results

The best prediction numerical codes the designer might employ, the closest rig test rig experimental people might set up, nevertheless the ultimate evidence on the performance of the cooling system must still be obtained from engine test. Common practice is to make use of thermal paints, despite its limitations.

In figures 4.8, 4.9 and 4.10 the results of these tests are presented at three blade sections, namely tip, mid-span and hub, in terms of blade metal surface temperature. The temperature derived from the thermal paint colour change was firstly corrected to take into account the coating effect induced by the paint itself. The temperature relevant to the standard and the modified configuration are then compared to the values calculated for the standard configuration. The calculated and thermal paint values show good agreement.

Optimization of cooling system

The need to improve the heat transfer at blade tip was faced with the constraint of minimizing the impact on the industrial production process and tooling. The simplest solution of moving some of the turbulence promoters from blade hub to blade tip in the leading and trailing edge channels was first checked on the perspex model. In addition the pressure inlet-outlet ratio was modified with respect to the trailing edge channel, according to the coolant driving pressure available on engine. The coolant working point, in terms of mass flow distribution among channels, was modified as follows :

NEW MASS FLOW DISTRIBUTION

Channel	Standard	Modified
1	34.9 %	30.6 %
2	35.2 %	31.9 %
3 total	29.8 %	37.5 %

As it can be seen the mass flow was increased in channel 3 (trailing edge), with consequent reduction of the mass flow in channels 1 & 2.

The effect of the new location of the ribs on the heat exchange has been plotted in the already presented figures 4.5, 4.6 and 4.7 for sake of comparison. It is possible to notice that the effect of the ribs in terms of location of the maximum Stanton number is somewhat shifted towards the blade tip. After a short smooth surface zone, the presence of a new ribbed zone promotes an effective heat transfer enhancement at the tip of the blade.In order to enhance the heat exchange at the tip, without increasing too much the pressure losses, the solution of interrupting the ribbed surface for some channel length and to place ribs at the blade tip, was introduced .

It is nevertheless our opinion that if we had simply extended the ribbed zone length towards the blade tip, we would have obtained a less positive effect on the heat transfer enhancement at the blade tip, because the effectiveness of continuous ribs would probably have been reduced by the "extremity effect".

Of course, also the friction factor rises in the new ribbed zone of channel 1, while it stays constant in channel 2, as it can be seen in fig.4.3 and 4.4. Again this data is reported togheter with the standard configuration for sake of comparison.

Relying on the good agreement shown by the blade metal surface temperature calculated by making use of measured internal heat transfer coefficients, the calculation was performed again, introducing the new heat transfer distribution. The results are plotted in fig. 4.8, 4.9 and 4.10, where they are compared both to the previously calculated and measured values.

As expected, a lower metal temperature is evaluated at the tip of the modified configuration, due to the increased internal heat transfer coefficient induced by the turbulence promoters. The decrease in metal temperature averages 20 K. On the contrary, the hub section temperature is slightly higher as a result of the absence of the turbulators. The mid-span section remains basically unchanged.

5. CONCLUSIONS

The transient technique using liquid crystal as a surface temperature indicator proved to be very useful in the process of obtaining reliable prediction of the metal temperature distribution in actual engine components. It allows real reduction in the time and cost of new component development.

It is thought to be of the utmost importance to pursue further the development of this technique in order to overcome the problems of simulating the effects of the centrifugal force field present in rotating baldes.

On the other hand the present potentiality of the technique are certainly beyond the reported application. In Fiat Avio Fluidodynamic Laboratories more complex blade cooling devices, including impingement cooling, are currently being investigated.

REFERENCES

1.) Clifford, R.J., Jones, T.V. and Dunne, S.T., Techiniques for obtaining detailed heat transfer coefficient measurement within gas turbine blade and vane cooling passages, ASME 1983

2) Colladay, R.S., Stepka, F.S., Similarity constraints in testing of cooled engine parts, NASA TN D-7707, June 1974

3) Han, J.C., Park, J.S. and Lei, C.K., Heat transfer and pressure drop in blade cooling channels with turbulence promoters, NASA Report 3837, November 1984

4) Ireland, P.T. and Jones T.V., The measurement of local heat transfer coefficients in blade cooling geometries, AGARD 390, May 1985

5) Han, J.C., Heat transfer and friction characteristics in rctangular channels with ribs turbulators, ASME Vol. 110, May 1988

6) Han, J.C., Zhang, Y.M., Lee, C.P., Augmented heat transfer in square channels with parallel, crossed and V-shaped angled ribs, ASME Vol. 113, Aug. '91

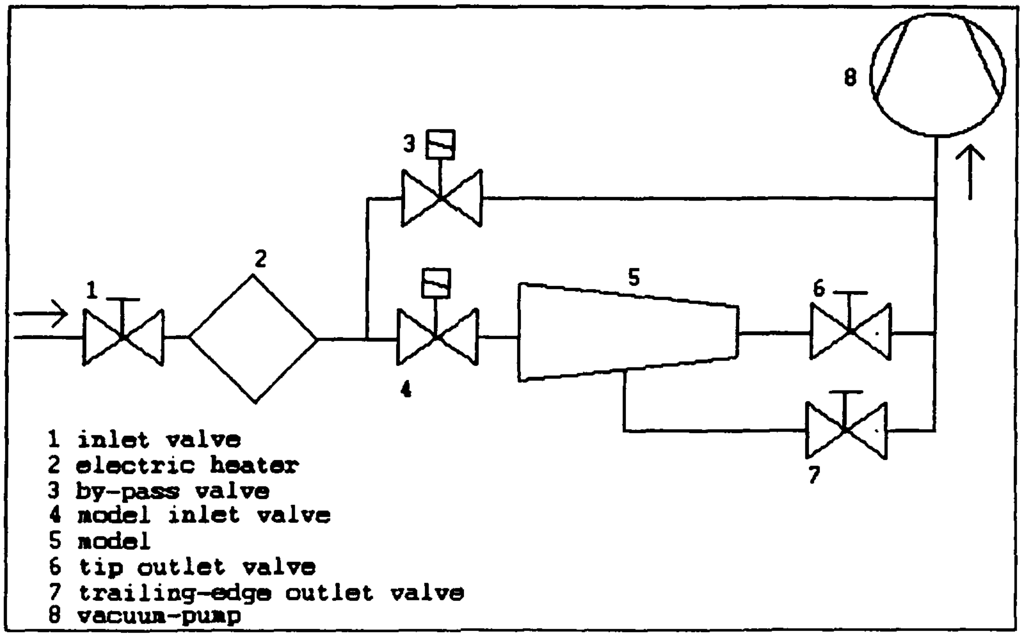
8
3
2
1
5
6
4
7
1 inlet valve
2 electric heater
3 by-pass valve
4 model inlet valve
5 model
6 tip outlet valve
7 trailing-edge outlet valve
8 vacuum-pump

Fig. 3.1 - Test rig (schematic)

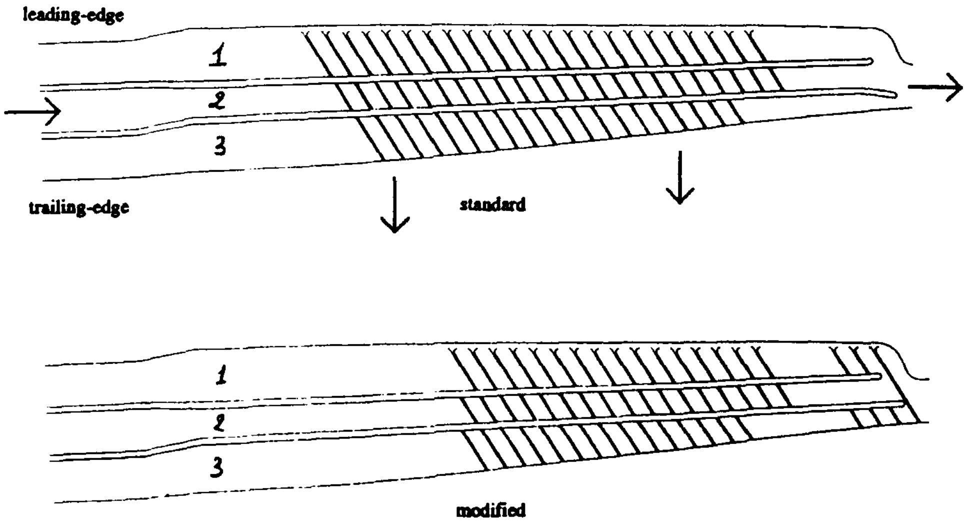
leading-edge
1
2
3
trailing-edge
standard
1
2
3
modified

Fig. 3.2 - Tested blade configurations

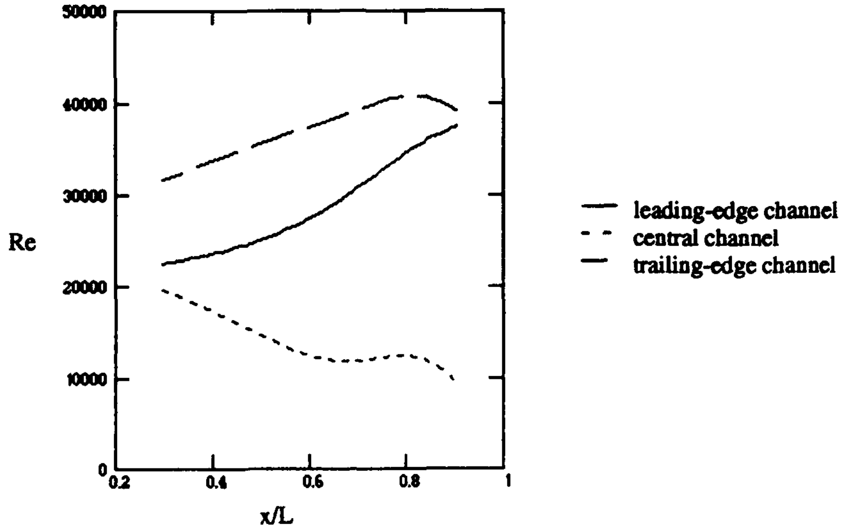

Fig. 4.1 - Standard configuration - Reynolds number distribution

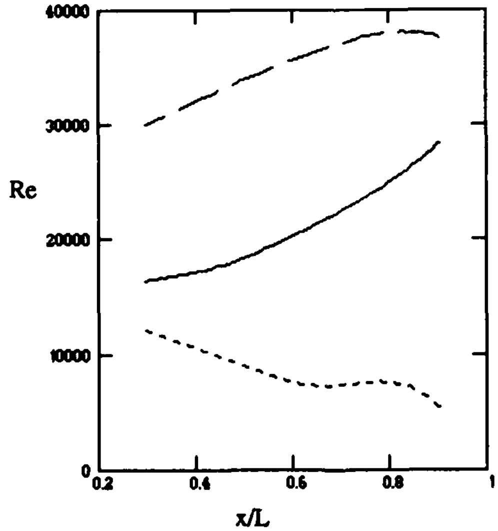

Fig. 4.2 - Modified configuration - Reynolds number distribution

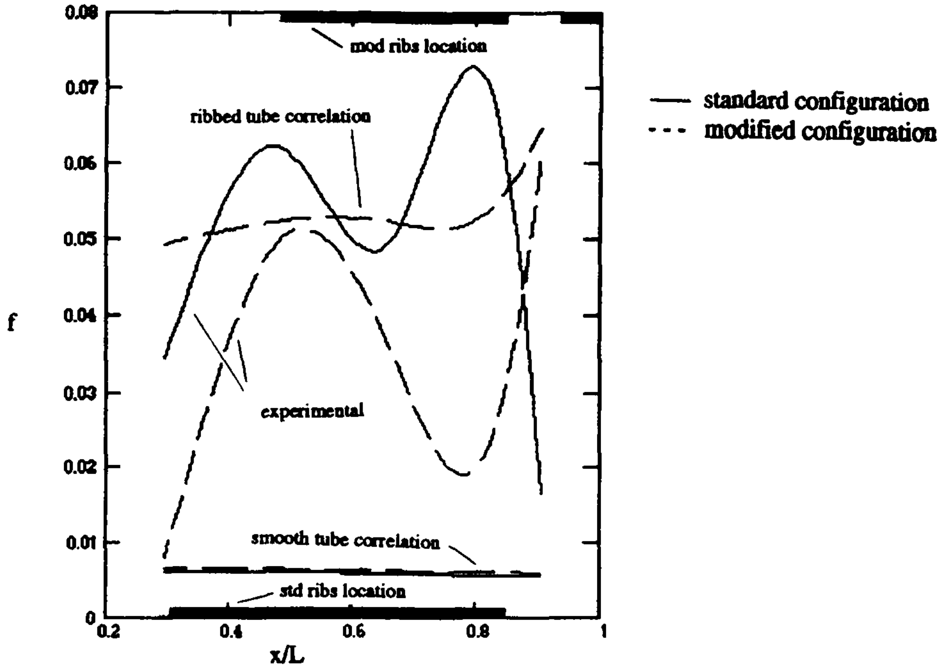

Fig. 4.3 - Leading-edge channel friction factor distribution

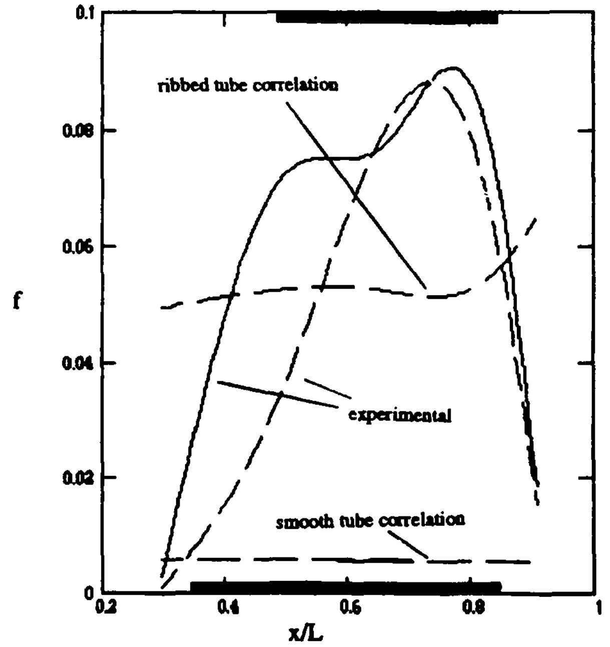

Fig. 4.4 - Central channel friction factor distribution

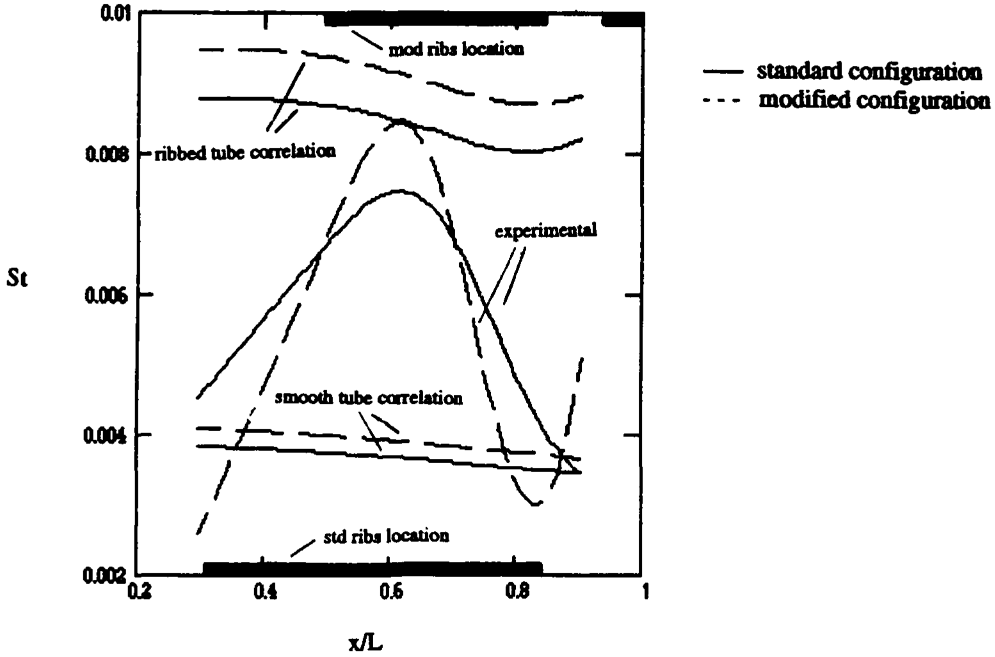

Fig. 4.5 - Leading -edge channel Stanton number distribution

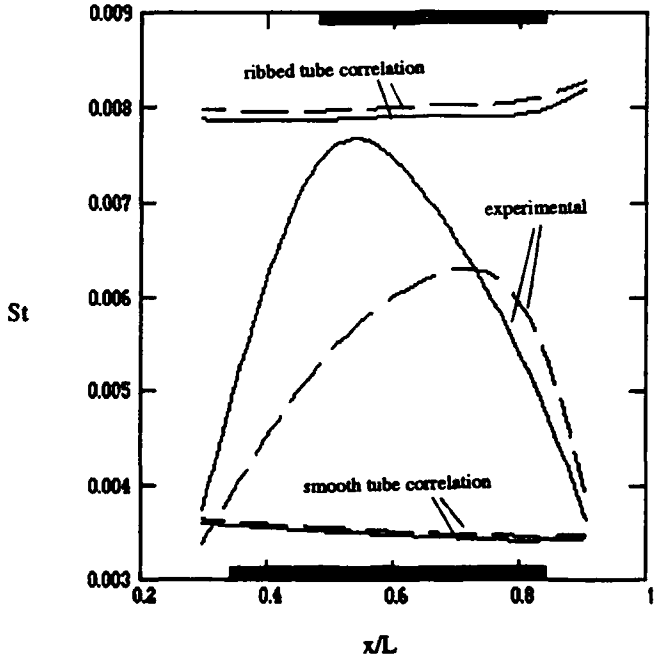

Fig. 4.6 - Central channel Stanton number distribution

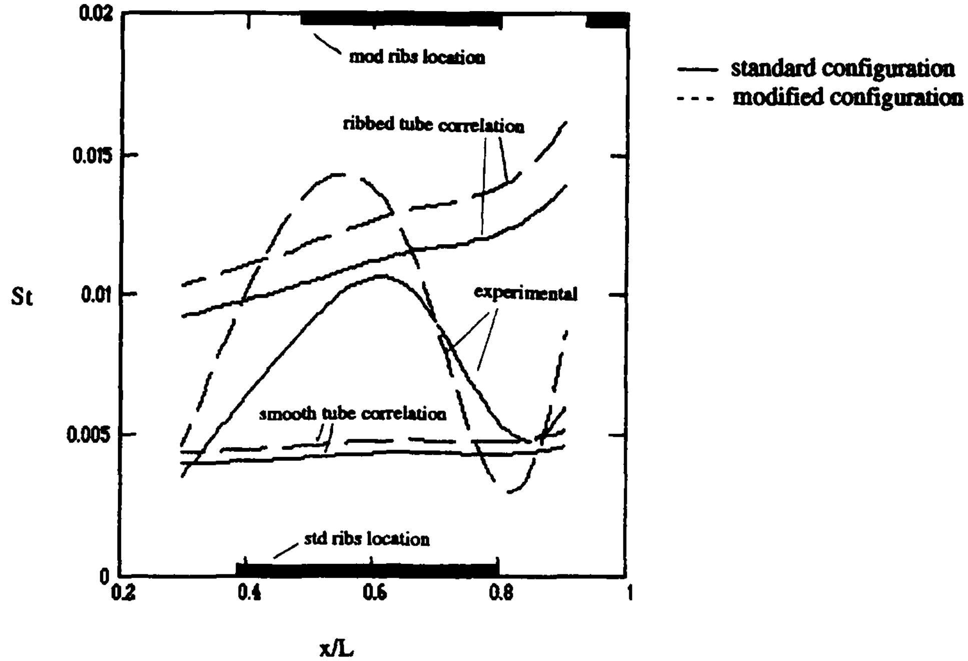

Fig. 4.7 - Trailing-edge channel Stanton number distribution

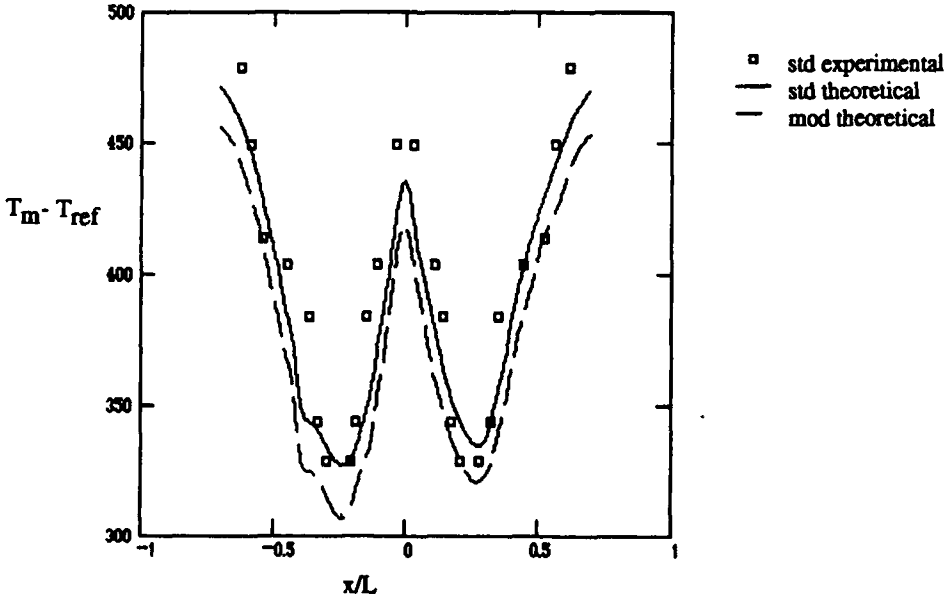

Fig. 4.8 - Tip section surface metal temperature

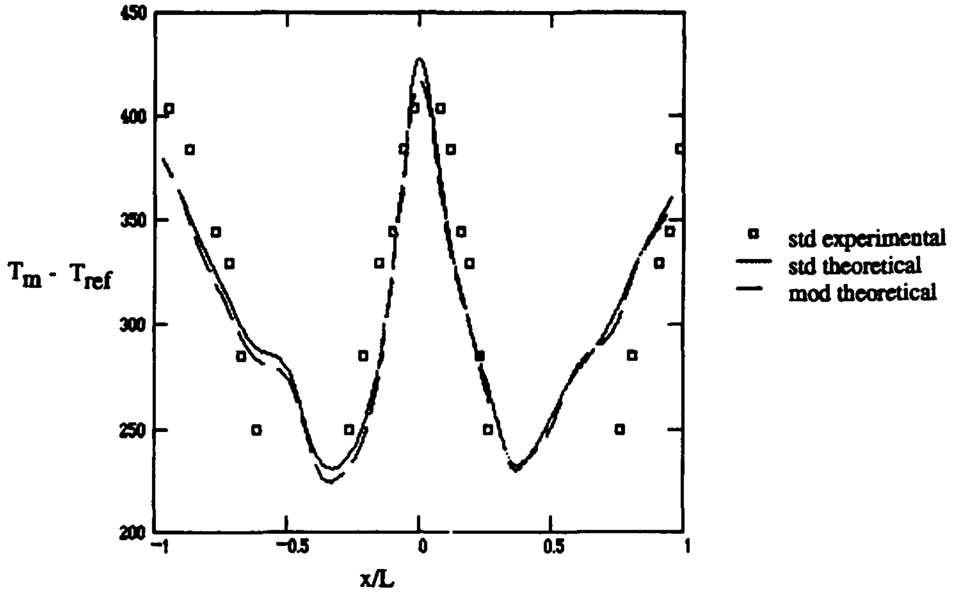

Fig. 4.9 - Mid-span section surface metal temperature

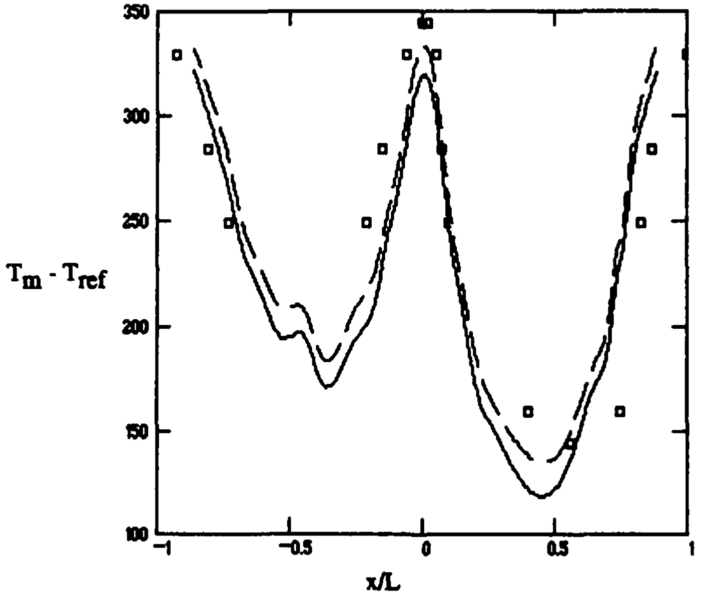

Fig. 4.10 Hub section surface metal temperature

Discussion

QUESTION 1:

DISCUSSOR: M. Owen, University of Bath

The finite-difference solution requires knowledge of the variation of surface temperature with time in order to calculate the heat transfer coefficient. As only one temperature-time point (that is, the time at which the crystals change state) is known, how is the heat transfer coefficient calculated?

AUTHOR'S REPLY:

The solution of the of equation set presented is actually based on a given variation of surface temperature with time. This temperature evolution is based on a guessed value for the heat transfer coefficient, h. The resulting local surface temperature at a given time will be the observed one (liquid crystal melting time and temperature) at that location, only if the assumed value of h is the actual one. The numerical code iterates the solution with an updated h until the calculated value of the surface temperature at a given position and time coincides with the experimental one.

QUESTION 2:

DISCUSSOR: M. Owen, University of Bath

The one-dimensional solution is only valid if $\frac{\partial^2 T}{\partial y^2}, \frac{\partial^2 T}{\partial z^2} << \frac{\partial^2 T}{\partial x^2}$. Is this always valid in your experiments?

AUTHOR'S REPLY:

Whether the lateral conduction can be neglected or not is related to the conductivity of the model material and to the duration of the experiment. In our case, the conductivity and duration were small enough such that the diffusion depth of the temperature pulse is small, and the surface temperature can actually be considered constant within small lateral distances.

FUNDAMENTAL STUDIES OF IMPINGEMENT COOLING THERMAL BOUNDARY CONDITIONS.

Lucas, M. G., Ireland, P. T., Wang, Z. and Jones, T. V.
Department of Engineering Science,
University of Oxford,
Parks Road, OXFORD.
OX1 3PJ

Pearce, W. J.
Rolls Royce PLC.,
Filton, BRISTOL.
BS12 7QE

ABSTRACT

Measurements have been made of the local heat transfer at the surface of a flat plate underneath a confined impinging jet. Thermochromic liquid crystals were used to measure the surface temperature of a uniformly heated plate cooled by an impinging jet. The temperature of the wall through which the jet passes has been controlled and experiments have been performed to measure the two heat transfer coefficients which arise from this three temperature problem. The effect of Reynolds number and plate to jet spacing on heat transfer has been investigated. The heat transfer results are discussed in terms of the interpreted flow field.

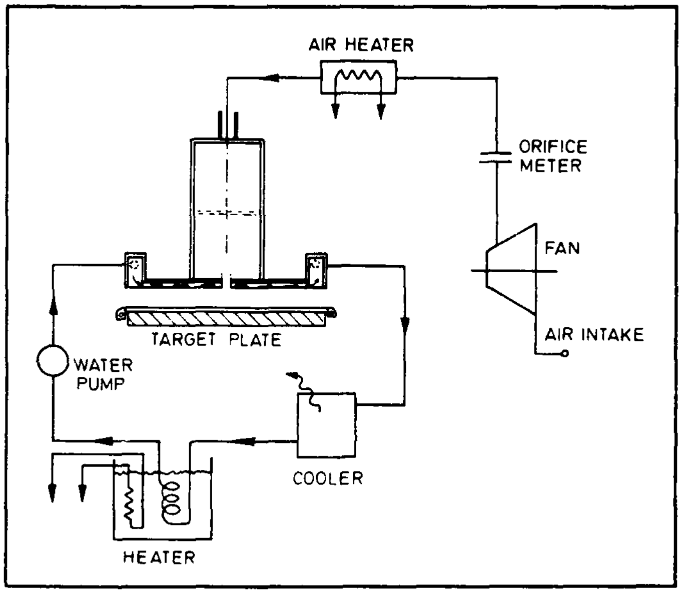

Figure 1 Schematic diagram of the experimental apparatus.

1. INTRODUCTION

External heat transfer coefficients in the vicinity of the leading edge of turbine blades are locally very high and heat conduction within the low conductivity material is not sufficient to smooth out the effect of concentrated heating on metal temperatures. The internal heat transfer coefficient at this location must be set to achieve adequate cooling, Suo (1985), and impingement cooling is often used as a means of producing high, localised heat transfer coefficients. A single row of impinging jets has been used in many designs to cool the blade leading edge. A thorough investigation of this geometry was reported by Bunker and Metzger (1988) who used a transient technique to produce full distributions of heat transfer coefficient. Obot et al. (1979) showed that the shape of the hole had a significant effect on the heat transfer beneath a single jet. In the present work, the hole was modelled at 40 times engine size as a sharp edged circular passage through the impingement (top in figure (3)) plate. This is representative of laser cut holes used in current impingement tube geometries, Van Treuren (1992). The effect of nozzle geometry on the heat transfer beneath a single impinging jet was investigated by Obot et al. (1979). In the present work, great care has been taken in the specification of the thermal boundary conditions, and the temperature of the plate from which the jet issues has been controlled and accurately measured. Application of the principle of superposition (section 3) shows that the heat transfer to the surface is quantified by two heat transfer coefficients. Both heat transfer coefficients have been measured for the single confined jet for a range of Reynolds numbers and *z/d* ratios. The jet Reynolds numbers investigated were 7500, 15000 and 30000 and the plate z/d used were 1.0, 2.0 and 3.0. The impingement hole length was the same as its diameter for all tests.

2. EXPERIMENTAL METHOD AND APPARATUS

A schematic diagram of the apparatus is given in figure (1). Air is drawn from atmosphere through the fan and passes through the orifice flow meter and heater into the plenum. A plastic foam sheet (permeance 0.23m/secPa) is located in the plenum to distribute air flow uniformly above the hole. The

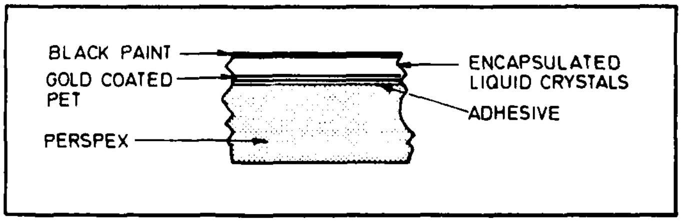

Figure 2 Heated surface used in the first method (not to scale).

Table I Nomenclature.

A	target wall temperature in case (a), fig.(5)
B	target wall temperature in case (b), fig.(5)
C_p	pressure coefficient, $(p-p_e)/(p_o-p_e)$
d	hole diameter
EFF	non-dimensional adiabatic temperature, eq.(8)
h	overall heat transfer coefficient, eq.(5)
h_j	jet heat transfer coefficient, eq.(4)
h_p	plate heat transfer coefficient, eq.(4)
k	fluid thermal conductivity
Nu	Nusselt number, hd/k
Nu_j	h_jd/k
Nu_p	h_pd/k
P	pressure
q	heat flux
r	distance from hole centreline along target plate
R	resistance per square of heater
Re_j	jet Reynolds number
T	temperature
u,v,w	velocity components
x,y,z	coordinates
X	measurand
z	plate separation
Greek	
α	molecular diffusivity
θ	dimensionless plate temperature, eq.(5)
ε	turbulent diffusivity or uncertainty
Subscripts	
ad	adiabatic
c	liquid crystal
e	exit from the confinement
j	jet
o	total conditions
p	plate
w	wall

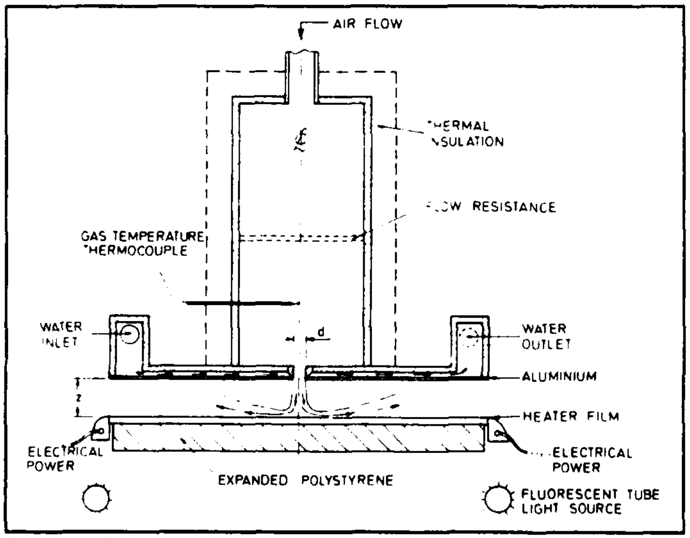

Figure 3 Detail of the test geometry.

oil of wintergreen method of Langston and Boyle (1982) was used to determine the direction of surface shear on the target plate beneath the jet. In this way it was confirmed that the air flows radially out from the stagnation point without swirl. For the present work, the jet Mach number is always less than 0.1 so the flow can be treated as incompressible. The temperature of the air in the thermally insulated plenum is measured by a thermocouple and power to the air heater is regulated by a P.I.D controller.

Two means of providing the uniform heat flux were used in these tests. In the first application of the steady state method, the heat is supplied to the perspex sheet by an electrical heater pad similar to that used by Baughn et al. (1988). The gold side of the heater is glued to the perspex, and a coating which comprises two types of encapsulated thermochromic liquid crystal is sprayed over the top, figure (2). The use of thermochromic liquid crystals in heat transfer measurements has been described recently by Jones (1992). A thermally thin layer of black ink is then sprayed on top and the composite coating is viewed from the perspex side. In this way the crystal is observed through the heater pad, glue and perspex. Oblique illumination is provided by two fluorescent tubes located as shown in figure (3) and the video camera is positioned approximately one metre beneath the target plate on the centreline indicated. Heat loss through the perspex is made negligible by allowing the sheet to achieve steady state whilst a 45mm thick sheet of expanded polystyrene is attached to the viewing side. This sheet is then removed just before the position of the liquid crystal colour play contours is recorded by a video camera. The liquid crystal colour display is calibrated in situ using a thin (0.125mm) foil thermocouple fixed to the top (non conducting) side of the heater sheet. The liquid crystal and black paint are applied over this sensor.

The second method was adopted part way through the series of tests to increase the data rate. A thin (0.8mm) sheet of perspex is used as the target plate with an Aluminium heater foil attached to the surface exposed to the impinging jet, figure (4). Heat lost from the opposite side is made negligible by placing a 70mm thick sheet of polystyrene beneath the perspex sheet. Since light can not be transmitted through this heater and the target surface can not be viewed from the impingement plate side, encapsulated liquid crystals are applied to the side *away* from the jet.

In the analysis of the experimental data, heat conducted into the perspex is assumed to be negligible. This is valid provided that heat lost from the surface away from the foil is very small and that heat conducted laterally can be neglected. Sufficient expanded polystyrene was used in both methods to ensure that the former criterion was always satisfied. The effect of lateral conduction on the measured heat transfer coefficient was assessed for both methods by solving Laplace's equation in two dimensions within the perspex. Previous workers have used the gold film method and the conduction analysis confirmed that no correction was necessary to account for lateral conduction. There are few reports of experiments which position the thermometer on the outside surface of thin walled model. Dunne (1983) showed that, for a thin walled transient method which used phase change paints on the external

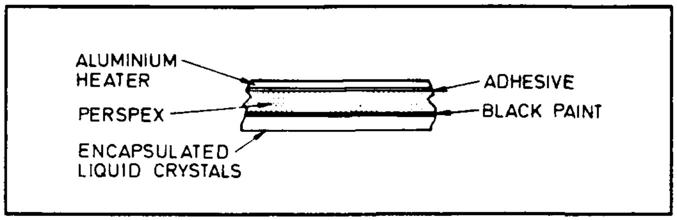

Figure 4 Heated surface used in the second method (not to scale).

surface, errors due to lateral conduction only became important when the second derivative of the substrate temperature were large. To the first order, the largest second derivatives in temperature occur at the location of the largest second derivatives in *h*. This will also be true for steady state techniques. For both methods used in the present work, the effect of conducted heat was assessed for the worst case (highest second derivative) distributions of overall *h*. The error in calculated *h* was less than 1.0% and hence no correction was applied.

The temperature of the impingement plate is held constant by passing water through the passage indicated in the figure. The water temperature is controlled by a second P.I.D. controller which governs the power supply to the water tank heater. The plate temperature was measured and for all of the tests was found to be within 0.1°C of the water temperature. For low plate temperature tests, heat acquired in the plate passage and power supplied by the pump exceed the heat losses. Under these conditions, an automotive heat exchanger (radiator) is used to cool the water flow.

Heat transfer measurements are made by setting the jet massflow rate to achieve the correct jet Reynolds number. The required jet temperature and the plate temperature are entered into the controllers. Once steady conditions have been achieved, the position of the liquid crystal colour display is logged by a video system at different foil heater power settings. The convective heat flux is calculated from the current supplied to the heater pad and the resistance per square.

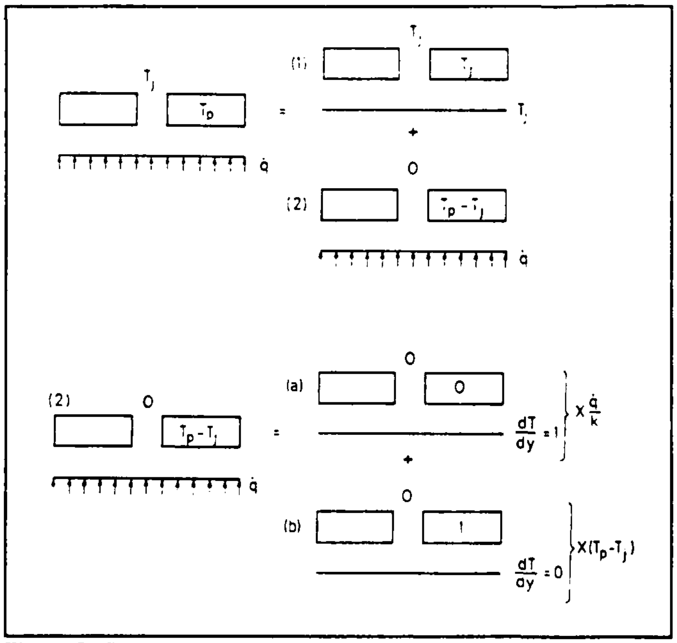

Figure 5 Component temperature fields.

The radiative heat flux from the heater foil into the cavity was estimated by calculating the heat transferred between two flat parallel grey surfaces. Over the full target plate, the net heat lost to radiation is small on account of the low emissivity of the aluminium impingement plate. For the worst case, ink coated gold heater at 41.1°C and impingement plate at 20°C, the radiative heat transfer coefficient was less than 1.0W/m²K.

3. LINEAR MODEL

The thermal boundary conditions for these tests are an isothermal impingement plate and a uniform heat flux boundary condition at the target surface[1]. Since the energy equation

$$u.\frac{\partial T}{\partial x} + v.\frac{\partial T}{\partial y} + w.\frac{\partial T}{\partial z} = \frac{\partial}{\partial x}\left((\alpha+\epsilon)\frac{\partial T}{\partial x}\right) + \frac{\partial}{\partial y}\left((\alpha+\epsilon)\frac{\partial T}{\partial y}\right) + \frac{\partial}{\partial z}\left((\alpha+\epsilon)\frac{\partial T}{\partial z}\right) \qquad (1)$$

is linear in temperature, the principle of superposition can be used to relate the actual temperature field to the sum of other temperature field solutions to this equation. Referring to figure (5), the component fields could be chosen to be the isothermal field (1) and field (2). Importantly, temperature gradients do not exist in (1) so that the heat flux at any surface must be determined by (2). Since the energy equation is homogenous, any solution for the temperature field can be multiplied by a constant factor and remain a solution provided that the summed component fields match the required boundary conditions. Hence, field (2) can be broken down into the sum of:-

- The product of q/k with (a), the field with zero temperature at the impingement plate and in the jet plenum and unit temperature gradient at the target plate.
- The product of T_p-T_j with (b), the field with zero temperature gradient at the target plate, uniform unit temperature at the impingement plate and zero jet plenum temperature.

The temperature along the target plate in solution (2) (this is T_w- T_j) can thus be written as:

$$T_w - T_j = \frac{q}{k}A + (T_p - T_j)B \qquad (2)$$

where A and B are constants. In fact A corresponds to the target wall temperature for case (a) and B is the target wall temperature for case (b). This equation can be rearranged so that the heat flux can be expressed as

---

[1] The hybrid boundary conditions correspond to those of the third kind specified by Lundberg et al (1972) for flow through concentric annuli.

$$q = \frac{(1-B)}{A}k\,(T_w - T_j) + \frac{B}{A}k\,(T_w - T_p) \qquad (3)$$

In other words, the heat flux is determined by two heat transfer coefficients,

$$q = h_j(T_w - T_j) + h_p(T_w - T_p) \qquad (4)$$

The heat transfer coefficient results are presented in full in the following section and discussed in section 6.

4. HEAT TRANSFER MEASUREMENTS

Measurements were made of both heat transfer coefficients at three jet spacings for a range of Reynolds numbers. In each case, the heater foil power required to affect liquid crystal colour play was measured for different crystal colour play positions. As each test proceeded, the power was increased in increments to move the colour display contour(s) in steps over the full surface of the target plate. In this way, as the power was increased, the crystal colour display moved from the region of lowest convective heat flux to the most cooled location.

The surface heat flux required to produce colour display at one stated set of conditions is shown in figure (6). By dividing the heat flux by the difference between the local wall and the gas temperature, an overall heat transfer coefficient can be defined. The overall heat transfer coefficient is

$$h = h_j + h_p\left(\frac{T_w - T_p}{T_w - T_j}\right) = h_j + h_p\theta \qquad (5)$$

where θ is the dimensionless plate temperature. This heat transfer coefficient (non dimensionalised by multiplying by *d*/*k*) at three radial positions is presented as a function of θ in figure (7). Two different liquid crystals (40.1°C and 31.1°C as indicated by the data labels) were used to obtain these data by applying a double crystal coating. From equation (5), the intercept with the *Nu* axis is the dimensionless jet heat transfer coefficient and the slope is the dimensionless plate heat transfer coefficient. It can seen that both the overall heat transfer coefficient and the jet heat transfer coefficient decrease with distance from the stagnation point. Interestingly, the plate heat transfer coefficient *increases* with radial distance. The variation of the heat transfer coefficients with position is discussed in section (7).

Having demonstrated that the superposition model could be used to analyse the data and that the apparatus was operating properly, it was possible to find the two unknown heat transfer coefficients, h_j and h_p, by using only two tests. Thus equation (4) could be written twice with different plate or jet temperatures, then these two equations rearranged to give h_j and h_p explicitly (equations (6) and (7)).

$$h_j = \frac{q_1(T_{w2} - T_{p2}) - q_2(T_{w1} - T_{p1})}{(T_{w1} - T_{j1})(T_{w2} - T_{p2}) - (T_{w2} - T_{j2})(T_{w1} - T_{p1})} \qquad (6)$$

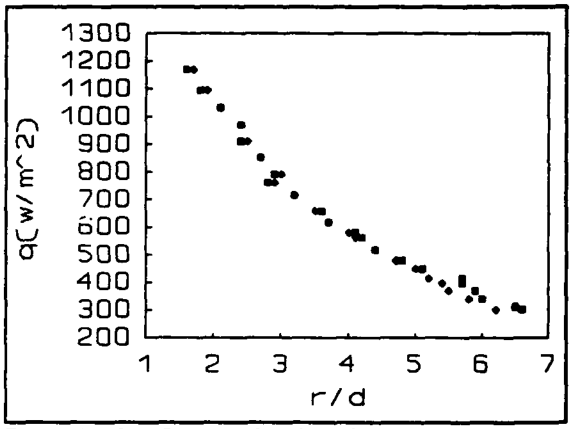

Figure 6. Heat flux as a function of radial position. z/d=2, Re_j=7500, T_p=23°C, T_j=23°C and T_c=40.1°C. The two types of marker indicate different sides of the jet.

$$h_p = \frac{q_1(T_{w2} - T_{j2}) - q_2(T_{w1} - T_{j1})}{(T_{w1} - T_{p1})(T_{w2} - T_{j2}) - (T_{w2} - T_{p2})(T_{w1} - T_{j1})} \qquad (7)$$

The measured dimensionless heat transfer coefficients are shown in figures (8) to (16). Since it would have been very time consuming to adjust the power to position the crystal colour display at specific locations, the heat transfer coefficients are calculated by interpolating for the heat fluxes (q_1 and q_2) at the locations of the presented data.

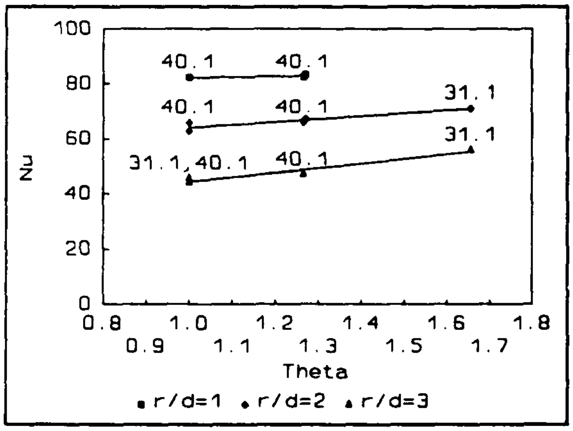

Figure 7 Overall Nusselt number as a function of dimensionless plate temperature at three different radial positions. The figures next to the data points are the liquid crystal display temperatures. Re_j=7500, z/d=2.

Uncertainty analysis.

The experimental uncertainty, ε_h, in both *h*s was calculated as being less than 4% of the total heat transfer coefficient for typical test conditions. Values of the terms used in the analysis are given in the table below, where the subscripts 1 and 2 refer to the separate experiments performed to obtain h_j and h_p.

X_i	$(T_c-T_j)_1$	$(T_c-T_p)_1$	$(T_c-T_j)_2$	$(T_c-T_p)_2$	q_1	q_2
ε_i	0.14 °C	0.14 °C	0.14 °C	0.14 °C	1.32 W/m^2	0.62 W/m^2
$\partial h/\partial X_i$	3.9 W/m^2K^2	2.9 W/m^2K^2	24.8 W/m^2K^2	18.6 W/m^2K^2	0.22 K^{-1}	0.1 K^{-1}

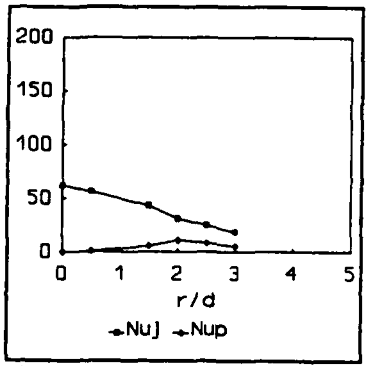

Figure 8. Separate Nusselt numbers with z/d=1, Re=7500.

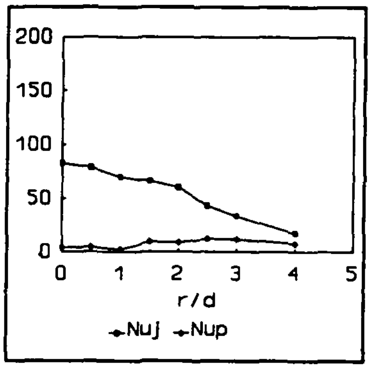

Figure 9. Separate Nusselt numbers with z/d=1, Re=15000.

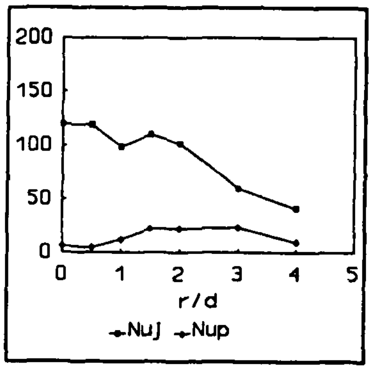

Figure 10. Separate Nusselt numbers with z/d=1, Re=30000.

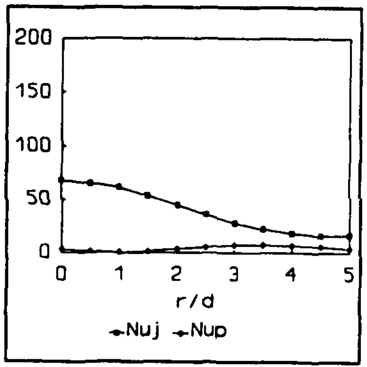

Figure 11. Separate Nusselt numbers with z/d=2, Re=7500.

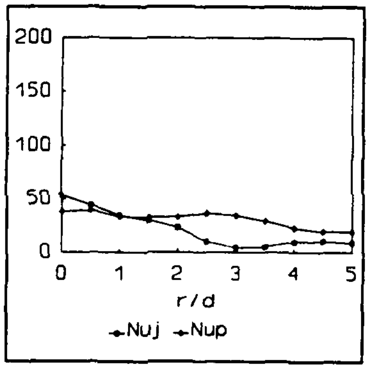

Figure 12. Separate Nusselt numbers with z/d=2, Re=15000.

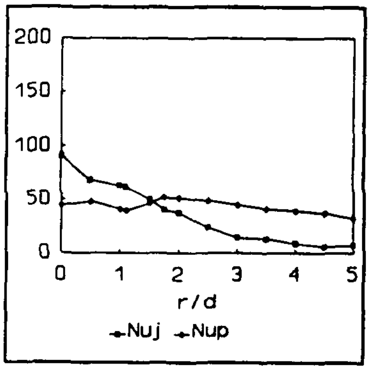

Figure 13. Separate Nusselt numbers with z/d=2, Re=30000.

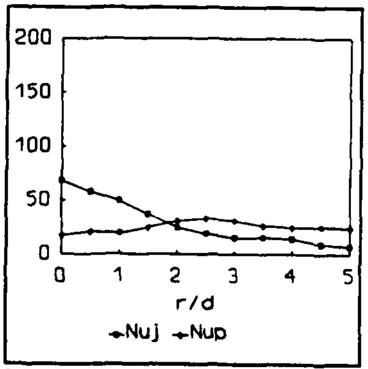

Figure 14. Separate Nusselt numbers with z/d=3, Re=7500.

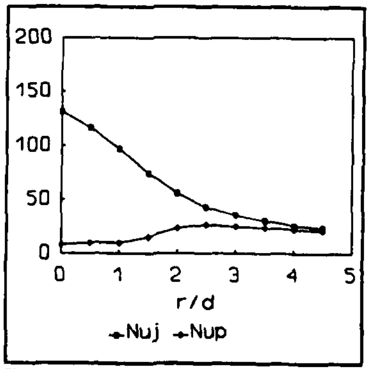

Figure 15. Separate Nusselt numbers with z/d=3, Re=15000.

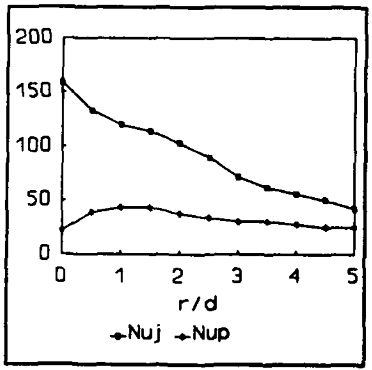

Figure 16. Separate Nusselt numbers with z/d=3, Re=30000.

5. PRESSURE AND FLOW MEASUREMENTS

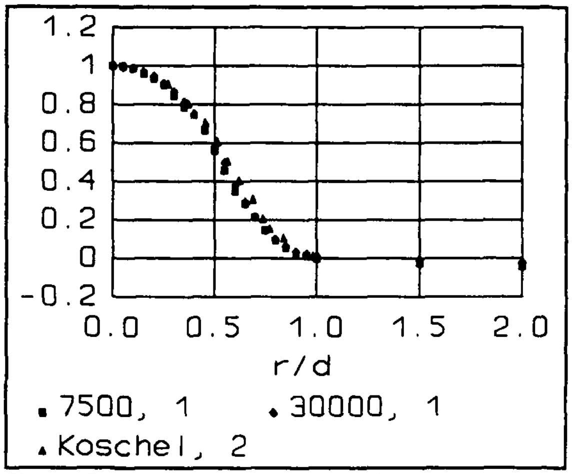

Figure 17. C_p along the target plate surface as a function of r/d, z/d=1.

The pressure coefficient along the target plate is presented in figures(17) to (20) where the legends refer to the jet Reynolds number and z/d respectively. In the impingement region the data are very close to the free jet data after Koschel who tested at Re_j=27,500. The pressure is highest at the stagnation point, where it recovers the plenum total pressure, and then decreases with distance as the flow accelerates in the impingement region. At r/d greater than 1.0 the gentle increase in pressure is evidence of the flow slowing down as it diffuses radially. Similar pressure distributions were measured for a z/d of 5 (not presented) although the plenum pressure was not recovered at the stagnation point.

A simple investigation of the flow field was performed using a small (5mm) tuft suspended on a nylon line at a jet Reynolds number of 30000, figure (21). The tuft was able to rotate freely and was used to determine the flow direction. The jet Reynolds number was decreased to 15000 for the z/d=1 configuration and no significant change in the interpreted flow field was detected. It is interesting to note the large extent of the air which flows back towards the jet along the top plate. For the largest spacing tested (z/d=3), this doughnut shaped recirculation vortex extended almost to the edge of the square plate. The same flow field was observed by Saripalli for single confined jets. He correlated the confinement diameter at which flow started to be drawn back from the surroundings against the plate spacing (presented in Bower et al. (1981)).

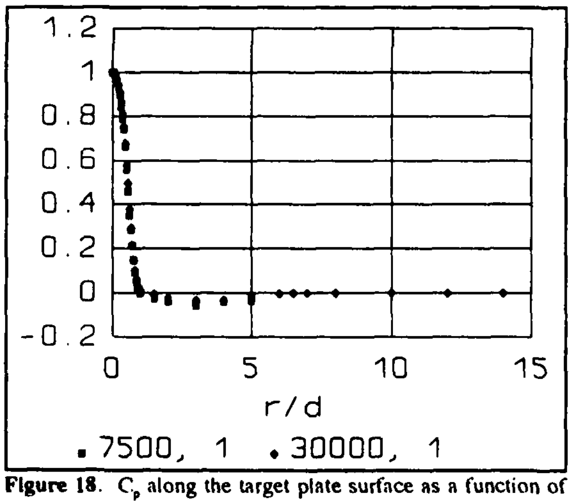

Figure 18. C_p along the target plate surface as a function of r/d, z/d=1.

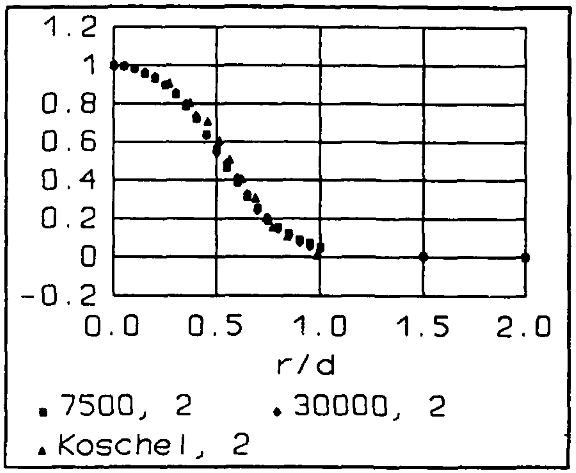

Figure 19. C_p along the target plate surface as a function of r/d, z/d=2.

The discharge coefficient was measured for all three plate spacings and was found to be a weak function of both Reynolds number, over the range 7500 to 30000, and of z. A value of 0.83±0.03 was measured for the confined jet.

6. DISCUSSION OF THE RESULTS

In all cases the jet heat transfer coefficient is highest at the stagnation point and its profile bears a marked similarity to that measured beneath rows of jets impinging onto curved surfaces (Bunker and Metzger (1988) and Pagenkopf and Hennecke (1992)).

Stagnation point heat transfer.

The overall dimensionless heat transfer coefficient ($Nu_j + Nu_p$) at the stagnation point is presented in figure (22). This corresponds to the Nusselt number when the plate temperature is the same as the jet temperature and is the most appropriate

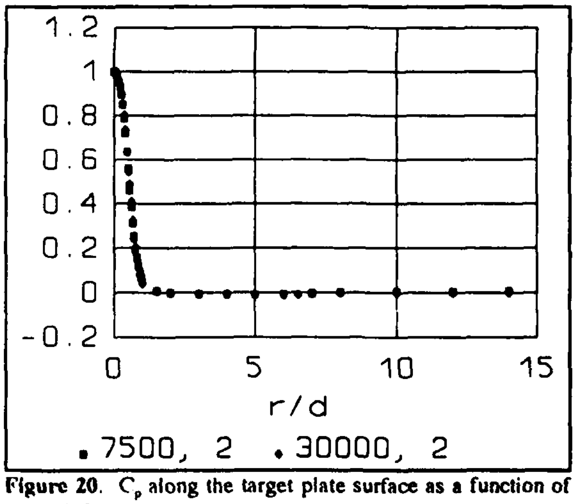

Figure 20. C_p along the target plate surface as a function of r/d, z/d=2.

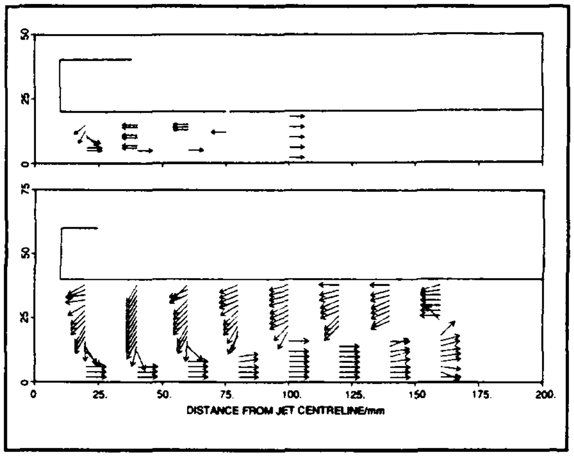

Figure 21. Flow field interpreted from the tuft deflection at Re_j=30,000, d=20mm.

case to compare with free jet data when the entrained air from the surroundings is at the same temperature as the jet. In the present work, the jet entrains air from the enclosure which passes along the surface of the impingement plate. For the three spacings tested, the heat transfer increases with Reynolds number. The heat transfer levels for z/d spacings of 1 and 2 are practically the same. The same insensitivity to plate spacing was observed for free jet data by Yan et al. (1992) at values of z/d of 2 and 4. This is explained by the presence of the potential core of the jet which extends to the plate (C_p=1.0) for smaller spacings. The higher heat transfer levels measured by these authors could either be due to the absence of the enclosure, or the fact that the jet flow was fully developed pipe flow with greater turbulence on the centreline than the short orifice used in the present work. The latter explanation is more reasonable since the current pressure data is very similar to the free jet data (section 5). The Nusselt number levels increase markedly for the spacing of 3D. The same effect can be seen for the free jet, but at the greater spacing of 6D (not shown here). This increase is associated with the end of the potential core (C_p is less than 1.0 for the confined jet at z/d=5) and is due to the arrival of turbulence from the shear layers at the stagnation point.

Of great interest is the significance of h_p. This heat transfer coefficient increases with Reynolds number at all spacings and its effect is most pronounced for the z/d=2 configuration where, at r/d>~2, its value exceeds the jet heat transfer coefficient. In this region, the driving gas temperature must be strongly influenced by contact between the recirculating flow and the impingement plate. It is thought that this effect is more pronounced for the z/d=2 and z/d=3 geometries since, in both cases, the extent of the recirculation is much greater than for the z/d=1 case.

Adiabatic wall temperature.
The dimensionless adiabatic wall temperature can be calculated from the two heat transfer coefficients by rearranging equation (4) to give

$$EFF = \frac{T_{ad}-T_p}{T_j-T_p} = \frac{h_j}{h_j+h_p} \qquad (8)$$

In cases where the plate heat transfer coefficient is large, the adiabatic temperature can be seen to be significantly different to the plenum temperature. A change in the temperature potential beneath free jets was measured by Striegl and Diller (1984) for a single slot jet when the temperature of the surroundings was increased to the target plate temperature. More recently Baughn et al. (1991) presented values of the effectiveness for a circular free jet. The effectiveness decreased continuously with r/d although the large reduction in effectiveness for r/d<2 measured for the confined jet with z/d=2 was not observed by these authors.

7. CONCLUSIONS

(1) A theoretical description of the effect of impingement plate temperature has been proposed based on superposition of solutions to the temperature field. The analysis introduced new heat transfer coefficients which have been measured. The theoretical model was verified in a series of tests.

(2) A steady state double test method has been developed for measuring these heat transfer coefficients for a uniform heat flux boundary condition.

(3) The temperature of the plate has been shown to have a significant effect on the overall heat transfer at the target plate for the z/d=2 and z/d=3 configurations. It is thought likely that a similar effect is present for curved target surfaces.

8. ACKNOWLEDGEMENTS

The authors gratefully acknowledge the support of the Science and Engineering Research Council, the Ministry of Defence (Procurement Executive) and Rolls-Royce Plc for the work

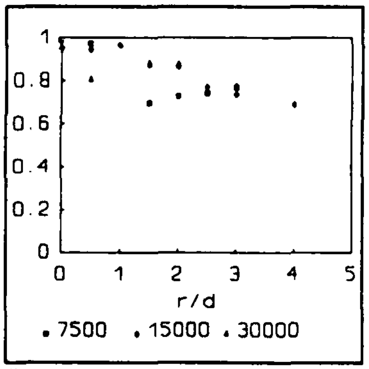

Figure 22
EFF as a function of r/d, z/d=1.

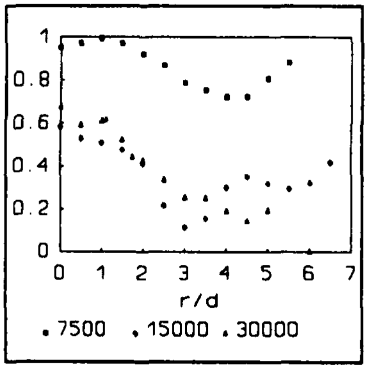

Figure 23
EFF as a function of r/d, z/d=2.

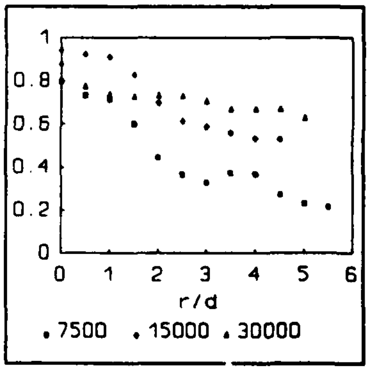

Figure 24
EFF as a function of r/d, z/d=3.

reported here. The technical expertise of Mr. P.J. Timms was much appreciated.

9. REFERENCES

Baughn, J. W., Hechanova, A. E. and Yan, X.
" An experimental study of entrainment effects on the heat transfer from a flat surface to a heated circular impinging jet."
Journal of heat transfer, vol., 113, pp.1023-1025., 1991.

Baughn, J. W., Ireland, P. T., Jones, T. V. and Saniei, M.
" A comparison of the transient and heated-coating methods for the measurement of local heat transfer coefficients on a pin fin."
Paper 88-GT-180, *33rd ASME International gas turbine and aeroengine congress and exposition, Amsterdam*, 1988.

Bower, W. W, Saripalli, K. R. and Agarwal, R. K.
" A summary of jet impingement studies at Mc Donnell Douglas Research Laboratories."
Paper AIAA-81-2613, *AIAA/NASA Ames, VSTOL Conference, Palo Alto, California*, 1981.

Bunker, R. S. and Metzger, D. E.
" Local heat transfer in internally cooled turbine airfoil leading edge regions - Part I: Impingement cooling without film coolant extraction."
ASME Winter Annual Meeting, 1988.

Dunne, S. T.
" A study of flow and heat transfer in gas turbine blade cooling passages."
D. Phil. thesis, *University of Oxford*, 1983.

Jones, T.V.
" Aerodynamic and heat transfer testing."
Liquid crystals today, vol. 2., pp. 4-5, 1992.

Koschel, W.
" Experimental results on heat transfer rates of single and multiple air jets impinging normally onto walls."
Berlin University.

Langston, L. S. and Boyle, M. T.
" A new surface flow visualisation technique."
Journal of fluid mechanics, vol. 125, pp. 53-57, 1982.

Lundberg, R.E., Reynolds, W.C. and Kays, W.M.
" Heat transfer with laminar flow in concentric annuli with constant and variable wall temperature and heat flux."
NASA TN D-1972, 1963.

Obot, N. T., Majumdar, A. S. and Douglas, W. J. M.
" The effect of nozzle geometry on impingement heat transfer under a round turbulent jet."
AMSE Winter Annual Meeting, 1979.

Pagenkopf, U. and Hennecke, D. K.
" Local and average transfer coefficients due to different impingement arrangements for blade cooling applications."
International centre for heat and mass transfer conference, Athens, Greece, 1992.

Striegl, S. A. and Diller, T.E.
" The effect of entrainment temperature on jet impingement heat transfer."
Journal of heat transfer, vol. 106, pp.27-33, 1984.

Suo, M.
" Turbine Cooling."
In *Aerothermodynamics of aircraft engine components*, edited by G. C. Oates, AIAA education series, Chapter 5, 1985.

Van Treuren, K.
" Impingement cooling studies"
Msc transition report, *Department of Engineering Science, University of Oxford*, 1992.

Yan, X., Baughn, J. W. and Mesbeh, M.
" The effect of Reynolds number on the heat transfer distribution from a flat plate to an impinging jet."
Accepted for the *ASME winter annual meeting, Anaheim, California*, 1992.

Discussion

QUESTION 1:

DISCUSSOR: G. Andrews, University of Leeds

The flow recirculation within the impingement gap to which you refer, is an important feature of impingement heat transfer which has received little study. My research group at Leeds made the first publication on the effect at the last AGARD heat transfer meeting in 1985 and in four papers since then (Ref 1 - 5). The recirculation is responsible for the impingement jet surface heat transfer which you have measured. However, this effect is minimized for the single jet geometry that you used and is much stronger for arrays of jets as used in blade cooling and in the work at Leeds. Multi-recirculation zones are set up having about one half the size of the impingement jet-pitch, so that there is a double counter rotating vortex between each impingement jet row. The conductive recirculating jet velocity can be a major function of the initial impingement jet velocity and the surface averaged jet-plate heat transfer coefficient can be about fifty percent of that on the impingement wall, and this is higher for $Z/D < 1$. For low coolant mass flow rates this results in significant heating of the impingement jet wall which in turn heats the impingement jet.

This effect is also present when film cooling fluid extraction or impingement/effusion cooling occurs as discussed in Paper 30 of this symposium. This geometry, although it appears more complicated, is actually easier to analyze since each impingement/film hole has a source and sink for the fluid. For impingement jet arrays, the complex jet recirculation aerodynamics are influenced by the impingement gap crossflow and there has been, to my knowledge, no attempt at predicting these complex aerodynamics.

Do you intent to extend your work to arrays of impingement jets and to film cooling jet extractions?

References:

1. Andrews, G.E., Asere, A.A., Hussain, C.I. and Mkpadi, M.C., 1985 "Full coverage impingement heat transfer; the variation in pitch to diameter ratio at a constant gap" AGARD CP 390, Heat transfer and cooling in gas turbines, pp. 26.1 - 26.13.
2. Andrews, G.E., Asere, A.A., Hussain, C.I. and Mkpadi, M.C., Transpiration and impingement/effusion cooling of gas turbine combustion chambers, Proc. Seventh ISABE, Beijing, AIAA, pp. 794 - 803, 1985.
3. Andrews, G.E., Asere, A.A., Hussain, C.I., Mkpadi, M.C. and Nazari, A., Impingement/effusion cooling: overall wall heat transfer, ASME Paper 88-GT-290, 1988.
4. Al, Dabagh, A.M,. Andrews, G.E., Abdul Hussain, R.A.A., Husain C.I., Nazarai, A. and Wu, J., Impingement/Effusion Cooling: the influence of the number of impingement holes and pressure loss on the heat transfer coefficient, ASME Paper 89-GT-188, 1989, also published in ASME Transactions, 1990.
5. Andrews, G.E., Al Dabagh, A.M., Asere, A.A., Bazdidi-Tehrani, F., Mkpadi, M.C. and Nazari, A., "Impingement/Effusion Cooling," AGARD PEP 80th Symposium, 1992, Paper 30.

AUTHORS' REPLY:

The authors thank Dr. Andrews for his interesting question and acknowledge the extensive work of his research group in the field of impingement cooling. The interaction of the impingement plate with the target plate is clearly of great interest to the designers of combustion chambers as well as to turbine blade designers. However, the influence of the impingement plate temperature on the target wall heat transfer coefficient does not appear to have been previously quantified. The current investigation is to be extended to measure this effect in impingement arrays with and without film cooling.

PREDICTION OF JET IMPINGEMENT COOLING SCHEME CHARACTERISTICS (AIRFOIL LEADING EDGE APPLICATION)

A. Riahi
H. J. Saabas
W. Abdel Messeh
Pratt & Whitney Canada Inc.
1000 Marie Victorin
Longueuil, Quebec, Canada.

ABSTRACT

A control volume finite difference method based on the work of Rhie in conjunction with (1) a high Reynolds k-ϵ model and (2) a two layer turbulence model has been used to predict the heat transfer coefficients underneath an impinging circular jet in the absence of crossflow. The numerical results are compared to experimental measurements for two different impingement height to jet diameter ratios: $H/D=2$, and 10. The comparisons indicate that although both the k-ϵ and the two layer turbulence models are adequate in the prediction of the flow field, the two layer model resulted in heat transfer predictions that were closer to experimental observations. It was also observed that the predicted heat transfer coefficients for the case of $H/D=2$ were sensitive to the assumed jet exit turbulence levels, whereas they were not for $H/D=10$. This information is useful to the designer of cooled turbine components.

NOMENCLATURE

D	jet diameter
H	distance between jet outlet and impingement plate
h	heat transfer coefficient
k	turbulent kinetic energy
L	mixing length
n	coordinate normal to wall
Nu	Nusselt number $=hD/\lambda$
p	pressure
P	production of turbulent kinetic energy
Re	Reynolds number $=\rho V_j D/\mu_l$
S	volumetric source term
T	temperature
u	mean velocity component
V_j	average jet outlet velocity
x, y, z	Cartesian coordinates

Greek Symbols

ϵ	dissipation of turbulent kinetic energy
Γ	diffusion constant
λ	thermal conductivity
ϕ	transported scalar
ρ	density
μ_t	turbulent viscosity
μ_l	laminar viscosity

Subscripts

ϕ	pertaining to transported scalar ϕ
i, j	indices in Cartesian tensor notation
w	wall

Superscripts

$'$	fluctuating component
e	effective
l	molecular
t	turbulent

1 INTRODUCTION

The high turbine inlet temperatures encountered in many modern gas turbine engines necessitate the cooling of the turbine components. One cooling scheme that offers high heat transfer coefficients, as well as control over the distribution of the coolant heat transfer is impingement. This type of cooling can be found within stator and rotor aerofoils, as well as on vane platforms, and shroud housings. The level of heat transfer is dependent on many variables: (1) the geometry of the impingement array, including the impingement plate to impingement surface spacing [2, 12, 13, 17, 19, 29]; (2) the presence and temperature of a cross flow [8, 9, 11, 16, 22]; (3) the level of turbulence in the jet [18]; (4) the jet outlet conditions (velocity, turbulence profiles) [11, 5, 6] and (5) the manner in which the jet flow leaves the domain of interest after impingement [15, 22]. A recent review of the impingement literature has been compiled by Downs [7].

The level of impingement heat transfer obtained in any given cooling scheme design is a function of many flow and geometrical parameters. Often, experimental data for the array geometry and domain outflow boundaries used in the design do not exist. It would be costly to test each design configuration experimentally. Furthermore, it is not feasible to perform these tests within the time frame allowed for the design. Computational Fluid Dynamics (CFD) is one method that will ultimately allow for a tool whereby the effects of a change of any of the above mentioned parameters on the heat transfer can be quantified.

The computer simulation of any flow of interest requires (1) a mathematical model of the physical problem which includes the partial differential equations, turbulence models and boundary conditions that govern the distribution of the unknown dependent variables in the region of interest; (2) a numerical method for the solution of the mathematical model; and (3) a computer implementation of the numerical method. The mathematical model in conjunction with a given numerical solution procedure is referred to as a numerical model.

For a numerical model to be useful, all three of the aforementioned requirements have to be met successfully. The appropriateness of a proposed mathematical model can be ascertained by comparing the results of a numerical solution to experimental data, in which detailed boundary information has also been measured. In view of this, the purpose of this paper is to predict the heat transfer coefficients under a single circular jet impinging on a flat plate with no imposed cross flow for two different jet plate to impingement surface spacings: $H/D = 2$, and 10. These values are typical of the range encountered in gas turbine engines. The numerical predictions from this study will be compared to experimental data available in the literature. This will allow for an evaluation of the appropriateness of the chosen mathematical model, as well as provide some insight into the flow and heat transfer characteristics of an impinging jet.

2 MATHEMATICAL MODEL

The thermofluid behaviour of a steady incompressible impinging jet can be described by a set of time averaged partial differential equations that can be written in the following general form:

$$\frac{\partial \rho u_j \phi}{\partial x_j} = \frac{\partial}{\partial x_j}\left(\Gamma^l_\phi \frac{\partial \phi}{\partial x_j} - \rho\overline{u'_j \phi'}\right) + S_\phi \qquad (1)$$

where ϕ can represent the three components of velocity, temperature, turbulent kinetic energy, dissipation of turbulent kinetic energy, or any other transported scalar. When ϕ represents the velocity components, the S_ϕ terms includes the appropriate pressure gradients. The turbulent stresses $(-\rho\overline{u'_j\phi'})$ are modelled using an Boussinesq eddy viscosity concept [14] whereby they are set equal to mean flow gradients multiplied by a scalar turbulent diffusion constant. Under this assumption, equation 1 can be written as:

$$\frac{\partial \rho u_j \phi}{\partial x_j} = \frac{\partial}{\partial x_j}\left(\Gamma^e_\phi \frac{\partial \phi}{\partial x_j}\right) + S_\phi \qquad (2)$$

Γ^e_ϕ is an effective diffusion constant and is given by

$$\Gamma^e_\phi = \Gamma^l_\phi + \Gamma^t_\phi \qquad (3)$$

where the superscripts l and t refer to molecular and turbulent quantities. The coefficients Γ^e_ϕ, the source terms S_ϕ are defined for different transport variables ϕ in Table 1.

Two different turbulence models were used in this study. In both models, the turbulent viscosity μ_t is calculated using the $k-\epsilon$ model in the fully turbulent regions away from the wall [21]:

$$\mu_t = C_\mu \rho \frac{k^2}{\epsilon} \qquad (4)$$

However, the models differ in the treatment of the near wall region, where viscosity has an important effect. The first model uses standard wall functions to bridge the near wall region [21], where as the second model uses a two layer approach [28] where the van Driest mixing length formulation [14] is used to obtain an expression for the turbulent viscosity:

$$\mu_t = \rho L^2 \left|\frac{\partial u}{\partial n}\right| \qquad (5)$$

where, L is given by:

$$L = \kappa n \left[1 - \exp\left(\frac{y^+}{A}\right)\right] \qquad (6)$$

A is equal to 26, κ is 0.40, and y^+ is given by:

$$y^+ = \frac{n \tau_s^{1/2} \rho^{1/2}}{\mu_l} \qquad (7)$$

where τ_s is the wall shear stress. This approach is more economical in terms of the number of grid points required to resolve the near wall regions when compared to low Reynolds number turbulence models, and offers more accuracy in the analysis of separated flows when compared to high Reynolds number $k-\epsilon$ models [28]. Furthermore transition effects can be modelled through empirical constants used in the mixing length expressions.

It is acknowledged that this turbulence model can not capture all the physics associated with a jet impinging on a flat plate. For example, the effects of the streamline curvature on the turbulence are not accounted for. However, this turbulence model does include enough complexities to capture some of the physics of the flow and has been used successfully for two-dimensional investigations of a plane jet impinging on a flat surface [3, 4, 24], and impingement/effusion cooling [1] studies. Chuang and Wei [4] present comparisons between predicted and measured ground pressure distributions and centerline velocity decay profiles for a impingement height to jet diameter ratio of two. The numerical predictions are in good agreement with the observations, but the centerline velocity decay profile

ϕ	Γ^e	S
1	0	0
u_i	$\mu_t + \mu_l$	$-\partial p/\partial x_i + S^i$
k	μ_t/σ_k	$P - \rho\epsilon$
ϵ	$\mu_t\sigma_\epsilon$	$\left(C_1\epsilon P - C_2\rho\epsilon^2\right)/k$

$C_1 = 1.44, C_2 = 1.72, C_\mu = 0.09, \sigma_k = 1.0 \sigma_\epsilon = 1.3$

$P = \mu_t \left(\frac{\partial u_i}{\partial x_j} + \frac{\partial u_j}{\partial x_i}\right) \frac{\partial u_i}{\partial x_j}$
μ_t given by equations 4 or 5

Table 1 Governing Equation Variables

was sensitive to the assumed velocity profile at the jet exit. Their predictions also indicate high levels of k on either side of the jet and on the ground plane. The levels of k are high on the edges of the jet as a result of the high production of turbulent kinetic energy brought about by the shear stresses between the jet and the ambient fluid. They state that the large k zone on the ground plane is due to flow deflection and acceleration [4]. The numerical predictions also indicate the presence of a potential core extending from the jet inlet to just above the ground plane. No heat transfer predictions are presented.

Nixon [23] reports on a complementary numerical/experimental study of circular jets with an impingement height of thirty jet diameters. In this work Algebraic Stress Models (ASM) were also considered. They observed that the ASM did not give a significant improvement over the standard $k-\epsilon$ model in the prediction of flow field associated with an impinging jet. Furthermore, they reported that the ASM was twice as expensive as the k-ϵ model, and not as stable.

Recently, Knowles and Bray [20] performed computations for a normal impinging jet in a cross-flow using the standard $k-\epsilon$ turbulence model. They investigated both a circular free jet, and an impinging circular jet with no crossflow. The computations were done using an 2-D axisymmetric grid. They present predictions for the free jet axial velocity decay for various jet exit turbulence intensities and Mach numbers, assuming a uniform nozzle velocity profile. Their results indicate (1) that the use of the k-ϵ model results in an overprediction of the jet spreading rate when compared to the results of Donaldson and Snedeker [5] and (2) that increasing the jet exit turbulence intensity shortens its potential core. For the impinging jet they consider H/D ratios of 7.5 and 24, and compare the spreading and decay rate of the wall jet (produced by the impingement jet) to experimental data. However, no heat transfer predictions were made.

The k-ϵ model has been used extensively in the prediction of the flow field associated with an impinging jet. However, there is little information concerning the appropriateness of this model in the prediction of heat transfer underneath an impinging jet. This information is required in the design of cooling schemes for gas turbine hardware. Furthermore, the designer should be aware of the effects of different jet exit assumptions on the resulting heat transfer distribution. This paper provides comparisons between numerical predictions and experimental observations of heat transfer coefficients, discusses the effects of varying the jet exit turbulence intensity, and offers suggestions for improving the heat transfer predictions.

3 NUMERICAL SOLUTION PROCEDURE

The numerical solution procedure adopted in the present study is based on the work of Rhie and Chow [25]. The numerical solutions presented in this paper were obtained using the computer code NASTAR written by C. Rhie. This method is a Control Volume Finite Difference Method that solves for the Cartesian velocity components and pressure using a non-staggered grid. In this approach the domain is divided into a number of control volumes over which the governing equations are integrated. The ability of this numerical solution procedure to provide accurate solutions to the mathematical model described above for a range of problems has been demonstrated [25, 26, 27].

4 NUMERICAL DETAILS

A schematic of the physical problem is presented in Figure 1. A single circular jet of diameter (D) 1.52 cm impinges on a flat plate that is a distance H from the jet outlet plane. There is no imposed crossflow. The total temperature of the jet at its outlet is set equal to the ambient temperature (21.1°C). The velocity profile in the jet was assumed to be either (1) uniform at a value of V_j, or (2) given by a 1/7th power profile. The turbulent kinetic energy (k) and its dissipation rate (ϵ) at the jet outlet were calculated as follows:

$$k = 1.5 \times (T.I. \times V_j)^2 \tag{8}$$

where $T.I.$ is the assumed turbulence intensity.

$$\epsilon = C_\mu k^{1.5}/0.03D \tag{9}$$

The inherent symmetry of the problem was exploited, and hence the computational domain incorporates one quarter of the jet with the center of the jet located at (x,y,z) = (0,0,H). The problem was solved in three-dimensions as the next step in the analysis is to include a cross-flow. The computations were performed in a parallepiped (box-shaped) domain that extended from the plane of symmetry $x/D = 0$ to a plane downstream at $x/D = 20$ in the axial direction, from the

jet inlet plane $z = H$ to the impingement plate $z = 0$ in the radial direction, and from the symmetry plane $y = 0$ to a slip boundary at the plane y/D=15. H/D values of 2 and 10 were considered in this study.

The boundary conditions on the various faces of the calculation domain were as follows:

- **Symmetry Planes:** On the planes $x = 0$, and $y = 0$, the combined convective/diffusive flux was set to zero.
- **Outflow:** The plane $x = 20D$ was treated as an outflow boundary.
- **Walls** The upper (excluding jet outlet) and lower plates ($z = H, 0$) were treated as follows: No slip conditions were imposed, and numerical predictions were obtained for the cases of adiabatic walls, and for the cases of an imposed uniform temperature (T_w). These different runs were required in order to allow for a comparison with the heat transfer data in the literature [13] where the adiabatic wall temperature was used in defining the heat transfer coefficient.
- **Jet Exit:** the velocity components, k, ϵ and temperature were specified at the jet outlet.

The number of grid points used in the x and y directions were 35 and 31 respectively. In the z direction the number of grid points used depended on the H/D of the domain and the wall boundary conditions used. For an H/D of 2, the number of grid points used for the high Reynolds number turbulence model and the two layer model were 20 and 40, respectively. The corresponding numbers for H/D=10 were 31 and 49.

5 RESULTS

The discussion of results is divided into two parts, based on the near wall treatment of the flow, viz : (1) wall functions application and (2) the two- layer model. In each section the highlights of these two near-wall treatments will be given for H/D of 2 and 10.

5.1 Standard Wall Functions

The results presented in this section pertain to the flow and heat transfer predictions, using the standard wall functions to bridge the near wall region [21].

The velocity vector plots, in the vicinity of the hole, on the planes of symmetry are presented in Figures 2 and 3 for $H/D = 2$ and 10, respectively. The flow pattern indicates that for $H/D = 2$, the jet impinges on the bottom plate with approximately the same profile as that prescribed at the hole exit plane. This implies that there is a minimal interaction between the bulk of the jet flow and the surrounding fluid. The shear effects are absent and the jet exhibites a potential flow characteristics (similar to the potential core of a free jet). However, for $H/D = 10$, the effect of shear stress on the velocity profile is apparent. The jet expands and entrains fluid from surroundings; this slows down the jet core velocity as can be seen in figure 3. Close examination of the vector plot, reveals that the region in which the shear effects are minimal (i.e. potential core region) persists up to approximately $z/D = 5$. The above observations are in agreement with previous studies (e.g. [5],[6],[10] etc.).

Figure 4 shows the comparison between the predicted dimensionless jet centerline pressure and the corresponding experimental profile [5] at the plane of symmetry (y=0) for the case of H/D=2. Good agreement can be observed. The mean jet centerline velocity (along the jet) for the case of H/D=10 is also compared to the available experimental data [5] in Figure 5. The comparison is only shown in the region outside the potential core (viz $z/D > 6$) where the experimental data were reported. The prediction is in good agreement with the experimental measurements.

At this point it was concluded that the mean flow characteristics pertinent to impinging circular jet can be adequately predicted, using the standard $k-\epsilon$ turbulence model in conjunction with wall function formulation .

Attention was then focused on to the heat transfer prediction capability of the present formulation. The predicted Nu along the impingement plate on the symmetry plane (y=0) for H/D=2 is presented in Figure 6. Two cases were considered namely, jet turbulence intensities of 1% and 10% at the hole exit plane. It is evident that though the predicted Nu exhibites strong jet turbulence intensity dependency, neither of the cases compared well against the reported experimental data [13]. An interesting feature observed from the predicted profile is that in the case of high jet turbulence intensity, the peak Nu occurres at the edge of the jet (i.e. $x/D = 0.5$). Review of the turbulence intensity distribution ($u' = \sqrt{2k/3}$) along the same plane (i.e. at the nodal point adjacent to the impingement wall) shows that the maximum u' occurres at the same location (Fig 7). This suggests that firstly the jet does not expand as it approaches the impingement plate and secondly the maximum turbulence kinetic energy is nearly the same as that convected by the jet from the exit plane of the hole to the impingement plate. On the other hand for the case of low jet turbulence intensity, the peak Nu occurres beyond the edge of the jet (i.e. $x/D = 1.6$), corresponding to the location at which the peak turbulence intensity occurres (Fig. 7). It is evident that the rate of production of turbulence energy in the vicinity of the wall in this case, out-weights the convected turbulence energy from the hole exit plane. The experimental data also suggests that the peak Nu occurres beyond the edge of the jet (i.e.at $x/D = 2$). Goldstein et al. attributed this local peak to the presence of vortex ring surrounding the jet; the vortex ring is believed to promote mixing (i.e. turbulence kinetic energy) and hence heat transfer.

In-overall the agreement between the predicted and measured heat transfer coefficient is very poor. One source of discrepancy could be due to the application of wall functions for heat transfer prediction.

The predicted Nu along the impingement plate on the symmetry plane (y=0) for the case of H/D=10 is presented in Figure 8. Two cases were again considered, namely, jet turbulence intensities of 1% and 10% at the hole exit plane. It is evident that neither of the cases compared well against the reported experimental data [13]. The peak Nu occurres at the stagnation point ($x/D = 0$) for both calculation and measurement, corresponding to the location of maximum turbulence intensity as shown in Figure 9.

An interesting feature observed from the predicted profile is that the Nu is independent of the turbulence intensity imposed at the hole exit plane. This suggests that the turbulence energy distribution at the wall is governed by the shearing effects and is generally independent of the turbulence convected by the jet towards the impingement plate. The source of discrepancy between the measured and predicted Nu profile could again be due to the application of wall functions for heat transfer prediction.

At this point it was decided to use the two layer model for heat transfer prediction.

5.2 Two Layer Turbulence Model

Two inherent significant assumptions on the heat transfer characteristics, when applying the wall function formulation, are :

1. Reynolds analogy is invoked, which assumes that the heat diffusion rate is proportional to momentum diffusion rate, i.e. $\nu_t \sim \lambda_t$ which is not necessarily valid; a good example is the case of separating, re-attaching flows, where at the point of re- attachment the wall shear stress is zero while the wall heat flux is maximum.
2. The wall function formulation assumes a logarithmic temperature profile near the wall, in analogy with the near wall velocity profile.

In order to avoid the above assumptions, the conservation equations are solved to the wall using the two layer model [28]. In this model, the molecular thermal conductivity is used to calculate the wall heat flux, the pre-requisit of which is that the nodal point adjacent to the wall should be located inside the laminar sublayer region.

The calculations were repeated for both cases of $H/D = 2$ and $H/D = 10$, using the two layer turbulence model. The wall function calculations revealed that the rate of heat transfer to the boundary is independent of the jet turbulence intensity imposed at the hole exit plane for the case of $H/D = 10$. It was thus decided to first carry out the calculation for the case of $H/D = 10$ with the jet turbulence intensity at the hole exit plane set to $u' = 1\%$.

Figure 10 shows the comparison between the calculated Nu and the corresponding Goldstein et al. data. Clearly a much improved agreement can be observed, particularly near the stagnation region ($x/D = 0$). The maximum discrepancy of 25% occurres in the region of $3 < x/D < 4$. Grid refinement to improve the agreement was not carried out due to time limitation.

The same calculation was carried out for the case of $H/D = 2$ with the jet turbulence intensity at the hole exit plane set to $u' = 1\%$. Figure 11 shows the comparison between the calculated Nu and the corresponding data. Poor agreement is observed, suggesting that the two layer model does not perform well for this case. However, by reviewing the dimensionless distance between the nodal point adjacent to the wall and the wall ($y^+ = n\tau_s^{1/2}\rho^{1/2}/\mu_l$), it is observed in Figure 12 that the nodal point might not have lied in the laminar sub-layer region, with the present grid arrangement. C. Rhie [25] recommends that for successful two layer model applications, the first nodal point adjacent to the boundary should be located at $y^+ \leq 2$.

The grid arrangement was refined to insure the recommended criterion is met before any firm conclusion about the merits of the two layer model is made. Figure 13 shows the comparison between the measured and calculated Nu using the refined grid arrangement. The agreement has not improved, even-though the $y^+ \leq 2$ condition has been met. It can be seen that neither the location nor the magnitude of the peak Nu has been predicted correctly.

It is suspected that the implementation of the two layer model in the present code might be the cause of this discrepancy. In depth review of the implementaion reveals that the y^+ value at every x location in equation 6 is calculated based on the maximum shear stress in that plane, as opposed to the local nodal value. This might result in a smaller predicted sublayer region, giving rise to a higher heat transfer coefficient (i.e.larger temperature gradient). The effects of this form of implementation on the heat transfer distribution will be investigated by present authors in the near future. Also the two layer model in general might not be adequate for this type of heat transfer prediction. Other turbulence models (e.g. low Reynolds number turbulence model) might be investigated in future.

6 Conclusion

Based on the present numerical study of an impinging circular jet on a flat plate, in the absence of cross-flow effects, the following conclusions have been made:

1. The mean flow characteristics of impinging circular jets can be adequately predicted with the standard $k-\epsilon$ turbulence model in conjunction with the wall functions.
2. The potential core of the jet persist up to 5 hole diameter away from the hole exit plane. Hence, the impingement plate located at distances smaller than 5 hole diameter away from the hole, is subjected to a small rate of heat transfer, owing to the low rate of turbulence and mixing process in the potential core region.
3. The application of wall functions does not yield satisfactory heat transfer prediction.
4. The rate of heat transfer is a strong function of the jet's turbulence intensity imposed at the exit of the hole for $H/D = 2$.
5. Application of the two layer turbulence model improves the heat transfer prediction capability for $H/D = 10$, provided that the $y^+ \leq 2$ condition is satisfied. The present implementation of the two layer model does not adequately predict the heat transfer characteristics for $H/D = 2$.

7 References

[1] Al Dabagh, A.M. et al. Impingement/Effusion Cooling: The Influence of the Number of Impingement Holes and Pressure Loss on the Heat Transfer Coefficient, *ASME Journal of Turbomachinery*, **112**, pp. 467-476, July 1990.

[2] Behbahani, A.I., Goldstein, R.J., Local Heat Transfer to Staggered Arrays of Impinging Circular Air Jets, *ASME Paper No. 82-GT-211.*

[3] Chuang, S, et al. Numerical Simulation of Twin-Jet Impingement on a Flat Plate Coupled with Cross-Flow, *International Journal for Numerical Method in Fluids*, **14**, pp.459-475, 1992.

[4] Chuang, S., Wei, C., Computations for a Jet Impinging Obliquely on a Flat Surface, *International Journal for Numerical Methods in Fluids*, **12**, pp. 637-653, 1991.

[5] Donaldson, C. Dup., Snedeker, R.S., A Study of Free Jet Impingement. Part 1. Mean Properties of Free and Impinging Jets, *Journal of Fluid Mechanics* **45**, 2, pp. 281-319, 1971.

[6] Donaldson, C. Dup., Snedeker, R.S., Margolis, D.P., A Study of Free Jet Impingement. Part 2. Free Jet Turbulent Structure and Impingement Heat Transfer, *Journal of Fluid Mechanics*, **45**, 3, pp. 477-512, 1971.

[7] Downs, S.J., Jet Impingement Heat Transfer - A Literature Survey, *Rolls Royce Ltd., Report No. PNR-90360*, 1987.

[8] Florshuetz, L.W., Isoda, Y., Flow Distributions and Discharge Coefficient Effects for Jet Array Impingement with Initial Crossflow, *ASME Paper No. 82-GT-156.*

[9] Florshuetz, L.W., Metzger, D.E., Su, C.C., Heat Transfer Characteristics for Jet Array Impingement with Initial Crossflow, *ASME Paper No. 83-GT-28*

[10] Gauntner, J.W., Livingood, J.N.B., Hrycak, P., Survey of Literature on Flow Characteristics of a Single Turbulent Jet Impinging on a Flat Plate, *NASA Technical Note TN D-5652*, 1970.

[11] Goldstein, R.J., Behbahani, A.I., Impingement of a Circular Jet With and Without Cross Flow, *International Journal Heat and Mass Transfer*, **25**, 9, pp.1377-1382, 1982.

[12] Goldstein, R.J., Timmers, J.F., Visualization of Heat Transfer from Arrays of Impinging Jets, *International Journal of Heat and Mass Transfer*, **25**, 12, pp. 1857-1868, 1982.

[13] Goldstein, R.J., Behbahani, A.I., Heppelmann, K.K., Streamwise Distribution of the Recovery Factor and the Local Heat Transfer Coefficient to an Impinging Circular Air Jet, *International Journal Heat and Mass Transfer*, **29**, 8, pp.1227-1235, 1986.

[14] Hinze, J.O., *Turbulence*, McGraw-Hill Book Co., New York, 1959.

[15] Hollworth, B.R., Dagan, L., Arrays of Impinging Jets with Spent Fluid Removal Through Vent Holes on the Target Surface, Part 1: Average Heat Transfer, *ASME Paper No. 80-GT-42*, presented at the ASME Gas Turbine Conference, New Orleans, La., March 10-13, 1980.

[16] Hollworth, B.R., Gero., L.R., Entrainment Effects on Impingement Heat Transfer: Part II-Local Heat Transfer Measurements, *ASME Journal of Heat Transfer*, **107**, pp.910-915, November, 1985.

[17] Hollworth, B.R., Berry, R.D., Heat Transfer from Arrays of Impinging Jets with Large Jet-to-Jet Spacing, *ASME Journal of Heat Transfer*, **100**, pp.352-357, May 1978.

[18] Hookendoorn, C.J., The Effect of Turbulence on Heat Transfer at a Stagnation Point, *International Journal of Heat and Mass Transfer*, **20**, pp.1333-1338, 1977.

[19] Hrycak, P., Heat Transfer From a Row of Impinging Jets to Convave Cylindrical Surfaces, *International Journal of Heat and Mass Transfer*, **24**, 24, pp.407-419, 1981.

[20] Knowles, K., Bray, D., Computation of Normal Impinging Jets in Cross-Flow and Comparison with Experiments, *International Journal for Numerical Methods in Fluids*, **13**, pp. 1225-1233, 1991.

[21] Launder, B.E., Spalding, D.B., The Numerical Computation of Turbulent Flows, *Computer Methods in Applied Mechanics and Engineering 3*, pp. 269-289, 1974.

[22] Metzger, D.E. et al., Heat Transfer Characteristics for Incline and Staggered Arrays of Circular Jets with Crossflow of Spent Air, *ASME Journal of Heat Transfer*, **101**, 3, 1979.

[23] Nixon, D., A Fundamental Study of Jet Flows, *USAF Office of Scientific Research/Nielsen Engineering and Research: Report No. NEAR-TR-345 OR AFOSR-TR-86-0896*, 1986.

[24] Ravi, R., Deshpande, M.D., Computation of Plane Jet Impingement on a Plate, *National Aeronautical Lab (India) Report No. NAL-TM-FM-8602*, 1986.

[25] Rhie, C.M., Numerical Study of Turbulent Flow Past an Airfoil with Trailing Edge Separation, *AIAA Journal*, **21**, 11, Nov., 1983

[26] Rhie, C.M., Chow, W.L., A Pressure Based Navier Stokes Solver Using the Multigrid Method, *AIAA 86-0207*, 1986.

[27] Bansod, P., Rhie, C.M., Computation of Flow Through a Centrifugal Impeller with Tip Leakage, *AIAA paper 90-2021*, 1990.

[28] Rodi, W., Experience with Two-Layer Models combining the $k-\epsilon$ Model with a One-Equation Model Near The Wall, *AIAA paper 91-0216*, presented at the 29th Aerospace Sciences Meeting, Jan. 7-10, 1991.

[29] Saad, N.R. et al. Local Heat Transfer Characteristics for Staggered Arrays of Circular Impinging Jets with Cross-Flow of Spent Air, *ASME paper No. 80-HT-23*.

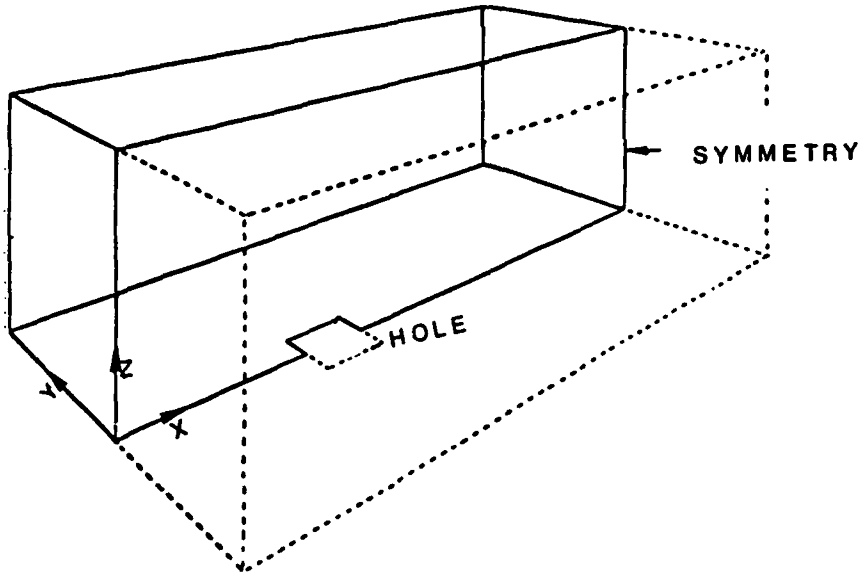
SYMMETRY
HOLE
Z
Y
X

Figure 1: Schematic of the Geometry Under Present Investigation

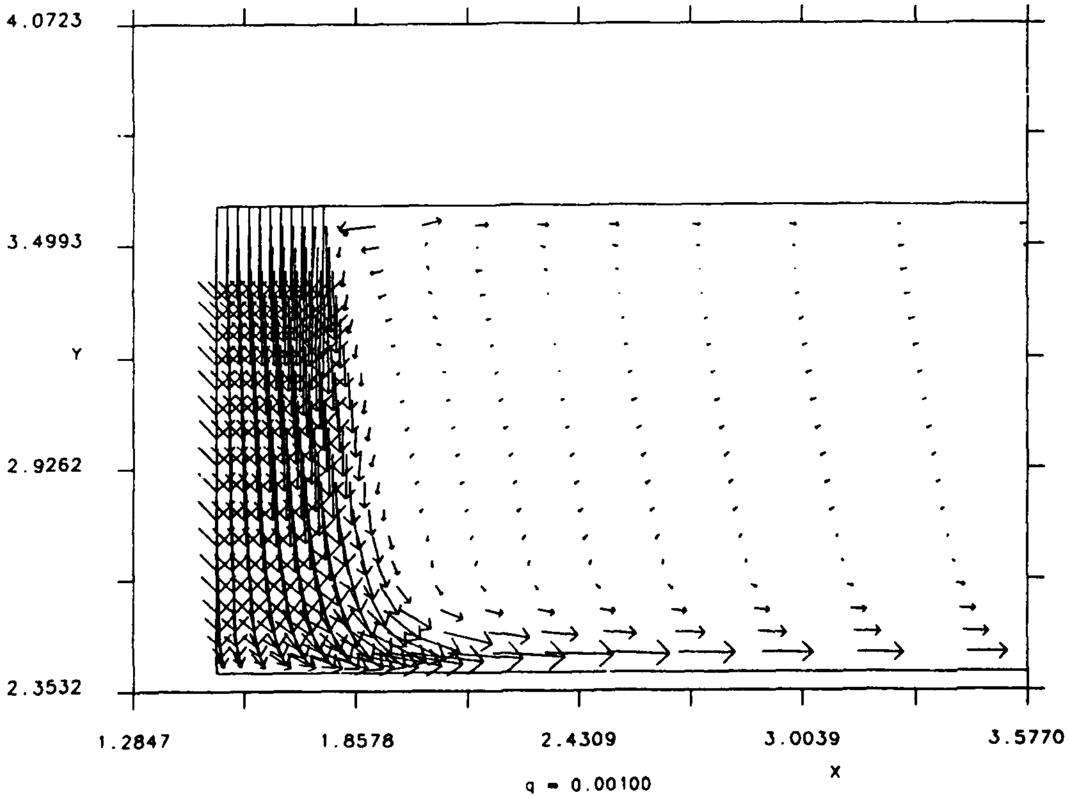

Figure 2: Vector Plot of the Flow in the Vicinity of the Hole, at the Plane of Symmetry, for $H/D = 2$

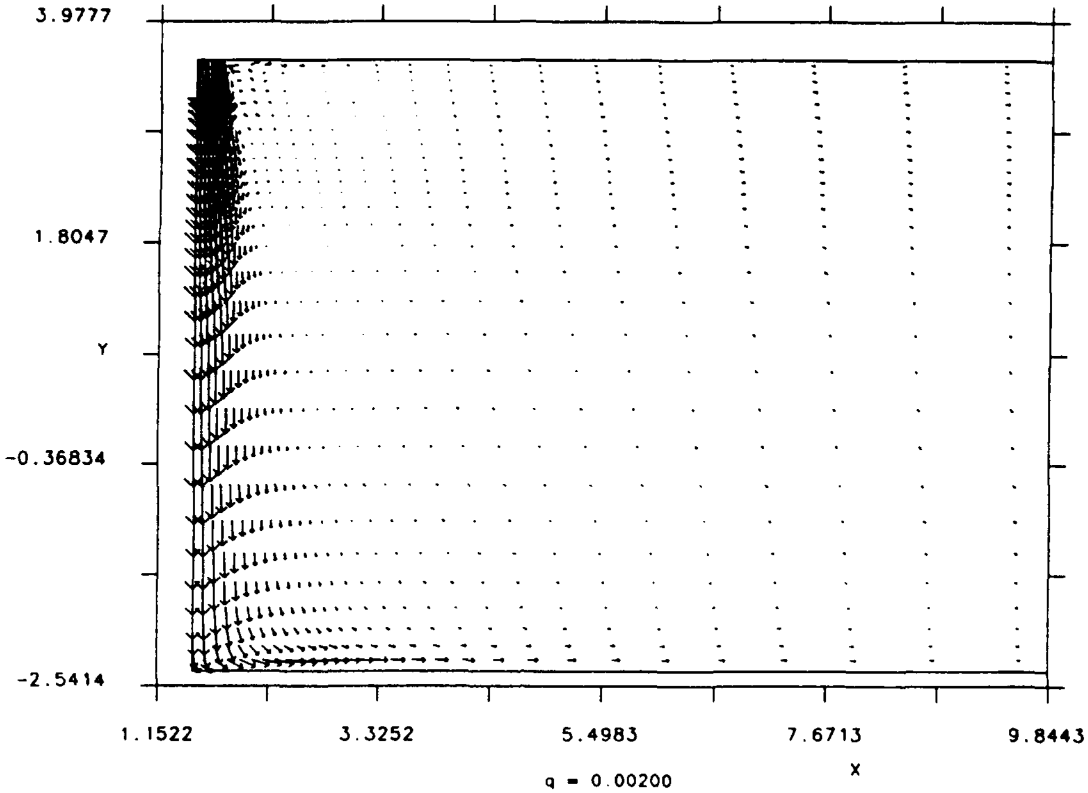

Figure 3: Vector Plot of the Flow in the Vicinity of the Hole, at the Plane of Symmetry, for $H/D = 10$

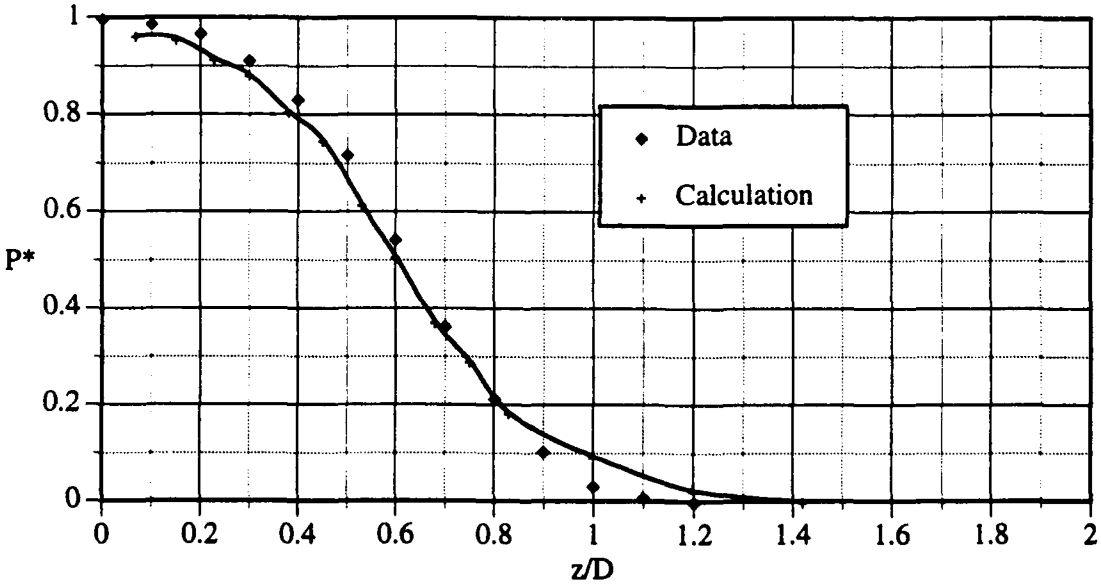

Figure 4: Comparison Between the Calculated Dimensionless Pressure Along the Jet Center-Line and the Corresponding Data of Donaldson,C [1971] for $H/D = 2$ $P^* = (P - P_\infty)/(P_0 - P_\infty)$

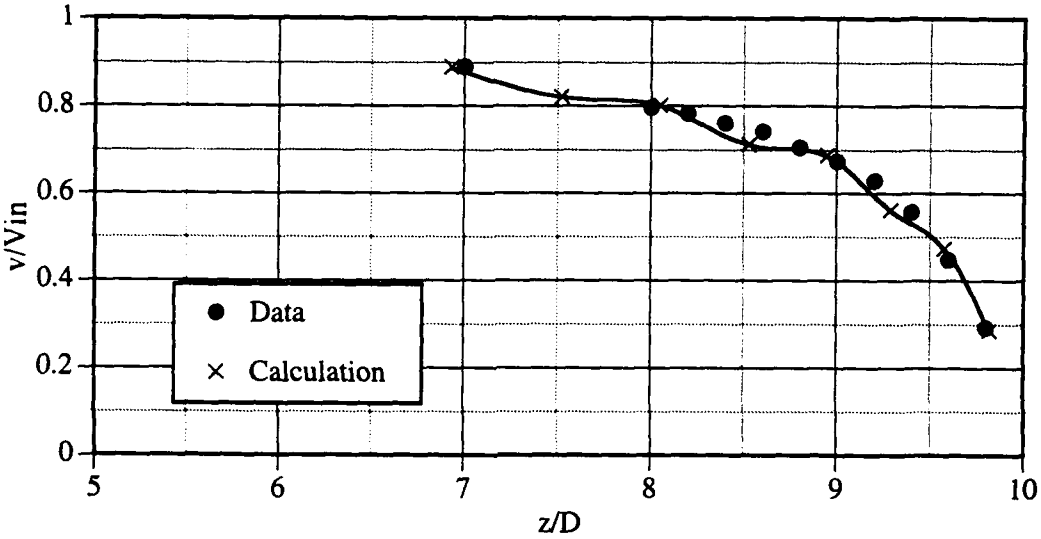

Figure 5: Comparison Between the Calculated Dimensionless Velocity Along the Jet Center-Line and the Corresponding Data of Donaldson, C. [1971] for $H/D = 10$, V_{in} = Jet Velocity at the Exit Plane of the Hole

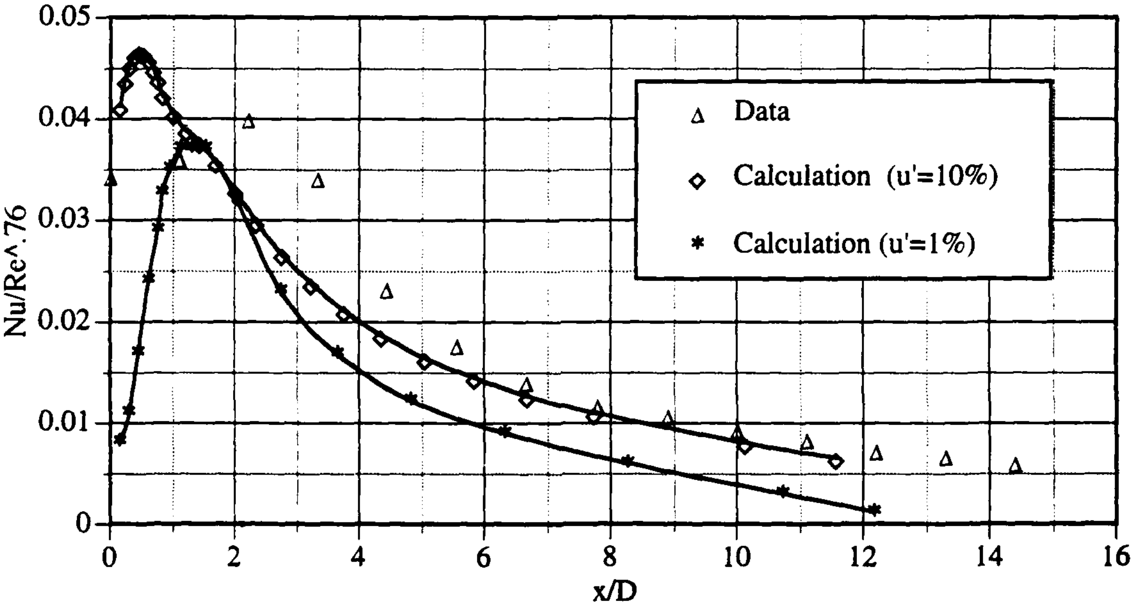

Figure 6: Comparison Between the Calculated $Nu/Re^{0.76}$ Along the Impingement Plate and the Corresponding Data of Goldstein et al. [1982] for $H/D = 2$, Using Wall Functions

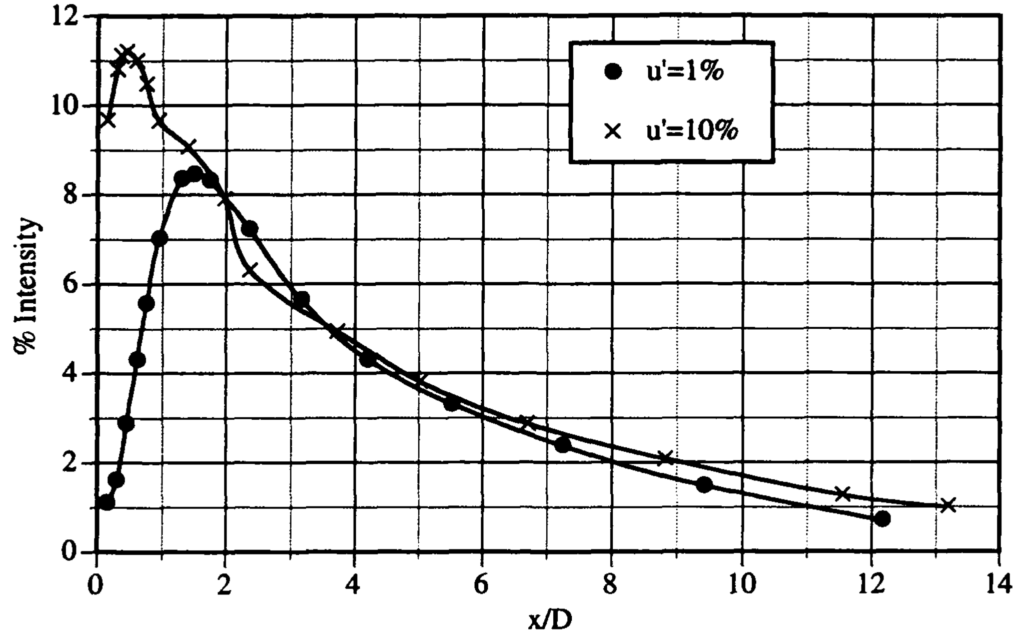

Figure 7: Calculated Turbulence Intensity Distribution Along the Impingement Plate for $H/D = 2$ Using Wall Functions

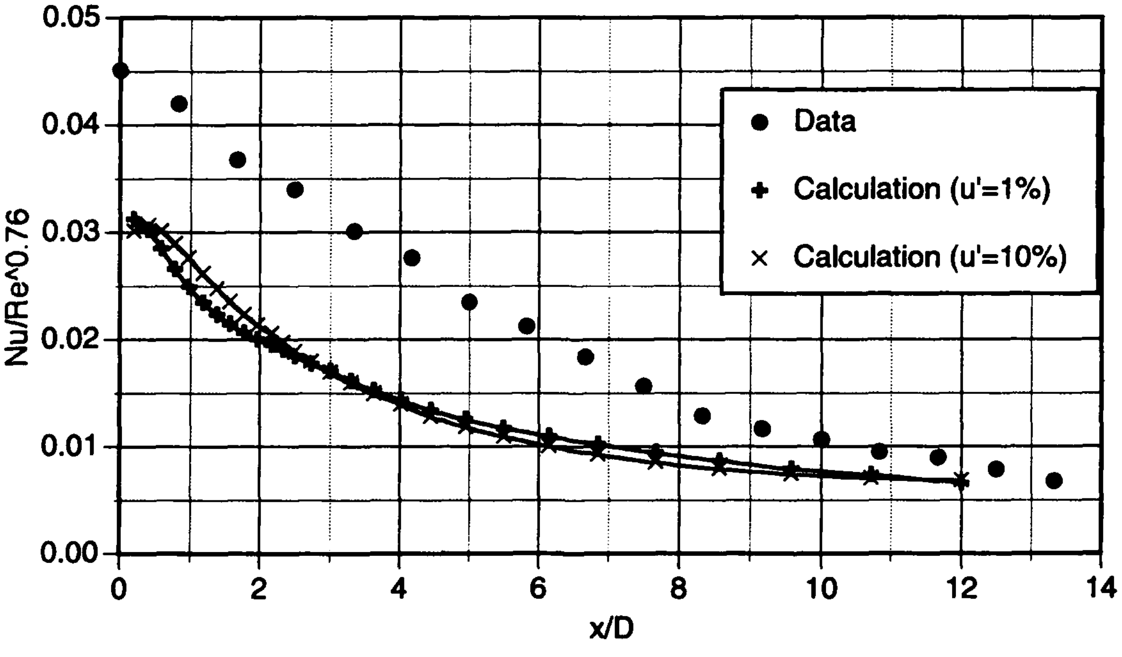

Figure 8: Comparison Between the Calculated $Nu/Re^{0.76}$ Along the Impingement Plate and the Corresponding Data of Goldstein et. al. [1982] $H/D = 10$, Using Wall Functions

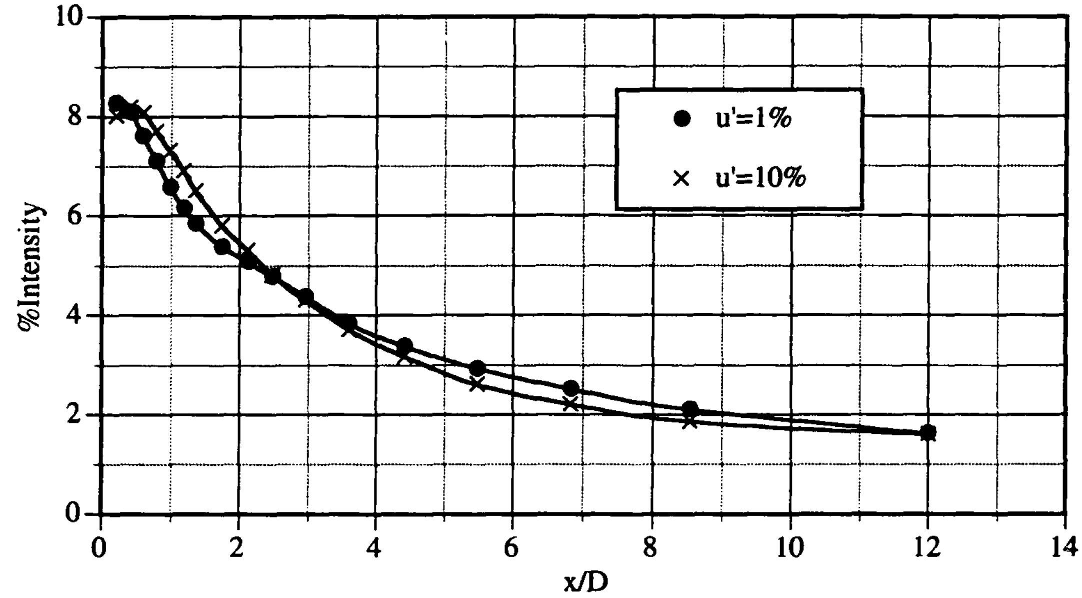

Figure 9: Calculated Turbulence Intensity Distribution Along the Impingement Plate for $H/D = 10$ Using Wall Functions

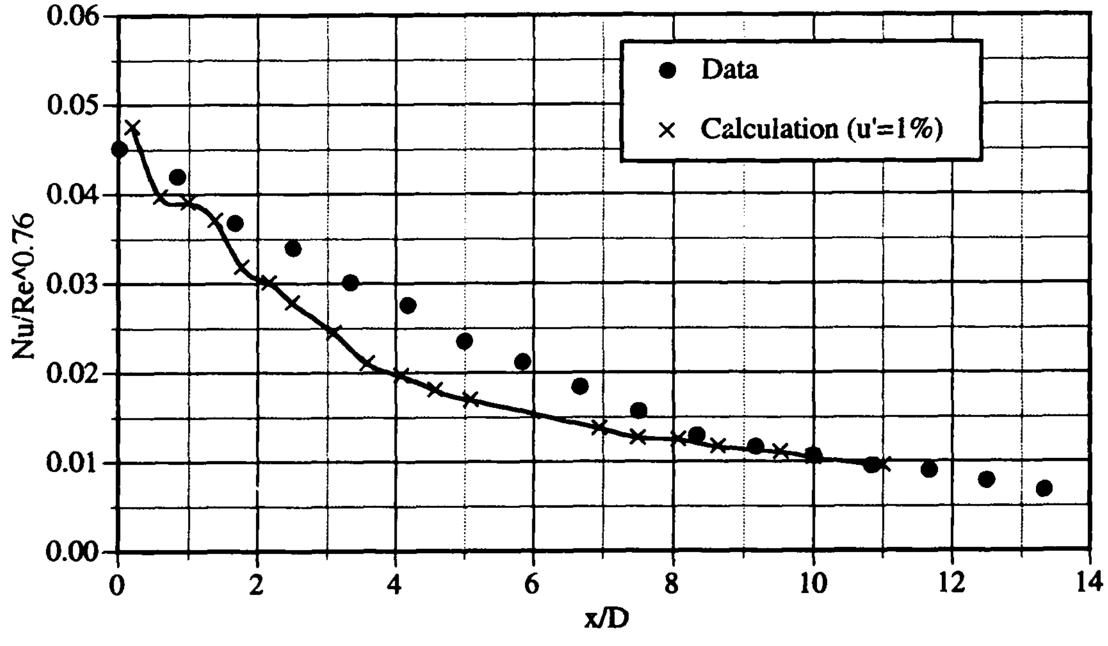

Figure 10: Comparison Between the Calculated $Nu/Re^{0.76}$ Along the Impingement Plate and the Corresponding Data of Goldstein et. al. [1982] for $H/D = 10$, Using Two Layer Model.

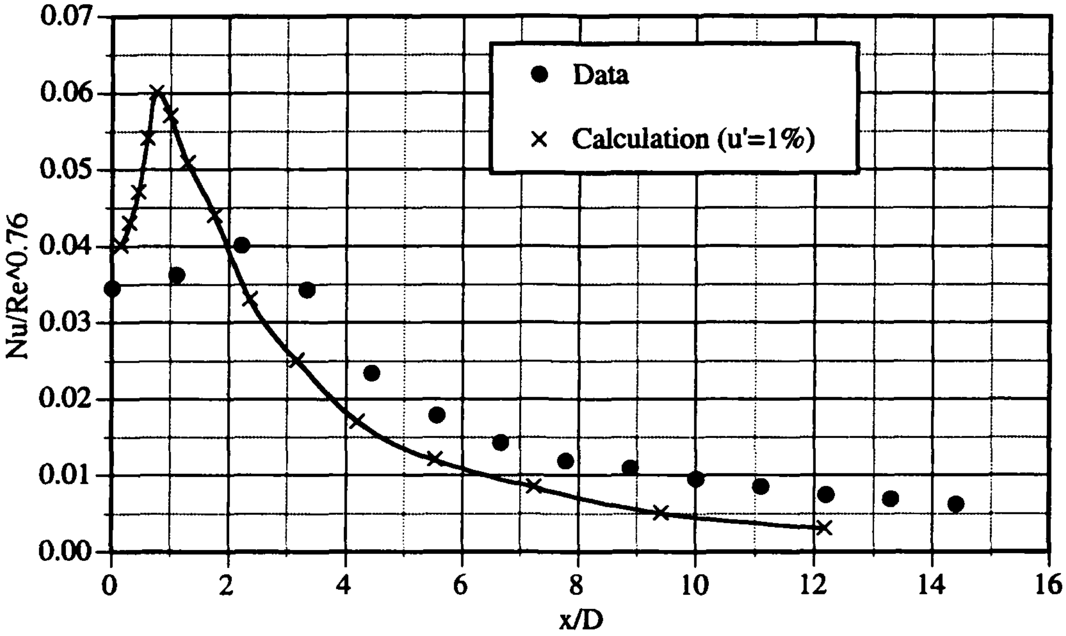

Figure 11: Comparison Between the Calculated $Nu/Re^{0.76}$ Along the Impingement Plate and the Corresponding Data of Goldstein et. al [1982] for $H/D = 2$, Using Two Layer Model

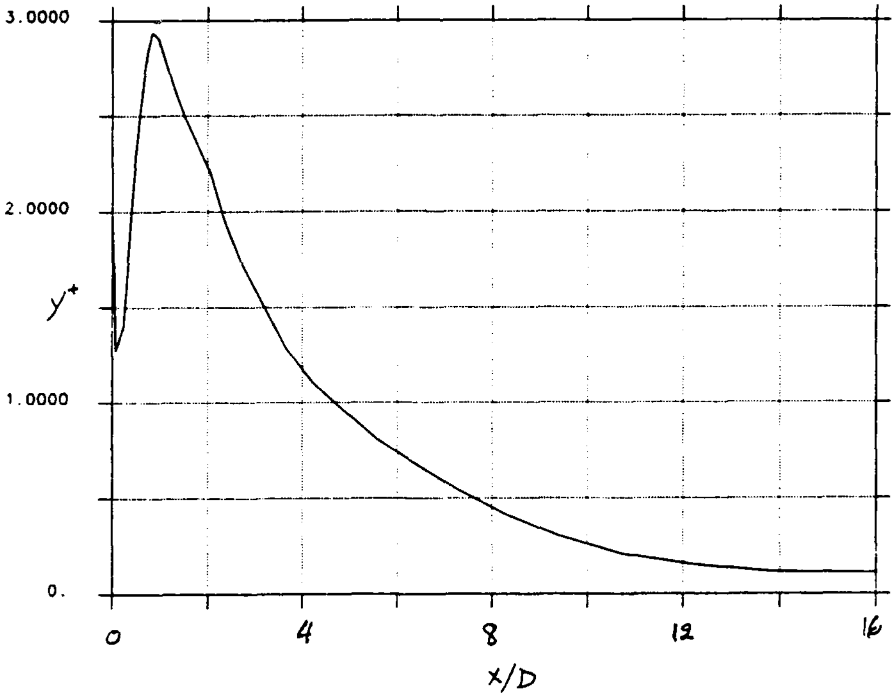

Figure 12: Calculated Dimensionless Distance of The First Nodal Point Away From The Wall (y^+), Along the Impingement Plate for $H/D = 2$ Using Two Layer Model

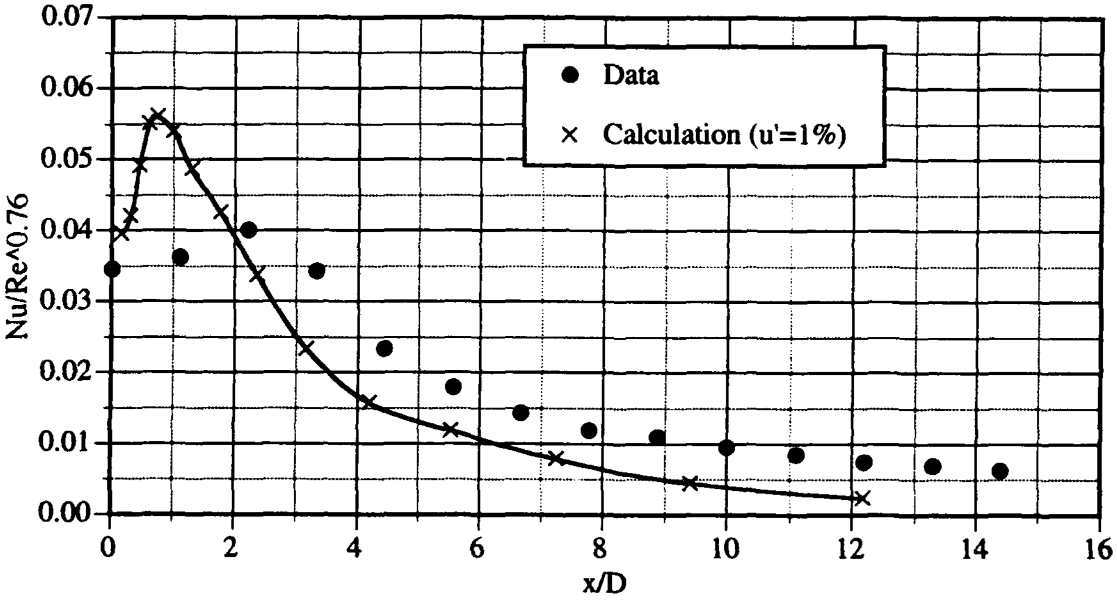

Figure 13: Comparison Between the Calculated $Nu/Re^{0.76}$ Along the Impingement Plate and the Corresponding Data of Goldstein et. al. [1982] for $H/D = 2$, Using Two Layer Model

An L2F-Measurement Device with Image Rotator Prism for Flow Velocity Analysis in Rotating Coolant Channels

M. Beversdorff, O. Hein*, R. Schodl
DLR, Institute for Propulsion Technology
P.O. Box 90 60 58, W-5000 Cologne 90, Germany

ABSTRACT

For further improvement of the turbine blade cooling process the knowledge about the heat transfer in radial coolant channels has to be deepened. Due to rotation the velocity distribution as well as the turbulence structure and therefore the heat transfer will be influenced. To carry out experimental data of the flow field within a rotating duct a non-intrusive continuous measuring system (Laser-Two-Focus) with an image rotator prism is presented. The design of the system is explained in detail. Problems of application are discussed and results of the first successful measurements compared with numerical results are presented.

NOMENCLATURE

d	duct inner diameter
L	duct length
dp	particle diameter
Tu	turbulence parameter
	laserlight wavelength
s	start-stop-focus separation
R_{max}	maximum radius of measurement location
n_{max}	maximum rotational speed
g	earth acceleration
p	static presssure
u	axial flow velocity
α	divergence angle of prism BS
γ	inclination angle
F	focal point
L	probe volume length
Re	Reynolds number
SS	suction side
PS	pressure side
SPP	Schmidt-Pechan image rotator prism
S1 to S4	mirrors
L1, L2, L3	lenses
MV	measurement volume
SF	sending fiber (monomode)
RF	receiving fiber (multimode)
BS	beam splitter prism
LU	launching unit
OH	optical head
DU	detector unit
ESP	electronical signal processing

INTRODUCTION

The improvement of power, efficiency and operational lifetime of jet engines demands higher performance from the cooling of turbine blades to cope with the increase of temperature and pressure load.

Accurate correlations for the design of the cooling configuration based on detailed knowledge of the gas and coolant flow and the heat transfer are necessary.

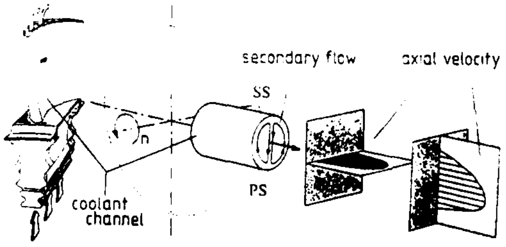

Fig.1: Turbine blade with radial coolant channel and typical flow field development

In the rotating components strong centrifugal and Coriolis forces cause a complex flow structure inside the coolant channels. The change in friction due to the secondary flow has an influence on heat transfer and pressure drop behaviour. A typical view of a cooled turbine blade and a view of the flow pattern inside a channel with circular cross-section rotating orthogonal to the turbine axis is shown in Fig.1.

---

*Now Siemens-KWU

A numerical method has been developed to calculate the heat transfer in coolant channels Ref.[1]. To verify the predicted data, experiments on pressure drop behaviour and flow field measurements were done at DLR Cologne.

A large-scale coolant duct, (Fig.2), with a diameter d = 16mm and a length to diameter ratio L/d = 20 within a cantilevered rotor of 1m outer diameter was designed for the investigation. The maximum rotational speed of the rotor was 3000rpm. The measurement positions were located at the relative length x/d of 3, 10 and 20. The flow in the duct was provided by cleaned, pressurized air and controlled by mass flow meters at the specially sealed inlet and outlet of the hollow rotor shaft. The flow direction can be changed from radial inward to radial outward.

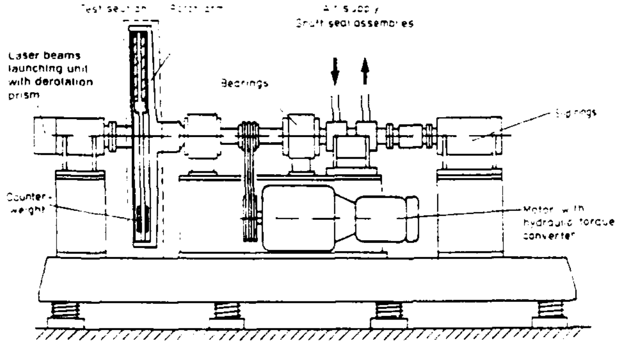
Test section
Rotor arm
Air supply
Shaft seal assemblies
Laser beams launching unit with derotation prism
Bearings
Slip rings
Counter-weight
Motor with hydraulic torque converter

Fig.2: Schematic of the test rig

For the non-intrusive flow measurements a Laser-Two-Focus velocimeter was applied.

LASER-TWO-FOCUS VELOCITY MEASUREMENTS

The Laser-Two-Focus technique is a well known method in turbomachinery flow analysis, Ref.[2]. The main applications are: high speed, narrow flow channels and low turbulent flows in axial and radial compressors or turbines and cascade wind tunnels.

The principle is a time-of-flight measurement of very small particles in the flow, dp < 0.5 microns, which have a good flow following behaviour (Fig.3). The optical setup is described in detail in Ref.[3]. Typically the two beams are focussed down to 10 microns and are separated about 300 microns.

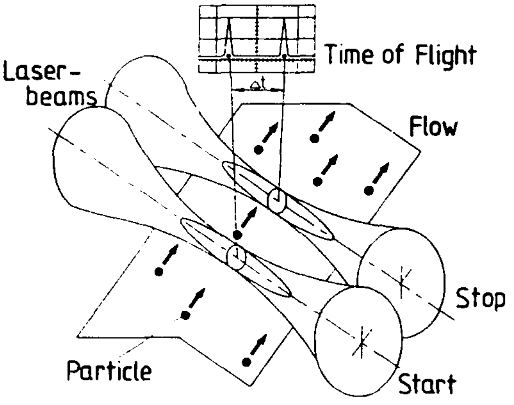

Fig.3: Principle of the Laser-Two-Focus velocimeter

When the natural particle concentration is not sufficient artificial seeding is provided to reduce the measuring time. To get results of mean flow velocity, mean flow angle and turbulence intensities with sufficient confidence numerous start-stop events have to be detected and statistically evaluated. In a first approach one might believe that the L2F-system could be operated the same way on the duct flow as on usual turbomachine applications. This, however, ist not a very pratical solution. In the turbomachine case the probe volume is figured through locally fixed casing windows to a certain rotor blade passage position, which changes circumferentially during rotation. Since the L2F-system is active in every blade passage the flow is always present in the probe volume and measurements are continuously possible.

Considering the duct flow measurements can only be carried out during the very short time period when the rotating duct passes the fixed measuring volume. This time period is typically only about 1/1000 of the rotor revolution time and therefore the resultant measuring time is about 1000 times longer than in an usual turbomachine application. This cannot be tolerated. The only way to overcome this drawback is to have the measuring system continuously operating in the rotating frame.

One solution of the problem would be to install the complete optical head of the measuring system on the rotor. This, however, is not possible with a normal L2F-system with the big Ar^+-Ion laser. A laser diode system which is much smaller and just under development in the institute could be a possible choice, but adjustment problems of the complex optical setup cannot be avoided in an enviroment of vibrations and high centrifugal forces. We decided therefore to place only a single part of the optical system on the rotor and to have the most parts of the optics separated from the rotor in a stationary location. The collimated light from the L2F-system is launched into the rotor concentric to the rotor axis and guided by mirrors to the lens, which is mounted on the rotor, but movable to focus the laser beams to different probe volume locations.

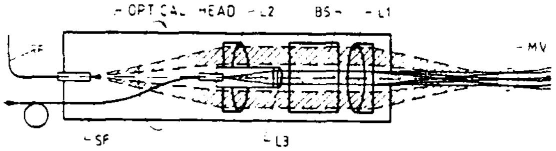

Fig.4: Optical beam path of the fiber optic Laser-Two-Focus velocimeter

A new developed L2F probe (Ref.[3]) with fiber technique, Fig.4, seemed to be ideal for this application. The beams between the beam splitter and the focussing lens are parallel. The small, lightweight optical head is fixed on the rotor pedestal avoiding relative motions between optical head and rotor.

The separation of the lens from the optical head caused a negative effect on the measuring volume. As shown in Fig.5, the dividing point of the beam splitter and the focal plane are no more identical as they should be and so the beams in the measuring volume are no longer parallel, but slightly inclined. The inclination angle γ depends on the distance between lens and beam splitter and causes different beam separations as a function of the probe volume lenght L. The different beam separations in the measuring volume will cause different time-of-flight measurements so that for example in laminar flows an artificial turbulence is indicated. However, theoretical calculations and experimental results in a jet flow showed, that the maximum distance between lens and beam splitter of 800mm will result in a relative error of only 0.3% at a turbulence level Tu = 4%. The statistically evaluated mean velocity is not influenced.

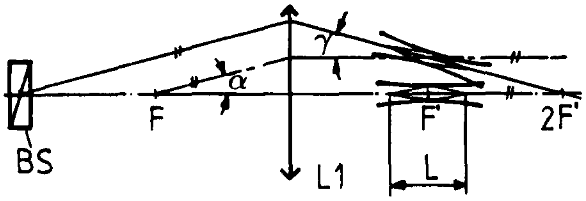

Fig.5: Distortion of the measuring volume due to the separation of BS and L1

THE OPTICAL SET-UP

The schematic set-up of the L2F measuring device is shown in Fig.6.

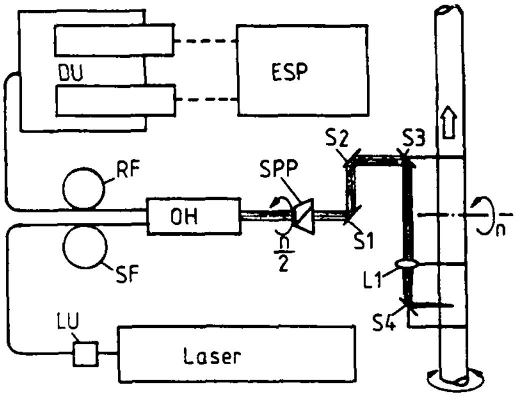

Fig.6: Set-up of the Laser-Two-Focus device at the rotating duct

The multicolored light from a 4W-Argon Laser is guided through a monomode fiber SF to the optical head. There the laser beam is divided by a color dispersion prism. The divergence angle between the beams with a wave length λ of 514nm (start) and λ of 488nm (stop) is α = 0.17°. This results in a beam separation s of 292 microns with a focussing lens L1 of 100mm focal length. The parallel beams are directed through an image rotator prism SPP and by four mirros S1 to S4 perpendicular into the duct.

The image rotator (Schmidt-Pechan-prism, Fig.7) is necessary to keep the orientation of the start and stop beams - the measurement plane - always parallel to the duct axis. Without this additional optical component the measurement plane would turn counter-clockwise when the rotor is turned clockwise. The image rotator compensates this motion if it is rotated clockwise with half the rotor frequency.

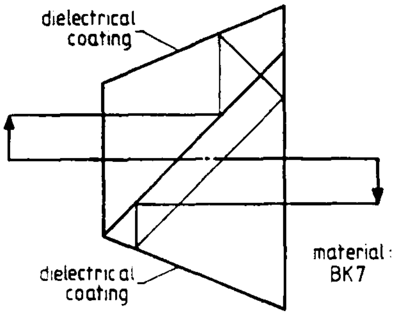

Fig.7: Schmidt-Pechan image rotator prism

The angular stability of the measurement-plane is excellent by the use of a belt gear. Many efforts had to be done to solve the adjustment problem of the prism in the optical beam path. A model rotor was designed to study the problem and a procedure was found to do this very accurately. The local variation of the measuring volume, which is a measure of the adjustment quality, we achieved was less than 30 microns.

The four mirror arrangement with two mirrors fixed at the duct enabled the system to measure at different lines of sight with respect to the rotational axis within an angle range of ±100°, (Fig.8).

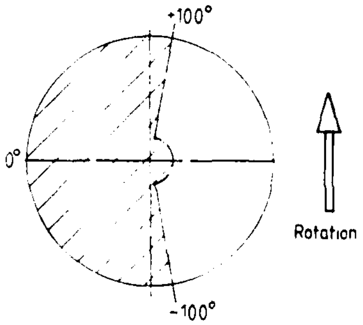

Fig.8: Cross-section of the duct with the observeable (hatched) area

The lens L1 is traversable by a DC-motor up to 10mm, so that the measuring volume can be traversed over half the duct diameter. The position is controlled by a potentiometer. The electrical connections to the DC-motor and the potentiometer are enabled with slip-rings on the rotor shaft.

The described positioning possibilities enabled the system to measure more than one half of the circular cross section of the duct. If a symmetrical flow is assumed, the flow pattern in the other half can be treated as a reflected image.

The scattered light from particles out of the probe volume is directed backwards through the optical set-up. The different colors from start and stop are recombined to one multicolor beam by the dispersion prism in the optical head. This light is guided with a multimode fiber to a detector unit and the signal processing electronics.

Measurements at different ratios x/d of duct length were possible by mounting the duct section with the integrated window for optical access and the traverse mechanism for the lens at the desired position. Ratios x/d of 3, 10 and 20 were choosen.

Particular attention was taken on the design and the estimation of the loads on to the mechanical and optical parts, especially on the achromatic lens. Due to the high centrifugal acceleration of 4000g at a radius R_{max} = 400mm, and n_{max} = 3000rpm, there were some doubts that the lens would keep it optical quality.

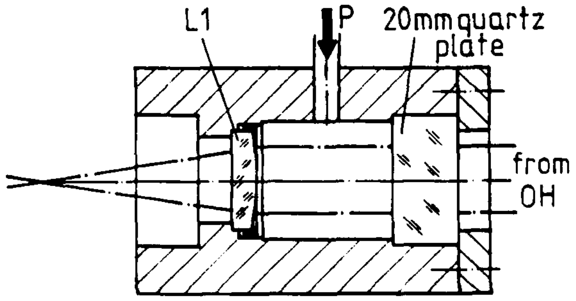

Fig.9: Pressure chamber for lens stress simulation

Therefore, a small pressure chamber (Fig.9) was manufactured to check the lens with an equivalent load. Which is corresponding to a pressure p of 10bar. A parallel light beam was directed through the plane window to the focussing lens and the focal plane was magnified. Then the pressure in the chamber was increased up to 10bar. There were no significant changes in the focal plane observeable.

Artificial seeding was done at the inlet of the rotor shaft by a particle generator atomizing a Glycerin-Alcohol mixture.

DISCUSSION OF PROBLEMS DURING THE MEASUREMENTS

Some difficulties occured during the first tests and handicapped the measurements. In the original design the window (2mm BK7 plate) was in a position close to the wall and parallel to the duct axis to get minimum disturbance of the flow. This caused the following problems:

- Reflections from the window into the receiving optics resulted in a drastical reduction of signal-to-noise ratio. Multiple reflections in the image rotator may cause this problems.
- The window got dirty after very short measuring time and made further measurements impossible. The soiling was caused by oil from the air supply shaft seals which crept along the duct wall and not so much from seeding particles.

The cleaning of the window took a lot of time, because the rotor was fully capsuled and had to be dismounted for this purpose.

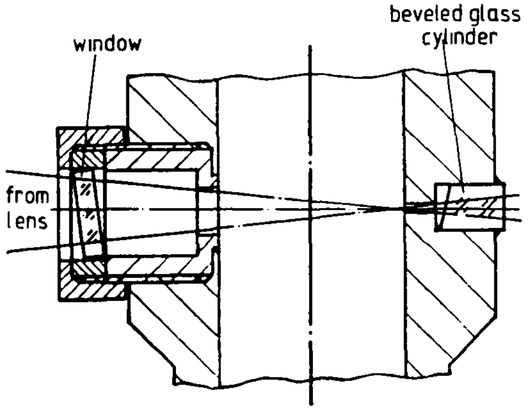

Fig.10: View of the duct section with the integrated window

By a change in the design (Fig.10) both problems were solved.

The window was separated by 10mm from the duct wall and was inclined by 7 degrees. The remaining hole in the wall is about 4mm in diameter.

The inclined glass surface directed the reflections out of the receiving optics. The backplaced window prevented soiling for hours and the hole in the wall showed no observeable disturbance in the flow field behind the duct axis.

Another problem occured at close to the wall measurements, because the minimum distance achieved was about 1.5mm. Normally, a L2F-system is capable to measure down to 0.2mm perpendicular to a wall, but the unconventional beam path had a negative effect on this capability. To obtain measurements from the boundary layer close to the wall a small hole was drilled into the rearwall, ∅ 1.2mm, to reduce background flare. The hole was closed with a beveled glass cylinder to avoid reflections into the optics.

Since the flow is stationary, the influence of the hole of such a small size is negligible.

A secondary effect of this modification was a more easy way to adjust the measuring volume normal to the duct axis, because now the laser beam had to be positioned only to the center of the two windows, which can be easy observed.

COMPARISON OF EXPERIMENTAL AND NUMERICAL RESULTS

First measurements were carried out at a relative length x/d of 20 and a flow from the outer radius to the cen-

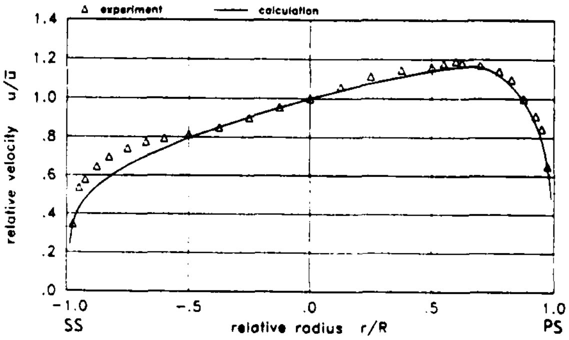

Fig.11: Axial velocity profile from SS to PS for n= 1500rpm, Re=60000

ter at a rotational speed of 1500rpm.

The following figures show the axial velocity distribution in the plane from the suction side to the pressure side and in the perpendicular plane. The symbols are representing the experimental results and the solid lines were generated from numerical results.

In Fig.11 the velocity profile from suction side to pressure side is shown, which confirmed the expected asymmetrical distribution. While the velocity profile in the perpendicular plane in Fig.12, is symmetrical. The observable differences between the results are more related to the circumstance that in the experiments the flow field was not yet fully developed. This is caused by differences in the inlet conditions of the experiment in comparison to the assumptions made by numerical calculations.

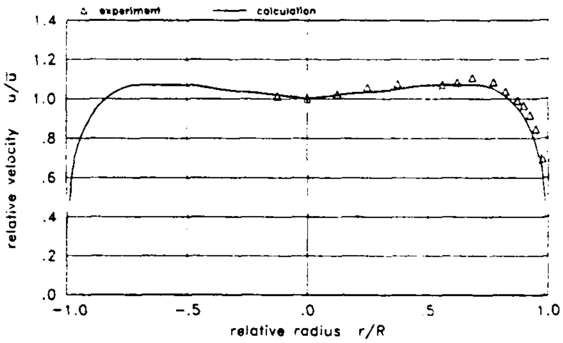

Fig.12: Axial velocity profile perpendicular to SS-PS for n=1500rpm, Re = 60000

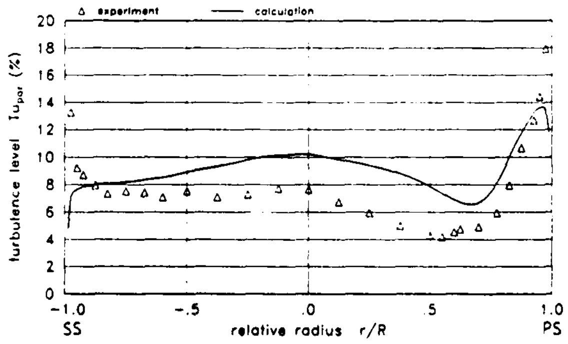

Fig.13: Turbulence distribution from PS to SS for n = 1500rpm, Re = 60000

Finally, in Fig.13 the turbulence distribution from suction side to pressure side is shown. There are also deviations from the calculated values, specially from the center to the suction side. The reasons therefore seemed to be also the inlet conditions. A more detailed presentation and discussions of the results will be given in Ref.[4].

CONCLUSION

The results obtained from the experiments showed, that the proposed L2F device with an image rotator is a very suitable method to determine the flow field in a small rotating flow channel.

The measurements will be carried on at increased rotational speeds and also the buoyancy effects due to a heated tube wall on the flow field will be studied.

REFERENCES

[1] H.P. Berg et al.: "The Effect of Roation on Local Coolant Side Flow and Heat Transfer in Turbine Blades". The 10th ISABE, Nottingham, UK, 1991, ISABE 91-7016.

[2] R. Schodl: "Laser-two-focus velocimetry." In "Advanced Instrumentation for Aero Engine Components", Philadelphia, USA, 1986, AGARD-CP-399, paper 7.

[3] R. Schodl: "Laser-two-focus techniques". In "Measruement Techniques in Aerodynamics", von Karman Institute for Fluid Dynamics, Lecture Series 1989-05, Rhode-St. Genèse, Belgium.

[4] M. Elfert: "The Effect of Rotation and Buoyancy on Flow Development in a Rotating Circular Coolant Channel", to be published in the proceedings of the 2nd Int. Symp. on Engineering Turbulence Modelling and Measurements, June 1993, Florence, Italy.

Discussion

QUESTION 1:

DISCUSSOR: N. Hay, University of Nottingham

Regarding the problem of oil on the window, we had a similar problem in a combustion situation and we solved it by using film cooling techniques: we blew clean air across the window from a slot upstream. Would it be possible to use the same approach in this case?

AUTHOR'S REPLY:

I think it would be possible. Normally we use a similar cleaning device where solvent is blown out of some holes upstream from time to time to clean the window. In the present case, since it is complicated to adapt the method to the rotating duct, we decided to separate the window from the duct.

LOCAL HEAT TRANSFER MEASUREMENT WITH LIQUID CRYSTALS ON ROTATING SURFACES INCLUDING NON-AXISYMMETRIC CASES

D.E. Metzger and Y.K. Kim
Mechanical and Aerospace Engineering Department
Arizona State University
Tempe, AZ 85287-6106
U.S.A.

ABSTRACT

An overview and summary of test methods and results are given for the problem of measuring local heat transfer on rotating surfaces that model gas turbine engine disks. Disk-cavity situations generically similar to those encountered in the high pressure stage disk cooling are considered, with cooling air supplied both at or near the wheel centerline as well as through single or multiple jets impinging outboard on the wheel near the blade attachment region. In some situations provision has been made for ingestion into the disk-cavity from the gas path region radially outboard of the disk. Local heat transfer rates in all cases are determined from the color display from a thin coating of encapsulated liquid crystals sprayed onto the disk, in conjunction with use of a video camera and computer vision system. For cases with axisymmetric disk surfaces, the coated surfaces are illuminated and viewed continuously, and detailed radial distributions of local Nusselt number are obtained. For non-axisymmetric disk surfaces, such as encountered in the vicinity of boltheads, the disk is illuminated with stroboscopic light and a method has been developed and used to synchronize the computer frame-grabber with the illumination.

NOMENCLATURE

A	heat transfer area
c_p	specific heat
E	entrainment supply flow ratio, $= Q_e/Q_p$
h	convection heat transfer coefficient
k	thermal conductivity
m	total coolant mass flow rate
Nu	Nusselt number, $= hr_o/k$
q	local surface heat transfer rate
Q	total measured coolant volumetric flow rate
Q_e	measured entrainment volumetric flow rate
Q_p	calculated free disk pumping flow
r	radial coordinate
r_o	disk radius
r_i	impingement radius
R	jet supply flow ratio, $= Q/Q_p$
Re_m	flow Reynolds number $= Q/2p\ zn$
Re_r	disk rotational Reynolds number $= wr_o^2/n$
t	temperature
t_i	initial temperature
t_r	reference temperature
t_s	local surface temperature
z	rotor-to-stator spacing
α	thermal diffusivity
ν	fluid kinematic viscosity
μ	fluid dynamic viscosity
ω	angular velocity
ρ	fluid density
θ	time
τ	time step

INTRODUCTION

Current aircraft propulsion engines and rocket engine turbopumps employ very high axial turbine stage inlet temperatures for the hot working gases that flow along the hot gas path at the outer boundary of the rapidly rotating turbine disks. A perennial major concern in turbine design is the ingestion of fluid from the hot gas path into into the disk-stator cavity where it can increase both temperature level and temperature gradients within the highly stressed disk. The pumping ability of the rotating disk produces an inherent tendency of the disk for cavity evacuation, and induces the hot gases into the cavity unless the disk pumping appetite is provided for by separately supplied cooling flows. The amount of coolant necessary to prevent hot gas ingestion into the cavity is important in engine design, because of the cycle penalty associated with it and the resulting need to minimize its use.

Detailed convection heat transfer information over the entire face of turbine disks is also needed in general in order to specify a cooling design that will insure acceptably low metal temperatures and temperature gradients, consistent with desired durability. Despite this need for detailed heat transfer information on rotating surfaces, such information has been acquired only slowly starting with, among others, the analysis of von Karman [1] and the experiments of Cobb and Saunders [2] and Kreith, et al [3]. A concise review of literature addressing both the fluid mechanics and heat transfer aspects of the subject through 1982 is provided by Owen [4].

In general, cooling air can be provided to the disk or disk-cavity in different ways, with one of the most common methods using supply at or near the disk axis, followed by radially outward flow along the disk. The emphasis in such schemes is usually placed upon purging the cavity of hot gases. A second method involves the direct impingement of coolant jets onto the disk surface, usually near the disk periphery in an attempt to provide more cooling to the blade attachment region. This latter method has long been considered to be a potentially very effective method for turbine cooling, but a method where heat transfer mechanisms are not well understood. Some early measurements on actual cooled turbine hardware [5] revealed anomalous results where heat transfer unexpectedly decreased with increasing disk speed. Subsequent laboratory studies with jets impinging on plane rotating surfaces, eg Popiel, et al [6], Metzger and Grochowsky, [7], Metzger et al [8], Bogdan, [9], and Popiel and Boguslawski [6] have shown that a single isolated jet can easily be too weak to effectively penetrate the boundary layer flow induced by the disk rotation. Since jet impingment schemes always involve a finite number of jets spaced around the disk at intervals, there is always concern that hot gas flow can penetrate into the cavity at the spaces between the jets, and even that the jet flow may actually induce and exaggerate the radially inward hot gas flow.

The interaction of an impinging jet onto a surface with boundary fluid pumped by the surface motion is quite different than the usual interaction of a jet with a cross-flow. In the case of the moving surface, the jet encounters an ever stronger cross-flow as it nears the surface, whereas in the more usual stationary surface case, the cross-flow must reduce to zero at the surface. Some recently published data [10], with sets of three impinging jets set close together, suggest that the heat transfer effect of multiple jets may be predictable by superposition of single jet performance, but this conclusion is questionably applied to disk cooling situations with jets closely spaced over the full 360 degrees. Both centrally supplied coolant supply and radially outboard jet supply, both with single and multiple jets, have been investigated with the methods described herein. The paper focuses on the experiemntal modeling and methods employed and gives an overview of results obtained in terms of the effects of various parameters such as coolant flow Reynolds number, jet supply versus central supply, radial position of jets, and the contour of the disk.

EXPERIMENTAL METHODS AND APPARATUS

The acquisition of heat transfer information for turbine disks has been slow and knowledge is still very incomplete because of the expense and complexity usually involved with making local heat transfer measurements on rotating surfaces. Conventionally, such measurements involve mounting expensive heat flux gages, or spot heaters and thermocouples, on the disk surface, and transmitting electrical power and measurement signals from and to the rotating apparatus through slip rings. In the present study, very localized convection heat transfer rates are obtained by utilizing remotely viewed liquid crystal surface coatings together with a thermal transient test procedure.

In the present method, encapsulated liquid crystal coatings are sprayed directly onto the disk test surface and their response is observed and processed during the transient with automated computer vision and data acquisition systems. Local convection coefficients are calculated from the transient thermal response of the test surface, as determined by color indications from the thin coating. This technique applied to rotating surfaces has been developed over the past few years at Arizona State University [10] and at the University of Karlsruhe in Germany [11], in both cases applied to a situation where the disk is cooled by jets. Adaptation of the technique to the present configuration and preliminary results have been previously presented by Metzger and Kim [12].

A significant advantage of the present test method concerns the proper modeling of the thermal boundary conditions on all the wetted surfaces. In many instances of practical interest, the flow in the wheel-space between rotor and stator often contains recirculating regions where the flow exchanges heat with both the stator and the rotor. In most previous testing, the disk is usually the only active heat transfer surface and heat transfer to or from the stationary surfaces is not properly modeled or accounted for in the experiments. In the present tests, all surfaces are heat transfer active.

Measurement Theory and Procedures The test procedures and data reduction theory used in this investigation are essentially identical to those described in Metzger and Larson [13] and Metzger and Bunker [13], and only a brief overview is presented here. In the technique used, detailed local convection coefficients over the test region of interest are deduced from measurements of local transient wall temperature responses to the driving convective heating load based on well established one-dimensional conduction theory.

The wall temperature response for one-dimensional heat conduction in a semi-infinite solid object to a step change in ambient fluid temperature is described by the following classical solution.

$$(t_s - t_i)/(t_r - t_i) = 1 - \exp(h^2\alpha\theta/k^2) \cdot \operatorname{erfc}(h\sqrt{\alpha\theta}/k) \qquad (1)$$

If material properties are known, the heat transfer coefficient h can be inversely obtained from Eq. 1 with measurements of transient wall temperature response and fluid temperature t_m. For a simplified flow situation, the driving fluid temperature t_m may be considered as the local mixed mean temperature. However, in less restricted cases, t_m can be substituted by a more readily measurable reference temperature t_r and h can be redefined accordingly.

In actual experiments, a true step change in fluid temperature is nearly impossible to achieve and generally the reference temperature will be a function of time. In this case the solution given by Eq. 1 is still valid as a fundamental solution but is used for a series of step changes in $t_r(\theta)$ using Duhamel's superposition theorem, ie:

$$t - t_i = \sum_{i=1}^{N} U(\theta - \tau_i)\, \Delta t_r \qquad (2)$$

where:

$$U(\theta - \tau_i) = 1 - \exp\left[\frac{h^2\alpha(\theta - \tau_i)}{k^2}\right] \operatorname{erfc}\left[\frac{h\sqrt{\alpha(\theta - \tau_i)}}{k}\right] \qquad (3)$$

For the acrylic plastic test surface material used, the depth of heating into the disk over the time duration needed to complete the test is less than the disk thickness. In addition, departure from one-dimensionality because of finite lateral conduction in the disk is not expected to have a significant effect on the local surface temperature response for the surface heat transfer gradients anticipated, as shown by Vedula, et al [14] and Metzger and Larson [13].

In the technique used, the transient surface temperature information is provided by the application of a temperature indicating coating material and a PC-based image processing system employing the frame grabber. The coating material used for this study is an commercially available encapsulated chiral nematic thermochromic liquid crystal (TLC), applied to the test surface using an airbrush. The TLC displays colors in response to temperature changes as a result of lattice reorientation of the crystal. When sprayed as a thin layer, the TLC is essentially clear and displays color with increasing temperature in sequence of red, green, blue, and back to clear.

The nominal temperatures for red, green, and blue displays of the present chiral nematic TLC are 38.4 C, 39.8 C, and 43.5 C, respectively. The process is reversible such that the calibration of temperature remains unchanged for a large number of cycles under laboratory conditions. While all TLC type coatings assume a finite time response for the lattice rotations, Ireland and Jones [15] have shown that micro-encapsulated chiral nematic coatings on the order of 10^{-3} cm thick require only a few milliseconds for this action. This time lag is negligible in comparison with the thermal transients of the present study.

A typical experimental run begins with heating laboratory compressed air up to a desired temperature while the test section is maintained at room temperature. A three-way ball diverter valve is used to route the heated air away from the test section until the air temperature reaches a preselected steady state value indicated by a monitoring thermocouple in the diversion line. When steady state is nearly reached in the diversion line, the disk is brought to the desired test speed as rapidly as possible to minimize any possible temperature rise within the test region due to frictional heating. Typically the disk speed can be stabilized within two minutes with less than 0.5 C increase in the recirculating air initially at room temperature. The heated air is then suddenly re-routed to the test section as the frame grabber and data log system for air temperature measurements are initiated simultaneously. For tests with entrainment flow, the secondary air flow at room temperature is also initially passed away from the test section by a second diverter valve and re-routed simultaneously with the main flow, For the test cases with 19-jet supply, it was necessary to preheat the plenum chamber in order to improve the reference air temperature response particularly at lower flowrates.

As the test surface is heated by introduction of flow at elevated temperature, the local color information from TLC captured by a color video camera is digitized pixel-by-pixel with the frame grabber in reference to a pre-set threshold corresponding to the calibrated color intensity. The outcome of this image digitization process is a pixel time-temperature matrix covering the entire test region monitored by the video camera. This information together with the transient reference temperature data suffices to obtain the local heat transfer coefficients with a relatively high resolution using Eq. 2.

The pre-set threshold for the desired color is determined by calibrating the image processing system against a TLC-coated copper bar. The temperature response of the copper bar to a heat input load is monitored by a thermocouple embedded in the bar. By varying the input threshold values, an optimum threshold and corresponding wall temperature can be acquired for given lighting conditions.

Apparatus Figure 1 shows a schematic of the test apparatus used. Fig. 2 shows cross sections of the disk and stator assemblies used, except where noted, for the experimental results to be discussed. Rotational speeds up to 10,000 rpm have been achieved by a 3/4 HP induction motor driving an enclosed and sealed twin bearing quill through a flat belt. Continuously variable speed adjustment is provided by an autotransformer, and the disk speed is continuously monitored with a photoelectric pickup and a digital frequency counter.

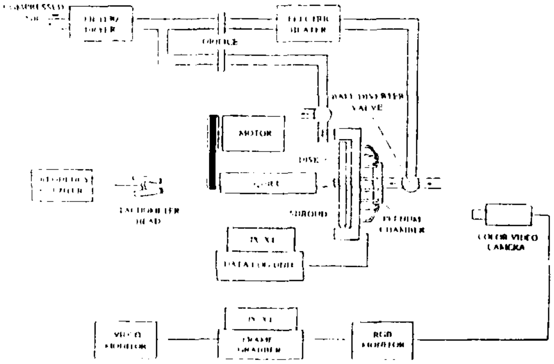

Fig. 1 Apparatus Schematic

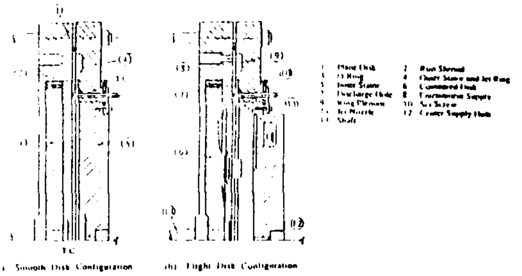

(a) Smooth Disk Configuration (b) Light Disk Configuration

Fig. 2 Disk and Stator Assembly Cross Section

The disks have been constructed of clear acrylic plastic with a radius of 4.75 in. (12.065 cm) in two versions: a smooth (plane) configuration and a contoured configuration. The smooth version has plane parallel disk and stator surfaces over the full radius with variable disk-to-stator spacing. The contoured version has been machined with shaping on both disk and stator that more closely approximate the disk cavity boundaries common in turbine stages. Air can be supplied to the cavity either through a single large inlet hole at the stator center line or through single or multiple jets as shown in Fig. 2. Simulated boltheads have been fabricated from lightweight balsa and are attached to the contoured disk. The disk thickness varies between 0.354 in (0.899 cm) and 0.58 in (1.473 cm) along the radius. Both test disks have seventy eight equally spaced 0.053 in (0.135 cm) diameter holes at 4.6 in (11.684 cm) radius which simulate rotating cavity coolant discharge flow passages, such as through the blade roots at firtree attachment joints.

The shroud assemblies consist of three components made of acrylic plastic and aluminum. The front shroud piece is interchangeable to produce different disk and stator arrangements. The disk is maintained parallel to the stator with a shroud support assembly attached to the bearing housing and the spacing is adjusted by moving the entire shroud assembly in the axial direction. The front shroud has an acrylic viewing window (machined to match the shroud contour) which permits visual observations over the entire disk radius.

In the tests reported here with coolant impinging onto the disk from jets, 19 jets, equally spaced around the full 360 degrees were used. The jet supply nozzles were made of brass each having a nozzle tip with a 0.052 in (0.132 cm) exit diameter, soldered to a 0.125 in (0.318 cm) ID tube. The nozzle tips were configured such that the jets they produce issue at an angle of 45 degrees to the axial direction. In the current 19-jet version, the supply nozzles were installed through 19 equally spaced positioning holes at 4.305 in (10.935 cm) radius from the shroud center Each nozzle is individually fixed with a set screw allowing two degrees of freedom for adjustment: axial translation and full 360 degree azimuthal rotation.

The impingement gap between disk and nozzle tip was maintained as 0.25 in (0.635 cm) for the present testing and the disk-to-stator spacing was maintained as 0.5 in (1.27 cm) for all smooth disk tests. The corresponding settings for the contoured disk tests were 0.19 in (0.483 cm) and 0.44 in (1.118 cm) at the impingement radius The azimuthal angle for each nozzle was fixed at 13 degrees radially outward for all tests. All jet supply nozzles are connected to a plenum chamber located near the front shroud through heat resistant plastic tubes. The plenum chamber serves as a flow distributor and is essentially a hollow disk with manifold holes configured such that heated air enters the chamber axially through one inlet port and exits radially in equal parts distributed equally spaced holes on the rim. It was fabricated from a reinforced plastic (Lexan) and equipped with guard heaters to minimize heat losses. The guard heaters were found necessary in order to insure that the jet exit temperature remained high enough to produce a useable display of the disk liquid crystal surface coating. For tests with a single center supplied jet, the multiple jet plenum chamber is by-passed. In this case the heated air is directly injected axially through a 0.227 in (0.577 cm) diameter hole located at the center of the front shroud.

In the present testing, the possiblity of entrainment/ingestion from the hot gas path radially outboard of the disk was similated by providing a controlled, separately metered amount of secondary flow, supplied to a separate plenum chamber with design similar to the jet supply plenum. Room compressed air is divided into eight equal parts passing through the plenum chamber and delivered to the rear of the shroud rim by plastic tubes. Each jet first impinges onto a circumferential groove machined into the opposite facing shroud component and serving as a settling chamber. It is then introduced radially into the test section through a circumferential gap. The degree to which it is entrained into the disk cavity, as opposed to rapid turning and axially exit, can be at least partially indicated by its detected effect on the disk local heat transfer.

With the present disk and shroud arrangement, all discharge flow is forced out through the seventy-eight discharge holes near the disk rim and the disk-to-rim clearance gap which was measured to be 0.018 in (0.046 cm). The flowrates for all flows were measured using ASME standard orifices. The uniformity of the distribution of flow through the multiple jets was independently checked using a precision rotometer, and were found to be uniform within ±5%.

Thermocouples to measure the driving jet temperature are located within the jet supply nozzles near their exit. Five additional thermocouples were installed on the front shroud to monitor midpoint temperature variations at various locations within the wheel space. All thermocouples used were type K (Chromel-Alumel) with nominal wire diameter of 0.00314 in (0.0798 mm). The transient responses of the seven thermocouples monitoring jet and wheel space region temperatures were recorded through a data log unit (Fluke 2400 B Intelligent Computer Front End) with a 0.4 sec sampling interval for each thermocouple.

RESULTS AND DISCUSSION

Experimental Uncertainties To minimize experimental uncertainties, the temperature of the supplied flow is chosen so that the color threshold is not reached until sufficient time has elapsed after the start of flow (usually 10 seconds or more) to insure that the elapsed time can be determined accurately. Also, the flow temperature is chosen so that the elapsed time and corresponding penetration of the temperature pulse into the surface are small enough (usually less than 60 seconds) to insure that the test surface can be treated as semi-infinite as assumed in the data reduction. All of the results presented were obtained with threshold times satisfying these constraints, and the uncertainty in the measured convection coefficients is estimated to be ±10 percent by the methods of Kline and McKlintock [16].

Figure 3 shows the nature of results obtained to fully characterize the radial variation in convection coefficient, h, presented non-dimensionally as a radially local Nusselt number. Nu is based on outer disk radius, r_o, so that the values reflect changes in h. These results are typical of all full-radius testing in that the convection coefficients vary over a large range and several tests with different supply temperatures are necessary to cover the entire range without violating the test requirements listed in the previous paragraph. In the ranges where results from two tests overlap, there is generally good agreement well within the estimated experimental uncertainty. Further confidence is given by comparison with previous results [10] obtained for similar conditions but with a different test disk and different liquid crystal coating. The dashed lines on Fig. 3 show these previous results for the case of $Re_r = 2.71 \times 10^5$ with $Re_m = 1360$ (lower line) and 1900 (upper line). The convection coefficient is based on the disk surface - jet inlet temperature difference in this and in all of the results presentations that follow.

Effect of Impingement Radius for Single Jet Impingement

Figure 4 shows typical measured single-jet Nu variations that illustrate the effect of jet nozzle location, with r_i/r_o varied from zero to 0.8 in 0.2 increments, while disk speed and jet flowrate is held constant. These results were obtained with an earlier plane disk/ plane stator arrangement [10] with radial exit of the supplied flow at the edge of the disk. For a given impingement flow and disk speed, the local radial convection coefficients attained with impingement onto the disk center appear to establish the general level of the maximum heat transfer possible at the various radii, regardless of the impingement radius. Impingement at radial outboard locations does, however, increase the local heat transfer in the vicinity of impingement over what would be the case with center-supplied flow, with the increase ranging from a very small amount at $r_i/r_o = 0.2$ to about 80 percent at $r_i/r_o = 0.8$. Distributions such as this show generally that the radial average heat transfer decreases with increasing impingement radius, so that most effecient use of this type of disk cooling is obtained with center impingement. However, in a given application, it may be desirable to tailor the radial heat transfer distribution, and the results of Fig. 4 indicate that off-center impingement can be an effective means of doing so.

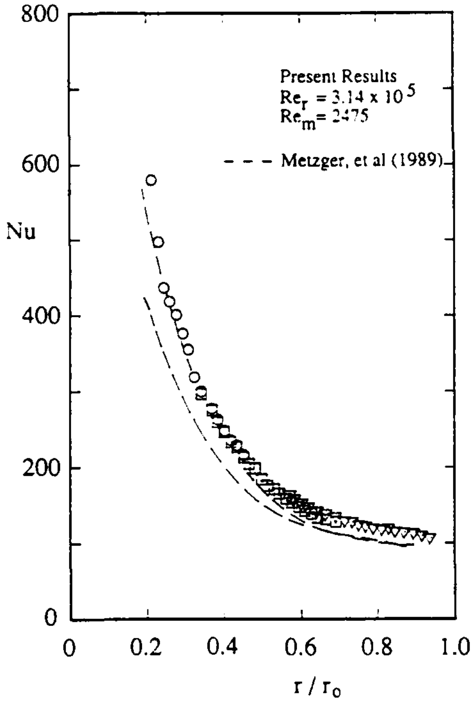

Fig. 3 Typical Radial Nu Distribution Obtained With Three Supply Temperatures

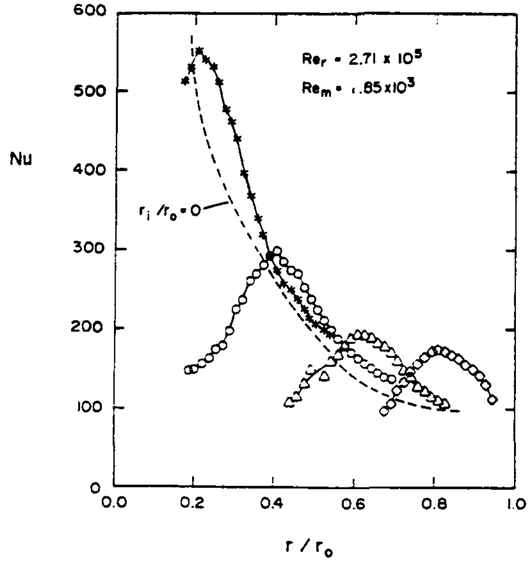

Fig. 4 Nu for Single Jet Supply, Effect of Impingement Radius

Single Center Supply, Effects of Contour and Flowrate

Figures 5-7 show measured local heat transfer rates obtained with the contoured disk and stator arrangement, with air supplied to the cavity only through the center inlet. In these tests, the data as a function of radius, especially in the mid-radius region, is sparse as a consequence of difficulties associated with observing the liquid crystal responses through the contoured plexiglas viewing window. It was found impossible to illuminate the test surface uniformly over the entire radius, therefore a separate calibration applicable to each region of interest was conducted and the data was reduced accordingly.

Figure 5 shows typical local Nusselt number results for values of Re_r and Re_m of 3.14 x 10^5 and 2505, respectively. For comparison, the corresponding results obtained with the plane disk and stator as presented in Metzger and Kim [12] are indicated by the dashed line, and show good agreement with the contoured results. The finding that heat transfer is largely insensitive to the disk contour is in agreement with a previous study by Metzger, et al [8] that included the effect of disk shape on heat transfer. Apparently, the very large tangential component of the disk pumped flow minimizes the effects of disk contour.

Figures 6 and 7 show additional results for the contoured disk and stator combination, for $Re_m = 3.14 \times 10^5$ and 5.38×10^5, respectively. For each value of rotational Reynolds number, three values of flow Reynolds number were tested. The results all display similar radial distributions, with Nusselt number levels increasing with increasing Re_m as for the plane disk cases. Also indicated on these and subsequent figures is R, the ratio of supplied flow rate, Q, to the calculated turbulent pumping flow evaluated from the von Karman expression: $Q_p = 0.0697 \pi r Re_r^{0.8}$. For the results in Figs. 5-7, the full disk ($r = r_o$) pumping flow is used.

It is evident from Figs. 5-7 that with single center jet supply, quite high heat transfer rates (for a given surface temperature - coolant inlet temperature difference) are present near the disk center as a result of both impingement and undiminished temperature difference. However, the high central region heat transfer rates decrease rapidly with radius as the coolant looses its impingement character and as the coolant-to-surface temperature difference diminishes. An important question when considering the use of central coolant supply schemes is how the magnitude of heat transfer rate remaining at the important outer radius position compares with cases where the coolant is introduced through one or more jets located at some distance radially outboard of the disk center. This question is considered in the following section for the case of the multiple jet supply arrangement investigated.

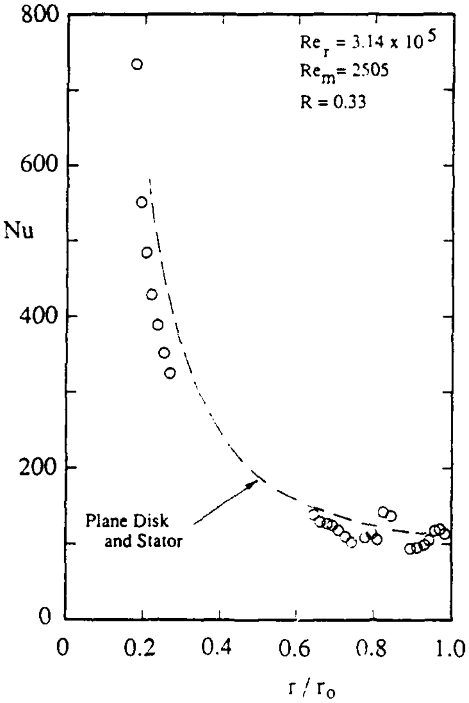

Fig. 5 Effect of Disk Contour on Nu

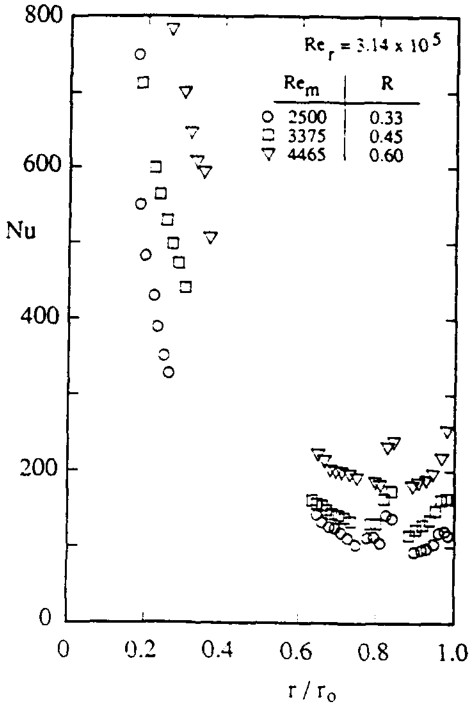

Fig. 6 Nu for Center Supply, Contoured Disk Effect of Re_m on Nu at Re_r=3.14 x 10^5

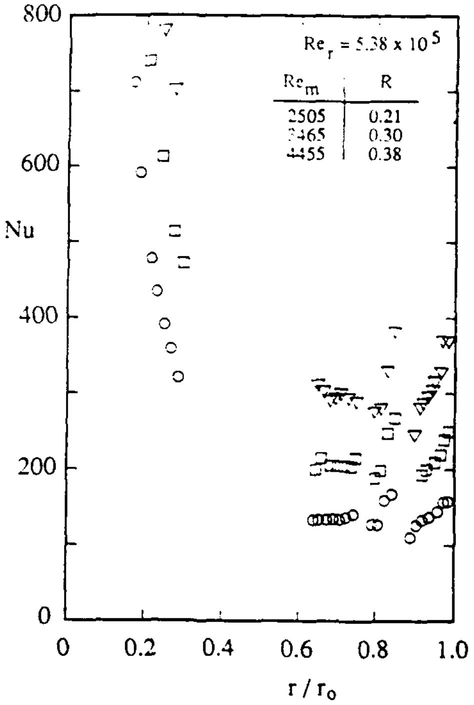

Fig. 7 Nu for Center Supply, Contoured Disk Effect of Re_m on Nu at Re_r=5.38 x 10^5

Effects of Multiple Jet Outboard Impingement Figures 8 and 9 present results obtained using the contoured disk and stator with coolant supplied through 19 equally spaced jets. In these figures, local Nusselt numbers are again based on the measured heat transfer rates and the disk surface - jet inlet temperature difference. Figure 8 shows parametrically the effect of variations in Re_m from 2520 through 4430 (and corresponding variations in R from 0.22 through 0.38, with R evaluated with the impingement radius) while Re_r is maintained constant at 5.85×10^5. All three sets of results exhibit peak values of local Nusselt number right at the impingement radius, with rapid radial decreases on both sides of the impingement location. The fact that measurable results are not obtained radially inward of the values shown indicates that the heat transfer effects of the jet array do not, to any significant extent, propagate radially inward.

The dependence of the local heat transfer rates on the value of Re_m is seen in Fig. 8 to be relatively weak. A decrease in coolant flowrate of nearly 50 percent results in only about an 11 percent decrease in the impingement heat transfer rates averaged over their effective radial positions. This is in contrast to the greater dependence on Re_m measured with central coolant supply, as indicated for the corresponding value of Re_r in Fig. 7. The difference is thought to be strongly associated with the reduction in the coolant-to-surface temperature difference that occurs in the radial outflow direction with central supply.

The values of Nu in the outboard disk regions with central supply of coolant can be obtained from Fig. 7, and then compared with the jet supply values shown in Fig. 8, for almost identical values of Re_m (indicating the same amount of total coolant flow.) The relative lack of dependence of the jet supply on Re_m combined with more significant dependence for the central supply act to create a variation with Re_m of the relative heat transfer performance of these two supply schemes. For the lower values of Re_m, the values of Nu at the impingement radius location are significantly higher than those achieved with central supply of the same total coolant flow. In fact, for a nominal Rem value of 2500, the peak jet supply Nu values are approximately 100 percent greater than the corresponding central supply values. Stated another way, this also means that the same peak cooling rates can be achieved with jet supply flow with only about 60 percent of the flow required if centrally supplied.

Figure 9 shows parametrically the effect of variations in Re_r from 3.14 x 105 to 5.38 x 105 (and corresponding variations in R from 0.32 through 0.45, again evaluated with the impingment radius) while Re_m is maintained approximately constant in the range 4430 - 4470. All three sets of results again exhibit peak values of local Nusselt number right at the impingement radius, with a rapid radial decreases on both sides of the impingement location. The peak values are almost completely independent of the variation in Re_r, indicating that they are dictated exclusively by the jet flow, which remains constant in this presentation. Such behavior is consistent with behavior expected for what we have termed in prior studies as the jet-dominated flow regime, and is consistent with recent detailed flowfield maps made in the interaction region between a single impinging jet and the pumped boundary layer on a rotating disk Brodersen and Metzger [17]. Also, although the flowrate associated with each individual jet in the 19 jet array is smaller than that associated with impingement dominated conditions in previous studies, it appears that the 19 jets acting together, at relatively close circumferential spacings, do thermally penetrate the pumped boundary layer to effectively cool the surface. The recent flowfield mapping indicates that the direction of the pumped disk flow is almost entirely tangential in the inner layers where the interaction between disk and jet is dictated. With 19 jets closely spaced as in the present configuration, the upstream jets appear to shield each individual jet from the full effect of the pumped flow and allow the jets to penetrate better than would a single jet with the same flow.

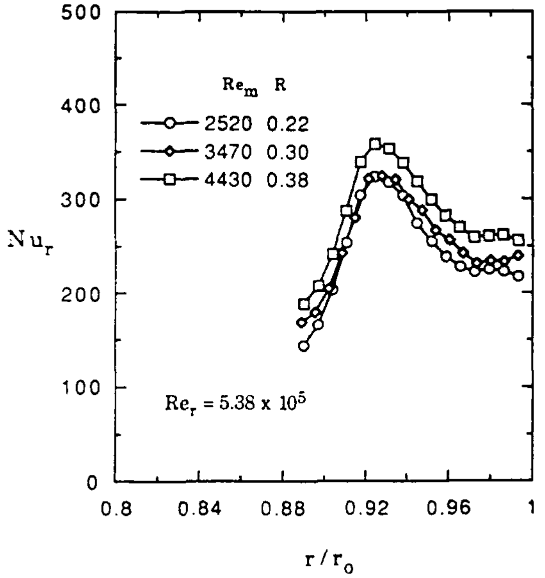

Fig. 8 Nu for Outboard Jet Supply, Contoured Disk
Effect of Re_m on Nu at $Re_r=5.38 \times 10^5$

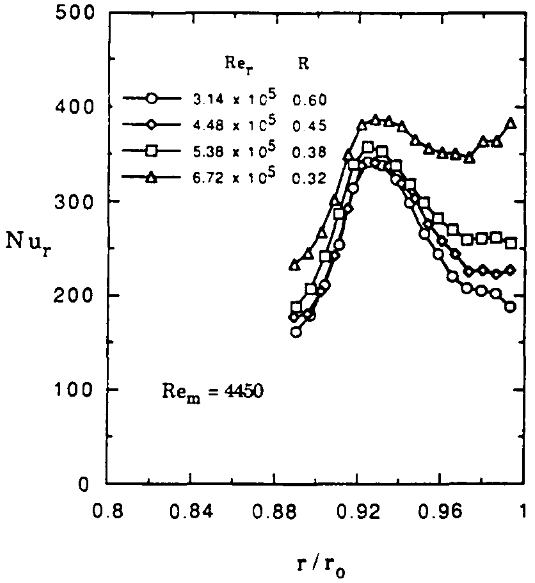

Fig. 9 Nu for Outboard Jet Supply, Contoured Disk
Effect of Re_r on Nu at Re_m=4450

Effect of Entrainment Flow

Figures 10-13 show, for the 19 jet supply, the measured effects of simulating an entrainment flow from the blade passages by supplying a measured secondary flow to the disk-cavity region through a gap in the outer rim shroud. This flow is supplied at room air conditions so it is initially at the same temperature as the test disk. As the disk temperature increases during a test under the influence of the heated cooling jets, the difference between the disk surface and simulated entrainment flow increases, and tends to drive the surface heat transfer in a direction opposing that of the coolant jets. Thus, if the entrainment flow is significantly intruding into the disk cavity, its presence will be evident through a measured decrease in local disk heat transfer rates.

For each of the combinations of Re_m and Re_r shown in Figs. 10-13, two values of simulated entrainment flowrates were investigated, nominally values of 6% and 10% of the calculated turbulent pumping flow based on the outer disk radius. For direct comparison, the previous results (0% entrainment) are re-plotted on these figures. It is immediately apparent that the presence of the simulated entrainment flow is felt on the disk surface, and that the effects are observed more strongly as entrainment flow increases. Nevertheless, the effects are relatively small, and indicate that the jets are still quite effective in cooling the local region of the disk near their impingement radius.

It should be emphasized that these results in Figs. 10-13 only serve to qualitatively indicate the presence of a heat transfer effect from the entrainment flow, and that they are insufficient to fully characterize the heat transfer effect quantitatively. In general the jet and entrainment flow temperatures will be quite different, and together with the disk surface temperature, constitute a three-temperature convection situation where information on both convection coefficient and another parameter (usually termed effectiveness) are necessary to describe the heat transfer phenomenon, similar to the situation encountered with film-cooling injection onto a surface.

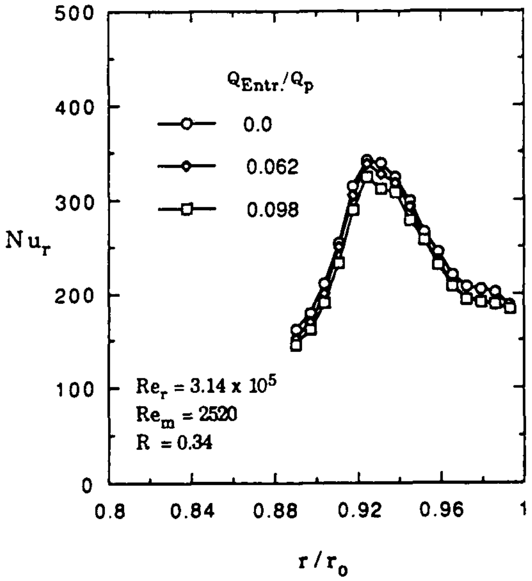

Fig. 10 Effect of Entrainment on Nu, Contoured Disk
Re_r=3.14 x 10^5, R=0.34

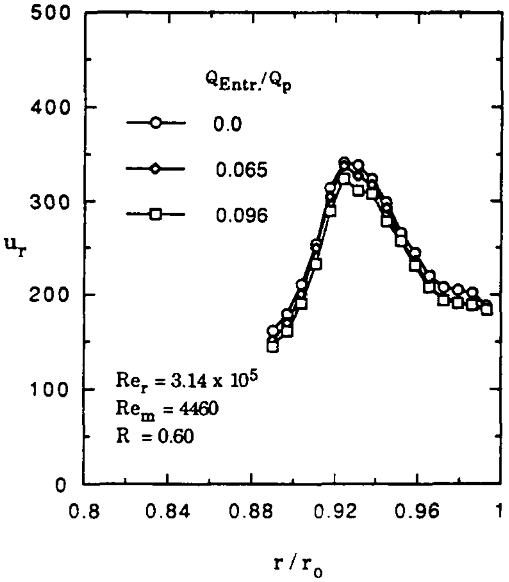

Fig. 11 Effect of Entrainment on Nu, Contoured Disk
Re_r=3.14 x 10^5, R=0.60

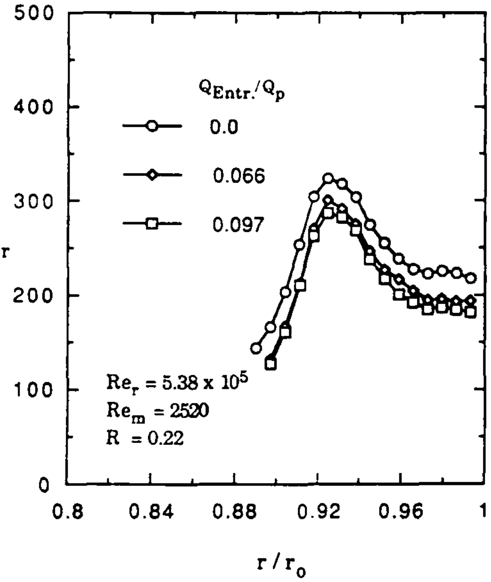

Fig. 12 Effect of Entrainment on Nu, Contoured Disk
Re_r=5.38 x 10^5, R=0.22

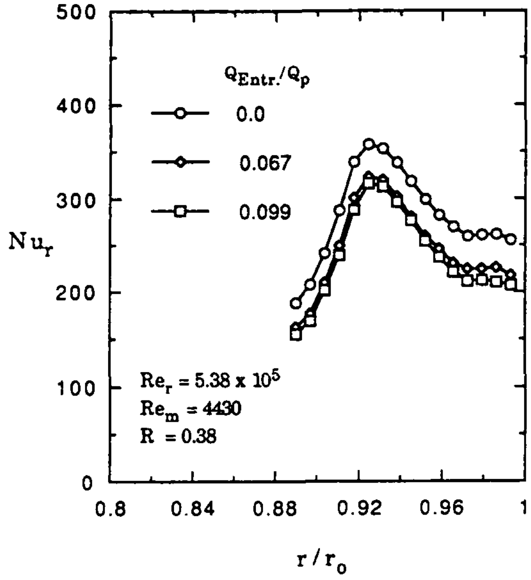

Fig. 13 Effect of Entrainment on Nu, Contoured Disk Re_r=5.38 x 10^5, R=0.38

Effect of Boltheads Figs. 14 and 15 show the measured effects, on local heat transfer near the impingement radius, of the presence of simulated boltheads located radially inward on the disk surface, for a single combination of Re_m and Re_r, for two values of entrainment flow percentage, respectively. In both instances the measured local Nusselt number values obtained with the boltheads in place are generally slightly lower than those measured without boltheads. This trend is plausibly explained by the presence of a larger pumped flow with the bolts in place which interacts more with the impingement flow to reduce the penetration of the jets to the disk surface, although the data base is obviously not large enough to support any but the most tentative speculations. Nevertheless, even though the effects are small in these two instances, the effect is in the direction of decreased cooling capacity of the jet flow, and deserves to be investigated over a much wider range of conditions.

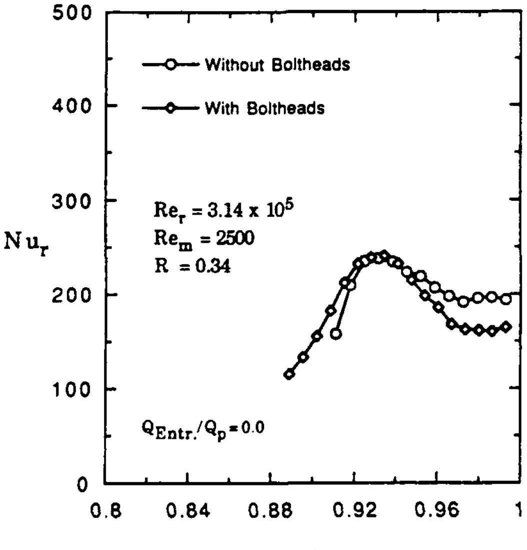

Fig. 14 Effect of Boltheads on Nu Without Entrainment, Contoured Disk

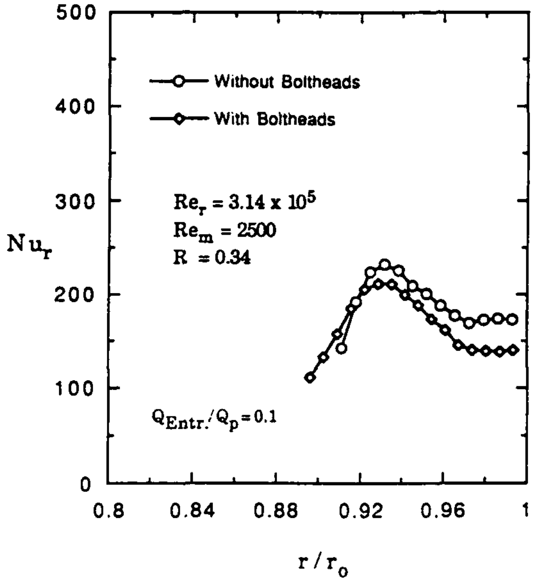

Fig. 15 Effect of Boltheads on Nu With Entrainment, Contoured Disk

Non-Axisymmetric Local Heat Transfer Variations Finally, Figs 16 and 17 describe tests conducted to obtain local Nusselt numbers around the simulated boltheads. The tests were conducted for a typical set of conditions using strobe illumination and a sychronized frame-grabbing procedure.

Such three-dimensional surface elements, or protrusions into the disk flow, will necessarily cause both the flow and heat transfer distributions to depart from axisymmetric over some region extending both radially inward and radially outward from their location on the disk. In general the radial extent of the effect as well as the magnitude of circumferential variations set up in the disturbed region can be important in that they potentially add additional thermal stresses to an already highly stressed disk.

Figure 16 shows a sketch of a portion of the disk and boltheads with the character of the local radial and circumferential heat transfer variations obtained. As might be expected, the heat transfer distributions are different on the upwind and downwind sides of the boltheads. This difference is shown quantitatively in Fig. 17 in terms of variations along typical uwind and downwind radial lines indicated A and B in Fig. 16.

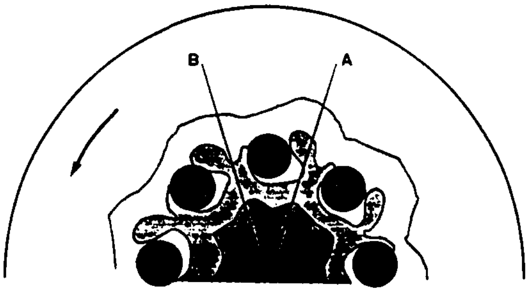

Fig. 16 Nu Contours Around Boltheads

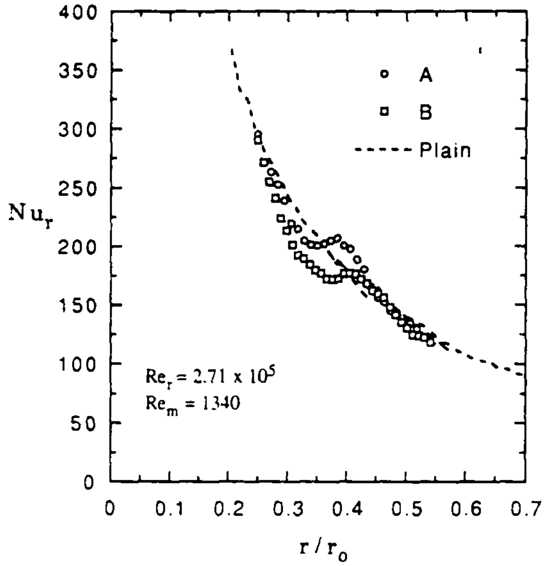

Fig. 17 Effect of Boltheads on Radial Nu Distribution

SUMMARY

The work presented can be summarized as follows:

- The acquisition of detailed local convection heat transfer coefficient distributions on models of both plane and contoured turbine disks using acrylic disk, thin spray-applied coats of encapsulated liquid crystals as surface temperature indicators, transient testing, and a computer-vision system has been successfully demonstrated. The method offers an affordable means of local disk heat transfer information, and could be useful in an interactive way to rapidly assess the effects of design alternatives or changes.

- The method has been employed thus far to acquire axisymmetric convection heat transfer information from both plane and contoured rotating disks with two different coolant supply schemes.

- Except for minor variations, the convection coefficients for the contoured disk and stator configuration are very similar to those for the plane disk and stator, both in magnitude and distribution. This observation concurs with the very limited prior information on the independent effect of disk shape and is plausible, so it appears appropriate to conclude that the effect of disk contour on heat transfer is minor.

- For coolant supplied from the center of the disk cavity, the local heat transfer rates decrease monotonically from center to disk rim along the disk face.

- For coolant supplied to the disk face from a jet ring near the disk outer radius, the location of significant coefficient magnitudes is restricted to the outer radius region, but the results indicate that the same magnitude of local cooling effect can be obtained with the jet supply at lower values of total coolant flowrate than required with central supply.

- For the present multiple jet tests, the measured heat transfer effect of the multiple jets is more significant than found in previous studies, despite the fact that the flowrate from each individual jet is no more than two percent of the calculated disk pumping flow. The combination of closely spaced jets around the complete circumference and the presence of a closely spaced stator is thought to act to improve jet penetration through the pumped boundary layer to the moving surface.

- Although the presence of both simulated entrainment and boltheads on the disk act to reduce the cooling rates for a given jet flow and disk speed, neither appears to cause a major degradation in the multiple jet cooling performance, at least over the parameter ranges covered in this study.

- The feasibility of obtaining non-axisymmetric local heat transfer variations in both the radial and circumferential directions around three-dimensional disk surface protrusions such as boltheads has been demonstrated using the same transient test procedures with the substitution of strobe illumination and synchronization of the frame-grabber. The limited information acquired shows a disk surface heat transfer effect within only a small radial region around the protrusion, but the interaction of the pumped flow with outboard cooling jets indicates that boltheads do increase the pumped flow.

ACKNOWLEDGEMENTS

This work was conducted with financial support from the Rocketdyne Division of Rockwell International Corporation through NASA Marshall Space Flight Center.

REFERENCES

1. vonKarman, T., "Uber Laminare und Turbulente Reibung. Z.", Angew. Math. Mech., *1*, 1921, p. 233.

2. Cobb, E.C., and Saunders, O.A., "Heat Transfer from a Rotating Disk", *in* "Royal Society", A236, 1956, p. 343.

3. Kreith, F., Taylor, J.H., and Chong, J.P., "Heat and Mass Transfer from a Rotating Disk", Journal of Heat Transfer, Trans. ASME, *81*, 1959, pp. 95-105.

4. Owen, J.M., "Fluid Flow and Heat Transfer in Rotating Disc Systems", *in* "Heat and Mass Transfer in Rotating Machinery", D.E. Metzger and N.H. Afgan, Editors, Washington, D.C., Hemisphere Publishing Corporation, 1984, pp. 81-103.

5. Devytov, V.I., "Investigation of Heat Transfer for Two Versions of Turbine Disk Cooling", Aviatsionnaya *Tekhnika, 8, 2, 1965, pp. 56-64.*

6. Popiel, C.O., and Boguslawski, L.,"Local Heat Transfer from a Rotating Disk in an Impinging Round Jet", Journal of Heat Transfer, Trans. ASME, *108*, 1986, pp. 357-364.

7. Metzger, D.E., and Grochowsky, L.D. "Heat Transfer Between an Impinging Jet and a Rotating Disk", Journal of Heat Transfer, Trans. ASME, *99*, 1977, pp. 663-667.

8. Metzger, D.E., Mathis, W.J., and Grochowsky, L.D., "Jet Cooling at the Rim of a Rotating Disk", Journal of Heat Transfer, Trans. ASME, *101*, 1979, pp. 68-72.

9. Bogdan, Z., "Cooling of a Rotating Disk by Means of an Impinging Jet", *in* . "7th International Heat Transfer Conference", 3, 1982, pp. 333-336.

10. Metzger, D.E., Bunker, R.S., and Bosch, G., "Transient Liquid Crystal Measurements of Local Heat Transfer on a Rotating Disk with Jet Impintement", 1989, ASME Paper No. 89-GT-287.

11. Bunker, R.S., Metzger, D.E., and Wittig, S., "Local Heat Transfer in Turbine Disk Cavities: Part I--Rotor and Stator Cooling with Hub Injection of Coolant", 1990, ASME Paper No. 91-183.

12. Metzger, D.E., and Kim, Y.W., "Experimental Modeling of Jet-Ring Turbine Disk Cooling", 1991, AIAA Paper No. 91-0343.

13. Metzger, D.E., and Larson. D.E., "Use of Fusion Point Surface Coatings for Local Convection Heat Transfer Measurements in Rectangular Channel Flows with 90-Degree Turns", Journal of Heat Transfer, Trans. ASME, *108*:, 1986, pp. 48-54.

14. Vedula, R.P., Bickford, W., and Metzger, D.E., "Effects of Lateral and Anisotropic Conduction on Determination of Local Convection Heat Transfer Characteristics with Transient Tests and Sufrace Coatings", Collected Papers *in* Heat Transfer, ASME Publication HTD-14, 1988, pp. 21-27.

15. Ireland, P.T., and Jones, T.V., "The Response Time of a Surface Thermometer Employing Encapsulated Thermochromic Liquid Crystals", Journal of Physics, *E, 20*, 1987, pp. 1195-1199.

16. Kline, S.J., and McClintock, F.A., "Describing Uncertainties in Single Sample Experiments", Mechanical Engineering, *75*, 1953, p. 3.

17. Brodersen, S., and Metzger, D.E., "Experimental Investigation of the Flowfield Resulting from the Interaction Between an Impinging Jet and a Rotating Disk", Experimental Thermal and Fluid Science, *5*, 1992, pp. 351-358.

THE SWOLLEN POLYMER TECHNIQUE AND ITS USE FOR HEAT TRANSFER INVESTIGATIONS ON FILM COOLED SURFACES

by

N. Hay and D. Lampard
Dept of Mechanical Engineering
The University of Nottingham
University Park, Nottingham NG7 2RD
United Kingdom

N. Macleod
University of Edinburgh

SUMMARY

The Swollen Polymer Technique is a mass transfer analogy method of obtaining heat transfer data. It is similar in principle to the naphthalene method but has the advantage that it can be combined with interferometric measuring methods giving a panoramic view of the distribution of the transfer coefficient over the working surface. Also the mass transfer process is reversible and the working surface can be used repeatedly.

Changes in thickness of a polymer coating on the working surface, initially swollen with an ester, are measured, using holographic interferometry to yield a fringe pattern depicting loci of equal transfer coefficient over the surface.

The paper describes the basis of the method, the equipment required to implement it, the precautions necessary for its successful use, its advantages, limitations and future potential.

The technique yields data useful in the design process. Examples of its application to film cooled surfaces are given, including the effects of geometry, density ratio and acceleration of the mainstream flow on the heat transfer coefficient.

Extension of the technique for the simultaneous measurement of effectiveness and heat transfer coefficient is described and its further extension for use with curved surfaces is outlined.

A recent development to the technique itself by the use of a thermoplastic plate for recording the holograms opens up the possibility of further advancement using electronic image processing.

SYMBOLS

c	concentration of swelling agent in fluid, kg m^{-3}
C	fluid specific heat capacity, kJ kg^{-1} K^{-1}
d	hole diameter, m
D	diffusivity of transferred material (swelling agent) in fluid, m^2s^{-1}
D_l	diffusivity of swelling agent in coating, m^2s^{-1}
h	heat transfer coefficient at surface location (x,y), W $m^{-2}K^{-1}$
H	greatest value of h for air-operated prototype that can be estimated with specified precision from mass-transferring air-operated mass-transferring model of scale factor S, W $m^{-2}K^{-1}$
H^1	greatest value of h for water-operated prototype that can be estimated with specified precision from water-operated mass-transferring model of scale factor S, W $m^{-2}K^{-1}$
H^o	greatest value of h for prototype, operating with any fluid, that can be estimated with specified precision from mass-transferring model operating with air or water, Watts $m^{-2}K^{-1}$
k	mass transfer coefficient at (model) surface location (x,y), m s^{-1}
K	greatest value of k for transfer to air determinable with specified precision in an experiment of duration τ, m s^{-1}
K^1	greatest value of k for transfer to water determinable with specified precision in an experiment of duration τ, m s^{-1}
Ka	acceleration parameter $\equiv \nu\ (du_g/dx)/u^2_g$
l	characteristic dimension of prototype or model, m
M	blowing rate $\equiv \rho_c\ u_c/\rho_g\ u_g$
m"	mass transfer per unit area, kg m^{-2}
n	fringe order
p	vapour pressure of swelling agent, mm Hg
q"	heat flux at surface location (x, y), W m^{-2}
s	change of coating thickness (surface recession) occurring in time interval t at location (x,y), m
S	scale factor of model = l_M/l_P
S'	Pitch of film cooling holes (Fig. 11), m
t	duration of exposure of model to convective transfer, s
T	temperature, °K
u	fluid velocity, m s^{-1}
x, y,	coordinates of point in transferring surface, m
z	perpendicular distance from surface at point (x,y), m

Greek

α	angle of injection, degrees to the surface
Δ_{cs}	difference between fluid concentrations at solid surface and in bulk of stream, kg m^{-3}
χ	thermal conductivity of fluid, W m^{-1}K^{-1}
λ	wavelength of (laser) light used in interferometry, nm (m x 10^{-9})
μ	fluid viscosity, kg m^{-1}s^{-1}
ν	fluid kinematic viscosity $\equiv \mu/\rho$, m^{2}s^{-1}
ρ	fluid density, kg m^{-3}
ρ_t	density of swelling agent, kg m^{-3}
τ	fixed duration specified for mass transfer model experiments, s
η	film cooling effectiveness

Suffixes

aw	adiabatic wall
B, b	condition in bulk of fluid stream, far from surface.
c	film cooling flow
g	mainstream flow
M	for (mass transferring) model system
P	for prototype system
w	wall
S, s	condition in fluid stream adjacent to, and in equilibrium with, surface
o	without film cooling injection

Dimensionless

Pr	Prandtl number, = $\mu C_p/\chi$
Re	Reynolds number, $\rho u l/\mu$
Sc	Schmidt number, = $\mu/\rho D$

1. INTRODUCTION

The Swollen Polymer Technique is a mass transfer measurement technique which, through the heat/mass transfer analogy, gives high resolution mapping of the heat transfer coefficient over extended areas.

It was originally developed by one of the authors (N Macleod) and has since been applied to a wide range of heat transfer problems. The most extensive use has been in the study of film cooling. Here, the provision of a 'map' as a direct output, Fig. 1, is invaluable not only in revealing potential hot spots, but also in giving an insight into the changes occurring in the complex flow pattern as injection parameters are varied.

This gives the technique an immediate obvious advantage both over thermal methods relying on point measurement of heat flux or temperature, and over the familiar naphthalene mass transfer technique which requires computer processing of profilometric measurements to generate a map.

The advantages of the Swollen Polymer Technique over thermal techniques using infra-red scanning [1] or liquid crystals [2,3] for surface temperature measurement stem from the absence of any requirement to view the surface during its exposure to the flow. This makes for easier rig design, and eliminates errors arising from non-homogenous fluid optical properties. These can result in errors in locating the point at which the measurement is made.

Despite these advantages, and others, such as rapid test surface restoration, the Swollen Polymer Technique has yet to be widely adopted. Perhaps this is due to worries related to the possible complexity of the holographic interferometry or of other elements of the technique, or to uncertainties regarding the accuracy or applicability of the results.

It is the purpose of this paper to demonstrate that the Swollen Polymer Technique is a well-developed and thoroughly tested system for the accurate and reliable estimation of heat transfer data.

2. ANALOGY BETWEEN CONVECTIVE HEAT AND MASS TRANSFER

In all processes of forced convection the fundamental transport mechanism is diffusion. Diffusion is effected by continual and widespread random agitation, either of molecules or of macroscopic eddies. Where the diffusate, or diffusing entity, does not itself significantly influence these random motions, the diffusion is governed by an equation whose form is the same for different diffusates, viz.

Diffusate Flux Vector =
-Diffusivity x ∇. (diffusate concentration)

For heat diffusion (conduction), the diffusate is thermal energy and the general relation becomes Fourier's Law; for mass diffusion, it becomes Fick's law.

The magnitude of the diffusivity is generally different for different diffusates in the same fluid, particularly for the molecular diffusion of heat, mass and momentum in liquids. For laminar flow, the diffusional processes for mass and heat in convective transfer are both purely molecular, and the ratio of the mass and heat transfer coefficients for strictly similar model and prototype systems is everywhere proportional to the ratio of the appropriate molecular mass and thermal diffusivities. For transfer to turbulent flow, however, only a proportion of the overall diffusional process is molecular; the remainder, outside the viscous sub-layer next to the wall, is by eddy transport, for which the diffusion coefficients for mass and heat at the same point are generally more nearly equal [9]. Thus the mass and heat transfer coefficients are not proportional to the corresponding molecular diffusivities, but show a weaker dependence on these. There is evidence, both theoretical and experimental, that this dependence is approximately as $(\text{diffusivity})^{0.67}$, at least over a small range of diffusivity. Expressed in dimensionless terms, the currently accepted relationship between heat and mass transfer coefficient and the corresponding molecular thermal and mass diffusivities for dynamically similar prototype and model systems is accordingly:

$$\frac{\left(\dfrac{h}{u_p \rho_p C_p}\right)}{\left(\dfrac{k}{u_M}\right)} = \left(\frac{Sc}{Pr}\right)^{0.67} \qquad (1)$$

Where Sc/Pr differs greatly from unity there are theoretical reasons for doubting that the RHS of (1) accurately represents the form of the Sc-Pr function. This need not undermine confidence in the validity of mass/heat transfer modelling, however, if equation (1) is applied in an indirect way. If h_1 and h_2 are heat transfer coefficients at points 1 and 2 on the prototype and k_1 and k_2 are measured mass transfer coefficients at corresponding points on the model operated under corresponding conditions (in particular, at the same Re), then whatever the correct form of the dependence of the transfer coefficients on Sc and Pr, eqn. (1) gives

$$\frac{h_1}{h_2} = \frac{k_1}{k_2} \qquad (2)$$

Thus if point 2, say, is so chosen that h_2 is known there for the experimental flow, h_1 can be found from the measured ratio k_1/k_2 for the model. An additional advantage of this procedure is that equation (2) does not contain the Schmidt number of the mass-transfer system, so that k_1/k_2 can be found directly from experimental determinations of any linear measure of k, without knowledge of any physical property of the transferred substance, such as would be needed to evaluate k_1 or k_2 separately.

There is now a very substantial literature testifying to the validity and practical utility of equation (2), whatever doubts may remain about the status of equation (1) and about physical property values for model materials in relation to absolute determinations of h.

3. SWOLLEN POLYMER HOLOGRAPHIC TECHNIQUE

The essence of this technique is that changes in the thickness of a permanent elastomeric surface coating, initially swollen to equilibrium with the volatile or soluble mass-transferring agent, are measured by holographic comparisons of the initial surface configuration with that after exposure to the convecting fluid stream for a known time [5]. Superimposition of holograms of initial and subsequent surface states yields a system of interference fringes overlying the image of the surface, Fig. 1. The fringes are isosystolic lines, or loci of constant recession -in effect, contours of coating thickness change, the contour interval being of the order of the wavelength of the coherent (laser) light employed. The superimposed holograms constitute an interferogram, a contour map of the surface showing the amount of mass transferred in the time interval between initial and subsequent observations as a function of position on the surface (conveniently registered by a ruled grid of reference lines) over the whole field of view.

More particularly, if the recession or coating thickness change occurring over time t has the value s for all points on a given contour, it is readily shown that the mass transfer flux at all such points for the transferred material of density ρ_1 is $\rho_1 s/t$. If $\Delta c_s = (c_s - c_b)$ is the driving force for the transfer, the transfer coefficient k is thus given for all points on the contour as: $k = \rho_1 s/t.\Delta c_s$.

4. OPTICAL PRINCIPLES AND PRACTICE

The basic optical arrangement required for making initial and subsequent-state holograms of a mass-transferring model surface is shown schematically in Figure 2. The essential optical principle is the convergence at the photographic plate or other recording surface of two beams from the same coherent light source (here a He-Ne laser) of wavelength λ, one beam having been modulated by reflection from the test plate while the other provides a smooth reference field of illumination. The interference pattern formed at the recording surface by superposition of these optical fields registers the phase and intensity distribution in that plane of the wave-front originating from the test plate, and may be reconstructed from its encoded record, once that is made permanent as a hologram, by illuminating the recording with the reference beam alone. The eye (or a television camera) placed behind the hologram then sees a virtual image of the test surface in front of the hologram, in the position occupied by the test plate when the hologram was recorded.

If meanwhile the test plate still occupies, or is restored exactly to, its original position, its virtual reconstructed image is superimposed upon the surface itself. If any part of this test surface is displaced from its original location through such a distance that the light reaching the observer from it is out of phase with that appearing to originate from the corresponding part of its virtual image, destructive interference will make the displaced region appear darker. When viewed through the initial-state hologram, the loci of all points displaced equally from their initial (or virtual image) positions will be light or dark bands or fringes, according to whether the optical path change is an even or odd number of $\lambda/2$ increments.

In the arrangement of Fig. 2, the mass-transferring coating is a transparent layer overlying a fixed diffusely reflecting surface. Recession of the coating surface, and change in coating thickness, changes the optical path length of the object beam (though not its geometrical path length) because the refractive index of the coating elastomer is greater than that of air. The consequent relation between recession distance and number of fringes generated depends not only on this refractive index difference but also on the angles of viewing and observation, and is given in [5].

Fig. 3 details the sequence of operations in our most usual application of these principles, and Fig. 4 shows the holographic apparatus used in the film cooling investigation at Nottingham. This is contained within a chamber where temperature is maintained constant and equal to that of the wind tunnel in which the demountable test-piece is exposed to the flow. This is vital, as temperature changes result in changes in the thickness of the coating substrate which are experimentally indistinguishable from those arising in the coating due to mass transfer.

After the initial hologram is made, the mass-transferring test-piece is removed from the anti-vibration optical table and special environment required for successful holography and placed in the wind-tunnel, Fig. 5, or other flow system.

During the subsequent timed exposure to the experimental flow, the transferring surface need neither be visible from, nor connected to, any data gathering station outside the test equipment; the coating develops its own self-contained record of the pattern of transfer as the experiment proceeds. This record is made visible, after the test-piece is replaced in its kinematic mount on the holographic table, either by viewing it through the developed hologram of its original state (live-fringe technique), or by using the still undeveloped plate, which is developed subsequently (frozen-fringe), or double exposure, method). The latter gives directly a robust permanent record; but the live-fringe technique has the advantage of allowing local maxima and minima of mass transfer rate to be identified unambiguously on the contour pattern. This is achieved by minutely displacing the developed hologram towards the object, eg. by gently deflecting it by light finger presure; during this movement the fringes appear to move outwards from points of maximum recession and converge upon those of minimum transfer [6]. In any case, the interference fringe pattern thus generated, registering the difference between final and initial surface configurations, can either be photographed or video-recorded.

To interpret this fringe or contour map in terms of absolute, or even relative, surface recessions or rates of transfer, we require to know fringe order numbers. These are readily found by independent measurements of surface recession at one or two selected points in the fringe field. In our work, we have used free-jet air gauging for such point measurements. Fig. 6 shows the air gauge and kinematic mount used at Nottingham [7]. A potential source of error, that of mass transfer to the flow of air from the gauge, can be virtually eliminated by saturating the air supply to the gauge with the mass transferring agent.

Local coating-thickness changes corresponding to many fringes can in this way be measured to a fraction of a fringe, and thus with great precision. The spatial resolution of these measurements over the surface is limited only by the grain size of the photographic or other recording medium.

In our experiments the laser light wavelength is 633 nm, so even in a model of small dimensions operated at high flow Reynolds numbers, accurately measurable surface recession can be far smaller than the fluid viscous sub-layer thickness. Thus, although the method registers mass transfer through configurational changes in the flow boundaries, these changes can be kept so small as to have no significant effect on the flow.

5. PHYSICO-CHEMICAL PRINCIPLES OF SWOLLEN POLYMER TECHNIQUE AND THE CHOICE OF SWELLING AGENT

A polymer surface-coating initially swollen to equilibrium with a volatile or soluble swelling agent diminishes in thickness as the transferable material is removed from its surface. For some time, ie. until the swelling agent concentration falls significantly, the coating shrinks at the same rate as would a (solidified) surface layer of the pure swelling agent under the same conditions of convective transfer.

The volume of the swollen material is simply the sum of the component volumes. For a thin polymer coating bonded to a rigid substrate, and thus of fixed superficial area, volume changes are proportional to changes of thickness. The local coating recession at any point is thus the volume of swelling agent transferred per unit area of coating at that point.

On this basis, the properties of the polymer are irrelevant to the interpretation of the holographic record of recession rate in terms of mass transfer coefficients. It follows that any swellable stable polymer that can conveniently be deposited as a strongly adherent transparent surface coating on a suitable (diffusely reflecting) model substrate may be chosen for this application. The room-temperature vulcanising (RTV) silicone elastomer, GE 615, available as a liquid from Dow Corning, is found very convenient for the purpose. After mixing with the proprietary catalyst it may be painted or solvent-sprayed to form a coating a few tenths of a millimetre thick on the surface of a light alloy model previously treated with the recommended primer to promote bonding; a few minutes or hours later, depending on the age of the liquid sample and the ambient temperature, the coating forms a firm elastic film, see Fig. 7. Curing is completed in 24-48 hours, after which the film can be swollen to equilibrium by immersion for a few hours in a bath of the swelling agent chosen. After removal from the bath and freeing from superficial liquid droplets by blotting with absorbent paper, the coated model is ready for use in a mass transfer experiment.

The coating can be re-swollen for subsequent experiments simply by re-immersion in the liquid bath. With the swelling agents recommended below, it appears to suffer no deterioration, even after dozens of repetitions of the swelling-shrinking cycle.

Regarding the choice of swelling agent, the above arguments imply that this, also, can be fixed simply by considerations of values of coefficients at different points on the same surface. It is not even necessary in principle to know the physical properties of the swelling agent (assuming that its concentration in the experimental stream nowhere approaches saturation); eqn. (2) above shows that the ratio of transfer coefficients at any two points appearing on the same mass-transfer interferogram is the ratio of the fringe orders at those points, if the concentration driving force for mass transfer, $c_s - c_b$ is the same at both locations - eg. if the swelling agent concentration in the experimental fluid stream is everywhere very small, so that $c_s - c_b \sim c_s$ throughout.

There are nevertheless quite stringent practical limitations on choice of swelling agent in all cases.

This is because such swelling agents must give sufficiently low rates of mass transfer in situations of practical interest to generate reasonably small (ie. countable) numbers of interference fringes in an experimental period long enough for the flow start-up and stopping periods to be negligible. This means that the swelling agent must be of exceptionally low vapour pressure or solubility, such as is neither easily determined nor reliably estimated from standard correlations. Consequently the choice of swelling agents is strictly limited, particularly if absolute values of heat transfer coefficient are required.

Details of three swelling agents found suitable by us, together with recently determined and verified physical property data, are given in Table 1.

These recommended swelling agents satisfy a further limitation on the choice of swelling agent, viz that it must have a sufficiently powerful swelling action on the coating elastomer used. Here the fundamental requirement is that a coating of acceptable thickness, swollen initially to equilibrium, should contain enough swelling agent to allow subsequent transfer of an accurately measurable amount without a significant fall in surface concentration from the initial (saturation) value.

A mathematical treatment of this latter requirement is given in [8]. The results of this analysis show that for experiments of fixed duration, τ, depletion effects set an upper limiting value for the transfer coefficient that can be measured with any specified accuracy using a given swelling agent/polymer coating system. This limiting value of the coefficient is independent of coating thickness when that exceeds a critical magnitude of order $\sqrt{D_1\tau}$.

Table 1 gives results for such limiting values according to the analysis of Ref 8. These have been calculated for the three swelling agents most commonly used by us and for GE RTV 615 silicone rubber coatings of more than the critical thickness (approximately 1.5×10^{-4} m for $\tau = 300$ s). Here K and K^1 are the greatest values of coefficients of mass transfer to air and water respectively, determinable interferometrically with an error due to coating depletion not exceeding 2-3% of K or K^1 in experiments lasting 5 minutes.

The implications of these limitations on k for the simulation of heat transfer equipment by 'cold' polymer-coated scale models are shown directly in the last two columns of the table. Here H and H^1 are the largest values of heat transfer coefficients (to air and water respectively) that can be estimated with 2-3% accuracy for a prototype system from five-minute measurements on a geometrically similar mass-transferring model S times as large, coated with the materials detailed in the table, operated at the same Reynolds number with the same fluid.

These values are obtained as

$$\frac{H}{S} = K\rho_p C_p \left(\frac{Sc}{Pr}\right)^{0.67} \tag{3}$$

from equation (1) (and H^1 similarly), on the basis that $u_p/u_M = S$, when the model and prototype Reynolds numbers are equal and the fluids are the same. When the fluids are not the same, the following more general expression can be arrived at from equation (1) for H°/S

$$\frac{H^\circ}{S} = K\,\frac{\mu_p\,\rho_M\,C_p}{\mu_M}\left(\frac{Sc_M}{Pr_p}\right)^{0.67} = \frac{\nu_p}{\nu_M}\left(\frac{Pr_M}{Pr_p}\right)^{0.67} \frac{I}{:} \tag{4}$$

- if the model is operated with air. If the model fluid is water, H^1 replaces H in this expression.

6. OPTIMAL OPERATING CONDITIONS FOR COATED COLD MODELS

When planning to simulate the performance of convective heat transfer ('prototype') equipment with a coated mass transferring 'cold' model, the experimenter can use equation (4) and the given table of H values to choose the swelling agent, experimental fluid and scale factor S so as to ensure that no significant modelling errors arise from GE 615 coating depletion (de-saturation) in a five minute experiment. It is first necessary to estimate approximately a value for h_p, the maximum (local) heat transfer coefficient value which it is desired to determine for the prototype. Then, from equation (4), a coated model S times as large as the prototype will allow estimation of prototype heat transfer coefficients with an error due to coating depletion not exceeding 2-3% in a 5-minute period of transfer if

$$\frac{h_p}{S} < \frac{\nu_p}{\nu_M}\left(\frac{Pr_M}{Pr_p}\right)^{0.67} \frac{H_M}{S} \tag{5}$$

- where H_M/S has the value of H/S in the table if the model is air-operated and H^1/S if the model fluid is water.

As an example of the modelling choices to which this leads, we may consider a particular cold model study of gas-turbine blade film-cooling. Here, previous results had indicated that h_p, the greatest value of the heat transfer coefficient at the blade surface under the most extreme flow conditions to be investigated, would be of the order 200 Watts $m^{-2}K^{-1}$. Assuming for the present purpose that the prototype fluid has approximately the properties of air, and assuming also that we wish to use air, rather than water, as the model fluid, we then have

$$\frac{200}{S} < \frac{H}{S}\; W\,m^{-2}\,K^{-1} \tag{6}$$

Reference to the H/S values given in the table shows that the first two swelling agents listed there would be suitable only for S > 4 or 5, ie. for a model much larger than the prototype. Thus, if it were desired to use a model of the same size as the prototype, n-Tetradecane would be the swelling agent of choice in the air-operated model.

With this swelling agent, a scaling factor S = 1 and h for the prototype nowhere greater than 200 W $m^{-2}K^{-1}$, k for the air-operated model would not exceed 200/600 x 17 x 10^{-2} ms^{-1}, ie. ⅓ K. It follows that in a five-minute experiment the coating recession would nowhere exceed one-third of that corresponding to significant depletion. Thus, if the duration of these experiments were limited to τ, the numbers of fringes observed would everywhere be unduly and unnecessarily small and the percentage error on each recession measurement and k value would be correspondingly large. The coating-depletion error would, of course, at the same time be reduced below the 2-3 % assumed in the table; but this reduction would fall far short of compensating for the increased percentage error in recession measurement. Clearly, the resultant percentage error in k would be minimised by continuing the transfer to the point where coating depletion began to become significant in relation to the error in measuring the coating recession - in this case, by extending the duration of the experiment to about 3 x τ, or 15 minutes.

In general, therefore, the optimum duration of a model experiment designed to maximise the accuracy of h estimation for the prototype is given approximately by

$$t = \tau \frac{\left(\frac{H}{S}\right)}{\left(\frac{h_p}{S}\right)} = 300 \frac{\left(\frac{H}{S}\right)}{\left(\frac{h_p}{S}\right)} \text{ seconds} \qquad (7)$$

- assuming, for the coating materials given here, a coating thickness of at least 1.5×10^{-4} m, ensuring that the saturated coating has adequate swelling-agent capacity.

7. APPLICATION OF THE METHOD TO THE ESTIMATION OF HEAT TRANSFER COEFFICIENTS ON FILM COOLED SURFACES

The easy surface restoration of the polymer coating simply by soaking in a bath of swelling agent is a very attractive feature of the method for film cooling studies, in which various injection geometries are tested over a wide range of flow parameters. The basic operational steps for obtaining a hologram with fringes corresponding to contours of constant mass or heat transfer coefficient have already been covered. Some of the necessary precautions have also been mentioned: in particular, the need to keep the test plate temperature constant to avoid the appearance of fringes resulting from thermal strains. In our experiments at Nottingham, both the holographic apparatus and the wind tunnel working section are contained in temperature- controlled chambers, and the flow temperature is also controlled to ensure a fixed, uniform temperature throughout.

The resulting repeatability is evident from the fringes shown in Fig. 8, and the associated interpretation beneath it. Note the very high spatial resolution which permits fringes to be resolved within small distances from the 2.3 mm diameter injection holes. Note also that, in accordance with Section 2, the results are presented as a ratio, h/h_0, to remove the sensitivity to Sc. Only a part of the hologram is shown here. There is a region of flow visible on the photograph from which the Figure is taken which is unaffected by the injected flow, thus permitting the fringe number corresponding to h_0, to be determined.

A considerable body of data has been collected using the method. Fig. 9 shows correlated data demonstrating the effects of mainstream acceleration upon the heat transfer coefficient under cooling films. It will be noted that the data includes cases with a density ratio of 1.52, modelling the real engine conditions more closely. The sensitivity of the heat transfer coefficient distribution, and the associated flow field, to density ratio rate can be gauged from Fig. 10 in which the blowing rate is maintained constant at unity for density ratios of 1 and 1.52.

The modelling of elevated density ratios in isothermal flows requires foreign gas injection. In the present case, carbon dioxide was used. Although diffusion rates for the swelling agent vapour differ between air and carbon dioxide, this was found to have no discernible effect (13) and it was thus concluded that the swollen polymer technique gives precise and detailed measurements of heat transfer coefficients under conditions modelling the most essential of those for the real engine.

8. EXTENSION OF THE METHOD FOR EFFECTIVENESS MEASUREMENT

Two mechanisms control the heat transfer to film cooled surfaces. As already seen, the stirring effect of injecting a flow in a cross-stream increases the heat transfer coefficient above that for the boundary layer, ie. $h/h_0 > 1$. Reduced heat transfer will only result if the temperature of the injected film is sufficiently low. This thermal dilution is usually given in terms of an adiabatic wall effectiveness.

$$\eta_{aw} = \frac{T_g - T_{aw}}{T_g - T_c} \qquad (8)$$

where T_g, T_c, T_{aw} are the mainstream, the coolant gas and the adiabatic wall temperature respectively.

It is easily shown that

$$\frac{(q'')_w}{(q'')_g} = 1 - \eta_{aw} \qquad (9)$$

where subscripts w and g denote film heat fluxes measured with coolant temperatures equal to the wall and gas temperature respectively. It is evident that a thermal experiment can easily be conducted to determine η_{aw}, simply by passing gases at the wall and mainstream temperatures to separate sections of the injection arrangement.

In the analogous mass transfer experiment, the concentration at the wall is equivalent to the wall temperature, and, in the swollen polymer technique, this concentration is set by the vapour pressure of the swelling agent. To model the condition of coolant temperature equal to wall temperature, all that is necessary is to saturate the coolant airstream with swelling agent, while maintaining isothermal conditions. The modelling of coolant temperature equal to free stream temperature requires only the absence of swelling agent in both coolant and main stream, as in the earlier transfer coefficient measurements, so that it should, in principle, be possible to determine both the heat transfer coefficient and the film cooling effectiveness from a single experiment.

An injection system comprising two adjacent identical slots was constructed to test these ideas. Air saturated with swelling agent vapours was fed to one, while the other was fed with normal air. A double-exposure interferogram was obtained covering the flow field downstream of both slots.

At any streamwise location then, the mass transferred corresponded to the fringe order at that point. Thus, the ratio of the fringe orders at any location downstream of the two slots gave the corresponding ratio of the mass transfer from which η_{aw} could be determined using

$$\frac{(m'')_{sa}}{(m'')_{a}} = \frac{n_{sa}}{n_{a}} = 1 - \eta_{aw} \qquad (10)$$

where subscripts 'a' and 'sa' denote 'air' and 'saturated air' respectively.

It proved relatively easy to satisfy the underlying assumptions of identical slot geometries and isothermal conditions. Achieving the necessary 100% saturation level was more problematic because of the exceedingly low vapour pressure of the swelling agent. It proved necessary to spray swelling agent into a heated chamber, and then to pass the mixture through a cooler and droplet separator to achieve fully saturated conditions at the wind tunnel flow temperature.

Comparison with thermal measurements of effectiveness from [14] are shown in Fig. 11. The results are close bearing in mind that all are subject to experimental error. Both sets of data show the optimum effectiveness to be given by the middle value of blowing rate, 0.64.

9. EXTENSION OF THE METHOD TO CURVED SURFACES

Curved surfaces present two problems; the coating of the surface with polymer, and the interpretation of the fringe pattern, as the optical path length becomes a complex function of position.

A method of casting a smooth coating of even thickness was devised, see Fig. 12. While an even thickness is not a prerequisite of the method, smoothness and dimensional accuracy of the finished surface are clearly desirable.

The second problem, that of fringe order interpretation, can be solved with the aid of geometric analysis and a computer. Clearly, this problem would be eased if the fringe data could be read electronically directly from the hologram.

We have found that the thermoplastic holographic recording system offered commercially by the Newport Corporation [15], used in conjunction with a video camera and recorder, offers a more user-friendly, largely automatic, replacement for ordinary photography in holographic mass transfer techniques, thus extending their range and ease of application in every way. It is noteworthy that the Newport thermoplastic recording system yields holographic interferograms showing spatial resolution at least equal to that of conventional photographic holograms.

10. THE NEWPORT THERMOPLASTIC HOLOGRAPHIC RECORDING SYSTEM

The distinguishing feature of this system is the thermoplastic photo-conductive recording plate used in place of a conventional photographic medium to record holograms. Where light falls on this composite transparent plate of several functionally distinct layers, the altered conductivity of the photo-sensitive layer changes the distribution of electric charge which has previously been applied by corona discharge at the outer surface. Application of a second charge to the surface then enhances the extent of this redistribution of the electric field. When the thermoplastic layer of the laminated plate is heated, by passage of an electric current through the conductive backing, the transparent softened plastic is electrostatically compressed and deformed locally according to the local magnitude of the charge gradient across it. On cooling, the solidified plastic layer thus registers the pattern of light and darkness to which it was originally exposed as variations of surface level; and the resulting pattern of ridges and hollows can diffract the incident light in the same way as the lines of developed grains in the emulsion of a conventional hologram recorded photographically. Because the thermoplastic is homogenous and of such high electrical resistance as to sustain large lateral charge gradients, the attainable spatial frequency of the lateral variations of thickness change, and hence the spatial resolution of the record, rivals that even of the finest-grain photographic emulsions. It is thus well adapted to record visible-light holograms.

On irradiating the plate with uniform intense light, all residual charge leaks away to the earthed conductive backing; electric heating of the thermoplastic layer then allows its surface to flow into the original planar configuration under the action of surface tension, obliterating the record. The plate is then ready for a fresh exposure.

This high-resolution system of optical recording has the significant advantage, compared with photography, that it entails no chemical processing. The Newport system, comprises the recording device or camera, with its inbuilt corona plate-charging mechanism and substrate-heating circuity, together with a Controller cabinet and electrically operated shutters for interrupting object and reference beams. With this equipment all operations required to produce a stable record of the pattern of illumination at the plate can be carried out in situ and in an automated sequence. Moreover, the complete record/erase cycle - the erasing of one hologram and recording of another on the same re-usable plate - can be completed in one minute, simply by pressing a switch on the Controller. The thermoplastic system approaches in this respect the convenience of ESPI (which the present authors have also used for mass transfer measurement [16]), while far surpassing that in fringe resolution and image quality, being based on true holography.

Live - or frozen-fringe interferograms can be obtained from thermoplastically recorded holograms in the usual way; and these can be video recorded if a television camera is placed at C in Fig. 2, just as when conventional photography is used to form the holograms [17]. The use of a television camera necessarily degrades the image quality of the interferogram and gives poorer spatial resolution than can be obtained with photographic recording; but it promises great advantages in respect of any subsequent image processing step. Thus, for example, if the object surface is curved, the signal from the video camera can readily be input to a computer programmed to generate and display on the monitor the pattern of transfer coefficient variation corrected for optical distortion by the surface curvature.

11. CONCLUSIONS

- The numerous advantages of the Swollen Polymer Technique over both thermal and other mass transfer techniques have been outlined.

- Guidelines and precautions have been specified which will allow precise, high resolution heat transfer data over extended areas to be obtained.

- It has been shown that the ratios of heat transfer coefficients at points on a surface can be deduced from the ratios of the fringe orders independent of the Schmidt number and of other thermo-physical properties of the polymer/swelling agent system.

- Guidelines have been given for the rational, optimum selection of the swelling agent at the planning stage of an experiment.

- Examples of the application of the technique to film cooling heat transfer studies have demonstrated both the repeatability and reliability of the results, and the capability of modelling the most important parameters.

- An extension of the method permitting the simultaneous measurement of both the heat transfer coefficient and the film cooling effectiveness has been demonstrated.

- New developments in data collection which should ease the problem of fringe pattern interpretation on curved surfaces have also been described.

REFERENCES

1. Sasaki, M., Takahara, K., Kumagai, T. and Kumano, M., Film Cooling Effectiveness for Injection from Multirow Holes. Trans ASME (J.Eng.Power) 101, 101-8, 1979.

2. Cooper, T.E., Field and Meyer, J.F., Liquid Cyrstal Thermography and its Application to the Study of Convective Heat Transfer. Trans ASME (J.Ht.Transf.) 97, 442-450, 1975.

3. Hippensteele, S.A., Russel, L.M. and Stepka, F.S., Evaluation of a Method for Heat Transfer Measurements and Thermal Visualisation using Liquid Crystals. Trans ASME (J.Ht.Transf.) 105, 184-9, 1983.

4. Transport Phenomena, Bird, R.B., Stewart, W.E. and Lightfoot, W.N., p 629, John Wiley and Sons Inc., New York 1960.

5. Kapur, D.N. and Macleod, N., The Determinaiton of Local Mass Transfer Coefficients by Holographic Interferometry. Intl.J.Heat Mass Transfer 17, 1151-1162, 1974.

6. Holographic and Speckle Interferometry, Jones, R. and Wykes, C., p 93, Cambridge University Press 1983.

7. The Heat Transfer coefficient on Film Cooled Surfaces, H.D. Ammari, Ph.D. Thesis, University of Nottingham, 1989.

8. Macleod, N. and Todd, R.B., The Experimental Determination of Wall-Fluid Mass Transfer Coefficients using Plasticised Polymer Surface Coatings. Intl.J.Heat Mass Transfer 16, 485-504, 1973.

9. Paterson, W.R, Colledge, R.A., MacNab, J.I and Joy, J.A., Solid-Gas Mass Transfer Coefficients by the Swollen Polymer Method: Proving of Swelling Agents. Intl.J.Heat Mass Transfer 30, 279-287, 1987.

10. Heat and Mass Transfer at the Wall of a Packed Bed at High Reynolds Numbers, Colledge, R.A., Ph.D. Thesis, University of Cambridge, 1986.

11. Witherspoon, P.A. and Bonoli, L., Correlation of Diffusion Coefficients for Paraffin, Aromatic and Cycloparaffin Hydrocarbons in Water. Ind.Eng.Chem. Fundamental 8, 589-591, 1969.

12. Fuhner, H., Die Wasserloslichkeit in homologen Reihen. Ber. 57, 510-515, 1924.

13. Ammari, H.D., Hay, N. and Lampard, D., Simulation of Cooling Film Density Ratios in a Mass Transfer Technique. ASME Paper No 89-GT-200, Gas Turbine Conf. Toronto, 1989.

14. Hartnett, J.P., Birkebak, R.C., and Eckert, E.R.G., Velocity distribution, temperature distribution effectiveness, and heat transfer for air injection through a tangential slot into a turbulent boundary layer. ASME Jnl. of Heat Transfer, 83, pp 293-306, 1961.

15. Colburn, W.S. and Tompkins, E.N., Improved Thermoplastic-Photoconductor Devices for Holographic Recording. Applied Optics 13, 2034-2491, 1974, see also: Newport Ltd (UK), Pembroke House, Thompsons Close, Harpenden, Herts. A15 4ES for details of HC 320 Holographic Device.

16. Hyne, N. and Macleod, N., The use of Speckle Pattern Interferometry for Convective Mass Transfer Measurement. Inst.Chem.Engrs. Symposium Series No. 90, 147-152, 1984.

17. Interferometric Measurement of Local Mass Transfer Rates to an Impinging Jet, N. Gholizadeh. Ph.D. Thesis, University of Edinburgh, 1992.

18. Ammari, H.D., Hay, N., and Lampard, D., Effect of acceleration on the heat transfer coefficient on a film cooled surface. ASME Jnl. of Turbomachinery, 113, No. 3, July 1991, pp 464-471.

19. Ammari, H.D., Hay, N., and Lampard, D., The effects of density ratio on the heat transfer coefficient from a film cooled flat plate. ASME Jnl. of Turobmachinery, 112, No. 3, July 1990, pp 444-450.

20. Hay, N., Lampard, D., Maali, R., and Burns,I., Simultaneous determination of heat transfer coefficient and adiabtic wall effectiveness on a film cooled surface using the swollen polymer technique. Proc. 8th. Int. Heat Transfer Conf., San Francisco, 1986.

21. Macleod, N. and Ruess, T., The radial transfer of mass to an annular stream of liquid between coaxial rotating cylinders. Chem.Eng.Sci. 30, 235-242, 1975.

22. The profilometric determination of mass transfer coefficients by holographic interferometry, D.N. Kapur. Ph.D. Thesis, University of Edinburgh, 1973.

23. Macleod, N., The swollen polymer technique for mass transfer rate measurement at solid-fluid interfaces. Intl.J.Heat Mass Transfer, in press.

TABLE 1 Properties [*] [9,10] of Three Swelling Agents used with GE RTV 615 Clear Silicone Rubber Surface Coatings for Mass Transfer Measurement by the Swollen Polymer Technique, together with limiting values of transfer coefficients to air and water accurately determinable with them in experiments of 300 s duration.

Swelling Agent	Mol. Wt	Vapour pressure, p (mm. Hg) $\log_{10}p = X - Y/T$ $293<T<328$	Solubility in water, c_s (kg m^{-3}) $292<T<298$	Density ρ' (kg m^{-3})	Sc in air	Sc in water	K m s^{-1} [23]	K^1 m s^{-1} [23]	H/S W m^{-2} K^{-1} [23]	H^1/S W m^{-2} K^{-1} [23]
1-Me Naphthalene	142.19	0.0459 (293°K) X = 8.1083 Y = 2768.69	-	1.029×10^3	2.59	-	1.7×10^{-2}	-	49.1	-
Ethyl Salicylate	166.17	0.0429 (293°K) [21] X = 8.8870 Y = 3005.49	2.9×10^{-1} (293°K) $c_s = 0.014T - 3.812$ [21, 22]	1.132×10^3	2.86	1260 [21]	1.5×10^{-2}	2.0×10^{-5}	46.3	2.71×10^3
n-Tetradecane	198.38	0.0090 (293°K) X = 10.7020 Y = 3738.01	$>1.4 \times 10^{-2}$ [x] (293°K)	0.765×10^3	3.51	2100 [+]	17.0×10^{-2}	1.2×10^{-3} [x]	600	$>2.29 \times 10^6$

[*] At 20°C (293°K), except where otherwise stated.

[+] Estimated according to [11].

[x] Based on data for octane [12].

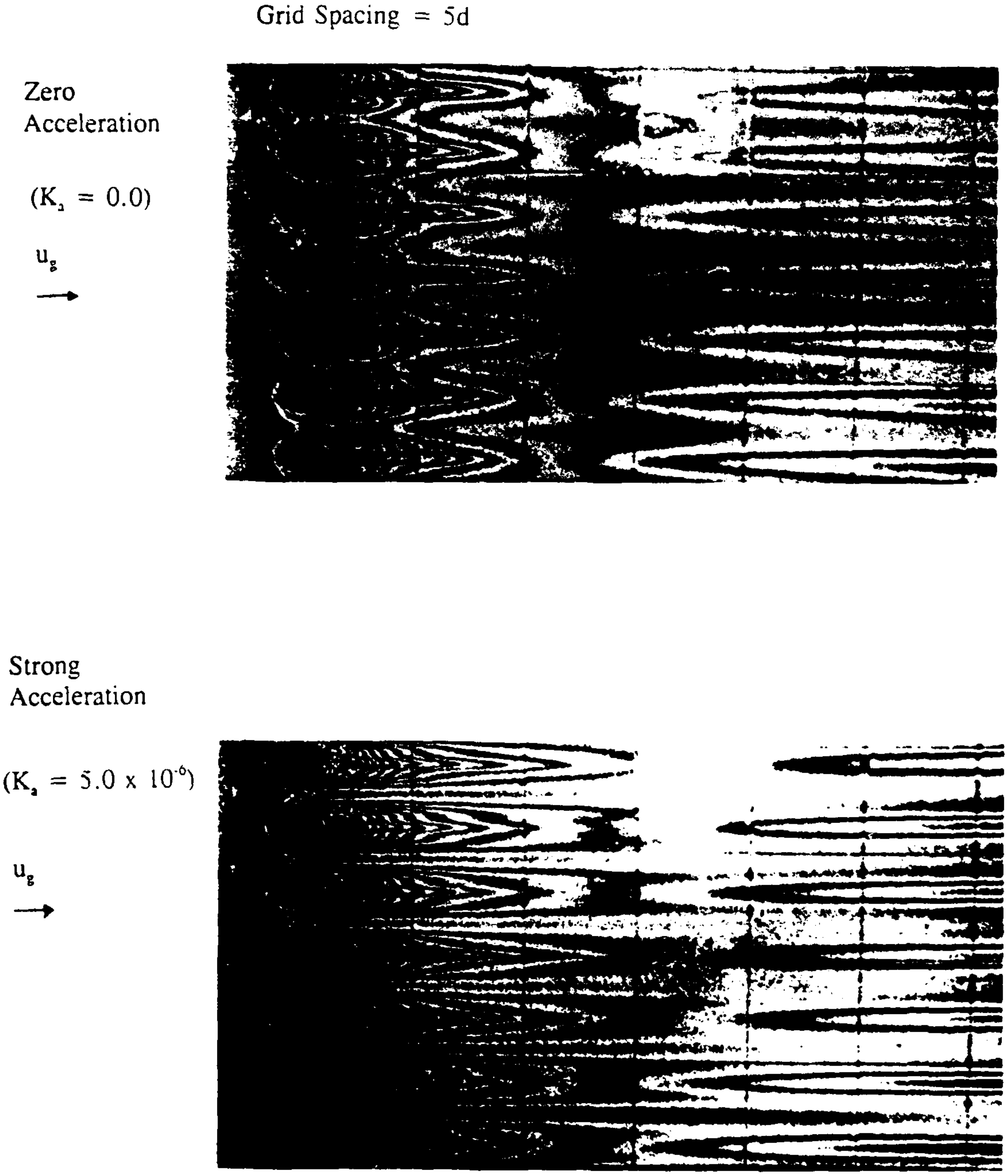

Grid Spacing = 5d

Zero Acceleration

$(K_a = 0.0)$

u_g →

Strong Acceleration

$(K_a = 5.0 \times 10^{-6})$

u_g →

Figure 1 Interference fringes showing the effect of mainstream flow acceleration on the heat transfer coefficient distribution for air injection through a row of 35° holes at blowing rate = 1. [Ref 18]

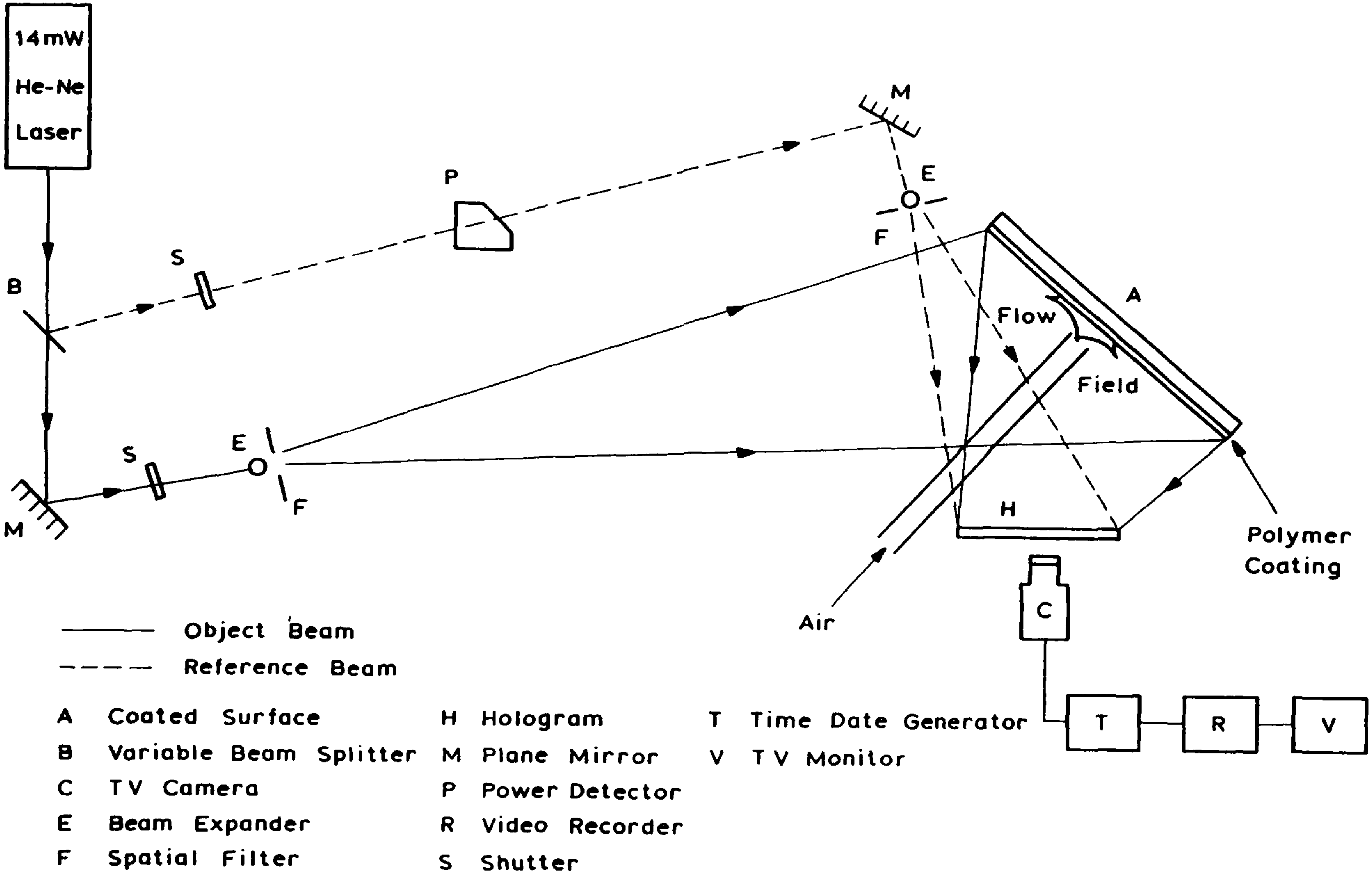
14mW
He-Ne
Laser
B
S
P
M
E
F
M
S
E
F
A
Flow
Field
H
Polymer Coating
Air
C
T
R
V
Object Beam
Reference Beam
A Coated Surface
B Variable Beam Splitter
C TV Camera
E Beam Expander
F Spatial Filter
H Hologram
M Plane Mirror
P Power Detector
R Video Recorder
S Shutter
T Time Date Generator
V TV Monitor

Figure 2 Holographic Arrangement

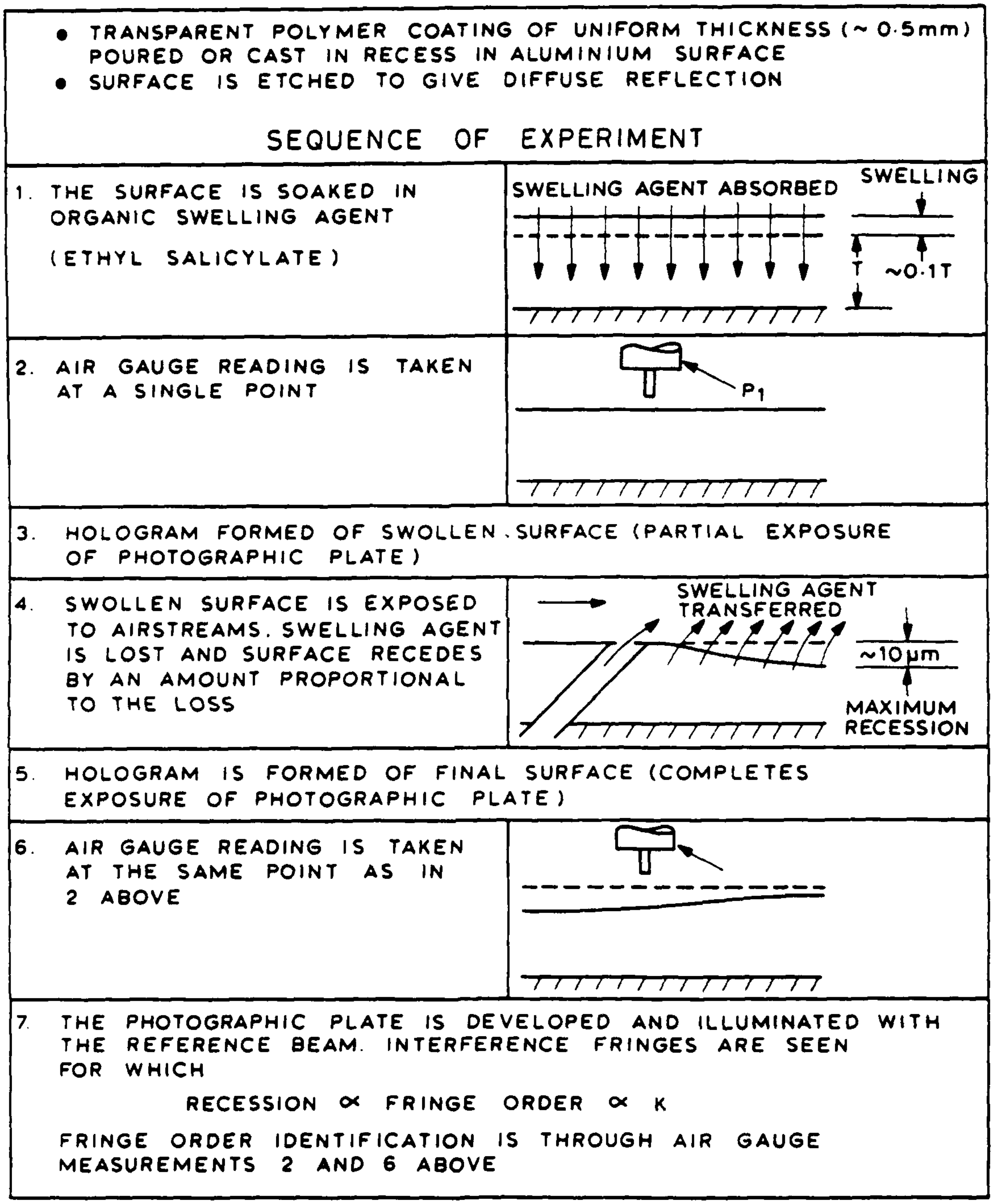

- TRANSPARENT POLYMER COATING OF UNIFORM THICKNESS (~ 0.5mm) POURED OR CAST IN RECESS IN ALUMINIUM SURFACE
- SURFACE IS ETCHED TO GIVE DIFFUSE REFLECTION

SEQUENCE OF EXPERIMENT

1. THE SURFACE IS SOAKED IN ORGANIC SWELLING AGENT (ETHYL SALICYLATE)

2. AIR GAUGE READING IS TAKEN AT A SINGLE POINT

3. HOLOGRAM FORMED OF SWOLLEN SURFACE (PARTIAL EXPOSURE OF PHOTOGRAPHIC PLATE)

4. SWOLLEN SURFACE IS EXPOSED TO AIRSTREAMS. SWELLING AGENT IS LOST AND SURFACE RECEDES BY AN AMOUNT PROPORTIONAL TO THE LOSS

5. HOLOGRAM IS FORMED OF FINAL SURFACE (COMPLETES EXPOSURE OF PHOTOGRAPHIC PLATE)

6. AIR GAUGE READING IS TAKEN AT THE SAME POINT AS IN 2 ABOVE

7. THE PHOTOGRAPHIC PLATE IS DEVELOPED AND ILLUMINATED WITH THE REFERENCE BEAM. INTERFERENCE FRINGES ARE SEEN FOR WHICH

$$\text{RECESSION} \propto \text{FRINGE ORDER} \propto K$$

FRINGE ORDER IDENTIFICATION IS THROUGH AIR GAUGE MEASUREMENTS 2 AND 6 ABOVE

Figure 3 Description of the technique

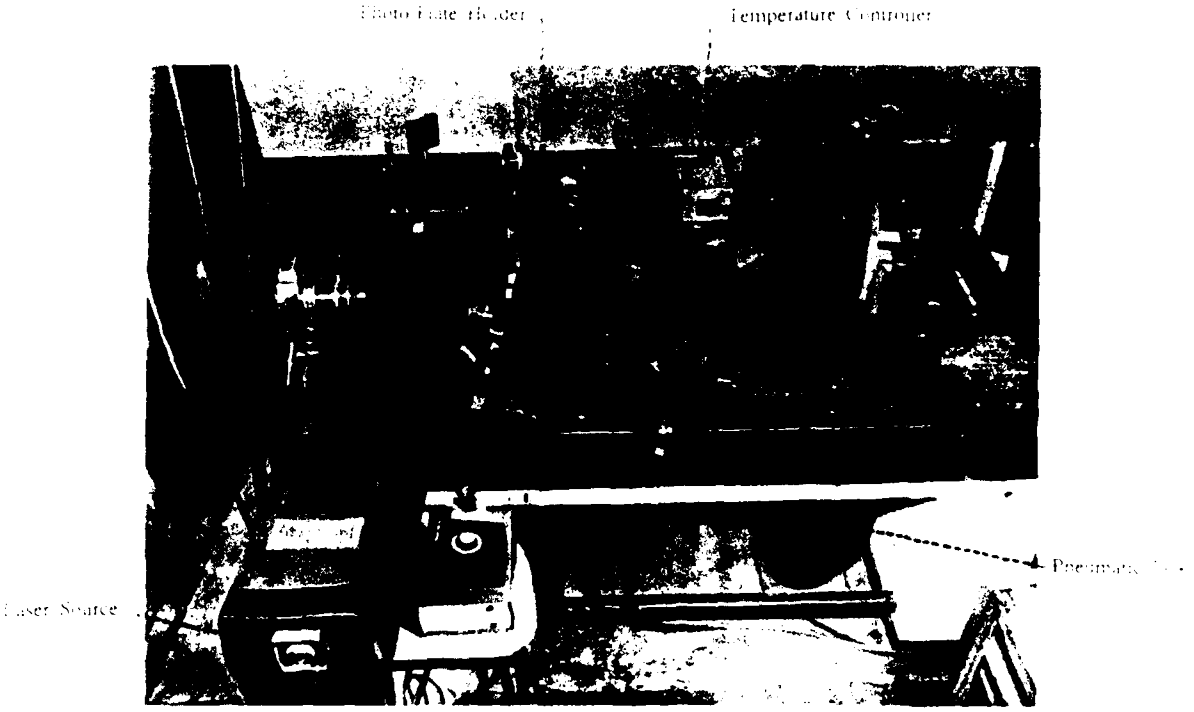
Photo Plate Holder
Temperature Controller
Pneumatic
Laser Source

Figure 4 View of the holographic set up

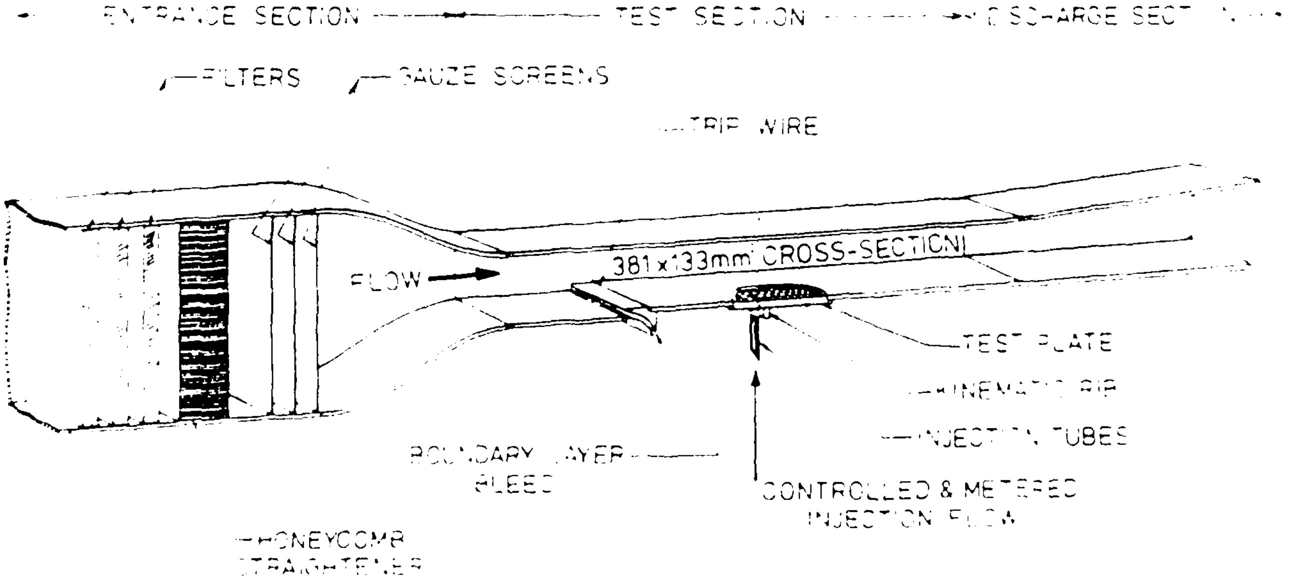
ENTRANCE SECTION
TEST SECTION
DISCHARGE SECTION
FILTERS
GAUZE SCREENS
TRIP WIRE
381 x 133mm CROSS-SECTION
FLOW
TEST PLATE
KINEMATIC RIG
INJECTION TUBES
BOUNDARY LAYER BLEED
CONTROLLED & METERED INJECTION FLOW
HONEYCOMB STRAIGHTENER

Figure 5 Layout of the wind tunnel

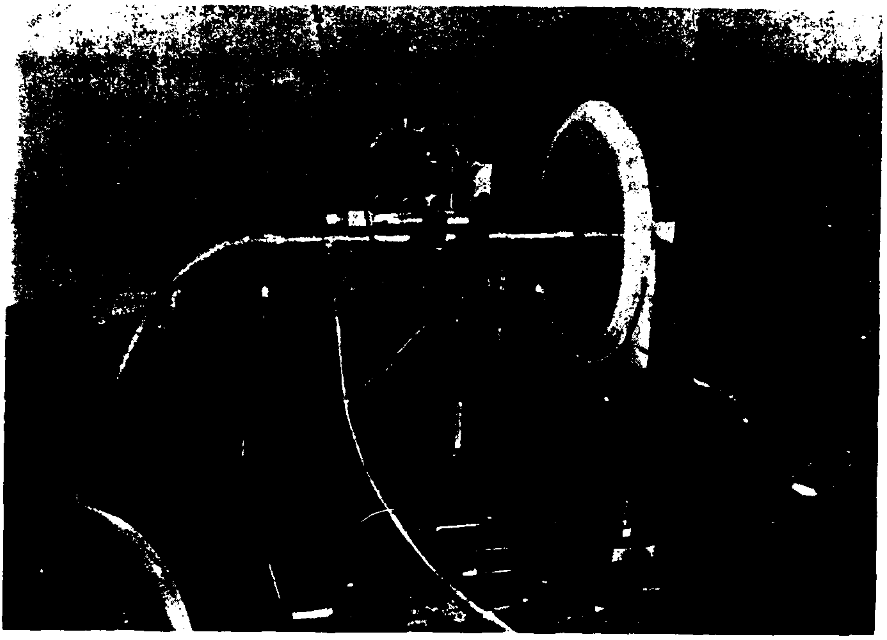
Probe Assembly
Air-Gauge Kinematic Bracket
Air-Gauge Supply Tube
Kinematic Mount

Figure 6 Air-gauge assembly

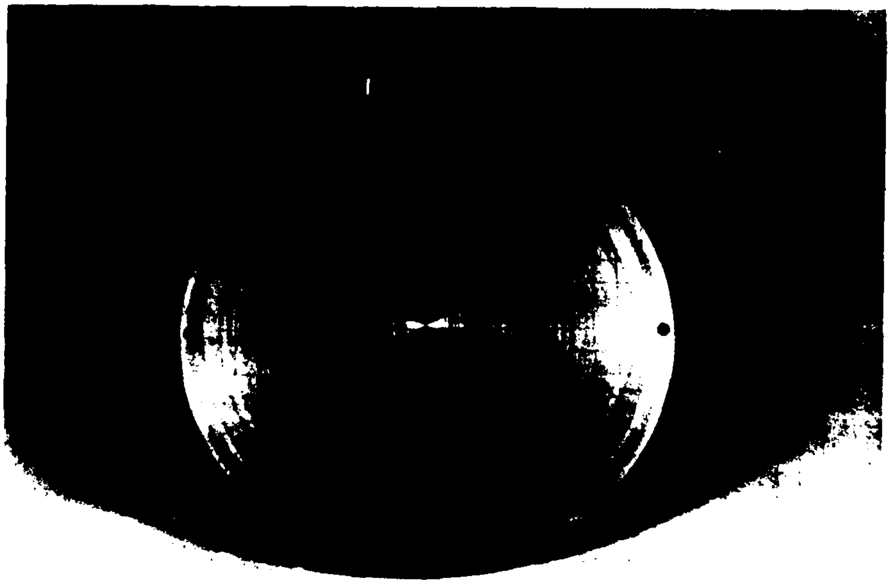

Figure 7 Test plate

Grid Spacing = 5d

Test Number 171

u_g →

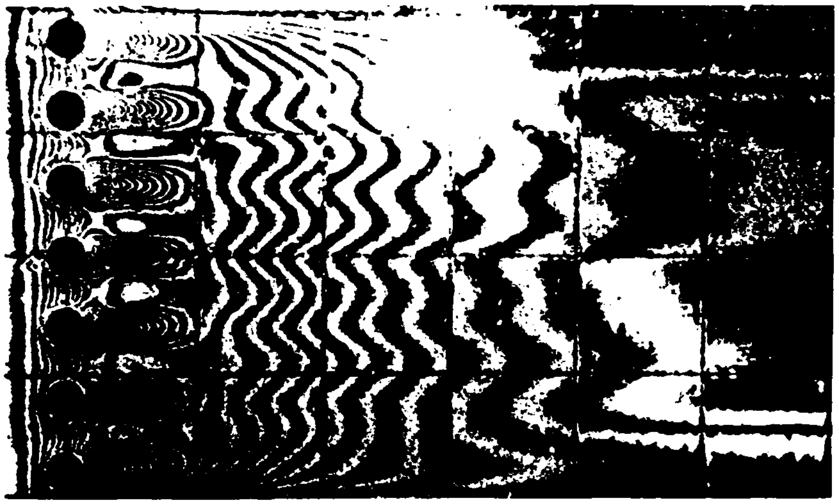

Test Number 173

u_g →

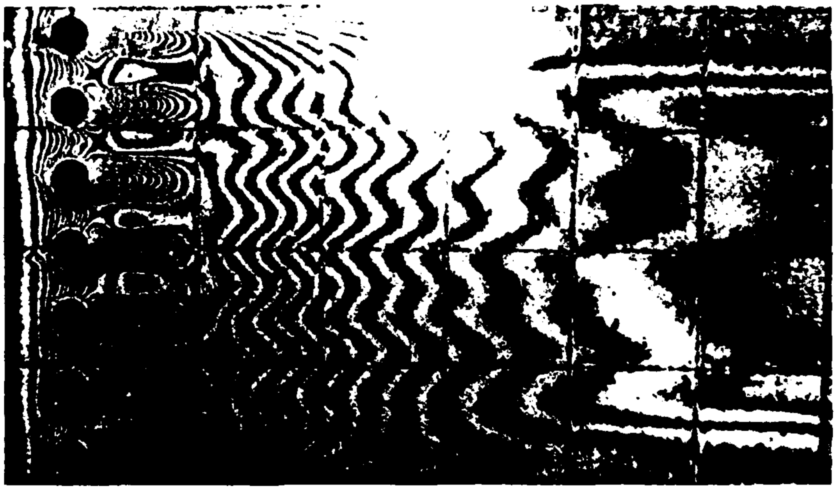

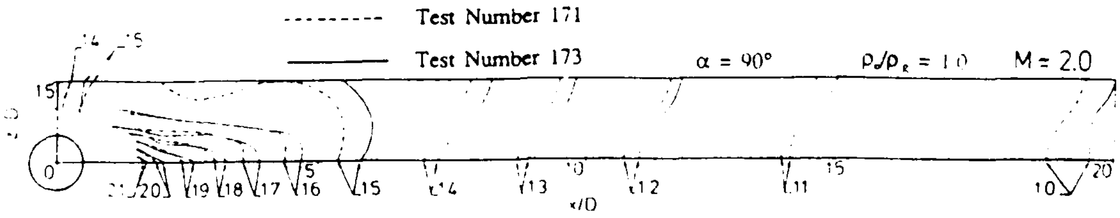

Figure 8 Repeatability check on fringe patterns and associated h/h_o for normal injection with blowing rate = 2. [Ref 7]

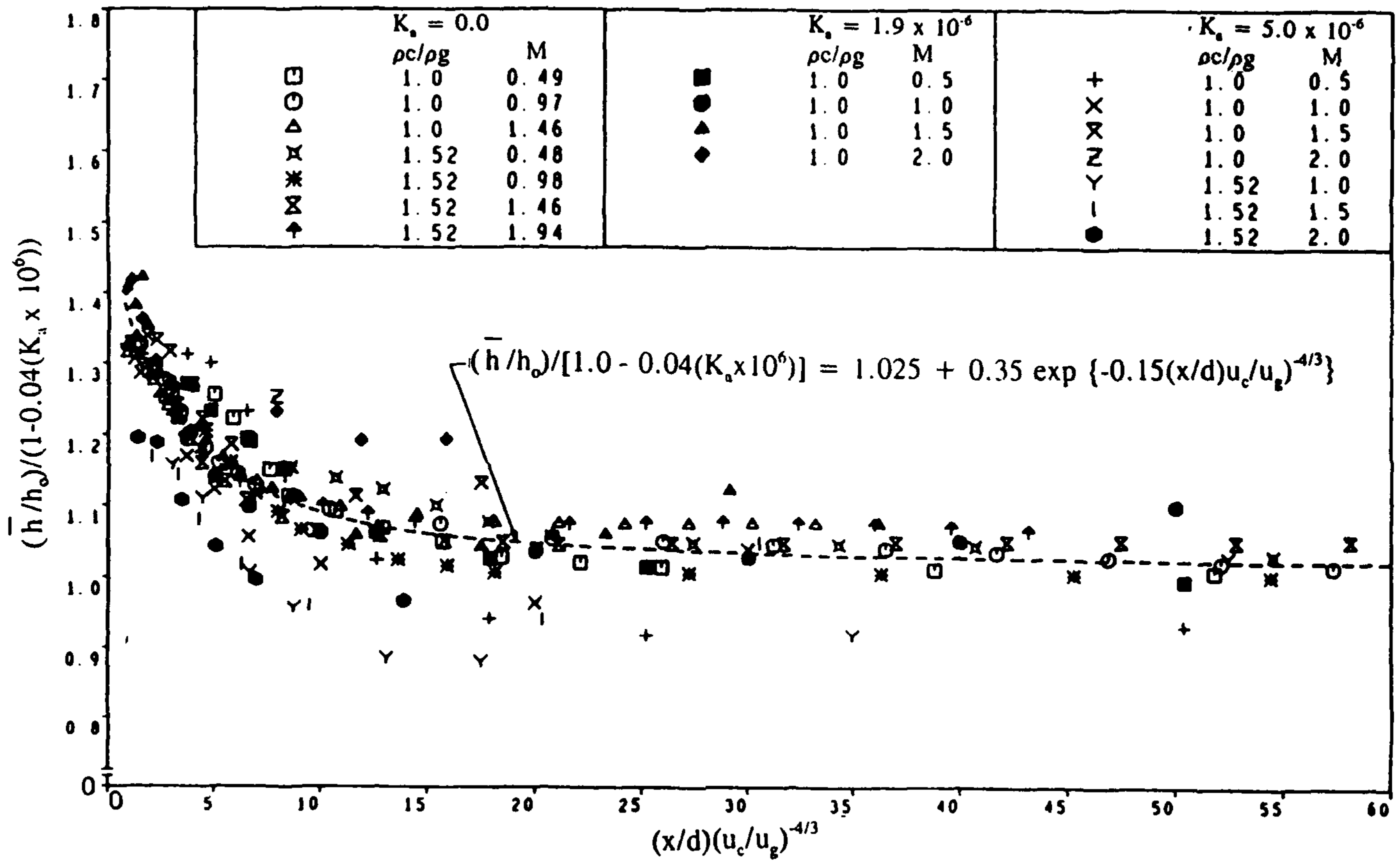

Figure 9 Correlation of $\bar{h}/h_o$ data for $0.0 \le K_a \le 5 \times 10^{-4}$ and $0.5 \le u_c/u_g \le 1.5$, row of holes, $\alpha = 35°$. [Ref 18]

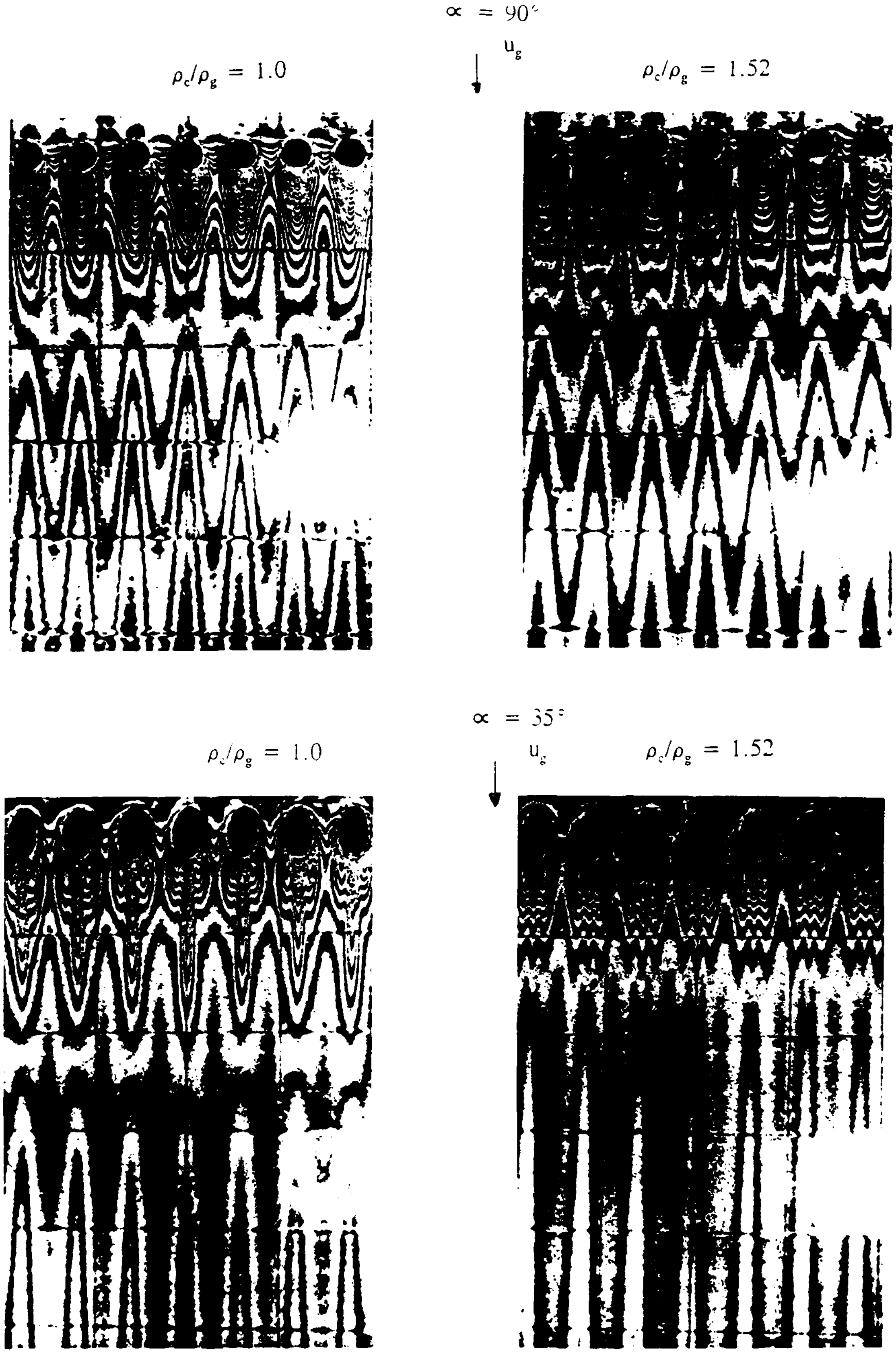

Figure 10 Effect of density ratio variation on the heat transfer coefficient distribution for 90° and 35° injection through a row of holes at blowing rate = 1. [Ref 19]

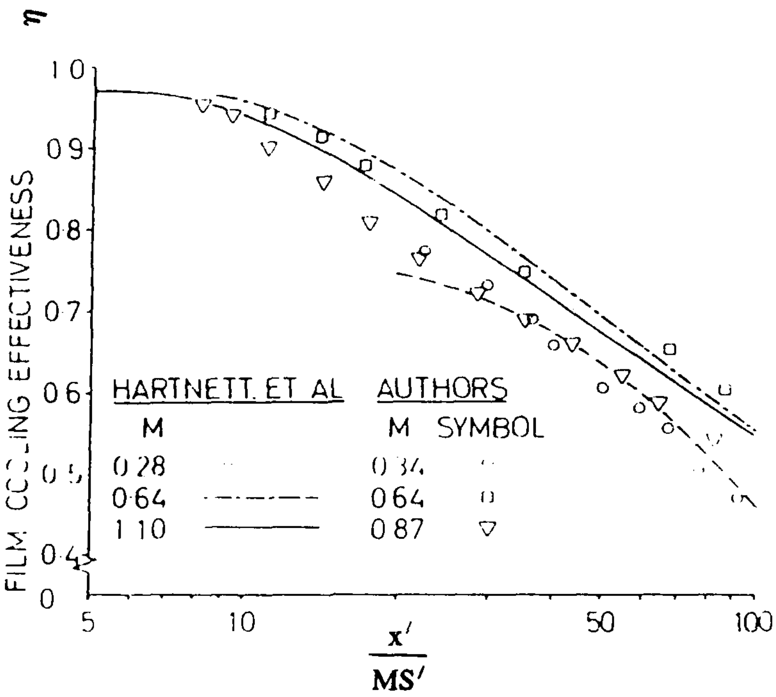

Figure 11 Validation of the technique for the measurement of η_{aw}. [Ref 20]

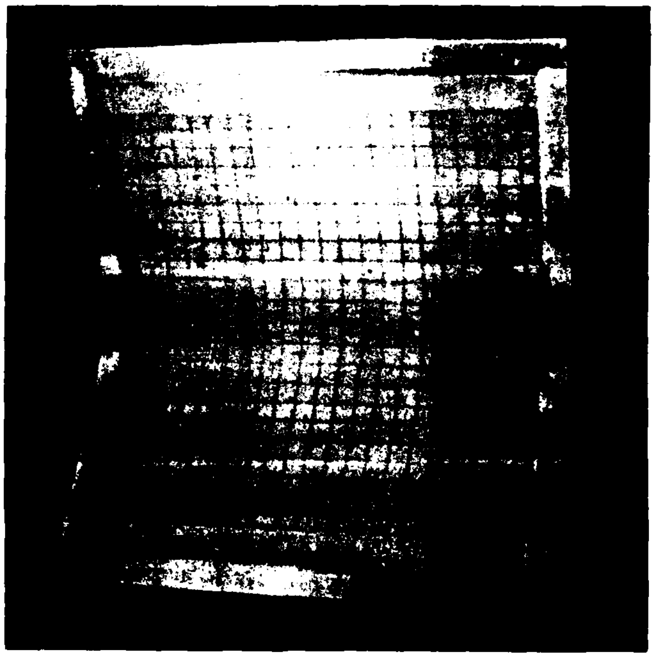

Figure 12 Concave test plate

Discussion

QUESTION 1:

DISCUSSOR: H.B. WEYER, Institut fur Antriebstechnik

What is the effect of Mach Number? With an increasing Mach number the differences in surface temperature - due to stagnation - become more evident. This must have some influence on the evaporation of the swelling agent.

AUTHOR'S REPLY:

The method is suitable for low Mach number flows only. We use a velocity of 20 to 35 m/s. At high Mach numbers there will be, as you say, a temperature rise in the boundary layer. This affects the saturation vapour pressure of the swelling agent which is very sensitive to temperature. Thus the concentration gradient driving the mass transfer is no longer known and it is no longer possible to derive a mass transfer coefficient from the measurement of surface recession.

QUESTION 2:

DISCUSSOR: H.B. WEYER, Institut fur Antriebstechnik

Blade aerodynamics is very sensitive to the blade shape. How precise is the coating with respect to blade shape variations?

AUTHORS REPLY:

Using a casting method it is possible to produce very smooth surfaces and very accurate coating thickness. The thickness of the coating does not have to be even all over because we measure changes in the thickness after swelling.

Coating a blade is, therefore, possible, but in regions where there might be a curvature in two planes the interpretation of the holographic image becomes too difficult. When there is curvature in one plane only, such as occurs on the flank of a blade, a correction depending on position has to be applied to the fringe order read from the hologram, but apart from that there are no problems.

QUESTION 3:

DISCUSSOR: L. de Chanterac, DRET/ Service des recherches

Do you think that reversible utilization of the swollen polymer technique is possible and that a dynamic heat transfer coefficient could be obtained with this method?

AUTHOR'S REPLY:

The swollen polymer technique is a reversible process since the working surface can be reactivated simply by dipping it again in swelling agent.

Regarding measurement of the dynamic heat transfer coefficient this is possible with the "live fringe" technique (Fig. 2). One would then count the number of fringes passing per unit time and that reflects the instantaneous values of the mass (or heat) transfer coefficient. A video recording would be useful in this case for the analysis to be done later at leisure. The "live fringe" passing rate could be different for different positions on the surface observed and thus the measurements could give space as well as time resolved values.

The USAF Advanced Turbine Aerothermal Research Rig (ATARR)

by

C.W. Haldeman Jr. and M.G. Dunn
Calspan Corp., Advanced Technology Center
Buffalo, New York

and

C.D. MacArthur and C.G. Murawski
Aero Propulsion and Power Directorate
Air Force Wright Laboratory, WPAFB
Dayton, Ohio

ABSTRACT

The Advanced Turbine Aerothermal Research Rig (ATARR) has been under development and construction at Wright-Patterson Air Force Base for the past three years. Construction of the facility is now complete and demonstration experiments are underway. These demonstration experiments involve use of an instrumented turbine stage (both surface pressure and surface heat flux instrumentation) to obtain measurements for comparison with predictions, flow path measurement of total pressure, total temperature, and static pressure to determine flow path uniformity, as well as instrumentation to ascertain proper operation of all facility components.

At the time of this writing, the experiments designed to obtain the data just mentioned are underway but results are not available. Therefore, the written paper will be confined to a description of: (1) the facility and its design capabilities, (2) a description of the operation of the major components with limited supporting data, e.g., main valve opening and closing times, and (3) a brief description of an uncertainty analysis that has been completed for the instrumentation and aero-performance measurements.

Nomenclature

General

h = total enthalpy
L = losses
N_{Phy} = rotor physical speed
P_o = total pressure of incoming gas
P_{ref} = reference pressure, 14.7 psia
Q_w = heat transfer to walls
T_o = total temperature of incoming gas
T_{ref} = reference temperature, 516°R
W = measured work done by turbine
$\dot{W}$ = weight flow of test gas
δ = nondimensional pressure, P_o/P_{ref}
γ = specific heat ratio
η_{ad} = adiabatic efficiency
η_{fu} = fundamental efficiency
η_{meas} = measured efficiency
θ = nondimensional temperature, T_o/T_{ref}

Subscripts

d = downstream of stage
d,is = ideal, isentropic conditions downstream of stage
u = upstream of stage

1. INTRODUCTION

For the past fifteen years, several groups have pioneered the development of short-duration facilities and the associated instrumentation for the investigation of phenomena relating to high-pressure turbines. For the facilities just mentioned, the term short-duration has been used in the past to mean test times on the order of tens of milliseconds to a few hundred milliseconds. The short duration test capability is becoming an increasing attractive alternative to conventional "long run-time" testing. By "long run-time" has been meant test times on the order of hours. The promise of major cost savings coupled with the ability to measure new quantities not possible in conventional facilities has motivated this interest in short-duration facility development. One of the most significant aspects of the ATARR facility discussed in this paper is that even though it is considered to be of the short duration class, the test time is on the order of seconds instead of milliseconds.

To review the short-duration facility development history for a moment, the application of the isentropic light piston compression tube for turbine research was pioneered at Oxford University by Schultz and co-workers (e.g., see Ref. 1) and a sector of high-pressure turbine vanes was instrumented with thin-film heat-flux gages and used as the test article. The test time for the Oxford facility is on the order of a few hundred milliseconds. Dunn and co-workers at Calspan used the shock tunnel to initially obtain measurements for a sector of a high-pressure turbine vane row (e.g., see Ref. 2) followed by replacement of the vane sector with a full stage rotating turbine (Ref. 3). The test time for this facility is on the order of tens of milliseconds. Louis at the Massachusetts Institute of Technology investigated the use of both the shock tube and the blowdown facility (Ref. 4) for the investigation of factors affecting heat transfer in turbines. The test times for his facilities were also on the order of milliseconds. Richards and co-workers at the Von Karman Institute also developed a light piston facility (e.g., see Ref. 5) to perform measurements on a high-pressure turbine vane sector (e.g., see Ref. 6). Epstein and co-workers at the Massachusetts Institute of Technology designed and built a low pressure blowdown facility (e.g., see Ref. 7) to perform measurements on a high-pressure turbine vane row. This facility is different than the one described in Ref. 4. The test time associated with the MIT blowdown turbine facility is on the order of a few hundred milliseconds.

The primary force driving the development of ATARR at WPAFB was the potential for being able to measure heat transfer and aero-performance simultaneously for advanced technology military engines. To this end, it was decided to build a large blowdown facility with a test time on the order of one to five seconds. The test time duration for this particular facility is determined by the weight flow rate that must be supplied to the turbine and by the amount of power that the eddy current brake must absorb because of work extracted by the turbine rotor from the test gas. One objective of ATARR is to measure either the cooled or uncooled turbine efficiency to within ± 0.25% of the "true" value within a 95% confidence limit. Achieving this goal will make ATARR competitive with the best conventional facilities for aero-performance evaluation. Another objective of the facility is to determine the thermal (cooling) performance of new turbine designs.

In the remainder of the paper, Section 2 presents a discussion of the facility and its components, Section 3 presents a brief description of the operation of one of the major components (the main valve) and Section 4 presents a brief description of an uncertainty analysis used to define the instrumentation and facility parameter requirements.

2. DESCRIPTION OF THE FACILITY

It was noted earlier that ATARR was designed and constructed to meet the specific needs of the turbine components group at WPAFB. This group is charged with the responsibility of developing new engine technology and, in particular, with the development of more advanced, higher work output, and higher operating temperature turbines for future military applications. More specifically, the goal is to achieve significant increases in turbine inlet temperature while at the same time reducing the flow rate of cooling air accompanied by work and speed increases. The increases in material stress associated with this goal are substantial. There are a number of new design concepts that have promise for increases in turbine performance such as super effective cooling designs, 3-D aerodynamic design, vaneless HP/LP systems and metal/non-metal composites. These concepts can be more reliably incorporated into military engine design if extensive testing has been performed to validate their usefulness.

The ATARR has been a cooperative effort with Calspan, MIT, Belcan, Allison, and the USAF all contributing. The facility is designed to accommodate full scale (either vane row alone or full stage) engine hardware and to subject this hardware to test conditions consistent with actual engine operation. By taking advantage of scaling relationships, the important nondimensional groups which determine the behavior of the turbine stage can be reproduced and at the same time operate at test conditions that do not subject the instrumentation to conditions as harsh as those associated with actual engine conditions. The blowdown facility is one for which the supply tank temperature and pressure change during the course of a given experiment and it is, therefore, necessary to carefully measure the flowpath parameters so that the appropriate nondimensional groups can be duplicated. The specific parameters that can be duplicated with this facility are: flow function $\left(\dot{W}\sqrt{\theta}/\delta\right)$, corrected speed $\left(N_{Phy}/\sqrt{\theta}\right)$, specific heat ratio of the turbine inlet gas (γ), pressure ratio across the stage, ratio of gas temperature to wall temperature, ratio of gas temperature to coolant temperature, Reynolds number, Mach number, and Prandtl number. These parameters will be duplicated during a portion of the test time duration, but not during the entire test time. Each experiment is designed to maximize this portion of the test time within the constraints imposed by the eddy current brake. This power absorbing device is programmed to maintain the proper corrected speed for the maximum period of time. This maximum operating time of the eddy current brake is determined by the temperature increase of the brake drum during the blowdown time as a result of dissipating the power extracted from the test gas by the rotor.

Figure 1 is a sketch of the ATARR. The test gas supply tank shown on the far left has a volume of approximately 3,200 ft.^{3} and designed to be pressurized to 180 psia while being heated to 550°F. Any combination of pressure and temperature between these maximums can be utilized. The test gas would normally be nitrogen or a mixture of nitrogen and carbon dioxide in order to duplicate the appropriate nondimensional groups. The supply tank is insulated with four inches of fiberglass with a 0.020 inch aluminum jacket to minimize heat loss to the room. Not shown on the sketch, but located internal to the supply tank is a variable speed fan and an electrical heater. The supply tank insulation and fan/heater combination were designed to produce axial temperature uniformity on the order of 0.8°F (over the 20 ft. length of the tank). It is estimated that for a typical run, the majority of the test gas would be taken from about one-third of the supply tank. The supply tank is instrumented with

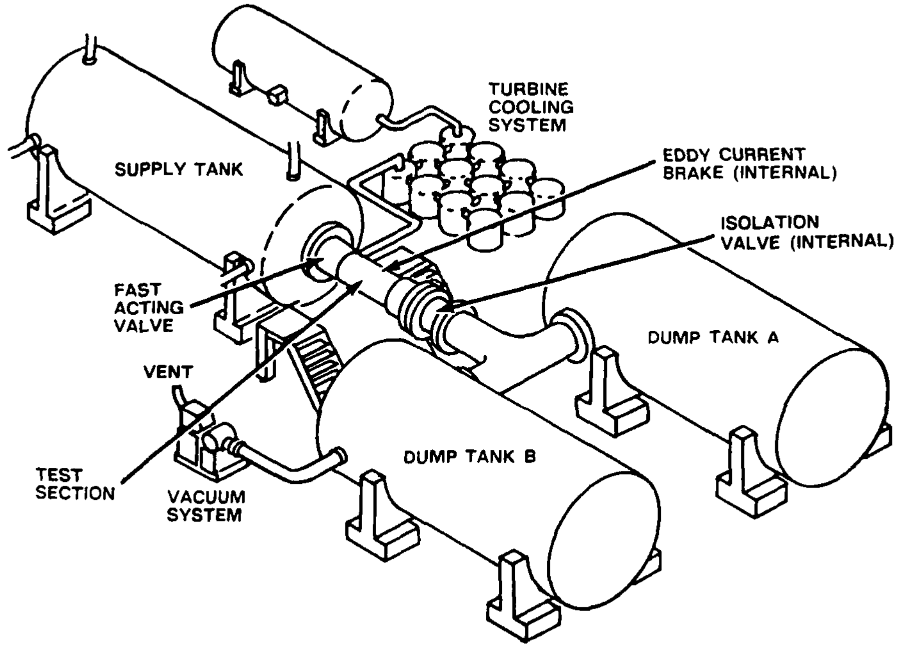

Figure 1 Sketch of Advanced Turbine Aerothermal Research Rig (ATARR) Configuration

resistance temperature detectors (RTD's) in order to measure the axial and the radial temperature uniformity. Temperature measurements are currently underway, but not available for presentation at this time.

Located internal at one end of the supply tank is a fast acting valve (which has moving components weighing about 600 lbs.) that is designed to open in approximately 100 milliseconds, remain open for a pre-determined time period, and then close in approximately 100 milliseconds. Careful control of both the opening and closing of the valve are critical to avoid structural damage. Of particular concern is the requirement that valve closing must be done in a way that closes off a large portion of the flow area very quickly, but then covers the remaining portion of axial travel at a lower velocity in order to avoid hard impact between the valve and the bumper. The bumper is spring loaded and designed to accommodate a reasonable impact velocity, but not a velocity that it so large that the springs become fully compressed. It is important that this valve close within the prescribed time interval because the eddy brake is not designed to absorb the power extracted by the turbine indefinitely. There is sufficient gas in the supply tank to cause turbine runaway if the supply tank valve were to remain open and if there were no other way to terminate the flow. However, to mitigate this potentially dangerous situation, there is an emergency valve (located downstream of the test section and referred to as an isolation valve on Figure 1) that can be driven closed using a deluge valve. This deluge valve would be fired in the event of a potential turbine run away.

Downstream of the supply tank main valve is the test section which houses the turbine that is being investigated. Internal to this test section are several other essential components and instrumentation associated with the facility. Figure 2 is a sketch of some of these components and the facility instrumentation locations. Table 1 is a tabulation of the specific (non-stage) instrumentation location, type, and expected accuracy.

Table 1 describes the instrumentation located in the supply tank. The primary instrumentation at location 1 are the RTD's and the Baratron unit. Ahead of the turbine stage there is a boundary layer bleed designed to remove the boundary layer associated with the incoming flow. Also located ahead of the turbine stage in the flow path are rakes

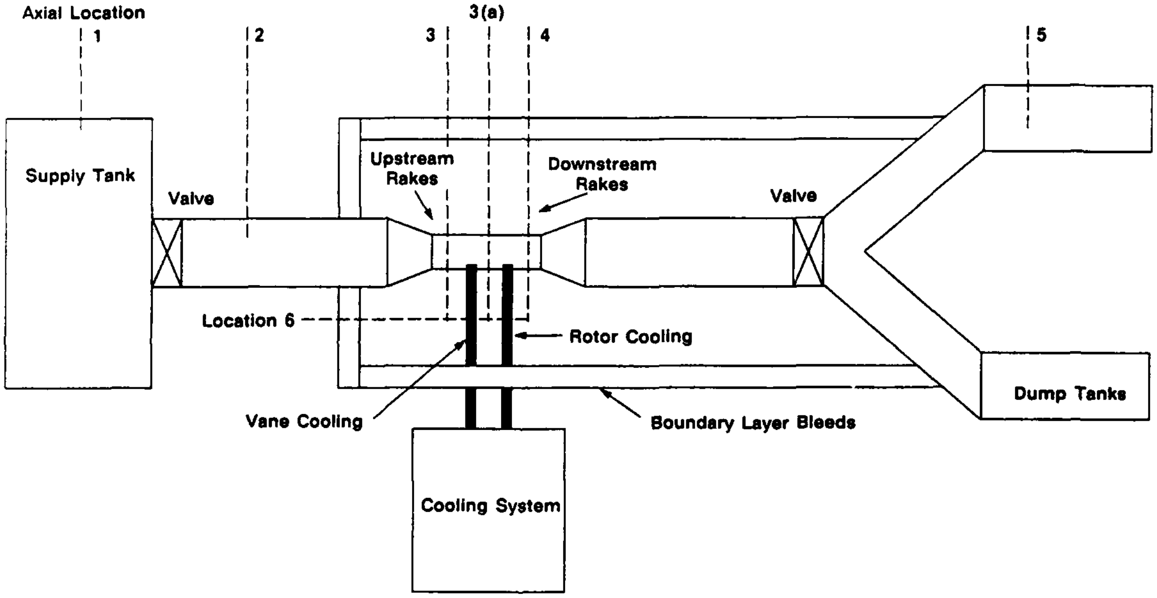

Figure 2 Sketch of ATARR Instrumentation Locations

Table 1 Facility Instrumentation

Location	Type of Sensor (number)	Expected Accuracy
Axial location 1: Supply Tank	RTD's (20) Baratron Units (1) Endevco 8540-100	.1°K or .02% FS .1 psi (.1% FS) Need to Calibrate
Axial Location 2: Inlet	Baratron Units (1)	.1 psi (.1% FS)
Axial location 3: Upstream Rake Position	1 Total Temp. Thermocouple Rake (4 sensor Type E 1 Mil) 1 Total Press. Rake (4 sensor Endevco 8534A-100) 2 static pressure Endevco 8530C-100	Need to Calibrate Need to Calibrate Need to Calibrate
Axial Location 3(a) Torquemeter Located on Drive Shaft	Strain gauges	Calibrated to within 0.25% FS
Axial Location 4: Downstream Rake Position	1 Total Temp. Thermo-couple Rake (4 sensor Type E 1 mil) Total Pres. Rake (Endevco 8534A-100) 2 static Press (Endevco 8530C-100)	Need to Calibrate Need to Calibrate Need to Calibrate
Axial Location 5: Dump Tank	Static Pressure (Endevco 8530C-100)	Need to Calibrate
Axial Location 6: Cooling Lines	Total Temp. Thermocouples (4) Pressure (not specified)	Need to Calibrate

of total pressure and total temperature. Similar rakes of total pressure and total temperature are located in the flow path downstream of the rotor. For the demonstration experiments, these rakes are fixed in position, but in the future traversing units will be added to this configuration. A photograph of one of the total pressure rakes is given in Figure 3(a). A close-up photograph of a pressure probe is given in Figure 3(b). One of the total temperature rakes is shown in Figure 3(c). The thermocouple housed in these probes is butt welded Type E wire and is 0.001-in. diameter. The design and construction of the thermocouple probes is very similar to that reported in Ref. 8. Wall static pressure is measured at the rake locations.

The vane portion of the particular turbine stage being used for the demonstration experiments is shown in Figure 4(a), 4(b), and 4(c). Figure 4(a) illustrates the miniature flush diaphragm Kulite pressure transducers placed at midspan on both the pressure and suction surfaces and a contoured leading-edge insert (at midspan) containing platinum thin-film heat-flux gages. Figure 4(b) is a photograph of two contoured strip inserts (at midspan) containing platinum thin-film heat-flux gages. Figure 4(c) is a photograph of numerous button-type heat-flux gages located at 20%, 50%, and 80% of span on the airfoil surface and on the hub and tip endwall. With the exception of the button-type gages, the Pyrex substrate was designed to be sufficiently thick to avoid

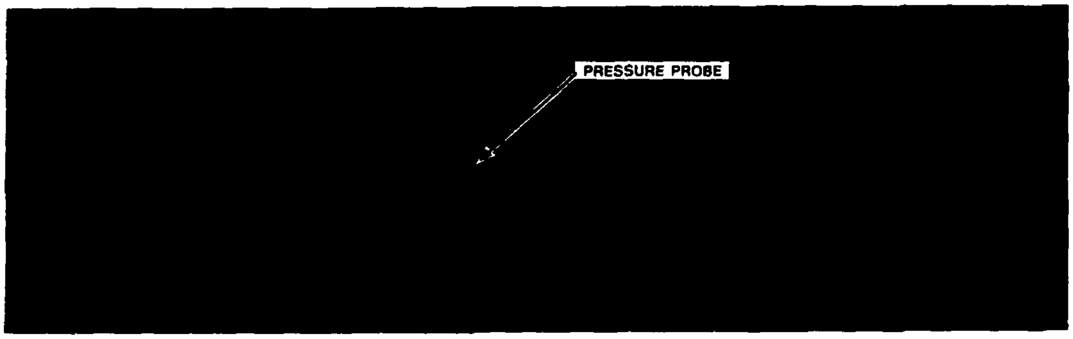

Figure 3(a) Photograph of Upstream Total Pressure Rake

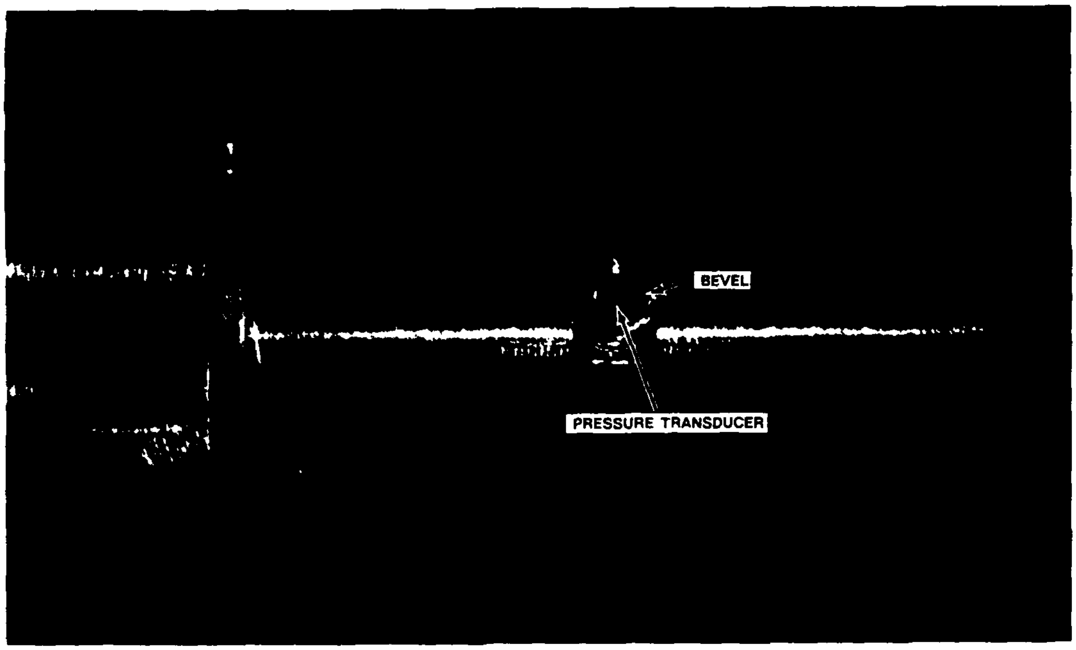

Figure 3(b) Close-Up Photograph of Total Pressure Probe

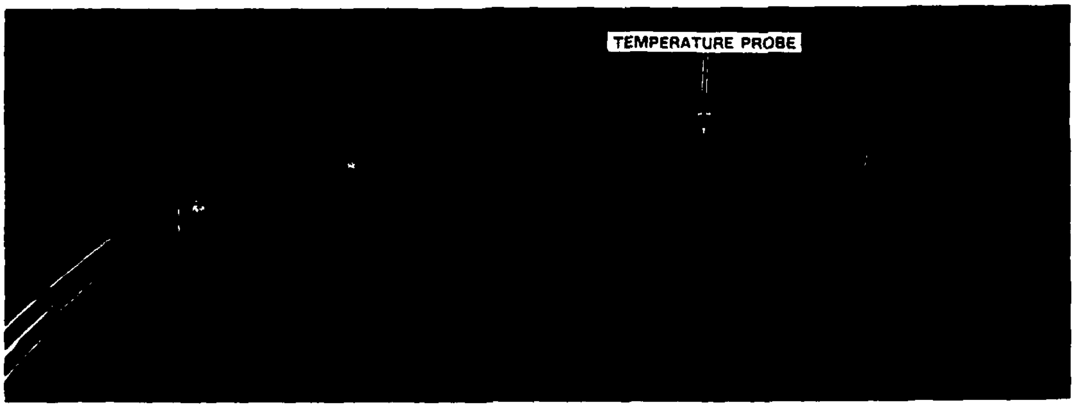

Figure 3(c) Photograph of Downstream Temperature Probe

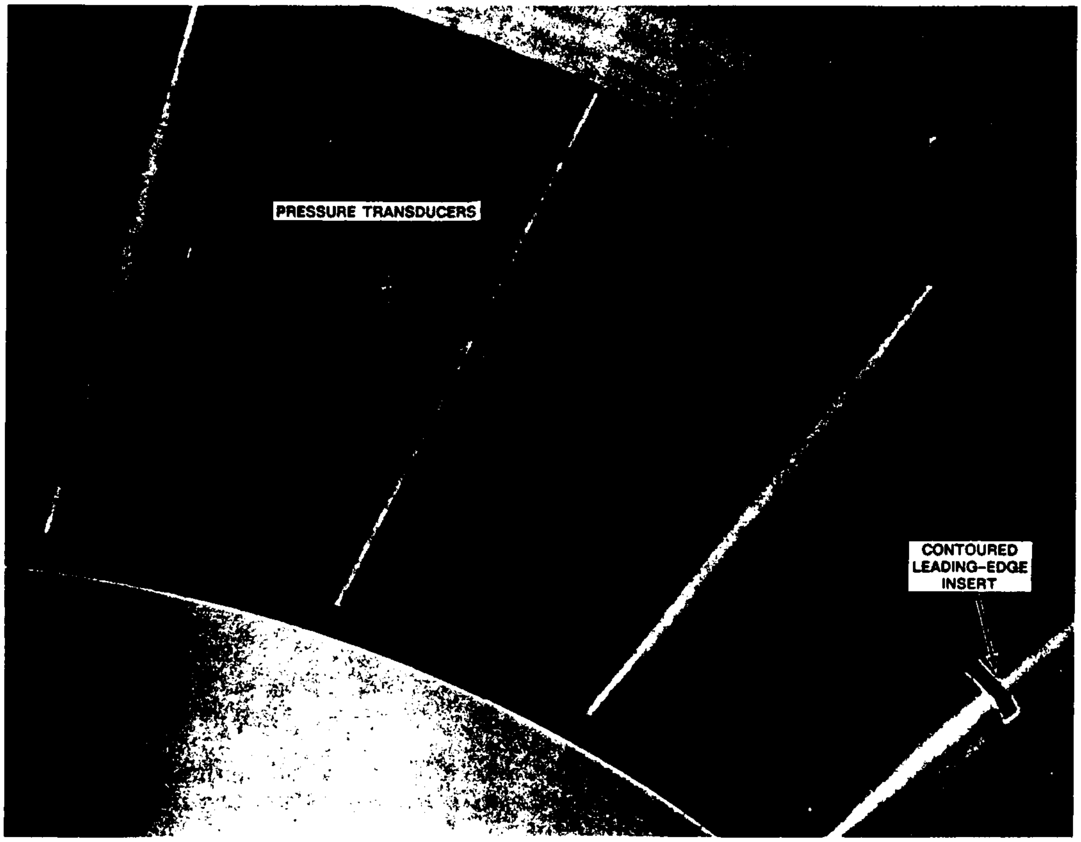
PRESSURE TRANSDUCERS
CONTOURED LEADING-EDGE INSERT

Figure 4(a) Instrumentation on Vane Airfoils

CONTOURED STRIP INSERTS

Figure 4(b) Instrumentation on Vane Airfoils (Cont.)

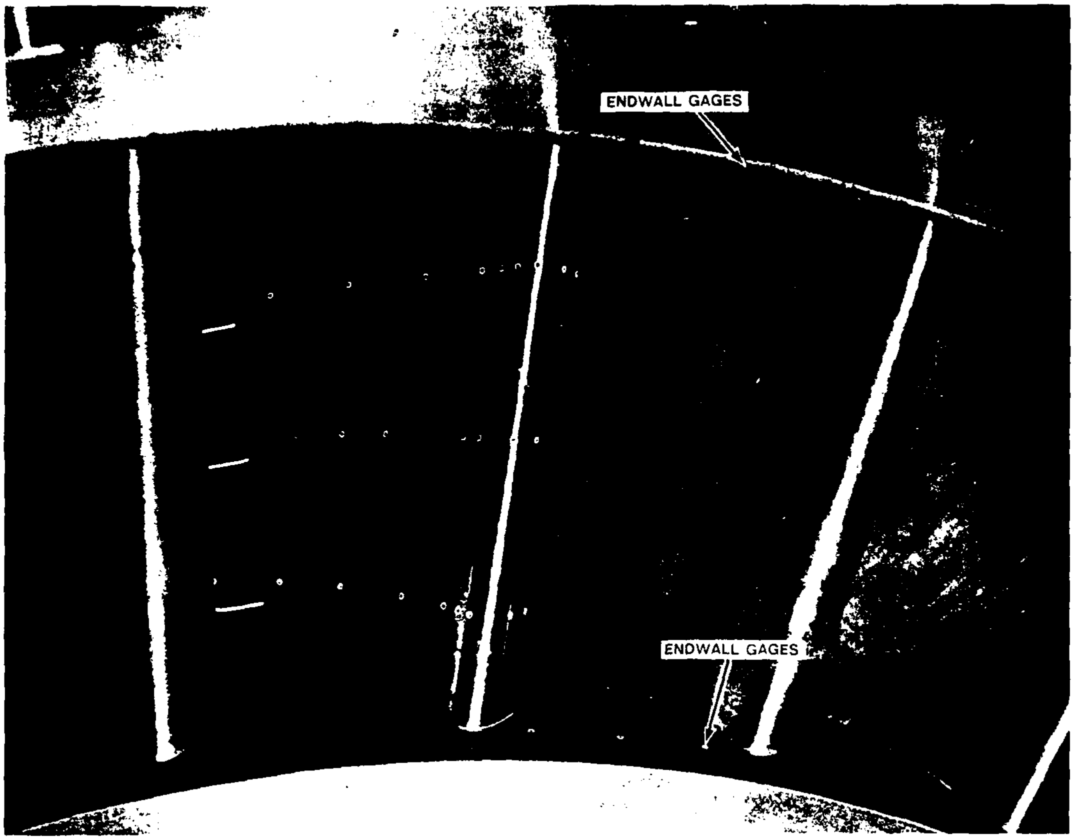

Figure 4(c) Instrumentation on Vane Airfoils (Cont.)

backside heating (and, therefore, preserving the one-dimensional approximation for data reduction) for test duration on the order of one second. The rotor portion of this stage is not shown, but it is instrumented in a similar manner.

The downstream isolation valve, shown in Figure 1, serves the function of providing a downstream flow control device which is used to achieve the desired stage pressure ratio by adjusting the flow area. Further, this valve can be used to isolate the test section from the dump tank permitting pressurization of the test section prior to and after an experiment in order to obtain a calibration of the pressure transducers. For the purposes of this calibration the Baratron pressure measuring device, which has a detector in the test section as well as the supply tank, is considered to be the standard against which the calibration is performed.

Two dump tanks of volume equal to approximately 3,200 ft.^{3} each are connected to the test section as shown. Prior to a run, the dump tanks and the test section are evacuated using the Stokes vacuum pump and Roots blower shown on the schematic of Figure 1. The dump tanks and the test section are routinely evacuated to a pressure of approximately 0.7 torr prior to initiation of an experiment. The eddy current brake noted on Figure 1 is a scaled up version of the one used at MIT (see Ref. 7) and was designed by Dr's. G. Guenette and A. Epstein of MIT. As previously noted, the turbine inlet total temperature decreases as the supply tank blows down. The current supplied to the coils of the magnets surrounding the rotating drum is on the order of 600 amperes of pulsed DC current supplied by a programmable SCR power supply. The brake can absorb power at a maximum of 4 megawatts at 7,500 rpm. The current to the magnets is programmed in order to maintain proper corrected rotor speed during the blowdown process. The rotating component of this brake is constructed of Inconel 718 and can be heated to approximately 1,000°F without significant loss of strength. A pyrometer looking at the brake drum surface can be used to monitor this temperature. For a large high pressure turbine (similar to the one shown in Figure 4) of the 25 megawatt class (engine conditions), the time for the brake temperature to reach the 1,000°F limit is about two seconds. In general, either the vane exit or the rotor exit (or both) of the turbine stage would be choked during the experiment. Regardless of whether or not the stage is choked, the previously mentioned isolation valve (which also serves as an emergency shut off valve) will remain choked for a wide range of conditions which serves to maintain the proper pressure ratio across the turbine stage.

The shaft on which the rotor component is mounted contains a torque meter which derives its signal from strain gauges mounted on a necked-down portion of the drive shaft. The torque meter was calibrated prior to final assembly of the rotating package to an accuracy of 0.25% of full scale. Data obtained with this device will be used as part of the turbine stage efficiency determination which will be described in Section 4. The rotating component is initially brought to the proper speed in the evacuated test section using a variable speed electric motor. This motor is attached to the end of the shaft nearest the return iron of the eddy current brake. At the other end of the shaft is mounted a 200 channel slip ring unit that is used to transfer the data from the rotating component to the laboratory data recorders.

Figure 5 is a photograph of the ATARR as it currently exists. The insulated supply tank can be seen on the far left, the external flange of the fast acting valve is to the right of the supply tank, a transition piece from the valve to the test section which contains the boundary layer bleed cannot be seen, the test section is relatively short in axial dimension and is bounded by the two flanges that can be seen, and the stair up to a platform providing access to one side of the test section is in the center of the photograph. The isolation valve

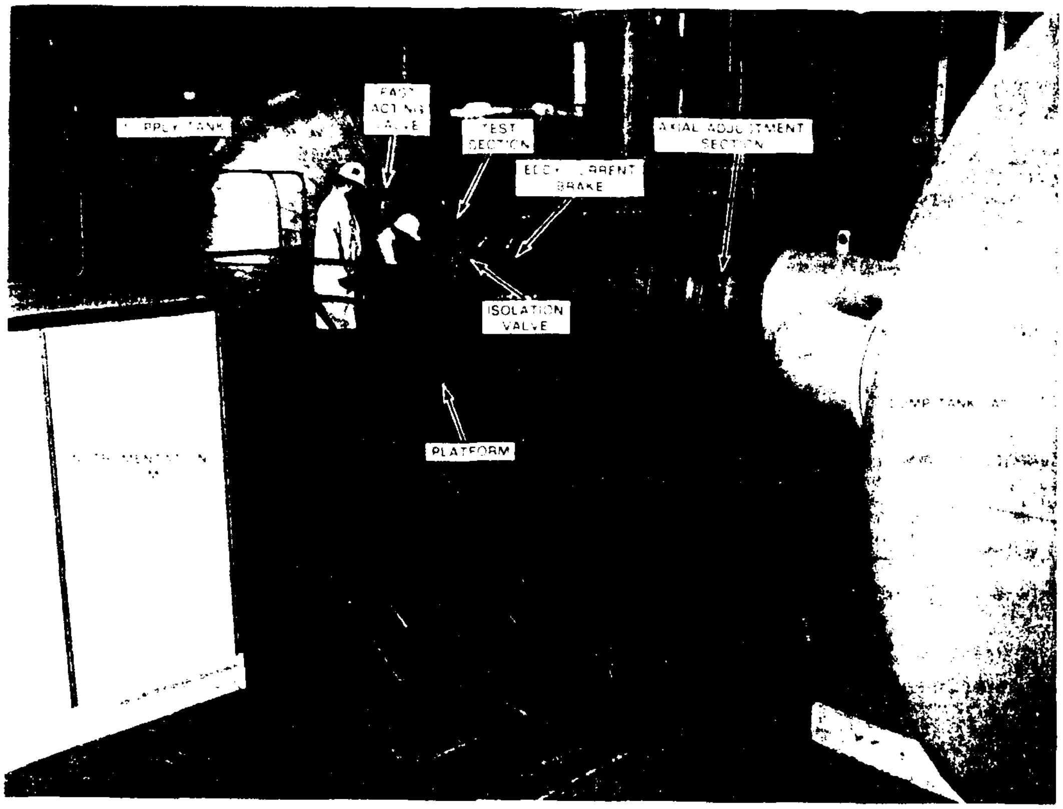
SUPPLY TANK
FAST ACTING VALVE
TEST SECTION
EDDY CURRENT BRAKE
AXIAL ADJUSTMENT SECTION
ISOLATION VALVE
PLATFORM
INSTRUMENTATION
DUMP TANK

Figure [illegible] Test stage of the ATARR

[illegible]

Table 2 Major Features of Data Acquisition System

[illegible]

Table 3 The ATARR Data Acquisition Computer System

- Sun 4/330 Computer System
- 32 Megabytes of Memory
- 2 x 1.2 Gigabyte Disk Drives (Removable)
- 1600/6250 BPI 9-Track 1/2 Inch Tape Drive
- Sun GX 19 Inch Color Graphics Display
- IEEE-488 (GPIB) Instrumentation Bus
- Ethernet TCP/IP Communications
- Appletalk Based QMS Printer/Plotter
- Sun OS UNIX Operating System

A comprehensive software suite has been written to reduce the raw data to the important engineering results and display them graphically. Figure 7 is a block diagram of the software structure functional decomposition. The data acquisition system consists of three major functions: software interfaces, user interfaces, and system management. Within each of these major functions are several service blocks as noted on the figure.

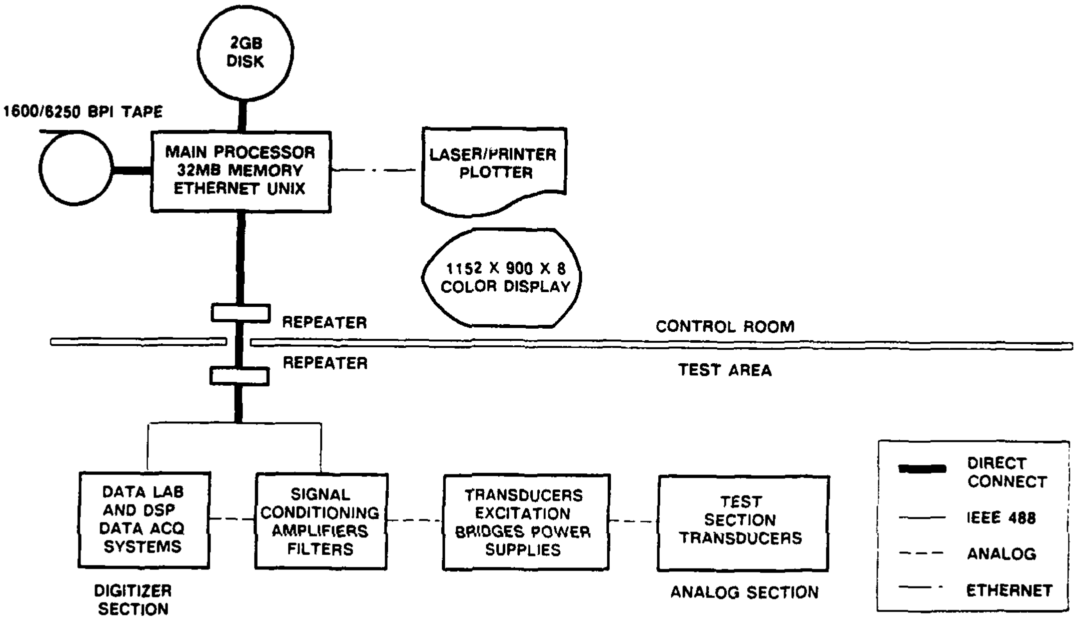
2GB DISK
1600/6250 BPI TAPE
MAIN PROCESSOR 32MB MEMORY ETHERNET UNIX
LASER/PRINTER PLOTTER
1152 X 900 X 8 COLOR DISPLAY
REPEATER
CONTROL ROOM
REPEATER
TEST AREA
DATA LAB AND DSP DATA ACQ SYSTEMS
SIGNAL CONDITIONING AMPLIFIERS FILTERS
TRANSDUCERS EXCITATION BRIDGES POWER SUPPLIES
TEST SECTION TRANSDUCERS
DIGITIZER SECTION
ANALOG SECTION
DIRECT CONNECT
IEEE 488
ANALOG
ETHERNET

Figure 6 Block Diagram of The ATARR Data Acquisition System

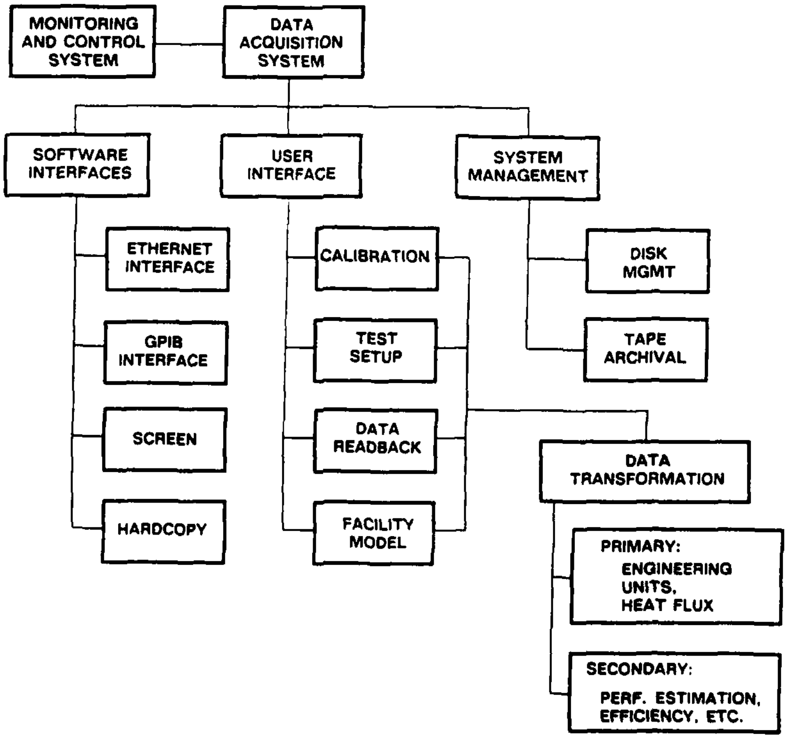
MONITORING AND CONTROL SYSTEM
DATA ACQUISITION SYSTEM
SOFTWARE INTERFACES
USER INTERFACE
SYSTEM MANAGEMENT
ETHERNET INTERFACE
GPIB INTERFACE
SCREEN
HARDCOPY
CALIBRATION
TEST SETUP
DATA READBACK
FACILITY MODEL
DISK MGMT
TAPE ARCHIVAL
DATA TRANSFORMATION
PRIMARY: ENGINEERING UNITS, HEAT FLUX
SECONDARY: PERF. ESTIMATION, EFFICIENCY, ETC.

Figure 7 The ATARR Software Structure Functional Decomposition

3. OPERATION OF SUPPLY TANK MAIN VALVE

As previously mentioned, the valve separating the supply tank from the test section is one of the major components of the ATARR. This valve must open quickly, remain open for a prescribed period of time, and close quickly. There are several reasons why proper operation of the supply tank main valve is essential, e.g., safety, flow quality, and avoidance of damage to other facility components. A simple gas dynamic model describing the operation of the actuating cylinder and the main valve which it drives was developed in order to predict the valve operation. Results obtained from the prediction model are compared with experimental results in the following paragraphs.

Figure 8(a) presents a comparison between an experimentally determined axial position vs. time history and a corresponding prediction. The prediction is obtained from an unsteady model initially developed at MIT and modified at Calspan to predict the operational characteristics of the valve and associated activation system. After the supply tank valve has moved approximately 8.5 inches in the axial direction, it is essentially fully open. The weight flow requirements of the turbine stage located in the test section are fully met by the corresponding flow area and any additional area at the valve will not result in additional weight flow. As can be seen from Figure 8(a), the travel for the particular case shown was approximately 10 inches. The time required for the valve to move approximately 9 inches was about 100 ms which is well within the design goal of the system. Closing of the valve is shown on the right side of Figure 8(a). The valve accelerates rapidly from the 10 inch position to about 2 inches in approximately 100 ms and then slows down over the remainder of the axial travel in order to avoid hard impact with the bumper. The time required to close off about 90% of the available flow area is well within the design requirements.

Figure 8(b) presents a comparison between the measured and predicted pressure histories associated with the opening and closing actuator legs of the system. Included on this figure are the pressure in the opening line and the pressure in the closing line. To the left hand side of the figure is the valve opening sequence and at about 2.4 seconds the valve closing sequence is initiated. The predicted peak in the opening pressure at about 0.2 seconds is above the data which is characteristic of the model and the closing pressure is underpredicted while the valve is open and overpredicted while the valve is closed. The opening pressure is well predicted throughout the entire sequence of events. Figure 8(c) presents a comparison between the opening and closing reservoir pressures for the duration of valve operation. In general, for Figures 8(a) - 8(c) the agreement between the prediction and the experimental data is shown to be reasonably good.

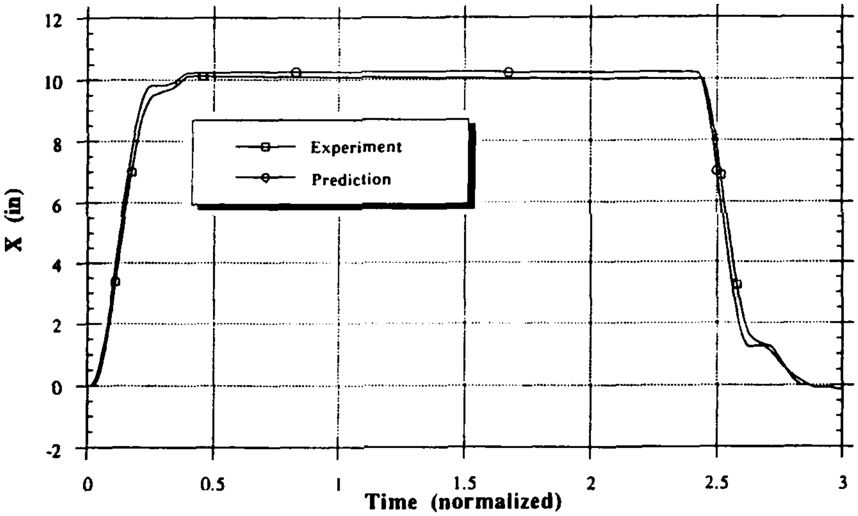

Figure 8(a) Comparison Between Experiment and Prediction For Supply Tank Valve Motion

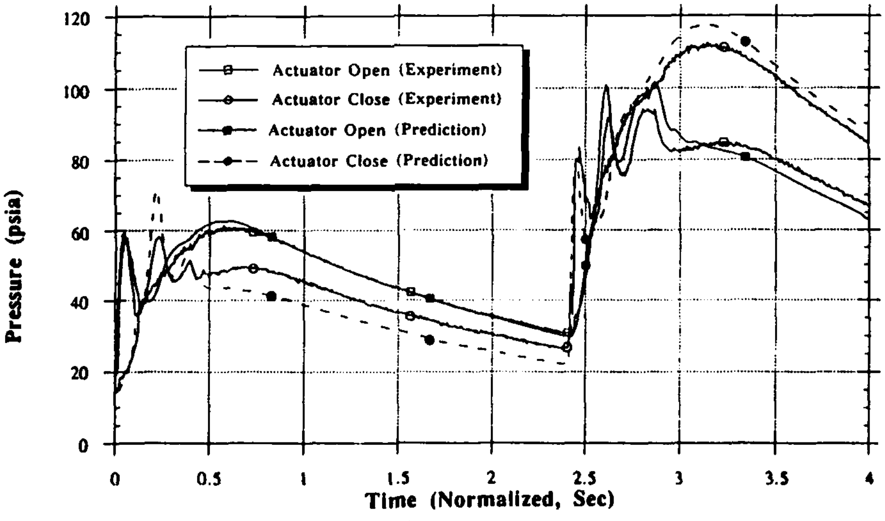

Figure 8(b) Comparison Between Experiment and Prediction For Valve Pressure Histories

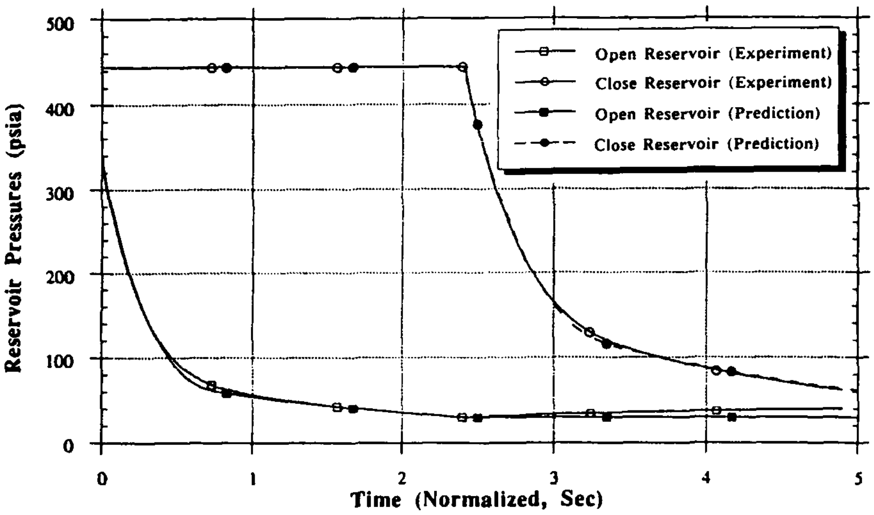

Figure 8(c) Comparison Between Experiment and Prediction For Reservoir Pressure Histories

4. SUMMARY OF UNCERTAINTY ANALYSIS FOR AEROPERFORMANCE MEASUREMENTS IN THE ATARR

There are many problems associated with making aeroperformance measurements of turbine stage efficiency in any facility, long run time or short duration. The goal set for the ATARR was to be able to measure turbine efficiency to within ± 0.25% of the "true" value within a 95% confidence limit. Because a great many of the assumptions used in the calculation of efficiency cannot, in general, be verified independently, the "true" efficiency becomes a function of the assumptions made about the testing process, the working fluid, etc. which comprise the basis of the efficiency calculation. Within any given basis, preliminary estimates described in detail in Ref. 7 suggest that single-sample data of approximately ± 0.8% accuracy can be obtained and through the use of common statistical techniques. The material presented here is a brief summary of the material presented in Ref. 7 which is a condensation of a more detailed report (Ref. 8). The topics addressed in Ref. 7 include: the accuracy required in each measurement quantity, the choice of alternative (but equivalent) efficiency definitions, the determination of the proper working fluid and the working fluid properties.

The desired 0.25% efficiency accuracy for the ATARR facility could easily be overshadowed when comparisons are made with data taken in other facilities because of differences in the testing methods. It is argued in Ref. 9 that the proper way of comparing efficiencies taken from different facilities is to "correct" the indicated efficiency to account for losses and obtain an efficiency measure which is independent of the test process. Uncooled turbines operate in long-duration facilities at conditions which are close to adiabatic, while the same turbines in short-duration facilities would have higher heat-transfer losses. However, the assumption of adiabatic conditions is not appropriate for either long or short-duration facilities when cooled turbines are tested. Cooled hardware in short-duration tests would be expected to experience additional heat-loss effects above those that would occur if the same turbine were tested in a long-duration facility. To compare measurements taken in these two facilities one has to correct for the fundamental differences in the testing process.

The thermodynamic efficiency measured in any facility is given by:

$$\eta\Big|_{meas} = \frac{\text{Measured Change in Energy State of the Working Fluid Across a Turbine}}{\text{Ideal Change in Energy of the Fluid for the Same Pressure Change}}$$

which for constant mass flow and no energy addition or removal (adiabatic flow), translates into:

$$\eta\Big|_{meas} = \frac{h_u - h_d}{h_u - h_{d,is}} \qquad (1)$$

Where the subscripts u and d represent the conditions upstream and downstream of the stage, respectively and $h_{d,is}$ represents the resulting enthalpy of the fluid if it were to be expanded isentropically to the measured downstream pressure. Equation 1-1 represents the measured efficiency in any testing facility. But this measure can be influenced by energy losses which are not directly related to the stage performance. They would include energy loss by heat transfer to surfaces and mass flow leakage through seals. An accounting process must be done since any energy lost in this manner is not available to do work on the turbine. If the sum of all the losses are labeled as L then the fundamental efficiency is:

$$\eta_{Fu} = \frac{h_u - h_d - L}{h_u - h_{d.is}} \qquad (2)$$

The work described in Ref. 9 has only been concerned with the heat-transfer losses which occur during the testing of a turbine stage. Accounting for only these losses (Q_w, the heat transfer to the walls) creates an adiabatic efficiency:

$$\eta_{ad} = \frac{h_u - h_d - Q_w}{h_u - h_{d.is}} \qquad (3)$$

There is the possibility that losses exist in both the testing facility and the stage which are not heat-transfer losses, and thus an adiabatic efficiency could still be dependent on the testing process. Only a measurement of efficiency which accounts for all losses (such as equation 2) can be used when comparing data taken in different facilities.

In general, long-duration facilities are assumed to have no heat losses and negligible mass flow losses (although these assumptions need to be verified for each facility) implying that L=0. Under these assumptions the long-duration facility measures the adiabatic efficiency and the fundamental efficiency. In a short-duration facility there will be heat transfer because of the isothermal nature of the facility and the enthalpy change would need to be corrected for these losses to determine the adiabatic efficiency. Further to convert to a fundamental efficiency, other losses besides heat transfer need to be quantified. Thus to convert an efficiency measurement in any testing facility to an adiabatic efficiency requires the knowledge of one of two variables: the adiabatic enthalpy ($h_{d,ad}$) or the heat-transfer losses in the system (Q_w). But to convert to a fundamental efficiency which is the only efficiency measurement which is independent of the testing process requires a knowledge of all the losses in the system (L). To avoid the problem of trying to determine L accurately in a short-duration facility, a second method, using the work extracted by the turbine, can be used to determine the change in enthalpy across the stage. If all the energy dissipated by the gas across the stage is transformed into work then:

$$W = h_u - h_d - L \qquad (4)$$

and W can replace the numerator in equation 1-2. These two methods are commonly referred to as the thermodynamic method and the mechanical method for measuring efficiency.

One of the unique differences between the thermodynamic technique and the mechanical technique is that the mechanical method provides the fundamental efficiency directly. Using the thermodynamic technique introduces a dependency on the testing process which directly influences the loss term L and complicates the process of comparing data taken in different facilities. The mechanical method also has its drawbacks. It assumes that all the energy change that occurs across the turbine stage gets translated into useful, measurable work and not other forms of potential energy (such as turbulence) which are not directly measured.

In addition to the testing process, assumptions about the gas properties and other topics which might seem extraneous to the main uncertainty analysis play key roles in determining the context in which the efficiency measurements are made. It is clear that as long as this "context" or "basis" remains consistent, efficiency measurements can be directly compared. For these reasons the analysis described here is not an error budgeting process, rather it is geared to evaluating different measurement uncertainties and grouping them according to different data processing procedures. In this way estimates can be made as to how much the final uncertainties can be reduced. Thus, for the majority of this work we will be using single-sample data. Discussion of statistical techniques which could be used to combine different measurements and increase the accuracy beyond the point of the individual measurements are described in Ref. 7.

Several different problems which confront the engineer when measuring efficiency are examined in Ref. 7, but the details of that examination cannot be repeated here. Because the ATARR will be used to test a variety of turbines, specific estimates of the obtainable accuracies are not given in detail; rather, the equations are developed which will allow adequate prediction of the uncertainty in the measured efficiency for any stage configuration.

It is shown in Ref. 7 that the definition of efficiency and the physical basis for its determination are more significant in comparing data from different facilities than the repeatability of the measurements themselves. Within the constraints of consistent definition and basis, efficiency measurements with accuracies better then 0.25% are achievable. In programs where test data are to be compared with data from other facilities, the specific method of determining efficiency must be carefully considered. Factors such as the specific gas properties, the defining equation of state of the gas, and the isentropic relationships used, can result in differences in the obtained efficiency. Whether the thermodynamic or the mechanical method is better for measuring efficiency is strongly dependent on the objectives of the testing program as well as the turbine configuration and how the loss term is treated. If a satisfactory estimate of the loss term is not available, then realistically only the mechanical method can be used.

5. SUMMARY COMMENTS

A brief description of the Advanced Aerothermal Research Rig (ATARR) currently under development at Aero Propulsion and Power Directorate of Wright Patterson Air Force Base has been presented. ATARR is the first large scale, short duration turbine facility built in the United States for integrated aerodynamic and heat transfer testing. It has been built both to extend our capability to validate turbine designs and provide affordable turbine performance testing.

REFERENCES

1. Schultz, D.L., Jones, T.V., Oldfield, M.G.G., and Daniels, L.C., "A New Transient Facility for the Measurement of Heat Transfer Rates," AGARD, CP229, 1977.
2. Dunn, M.G. and Stoddard, F.J., "Development of a Shock-Tunnel Technique for the Measurement of Heat-Transfer Rate to Gas Turbine Components," 11th International Symposium on Shock Tubes and Waves, July 1977.
3. Dunn, M.G. and Hause, A., "Measurement of Heat Flux and Pressure in a Turbine Stage," ASME J. of Engr. for Power, Vol. 104, No. 1, pp. 215-223, January 1982.
4. Louis, J.F., "Investigation of Factors Affecting Heat Transfer to Turbine End Walls," Technical Report AFAPL-TR-73-93, October 1973.
5. Richards, B.E., "Isentropic Light Piston Facilities for Simulation of Hot Flows Through Turbines," VKI Lecture Series 78, Advanced Testing Techniques in Turbomachines, April 1975.
6. Consigny, H. and Richards, B.E., "Short Duration Measurements of Heat-Transfer Rate to a Gas Turbine Rotor Blade," ASME J. of Engr. for Power, Vol. 104, pp. 542-551, July 1982.
7. Epstein, A.H., Guenette, G.R., and Norton, R., "The MIT Blowdown Turbine Facility," ASME Paper 84-GT-116, June 1984.
8. Dunn, M.G., Lukis, G., Urso, M., Hiemenz, R.J., Orszulak, R., and Kay, N.J., "Instrumentation for Gas Turbine Research in Short-Duration Facilities," Aerospace Congress and Exposition, Long Beach, CA, 15-18 October 1984, Paper No. 841504.
9. Haldeman, C. Jr., Dunn, M., MacArthur, C., and Cohrs, B., 1991, "Uncertainty Analysis of Turbine Aerodynamic Performance Measurements in Short Duration Test Facilities," AIAA Paper No. AIAA-91-2131, 27th Joint Propulsion Conference, Sacramento, CA.
10. Haldeman, C.W. and Dunn, M.G., "Uncertainty Analysis for the Advanced Turbine Aerothermal Research Rig (ATARR)," Calspan Report No. 7733-3, to be published.
11. Guenette, G.R., Epstein, A.H., and Ito, E., "Turbine Aerodynamic Performance Measurements in Short Duration Facilities," AIAA Paper 89-2690, AIAA/ASME/SAE/ASEE 25th Joint Propulsion Conference, Monterey, CA, July 10-12, 1989.

Discussion

QUESTIONS 1 & 2:

DISCUSSOR: P. Harasgama, ABB

How are you going to achieve the stated accuracy of 0.25% on aerodynamic performance and have you demonstrated an instrumentation technology that can achieve such levels of measurement accuracy?

DISCUSSOR: T. Arts, von Karman Institute

With the presented design of pressure probe rakes, taking into account blockage effects and how shock interactions in transonic flows, is the 0.25% goal really feasible or achievable?

AUTHORS' REPLY (to related questions above):

The topic, while conceptually easy, is extremely complicated to document and the results are susceptible to multiple interpretations. This paper was an overview of the ATARR facility, discussing only small parts of our uncertainty analysis. A more detailed discussion of our early uncertainty analysis was presented at the Sacramento Joint Propulsion Conference[1] based on underlying research done at Calspan. Since the completion of Reference 1, additional work has been done on the uncertainty analysis and the will soon be documented[2]. In essence, Reference 1 focused on the best ways of combining temperature and pressure data to obtain the efficiency with the highest degree of accuracy, not how to reduce the instrument uncertainty which contributes to the measurement uncertainty. Reference 1 can be summarized by four statements:

1) Measurements of 0.25% efficiency are possible given existing instrument technology by properly performing calibrations and reducing other sources of error (such as A/D conversion, amplifier drift, etc.) to a minimum.

2) Real gas effects can be of the same magnitude as the total instrument uncertainty, making relative accuracies of 0.25% (i.e. the difference between two tests in the same facility) easier to achieve than an absolute measurement.

3) None of the problems in making high-accuracy measurements are endemic to short of medium duration facilities[3]. Thus if a particular group is claiming 0.25% efficiency measurements on a facility, the same instrumentation calibration used at ATARR should achieve the same accuracy.

4) Variations between facilities will probably dominate the overall absolute error in efficiency measurements, making comparisons of measurements on the same turbine hardware in different facilities difficult at best.

However, we believe that 0.25% efficiency measurements are a good target, worthy of continued pursuit. It forced those of us associated with ATARR to do an in-depth uncertainty analysis before the final instrumentation was installed, and it forced us to run critical tests on the entire system. Tests which are often done after facilities are built, were done prior to facility completion, helping to locate and correct potential problems. This is, as Moffat[4] has suggested one of the key roles of a proper uncertainty analyses. The results of our analysis revealed several potential problems in the selected A/D system and instrumentation.

1) Static calibration of both pressure and temperature standards to the required accuracy were accomplished. We are presently using these standards to calibrate temperature and pressure rakes. Preliminary data demonstrate information shows that

static calibration of the pressure rakes and RTD's (resistance temperature devices) can be done to the required accuracy levels. We are still in the process of calibrating thermocouple rakes. However, using these diagnostics in a dynamic system requires and entirely different calibration facility, allowing independent variation of Mach number, radiation, and facility time constants to assure proper calibration of the recovery factors. A detailed design of the required facility, in particular, using the ATARR itself to calibrate the rakes.

2) The A/D system purchased was a software programmable amplifier, A/D system with internal calibration capabilities. The goal was to decrease the overall test set-up time and to reduce the number of personnel required to run the facility. Several problems were noted:

a) When calibrating the A/D system, the internal ground was different from the external ground, causing an unexpected offset in the amplifiers which was on the order of 2-3 counts.

b) The attenuators caused excessive noise in the output signal. The manufacturer was able to retrofit the system prior to facility commissioning in order to resolve these problems.

c) One of the analog switches used to switch gains on the amplifier has a strong temperature dependency. This creates a variation in the gain of about 1.5%, at a gain of 1000, from a 10°C temperature rise. Redesigned amplifiers are now available, alleviating the problem. For the old amplifiers which still exist in the system, a fan unit was installed which stabilized the temperatures and reduced the problem considerably. Further, calibrating the amplifiers immediately before and after a test documents any amplifier drift and allows for correction.

The overall accuracy of the instrumentation system is a function of how well one can statically (i.e. at one point in time) calibrate the system, and how well one can document the total system drift. The following is an outline of the calibration procedure as a function of time that we are currently using:

Step 1 (One-twos month before instrument installation in facility):
  Several laboratory calibrations are done on the instruments to verify their performance as a function of their primary and secondary variables (i.e. pressure transducer evaluated based on pressure and temperature). These are done over time to verify drift. Each instrument calibration is flanked by an amplifier calibration to evaluate any drift in the amplifiers.

Step 2 (Installation):
  The instruments are installed in the facility. Data at room conditions is obtained to verify that no ground loops have been created and/or that there is no increase in noise levels.

Step 3 (Testing):
  3a (Morning of the experiment): Calibrate all amplifiers
  3b (Immediately before experiment): Fill supply tank and test section, do pre-test pressure calibrations, verify temperature uniformity in the test section
  3c (Test): Run the experiment
  3d (Post-test data): Take data during cool-down time
  3e (Immediately after experiment) Fill supply tank and test section, do post-test pressure calibrations, verify temperature uniformity in test section
  3f (After experiment): Calibrate all amplifiers

All of these steps may not need to be done in all cases, but we will start with this system to verify our overall instrument drift. It should be evident from this discussion that significant time is required to obtain the desired accuracy. This level of accuracy lengthens overall testing time.

In summary, this type of measurement accuracy is right on the edge of what is achievable using existing technology, but with new calibration techniques. We believe it to be a good goal for instrumentation since it is both defined and achievable. Since we are still in the process of calibrating our instruments, we do not have a definitive experimental answer yet. In addition, we will not know what our dynamic accuracy is until we build the separate calibration facility noted earlier. However, we have gone to great length to document our work, in the hope that whatever our results, our experience will point us towards better instrument designs and data reduction techniques.

References

1. Haldeman, C., M. Dunn, J. Lotsof, C. MacArthur and B. Cohrs "Uncertainty Analysis of Turbine Aerodynamic Performance Measurements in Short Duration Test Facilities" AIAA/SAE/ASME/ASEE 27th Joint Propulsion Conference, June 24-26, 1991 Sacramento, CA, AIAA-91-2131
2. Haldeman, C. and M. Dunn "Uncertainty Analysis for the Advanced Turbine Aerothermal Research Rig (ATARR)", Calspan Report No. 7733-3 (to be published)
3. Short duration facilities are considered to be in the 1-50 ms test time frame (Calspan shock tunnels), medium duration would be in the 0.25 to 5 second test time (MIT Blowdown turbine and ATARR), and long duration facilities may run for many minutes or hours
4. R.J. Moffat "Contributions to the Theory of Single-Sample Uncertainty Anaysis", Journal of Fluids Engineering, Transactions of ASME, June 1982, Vol. 104, p. 250-260

TRANSIENT THERMAL BEHAVIOUR OF A COMPRESSOR ROTOR WITH AXIAL COOLING AIR FLOW AND CO-ROTATING OR CONTRA-ROTATING SHAFT

C. Burkhardt, A. Mayer, E. Reile
MTU Motoren-und Turbinen-Union München GmbH
8000 München 50, Germany

Abstract

Heat transfer measurements were made in a five-cavity compressor drum rig, in which cooling air passed axially through the centre of the discs. The rig also contained a central drive shaft which could be either co- or contrarotated.
Tests were conducted for different mass flow rates, rotational speeds and air temperatures. Typical engine conditions for steady state and transient operating conditions were simulated. Local Nusselt numbers were obtained for the discs of one cavity and compared with other published results. Furthermore an investigation into the effect of co and contrarotating shaft on the surface temperatures of the discs and on the Nusselt number distribution was also carried out. It was found that the direction of rotation and speed of the shaft influenced the disc temperatures as well as the Nusselt numbers.

NOMENCLATURE

a	inner radius of cavity
b	outer radius of cavity
g	acceleration due to gravity
G	gap ratio, = s/b
Gr_L	local Grashof number, $= \rho^2 \Omega^2 r L^3 \beta \Delta T/\mu^2$
k	thermal conductivity
L	characteristic length, = b-r
m	coolant mass flow rate
N	rotational speed
Nu_L	local Nusselt number $= q_{c,s} \cdot L/(Ts-Tref) \cdot k$
p	pressure
q	heat flux
r	radial coordinate
Re_z	axial Reynolds number, $= 2\rho Wa/\mu$
Re_ϕ	rotational Reynolds number, $= \rho \Omega b^2/\mu$
s	axial distance between discs
t	time
T	temperature
T_{ref}	reference air temperature, T_5 in this paper
W	bulk-average axial velocity at inlet to cavity
x	nondimensional radial coordinate = r/b
x_{io}	inner-to-outer radius ratio
x_{si}	shaft-to-inner disc radius ratio
z	axial coordinate
β	coefficient of volumetric expansion
ΔT	temperature difference, $=1/T_{ref}$
ϵ	axial Rossby number, $= W/\Omega a$
θ	nondimensional surface temperature, $= (T_s-T_{ref})/(T_{s,max} - T_{ref})$
μ	dynamic viscosity
ν	kinematic viscosity, μ/ρ
ρ	density
Ω	angular speed of cavity

Subscripts

c	pertaining to convection
hub	hub of disc
L	pertaining to characteristic length
max	maximum value
rim	rim of the disc
R	pertaining to rotor
s	value at disc surface
SH	pertaining to shaft

1. Introduction

In a gas turbine engine, it is often the case that cooling air, to be used in the turbine, is passed through the centre of the compressor discs. Some of this air can enter the cavities between adjacent corotating compressor discs as a result of rotationally induced buoyancy effects: the flow inside the cavities is significantly affected by the temperature difference between the discs and coolant as well as the radial temperature profile.
Since the designer must be able to control the thermal behaviour of the rotor, an understanding of the heat transfer phenomena is of paramount importance. On the basis of this knowledge the stress levels, fatigue life and radial growth can be predicted. There are only a few publications which help designers understand the fluid dynamics and the heat transfer in rotating cavities with an axial throughflow. Moreover, the limited work that does appear (Ref. 1) has, in contrast to the present paper, concentrated on single plane disc cavities without a heated shroud and with disc temperature profiles that did not always reflect those in an engine compressor.
This paper concentrates on the understanding of the heat transfer process, under simulated engine conditions, in a five cavity compressor drum rig (see fig. 1) with an axial throughflow of coolant. The rig also contained a central drive shaft which could be either co -or contrarotated. For the analysis of the test results, measured disc surface temperatures were used as boundary conditions to solve the heat conduction equation for the discs. From the computed surface heat fluxes the local Nusselt numbers were obtained.

2. Rig Tests

2.1 Geometry

Fig. 1 shows the configuration used for the rig tests described in this paper. The drum assembly, which was driven by an electric motor, comprised the last four discs of a high pressure compressor and reached a maximum speed of 15500RPM. The rotor cavity geometry and the materials used corresponded to those of an engine design.

The shaft was driven by the use of an air impeller (not shown in fig. 1) and it could be either co- or contrarotated relative to the drum assembly. In the former case the maximum shaft speed was + 12000RPM (the same as the drum); in the latter case the maximum shaft speed was -11400 RPM.
In this paper only the temperature measurements from the middle cavity, formed between discs 2 and 3, are discussed. This cavity had an inner-to-outer radius ratio, x_{io}, of 0.286, a gap ratio, G, of 0.256 and a shaft-to-inner disc radius ratio, x_{si}, of 0.793.

2.2 Air System

To simulate the engine compressor stage temperature, as shown in Fig. 1 hot air, supplied through a pipe arrangement, was impinged onto the outer surface of the drum.
Cooling air was supplied through inlet ports arranged in the hub area upstream of the first disc. This air passed axially through the annulus between the central shaft and the hub of each successive disc before leaving the rear of the drum assembly through outlet ports.

The test facility included two main air lines supplying hot and cold air respectively. The temperatures of the impingement and cooling air were controlled by valves. For the transient tests, all valves were simultaneously switched from cold to hot or vice versa.

2.3 Instrumentation and data acquisition

The drum assembly was instrumented with 44 Ni-Cr-Ni thermocouples. The transmission capacity from the rotor system was limited to 20 simultaneous signals. Therefore, three instrumentation arrangements were provided. By repeating a test and altering the arrangement it was possible to obtain measurements from all the thermocouples for any particular test condition. The thermocouple locations for the middle cavity can be seen in Fig. 1. A pyrometer was also installed in order to obtain more information on the shroud temperature at the outer surface of the middle cavity.
Two different data recording systems were used. The first recorded all measurements and was predominately used for steady state tests. Moreover this system allowed spot checks to be made. The second system which was used for all transient runs, allowed up to 40 signals per second. A smoothing technic was employed to obtain values every 1.5 seconds. Both systems were calibrated and checked regularly to minimize experimental inaccuracies; the maximum difference noted between any two thermocouples was less than 1.0 K at ambient temperatures. The measurement errors at test conditions could not be precisely determined but were estimated to be about ± 1 %.
The coolant mass flow was measured at the assembly exit by an orific plate, and using gas analysis to determine any leakage through the seals. This technique produced an uncertainty of ±3% and ±2% at low and maximum flow rates respectively. The additional leakage through the min flanges was estimated to be 1% of the central axial flow at the full load condition for the middle cavity. Errors in pressure and rotor speed were negligibly small.

2.4 Test Conditions

Tests were carried out for simulated full load and idle conditions as well as acceleration and deceleration. For the steady state tests, whilst keeping all other parameters constant, the effect of the following on the disc temperature and heat transfer was investigated:
- rotor/shaft speeds
- coolant mass flow rates
- coolant/impingement temperatures

Transient tests were carried out between the idle and full load steady state conditions for different mass flow rates and for both a co- and contrarotating shaft. The steady state conditions for simulated full load and idle are listed in Table 1.
Fig. 2 shows the main conditions for the transient tests. For an acceleration test, the cooling flow rate, pressure and rotor speed reached their specified values after approximately 10 - 15 s. For the impingement air it was more than 100 s. Due to the thermal inertia of the casing, the coolant air temperature required a longer time period to reach its specified value.

3. Data Analysis

If the temperature histories at the surface of a solid are known, then the internal temperature distribution can be computed by solving the time dependent heat conduction equation; this is termed a direct heat conduction problem. Once the temperature field has been calculated, the surface heat fluxes and the subsequent Nusselt numbers can be determined.
The computation was carried out using the thermal analysis program P/THERMAL (PDA). This is a hybrid analysis technique based on the combined use of finite elements and the heat balance finite difference method. The computational analysis included the effects of radiation. The calculations were carried out with the aid of a 2-dimensional axisymmetric finite element model. The grid, which is illustrated in Fig. 3, comprised 396 material elements and 82 convective elements. The latter were used to obtain surface heat fluxes. The shape of the cavity, modelled by the finite elements, is a reasonable approximation to the geometry shown in Fig. 1.

The mid plane of each of the two discs was assumed to be adiabatic ($\partial T/\partial z = 0$). This assumption, which has been used in Ref. 2 is considered to be suitable for relatively thin discs with large radial temperature gradients.
As can be seen from Fig. 1, the number of thermocouples used for the calculation was limited to only four per disc.
Due to the fact that, for each timestep, temperature values had to be allocated to the individual surface nodes of the grid, interpolated measured temperatures were required. Ref. 3 discussed an investigation into interpolation procedures whereby the number of measurement locations was considered. From these results, it can be deduced that for the present case a "Bessel interpolation" polynomial is the most suitable. Thermocouples M5, M9, M13, M16 were used for the upstream disc and M6, M10, M14, M16 for the downstream disc. As an example, Fig. 4 shows the results of interpolated surface temperatures versus radius for several timesteps for the upstream and downstream discs.

The coolant air passed through the narrow annulus between the shaft and the bore of the discs, $r_{sh} < r < a$. As a boundary condition the bore surface temperatures were assumed to be isothermal; the measured temperatures M5 and M6 were used for discs 2 and 3 respectively. Thermocouples M18 and M19 were used to determined the temperature at the outer surface of the shroud of the middle cavity. During later tests the signal from a pyrometer (as shown in Fig. 1) was also recorded to improve this boundary condition.

In the numerical procedure, a maximum timestep of 2 sec was chosen. The initial conditions were obtained by solving the steady state conduction equation with $(\partial T/\partial t) = 0$ and using the boundary conditions described above.
The local Nusselt number is defined by :

$$Nu_L = q_{c,s} \cdot L \; / \; (T_s - T_{ref}) \cdot k \qquad (1)$$

where L is a characteristic length, T_s is the local disc surface temperature, T_{ref} is a suitable reference temperature, and k the thermal conductivity of the fluid which is evaluated at T_{ref}. Following the suggestion of Ref. 4, for these tests the characteristic length used was (b-r), and T_5 was used for the reference temperature, T_{ref}.

4. Rig Test Results

4.1 Temperature Profiles

Since the flow inside the cavity is affected by buoyancy forces the disc temperature distribution has a significant effect on the disc heat transfer. Fig. 5 shows the variation of nondimensional surface temperature, θ , against nondimensional radial coordinate, x, where $\theta = (T_s - T_{ref})/(T_{s,max} - T_{ref})$ and x = r/b and the subscript 'max' is used to denote the maximum disc surface temperature for the test. The curves shown are for the full load condition.

4.2 Transient tests

The transient loadcases included both accelerations and decelerations, similar to actual engine conditions, for three different coolant air flow rates as well as with either a co- or contrarotating central shaft. Table 1 shows the steady state conditions at the beginning and end of the transients mentioned above.

Fig. 6 illustrates results in terms of Nusselt number variation with time for a contrarotational shaft. Test results for two different cooling flow rates for an acceleration and a deceleration are presented for the upstream and downstream discs. Most of the calculated Nusselt numbers are positive which implies that heat is convected from the disc surface to the fluid. The results are valid for the following ranges of characteristic parameters:

$$2.7 \cdot 10^4 \leq Re_z \leq 9.5 \cdot 10^4, \; 1.9 \cdot 10^6 \leq Re_\phi \leq 5.6 \cdot 10^6, \; 0.08 \leq \beta \Delta T \leq 0.14$$

Also shown in Fig. 6 is the correlation of Ref. 4 given as:

$$Nu_L = 0.0054 \, Re_z^{0.3} \, Gr_L^{0.25} \qquad (2)$$

This was obtained from experimental results where both discs had the same temperature distribution which increased with radius.

The correlation shown corresponds to the steady state condition at the end of the transient process. As can be seen, it reasonably predicts the heat transfer for the central and outer radii of the discs.

From the results it is possible to state the following:

- The Nusselt numbers determined for the upstream disc 2 are greater, than those for the downstream disc 3.
- For the time range shown, in the main, the upstream disc has Nusselt numbers which are greater in the hub area than those at the larger radii; this occurs for both acceleration and deceleration.
- For the downstream disc, the Nusselt numbers are generally smaller in the hub area than at the outer radii for acceleration. For deceleration, however, the opposite occurs at the beginning of the transient period but as time increases the Nusselt numbers decrease and become invariant with radius.
- The difference in Nusselt numbers between the upstream and downstream discs is more significant at the lower radii.
- For all transient tests, there is a greater variation of Nusselt number with time at the lower radii.
- An increase in coolant flow rate from 30% to 100% of the maximum decreases the Nusselt numbers on the upstream disc and increases them on the downstream disc.

It should be born in mind that the choice of reference temperature, T_{ref}, is important in correctly computing the Nusselt numbers. In the present work a common reference temperature, T5, was used for both the upstream and downstream discs of the middle cavity. *Indeed, if the heat* fluxes, rather than the Nusselt numbers, are compared, the differences between the discs are greatly reduced.

4.3 Steady State Tests

In order to assess in more detail the effects of cooling flow rate on the heat transfer, steady state tests were carried out in which all parameters but the flow rate was kept constant.
For both the idle and full load conditions, three flow rates were used: 30%, 60% and 100% of the values shown in Table 1. For the upstream disc Fig. 7 shows the effect of the flow rate on the radial temperature profile for both load conditions. Similar graphs were obtained for the downstream disc.
Fig. 8 shows the Nusselt numbers, for the three flow rates for the upstream and downstream discs under the full load condition. As was noted above for the transient results an increase in flow rate decreases the heat transfer on the upstream disc but decreases the heat transfer on the downstream disc.
The results presented so far were all obtained with a contrarotating shaft. Fig. 9 illustrates the effect of shaft rotational speed ranging from maximum contrarotation (-11400 RPM) to corotation (+12000 RPM) on the steady state cooling air and disc temperatures. For each shaft rotational speed, tests were carried out with three different coolant flow rates whilst keeping all other variables constant. Although T_1 was constant for all shaft speeds, T5 varied slightly. This is probably due to the heat transfer effect of the two upstream cavities. The disc temperatures decrease as the shaft speed approaches the drum speed. This effect is more pronounced for the higher flowrates and the downstream disc. Fig. 10 shows that, as the

shaft speed varies from its maximum contra to its maximum corotational values, there is a continuous increase in the Nusselt numbers for both discs.

5. Conclusions

Heat transfer experiments have been conducted using a five cavity compressor drum rig with an axial throughflow of coolant air.
The results from one of the cavities have been presented. The geometry comprised an inner-to-outer radius ratio, x_{io}, of 0.286, and a gap ratio, G, of 0.256. The rig also contained a central drive shaft, with a shaft-to-inner disc radius ratio of, x_{si}, 0.793, which could be either co- or contrarotated. Simulated compressor radial disc temperature profiles (increasing with radius) were used for the rig tests.

The local Nusselt numbers were obtained from the conduction solution using boundary conditions which included measured disc surface temperatures. The results were obtained for the following ranges of characteristic parameters:

$2.7\cdot10^4 \le Re_z \le 9.5\cdot10^4$, $1.9\cdot10^6 \le Re_\phi \le 5.6\cdot10^6$, $0.08 \le \beta\Delta T \le 0.14$

The main conclusions are:
- Under identical test conditions, the heat transfer for the upstream disc tends to be greater than that for the downstream disc.
- The upstream disc has Nusselt numbers which are greater in the hub area than those at the larger radii for both acceleration and deceleration. For the downstream disc, the Nusselt numbers are smaller in the hub area than at the outer radii for acceleration. For deceleration, however, the opposite occurs at the beginning of the transient period but as time increases the Nusselt numbers decreases and become invariant with radius.
- An increase in flow rate decreases the heat transfer on the upstream disc but increases the heat transfer on the downstream disc.
- For the variation of the shaft rotational speed ranging from - 11400 to + 12000 RPM, whilst all other parameters were kept constant, the steady state disc temperatures tend to decrease as the shaft speed approaches the drum speed. This effect , which is greater for the downstream disc, is more pronounced for larger coolant flow rates. In addition, for both discs the Nusselt number increase as the shaft speed approaches that of the drum.

The present work has only concentrated on the disc heat tansfer. However, a simple heat balance for the middle cavity, using the difference between the cavity inlet and outlet temperatures shows that the heat flux from the shroud is indeed greater than that from both discs. This is a topic which needs further attention as discussed in Ref. 5.

In response to this and other questions, the analysis is continuing at present, and it is hoped to obtain correlations that could be of use to the designer.

This work has presented results from simulated engine geometries and conditions. To fully understand the complex flow and heat transfer phenomena in rotating cavities with an axial throughflow, a combined theoretical and experimental study is required including rigs such as that described here and simplified geometries as discussed in Ref. 4.

References

Ref. 1 Owen, J.M.
Flow and heat transfer in rotating disc systems; ICHMT International symposium in heat transfer in turbomachinery, Athens, August 1992

Ref. 2 Long, C.A.
Transient analysis of temperature measurements on discs of the RB199 H.P. vented-rotor compressor, University of Sussex; 86/TFMRC/87, June 1986

Ref. 3 P.G. Tucker, C.A. Long
A finite element analysis of compressor disc heat transfer using the transient conduction method with sparse boundary collocation points, Second international conference on advanced computational methods in heat transfer, 1992, Milan, Italy

Ref. 4 P.R. Farthing, C.A. Long, J.M. Owen and J.R. Pincombe
Rotating cavity with axial throughflow of cooling air; ASME, 90-GT-16

Ref. 5 Long C.A., Tucker P.G.
Shroud heat transfer measurements from a rotating cavity with an axial throughflow of air; ASME, 92-GT-69

			IDLE	FULL LOAD
N_R	ROTOR SPEED	RPM	8000	12000
N_{SH}	SHAFT SPEED	RPM	-4000	-8000
m	COOLING FLOW RATE	kg/s	0.08	0.35
p	PRESSURE	bar	1.16	2.76
T5	REFERENCE AIR TEMP.	K	340	392
M18	SHROUD TEMP. AT DISC 2	K	440	577
M19	SHROUD TEMP. AT DISC 3	K	448	610

Table 1 Initial and final steady state conditions for the transient runs

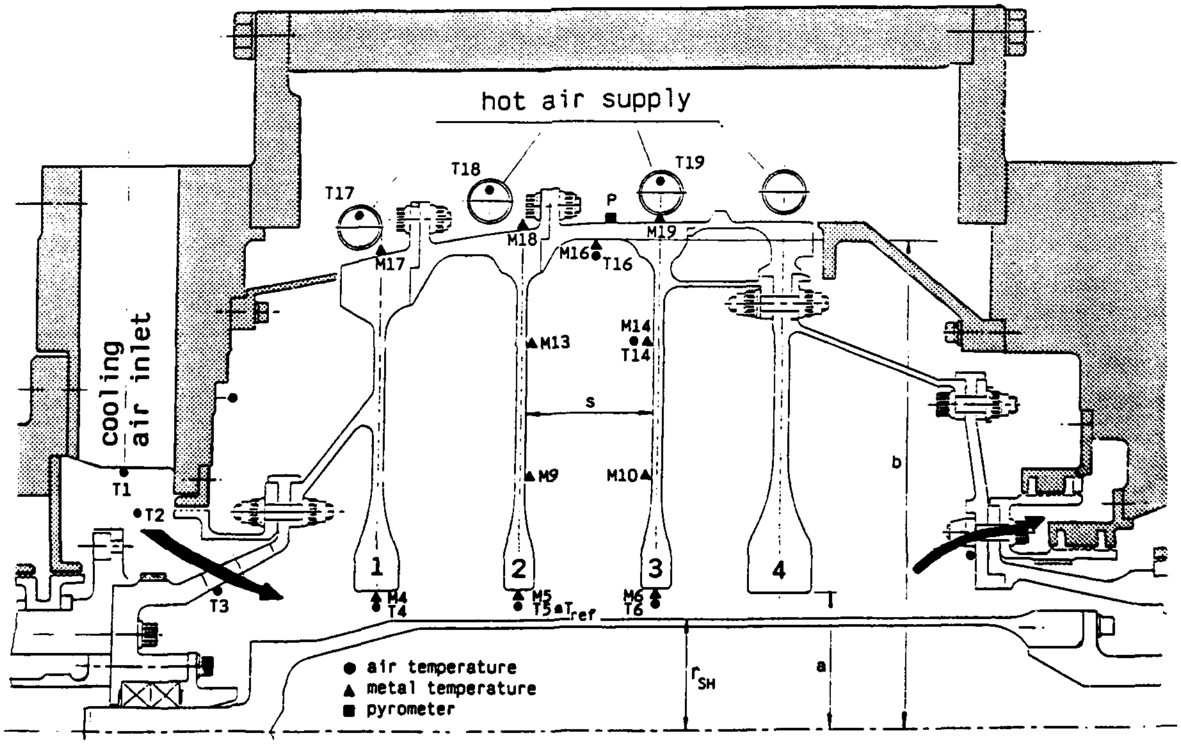
hot air supply
T17
T18
T19
P
M17
M18
M16
T16
M19
M14
T14
M13
s
M9
M10
b
cooling air inlet
T1
T2
T3
1
2
3
4
M4
T4
M5
$T5 = T_{ref}$
M6
T6
r_{SH}
a
● air temperature
▲ metal temperature
■ pyrometer

Fig.1 Cross-section through the compressor test rig

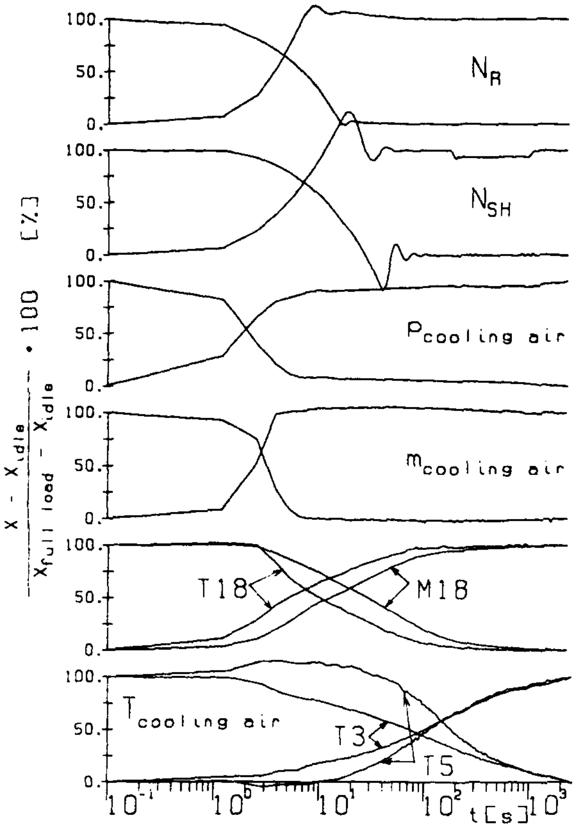

Fig.2 Transient behaviour of main parameters for simulated acceleration and deceleration

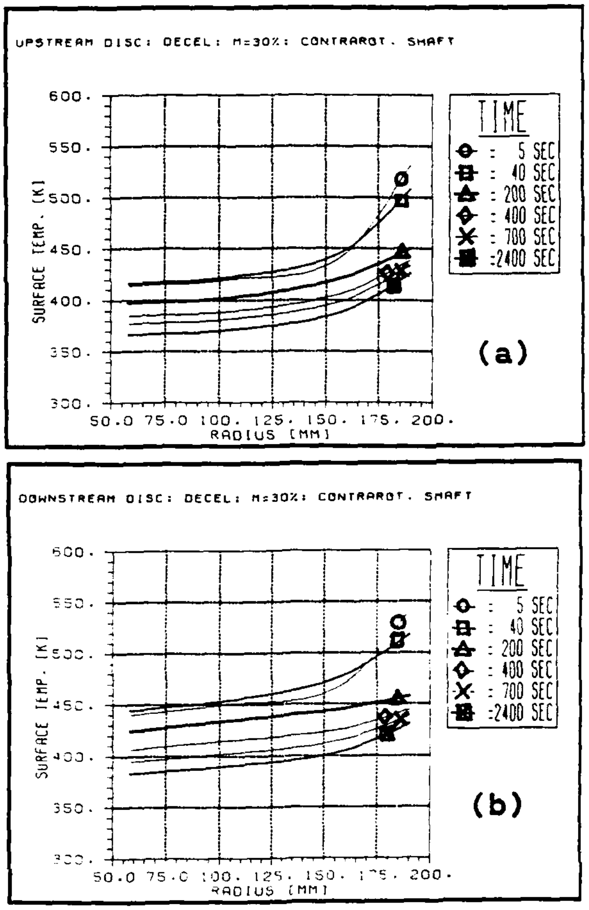

Fig.4 Interpolated surface temperatures versus radius during a deceleration;
(a) for the upstream disc
(b) for the downstream disc

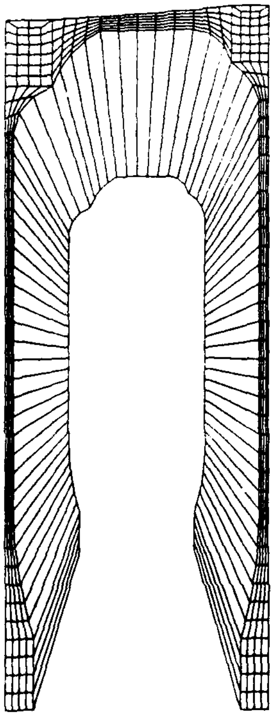

Fig.3 Finite element grid for the discs and shroud of the middle cavity

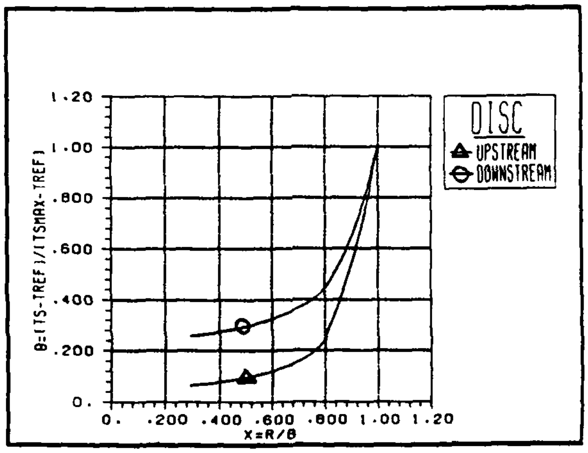

Fig.5 Nondimensional surface temperature versus nondimensional radius for the upstream and downstream disc

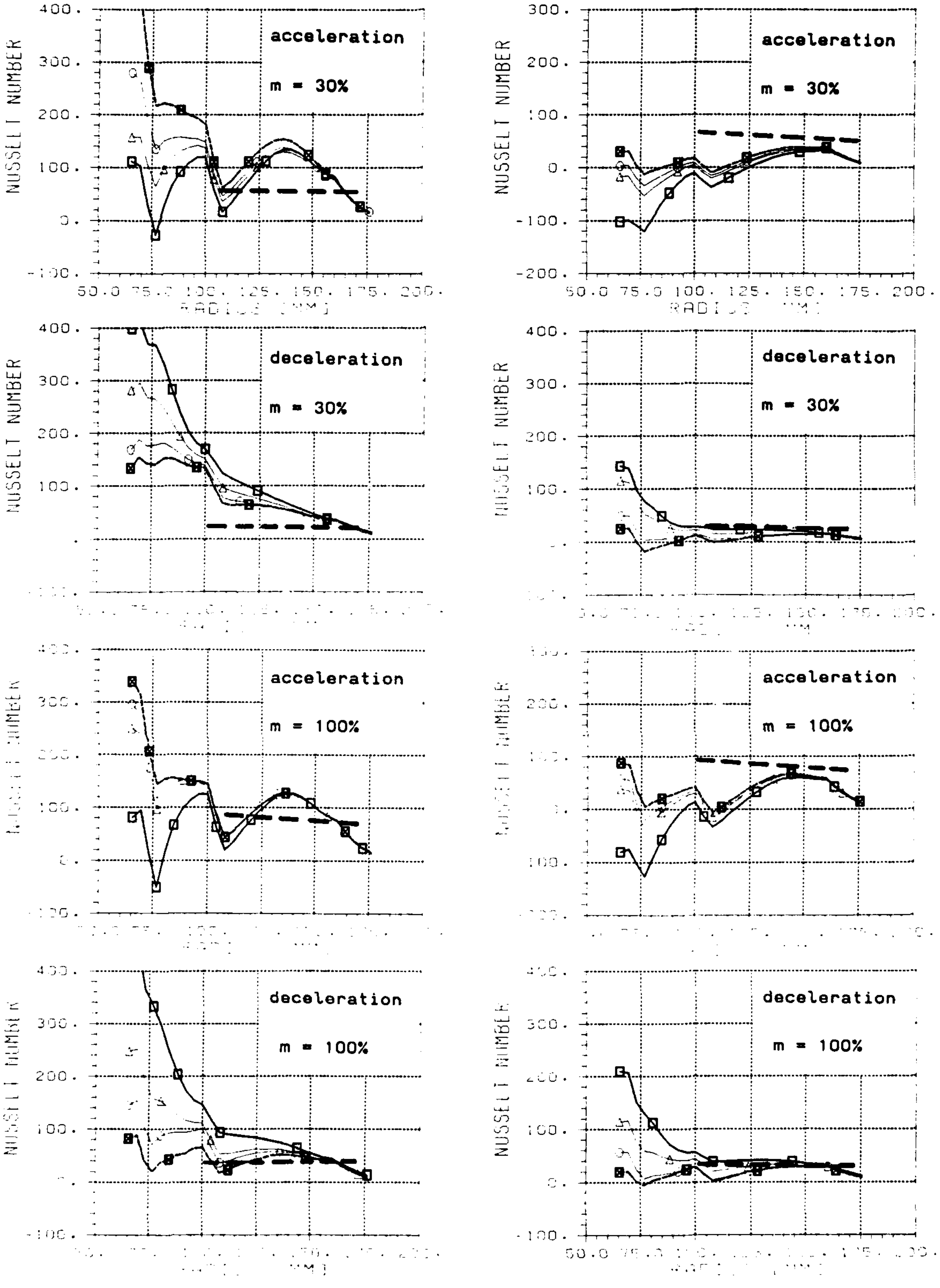

upstream disc

downstream disc

Fig.6 Radial variation of Nusselt number during an acceleration and decleration with a contrarotating shaft

— — — correlation (2)

The results are valid for the following ranges of characteristic parameters:

$2.7 \cdot 10^4 \leq Re_z \leq 9.5 \cdot 10^4$, $1.9 \cdot 10^6 \leq Re_\phi \leq 5.6 \cdot 10^6$, $0.08 \leq \beta\Delta T \leq 0.14$

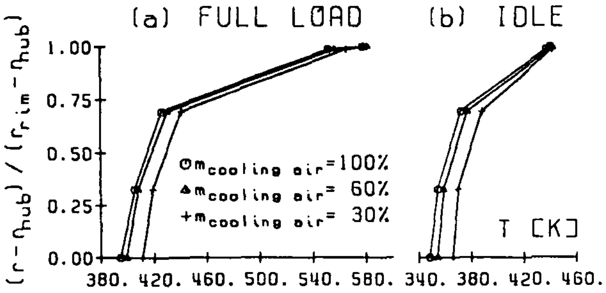

Fig.7 Effect of cooling flow rate on the radial temperature distribution for disc 2

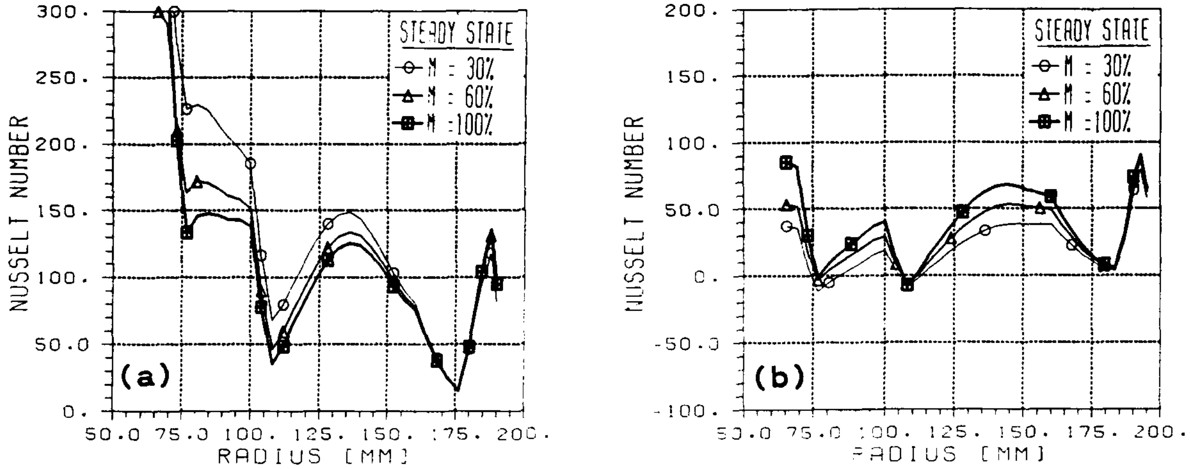

Fig.8 Effect of cooling flow rate on the Nusselt numbers at full load and a contra-rotational shaft for the (a) upstream and (b) downstream disc

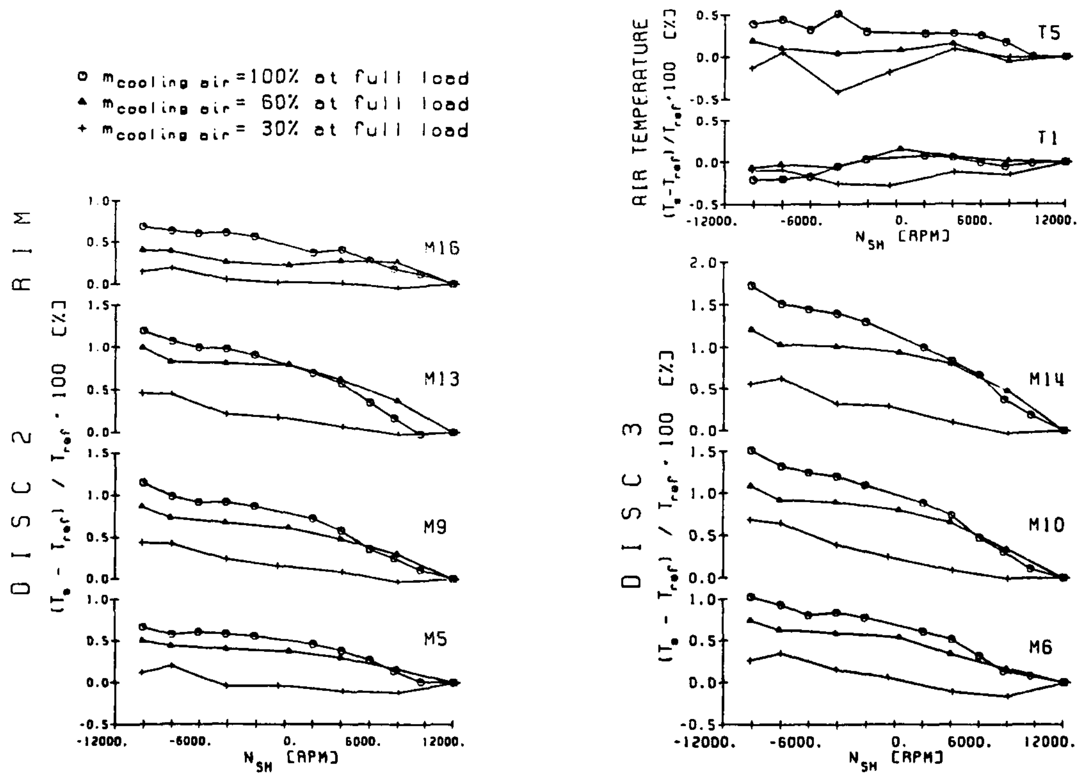

Fig.9 Effect of shaft rotational speed on the cooling air and disc temperature for three different cooling flow rates.

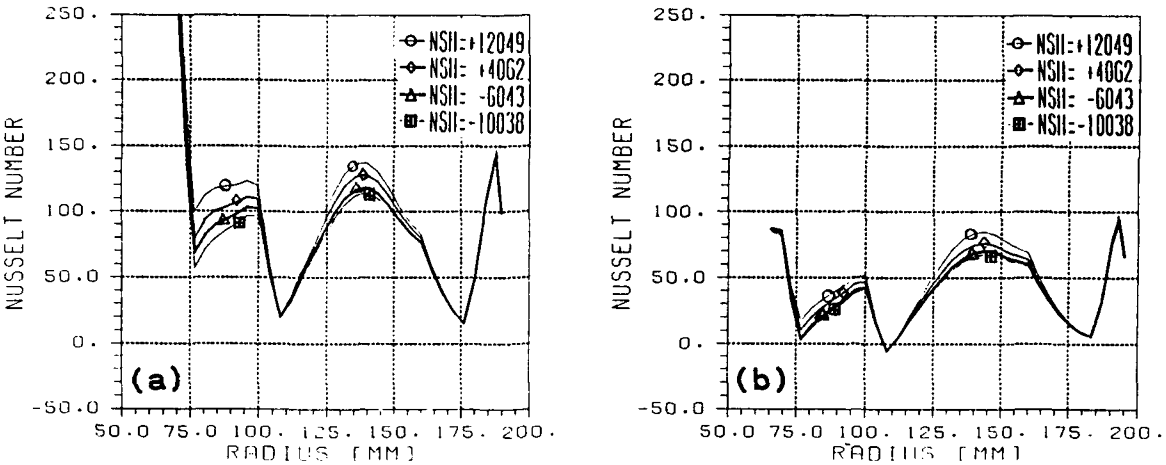

Fig.10 Effect of shaft rotational speed on the disc Nusselt number at full load for (a) upstream disc and (b) downstream disc

Discussion

QUESTION 1:

DISCUSSOR: J. Dixon, Rolls Royce

I note that radiation has been taken into account in the analysis of the rotating cavity with axial throughflow and heated shroud. Was radiation found to be significant?

AUTHOR'S REPLY:

From the literature it is well known that radiation can have a significant effect on the heat transfer in cavities with discs having different surface temperatures. In the present work, calculations with and without radiation revealed that the difference in heat flux was approximately 10 - 15%.

QUESTION 2:

DISCUSSOR: M. Owen, University of Bath

The authors are to be congratulated for obtaining Nusselt numbers from the compressor disks of an actual engine. The evaluation of Nusselt numbers from measured surface temperatures is a badly conditioned problem, and small errors in the measured temperature can cause large errors in the computed Nusselt numbers. Also the effect of uncertainties in the boundary conditions on the bore of the discs can cause uncertainties in the compiled Nusselt numbers at the small radii of the disc. Are the variations of the Nusselt number near the center of the disc caused by physical effects or errors? Having said that, it is pleasantly surprising to see that experimental conditions (obtained from rig at different conditions from the engine) agree under many conditions with the values of the Nusselt number measured by the authors, particularly at the larger radii.

AUTHOR'S REPLY:

A numerical study into the variation of temperature profiles in the bore region is being carried out at present in order to find out whether the variation of Nusselt number is caused by physical effects or by errors in interpolation or measurement respectively.

CALCULS AEROTHERMIQUES D'ECOULEMENTS DANS DES CAVITES INTERDISQUES DE TURBINES

D. Dutoya
ONERA, direction de l'Energétique
29, avenue de la Division Leclerc, BP 72
92322 CHATILLON sous BAGNEUX, FRANCE

Ph. Poncelin de Raucourt
Snecma, département Turbines et Aérothermique, YKLR1
Centre de Villaroche,
77550 MOISSY-CRAMAYEL, FRANCE

RESUME

Les températures de fonctionnement des turbomachines obligent les constructeurs à refroidir les parties du moteur situées en aval de la chambre de combustion et notamment les turbines.

La connaissance de l'écoulement d'air dans les circuits de ventilation est indispensable pour optimiser le refroidissement des moteurs. Afin de déterminer précisément les phénomènes d'échanges de chaleur et les efforts aérodynamiques sur les parois de cavités de formes complexes, Snecma utilise le code MATHILDA développé à l'ONERA.

Le code MATHILDA résout les équations de Navier-Stokes tridimensionnelles, pour des écoulements de fluide compressible. Les équations sont traitées à l'aide d'une méthode volumes finis sur un maillage structuré. Le schéma de résolution est décentré d'ordre 2, Une méthode implicite de type ADI permet de stabiliser et accélérer le calcul.

Cet article présente les travaux de validation du code MATHILDA pour des applications aux écoulements dans des cavités interdisques. Les cas présentés ont été étudiés par la mise en oeuvre de la version bidimensionnelle axisymétrique.

Deux types de cavités expérimentales ont servi aux validations, des cavités Rotor/Stator et des cavités Rotor/Rotor. Les solutions obtenues, comparées aux mesures expérimentales, sont satisfaisantes, d'un point de vue aérodynamique et d'un point de vue thermique.

Le dernier calcul, sur une configuration réelle de cavité interne de moteur, permet d'appréhender les difficultés rencontrées dans la mise en oeuvre de ce type de modélisation, et de mesurer l'apport d'un code résolvant les équations de Navier-Stokes pour la description des écoulements de refroidissement.

INTRODUCTION

Les performances atteintes par les turboréacteurs actuels sont obtenues en partie grâce à une température de fonctionnement de la turbine très élevée. Ce très haut niveau de température des gaz qui circulent dans le moteur oblige les motoristes à refroidir les pièces en contact avec l'air chaud.

Pour assurer le refroidissement des éléments de turbines, de l'air froid est prélevé dans le compresseur et acheminé au travers de circuits de ventilation vers les disques et aubes de turbines. Les géométries de ces circuits sont généralement complexes, et induisent des écoulements où les effets physiques sont délicats à modéliser (fortes recirculations, gradients de températures importants, phénomènes de parois, échanges de chaleur et efforts aérodynamiques ...).

Pour concevoir les canaux et les cavités par lesquels passe l'air de refroidissement, et pour compléter les outils classiques de dimensionnement que sont les corrélations, Snecma utilise le code MATHILDA développé à l'ONERA/OE [1], et participe à sa validation. Le code MATHILDA est présenté dans une première partie.

La première phase d'industrialisation du code pour son application aux écoulements dans les cavités interdisques est la validation dans des configurations expérimentales.

Plusieurs installations fournissent les données qui serviront de base de comparaison pour les calculs. Ces bancs sont le banc CRETE [2], situé à l'ONERA, et qui simule l'écoulement dans une cavité Rotor/Stator, le banc BEATRICE [3] situé chez Snecma, qui représente l'écoulement dans une cavité Rotor/Rotor de type cavité entraînée. Pour compléter la validation, des données expérimentales issues de la bibliographie [4] sont utilisées.

Les comparaisons calcul/expérience portent généralement sur les coefficients d'échanges, les pressions, les coefficients de moment, l'appréciation qualitative de l'écoulement. Elles font l'objet de la deuxième partie de cet article.

Enfin un calcul sur une géométrie réelle de cavité est présenté dans une troisième partie. Cette application permet de se rendre compte de la complexité des géométries rencontrées, de la variété des phénomènes physiques qui se développent et de l'intérêt d'un calcul Navier-Stokes pour la prévision de ce genre d'écoulement.

1 PRESENTATION DU CODE MATHILDA

1.1 Généralités

Le code MATHILDA a été utilisé pour calculer divers types d'écoulements turbulents dans des cavités, subsoniques ou supersoniques, stationnaires ou non [5]. Aujourd'hui, la majorité des applications concerne l'étude des transferts de masse et d'énergie dans les circuits de ventilation et de refroidissement des turbomachines. La première étape du processus de validation a consisté à analyser la stabilité de l'algorithme, à mesurer la précision des résultats en fonction de la finesse du maillage, et à évaluer les performances des modèles physiques. Cette étude s'est faite sur des configurations simples [6-7-8]: canaux fixes ou en rotation, cavités annulaires entre disques parallèles.

1.2 Modèles physiques et schémas numériques

Le code MATHILDA permet d'intégrer les équations instationnaires de bilan de l'aérothermique (masses, impulsion, énergie, etc...) sur un maillage curviligne quelconque à deux ou à trois dimensions. Le vecteur vitesse, les gradients et les tenseurs sont mesurés dans un repère cartésien qui peut éventuellement être mobile.

Le fluide considéré est un mélange non réactif de gaz parfaits, dont les propriétés thermodynamiques peuvent varier linéairement avec la température. La modélisation des transferts turbulents repose sur l'hypothèse de Boussinesq. La viscosité tourbillonnaire est reliée à deux quantités caractéristiques de la turbulence: son énergie cinétique K, et une échelle de longueur L, qui représente la taille des gros tourbillons. Ces deux quantités peuvent être calculées en chaque point soit grâce à une hypothèse d'équilibre de type algébrique (modèle de longueur de mélange de Prandtl), soit par intégration d'une ou de deux équations de bilan (modèles K et K-L), [1].

En tridimensionnel, le réseau de calcul est un empilement d'hexaèdres adjacents deux à deux, dont la forme et l'agencement peuvent être quelconques: il se compose en général d'un ensemble de sous-domaines limités par six portions de surface sur lesquelles les maillages coïncident. Ce mode de structuration permet de prendre en compte des géométries assez complexes. Chaque élément de volume (ou cellule) est limité par six facettes (ou interfaces). Les paramètres géométriques nécessaires à l'algorithme d'intégration – volumes et vecteurs surface – sont calculés à partir des coordonnées des noeuds du maillage [1], de manière à garantir la conservativité du système.

Toute interface peut être a priori choisie comme un élément de paroi fixe ou tournante, sur laquelle on impose, en plus de la vitesse angulaire, un niveau de température ou un flux de chaleur. Sur les bords du domaine de calcul, les autres types de limites possibles sont: les entrées de fluide à conditions génératrices imposées ou celles à débit donné, les sorties à pression statique fixée en subsonique, les plans de symétrie, les surfaces de périodicité, etc.

Les équations de bilan sont discrétisées sur chaque cellule, suivant la technique des volumes finis. Les flux à travers les interfaces sont exprimés en fonction de l'état de l'écoulement au centre des cellules environnantes: de part et d'autre de chaque interface, deux états plus ou moins décentrés sont obtenus à l'aide d'interpolations paraboliques de type "MUSCL", qui sont corrigées par une procédure de "limitation des pentes"; la partie réversible des flux (Euler) est alors calculée à l'aide d'un schéma basé sur la décomposition de la matrice jacobienne suivant ses trois sous-espaces propres [9]; les frottements et les flux de diffusion sont calculés au centre des hexaèdres grâce à la formulation intégrale de Green [1], puis sont interpolés et projetés sur les interfaces. Lorsque le maillage au voisinage des parois est trop grossier pour capter les sous-couches visqueuses, un modèle algébrique d'échanges pariétaux, basé sur l'approximation de Couette, permet de faire le pont entre condition de non-glissement et calcul au point courant.

Le système d'équations différentielles ordinaires ainsi obtenu est intégré à l'aide d'un schéma implicite d'ordre un ou deux, qui permet dans une certaine mesure d'échapper à la limitation CFL du pas de temps. Le système d'équations obtenu après linéarisation est factorisé suivant les trois directions du maillage, et le travail consiste à résoudre successivement trois séries de systèmes tridiagonaux par blocs. Les systèmes linéaires correspondant à une direction donnée sont indépendants les uns des autres: ils sont classés suivant leur taille, puis traités par lots, ce qui permet une vectorisation efficace de l'ensemble de l'algorithme [10].

2 VALIDATIONS EXPERIMENTALES

2.1 Ecoulement dans une cavité Rotor/Stator

Montage expérimental

Le montage du banc CRETE est présenté sur la figure 1. Il se compose de deux disques parallèles dont l'un est mis en mouvement de rotation autour de leur axe commun.

La cavité est alimentée par le moyeu, l'air étant éjecté à la périphérie. Le rayon maximum est de 300 mm, l'entrefer de 30mm.

La vitesse de rotation est égale à 6000 tr/mn, ce qui correspond à un nombre de Reynolds de l'ordre de 10^6. Le débit d'alimentation est égal à 150 g/s, l'écoulement étant centrifuge.

Des mesures de pressions et de vitesses sont réalisées en deux positions radiales qui correspondent aux rayons réduits 0.41 et 0.78, sur toute la hauteur de l'entrefer.

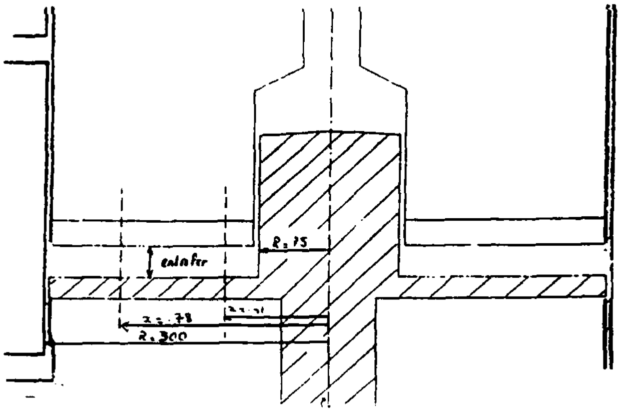

Figure 1 : Montage CRETE, cavité Rotor/Stator

Résultats numériques

Etant données la géométrie du dispositif expérimental, les conditions d'alimentation en air et la vitesse de rotation, l'écoulement est considéré comme axisymétrique. Le maillage dans un plan axial (figure 2) comporte 40 points dans la direction radiale et 37 points dans la direction axiale. Des resserrements près des parois assurent la présence des premières mailles dans la couche limite turbulente.

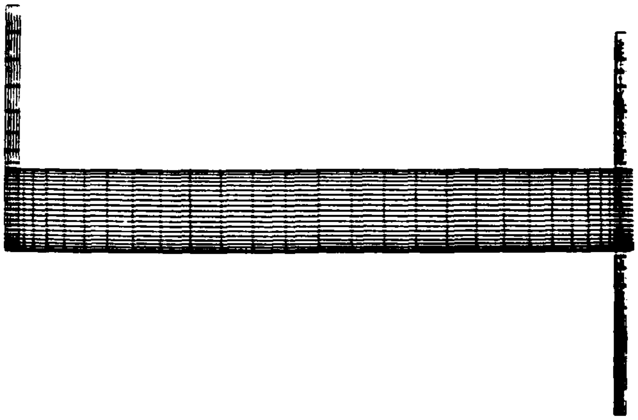

Figure 2 : Montage CRETE, maillage 37x40

La visualisation des vecteurs vitesse (figure 3) montre une recirculation importante dans la cavité qui s'étend jusqu'au rayon réduit r=0,5 et une autre située près de l'éjection qui est moins étendue. L'effet de la centrifugation le long du rotor est marqué par des vecteurs vitesse plus importants que pour le stator.

L'examen de l'évolution du coefficient d'entraînement en fonction de l'entrefer montre un bon accord avec les mesures pour le rayon r=0,78 (figure 4) et un résultat légèrement moins bon pour r=0,41 (figure 5). Cette différence s'explique par la localisation du rayon 0,41 dans une zone de recirculation, les calculs ayant été réalisés avec un modèle algébrique de longueur de mélange. L'influence de la recirculation se fait surtout sentir près du stator, alors que près du rotor l'effet d'accélération centrifuge guide l'écoulement et atténue l'effet de cette recirculation.

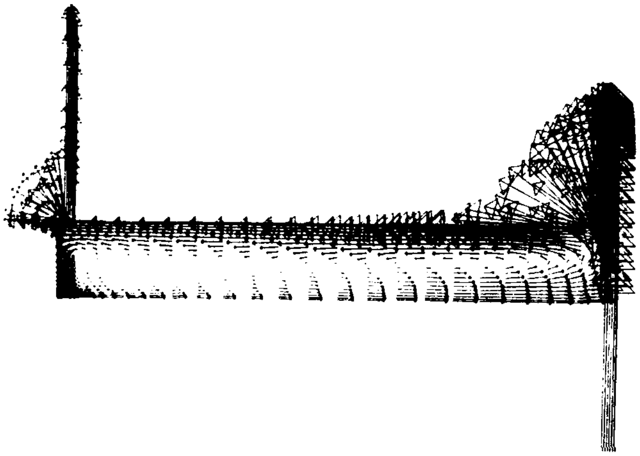

Figure 3 : Montage CRETE, vecteurs vitesse

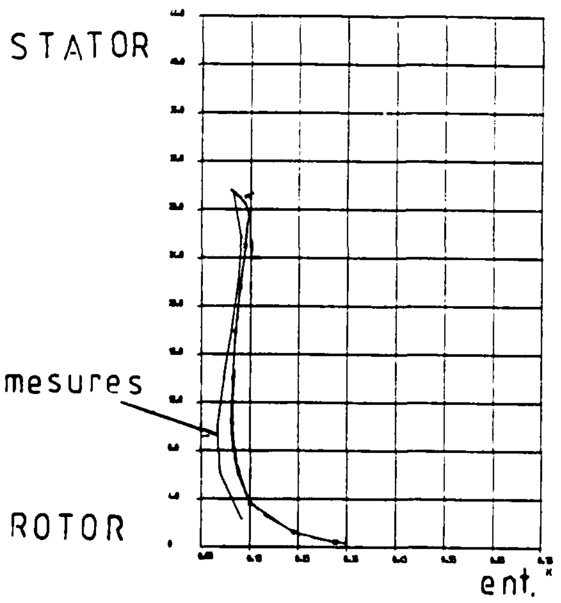

Figure 4 : Montage CRETE, coefficient d'entraînement, r= 0,78

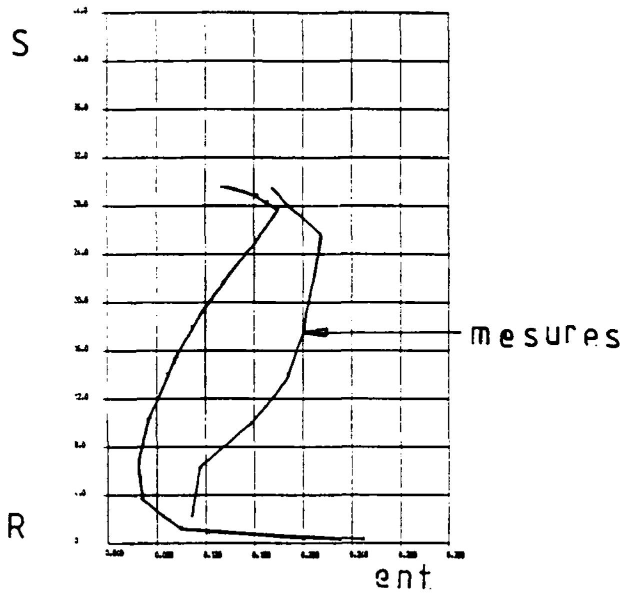

Figure 5 : Montage CRETE, coefficient d'entraînement, r=0,41

Sur ce cas ont été réalisés des tests d'initialisation du calcul. En effet la très grande diversité de géométries qui peuvent être traitées par MATHILDA a obligé d'implanter une phase de démarrage du calcul qui part du repos à l'instant initial. Une technique purement numérique consiste à initialiser le calcul turbulent par un calcul laminaire. La figure 6 montre l'intérêt de cette mise en oeuvre sur l'évolution du résidu pour l'équation de conservation de la masse. Les résidus décroissent d'un facteur 100 après 3000 itérations, dans le cas d'une initialisation turbulente avec un pas de temps égal à 30 CFL. Pour le même nombre d'itérations et le même pas de temps, l'initialisation laminaire permet une décroissance d'un facteur 10000.

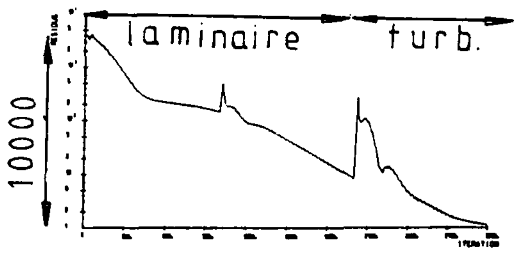

initialisation laminaire

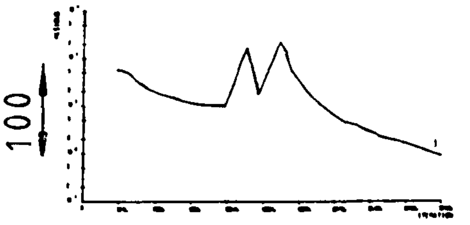

initialisation turbulente

Figure 6 : Montage CRETE
Influence de l'initialisation sur la convergence du calcul

2.2 Ecoulement dans une cavité entraînée

Montage expérimental

Le montage BEATRICE (figure 7) permet d'étudier les phénomènes de convection dans les cavités Rotor/Rotor. Il représente une cavité formée de deux disques chauffés en rotation, alimentée en air par le moyeu.

Le disque aval est instrumenté en thermocouples pour permettre les mesures de coefficients d'échanges.

Pour le cas étudié les conditions d'écoulements sont les suivantes :

- vitesse de rotation : 5317 tr/mn
- débit : 2,60 kg/s
- pression totale d'alimentation : 5,42 bars
- température totale d'alimentation : 71,66 °C

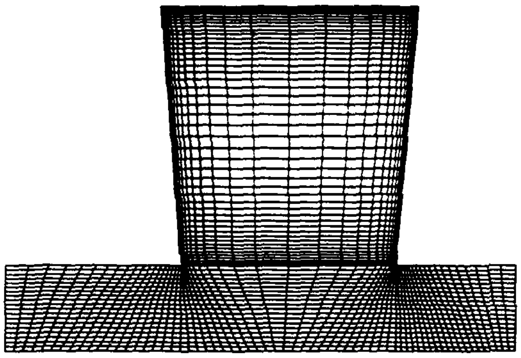

Figure 7 : Montage BEATRICE
Maillage 65 x 65 points

Résultats numériques

Le maillage utilisé pour les calculs comprend 65 points dans la direction radiale et 65 points dans la direction axiale. Le maillage (figure 7) est resserré près des parois afin de respecter le domaine de validité des lois de paroi.

Les calculs ont été réalisés avec un modèle de turbulence de type longueur de mélange. En plus des conditions de température et de pression totales, de taux de turbulence et de longueur de mélange, la prérotation du fluide est imposée en entrée de cavité.

Le pas en temps adopté pour faire avancer la solution vers l'état stationnaire est égal à 40 CFL. A l'instant initial, le fluide a un mouvement de rotation uniforme dans toute la cavité, les couches limites dynamiques et thermiques ne sont pas initialisées.

Les flux de chaleur et frottements n'étant pas fixés après 10000 itérations, le calcul a été poursuivi jusqu'à l'itération 20000. Cela correspond à un temps CPU d'une heure sur le calculateur CRAY YMP de l'ONERA, soit 8 µs par point, par itération et par équation.

L'évolution des résidus (figure 8) montre la bonne convergence du code sur les cinq variables conservatives du calcul.

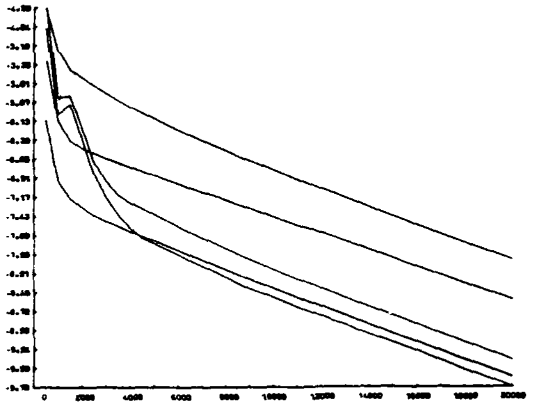

Figure 8 : Montage BEATRICE
Evolution des résidus en fonction des itérations

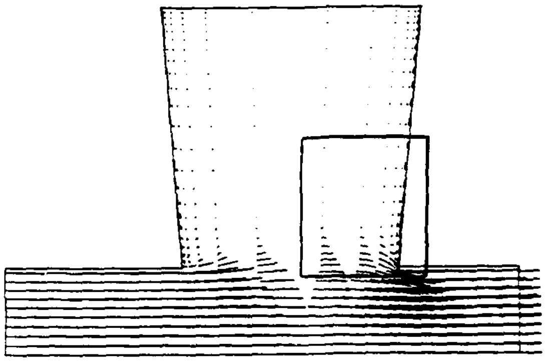

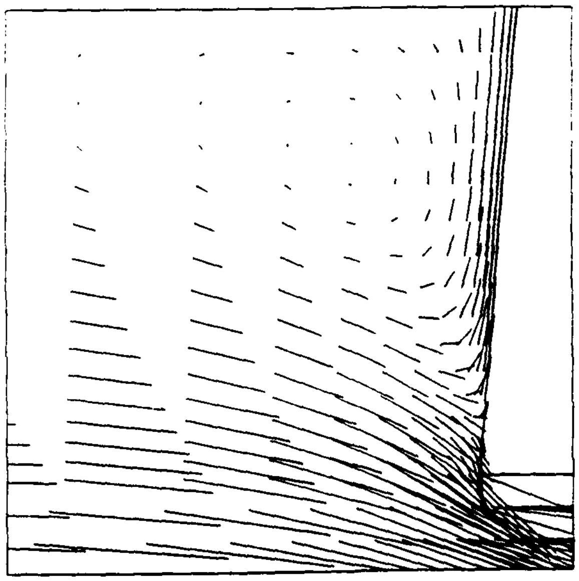

Figure 9 : Montage BEATRICE
Champ de vitesses

Entre les deux disques l'écoulement est essentiellement axisymétrique (effet d'entraînement). La figure 9 montre la faible pénétration du débit dans la cavité. On peut aussi noter la présence des effets centrifuges sur les couches limites qui se développent sur les parois verticales. Enfin une recirculation apparaît par effet d'entraînement par le fluide débitant du fluide résidant dans la cavité.

Le coefficient d'échange qui est mesuré (figure 10) correspond au rapport du flux de chaleur sur la différence de température entre la paroi et le fluide débitant (α = Qp / (Tp - Ttre) où Ttre est la température totale relative à l'entrée de la cavité). Les courbes 1 et 2 de la figure 10 montrent le coefficient d'échange calculé par MATHILDA après respectivement 10000 et 20000 itérations. La différence entre les deux calculs n'excède pas 10% de la valeur expérimentale et la différence entre les mesures et les calculs est toujours inférieure à 20% sauf pour le fond de la cavité.

Un test sur l'influence de la prérotation du fluide sur le calcul des coefficients d'échange sur le disque aval a été réalisé. La vitesse de rotation a été annulée. La courbe 3 de la figure 10 montre le résultat obtenu pour le calcul des coefficients d'échanges. Pour les rayons élevés (entre 0.2 m et 0.24 m) il y a une différence de l'ordre de 20% avec le calcul précédent. Plus près du moyeu la différence est moins importante, dans cette zone de l'écoulement la vitesse axiale est prépondérante et l'effet de la prérotation se fait moins sentir.

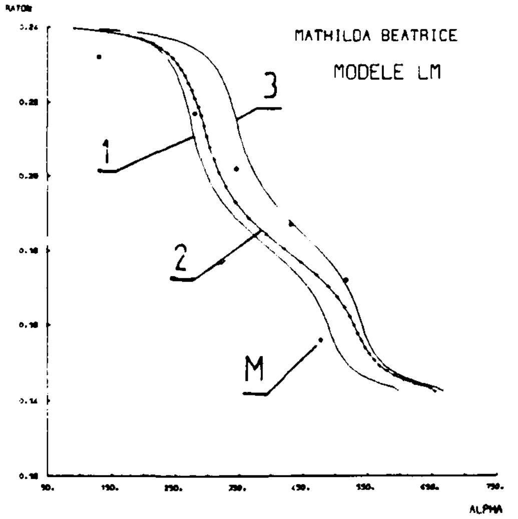

Figure 10 : Montage BEATRICE
Evolution du coefficient d'échange à la paroi en fonction du rayon

2.3 Ecoulement dans une cavité Rotor/Rotor

Montage expérimental

Les données expérimentales utilisées pour ce troisième exemple de validation sont fournies par les études d'Owen et Rogers [4] sur les systèmes en rotation.

La géométrie se compose de deux disques parallèles en rotation avec une alimentation axiale au moyeu et une sortie radiale en périphérie. La modélisation choisie est bidimensionnelle et axisymétrique; les trous d'éjection du fluide sont donc remplacés par une fente équivalente, c'est à dire respectant le débit total sortant de la cavité.

Le disque aval est instrumenté en thermocouples et l'on dispose de données expérimentales pour les coefficients d'échange sur la paroi.

Plusieurs régimes de rotation et plusieurs débits d'injection ont été étudiés par les auteurs. Nous présentons les résultats pour deux valeurs de débit D=0,1 kg/s et D=0,05 kg/s, et pour une valeur de la vitesse de rotation égale à Ω = 207 rd/s.

Résultats numériques

Le maillage utilisé pour les calculs est composé de 81 points dans la direction axiale et de 81 points dans la direction radiale (Figure 11). Les resserrements du maillage près des parois verticales permettent de placer les premiers points de maillage dans la zone logarithmique de la couche limite turbulente.

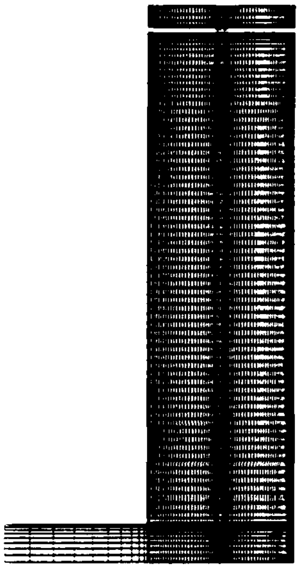

Figure 11 : Cavité Rotor/Rotor
Maillage 81 x 81 points

Pour cette configuration les calculs ont été réalisés avec le modèle K-L.

Les figures 12 et 13 montrent les vecteurs vitesses pour les conditions de débit D=0,1 kg/s et D=0,05 kg/s.
On peut observer, notamment pour le débit le plus élevé, la structure classique de l'écoulement dans une cavité Rotor/Rotor. En effet l'écoulement peut se décomposer en plusieurs zones, la région source ou zone de recirculation, située dans la partie inférieure de la cavité (moitié de la cavité pour D=0,1 kg/s et tiers de la cavité pour D=0,05 kg/s), le noyau ou zone d'écoulement purement tangentiel dans des conditions isothermes, situé dans la partie supérieure de la cavité, et enfin les couches d'Ekman qui se développent le long des parois.

La comparaison entre les tailles de recirculations calculées et celles mesurées montre un bon accord, la différence dans les deux cas étant de l'ordre de 5%.

Les mesures expérimentales permettent de valider le code sur les coefficients d'échange calculés sur le disque aval de la cavité. Les résultats montrent que la qualité des résultats dépend fortement de la nature de l'écoulement. En effet les résultats numériques et les mesures se recoupent bien pour la partie de paroi qui se trouve en face du noyau. En revanche ils sont moins précis pour la zone de paroi correspondant à la zone source, ce qui se voit sur la figure 14 pour D=0,1 kg/s et sur la figure 15 pour D=0,05 kg/s. Ce comportement s'explique par l'utilisation de lois de parois qui ont été calibrées pour des écoulements de couches limites et dont la validité pour les écoulements décollés n'est pas assurée.

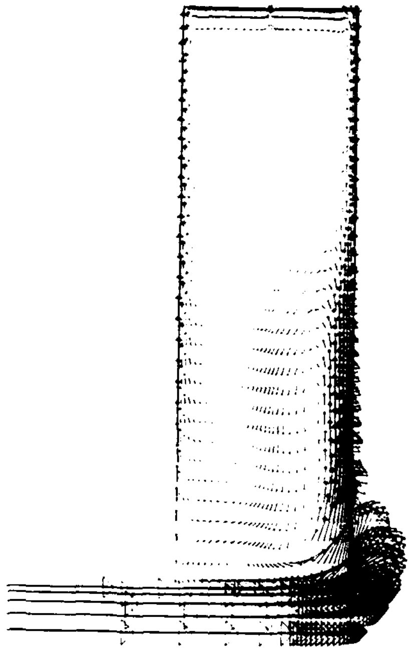

Figure 12 : Cavité Rotor/Rotor, D=0,1 kg/s, Ω=207 rd/s Vecteurs vitesses

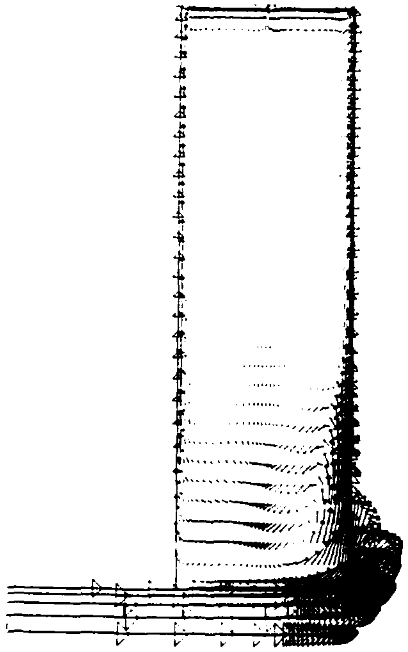

Figure 13 : Cavité Rotor/Rotor, D=0,05 kg/s, Ω=207 rd/s Vecteurs vitesses

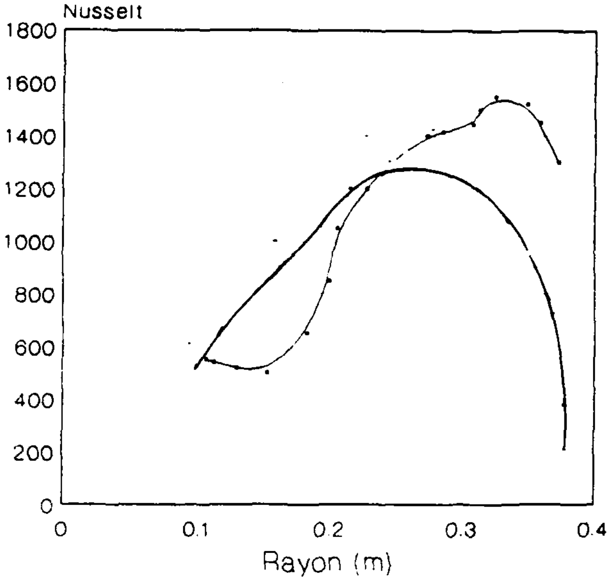

Figure 14 : Cavité Rotor/Rotor, D=0,1 kg/s, Ω=207 rd/s Coefficient d'échange sur la paroi aval

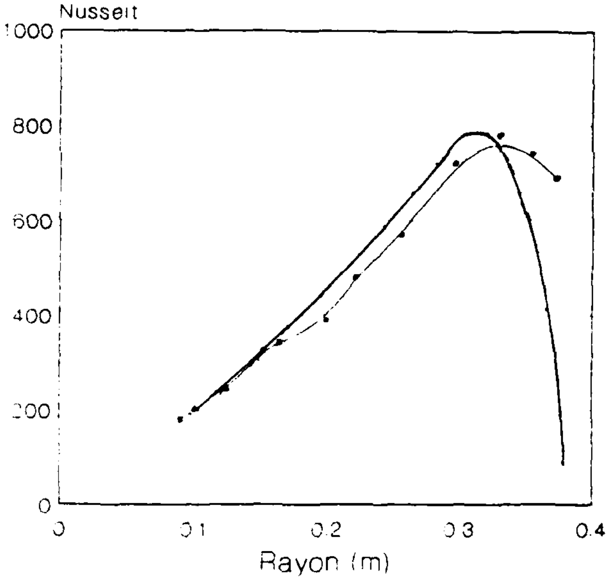

Figure 15 : Cavité Rotor/Rotor, D=0,05 kg/s, Ω=207 rd/s Coefficients d'échange sur la paroi aval

3 VALIDATION SUR UN CAS MOTEUR

Les trois exemples de validations présentées précédemment mettaient en oeuvre des géométries simples. De plus les conditions de fonctionnement de ces bancs expérimentaux ne sont pas toujours représentatifs des écoulements dans les moteurs. Ce dernier exemple de calcul dans une configuration Rotor/Stator que nous présentons est typique des applications du code MATHILDA pour le dimensionnement des moteurs d'avions.

La géométrie modélisée représente une cavité de prélèvement d'air froid sous compresseur. Il s'agit donc d'une cavité comprise entre un stator S (figure 16) et deux rotors R1 et R2. De l'air est prélevé dans la veine en amont et en aval du stator et évacué par un orifice de prélèvement P. La hauteur de veine complète n'est pas prise en compte, on ne modélise que 50% de celle-ci, l'effet du prélèvement sur l'écoulement dans la veine étant limité.

Les conditions de fonctionnement représentées sont :
- vitesse de rotation 10000 tr/mn
- pression statique dans la veine 20 bars
- pression statique au prélèvement 16 bars
- débit d'air dans la veine 150 kg/s
- température de paroi 750 – 800K
- température d'air 750K

Le maillage réalisé (figure 16) pour le calcul compte 155 points dans la direction radiale et 200 points dans la direction axiale.

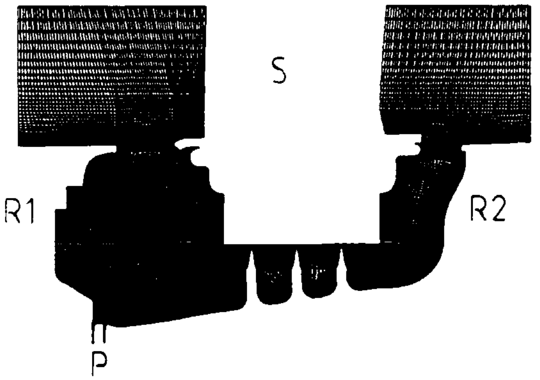

Figure 16 : Cavité Rotor/STATOR, cas moteur
Maillage 155 x 200 points

Les buts de cette validation sont de comparer les valeurs de débits calculés en différents points de la cavité avec les valeurs données par les méthodes de dimensionnement, et aussi d'étudier la structure de l'écoulement afin de prévoir les transferts de chaleur.

Les principales caractéristiques de cet écoulement sont l'équilibre des débits qui passent en amont et en aval du stator, la présence de recirculations et les échanges de chaleur relativement peu élevés.

Le champ des vitesses en amont du stator (figure 17a) montre la forte recirculation qui s'établit dans toute la cavité et qui conduit le fluide vers l'orifice de prélèvement. Il faut noter que cette recirculation en induit une autre plus faible, contrarotative, à la sortie du labyrinthe et qu'elle entraîne une partie de l'air provenant de ce labyrinthe vers le prélèvement. Dans cette zone l'entraînement du fluide par le rotor reste faible, la vitesse dans le plan méridien étant prépondérante par rapport à la vitesse tangentielle.

Dans la cavité en aval du stator (figure 17b) deux recirculations contrarotatives se développent, l'écoulement le long du rotor étant centripète pour celle se situant dans la partie supérieure de la cavité et centrifuge pour celle occupant la partie inférieure. Cela signifie que l'introduction de l'air de la veine dans la cavité se fait le long du rotor.

Dans le labyrinthe (figure 17c) on retrouve une certaine périodicité de l'écoulement dans les deux cavités. Là encore on note la présence de deux recirculations, le fluide étant entraîné près du stator par le débit qui passe de la cavité aval vers la cavité amont.

Toutes ces recirculations ont une influence sur la répartition de température dans l'ensemble de la cavité. Sur la figure 18 qui représente les lignes iso-température totale, l'augmentation de densité des lignes iso indique l'échauffement du fluide.

Dans la cavité en amont du stator le fluide au centre de la recirculation est à la même température que dans la veine. Le phénomène de réchauffement le long du rotor est propagé par le mouvement de recirculation.

Il faut noter l'importance du réchauffement de l'air au passage du labyrinthe et l'effet des recirculations contrarotatives.

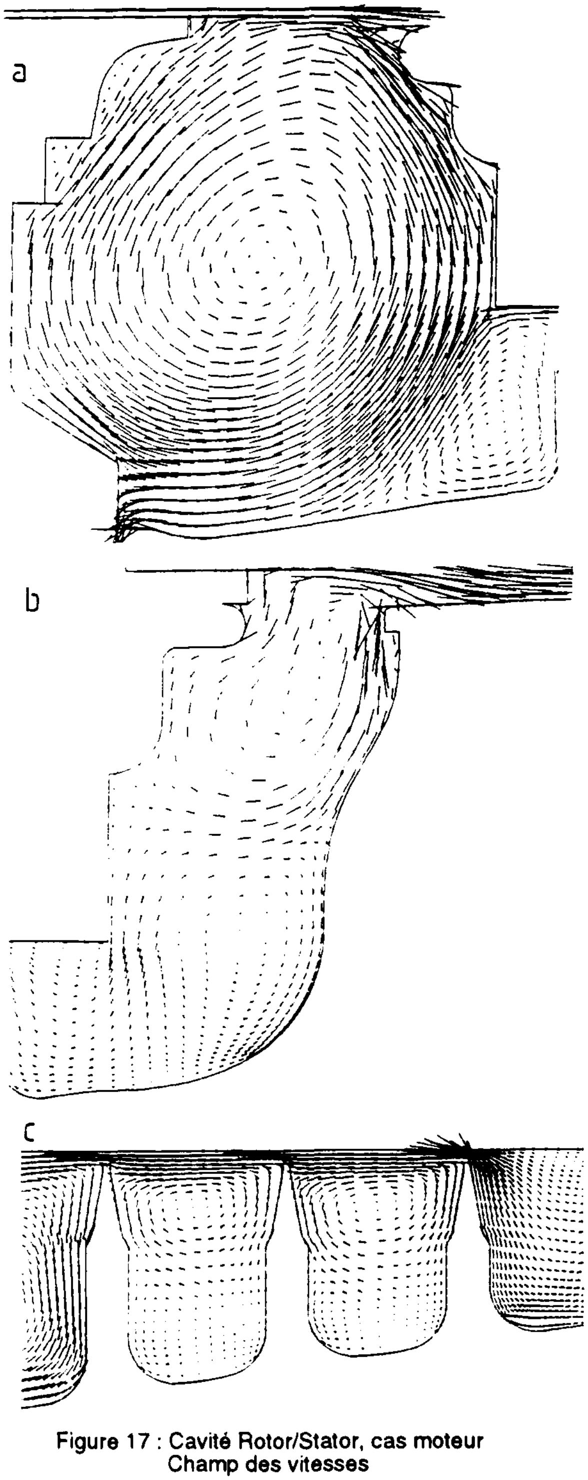

Figure 17 : Cavité Rotor/Stator, cas moteur
Champ des vitesses

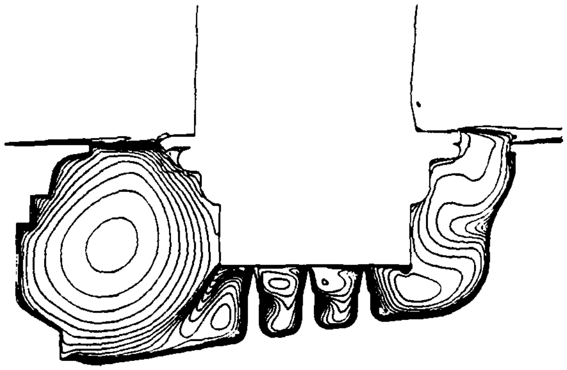

Figure 18 : Cavité Rotor/Stator, cas moteur
Lignes iso-température totale

CONCLUSION

Des calculs de validation aérothermique du code MATHILDA en configuration bidimensionnelle axisymétrique ont été réalisés pour des écoulements dans des cavités Rotor/Stator et Rotor/Rotor.

La comparaison des résultats de calculs et des mesures expérimentales a montré un accord satisfaisant d'un point de vue aérodynamique et d'un point de vue thermique.

La phase d'initialisation joue un rôle important sur la vitesse de convergence du calcul.

L'utilisation d'un code de calcul basé sur la résolution des équations de Navier-Stokes permet une analyse complète des phénomènes apparaissant dans les cavités complexes de turbomachines.

Néanmoins des développements restent nécessaires pour améliorer le temps de calcul, la validité des lois de parois dans le cas d'écoulements décollés, l'application du modèle K-L aux écoulements à bas nombre de Reynolds et la mise en oeuvre d'un calcul sur des géométries complexes.

Plusieurs évolutions sont actuellement testées (modèle K-L amélioré) ou développées (version multi-domaines du code) à l'ONERA.
D'autre part les travaux de validation se poursuivent chez Snecma sur des configurations expérimentales et sur des applications réelles aux cavités de refroidissement des moteurs.

REMERCIEMENTS

Nous tenons à remercier Madame Noiret et Monsieur Coulon qui ont réalisé, chez Snecma, certains des calculs présentés dans cet article.

REFERENCES

[1] D. DUTOYA, M. ERRERA, "Le code MATHILDA: modèles physiques, réseau de calcul et méthode numérique", ONERA - RT n° 42/3473 EN (1991).

[2] P.J. MICHARD, "Réalisation du banc CRETE, description du montage", Rapport ONERA RT 34/3473 EY.

[3] E. BOTREL, I. LAPIDUS, A.E. BOURGUIGNON, "Projet de spécification de la machine de convection dans les rotors", Note YKLT n°1678/88 Snecma-Villaroche.

[4] J.M. OWEN, R.H. ROGERS, "Flow and heat transfer in rotating disc systems", Research Studies Press LTD Tauntour, Somerset, UK.

[5] M. ERRERA, D. DUTOYA, "MATHILDA, un code multidimensionnel d'aérothermique", Entropie, n° 62, (1991).

[6] D. DUTOYA, ONERA RT n° 43/3473 EY (1991).

[7] D. DUTOYA, M. ERRERA, J.P. MICHARD, A. RISTORI, "Présentation d'un code de calcul d'écoulements compressibles 3-D dans des canaux et des cavités de forme complexe", Symposium PEP/AGARD, San Antonio (USA), 27-31 mai 1991.

[8] D. DUTOYA, Ph. PONCELIN de RAUCOURT, "A 3D compressible Navier-Stokes code for a Boundary Layer in a S-shaped Channel Calculation", ERCOFTAC Workshop on Numerical Simulation of Unsteady Flows, Transition to Turbulence and Combustion, Lausanne, 26-28 mars 1990.

[9] D. DUTOYA, M. ERRERA, "Une décomposition formelle du jacobien des équations d'Euler. Application à des schémas numériques décentrés", La Recherche Aérospatiale, n° 1992-1 (janvier-février 1992).

[10] P. VAQUEZ, P. ERRERA, D. DUTOYA, "Vectorisation d'un solveur Navier-Stokes implicite", La Recherche Aérospatiale, n° 1991-1 (janvier-février 1991).

Discussion

QUESTION 1:

DISCUSSOR: J.W. Chew, Rolls Royce

I was very interested in your results, particularly those for the rotor-rotor example with axial throughflow. Are the experimental data that you compare with generally available?

AUTHOR'S REPLY:

Yes, this data will be published. We will compile all the results in a publication shortly.

QUESTION 2:

DISCUSSOR: M. Owen, University of Bath

The flow in a rotating cavity with an axial throughflow is often nonaxisymmetric. Have you computed the three-dimensional flow for the case? If so, have you found cases where the flow is nonaxisymmetric?

AUTHOR'S REPLY:

We have purposely tried to choose our configurations for their nearly axisymmetric behavior because we are interested in the entrainment effect. We have, however, started three-dimensional calculations with the aim of showing that the axisymmetric calculations can be used for industrial applications even if they are not perfect. We don't think that the flow is purely axisymmetrical, but we do think that the assumption is sufficient for our purpose at this time. We know that when you're injecting a flow in a cavity behind a blading you have a heterogeneity in the pressures in the tangent direction and that this will have a three-dimensional effect on the flow in the cavity. The three-dimensional calculations will determine the error in our present method of treating the problem.

STUDY OF FLOW STRUCTURE IN ROTATING CAVITIES: NUMERICAL PREDICTIONS OF LAMINAR AND TURBULENT, STEADY AND UNSTEADY FLOWS.

P. Maubert, R. Schiestel, L. Elena, A. Randriamampianina, A.M. Chaouche,
E. Crespo del Arco & P. Bontoux
Institut de Mécanique des Fluides, IM2, Unité Mixte 34 CNRS
1, rue Honnorat. F-13003 Marseille, France.

SUMMARY

The flow regimes in rotating cavities (modelling co-rotating disks or rotor-stator systems), with or without throughflow, are studied by numerical approach using different techniques: spectral and finite volume methods. Comparisons between these techniques have been carried out for a typical test case. The solutions have been also compared satisfactorily to asymptotical approximations and to experimental results. The computations with spectral methods have been carried out until the onset of unsteady instabilities and transition to turbulence. The turbulent regimes have been treated with finite volume method based on modelling derived from k-ε or algebraic model of second order.

LIST OF SYMBOLS

a	Inner radius of the cavity
b	Outer radius of the cavity
c	Axial clearance of the exit
C_w	Mass flow rate (=$Q/\nu b$)
D_t	Particle derivative
Fr	Froude number (=$\Omega^2\Delta R/g$)
g	Gravity acceleration
G	Gap ratio (=s/b)
h	Half of axial width of the cavity
L	Aspect ratio (=$\Delta R/2h$)
p	Mean pressure
p'	Fluctuating pressure
Pr	Prandtl number (=ν/χ)
Q	Volumetric flow rate
r	Radius
R	Normalized radius (=r/s)
Ra	Rayleigh number (=$g\beta\Delta T\Delta R^3 Pr/\nu^2$)
R_{ij}	Reynolds stress tensor $\left(=\overline{u'_i u'_j}\right)$
R_m	Curvature parameter (=$(a+b)/\Delta R$)
Re	Reynolds number (=$2\Omega\Delta R^2/\nu$)
Re_T	Geostrophic Reynolds number (=$\delta V_g/\nu$)
Re_Ω	Rotational Reynolds number (=$\Omega b^2/\nu$)
Ro	Turbulent Rossby number (=$\varepsilon/k\Omega$)
Roth	Thermal Rossby number (=$\beta\Delta T$)
s	Axial width of the cavity (=2h)
T	Mean temperature
T_a	Temperature at r=a
T_b	Temperature at r=b
T_0	Reference temperature (=$(T_b+T_a)/2$)
t'	Fluctuating temperature
U_i	Mean velocity
u'_i	Fluctuating velocity
U_{IN}	Axial mean velocity at inlet (at z=0)
V	Normalized radial velocity (=$U_r/\Omega r$)
V_g	Geostrophic velocity
V_{IN}	Radial mean velocity at inlet (at r=a)
W	Normalized circumferential velocity (=$U_\theta/\Omega r$)
z	Axial coordinate
Z	Normalized axial coordinate (=z/s)
β	Thermal expansion coefficient
χ	Thermal diffusivity
δ	Ekman layer thickness
δ_{ij}	Unit tensor
ΔE	Source thickness
ΔK	Sink thickness
ΔR	Radial width of the cavity (=b-a)
ΔT	Temperature difference (=T_b-T_a)
ε	Dissipation rate of turbulent kinetic energy
$\tilde{\varepsilon}$	Isotropic part of dissipation rate
ε_{ipq}	Alternate tensor
ε_r	Geostrophic Rossby number (=$V_g/\Omega r$)
λ_{lam}	Laminar flow parameter (=$2.828\, C_w Re^{-1/2}(R_m+1)^{-1/2}$)
ν	Kinematic viscosity
ρ	Density
θ	Circumferential coordinate
ω_p	Rotation vector (=$(\Omega,0,0)$)
Ω	Angular speed
Ψ	Streamfunction
ζ	Vorticity

1. INTRODUCTION

The knowledge of the flow structure and heat transfer inside rotating disk systems is of crucial importance for high speed gas turbine design. Improving the performances of the gas turbines at very high temperatures is a difficult task that has led the designers to focus their interest on the fluid cooling system. In order to perform high levels for developed power and to improve the thermal efficiency in turbomachinery, the main flow is heated up to 1800°K at the exit of the combustion chamber. This fact leads to heat transfers from the hot fluid that produce temperature increases in the vital components of the motor, such as turbine blades and disks. In spite of important progress in the field of materials resistance, the blades and the disks of the turbines cannot bear such thermal gradients. These will result in a dilatation of the various components that should be overcome by loosing distances between solid structures, and then a decrease of efficiency.

In order to remedy to this problem, the components of the motor must be irrigated by using the flow of "cool" air drawn from the stages of the high pressure compressor. The objective is thus to get a precise description of the type of flow structures and of the distribution of temperatures in the circulation of cooling fluid between disks. Optimizing the machine efficiency results from favorable geometry and flow circulation but also from preserving the main flow from perturbations due to an introduction of cooling air.

In the case of cavities subjected to block rotation, the essential objective is to know how the cooling air can be renewed by the cooling flow rate. For the rotor-stator systems, in addition to the renewing process, it appears the problem of the injection of cooling air in the main flow and the possible reverse flow of hot air inside the cavity.

Previous studies

Many experimental, numerical and theoretical studies have been devoted to the flow between rotating coaxial disks. The basic model corresponding to the flow over a free disk has been studied for the first time by Von Karman [1] using an integral method. Numerous experimental studies have been carried out by Owen and co-workers (ref. [3] to [12]). A general survey of the typical flow structures is given in ref. [2].

We shall consider two main cases: the rotating cavity with a radial throughflow and the flow between a rotating disk and a stationary casing. In the first case, the structure of the flow is typical of a source sink flow in which four regions can be distinguished: the source region at the inlet, the sink region at the outlet, the Ekman layers along the lateral walls and a central core of geostrophic flow. The thickness of the Ekman layers is controlled by the rotation speed and the extent of the source region is mainly governed by the coolant flow rate C_W. Owen and Pincombe have made theoretical studies relying on Hide's solutions [13]. They have made also visualizations and laser doppler measurements [11] in the rotating cavity with axial inlet and radial outlet through a cylindrical perforated shroud and found spatially periodic instabilities associated with laminar-turbulent transition at large flow rates. The associated heat transfer problem has been studied by Owen and Bilimoria [9], Owen and Onur [10] and also Northrop and Owen [6,7]. Theses authors have identified several forced convection regimes and they have given correlations for the Nusselt numbers on the upstream wall.

One of the first experimental studies of the fluid mechanics associated with the rotation of a smooth disk enclosed in a cylindrical chamber was that of Daily and Nece [14]. The authors have distinguished four regimes: merged laminar boundardy layers, separate laminar boundary layers, merged turbulent boundary layers, separate turbulent boundary layers. In each case moment coefficients were measured. Daily *et al.* [15] also studied enclosed disk systems using a similar test rig and gave more detailed measurements including mean velocity profiles. More recently, a very detailed experimental investigation on enclosed rotating disks has been undertaken by Itoh *et al.* [16]. The authors have made measurements of the mean velocity distributions and all the six components of the Reynolds stress tensor. Velocity distributions in the boundary layers are shown to be similar at constant local Reynolds numbers.

Numerical approach has been developed by Chew [17] for laminar flow [18]. Koosinlin, Launder and Sharma [19] considered the turbulent case using a mixing length model taking into account the rotation effects through a rotation Richardson number in the spirit of Bradshaw approach [20]. Sharma [21,22] applied the low Reynolds number k-ε model to the flow on a free disk. The k-ε model was also used by Chew [23] to predict turbulent flow in a rotating cavity with radial flux using wall functions approximation near the solid boundaries. However, for several reasons (wall treatment, convergence of iterative process) the model failed to predict the essential characteristics of the flow and the author points out the need of a more refined insight. Chew used afterwise [24] the mixing length approach and found good agreement with experimental data. The rotating cavity with radial flux has been studied by Morse [25] with a modified low Reynolds number k-ε model which allows a far more realistic description of the Ekman layer region using a refined mesh near the wall. More recently, Iacovides and Theofanopoulos [26,27] used second order modelling developed in Launder's group to predict various rotating disk configurations including: corotating disks with radial inlet or outlet, enclosed disks with and without throughflow, corotating disks in an enclosure. In the fully turbulent core the authors use the k-ε model or an algebraic stress model while in the near wall region a mixing length with Van Driest type correction is used.

Considering the complexity of the flows under consideration including effect of rapid rotation on turbulence, confinement and wall effects on turbulence with Ekman layers development, interaction with heat transfer, a general predictive method is still not available. Advanced turbulence models have to be tested in simple geometries which are representative of the physical interactions involved and for which experimental data are available for comparisons.

2. GEOMETRIES

The flow between corotating compressor or turbine disks and that between a turbine disk and an adjacent stationary casing can be respectively modelled by a rotating cavity and by a rotor-stator system. The basic geometries, studied in this paper, are illustrated in Figure 1. This comprises a rectangular section of an annular domain of height s(=2h) in the axial, z-direction and from r=a to r=b in the radial, r-direction.

The different configurations correspond to:

- differentially heated cavities (RCT);
- rotating cavities submitted to a source-sink throughflow with radial outflow and radial (RCR) or axial (RCA) inflow;
- differentially rotating (rotor-stator) cavities (RS1 and RS2).

To examine the influence of thermal gradients on systems with uniform rotation (Problem RCT), the two vertical cylinders are held at constant temperatures, T_a and T_b, and the gravity vector is oriented antiparallel to the vertical axis of rotation. For Problems RCR and RCA, involving a superposed throughflow, the sections corresponding to the source and sink of fluid rotate at the same angular velocity as the endwalls. For differential rotation (Problems RS1 and RS2), one endwall (the stator) is stationary while the other endwall (the rotor) and the outer cylinder (shroud attached to the rotor) rotate at the same rate. The inner cylinder of the configuration is either held at the same rotation rate Ω (RS1) or stationary (RS2).

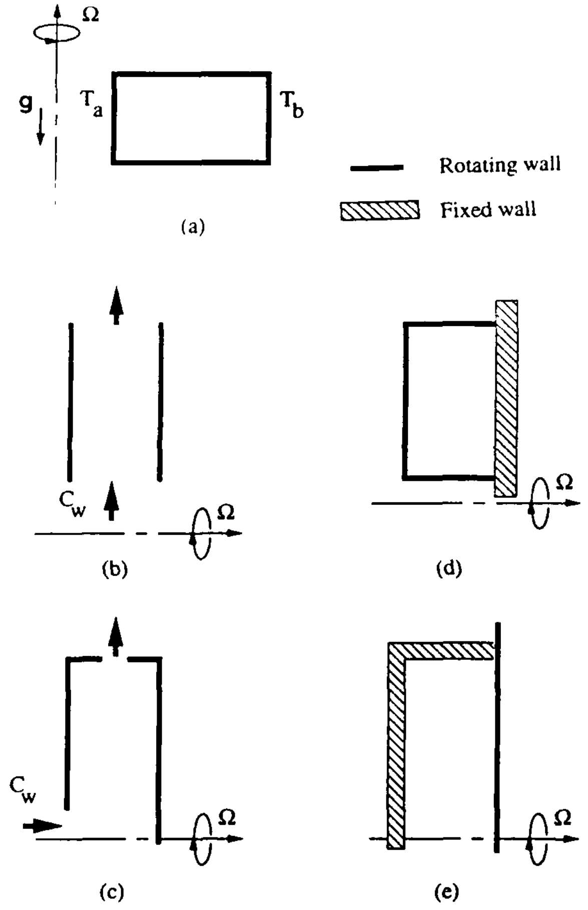

Figure 1. Geometries: Differentially heated cavity (RCT) (a); Rotating cavity with radial (RCR) (b) or axial (RCA) (c) inflow; Differentially rotating cavities (RS1, RS2) (d, e).

3. GOVERNING EQUATIONS

The general governing equations are written for a newtonian fluid with the Boussinesq approximation. The density is taken to be constant except in the effective body force terms (buoyancy, Coriolis and centrifugal) as suggested by Homsy and Hudson [28], De Vahl Davis *et al.* [29] and Randriamampianina *et al.* [30]. That is:

$$\rho = \rho_0\left\{1-\beta(T-T_0)\right\} \qquad (1)$$

where ρ_0 and $T_0(=(T_b+T_a)/2)$, are the reference density and temperature, and β is the thermal expansion coefficient.

The Navier-Stokes and energy equations are considered in the time dependent form and axisymmetry is assumed. Different scalings for the velocity are used depending on the mechanism studied [31]. The geometry is defined by the aspect ratio $L=\Delta R/2h$ and the curvature parameter $R_m=(a+b)/\Delta R$. The physical parameters are characterized by the following dimensionless groups:

- the Prandtl number, $Pr=\nu/\chi$,
- the Reynolds number, $Re=2\Omega\Delta R^2/\nu$,
- the Froude number, $Fr=\Omega^2\Delta R/g$,
- the Rayleigh number, $Ra=\beta\Delta T g\Delta R^3 Pr/\nu^2$,
- the mass flow rate, $C_w=Q/\nu b$.

For the RCR configuration, the forced flow at the source is parallel and modelled by a given radial velocity profile; the flow is also assumed to rotate with the same angular velocity as the cavity walls. At the sink, a Dirichlet type condition is used for the velocity components.

4. ASYMPTOTIC SOLUTIONS

Analytical solutions cannot be obtained for the entire flow field of all the problems considered, so the theoretical models are based on asymptotic boundary layer solutions (Stewartson [32], Robinson [33], Hunter [34], Hide [13], Homsy and Hudson[28]).

4.1. Problem RCT - Rotation and Buoyancy Driven Convection

For the range of parameter values considered, the flow is governed by the competition between buoyancy, Coriolis and centrifugal forces which successively dominate as the rotation rate is increased. For small Froude numbers (Fr<<1) the centrifugal force is negligible and associated boundary layer regimes have been investigated theoretically by Robinson [33] and by Hunter [34] for R_m>>1. These flows can be decomposed into three distinct zones: the core, the Ekman and the Stewartson layers. Asymptotic solutions for the radial and azimuthal velocities have been determined for the Ekman layers. These layers develop along the radial walls when Re>>1 and Roth/Fr<<1, (with $Roth=\beta\Delta T$). The solutions are expressed as follows (see Randriamampianina *et al* [30]):

$$u_A = V_{Aref}\left[e^{\zeta_1}\sin\zeta_1 + e^{-\zeta_2}\sin\zeta_2\right] \qquad (2)$$

$$v_A = V_{Aref}\sqrt{L}\left[1-e^{\zeta_1}\cos\zeta_1 + e^{-\zeta_2}\cos\zeta_2\right] \qquad (3)$$

where:

$$V_{Aref} = \frac{Ra}{4L^{5/2}Re},\ \zeta_1 = A(z-1),\ \zeta_2 = A(z+1),\ \text{and}$$

$$A = \frac{Re^{1/2}}{2\sqrt{2L}} \qquad (4)$$

The maximum values of velocity are:

$$u_{A\max} = \frac{e^{-\pi/4}Ra}{4\sqrt{2}L^{5/2}Re}, \tag{5}$$

and when $Re \longrightarrow \infty, v_{A\max} \longrightarrow \frac{Ra}{4L^2 Re}$ (6)

4.2. Problem RCR - Rotation with superposed radial flow

These flows can be decomposed into four zones: core, Ekman layers, source and sink regions. Entering fluid is entrained into boundary layers in the source region. The flow is then distributed into the two non-entraining Ekman layers, separated by an inviscid core. Fluid leaves at the outer radius via a sink region. For high rotation rates, Re>>1, the Coriolis force dominates at some distance from the inlet section, where the non linear terms are negligible. The asymptotic solution for this case applies to the Ekman boundary layer with the velocity expressed as follows:

$$u_B = V_{Bref}(r)\left[e^{\zeta_1}\sin\zeta_1 + e^{-\zeta_2}\sin\zeta_2\right] \tag{7}$$

$$v_B = V_{Bref}(r)\left[-1 + e^{\zeta_1}\cos\zeta_1 + e^{-\zeta_2}\cos\zeta_2\right] \tag{8}$$

where $$V_{Bref}(r) = \frac{C_w Re^{1/2}(R_m + 1)}{4\sqrt{2}\pi L(R_m + r)} \tag{9}$$

with ζ_1, ζ_2 and A defined as in the former section by relation (4).

These relations (7)-(8) are valid when the respective thicknesses of the source and the sink regions, Δ_E and Δ_K, are very large compared to the Ekman layer thickness. Δ_E and Δ_K are approximated by Hide[13] as:

$$\frac{\Delta_E}{\Delta R} = \alpha_{EK}\left[\left(1 + \frac{1}{4}X_a^{1/2}\right)^{1/2} + \frac{1}{2}X_a\right] \tag{10}$$

$$\frac{\Delta_K}{\Delta R} = \alpha_{EK}\left[\left(1 + \frac{1}{4}X_b^{1/2}\right)^{1/2} - \frac{1}{2}X_b\right] \tag{11}$$

where $\alpha_{EK} = \frac{3}{L^{1/2}(2Re)^{1/4}}$

and

$$X_b = \frac{L^{1/2}C_w}{6\pi(2Re)^{1/4}}, \; X_a = X_b\frac{(R_m + 1)}{(R_m - 1)} \tag{12}$$

These two last dimensionless parameters were introduced by Hide[13] to scale the influence of the non linear terms over the viscous ones, respectively at the sink (X_b) and the source (X_a) regions. Then, for the linear case, X_b and $X_a << 1$, $\Delta_E = \Delta_K$. For the non linear regime, X_b and $X_a >> 1$, the two thicknesses can be quite different: $\Delta_E > \Delta_K$.

4.3. Problem RS - Differential Rotation Driven Flow

Daily and Nece [14] empirically delimited the existence of four regimes. There are two laminar (I and II) and two turbulent (III and IV) regimes. Their appearance depends on the values of the gap ratio G and the Reynolds number Re. In a fixed reference frame, the asymptotic (laminar) solutions are given below.

- Regime I (laminar merged boundary layers) ([35]):

$$u_{C1} = -V_{Cref}(r)\frac{Re}{96L^2}\left[\frac{(z-1)^3}{4} + \frac{(1-9z)}{5}\right](z-1) \tag{13}$$

$$v_{C1} = -V_{Cref}(r)\frac{(z-1)}{2} \tag{14}$$

where $$V_{Cref}(r) = \frac{Re(R_m + r)}{8L} \tag{15}$$

- Regime II (laminar separate boundary layers):

$$u_{C2} = V_{Cref}(r)\left[\beta e^{\zeta_5}\sin\zeta_5 + (1-\beta)e^{-\zeta_6}\sin\zeta_6\right] \tag{16}$$

$$v_{C2} = V_{Cref}(r)[\beta(1 - e^{\zeta_5}\cos\zeta_5) + (1-\beta)e^{-\zeta_6}\cos\zeta_6] \tag{17}$$

where $\zeta_5 = -A\beta^{1/2}(z-1)$ and $\zeta_6 = A(z+1)$. Here β is solution of $1 - \beta - \beta^{1/2} = 0$, which arises from the mass conservation condition (see Owen and Rogers[36]).

5. MODELLING OF TURBULENT REGIMES

The geometries of flow under consideration are axisymmetrical with a rectangular section. The first one (Figure 1c) is a simplified representation of two corotating gas turbine disks where cooling air is fed through a central hole. Rotation produces a source-sink flow which has been studied experimentaly by Pincombe [37,38]. The second (Figure 1d) corresponds to the closed rotor-stator system like the one studied by Daily and Nece [14], while the geometry (Figure 1e) considered by Itoh et al. [16] is not limited axially.

The governing equations for the conservation of mass and momentum are deduced from the Navier-Stokes equations by statistical averaging. They are written in a rotating frame of reference with Boussinesq approximation applied to the centrifugal and Coriolis forces γ_j:

$$D_t U_i = -p_{,i} - R_{ij,j} + \nu U_{i,jj} + (1/2\Omega^2 r^2)_{,i} - 2\varepsilon_{ipq}\omega_p U_q + \beta\gamma_j F_{Ti,j}$$

$$U_{j,j} = 0 \tag{18}$$

We used two types of turbulence models: on the one hand a low-Reynolds number k-ε model and on the other hand a zonal approach with second order turbulence modelling in the core region.

The zonal approach had been used by C.R. Yap [39] to solve accurately the wall region by connecting a high Reynolds number ASM model applied far the wall to a mixing length model or a one-equation model applied in the wall adjacent region. In present calculation we use a low Reynolds number k-ε model in the region adjacent to the wall and an ASM high Reynolds number model in the central core.

The equations for energy and dissipation of turbulence in the framework of Boussinesq approximation read [32]:

$$D_t k = P + G - \varepsilon + D(k) + \nu k_{,jj} \qquad (19)$$

P	Turbulence production by mean flow
G	Extra production term due to density variations
ε	Viscous dissipation
$D(k)$	Turbulent diffusion.

$$D_t \tilde{\varepsilon} = \Sigma^+ - \Sigma^- + \Sigma^s + \Sigma^T + D(\tilde{\varepsilon}) + \nu \tilde{\varepsilon}_{,jj} \qquad (20)$$

Σ^+, Σ^-	Source and sink terms
Σ^s	Additive source for low Reynolds numbers Re_T
Σ^T	Additive source due to density variations
$D(\varepsilon)$	Turbulent diffusion.

When k-ε closure is used, the Reynolds stresses are given by:

$$R_{ij} = \frac{2}{3} k \delta_{ij} - \nu_t (U_{i,j} + U_{j,i}) \qquad (21)$$

ASM modelling is constructed from the transport equations for the turbulent Reynolds stresses in a rotating frame of reference:

$$D_t R_{ij} = P_{ij} + G_{ij} + \Omega_{ij} + \Phi_{ij} + D_{ij}(R_{ij}) - \varepsilon_{ij} \qquad (22)$$

P_{ij}	strict production term
G_{ij}	production term due to density variations
Ω_{ij}	extra production term corresponding to the explicit effect of rotation
Φ_{ij}	pressure-strain correlation
$D_{ij}(R_{ij})$	turbulent diffusion
ε_{ij}	viscous dissipation.

Main closure hypotheses rely on the standard LRR model [37]. Algebraic modelling is usually achieved using Rodi's hypothesis. We propose here a modified Rodi's hypothesis based on objective tensors [53]:

$$D_t R_{ij} - \frac{1}{2} \Omega_{ij} - D_{ij}(R_{ij}) = \frac{R_{ij}}{k} \big(D_t(k) - D(k) \big) \qquad (23)$$

The algebraic model is directly derived from (23). Temperature gradients interact with the turbulent flow when density changes occur. Only a first approach will be considered here, limited to relatively small temperature differences, using Boussinesq approximation. In the temperature equation :

$$D_t T = -F_{Tj,j} + \frac{\nu}{Pr} T_{,jj} \qquad (24)$$

the turbulent flux F_{Tj} is approximated by a gradient hypothesis. In the algebraic stress modelling framework, a tensorial diffusivity is used. The present approach utilizes a crude approximation based on a direct extension of Boussinesq hypothesis, supposed to act on the Coriolis forces terms.

6. NUMERICAL APPROXIMATION

6.1 Navier-Stokes solution

The Navier-Stokes and energy equations are expressed in a vorticity-streamfunction formulation and solved by spectral methods based on Chebyshev expansion. The tau-method was previously used to study the competition between buoyancy and rotation forces in a confined cavity (Randriamampianina *et al* [30]). Associated to the collocation method, a combined Adams-Bashforth/ second order backward Euler scheme proposed by Vanel *et al.* [40] and Ehrenstein and Peyret [41] was chosen for its good stability properties. At each time step the problem is reduced to the resolution of two Helmholtz equations, and a Stokes problem comprising equations for the vorticity and streamfunction. The solution is achieved by using the matrix diagonalization technique proposed by Haidvogel and Zang [42], extended to the collocation method for an axisymmetric configuration (Chaouche *et al.* [43]).

6.2 Turbulence equation solution

The system of partial differential equations is solved by finite volume method, using an outgrowth of the TEAM code (UMIST, Manchester). Steady convection-diffusion equations are written in the generic form:

$$\left(\rho U_i \Phi - \frac{\nu_t}{Pr_\Phi} \Phi_{,i} \right)_{,i} - S_\Phi = 0 \qquad (25)$$

They are then integrated over a control-volume surrounding each interior node of the mesh. These give raise to an algebraic system involving five points relations:

$$A_P \Phi_P = \sum_{j=N,S,W,E} A_j \Phi_j + B_P \qquad (26)$$

The code uses the standard shifted MAC type grids for the treatment of velocity-pressure linkage. The pressure field is calculated using the SIMPLER algorithm that proved to be more robust in the case of strong rotation rates. Convection-diffusion terms are discretized using a power law scheme [44]. The discretized equations are treated successively, the coupling between equations being solved iteratively. The linear systems are solved by a line by line and raw by raw application of Thomas algorithm. At each iteration step, the components of the full Reynolds stress tensor are obtained by solving a 6x6 linear system by direct method.

Moreover, strong rotation rates often lead to severe stability problems. They have been overcome by several stabilization techniques including a partial implicitation of Coriolis terms [53], stabilization practices introduced by Huang and Leschziner [45] for the numerical implementation of second order closures, solution of the 6x6 system for Reynolds stress components by direct method instead of the successive solution of normal and shear components proposed in ref [45] for non-rotating situations.

The grid is composed of at least 66x80 discretization points. The density of the mesh is increased near the wall region. The connection between ASM and k-ε models requires particular attention to insure consistency at the interfaces of control volumes. At intermediate control volumes the flux is calculated by k-ε model on the outer side and by ASM on the inner side. The changing of model is made at a distance of the wall approximately equal to 1/15 of the caviy width.

Of course, mesh tests have been made with various number of points and various distributions showing that the grids used give practically grid-independant results. Typically about 2000 iteration steps are necessary to reach steady state, corresponding to a CPU total time ranging from 1 to 2 hours approximately on CRAY2 computer.

The boundary conditions are of four types: inlet, symmetry line, wall and outlet. At the walls, the use of low Reynolds number k-ε model make the calculation free of any type of wall function treatment. All quantities are put to zero (k, ε, R_{ij}). At the axis of symmetry, gradients of scalars and normal stresses vanish while shear stresses go to zero. At inlet, profiles of all quantities are imposed. We introduced an initial turbulence level of $k/U^2=10^{-3}$. We found however that this precise value is of very weak influence on the main flow inside the cavity. At outflow, a free boundary is supposed:

$$\text{if } V_{r,exit}>0 \qquad dF/dr=0$$
$$\text{if } V_{r,exit}<0 \qquad F=F_{exit}$$

where F stands for any quantity except V_r which is calculated from continuity and pressure assumed to be constant.

7. RESULTS

7.1. Problem RCT: Rotation and buoyancy driven convection (see Figure 1.a)

The temperature difference (ΔT) and the temperature level (T_0) inside the cavity are taken to be constant, and the angular velocity Ω is varied up to $\Omega=250$ rad/sec (for $\Delta R=4$cm). The geometry is defined by the aspect ratio $L=1$ and the curvature parameter $R_m=2$, with the Prandtl and Rayleigh numbers set to $Pr=0.71$ and $Ra=3500$ respectively. Two values of the thermal Rossby number, Roth, are mainly considered, $Roth=2.x10^{-2}$ and $4.x10^{-4}$, for $Re/Fr^{1/2}$ fixed respectively at 500 and 3370, within a wide range of rotation rates: $4.x10^{-4} \leq Fr \leq 4.x10^4$ and $10<Re<10^5$.

Three major types of steady regimes have been observed: the buoyancy driven regime (BDR), the Coriolis force dominated regime (COR) and the centrifugal force dominated regime (CER). The BDR corresponds to the classical convective flow driven through buoyancy forces generated from density variations by an orthogonally-imposed temperature gradient and gravitational acceleration. The COR signifies the increasing influence of rotation, and for $Roth<0.2$ this results in the reduction of the basic thermal convection (originating from BDR). The effect of rotation at large Ω and/or large Roth ($Roth \geq 0.2$) is seen in the CER. This regime occurs when the centrifugal force dominates over the other, the resulting thermal convection is generated by the imposed thermal gradient and colinear centrifugal acceleration.

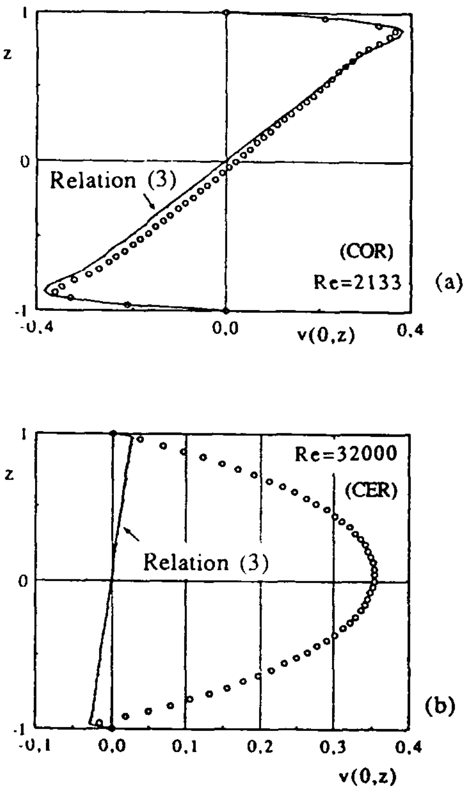

Figure 2. Problem RCT: Comparisons of the computed collocation solution with the asymptotical solution (equation (3), Hunter [34]). Azimuthal velocity profiles versus z at r=0 for Re=2133 (a); Re=32000 (b). COR (a) and CER (b) regimes for Roth=0.0004.

A comparison between the computed solutions obtained with the collocation method (at the mid-cavity along vertical axes) with the asymptotic solution given by relation (3) for two values of Re with $Roth=4.x10^{-4}$ is shown in Figures 2.a, b. In Figure 2.a, the computed azimuthal velocity profile is in good agreement with the asymptotic solutions for Re=2133. This corresponds to the COR. Since in the asymptotic solutions R_m is infinite, at the centre of the cavity the azimuthal velocity vanishes; this does not occur in the computed values of azimuthal velocity. At larger value of Re, Re=32000 (Figure 2.b), the computed azimuthal velocity profile progressively deviates from the asymptotic solution, and involves an azimuthal flow in the core with greater rotation than the side walls. This later configuration corresponds to the CER so it is not surprising that there are differences with the theoretical solution (3) which applies for the COR.

Discussion of the regimes

The variation of maximum radial and azimuthal velocities with Re are shown in Figures 3a and b, respectively. The differences noted above become apparent when comparing the Re-dependence of the computed velocities with those from the asymptotic solutions (5)-(6). The three regimes are characterized by the following features: in the BDR, the dimensionless (with respect to χ/h)

velocity remains independent of Re; in the COR the velocities are reduced following a 1/Re dependence; in the CER the flow structure is changed by the dominant centrifugal force and velocities increase as Re. The rate of increase actually depends on the value of Roth; for large values of Roth, the transition to CER occurs earlier. The phenomena arise due to the application of the Boussinesq approximation to the centrifugal force. This is evident upon inspection of the coefficient associated with the centrifugal force.

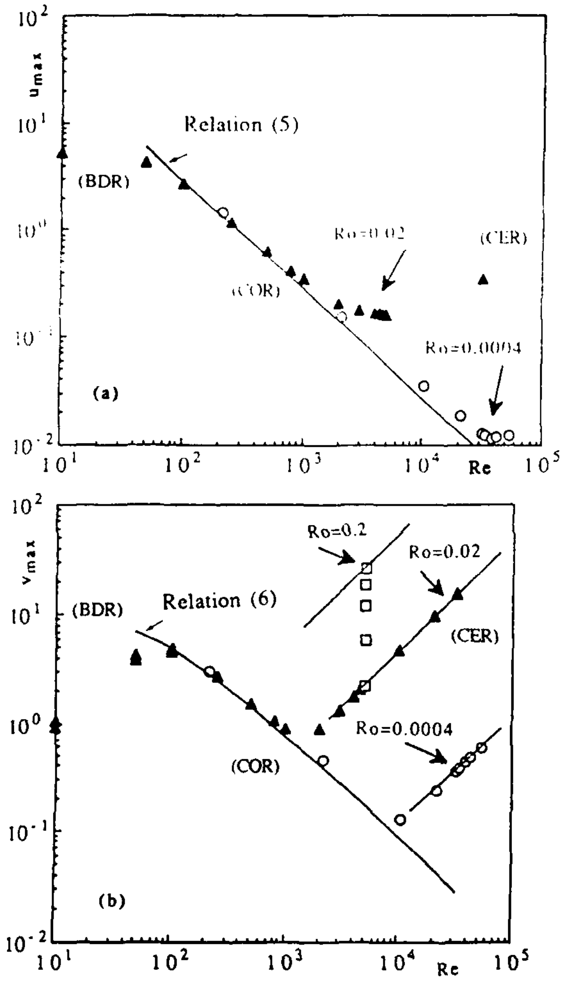

Figure 3. Problem RCT: Re-dependence of the extrema of radial (a) and azimuthal (b) velocities computed with both collocation and tau methods. Comparisons with asymptotical solutions (5) and (6) of Hunter [34]. BDR, COR and CER for Roth=0.0004 and 0.02; CER for 0.02≤Roth≤0.2.

7.2. Problem RCR: Rotation with superposed radial flow (see Figure 1.b)

The problem was previously investigated by several authors using theoretical, numerical and experimental approaches (Bennetts and Jackson [46], Hyun [47], Owen and Pincombe [11], Chew *et al.* [48]). In the work discussed here the computations were performed with L=2.267 and R_m=13.94.

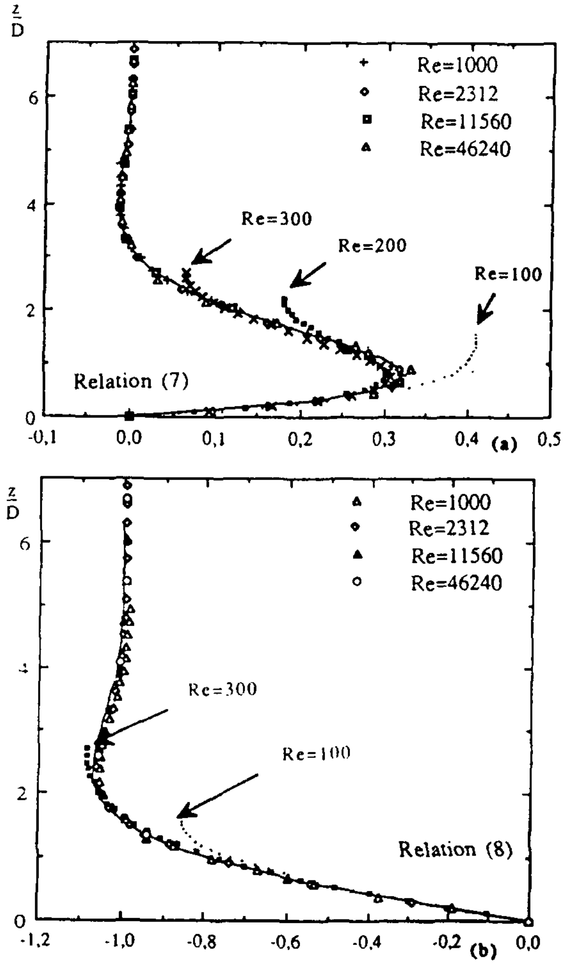

Figure 4. Problem RCR: Comparisons of the variations of the computed profiles versus z/D with the asymptotic solutions of Hide [13], at r=0 for C_W=0.0463 and for various Re, 100 ≤ Re≤46240: radial velocity with relation (7) (a); azimuthal velocity with relation (8) (b).

Problem RCR was studied over a range of parameters corresponding to different regimes.

The steady regimes range from an "annular Poiseuille" (P) type flow (which occurs at low rotation rates), to linear (LEK) and nonlinear (NLEK) Ekman regimes which occur at large rotation rates with developed Ekman layers (see Hide [13]). The linear regime corresponds to a relatively small radial flow and is characterized by the equality of the thicknesses of source and sink regions. The nonlinear regime corresponds to relatively large radial flow rates and is characterized by the thickening of source region and a diminishing sink region.

The accuracy of the collocation solutions is studied for the boundary layer configuration in the linear case and with various resolutions ranging from 16x16 to 64x64.

The investigations of the LEK, NLEK regimes at large values of Re and C_w are made up to the onset of oscillatory behaviour using a 40x40 resolution.

The P, LEK and LEK regimes

The axial variations of the radial and the azimuthal velocities at the mid-radial section are shown in Figure 4.a, b, for several values of Re and for $C_w=0.0463$. Comparisons are made with the asymptotic solutions (7)-(8), where $D=(\nu/\Omega)^{1/2}$ corresponds to one third of the theoretical Ekman layer thickness. The asymptotic solutions give better than order of magnitude estimates of the maximum velocities, even during the transition from P to LEK regimes ($Re \leq 300$).

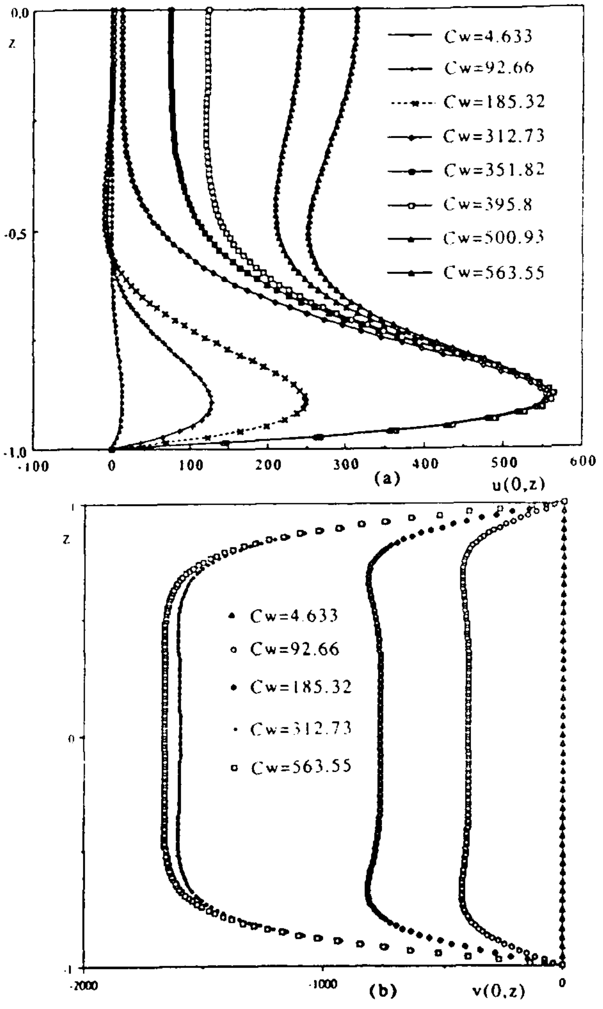

Figure 5. Problem RCR: Radial (a) and azimuthal (b) velocities profiles versus z for different values of C_w ($4.633 \leq C_w \leq 563.55$) and Re=2312 at r=0: LEK and NLEK regimes.

We have investigated the NLEK regime by increasing C_w up to $C_w=564$, at a constant value of Re, Re=2132. This corresponds to $\lambda_{lam} \leq 2.31$, where $\lambda_{lam}=2\sqrt{2}\,C_w Re^{-1/2} (R_m+1)^{-1/2}$ is the laminar flow parameter defined by Owen *et al.* [36]. As mentioned by Hide [13], although the non linear terms are negligible inside the Ekman layers, they can be important, even dominant, in the source and sink regions. This results in a thickening of the source region. The azimuthal velocity pattern for $C_w>350$ reflects a strong radial stratification and the minimal velocity occurs just close to the outlet section where the remaining Ekman layers are found. If we consider as previously the radial and azimuthal velocity profiles along the axial direction at the central location of the cavity (Figures 5.a,b), we observe in a first stage (for $C_w<320$) an increase, then a stabilization of the velocity in the Ekman layers. The increase of the mass flux results in an increase of the radial flow in the core: between $C_w= 312$ and 564 the velocity in the core varies from nearly zero (Ekman regime) to about 350 while the velocity in the shear layer remains at about 580. For the azimuthal velocity, there is a variation from nearly zero to about 1600 over the range of C_w studied.

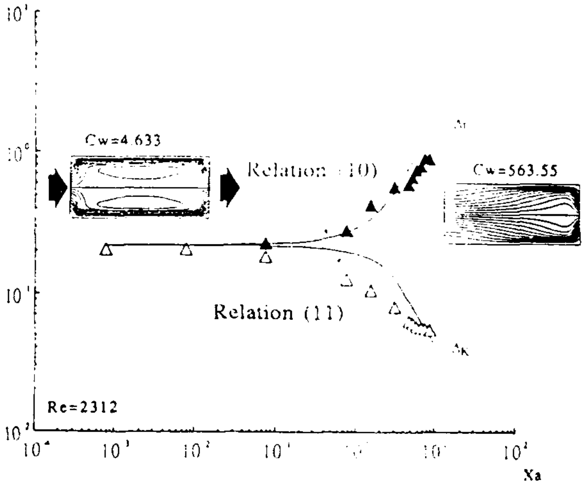

Figure 6. Problem RCR: Variations of the source and sink thicknesses versus X_a. Comparison of computed values with asymptotic solutions (10)-(11) from Hide [13]: LEK and NLEK regimes.

Significant differences also occur when using expression suggested by Faller [50] for the geostrophic velocity in the NLEK regime. However, we note that for the range of parameters considered in this study that the (non linear) relation given by Faller [50] does not result in any improvement in Hide's (linear) estimate. The actual variations of the sizes of the inlet and outlet regions as a function of X_a (defined in (12)) are shown in Figure 6 together with Hide's theoretical estimates. Typical streamlines are presented for the two regimes. The LEK is well predicted by the two solutions for $X_a<0.1$, as well as the transition to NLEK. Differences are observed for the NLEK, especially in the thickness of the sink region.

Time-dependent regimes

When increasing the rotation rate at large mass fluxes, transition to time-dependent regimes was observed. The computations were carried out in the case of an annular cavity of aspect ratio L=3.37 and curvature parameter $R_m=1.22$. Owen et al. [11,12] have found experimentally laminar and turbulent flows in the same configuration.

Two types of instabilities, A and B, have been observed experimentally by Faller [50] and Tatro and Mollö-Christensen [51]. The onset of these instabilities depends on the local Reynolds number ($Re_T=\delta V_g/\nu$) and Rossby number ($\varepsilon_T=V_g/\Omega r$) where V_g, δ, are the geostrophic velocity at the radial distance r and the Ekman layer thickness, respectively.

The numerical simulations were obtained while varying the dimensionless flow rate C_W for fixed rotation rate, Re=40580. The initial condition for each run, was generally the solution obtained for a lower C_W. In some cases, the uniqueness of the solution was confirmed by taking different initial conditions for the computations and we did not find any evidence of coexistence of different solutions. When increasing the mass flow rate, $80 \le C_W \le 150$, the flow becomes chaotic following a sequence S → P1 → QP → P5 → NP (see Figure 7).

For $C_W \le 100$ the flow is steady (S) with NLEK structure. In this range, the flow obtained from computations presents the four aforementioned regions described by Hide [13] and observed experimentally by Owen et al. [12]. The lowest value of the flux at which the oscillation is observed is taken as the critical point. The quantities V_g and δ are measured, then giving ε_T and Re_T. Two empirical laws,

$Re_T(A)=56.3+58.4\varepsilon_T(A)$ and

$Re_T(B)=124.5+3.7\varepsilon_T(B)$,

relate the critical values for the onset of the two instabilities, A and B, found experimentally. For $C_W=100$, using the computed values of δ and V_g at the center of the cavity, the numerical values of the local parameters are: $\varepsilon_T=0.6$ and $Re_T=95$. The empirical critical parameters for the two instabilities, corresponding to $\varepsilon_T=0.6$, are $Re_T(A)=92$ and $Re_T(B)=127$. Thus, according to the empirical relations, the type A instability should be found. (The experimental accuracies in the critical Re_T for the instabilities are estimated as 5% for the type A and 2% for the type B.) Increasing the dimensionless flow rate up to $C_W=120$, the flow becomes time-dependent. The regime is oscillatory, denoted by P1, and the frequency is f=80.8 (T=1/f=0.0124). At $C_W=120$, the local parameters are $\varepsilon_T=0.8$ and $Re_T=124$. According to the empirical laws, the critical parameters for this value of the Rossby number are $Re_T(A)=102$ and $Re_T(B)=127$. A transition to a quasiperiodic regime is observed when C_W is increased up to 132. This regime, denoted QP, has two incommensurate frequencies f=81.3 and f'=11.9, (T=0.0123 and T'=0.084 respectively). For the numerical solution at $C_W=132$ the computed values of the Rossby and the Reynolds numbers are $\varepsilon_T=0.9$ and $Re_T=136$. For $\varepsilon_T=0.9$ the empirical laws give the critical values $Re_T(A)=107$ and $Re_T(B)=128$. When C_W is further increased to 135, the frequencies of the motion are f=85.2 and f'=16.7, giving $f/f' \cong 5$. Thus, both frequencies have locked in a new periodic-5 regime, denoted P5. A further increase of the mass flow rate C_W to 136 yields to a chaotic regime (NP).

Investigations are in progress in the case of varying rotation rate Re at constant mass flux rate C_W (see Figure 7). The preliminary results show complex transitions.

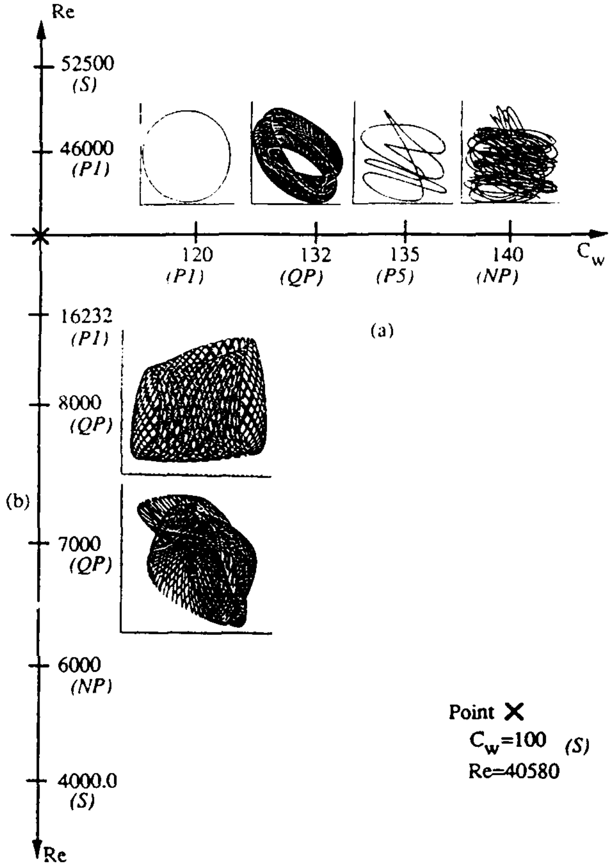

Figure 7. Problem RCR: Scenarii of transition to chaotic motion. Phase diagrams: effect of mass flow rate C_W at constant rotation rate Re=40580 (a); effect of the rotation rate Re at constant mass flow rate C_W=100 (b). (S) steady regime; (P1) periodic regime; (QP) quasiperiodic regime; (P5) periodic regime; (NP) aperiodic regime.

7.3. Turbulent modelling for problem RCA: Rotation with superposed axial flow (see Figure 1.c)

The main characteristic of the flow in the cavity subjected to solid body rotation is the development of two Ekman layers that are described in Figure 8 for the upstream side of the cavity.

The rotational Reynolds number is equal to $Re_\Omega=2.x10^5$ and the coolant flow rate $C_w=1092$. This case has been experimentally studied by Pincombe [37, 38]. The geometry is defined by: s/b=0.1333, a/b=0.1, c/s=0.58 (corresponding to L=6.75 and R_m=1.22).

The general agreement between calculations and measurements is satisfactory, but the calculation seems to underestimate somehow the Ekman layer thickness.

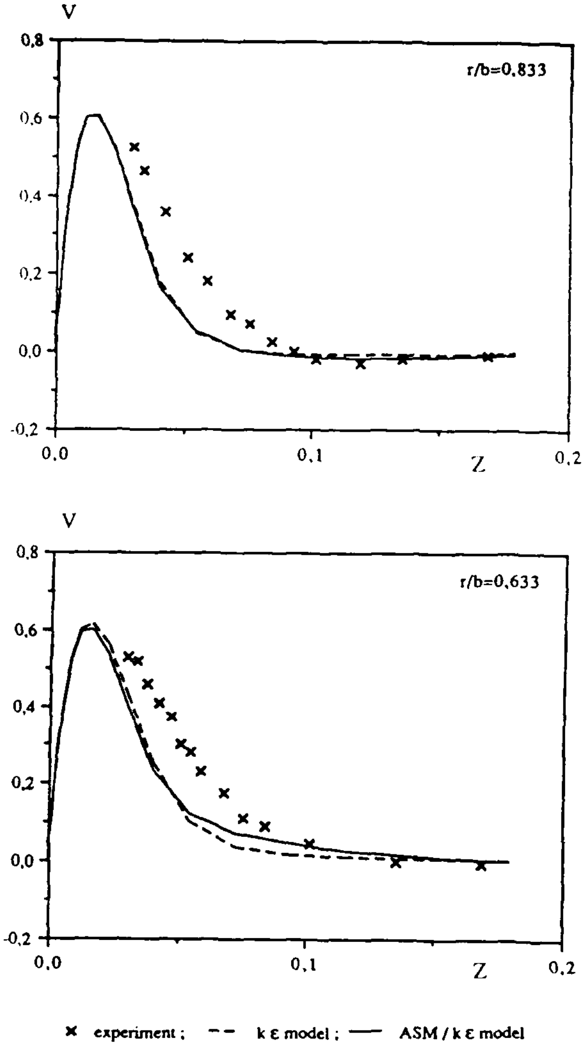

Figure 8. Problem RCA: Radial profile of velocity in the upstream boundary layer.

The numerical results support the idea that the fine description of the near wall region is crucial to obtain realistic predictions [22, 52] and that the fully turbulent region is less critical although the streamlines can be modified by the choice of the model in the core region (Figures 9 and 10). It is known that the Ekman layer velocity profiles can be improved by using a modified version of the low-Reynolds number k-ε model. For instance the Morse's formulation [22] has been devised for such purposes but contains additional empirical terms. The aim of present calculations is rather to explore ASM model coupling. Indeed, the k-ε and ASM predictions are not drastically different, reaching thus an analogous conclusion as reference [24] as far as the Ekman layer zone is concerned. However, a closer look reveals that the size and the position of the recirculation bulb within the source region is model dependant (Figures 9 and 10). In fact, the second order model which contains essential effects of rotation on turbulence (production terms and modelled redistribution terms) is more adequate to simulate turbulence field under rotation, particularly in the source region and in the sink flow region.

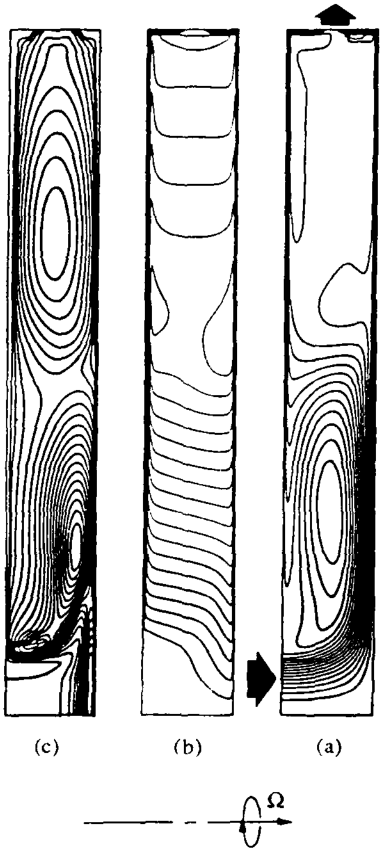

Figure 9. Problem RCA: Streamlines (a), isovalues of circumferential velocity (b) and turbulent kinetic energy (c): k-ε model.

In particular, equation (23), particularized for the shear stresses, shows an apparent viscosity reduction at high rotation rates (depending on the turbulent Rossby number) and provides thus a possible explanation for the influence of turbulence closure on the shape of recirculating bulb within the source region [53].

In turbulent flow the height of the source region can be estimated by supposing that the origin of the Ekman layer is located at a radial position where the imposed mean velocity of injected fluid is equal to the entrainment velocity on a free disk. For turbulent flow, this gives:

$$r_i/b = \alpha \, C_w^{5/13} / Re_\Omega^{4/13}$$

This equation supports the idea that the limit of the whole source region is governed by the establishment of the Ekman layer itself. Ref [2] suggests that coefficient

$\alpha=1.80$ gives the best agreement with measured values. In fact, the values given by the calculation $r_i/b=0.62$ for the k-ε model and 0.65 for the ASM model (radius at which the streamfunction reaches at the midline a value equal to the half of its maximum) are fairly well represented by this correlation which gives $r_i/b=0.64$.

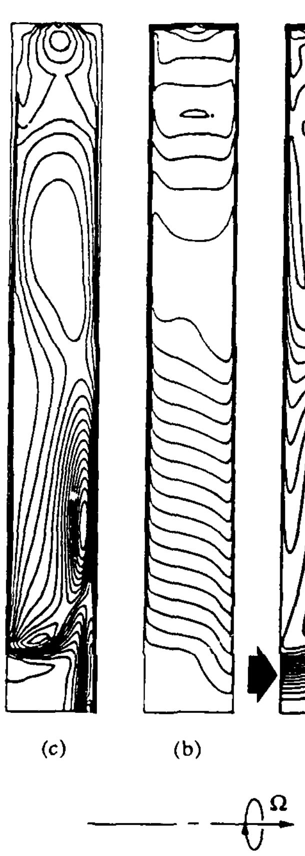

Figure 10. Problem RCA: Streamlines (a), isovalues of circumferential velocity (b) and turbulent kinetic energy (c): ASM model.

Predictions of mean circumferential velocity are given on Figure 11 for the midline axial position showing good agreement with the experimental results of Pincombe. Figures 9c and 10c give the turbulent energy distributions in the cavity. The levels of kinetic energy predicted by the two models (normalized by the wall shear stress) look very similar. It appeared also that the individual normal stresses predicted by the modified ASM model are always far from isotropy, a situation in favour of second order closure.

The associated heat transfer problem has been considered in a similar geometry corresponding to the experiment of A. Northrop and J.M. Owen [7] in which:

$s/b=0.138$, $a/b=0.104$, $c/s=0.152$ and $Re_\Omega=6.5\times10^5$, $C_w=7000$.

Here, we limited the calculations to constant wall temperature heating. Nusselt numbers are known to be very sensitive to the sublayer modelling. Calculations using the low Reynolds number k-ε model proved to be distinctly superior to the ones obtained by wall function approach ([39]). Figure 12 compares local Nusselt numbers predictions using k-ε with experimental results. If some discrepancies still remain, the order of magnitude is correct as well as the shape of the curve. However, we must remark that the Boussinesq approximation used in present calculations can only give a rough prediction. Indeed, temperature differences reaching ΔT=100°C can produce important density variations that influence mass conservation equation and make the Boussinesq hypothesis questionable in present case.

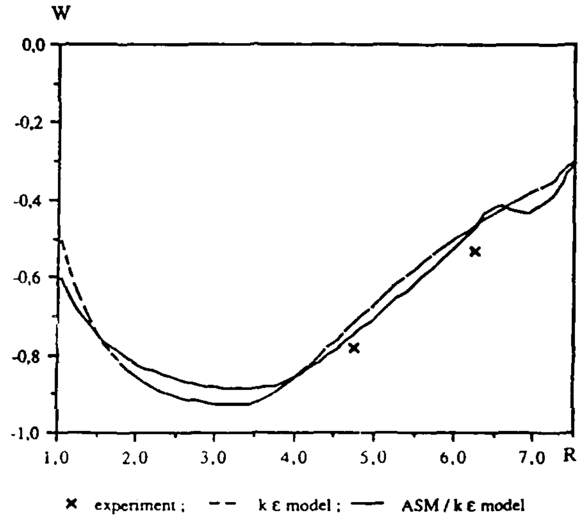

Figure 11. Problem RCA: Midline circumferential profile.

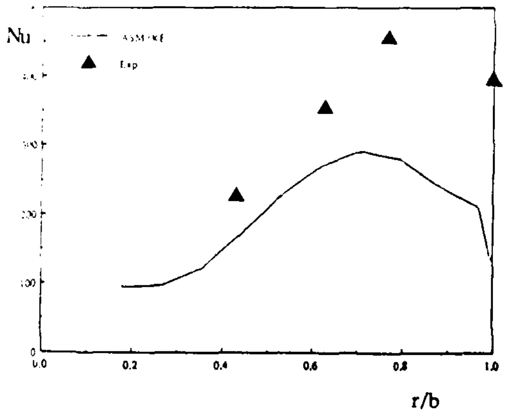

Figure 12. Problem RCA: Nusselt numbers on the upstream wall (low Reynolds number).

7.4. Problem RS1: Differential Rotation Driven Flow (see Figure 1.d)

The problem is specific with respect to the two former ones (RCT and RCR) as it concerns a large extension in the radial direction, L=10 (G=1/11), which brings additional difficulties concerning the adequacy of resolution. Another difficulty comes from the occurence of discontinuities at the corners between to the rotating and stationary walls. In the collocation method, the discontinuity is simply assigned between the corner point and the first inner collocation point. The annulus is also closer to the rotation axis than for the two previous problems, with a curvature parameter, $R_m=1.2$.

Flow regimes

The basic flow pattern consists of a radially outward flow adjacent to the rotor, a radially inward flow adjacent to the stator with an axial flow from the rotor side to the stator side along the shroud surface. The flow is of Couette type, and is dominated by diffusive motion and the recirculation cell is localized towards the shroud (regime I). When the rotation rate is increased, the strength of the flow driven by the rotating wall increases and there is a "hydraulic" jump at the corner between the rotor and the outer shroud due to the confinement. In this small region, the motion is locally reversed as the flow moves toward the axis at the border of the Ekman layer. It then flows axially toward the stationary wall where it is decelerated. The rotor and the stator layers are clearly separated by an inviscid core (regime II). There is a slight

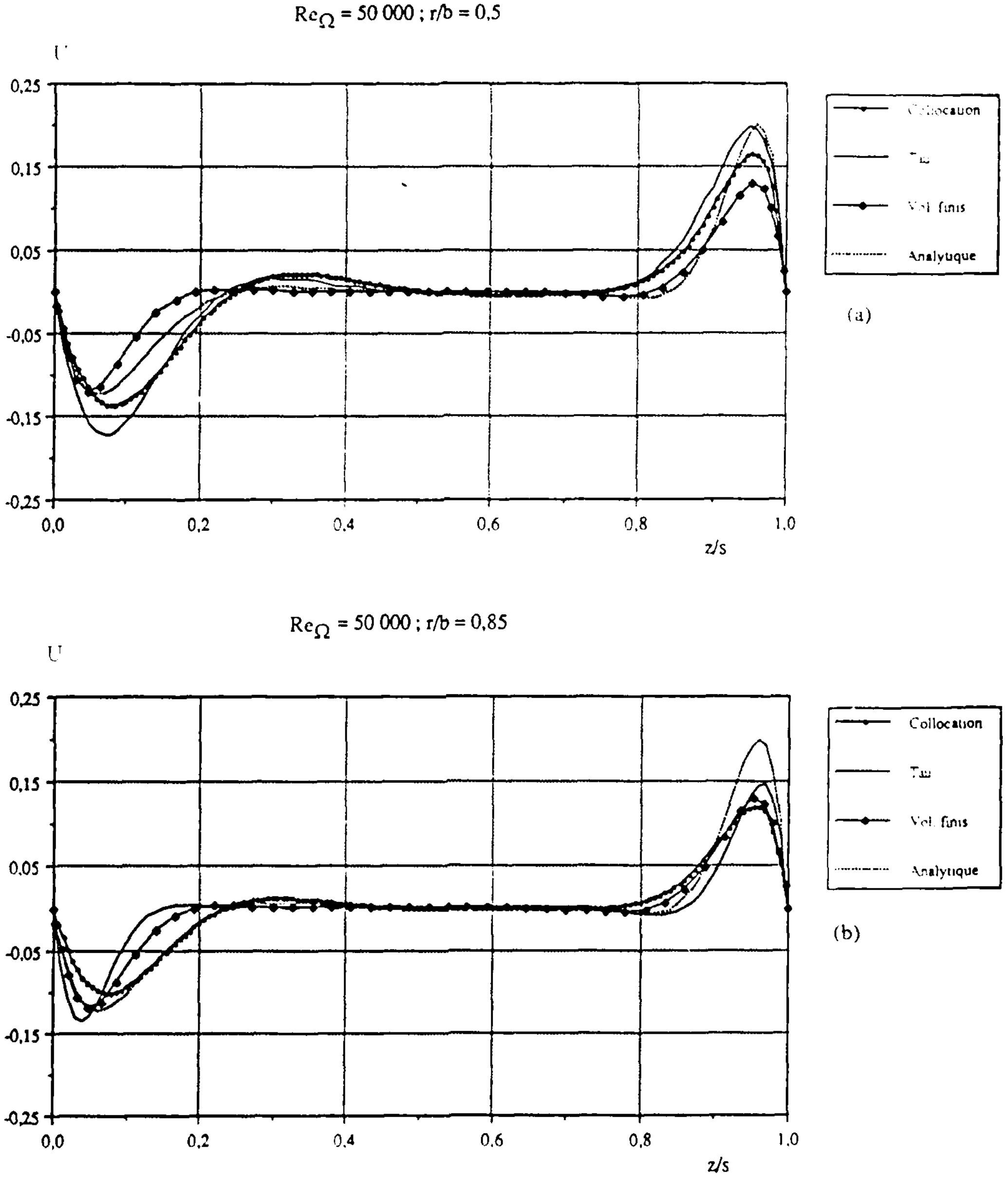

Figure 13. Problem RS1: Comparisons of computed solutions obtained with spectral (Collocation, Tau) and finite volume methods, and asymptotical solution (16), at r/b=0.5 (a) and r/b=0.85 (b), for $Re_\Omega=5.x10^4$.

asymmetry, with thickening at the stator due to the increased shear induced by the non-rotating wall.

Discussion of the solutions

The computed solutions obtained with the three tau, collocation and finite volume approximations were compared for $Re_\Omega=5.\times10^4$ at two radial locations in Figure 13. Separate boundary layers are clearly visible with the formation of the core region (regime II). There is also an asymmetry in the thicknesses of the rotor and stator boundary layers and a weak reverse flow occurs in the stator side. The three solutions agree pretty well, with limited differences at r/b=0.85, closer to the shroud. They move aside the asymptotical solution (16), taken with β=0.382. We recall that this was provided for infinite systems. Differences are more pronounced at the mid-cavity, r/b=0.5.

The transition between regimes I and II is seen in Figure 14, which shows the variation of $u_{max}/(r+R_m)$ with Re. This group was chosen to remove the dependency on r of the theoretical solution (see relation (15)). The radius is taken as that where the radial velocity is a maximum. From both the theoretical and the computed solutions, transition between regimes I and II seems to occur at $Re_\Omega\geq5.\times10^3$.

Time-dependent regimes were observed for higher values of rotation rates, and the study of the transition to turbulent regimes is reported thoroughly elsewhere.

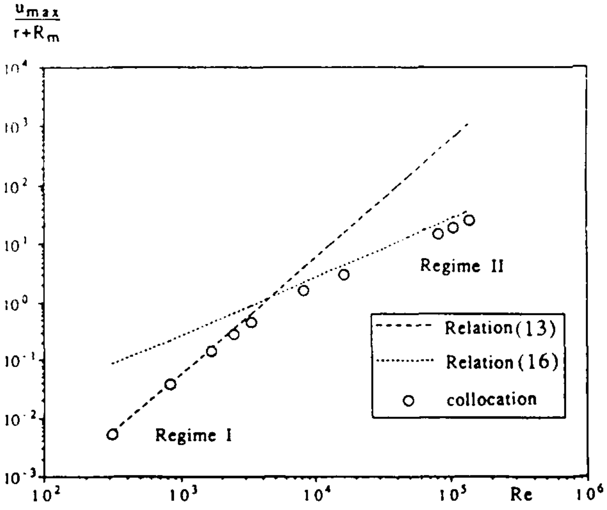

Figure 14. Problem RS1: Variation versus Re of the maximum radial velocity ($u_{max}/r+R_m$). Comparisons of computed solutions with analytical solutions (13) and (16) for regimes I and II.

7.5. Turbulent modelling for problem RS2: Differential rotation driven flow (see Figure 1.e)

The flow due to an enclosed rotating disk is a simplified model of the flow between rotor and stator in turbomachinery. The calculations shown here correspond to the experimental apparatus of Itoh *et al.* [16] in which a disk was rotated in a cylindrical cavity (Figure 1e). The rotational Reynolds number reaches a value of 10^6.

Figure 15 shows the radial velocity profiles for various radial positions. If the thickness of the wall layer is clearly underpredicted, the qualitative decrease of the peak velocity near the rotor when the radius increases is correct. Near the rotor the secondary extremum of the profiles obtained from calculation is also suggested by measurements. The profiles for the circumferential velocity show the same trends (Figure 16), the central core with constant rotation speed is well predicted except in the very top of the cavity.

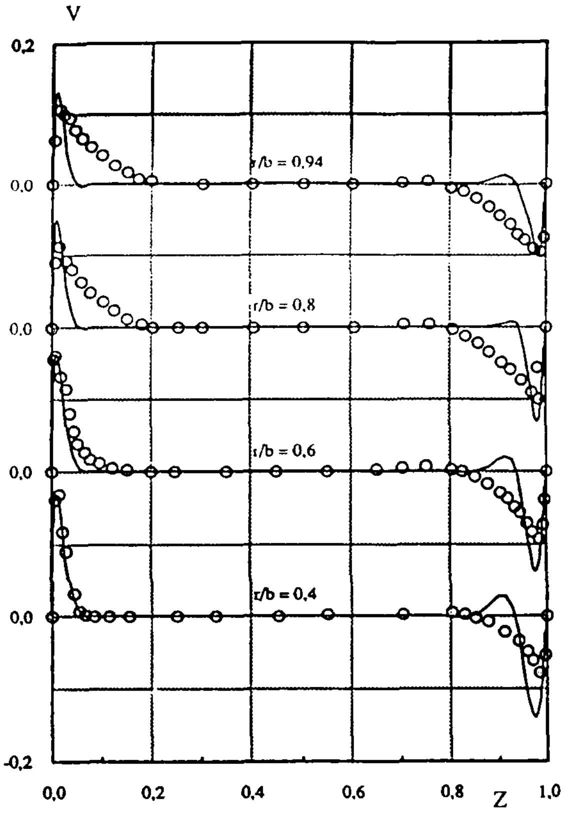

Figure 15. Problem RS2: Radial component of mean velocity , $Re_\Omega= 10^6$; o experiment; -- k ε model.

Figures 17 and 18 show the velocity profiles in the boundary layers at r/b=0.80 for different values of the rotational Reynolds number. Like in wall jets, the thicknesses b_r and b_s are defined by the distance from the wall where the value of velocity becomes half of its maximum values v_{mr} and v_{ms} respectively on the rotor and on the stator. The circumferential velocity profiles are normalized with Wrc which is the circumferential velocity at the midline Z=0.5. Figures 19 and 20 compare the velocity profiles at various radii for different rotational Reynolds number varied in such a way that the local Reynolds number $r^2\,\Omega/\nu$ is constant. The self-similarity found by Itoh *et al.* [16] is not exactly reproduced. In spite of the differences found between the profiles, the maximum of radial velocity in the Ekman layers and the thicknesses b_r and b_s are indeed in acceptable agreement as we can see in Table 1. The length and the velocity scales calculated are for $r^2\Omega/\nu$=3.6 10^5:

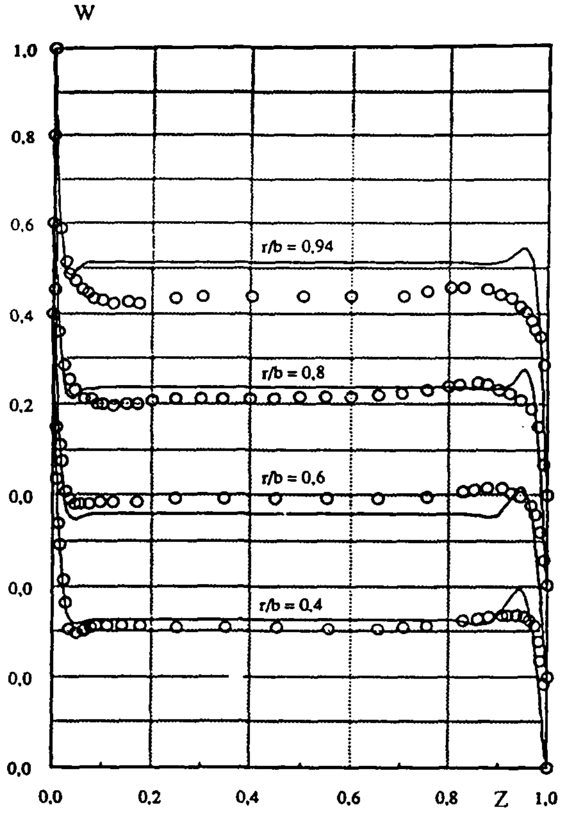

Figure 16. Problem RS2: Circumferential component of mean velocity, $Re_\Omega=10^6$; o experiment; -- k ε model.

Re_Ω	$5.6\ 10^5$	10^6
b_r	0.036	0.028
b_s	0.045	0.042
v_{mr}	0.150	0.162
v_{ms}	- 0.131	- 0.138

Table 1. Problem RS2: Characteristic values in Ekman layer

Figure 21 gives an illustration of the velocity field for streamlines and circumferential component of velocity. The turbulent kinetic energy (Figure 22) is generally concentrated in the top of the cavity where the rotational Reynolds number is larger.

Several cases have been calculated with geometry (1.e) which is close to the experiments of Daily and Nece [14]. For rotational Reynolds numbers comprised between $2.x10^5$ and $6.x10^5$ the numerical calculations can give a laminar solution (decaying turbulent energy going to zero) or a true turbulent solution, depending on the initial conditions chosen to start the calculation. Figures 23 and 24 give velocity plots in the case where turbulence is vanishing to give a laminar flow. Figures 25 and 26 are the truly turbulent solutions that clearly show a different pattern for the streamlines.

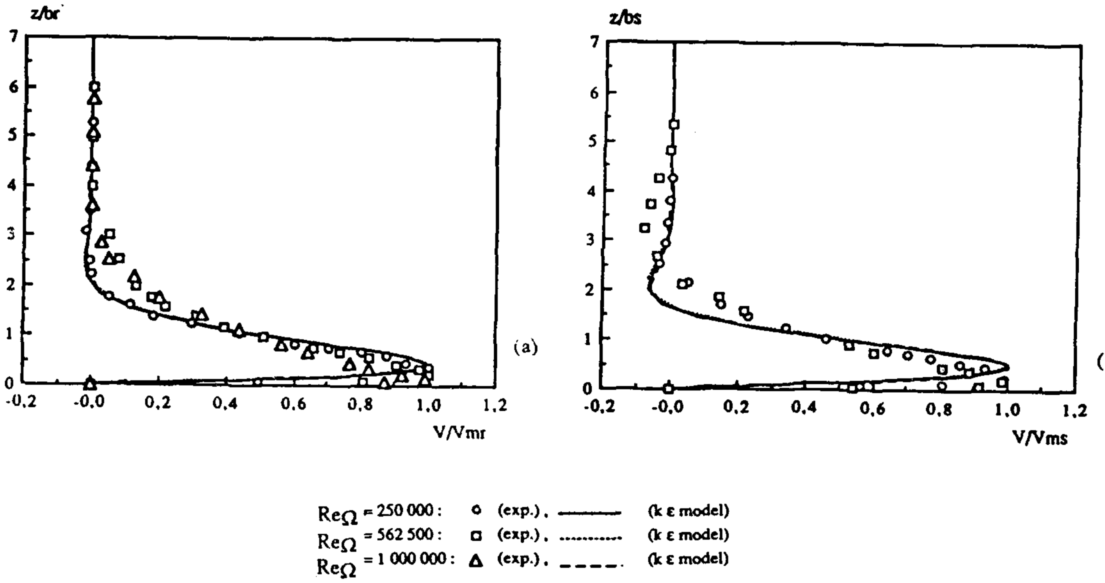

Figure 17. Problem RS2: Radial velocity component in boundary layers for the rotor (a) and the stator (b).

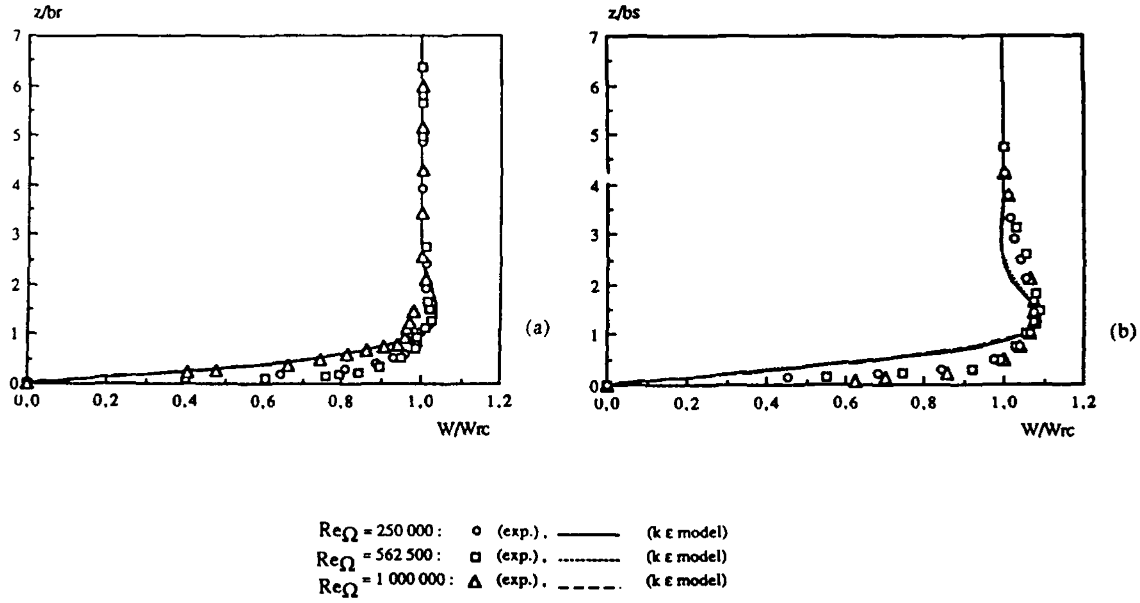

Figure 18. Problem RS2: Circumferential velocity component in boundary layers for the rotor (a) and the stator (b).

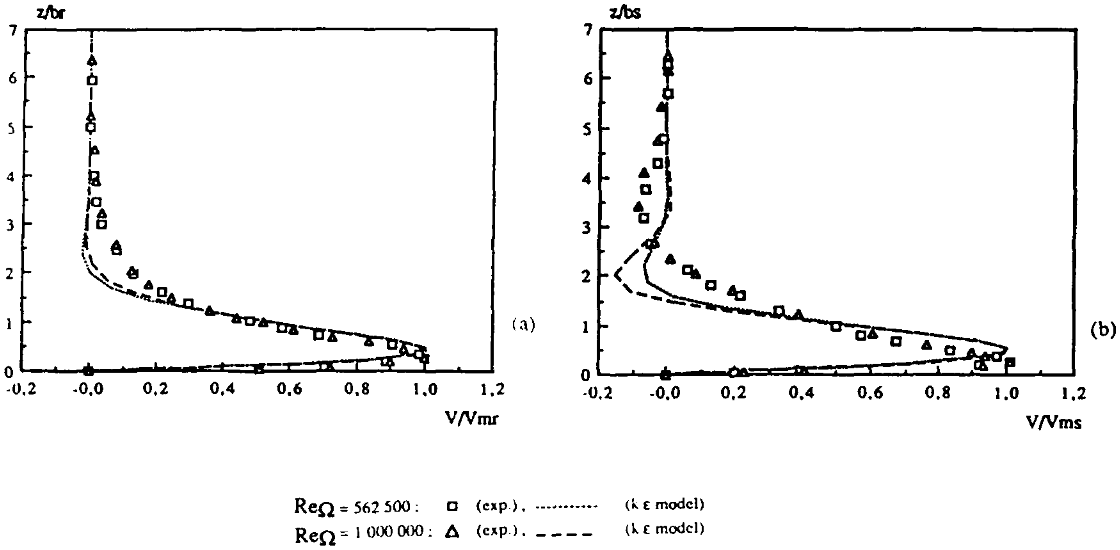

Figure 19. Problem RS2: Radial velocity component in boundary layers for the rotor (a) and the stator (b).

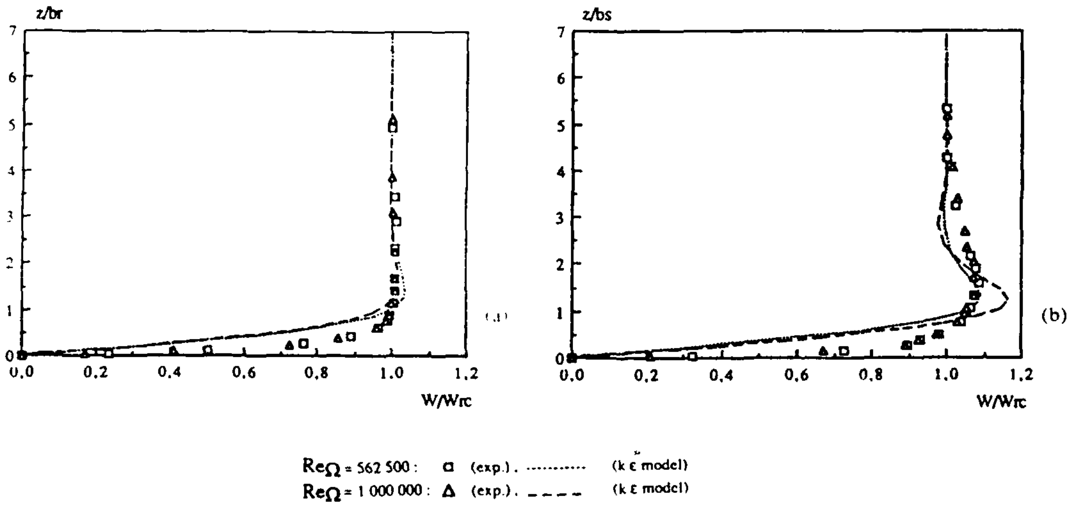

Figure 20. Problem RS2: Circumferential velocity component in boundary layers for the rotor (a) and the stator (b).

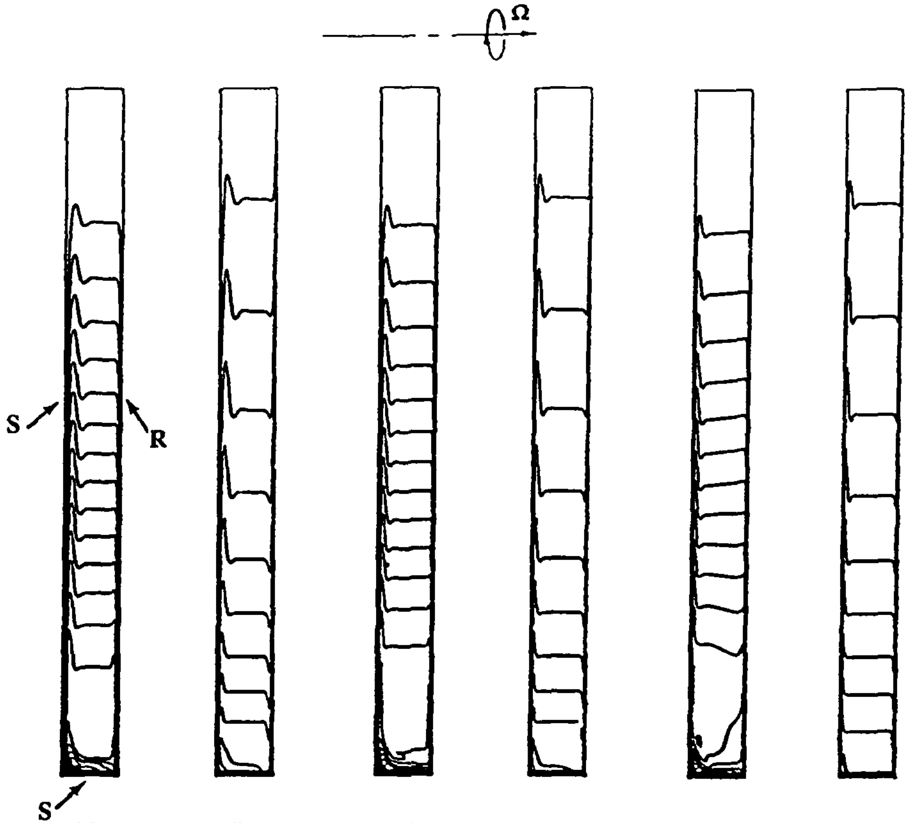

(a) (b) (c) (d) (e) (f)

Figure 21. Problem RS2: Streamlines and isovalues of circumferential velocity. $Re_{\Omega}=2.5\text{x}10^5$ (a,b); $Re_{\Omega}=5.625\text{x}10^5$ (c,d); $Re_{\Omega}=10^6$ (e,f).

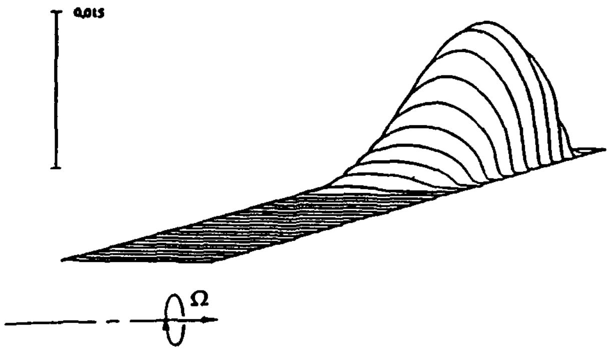

Figure 22. Problem RS2: View of the turbulent kinetic energy distribution for $Re_{\Omega}=10^6$.

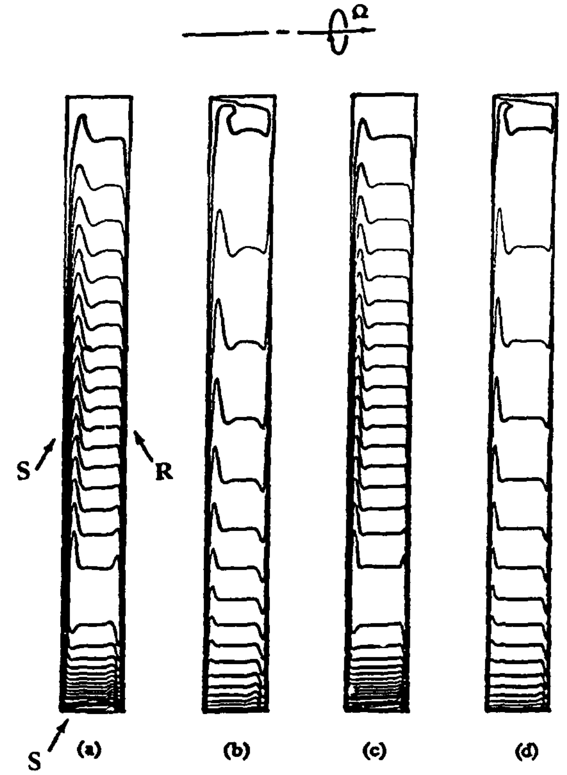

Figure 23. Problem RS2: Laminar flow (streamlines and isovalues of circumferential velocity) $Re_{\Omega}=10^5$ (a,b); $Re_{\Omega}=2.x10^5$ (c,d).

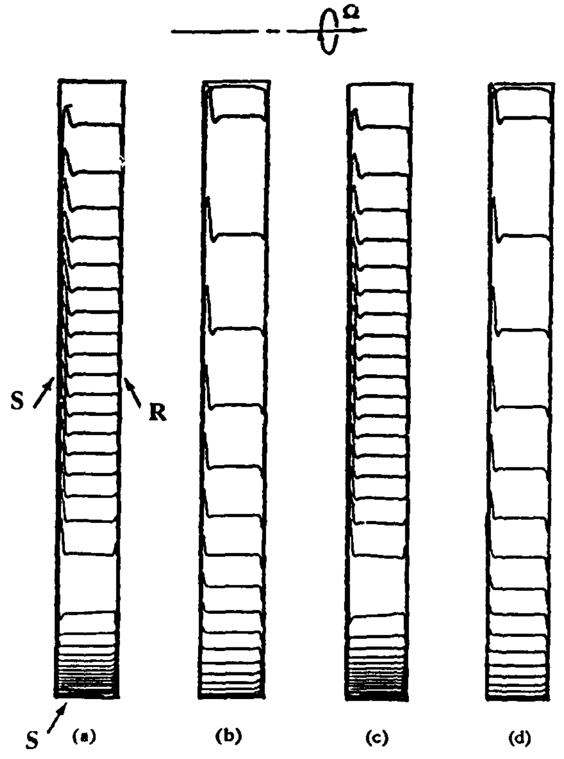

Figure 24. Problem RS2: Laminar flow (streamlines and isovalues of circumferential velocity) $Re_{\Omega}=5.x10^5$ (a,b); $Re_{\Omega}=6.x10^5$ (c,d).

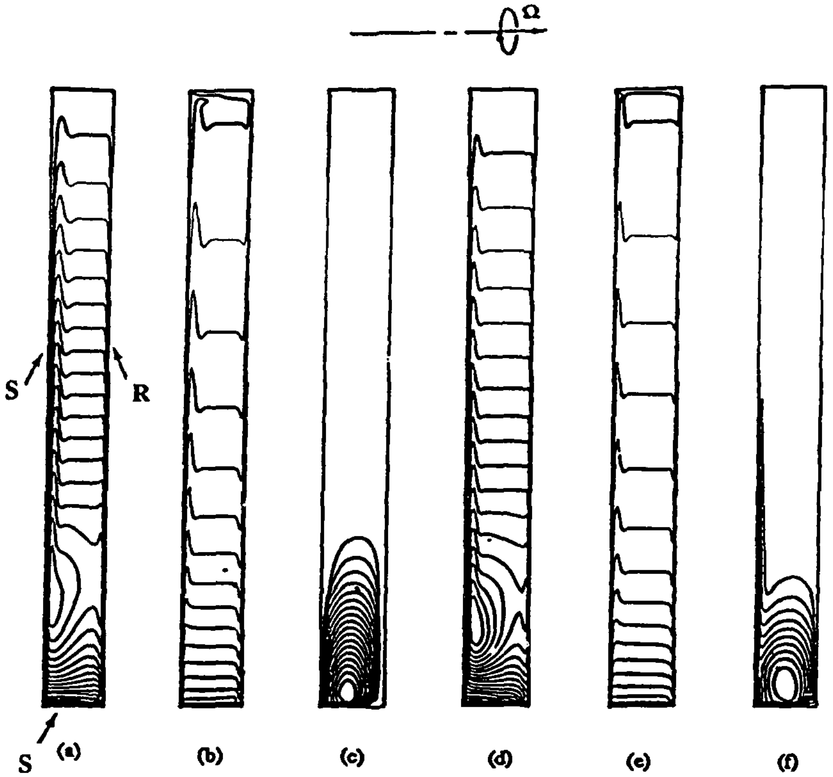

Figure 25. Problem RS2: Velocity and turbulent field (streamlines, isovalues of circumferential velocity and turbulent kinetic energy) $Re_{\Omega}=2.x10^5$ (a,b,c); $Re_{\Omega}=5.x10^5$ (d,e,f).

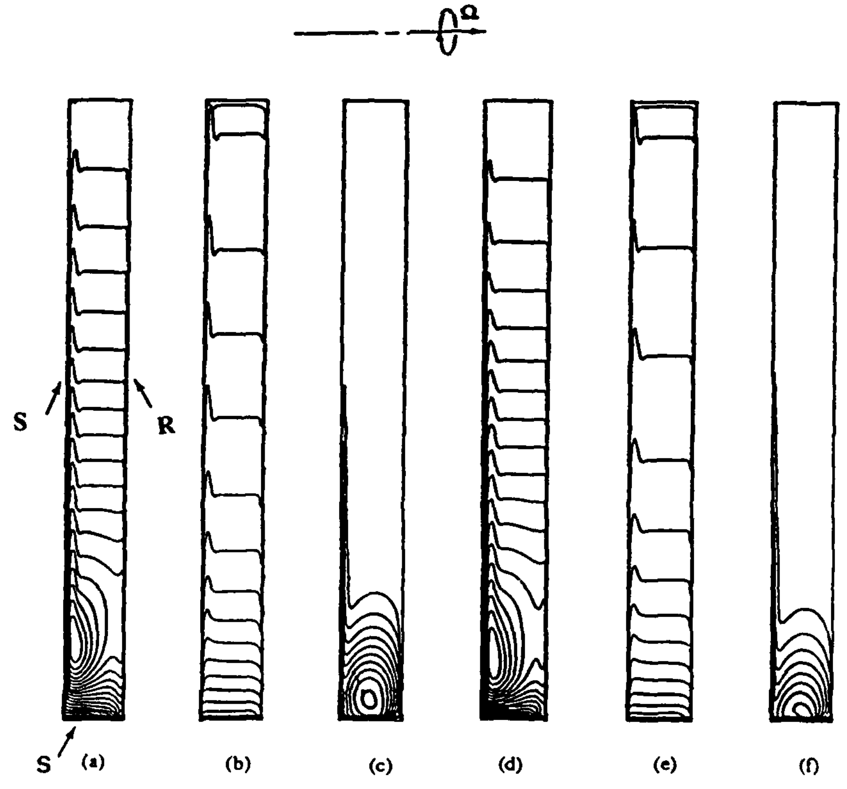

Figure 26. Problem RS2: Velocity and turbulent field (streamlines, isovalues of circumferential velocity and turbulent kinetic energy) $Re_{\Omega}=6.x10^5$ (a,b,c); $Re_{\Omega}=10^6$ (d,e,f)

8. CONCLUSIONS

Different numerical methods were used to investigate three test cases of rotating flow system. These involve the action of buoyancy forces, superposed radial flow, and shear induced by differential rotation. The effects of Rayleigh number, mass flow rate, Reynolds and Froude numbers together with geometric parameters and the transition between regimes are investigated. The results are validated by comparisons with those obtained with asymptotic solutions and with available experimental measurements.

In the first problem (RCT), we have delineated the successive transition from the buoyancy driven regime (BDR) to the Coriolis force dominated regime (COR) and to the centrifugal force dominated regime (CER). The occurence of the COR regime is affected by the value of the thermal Rossby number.

In the second problem (RCR), for steady flows, the computations reveal successive cylindrical Poiseuille (P) and Ekman layer (LEK and NLEK) regimes. The pseudospectral solutions give an accurate prediction of the steady Ekman layer which involve very steep gradients near the rotating walls. This method allows the direct treatment of boundary conditions in the physical space.

For time-dependent regimes, a succession of complex bifurcations (P1 --> QP --> P5 --> NP) was found when varying the mass flow rate C_w at constant Reynolds number Re and when varying Re at constant C_w (Maubert *et al.* [49]). A rather good agreement is already obtained with respect to experiments (Owen and Pincombe [11]).

The third problem (RSA) involves differential rotation. This case shows that the collocation method can be used to treat the discontinuity at the junction between rotating and stationary surfaces, as in classical finite difference method, but with higher accuracy.

In the case of problem RS1, the transition to time-dependent motion is not yet as clearly identified as in problem RCR. Owing to the large extension of the domain ($\Delta R >> s$) the transition does not simply result in a succession of bifurcations of periodic regimes but occurs more abruptly (Daily and Nece [14], Chaouche [56], Randriamampianina *et al.* [54]).

Further extensions of the spectral methods are in progress for the investigation of more actual rotating machine configurations: in particular, for the complex geometries by considering multidomain techniques (Raspo, Ouazzani and Peyret [57]), and for the fully three-dimensional configurations.

In the case of turbulent regimes (Problems RCA and RS2) the main modelling difficulties come from the characteristics of the flows under consideration that are the strong rotation rates and the confinement between the walls. The effect of confinement that makes the flow dominated by the Ekman layers can be described properly only by a fine resolution of the viscous sublayer. Within the limits of the section of the flow which is governed by the two Ekman layers, a first order low Reynolds number model seems sufficient to describe the wall region. However, the source region in the case of geometry 1.c with recirculation vortex is more complicated in its structure and second order modelling which is potentially more general seems necessary in this case. The same remark apply for the sink flow in the exit portion of the cavity. The benefit of second order modelling may in consequence appear in both moderate rotation rates (with an extended source region) and at very high rotation rates (with strong effect of rotation on the turbulence field itself). In the case of geometries 1d and 1e the two-equation model can give good qualitative behaviour but important discrepancies remain when the calculation is compared to the measurements of Itoh *et al.* [16] showing that a more refined modelling of the rotation on the turbulence field is necessary. To conciliate the previous remarks, low Reynolds number second order modelling is probably the appropriate way to extend research work.

Acknowledgments: The computations were carried out on both Cray 2 and Cray YMP computers with support from CCVR and CNRS, and from IMT and Conseil Regional PACA, respectively. Also, research support from DGA (contract n° 90/1539), DRET (Group 6, contract n° 9034212), SNECMA (Group YKL), GDR MFN (CNRS), Conseil Régional PACA (contract n° 91/04332, and Intl. Exchange Progs. n° 90/07519, 90/06645 and 91/04304), Ministère des Affaires Etrangères (Action Integrée n° 92/147). The authors want to acknowledge Drs R. Peyret, I. Alexander, C. A. Long for fruitful discussions. They wish to thank Prof. B.E. Launder for his collaborative action in numerical modelling, and also Dr. M.P. Chauve for useful discussions on experimental data.

REFERENCES

1. Th. Von Karman, 'Überlaminare und turbulenter Reibung', *Z. Angew. Math. Mech.*,**1**, 233 (1921).

2. J.M. Owen, 'Fluid flow and heat transfer in rotating disc systems', *XIV Int. Centre for heat and mass transfer. Symposium on heat and mass transfer in rotating machinery*, Dubrovnick (Sept. 1982).

3. M. Firouzian, J.M. Owen, J.R. Pincombe and R.H. Rogers, 'Flow and heat transfer in a rotating cylindrical cavity with a radial inflow of fluid. Part 1: The flow structure', *Int. J. for Heat and Fluid flow*, **6**, Part 4, 228-234 (1985).

4. M. Firouzian, J.M. Owen, J.R. Pincombe and R.H. Rogers, 'Flow and heat transfer in a rotating cylindrical cavity with a radial inflow of fluid. Part 2: Velocity, Pressure and Heat transfer measurements', *Int. J. for Heat and Fluid flow*, **7**, Part 1, 21-28 (1986).

5. C.A. Long and J.M. Owen, 'The effect of inlet conditions on heat transfer in a rotating cavity with a radial outflow of fluid', *31st Int. Gas. Turbine Conference and Exhibition*, Düsseldorf, RFA, paper n°**86-GT95**, (June 8-12 1986).

6. A. Northrop and J.M. Owen, 'Heat Transfer measurements in rotating disk systems, part 1: the free disk', *Int. J. Heat and Fluid Flow*, **9**, Part 1, 19-26 (1988).

7. A. Northrop and J.M. Owen, 'Heat transfer measurements in rotating disk systems, part 2: the rotating cavity with a radial outflow of cooling air', *Int. J. Heat and Fluid Flow*, **9**, Part 1, 27-36 (1988).

8. J.M. Owen, 'Ekman layers: a unifying theme for flow in rotating disk systems', *Internal report 86/TFMRC/97*, School for Engineering and Applied Sciences, Univ. of Sussex (1986).

9. J.M. Owen and A.D. Bilimoria, 'Heat transfer in rotating cylindrical cavities', *J. Mech. Engrg. Sci. I Mech. E*, **19**, Part 4, 175-187 (1977).

10. J.M. Owen and H.S. Onur, 'Convective heat transfer in a rotating cylindrical cavity', *Transactions of the ASME*, paper n°**82-GT-151** (1982).

11. J.M. Owen and J.R. Pincombe, 'Velocity measurements insides a rotating cylindrical cavity with a radial outflow of fluid', *J. Fluid Mech.*, **99**, Part 1, 111-127 (1980).

12. J.M. Owen, J.R. Pincombe and R.H. Rogers, 'Source-Sink flow inside a rotating cylindrical cavity', *J. Fluid Mech.*, **155**, 233-265 (1985).

13. R. Hide, 'On source-sink flows in a rotating fluid', *J. Fluid Mech.*, **32**, 737-747 (1968).

14. J.W. Daily, R.E. Nece, 'Chamber dimension effects on induced flow and frictional resistance of enclosed rotating disks', *J. Basic Engng.*, 217-232 (1960).

15. J.W. Daily, W.D. Ernst and V.V. Asbedian, 'Enclosed rotating disks with superposed throughflow: mean steady and periodic unsteady characteristics of induced flow', Report n°**64**, *Hydrodynamics Lab.*, Massachusetts Institute of Technology, (1964).

16. M. Itoh, Y. Yamada, S. Imao, M. Gonda, 'Experiments on turbulent flow due to an encosed rotating disk', *Engineering Turbulence Modelling and Experiments* Ed. by W. Rodi, E.N. Garic, Elsevier, 659-668 (1990).

17. J.W. Chew, 'Development of a computer program for the prediction of flow in a rotating cavity', *Int. J. Num. Meth. Fluids*, 4, 667-683 (1984).

18. J.W. Chew, 'Computation of convective laminar flow in rotating cavities', *J. Fluid Mech.*, **153**, 339-360 (1985).

19. M.L. Koosinlin, B.E. Launder and B.I. Sharma, 'Prediction of momentum, heat and mass transfer in swirling, turbulent boundary layers', *J. Heat Transfer*, ASME, **96**, 204-209 (1974).

20. P. Bradshaw, *Complex turbulent shear flows*, Agardograph 169 (1973).

21. B.E. Launder and B.I. Sharma, 'Application of the energy-dissipation model of turbulence to the calculation of the flow near a spinning disk', Letters in *Heat and Mass Transfer*, **1**, 131 (1974).

22. B.I. Sharma, 'Prediction of mass transfer near a rotating disk at high Schmidt numbers and high swirl rates', *Int. J. Heat Mass Transfer*, **21**, 1355-1356 (1978).

23. J.W. Chew, 'Prediction of flow in rotating disk systems using the k-E turbulence model', *Trans. of the ASME* , paper n° **84-GT-229** (1984).

24. J.W. Chew, 'Computation of flow and heat transfer in rotating disk systems', *2nd ASME-JSME thermal engineering Conference*, Hawaï, USA, **3**, 361 (1987).

25. A.P. Morse, 'Numerical prediction of turbulent flow in rotating cavities', *32th International Gas Turbine Conference*, Anaheim, California, ASME, paper n° **87-GT-74** (1987).

26. I.P. Theofanopoulos, 'Numerical computation of turbulent flow in rotating disk cavities', *Ph. D. Thesis*, UMIST, Univ. of Manchester, (1988).

27. H. Iacovides and I.P. Theofanopoulos, 'Turbulence modelling of axisymmetric flow inside rotating cavities', *Int. J. Heat Fluid Flow*, **12**, Part 1, 2-11 (1991)

28. G.M. Homsy & J.L. Hudson, 'Centrifugally driven thermal convection in a rotating cylinder', *J. Fluid Mech.*, **35**, Part 1, 33-52 (1969).

29. G. De Vahl Davis, E. Leonardi & J.A. Reizes, 'Convection in a rotating annular cavity', in *Proc. XIVth Int. Center for Heat and Mass Transfer Symposium*, Dubrovnik, Yugoslavia (1982).

30. A. Randriamampianina, P. Bontoux & B. Roux, 'Ecoulements induits par la force gravifique dans une cavité cylindrique en rotation', *Int. J. Heat Mass Tranfer*, **30**, 1275-1292 (1987).

31. A.M. Chaouche, P.A. Maubert, A. Randriamampianina and P. Bontoux, 'Pseudo-spectral Collocation-Chebyshev Methods for Axisymmetric Flows in Rotating Annular Domains', *Intl. J. Num. Meth. in Fluids* (submitted, 1992).

32. K. Stewartson, 'On almost rigid rotations', *J. Fluid Mech.*, **6**, 17-26 (1957).

33. A.R. Robinson, 'The symmetric state of a rotating fluid differentially heated in the horizontal', *J. Fluid Mech.*, **6**, 599-620 (1959).

34. C. Hunter, 'The axisymmetric flow in a rotating annulus due to a horizontally applied temperature gradient', *J. Fluid Mech.*, **27**, 753-778 (1967).

35. P.A. Maubert, Thèse de Doctorat, Université d'Aix-Marseille II (en préparation, 1992).

36. J.M. Owen & R.H. Rogers, *Heat Transfer in Rotating-Disc Systems: Rotor-Stator Systems, Vol. 1*, Ed. W.D. Morris, John Wiley & Sons Inc (1989).

37. J.R. Pincombe, 'Velocity measurements in the MkII rotating cavity rig with a radial outflow',

Thermofluid Mechanics Research Centre. University of Sussex **81/TFMRC/21** report (1981).

38. J.R. Pincombe, 'Optical measurements of the flow inside a rotating cylinder', *Ph. D. Thesis*, University of Sussex (1983).

39. C.R. Yap, 'Turbulent heat and momentum transfer in recirculating and impinging flows', *Ph. D Thesis*, University of Manchester UMIST, TFD/87/1 report (1987).

40. J.M. Vanel, R. Peyret & P. Bontoux, 'A pseudo-spectral solution of vorticity-stream function equations using the influence matrix technique', *Num. Meth. Fluids Dynamics*, K.W. Morton and M.J. Bains Eds., Clarendon Press, 463-475 (1986).

41. U. Ehrenstein & R. Peyret, 'A Chebyshev-collocation method for the Navier-Stokes equations with applications to double diffusive convection', *Int. J. Numer. Meth. Fluids*, **30**, 427-452 (1989).

42. D.B. Haidvogel & T.A. Zang, 'The accurate solution of Poisson's equation by expansion in Chebyshev polynomials', *J. Comput. Phys.*, **30**, 137-180 (1979).

43. A. Chaouche, A. Randriamampianina & P. Bontoux, 'A Collocation Method Based on an Influence Matrix Technique for Axisymmetric Flows in an Annulus', *Comput. Methods Appl. Mech. Eng.*, **80**, 237-244 (1990).

44. S.V. Patankar, *Numerical heat transfer and fluid flow*, Mac Graw Hill (1980).

45. P.G. Huang and M. A. Leschziner, Stabilization of recirculating flow computations performed with second moments closures and thired order discretization', *Vth Int. Symp. on Turbulent Shear Flows*, Cornell University (1985).

46. D.A. Bennetts & W.D.N. Jackson, 'Source-sink flows in a rotating annulus: a combined laboratory and numerical study', *J. Fluid Mech.*, **66**, 689-705 (1974).

47. J.M. Hyun, 'Source-sink flows of stratified fluid in a rotating annulus', *J. Fluid Mech.*, **145**, 112-125 (1984).

48. J.W. Chew, J.M. Owen & J.R. Pincombe, 'Numerical predictions for laminar source-sink flow in a rotating cylindrical cavity', *J. Fluid Mech.*, **143**, 451-466 (1984).

49. P. Maubert, A. Chaouche, E. Crespo del Arco & P. Bontoux, 'Régimes d'écoulement instationnaires dans une cavité annulaire tournante soumise à un flux radial forcé', *C. R. Acad. Sci. Paris*, (in print) (1992).

50. A.J. Faller, 'An experimental study of the instability of the laminar Ekman boundary layer', *J. Fluid Mech.*, **15**, 560-575 (1963).

51. P.R. Tatro & E.L. Mollö-Christensen, 'Experiments on Ekman layer instability', *J. Fluid Mech.*, **28**, 531-543 (1967).

52. T. Rezoug, 'Approche numérique de la convection thermique turbulente dans les cavités en rotation', *Thèse de Doctorat*, Univ. d'Aix-Marseille II (1990).

53. R. Schiestel, L. Elena, T. Rezoug, 'Numerical modelling of turbulent flow and heat transfer in rotating cavities' *J. Numerical Heat Transfer*, (to appear, 1993)

54. A. Randriamampianina, P. Tucker & L. Elena, 'Accurate numerical predictions of flow structure in shrouded rotor-stator system'. To be submitted.

55. D. Dijkstra & G.F.J. Van Heijst, 'The flow between two finite rotating disks enclosed by a cylinder', *J. Fluid Mech.*, **128**, 123-154 (1983).

56. A. Chaouche, 'Une méthode de collocation pour la prédiction et l'analyse des écoulements et des transferts dans les milieux en rotation rapide', Thèse de Doctorat, Université d'Aix-Marseille II (1991).

57. I. Raspo, J. Ouazzani & R. Peyret, Internal report (1992).

Discussion

QUESTION 1:

DISCUSSOR: M. Owen, University of Bath

The authors have presented some very interesting results for a wide range of rotating-disc problems. There appears to be a problem with the turbulent computations, where , as shown in Figure 15, the computations have "locked on" to the laminar solutions while the data of Itoh et al. show that turbulent flow occurs. Computations presented by Wilson et al. (1992) show that low-Reynolds-number k-ε models can give accurate computations for this case. Could the authors comment on this discrepancy?

AUTHOR'S REPLY:

The flow in rotating cavities is often complicated by the occurrence of laminar-turbulent transition within the flow. Indeed in Figure 15 of the present paper, the calculated flow near the stator has locked on to a quasi-laminarized solution. The result is very sensitive to the particular choice of the low-Reynolds number version of the k-ε model. We have used here the Launder and Sharma approach. In particular, $f_\mu = \exp[-3.4/(1 + Re_T/50)^2]$ which is different from the approach used by Wilson et al. (1992). No doubt this change is sufficient to modify the transitional behaviour of the model. Many low-Reynolds number k-ε models have been proposed in the scientific literature. A comparative assessment of these different approximations would be interesting in such complex flow situations.

MODELLING THERMAL BEHAVIOUR OF TURBOMACHINERY DISCS AND CASINGS

by

R.D. Monico and J.W. Chew
Rolls-Royce plc
PO Box 31
Derby DE2 8BJ
United Kingdom

ABSTRACT

The thermal behaviour of discs and casings in gas turbine engines has important effects on engine performance and integrity and theoretical or computer modelling of these effects is an essential part of the design process. In this paper the current status of thermal modelling is reviewed, problem areas are identified, examples of where application of the latest numerical and modelling techniques have led to improvements are given, and prospects for further developments are discussed. It is concluded that, although recent research and computing advances are improving the predictive capability, considerable scope for further improvement remains.

1. INTRODUCTION

Thermal modelling of discs and casings is required for prediction of component life and movements. Accurate predictions of the transient temperature distributions are needed so that the designer may minimise component weights while achieving the required life, controlling running clearances and maintaining the annulus line. Rotor tip clearance control has a direct effect on turbine and compressor efficiencies and on compressor surge margin. As engine operating temperatures and efficiencies have increased over the years so more attention has been given to their thermal behaviour; this trend is expected to continue.

Typically, a thermal model will consist of a heat conduction solution for the components coupled through boundary conditions to models of convective heat transfer and radiation. Features such as frictional heating of the air, ingestion of mainstream gas into the inter-disc cavities, thermal barrier coats, impingement cooling, contact resistance and flow leakage may have to be accounted for. Predictions are required for engine cycles through which the engine temperatures vary widely. Additional coupling of the convective flow and component temperatures occurs through dependency of the flow on seal clearances and buoyancy effects. In addition to the formidable problem of producing accurate models of the physics, there is the additional challenge of achieving fast turn-around times and minimising costs so that full impact on the design can be achieved.

No attempt will be made to give a historical account of the development of this subject, but it may be noted that use has been made of finite element and finite difference heat conduction models for about two decades. During this time considerable experience and 'engineering know-how' has been accumulated in deriving boundary conditions for the conduction solutions. Extensive matching of model predictions to engine temperature measurements has ensured that models are validated to a high level. However, in some cases, the modelling assumptions used may not accurately represent some of the physical processes involved. Hence extrapolation (for example, to a new engine operating condition) without matching to test data would be potentially hazardous. At the present time the mathematical models and empirical correlations underlying the thermal model are progressively being improved. This is expected to lead to fewer engine tests being required, improved designs and fewer surprises.

In the next section of this report various aspects of the thermal models are discussed in some detail. Examples of model validation and results are then given in section 3. In section 4, some of the problem areas where further research is required are highlighted and the main conclusions are summarised in section 5.

2. THE THERMAL MODEL

2.1 Heat conduction solution

The temperature field within the components is obtained through solution of the transient, variable property, heat conduction equation. Numerous software packages are available for tackling this problem, but few, if any, are specifically adapted to the present application. Obvious requirements of the software are that it should be accurate and have sufficient flexibility in the specification of boundary conditions. For use as a design tool the program should also be efficient in terms of both the computing and engineer's time and should be easy to use, with appropriate boundary condition options being readily available.

In recent years Rolls-Royce have replaced earlier finite difference and finite element heat conduction solvers with more efficient finite element methods (see Armstrong and Edmunds (1)). Particular features of the present method include automatic time step setting, mesh generation and mesh adaption to achieve a user specified accuracy. Combining these features with fast and stable numerical methods, powerful input and output processing capability, and a library of boundary condition options means a very effective thermal modelling facility has been produced. With numerical aspects of the problem largely automated the engineer is free to concentrate on boundary condition specification and application of the model.

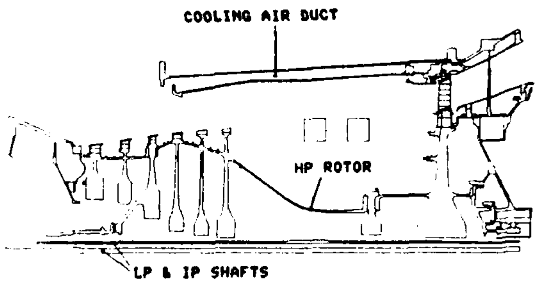

FIGURE.1. 2D AXISYMMETRIC GEOMETRY FOR TURBINE DISC ANALYSIS

An example of the geometry considered in a thermal model is shown in Figure 1. In this case the main interest is in the H P rotor behaviour. However, to complete the model it was appropriate to include the IP and LP shafts, a cooling air duct and some other stationary components in the calculation. With these components included the specification of inlet air temperatures is simplified. Figure 2 shows part of the automatically generated finite element mesh for this example. Note, that some approximation is necessary when three dimensional features such as blades and struts are included in an axisymmetric model such as that shown in the figure.

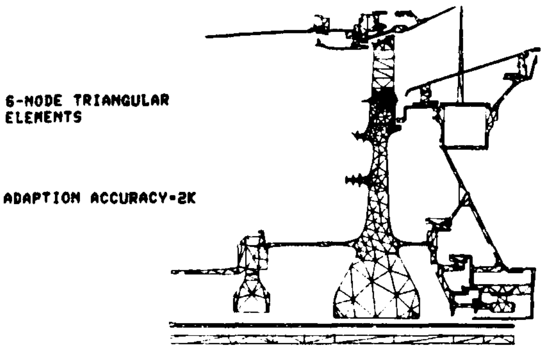

FIGURE.2. AUTOMATIC ADAPTIVE MESH OF TURBINE DISC REGION

While the use of axisymmetric models is standard design practice for both discs and casings, three dimensional analysis is now being increasingly employed as further performance benefits are sought. The automatic finite element methods of Armstrong and Edmunds are also applied in 3D, enabling complete 3D problems to be tackled efficiently. Examples of 3D finite element meshes are shown in Figure 3. For the casing (see Figure 3a) the model was used to estimate thermal distortion which can adversely affect the running clearances. For the turbine disc shown in Figure 3b there was particular interest in the temperature distribution around blade cooling air feed holes that pass through the disc rim and blade root.

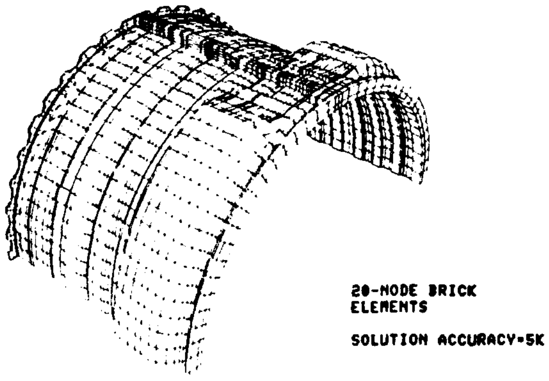

FIGURE.3A. 3D MESH OF COMPRESSOR CASING USED IN ASYMMETRIC TIP CLEARANCE PREDICTIONS

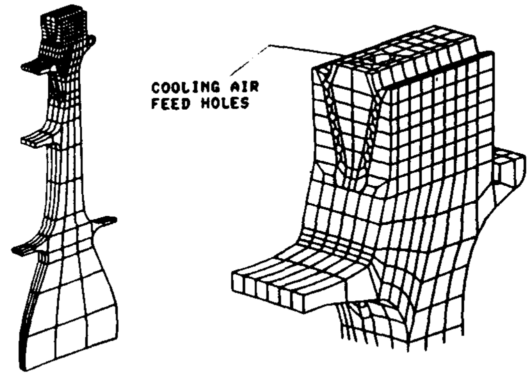

FIGURE.3B. TURBINE DISC SEGMENT 3D HEAT TRANSFER MODEL

2.2 Convective boundary conditions

Specification of convective boundary conditions is a major source of difficulty and uncertainty in the thermal models. However, as will be shown in section 3, a methodology has been developed which reproduces engine measurements reasonably well. Traditionally, convective boundary conditions are modelled through the specification of air temperature and heat transfer coefficients. This basic approach is retained in present models although increasingly sophisticated methods are used to estimate heat transfer coefficients and gas temperatures.

Main gas path temperatures are usually estimated from throughflow calculations for the mainstream (which may be adjusted to agree with measurements). These temperature estimates are themselves subject to some uncertainty, due to such effects as radial temperature variations in the annulus which are difficult to model reliably, and this uncertainty transfers to the thermal model. Gas temperatures in other parts of the engine are usually estimated from energy balances for the secondary air flows, taking account of heat transfer and 'windage' work. While this is straight forward in some situations, such as flow along a duct, it can be difficult where the flow distribution is uncertain. A good example of the latter case is axial throughflow between two co-rotating compressor discs where the degree to which the throughflow penetrates into the inter-disc cavity may have to be estimated. In such cases the engineer may have to make questionable assumptions regarding the flow and will rely on comparison with measurements to show up any discrepancies in the predictions. With experience, accepted modelling techniques have been established and these techniques embody a database of engine measurements.

Heat transfer coefficients based on local gas temperatures are generally used, as this avoids some of the gross errors that can occur if a remote gas temperature is employed. Considerable use is made of well known empirical Nusselt number correlations for such cases as duct flow, 'free' rotating disc flow, flow over flat plates and natural convection from flat plates and cylinders. While correction factors are often needed to account for the non-ideal engine conditions, use of these correlations goes some way to ensuring the correct scaling of the heat transfer coefficients through a flight cycle. Buoyancy effects due to rotation are sometimes modelled by replacing gravitational acceleration with centripital acceleration in correlations for natural convection. (Some support for this method is given by the data of Long and Tucker (2) but, in general, its validity is unproven.) Further, more specialist, empirical correlations may also be used. These include labyrinth seal heat transfer (eg. Waschka et al (3)), rotating drum heat transfer (eg. Childs et al (4)), rotating disc windage (eg. Daily and Nece (5)) and impingement heat transfer which is discussed further below. As for the flow distribution, experience with this approach to specification of heat transfer coefficients, has led to the establishment of accepted modelling techniques.

Impingement heat transfer is commonly used on turbine casings to provide control of casing temperatures and displacements in support of tip clearance optimisation. It is also encountered on rotating discs due to air jets resulting from passage through cooling air system restrictors or seals. Heat transfer associated with impingement is extremely difficult to model accurately because of its strong dependence on geometry and flow conditions. This is reflected by the wide and varied empirical correlations available on the subject (eg. Downs & James (6)). The traditional approach to determining impingement heat transfer coefficients for engine applications has been to derive them from appropriate test measurements. However, a knowledge-based database for impingement heat transfer has recently been developed (see Moss (7)) which contains a very extensive set of impingement correlations from existing literature. By selection of a set of keywords together with specification of parameter values defining the flow conditions, coefficients are evaluated for all correlations that satisfy the selected criteria. With links to the impingement database from the finite element system it is planned to automate the selection and evaluation of impingement heat transfer correlations with much greater reliability and less dependence on test measurements.

Convective heat transfer in rotating disc cavities has been the subject of a sustained research effort over recent years (see, for example, Owen (8) and Chew (9)) and some definite advances in this area can be identified. Computational fluid dynamics (CFD) methods and momentum-integral techniques have been developed for this application and are now being used to assist in thermal modelling. Examples of the capabilities of these two methods and comparison with heat transfer measurements are given by Chew and Rogers (10) and Iacovides and Chew (11). Of the two methods the integral technique is the more computationally efficient, and some success has been had in coupling this method to the heat conduction solution. CFD methods are potentially the more powerful predictive tool, but their computational requirements have, to date, limited their application to 'stand-alone' calculations. It is reassuring to note that when heat transfer predictions from the two models have been compared with the assumptions used in earlier thermal models, reasonable agreement has usually been found.

An example of a CFD calculation for the cavity in front of a turbine disc, from Virr (12) is shown in Figure 4. This illustrates both the capability of CFD methods and the complexity of the flow. In this axisymmetric calculation drag due to oil system pipes crossing the lower part of the cavity has been included in the model. Such features have a significant effect on the tangential velocity of the fluid in the cavity and hence the surface heat transfer. Note also that the flow inlets to the cavity are modelled as axisymmetric slots rather than discrete holes or nozzles as occur in practice. In this example, flow is highly swirled at the outer inlet and this affects the flow structure in the outer part of the cavity.

A further important aspect of the convection problem is gas ingestion in the turbine, where contamination of the cooling air by the hot mainstream gas may lead to overheating of the discs.

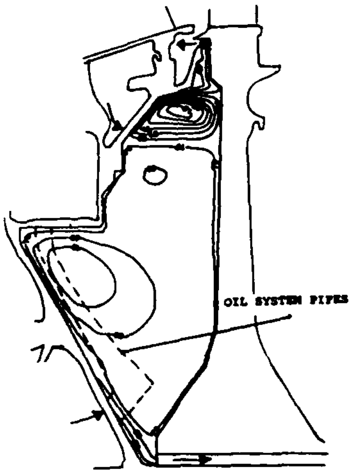

FIGURE.4. PREDICTED STREAMLINES FOR A TURBINE DISC CAVITY

Empirical correlations and models are available in the open literature for estimating ingress due to disc pumping (eg. Bayley and Owen (13), Daniels et al (14) and Chew et al (15)). Proprietary methods have been available for some years in Rolls-Royce for estimating ingestion driven by the mainstream pressure distribution (eg. Campbell (16)) and this problem is now receiving more attention from the research community (eg. Green and Turner (17)). CFD is also beginning to contribute in this area. Figure 5 shows some recent three-dimensional, steady CFD results for flow ingestion into a model disc cavity simulating Green and Turner's experimental set-up. Initial comparisons with measurements are very encouraging. Note, however, that for a full description of the problem, unsteady calculations may be required.

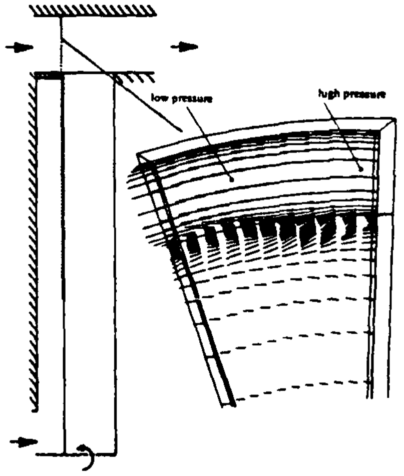

FIGURE.5. PREDICTED VELOCITY VECTORS SHOWING MAINSTREAM GAS INGESTION THROUGH AN AXIAL CLEARANCE SEAL

2.3 Other Boundary Conditions

In addition to convective heat transfer the thermal model will usually require the specification of further complex boundary conditions, which have a significant effect on the disc or casing thermal behaviour.

Contact resistance is of particular importance in the thermal analysis of turbine casings, where high conductive heat fluxes from nozzle guide vane segments to turbine casings are restricted by the imperfect contact between these components. Build tolerances, pressure variations and axial movements, combine to give great variability in the resulting casing temperature. The conventional approach is to measure contact resistance via thermocouples either side of the contact region and derive boundary conditions to reproduce the measured temperature difference. However, work is now in progress to incorporate a predictive capability, where the thermal resistance is calculated from empirical correlations and a knowledge of the contact conditions.

Thermal barrier coatings are increasingly being used in a variety of applications to reduce the heat transfer rate to components, either as a means of improving clearance control or to enhance the component integrity/life by reducing temperatures. The low conductivity of barrier coats and their bonding agents, together with their thin nature can lead to severe numerical instability if handled in the finite element conduction solution. Techniques have therefore been developed to represent the effects of thermal barrier coatings by specifying an overall effective heat transfer coefficient assuming a composite wall. This simple approach allows the effect of thermal coatings to be evaluated, in fast turn around times.

While the majority of thermal problems associated with turbomachinery discs and casings are usually dominated by convective heat fluxes, there are some instances where radiation can become significant, and must be accounted for in the heat transfer solution. Turbine casings with low external convective cooling are a typical example of where radiation effects must be included in the thermal model. The finite element methods of Armstrong & Edmunds (1) include full specification of radiative boundary conditions complete with automatic view factor calculation.

The ability of cooling air or annulus gas to penetrate even highly loaded flanged assemblies means that the effects of flange leakage must also be accounted for in the thermal model. The main problem in modelling such leakage is in determining the conditions under which such leakage will be present and representing the transient nature of the flow. However, with a comprehensive database of identified leakage from engine testing, together with flexible boundary condition input generation facilities, the thermal effects of flange leakage can be accounted for.

2.4 Thermo-Mechanical Coupling

Thermal and structural finite element analysis in support of clearance control and optimisation have conventionally been completed separately using codes developed for each type of analysis, with links to feed in previously calculated temperature distributions in specific deflection or stress predictions.

The automatic finite element analysis system now in use, has the capability to complete either separate or combined, linear or non-linear, thermal and mechanical analyses. This is having a significant effect not only on the time taken to complete clearance predictions but also in the technical methods used. Improvements in turn-around times of over 50% have been evident since the introduction of thermo-mechanical coupling. By using a common model for the temperature and displacement calculations unnecessary duplication of work is eliminated and geometry and boundary conditions are defined only once. Static pressures and component rotational speeds specified for use in empirical heat transfer correlations, can also be used to apply pressure and centrifugal loads in the structural analysis.

The coupling of temperature and displacement predictions also provides the opportunity for improvements in the technical methods used in some thermal problems. A good example of this is labyrinth seal clearance predictions. In this type of problem, temperature and displacement analyses of the rotating and static seal members are required to determine seal clearance characteristics and minimise parasitic air leakage. However, large transient changes in seal clearance are often experienced following severe engine throttle movements, causing large variations in seal flow, heat transfer and windage. The seal clearance characteristic, which is needed for the temperature calculation, thus depends on the displacement calculation. Combined thermo-mechanical analysis "opens up" the possibility of a linked interactive solution by the finite element system.

3. MODEL VALIDATION & RESULTS

Improvements in boundary condition predictive methods, coupled with a growing database of validation results, has led to greater accuracy in temperature predictions, but confirmation and correction of assumptions remain an essential part of thermal modelling. To aid the engineer in adjusting boundary assumptions, the finite element code includes inverse analysis capabilities, enabling the automatic optimisation of properties such as surface heat transfer coefficient to achieve agreement of the thermal model with component measurements to an accuracy required by the engineer. This approach not only reduces the time taken for the validation process, but also has the potential to identify new or improved Nusselt No. heat transfer correlations.

A number of techniques can be used to achieve model validation and ensure that the modelling accurately represents the true thermal behaviour. The principal methods used and application of the models are briefly described in the following sub-sections.

3.1 Temperature Validation

The temperature validation process consists of the detailed measurement of rotor disc and casing metal temperature distributions using thermocouples at selected key locations. Typically a six stage axial flow compressor validation test will include in excess of 250 thermocouples to identify axial, radial and circumferential temperature variations. In addition to the metal temperature data, where possible, the measurement of surrounding fluid properties (pressure, temperature) is completed to ensure accurate representation of convective boundary conditions in the thermal model. Figures 6a & 6b show typical instrumentation locations for a turbine disc validation test.

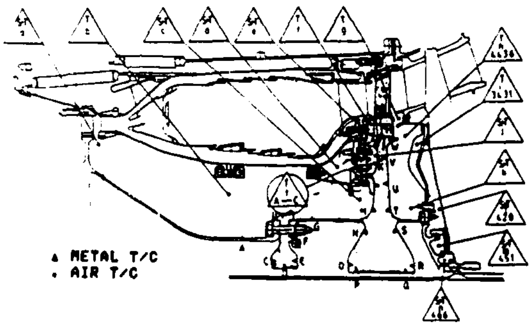

FIGURE.6A. INSTRUMENTATION FOR TURBINE DISC VALIDATION TEST

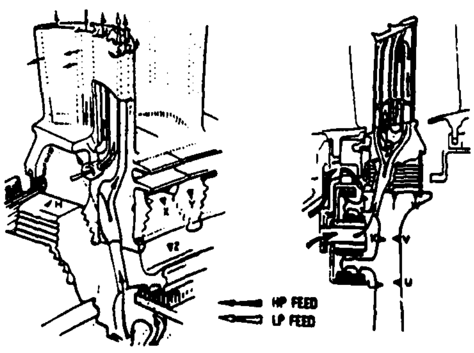

FIGURE.6B. INSTRUMENTATION FOR 3D MODEL VALIDATION

One of the primary objectives of temperature validation is confirmation of heat transfer coefficient assumptions. Measurements are taken over specific transient cycles that lead to severe convective heat fluxes. By comparison of the temperatures predicted by the model with those measured on the discs and casings, it is possible to ensure that the thermal behaviour of the model accurately reproduces the measured characteristics at all transient and steady state operating conditions. Figure 7a shows a comparison between thermal model predictions and disc temperature measurements at a steady state engine condition. Temperature comparisons for a single location of a typical transient cycle are shown in Figure 7b.

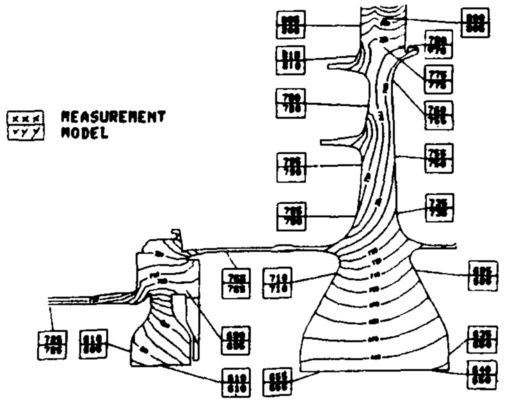

FIGURE.7A. STEADY STATE DISC TEMPERATURE VALIDATION

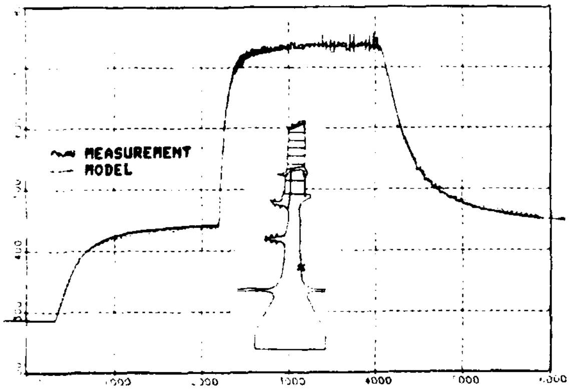

FIGURE.7B. TRANSIENT DISC TEMPERATURE VALIDATION

3.2 Displacement Validation

While component temperature measurements play an important role in the validation of thermal movements, it is also necessary to validate displacement predictions to confirm structural modelling assumptions. Displacement validation can include a variety of different measurement techniques, which include:

x-rays transient	- steady state and video recording provides relative movements for use in the optimisation of annulus line definition, labyrinth seal clearances and rotor blade tip clearances. This technique is particularly useful for otherwise inaccessible locations, and is inobtrusive (does not disturb the feature being measured).
tip clearance probes	- direct measurement of rotor path clearance ensures correct disc and casing modelling, including 3 dimensional effects.
ovality probes	- usually utilised in combination with tip clearance probes, localised casing distortions can be identified.
strip data	- dimensional measurement of rotor and casing or labyrinth seal members following engine running may be used in comparison with clearance/closure characteristics predicted by the thermal/structural model for the same engine running.

As with temperature validation, the difficulty in accurately predicting component deflections means revision of modelling assumptions may be required.

Figure 8. gives a comparison of predicted closure for a turbine labyrinth seal and x-ray derived measurements for a square cycle accel/decel test. These results highlight the close coupling required between thermal and structural modelling, with the transient changes in seal clearance causing large variations in seal flow, heat transfer, windage and temperature rise.

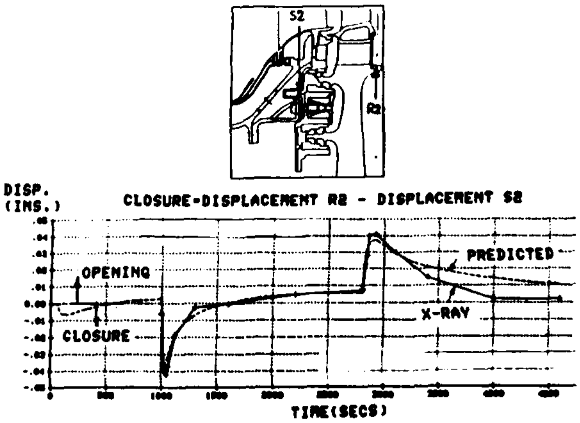

FIGURE.8. COMPARISON OF PREDICTED AND X-RAY CLOSURE CHARACTERISTICS FOR LABYRINTH SEAL

3.3 Results

Once the validity of a thermal model has been established, temperature and displacement predictions can be reliably calculated for any required transient altitude or test bed cycle. The thermal model results are ultimately used in further detailed stressing or performance calculations and analysis of model results can facilitate productive design optimisation.

Figure 9 shows predicted casing temperature distributions for a turbine casing assembly subject to external impingement cooling, internal contact resistance and local gas leakage. Accurate prediction of these temperatures is critical in determination of rotor tip clearances and casing integrity.

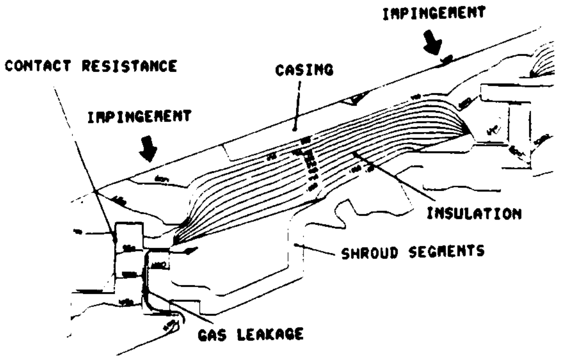

FIGURE.9. PREDICTED TEMPERATURES FOR A TURBINE CASING ASSEMBLY

3D temperatures used to calculate local stresses around the blade cooling air feed holes in a turbine disc rim are given in Figure 10. 3D thermal modelling of this area helped to provide understanding of why the holes were not the life-limiting feature predicted by a 2D analysis.

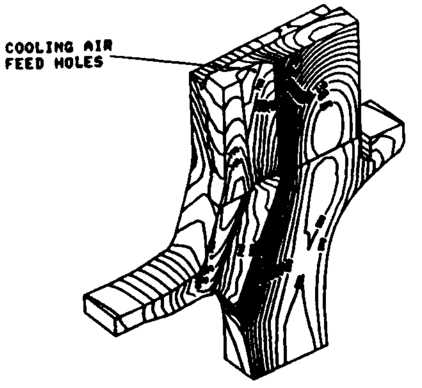

FIGURE.10. PREDICTED 3D TEMPERATURE DISTRIBUTIONS AROUND BLADE COOLING AIR FEED HOLES OF TURBINE DISC MODEL

4. PROBLEM AREAS

Through experience of producing and validating thermal models certain areas where problems are most frequently encountered and where further work would be useful can be identified. Some of these are highlighted in this section.

Not surprisingly, many of these areas correspond to situations where the physics is not well understood or there is a lack of relevant data available. Others are related to the need for fast job turn-around times and minimum cost of the thermal modelling.

Some problems are relevant to compressor rotor, turbine rotor and casings, others are more component specific. Considering first the more general problem areas, the need for efficient mechanisms for incorporating CFD predictions in the thermal modelling process is worth emphasising. Ideally, from the modeller's viewpoint, the heat conduction and CFD calculations should be fully linked, but this would require considerable computing resource and may increase job turn-around times unacceptably. While recognising that CFD will give improvements in predictive capability in the future, such limitations as turbulence modelling, high computing cost and poor code robustness must also be acknowledged. At present application of CFD codes must be supervised by specialists, only certain classes of flow can be reliably predicted, and considerable judgement is required in applying results to the thermal model.

The extent to which three-dimensional effects can be properly accounted for in the axisymmetric models is clearly limited. Such effects as heat conduction from blades to disc, around cooling air holes and bolt-heads, and many casing geometries are intrinsically three-dimensional. A move towards more three-dimensional analysis can therefore be expected in the future. For a rigorous treatment, the three-dimensional nature of the convective boundary conditions will also have to be modelled; this will certainly present further problems to the design engineer.

In compressors, both the inter-disc cavities and the 'stator well' cavities just inside the mainstream annulus (see Figure 11) can present modelling problems.

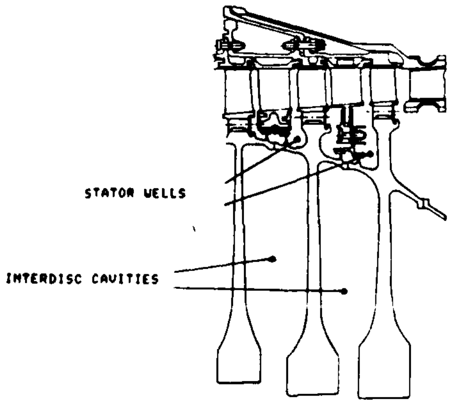

FIGURE.11. COMPRESSOR STATOR WELL AND INTERDISC CAVITIES

For a cavity between co-rotating discs with a central axial throughflow, but no net radial flow, it has been found that the nature of the convection following an engine acceleration may be quite different from that during a deceleration. This is consistent with buoyancy effects being important as the rotor temperature distributions are quite different for these two conditions. Research studies for this problem indicate that the flow may be both three-dimensional and unsteady (Farthing et al (18)).

For stator wells, it is thought that windage heating, blade platform and root leakage, seal clearances, mainstream gas ingestion, and recirculation of hot air ejected from the front half of the wells back into the rear half of the well can significantly affect the heat transfer. The significance of each of these effects depends on the detailed design and temperature prediction can be both difficult and time consuming.

In turbines, mainstream gas ingestion is perhaps the prime area of difficulty. As discussed above CFD is beginning to contribute to an understanding of this problem, but further work is needed. Impingement of inclined jets onto rotating components, as may occur in a pre-swirled blade cooling feed system, is a further situation for which there is a lack of data.

For casings, natural convection can be an important heat transfer mechanism and there is some uncertainty regarding the effect of vibration here. Other problems to be addressed in casing modelling include impingement heating or cooling and contact resistances.

The above survey of problem areas is by no means complete but illustrates the limitations of current methods. As there are considerable differences between engine geometries and as designs continue to evolve, so new challenges are continually presented to the thermal modeller. Concepts such as active tip clearance control and contra-rotating engines may need to be modelled in the future and so the need is for generally applicable modelling methods as opposed to correlations for specific applications.

5. CONCLUSIONS

Thermal modelling of discs and casings is a valuable element of the engine design process. When properly validated, models give useful estimates of temperature distribution for stress and movement calculations. With an advanced finite element solver for the heat conduction problem, used in conjunction with powerful geometry and boundary condition software, thermal predictions can be readily attained and design proposals fully assessed.

Further benefits could be obtained from thermal modelling if more general modelling techniques could be developed, so reducing the reliance on engine test validation. Some progress is being made towards this with application of recent research results and CFD methods. Prospects for continued improvement are good as increasing computing power will undoubtably allow more flexibility in the modelling. In particular, increased use of CFD and three-dimensional heat conduction solutions is expected. It should be noted, however, that some formidable problems must be resolved before fully comprehensive and reliable predictions are possible.

ACKNOWLEDGEMENTS

The authors gratefully acknowledge contributions to this paper from our colleagues in the Heat Transfer and Systems groups at Rolls-Royce plc.

REFERENCES

1. Armstrong, I. and Edmunds, T. M., "Fully Automatic Analysis in the Industrial Environment", in Proc. second Int. Conf. on Quality Assurance and Standards in Finite Element Analysis, NAFEMS, 1989.
2. Long, C.A. and Tucker, P.G., "Shroud Heat Transfer Measurements from a Rotating Cavity with an Axial Throughflow of Air". ASME paper 92-GT-69., Koln, 1992.
3. Waschka, W., Wittig, S. and Kim, S., "Influence of High Rotational Speeds on the Heat Transfer and Discharge Coefficients in Labyrinth Seals."ASME paper 90-GT-330, 1990.
4. Childs, P.R.N., Turner, A.B., Vaughan, C.M., Rayner, D. and Bayley, F.J. "Heat Transfer to a Rotating Drum in an annulus with a Stator Blade Row and Axial Throughflow". ASME paper 92-GT-249, 1992.
5. Daily, J.W. and Nece, R.E., "Chamber Dimension Effects on Induced Flow and Frictional Resistance of Enclosed Rotating Disks". ASME J. Basic Engineering, 1960, pp 217-232, 1960.
6. Downs, S.F. and James, E.H., "Jet Impingement Heat Transfer - A Literature Survey" ASME paper 87-HT-35, 1987.
7. Moss M.A."A Knowledge Based Database System For Jet Impingement Heat Transfer" Nottingham Polytechnic Thesis, 1992.
8. Owen, J.M., "Air-cooled Gas Turbine Discs: A Review of Recent Research." Int. J. Heat and Fluid Flow, vol. 9, pp. 354-365, 1988.
9. Chew, J.W., "Prediction of Rotating Disc Flow and Heat Transfer in Gas Turbine Engines" Proc. third Int. Symp. on Transport Phenomena and Dynamics of Rotating Machinery, 1990.

10. Chew, J.W. and Rogers, R.H., "An Integral Method for the Calculation of Turbulent Forced Convection in a Rotating Cavity with Radial Outflow" Int. J. Heat and Fluid Flow, vol. 9, pp 37-48, 1988.

11. Iacovides, H and Chew, J.W., "The Computation of Convective Heat Transfer in Rotating Cavities" Int. J. Heat and Fluid Flow, To appear

12. Virr, G.P. unpublished work, Rolls-Royce 1991.

13. Bayley, F.J. and Owen, J.M., "The Fluid Dynamics of a Shrouded Disk System with a Radial Outflow of Coolant". ASME J. Engng Power, vol, 92, pp 335-341. 1970.

14. Daniels, W.A., Graber, D.J., Martin, R.J. and Johnson, B.V., "Rim Seal Experiments and Analysis for Turbine Applications". ASME paper 90-GT-131, 1990.

15. Chew, J.W., Dadkhah, S. and Turner, A.B., "Rim Sealing of Rotor-Stator Wheelspaces in the Absence of External Flow" ASME paper 91-GT-33, 1991.

16. Campbell, D.A. "Gas Turbine Disc Sealing System Design "AGARD Conf on Seal Technology in Gas Turbine Engines, AGARD-CP-237. 1978. and Unpublished work, Rolls-Royce.

17. Green, T. and Turner, A.B., "Ingestion into the Upstream Wheelspace of an Axial Turbine Stage" ASME paper 92-GT-303, 1992.

18. Farthing, P.R., Long, C.A., Owen, J.M. and Pincombe, J.R., "Rotating Cavity with Axial Throughflow of Cooling Air: Flow Structure" ASME paper 90-GT-17, 1990.

Discussion

QUESTION 1:

DISCUSSOR: N. Selçuk, Middle East Technical University

Which type of radiative boundary condition have you used in your model?

AUTHOR'S REPLY:

The finite element program includes an option for radiative heat transfer between surface zones using the view factor method with gray body assumptions.

QUESTION 2:

DISCUSSOR: D.K. Hennecke, Darmstadt

For the calculation of disk temperatures you need the temperature, mass flow and transient temperature variation of the surrounding air. Do you calculate the values starting at the source of the flow and follow it along its way to the turbine disk or do you use measurements? In particular, did you employ calculated or measured values in Figure 7?

AUTHORS' REPLY:

CHEW: We generally do include energy balances along the flow path from the source to the disc to give the air temperature. Validation tests included air temperature measurements and if necessary the initial model was corrected to ensure correct reproduction of the local air temperature. My colleague Jeff Dixon may be better able to answer your question concerning Fig. 7.

DIXON: In Figure 7 the air temperatures adjacent to the side surface are calculated within the model and compared with the measured cooling air temperatures. The air temperature at position k from figure 6a is the relevant boundary condition for metal temperature position T on the disc, shown as a time-history plot in figure 7b. The model determines 'its own' transient boundary air temperatures, mass flows and heat transfer coefficients, starting from the off-take position (i.e., main annulus position).

QUESTION 3:

DISCUSSOR: M. Owen, University of Bath

It is encouraging that considerable progress has been made in applying computational techniques to engine design and that the pace of this program is likely to quicken over the coming years. It is even more encouraging for research workers that there are still many unsolved rotating disc problems for the future.

Could you explain how the heat transfer coefficient was calculated for the computation shown in Figure 7a,b?

AUTHOR'S REPLY:

CHEW: A factored free-disc heat transfer coefficient was used for the turbine disc. The factor was kept constant throughout the test cycle.

DIXON: The standard free-disc correlation is used for the disc position shown as a time-history plot in the figure 7b. The good thermal matching is obtained with factors close to 1.0 at this and similar locations based on local air temperature. Other locations also shown in Figure 7a of the paper require different correlations as appropriate, e.g. a modified duct flow correlation in the disc core, and a modified natural convection correlation in the rotating cavities inboard of the drive arms.

Again factors and correlations are kept constant throughout the power range and during accelerating and decelerating portions of the cycle. It is very important to use the local air temperature to get the right heat flux for thermal matching in this class of problems.

FLOW AND HEAT TRANSFER BETWEEN GAS-TURBINE DISCS

X. Gan, M. Kilic and J.M. Owen
School of Mechanical Engineering
University of Bath
Claverton Down, Bath, BA2 7AY, UK

SUMMARY

The paper provides both a brief review of some recent research into the flow and heat transfer associated with the turbine and compressor discs of gas-turbine engines and some new results for flow between contra-rotating turbine discs. Elliptic solvers, parabolic solvers and integral methods have all been applied successfully to some important axisymmetric boundary-layer-dominated flows, and multigrid elliptic solvers used in conjunction with parallel computers offer great promise for the future computation of nonaxisymmetric flows. LDA velocity measurements and computations have given fresh insight into the flow between contra-rotating turbine discs. Batchelor-type flow, in which there are boundary layers on the discs and a shear layer in the midplane, has been computed for laminar flow but has not been observed in practice, even at local rotational Reynolds numbers as low as 2.2×10^4. The actual flow structure comprised radial outflow in boundary layers on the discs and a central core of radial inflow in which rotational effects were weak. Although the flow in the core was always turbulent, the flow in the boundary layers was laminar for rotational Reynolds numbers up to at least 1.2×10^5. Agreement between the computed turbulent velocities and the measured values was good for Reynolds numbers above 4.5×10^5.

LIST OF SYMBOLS

a, b	inner, outer radius of disc	
c	constant or inlet swirl-fraction	$(= V_\phi/\Omega r$ at $r = b)$
C_d	discharge coefficient	
C_m	moment coefficient	$(= M/\tfrac{1}{2}\rho\Omega^2 b^5)$
C_p	specific heat at constant pressure	
C_P	pressure coefficient	$(= \Delta p/\tfrac{1}{2}\rho\Omega^2 b^2)$
C_w	nondimensional flow rate (positive for radial outflow, negative for inflow)	$(=Q/\nu b)$
G	gap ratio	$(=s/b)$
G_c	shroud-clearance ratio	$(=s_c/b)$
Gr_x	Grashof number	$(=\Omega^2 r^4 \beta \Delta T/\nu^2)$
k	thermal conductivity of fluid	
$\dot{m}$	mass flowrate	
M	frictional moment on one side of disc	
n	exponent for power-law temperature profile	
Nu	local Nusselt number	$(=q_s r/k(T_s - T_{ref}))$
Nu*	modified local Nusselt number	$(= q_s r/k(T_s - T_{s,ad}))$
p	static pressure	
Pr	Prandtl number	$(= \mu C_p/k)$
q	heat flux from disc to cooling air	
r	radial location	
Re_w	external flow Reynolds number	$(= Wb/\upsilon)$
Re_z	axial Reynolds number	$(=2Wa/\upsilon)$
Re_ϕ	rotational Reynolds number	$(=\Omega b^2/\upsilon)$
s	axial clearance between discs or between rotor and stator	
s_c	shroud clearance	
T	temperature	
U	representative velocity	
V_r, V_ϕ, V_z	radial, tangential, axial components of velocity in a stationary frame	
W	appropriate axial component of velocity	
x	nondimensional radius	$(=r/b)$
x_a	radius ratio	$(=a/b)$
z	axial distance from disc	
β	coefficient of volumetric expansion	
Δp	pressure difference	
ΔT	temperature difference	
λ_T	turbulent flow parameter	$(=C_w Re_\phi^{-0.8})$
μ	absolute viscosity	
υ	kinematic viscosity	(μ/ρ)
ρ	density	
ϕ	sealing effectiveness	$(=C_w/(C_w + C_{w,in}))$
Ω	angular speed of disc	

Subscripts

ad	adiabatic value
eff	effective value
fd	free-disc value
in	relating to ingress
max	maximum value
min	minimum value (to prevent ingress)
ref	reference value (inlet conditions for cavity)
∞	value at infinity

1. INTRODUCTION

Fig. 1 shows a schematic diagram of the rotating-disc systems used to model the flow and heat transfer associated with turbine and compressor discs in gas-turbine engines. Fig. 1a, the free disc, is the datum case for all rotating-disc systems although in the engine a disc usually rotates close either to a stationary casing, as in Fig. 1b, or to another rotating disc, as in Figs. 1c - 1f. Fig. 1c represents air-cooled corotating turbine discs, and Fig. 1d represents the case where air, for cooling the turbine, is extracted radially inward between two high-pressure compressor discs. In some aero-engines, the cooling air passes axially through the centre of a stack of compressor discs, and this case is modelled by Fig. 1e. Contra-rotating turbine discs, as shown in Fig. 1f, may be used in future generations of ultra-high-bypass-ratio engines to drive contra-rotating fans; contra-rotating turbine blades obviate the need for one row of stator blades, thereby saving weight and space. All these systems share certain characteristics.

It is convenient to define some of the nondimensional variables that specify the system. The nondimensional radii, x and x_a, are defined as

$$x = \frac{r}{b}, \quad x_a = \frac{a}{b} \tag{1.1}$$

the gap ratio, G, as

$$G = \frac{s}{b} \tag{1.2}$$

the shroud-clearance ration, G_c, as

$$G_c = \frac{s_c}{b} \tag{1.3}$$

the rotational Reynolds number, Re_ϕ, as

$$Re_\phi = \frac{\rho \Omega b^2}{\mu} \tag{1.4}$$

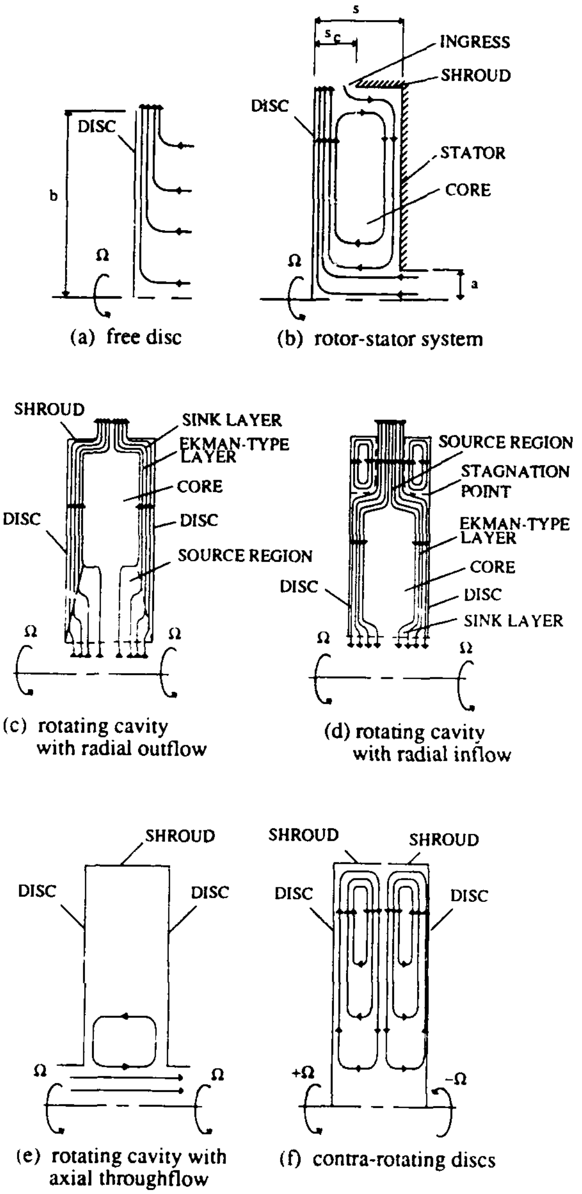

(a) free disc (b) rotor-stator system

(c) rotating cavity with radial outflow (d) rotating cavity with radial inflow

(e) rotating cavity with axial throughflow (f) contra-rotating discs

Fig. 1 Schematic diagram of rotating-disc systems

and the nondimensional flowrate (for a superposed inflow or outflow), C_w, as

$$C_w = \frac{\dot{m}}{\mu b} \qquad (1.5)$$

Two axial Reynolds numbers are used: Re_z for the rotating cavity with axial throughflow, and Re_w for the rotor-stator system with an external axial flow, where

$$\mathrm{Re}_z = \frac{2\rho W a}{\mu}, \quad \mathrm{Re}_w = \frac{\rho W b}{\mu} \qquad (1.6)$$

Although it is not an independent nondimensional parameter, the turbulent flow parameter, λ_T, is defined as

$$\lambda_T = C_w \mathrm{Re}_\phi^{-4/5} \qquad (1.7)$$

For flows in which buoyancy effects are important (as in the case of a heated rotating cavity with an axial throughflow of cooling air), the local Grashof number, Gr_x, is often defined as

$$Gr_x = \frac{\rho^2 \Omega^2 r^4 \beta \Delta T}{\mu^2} = \beta \Delta T \left(x^2 \mathrm{Re}_\phi\right)^2 \qquad (1.8)$$

where ΔT is the local temperature difference between the surface of the disc and the air at inlet to the system.

In addition to the above defining parameters, there are several nondimensional variables of importance to the engineer. The moment coefficient, C_m, is defined as

$$C_m = \frac{M}{\frac{1}{2}\rho \Omega^2 b^5} \qquad (1.9)$$

where M is the frictional moment on one side of the disc. The pressure coefficient, C_p, is defined as

$$C_p = \frac{\Delta p}{\frac{1}{2}\rho U^2} \qquad (1.10)$$

where Δp and U are representative pressure differences and velocities, respectively. (For example, for a rotating cavity, Δp is the radial pressure drop and $U = \Omega b$; for a rotor-stator system with an external axial flow, Δp is the circumferential pressure variation and $U = W$, the axial velocity of the external flow.)

The local Nusselt number, Nu, and the modified Nusselt number Nu*, are defined as

$$Nu = \frac{rq}{k\left(T_s - T_{ref}\right)}, \quad Nu^* = \frac{rq}{k\left(T_s - T_{s,ad}\right)} \qquad (1.11)$$

where T_{ref} is a suitable reference temperature (for example, the temperature of the air at inlet to the system) and $T_{s,ad}$ is the adiabatic-disc temperature (see ref. 1 for the details).

For the rotor-stator system in particular, the designer needs to estimate $C_{w,min}$, the minimum value of C_w necessary to prevent the ingress of hot mainstream gas into the wheel-space. In most gas turbines, $C_w < C_{w,min}$ and ingress occurs. Under these conditions, it is useful to define the sealing effectiveness, ϕ, as

$$\phi = \frac{C_w}{C_w + C_{w,in}} \qquad (1.12)$$

where $C_{w,in}$ is the nondimensional flowrate of the ingested fluid.

Another useful quantity, which is used as a datum flowrate by many research workers, is the nondimensional free-disc entrainment rate, $C_{w,fd}$, or the free-disc turbulent flow parameter, $\lambda_{T,fd}$, where (see ref. 1),

$$C_{w,fd} = 0.22\ \mathrm{Re}_\phi^{0.8}, \quad \lambda_{T,fd} = 0.22 \qquad (1.13)$$

For turbine-disc cooling, C_w is usually less than $C_{w,fd}$.

Before discussing rotating-disc systems in more detail, it may be helpful to highlight some of the important characteristics of isothermal rotating cavities with a superposed radial inflow or outflow. In both these "source-sink flows", there is a source region that distributes the incoming flow into the boundary layers on the discs : in the source region, the boundary layer entrains fluid; outside the source region, nonentraining Ekman-type layers are formed. The flow leaves the cavity via the sink layer, and the interior core between the sink layer, the Ekman-type layers and the source region rotates with a tangential velocity, V_f : for radial outflow in the boundary layers, $V_\phi < \Omega r$; for inflow, $V_\phi > \Omega r$.

The flow in the source region approximates to a free vortex where

$$\frac{V_\phi}{\Omega r} = c_{eff} x^{-2} \qquad (1.14)$$

where the constant c_{eff} is referred to as the "effective swirl fraction". If, for radial inflow, the air enters the cavity with a tangential velocity equal to that of the peripheral shroud, such that c_{eff} is unity, then equation (1.14) suggests that, for $x << 1$, $V_\phi >> \Omega r$, and the resulting pressure drop can be very large. If, however, $c_{eff} < 1$, then equation (1.14) implies that $V_\phi = \Omega r$ when $x = \sqrt{c_{eff}}$; for $x > \sqrt{c_{eff}}$, the flow in the boundary layer is radially outward, and for $x < \sqrt{c_{eff}}$ it is radially inward. This creates the recirculation inside the source region shown in Fig. 1d, and the mixing that occurs between the recirculating fluid and the incoming air means that the magnitude of the "effective swirl fraction" differs from the "initial swirl fraction" that is imparted to the incoming air by the holes or nozzles in the shroud. As discussed below, this effect can be used to advantage to control V_ϕ and to reduce the pressure drop associated with extracting cooling air between corotating compressor discs.

The need to improve the effectiveness of the internal-air systems of gas-turbine engines has led to a large increase in the research carried out over the last few years. The first volume of the research monograph by Owen and Rogers (1) concentrated on rotor-stator systems, and the second volume, which should appear next year, will deal mainly with rotating cavities; comprehensive reviews of rotating-disc systems are also given in refs. 2 and 3. In Sections 2 and 3 of the paper, an outline is given of recent computational developments and experimental measurements for rotating-disc systems in general, and Sections 4 and 5 concentrate on some new experimental and computational results for contra-rotating discs in particular.

2. RECENT DEVELOPMENTS IN COMPUTATIONAL TECHNIQUES

2.1 Elliptic solvers

Elliptic solvers using TEACH-type finite-volume methods have proved effective for computing the flow and heat transfer in many rotating-disc systems. The version of the low-Reynolds-number k-ε turbulence model developed by Morse (4-7) has been used to obtain good agreement with experimental data for rotating cavities and rotor-stator systems. Fig. 2 shows a comparison between the tangential velocities computed by Morse (4) and the values measured by Pincombe (8) for a rotating cavity with a radial outflow of air.

Lapworth and Chew (9) were able to obtain good agreement with experimental data for a number of systems using the mixing-length model, which is usually adequate for those flows that are dominated by the boundary layers on the discs. Iacovides and Theofanopoulos (10) used a "zonal turbulence modelling approach" in which one of two mixing-length models was used in the boundary layers and either the k-ε model or the algebraic-stress model was used in the turbulent core region outside the boundary layers. They compared their computed results with experimental data for both rotor-stator systems and rotating cavities, and concluded that the modelling of the turbulent core was of marginal importance in these boundary-layer-dominated flows. Neither of the two mixing-length models tested was universally successful; one worked better for rotor-stators, and the other for rotating cavities.

Multigrid methods are proving to be an effective way of reducing the long computing times necessary to achieve so-called grid-independent solutions. By using a series of progressively coarser grids, it is possible to accelerate the reduction of "low-frequency" errors, which are difficult to reduce on a fine grid. As a consequence, linear convergence (where the computing time is proportional to the number of fine grid nodes) can be achieved rather than the quadratic convergence associated with conventional iterative schemes. This technique was first applied to laminar rotating-disc systems by Lonsdale (11), and his work was later extended by Vaughan *et al* (12) to include variable-property fluids, turbulent flow and heat transfer. Using a mixing-length model, with the van Driest modification, the authors computed the flow in a rotor-stator system at $Re_\phi = 4.4 \times 10^6$ using a 65 x 65 grid and achieved a saving of computing time of 87% compared with a single-grid solver. Recently, Wilson *et al* (13) have modified this multigrid solver for use on a parallel computer. For laminar flow in a rotor-stator system, the combined use of multigrid and four processors gave a speed -up of over 20 compared with single-grid computations on one processor; for turbulent flow, using a variant of Morse's low-Reynolds-number k-ε model, the equivalent speed-up was seven.

Many of the rotating-disc flows associated with gas-turbine engines are three-dimensional and unsteady, and multigrid methods and parallel computing are likely to play an important part in these difficult computations. However, for boundary-layer-dominated flows, the methods outlined below may be more appropriate.

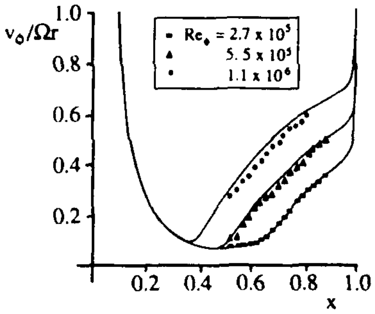

Fig. 2 Radial variation of $v_\phi/\Omega r$ in the midplane of a rotating cavity with a radial outflow of air for $C_w = 2500$.
— computation of Morse (4)
Data of Pincombe (8)

2.2 Parabolic solvers

Ong and Owen (14-16) have applied an efficient parabolic solver, based on the Keller Box method, to the flow and heat transfer associated with free discs and rotating cavities. For turbulent flows, a mixing-length model, with the van Driest modification, was found to give good agreement with measured velocity profiles, moment coefficients and Nusselt numbers. Fig. 3 shows a comparison between the Nusselt numbers computed by the parabolic solver and those measured by Northrop and Owen (17) for a free disc.

Reverse flow can occur in the boundary layers on discs rotating in a fluid that is itself rotating (see ref. 1). For a rotating cavity with a radial outflow of fluid, there is a region of radial inflow at the edge of the boundary layer. As parabolic solvers integrate the equations by "marching" in the radial direction, this reverse flow presents a problem. Although this can be overcome by iterating alternately in the positive and negative radial directions, in practice the reverse flow region has little effect on the accuracy of the computed moment coefficients and Nusselt numbers.

Parabolic solvers are very fast, taking around five minutes of computing time on a VAX 8530 computer to solve the boundary-layer equations using a grid with around 100 axial grid nodes. (For elliptic solvers, most computation is carried out with less than 100 axial grid nodes across the entire cavity, and computing times are measured in hours rather than minutes.)

2.3 Integral methods

For boundary-layer-dominated flows, integral methods are simple to use, are computationally efficient and can produce solutions for moment coefficients, pressure coefficients and Nusselt numbers that are accurate enough for most engineering applications.

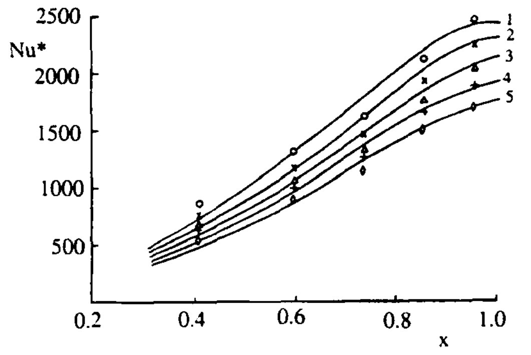

Fig. 3 Radial variation of local Nusselt numbers for the free disc: Pr = 0.71

Experiment (ref. 17)	○	×	△	+	◇
Computed curve (ref.16)	1	2	3	4	5
$Re_\phi/10^6$	3.20	2.66	2.40	2.14	1.88

The solution of the momentum-integral equations by Owen, Pincombe and Rogers (18) for flow in rotating cavities was extended by Chew and Rogers (19) to include variable-property fluids and the energy equation. For turbulent flow, the latter authors used power-law velocity profiles and a modified form of the Reynolds analogy. The second-order partial differential equations of the boundary layer are then integrated to produce three first-order nonlinear ordinary differential equations that can be solved by standard techniques, such as the Gear method.

Variations of this technique have been used successfully for rotating cavities and rotor-stator systems, and Fig. 4 shows the comparison between Nusselt numbers computed by the integral method and those measured by Northrop and Owen (20) for a heated rotating cavity with a radial outflow of cooling air. "Positive profile" refers to a radial distribution of disc-temperature that increases radially; "negative profile" refers to one that decreases radially. As can be seen, Nu depends on the temperature distribution, and for negative profiles negative values of Nu have been measured and computed.

3. SOME RECENT EXPERIMENTAL MEASUREMENTS

3.1 Rotating cavities

Northrop and Owen (20) measured the local Nusselt numbers in a rotating cavity with a radial outflow of cooling air, and determined the effect of Re_ϕ, C_w and disc-temperature distribution on the heat transfer. The Nusselt numbers have been computed successfully using the integral methods, parabolic solvers and elliptic solvers described in Section 2 at values of Re_ϕ up to 3.2×10^6. Farthing and Owen (21) conducted flow visualization and made heat transfer measurements for the case where "cobs", or bulbous hubs representative of those found on turbine discs, were attached to the centre of the discs. The flow structure was found to be similar to source-sink flow between plane discs (see Section 1) and, as long as the source region did not fill the cavity, the integral equations provided a reasonable estimate of the Nusselt numbers. For the radial inflow case, Farthing *et al* (22) compared measured Nusselt numbers on an experimental rig with those obtained from an instrumented compressor disc and with values computed using the integral equations. Although there were large experimental uncertainties, the overall agreement between the results was regarded as encouraging.

Two ways of reducing the large pressure drops associated with extracting cooling air radially inwards between corotating compressor discs were investigated in refs. 23 - 25. The first way was the attachment of radial fins to one of the discs; the second used peripheral de-swirl nozzles to control the swirl of the incoming air. For the finned disc, flow visualization revealed that the conventional source-sink flow structure still occurred inside the rotating cavity, and the integral equations were able to predict the resulting pressure drops with reasonable accuracy. Without the fins, free-vortex flow can result in pressure drops an order-of-magnitude greater than those associated with solid-body rotation; with the fins, the pressure drop can be reduced to little more than the solid-body value. Using de-swirl nozzles, it is possible to make c_{eff} zero (see equation (1.14)) thereby reducing the pressure drop downstream of the nozzles to virtually zero. However, the resistance of the nozzles themselves is such that the overall pressure drop in the system is always greater than that associated with solid-body rotation. Again, the integral equations produced acceptable predictions of the pressure drop and were able to explain some of the previously inexplicable phenomena associated with the use of de-swirl nozzles.

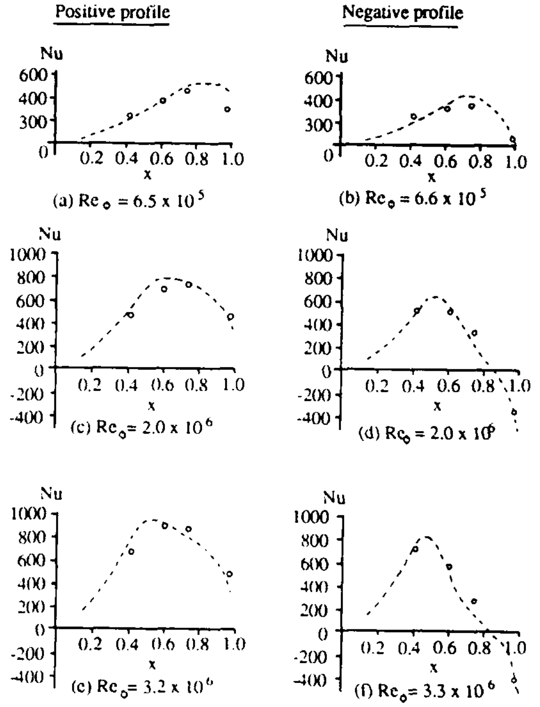

(a) $Re_\phi = 6.5 \times 10^5$ (b) $Re_\phi = 6.6 \times 10^5$ (c) $Re_\phi = 2.0 \times 10^6$ (d) $Re_\phi = 2.0 \times 10^6$ (e) $Re_\phi = 3.2 \times 10^6$ (f) $Re_\phi = 3.3 \times 10^6$

Fig. 4 Effect of disc-temperature profiles and Re_ϕ on radial variation of Nu for $C_w = 7000$
○, fluxmeter measurement (ref.20)
----, integral solutions (ref.19)

As discovered by Farthing *et al* (26,27) vortex breakdown and buoyancy-induced flow conspire to create a nonaxisymmetric flow structure inside a heated rotating cavity with an axial throughflow of cooling air. The Coriolis forces, associated with the simultaneous radial outflow of cold air and inflow of hot air, are created by cyclonic and anti-cyclonic circulations inside the cavity : the low and high pressure caused by these circulations creates a circumferential pressure distribution. The Nusselt numbers depend on Re_z and Gr_x (defined in equations 1.6 and 1.8) as well as on the radial distribution of the surface temperature of the discs. Some simple correlations were obtained that suggested that the free convection inside the cavity was laminar ($Nu \propto Gr_x^{1/4}$) rather than the turbulent ($Nu \propto Gr_x^{1/3}$) for Grashof numbers of order 10^{12}. The free convection is relatively weak, and radiation from the hot to the cold disc can be of a similar magnitude to that of the convection.

Long and Tucker (28) made measurements from the heated shroud of a rotating cavity with an axial throughflow of cooling air. They also measured the air temperature inside the cavity, and this showed cyclical variations with a period consistent with measurements of the tangential velocity in the core made by Farthing *et al* (26). The average Nusselt numbers for the shroud were similar in magnitude to those for laminar free convection from a horizontal plate (with the gravitational acceleration replaced by $\Omega^2 b$).

Although elliptic solvers have proved effective for source-sink flows, there is no published evidence, at the time of writing, of their successful use in computing accurately the Nusselt numbers for the axial-throughflow case.

3.2 Rotor-stator systems

Millward and Robinson (29) made heat transfer and windage measurements for an air-cooled disc, with and without boltheads attached to it, for rotational Reynolds numbers up to $Re_\phi = 1.7 \times 10^7$. The boltheads increased both the windage torque and the local heat transfer rates compared with a plane disc. However, for reasons the authors could not explain, the use of a bolt cover could actually reduce the windage torque compared with a plane disc. Daniels *et al* (30) made windage measurements up to $Re_\phi = 1.6 \times 10^7$ and found, like Zimmermann *et al* (31), the extra torque depended on the number, location and shape of the boltheads on the disc.

Bunker *et al* (32,33) used a transient thermochromic liquid-crystal technique to measure Nusselt numbers on an air-cooled acrylic disc up to $Re_\phi = 5 \times 10^5$. Air was injected by a nozzle located either at the centre of the disc or at one of three other radial locations; for large values of the gap ratio, G, the overall heat transfer was maximized by injecting the air at the centre; for small G, it was maximized by injecting at one of the other locations.

Staub (34) used a steady-state liquid-crystal technique to measure Nusselt numbers, in a model of a turbine wheel-space, for Re_ϕ up to 9×10^6. As well as supplying coolant (either Freon or air) though an inner seal, fluid was also injected through pre-swirl nozzles in the stator. He found that there is a "rotation-dominated regime", where Nu increases as Re_ϕ increases, and a "flow-dominated regime", where Re_ϕ has little effect on the heat transfer. The transition between the two regimes occurs when $C_w \approx C_{w,fd}$ (see equation (1.13)).

The "ingress-problem" mentioned in Section 1 has aroused considerable interest in the past few years (refs. 35-45). For the case where there is an external axial flow of fluid, representing the mainstream flow in a gas turbine, there is a "rotation-dominated regime" and an "external-flow-dominated regime". In the former regime, the pressure inside the wheel-space decreases, and ingress correspondingly increases, with increasing rotational speed; this is caused by the rotating core of fluid, between the boundary layers on the rotor and stator, creating a large radial pressure gradient in the wheel-space. In the latter regime, circumferential pressure variations in the external flow can allow the external flow to enter the wheel-space through the peripheral seals in regions of high external pressure and leave in regions of low pressure; under these conditions, the rotational speed has little effect on ingress.

For the rotation-dominated regime, Phadke and Owen (35) obtained correlations of $C_{w,min}$ with the shroud-clearance ratio, G_c, and the rotational Reynolds number, Re_ϕ, for a number of different seal geometries. They concluded that certain types of radial-clearance seals were superior to axial-clearance ones.

Daniels *et al* (39) made concentration measurements inside the wheel-space to quantify the nondimensional ingress, $C_{w,in}$. Using the definitions given in equations 1.7 and 1.12, they showed that the sealing effectiveness, ϕ, can be approximated by

$$\phi = 1 - e^{-\alpha\lambda_T} \qquad (3.1)$$

where α is a constant that depends on the seal geometry.

Chew (40) used the integral technique to estimate $C_{w,min}$, or $\lambda_{T,min}$, and proposed that, for $C_w < C_{w,min}$,

$$C_{w,in} = 0.2\left(C_{w,min} - C_w\right) \qquad (3.2)$$

from which it follows that

$$\phi = \frac{\lambda_T}{0.8\,\lambda_T + 0.2\,\lambda_{T,min}} \qquad (3.3)$$

For axial-clearance seals, his model showed reasonable agreement with the measurements of Daniels *et al* (39) and those of Chew *et al* (41).

For the external-flow-dominated regime, Phadke and Owen (37) used a simple one-dimensional model to show that

$$C_{w,min} = c C_d G_c \,\mathrm{Re}_z \sqrt{C_{P,max}} \qquad (3.4)$$

where c is an empirical constant, C_d the discharge coefficient for the seal, and G_c, Re_z and C_p are defined by equations (1.3), (1.6) and (1.10); $C_{P,max}$ is based on the maximum circumferential pressure difference in the external flow.

Hamabe and Ishida (45) extended the above model to calculate the sealing effectiveness for the external-flow-dominated regime. $C_{w,min}$ was calculated from equation (3.4) using measured values of the circumferential pressure distribution in the external flow and integrating this distribution to evaluate c. The values of ϕ calculated in this way were in good agreement with concentration measurements made in the wheel-space.

There is no published evidence that elliptic solvers have been used successfully to tackle the ingress problem. Like the heated rotating cavity with an axial throughflow, the problem provides a challenge for the CFD practitioner.

4. EXPERIMENTAL APPARATUS FOR CONTRA-ROTATING-DISC MEASUREMENTS

4.1 Rotating-disc rig

Fig. 5 shows a schematic diagram of the rotating-disc rig used for the measurements described below. Each disc, which is 762 mm diameter, can be rotated up to 4000 rev/min by means of a variable-speed electric motor, and the speed was measured to an accuracy of ±1 rev/min. The upstream disc and shrouds were made from transparent polycarbonate, which limited the speed to 1500 rev/min. Each shroud was mounted on silicon-foam rubber, of 12 mm radial thickness, which made the effective outer radius of the cavity (measured to the inner surface of the shrouds) b = 391 mm. The axial spacing between the two discs was s = 47 mm, and the axial clearance between the stationary shrouds was $s_c \approx 1$mm; the latter clearance tended to increase with increasing rotational speed, and the estimated value for the tests described below is around 4 mm.

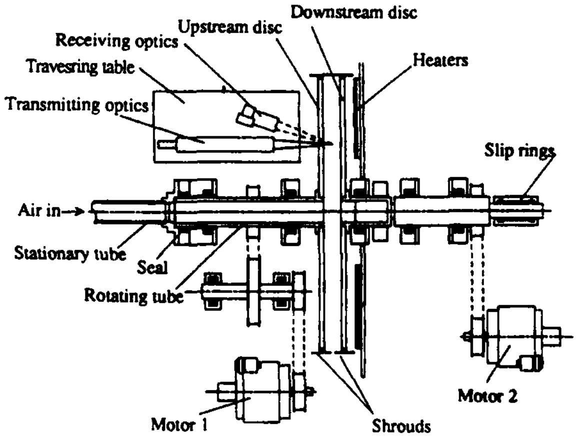

Fig. 5 Schematic diagram of contra - rotating - disc rig

The upstream disc, which could be rotated in either direction, was mounted on a hollow shaft through which air could be supplied to the system by means of a centrifugal compressor. The air entered the cavity, at a radius of a = 50 mm, through a rotating, cylindrical, porous surface; the latter was made from two gauze tubes, each attached to one of the discs. The downstream disc, which was made from steel, was instrumented with fluxmeters and thermocouples, the signals being taken out via sliprings to a computer-controlled data-acquisition system. This disc could be heated to around 100°C by stationary radiant electric heaters.

The tests described below were conducted under isothermal conditions with no superposed flow of air.

4.2 Optical instrumentation

Velocity measurements were made using a single-component laser Doppler anemometry (LDA) system. The system comprised a 4W Spectra Physics 164A argon-ion laser, TSI transmitting optics, frequency shift and receiving optics, and a TSI IFA-750 signal processor. The optics were mounted on an x-y traversing table in an off-axis back-scatter configuration, as shown in Fig. 5. The laser was connected to the transmitting optics by a fibre-optic cable, and the wavelength and power at the probe volume were 514.5 nm and 200 mW respectively. A Bragg-cell acousto-optic modulator provided a frequency shift of 40 MHz, and this was "down-mixed" to produce a frequency shift in the range 2 KHz to 10 MHz. The beam spacing was 50 mm, and a converging lens of 120 mm focal length produced a probe volume of 0.34 mm length, 34 μm diameter and a fringe spacing of 1.39 μm.

The IFA-750 processor is a "burst correlator" capable of measuring Doppler signals up to 90 MHz with signal-to-noise ratios (SNR) as low as -5dB. It was used in conjunction with a Viglen II PC to provide a computer-controlled system of measurement. As soon as the Doppler signal had been validated by the processor, the PC controlled the movement of the x-y table, positioning the optical probe volume in its next location. It was possible to achieve an entire axial distribution of either the radial or the tangential component of velocity without user control. It was necessary, however, to rotate the transmission optics manually through 90° to obtain the second component.

The optical axis was normal to the polycarbonate disc, and the probe volume could be located with an axial uncertainty of 0.13 mm by using a "target" on the stationary steel disc. It should be pointed out, however, that neither disc was flat : the steel disc had a "run-out" of around ±0.25 mm and the polycarbonate disc ±1.1 mm. Despite this, it was possible to obtain velocity measurements as close as 0.5 mm from the polycarbonate disc, but flare from the steel disc meant that under some conditions it was not possible to get closer than 1.5 mm. The spectral distribution of the Doppler frequency produced by the IFA-750 processor meant that the presence of the disc could be readily detected as a second peak in the distribution; this could be filtered out to remove the disc contribution from the signal, and it was therefore possible to obtain measurements close to the polycarbonate disc despite the large run-out. It was also possible to obtain signals when the probe volume was actually inside the polycarbonate disc : this was used to validate the measured tangential component of velocity which, at the disc surface, was within 0.5% of the independently-measured angular speed of the disc.

For the tests described below, the air inside the cavity was "seeded" with oil particles, of around 1 μm diameter, produced from a Dantec particle generator. The particles were released into the air surrounding the disc, and sufficient numbers were ingested into the wheel-space, through the clearance between the shrouds, to produce satisfactory Doppler signals. For the radial component of velocity, however, it could take up to one minute to obtain the 2000 samples necessary to achieve a validated measurement.

5. FLOW BETWEEN CONTRA-ROTATING DISCS

5.1 Numerical solutions

The multigrid elliptic solver described by Wilson *et al* (13) was used for the computations described below, and the basic equations and the k-ε turbulence model are listed in the Appendix. The turbulence model was not completely integrated into the multigrid scheme : the k-ε equations were solved only on the finest grid, and restricted values and defects were not updated on the coarser grids. Only one i860 processor of the Meiko 16-node computing surface used by Wilson *et al* was employed for the computations described here.

Advantage was taken of the geometrical symmetry about the midplane, z = 1/2s. Computations were carried out only for $o \leq z \leq 1/2s$, and the computed velocities were "reflected" about the midplane to enable comparisons with experimental data for $0 \leq z \leq s$. A 65 x 113 (axial x radial) nonuniform grid was used : grid expansion factors were employed to ensure fine grid spacing near the disc and shroud (and, for laminar flow, near the midplane). For turbulent flow, there were several grid nodes in the viscous sublayer on the disc. Morse (5) suggests that a value of $y+ < 0.5$ for the first node near the wall should ensure sensible grid-independence of the computed moment coefficients; this condition was applied to the computations discussed below. The convergence for the numerical solution was based on the normalized root-mean-square (RMS) change per iteration for each of the computed variables; a normalized RMS change of 10^{-4} was used as the criterion. For turbulent flow, using a 3-level multigrid, the typical computing time on a single i860 processor was around one hour.

Fig. 6 shows the computed velocity profiles for laminar flow at $Re_\phi = 2.3 \times 10^5$ and G = 0.12 This reveals the flow structure predicted by Batchelor (46) from consideration of the solutions for laminar flow between infinite rotating discs. He deduced that there should be radially outward flow in thin boundary layers on the discs and radially inward flow in a thin shear layer in the midplane; contra-rotating cores of fluid occur between the shear layer and the boundary layers, and fluid moves axially across the core from the shear layer to be entrained by the boundary layers.

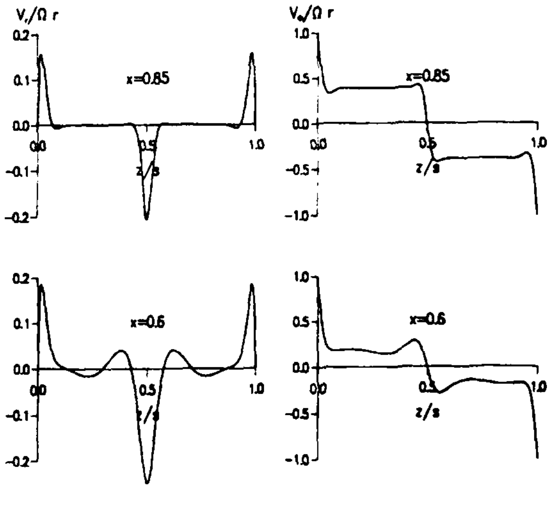

Fig. 6 Computed laminar velocity profiles between contra-rotating discs: G = 0.12, $Re_\phi = 2.3 \times 10^5$

Stewartson (47) came to different conclusions and maintained that, although boundary layers would form on the discs, there would be neither a shear layer nor contra-rotating cores.

The so-called Batchelor-Stewartson controversy has been the subject of many studies, and the interested reader is referred to the comprehensive review of Zanbergen and Dijkstra (48) for further details. Suffice it to say here that there are multiple solutions for the infinite-disc problem, of which Batchelor's and

Stewartson's are but two possibilities. For finite geometries, however, there is usually only one solution : for the computations shown in Fig. 6, Batchelor-type flow occurs.

The fact that a flow can be computed does not, of course, mean that it can exist in the real world. Fig. 6 shows that there are many points of inflexion in the velocity profiles, particularly in the shear layer, and these are associated with instability. Not shown in Fig. 6 are the thin boundary layers on the shrouds in which two contra-rotating flows move axially towards each other to meet in the midplane. Whilst the computations ensure that this flow remains laminar, nature does not. This is discussed below.

5.2 Comparison between computed and measured results

Figs. 7 and 8 show the computed and measured velocities, from x = 0.6 to 0.85, for G = 0.12 and $Re_\phi = 2.3 \times 10^5$ and 1.25×10^6 respectively. Referring to Fig. 7, the following observations can be made.

(i) Neither the measurements nor the computed turbulent velocities show the Batchelor-type flow structure displayed by the computed laminar results. Instead of the thin shear layer and the two contra-rotating cores, radial inflow occurs inside a large central core that extends between the boundary layers on the discs and in which the tangential velocity is relatively small.

(ii) For x = 0.6 and 0.7, there is good agreement between the computed laminar radial velocities and the measured values in the boundary layers on the discs; for x = 0.85, there is good agreement between the computed turbulent radial and tangential velocities and the measured values.

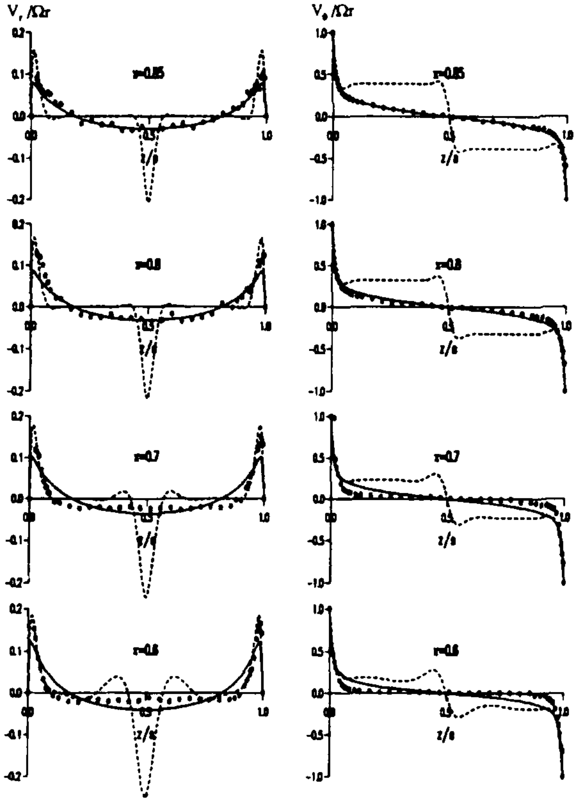

Fig 7 Comparison between computed and measured velocity profiles between contra-rotating discs: G = 0.12, $Re_\phi = 2.3 \times 10^5$.
— — laminar computations;
—— turbulent computations;
o experimental measurements.

These observations lead to the following conclusions.

(i) There is no evidence of laminar flow in the core even at local rotational Reynolds numbers as low as $x^2Re_\phi = 8.28 \times 10^4$. (Measurements made at rotational speeds of around 60 rev/min have found no evidence of laminar flow in the core at local Reynolds numbers as low as $x^2Re_\phi = 2.2 \times 10^4$.) This is attributed to the inherent instability of Batchelor-type flow.

(ii) The boundary layers on the discs remain laminar until at least $x^2Re_\phi = 1.1 \times 10^5$. Transition starts before $x^2Re_\phi = 1.47 \times 10^5$, and the flow becomes fully turbulent before 1.66×10^5.

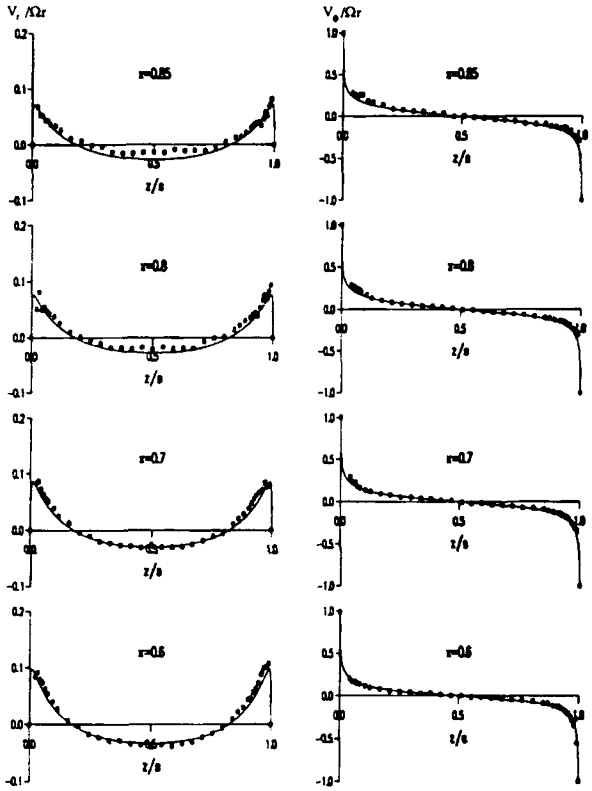

Fig 8. Comparison between computed and measured velocity profiles between contra-rotating discs : G = 0.12, $Re_\phi = 1.25 \times 10^6$.
—— turbulent computations;
o experimental measurements.

(For the free disc, see ref. 1, laminar flow usually becomes unstable around $x^2Re_\phi = 2 \times 10^5$ and transition to turbulence is usually complete by 3×10^5. A highly polished disc can delay transition; surface roughness or atmospheric disturbances can advance it.) For the contra-rotating discs, the high turbulence level in the flow entrained by the discs from the central core is presumed to be responsible for the early transition. The turbulence model exhibits "premature transition" : computed transition on the discs starts before $x^2Re_\phi = 3.8 \times 10^4$.

Fig. 8 shows that for $Re_\phi = 1.25 \times 10^6$ there is generally good agreement between the computed turbulent velocities and the measured values. Even at x = 0.6, where $x^2Re_\phi = 4.5 \times 10^5$, the flow is completely turbulent.

6. CONCLUSIONS

For the computation of axisymmetric flow and heat transfer in rotating-disc systems, elliptic solvers, parabolic solvers and integral methods all have a part to play. For boundary-layer-dominated flows, all three techniques can be used, and simple mixing-length models are often adequate for computing turbulent flows. Two (nonaxisymmetric) problems of practical importance that have yet to be predicted accurately by elliptic solvers (or by other methods) are the heated rotating cavity with an axial throughflow and the ingress problem for a rotor-stator system. With increasing use of multigrid methods and parallel computers, it is likely that both these and other nonaxisymmetric problems will be solved in the coming years.

A multigrid elliptic solver, using a low-Reynolds-number k-ε model for turbulent flow, and LDA measurements have been used to give new insight into the axisymmetric flow between contra-rotating discs. The laminar computations show Batchelor-type flow with radial outflow confined to thin boundary layers on the discs and inflow in a thin shear layer in the midplane; between the two boundary layers and the shear layers are cores of contra-rotating fluid. Although there is experimental evidence for laminar boundary-layer flow on the discs (at local rotational Reynolds numbers up to at least $x^2Re_\phi = 1.1 \times 10^5$), no evidence has been found for the shear layer and contra-rotating cores (even for Reynolds numbers as low as $x^2Re_\phi = 2.2 \times 10^4$). The velocity measurements, and the turbulent computations, show that radial inflow occurs inside a single central core that extends between the two boundary layers and in which the tangential velocity is relatively small. Although the turbulence model predicts premature transition from laminar to turbulent flow in the boundary layers, the fully turbulent computations (for $x^2Re_\phi \geq 4.5 \times 10^5$) are in good agreement with the measured velocities.

Future work on contra-rotating discs will include the effects of superposed flow and heat transfer.

ACKNOWLEDGEMENTS

The authors wish to thank the Ministry of Defence and the Science and Engineering Research Council (SERC) for supporting the work described in this paper; in particular, the Meiko parallel computer and much of the TSI LDA system was provided by SERC. We also wish to thank the Turkish Government for providing financial support for Mr Kilic.

REFERENCES

1. Owen, J.M. and Rogers, R.H., Flow and heat transfer in rotating-disc systems. Vol 1: rotor-stator systems, Research Studies Press, Taunton, 1989
2. Owen, J.M. Recent developments in rotating-disc systems. Proc. I Mech E Conf. on Turbomachinery: Latest developments in a changing scene, pp 83-89. Mechanical Engineering Publications, London, 1991.
3. Owen, J.M. Air-cooled gas-turbine discs:a review of recent research. Int.J. Heat Fluid Flow, vol. 9, pp 354-365, 1988.
4. Morse, A.P. Numerical prediction of turbulent flow in rotating cavities. J.Turbomachinery, vol. 110, pp 202-212, 1988.
5. Morse, A.P. Assessment of laminar-turbulent transition in closed disc geometries. J.Turbomachinery, vol. 113, pp 131-138, 1991.
6. Morse, A.P. Application of a low Reynolds number k-e turbulence model to high-speed rotating cavity flows. J.Turbomachinery, vol. 113, pp 98-105, 1991.
7. Morse, A.P. and Ong, C.L. Computation of heat transfer in rotating cavities using a two-equation model of turbulence, J.Turbomachinery, vol. 114, pp 247-255, 1992.
8. Pincombe, J.R. Optical measurements of the flow inside a rotating cylinder. D.Phil. thesis, University of Sussex, 1983.
9. Lapworth, B.L. and Chew, J.W. 1990 A numerical study of the influence of disc geometry on the flow and heat transfer in a rotating cavity. 35th ASME International Gas Turbine and Aeroengine Congress and Exhibition, Brussels, 90-GT-136, 1983.
10. Iacovides, H. and Theofanopoulos. Turbulence modelling of axisymmetric flow inside rotating cavities. Int.J.Heat Fluid Flow, vol. 12, pp 2-11, 1991.
11. Lonsdale, G. Solution of a rotating Navier-Stokes problem by a nonlinear multigrid algorithm.J Comp. Phys., vol 74, pp 177-190, 1988.
12. Vaughan, C.M., Gilham, S. and Chew, J.W. Numerical solutions of rotating disc flows using a non-linear multigrid algorithm. Proc. 6th Int. Conf. Num. Meth.Lam.Turb.Flow., Swansea, pp 66-73 (Pineridge Press), 1989.
13. Wilson, M., Kilic, M. and Owen, J.M. Computation of flow in rotating disc systems. ICHMT Int. Symp. on Heat Transfer in Turbomachinery, Athens, 1992.
14. Ong, C.L. and Owen, J.M. Boundary-layer flows in rotating cavities. J. Turbomachinery, vol 111, pp 341-348, 1989.
15. Ong, C.L. and Owen, J.M. Prediction of heat transfer in a rotating cavity with a radial outflow.J.Turbomachinery, vol. 113, pp 115-123, 1991.
16. Ong, C.L. and Owen, J.M. , 1991, Computation of the flow and heat transfer due to a rotating disc. Int.J. Heat Fluid Flow, vol. 12, pp 106-115, 1991.
17. Northrop, A. and Owen, J.M. Heat transfer measurements in rotating-disc systems. Part 1: The free disc. Int.J.Heat and Fluid Flow, vol. 9, pp 19-26, 1988.
18. Owen, J.M., Pincombe, J.R. and Rogers, R.H. Source-sink flow inside a rotating cylindrical cavity. J.Fluid Mech., vol. 155, pp 233-265, 1985.
19. Chew, J.W. and Rogers, R.H. An integral method for the calculation of turbulent forced convection in a rotating cavity with radial outflow. Int.J.Heat Fluid Flow, vol. 9, 1988.
20. Northrop, A. and Owen, J.M. Heat transfer measurements in rotating-disc systems. Part II: The rotating cavity with a radial outflow of cooling air. Int. J. Heat Fluid Flow, vol. 9, pp 27-36, 1988.
21. Farthing, P.R. and Owen, J.M. The effect of disc geometry on heat transfer in a rotating cavity with a radial outflow of fluid. J.Engng. Gas Turbines Power, vol. 110, pp 70-77, 1988.
22. Farthing, P.R., Long, C.A. and Rogers, R.H. Measurement and prediction of heat transfer from compressor discs with a radial inflow of cooling air. 36th ASME International Gas Turbine and Aeroengine Congress and Exhibition, Orlando, 91-GT-53, 1991.
23. Chew, J.W., Farthing, P.R., Owen, J.M. and Stratford, B. The use of fins to reduce the pressure drop in a rotating cavity with a radial inflow. J.Turbomachinery, vol. 111, pp 349-356, 1989.
24. Farthing, P.R., Chew, J.W. and Owen, J.M. The use of de-swirl nozzles to reduce the pressure drop in a rotating cavity with a radial inflow. J.Turbomachinery, vol. 113, pp 106-114, 1991.

25. Farthing, P.R., and Owen, J.M. De-swirled radial inflow in a rotating cavity. Int.J.Heat Fluid Flow, vol. 12, pp 63-70, 1991.

26. Farthing, P.R., Long, C.A., Owen, J.M. and Pincombe, J.R. Rotating cavity with axial throughflow of cooling air: flow structure. J.Turbomachinery, vol. 114, pp 237-246, 1992.

27. Farthing, P.R., Long, C.A., Owen, J.M. and Pincombe, J.R. Rotating cavity with axial throughflow of cooling air: heat transfer. J.Turbomachinery, vol. 114, pp 229-236, 1992.

28. Long, C.A. and Tucker, P.G. Shroud heat transfer measurements from a rotating cavity with an axial throughflow of cooling air. 37th ASME International Gas Turbine and Aeroengine Congress and Exhibition, Cologne, 92-GT-69, 1992.

29. Millward, J.A. and Robinson, P.H. Experimental investigation into the effects of rotating and static bolts on both windage heating and local heat transfer coefficients in a rotor/stator cavity. 34th ASME International Gas Turbine and Aeroengine Congress and Exhibition, Toronto, 89-GT-196, 1989.

30. Daniels, W.A., Johnson, B.V. and Graber, D.J. Aerodynamic and torque characteristics of enclosed co/counter rotating disks. 34th ASME International Gas Turbine and Aeroengine Congress and Exhibition, Toronto, 89-GT-177, 1989.

31. Zimmermann, H., Firsching, A., Dibelius, G.H., and Ziemann, M. Friction losses and flow distribution for rotating disks with shielded and protruding bolts. J.Engng Gas Turbines Power, vol. 108, pp 547-561, 1986.

32. Bunker, R.S., Metzger, D.E. and Wittig, S. Local heat transfer in turbine disk-cavities. Part I: Rotor and stator cooling with hub injection of coolant. J.Turbomachinery, vol. 114, pp 211-220, 1992.

33. Bunker, R.S., Metzger, D.E. and Wittig, S. Local heat transfer in turbine disk-cavities. Part II: Rotor cooling with radial location injection of coolant. J.Turbomachinery, vol. 114, pp 221-228, 1992.

34. Staub, F.W. Rotor cavity flow and heat transfer with inlet swirl and radial outflows of cooling air. 37th ASME International Gas Turbine and Aeroengine Congress and Exhibition, Cologne, 92-GT-378, 1992.

35. Phadke, U.P. and Owen, J.M., 1988, Aerodynamic aspects of the sealing of gas-turbine rotor-stator systems. Part I: The behavior of simple shrouded rotating -disk systems in a quiescent environment. Int.J.Heat Fluid Flow, vol. 9, pp 98-105, 1988.

36. Phadke U.P. and Owen, J.M. Aerodynamic aspects of the sealing of gas-turbine rotor-stator systems. Part II: The performance of simple seals in a quasi-axisymmetric external flow. Int.J.Heat Fluid Flow, vol. 9, pp 106-112, 1988.

37. Phadke, U.P. and Owen, J.M. Aerodynamic aspects of the sealing of gas-turbine rotor-stator systems. Part III: The effect of nonaxisymmetric external flow on seal performance. Int.J.Heat Fluid Flow, vol. 9, pp 113-117, 1988.

38. El-Oun, Z.B., Neller, P.H. and Turner, A.B. Sealing of a shrouded rotor-stator system with pre-swirl coolant. J.Turbomachinery, vol. 110, pp 218-228, 1988.

39. Daniels, W.A., Johnson, B.V., Graber, D.J. and Martin, R.J. Rim seal experiments and analysis for turbine applications. 35th ASME International Gas Turbine and Aeroengine Congress and Exhibition, Brussels, 190-GT-131, 1990.

40. Chew, J.W. A theoretical study of ingress for shrouded rotating disc systems with radial outflow. 34th ASME International Gas Turbine and Aeroengine Congress and Exhibition, Toronto, 89-GT-178, 1989.

41. Chew, J.W., Dadkhah, S. and Turner, A.B. Rim sealing of rotor-stator wheelspaces in the absence of external flow. 36th ASME International Gas Turbine and Aeroengine Congress and Exhibition, Orlando, 91-GT-33, 1991.

42. Dadkhah, S., Turner, A.B. and Chew, J.W. Performance of radial clearance rim seals in upstream and downstream wheelspaces. 36th ASME International Gas Turbine and Aeroengine Congress and Exhibition, Orlando, 91-GT-32, 1991.

43. Green, T. and Turner, A.B. Ingestion into the wheelspace upstream of an axial turbine rotor. 37th ASME International Gas Turbine and Aeroengine Congress and Exhibition, Cologne, 92-GT-303, 1992.

44. Bhavnani, S.H., Khilnani, V.I., Tsai, L.C., Khodadadi, J.M., Goodling, J.S. and Waggott, J. Effective sealing of a disk cavity using a double-toothed rim seal. 37th ASME International Gas Turbine and Aeroengine Congress and Exhibition Cologne, 92-GT-379, 1992.

45. Hamabe, K. and Ishida, K. Rim seal experiments and analysis of a rotor-stator system with nonaxisymmetric main flow. 37th ASME International Gas Turbines and Aeroengine Congress and Exhibition, Cologne, 92-GT-160, 1992.

46. Batchelor, G.K. Note on a class of solutions of the Navier-Stokes equations representing steady rotationally-symmetric flow. Quart. J. Mech. Appl. Math., vol. 4, pp 29-41, 1951.

47. Stewartson, K. On the flow between two rotating coaxial discs. Proc. Camb. Phil. Soc., vol. 49, pp 333-341, 1953.

48. Zanbergen, P.J. and Dijkstra, D. Von Karman swirling flows. Ann. Rev. Fluid Mech., vol. 19, pp 465 - 491, 1987.

49. Lam, C.K.G. and Bremhorst, K.A. Modified form of the k-e model for predicting wall turbulence. Fluids Eng., vol. 103, pp 456-460, 1981.

APPENDIX A: CONSERVATION EQUATIONS

The axisymmetric equations for conservation of momentum, mass, and model turbulence quantities k and ϵ can be written in the following form using a cylindrical-polar co-ordinate system (r,ϕ,z) with velocity components (v_r, v_ϕ, v_z):

$$\frac{\partial}{\partial z}(\rho v_z \phi) + \frac{1}{r}\frac{\partial}{\partial r}(r\rho v_r \phi) = \frac{\partial}{\partial z}(\Gamma_z \frac{\partial \phi}{\partial z})$$

$$+\frac{1}{r}\frac{\partial}{\partial r}(r\Gamma_r \frac{\partial \phi}{\partial r}) + S_\phi$$

where ϕ represents the transported variables v_r, v_ϕ, v_z, k or ϵ, and the continuity equation is recovered by setting $\phi = 1$. S_ϕ contains all source terms including the pressure gradient. Γ_z and Γ_r are the effective diffusivities comprising both laminar and turbulent components. The relevant expressions are given in Table A.1.

The effective viscosity is $\mu_{eff} = \mu + \mu_t$, where μ_t is determined from the computed turbulence quantities k and ϵ. Further details of the turbulence closure are given in Appendix B.

Table A.1

ϕ	Γ_z	Γ_r	S_ϕ
v_z	$2\mu_{eff} - \mu$	μ_{eff}	$-\frac{\partial}{\partial z}(p + \frac{2}{3}\rho k)$ $+\frac{1}{r}\frac{\partial}{\partial r}(r\mu_{eff}\frac{\partial v_r}{\partial z})$ $-\frac{2}{3}\frac{\partial}{\partial z}(\nabla \cdot \mathbf{v})$
v_r	μ_{eff}	$2\mu_{eff} - \mu$	$-\frac{\partial}{\partial r}(p + \frac{2}{3}\rho k)$ $-(2\mu_{eff} - \mu)\frac{v_r}{r^2}$ $+\frac{\rho v_\phi^2}{r} + \frac{\partial}{\partial z}(\mu_t \frac{\partial v_z}{\partial r})$ $-\frac{2}{3}\frac{\partial}{\partial r}(\nabla \cdot \mathbf{v})$
v_ϕ	μ_{eff}	μ_{eff}	$-\frac{\rho v_z v_\phi}{r} - \mu_{eff}\frac{v_\phi}{r^2}$ $-\frac{v_\phi}{r}\frac{\partial \mu_{eff}}{\partial r}$
k	$\mu + \frac{\mu_t}{\sigma_k}$	$\mu + \frac{\mu_t}{\sigma_k}$	$P - \rho\epsilon - D$
ϵ	$\mu + \frac{\mu_t}{\sigma_\epsilon}$	$\mu + \frac{\mu_t}{\sigma_\epsilon}$	$\frac{\epsilon}{k}(c_{\epsilon 1}P - c_{\epsilon 2}\rho\epsilon)$ $+E - F$

APPENDIX B:
LOW-REYNOLDS-NUMBER $k - \epsilon$ TURBULENCE MODEL

The terms given in Table B.1 are based on the model used by Morse(refs 4–6), in which D, E and F are extra terms added to the high-Reynolds-number form of the model, to represent near-wall behaviour. The production rate P of turbulent kinetic energy (k) is given by:

$$P = \mu_t[2\left((\frac{\partial v_z}{\partial z})^2 + (\frac{\partial v_r}{\partial r})^2 + (\frac{v_r}{r})^2\right)$$
$$+(\frac{\partial v_z}{\partial r} + \frac{\partial v_r}{\partial z})^2 + (\frac{\partial v_\phi}{\partial z})^2 + (r\frac{\partial}{\partial r}(\frac{v_\phi}{r}))^2]$$

The empirical coefficients appearing in the model are given by:

$C_\mu = 0.09$; $C_{\epsilon 1} = 1.44$;
$C_{\epsilon 2} = 1.92 - 0.43exp(-Re_t^2/36)$;
σ_k=1.0; σ_ϵ=1.22

The turbulent viscosity includes a near-wall damping function f_μ where

$$\mu_t = C_\mu f_\mu \rho k^2/\epsilon$$

The version of f_μ used by Morse for single-grid codes was found by the present authors to give convergence difficulties in the multigrid code. The problem was overcome by using a version of f_μ employed by Lam and Bremhorst (ref.49) where

$$f_\mu = [1 - exp(-A_\mu Re_y)]^2(1 + \frac{A_t}{Re_t})$$
$$Re_t = k^2/\nu\epsilon$$

and

$$Re_y = k^{1/2}y/\nu$$

For the computations presented in this paper,

$A_\mu = 0.029$
$A_t = 25$

and f_μ was never allowed to exceed unity (some velocity profiles were computed on a single–grid code using Morse's version of f_μ; these showed little difference from the results presented here).

The approximations for the Reynolds stresses $\rho v_i' v_j'$ appearing in the time-averaged Navier-Stokes equations for axisymmetric flow are given in Table B.2.

Table B.1

$D = 2\mu[(\frac{\partial k^{1/2}}{\partial z})^2 + (\frac{\partial k^{1/2}}{\partial r})^2]$
$E = \frac{2\mu\mu_t}{\rho}[(\frac{\partial^2 v_r}{\partial z^2})^2 + (\frac{\partial^2 v_\phi}{\partial z^2})^2]$ $+\frac{2\mu\mu_t}{\rho}[(\frac{\partial^2 v_z}{\partial r^2})^2 + (\frac{\partial^2 v_\phi}{\partial r^2})^2]$
$F = 2\mu[(\frac{\partial \epsilon^{1/2}}{\partial z})^2 + (\frac{\partial \epsilon^{1/2}}{\partial r})^2]$

Table B.2

$\rho\overline{(v_r')^2} = \frac{2}{3}\rho k - 2\mu_t\frac{\partial v_r}{\partial r}$	$\rho\overline{v_r' v_\phi'} = -\mu_t r\frac{\partial}{\partial r}(\frac{v_\phi}{r})$
$\rho\overline{(v_\phi')^2} = \frac{2}{3}\rho k - 2\mu_t\frac{v_r}{r}$	$\rho\overline{v_r' v_z'} = -\mu_t(\frac{\partial v_r}{\partial z} + \frac{\partial v_z}{\partial r})$
$\rho\overline{(v_z')^2} = \frac{2}{3}\rho k - 2\mu_t\frac{\partial v_z}{\partial z}$	$\rho\overline{v_\phi' v_z'} = -\mu_t\frac{\partial v_\phi}{\partial z}$

Discussion

QUESTION 1:

DISCUSSOR: D.J. Way, Defense Research Agency, Pyestock

How do you see our production capabilities advancing in the next ten years?

AUTHOR'S REPLY:

If the use of CFD methods in the design of internal air systems is to increase over the next decade then it will be necessary to provide reliable experimental data for the validation of the CFD codes. The rotating-disc research at the University of Bath is contributing to this area and, as long as funding continues from industry and government agencies, the next decade should see a significant advance in this area. However, one of the many unfortunate effects of the present recession is to reduce the investment in research, and without a crystal ball it is impossible to say what effect this will have on future progress.

QUESTION 2:

DISCUSSOR: J.W. Chew, Rolls Royce

A difficulty in deciding which low-Reynolds-number k-ε model to use across a range of different rotating disc flows is that different near-wall damping functions are used in the various papers on this subject. Do you intend to repeat earlier comparisons with data using your recommended treatment?

AUTHOR'S REPLY:

We have used variants of the Morse model and the Launder-Sharma model for rotating-disc computations. As shown in this paper, the Morse model works well, but the Launder-Sharma model is easier to implement in multigrid solvers and it gives better results for transition flows between contra-rotating discs. Mr. Kilic is currently computing the results for contra-rotating discs using the Launder-Sharma model.

Heat Transfer and Leakage in High-Speed Rotating Stepped Labyrinth Seals

W. Waschka, S. Wittig, S. Kim and Th. Scherer

Lehrstuhl und Institut für Thermische Strömungsmaschinen
Universität Karlsruhe (T.H.)
Kaiserstr.12, W-7500 Karlsruhe (Germany)

ABSTRACT

A new experimental and numerical research program was conducted to determine the effects of rotation on the leakage loss and the heat transfer coefficients of compressible flows in modern high performance labyrinth seals. In this study, the interest is focused on divergent shaped stepped labyrinth seals. That type of labyrinth seal is the last one within a row of different labyrinth seals, investigated at the University of Karlsruhe: straight-through, staggered labyrinth seals and convergent shaped stepped labyrinth seals have been the other geometries.

For heat transfer and leakage loss measurements our high temperature test facility was used, providing realistic conditions of gas temperatures, pressure ratios as well as a wide range of axial and peripheral Reynolds numbers . In addition, numerical codes have been verified by experimentally obtained data. Heat transfer coefficients for the stator and the rotor are derived utilizing the well-known standard k-ϵ model and the Stanton-analogy.

The following report will discuss first some new rotational effects, which are significant for the divergent shaped seal. In addition, these results will be compared with those obtained from our other seal geometries studied.

NOMENCLATURE

A	m^2	flow area, $A = 2\pi r_{eff} s$
C_D	-	discharge coefficent
$\bar{c}_{as}$	$\frac{m}{s}$	mass averaged axial velocity
c_P	$\frac{kJ}{kgK}$	specific heat capacity
c_μ	-	constant value
k	$\frac{m^2}{s^2}$	turbulent kinetic energy
$\dot{m}$	$\frac{kg}{s}$	mass flow rate
n	$\frac{1}{s}$	rotational speed
Nu	-	Nusselt number, $Nu = \frac{\alpha \cdot 2s}{\lambda_{T_{str}}}$
$\dot{q}$	$\frac{W}{m^2}$	specific heat flux
P	-	constant value
p	$\frac{N}{m^2}$	pressure
Pr	-	Prandtl number
R	$\frac{kJ}{kgK}$	specific gas constant
r	m	radius
Re_{as}	-	axial Reynolds number $Re = \frac{\dot{m} \cdot 2 \cdot s}{\mu_{(T_{str})} A_{ref}}$
Re_u	-	rot. Reynolds number $Re_u = \frac{u_m \cdot s}{\mu_{(T_{str})}}$
s	m	gap- width
T	K	temperature
u	$\frac{m}{s}$	circumferential velocity
u^+	-	dimensionless velocity
α	$\frac{W}{m^2K}$	heat transfer coefficent
κ	-	isentropic coefficent
λ	$\frac{W}{mK}$	thermal conductivity
μ	$\frac{kg}{ms}$	dynamic viscosity
ρ	$\frac{kg}{m^3}$	density

Subscripts:

max	maximum value
meas	measured value
num	numerical value
ref	reference value
s	refering to the flow
t	turbulent
w	value of wall
o	with no rotation
0	settling chamber
∞	behind the seal

INTRODUCTION

Despite their unavoidable leakage, labyrinth seals remain the widely used sealing elements in turbo engines. Especially in modern aero engines, which are operating at extremely high gas temperatures and rotational speeds, labyrinth seals are often the only chance to provide the required reliability. Of course, in some few applications, labyrinth seals could have been substituted by contact seals, such as brush seals or carbon seals, which provide a smaller leakage rate. However, that substitution was limited to more moderate conditions, i.e. related to bearing chambers or to small shaft radii.

To restrict the undesired leakage to a minimum, labyrinth seals have to work at very small running clearances. As a consequence, thermal delatations can strongly effect the leakage characteristic of the seal. The thermal load of the seal as well as of important engine parts, which are in direct contact to the seal, is another designers problem. To provide high efficiency and sufficient reliability of the whole engine, therefore detailed informations of the leakage flow and the heat transfer from the hot gas to the labyrinth components are an utmost premise. Although a lot of experimentally and numerically obtained data on the leakage characteristic and the heat transfer are available (Sheinin (1961), Shvets (1963), Kapinos and Gura (1970, 1973), Metzger and Bunker (1985), Wittig et al. (1985, 87, 89)), it has to be recognized that most studies do not consider rotational effects. Moreover, the majority of the limited number of data are confined on the leakage problem. Thus, informations on rotational effects, which might influence both, heat transfer and leakage rate, are not commonplace. Of course, in many previous applications of labyrinth seals the

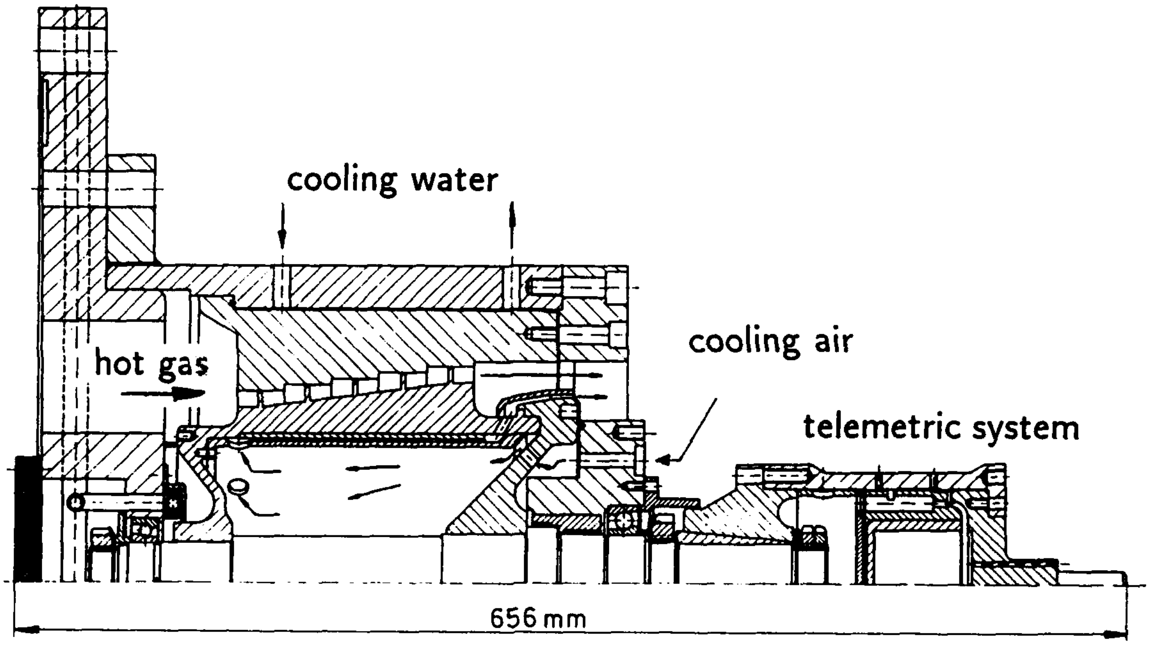

Fig. 1: Test Section for Divergent Stepped Labyrinth Seal

shaft speeds were small compared to the axial flow velocity and thus could have been neglected, tested by several authors (i.e. Yamada (1962), Stocker (1978)). But this is no more true for current applications, where the tip of the fins often reaches supersonic velocities and the flow rate could have been decreased by smaller clearences and improved seal design. As a consequence, in many cases the peripheral velocity of the seal exceeds the axial velocity of the flow.

At the University of Karlsruhe a research program has been conducted, focusing onto the rotational effects. The present report is an extension of our previous puplications (see Waschka et al. (1989, 1991)), dealing with straight-through, staggered and convergent shaped stepped labyrinth seals. In this study, main interest is directed onto the rotational effects on the heat transfer and the leakage in divergent shaped labyrinth seals. To provide a general understanding the following discussion will include results of the other geometries, studied in our test rig, as well.

EXPERIMENTAL FACILITY AND INSTRUMENTATION

The new test section for the stepped labyrinth seal (Fig. 1) is similar to our earlier test sections, where straight through and staggered labyrinth seals have been studied (Waschka et al., 1990, 1991), therefore only short description will be included here. It consists of an inner rotating part with five fins and a stationary outer part. Geometrical quantities are given in Tab. 1. To avoid a buckling of the rotor, which would be very critical for the later analysis of the leakage rates and the heat transfer, the two seal supporters are kept flexible. The rotor is driven by an electrical motor (max. 3000 rpm) in connection with a flat belt drive (transmission 1:7).

	[mm]
gap- width	0.4 – 0.6
fin height	9.5
step height	3.7
pitch	28.0
fin radius	125.0

Tab. 1: Geometrical data

A conventional rotor support was chosen to avoid eccentricities of the heavy rotor. Profiled struts, which support the frontbearing, provide undisturbed flow conditions at the entrance of the seal. A labyrinth seal between the bearing support and the rotor reduces the pre- swirl, induced by the rotating front disk of the rotor. This is necessary, as the amount of the pre- swirl has a dominant effect on the heat transfer at the entry of the labyrinth seal (Wittig et al., 1990).

For the determination of the heat transfer coefficients, a steady state method has been chosen, which requires a cooling of the labyrinth components. Thus real engine conditions are provided. Whilst cold air is used as cooling fluid for the rotor, the stator is water cooled. However, smooth gas temperature profiles across the gap and the cavities are ensured by keeping the rotor and stator wall temperatures at equal temperature levels, preheating the cooling water. In addition, the air cooling system of the rotor is combined with a thrust balance to minimise the axial load of the bearings.

Air for the test section is supplied by a compressor (Fig. 2) with a pressure ratio of 4.0 and a maximum mass flow of 0.5 kg/s. The mass flow rate is determined by one of three orifice meters, applicable to the appropriate measurement range and connected to a precision water pressure gauge. Further downstream, a 150 kW electrical heater provides maximum gas temperature of 400 °C. Before en-

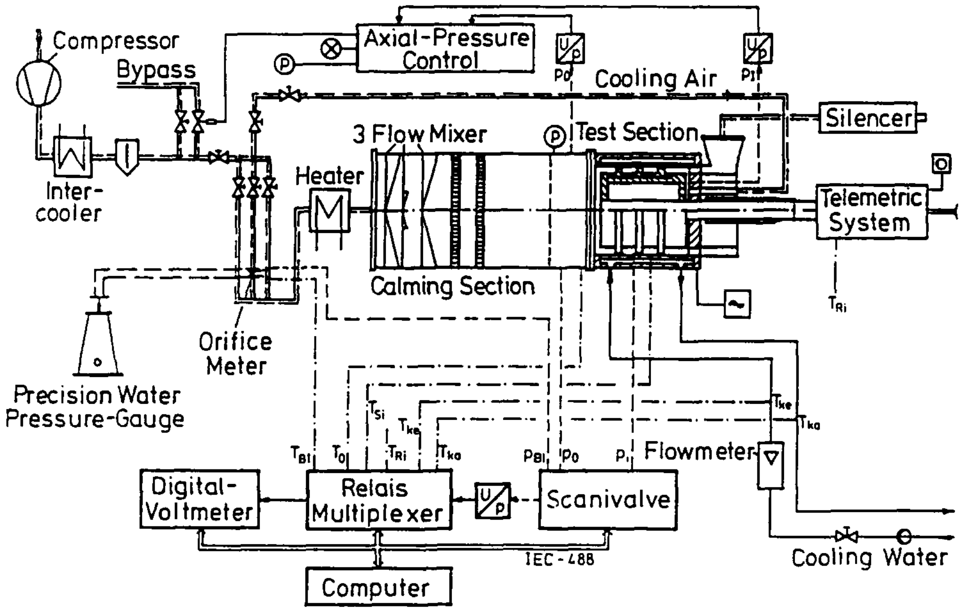

Fig. 2: Test Facility

tering the test section, temperature and velocity profiles are smoothened in a specially designed plenum chamber.

Instrumentation

For the analysis of the labyrinth seal losses, a dimensionless discharge coefficient is used, which is defined as:

$$C_D = \frac{\dot{m}_{meas}}{\dot{m}_{ideal}} \tag{1}$$

where $\dot{m}_{ideal}$ is determined as the mass flow through an ideal nozzle, with identical cross-sectional flow area as in the gap of the labyrinth seal and overall pressure ratio. $\dot{m}_{ideal}$ is calculated in the usual way

$$\dot{m}_{ideal} = \frac{\dot{Q}_{ideal} \cdot p_o \cdot A}{\sqrt{\bar{T}_g}} \tag{2}$$

with

$$\dot{Q}_{ideal} = \left(\frac{p_\infty}{p_o}\right)^{\frac{1}{\kappa}} \sqrt{\frac{2\kappa}{R \cdot (\kappa - 1)} \left[1 - \left(\frac{p_\infty}{p_o}\right)^{\frac{\kappa-1}{\kappa}}\right]} \tag{3}$$

for subcritical pressure ratios. For supercritical pressure ratios the value of Q_{ideal} is equal to the maximum value at

$$\left(\frac{p_\infty}{p_o}\right)_{crit} = \left(\frac{2}{\kappa + 1}\right)^{\frac{\kappa}{\kappa-1}} \tag{4}$$

To suppress cooling effects while calculating discharge coefficients for flows with heat transfer (which could lead to discharge coefficients bigger than 1), choice of correct temperature in eq. 2 is important to avoid misunderstanding results. Instead of using the temperature at the entrance of the labyrinth a mean temperature $\bar{T}_g$ was taken by considering temperature distribution along the complete seal. To describe substantial properties of the flow through labyrinth seals, the axial Reynolds number and a rotational Reynolds number were found to be the characteristic dimensionless parameters. These dimensionless numbers are defined as follows:

$$Re_{ax} = \frac{\dot{m} \cdot 2s}{\mu_{(T_g)} \cdot A_{ref}} \tag{5}$$

and

$$Re_u = \frac{u_w/2 \cdot 2s}{\nu_{(T_g)}} \tag{6}$$

The reference cross-sectional area is calculated by $A_{ref} = 2 \cdot \pi \cdot r_{i,ref} \cdot s$, which is based on the radius of the third fin ($r_{i,ref}$). For an accurate analysis, the determination of the actual gap- width is one of the most critical elements, as centrifugal growth and thermal expansions reach under certain conditions 50% of the original clearance. Therefore, a specially designed clearanceometer was used as described by Waschka et al. (1990). Above the fins one of the capacitive clearance gauges is mounted in the stator. Two additional capacitive clearanceometers are located at the first and the last fin to determine the eccentricity of the rotor. To reduce the rotor eccentricity and displacement to a minimum (e=5 μm) high precision spindle bearings with an extremely small bearing play are used.

The local heat transfer coefficient is derived from

$$\alpha = \frac{d\dot{Q}}{dA \cdot (T_g - T_w)} \tag{7}$$

with the local heat flux $d\dot{Q} = -\lambda \cdot \nabla \cdot T|_{wall}$ determined from the two dimensional temperature distribution in the stator and the rotor. For the calculation of the temperature distribution a finite element program has been used, which requires the wall temperatures T_w at each boundary knot of the finite element mesh. Therefore, local measured values are interpolated by rational spline functions. All surface temperatures and gas temperatures T_g were measured by NiCr-Ni thermocouples. In Fig. 3, the principle instrumentation in one cross-sectional area is shown. The

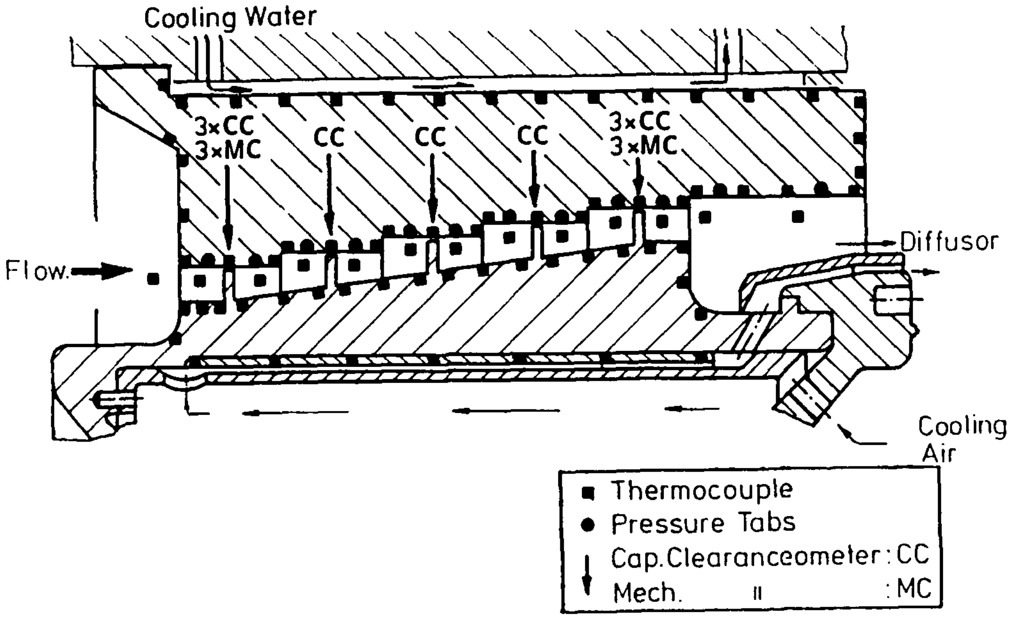

Fig. 3: Instrumentation

27 thermocouples of the rotor are integrated into the rotating part of the telemetrical system, which includes time multiplexer, amplifier, temperature compensation and frequency modulation of the signals. Total uncertainty of the calibrated system is less than 1 K. Due to the limited number of available channels, the fins are not instrumented. But the heat flux is determined at the root of the fins. Thus the calculated heat transfer coefficients for the regions of the fins are equivalent with fin heat transfer coefficients.

To provide information regarding rotational symetrically boundary conditions, the stator was instrumented with thermocouples, pressure tabs and capacitive and mechanical clearanceometers in three different cross-sections. The gas temperatures were also recorded at three different cross-sectional positions in the plenum chamber, in the center of each cavity and at the exit of the seal.

In addition, mean heat transfer coefficients were calculated by averaging the local values. To describe the influence of rotation on the heat transfer, Nusselt numbers are used for the rotor as well as for the stator:

$$Nu = \frac{\alpha \cdot 2s}{\lambda_{(\hat{T}_s)}} \tag{8}$$

Further information is obtained by measuring the static pressures in the plenum chamber, the cavities and a half pitch downstream the last fin. All pressure tabs are linked via a scanivalve with pressure gauge (max. 5 bar). In addition, a precision water pressure gauge was used in the case of small pressure differences across the seal. All pressure, temperature and capacitive signals as well as the rotational speed are recorded by a data acquisition system.

NUMERICAL CODE

Our numerical code has been developed during the past years at our Institute and has been already described in an earlier report (Waschka et al., 1991, Scherer et al.,1992). Based on a quasi three-dimensional finite volume method, it accounts for the elliptic character of the flow. All three velocity components are solved as well as the energy equation. In order to calculate the pressure distribution of the flow field, the well-known SIMPLEC algorithm (van Doormal and Raithby, 1984) is adopted and has been extended by us to compute various flow problems (Wittig, Bauer, Noll, 1987). Turbulence is considered by the standard $k-\epsilon-$ model and heat transfer is calculated using the wall function, which is given by Pun and Spalding (1976).

$$\dot{q} = \frac{c_\mu^{0.25} k^{0.5}}{Pr_t(u^+ + P)} c_P \rho (T_g - T_w) \tag{9}$$

with

$$P = 9.0(\frac{Pr}{Pr_t} - 1)(\frac{Pr}{Pr_t})^{-0.25} \tag{10}$$

For the solution of time-averaged Navier Stokes equations and the energy equation, two different schemes are employed: First predictions have been made with a semi implicit procedure (SIP, Stone 1968). That method has been extended by a conjugate gradient method (CG) recently, which has reduced the required CPU time to about 8 minutes on an IBM 3090 computer. For the calculation a grid of 140 · 95 lines was chosen. Further refinements were tested. However, although the local solution of the velocity field was improved, they do not affect either the global discharge coefficients nor the Nusselt numbers.

Several differencing schemes has been tested as well. However, calculations of the flow through labyrinth seals are quite difficult to perform, because of the relatively high ratios of fin height to gap- width. Only the stable upwind scheme provides a stable solution.

To verify our experiments the measured wall temperature distribution at the cold sides of the seal components and the inlet gas temperature have been used.

DISCUSSION

The present study is an extension of our earlier work on non-rotating scaled up (2:1) labyrinth seals. Pressure distributions, friction factors as well as scaling effects are discussed elsewhere by Wittig et al. (1982 and 1987a,b). In this report focus is directed especially towards the influence of rotational speeds.

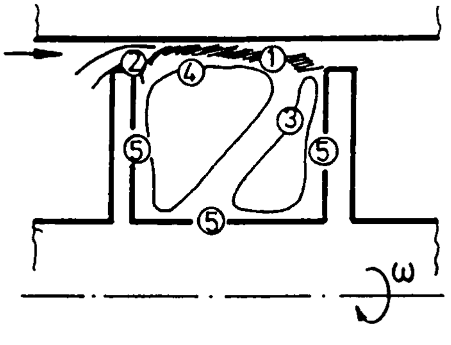

Fig. 4: Rotational effects

If one seal element is rotating, there are several rotational effects, which can influence the leakage rate and the heat transfer, summarized in the diagrammatic sketch of a straight-through labyrinth (Fig. 4). One effect is indicated by mark (1): Due to centrifugal forces the shearlayer shifts radially outward, thus reducing the effective gap- width. An additional decrease of the effective gap- width is to be expexted in the near region of the tip of the fins (2), as the main flow there is partially removed by an centrifugal force driven outflow from the chamber. Moreover, even the quasi two-dimensional flow field in the co-axial cross sectional area can significantly change. So, it is well-known, that in the chamber of straight-through labyrinth seals a second vortex can establish (3), whereas in divergent shaped stepped seals the main flow is deflected to the bottom of the cavity (Fig. 5b). Another effect, which is due to an additional peripheral velocity component, is a drastical increase of the shear stresses (Fig. 4, (4),(5)), which leads to higher rates of turbulent kinetic energy respectively their dissipation.

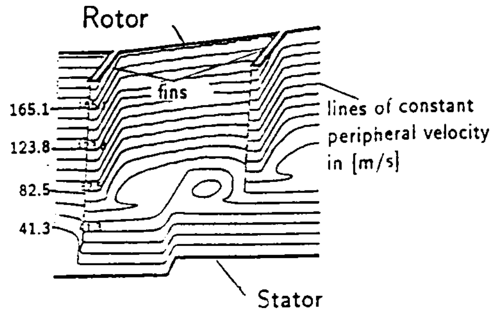

Fig. 5a: Circumferential Velocity

In Fig. 6 the predicted distribution of the turbulent kinetic energy k for 15.000 rpm is compared to that without rotation. High differences occur along the wall and in the shear layers between the recirculation zones, with a higher production rate of turbulence at maximum rotational speed. Therefore, it is to conclude, that the flow resistance increases. However, that augmentation of k can not directly be contributed to a reduction of the leakage rate, because some portion of the dissipated power is replaced by energy transfer from the rotating wall to the fluid. Nevertheless, the static temperature of the flow can drastically increase in downstream direction by that power dissipation as has been discussed by McGreehan et al. (1989) and Waschka et al. (1991), affecting via smaller fluid density the leakage rate as well. The amount of temperature rise is dependent on the pre- swirl at the entrance of the seal, the heat transfer from the gas to the labyrinth components and the geometry of the seal itself. For our experiments, the static temperature T_g was little affected, with an maximal rise of the static temperature across the seal measured to be 3.4 K, at highest rotational speeds of 8000 rpm and overall labyrinth pressure ratio of 1.8. Despite a longer residence time of the flow within the seal, the temperature rise was smaller at low pressure ratios ($\pi = 1.01$, $\Delta T = 1.6°C$), be-

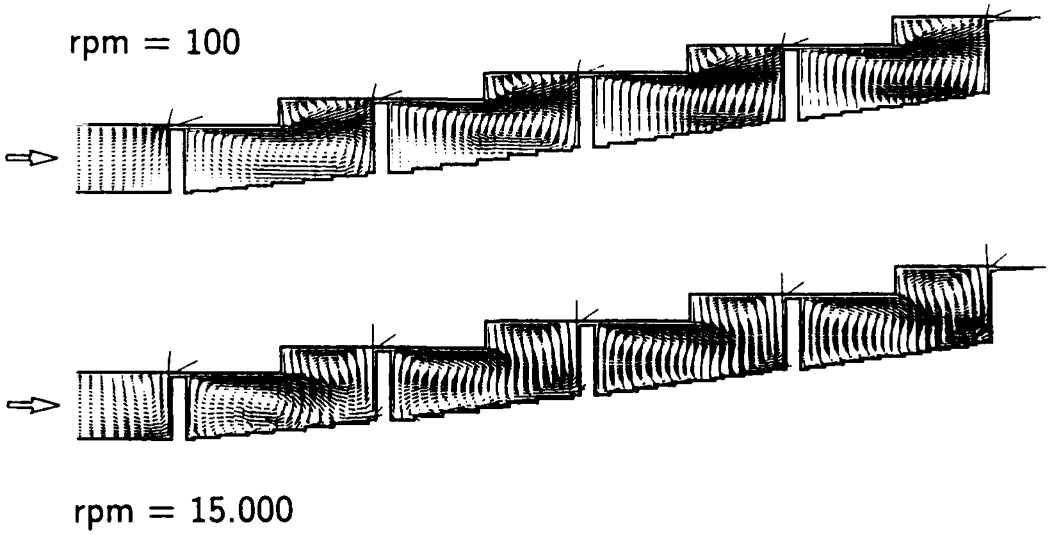

Fig. 5b: Velocity Vectors (Axial and Radial Component)

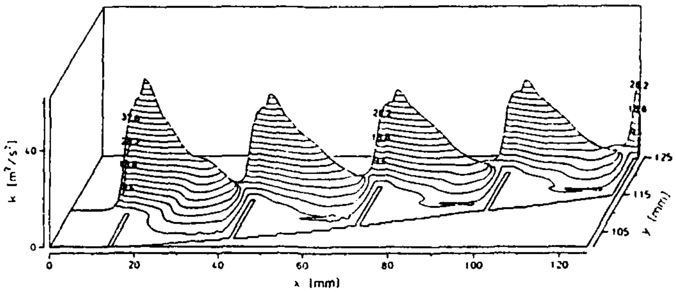

rpm = 100

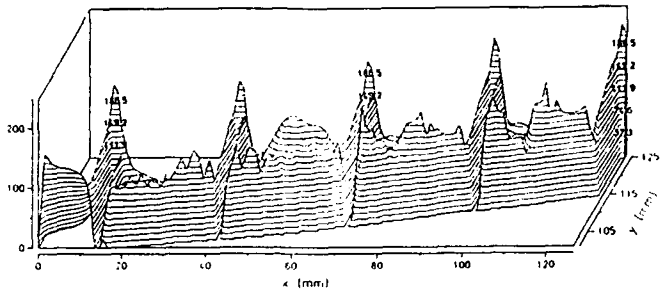

rpm = 15.000

Fig. 6: Turbulent Kinetic Energy — Influence of Rotation

cause the dissipated power was reduced by the heat transfer to the walls. Since the temperature rise has been only very small, the discharge coefficients were calculated by labyrinth-averaged gas temperature $\bar{T}_g$ only, as introduced in eq.2. However, for many technical applications the peripheral velocity of the seal is higher than tested under prevailing conditions and the power dissipation is of considerable relevance, as is shown in a seperate report by Scherer, Waschka and Wittig (1992).

Especially for radial or half-radial seals, such as stepped labyrinth seals, an additional pressure drop across the seal, originated by centrifugal forces, must be considered by the designer too. Dependent on the main flow direction, that effect can lead either to an significant decrease (convergent shape) or an increase (divergent shape) of the leakage rate. Since the amount of that effect strongly depends on the seal geometry either (i.e seal radius at entrance and exit), for general comparability of different seal geometries an isolation of this additional pressure drop across the seal Δp_p is required. Therefore, Δp_p was calculated by an integration of the determining equation

$$dp = \omega_s{}^2 \cdot \rho_s \cdot r_s \cdot dr_s \qquad (11)$$

with the index s refering to the flow. The densities were determined by measuring the temperature and pressure distribution, while the angular velocity of the flow ω_s is based on numerical data. However, frequently the flow field is not known in detail. In this case, good results for the pressure correction will be achieved, if an averaged peripheral velocity of the flow as $\bar{u}_s = 0.4 \cdot u_w$ is assumed. A strong effect was evident especially for the small overall pressure ratio of 1.01. At 10.000 rpm Δp_p reaches about 75% of the total pressure drop across the seal, whereas at the total pressure ratio of 1.8 the relative effect was smaller than 1%. Nevertheless, for general application of the discharge coefficients, this effect has been taken into account, utilizing the net pressure drop $\Delta p_{net} = \Delta p_{tot} - \Delta p_p$ for the calculation of the ideal mass flow ratio via eq.2.

Although the principle of these effects is known, only very few data are available for their quantification, especially for the heat transfer . In Fig. 7 the net-discharge coefficients are plotted as a function of the axial Reynolds number for different rotational speeds. Especially at small Reynolds numbers, a large decrease of the discharge coefficients with increasing rotational speeds becomes evident. A closer examination of the effect reveals the ratio of peripheral to axial Reynolds number as dominant parameter. That is illustrated by Fig. 8, where the rotation dependent change of the same discharge coefficients as shown in Fig. 7 is plotted as a function of the velocity ratio u_w/c_{ax}. This ratio can be seen as a measure of the ratio of circumferential to axial momentum of the flow. Obviously, the distribution of the data as well as the onset of the rotational effect is characterized by that velocity ratio. Same distribution is found for both gap- witdh of 0.4 mm and 0.6 mm. This result agrees very well with our previously obtained data for convergent shaped seal, with extremely small differences in the amount of that decrease only.

The improving of our numerical program and the verification of the experiment has been another goal of our study. For comparisons, both experimentally and numerically obtained data, indicated by the line, are plotted in Fig. 8. An excellent agreement confirms that even the turbulence of labyrinth seal flow is non-isotropic, the $k - \epsilon$ model provides extremely reasonable results.

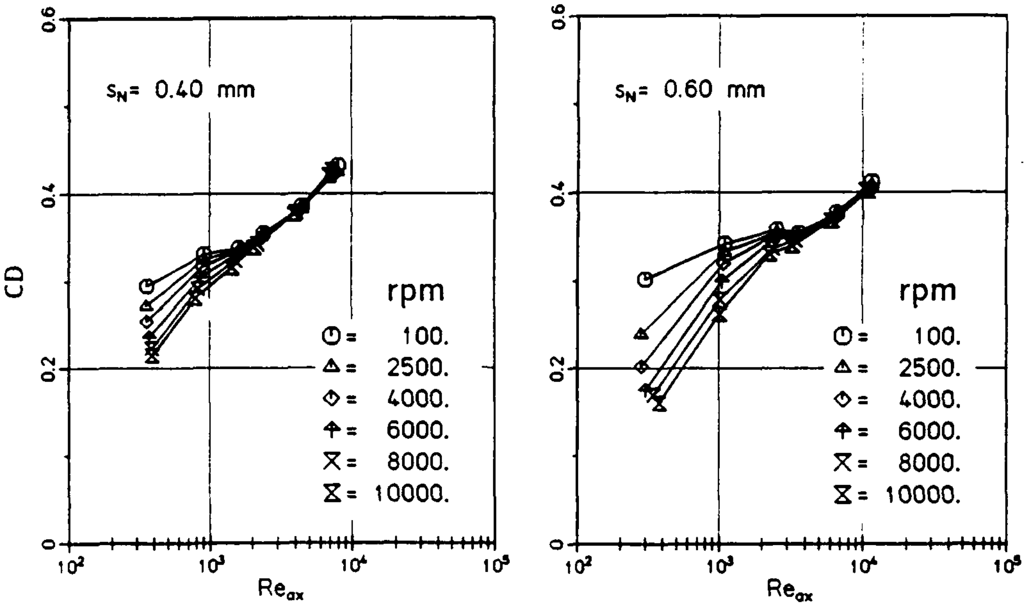

Fig. 7: Discharge Coefficients — Influence of Rotation

Heat transfer measurements were performed in addition to the flow measurements discussed. Gas temperatures at seal inlet of 350°C have been provided and wall temperatures were kept at 35°C for the cold side of the stator and 60°C for the rotor side. In Fig. 9 the distribution of the heat transfer coefficients for the stator and the rotor is shown for a pressure ratio of 1.8 and rotational speeds, varying from 0 to 8000 rpm. Two parallel lines indicate the position of the steps, whereas single lines mark the positions of the fins. It has to be mentioned, that the fins itself are not instrumented with thermoelement couples, which is due to a limitation given by the telemetric system. However, heat input to the rotor via the fins is considered by locating thermo-couples very close to the bottom of the fins.

Fig. 9 reveals an increase of the local heat transfer coefficients towards higher rotational speeds, with a slightly higher relative augmentation at the entrance, and a nearly constant amount downstream of the second fin; similar for the stator and for the rotor. The stronger effect at the entrance region of the seal is due to the very high acceleration of the flow in circumferential direction. Since the acceleration length also depends on the pre- swirl, identical inlet conditions were ensured, using profiled struts for the

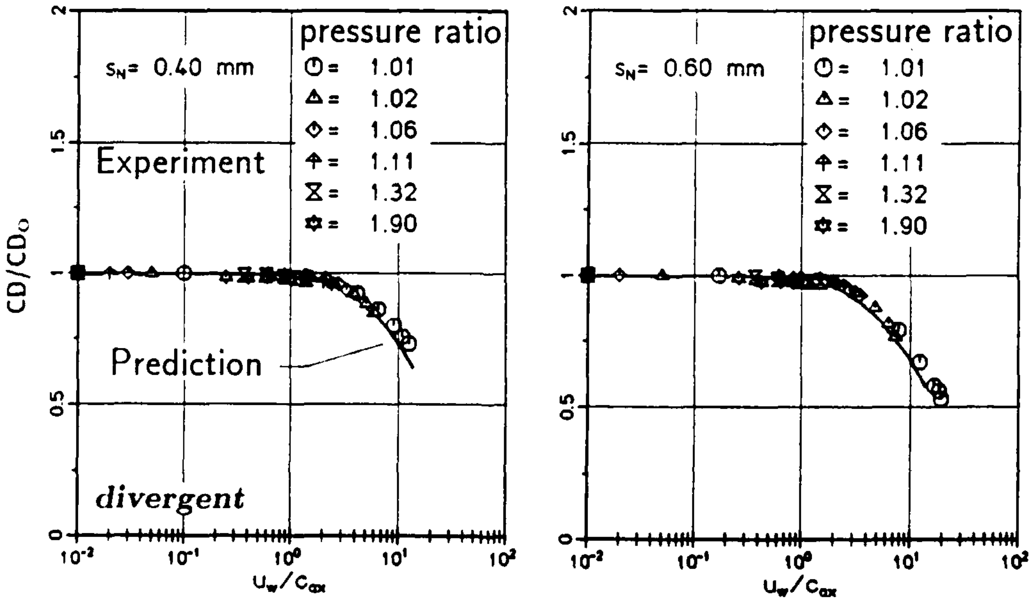

Fig. 8: Discharge Coefficients — Influence of Velocity Ratio

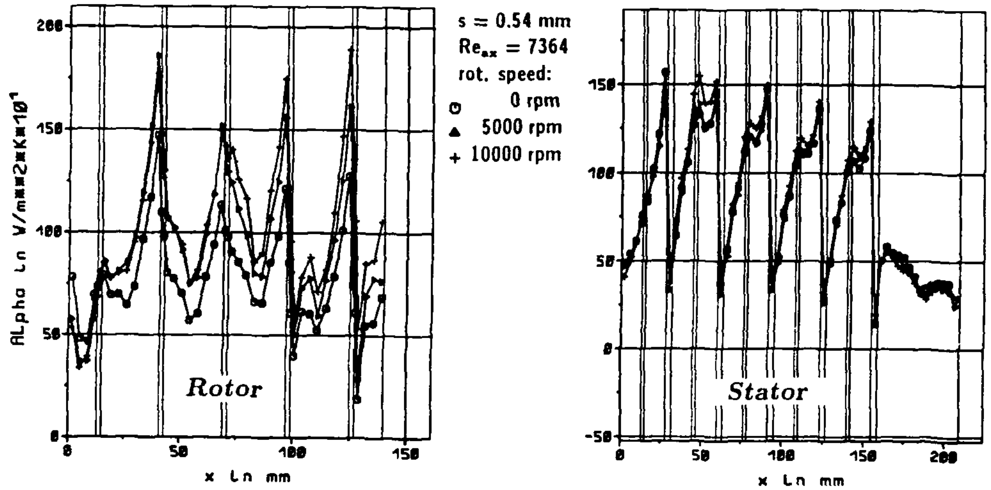

Fig. 9: Local Heat Transfer Coefficients — Influence of Rotation

reduction of the pre- swirl.

It has been already mentioned, that although the geometry of divergent and convergent shaped stepped labyrinth seals are in principle identical, opposite flow directions lead to completely different velocity fields, which consequently does affect the heat transfer from the hot gas to the labyrinth components as well. Fig. 5b presents a plot of the quasi two-dimensional flow field in a co-axial cross-sectional area at 15.000 rpm. Detailed information on the peripheral velocity component within the cavity is given in Fig. 5a. In contrary to divergent shaped seal, where the main flow seperates at the backward step and impinges further downstream onto the fin, in convergent shaped stepped seals the main flow direction is diverted by the steps of the stator towards the bottom of the chamber. Since impingement is commonly related with high heat transfer rates, in convergent shaped seal highest heat transfer rates occur at the forward step and the bottom of the cavity (Waschka et al., 1991), whilst in the divergent shaped seal a maximum is revealed at the fins.

Another difference becomes evident, if the shaft is rotating. Whilst in convergent shaped stepped seals rotation does not qualitatively affect the two-dimensional co-axial velocity field and only leads to an increase of the vortex strenght of the two counterrotating vortices, for divergent shaped seals the situation is considerable different. Here, in the near region of the rotating fins the fluid is radially driven outward, because of the centrifugal forces. Thus, to satisfy continuity, the main flow, which originally impinges on somewhere close to the midst of the fin, is suct to the bottom of chamber, as shown in Fig. 5b. However, a comparison of the influence of rotation on the global Nusselt

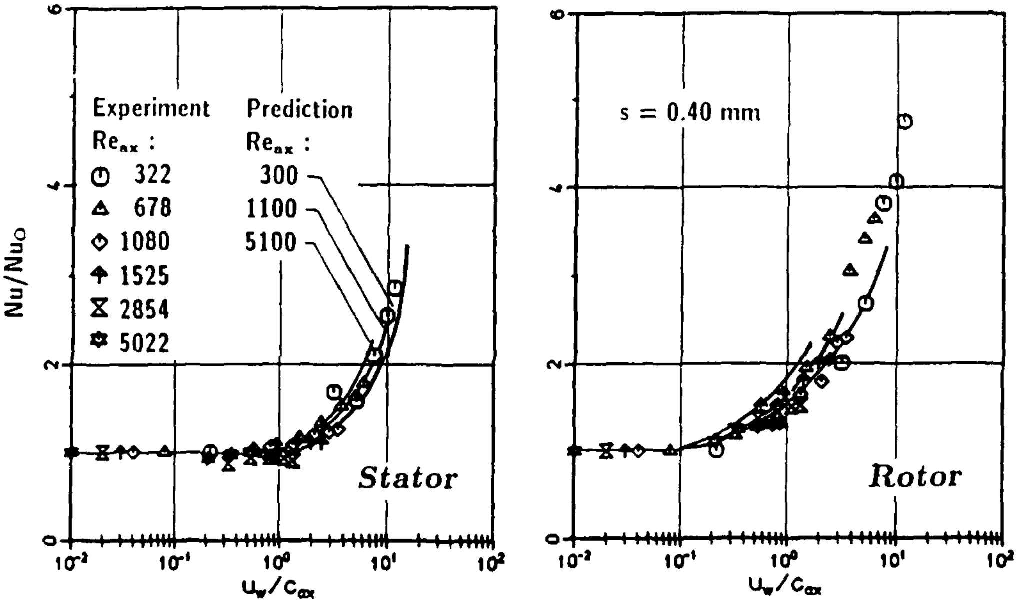

Fig. 10: Nusselt Numbers — Influence of Rotation, $s = 0.4$ mm

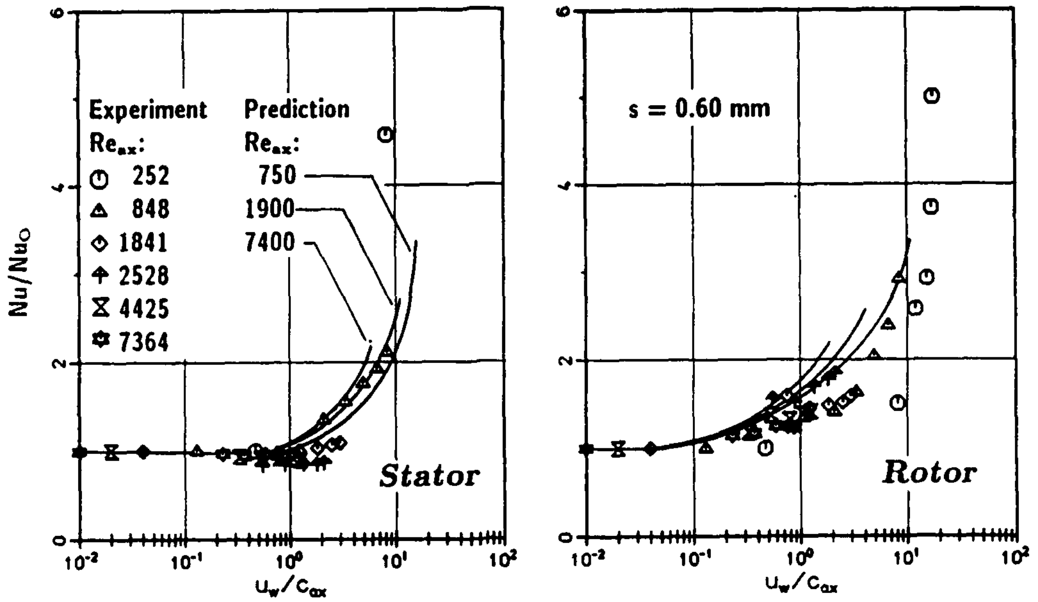

Fig. 11: Nusselt Numbers — Influence of Rotation, $s = 0.6\ mm$

numbers (Fig. 10;11) reveals only slight differences between both stepped seals. Correlations of Nusselt numbers for no rotation Nu_o have been presented by (Wittig et al. (1987)):

$$Nu_o = 0.747 \cdot {Re_{ax}}^{0.8} \cdot (t/s)^{-0.5} \qquad (12)$$

for the stator and

$$Nu_o = 1.673 \cdot {Re_{ax}}^{0.6} \cdot (t/s)^{-0.71} \qquad (13)$$

for the rotor. The correlation is valid for $10^3 \leq Re \leq 1.8 \cdot 10^4$ and $15.6 \leq (t/s) \leq 117$. In Fig. 10a for the stator and in Fig. 10b for the rotor the ratio of the Nusselt number at a certain rotational speed to the basic Nusselt number Nu_o is plotted versus the velocity ratio u_w/c_{ax}. Similar to the discharge coefficients discussed, an incipience of rotational effects is obvious on the heat transfer as well, if the velocity ratio u_w/c_{ax} is about 1. Towards higher rotational speeds the Nusselt numbers increase. However, a comparison of the data for the rotor to those of the stator reveals a stronger effect for the rotor. For a maximum measured momentum ratio of 10, the Nusselt numbers increase by a factor of 2 for the stator and by a factor of 4 for the rotor. This difference can be explained by the distribution of the peripheral velocity in the near region of the walls. Near the rotor, predictions showed (Fig. 5b) that the gradient of the peripheral velocity normal to the wall is more than 2 times higher than the gradient near the stator. Within most parts of the seal chambers the peripheral velocity is about $u_s = 0.35 - 0.45 \cdot u_w$. As a consequence, local momentum ratio seems to be best suited to describe rotational effects on the heat transfer. Influence of other parameters, as pressure ratio or gap- width was found to be comparatively small.

SUMMARY

Heat transfer and leakage loss measurements and predictions were performed for compressible flows in divergent shaped stepped seals with high rotational speeds. Results show a strong influence of rotation on the leakage rate as well as on the heat transfer. Especially for high altitude flight conditions, where small Reynolds numbers occur, rotation can lead to a significant improvement of the leakage behaviour but also to a critical augmentation of the Nusselt numbers. Excellent agreement between experiments and predictions were found.

Future work is directed towards a detailled study regarding the influence of pre- swirl on leakage rates, heat transfer and power dissipation in typical labyrinth seals.

LITERATURE

1. van Doormal,J.; G. Raithby (1984): Enhancements of the SIMPLE Method for Predicting Incompressible Fluid Flows. Num. Heat Transfer, Vol. 7.

2. McGreehan, W.F.; S.H. Ko (1989): Power dissipation in smooth and honeycomb labyrinth seals. ASME Conference, 89-GT-220.

3. Metzger, D.E.; R.S. Bunker (1985): Heat Transfer for Flow through Simulated Labyrinth Seals. ISROMAC, 1985, Honolulu, USA.

4. Morrison, G. L.; D. Chi (1985): Incompressible Flow in Stepped Labyrinth Seals. ASME 85-FE-4

5. Pun, W. M.; D. B. Spalding (1976): A General Computer Program for Two-Dimensional Elliptic Flows. Imperial College of Science and Technology, Heat Transfer Section, HTS/76/2

6. Rhode D.,L.; R.I. Hibbs (1989): A Comparative Investigation of Corresponding Annular and Labyrinth Seal Flowfields. ASME 89-GT-195. Toronto,Canada.

7. Scherer, Th.; Waschka, W.; Wittig, S. (1992): Numerical Predictions of High- Speed Rotating Layrinth Seal Performance: Influence of Rotation on Power Dissipation and Temperature Rise. International Symposium on Heat Transfer in Turbomachinery, Athens, Greece.

8. Shvets, I.T.; V.Y. Khavin; E.P. Dyban (1963): Heat Exchange in Labyrinth Seals of Turbine Rotor (russ). Energomashinostroenie, Vol.12, pp. 8-12

9. Stocker,H.L. (1978): Determining and Improving Labyrinth Seal Performance in Current and Advanced High-Performance Gas Turbines. AGARD-CP-237.

10. Stone, H. (1968): Iterative Solution of Implicit Approximations of Multidimensional Partial Differential Equations. SIAM J.Num. Anal., Vol.5, No. 3, pp. 530-558

11. Waschka, W.; S. Wittig, S.Kim (1990): Influence of High Rotational Speeds on the Heat Transfer and Discharge Coefficients in Labyrinth Seals. ASME , 90-GT-330

12. Waschka, W.; S. Wittig, T. Scherer, S.Kim (1991): Leakage Loss and Heat Transfer in High-Speed Rotating Labyrinth Seals. 91-Yokohama-IGTC-34.

13. Wittig, S. (1990): Heat Transfer Analysis in Rotating Gas Turbine Components. ISROMAC-3, Vol.1, pp.1, Honolulu, Hawaii, 1990.

14. Wittig, S.; U. Schelling; S. Kim; K. Jacobsen (1987): Numerical Predictions and Measurements of Discharge Coefficients in Labyrinth Seals. ASME 87-GT-188, Anaheim, California

15. Wittig, S.; K. Jacobsen; U. Schelling; S. Kim (1987): Heat Transfer in Stepped Labyrinth Seals. ASME, 87-GT-92

16. Wittig, S.; H.J. Bauer and B. Noll (1987): On the Application of Finite- Difference Techniques for the Computation of the Flow Field in Gas Turbine Combustors with Complex Geometries. AGARD Conference Proceedings No. 422, Chania, Crete, Greece

17. Yamada, Y. (1962): On the Pressure Loss of Flow between Rotating Co-Axial Cylinders with Rectangular Grooves. Bull. of ISME 5, Nr.20, p.642-651.

Discussion

QUESTION 1:

DISCUSSOR: C. Hah, NASA Lewis Research Center

What is the Mach number range of the flow?

AUTHOR'S REPLY:

The maximum Mach number was very close to unity. However, at these high Mach numbers the velocity ratio was far below unity so no effect of rotation was found on either the leakage or heat transfer. It is no problem, however, to predict the flow and the heat transfer at this rotational speed as shown in the presentation.

QUESTION 2:

DISCUSSOR: C. Hah, NASA Lewis Research Center

What was the boundary conditions at inflow and outflow for the numerical analysis?

AUTHOR'S REPLY:

The outflow conditions for the numerical calculations were parabolic outflow conditions (von Neumann condition). The flow inlet conditions were preswirl ratios of 0.5 (tangential velocity of the fin divided by the axial velocity of the flow at the entrance of the seal). In general, the preswirl ratio has a strong effect on the heat transfer rates at the inlet region of rotor and states. For comparison reasons, the boundary condition was chosen in accordance to the experimental boundary conditions. In addition, I think that for most engine applications we will find a preswirl ratio of 0.5 as well.

Fluid Flow and Heat Transfer in the Entrance Region of an Annulus Between Independently Rotating Tubes with a Turbulent Axial Flow

H. Pfitzer, T. Rothe and H. Beer
Institut für Technische Thermodynamik
Technische Universität Darmstadt
Petersenstraße 30
6100 Darmstadt
Germany

SUMMARY

Experimental and numerical investigations of turbulent flow and heat transfer have been performed in the entrance region of a concentric annulus between independently rotating tubes. The horizontally mounted test section has an electrically heated outer wall and an adiabatic inner wall. The mean heat transfer rate in the hydrodynamic and thermal entrance region as well as the local Nusselt number at the axial position $z/d_h \approx 60$, which is the end of the rotating annular channel, were determined experimentally. Hotwire- and thermocouple-probes allowed for measurement of velocity and temperature distributions at the end of the annulus. Numerical predictions, applying a k-ε eddy viscosity model with a modification by the flux Richardson number, are compared with the experimental results. The comparison shows that general effects of the rotation can be predicted quite well with the aid of a simple turbulence model. Due to stabilizing or destabilizing effects of centrifugal forces in the fluid and due to the additional shear stress, the rotation of the inner and the outer tube influences remarkably fluid flow and heat transfer in the annulus.

LIST OF SYMBOLS

Nomenclature

c_p	specific heat at const. pressure
d_h	hydraulic diameter ($d_h = 2\, r_2(1-\kappa)$)
k	turbulent kinetic energy ($k = ½\, \overline{v_i v_i}$)
L	length of rotating test section
N_1	rotation rate of inner tube ($N_1 = V_{\varphi 1} / \bar{V}_z$)
N_2	rotation rate of outer tube ($N_2 = V_{\varphi 2} / \bar{V}_z$)
Nu_z	local Nusselt number
Nu_m	mean Nusselt number
p	time mean static pressure
Pr	Prandtl number
$\dot{q}_w$	heat flux density at outer wall
Re_z	flow-rate Reynolds number ($Re_z = \bar{V}_z\, d_h /\nu$)
$Re_{\varphi 1}$	rotational Reynolds number at inner tube ($Re_{\varphi 1} = V_{\varphi 1}\, d_h /\nu$)
$Re_{\varphi 2}$	rotational Reynolds number at outer tube ($Re_{\varphi 2} = V_{\varphi 2}\, d_h /\nu$)
Ri_f	flux Richardson number (eq. 15)
r	radial coordinate
r_1	radius of inner tube
r_2	radius of outer tube
r_m	radius of annular center line $r_m = (r_1+r_2) / 2$
s	gap width ($s = r_2 - r_1$)
t	rms temperature fluctuation
T	time mean temperature
Ta	Taylor number
v_r, v_φ, v_z	rms velocity fluctuations in r,φ,z-direction
$\overline{v_i t}$	turbulent heat flux
$\overline{v_i v_j}$	kinematic Reynolds stress
V_r, V_φ, V_z	time mean velocity in r,φ,z-direction
$\bar{V}_z$	mean axial velocity over annular cross section
z	axial coordinate

Greek Symols

α	heat transfer coefficient
e	dissipation rate of turbulent energy ($e = \nu\, \overline{\partial v_i/\partial x_j \cdot \partial v_i/\partial x_j}$)
ε	modified dissipation rate (eq. 14)
Θ	dimensionless temperature (eq. 4)
κ	radius ratio ($\kappa = r_1 / r_2$)
λ	thermal conductivity
μ	dynamic viscosity
ν	kinematic viscosity
ρ	density
τ	shear stress
φ	tangential coordinate

Subscripts and Superscripts

b	bulk
1	inner wall
2	outer wall
0	at z=0
kr	critical
m	mean
t	turbulent
w	wall
ˉ	dimensionless

1. INTRODUCTION

In rotating machinery, e.g. electrical and turbomachinery, chemical mixing and separation devices etc., rotating fluids are of importance. Therefore, fluid flow and heat transfer in rotating channels have gained increased interest since many years.

Taylor (Ref. 1) investigated the stability of the flow between two concentric rotating cylinders. He found regular toroidal vortices in the annular gap for rotational speeds of the inner cylinder above a critical value. These socalled Taylor vortices develop because of an instability of the laminar flow due to a strong decrease of centrifugal forces with increasing radius. In a closed annular gap with no axial throughflow and with a rotating inner tube, Taylor vortices will arise at Taylor numbers $Ta_{kr} \geq 41.2$.

$$Ta = \frac{V_{\varphi 1}(r_2 - r_1)}{\nu} \sqrt{\frac{s}{r_m}} \qquad (1)$$

With the aid of a bifurcation analysis for $Re_z \rightarrow 0$, Chandrasekhar (Ref. 2) found a stabilizing effect by an imposed axial flow. For small flow-rate Reynolds numbers Re_z, the critical Taylor number increases according to

$$Ta_{kr}(Re_z) = Ta_{kr}(Re_z = 0) + 26.5\,Re_z^2 \qquad (2)$$

The combined axial and rotational flow in an annulus with a rotating inner cylinder was studied experimentally by Kaye and Elgar (Ref. 3). For flow-rate Reynolds numbers $Re_z < 2000$, four flow regimes were detected in the annular gap

- laminar flow
- laminar flow with Taylor vortices
- turbulent flow
- turbulent flow with Taylor vortices.

The changes in the structure of the vortices with increasing axial velocity were investigated by Gu and Fahidy (Ref. 4) by visualization. At small axial flows the individual Taylor cells get inclined and partial overlapping begins to appear. With further increase in the axial flow rate, the cell structure degenerates progressively to a disorderly pattern. At high axial flow rates the Taylor cells are hardly detectable and the complete degeneration of Taylor vortices is assumed.

Kuzay (Ref. 5) experimentally studied the turbulent flow and heat transfer in a concentric annulus between a stationary and uniformly heated outer tube and a rotating adiabatic inner tube. The rotation rate $N_1 = V_{\varphi 1} / \bar{V}_z$ was varied up to 2.8 in the flow-rate Reynolds number range $1.5 \cdot 10^4 < Re_z < 6.5 \cdot 10^4$. Imposing a rotation to the axial flow, he found that the wall temperature of the outer tube diminished and the radial temperature profiles at the end of the heated annular gap, with a length of 36 hydraulic diameters, appreciably flattened. With increasing rotation, the inner boundary temperature rises while the outer wall temperature drops sharply. Therefore, the Nusselt number of a mixed-mode flow increases with increasing rotational velocity of the inner tube.

This paper describes the effect of independently rotating inner and outer tube of a concentric annulus on the velocity and temperature distribution and on the heat transfer to a fluid flowing inside the annular gap. Fluid flow and heat transfer were studied experimentally and numerically in the hydrodynamic and thermal entrance region. The effects of centrifugal forces, due to tube rotation, are visualized by velocity, temperature and Nusselt number distributions. To our knowledge these are the first investigations performed in an annulus between co-rotating and counter-rotating tubes with turbulent axial flow.

2. EXPERIMENTS

A schematic outline of the horizontally mounted experimental apparatus is shown in Fig. 1. The rotating and heated test section has a length of $L/d_h = 60.94$, with a radius ratio $r_1 / r_2 = 0.8575$ and an outer tube i. d. of $D = 180$ mm. The outer tube is heated electrically with a thin heating foil by means of a slip ring arrangement. The inner tube is made of synthetic, low conductivity material to obtain adiabatic conditions and is coated with a very thin tin foil to minimize heat radiation.

In order to measure the axial development of the wall temperatures, both tubes are instrumented with thermocouples. The thermoelectric voltages were transmitted from the inner rotating tube to the stationary instrumentation with the aid of slip rings and from the outer rotating tube by a telemetric device.

At the end of the heated and rotating section a cylindrical three-hole aerodynamic probe as well as a hotwire probe could be inserted into the annular gap through small holes and traversed in radial direction, in order to obtain axial and tangential velocity profiles. Step motors rotate the probe automatically against the main flow direction of the fluid. Temperature profiles could be detected by a traversable thermocouple probe on the other side of the annular gap at the end of the rotating test section.

Air is supplied by a centrifugal blower which is arranged at the end of the test rig to avoid heating of the air outside the test section. The inlet consists of an air filter, honeycombs and two wire mesh screens. The inlet section has a non-rotating length of six hydraulic diameters ($d_h = 2(r_2 - r_1)$) with the same radius ratio as the rotating test section. Behind the heated test section a mixing chamber for measuring the exit bulk temperature, a downstream nonrotating pipe, a Venturi nozzle for measuring the flow rate and the centrifugal blower are arranged. Rotation of both tubes was accomplished by means of two variable speed d.c. motors and pulley drives. The drive mechanisms provided continuous variation of the rotational speed from 50 to 2000 r.p.m. .

The flow-rate Reynolds number Re_z was varied in the range $3000 \leq Re_z = \bar{V}_z d_h / \nu \leq 30000$ up to rotational Reynolds numbers $Re_{\varphi 1} = V_{\varphi 1} d_h / \nu \leq 20000$ at the inner tube and $Re_{\varphi 2} = V_{\varphi 2}\, d_h / \nu \leq 30000$ at the outer tube. Heat transfer coefficients and Nusselt numbers were determined from measurements of the inlet and outlet air temperatures, the wall temperatures of the outer heated tube and the mass flow. The local Nusselt number is

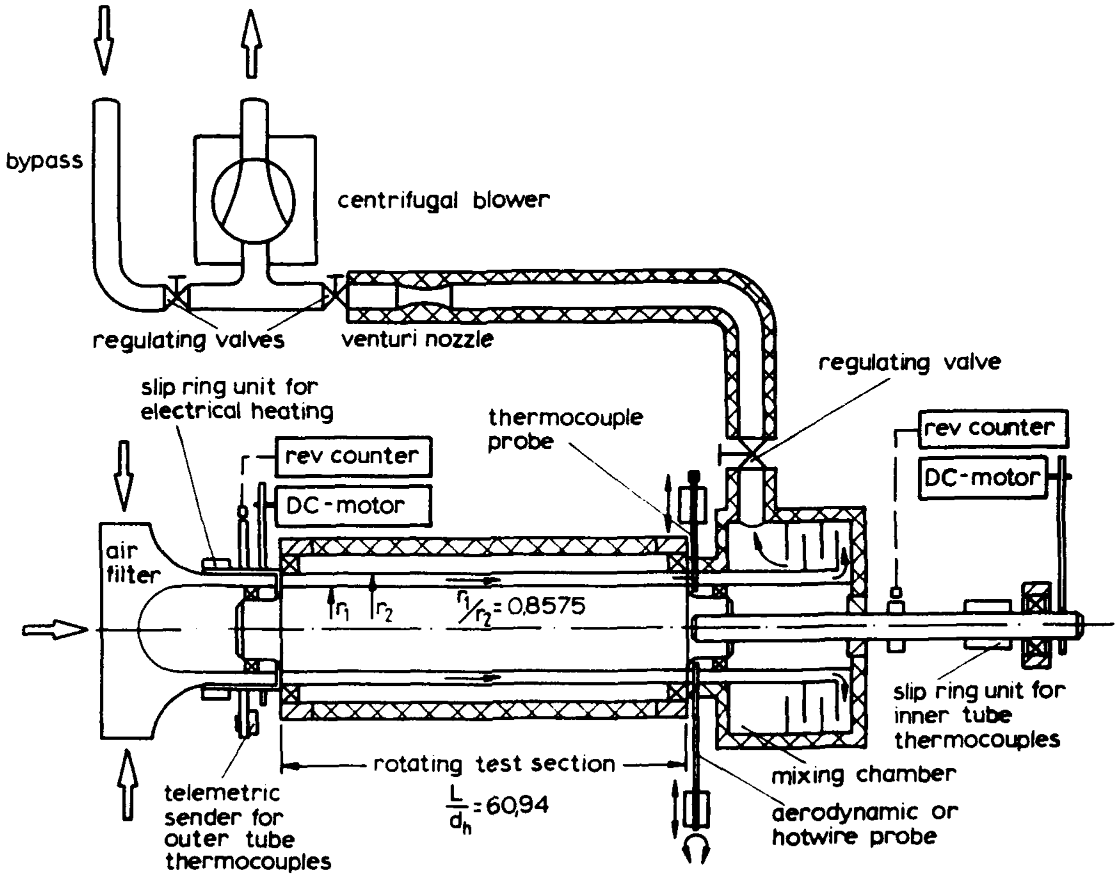
bypass
centrifugal blower
regulating valves
venturi nozzle
regulating valve
slip ring unit for electrical heating
thermocouple probe
rev counter
DC-motor
rev counter
DC-motor
air filter
r_1
r_2
$r_1/r_2 = 0{,}8575$
slip ring unit for inner tube thermocouples
rotating test section
mixing chamber
telemetric sender for outer tube thermocouples
$\frac{L}{d_h} = 60{,}94$
aerodynamic or hotwire probe

Fig. 1: Experimental apparatus

based on the local difference between wall temperature and fluid bulk temperature. With a uniform outer heat flux density $\dot{q}_w$, the local Nusselt number can be expressed as:

$$Nu_z = \frac{\alpha \, d_h}{\lambda} = \frac{\dot{q}_w \, d_h}{(T_w - T_b)\, \lambda} \tag{3}$$

After introducing the dimensionless temperature

$$\Theta = \frac{T - T_0}{\dot{q}_w \, \frac{d_h}{\lambda}} \tag{4}$$

the local Nusselt number Nu_z can be calculated from the local difference between the dimensionless wall temperature and the fluid bulk temperature.

$$Nu_z = \frac{1}{\Theta_w - \Theta_b} \tag{5}$$

The fluid bulk temperature in an annulus with uniformly heated outer wall and adiabatic inner wall, increases linearly as a function of the dimensionless axial coordinate $\hat{z} = z/d_h$.

$$\Theta_b = \frac{4\, \hat{z}}{Re_z \, Pr \, (1+\kappa)} \tag{6}$$

The mean Nusselt number Nu_m is calculated with the aid of the mean temperature difference determined by numerical integration of the local temperature differences over the length of the rotating test section.

3. EXPERIMENTAL HEAT TRANSFER RESULTS

In the experimental investigations of heat transfer in the hydrodynamic and thermal entrance region, a significant influence of rotation on heat transfer and fluid flow was observed.

In Figs. 2 - 5 the measured mean Nusselt numbers, Nu_m, at different flow-rate Reynolds numbers are plotted as functions of the two rotation rates N_1 and N_2. In this presentation Nu_m has been divided by the Nusselt number $Nu_{m,0}$, measured for the non-rotating annulus. With stationary outer tube ($N_2 = 0$) and increasing N_1, a remarkable rise in the Nusselt number can be observed. An additional counter-rotating outer tube ($N_2 < 0$) again leads to a small increase of the Nusselt number. On the other hand the heat transfer rates decrease down to their minimum, in the case of co-rotating tubes ($N_2 > 0$), when the tubes have nearly the same number of revolutions. In the region $0.6 < N_1 / N_2 < 0.9$ a small decrease of the Nusselt number can be detected. A sole rotation of the outer tube has only an unimportant influence on the heat transfer rate in the range of Reynolds numbers under consideration.

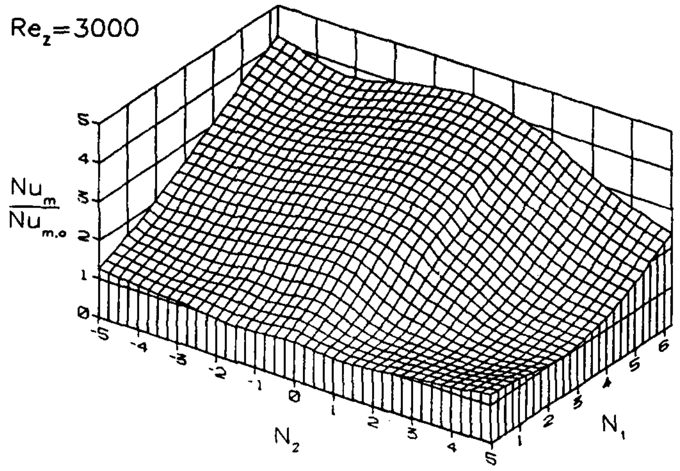

Fig. 2: Three-dimensional representation of the measured mean Nusselt numbers Nu_m as a function of N_1 and N_2 at Re_z = 3000 .

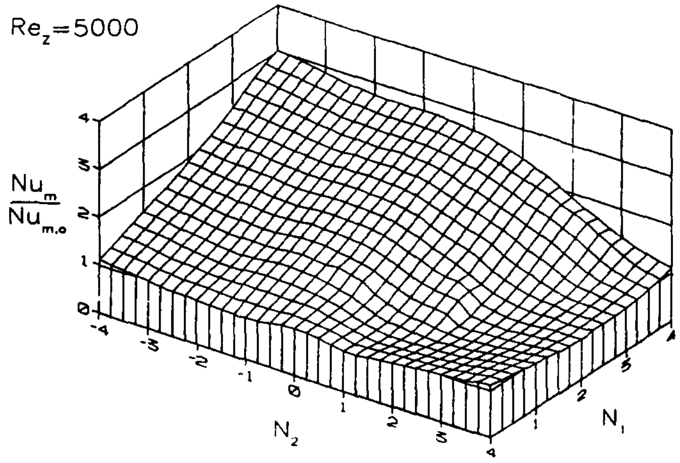

Fig. 3: Three-dimensional representation of the measured mean Nusselt numbers Nu_m as a function of N_1 and N_2 at Re_z = 5000 .

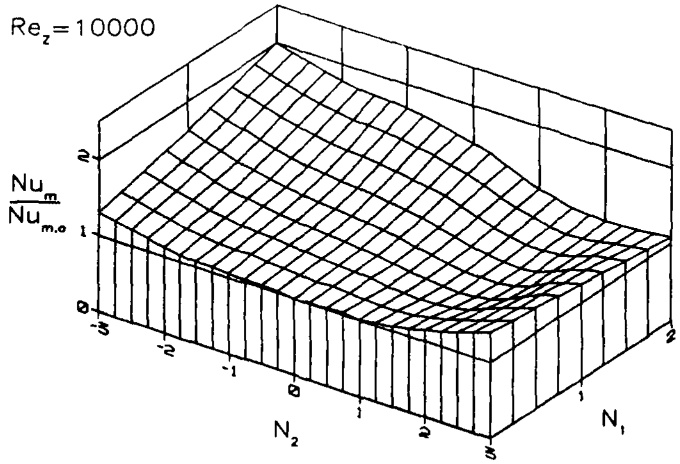

Fig. 4: Three-dimensional representation of the measured mean Nusselt numbers Nu_m as a function of N_1 and N_2 at Re_z = 10000 .

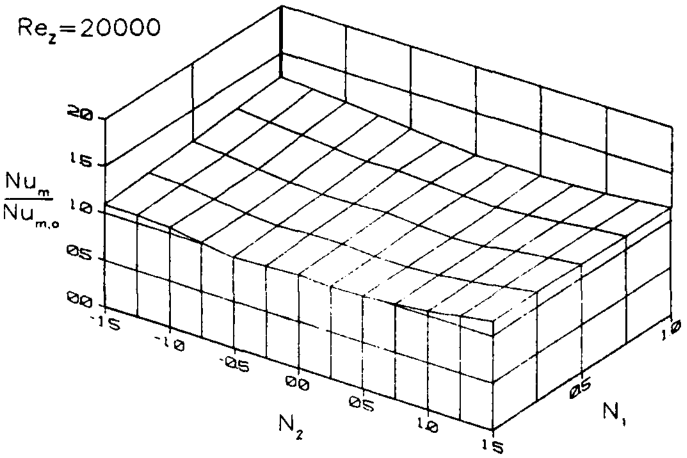

Fig. 5: Three-dimensional representation of the measured mean Nusselt numbers Nu_m as a function of N_1 and N_2 at $Re_z = 20000$.

At high flow-rate Reynolds numbers, $Re_z = 30000$, measurements could be made only for rotation rates $N < 1$. In this case no significant changes in heat transfer were determined.

Co-rotating or counter-rotating tubes have a very different influence on heat transfer in an annular gap, as revealed above. Heat transfer will decrease with radially growing tangential velocity and small differences between the rotational speeds of the two tubes. In contrast to this, the heat transfer rates rise with radially decreasing tangential velocity and very different rotational speeds of the tubes. This behavior can be explained by the different effects of a stabilizing or destabilizing distribution of centrifugal forces in the fluid, caused by the radially growing or diminishing tangential velocity on the one hand and an increasing shear stress, due to a growing difference between both rotational speeds on the other hand. In the case of counter-rotating tubes both turbulence intensifying effects of a radially decreasing tangential velocity near the inner wall and a large difference in rotational speeds superimpose. In an annulus with co-rotating tubes the turbulence suppression by a stabilizing centrifugal force distribution and small differences between the rotational speeds causes a small decrease in Nusselt number.

Finally, it should be pointed out that all experimental results have been gained for a radius ratio $r_1 / r_2 = 0.8575$.

4. THEORETICAL ANALYSIS

4.1 Conservation Equations

The calculation is based on the time-averaged boundary layer type conservation equations of mass, momentum and energy in an axisymmetric cylindrical coordinate system. The basic equations for an incompressible fluid with constant fluid properties are:

$$\frac{\partial}{\partial z}(\rho r V_z) + \frac{\partial}{\partial r}(\rho r V_r) = 0 \tag{7}$$

$$\frac{\partial}{\partial z}(\rho r V_z^2) + \frac{\partial}{\partial r}(\rho r V_r V_z) = \frac{\partial}{\partial r}\left(r \mu \frac{\partial V_z}{\partial r}\right) - r \frac{\partial p}{\partial z} - \frac{\partial}{\partial r}\left(r \rho \overline{v_r v_z}\right) \tag{8}$$

$$\frac{\partial}{\partial z}(\rho r^2 V_z V_\varphi) + \frac{\partial}{\partial r}(\rho r^2 V_r V_\varphi) = \frac{\partial}{\partial r}\left[r \mu \frac{\partial (r V_\varphi)}{\partial r} - 2 \mu r V_\varphi\right] - r^2 \frac{\partial}{\partial r}(\rho \overline{v_r v_\varphi}) - 2 r \rho \overline{v_r v_\varphi} \tag{9}$$

$$\frac{\partial p}{\partial r} = \rho \frac{V_\varphi^2}{r} \tag{10}$$

$$\rho c_p \left[\frac{\partial}{\partial z}(r V_z T) + \frac{\partial}{\partial r}(r V_r T)\right] = \frac{\partial}{\partial r}\left(r \lambda \frac{\partial T}{\partial r}\right) - \frac{\partial}{\partial r}\left(r \rho c_p \overline{v_r t}\right) \tag{11}$$

The correlations of velocity fluctuations in eq. (8) and (9) which are the Reynolds stresses and the correlation of velocity fluctuation and temperature fluctuation in eq. (11) which is the turbulent heat flux, are evaluated with a modified k-ε eddy-viscosity model.

4.2 Turbulence Model

The turbulence model applied to the present calculations is the k-ε two equation model for near-wall flows according to Launder and Sharma (Ref. 7), modified by the Richardson number as proposed by Rodi (Ref. 8). The kinetic energy of turbulence k and its dissipation rate ε are calculated from the following transport equations:

$$\frac{\partial}{\partial z}(\rho r V_z k) + \frac{\partial}{\partial r}(\rho r V_r k) = \frac{\partial}{\partial r}\left[r\left(\mu + \frac{\mu_t}{\sigma_k}\right)\frac{\partial k}{\partial r}\right] + r\mu_t\left[\left(\frac{\partial V_z}{\partial r}\right)^2 + \left(r\frac{\partial}{\partial r}\left(\frac{V_\varphi}{r}\right)\right)^2\right] - 2r\mu\left(\frac{\partial\sqrt{k}}{\partial r}\right)^2 - r\rho\varepsilon \tag{12}$$

$$\frac{\partial}{\partial z}(\rho r V_z \varepsilon) + \frac{\partial}{\partial r}(\rho r V_r \varepsilon) = \frac{\partial}{\partial r}\left[r\left(\mu + \frac{\mu_t}{\sigma_\varepsilon}\right)\frac{\partial \varepsilon}{\partial r}\right] + C_{\varepsilon 1}(1 + C_{\varepsilon 3}Ri_f)\, r\mu_t\frac{\varepsilon}{k}\left[\left(\frac{\partial V_z}{\partial r}\right)^2 + \left(r\frac{\partial}{\partial r}\left(\frac{V_\varphi}{r}\right)\right)^2\right] - C_{\varepsilon 2} f_2 r\rho\frac{\varepsilon^2}{k} + 2r\nu\mu_t\left[\frac{\partial}{\partial r}\sqrt{\left(\frac{\partial V_z}{\partial r}\right)^2 + \left(r\frac{\partial}{\partial r}\left(\frac{V_\varphi}{r}\right)\right)^2}\right]^2 \tag{13}$$

with

$$\varepsilon = e - 2\nu\left(\frac{\partial\sqrt{k}}{\partial r}\right)^2 \tag{14}$$

the modified dissipation rate of turbulent kinetic energy and

$$Ri_f = \frac{2V_\varphi\frac{\partial}{\partial r}\left(\frac{V_\varphi}{r}\right)}{\left(\frac{\partial V_z}{\partial r}\right)^2 + \left(r\frac{\partial}{\partial r}\left(\frac{V_\varphi}{r}\right)\right)^2} \tag{15}$$

The flux Richardson number, defined by equation (15), describes the effect of streamline curvature on turbulence. The streamline curvature will diminish turbulent transport in flows in which the angular momentum of the flow increases with radius and will augment it in the opposite case. The turbulent dynamic viscosity μ_t is determined from the relation which assumes an isotropic eddy viscosity.

$$\mu_t = C_\mu f_\mu \rho \frac{k^2}{\varepsilon} \tag{16}$$

The wall functions f_μ and f_2, proposed by Launder and Sharma (Ref. 7), are defined as follows:

$$f_\mu = \exp\left[\frac{-3.4}{\left(1 + \frac{Re_t}{50}\right)^2}\right] \tag{17}$$

$$f_2 = 1 - 0.3\exp(-Re_t^2) \tag{18}$$

with

$$Re_t = \frac{k^2}{\nu\varepsilon} \tag{19}$$

Most empirical constants in eqs. (12), (13) and (16) are those which are normally adopted in the k-ε model and are listed as follows: $C_\mu = 0.09$, $C_{\varepsilon 1} = 1.44$, $C_{\varepsilon 2} = 1.92$, $\sigma_k = 1.0$, $\sigma_\varepsilon = 1.3$.

The influence of the flux Richardson number on the dissipation rate ε in equation (13) is adjusted by the constant $C_{\varepsilon 3}$ which was determined according to experiments by Pfitzer (Ref. 6):

$Ri_f \le 0$: $C_{\varepsilon 3} = 0.9$

$Ri_f > 0$: $C_{\varepsilon 3} = 2.7$

The Reynolds shear stress terms $\rho\overline{v_r v_z}$ and $\rho\overline{v_r v_\varphi}$ in eqs. (8) and (9) are modelled by the aid of the turbulent viscosity and the velocity gradients as

$$-\rho\overline{v_r v_z} = \mu_t\frac{\partial V_z}{\partial r} \tag{20}$$

$$-\rho\overline{v_r v_\varphi} = \mu_t r\frac{\partial}{\partial r}\left(\frac{V_\varphi}{r}\right) \tag{21}$$

The turbulent heat flux in r-direction can be expressed as

$$-\rho\overline{v_r t} = \frac{\mu_t}{Pr_t}\frac{\partial T}{\partial r} \tag{22}$$

with the turbulent Prandtl number Pr_t. Kays and Crawford (Ref. 9) proposed the following distribution for the turbulent Prandtl number in a wall-bounded shear flow.

$$Pr_t^{-1} = \frac{1}{2Pr_{t,\infty}} + C\frac{\mu_t}{\mu}Pr\sqrt{\frac{1}{Pr_{t,\infty}}} - \left(C\frac{\mu_t}{\mu}Pr\right)^2 \times \left[1 - \exp\left(-C\frac{\mu_t}{\mu}Pr\,Pr_{t,\infty}\right)^{-1}\right] \tag{23}$$

with $Pr = 0.71$, $Pr_{t,\infty} = 0.65$ and $C = 0.1$ used in this analysis.

The local and the mean Nusselt number are calculated according to the definition in section 2.

4.3 Boundary Conditions

The parabolic nature of the boundary-layer equations requires that boundary conditions be provided on three sides of the solution domain. In addition to initial conditions for the momentum, turbulence and energy equations, the heat fluxes at the surfaces of both tubes are prescribed and the zero slip condition holds.

$$r = r_1: \quad V_r = 0,\ V_\varphi = V_{\varphi 1},\ V_z = 0,\ \frac{\partial T}{\partial r} = 0,\ k = 0,\ \varepsilon = 0$$

$$r = r_2: \quad V_r = 0,\ V_\varphi = V_{\varphi 2},\ V_z = 0,\ \frac{\partial T}{\partial r} = -\frac{\dot{q}_w}{\lambda},\ k = 0,\ \varepsilon = 0$$

$$z = 0: \quad p = p_0,\ V_\varphi = 0,\ V_z = V_z(r),\ T = T_0,\ k = k(r),\ \varepsilon = \varepsilon(r)$$

For simplification the inlet profile of the dependent variables V_z, k and ε are determined refering to a fully developed turbulent flow in an annulus without rotation.

The tangential velocity V_φ at the inlet section is set to zero, except at the tube walls.

The above-mentioned differential equations are solved numerically, applying a finite-volume method with 150 grid points, located in the radial direction at nonuniform intervals.

5. RESULTS AND DISCUSSION

In the experimental and numerical investigations of heat transfer in the hydrodynamic and thermal entrance region, a significant influence of rotation on heat transfer and fluid flow was observed. The radial distribution of the fluid velocity and the temperature were measured at the end of the test section ($z/d_h \approx 60$) and calculated for the same position. The special case, the inner tube rotating and the outer tube at rest, shall be presented first.

5.1 Rotation of the Inner Tube

For mere inner tube rotation, the measured velocity and temperature distributions are plotted in Figs. 6 - 8 . They are compared with numerical results, calculated with the aid of the above-mentioned theoretical model.

At the entry of the annulus an additional shear stress occurs in order to accelerate the fluid in tangential direction, due to the rotating inner wall. This causes an additional production of turbulent kinetic energy, enhanced by the radially decreasing angular momentum which destabilizes the flow.

With increasing rotation rate N_1, the velocity profiles in axial and tangential direction approach a more turbulent

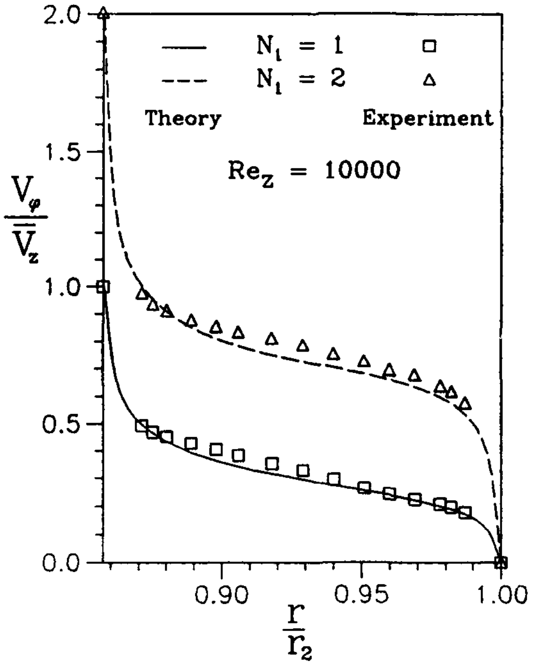

Fig. 7: Tangential velocity distribution in an annulus with a rotating inner tube and a stationary outer tube.

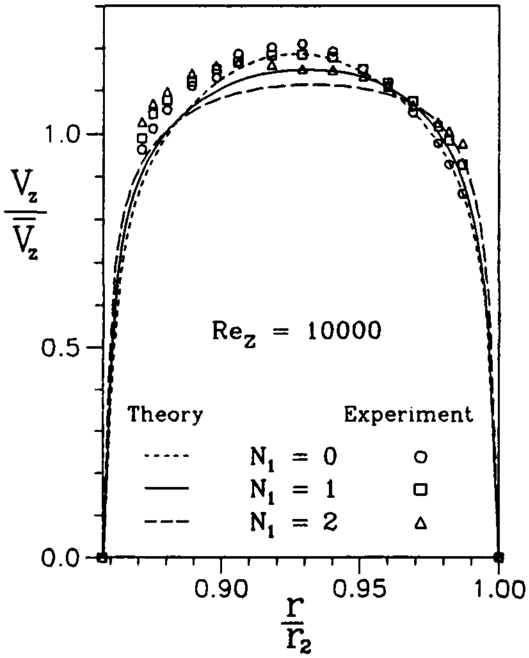

Fig. 6: Axial velocity distribution in an annulus with a rotating inner tube and a stationary outer tube.

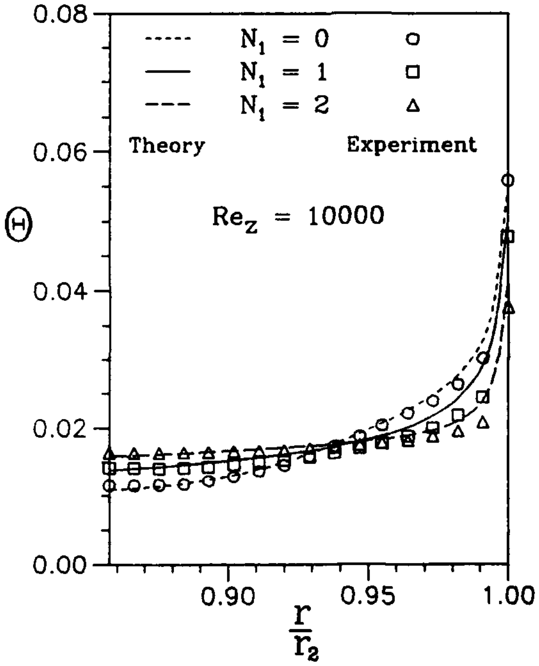

Fig. 8: Temperature distribution in an annulus with a rotating inner tube and a stationary outer tube.

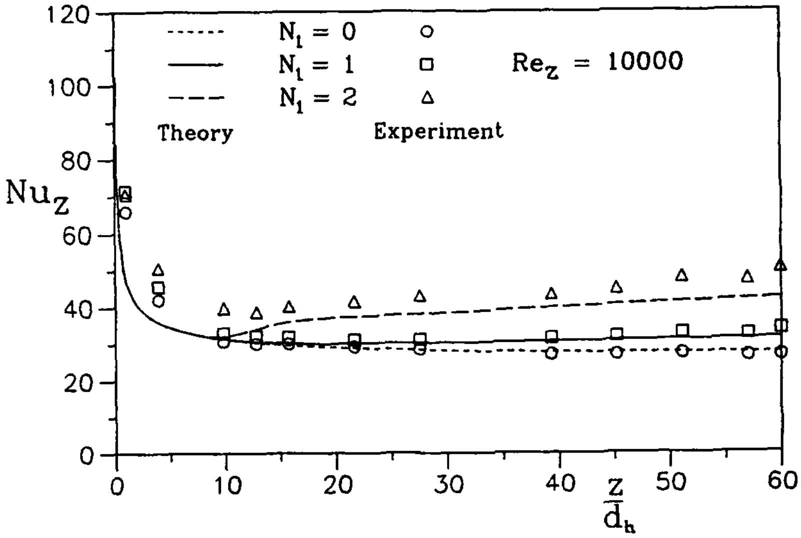

Fig. 9: Development of the local Nusselt number in an annulus with a rotating inner tube and a stationary outer tube.

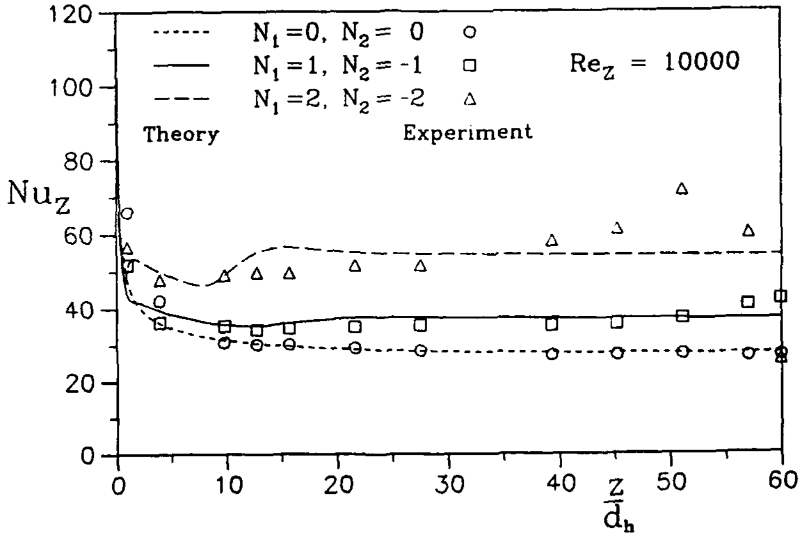

Fig. 10: Development of the local Nusselt number in an annulus with counter-rotating tubes.

shape which corresponds to increasing turbulent fluctuations in the fluid. The profiles get flattened in the core, whereas, an increase of the velocity gradients at both walls can be observed. It should be pointed out that the tangential velocity profile (Fig. 7) has not attained its fully developed shape at the axial position $z/d_h = 60$. In this case the tangential velocity at the centerline of the gap would be half the rotational speed of the inner tube, as calculated by Pfitzer (Ref. 6).

The radial temperature distributions, with the temperature normalized according to equation (4), change in the same way and get appreciably flattened by rotation. The outer wall temperature drops sharply with inner tube rotation and the profile continues towards the adiabatic inner wall with a slope more gentle than in the non-rotating case.

The development of the local Nusselt number Nu_z in axial direction is depicted in Fig. 9 . With uniform heating at the outer wall, the Nusselt number decreases throughout the length of the first ten hydraulic diameters, because of an increasing thermal boundary-layer thickness. As soon as the angular momentum reaches the outer wall, the heat transfer intensifies and especially for $N_1 = 2$, the Nusselt number increases remarkably.

5.2 Counter-rotating Tubes

For counter-rotating tubes, the effects of the rotation rates N_1 and N_2 on the axial and tangential velocity distribution

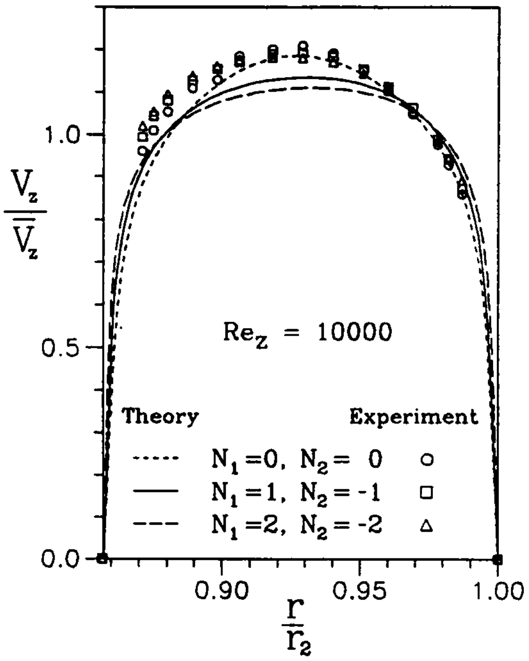

Fig. 11: Axial velocity distribution in an annulus with counter-rotating tubes.

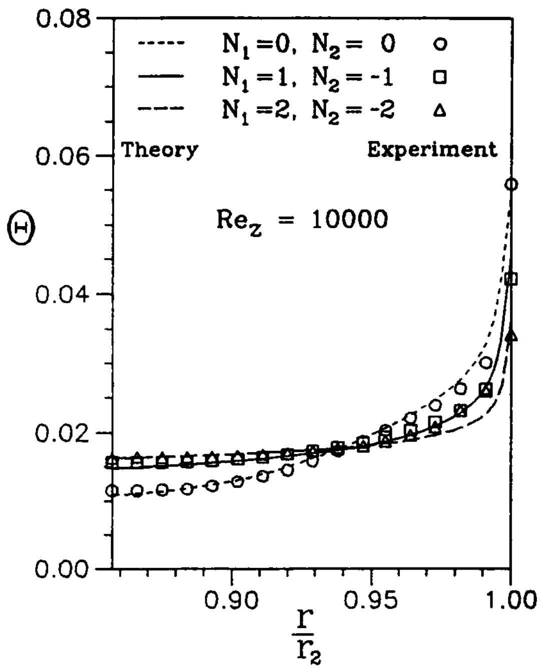

Fig. 13: Temperature distribution in an annulus with counter-rotating tubes.

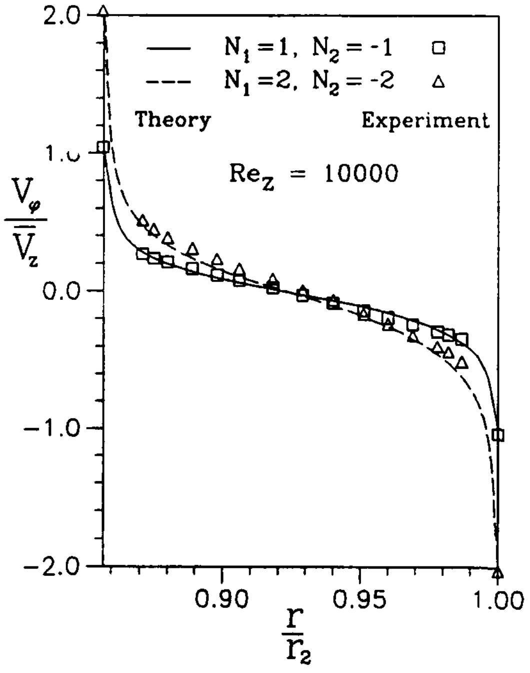

Fig. 12: Tangential velocity distribution in an annulus with counter-rotating tubes.

and on the temperature profile are depicted in Figs. 11 - 13 .

In this case an additional shear stress $\tau_{r\varphi}$ is induced by the rotation of the inner and the outer tube, enhancing the turbulent fluctuations from both sides of the gap. Besides that, the developing tangential velocity profile causes a stabilizing distribution of centrifugal forces ($Ri_f > 0$) in the outer half of the gap, and a destabilizing distribution ($Ri_f < 0$) in the inner half. Both phenomena are superimposed, whereby the turbulence suppressing effect of the positiv Richardson number in the outer half of the gap is of less influence than the turbulence enhancing shear stress $\tau_{r\varphi}$.

As for mere inner tube rotation, the velocity profiles in axial direction (Fig. 11) attain a more turbulent shape with increasing rotation rates N_1 and N_2 which corresponds to increasing turbulent fluctuations in the fluid. In Fig. 12 the experimental results of the tangential velocity are in close agreement with the theory. The analysis makes also evident that in this case the fluid flow is fully developed at $z/d_h \approx 60$.

Concerning the radial temperature distribution in Fig. 13, the same effects as for a sole rotation of the inner tube can be observed even more pronounced. The curves are alinged in an orderly manner in passing from the uniform heat flux outer boundary to the adiabatic inner boundary. At the outer wall a large temperature decrease can be detected. With increasing rotation in the opposite direction, the inner boundary temperature increases and the temperature at the outer wall decreases.

The development of the local Nusselt number Nu_z for counter-rotating tubes is plotted in Fig. 10 . A comparison with Fig. 9 for mere inner tube rotation reveals that the influence of turbulence intensification on heat transfer sets in closer to the entry with an additional outer tube rotation. Furthermore, a larger increase of the local Nusselt number Nu_z can be observed for counter-rotating tubes.

5.3. Influence of radius ratio

All experimental and theoretical results in this analysis have been gained for a radius ratio $r_1 / r_2 = 0.8575$.

Pfitzer and Beer (Ref. 10) studied the influence of the radius ratio on heat transfer with the aid of a theoretical model for fully developed flow. Their investigation leads to the following conclusion. In a narrow annulus and for specified rotation rates, the gradient of the circumferential velocity is larger than in a wide annulus. The larger shear stress $\tau_{r\varphi}$ in the fluid leads to an excitement of turbulence and, therefore, to an increase in heat transfer. On the other hand, the laminarizing effect of the distribution of the stabilizing centrifugal forces, expressed by the Richardson number, gains influence in a wide annulus.

6. CONCLUSIONS

In turbulent annular flow, inner and outer tube rotation produce significant effects on the velocity and temperature fields as well as on heat transfer rate. These effects were studied experimentally and numerically in the hydrodynamic and thermal entrance region of a concentric annulus between independently rotating tubes. In the theoretical study a modified k-ε Turbulence model was applied, taking into account the influence of streamline curvature on turbulence.

The investigations reveal a clear enhancement of the Nusselt number with increasing rotation of the inner tube. An additional counter-rotating outer tube leads to a further small increase in heat transfer. On the other hand the Nusselt number decreases with co-rotating tubes down to its minimum, when the outer tube rotates a little faster than the inner tube. The mere rotation of the outer tube, with the inner tube being at rest, has only an unimportant influence on heat transfer for the radius ratio $r_1 / r_2 = 0.8575$.

Finally, it has to be pointed out that Taylor vortices could not be detected using the hotwire probe in the range of parameters under consideration.

7. REFERENCES

1. Taylor, G.I., "Stability of a Viscous Liquid Contained Between Two Rotating Cylinders", Phil. Trans. Royal Society London, A 223, 1923, pp 289-343.
2. Chandrasekhar, S., "The Stability of Spiral Flow Between Rotating Cylinders", Proc. Roy. Society London, A 265, 1961, pp 188-196.
3. Kaye, J. and Elgar, E.C., "Modes of Adiabatic and Diabatic Fluid Flow in an Annulus with an Inner Rotating Cylinder", Journal of Heat Transfer, 80, 1958, pp 753-765.
4. Gu, Z.H. and Fahidy, T.Z., "Visualization of Flow Patterns in Axial Flow Between Horizontal Coaxial Rotating Cylinders", The Canadian Journal of Chemical Engineering, 63, 1985, pp 14-21.
5. Kuzay, T.M., "Turbulent Heat and Momentum Transfer Studies", Ph.D. Thesis, University of Minnesota, 1973
6. Pfitzer, H., "Konvektiver Wärmetransport im axial durchströmten Ringspalt zwischen rotierenden Hohlwellen", Doctoral Thesis, Technische Hochschule Darmstadt, 1991
7. Launder, B.E. and Sharma, B.I., "Application of the Energy-Dissipation Model of Turbulence to the Calculation of Flow Near a Spinning Disc", Letters in Heat and Mass Transfer, 1, 1974, pp 131-138.
8. Rodi, W., "Influence of Buoyancy and Rotation on Equations for the Turbulent Length Scale", 2nd Int. Symp. on Turbulent Shear Flows, London, 1979, pp 10.37-10.42 .
9. Kays, W.M. and Crawford, M.E., "Convective Heat and Mass Transfer", New York, McGraw-Hill Book Company, 1980 (ISBN 0 07 033457 9)
10. Pfitzer, H. and Beer, H., "Heat Transfer in an Annulus Between Independently Rotating Tubes with a Turbulent Axial Flow", Int. Journ. of Heat and Mass Transfer, 35, 1992, pp 623-633.

Discussion

QUESTION 1:

DISCUSSOR: W. Waschka, BMW Rolls Royce

What were the tangential to axial velocity ratios at the inlet of the annulus? That ratio strongly influences the heat transfer rates and the laminar/turbulent transition at the very entrance of the annulus.

AUTHORS REPLY:

As stated in the paper, the tangential velocity for all cases was equal to zero at the inlet of the test section.

QUESTION 2:

DISCUSSOR: D.T. Vogel, DLR

For which Reynolds number does transition occur?

AUTHOR'S REPLY:

Transition from laminar to turbulent flow depends upon flow Reynolds number Re_z and rotation rates N_1 and N_2. This investigation was restricted to turbulent flow. For the case of a rotating inner tube, the transition region was investigated experimentally by Kaye and Elgar (Ref. 3).

QUESTION 3:

DISCUSSOR: D.T. Vogel, DLR

Which inlet boundary conditions did you use for k and ε?

AUTHORS REPLY:

As stated in the paper, the inlet profiles of V_z, k and ε were determined using the results for a fully developed turbulent flow in a non-rotating annulus.

QUESTION 4:

DISCUSSOR: J.W. Chew, Rolls Royce

Your comparison between experimental and computational results shows some good agreement. To what extent is this dependent on the choice of the Richardson number multiplying factor $C_{\varepsilon 3}$ in the turbulence model?

AUTHOR'S REPLY:

Assuming $C_{\varepsilon 3} = 0$ leads to a maximum deviation of about three percent from the calculations shown in the paper. This statement is restricted to the radius ratio under consideration. In a narrow gap, where fluid flow is dominated by shear stresses the influence of $C_{\varepsilon 3}$ will be even smaller, whereas in wide gap the radial distribution of centrifugal forces is of importance and therefore the value of $C_{\varepsilon 3}$ will have a significant influence on calculated results in this case.

The Effect of Main Stream Flow Angle on Flame Tube Film Cooling

H. Klinger, D. K. Hennecke
Technical University Darmstadt
Petersenstr. 30, 6100 Darmstadt, Germany

SUMMARY

Generally film cooling configurations are positioned such that they are oriented perpendicular to the main stream flow direction. However in many cases, in particular combustor applications, different flow angles may occur. Then, due to the interaction between the main stream and the cooling film, a complex three-dimensional flow field with a vortex is formed. An experimental study was done to study the basic effects. The cooling configuration was a vertical slot which could be turned by up to about 60 degrees from the position perpendicular to the main stream. Velocity distributions were measured and the adiabatic film cooling effectiveness was determined using the liquid crystal technique. The results show that, along lines parallel to the slot, the film cooling effectiveness varies strongly, even with small slot turning angles. This would lead to hot and cold spots in a combustor application. A simple semi-empirical correlation for the average cooling effectiveness is derived using the main stream velocity component perpendicular to the slot.

LIST OF SYMBOLS

a_1, a_2, a_3, b, c	constants
B	width of test section
c_p	specific heat at constant pressure
f(), g()	function of
H	height of test section
I	intensity
i	graylevel
L	length of test section
M	mass flux ratio
n	frequency
p, q	columns, rows
Re_s	Reynolds number based on slot width
S	threshold value
s	slot width
T	temperature
Tu	intensity of turbulence
U, V	x- and y-velocity components
x, y, z	co-ordinates
α	slot angle relative to main stream flow
β	blowing angle
δ	boundary-layer thickness
η	film cooling effectiveness
ϑ	$=(T-T_m)$
λ	heat conductivity
ν	streamline angle
ρ	density
φ	reattachment angle
Subscripts	
aw	adiabatic wall
m	main stream
r	recirculation
s	slot stream
α	relative to flow angle

1 INTRODUCTION

Today's advanced gas turbines still have great potentials for improvement by a further increase in turbine entry temperatures along with higher compressor pressure ratios. The resulting higher temperature level in the combustor mixing zone requires a more intensive wall cooling. The cooling task is further complicated because of the higher cooling air temperature owing to the increased pressure ratio and the resulting lower cooling potential. The necessary improvement of the cooling effectiveness of pure film cooling is hardly achievable in light of today's already high standard [1, 2]. However, the cooling potential of the coolant can be better utilized by first using it for convective cooling of the combustor wall and then ejecting it as cooling film [3, 4]. This combined cooling concept may be realized, for instance, using square or triangular metal or ceramic surface elements that are impingement cooled on their back sides. The coolant is then ducted through slots between the elements and ejected into the combustor such that it forms cooling films. In this way, intersecting film cooling slots are formed that, depending on combustor geometry and swirl, are oriented towards the main stream flow direction under various angles. Thus, the usual perpendicular orientation of the film cooling slot configuration resulting in a two-dimensional flow field does not occur. Rather, a three-dimensional flow field with swirls transporting hot gas towards the wall resulting in hot regions may be expected.

The present basic study investigates the dependence of the adiabatic film cooling effectiveness

$$\eta = \frac{T_{aw} - T_m}{T_s - T_m} \qquad (1)$$

on the angle α of a single slot configuration (Fig. 1) and on the main stream to coolant mass flux ratio defined by

$$M_\alpha = \frac{\rho_s V_s}{\rho_m U_m \sin\alpha} . \qquad (2)$$

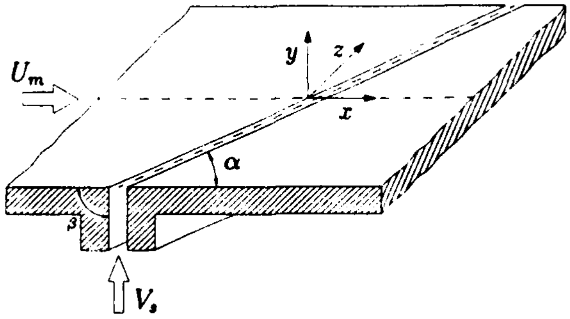

Figure 1: Slot geometry

For a better understanding of the basic phenomena, experiments were done on a simplified enlarged model with the main stream unheated. In all cases the slot was perpendicular to the surface, i. e. $\beta = 90°$.

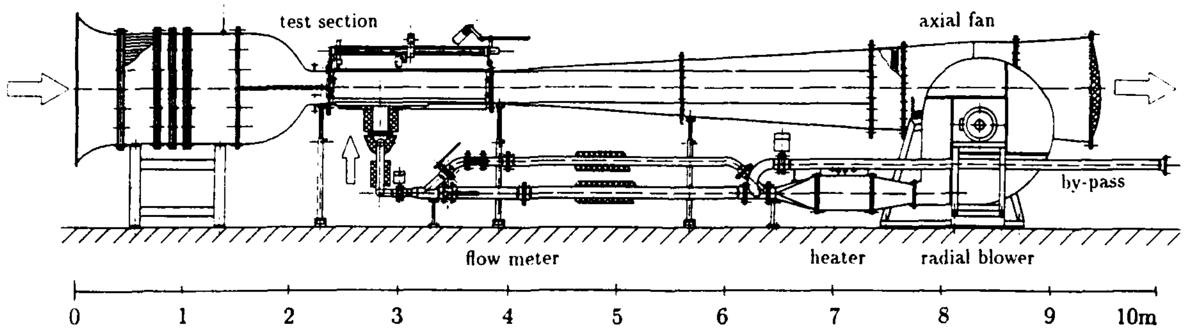

Figure 2: Experimental apparatus

2 EXPERIMENTAL APPARATUS

The experiments were done in the new combustor film-cooling rig (Fig. 2). It is an Eiffel type wind tunnel with a measuring section with height $H = 300$ mm, width $B = 360$ mm and length $L = 1500$ mm. The inlet section with flow straighteners and contraction was designed carefully resulting in a very uniform velocity distribution and a low turbulence level of $Tu_m < 0.2\%$. The main flow velocity can be varied continuously up to $V_m = 100$ m/s corresponding to $Re_m = 2.25 \cdot 10^6$ based on the hydraulic diameter. After passing the test section, the main stream flows through a diffuser, a blower and then into the ambient.

The film cooling slot was placed in a disk that forms part of the tunnel floor (Fig. 3). The disk can be rotated, thus the angle α of the slot relative to the main flow direction may be changed continuously between $\alpha = 90°$ and $30°$. For experimental ease, the main stream to coolant temperature ratio was not intended to be simulated and the coolant, rather than the main stream, was heated, typically by 30° to 100° C. The "coolant" flows through a blower, an orifice flow meter, through a settling chamber with flow straighteners and then into the film slot. There the turbulence level is $Tu_s < 0.6\%$ and the maximum velocity 160 m/s ($Re_s = 4.37 \cdot 10^5$) at $\alpha = 90°$ and 115 m/s ($Re_s = 3.14 \cdot 10^5$) at $\alpha = 30°$. The slot has movable sidewalls that can be adjusted such that for every angle α the slot extends only from one tunnel side wall to the other and the film flows perpendicularly into the main stream. Covers on both sides of the tunnel ensure that there is no leakage of coolant. The side walls and the top wall of the test section were made of perspex to facilitate flow visualization and optical measurements. The bottom wall including the disk were made of 20 mm thick Pertinax with heavy insulation on the outside to ensure near-adiabatic conditions.

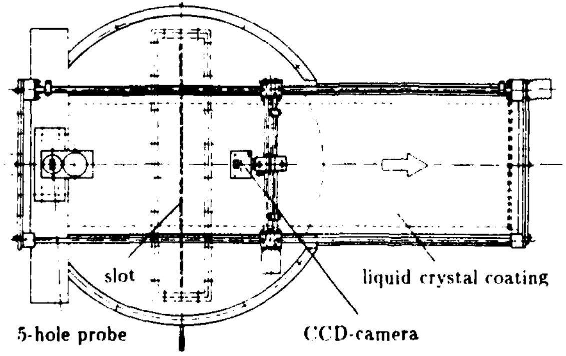

Figure 3: Test section

3 MEASUREMENT TECHNIQUES

Flow velocities were measured with five-hole probes and the turbulence level with hot-wire probes. The traversing of the probes and the data acquisition was done by computer control.

The surface temperature distribution behind the slot was determined by the well-known liquid crystal method [5, 6, 7]. Certain cholesterine liquid crystals have a temperature dependent selective reflection of light. Thus, isotherms on a surface coated with liquid crystals appear as lines of equal color. The coating of the encapsulated crystals used is thin enough so that it has negligible influence on the heat transfer. Thermocouples mounted flush in the surface provided additional temperature data for accuracy control and calibration. By selecting liquid crystals with a color range adjusted to the test conditions and varying the film temperature, extremely high resolutions of surface temperature distribution may be achieved.

For the data acquisition, an image processing system was used [8, 9]. A video camera mounted on top of the test section views onto the liquid crystal coated surface. Its analog signal is then fed into a personal computer with an analog-digital converter. A real time digitizer (PC Vision Plus/ Imaging Technology) with CCIR-Standard with a scanning frequency of 10 MHz and a pixel grid of 1024x512 with 8 bits each was used. The A/D-electronic-card has a processor that allows elementary memory operations in real-time. Further analyses, e. g. the processing of the pixel fields, are done on the processor of the personal computer. With the present system, the degree of discretization of a complete picture is 262,144 picture points, i. e. for the evaluation of a color line a square matrix of 512 lines and 512 columns with 256 steps of gray are readily available for the numerical analysis. With a test section width of 360 mm, there is a resolution of about 1.5 picture points/mm. The evaluation of the picture quality for the required preprocessing and adjustment of hardware is done with the intensity profile. Fig. 4 shows a section through a typical gray level distribution of a black and white picture. In this example the liquid crystal transition shows a distinct signal peak which differs clearly from the background noise.

For the identification of the calibrated edge of the color line, a threshold value method was used. Because there are pictures of different quality, it is necessary, in view of the large number of experiments, to read the respective intensities automatically. For this purpose, the frequency histogram is smoothed by averaging (Fig. 5a). The second peak as taken from the smoothed histogram represents all graylevels

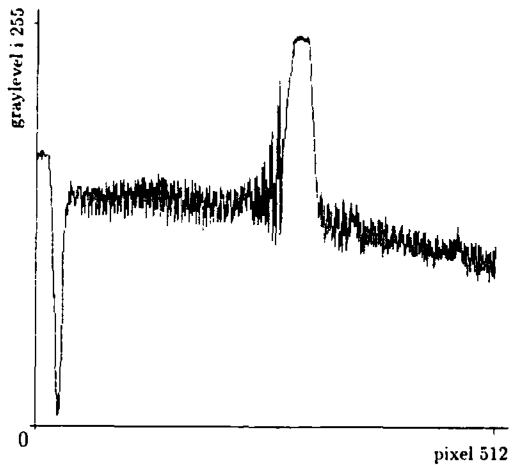

Figure 4: Distribution of intensity

of the transition line. Consequently a respective value as threshold can be determined by the signal flank according to the calibration. The high gradient of the peak on the downstream side leads to a weak minimum in the graylevel frequency directly in front of the signal maximum.

After differentiating according to

$$\frac{d\overline{n}}{di} \doteq \frac{\overline{n_i} - \overline{n_{i-i_0}}}{i - (i - i_0)}\ , \quad i = 0 \div 255 \qquad (3)$$

the threshold value S can be determined by analysing the above mentioned minimum in Fig. 5b.

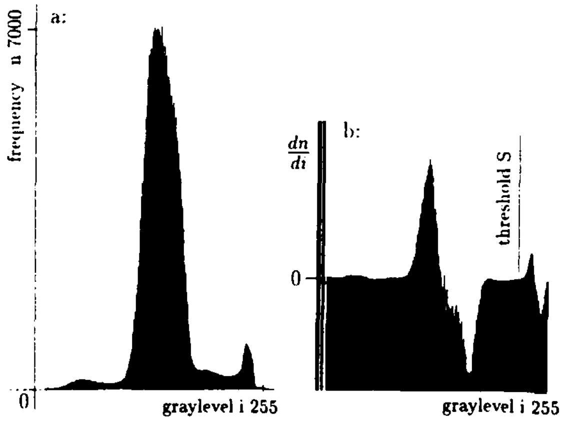

Figure 5: a: Smoothed histogram and b: diff. histogram with threshold value

The influence of the high-frequency scatter remaining after smoothing is best suppressed when i_o roughly corresponds to the width of the signal peak. Now, all pixels of the original image $f(p,q)$ are set to intensity I_1 or I_2 depending whether the values are below or above the threshold value S, thus obtaining a new image $g(p,q)$:

$$g(p,q) = \begin{cases} I_1\ , 0 \leq f(p,q) < S \\ I_2\ , S \leq f(p,q) \leq f_{max} \end{cases} \qquad (4)$$

where p and q represent the column and line number, respectively. Then ideally, the color change of the calibrated liquid crystal has the intensity I_2 and the background the intensity I_1. By subsequently evaluating the whole contour, the color transition line and, thus, the isotherm is determined. Due to positioning and focussing errors of the camera as well as the noise contribution to the image signal, the resolution may be in error by up to 6 pixels, corresponding to about 3 mm. The temperature is determined with an accuracy of about ±0.4 K.

4 RESULTS AND DISCUSSION

Experiments were done for the following values of M and α:

α	M	M	M	M	M	M
90.0 °	0.50	0.74	0.85	0.99	1.50	2.53
82.5 °	-	-	-	1.01	1.51	2.49
75.0 °	0.49	0.75	0.85	0.98	1.47	2.49
60.0 °	0.50	0.74	0.86	1.00	1.45	2.49
45.0 °	0.51	0.74	0.84	1.03	1.46	2.48
30.0 °	0.50	0.76	0.86	0.99	1.49	2.50

Detailed results will be presented only for a few test points but they serve as examples illustrating the tendencies observed in all tests [10].

A physically correct interpretation of the measured film cooling effectiveness distributions for various values of α is questionable without the knowledge of the flow field. Therefore, the velocity distributions were measured first.

4.1 Flow Field

The flow field was determined for all test conditions with $M > 1.0$ using a five-hole probe [11] traversed in the three coordinate directions through the whole test section.

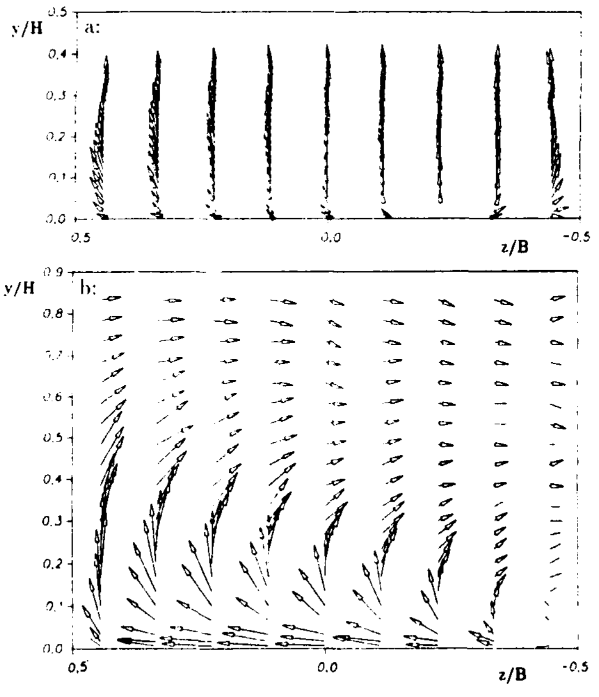

Figure 6: Flow field just before slot a(top): α=90 °, b(bottom): α=30 ° (x/s=-6.4, M=2.5, viewed downstream)

In Fig. 6 the velocity components in the y-z-plane of the flow field just before the slot is depicted for α = 90 ° (top) and for 30 ° (bottom). For the perpendicular configuration (α = 90 °) only a small deviation from the two-dimensional flow is observed as expected (Fig. 6a). However, turning the slot by 60 ° (α = 30 °), a strong effect of α may be observed (Fig. 6b). Close to the wall, the main stream approaching the slot with $\alpha = 30^\circ$ is deflected into the slot direction. Farther away from the wall, this deflection is reduced and, finally, reversed forming a large vortex. Taking the area-averaged flow angle for the two cases, a net deviation of the flow by 0.34° and 0.83°, respectively, was obtained substantiating the two- dimensionality in case of $\alpha = 90^\circ$ and the accuracy of the measurements. The flow deviation near the tunnel floor and farther away compensate, thus satisfying the continuity condition in an incompressible duct flow.

Due to the relatively strong momentum of the film normal to the main flow direction, flow separation and recirculation occur. This results in a more intense momentum and heat exchange, reducing more rapidly the cooling effectiveness than in case of a tangential ejection of cooling air. This flow field is characterized by a separation line at the downstream edge of the slot and a reattachment line. The results show that for smaller mass flux ratios M this reattachment line is parallel to the slot in the central region, even for large turning of the slot. The relative length $x_{\alpha,r}/s$ of the recirculation zone is a function of mass flux ratio M and slot angle α, with $M_s = M/\sin\alpha$ as the main correlating parameter as shown in Fig. 7. The data correlate well with

$$\left(\frac{x_{\alpha,r}}{s}\right)_\alpha = 15\left(\frac{M}{\sin\alpha}\right)^{\frac{3}{2}} . \qquad (5)$$

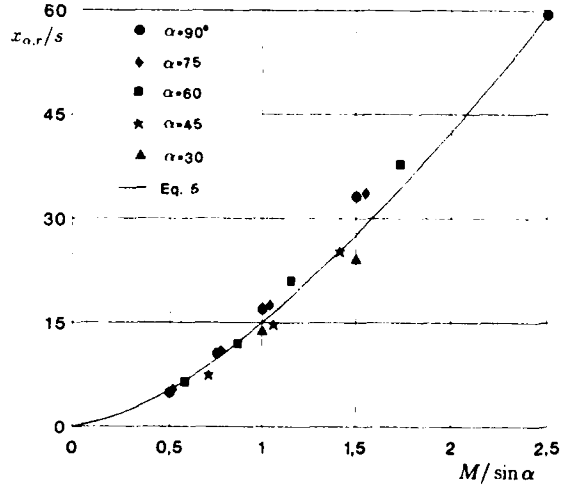

Figure 7: Length of recirculation zone

The following flow fields, Fig. 8, illustrate the situation in the plane at a distance $x/s = 74$ parallel to the slot. For $\alpha = 90^\circ$ (Fig. 8a) the flow is still essentially two-dimensional. These results are in good agreement with those of [12, 13]. However for $\alpha = 30^\circ$ (Fig. 8b), strong vortices may be observed making the flow very three-dimensional. It should be noted that the large velocity gradients in the vortex cores could not be resolved accurately with the five- hole-probes used. Characteristic for such flows is the stable structure of the vortex even at great distance behind the slot [14, 15].

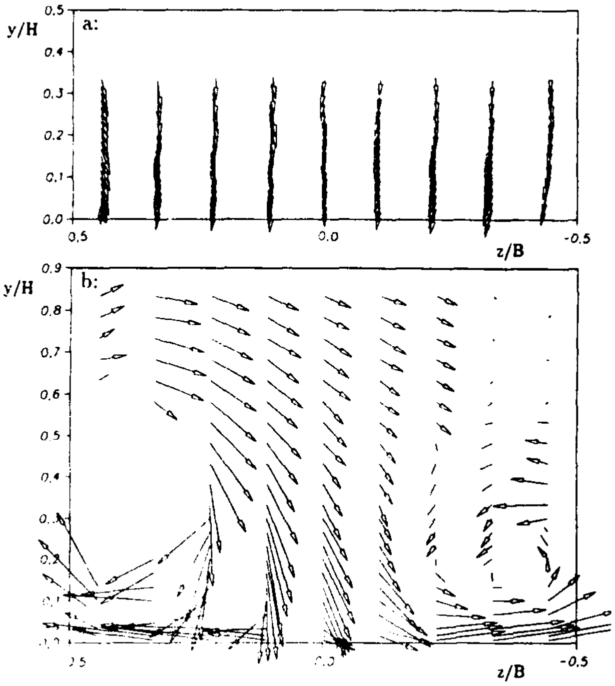

Figure 8: Flow field behind slot a(top): $\alpha=90^\circ$, b(bottom): $\alpha=30^\circ$ (x/s=74, M=2.5, viewed downstream)

Fig.8b displays a second smaller vortex also growing downstream like a cone. It is formed by the streamlines originating at the leading edge of the slot. The flow field and the surface streamlines behind an oblique slot are schematically depicted in Fig. 9. It shows the flow separations caused by strong pressure gradients. Due to the finite width of the channel, the slot has a finite length. The vortex starts at the forward slot end, and a vortex sheet rolls up in a cone-shaped manner. The vortex is three-dimensional, which means that the fluid particles move on spiral paths with increasing radius. With sufficiently large turning of the slot and high blowing rate, the vortex is stable increasing linearly along the slot. Therefore, there exists a similarity of the vortex velocity distributions.

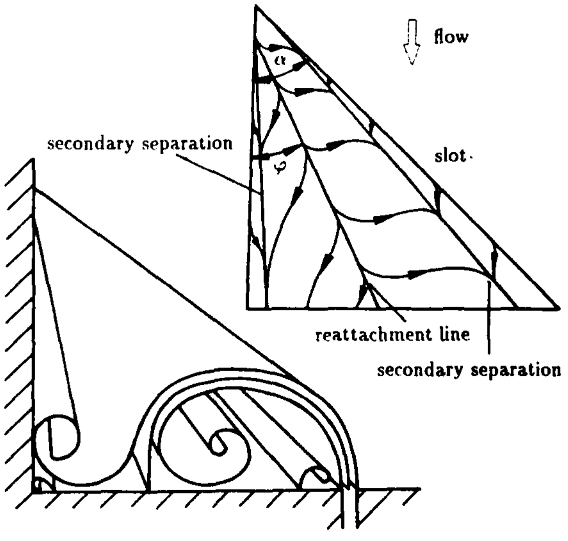

Figure 9: Schematic presentation of flow field

The separation line is again the slot trailing edge. As may be seen from Fig. 8b the flow near the wall separates into two opposite directions, forming a stagnation line which is a reattachment line. The vortex which starts at the upstream end the slot increases in the slot direction like a cone, thus the reattachment line forms an angle $\alpha - \varphi$ with the slot. Fig. 10 shows this angle $\alpha - \varphi$ as a function of the slot angle α with the mass flux ratio as parameter. The data points may be correlated by

$$\varphi = \alpha - \left[(a_1 + a_2 M + a_3 M^2)(90 - \alpha)^b e^{c(90-\alpha)}\right] \qquad (6)$$

with

$$\begin{aligned} a_1 &= -4.25 & b &= 0.9 \\ a_2 &= 11.5 & c &= -0.06 \\ a_3 &= -2.4\,. \end{aligned}$$

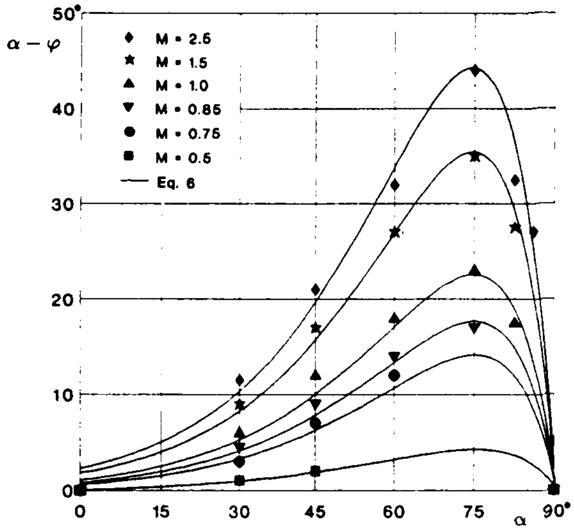

Figure 10: Reattachment angle of vortex flow

The data and Eq.(6) indicate that the flow field reacts already to a relatively small turning of the slot with the formation of a vortex having a steep reattachment angle.

The separation bubble has a recirculation length that corresponds to the blowing rate. Under the influence of the main stream, the slot inclination results in cross flow that transports the mass required to support the recirculation zone. Then the parallel and the inclined reattachment lines intersect as sketched schematically in Fig. 11. Apparently, with low blowing rates or small slot angles the mass flow induced by the cross velocity components is not sufficient to feed a steadily growing vortex. Then the reattachment parallel to the slot occurs. For this zone the symbol $2D_\alpha$ is chosen, because relative to the slot the flow is essentially two- dimensional but turned relative to the main flow direction by the angle α (Fig. 11b). With increasing turning of the slot or with higher blowing rates this $2D_\alpha$-zone becomes smaller and the intersection point moves towards the downstream slot end, until the cone-shaped three-dimensional vortex covers the whole channel width (Fig.11c).

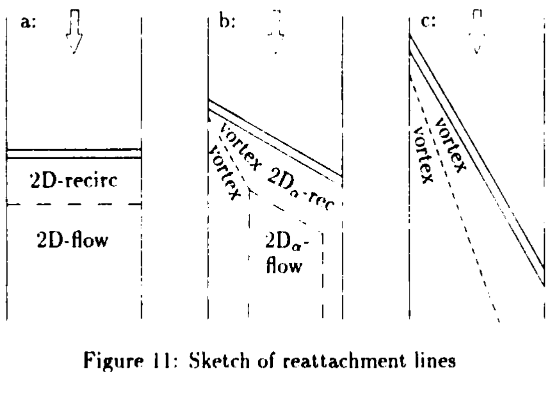

Figure 11: Sketch of reattachment lines

4.2 Film Cooling Effectiveness

At first, a comprehensive test program was done measuring the film cooling effectiveness for the $\alpha = 90°$ case, i. e. the two-dimensional situation, in order to establish the measuring technique and to permit comparisons with literature. Such a comparison with data from [16] to [20] was made and a comparison with [17] is shown in Fig. 12. Very good agreement may be observed, proving the applicability of the new test facility and the measuring technique.

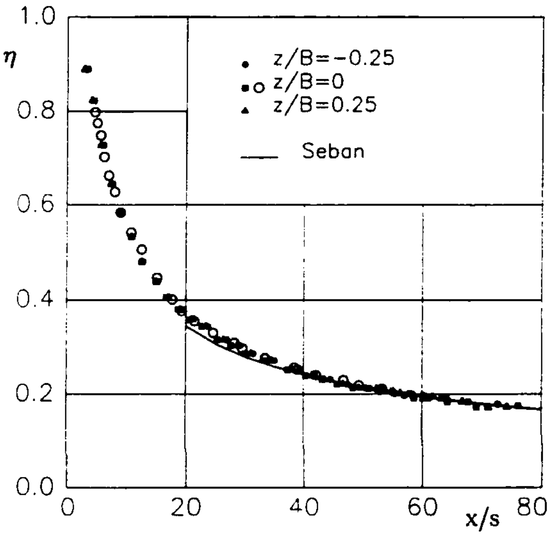

Figure 12: Film cooling effectiveness for normal main stream direction - Comparison with measurements from Seban et al. [17] ($\alpha = 90°$, $M = 0.5$)

In Fig. 13 measured isotherms are presented for a mass flux ratio $M = 0.5$ and slot angles $\alpha = 90°$; $60°$; $45°$; and $30°$. These plots are representative for the whole parameter variation. While Fig. 13a shows a nearly two-dimensional situation, Fig. 13b (slot turned by 30°) displays an unsymmetric distribution of the isotherms indicating a remarkable influence of slot angle already at relatively small slot turning, Fig. 13c and 13d. It can also be seen clearly that the isotherms in the $2D_\alpha$-zone run parallel to the slot, especially in the region close to the slot. The intersection of the reattachment line known from the measured flow field (Eq. 5) and the vortex recirculation line obtained from Eq. 6 marks off the $2D_\alpha$-zone at the upstream end of the slot. On the right hand side, there is another characteristic point on the reattachment line marking the second limit of the $2D_\alpha$-recirculation zone, thus establishing the width of this zone which exists even at the large slot turning. So the film cooling experiments support the $2D_\alpha$-behavior as observed in the flow field investigation.

With increasing distance from the slot, the direction of the film cooling air looses its influence on the flow field and the isolines turn towards the direction normal to the main flow. Owing to the change of flow direction that the main flow forces on the cooling flow, a stronger mixing results

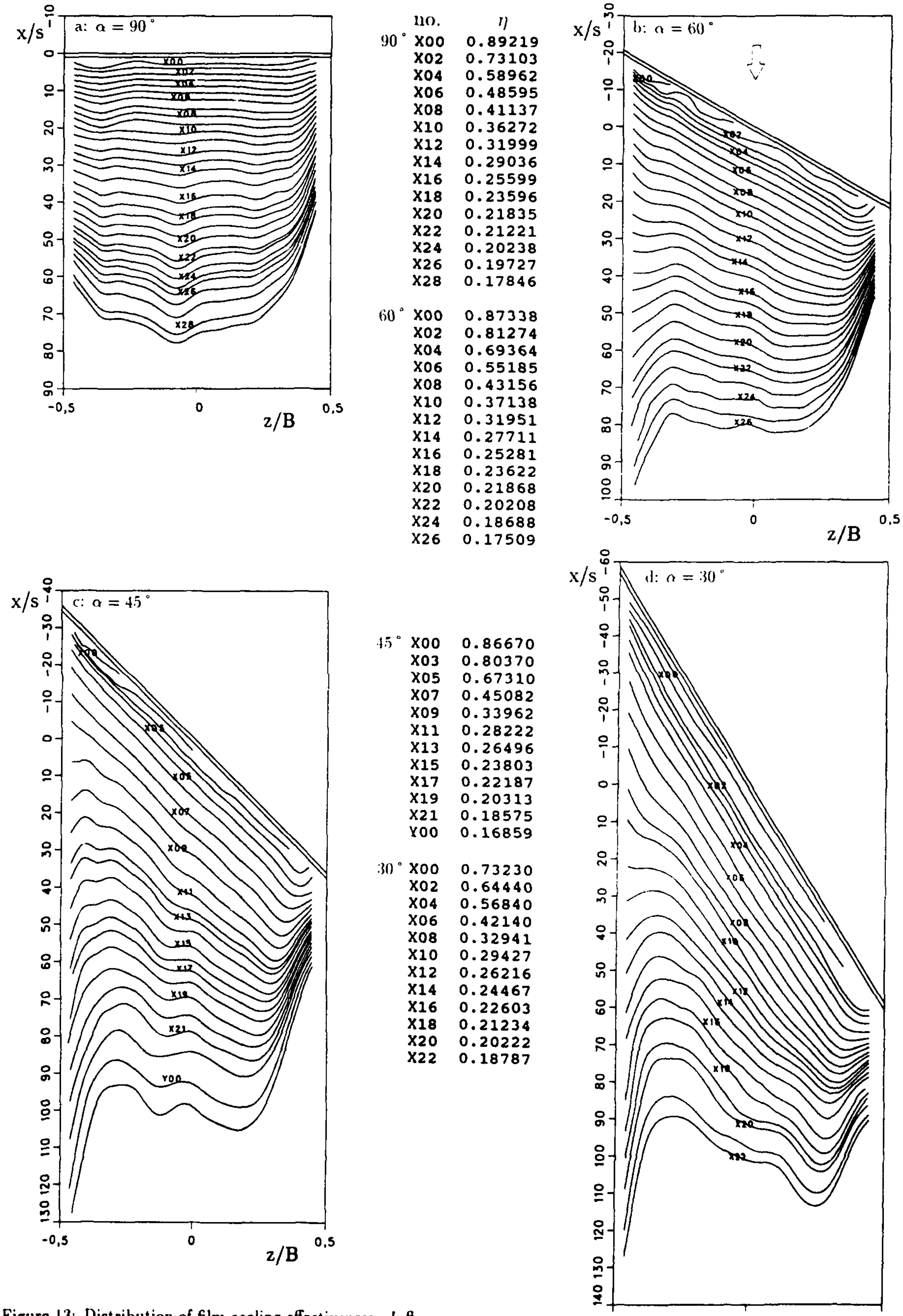

	no.	η
90°	X00	0.89219
	X02	0.73103
	X04	0.58962
	X06	0.48595
	X08	0.41137
	X10	0.36272
	X12	0.31999
	X14	0.29036
	X16	0.25599
	X18	0.23596
	X20	0.21835
	X22	0.21221
	X24	0.20238
	X26	0.19727
	X28	0.17846
60°	X00	0.87338
	X02	0.81274
	X04	0.69364
	X06	0.55185
	X08	0.43156
	X10	0.37138
	X12	0.31951
	X14	0.27711
	X16	0.25281
	X18	0.23622
	X20	0.21868
	X22	0.20208
	X24	0.18688
	X26	0.17509
45°	X00	0.86670
	X03	0.80370
	X05	0.67310
	X07	0.45082
	X09	0.33962
	X11	0.28222
	X13	0.26496
	X15	0.23803
	X17	0.22187
	X19	0.20313
	X21	0.18575
	Y00	0.16859
30°	X00	0.73230
	X02	0.64440
	X04	0.56840
	X06	0.42140
	X08	0.32941
	X10	0.29427
	X12	0.26216
	X14	0.24467
	X16	0.22603
	X18	0.21234
	X20	0.20222
	X22	0.18787

Figure 13: Distribution of film cooling effectiveness - Influence of flow angle (M=0.5)

than in the case of tangential injection. Closer to the slot, the flow separation with recirculation, leads to ingestion of main stream flow resulting in a marked reduction of cooling potential with increasing blowing rate.

The film cooling effectiveness for $\alpha = 90°$ is shown in Fig.14 as function of x along with an empirical correlation

$$\eta = 2.02\,(\frac{x}{M^{0.5}s})^{-0.505}\ ,\quad x/s > 20\ . \tag{7}$$

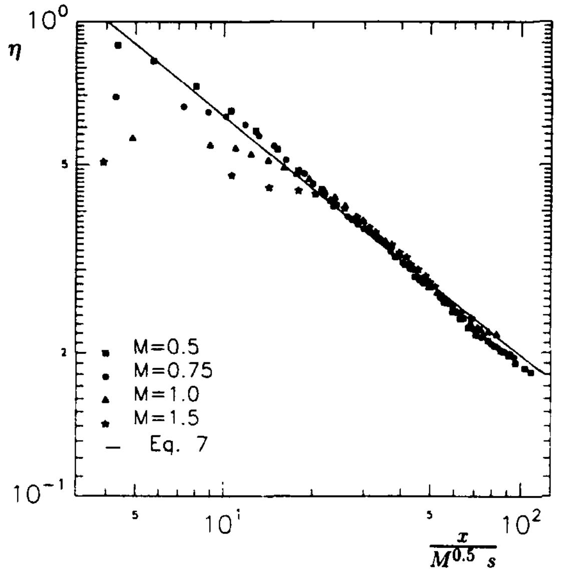

Figure 14: Film cooling effectiveness - Influence of mass flux ratio (α=90°, z/B=0)

It should be noted that the correlation could be achieved with $M^{0.5}$, rather than M that is usually taken.

Besides the $2D_\alpha$-recirculation zones, Fig.13 shows a distinct zone on the left and another one on the right hand surface region. On the left side higher values of effectiveness occur because cooling air is transported to this region as is indicated in Fig.9. In contrast the right side is characterized by a sharp drop in effectiveness. There, film cooling flow is directed away from the wall giving the main stream a chance to flow towards the surface resulting in a low effectiveness. This is further shown in Fig.15 for $\alpha = 45°$ where the variation of η with distance x from the slot for various lateral positions z is plotted. The low η near the downstream end of the slot may be noted.

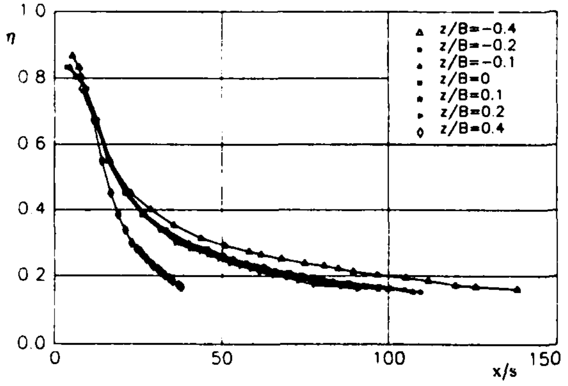

Figure 15: Film cooling effectiveness in characteristic regions (α=45°, M=0.5)

The results for all slot angles α may be correlated if M in Eq.7 is replaced by $M_\alpha = M/\sin\alpha$, Fig.16, with the full line according to

$$\eta_\alpha = 2.02(\frac{x\sin^{0.5}\alpha}{M^{0.5}s})^{-0.505}\ ,\quad x/s > 20\ . \tag{8}$$

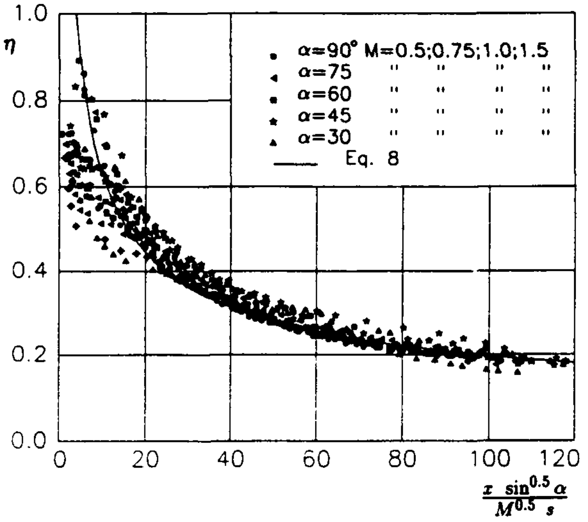

Figure 16: Film cooling effectiveness in the $2D_\alpha$-region (z/B=0)

This correlation essentially represents the efficiency behavior in the $2D_\alpha$-region. In addition to that the results indicate that the increase of η at the upstream slot end and the decrease of η at the downstream slot end nearly compensate.

It may be speculated that the end effects are strongly influenced by the windtunnel side wall boundary layers. In order to investigate this effect, a configuration was built consisting of two slots meeting at 90° as shown in Fig.17. This represents the single slot configuration with $\alpha = 45°$ with the left side wall boundary layer. By turning this configuration by 180°, the situation sketched at the right in Fig.17 is obtained simulating the downstream end of the single slot, again the tunnel side wall replaced by a symmetry plane. A remarkable agreement with Fig.13c may be observed indicating that the side walls act essentially as symmetry planes and the side wall boundary layers have only a minor influence on the flow field and on the variation of η resulting from the turning of the slot. This is supported by a comparison between the measured effectiveness and that computed with Eq.8 (Fig.18).

5 NUMERICAL CALCULATIONS

The experiments were complimented by numerical calculations using the finite element computer code FIDAP [21]. Turbulence was described by the standard k-ϵ-model. The constants are taken from [22]. A three-dimensional grid with 52,117 unevenly distributed elements was set up. In order to reduce the relative residuals to less than 1/1000 up to 250 iterations were done requiring 62.5 hours of CPU time on the IBM RS 6000-550 computer and using 60 Mbyte core memory. A result is shown in the center of Fig.17. The general η-distribution observed in the experiments is well reproduced, especially the formation of the $2D_\alpha$-region. However, the effects near the symmetry planes appear to be overestimated, probably due to limitations of the turbulence model used, considering the strong vortices in these

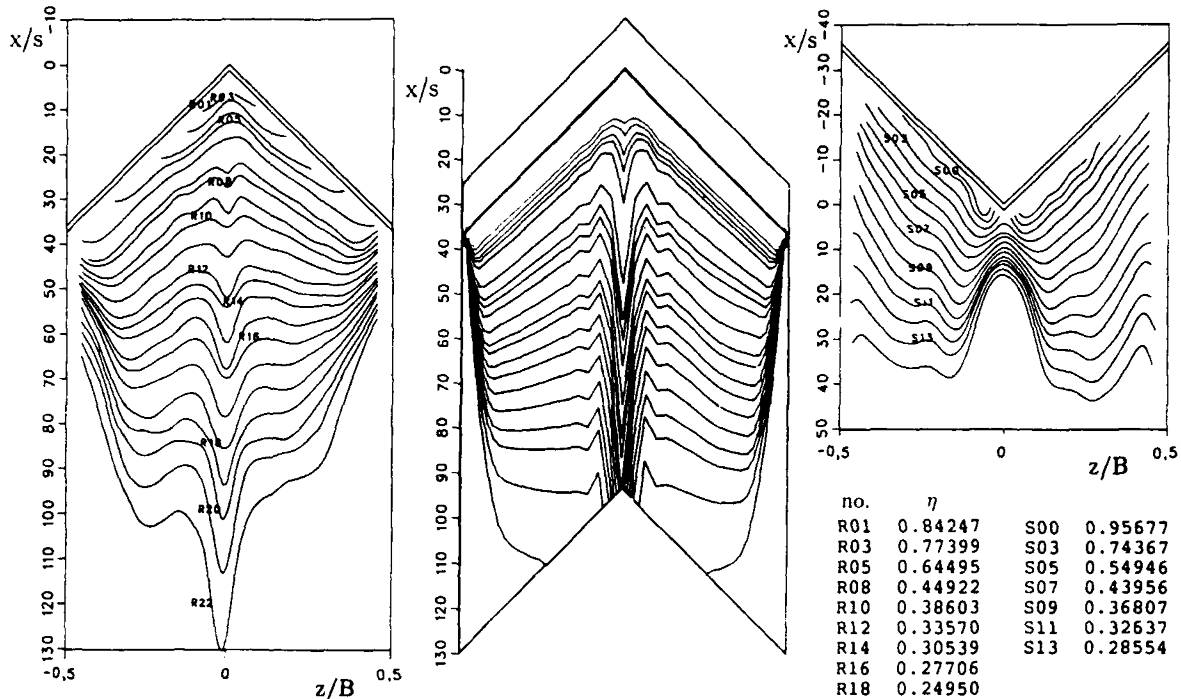

Figure 17: <- and >-slot configuration ($\alpha=45°$)

no.	η		
R01	0.84247	S00	0.95677
R03	0.77399	S03	0.74367
R05	0.64495	S05	0.54946
R08	0.44922	S07	0.43956
R10	0.38603	S09	0.36807
R12	0.33570	S11	0.32637
R14	0.30539	S13	0.28554
R16	0.27706		
R18	0.24950		
R20	0.22725		
R22	0.18722		

regions. This is also demonstrated in Fig.18 where very good agreement between the numerical calculation and Eq.8 may be seen for $z/B = \pm 0.25$, i. e. in the $2D_\alpha$-region, while the curves for $z/B = 0$ display a larger disagreement with the corresponding curves in Fig.18.

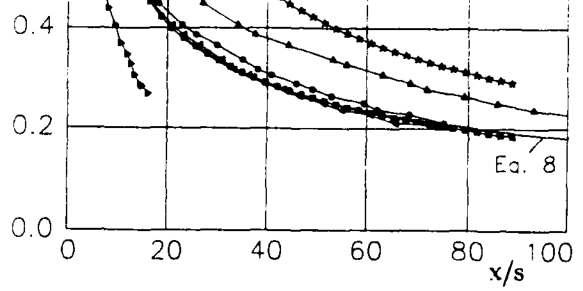

Figure 18: Film cooling effectiveness (<- and >-configuration) - Measurements and numerical results

6 THEORETICAL CONSIDERATIONS

For the region downstream of the reattachment line, a boundary layer flow may be assumed. Then, with further simplifications, the energy equation for the case of a perpendicular slot ($\alpha = 90°$) may be written as

$$\rho U \frac{\partial \vartheta}{\partial x} + \rho V \frac{\partial \vartheta}{\partial y} = \frac{\lambda}{c_p} \frac{\partial^2 \vartheta}{\partial y^2} , \tag{9}$$

with $\vartheta = T - T_m$. The boundary conditions are at $y = 0$: $U = V = 0$, $\partial\vartheta/\partial y = 0$ (adiabatic wall) and at $y = \infty$: $U = U_m$, $V = 0$, $\vartheta = 0$. With relatively small temperature differences between main stream and film, $\vartheta_s = T_s - T_m$, the integral form of the energy equation is

$$\int_0^\delta \rho U \vartheta \, dy = \rho_s V_s \vartheta_s s . \tag{10}$$

or, dividing by $\rho_m U_m$

$$\int_0^\delta \frac{\rho U}{\rho_m U_m} \frac{\vartheta}{\vartheta_s} \, dy = M s . \tag{11}$$

Introducing y/δ, the film cooling effectiveness can be obtained as

$$\eta = \frac{T_{aw} - T_m}{T_s - T_m} = \frac{Ms/\delta}{\int_0^1 \frac{\rho U}{\rho_m U_m} (\frac{T - T_m}{T_{aw} - T_m}) \, d\frac{y}{\delta}} . \tag{12}$$

The integral in this equation can be evaluated using the experimental data. It is nearly constant and is approximately 0.5. So for the following basic considerations it was set

$$\int_0^1 \frac{\rho U}{\rho_m U_m} (\frac{T - T_m}{T_{aw} - T_m}) \, d\frac{y}{\delta} = \frac{1}{2} . \tag{13}$$

Then the boundary layer growth δ as a function of blowing rate is evaluated. It turns out that the data of four different blowing rates correlate well with

$$\frac{\delta}{Ms} = (\frac{x}{M^{0.5}s})^{0.5} . \tag{14}$$

as is shown in Fig.19.

Introducing Eq.14 into Eq.12 yields

$$\eta = 2.0(\frac{Ms}{\delta}) = 2.0(\frac{x}{M^{0.5}s})^{-0.5} . \tag{15}$$

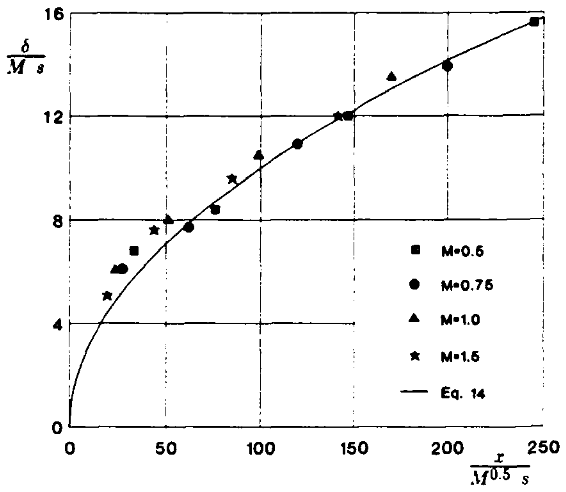

Figure 19: Growth of boundary layer - Influence of mass flux ratio

which is in good agreement with Eq.7 obtained empirically.

For an inclined slot, the mainstream velocity component $U_m \sin\alpha$ perpendicular to the slot is used resulting in

$$\eta = 2.0\left(\frac{x}{M_\alpha^{0.5} s}\right)^{-0.5} = 2.0\left(\frac{x \sin^{0.5}\alpha}{M^{0.5} s}\right)^{-0.5} . \qquad (16)$$

corresponding to the empirical Eq.8.

7 CONCLUSIONS

This investigation has shown that the turning of a film cooling slot relative to the main stream flow direction leads to a complex vortex flow strongly affecting the distribution of film cooling effectiveness:

- Depending on the slot angle, a cone-shaped vortex forms at the upstream end of the slot rolling up the stream surface originating from the slot trailing edge. This vortex is positioned at an angle relative to the slot and is essentially fed by the slot mass flow. It leads to an intensified film cooling effectiveness in that region.

- With lower blowing rates, but always with small turning angles, the mass flow added continuously in the vortex direction can support the growth of the vortex at its initial angle only to a certain limit. Then the vortex changes into a two-dimensional recirculation zone parallel to the slot ($2D_\alpha$-region). The effective velocity is the main stream velocity component normal to the slot. Using this velocity component in the mass flux ratio it is possible to correlate the cooling effectiveness by empirical and semi-empirical equations.

- At the side wall at the upstream end of the slot, the stream surface originating at the leading edge of the slot rolls up under the influence of the oblique film slot and forms a second vortex. This vortex collects film air in its core which leads to a marked increase in cooling effectiveness in the vortex region. However, at the opposite side wall at the downstream end of the slot, the velocity is directed away from the wall leading to an ingestion and admixing of main stream flow which results in a strong reduction of cooling effectiveness. In a practical application hot and cold spots would result.

- Taking the average along lines perpendicular to the main stream direction, the increased and decreased effectiveness values nearly compensate. The average values could be well correlated, using the main stream velocity component perpendicular to the slot.

- The boundary layers on the side walls of the test section have a minor influence. Thus, the side walls have the effect of symmetry planes.

ACKNOWLEDGEMENT

The authors are indebted to the Bundesministerium für Forschung und Technologie (German Ministry of Research and Technology) which supported the work through the Arbeitsgemeinschaft Hochtemperatur-Gasturbine, AG-Turbo.

REFERENCES

[1] Goldstein, R. J.
Film Cooling
in: Advances in Heat Transfer
Academic Press, New York, Vol. 7, 1971, pp. 321-379

[2] Hartnett, J. P.
Mass Transfer Cooling
in: Handbook of Heat Transfer Applications
McGraw Hill, New York, 1985, pp. 1-111

[3] Colladay, R. S.
Importance of Combining Convection with Film Cooling
AIAA-Paper 72-8, San Diego, 1972

[4] Hennecke, D. K.
Heat Transfer Problems in Aero-Engines
in: Heat and Mass Transfer Problems in Rotating Machinery
Hemisphere, Washington, 1984, pp. 353-379

[5] Fergason, J. L.
Liquid Crystals in Nondestructive Testing
Applied Optics, Vol. 7, No. 9, 1968, pp. 1729-1737

[6] Stegemeyer, H.
Anwendung von cholesterinischen, flüssigen Kristallen zur Darstellung von Temperaturfeldern
VDI-Bericht Nr. 198, 1973, pp. 29-35

[7] Klein, E. J.
Application of Liquid Crystals to Boundary-Layer Flow Visualization
AIAA-Paper 68-376, San Francisco, 1968

[8] Schönfelder, H.
Bildkommunikation
in: Nachrichtentechnik
Springer, Bd. 11, 1983

[9] Wahl, F. M.
Digitale Bildsignalverarbeitung
in: Nachrichtentechnik
Springer, Bd. 13, 1984

[10] Klinger, H.
Untersuchung des Einflusses veränderlicher Anströmwinkel auf die Flammrohrfilmkühlung
Ph. D. Thesis, Techn. Univ. Darmstadt, 1992

[11] Everett, K. N.; Gerner A. A.; Durston, D. A.
Seven-Hole Cone Probes for High Angle Flow Measurement: Theory and Calibration
AIAA-Paper 82-0232, Orlando/USA, 1982

[12] Kamotani, Y.; Greber, I.
Experiments of Confined Turbulent Jets in Cross Flow
NASA-CR-2392, Lewis Research Center, 1974

[13] Mikhail, R.; Chu, V. H.; Savage, S. B.
The Reattachment of a Two-Dimensional Turbulent Jet in a Confined Cross Flow
Int. Association Hydr. Res., Vol. 3, Sao Paolo/Brazil, 1975, pp. 141-419

[14] Marsden, D. J.; Simpson, R. W.; Rainbird, W. J.
The Flow over Delta Wings at Low Speeds with Leading Edge Separation
College of Aeronautics Cranfield, Rep. No. 114, 1958

[15] Hummel, D.
Zur Umströmung scharfkantiger schlanker Deltaflügel bei großen Anstellwinkeln
ZfW, Nr. 15, Heft 10, 1967, pp. 376-385

[16] Scesa, S.
Effect of Local Normal Injection on Flat-Plate Heat Transfer
Ph. D. Thesis, Univ. of California, Berkeley, 1954

[17] Seban, R. A.; Chan, H. W.; Scesa, S.
Heat Tranfer to a Turbulent Boundary Layer Downstream of an Injection Slot
ASME-Paper 57-A-36, 1957

[18] Papell, S. S.
Effect on Gaseous Film Cooling of Coolant Injection Through Angled Slots and Normal Holes
NASA TN D-299, Langley Field, 1960

[19] Sivasegaram, S.; Whitelaw, J. H.
Film Cooling Slots: The Importance of Lip Thickness and Injection Angle
J. Mechanical Engineering Science, Vol. 11, 1969, pp. 22-27

[20] Foster, R. C.; Haji-Sheikh, A.
An Experimental Investigation of Boundary Layer and Heat Transfer in the Separated Flow Downstream of Normal Injection Slots
AIAA-Paper 74-678, Boston, 1974

[21] Fluid Dynamics International
General Introduction Manual
Rev. 6.0, Evanston, USA, 1991

[22] Demuren, A. O.; Rodi, W.; Schönung, B.
Systematic Study of Film Cooling with a Three-Dimensional Calculation Procedure
ASME-Paper 85-IGT-2, Beijing, 1985

Discussion

QUESTION 1:

DISCUSSOR: G. Andrews, University of Leeds

Is the geometry you have looked at unique to the ceramic tile wall construction you have mentioned? In a can or an annular combustor the cooling film slot is continuous around the combustor, normally at 90° to the axis. The flow may be at an angle to this due to swirl, but there can be no start or end point to the interaction circulation zone. Also, a more severe problem is where the angle of flow is not parallel to the wall, but is inclined toward the wall. This often occurs in combustors and can completely destroy the film cooling.

AUTHOR'S REPLY:

The complexity of flame tube surfaces requires small, triangular metallic or ceramic tile elements. The slots therefore are no longer perpendicular to the main stream direction. Such a situation can be seen in the figure below. Our basic studies focus only on a single slot geometry inclined with different angles to the main stream. Therefore a start and an end point occur at the side walls. The results with the <- and the >- configuration have shown further that there is no measurable effect of the side wall boundary layers. In addition to these configurations, the test section is prepared to investigate the film cooling effectiveness and the flow field behind an intersection point of two or more meeting slots. The latter configuration will be close to the one produced by the heat shield elements shown in the figure.

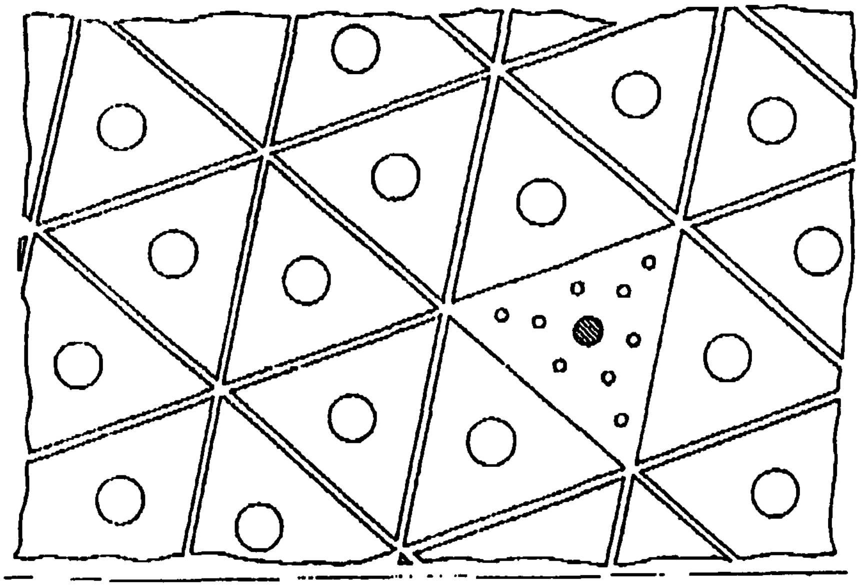

Ceramic tile technology to insulate complex combustor surfaces

QUESTION 2:

DISCUSSOR: J. Chew, Rolls Royce

Your experiment has some relevance to the turbine rim sealing problem where flow is ejected through the seal into the mainstream which has a tangential velocity component. Are you able to deduce discharge coefficients from your measurements?

AUTHOR'S REPLY:

It is possible to evaluate an average discharge coefficient $\overline{C_D} = \frac{\dot{m}_{s,real}}{\dot{m}_{s,real}}$ according to the static pressure taps and the pitot probes along the slot nozzle in combination with the mass flow we obtained for each test point. For example for a mass flow rate of M = 2.5 we have a nearly constant value of $\overline{C_D}$:

α	90°	75°	60°	45°	30°
$\overline{C_D}$	0.875	0.900	0.899	0.909	0.900

with $\dot{m}_{s,real}$ obtained by an orifice flow meter and $\dot{m}_{s,real} = \rho_s v_s A_{nozzle}$, $v_s = \sqrt{\frac{2}{\rho}(p_t - p)}$.

IMPINGEMENT/EFFUSION COOLING

G.E. Andrews, A.M. Al Dabagh, A.A. Asere, F. Bazdidi-Tehrani, M.C. Mkpadi and A. Nazari

Department of Fuel and Energy
The University of Leeds
LEEDS, LS2 9JT, UK

ABSTRACT

Impingement/effusion cooling offers one of the most effective ways of cooling gas turbine combustor walls and turbine blades. The design principles are reviewed and cooling effectiveness data presented for a range of typical geometries with holes at 90 degrees to the surface. The main variable studied was the number of impingement/effusion holes. Comparison was made with the effusion cooling effectiveness. Optimum configurations were demonstrated with a 0.7 overall cooling effectiveness at a mass flow per unit surface area of 0.2 kg/sm^{2}bar. This was equivalent to 10% of the combustor air flow for a typical gas turbine combustor. Data is also presented for the overall wall heat transfer coefficient. The mechanism of the enhanced heat transfer within the impingement/effusion double skin wall was investigated using a CFD code. This predicted the complex aerodynamics in the impingement gap and also gave good agreement with the measured overall heat transfer data.

NOMENCLATURE

Ah	Total hole internal surface area, m^2
Ax	Total hole approach surface area, Eq.9, m^2.
Cp	Specific heat of the wall material.
D	Hole internal diameter, m.
G	Coolant mass flow per unit wall area Ax at atmospheric pressure, kg/sm^2
h	Convective heat transfer coefficient, W/m^{2}K.
hu	Impingement and effusion hole inlet combined heat transfer coefficient, W/m^{2}K.
Hcf	Film heat transfer coefficient, W/m^{2}K.
k	Thermal conductivity of the coolant, W/mK.
L	Hole length, m.
m	Mass of the test plate heat transfer section, kg.
M	Blowing rate = effusion hole/hot gas cross flow density times velocity ratio
N	Number of holes per unit surface area, Ax, m^{-2}.
Nu	Nusselt number based on h and the hole diameter D, hD/k.
Pr	Prandtl number.
Re	Hole Reynolds number based on D and the coolant velocity in the hole.
Tpl	Effusion wall temperature, K.
Tim	Impingement wall temperature, K.
Tz	Predicted impingement gap temperature, K
Tw	Mean wall temperature, K.
X	Hole Pitch, m.

1. INTRODUCTION

Full coverage discrete hole film cooling, which is usually referred to as effusion cooling, offers a relatively simple technique for the efficient cooling of gas turbine combustor and turbine blade walls. Many gas turbine combustors use effusion cooling for the cooling of local hot spots on the wall, where a locally high coolant flow rate for the hot spot area is used. The present work is concerned with the cooling of the whole combustor surface area using this method of film cooling with a much lower proportion of the combustor air flow for cooling than is used for conventional film cooling techniques. Large reductions in the proportion of film cooling air flow are required for future lean burning low NOx combustor designs (8). These low NOx combustor designs require the maximum possible air flow in the primary zone and a dilution zone will still be required for pattern factor optimisation, consequently it is the film cooling air flow that has to be drastically reduced.

Although good film cooling can be achieved by suitable full coverage effusion cooling designs (1-4) the internal wall heat transfer is relatively low. The addition of impingement cooling through a double skin wall construction, as shown in Fig.1, increases the internal wall cooling whilst maintaining the good film cooling characteristics of the effusion wall (5,6), this results in very high overall cooling effectiveness characteristics. The same configuration can be used in turbine blades with the air feed to arrays of discrete film cooling jets coming through an impingement insert. The main design difference is the relative pressure loss between the impingement and effusion surfaces and hence the relative hole sizes. For combustor applications the main pressure loss can be arranged to be at the impingement surface for maximum impingement heat transfer. The effusion surface than has a low pressure loss which gives low effusion hole blowing rates and hence good film cooling characteristics. However, for the turbine blade application there is the complication of the large static pressure gradients around the blade surface. The pressure difference across the effusion holes is then significant and a large pressure loss at the impingement hole may not be possible. In this situation equal impingement and effusion flow areas may be necessary. The impingement/effusion aerodynamics and internal heat transfer are investigated in the present work for a situation of equal impingement and effusion hole sizes and number. In associated work the authors have investigated the influence of the relative number of holes between the impingement and effusion surfaces. Impingement and effusion holes at 90 degrees to the surface are used throughout this work.

Hollworth et al (9,10) for an X/D of 10 and effusion/impingement jet area ratio of 3.07 found an increase of 30% in the heat transfer due to the addition of effusion holes offset from the impingement holes. Andrews et al (5) found similar increases with values of 30% for an X/D of 10 with an effusion/impingement jet area ratio of 5.6 and 45% for an area ratio of 2.4. The double skin construction of impingement/effusion cooling, shown in Fig.1, permits the separate optimisation of the impingement and effusion hole geometries. The authors have previously shown that the maximum effusion cooling effectiveness in combustor configurations occurs for a large number of effusion holes with a low design pressure loss, or large hole size (2-4). However, impingement heat transfer is not sensitive to the number of holes used (11) but increases with reduction in hole size and pressure loss. These conflicting optimisation criteria can be accommodated if different impingement and effusion hole designs are used. The thermal separation of the two surfaces also minimises the wall thermal stresses, which is a major advantage of the technique over alternative efficient internal wall cooling designs such as Llamilloy or Transply (3).

Design considerations for the combustor wall applications of effusion and impingement cooling have been presented by the authors (1,12). Transpiration wall cooling offers the optimum wall cooling performance with the minimum air requirements. Andrews and Asere (13) and Andrews et al (3) have shown for a transpiration cooled wall that at low coolant flow rates both the film and internal wall cooling were important, but that at high coolant flow rates the film cooling was dominant. Thus, the optimum design of effusion cooling at low coolant flow rates must also maximize both the film and internal wall cooling components of the overall heat transfer. It is this region of low coolant flow rate that was of interest in the present work and the maximisation of the film and the impingement heat transfer was the design goal.

The bulk of the literature on discrete hole film cooling has been directed at obtaining adiabatic cooling effectiveness data and the many variables have been correlated by L'Ecuyer and Soechting (14). Often large scale test systems are used with rather limited ranges of geometries (15). Much less information is available on the film heat transfer coefficient and it is often assumed that simple flat plate convective heat transfer coefficients would apply. It has been shown by Hey and Lampart (16) that this is not valid for single rows of holes and by the authors for arrays of holes (2,3).

In spite of this large research effort on film cooling, there has been little comparable effort on the convective heat transfer from the wall to the film cooling air as it passes through the wall (17). The best way of enhancing this heat transfer is considered to be the addition of impingement cooling, but there have been few investigations of combined impingement/effusion cooling. The present work concentrates on the geometrical design aspects and is part of a large research programme directed at the identification of the optimum impingement and effusion geometries.

The effusion cooling is strongly influenced by the number of effusion holes (4) and by the hole size or pressure loss for a fixed number of holes (2,3). In the present work data is presented for low pressure loss effusion designs on the influence of the number of holes, using equal numbers of impingement and effusion holes. The aerodynamics in the impingement gap in the presence of effusion holes are complex and result in recirculation between the jets with heating of the impingement wall (6,7). These aerodynamics are investigated using 3D CFD predictions.

2. IMPINGEMENT/EFFUSION INTERNAL WALL AERODYNAMICS AND HEAT TRANSFER

The impingement/effusion aerodynamics in the gap between the two surfaces were investigated using 3D CFD using the FLUENT CFD code. The impingement/effusion hole configuration with the area of CFD computation marked is shown in Fig.1. The aerodynamics were identical for all the other elements and the computational element was chosen so as to minimise the computation time. The computational grid is shown in Fig.2 and the planes for which data is presented in detail are shown. 20,000 nodes were used in the computation, which started upstream of the impingement holes so as to model the flow contraction on entry to the impingement holes.

The predictions were carried out for an impingement and effusion X/D of 5 and a Z/D of unity and the results are shown in Figs.3-7. Figs. 3 and 4 show the 3D aerodynamics in the impingement gap. There was a strong recirculation in the gap with a reverse jet flow on the centreline of the impingement jet arrays offset from the effusion holes. This reverse flow is shown in Fig.3 to extend from the vertical plane 8 to 19 and was only absent just in line with the effusion hole. Previous 2D predictions of the aerodynamics had a reverse flow jet opposite the effusion jet (6). There was a further reverse flow jet midway between the effusion holes and the impingement holes, as shown at plane 4 in Fig.3. The impingement gap was thus filled with two triangular shaped recirculation zones of complex aerodynamics.

The flow very close to the effusion surface is shown in Fig.4 together with several horizontal planes in the impingement gap. The central region of the gap was predominantly a dead zone in the centre of the large recirculation zones. The highest velocities were on the effusion surface around the impingement point and around the entrance to the effusion hole. There was also a flow in the opposite direction on the impingement wall surface, this is also shown in Fig.3. These high velocity flows on the two surfaces give rise to high heat transfer coefficients. The gap recirculation also gives rise to convective heating of the impingement wall surface so that this wall will adopt a temperature higher than the coolant temperature but lower than the effusion wall. This heating of the impingement wall has been reported previously by the authors (6,7), it is also a feature of impingement heat transfer. For geometries with smaller impingement holes than effusion holes, as in the geometries discussed later, this gap recirculation is stronger and the heat transfer to both surfaces is enhanced.

The predicted effusion surface heat transfer coefficient distribution is shown in Fig.5. The highest heat transfer was in line with the impingement jet, as expected. The enhanced heat transfer due to the flow acceleration into the effusion hole is also demonstrated in Fig.5, although it occupies only a relatively small proportion of the surface area. The peak effusion hole enhanced heat transfer was approximately 60% of the peak impingement heat transfer. For the opposite surface the heat transfer predictions are shown in Fig.6. The is dominated by two peaks in the heat transfer due to the reverse flow jets discussed above. The peak heat transfer coefficient on this surface was approximately 50% of that on the impingement surface. The influence of the two triangular recirculation zones is clearly shown with a low heat transfer at the null point between the two zones. Heat transfer measurements on this surface have confirmed the high convective heat transfer coefficients.

The variation of the heat transfer coefficient along the impingement surface on the effusion wall is shown in Fig.7. This also shows a comparison with the local heat transfer coefficient measurements of Hollworth et al (9,10) and good agreement is shown along the centreline through the impingement jet, between the two effusion jets. Some local heat transfer coefficient measurements were also made using the experimental arrangement outlined below. These measurement are in good agreement with those of Hollworth et al (9,10) and with the present CFD predictions.

3. DETERMINATION OF THE IMPINGEMENT AND EFFUSION SURFACE HEAT TRANSFER.

3.1 Experimental Equipment

A large scale test rig was used which had a hollow effusion wall through which heated air flowed. Above and below this effusion wall was mounted impingement jet plates. The hollow effusion wall was instrumented with thermocouples and a transient cooling technique was used to determine the heat transfer coefficient. The hollow effusion wall consists of a pin-fin array, with the pins made of the effusion hole tubes. This same test rig has been used to determine the pin-fin heat transfer coefficients (18) and the same techniques were used in the present work.

The thin walled effusion surface and high heat transfer coefficients allowed low Biot number transient cooling techniques to be used. The thermocouples on the impingement jet approach surface, the effusion jet tube wall surface and the discharge surface allowed these three surface heat transfer coefficients to be determined. The outlet surface in the presence of a discharge impingement wall creates the same reverse flow aerodynamics as for the impingement jets. Thus for geometries with the same impingement and effusion holes these effusion outlet surface heat transfer measurements are the same as the reverse flow surface heat transfer coefficients.

3.2 Results.

The results were in the form of several local heat transfer coefficient measurements, some of which are shown in Fig.7. These were surface area averaged and these average results are shown in Fig.8 for the impingement surface or effusion jet inlet surface. These measurements are the combined influence of the impingement heat transfer and of the effusion hole approach heat transfer. The only previous measurements for this situation are those of Hollworth et al (9,10) and Fig.7 shows good agreement with the present results. Fig.8 shows that the impingement heat transfer had only a small influence of the impingement jet open area ratio, Af, for Af from 5.5-8.6%. For higher Af there was a reduction in the heat transfer.

Fig.9 compares the impingement surface, internal effusion hole and reverse flow surface heat transfer coefficients. The internal hole heat transfer is significant due to the turbulence created by the flow separation at the inlet, shown in Fig.3. The authors have previously extensively investigated the effusion hole heat transfer (19) using a solid wall test geometry that resulted in the measurement of the combined influence of the approach flow and internal wall heat transfer. The present measurements allow the separate determination of the short hole internal heat transfer coefficient. The reverse flow heat transfer, with a surface distribution shown in Fig. 6, is strongly influenced by Z/D as the surface velocities are increased at low Z/D. For a low Z/D Fig. 10 shows that the reverse flow surface heat transfer was as high as the impingement heat transfer. However, at Z/D greater than unity the reverse flow heat transfer was reduced by 40-50% below that of the impingement surface, as shown in Fig.9.

4. OVERALL IMPINGEMENT/EFFUSION WALL HEAT TRANSFER

The authors have previously developed a transient cooling technique that determined the combined influence of the impingement jet, effusion hole inlet and internal heat transfer on the effusion wall heat transfer coefficient (5,6). The experimental technique has been described previously (5,6) and consisted of electrically heating the solid metal test geometries and then removing the heat and determining the rate of temperature fall due to the impingement/effusion heat transfer. From the cooling time constant the surface averaged heat transfer coefficient was determined. This technique has been applied to the three impingement/effusion geometries, shown in Table 1, for which cooling effectiveness data is presented below. This wall heat transfer data is used in a heat balance programme (2) to compute the film heat transfer coefficient from the measured cooling effectiveness and the results of these film heat transfer computations are described later.

Table 1 Impingement/Effusion Geometries

Wall	N m^{-2}	D mm	X mm	X/D mm	L	152 mm	square test surface array
EFFUSION							
I	26910	1.31	6.1	4.7	6.35		25 x 25
V	9688	2.24	10.2	4.6	6.51		15 x 15
E	4306	3.27	15.2	4.7	6.35		10 x 10
IMPINGEMENT						Z mm	Z/D
1	26910	0.64	6.1	9.6	6.35	3.2	5.0
U	9688	1.00	10.2	10.2	3.32	4.5	4.5
4	4306	1.41	15.2	10.8	6.35	6.4	4.5

All the impingement effusion geometries in the present work had equal numbers of impingement and effusion holes in square arrays offset half a pitch from each other, as shown in Fig.1. Thus the walls in Table 1 were combined with the impingement and effusion surfaces of the same number of holes. The impingement gap, Z, was varied, in the film cooling studies, to keep the Z/D constant so that a variation in Z/D was not influencing the results. However, impingement heat transfer is not sensitive to this gap, if 2<Z/D<6 for impingement/effusion geometries (11) and in the internal wall heat transfer work this gap was constant at 10mm. This was used because in associated work the variation of the number of impingement holes was studied and the hole sizes were larger than in the present work and this gap was required to keep all the geometries within the above range of Z/D. Also a 10mm gap is typical of combustor wall cooling practical geometries. For gas turbine blade cooling applications a 3mm gap has been used, as generally larger values of N and hence smaller impingement hole sizes are used.

The influence of the number of impingement and effusion holes on the internal wall heat transfer is shown in Fig.11 as heat transfer coefficient as a function of G. The equivalent Nusselt/Reynolds number correlation is shown in Fig.12. There was very little influence of the number of holes on the internal wall heat transfer, as found for the impingement heat transfer alone (11). For the effusion cooling surface alone there was an influence of the number of holes (20) due to the greater number of hole inlet surfaces with enhanced heat transfer. However, for IMPINGEMENT/EFFUSION configurations the dominance of the impingement heat transfer eliminates any influence of the number of holes. The consequence of this is that the number of holes can be determined from the optimum film cooling geometry, as investigated below. Also, it is likely that a reduced number of impingement holes could be used relative to the effusion holes and this has been examined by the authors. A reduced number of impingement holes reduced the manufacturing costs as these holes are relatively small compared with the effusion holes if the same number of holes is used.

5. COOLING EFFECTIVENESS

5.1 Experimental Techniques

The cooling effectiveness was determined by placing the 152mm square test walls with its plenum chamber air feed into the wall of a 152mm by 76mm duct through which propane/air combustion product gases at 750K flowed at 25 m/s. Cold 300K film cooling air was used giving a practical coolant to crossflow density ratio of 2.5. This test facility has been described in detail in the authors previous papers (1-4). The duct wall was air externally air cooled and the duct wall temperature was set equal to that of the centre of the test section so as to minimise radiation interchange with the walls. A heat balance correction to the wall temperatures was used to account for surface emissivity differences and test wall temperature differences away from the centreline. For the 750K test temperature these corrections were small (<5%), except at very low coolant flow rates.

The test wall were all instrumented with at least 5 thermocouples on the centreline in the direction of the crossflow. These were mounted on the centreline between the rows of effusion holes and thus measured the hottest wall temperature at the furthest position from the effusion hole outlets. They were spaced at 25mm intervals in the axial crossflow direction and enabled the axial development in the cooling effectiveness to be determined. By using the same thermocouple positions on all the test walls the cooling effectiveness at the same axial positions could be determined.

In the present work with different numbers of holes, the number of upstream holes would be different at each axial position. The cooling effectiveness was defined as the gas to wall temperature difference divided by the gas to coolant temperature difference.

Boundary layer temperature profiles were also determined at the 37, 76 and 113mm axial positions. The film temperature immediately below the wall was determined in these traverses and this was used as equivalent to the adiabatic wall temperature and used to determine the adiabatic or film cooling effectiveness. This temperature was also determined on the centre of the effusion holes and was a worst case position rather than a locally averaged measurement. Comparison of these adiabatic and overall cooling effectiveness measurement gave an indication of the relative importance of the internal wall and film cooling in the overall wall cooling process.

5.2 Effusion Cooling

The overall and adiabatic film cooling effectiveness for the effusion walls alone at the 127mm axial position are shown as a function of the blowing rate, M, and the coolant mass flow rate per surface area in Figs. 13 and 14 respectively. The change in the number of holes was at constant X/D and this resulted in no change in the blowing rate for the same mass flow rate. The adiabatic cooling effectiveness results show two regions, one at low blowing rates and low G where the number of holes does not influence the cooling effectiveness and one at higher blowing rates and G where increasing the number of holes improves the adiabatic cooling effectiveness significantly. The change between these two region was at a blowing rate of approximately 0.5 and a G of 0.2 kg/sm^2.

These two regions correspond to attached and detached film cooling jets. If the effusion jets are turned by the crossflow and remain attached to the surface then optimum film cooling occurs. However, for 90 degree holes the jets are easily detached as the coolant flow increases and set up a stirred film boundary layer (1-4). However, the extra film cooling mass flow still produces an increase in the adiabatic film cooling effectiveness. The reason for the increase in the adiabatic cooling effectiveness with increasing number of effusion holes is that the holes are smaller and the jet penetration is lower and hence the boundary layer is less stirred by the jets. These has also been shown for effusion holes with a higher X/D (4), designed for single skin wall cooling applications. The jet stirring increases as the number of holes is reduced and the 4306 m^{-2} design has very little improvement in the adiabatic cooling effectiveness with G once jet separation has occurred.

Comparison of the overall and adiabatic cooling effectiveness results in Figs. 13 and 14 shows that the overall cooling effectiveness has the greatest difference from the adiabatic at low M and G. In this region, which is the design goal of the present work the internal wall heat transfer is very important, accounting for approximately 50% of the overall cooling effectiveness. At higher coolant mass flow rates the film cooling dominates the overall cooling. The importance of the internal wall cooling at low G means that the addition of impingement cooling may have its greatest impact in this region. Fig. 14 shows that for the largest number of holes a cooling effectiveness of 0.7 was achieved at a G of 0.2 kg/sm^2, which was the design goal in this work. However, effusion walls with an X/D of 4.7 have much too low a pressure loss to be used on their own in combustor walls and need an upstream restrictor to control the coolant flow total pressure loss. It is sensible to use an impingement wall for this purpose and also to further enhance the cooling effectiveness.

The above results were for the 127mm axial position. The axial variation in the adiabatic and overall cooling effectiveness is shown for all three test geometries in Fig.15 for a G of 0.17 kg/sm^2. The axial variation in cooling effectiveness was similar for the overall and adiabatic cooling effectiveness. There is no reason for there to be an axial variation in the wall heat transfer, provided the wall pressure loss is sufficient to ensure a uniform coolant distribution between the effusion holes, as it was in this work. Thus the axial variation in the overall cooling effectiveness was due to the development of the film cooling effectiveness. The coolant film grows with axial distance and provides increasing cool flow insulation from the mainstream gases with distance, this has been shown by the boundary layer temperature traverses (1-4).

The measured wall overall heat transfer coefficients (19,20) have been used in a heat balance computer programme to calculate the film heat transfer coefficient from the overall cooing effectiveness data. The results as a function of G are shown in Fig. 16 for the three test geometries. For a plane wall the wall heat transfer coefficient has been determined as 100 W/m^{2}K at the present hot gas test flow conditions. The results show a very strong influence of the number of effusion holes on the film heat transfer coefficient. A large number of effusion holes for the same X/D caused a reduction in the film heat transfer coefficient. this was also related to the increase in the adiabatic cooling effectiveness discussed above. The decreased hole size as the number of holes is increased for the same total hole area or X/D reduces the coolant jet penetration into the crossflow as this is a linear function of the hole diameter (2-4). Thus the coolant flow will be closer to the wall and there will be reduced mixing with the hot crossflow gases.

Fig.16 shows that for the 9688 and 26910 m^{-2} effusion walls the film heat transfer coefficient decreased as G was increased. This is a characteristic of porous or transpiration cooled walls (3) and indicates that near ideal film cooling has been achieved. The strong increase of the film heat transfer coefficient with G for the 4306 m^{-2} design is due to the strong stirring of the film by the large diameter coolant jets. At low values of G this design has attached jets and a similar film heat transfer coefficient to the other designs. This is also shown in Fig.17 where the axial variation of the film cooling effectiveness is shown for a G of 0.17 kg/sm^2. This also shows the axial reduction in the film heat transfer coefficient from the plane wall value as the film cooling boundary layer develops.

5.3 Combined Impingement/Effusion Cooling

The combined impingement/effusion walls investigated are shown in Table 1. They all had an impingement X/D of 10-11 and an effusion X/D of 4.7. The same number of holes and hole pitch was used for the two surfaces so that the main design difference was the hole diameter. The differences in hole diameter and in X/D causes a major difference in the pressure loss across the two surfaces. It may be shown (12) that the pressure loss is proportional to X/D to the power 4 at a constant mass flow. Thus the present X/D ratio between the two surfaces of 2.2 gave a pressure loss ratio of approximately 25. Thus if the impingement wall was operated at a combustor wall pressure loss of 3% then the effusion wall would only have a pressure loss of 0.12%. It is these very low effusion wall pressure losses than give the enhanced cooling effectiveness relative to our previous work with effusion walls of X/D of approximately 10.5 (4).

The adiabatic cooling effectiveness are not influence by the presence of the impingement wall and hence only the overall cooling effectiveness are presented for the impingement/effusion double skin walls. The axial variation of the overall cooling effectiveness for the three geometries investigated at a G of 0.37 kg/sm^2 are shown in Fig.18. Also the effusion results alone for N=9688 m^{-2} are shown for comparison. All three geometries had a high cooling effectiveness with 0.7 achieved at the leading edge and over 0.8 at the 127mm position. The increase relative to the effusion alone results was of the order of 0.1 cooling effectiveness due to the addition of the impingement heat transfer. The impingement cooling had a relatively greater influence at the leading edge, where the film cooling was not fully developed.

The overall cooling effectiveness as a function of G at the 127mm axial position for the three impingement/effusion geometries are shown in Fig. 19. The results for the 9688 m^{-2} effusion wall alone results are also shown for comparison. Very high cooling effectiveness at low G values are shown in Fig.19. For a G of 0.2 kg/sm^2, which will give full coverage combustor wall cooling using approximately 10% of the combustor total air flow, a cooling effectiveness above 0.7 for all three designs has been demonstrated with 0.75 achieved for the highest number of holes. For practical combustor primary zone operating conditions a 0.1 change in overall cooling effectiveness represents approximately 150C in metal temperature. Hence the near 0.1 improvement in cooling effectiveness due to the addition of impingement cooling is very significant.

At low coolant flow rates the influence of the number of holes is small. The difference between 9688 and 26910 holes/m^2 is small for G from 0.1 - 0.6. Hence, the practical optimum number of holes is 9688/m^2 as further increases do not provide any significant benefit and the additional manufacturing cost are large. The improvement in cooling effectiveness relative to the effusion results is greater the lower the number of effusion holes used. Comparison of Figs. 14 and 19 shows at all G a much smaller influence of the number of holes for the impingement/effusion designs than for the effusion wall alone. Part of the reason for this is that the internal gap aerodynamics discussed above act to make the surface heat transfer more uniform. Thus for the same surface area increasing the number of the impingement jets does not create a major improvement in the proportion of the surface at the highest heat transfer rates and so there is little improvement in the impingement heat transfer with the number of holes. However, the effusion cooling effectiveness is influence by the number of holes and hence as the number of holes is reduced the wall increases in temperature for the same coolant mass flow. The greater coolant to wall temperature difference than increases the heat removed by the impingement cooling. Hence the wall temperature change due to impingement cooling becomes greater for low numbers of holes. For full coverage combustor cooling the minimisation of the number of holes is a major design factor that affects the cost. Fig.19 shows that adequate impingement/effusion The aerodynamics of the impingement gap shown in Figs. 3 and 4 result in the heating of the impingement jet wall by the recirculating flow. This has been investigated for the IMPINGEMENT/EFFUSION tests by separate temperature measurement on the impingement jet wall. A dimensionless parameter Tz' has been used to quantify this heating.

$$Tz' = \frac{Tz - Tim}{Tpl - Tim}$$

The impingement gap temperature, Tz, was temperature of the recirculated jet after impingement surface heat transfer. It was computed from the measured impingement heat transfer coefficient and the computed impingement jet outlet temperature. It was this reverse flow at Tz that was responsible for heating the impingement jet wall. This heating caused the impingement jet to be heated above the coolant inlet temperature, thus reducing its cooling effectiveness. Thus any model of impingement/effusion cooling has to take into account this convective heating of the impingement jet wall, otherwise it will overpredict the cooling due to the impingement jets.

Fig.20 shows the values of Tz' as a function of G for the present three impingement/effusion geometries. The impingement gap aerodynamics are influenced by the gap width and Z/D. The present work was carried out at constant Z/D and it is not surprising that the impingement jet wall heating is relatively independent of N, as shown in Fig.20. At low coolant flow rates the impingement jet wall heating was very significant. Values of Tz' greater than unity are possible at low G. The higher wall temperatures and low coolant flow rates produce high recirculation jet temperatures which can be higher than the impingement jet wall temperature, as this is cooled by the coolant.

6. CONCLUSIONS

6.1 Impingement/effusion cooling with offset impingement and effusion holes produces complex aerodynamics in the impingement gap with two opposed triangular shaped recirculation zones between the impingement and effusion holes. The CFD work predicted the general features of this flow well and gave good agreement with the measured impingement heat transfer coefficient.

6.2 The recirculation in the impingement gap heats the impingement jet wall and this process must be taken into account if the coolant temperature changes and the internal wall overall heat transfer are to be correctly predicted.

6.3 There was no significant influence of the number of impingement/effusion jets on the overall internal wall heat transfer.

6.4 There was a very significant influence of the number of effusion jets on the film cooling and the film heat transfer coefficient. This was due to the increase in hole diameter as the number of jets was reduced and the associated increase in the jet penetration into the hot crossflow. Near ideal transpiration film cooling was achieved for the highest number of effusion holes investigated.

6.5 The addition of impingement cooling to the effusion cooling with X/D of 10.5/4.7 gave on average a 0.1 improvement in the overall cooling effectiveness. All three designs met the design criteria of a 0.7 cooling effectiveness at a G of 0.2 kg/m^2. This is equivalent to cooling the whole surface area of a combustor using only 10% of the total air flow. For the largest number of holes investigated a 0.7 cooling effectiveness was achieved with half of this coolant flow.

6.6 The number of impingement/effusion holes had a lower influence on the overall cooling effectiveness than was the case for the effusion wall alone. The impingement cooling had its greatest effect for the worst effusion design with the lowest number of holes.

ACKNOWLEDGEMENTS

We would like to thank the UK Science and Engineering Research Council for a research grant in support of part of this work (GR/D/53029). We would like to thank GEC-Ruston Gas Turbines for the manufacture of some of the test geometries and M.F. Cannon for valuable technical advice.

REFERENCES

1. Andrews, G.E. and Mkpadi, M.C., 1984, 'Full coverage discrete hole wall cooling: discharge coefficients', Trans. ASME, J.Eng.Power, Vol.106, pp.193-192.

2. Andrews, G.E., Gupta, M.L. and Mkpadi, M.C., 1985, 'Full coverage discrete hole film cooling: cooling effectiveness', Int.J.Turbo Jet Engines, Vol.2, pp. 199-212.

3. Andrews, G.E., Asere, A.A., Mkpadi, M.C. and Tirmahi, A., 1986, 'Transpiration cooling: contribution of film cooling to the overall cooling effectiveness', ASME Paper 86-GT-136, Int.J.Turbo Jet Engines, Vol.3, pp.245-256.

4. Andrews, G.E., Asere, A.A., Gupta, M.L., Mkpadi, M.C. and Tirmahi, A., Full coverage discrete hole film cooling: the influence of the number of holes and pressure loss, ASME Paper 90-GT-61, 1990.

5. Andrews, G.E., Asere, A.A., Hussain, C.I., Mkpadi, M.C. and Nazari, A., Impingement/effusion cooling: overall wall heat transfer, ASME Paper 88-GT-290, 1988.

6. Al Dabagh, A.M., Andrews, G.E., Abdul Husain, R.A.A., Husain, C.I., Nazari, A. and Wu, J., Impingement/Effusion Cooling: The influence of the number of impingement holes and pressure loss on the heat transfer coefficient, ASME Paper 89-GT-188, 1989, also published in ASME Transactions, 1990.

7. Andrews, G.E., Asere, A.A., Hussain, C.I. and Mkpadi, M.C., Transpiration and IMPINGEMENT/EFFUSION cooling of gas turbine combustion chambers, Proc. Seventh ISABE, Beijing, AIAA, pp. 794-803, 1985.

8. Andrews, G.E. et al, Low NOx combustor designs without premixing for aero-engine applications, Proc. European Propulsion Forum: Future Civil engines and the Protection of the Atmosphere, DGLR/AAAF/RAeS. DGLR-Bericht 90-01 pp. 161-174, 1990.

9. Hollworth, B.R. and Dagan, L., Arrays of impinging jets with spent fluid removal through vent holes on the target surface, Trans. ASME, J.Eng. Power, Vol.102, pp.994-999, 1980.

10. Hollworth, B.R., Lehmann, G. and Rosickowski, J., Arrays of impinging jets with spent fluid removal through vent holes on the target surface. Part 2: Local heat transfer, ASME Paper 81-HT-76, 1981.

11. Andrews, G.E., Durance, J., Hussain, C.I. and Ojobor, S.N., Full coverage impingement heat transfer: the influence of the number of holes, ASME Paper 87-GT-93, Trans. ASME, J. Turbo-machinery, Vol. 109, pp.557-563, 1987.

12. Andrews, G.E., Asere, A.A., Hussain, C.I. and Mkpadi, M.C., 1985a 'Full coverage impingement heat transfer: the variation in pitch to diameter ratio at a constant gap' AGARD CP 390, Heat transfer and cooling in gas turbines, pp. 26.1 - 26.13.

13. Andrews, G.E., Asere, A.A., Gupta, M.L. and Mkpadi, M.C., 1985, 'Full coverage discrete hole film cooling: the influence of hole size', ASME Paper 85-GT-47, Int.J.Turbo Jet Engines, Vol.2, pp. 213-225.

14. L'Ecuyer, M.R. and Soechting, F.O., 1985 'A model for correlating flat plate film cooling effectiveness for rows of round holes', AGARD CP 390, Paper 19.

15. Crawford, M.E., Kays, W.M. and Moffat, R.J., Full coverage film cooling, Part. 1: Comparison of heat transfer data for three injection angles, ASME Paper 80-GT-43, 1980.

16. Hay, N., Lampart, D. and Saluja, C.L., 1985, 'Effects of cooling films on the heat transfer coefficient on a flat plate with zero mainstream pressure gradient', ASME Paper 84-GT-40.

17. Andrews, G.E., Alikhanizadeh, M., Asere, A.A., Hussain, C.I., Khoshkbar Azari, M.S. and Mkpadi, M.C., 1986b 'Small diameter film cooling holes: wall convective heat transfer', ASME Paper 86-GT-225, Trans. ASME, J.Turbomachinery, Vol.108, pp.283-289.

18. Al Dabagh, A.M., Pin-Fin heat transfer: contribution of the wall and the pin the overall heat transfer, ASME Paper 92-GT-242, 1992.

19. Andrews, G.E., Alikhanizadeh, M., Bazdidi-Tehrani, F, Hussain, C.I. and Koshkbar Azari, M.S., 1987, 'Small diameter film cooling holes: the influence of hole size and pitch', ASME Paper 87-HT-28.

20. Andrews, G.E. and Bazdidi-Tehrani, F., 1989, 'Small diameter film cooling hole heat transfer: the influence of the number of holes', ASME Paper 89-GT-7.

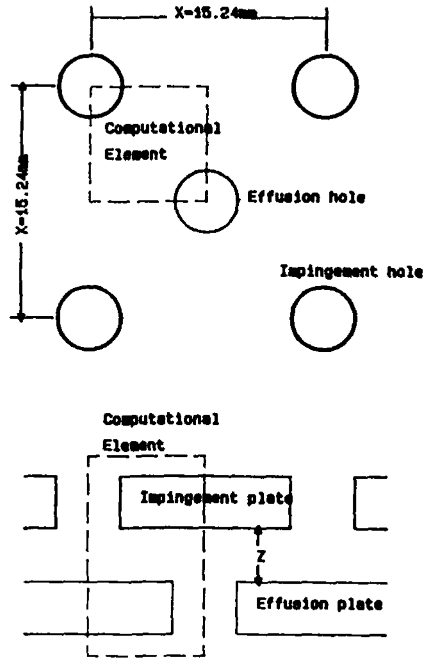
X=15.24mm
Computational Element
Effusion hole
X=15.24mm
Impingement hole
Computational Element
Impingement plate
Z
Effusion plate

Fig.1 Impingement/Effusion geometry and computational element location.

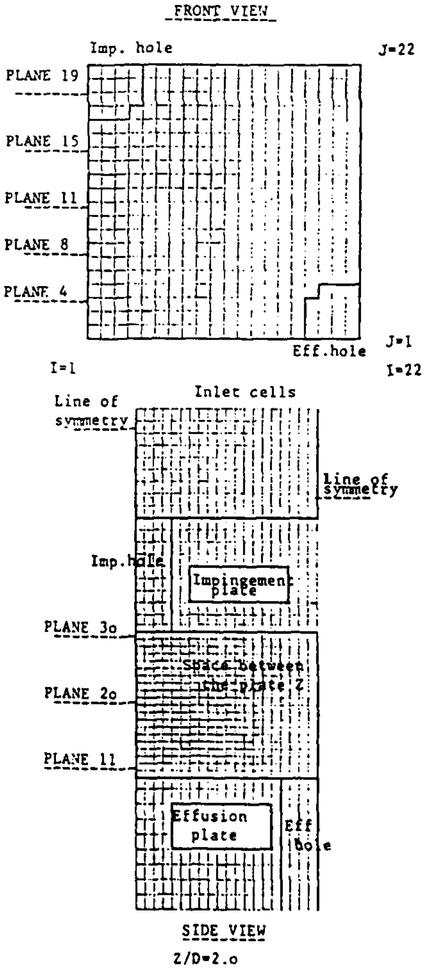
FRONT VIEW
Imp. hole
J=22
PLANE 19
PLANE 15
PLANE 11
PLANE 8
PLANE 4
Eff.hole
J=1
I=1
I=22
Inlet cells
Line of symmetry
Line of symmetry
Imp.hole
Impingement plate
PLANE 30
PLANE 20
PLANE 11
Space between the plate Z
Effusion plate
Eff hole
SIDE VIEW
Z/D=2.0

Fig.2 3D CFD Computational grid.

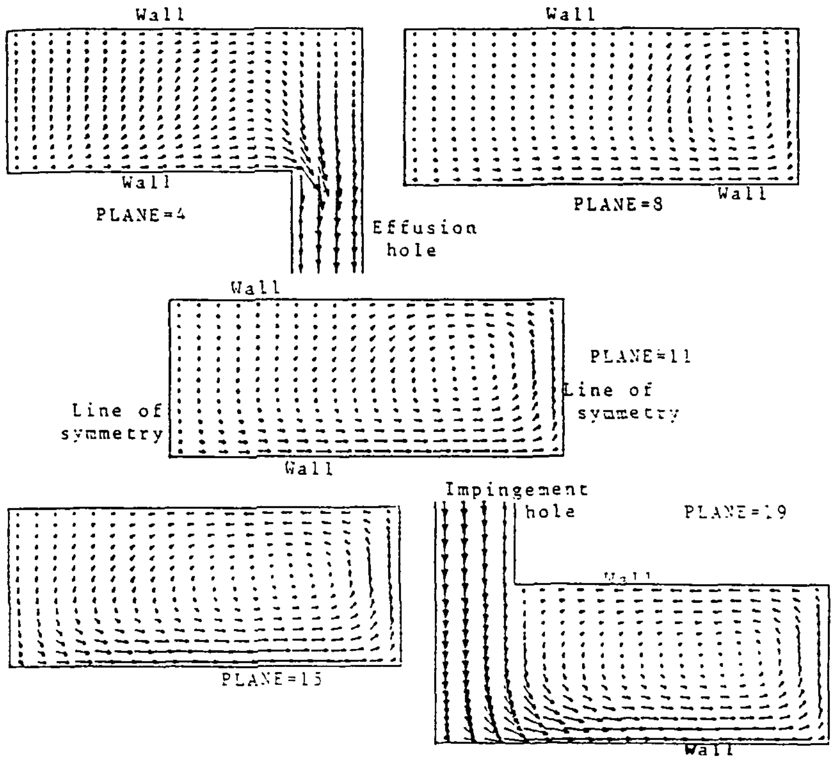

Fig. 3 Velocity vector in planes from side veiw for model of X/D=5.0, Z/D=1.0 .

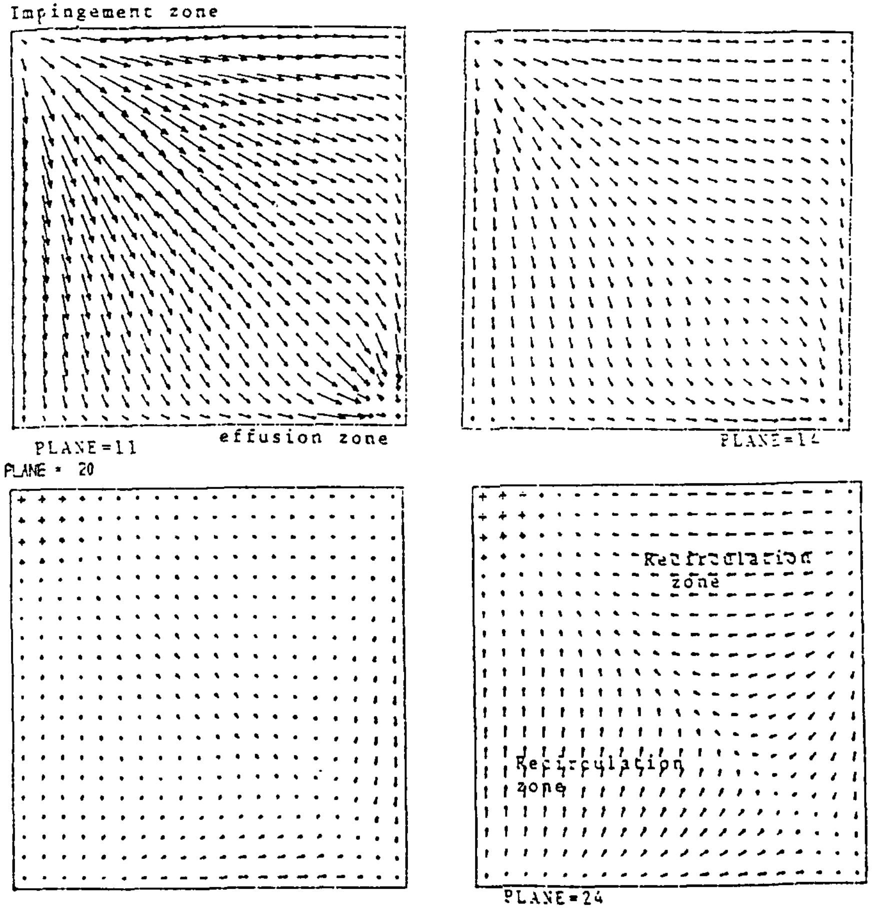

Fig.4 Velocity vector in planes from front view for model of X/D=5.0, Z/D=1.0.

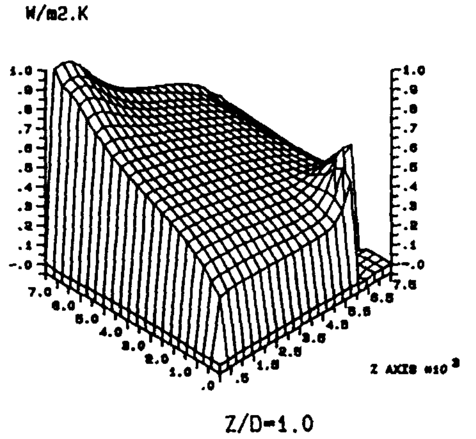

Fig.5 Heat transfer distribution at the impingement surface for X/D=5.0

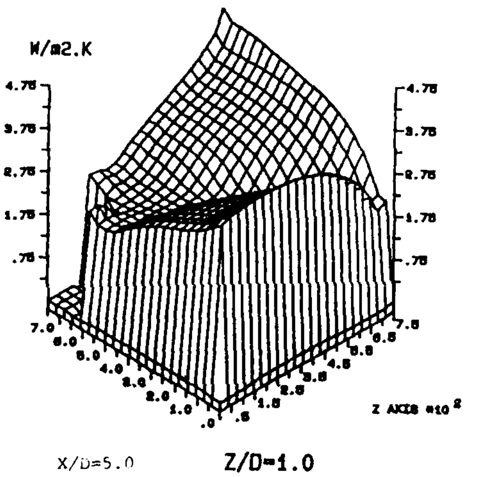

Fig.6 Heat transfer distribution at the surface opposite to the impingement surface.

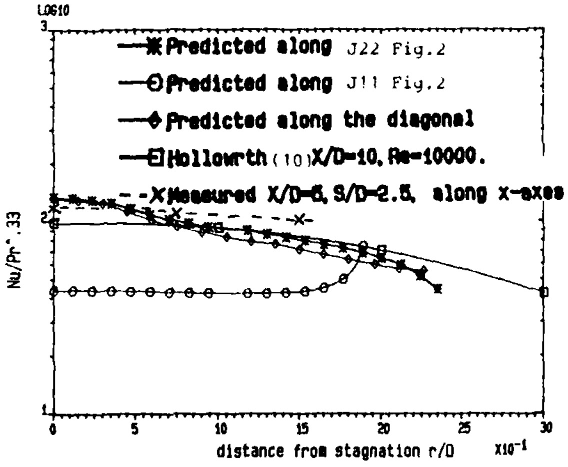

Fig. 7 Comparison of the predicted and measured heat transfer distribution at the impingement surface for X/D=5.0, Z/D=1.0, at Reynolds number=15000.

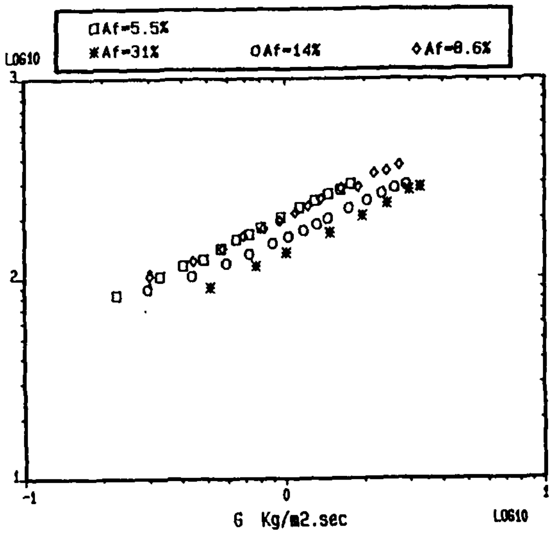

Fig. 8 Impingement heat transfer coefficient vs mass velocity for different open area at Z/D=0.5.

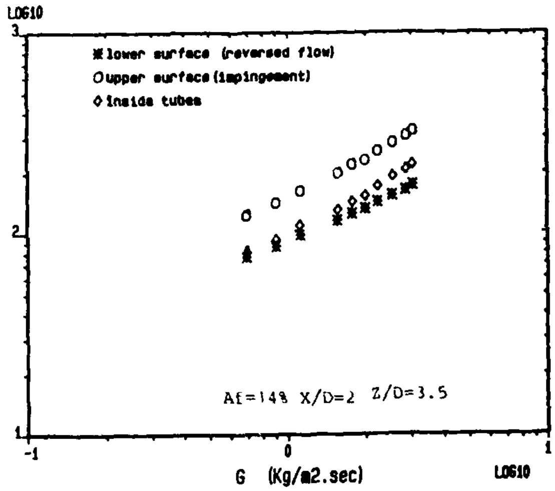

Fig. 9 Comparison of the heat transfer coefficient for the three surfaces of the impingement side.

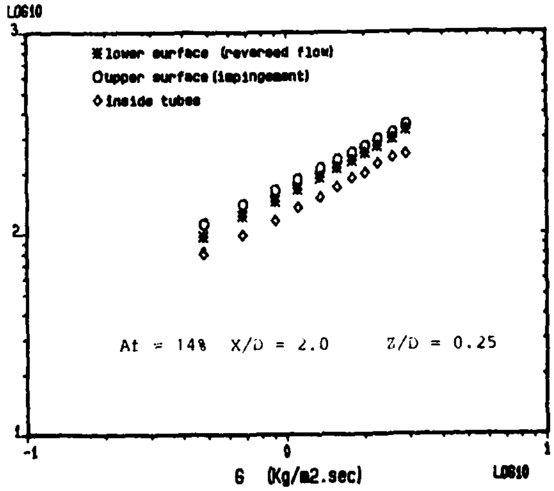

Fig. 10 Comparison of the heat transfer coefficient for the three surfaces of the impingement side.

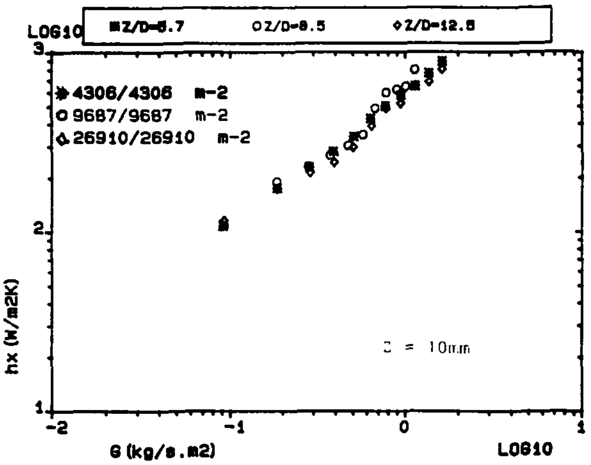

Fig. 11 Variation of heat transfer coefficient hx, as a function of G for increasing number of impingement /effusion holes at constant effusion X/D=4.7.

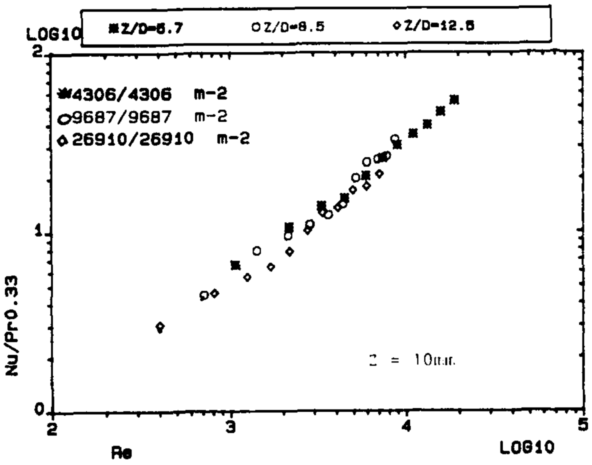

Fig. 12 Nu/Pr0.33 versus Re, the influence of Re on the heat transfer coefficient for range of Z/D, at constant effusion X/D=4.7.

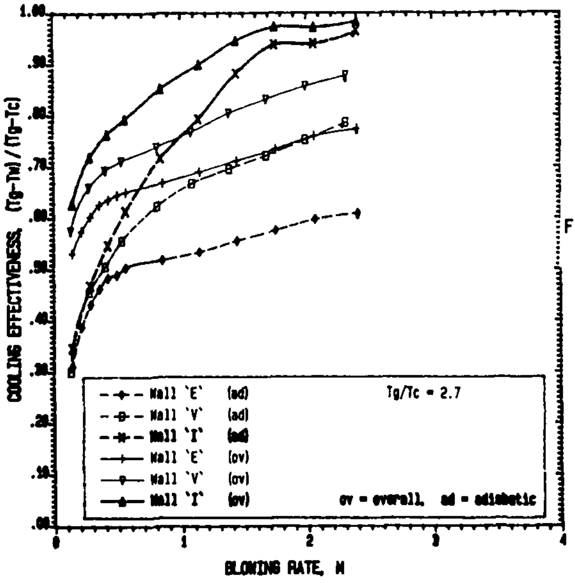

Fig. 13 Cooling effectiveness as a function of blowing rate, for comparison of walls I, V and E, at thermal station 5.

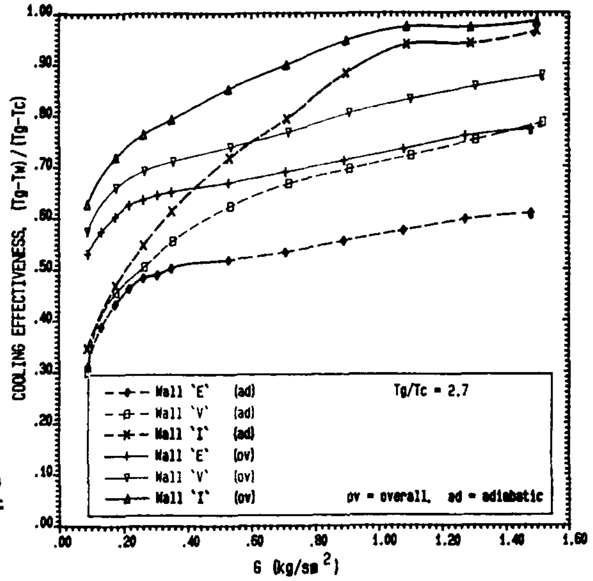

Fig. 14 Cooling effectiveness as a function of G, for comparison of walls I, V and E, at thermal station 5.

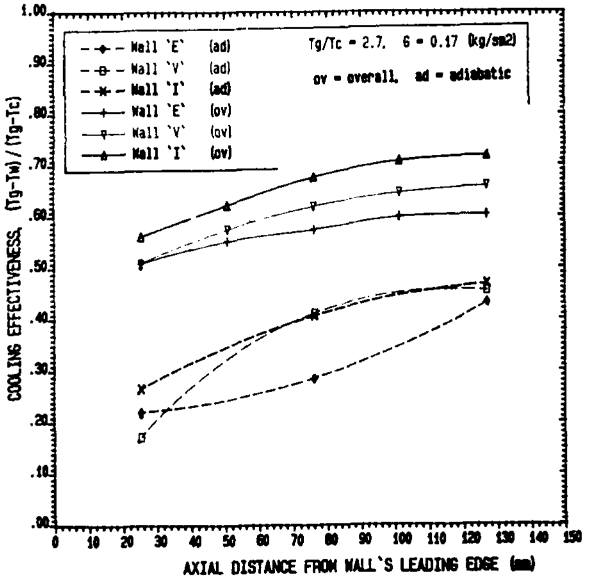

Fig. 15 Axial variation of cooling effectiveness for walls I, V and E, at fixed G and temperature ratio.

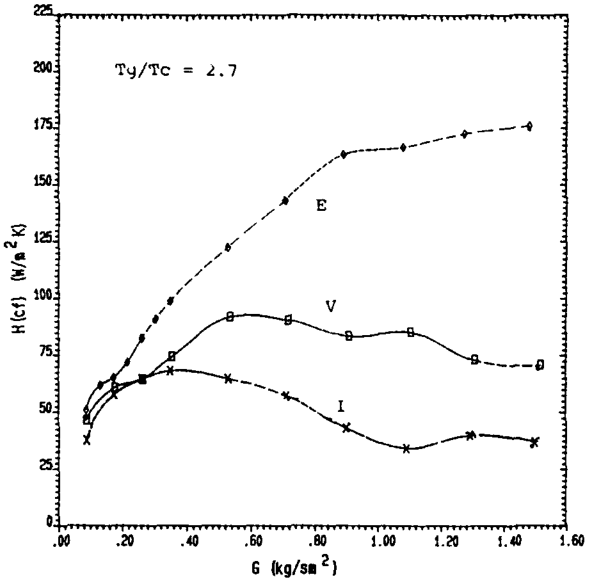

Fig.16 H(cf) versus G, for comparison of walls I, V and E at a fixed temperature ratio, at thermal station 5.

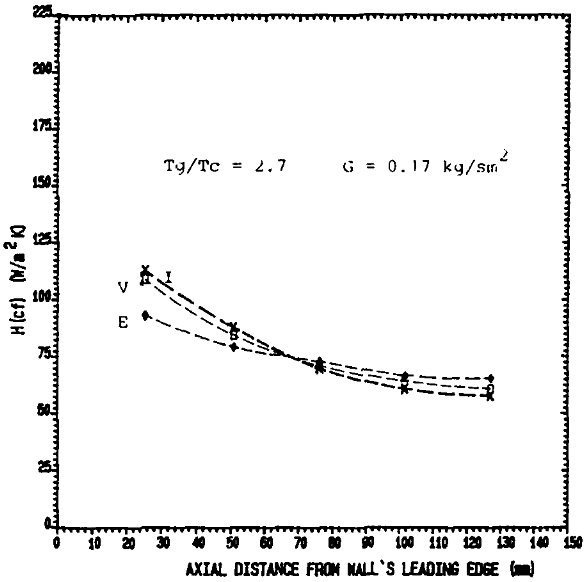

Fig.17 Axial variation of film heat transfer coefficient for walls I, V and E at fixed G and temperature ratio.

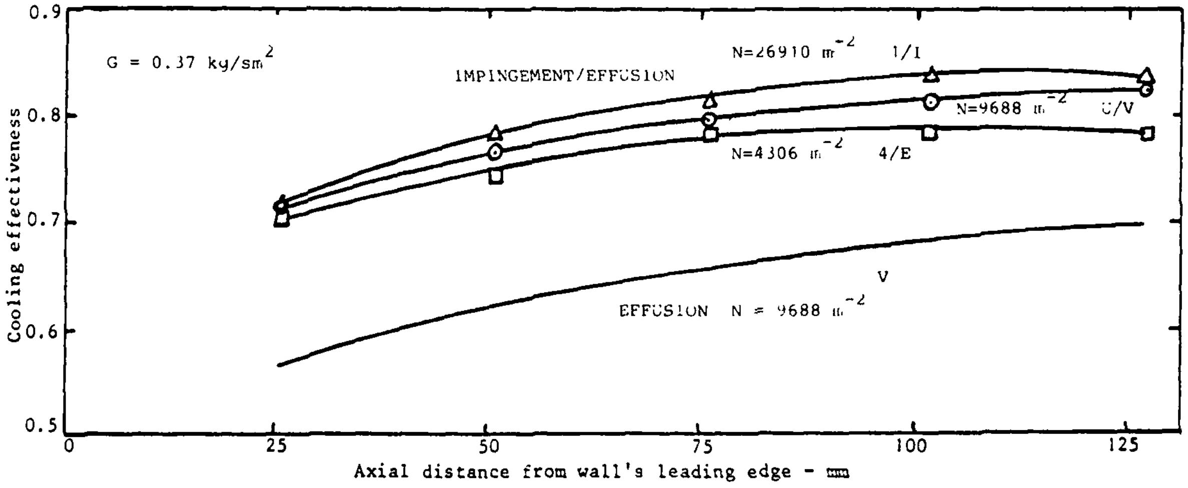

Fig.18 Axial variation of the overall cooling effectiveness at G=0.037 kg/sm^2

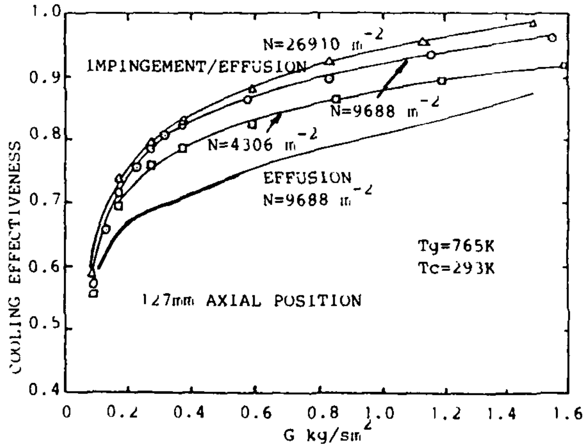

Fig.19 Overall cooling effectiveness as a function of G for three impingement/effusion cooling configurations with different N.

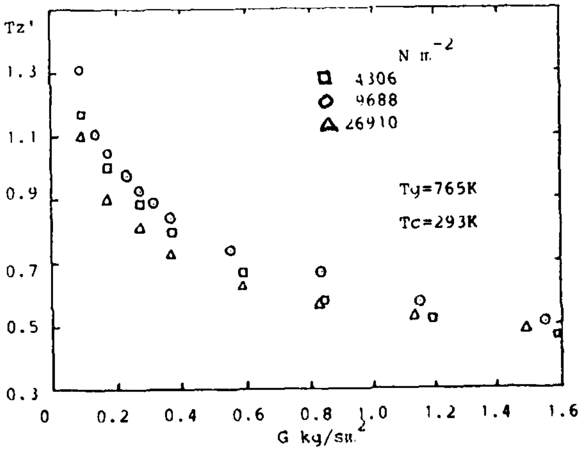

Fig.20 Impingement jet wall heating parameter Tz' as a function of G for the three impingement/effusion geometries at different N.

EVALUATION OF MULTI-DIMENSIONAL FLUX MODELS FOR RADIATIVE TRANSFER IN CYLINDRICAL COMBUSTION CHAMBERS

Nevin Selçuk
Department of Chemical Engineering
Middle East Technical University
Ankara 06531, Türkiye

SUMMARY

Four flux-type models for radiative heat transfer in cylindrical configurations were applied to the prediction of radiative flux density and source term of a cylindrical enclosure problem based on data reported previously on a pilot-scale experimental combustor with steep temperature gradients. The models, which are Schuster-Hamaker type four-flux model derived by Lockwood and Spalding, two Schuster-Schwarzschild type four-flux models derived by Siddall and Selçuk and Richter and Quack and spherical harmonics approximation, were evaluated from the viewpoint of predictive accuracy by comparing their predictions with exact solutions produced previously. The comparisons showed that spherical harmonics approximation produces more accurate results than the other models with respect to the radiative energy source term and that the four-flux models of Lockwood and Spalding and Siddalll and Selçuk for isotropic radiation field are more accurate with respect to the prediction of radiative flux density to the side wall.

LIST OF SYMBOLS

K_a	volumetric absorption coefficient of the medium [m^{-1}]
q	component of radiative flux density vector [Wm^{-2}]
Q	source term for radiative energy [Wm^{-3}]
R,Γ,Z	coordinate directions

Superscripts

~	dimensionless

1. INTRODUCTION

In a previous paper [1], the accuracy of several flux-type models for three-dimensional radiative heat transfer have been assessed by applying these radiation models to the prediction of distributions of radiative flux density and radiative energy source term of a rectangular enclosure problem and by comparing their predictions with exact solutions produced earlier by the same author [2]. The problem was based on data taken from a large-scale experimental furnace with steep temperature gradients typical of operating furnaces.

A significant number of industrial furnaces and combustors are cylindrical in shape. Therefore, it is considered necessary to evaluate the flux-type models produced earlier for cylindrical furnaces [3-6] by applying them to the prediction of radiative flux density and source term distributions of a cylindrical enclosure problem based on data reported previously on a pilot-scale experimental furnace [7] and by comparing their predictions with exact values reported previously [8].

The first radiation model is a Schuster-Hamaker type four-flux model for axi-symmetrical radiation field derived by Lockwood and Spalding [3]. The model is an extension of Schuster-Hamaker formulation to an axi-symmetrical radiation field. It utilizes the simplest and least accurate representation of the angular variation of intensity, that is, either plane parallel radiation in each spacial coordinate direction or an isotropic radiation field [3,9]. Two differential equations are then produced from first principles for each coordinate direction separately by carrying out radiative energy balances for the forward and backward directions, ignoring variations in the other coordinate directions. That is, in deriving each pair of equations, it is implicitly assumed that the situation under consideration is that of one dimensional variation in the coordinate direction considered, rather than the true multi-dimensional variation which the approximate equations are intended to model. Lockwood and Spalding also suggest that the multiplying coefficient appearing in their radiative energy balances should take values of K_a and $2K_a$ corresponding to the cases of parallel and isotropic emitted radiation respectively.

The second radiation model is a Schuster-Schwarzschild type four-flux model derived by Siddall and Selçuk [4]. The model is derived by consideration of the axi-symmetrical radiation field in a grey non-scattering medium in which significant radiative transfer occurs in either the radial or axial direction. Assuming that the transfer in the radial direction is negligible, a two-flux representation of the radiation is obtained by integrating the equation of radiative transfer at a point over two hemispheres whose diametric plane is normal to the axis of symmetry, utilizing the assumption that the intensity of radiation is uniform but different over each hemisphere. A similar Schuster-Schwarzschild [10] type treatment of the corresponding axi-symmetrical field in which transfer in the axial direction may be neglected produces another pair of two-flux equations, when the intensity of radiation in the diametric plane is assumed to be the arithmetic mean of the uniform but different intensities in the two hemispheres. These two pairs of two-flux equations represent an axi-symmetrical radiative field with significant transfer in both the radial and axial directions. Multiplying coefficient appearing in the radiative energy balances take the values of K_a and $2K_a$ for the cases of parallel and isotropic emitted radiation respectively.

The third radiation model is a Schuster-Schwarszchild type four-flux model produced by Richter and Quack [5]. In this model, the total solid angle surrounding a point is divided into four smaller solid angles-two of which are cones of half angle, 45°, in the forward and backward axial directions and the remaining two for all other forward and backward radial directons-in each of which intensity is assumed to be uniform. Integration of the equation of radiant energy transfer for each smaller solid angle, in turn, produces four differential equations in the unknown intensities.

The final radiation model is the spherical harmonics approximation derived for an axisymmetrical radiation field [6]. In this model the angular variation of intensity at a point is expressed by a series of spherical harmonics. By using the P_1 approximation (in which the series is truncated after the first four terms) and the equation of radiative transfer, the axisymmetrical radiation field within a grey, non-scattering medium is represented by three partial differential equations in the total incident flux density and the net radiant flux densities in the positive coordinate directions.

All these models had previously been employed as part of complete prediction procedures and predicted temperature and radiative heat flux distributions have been compared with experimentally determined data [3-6,9,11,12]. However, it has been found impossible to decide whether discrepancies between the predictions and measurements are attributable directly to the flux model employed or to inaccuracies in the submodels used for the prediction of flow, reaction etc.

The use of exact solutions for testing purposes provides a means for assessing the accuracy of predictions of these radiation models in isolation from the models of flow and reaction. Therefore, the accuracy of each of these radiations models had been tested by applying them to the prediction of distributions of radiative flux density and radiative energy source term of a cylindrical enclosure problem and by comparing its predictions with exact solutions reported previously [13,14].

In this paper, evaluations of these models for radiative transfer in cylindrical enclosures are reviewed from the points of view of both accuracy and computational economy.

2. THE TEST PROBLEM

The flux-type models considered have been tested by making predictions for a black-walled enclosure problem for which exact solutions have been produced previously [8]. The enclosure problem is based on data reported by Wu and Fricker [7] on a pilot-scale experimental furnace with steep temperature gradients typically encountered in industrial furnaces.

The experimental furnace under consideration is a vertical cylinder fired from the bottom end wall with natural gas and operates under atmospheric pressure. The side walls are water cooled. A detailed description of the data obtained from the experimental furnace and used as input data for flux-type models can be found elsewhere [8].

3. NUMERICAL SOLUTION PROCEDURE

The partial differential equations representing the radiation models under consideration have been re-cast into finite difference forms by using the control volume approach. As the variation of gas and wall temperatures is axi-symmetrical, the enclosure has been subdivided into 2x20 control volumes in the *r*-and *z*-directions, respectively. A medium grid point lies at the geometrical centre of each control volume and a surface grid point lies in the centre of each control volume face in contact with the walls of the enclosure. Hence the total number of medium and surface grid points are 2x20 and (2x2+20), respectively. The resulting sets of simultaneous algebraic equations have then been solved by the iterative procedure developed by Peaceman and Rachford [15] for numerical solution of the algebraic equations with a coefficient matrix of the tridiagonal type. This procedure can be described as 'forward elimination followed by backward substitution'.

4. EVALUATION OF THE FLUX MODEL PREDICTIONS

Point values of the dimensionless radiative energy source term and flux density for 2x20 medium grid points have been produced using:

(a) Lookwood and Spalding's four-flux model for plane parallel radiation-Model 1;

(b) Lokwood and Spalding's four flux model for isotropic radiaton-Model 2;

(c) Siddall and Selçuk's four-flux model for plane parallel radiation-Model 3;

(d) Siddall and Selçuk's four-flux model for isotropic radiation-Model 4;

(e) Richter and Quack's four-flux model-Model 5;

(f) Selçuk and Siddall's spherical harmonics model-Model 6.

The predictions of these models have been compared with the exact solutions reported previously in the literature [8].

In the discussion that follows, all physical quantities are expressed in dimensionless forms which are obtained by dividing them by the shortest dimension of the enclosure or by the maximum emissive power of the gas, depending on the quantity.

4.1. Source Term Distributions

Figure 1 shows the comparison between flux model predictions of the dimensionless source term and the exact values for points ($\tilde{R}$ = 0.25, $\tilde{\Gamma}$ = 0, $\tilde{Z}$). These grid points represent the points at the centre of the row of control volumes nearest to the furnace axis. It can be seen that the exact source term distribution follows the physically expected trend, rising steeply from the burner wall onwards, going through a maximum and decreasing continuously towards the exit. The maximum of the source term distribution occurs at the same location as the maximum of the temperature distribution. It can also be noted that the trend of the distributions predicted by the flux models is the same as that of the exact distribution and that the distributions are over predicted by Models 2,4, and 6 and underpredicted by Models 1,3 and 5.

Figure 2 illustrates the comparison between the exact values of the dimensionless source term and the distributions predicted by the flux models for grid points ($\tilde{R}$ = 0.75, $\tilde{\Gamma}$ = 0, $\tilde{Z}$). These grid points represent the medium points nearer to the side wall. It can be seen that good agreement is obtained and that the source term distributions for these grid points show smaller variation along the length of the furnace than those for other medium grid points. This is consistent with the uniform temperature distribution in the medium near the wall of the enclosure.

A condensed comparison of the flux model predictions of the dimensmionless source term values is contained in Table 1. Two values are given for each model; the maximum point percentage error and the average absolute percentage error both of which give measures of the accuracy of predicted source terms.

As can be seen from Table 1, Model 6 produces more accurate results than the other models.

Table 1. Comparison of flux model predictions of dimensionless source terms

Flux model	Maximum percentage error	Average absolute percentage error
Model 1	44.98	23.38
Model 2	-52.40	24.16
Model 3	48.84	22.67
Model 4	-79.54	28.34
Model 5	74.44	18.68
Model 6	-11.33	9.04

4.2. Flux Density Distributions

Figure 3 illustrates the comparison between the point values of the dimensionelss flux density to the side wall in the positive *r*-direction predicted by the flux models and exact solutions for surface grid points. It can be seen that Models 2 and 4 produce fairly good agreement and that Models 1,3, 5 and 6 underestimate the flux densities to the wall over the whole length of the enclosure.

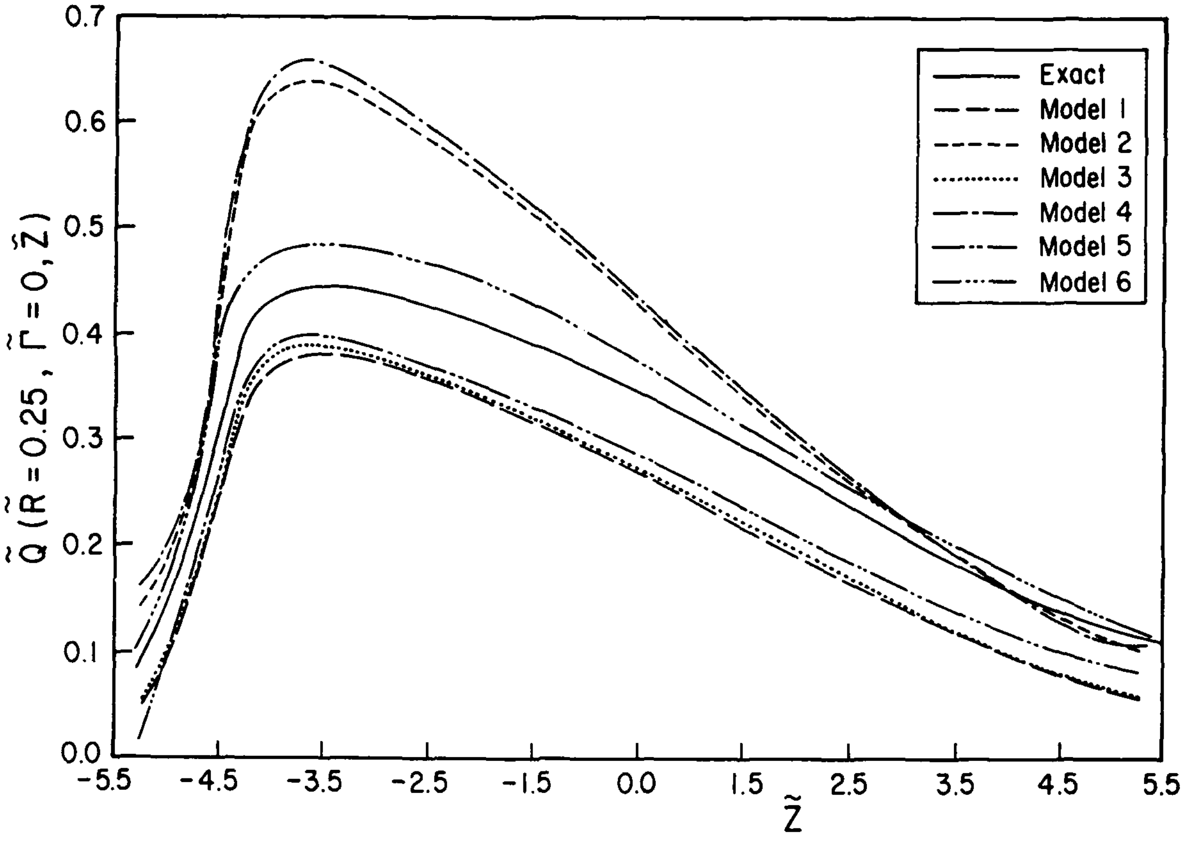

Figure 1. Comparison between the exact values and flux model predictions of dimensionless radiative energy source terms along ($\tilde{R}$ = 0.25, $\tilde{\Gamma}$ = 0, $\tilde{Z}$).

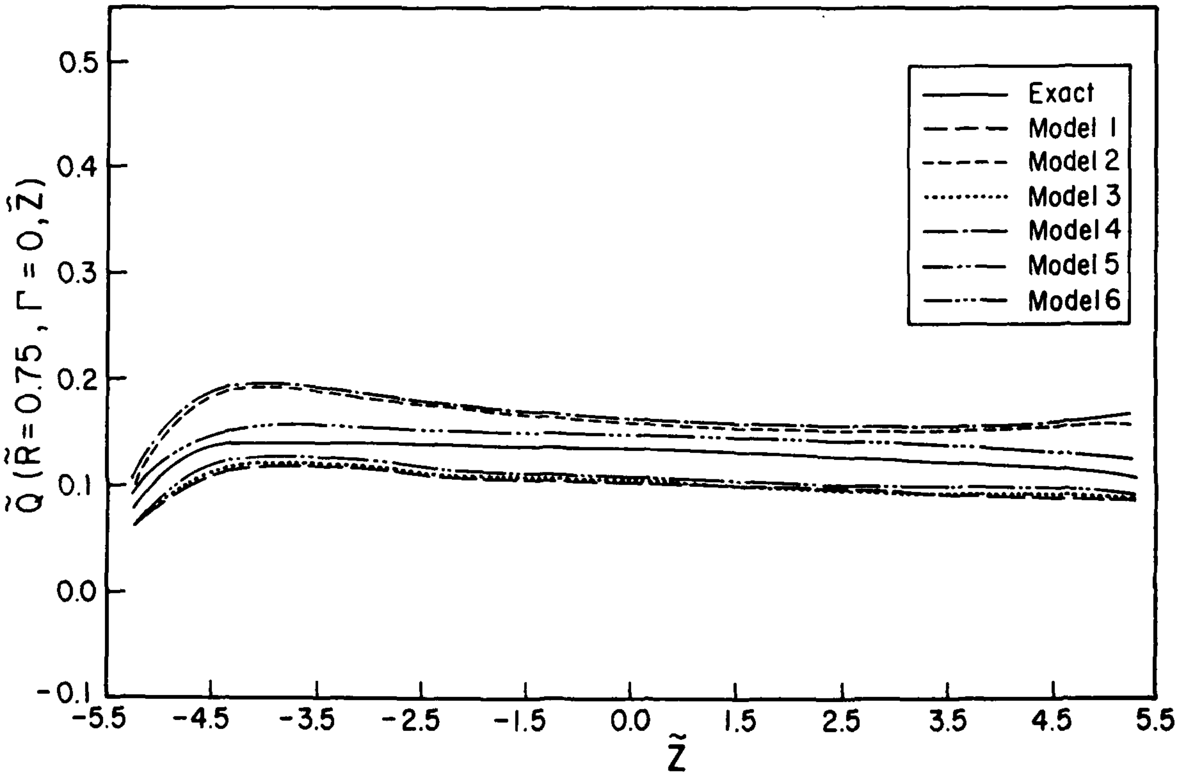

Figure 2. Comparison between the exact values and flux model predictions of dimensionless radiative energy source terms along ($\tilde{R}$ = 0.75, $\tilde{\Gamma}$ = 0, $\tilde{Z}$).

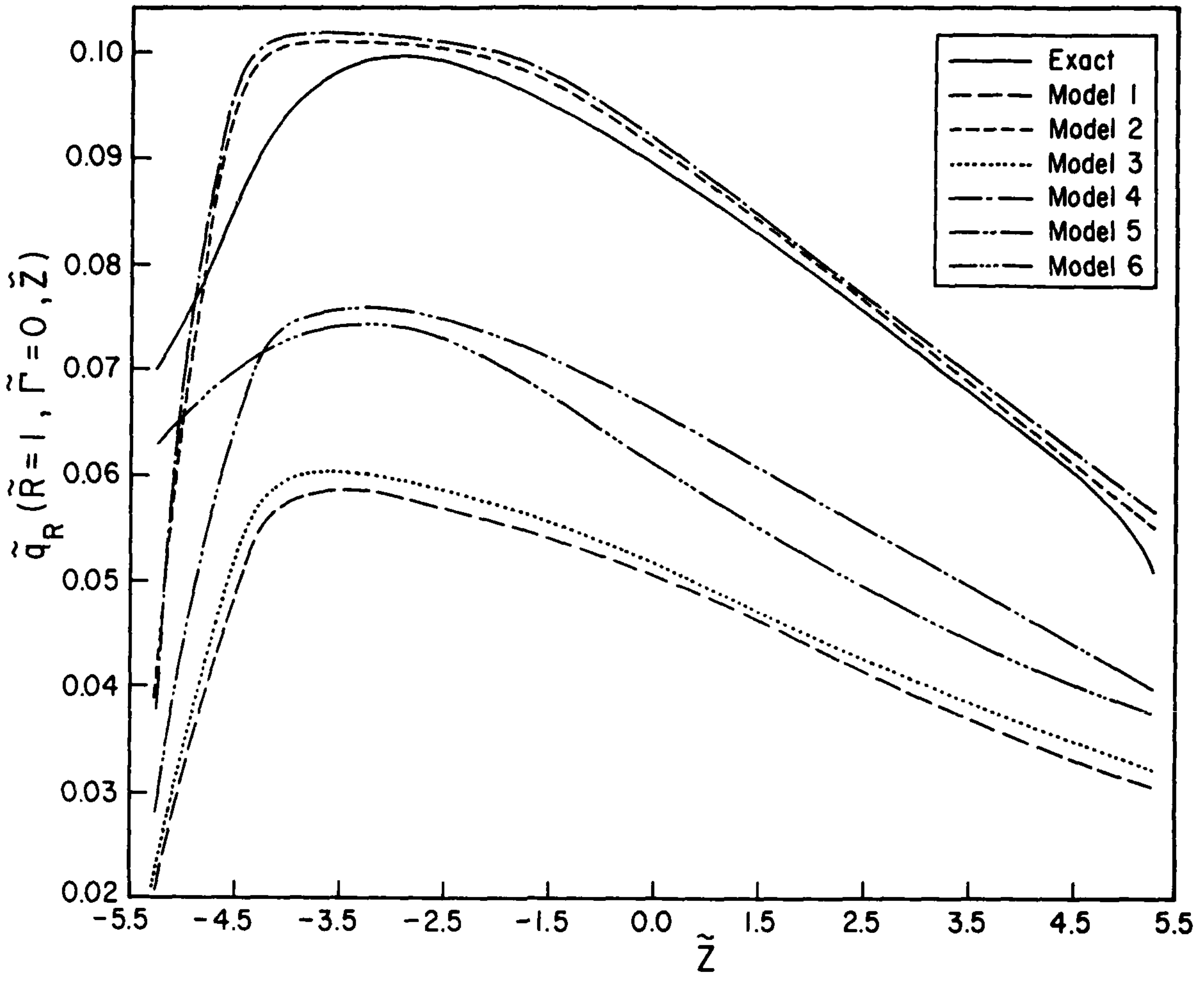

Figure 3. Comparison between the exact values and flux model predictions of dimensionless flux densities to the side walls.

A condensed comparison of the flux model predictions of the dimensionelss flux densities is contained in Table 2. As can be seen from Table 2, the level of agreement decreases in the following order: Model 2, Model 4, Model 6, Model 5, Model 3, and Model 1.

Table 2. Comparison of flux model predictions of dimensionless flux densities to the side wall

Flux model	Maximum percentage error	Average absolute percentage error
Model 1	69.20	44.24
Model 2	43.97	5.34
Model 3	70.11	43.54
Model 4	46.86	7.63
Model 5	59.37	27.07
Model 6	28.10	24.15

To provide a global check on the accuracy of the flux model predictions, the total rate of removal of radiative energy through the wall and the total rate of generation of radiative energy within the enclosed medium were calculated and compared with the exact values. Table 3 shows the errors in generated and removed radiative energy produced by the flux model predictions. It can be seen that the percentage errors in generated and removed radiative energy are almost equal for each model, implying that each model produces consistent results, although different from the exact values.

Table 3. Comparison of flux model predictions of the percentage errors in generated ana removed radiative energy

Flux model	Percentage error in generation	Percentage error in removal
Model 1	21.46	21.46
Model 2	-25.27	-25.27
Model 3	21.17	21.17
Model 4	-26.18	-26.18
Model 5	15.97	15.97
Model 6	-10.06	-10.06

5. CONCLUSIONS

Four flux-type models for cylindrical enclosures filled with an absorbing-emitting medium of constant properties have been applied to the prediction of distributions of the radiative flux density and the energy source term of a black-walled enclosure problem. The problem is based on data reported previously and a pilot-scale experimental furnace with steep temperature gradients typically encountered in industrial furnaces. The accuracy of the models have been tested by comparing their predictions with exact solutions reported earlier in the literature. On the basis of comparisons the following conclusions have been reached.

(1) The spherical harmonic model of Selçuk and Siddall proves to be a satisfactory method, previding a better agreement in radiative energy source term distributions than in the flux density distributions.

(2) The four-flux model of Richter and Quack is a reasonably satisfactory method of predicting both the radiative energy source term and flux density distributions.

(3) The four-flux models of Lockwood and Spalding and Siddall and Selçuk for an isotropic radiation field provide a useful method for predicting the flux density distributions at the walls of the enclosure. However, with regard to the distribution of the radiative energy source term, a relatively poor agreement is obtained.

(4) The four-flux methods of Lockwood and Spalding and Siddall and Selçuk for plane parallel radiation are not found satisfactory.

(5) Predictive ability of each model relative to the exact solutions are expected to remain the same for non-black walled enclosures although the order of magnitude of the accuracies might change.

REFERENCES

1. Selçuk, N., "Evaluation o Flux Models for Radiative Transfer in Rectangular Furnaces", Int.J. Heat Mass Transfer, 31, 1988. pp. 1477-1482.

2. Selçuk, N., "Exact Solutions for Radiative Heat Transfer in Box-Shaped Furnaces". ASME J. Heat Transfer, 107, 1985, pp. 648-655.

3. Lockwood, F.C and Spalding, D.B., "Prediction of a Turbulent Reacting Duct Flow with Significant Radiation", Thermodynamic Session, Proceedings Colloques d'Evion de la Societe Francaise, 1971, C 56-27.

4. Siddall, R.G. and Selçuk, N., "Two-flux Modelling of Two Dimensional Radiative Transfer in Axi-symmetrical Furnaces", J. Inst. Fuel, 49, 1976, pp. 10-20.

5. Richter. W. and Quack, R., "Mathematical Model of a Low-Volatile Pulvensed Fuel Flame", in Heat Transfer in Flames (Edited by N.H. Afgan and J.M.Beer), Scripta, Washington DC, 1974, pp. 95-110.

6. Selçuk, N. and Siddall, R.G., "Two-flux Spherical Harmonic Modelling of Two-dimensional Radiative Heat Transfer in Furnaces", Int. J. Heat Mass Transfer, 19, 1976, pp. 313-321.

7. Wu, H.L. and Fricker, N., "The Characteristics of Swirl-stabilized Natural Gas Flames: Part 2. The Behaviour of Swirling Jet Flames in a Narrow Cylindrical Furnace, J. Inst. Fuel, 49, 1976, pp. 145-151.

8. Selçuk, N. and Tahiroğlu, Z., "Exact Numerical Solutions for Radiative Heat Transfer in Cylindrical Furnaces", Int. J. Numer. Meth. Engng, 26, 1988, pp. 1201-1212.

9. Gosman, A.D. and Lockwood F.C., "Incorporation of a Flux Model for Radiation into a Finite-difference Procedure for Furnace Calculations, Proc.14th Symp. (Int.) on Combustion, The Combustion Institute, Pittsburgh, Pennsylvania, 1973, pp. 661-671.

10. Schwarzschild, K., "Equilibrium of the Sun's Atmosphere, Ges. Wiss. Göttingen, Nachr., Math.-Phys. Klasse, 1, 1906, pp.41-53.

11. Patankar, S.V. and Spalding, D.B., "Simultaneous Predictions of Flow Pattern and Radiation for Three-dimensional Flames, in Heat Transfer in Flames (Edited by N.H.Afgan and J.M.Beer), Scripta, Washington, DC, 1974, pp.73-94.

12. Selçuk, N., Siddall, R.G. and Beer, J.M., "A Comparison of Mathematical Models of the Radiative Behaviour of a Large-scale Experimental Furnace", Proc. 16th Int. Symp. of Combustion, The Combustion Institute, Pittsburgh, Pennsylvania, 1977, pp. 53-61.

13. Selçuk, N., "Evaluation of Flux Models for Radiative Transfer in Cylindrical Furnaces", Int. J. Heat Mass Transfer, 32, 1989, pp. 620-624.

14. Selçuk, N., "Evaluation of Spherical Harmonics Approximation for Radiative Transfer in Cylindrical Furnaces, Int. J. Heat Mass Transfer, 33, 1990, pp. 579-581.

15. Peaceman, D.W. and Rachford, H.H., "The Numerical Solution of Parabolic and Elliptic Differential Equations", J. Soc. Ind. Appl. Math., 3, 1955, pp. 1-28.

Discussion

QUESTION 1:

DISCUSSOR: G. Andrews, University of Leeds

Which is the most efficient radiation model to incorporate in CFD codes for gas turbine combustion applications, where there is no net heat loss due to radiation? Radiation heats the combustor walls which, in turn, transfer heat to the coolant which, in turn, is injected back into the combustion gas. Thus radiation can change combustion temperature profiles and hence NO_x, but how accurate does it need to be for adequate predictions? I understand that some of the more accurate radiation models cause large increases in CFD computation time.

AUTHOR'S REPLY:

As I have mentioned in my presentation, flux-type radiation models are the most economic methods as far as the computation time is concerned. Among the flux models that I have tested, P_1-spherical-harmonic models produce the best agreement with exact solution relative to the radiative energy source term. For gas turbine combustors where temperature distribution prediction is important, I would recommend the use of the P_1-approximation in CFD, as temperature distribution is proportional to the source term distribution. Its advantages are computational economy and good accuracy with respect to the source term.

QUESTION 2:

DISCUSSOR: Y.A. Gogus, Havacilik Muh Bol

Would you please tell me the relative position for the origin of the z axis.

AUTHOR'S REPLY:

For calculation purposes, the origin was taken to be the midpoint of the the axis of symmetry.

QUESTION 3:

DISCUSSOR: D.T. Vogel, DLR

What does the test furnace look like?

AUTHOR'S REPLY:

The furnace is a cylindrical combustion chamber 0.9m in diameter, 5m in height. It is a vertical chamber fired with natural gas from the bottom end wall. The sidewalls are water-cooled. For these calculations, the swirl number was zero.

QUESTION 4

DISCUSSOR: H. Weyer, ABB

Your paper deals with gas-solid wall interaction. What assumption did you make about the gas phase, i.e., gas composition, emissivity and absorption of gas components and soot?

AUTHOR'S REPLY:

Because the radiation has been treated in isolation from the flow and reaction, we only need a radiative boundary condition, and this stems from the assumption that the inner wall is black. As far as the gas composition is concerned it is typical and has CO_2 and H_2O vapour in it. The absorbing-emitting characteristics are calculated accordingly.

CALCULS D'ECOULEMENTS TURBULENTS REACTIFS DANS LES FOYERS AERONAUTIQUES

P. CAILLAU, F. DUPOIRIEUX

ONERA
29, avenue de la Division Leclerc
92322 CHATILLON Cedex - France

SOMMAIRE

Cet article décrit les progrès que nous avons accomplis récemment dans la modélisation de la combustion turbulente pour les applications à la propulsion. Nous rappelons brièvement les équations moyennées des écoulements turbulents réactifs, puis présentons le modèle Probabiliste EUlérien Lagrangien PEUL destiné au calcul des termes sources moyens des espèces et de l'enthalpie. La possibilité de prise en compte par ce modèle de mécanismes réactionnels à plusieurs espèces est appliquée à la prédiction des polluants et en particulier au calcul du NO thermique. En vue d'obtenir la meilleure prédiction possible de la composition chimique et de la température, trois mécanismes globaux d'oxydation du méthane sont successivement couplés au modèle PEUL et leurs résultats comparés. Deux applications sont ensuite étudiées.

La première application concerne une flamme prémélangée stabilisée par un écoulement de gaz chauds. Les résultats de calcul sont comparés aux résultats expérimentaux obtenus à l'ONERA et présentent un accord convenable, en particulier en ce qui concerne les profils de NO thermique. La seconde concerne une portion de chambre aéronautique annulaire. La comparaison des taux de production moyens obtenus avec un modèle de combustion turbulente à chimie rapide et avec le modèle PEUL met en évidence, dans ce cas, l'intérêt de ne pas faire l'hypothèse de chimie rapide.

LISTE DES SYMBOLES

φ : richesse

P : pression

T : température

ρ : densité

h : enthalpie

$\tilde{\Phi}$: moyenne de Favre de la variable Φ

Φ'' : fluctuations de la variable Φ, $\Phi = \tilde{\Phi} + \Phi''$

$\overline{\Phi}$: moyenne statistique classique de la variable Φ

u : composante du vecteur vitesse

μt : viscosité turbulente

Y_i : fraction massique de l'espèce i

$\tilde{\omega}_i$: taux de production moyen de l'espèce i

$\tilde{\omega}_h$: taux de production moyen de l'enthalpie

$\delta_{\alpha\beta}$: symbole de Kronecker

$\bar{\tau}_{\alpha\beta}$: tenseur moyen des contraintes visqueuses

$\bar{J}^i_\alpha$: vitesse moyenne de diffusion laminaire de l'espèce i

$\bar{J}^h_\alpha$: vitesse moyenne de diffusion laminaire de la chaleur

k : énergie cinétique de la turbulence

ε : taux de dissipation de k

τt : temps caractéristique de l'échelle moyenne de turbulence $\tau t = k/\varepsilon$

εv : taux de dissipation des fluctuations d'espèces

τv : temps caractéristique turbulent relatif aux échanges des espèces

τex : temps caractéristique d'échange du modèle IEM

D : coefficient de diffusion laminaire

Q_0^i : chaleur de formation de l'espèce i

INTRODUCTION

Nous présentons, dans cet article, une version du modèle de combustion turbulente PEUL (Probabiliste Eulérien Lagrangien) sur laquelle plusieurs mécanismes simplifiés d'oxydation du méthane à 1, 2 et 4 étapes ont été implantés et comparés. Le mécanisme de production des oxydes d'azote dans les gaz brûlés dit "mécanisme du NO thermique" a lui aussi été pris en compte et l'influence des schémas d'oxydation du méthane sur la vitesse de production de NO a été étudiée.

Les calculs ainsi réalisés ont été comparés aux mesures effectuées dans un canal rectangulaire bidimensionnel où une flamme air-méthane est stabilisée par un jet de gaz chauds.

A partir du même modèle de combustion turbulente, des calculs ont été menés dans une chambre de combustion aéronautique tridimensionnelle.

MODELISATION DE LA COMBUSTION TURBULENTE

La turbulence est caractérisée par des fluctuations de vitesse et des variables d'état (P, ρ, T, h). Les équations classiques de Navier-Stokes pour les grandeurs instantanées (quantité de mouvement, densité, enthalpie) ne nécessitent aucune hypothèse supplémentaire pour décrire un écoulement turbulent. Toutefois, à grand nombre de Reynolds, le calcul des structures turbulentes, nécessite des pas en temps et en espace extrêmement petits, et ne peut donc être effectué que pour des configurations simples, compte tenu de la puissance actuelle des ordinateurs.

Afin d'éviter cette limitation, nous avons utilisé l'approche classique qui consiste à résoudre les équations de bilan de la moyenne des grandeurs étudiées. Chaque grandeur Φ peut alors être décomposée en une composante moyenne $\tilde{\Phi}$ (il s'agit ici de la moyenne de Favre) et une composante fluctuante aléatoire Φ''.

Les équations moyennées que nous cherchons à résoudre sont les suivantes :

- Conservation de la masse

$$\frac{\partial \bar{\rho}}{\partial t} + \frac{\partial}{\partial x_\alpha} \bar{\rho} \tilde{u}_\alpha = 0$$

- Conservation de la quantité de mouvement

$$\frac{\partial}{\partial t} \bar{\rho} \tilde{u}_\beta + \frac{\partial}{\partial x_\alpha} \left(\bar{\rho} \tilde{u}_\alpha \tilde{u}_\beta + \bar{\tau}_{\alpha\beta} + \bar{P} \delta_{\alpha\beta} + \bar{\rho} \widetilde{u_\alpha'' u_\beta''} \right) = 0$$

$\bar{\tau}_{\alpha\beta}$ est le tenseur moyen des contraintes visqueuses.
$\delta_{\alpha\beta}$ est le symbole de Kronecker ($=1$ si $\alpha = \beta$, $=0$ si $\alpha \neq \beta$)

Conservation de la masse des espèces chimiques

$$\frac{\partial}{\partial t} \bar{\rho} \tilde{Y}_l + \frac{\partial}{\partial x_\alpha} \left(\bar{\rho} \tilde{u}_\alpha \tilde{Y}_l + \bar{j}_\alpha^l + \bar{\rho} \widetilde{u_\alpha'' Y_l''} \right) = \bar{\rho} \tilde{\omega}_l$$

où $\bar{j}_\alpha^l$ est la vitesse moyenne de diffusion laminaire et $\tilde{\omega}_l$ le taux de production chimique moyen de l'espèce i.

- Conservation de l'enthalpie

$$\frac{\partial}{\partial t} \bar{\rho} \tilde{h} + \frac{\partial}{\partial x_\alpha} \left(\bar{\rho} \tilde{u}_\alpha \tilde{h} + \bar{j}_\alpha^h + \bar{\rho} \widetilde{u_\alpha'' h''} \right) = \frac{\partial P}{\partial t} + \bar{\rho} \tilde{\omega}_h$$

où $\bar{j}_\alpha^h$ est la vitesse moyenne laminaire de diffusion de la chaleur.

5 termes inconnus apparaissent :

- les flux turbulents $\widetilde{u_\alpha'' u_\beta''}$ $\widetilde{u_\alpha'' Y_l''}$ $\widetilde{u_\alpha'' h''}$

- les termes de production moyens d'espèces et d'enthalpie $\tilde{\omega}_l$, $\tilde{\omega}_h$.

Les flux turbulents sont donnés par le modèle classique de turbulence k-ϵ à concept de viscosité turbulente [1].

$$\bar{\rho} \widetilde{u_\alpha'' u_\beta''} = -\mu_t \left(\frac{\partial \tilde{u}_\alpha''}{\partial x_\beta} + \frac{\partial \tilde{u}_\beta''}{\partial x_\alpha} \right) + \frac{2}{3} \bar{\rho} k \delta_{\alpha\beta} + \frac{2}{3} \delta_{\alpha\beta} \frac{\partial \tilde{u}_\gamma}{\partial x_\gamma}$$

avec $\mu_t = \bar{\rho} c_\mu \frac{k^2}{\varepsilon}$

où μ_t est la viscosité turbulente.

k est l'énergie cinétique de la turbulence et ϵ son taux de dissipation. Tous deux sont calculés à l'aide d'une équation de bilan.

La résolution des équations de bilan eulériennes moyennées est effectuée par le code 3D DIAMANT, développé à l'ONERA [2].

La technique de discrétisation utilisée est de type volumes finis. L'intégration des équations est effectuée par une méthode implicite à directions alternées.

Cette technique consiste à intégrer successivement les équations dans les 3 directions de l'espace. Elle a pour principal avantage de réduire considérablement le temps de calcul et le stockage mémoire nécessaire par rapport à une méthode où l'intégration implicite serait effectuée dans les 3 directions simultanément.

Les termes de production moyens d'espèces et d'enthalpie $\tilde{\omega}_l$ et $\tilde{\omega}_h$ sont donnés par le modèle de combustion turbulente PEUL proprement dit.

PRINCIPE DU MODELE PEUL

Le modèle PEUL dit "espace physique", consiste à suivre dans l'espace (U, Y_i, h, $\vec{x}$, t), un grand nombre de particules fluides dont la situation évolue sous contrainte de 2 types d'équations :

1- $\frac{d\vec{x}_p}{dt} = \vec{U}_p$

où $\vec{U}_p$ est la vitesse instantanée de la particule fluide, qui est décomposée en une partie moyenne donnée par le calcul eulérien moyen, et une partie fluctuante aléatoire, tirée au sort suivant une procédure décrite par ORMANCEY dans [3].

2- $\frac{dY_l}{dt} = \frac{\bar{Y}_l - Y_l}{\tau_\alpha} + \omega_l$

$$\frac{dh}{dt} = \frac{\bar{h} - h}{\tau_\alpha} + \omega_h$$

La modélisation du terme d'échange aux petites échelles entre la particule et son environnement, de type $\bar{\Phi} - \Phi / \tau_\alpha$ est due à AUBRY et VILLERMAUX [4].

Cette modélisation remplace le terme de diffusion de l'équation lagrangienne d'évolution de Y_i dans la particule :

$$\frac{dY_l}{dt} = \frac{\partial}{\partial x_\alpha} \left(-\rho D \frac{\partial Y_l}{\partial x_\alpha} \right) + \omega_l$$

où D est le coefficient de diffusion moléculaire de l'espèce i.

On montre facilement [5] que τ_{ex}, le temps caractéristique, peut s'écrire sous la forme :

$$\tau_{ex} = \tau_Y = \frac{\overline{Y'^2}}{D\dfrac{\partial Y'}{\partial x_\alpha}\dfrac{\partial Y'}{\partial x_\alpha}} = \frac{\overline{Y'^2}}{\varepsilon_Y}$$

où ϵ_y est le taux de dissipation des fluctuations d'espèces.

Le temps caractéristique d'échange τ_Y ou le taux de dissipation des fluctuations d'espèces ϵ_y apparaissent, comme le souligne BORGHI [6], dans de nombreux modèles de combustion turbulente, qu'il s'agisse des modèles à concept de flammelette, à transport de PDF ou à PDF présumée. Sa modélisation précise constitue un point délicat de la modélisation de la combustion turbulente.

Une hypothèse classique consiste à supposer que τ_Y est directement proportionnel à $\tau t = k/\varepsilon$, le temps caractéristique de l'échelle moyenne de la turbulence.

BEGUIER, DEKEYSER et LAUNDER [7] ont fait une étude bibliographique des expériences permettant d'estimer le rapport $R = \tau y/\tau t$ et ont conclu que R était compris entre 1,04 et 1,22.

C'est cette hypothèse que nous avons faite en prenant

$\tau ex = 0.25k/\varepsilon$

Les termes sources que nous souhaitons calculer sont ensuite simplement définis dans une maille I,J,K donnée, comme la moyenne statistique pondérée par le temps de séjour dans la maille, des contributions de chaque particule la traversant :

$$\tilde{\omega}'_{I,J,K} = \frac{\sum_{l=1}^{N}\sum_{m=1}^{P^l} \omega^l_{l,m}\cdot\Delta t_{l,m}}{\sum_{l=1}^{N}\sum_{m=1}^{P^l}\Delta t_{l,m}}$$

où N est le nombre de particules ayant traversé la maille I,J,K et P^l est le nombre de pas de temps mis par la particule l pour traverser la maille I,J,K.

Les termes sources moyens ainsi calculés sont ensuite "injectés" dans les équations eulériennes au niveau de chaque maille, puis de nouvelles particules sont lancées, de nouveaux taux moyens calculés, et ainsi de suite jusqu'à convergence du calcul.

La procédure employée est résumée sur la figure 1.

Le premier champ eulérien doit être calculé à l'aide d'un modèle de combustion turbulente simple (Eddy Break Up [8], CRAMER [9]) afin d'initialiser la procédure itérative.

PRISE EN COMPTE DE LA CINETIQUE CHIMIQUE

La prise en compte de cinétiques chimiques relativement complexes ne pose pas d'autre problème que celui du temps de calcul, puisque la vitesse de réaction intervient sous forme instantanée dans l'équation de bilan lagrangienne (les vitesses instantanées sont bien connues, seul le terme moyen prenant en compte l'influence de la turbulence nécessite une modélisation), l'influence de la turbulence sur la combustion étant prise en compte d'une part au niveau du temps caractéristique d'échange τ_{ex}, d'autre part, par la composante fluctuante stochastique de la vitesse des particules.

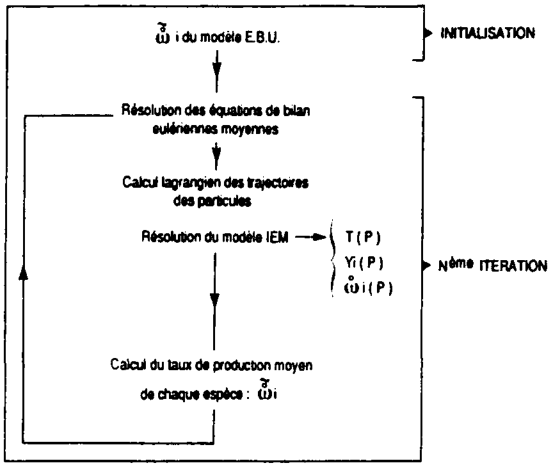
$\tilde{\omega}$ i du modèle E.B.U.
INITIALISATION
Résolution des équations de bilan eulériennes moyennes
Calcul lagrangien des trajectoires des particules
Résolution du modèle IEM
T (P)
Yi (P)
$\mathring{\omega}$ i (P)
Nème ITERATION
Calcul du taux de production moyen de chaque espèce : $\tilde{\omega}$i

Figure 1

Formation du monoxyde d'azote NO

Le NO produit dans les chambres de combustion provient soit de l'azote de l'air, soit de l'azote présent dans les combustibles impurs.

Nous allons ici nous intéresser aux deux principaux mécanismes de formation du NO à partir du N_2 de l'air :

- le mécanisme du NO thermique.
- le mécanisme du Prompt NO.

Mécanisme du NO thermique

Il consiste en une oxydation lente de N_2 par les radicaux O et OH présents dans les gaz brûlés. ZELDOVICH [10] propose le schéma cinétique suivant :

$O + N_2 \rightleftharpoons NO + N$
$N + O_2 \rightleftharpoons NO + O$
et ($N + OH \rightleftharpoons NO + H$)

La troisième réaction ne joue un rôle significatif que pour les richesses proches de 1.

Les radicaux O sont donnés en supposant la réaction $O_2 \rightleftharpoons 2O$ à l'équilibre.

Ce mécanisme ne joue un rôle important que si les radicaux O sont présents en quantité suffisante dans les gaz brûlés, c'est-à-dire si la température est élevée (T > 1800 K) et si les produits brûlés contiennent de l'oxygène, donc si le mélange est pauvre, ou très peu riche (OH joue alors un rôle). En pratique, au delà de richesse 1,10, le mécanisme du NO thermique n'intervient plus.

Dans ces conditions, le mécanisme du NO thermique joue un rôle prépondérant si, compte tenu de la lenteur de son mécanisme de formation, le temps de séjour des gaz brûlés dans la chambre est important.

L'importance respective des 2 mécanismes est mise en évidence sur la figure 2, présentant les mesures de FENIMORE [11] sur un brûleur à flamme plate :

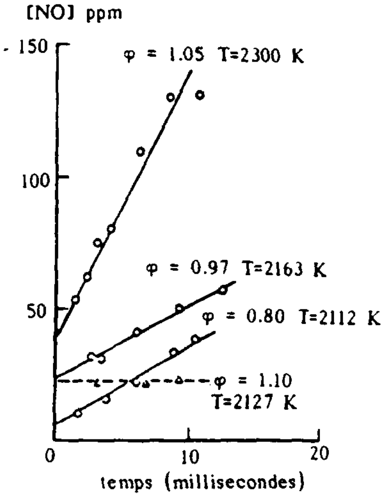

Figure 2

L'ordonnée à l'origine des courbes de mesure correspond au mécanisme du Prompt NO formé brusquement dans la flamme. Au delà, il s'agit du NO thermique.

La vitesse de formation du NO thermique croît sensiblement avec la richesse pour atteindre un maximum à richesse 1,05, puis décroît et s'annule finalement à richesse 1,10.

Mécanisme du PROMPT NO

Le NO formé rapidement dans la flamme peut être attribué à plusieurs mécanismes qui contribuent tous, dans des proportions variables, au niveau total de NO formé dans la flamme. DRAKE et BLINT [12], qui étudient la formation du NO dans les flammes laminaires prémélangées air-méthane à l'aide d'un schéma cinétique détaillé à 212 réactions, recensent 4 principaux mécanismes conduisant à la formation de NO dans le front de flamme :

1- Le mécanisme de ZELDOVICH associé à l'équilibre $O_2 \rightleftharpoons 2O$ qui conduit principalement à la formation du NO thermique dans les gaz brûlés.

2- Le mécanisme de ZELDOVICH associé (pour le calcul de O et OH) au "superéquilibre de O" qui consiste à supposer que les 4 réactions suivantes sont à l'équilibre :

$$\begin{aligned} H + O_2 &\rightleftharpoons OH + O \\ O + H_2 &\rightleftharpoons OH + H \\ H_2 + OH &\rightleftharpoons H_2O + H \\ CO + OH &\rightleftharpoons CO_2 + H \end{aligned}$$

3- Le mécanisme de FENIMORE [11] :

$$\begin{aligned} CH_2 + N_2 &\rightleftharpoons HCN + NH \\ CH + N_2 &\rightleftharpoons HCN + N \\ \text{puis} \quad HCN + O &\rightleftharpoons HCO + N \\ CN + O &\rightleftharpoons CO + N \\ N + O_2 &\rightleftharpoons NO + O \end{aligned}$$

4- Un mécanisme conduisant à NO à partir de N_2O, dont le rôle est mineur à basse pression (0,1----->1 atm) et dont l'importance croît si P augmente.

Nous retiendrons finalement que pour un régime de combustion pauvre, si le temps de séjour des gaz brûlés dans la chambre n'est pas trop court, le mécanisme du NO thermique contribue majoritairement à la quantité totale de NO formé. Par contre, au delà de la richesse 1,1, il ne joue plus aucun rôle et tout le NO produit l'est par le mécanisme du Prompt NO.

Compte tenu du régime de combustion pauvre des 2 configurations que nous avons étudiées dans cet article, nous nous sommes exclusivement intéressés au mécanisme du NO thermique. Toutefois, une extension au calcul partiel du Prompt NO avec le mécanisme de ZELDOVICH associé à l'hypothèse de superéquilibre peut être envisagée à court terme, alors que la prise en compte des mécanismes de FENIMORE ou du mécanisme n° 4 (N_2O), faisant tous deux intervenir des radicaux nécessitant une cinétique détaillée d'oxydation du combustible, n'est pas envisageable pour une raison évidente de temps de calcul.

Le mécanisme de ZELDOVICH de production du NO a été associé à plusieurs mécanismes simplifiés d'oxydation du méthane, afin de tester l'influence de différents paramètres.

On sait que le mécanisme de ZELDOVICH est essentiellement contrôlé par sa première réaction, dont la vitesse dépend beaucoup de la concentration de radicaux O, or cette dernière dépend elle-même fortement de la température. On peut donc s'attendre à ce que le mécanisme de ZELDOVICH soit sensible à celle-ci. Sachant que la température est contrôlée par le mécanisme d'oxydation du combustible, et en particulier par la prise en compte d'équilibres tels que $CO \rightleftharpoons CO_2$, $H_2 \rightleftharpoons H_2O$, il est intéressant de comparer différents mécanismes prenant en compte ou non ces différents équilibres.

Mécanismes d'oxydation du combustible

1- Schéma à 1 étape :

$$CH_4 + 2O_2 \longrightarrow CO_2 + 2H_2O$$

proposé par CATHONNET et al [13], WESTBROOK et DRYER [14], ne prenant en compte ni l'équilibre entre CO et CO_2, ni l'équilibre entre H_2 et H_2O.

2- Schéma à 2 étapes :

$$\begin{aligned} CH_4 + 3/2\ O_2 &\longrightarrow CO + 2H_2O \\ CO + 1/2\ O_2 &\rightleftharpoons CO_2 \end{aligned}$$

proposé par WESTBROOK et DRYER [14] et prenant en compte l'équilibre entre CO et CO_2.

3- Schéma à 4 étapes :

$$\begin{aligned} CH_4 + 2H + H_2O &\rightleftharpoons CO + 4\ H_2 \\ CO + H_2O &\rightleftharpoons CO_2 + H_2 \\ H + H + M &\rightleftharpoons H_2 + M \\ O_2 + 3\ H_2 &\rightleftharpoons 2\ H_2O + 2H \end{aligned}$$

proposé par PETERS [15] et prenant en compte les équilibres entre CO et CO_2, et entre H_2 et H_2O, ainsi que les radicaux H.

En raison de la prise en compte des radicaux H dont les temps caractéristiques de formation sont très courts, ce schéma nécessite un nombre d'itérations beaucoup plus important que les deux précédents (de 50 à 100 fois plus), ce qui s'avère pénalisant au niveau du temps de calcul.

Intégration des équations lagrangiennes

Rappelons que les équations lagrangiennes que nous devons intégrer sont de la forme :

Pour les espèces : $\frac{dY_I}{dt} = \frac{\overline{Y}_I - Y_I}{\tau_\alpha} + \omega_I$

$$I \in \{ CH_4, O_2, CO_2, CO, H_2, H, NO \}$$

En fait 3 des n espèces sont calculées à partir des bilans d'atomes C, H et O.

Pour l'enthalpie totale : $h_t = \sum_{I=1}^{N} Y_I \left(\int_{t^0}^{t} cp.\,dt + Q_I^0 \right)$

$$\frac{dh_t}{dt} = \frac{\overline{h}_t - h_t}{\tau_{ex}}$$

Les équations lagrangiennes pour les espèces s'avèrent particulièrement délicates à intégrer en raison du comportement très raide des termes sources ω_I . Une technique d'intégration implicite s'impose. Cependant, la technique classique qui consiste à linéariser les

termes sources $\omega_I^{N+1} = \omega_I^N + \sum_{J=1}^{N} \frac{\partial \omega_I}{\partial Y_J}\left(Y_J^{N+1} - Y_J^N\right)$

s'est avérée incapable d'empêcher l'annulation de la fraction massique des espèces qui tendent vers 0 (comme CH_4 ou O_2) et les instabilités numériques qui en découlent.

La technique d'intégration implicite utilisée a été choisie afin d'éviter cet inconvénient majeur. Son principe consiste à rendre implicites uniquement les termes consommant l'espèce i :

On décompose ω_I en ω_I^+ : production
et ω_I^- : consommation

puis on écrit : $\omega_I^{N+1} = \omega_I^{+N} + \omega_I^{-N} . \frac{Y_I^{N+1}}{Y_I^N}$

On obtient finalement :

$$Y_I^{N+1} = \frac{\frac{Y_I^N}{\Delta t} + \frac{\overline{Y}_I}{\tau} + \omega_I^{+N}}{\frac{1}{\Delta t} + \frac{1}{\tau} - \frac{\omega_I^{+N}}{Y_I^N}}$$

qui assure que Y_i^{N+1} demeure positif et différent de O.

Comparaison des schémas cinétiques à l'équilibre chimique

Les 3 schémas cinétiques d'oxydation du méthane présentés plus haut ont été implantés dans les équations lagrangiennes décrites au paragraphe précédent et intégrés pendant un temps suffisamment grand pour que l'équilibre chimique soit atteint. Les compositions chimiques obtenues et les températures associées sont présentées dans le tableau 1. Ils sont comparés aux résultats obtenus avec un code de calcul spécifique des équilibres chimiques prenant en compte plusieurs centaines d'espèces. Ces résultats nous donnent une indication sur la précision du calcul du NO formé que l'on va obtenir, puisque ce dernier se crée lorsque les réactions chimiques d'oxydation du combustible sont à l'équilibre.

On constate que le schéma à 1 étape provoque une surestimation de T de l'ordre de 40 K à richesse 0,8 et de près de 180 K à richesse 1, faute de prise en compte de CO et dans une moindre mesure de H_2 et H.

La prédiction de T est bien meilleure avec les schémas à 2 et 4 étapes à richesse 0,8 (moins de 10 K),

Tableau 1 : Comparaison des compositions chimiques obtenues à l'équilibre avec les 3 cinétiques globales d'oxydation du méthane à 1, 2 et 4 étapes, ainsi qu'avec un logiciel spécifique de calcul d'équilibres.

RICHESSE : 0,8

	CH_4	O_2 x 100	O x 10 000	CO_2 x 100	H_2O x 100	CO x 1 000	H	H_2	T
1 étape	10^{-8}	4,49	3,7	12,1	9,91				2 235
2 étapes	10^{-24}	4,74	3,13	11,4	9,91	4,45			2 204
4 étapes	10^{-7}	4,70	3,01	11,5	9,76	3,89	$2.18.10^{-5}$	$1,59.10^{-4}$	2 200
Calcul à l'équilibre	0	4,19	2,8	11,9	9,83	2,24	$5,8.10^{-5}$	$6,3.10^{-5}$	2 193

RICHESSE : 1,0

	CH^4	O_2	O x 10000	CO_2 x 100	H_2O x 100	CO x 1 000	H	H_2	T
1 étape	10^{-5}	$5,64.10^{-3}$	0,386	15,3	12,3				2 544
2 étapes	10^{-20}	$5,17.10^{-3}$	4,71	13,6	12,3	9,05			2 485
4 étapes	2.10^{-4}	$1,05.10^{-2}$	4,1	13,1	11,9	12,04	$3,45.10^{-5}$	$4,23.10^{-4}$	2 433
Calcul à l'équilibre	0	$9,03.10^{-3}$	3,72	12,6	11,8	15,89	$3,92.10^{-5}$	$4,54.10^{-4}$	2 368

mais se dégrade à richesse 1 : respectivement 110 K d'erreur et 80 K d'erreur.

On voit donc que les schémas à 2 et 4 étapes sont appropriés au calcul du NO thermique, sachant par ailleurs que le premier présente une bien plus grande simplicité d'intégration.

CALCUL D'UNE FLAMME PREMELANGEE AIR-METHANE STABILISEE PAR FLAMME PILOTE

Le modèle est testé dans le cas d'une flamme bidimensionnelle prémélangée turbulente à grande vitesse, stabilisée par une flamme pilote. Le dispositif expérimental est représenté sur la figure 3. Il a été développé par MOREAU [16] à l'ONERA en 1977. Sa section est carrée de 100 mm sur 100 mm. La flamme pilote est obtenue par la combustion d'un prémélange stoechiométrique air-méthane. La vitesse et la température sont respectivement 55 m/s et 600 K pour les gaz frais et 110 m/s et 2200 K dans les gaz brûlés. L'intensité de turbulence est environ de 10 % et peut être modifiée en introduisant différents types de grilles dans le courant amont.

Les calculs ont été effectués à richesse 0,8 pour laquelle la majorité des résultats expérimentaux sont fournis.

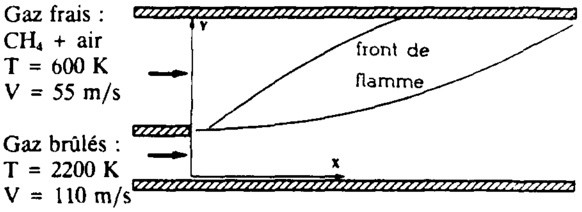

Figure 3

Les vitesses calculées sont comparées aux profils expérimentaux obtenus par vélocimétrie Doppler Laser par MOREAU et al [18]. Les profils de CH_4, CO, NO sont obtenus par prélèvement par sonde et chromatographie pour les deux premiers et chimiluminescence pour le dernier (Moreau [16]). Les profils de température sont obtenus par Diffusion Raman Anti-Stokes Cohérente (DRASC) [17].

On compare figure 4, les profils de vitesse moyenne calculés par le code DIAMANT et les mesures de MOREAU [18]. On constate un relativement bon accord entre simulation et expérience. L'erreur la plus importante est d'environ 10 m/s pour x = 122 mm.

Figures 5, 6 et 7 on compare des résultats lagrangiens moyens (calcul similaire au calcul du taux de réaction moyen $\widetilde{\omega}_l$) aux valeurs mesurées, respectivement pour la température, le rapport de la concentration de CH_4 sur celle de N_2 et le rapport de la concentration de CO sur celle de N_2.

En ce qui concerne la température, on constate que la valeur maximale calculée est environ supérieure de 150 K à la valeur mesurée. Une bonne partie de cet écart doit être due, d'une part aux pertes au niveau des parois non adiabatiques du montage expérimental, d'autre part aux pertes par rayonnement. Ni l'un ni l'autre de ces phénomènes n'ont été pris en compte dans la simulation numérique.

Les profils de méthane (figure 6) calculés et mesurés sont très proches. Par contre, on constate figure 7, que les profils moyens de CO calculés ne sont que qualitativement représentatifs des profils mesurés. Ce calcul relativement grossier de CO suffit cependant à donner une meilleure indication de la température, ce qui est favorable au calcul des oxydes d'azote.

Figure 8, on compare le niveau de NO thermique calculé au niveau total mesuré par MOREAU [16]. On constate que le NO thermique calculé est bien formé en aval de la zone moyenne de réaction où la température est élevée et les molécules de O_2 fortement dissociées en radicaux O.

Le niveau maximal de NO calculé est de l'ordre de 65 parties par million (ppm), alors que les mesures donnent 50 ppm. On constate un relativement bon accord tant qualitatif que quantitatif entre mesures et calculs.

CALCULS DANS UNE CHAMBRE AERONAUTIQUE ANNULAIRE

La seconde chambre de combustion étudiée est une partie d'une chambre annulaire. Une section de cette chambre est représentée sur la figure 9. Le maillage comporte 58 x 22 x 29 mailles respectivement dans les directions I, J et K.

Nous avons considéré une injection air-méthane et non air-kérosène comme dans la réalité, essentiellement en raison de la plus large gamme et de la meilleure connnaissance de cinétiques pour le méthane. Ce prémélange air-méthane riche (φ = 1,93) à 770 K et 15 bar entre par un injecteur tourbillonnaire dans le "bol" représenté sur la figure 9 à environ 140 m/s. A l'entrée de la chambre proprement dite, la vitesse est de l'ordre de 40 m/s.

De l'air à 770 K et 15 bar est injecté sous forme de 9 films parallèlement aux parois, afin de refroidir ces dernières. Ces films sont représentés F1 à F9 sur la figure 9.

Enfin, une série de trous primaires et de trous de dilution permettent l'injection d'air à 770 K et 15 bar. L'air de dilution est destiné à refroidir les gaz brûlés afin de permettre l'arrivée à basse température (1400,1600 K) sur les aubes de turbine en aval de la chambre et à réduire l'émission des oxydes d'azote.

La simulation numérique a été réalisée avec le code DIAMANT associé au modèle de combustion turbulente CRAMER [9] pour le calcul du champ de vitesse, de concentration et de température initial. 30 000 particules fluides ont été injectées dans les diverses entrées de la chambre, ce qui a permis le calcul du taux de réaction lagrangien moyen, ainsi que celui du champ moyen de NO.

Le champ de vitesse calculé est représenté figure 10 suivant les plans I =6 et J = 12. On observe nettement dans le plan I = 6 le mouvement du fluide dû à l'injecteur tourbillonnaire. Dans le plan J = 12, on constate la formation de zones de recirculations en fond de chambre, ainsi que l'injection par les trous primaires supérieurs et inférieurs.

On compare figure 11 le taux de réaction moyen $\widetilde{w_i}$ obtenu avec le modèle CRAMER et avec le modèle PEUL. Le modèle CRAMER est un modèle de combustion turbulente qui, au meme titre que le modèle Eddy Break Up fait l'hypothèse que la chimie est très rapide et que la réaction est contrôlée par le mélange, donc par la turbulence. Ceci se traduit par le fait que la combustion commence immédiatement à l'injection dans le bol avec le modèle CRAMER alors qu'avec le modèle PEUL, on constate que la réaction démarre un peu plus loin, à la sortie du bol, respectant ainsi un certain délai d'allumage caractéristique de la réaction chimique considérée.

Les deux modèles représentent par ailleurs correctement une zone de combustion secondaire ou le combustible imbrûlé dans le bol réagit avec l'air injecté par les trous de dilution.

La figure 12 présente le champ de température moyen obtenu avec le modèle PEUL. La température maximale (2220 K) est obtenue dans les gaz brûlés issus de la combustion principale riche. La combustion secondaire du méthane imbrûlé et de l'air de dilution provoque aussi un dégagement de chaleur, sans augmentation de température compte tenu du débit important d'air "froid" (770K) injecté. La température moyenne de sortie des gaz est de 1470 K.

On présente figure 13, le champ moyen de NO obtenu. On sait que le NO thermique se forme dans les régions à haute température (au dessu de 1800 K) riches en oxygène O_2, afin que la dissociation $O_2 \rightleftharpoons 2O$ crée suffisamment de radicaux O pour déclancher le mécanisme de ZELDOVICH. Il se crée ici un maximum de 30 ppm de NO thermique, la moyenne dans la section de sortie se situant à 6 ppm.

Compte tenu du régime de fonctionnement de la chambre (combustion primaire riche, pression élevée de 15 bar), il est fort probable qu'une quantité de NO bien plus importante se forme par le mécanisme du prompt NO et par celui passant par N_2O, qui n'ont pas été pris en compte dans cette étude.

CONCLUSION.

Plusieurs mécanismes globaux d'oxydation du méthane ainsi que le mécanisme de formation du NO thermique ont été couplés au modèle de combustion turbulente PEUL associé au code DIAMANT. Les résultats obtenus dans le cas de la chambre double flux montrent que le niveau de NO calculé est proche du niveau mesuré, pourvu que l'on adopte un mécanisme d'oxydation du combustible permettant une bonne estimation de la température , donc prenant au moins en compte l'équilibre entre CO et CO_2.

On sait par contre que dans le cas de la chambre aéronautique, le régime de combustion riche à haute pression fait que le mécanisme du NO thermique est minoritaire par rapport au mécanisme du PROMPT NO et à celui passant par N_2O, si bien que notre niveau calculé est très certainement inférieur au niveau réel.

On constate par ailleurs sur la forme des taux de réactions obtenus dans la chambre aéronautique, l'intéret que présente le modèle PEUL de ne pas faire d'hypothèses particulières sur le rapport des temps caractéristiques de la chimie et de la turbulence.

- Le code DIAMANT dont les résultats ont été présentés dans cet article a été développé dans le cadre de l'opération A3C [19].

- Nous remercions la Direction de la Recherche de RENAULT d'avoir participé au financement de cette étude.

BIBLIOGRAPHIE

[1] **LAUNDER BE**

Turbulence - Ed P. BRADSHAW
Topics in applied physics, Springer Verlog - 1976

[2] **PIT F., TICHTINSKY H., DUPOIRIEUX F.**

Calculs tridimensionnels d'écoulements réactifs dans les foyers de moteur d'avion.
3rd International Seminar on flame structure
ALMA- ATA - USSR - 1989

[3] **ORMANCEY A.**

Simulation du comportement des particules dans des écoulements turbulents.
Thèse de troisième cycle - 1984

[4] **AUBRY - VILLERMAUX**

J. Chem. Eng. Sci. - vol 30, p 457 - 1975

[5] **Ph. CAILLAU**

Développement et mise en oeuvre du modèle de combustion turbulente PEUL pour le calcul des écoulements réactifs dans les chambres de combustion de turbines à gaz.
Rapport technique ONERA - 1992

[6] **BORGHI R.**

Turbulent premixed combustion : further discussion on the scales of fluctuations.
Comb. and Flame - pp 304,312 - 1990

[7] **BEGUIER, DEKEYSER, LAUDER**

Ratio of scalar and velocity dissipation times scales in shear flow turbulence.
Phys. Fluids - 21(3) - 1978

[8] **SPALDING D.B.**

Mixing and chemical reaction in steady confined turbulent flames.
13th Symp. on Comb. - 1971

[9] **DUPOIRIEUX F.**

Calcul numérique d'écoulement avec réactions chimiques et comparaisons expérimentales.
Workshop on the gaz flame structure, Novosibirsk - 1986

[10] **ZELDOVICH, SADOVNIKOV, KAMENETSKII**

Oxydation of nitrogen in combustion
Academy of Science of the USSR, Moscow - 1947

[11] **FENIMORE C.P.**

Formation of nitric oxide in premixed hydrocarbon flames.
13th Symp. on Comb. - 1971

[12] **DRAKE, BLINT**

Calculations of NOX formation pathways in propagating laminar high pressure premixed CH_4/Air flames.
Comb. Sci. and Tech. 1991, vol 75, pp 261-285

[13] **CATHONNET, BOETTNER, GAILLARD**

Etude cinétique des réactions en combustion.
Rapport interne CNRS

[14] **WESTBROOK, DRYER**

Simplified reaction mechanisms for the oxidation of hydrocarbon fuels in flames.
Comb. Sci. and Tech. - vol 27, pp 31-43 - 1981

[15] **PETERS N, PACZKO G, LEFDAL PM**

Reduced reaction schemes for methane, methanol and propane flames.
21th Symp. on Comb. - 1986

[16] **MOREAU P**

Turbulent flame development in a high velocity premixed flow.
Communication AIAA - Los Angeles - 1977

[17] **MAGRE Ph., MOREAU P., COLLIN G., PEALAT M.**

Application de la méthode DRASC à la mesure de la température dans une flamme turbulente.
PEP AGARD on Advanced Intrumentation for Propulsion Components - 1986

[18] **MOREAU P., BOUTIER A.**

Laser Velocimetry measurements in a turbulent flame
16th Symp. on Comb. - 1976

[19] **DUPOIRIEUX F., HIRSINGER F.**

Modélisation des chambres de combustion.
Opération A3C - 3rd European Propulsion Forum, COLOGNE - 1990

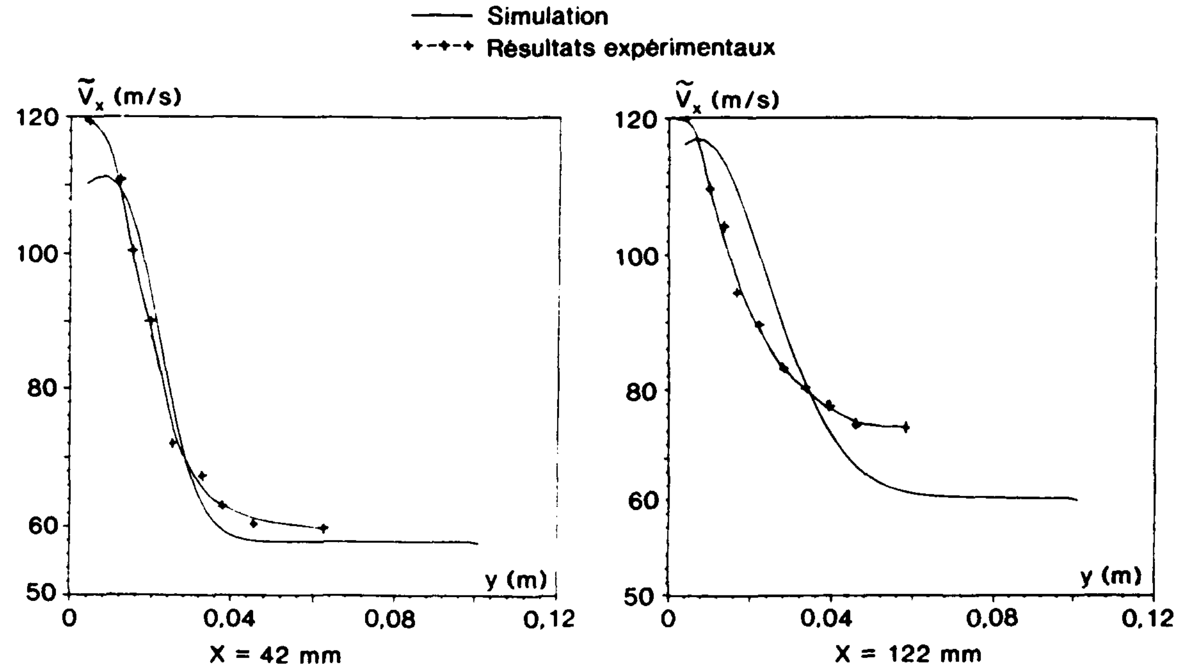

Figure 4 : Comparaison entre les profils de vitesse calculés et expérimentaux obtenus par Anémométrie Laser Doppler [17]

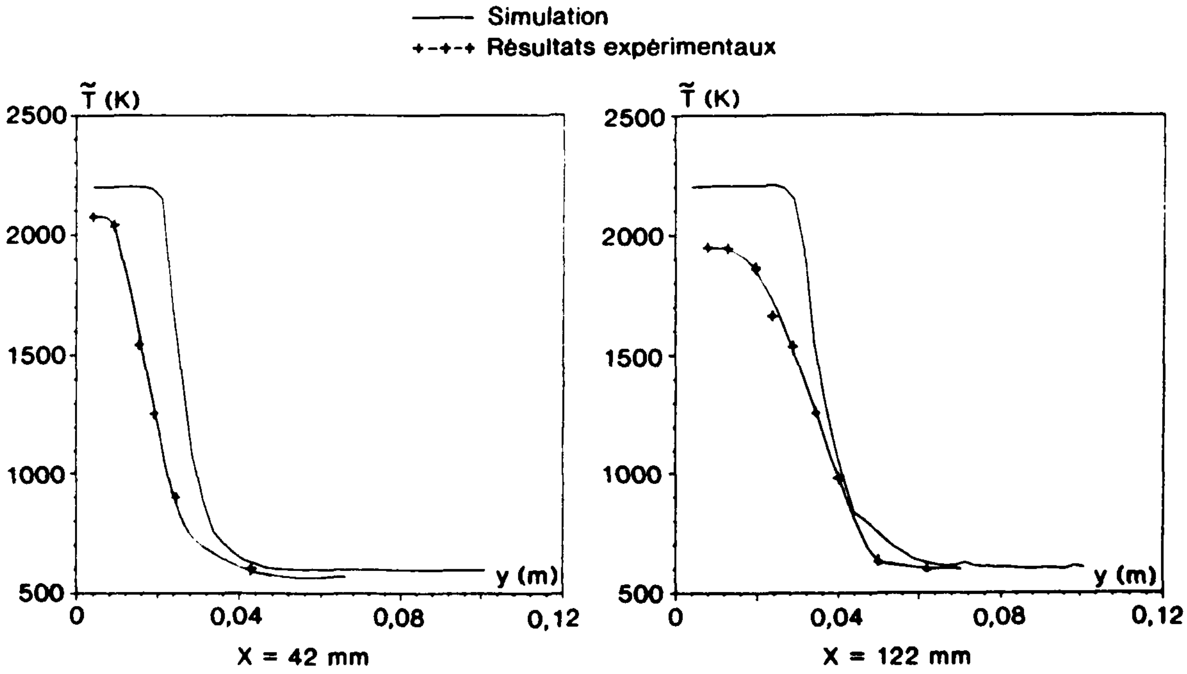

Figure 5 : Comparaison entre les profils de température calculés et mesurés par DRASC (MAGRE [17])

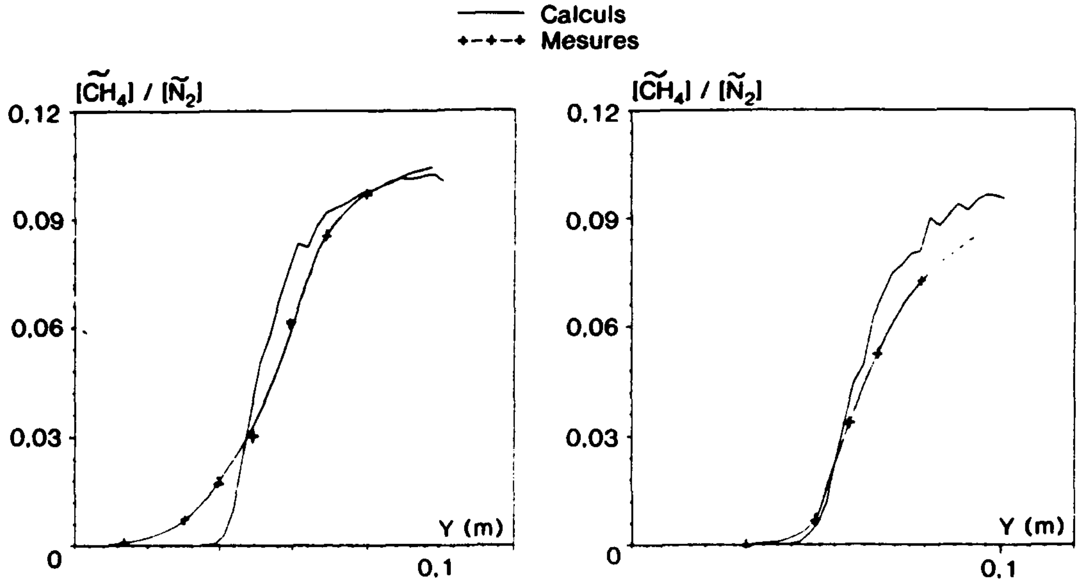

X = 322 mm

X = 522 mm

Figure 6 : Comparaison entre les profils de CH_4 calculés et mesurés

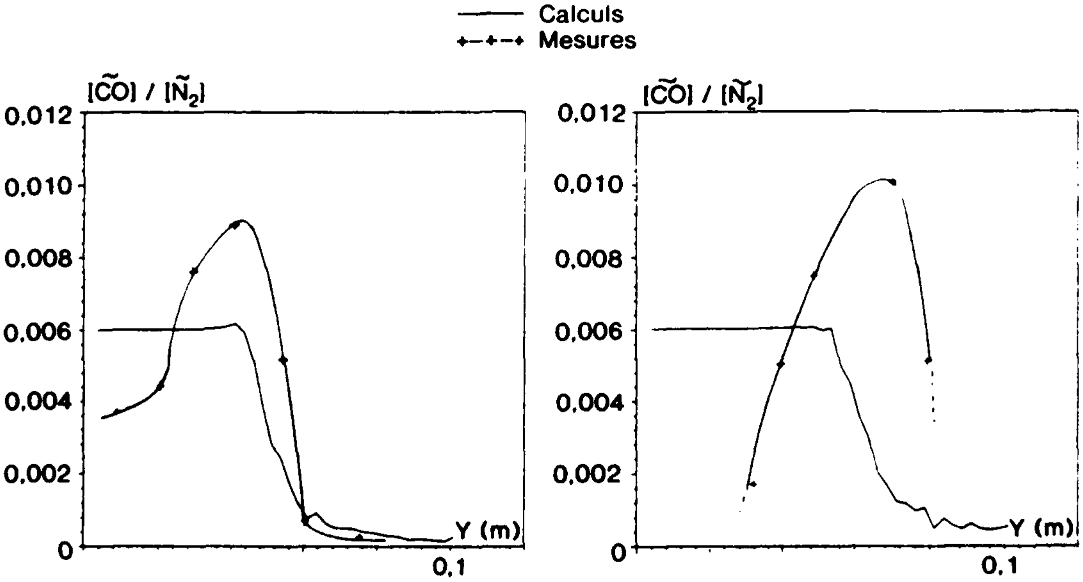

X = 322 mm

X = 522 mm

Figure 7 : Comparaison entre les profils de CO calculés et mesurés

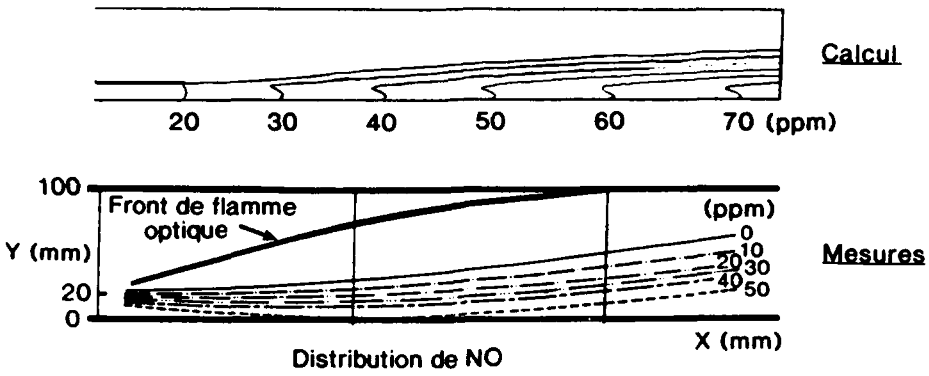

Figure 8 : Comparaison entre les isolignes de NO calculées et mesurées (MOREAU [16])

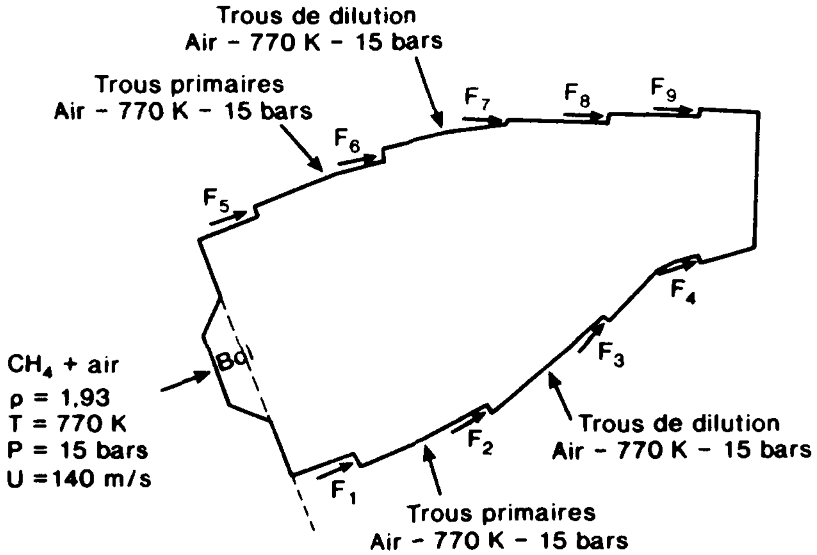
Trous de dilution
Air - 770 K - 15 bars
Trous primaires
Air - 770 K - 15 bars
F_7
F_8
F_9
F_6
F_5
F_4
F_3
F_2
F_1
Bd
CH$_4$ + air
ρ = 1,93
T = 770 K
P = 15 bars
U =140 m/s
Trous de dilution
Air - 770 K - 15 bars
Trous primaires
Air - 770 K - 15 bars

Figure 9 : Section de la chambre aéronautique - Représentation des différentes injections et conditions d'entrée

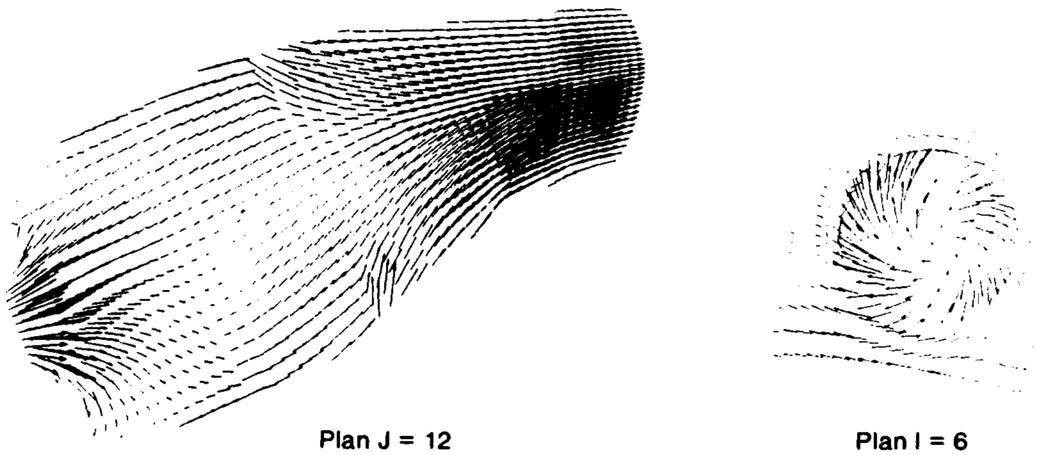

Plan J = 12

Plan I = 6

Figure 10 : Vecteurs vitesse calculés par simulation numérique avec DIAMANT

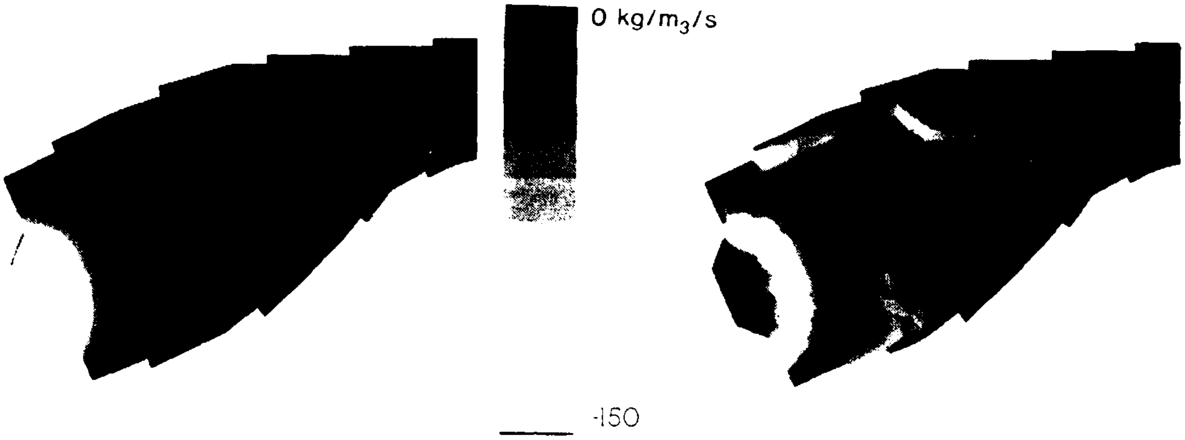

Modele CRAMER

Modèle PEUL

Figure 11 : Taux de réaction moyen $\widetilde{\omega}_{CH_4}$

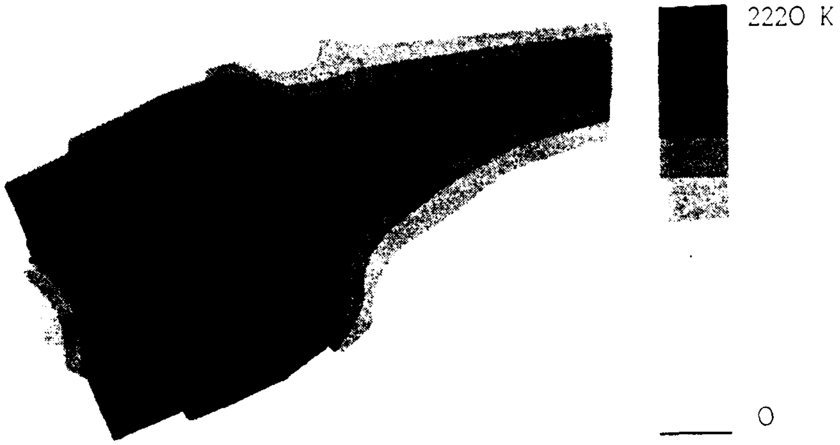

Figure 12 : Température eulérienne moyenne dans la chambre.

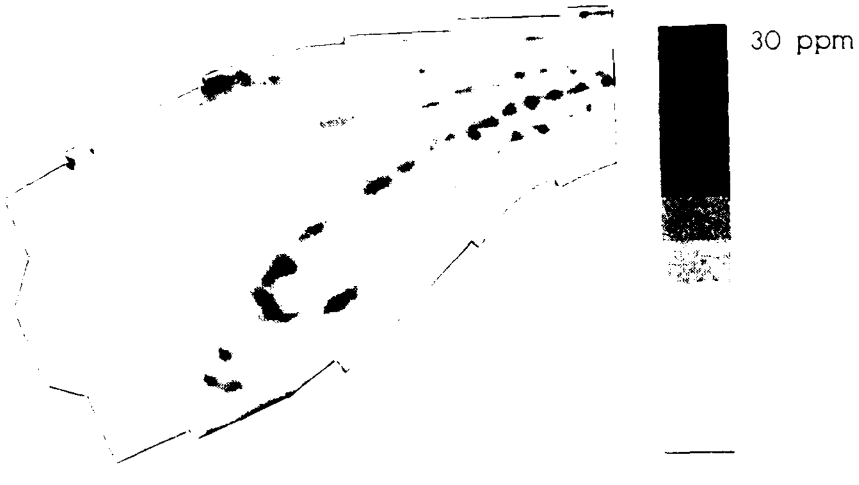

Figure 13 : Niveau de NO thermique moyen formé en parties par million

Discussion

QUESTION 1:

DISCUSSOR: N. Selçuk, Middle Eastern Technical University

I have not seen any temperature profiles for the two problems you have calculated. NO_x formation is strongly dependent on temperature and the temperature distribution is strongly affected by thermal radiation at the high temperatures that you are considering. Don't you think your NO_x estimation would be better if you incorporated thermal radiation with your predictions?

AUTHOR'S REPLY:

In parallel to the work presented here we have made some calculation of radiative transfer within the combustor and we have checked that the divergence of the radiative flux is negligible compared to heat release of the reaction. Therefore the temperature field should not be significantly influenced by the radiative transfer especially in the reaction zone where the prompt NO is supposed to be produced. These calculations did not take soot into account. The soot level is considered to be very low.

AERO-THERMAL DESIGN OF A COOLED TRANSONIC NGV AND COMPARISON WITH EXPERIMENTAL RESULTS

S.Colantuoni, A. Colella, L. Di Nola, D. Carbone, D. Marotta
ALFA ROMEO AVIO Societa' Aeromotoristica per Azioni
Research & Development
80038 Pomigliano d'Arco (NAPOLI) - ITALY

SUMMARY

The aerothermal design process applied to a Nozzle Guide Vane of a gas-generator axial-flow turbine for a compact advanced technology core engine is described.

The principal characteristics of the NGV are:

Overall Tip Radius, mm	108.8
Blade height , mm	19.7
Blade aspect ratio	0.53
Solidity	1.37
Mean Exit isentropic Mach Number,	0.95
Inlet Temperature, K	1450

The NGV is cooled by a combination of different solutions, like impingement cooling and film-cooling on the front side, and forced convection on the rear side, followed by a cooling ejection at pressure side near the trailing edge.

Representative results of the computational fluid-dynamics and of the thermal analysis of the NGV blade, together with some experimental data obtained from component test rig and engine demonstrator are presented and discussed.

LIST OF SYMBOLS

C	blade chord
Cp	specific heat at constant pressure for air
D	internal leading edge diameter
d	coolant hole diameter
FEM	Finite Element Method
F/C	film cooling
g	pitch
H	blade height
h	convective heat transfer coeff. q/(To-Tw)
HTC	heat transfer coefficient
k	thermal conductivity
L	coolant duct length
l	flat plate length
LE	leading edge
M	Mach number
m	local blowing rate $\rho cUc/\rho\infty U\infty$
NGV	Nozzle Guide Vane
Nu	Nusselt number
o	throat
OTDF	overall temperature distribution factor
P	pressure
Pr	Prandtl number $\mu Cp/k$
PS	pressure side
Re	Reynolds number $\rho U\infty C/\mu$
RTDF	Radial temperature distribution factor
CET	Combustor exit temperature
S	impingement holes spacing
s	curvilinear coordinate from stagnation point
SS	suction side
St	Stanton number
T	temperature
TE	trailing edge
TIT	turbine inlet temperature
Tu	freestream turbulence
U	velocity
W	mass flow rate
x	coordinate along axial chord
xc	coordinate along blade chord
y	coordinate in tangential direction
Z	impingement holes to cooled wall distance
α	film cooling hole axis angle
β	flow angle in blade-to-blade plane
ΔH	change in stagnation enthalpy
γ	specific heat ratio
ρ	density
ζ	Kinetic Loss Coefficient

Subscripts

c	coolant flow condition
O	total condition
1	upstream condition
2	downstream condition
ax	along the axial chord
∞	freestream flow condition
g	gas
o	without coolant injection
is	isentropic condition
r	recovery
w	condition at the wall

1 INTRODUCTION

A technological research program has been planned in 1987 at ARA-R&D to implement design methodology in the critical field of aerothermo-mechanics of HP turbine stages having high working temperature (1450 ÷ 1800 K). The future advanced technology is characterized by a compact geometry with severe design constraints and targets, like blade life goals and high aerodynamic performances achieved in the transonic range. Complex cooling system is required despite continuous improvements in materials properties. An increasing difficulty is due to cooling effectiveness that must be achieved with vanes of small dimension.

The first phase of this research project was to design and develop a gas generator turbine stage with the maximum possible inlet temperature without rotor blade cooling.

The cooled NGV aerodynamic design of a turbine working at high temperature required a system of computational tools in order to define the correct geometry of the blade. On the other hand an important task was the experimental validation of the design methodology, so that recently developed experimental techniques have been applied to verify the flow modeling and the computational approach used (see fig 1).

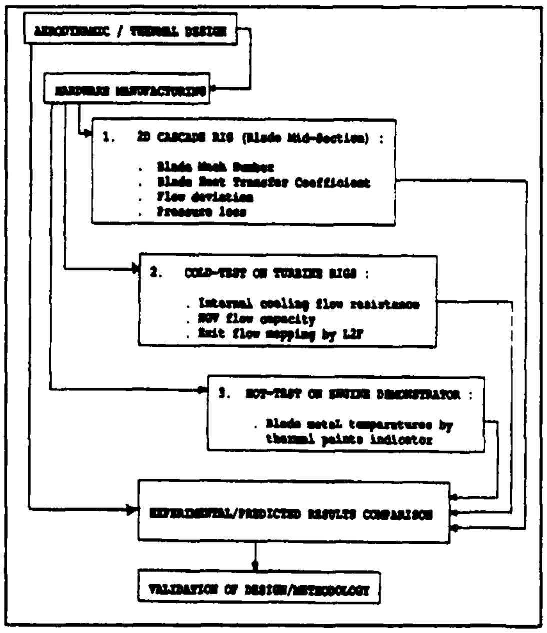
AERODYNAMIC / THERMAL DESIGN
HARDWARE MANUFACTURING
1. 2D CASCADE RIG (Blade Mid-Section) :
. Blade Mach Number
. Blade Heat Transfer Coefficient
. Flow deviation
. Pressure loss
2. COLD-TEST ON TURBINE RIGS :
. Internal cooling flow resistance
. NGV flow capacity
. Exit flow mapping by L2F
3. HOT-TEST ON ENGINE DEMONSTRATOR :
. Blade metal temperatures by thermal paints indicator
EXPERIMENTAL/PREDICTED RESULTS COMPARISON
VALIDATION OF DESIGN/METHODOLOGY

Fig 1 - Flow-chart of design validation

An experimental program on the different aspects of the aerothermal design has been planned.

Aerodynamic tests on blade mid section have been performed on solid vane at design point as well as off-design conditions in terms of Mach number, Reynolds number and inlet turbulence level.

On the other hand the performances of the film cooling have been measured at different blowing rates and temperature ratios. In order to provide the thermal design validation on the engine demonstrator, it was required to have a comprehensive knowledge of blade metal temperatures. The thermal indicator paints (TIP) method, that can provide pictorial evidence of peak temperatures and isothermal distributions on the NGV blades, has been chosen.

The design is described along with discussion of the results.

2 AERODYNAMIC DESIGN

2.1 Turbine design conditions

The project goal is to design a new single stage HP unshrouded turbine with uprating requirements of TIT (from actual 1250 to 1450 K) that fits in to existing engine hardware. Although the rotor blade can be uncooled (single crystal alloy) the NGV must be adequately cooled.

The turbine design conditions are based on driving a single stage centrifugal compressor at given speed :

inlet total pressure	681 Kpa
inlet total temperature	1450 K
inlet mass flow	2.82 kg/s
rotational speed	38100 RPM
power	825 kW

In order to meet target performances and life requirements, with geometrical and manufacturing constraints, including cost considerations, an iterative and interactive procedure has been adopted, to design the basic blade profiles. Then flow analysis has been performed on the final blade annular cascade by 3D Euler and Navier-Stokes solvers.

2.2 Mean line and through-flow analysis

The mean line design required a parametric study fixing some geometry parameters due to mechanical constrains (hub radius), varying tip radius and NGV TE angle, in order to optimize the performances.

Analysis study has been carried out to select blade velocity triangles. The through-flow calculation gives the following performances of turbine stage:

total-to-total pressure ratio	2.45
total efficiency	86.30 %
specific work , Δh	290.8 kJ/kg
flow factor , Ca/U	0.605
mean loading factor , $\Delta h/U^2$	1.865
work capacity , Δh/T	0.201 kJ/kgK

To get a better work distribution along the blade span the forced vortex design has been selected, imposing a constant meridional velocity gradient.
The flowpath of the turbine stage is presented in fig.2. The NGV exit Mach numbers are slightly supersonic (1.08 at the hub , 0.95 at the mid and 0.90 at the tip) and flow deviation is almost constant.

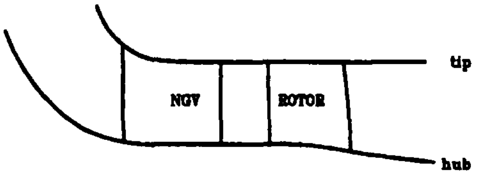
NGV
ROTOR
tip
hub

	Dhub	Dtip
NGV INLET	178.2	221.4
NGV EXIT	178.2	217.8
ROTOR INLET	177.1	217.8
ROTOR EXIT	171.8	217.8

Fig 2 - Meridional view of turbine flow-path

2.3 Detailed blade profile design

The blade profiles (hub, mid, tip) have been designed with an interactive code,based on an indirect method, a procedure is described in the flow-chart of fig 3.

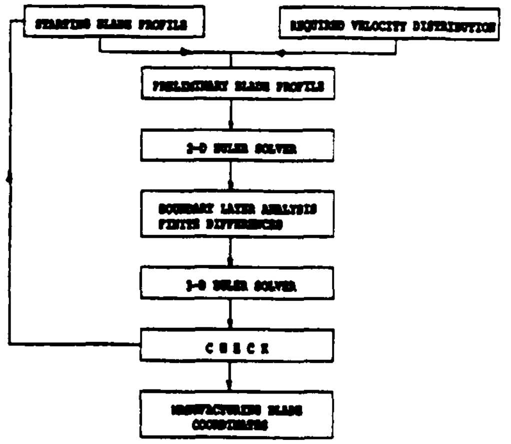
STARTING BLADE PROFILE
REQUIRED VELOCITY DISTRIBUTION
PRELIMINARY BLADE PROFILE
2-D EULER SOLVER
BOUNDARY LAYER ANALYSIS
FINITE DIFFERENCES
3-D EULER SOLVER
CHECK
MANUFACTURING BLADE
COORDINATES

Fig 3 - Flow-chart of design procedure

The blade coordinates are computed starting from a prescribed velocity distribution, that must satisfy aerodynamic requirement as well as mechanical and manufacturing constrains for cooled blade, than the flow have been analyzed by 2D Euler solver and the 2D boundary layer was also evaluated. In the final step 3D flow field analysis has been performed. For the aerodynamic design of the blade profiles, the following criteria has been used: an uniform loading distribution along the chord, with the maximum more near the TE, avoiding velocity peaks on the SS and reducing as far as possible the diffusion on the SS after the shock. The geometry of three blade sections have been defined (hub, mid and tip) (fig. 4). The mid section cascade (fig. 5) has the following geometrical characteristics:

radius	99.44 mm
pitch , g	27.29 mm
axial chord length , Cax	23.18 mm
chord length , C	37.15 mm
throat width , o	8.06 mm
pitch/chord ratio , g/o	0.73
TE thickness/throat, te/o	8.06 %
TE thickness, te	0.65 mm
TE thickness/chord , te/C	1.75 %
Stagger angle	50.03 deg
Gauging angle, arcos(o/g)	72.8 deg

The exit design flow conditions are :

exit flow angle, β_2	71.0 deg
isentropic exit Mach number,$M_{2,is}$	0.95
exit Reynolds number (chord), $Re_{2,is}$	$5.5x10^5$

The NGV blade number is 23 and the aspect ratio H/C=0.53 based on mean true chord.

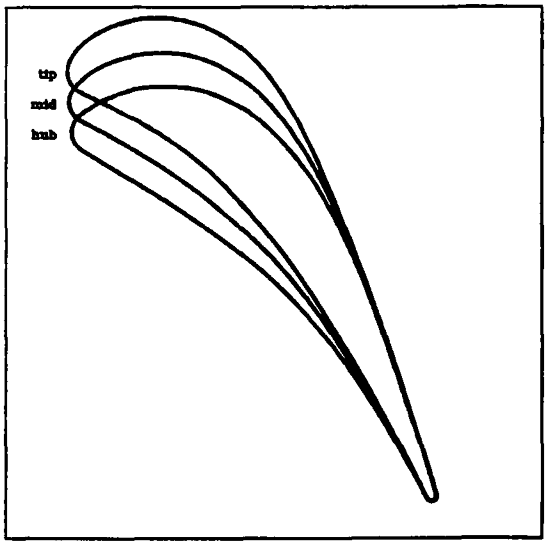

Fig 4 - NGV Blade sections

The cascade flowfields have been analyzed with a 2D time marching Euler code based on finite area approach [1].

The type H computational mesh size is 69x15. The convergence is checked on the evaluation of the exit flow angle. It is satisfactory to have maximum fluctuation less than 0.1 deg. The isentropic Mach number distribution vs the axial coordinate is showed in fig. 6. There is a gradual acceleration at SS up to max value of 1.1 at 72 % of the axial chord, followed by a weak oblique shock with ΔMach=0.05, than an oblique shock decelerate the flow to 0.98. Regular acceleration at PS is detected. The computed exit flow angle is 71.5.

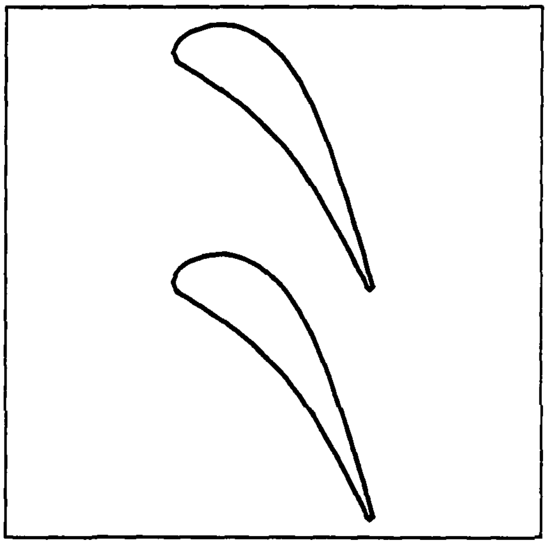

Fig 5 - Cascade geometry at mid blade height

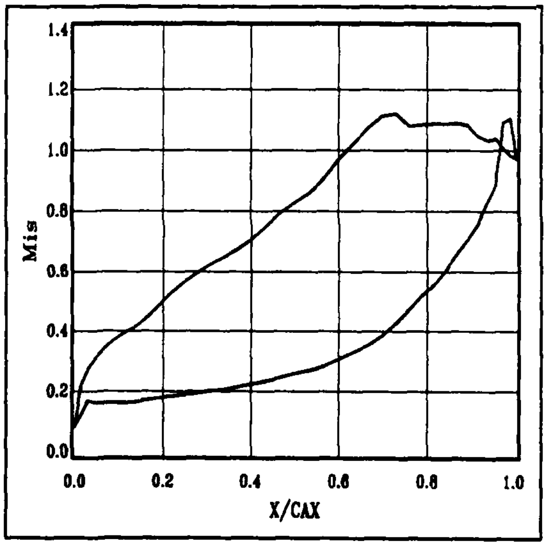

Fig 6 - Blade isentropic Mach Number (Euler 2D)

The blade-to-blade iso-Mach lines at the mid section is presented in fig. 7.

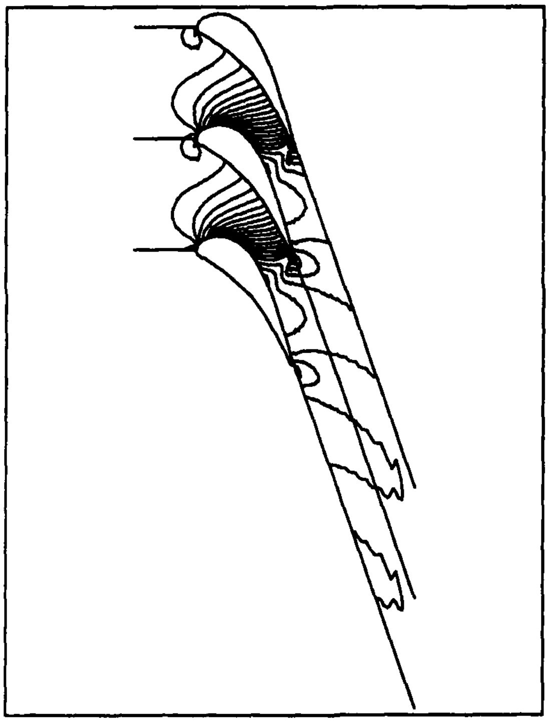

Fig 7 - 2D Euler analysis : iso-Mach lines at the mid section . $\Delta M=0.05$ Range=(0.05,1.2).

2.4 Euler 3D analysis

The final 3D geometry of the blade was obtained by stacking the blade sections such that the TE was straight (no tilt) and radial (no lean) in the meridional and axial views, respectively.

The analysis has been performed on the solid blade with a code based on time marching technique and finite volume discretization procedure [2]. The computational domain (H-mesh) used had a size of 71x21x21 with constant inlet boundary conditions. The pressure ratio at the hub exit was chosen to obtain a mid span outlet $M_{2,is} \sim 0.95$.

The $M_{2,is}$ distributions results relative to hub, mid and tip section are presented in fig. 8. There is at mid section more evident deceleration behind the shock with respect to the 2D calculation (fig. 6).

Let's note also that the maximum SS surface Mach number at the hub does not exceed 1.3.

The computed flow angle and Mach number at mid section are respectively equal to 70.9 and 0.95.

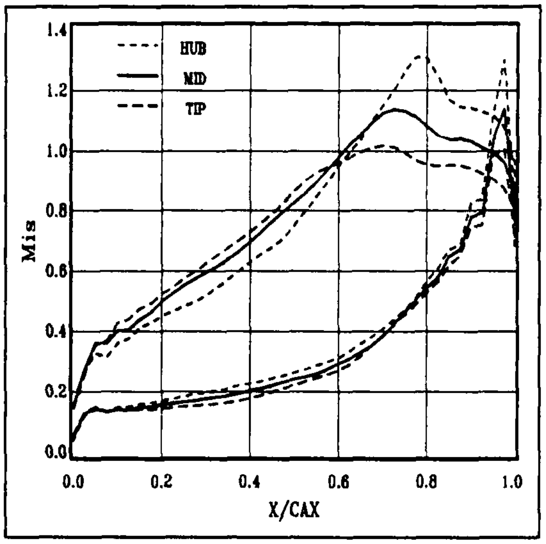

Fig 8 - Blade mach number distribution (Euler 3D)

In the fig.9 there are the 3D Euler analysis results in terms of average flow deviations and Isentropic Mach number distribution at the NGV exit along the blade span at about x/Cax=0.26 behind the TE.

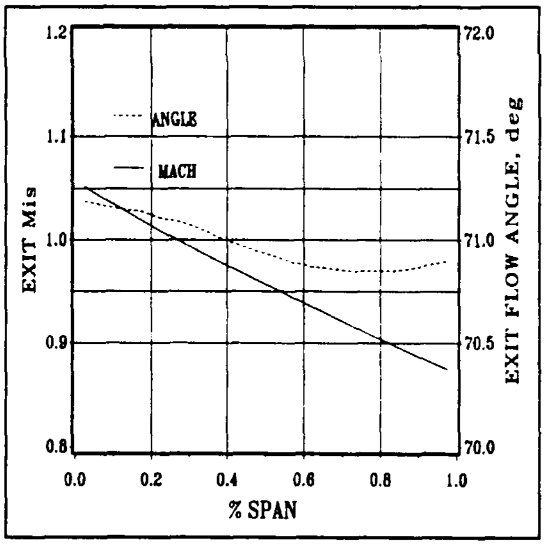

Fig 9 - Flow parameters at exit of blade (Euler 3D)

2.5 3D viscous analysis

At the time of the NGV aerodesign the viscous solver was not available, therefore this analysis has been done later, when the manufacturing process was in progress.

In the following some results of a steady state 3D viscous analysis are reported. The analysis solves the Navier-Stokes equations written in a Cartesian (x,y,z) coordinate system. The multistage Runge-Kutta scheme is used to advance the flow equations in time from an initial guess to a steady state. The turbulent viscosity is computed using an adaptation of the Baldwin-Lomax turbulence model to three-dimensional flows. The local time-stepping, residual smoothing and multigrid are used to accelerate convergence .

The three-dimensional grid was obtained by means of two-dimensional C-shaped grids (fig.10) interpolated linearly from hub to the tip of the blade.

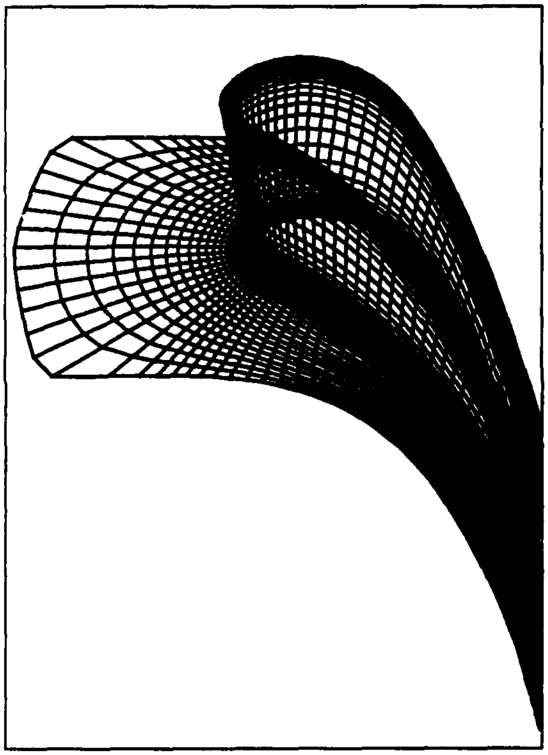

Fig 10 - Viscous analysis : computational mesh view

The calculation has been performed using 176 points around the blade, 32 blade-to-blade and 48 in radial direction . The initial grid spacing is about 0.03 % of the chord at the blade and 0.06 % of the blade height either at the hub and tip.

The analysis has been performed at the design conditions with the inlet total temperature distribution of the fig.11. A convergent solution with a total grid point of 270000 needs about 400 cycles of multigrid.

Computational results relative to blade-to-blade iso-Mach at mid section the fig. 12.

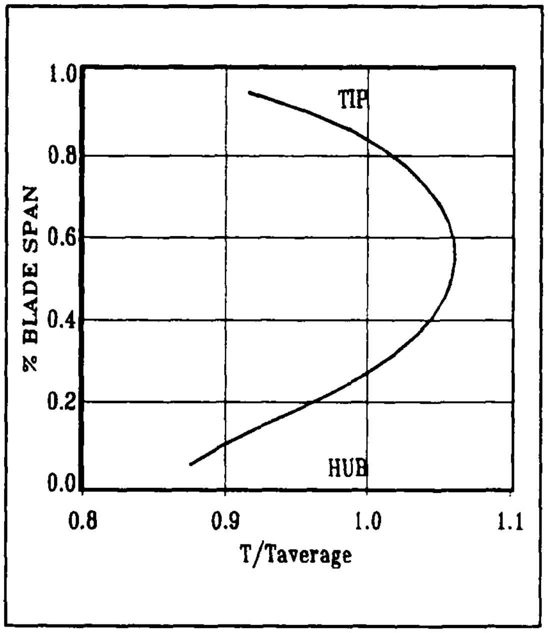

Fig 11 - 3D viscous analysis : inlet total temperature profile

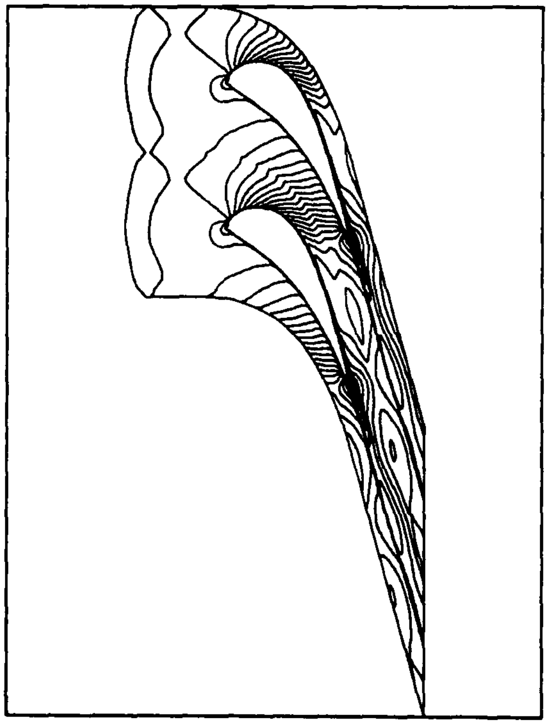

Fig 12 - 3D viscous analysis : isomach lines at the mid section. $\Delta M=0.05$; Range = (0.05,1.2)

3 THERMAL DESIGN

3.1 Design Requirements

Current materials cannot be exposed to temperatures above 1250 K without a dramatic decrease in life. Blades must be cooled if significantly higher turbine inlet temperature are desired. As the cooling scheme becomes more complex, a better understanding of the internal pressure and heat transfer coefficient distributions is necessary to be able to predict the hot section metal temperature accurately. In our case the freestream temperature is above this limit so the nozzle must be cooled.
The design target gas temperature distribution at the NGV inlet has a RTDF=0.10 and an OTDF=0.21, with an average TIT=1450 K. The average profile (fig. 11) has a peak temperature of 1549 K and a "worst" profile has a peak of 1645 K.

The design requirement of the cooling system is based on blade max metal temperature of 1050 °C with minimum cooling flow.

The cooling system definition for the NGV thermal design followed an integrated approach between the coolant flow path definition inside the blade, the evaluation of external and internal heat-transfer coefficients, the impact of the coolant flow on the aerodynamic performance of the blade row, and the 2D thermal analysis. As final result the metal temperatures distribution by a Finite Element Method (FEM) model has been estimated.

3.2 Internal coolant passage design

The design of the cooling passages is constrained by the following considerations:

- Stator blade internal heat transfer;
- Cooling flow pressure losses;
- Compatibility with fabrication methods.

The last one is the most restrictive of the three constraints and is so limiting that the design process, to a high degree, revolves around the limits placed on cooling passage geometry.
Fabrication constraints that limit the allowable core passage geometries are, generally, based on previous casting experience. These constraints are:

- minimum core cross-sectional area ;
- minimum length of unsupported core section (dependent on thickness of section);
- minimum core and wall metal thicknesses ;

Of course heat transfer considerations call for a complete coverage of the stator blade surface by adequate internal convective coefficients obtained via appropriate combinations of flow velocity, passage width, and wall surface roughness treatment. From this point of view it is necessary to take into account that coolant flow pressure loss is limited by available cooling air pressure from compressor bleed and the position along the stator blade surface, at which the cooling air is discharged. Mutual satisfaction of these considerations results in a successful design.

The design process consisted of selecting cooling concepts, compatibly with the established constraints, examining the ability of each to perform the required cooling and choosing the final conceptual scheme. Figure 13 shows the resulting concept used for the detailed design effort.

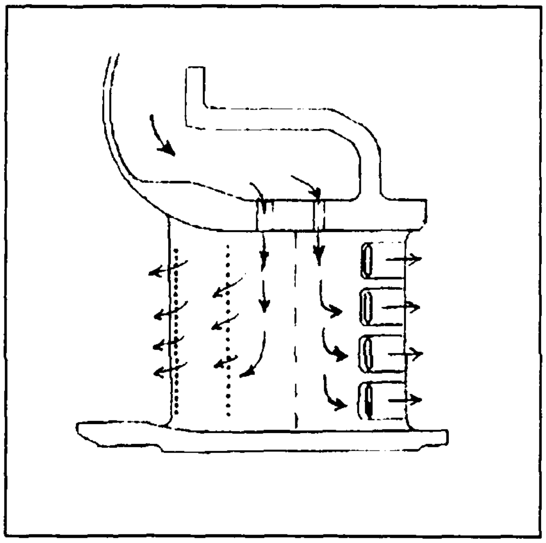

Fig 13 - NGV blade cooling flow scheme

The cooling air goes into the stator blade at the tip section and flows within the blade through two parallel cooling ducts.

In the forward duct the cooling air flows from the tip to hub blade direction, cooling the internal surface of the stator blade by impingement and the external surface by film cooling. The impingement cooling is realized by a perforated sheet inserted into the cavity (fig.14). After the impingement cooling the air discharges in the freestream at leading edge, pressure and suction regions from six rows of holes. When the cooling air flows from holes forms, on the stator blade surface, a protective cooling film that reduce the surface heat flux.

In the rearward duct the surface of the stator blade is cooled with combined mechanism of convective and film cooling at trailing edge. In fact the air that flows in the duct cooling the internal surface by convection, is discharged in the freestream from four slots on the pressure side near the trailing edge, thus film cooling this edge.

Design of the detailed area distribution and branching coolant flow circuitry has been accomplished using an internal coolant flow model. The method utilizes flow modeling within the stator blade passages via discreet elements that include frictional and bend losses, branching losses, restriction and expansion losses. The coolant passage wall temperature distribution and coolant inlet condition are a required input. Thus an interactive process between this code and the heat conduction code must be used since the wall temperature distribution is not known a priori. Fig. 14 shows the internal coolant flow distribution (the 1.8% of the inlet mass flow turbine in the forward duct and the 2.5% in the rearward duct for full NGV blade).

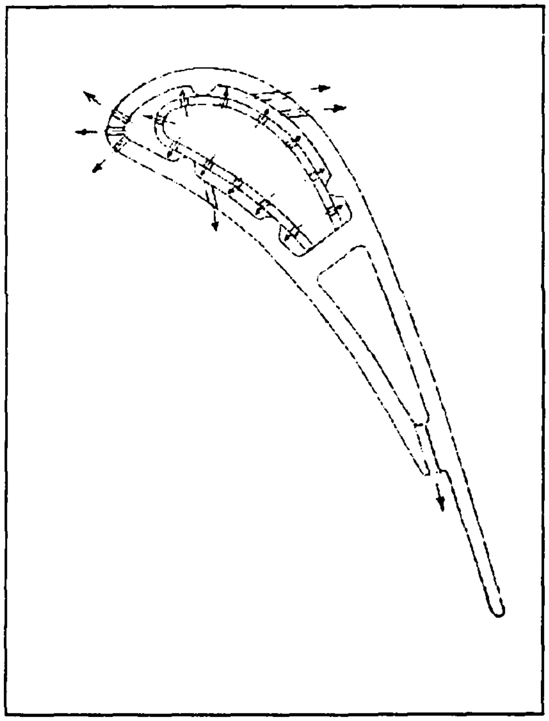

Fig 14 - Internal cooling system

3.3 Film-cooling design

Film cooling has been selected as the best method to cool the critical leading edge (LE) region (in the stagnation point, in fact, the hot gas heat transfer coefficient is very high up to about 3000 W/m²/K). This method, combined with impingement cooling on the internal surface, permits a good cooling of the LE. The cooling air, after the impingement cooling, is discharged in the hot gas boundary layer by three rows of holes (also a convection cooling through the holes is obtained in this way). The amount of the coolant and the geometrical characteristics of the rows (hole diameter, pitch to diameter ratio, number of holes for row and number of rows) have been defined to get a blowing ratio close to "1", in order to obtain a good cooling effectiveness without excessive usage of cooling air. As shows fig.14, the film cooling has also been used on the suction side (two rows of holes) and pressure side (one row). Sizing film cooling holes requires the knowledge of the discharge coefficient that has been initially estimated and then updated, based on experimental tests. In the Table I geometrical characteristics of the film cooling holes are reported.

Table I

	Row	N	d (mm)	S/d (-)	α (deg)
LE	LM	23	0.25	3.	50
	LS	24	0.25	3.	24
	LP	24	0.25	3.	77
SS	SS1	24	"	"	68
	SS2	23	"	"	68
PS	PS	24	"	"	155

The geometry of the thin trailing edge region precludes adequate cooling by internal convection alone, so the film cooling method, from four slots near this region, is used. The main characteristics of slots are :

Number of slots	4
Radial Length (mm)	3
Width (mm)	0.68
Distance from TE (% chord)	26.5

3.4 Nastran finite element method, element models and geometry related assumptions

The Nastran thermal analyzer code approximates the integrations of the 3D conduction equation for the finite element by a matrix form equation which relates, in steady-state condition, the temperature T at any point in the finite model of the structure, thermal conductivity, and heat flow due to the convection from the surfaces and the conduction within the structure. For the steady-state runs, the code verifies convergence of the solution after each iteration by comparing the maximum temperature change at every node against a preselected criteria.

In order to define both Mid-section 2D and 3D NGV geometrical models, was used PATRAN-2 as preprocessor code.

For the Mid section 2D finite elements model, QUAD4 conduction surface elements have been used. On the line of the QUAD4 elements, exposed to the hot gas or cooling air, HBDY elements (LINE type) have been used, for the convective heat exchange. The model is shown in fig 15.

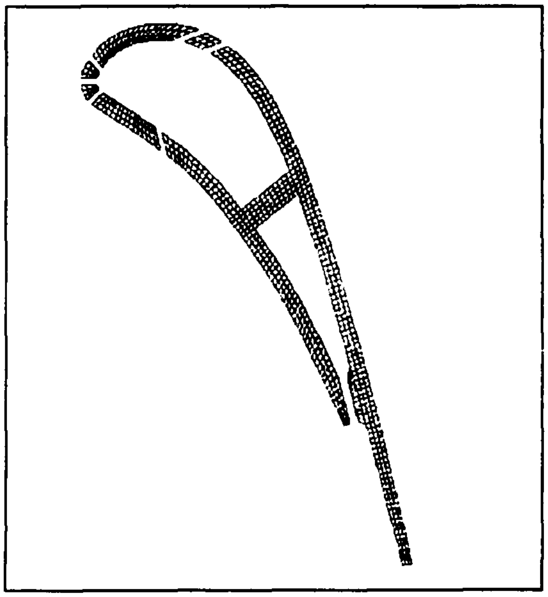

Fig 15 - 2D FEM model

The NGV solid model that includes the hollow blade with the hub and tip platforms, is shown in fig. 16.

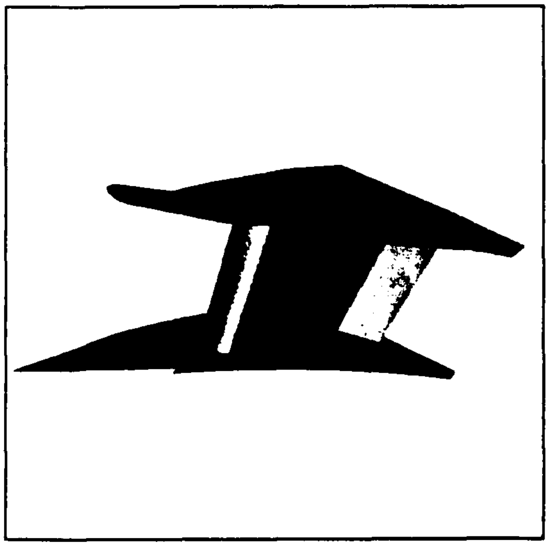

Fig 16 - 3D Solid Model

For the 3D finite elements model, HEXA and PENTA conduction solid element have been applied. On the surfaces of the HEXA elements where convective heat transfer (with hot gas or air cooling) are present, HBDY elements (AREA4 and AREA3 types) have been overlaid. To simulate the geometrical presence of film cooling holes and the convective heat transfer through the holes, FTUBE elements have been used. The solid model is composed by:

Grid Point	5005
Solid Element (HEXA)	2996
Solid Element (PENTA)	6
HBDY Boundary element (AREA4)	3503
HBDY Boundary element (AREA3)	8
HBDY Boundary element (FTUBE):	66

3.5 Mid Section blade thermal analysis

The model under consideration is the mid section of the stator blade. The equation governing steady state conduction is of the elliptic form. Therefore, heat transfer coefficients (HTCs) and relative total temperature boundary conditions are required on the external and internal surfaces cooling air passages.

Boundary conditions were specified according to different regions of heat transfer on the internal and external surfaces.

- Convection forced on leading edge, suction and pressure hot gas sides: HTCs on this surfaces in presence of film cooling have been initially estimated, than updated based on experimental tests performed at Von Karman Institute [3]. The measurement were performed in the short duration isentropic light piston compression tube facility with the platinum thin-film gauge technique. Fig. 17 show the heat transfer coefficients distributions for a nominal test condition (M_2=0.98, Re_2=5.5x10^5, Toc/To∞=0.4). The total temperature boundary condition is the hot gas total temperature To∞=1450K.

- Film cooling on trailing edge: The experimental configuration of the blade model tested did not have film cooling at trailing edge, therefore a theoretical approach has been used in this case. The HTC has been calculated by a modified version of two-dimensional finite difference boundary layer code STAN5 [4], without film cooling, and the total temperature boundary condition is the wall adiabatic temperature calculated from the "film effectiveness η":

$$T_{aw} = T_{o\infty} - \eta\,(T_{o\infty} - T_{oc})$$

where the film effectiveness is calculated by the Goldtsein [5] relationship for tangential injection from slot (Appendix A).

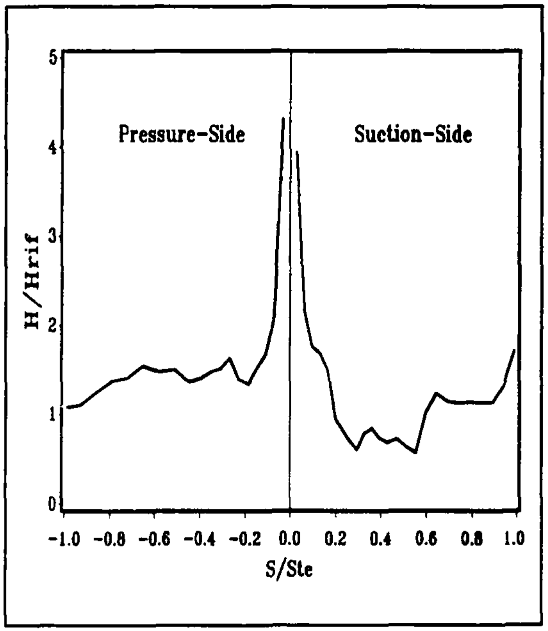

Fig 17 - Heat transfer coefficients

- Impingement cooling in the forward duct: The HTC has been calculated by the Kercher-Tabakoff [6] relationship for impingement realized through a square array of circular holes:

$$Nud = \varphi_1\ \varphi_2\ (Red)^k (Pr)^{1/3}\ (Z/d)^{0.091}$$

where the coefficients are presented in Appendix A.

- Impingement cooling on the internal LE surface: The HTC on the internal l.e. surface has been calculated by the Chupp [7] relationships for impingement realized through a row of circular holes on a concave semicilinder surface:

$$Nud(0) = 0.493\ (Red)^{0.7}(Pr)^{1/3}(d/S)^{0.8}\ \exp\{-0.85\ (d/S)\ (d/D)^{0.4}(Z/d)\}$$

for the Nusselt number in the stagnation point, and:

$$Nud = 0.706\ (Red)^{0.7}(Pr)^{1/3}(d/S)^{0.5}(d/D)^{0.6}\ \exp\{-1.27\ (d/S)^{0.5}(d/D)^{1.2}(Z/d)\}$$

for the average Nusselt number.

- Convection cooling in the rearward duct, holes and slots: In this passages the HTC is calculated by a turbulent flow in a short tube correlation [8]:

$$Nud = 0.023\ (Red)^{0.8}(Pr)^{1/3}\{1+(d/L)^{0.7}\}$$

The preliminary value of the cooling air total temperature Tco was 575 K.

The analysis is non-linear steady-state type, that means the thermal conductivity is temperature function. The final results for the Mid section stator blade analysis are presented in fig. 18.

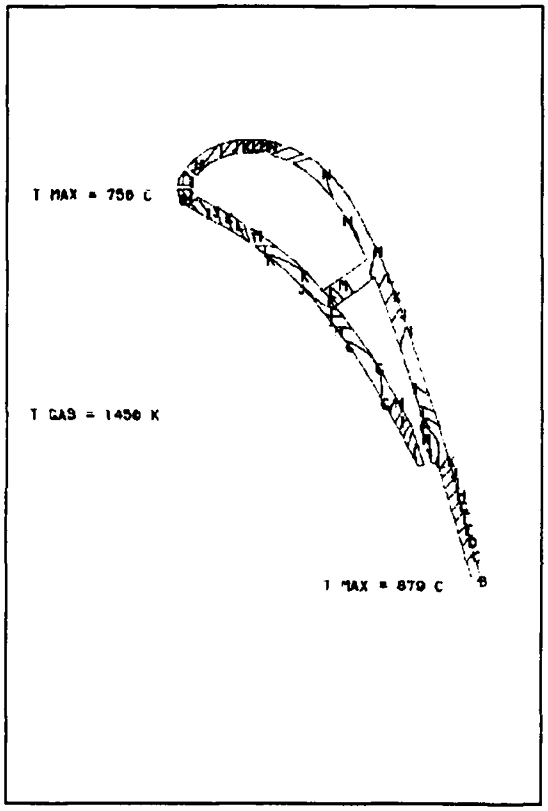

Fig 18 - Results of 2D thermal analysis

The ΔT between the iso-temperature is 25°C. The maximum temperature (= 879°C) occurs at the trailing edge, where the protection by film cooling, on the pressure side, is opposed from high heat flux on the suction side (here, in fact, the boundary layer is turbulent so the HTC are greater than laminar and transitional b.l. ones) and the protective film cooling on the suction side itself, realized from rows SS1 and SS2, is, by this time, vanished. In the forward part of the stator blade, the combined mechanism of impingement, film cooling and convection cooling (through film cooling holes) results very efficient, in fact the maximum temperature, occurs in the stagnation point, is about 750°C.

3.6 NGV 3D model thermal analysis

The model under consideration is the 3D model of the stator blade (fig. 16). As before the heat transfer coefficients (HTCs) and relative total temperature boundary conditions are required on the external and internal surfaces of the cooling air passages.

The HTCs on internal coolant passages and external surfaces were calculated as before, taking into account cooling air temperature increase, due to the heat transfer between the hot stator surfaces and the cooling air, that flows from tip to hub direction. Gas side HTCs have been considered constant along the blade span. Some other parts on which the boundary conditions were imposed are:

- Stator blade to blade inner and outer platforms, hot gas surfaces : The heat transfer coefficients are taken to be the mean of the suction and pressure surface values at the Hub and Tip sections.

- Inner and outer platforms hot gas surfaces upstream and downstream of the NGV : On hot surfaces, the use of twice HTC calculated by the correlation for a turbulent flow in a pipe, produce a realistic value. The hot gas total temperature has been assumed uniform.

- Inner and outer platforms cold surfaces: Over the outer shroud cold surface, for HTC calculation were used the expression for average value of a turbulent boundary layer on a flat plate:

$$Nul = 0.036\ (Rel)^{0.8}(Pr)^{1/3}$$

Over the inner shroud cold surface the HTC for annular duct forced convection correlation has been used. The cooling air temperatures have been estimated for the forward vane 625 K, the rearward vane 605 K, across the cooling holes 800 K.

Two calculations have been performed, one relative to the "average" vane (Tgas,ave= 1460 K, Tpeak= 1549 K) and one for the "hottest" vane (Tgas,ave= 1542 K, Tpeak= 1645 K).

The thermal maps of the blade are presented in figg. 19, 20. From the isothermal lines it is evident that the blade has a PS hotter than SS and the hottest regions are at TE and LE . Max metal temperatures are at TE 976 °C and at LE 955 °C in the case of average vane. More critical, but in any case below target limits, are the max values for the hotter vane, where at TE the temperature is 1033 °C and 1012 °C at the LE.

In correspondence to the SS rows there are lowest temperatures around 700 °C, due to convection cooling through the holes.

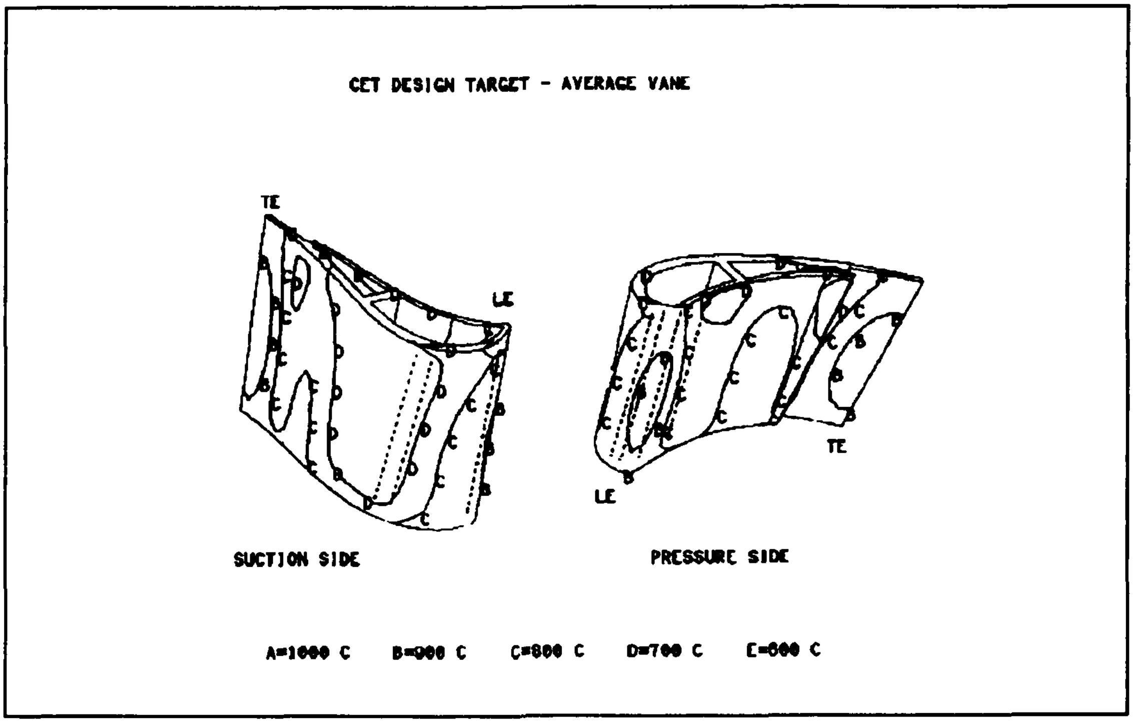
CET DESIGN TARGET - AVERAGE VANE
TE
LE
LE
TE
SUCTION SIDE
PRESSURE SIDE
A=1000 C
B=900 C
C=800 C
D=700 C
E=600 C

Fig 19 - Results of 3D thermal analysis - Design target - Average Vane

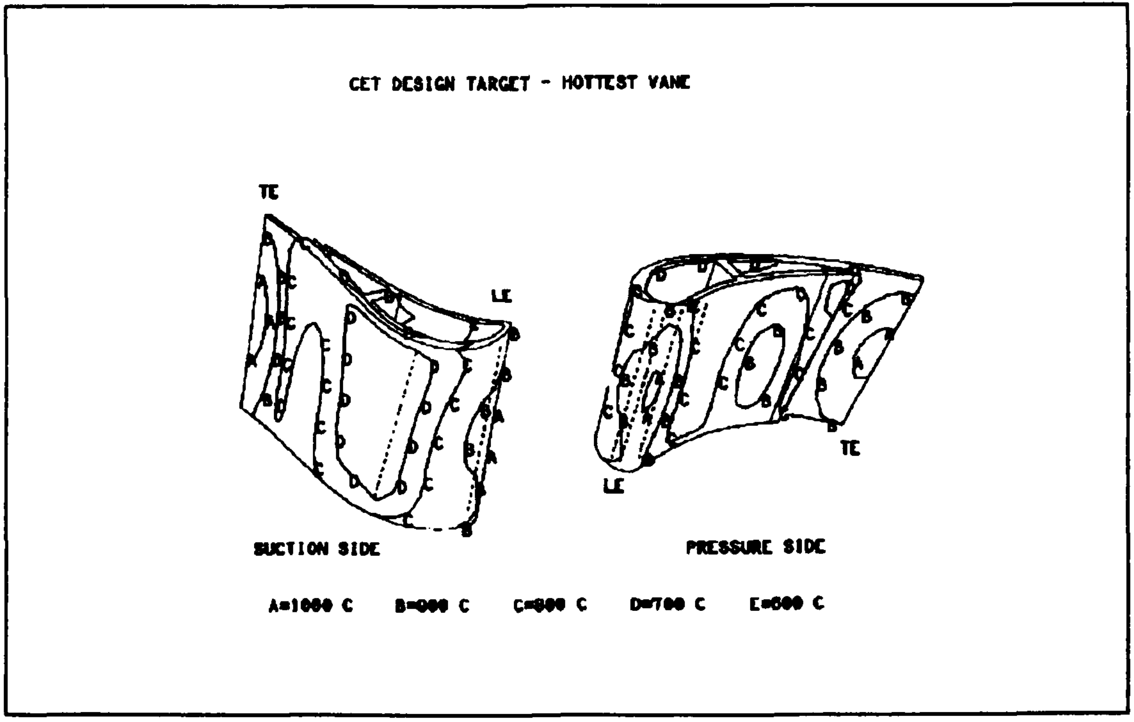
CET DESIGN TARGET - HOTTEST VANE
TE
LE
LE
TE
SUCTION SIDE
PRESSURE SIDE
A=1000 C
B=900 C
C=800 C
D=700 C
E=600 C

Fig 20 - Result of 3D thermal analysis - Design Target - Hottest Vane

4 AERODYNAMIC NGV TEST VERIFICATION ON CASCADE RIG

4.1 The facility, the model and the measurement techniques

The experimental investigation was carried out in the Von Karman Institute light piston compression tube facility [3]. The freestream gas conditions can be varied between 300 and 600 K and 0.5 and 7 bar. The typical test duration is about 400...500 ms.

The measurements presented were performed along a film cooled NGV mid section, mounted in linear cascade configuration. The model was scaled by an factor of 2. This cascade consisted of 5 blades (fig.21) with the central one instrumented either for static pressure measurements (blade velocity distribution) or for heat flux measurements (blade convective heat transfer distribution).

The heat transfer measurements are obtained via a transient technique using thin film gauges installed on a glass ceramic blade.

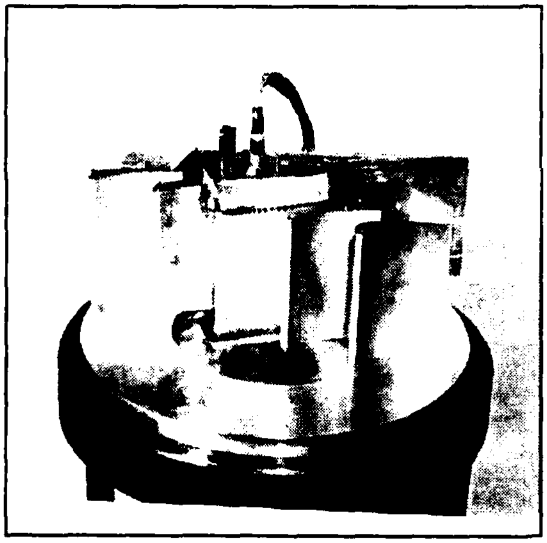

Fig 21 - Cascade Model

The coolant flow was supplied by a regenerative type cryogenic heat exchanger allowing the simulation of different coolant to freestream temperature ratios.

It is important to mention that only the blade used for heat flux measurements was film cooled. The velocity distributions were obtained along a smooth, uncooled profile.

The uncertainty on pressure measurements was of the order of ± 0.5 %, on temperature measurements of the order of ± 1.5 K, on the heat transfer coefficient of the order of ± 5%, on the integrated loss coefficient of the order of ± 0.2 points and on the exit flow angle ± 0.5 deg.

4.2 Test conditions

The test program was built up by varying the freestream conditions according to the following values : Mach 0.8 ÷ 1.2, Reynolds $0.4\text{x}10^5 \div 1.0\text{x}10^6$ Turbulence 1 % ÷ 6 %.

The freestream temperature was selected to be 362K for the Reynolds tests ($5.5\text{x}10^5$). For this test condition 3 values of the coolant to freestream temperature ratio were considered as well as 5 to 7 values of the blowing rate. All these tests were performed independently for the leading edge suction side and pressure side cooling configurations.

4.3 Blade velocity distribution

Blade isentropic Mach number distributions were obtained from local static pressure measurements, referred to the upstream total pressure. The blade used for this purpose is equipped with 27 static pressure tappings.

The blade velocity distributions were performed with the downstream dump tank open to atmosphere, in this way, the value of the downstream Reynolds number was not controlled. Anyway, the influence of this parameter on the velocity distribution presented under the form of a Mach number evolution is know to be small.

In the fig.22 the Isentropic Mach number in function of a coordinate (Xc) measured along the chord of profile for the condition $M_{2,is}$=0.95 is presented. The irregularities along the suction side are due to the local variation of the curvature of the profile.

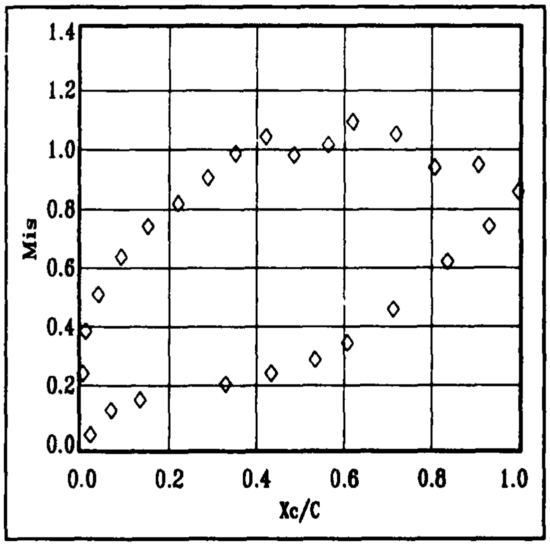

Fig 22 - Experimental isentropic Mach Number

4.4 Blade heat transfer distribution

The blade used for heat flux measurements was made of Macor glass ceramic and instrumented by means of 45 platinum thin film gauges.

In order to identify the effects of Mach number and Reynolds number as well as of freestream turbulence intensity on the convective heat transfer distribution along the profile, a first series of heat flux measurements were performed without any film cooling.

In the fig.23 the heat transfer coefficient distributions for $M_{2,is}=1.0$ are presented. The effects of turbulence level (1% and 6%) and Reynolds number ($0.55x10^6$ and $1.0x10^6$) are clearly evident. At Re of $0.55x10^6$ the effect of turbulence increases HTC but not the boundary layer state. At Tu of 6% the increase of Re appears that the boundary layer remains in a laminar state up to the rear part of the suction side and that transition occurs more or less at location of the suction side velocity peak. Along the pressure side, the boundary layer is in a transitional state. We can observe the small disturbs on the boundary layer status due to the film cooling holes presence to low Reynolds numbers. With additional test performed for downstream Reynolds number value of $1.0x10^6$ was observed that film cooling holes is sufficient to trigger the transition of the boundary layer.

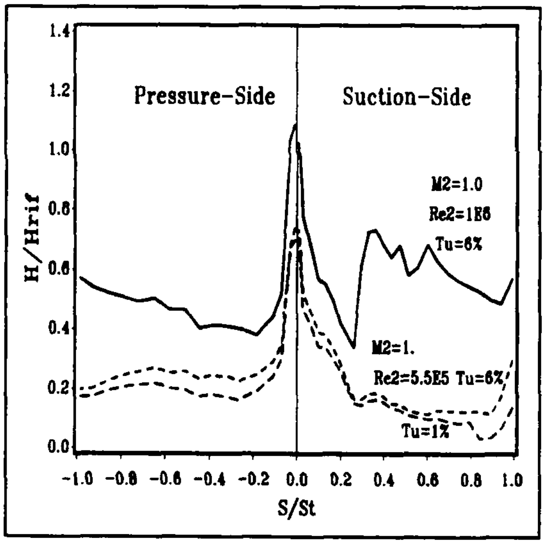

Fig 23 - Heat transfer coefficients for the uncooled blade

The heat transfer coefficient distributions film cooling were conducted independently for the three different cooling configurations : leading edge, suction side and pressure side.

For each case the heat transfer coefficient "h" is compared to the heat transfer coefficient "ho" obtained without any film cooling. The results are obtained at three different coolant to freestream temperature ratios varying the coolant mass flow (blowing ratio). The fig.24 shows the h/ho ratio relative to the nominal condition. The film cooling on the LE and PS seems to be effective, while the benefit on the SS is limited to the region immediately downstream the holes; further downstream the laminar to turbulent B.L. transition causes an HTC increase.

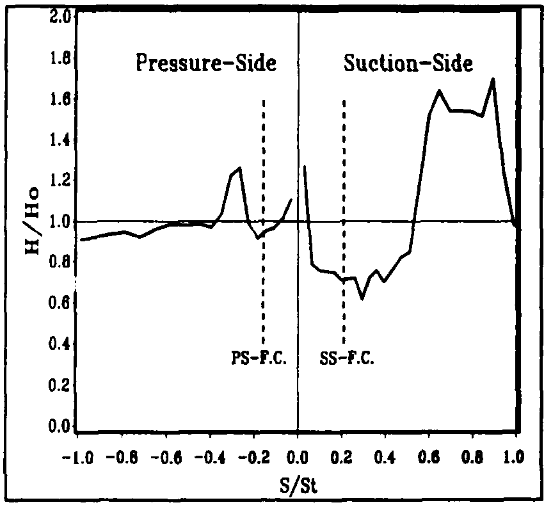

Fig 24 - Heat transfer coefficients with film cooling

In fig.25 the discharge coefficient evolution vs to coolant static to freestream total pressure ratio is given.

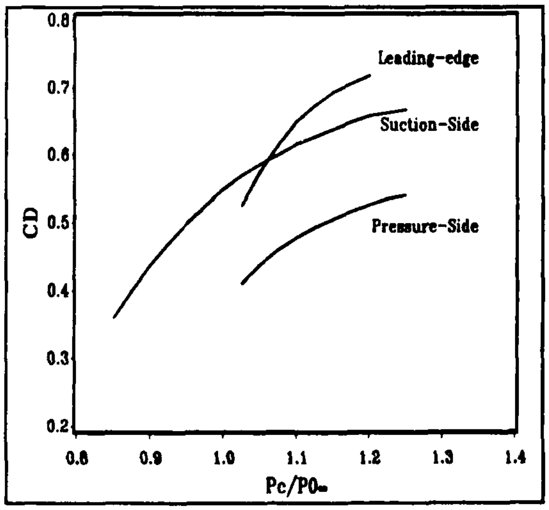

Fig 25 - Discharge coefficient through the film cooling holes

4.5 Cascade performances

This testing was carried out using 5 aluminium profiles none of the blade were equipped with film cooling holes.

Wall static pressure tappings were installed downstream of the cascade, in a plane parallel to the trailing edge plane and located at X/Cax =1.415 downstream. They covered a distance a little more than 2 pitches to verify the downstream periodicity of the flow and to determine the exit Mach number to the cascade. The downstream loss coefficient evolution as well as the exit flow angle were obtained by means of a fast traversing mechanism, transporting a Pitot probe over 2 pitches [9].

The test was built up by varying the following freestream conditions : To = 400 K, $M_{2,is}$ = 0.7 to 1.12, $Re_{2,is}$= $5x10^5$ to $1x10^6$, Tu = 0.8 %.

At the design point ($M_{2,is}$ = 0.95) the measured flow deviation is 71.0 deg and kinetic loss coefficient ζ_2=0.026.

4.6 Comparison with numerical predictions

The predicted Isentropic Mach number distribution around the solid blade at design point has been compared with the experimental one in fig.26.

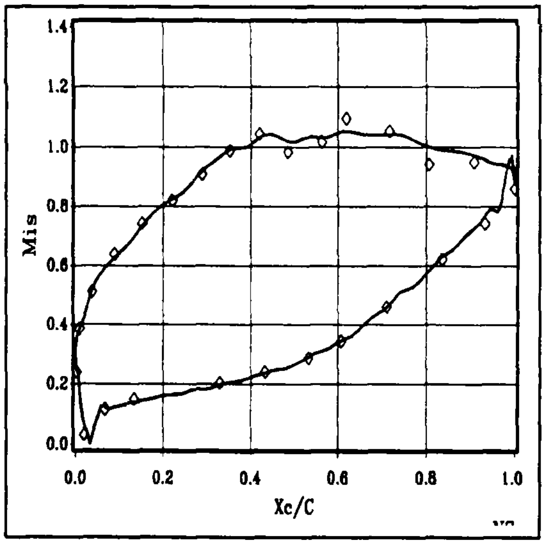

Fig 26 - Experimental blade isentropic Mach number distribution compared with 2D NS calculation (Solid Blade). M2is=0.95, Reis=$5.5x10^5$

The theoretical values have been obtained by 2D Navier Stokes code. The method uses a conservative formulation of the Reynolds-averaged 2D compressible Navier-Stokes equations. The Baldwin-Lomax turbulence model is adopted. The system of governing equations is solved by an explicit finite volume approach with the time integration performed by a three stage Runge-Kutta algorithm [10].

It can be seen that close agreement is obtained on the pressure side and suction side.

In fig.27 is reported the comparison between the experimental HTCs and that ones calculated by a modified version of the STAN5 code [4], at the condition M_2=0.98, Re_2=$5.5x10^5$, Tu=6%.

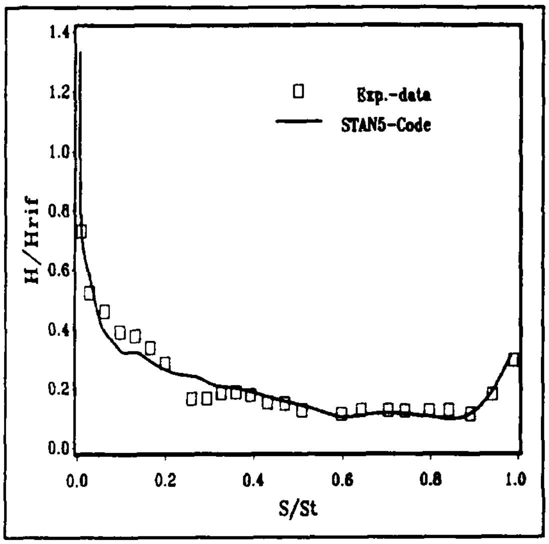

Fig 27 - Blade SS heat transfer coefficient. Experimental-theoretical comparison.

In the Fig. 28 is shown the comparison from NS code and measurements in terms of flow deviation and kinetic loss coefficient.

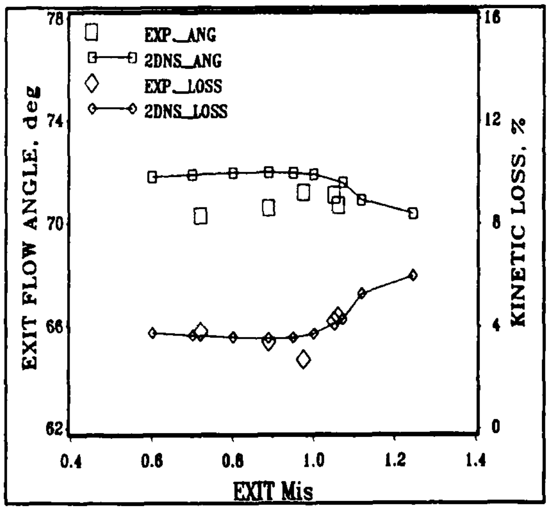

Fig 28 - Flow deviation and kinetic loss coefficient. Comparison from NS code calculations and measurements. (Solid Blade)

A good agreement is observed on the general trends. The increase of exit flow angle up to design $M_{2,is}$ = 0.95 is followed by a decrease more marked for $M_{2,is} \geq 1.05$. The value are overpredicted (in particular at lower $M_{2,is}$. Losses trend is correctly predicted with the increase above design $M_{2,is}$. A satisfactory correspondence between experimental numerical values is observed although calculations are based on fully turbulent flow over the blade surface.

5 THERMAL NGV TEST VERIFICATION ON ENGINE DEMONSTRATOR

An extensive experimental program actually is in progress on an engine demonstrator to verify the aerothermal and mechanical behavior of the full HP turbine stage. In particular, focusing on the NGV aerothermal design validation phase, the main results, up now available, are described.

5.1 Engine demonstrator

The demonstrator has been derived from an existing single-shaft turboprop engine of 600 SHP (SL ISA condition).

The lay-out of the engine demonstrator is presented in fig.29. The power section has a high-technology, single-stage centrifugal compressor dimensionated with a single-stage axial flow turbine to minimize the overall diameter of the power section. The combustor design is of the reverse annular flow type and fits compactly around the exhaust duct.

An exhaust cone has been dimensionated to set adequate value of the backpressure at the turbine stage exit.

The combustor has been derived from the existing one designed for 1250 K TET, which main fuel injector system has 9 T-shape vaporizers. There is also the fuel pilot system of 3 sprayers (torches) to start-up the engine.

Since the design test conditions for the HP turbine is 1450 K TET, more fuel flow must be burned into the existing combustor and consequently the thermal loading is higher on the liner.

The optimization of the combustor system it was necessary to achieve good performances in terms of pressure losses, combustion efficiency, liner life and OTDF/RTDF requirements, and so the redesign that satisfy the geometrical restrains and mechanical interfaces of the original engine has been done. However, in the initial phase of the experimental program a preliminary version of the combustor has been used, simply derived from the original configuration by an application of a thermal barrier coating (Bound coat NiCoCrAlYo and top coat ZrO2+Y+Cc applied with plasma spray), in order to avoid excessive liner metal temperature. Moreover, the fuel system uses the original 9 T-vaporizers and the 3 sprayers at same time, by which it is possible to inject the required value of the fuel at design condition.

5.2 NGV demonstrator hardware

The mechanical design of the NGV is showed in fig.30. The annular cascade is an integral casting ring (INCO 713 LC) that is connected on the hub platform by bolts to the compressor diffuser plate. The shroud platform is brazed to a ring shaped to get the convex wall of the 180 degree bend of the combustor. The shroud platform has two row of holes by which the cooling air fill the front and rear cavity of the blade.

The rows of film cooling holes on the blades have been realized by EDM technique. The hardware tested has same differences respect to the design values, the axial position of the hole rows on the SS surfaces for machining reasons have been realized 2 mm far away the design value, and the film cooling row holes at PS covers only 70% of blade height starting from the upper platform.

The manufacturing process of the sheet metal insert to provide impingement cooling reveals some difficulties so that the first prototype hardware had discrepancies respect to the design intent in terms of hole diameter, number of holes and spatial position.

5.3 Measurement techniques

The engine has been instrumented with thermocouples and total/static pressure devices at the compressor inlet/exit planes, to evaluate temperature and pressure ratio, and at the turbine exit plane to measure exit gas temperature (n° 18 shielded thermocouples) and total pressure (3 rakes, each with 3 probes). The engine inlet mass flow has been derived from static pressure measurements at the air-intake inlet plane by using a calibration curve.

The accuracy of the measurements is ± 2°C for the temperature, ±0.5 g/s for fuel flow, ± 1 kW for the Power and ± 1% for the mass flow.

A survey on the NGV metal temperature has been obtained applying thermal indicator paints (TIP). By this technique in a simple and effective way it is possible to obtain permanent visual records of peak temperature variation over the surfaces of the component.

The type developed by ROLLS-ROYCE, adopted by ARA Experimental Center since many years have high degree of accuracy and reliability (+/- 15 °C) at 1150 °C. They have the ability to survive in very hostile environments and work up to 1150 °C [11].

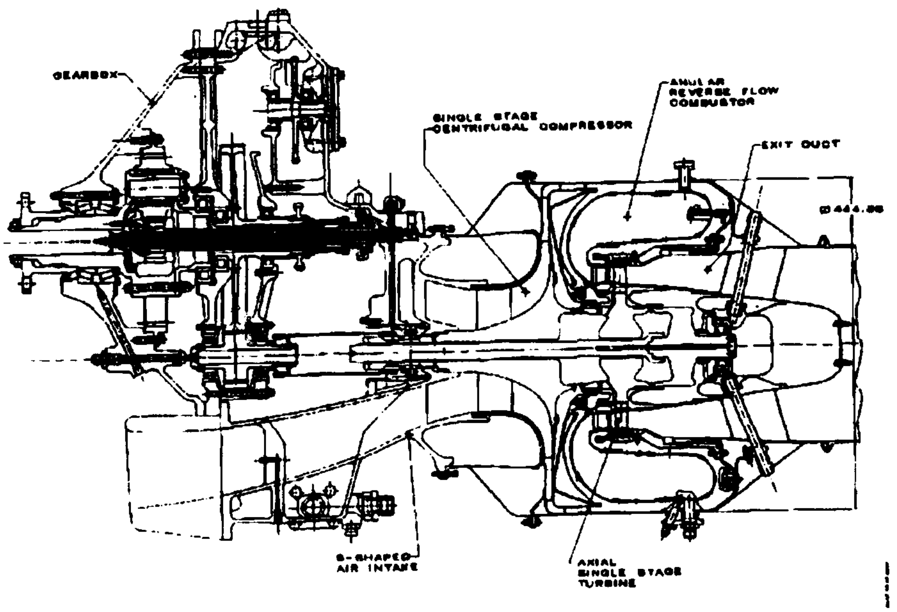
GEARBOX
SINGLE STAGE CENTRIFUGAL COMPRESSOR
ANULAR REVERSE FLOW COMBUSTOR
EXIT DUCT
Ø 444.86
S-SHAPED AIR INTAKE
AXIAL SINGLE STAGE TURBINE

Fig 29 - Engine Demonstrator Layout

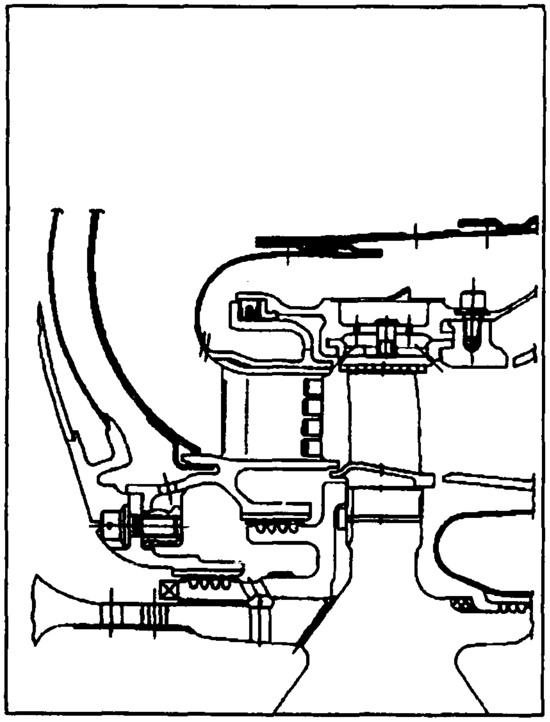

Fig 30 - Turbine Stage

The type applied on the NGV blade and platforms is the multichange type RR-TP6. This is a bound mixture of pigments which are chosen to exhibit distinct and irreversible color changes on exposure to elevated temperatures over the range from 520°C to 1150°C. The paint temperature change with temperature is given in table II for a 5 minute calibration. Each color band has been allocated a code letter to represent the results.

TABLE II

COLOR	FROM	TO	LETTER CODE
BLUE	<520		-
PALE BLUE GRAY	520	780	N
DARK BLUE GREY	780	960	T
BLUE	960	1040	P
MIDNIGHT BLUE	1040	1100	G
MATT BLACK	1100	1120	M
BLACK GLAZE	1120	1150	Y
DARK BLUE GLAZE		>1150	R

5.4 Engine test procedure

The demonstrator engine has been tested at ARA Experimental center using test cell n° 2. Engine power was absorbed in a water brake dynamometer.

Engine testing was carried out in two steps. The aim of the first one was to check the performances of the demonstrator, reaching the design conditions in terms of corrected speed (38100 rpm at ISA SL conditions), and fuel flow in order up to get TET design point target (1450 deg K). Since a direct measurement of turbine inlet temperature was not possible, the measured data have been processed using the "Power" method, i.e. from the power balance given by turbine, the one absorbed by the compressor and the one measured at the dynamometer (taking into account the mechanical losses due to the gear-box).

The following thermodynamic test conditions have been evaluated near the design point :

Corrected Engine inlet mass flow	2.62 kg/s
Corrected shaft power	225 HP
Compressor pressure ratio (T-S)	6.67
Exhaust gas temperature	1118 K
Turbine inlet gas temperature	1448 K

Taking into account uncertainty of the measurements, the average value of the TIT has been estimated with a precision of +/- 10 K.

The second test has been performed with same hardware. The TIP has been applied to the surfaces of the NGV by spray gun.

The following procedure has been adopted :

a) engine start-up, acceleration from idle-speed to 100% design speed, progressive loading by increasing fuel-flow at constant speed to reach required TIT, to set thermodynamic engine condition at the design point;

b) Five minutes of stable conditions at design point (TIT = 1450 K);

c) Rapid shut-down of the engine.

5.5 Thermal Indicator Paint Results

An overview of the results relative to a NGV sector of 120° is presented in the photographs of the fig.31 (looking from NGV inlet) and in fig.32 (looking from NGV outlet). It is evident the hot spot generated by the fuel sprayer.

Looking into details to the metal temperature distribution on each blade, two different situations can be distinguished : the blade situated on the main average gas temperature (fig.33) and the blade in correspondence to the gas hot spot (fig.34). On the LE in the first case several isolines are detected and the one at maximum temperature is 1100 °C . Since the greater is not visible, the peak metal temperature is between 1100 °C and 1120°C on the average vane.

Regarding the thermal situation at TE, the max temperature region is in the middle height of the blade, where in the case of average vane the temperature is between 960 °C and 1040 °C.

It is clearly evident that on both blades the PS surface is hotter than SS . Film cooling seems to be effective on the suction side, where the isothermal lines corresponding to temperature 780 °C are observed in the midspan zone on the blade. On the pressure side the film cooling is less effective in the front part of the blade.

5.6 Discussion on the results and comparison with predictions

A comparison between experimental results (figg. 33,34) and theoretical ones has been done. First of all a direct comparison with the thermal behavior predicted for the original NGV design it is possible (see figg.35,36). It must be remarked that these predictions are based on the target radial inlet gas temperature, and thermal gas loading around the blade is a replication of radial profile at NGV inlet.

Metal temperatures on the experimental NGV hardware are generally greater respect to the predictions at LE, and at front part of the blade. A quite strong radial temperature variation is observed on the experimental hardware respect to the predicted results.

A main responsible for that behavior is due to the combustor performance. In fact the combustor configuration used in the first test of the engine demonstrator is non-optimized to satisfy the target RTDF and OTDF. The prediction of the CET distribution, recently obtained from the solution of the 3D combustor reactive flow on a 120° combustor sector including 3 vaporizers an 1 fuel sprayer, reveals highly distorted gas temperature in correspondence to the NGV inlet plane as it is showed in fig.37. The predicted OTDF is 0.31 respect to the target value of 0.21 for which the NGV cooling system has been designed. So that the NGV has been exposed in the first demonstrator test to thermal conditions more severe than the ones for which has been designed, as is showed in fig.38.

Consequently two more NGV thermal simulations have been developed, using radial temperature profiles obtained from combustor calculations relative to the so called "tested hardware". Also in this case there is the assumption that gas temperature radial profile around the blade is constant from LE to TE. The results are showed in figg. 39,40.

From the comparison between figg. 33,34 vs fig 39,40 it is still evident that thermal behavior of NGV experimental hardware is different respect to predictions. Such differences are mainly due to 3 factors:

- tested hardware differences between original design and manufacturing vanes;
- gas temperature loading around the blade due to secondary flows;
- heat transfer coefficients distribution on the hot side and as well as on the cold air side.

To have an idea on the importance of the NGV hardware differences between the original design and the real prototype tested on the demonstrator a final simulation has been performed taking into account some of the aspects mentioned before.

Difficulties arose during the fabrication of the sheet metal insert to realize the impingement cooling for the first NGV prototype, force into a direction to a less efficient cooling system. By an estimation done a-posteriori the penalty of the HTC values on the internal side is -30 % around the PS and SS and -50% at LE.

On the other hand based on the inspection reports, the film cooling rows has been realized with holes diameter less than the design values. Due to others manufacturing difficulties to realize F/C rows on the PS as well as on the SS, the number of the holes has been reduced by 15 %. In conclusion for this first NGV prototype tested on the demonstrator, less cooling air was available through the front part of the blade and the cooling system was less efficient respect to the design intent.

The simulation of the NGV experimental hardware can be done taking into account more sophisticated flow modeling around the blade. In fact the predicted hot gas flow condition, got from combustor CFD solution, can by used as an input for the NS solver of the 3D flow in the NGV annular cascade. In this case the solver doesn't take into account the cooling flow, nevertheless the simulation can predict the flow behavior, i.e. the redistribution of the gas temperature through the cascade due to secondary flows (see fig.41).

The new thermal loading has been applied on the same NGV's FEM model, to get a more appropriate thermal prediction. Results of thermal numerical simulation are showed in fig.42 for the average vane.

It is clearly evident the effect of impingement cooling reduced performance on the metal temperatures around the blade LE, comparing fig 42 respect to fig 39 for the same inlet gas thermal loading LE region is hotter and peak temperature increase from 974 °C to 1105 °C.

It is interesting to observe the satisfactory level of simulation of the NGV experimental thermal behavior, comparing fig 42 respect to fig 33.

Isothermal lines B, C, D are present in the simulation like in the experimental results. LE predicted temperature is 1105 °C, where experimental value is between 1100 and 1120 °C. A quite good prediction is found on the SS. At PS the temperatures are underestimated close to the FC and overestimated far away form FC in the mid span of the blade. In the TE region thermal level is correctly simulated.

It must be remarked that the correlations applied to evaluate HTC for the impingement cooling system have been used at their limit of validity range, and this can explain thermal differences in the front part of the vane.

In the rear part of the blade the velocity distributions around the blade between hub, mid and tip, and the secondary flow effect on the HTC, are mainly responsible for the difference in the thermal behavior founded in the SS hub and tip region.

Conclusion Remarks

The aerothermal design of a low-aspect-ratio transonic, cooled nozzle guide vane for an advanced compact high temperature gas generator turbine stage is described.

The cooling system include impingement, forced convection and film cooling devices.

Aerodynamic cascade test on the scaled model (2:1) of mid span blade section have been performed to verify overall performances in terms of blade velocity distributions, flow deviation and pressure loss.

Heat transfer coefficients have been measured in absence and presence of film cooling on LE, SS and PS at different Reynolds, Mach number and turbulence level. These results contribute to update the predictions of the thermal behavior of the NGV blade in the engine conditions. On the other hand the validation of CFD tools for aerodynamic design has been performed.

Thermal test results on the engine demonstrator, obtained on NGV hardware, have been obtained by TIP technique.

The first NGV prototype experienced metal temperature at LE greater than predicted (1150 °C), because of manufacturing inconsistency respect to the design and thermal loading heavier than design target.

The lesson learned from this experience regards two critical aspects of the thermal design:

- design sensitivity to the manufacturing tolerances on small vane dimensions;
- accuracy of HTC predictions for impingement cooling.

Work is in progress to extende of the validity range of the correlations and to simulate the 3D viscous flows through the annulus cascade in order to evaluate HTC distribution.

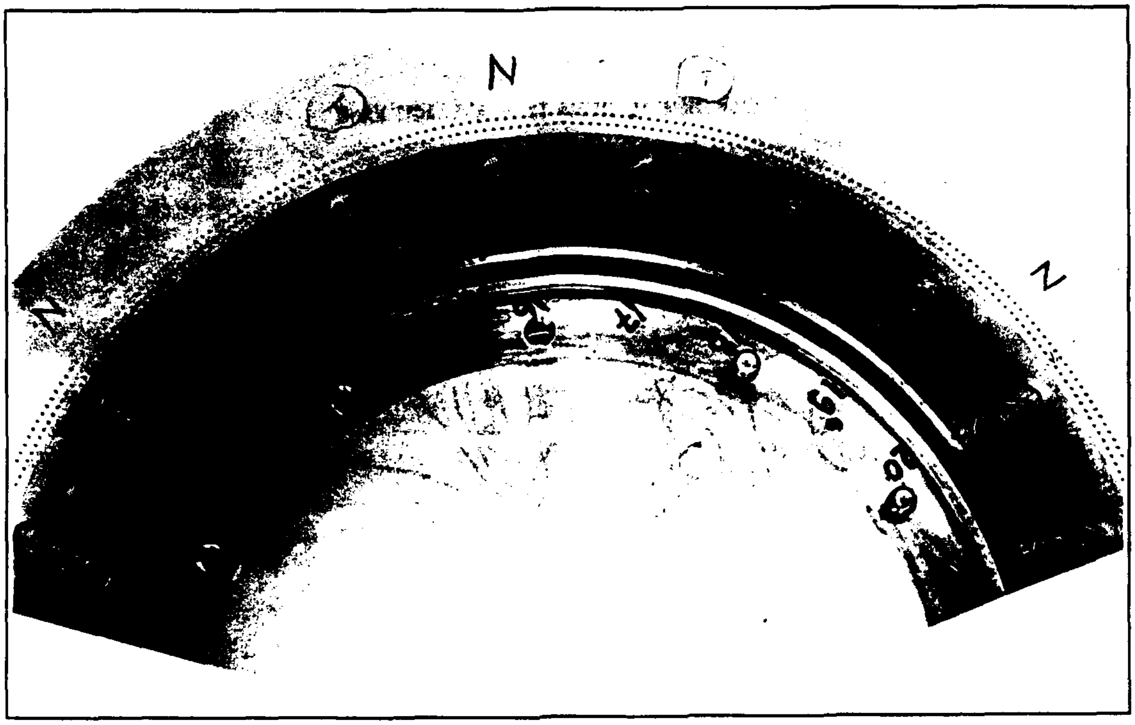

Fig 31 - TIP results looking from NGV inlet.

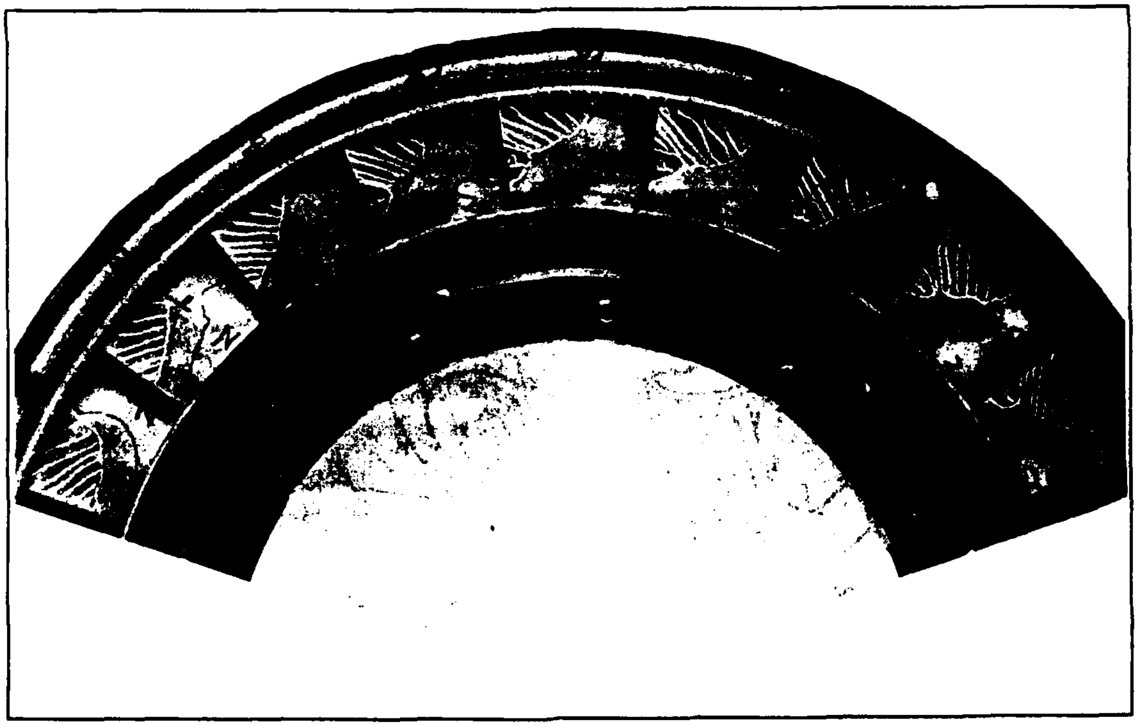

Fig 32 - TIP results looking from NGV outlet

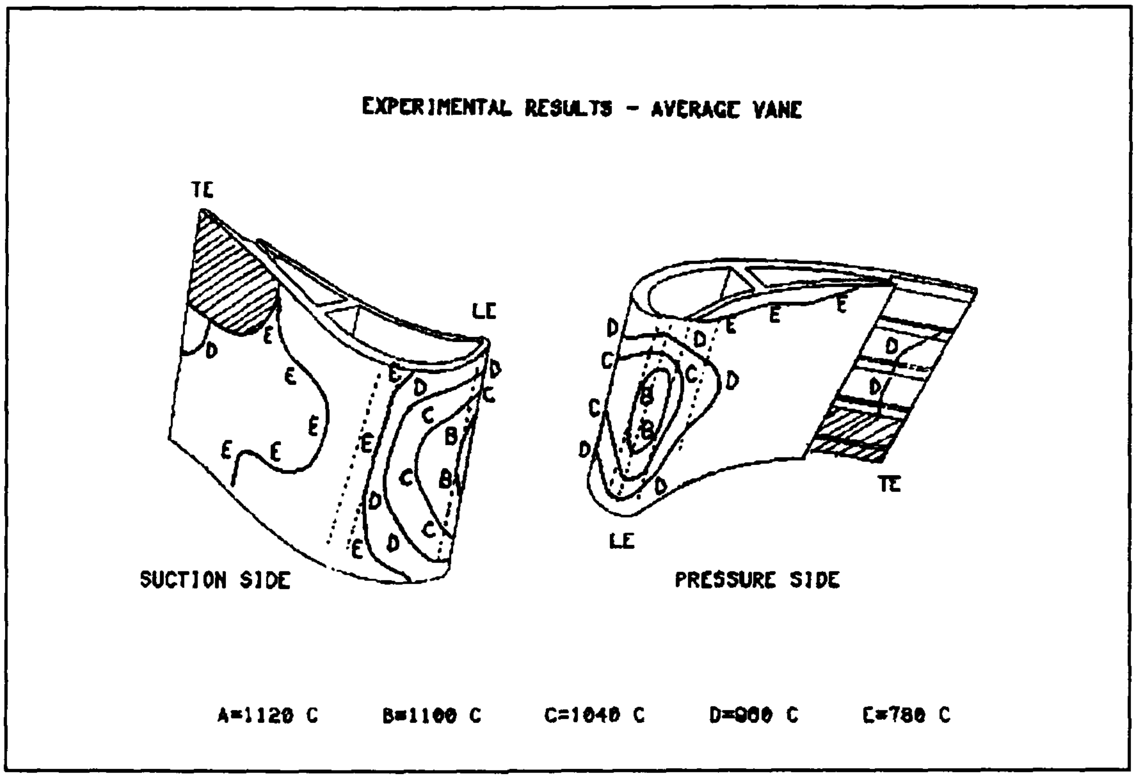
EXPERIMENTAL RESULTS - AVERAGE VANE
TE
LE
SUCTION SIDE
LE
TE
PRESSURE SIDE
A=1120 C
B=1100 C
C=1040 C
D=960 C
E=780 C

Fig 33 - Engine Demonstrator TIP test : results of average vane

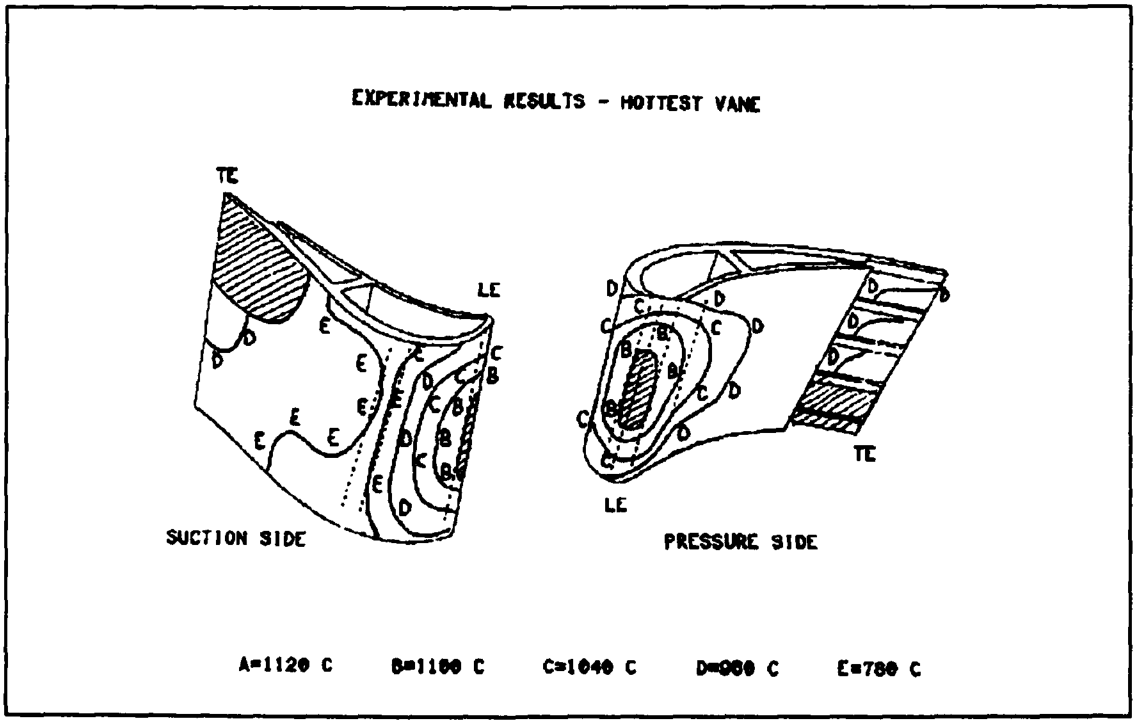
EXPERIMENTAL RESULTS - HOTTEST VANE
TE
LE
SUCTION SIDE
LE
TE
PRESSURE SIDE
A=1120 C
B=1100 C
C=1040 C
D=960 C
E=780 C

Fig 34 - Engine Demonstrator TIP test : results of Hottest vane

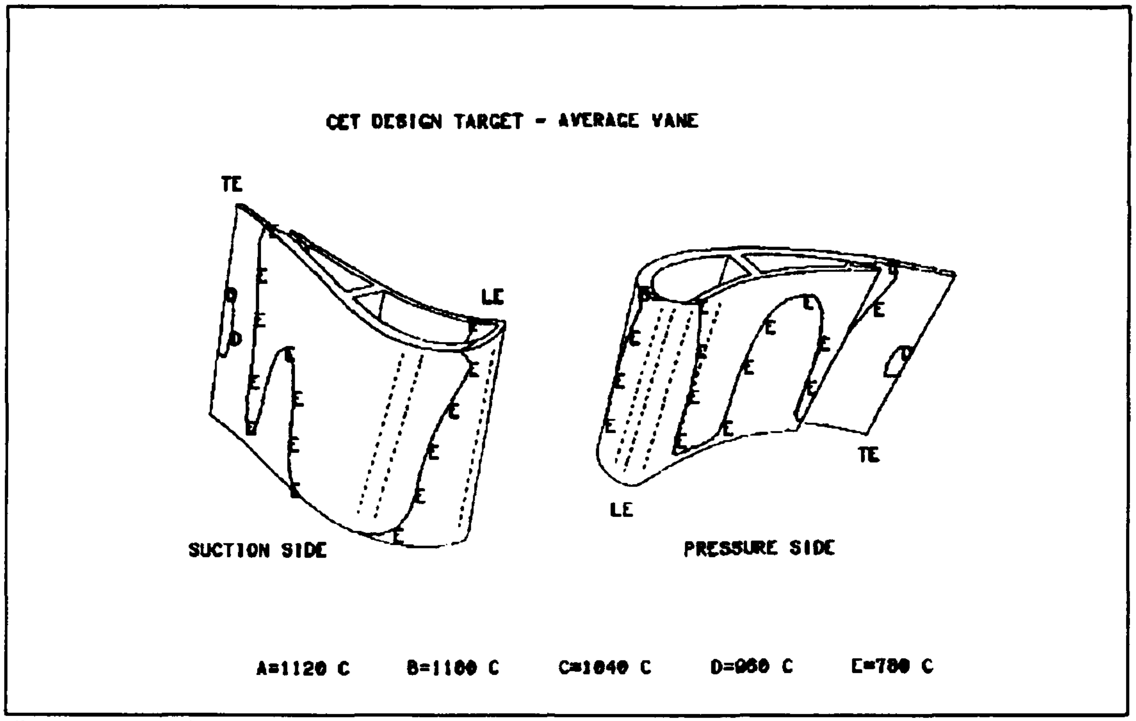
CET DESIGN TARGET - AVERAGE VANE
TE
LE
SUCTION SIDE
TE
LE
PRESSURE SIDE
A=1120 C
B=1100 C
C=1040 C
D=960 C
E=780 C

Fig 35- Results of 3D thermal analysis-Design target Average Vane

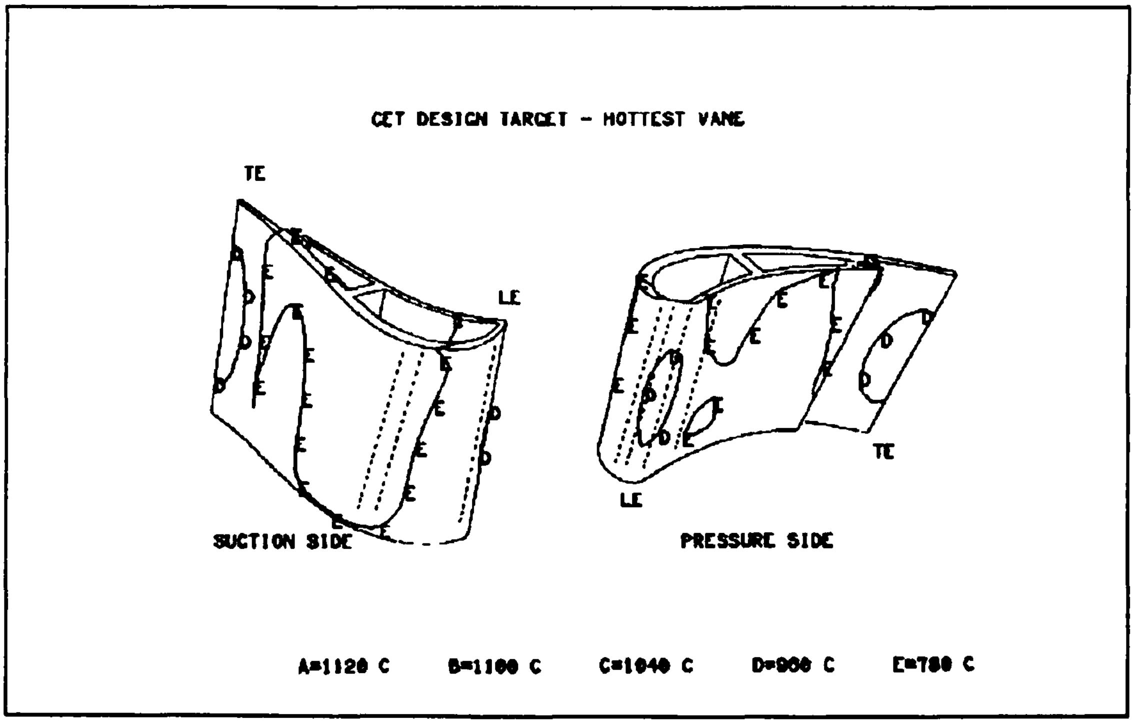
CET DESIGN TARGET - HOTTEST VANE
TE
LE
SUCTION SIDE
TE
LE
PRESSURE SIDE
A=1120 C
B=1100 C
C=1040 C
D=900 C
E=780 C

Fig 36 - Results of 3D thermal analysis - Design target Hottest Vane

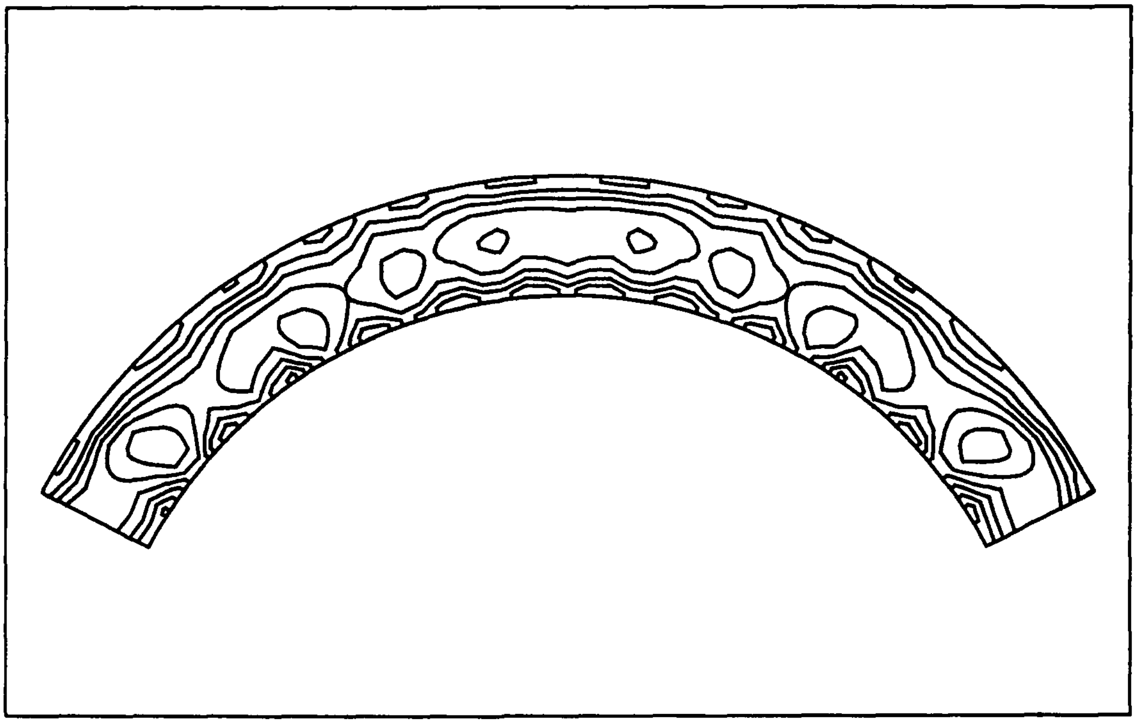

Fig 37 - Engine Demonstrator Tested Hardware : CET predictions. ΔT=100, Range=(1100÷1700 K)

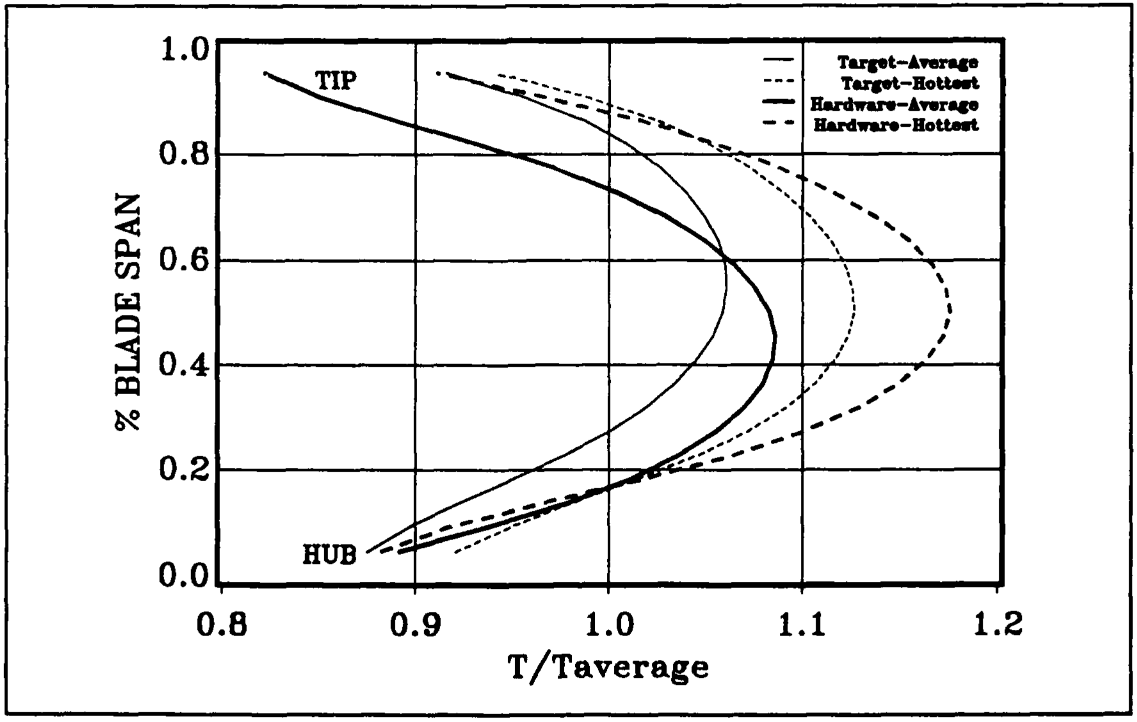

Fig 38 - CET radial profiles comparison

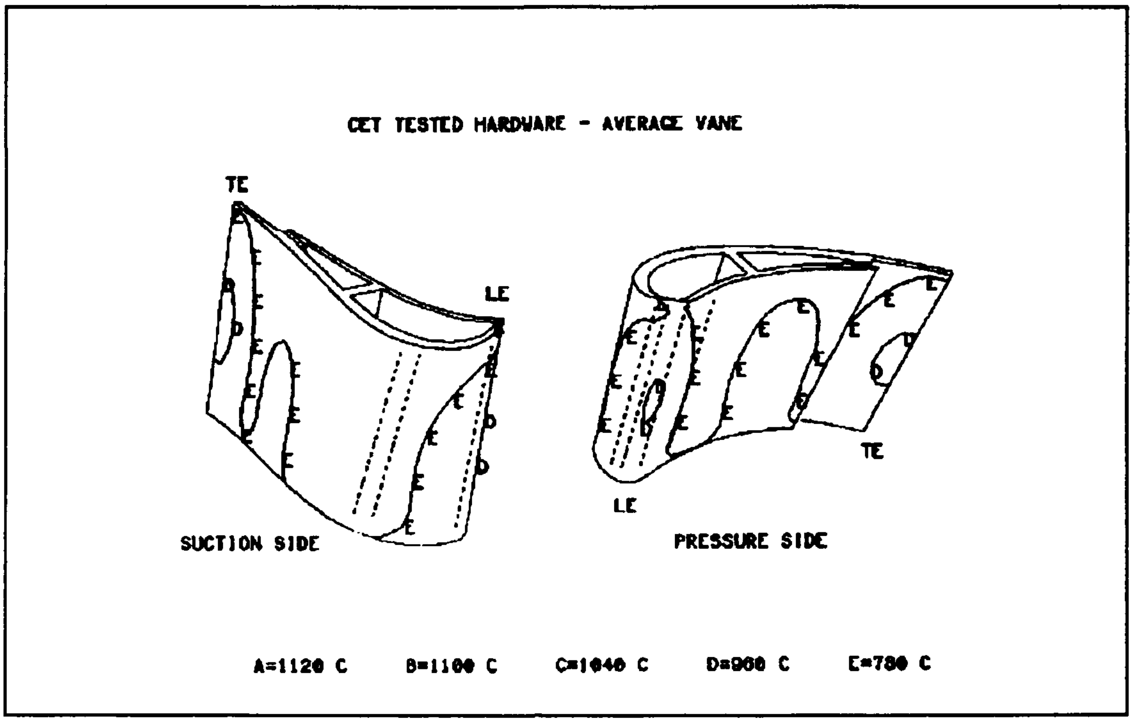
CET TESTED HARDWARE - AVERAGE VANE
TE
LE
SUCTION SIDE
LE
TE
PRESSURE SIDE
A=1120 C
B=1100 C
C=1040 C
D=960 C
E=780 C

Fig 39 - Results of 3D thermal analysis - CET Tested Hardware Average Vane

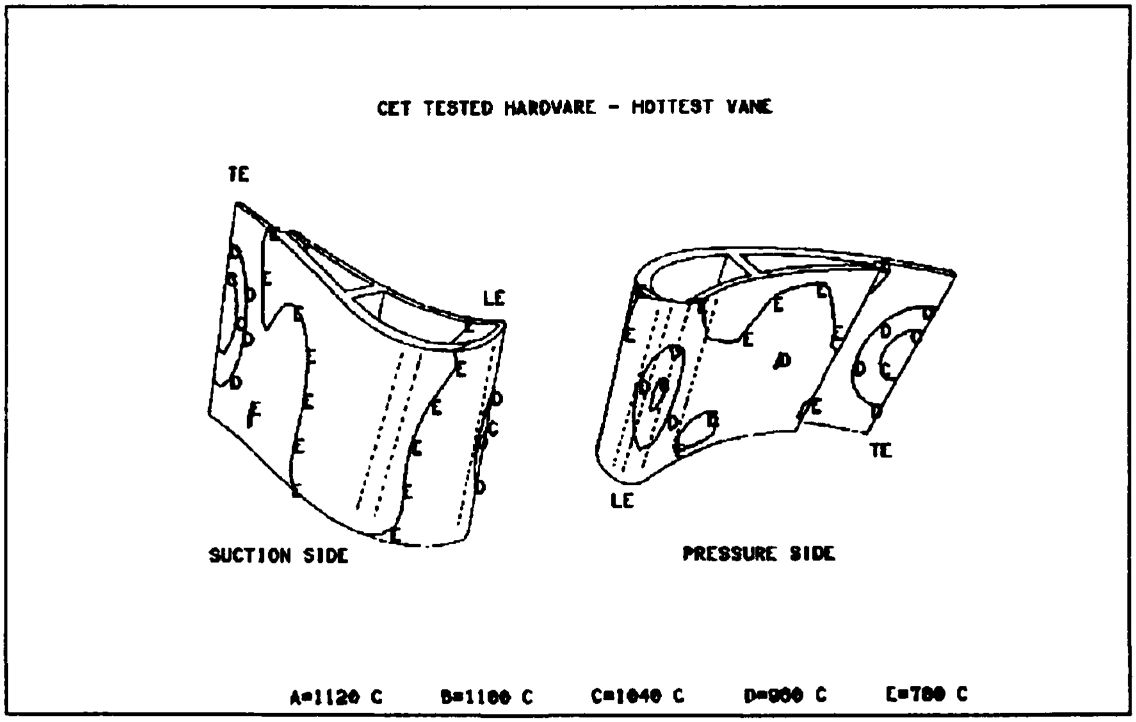
CET TESTED HARDWARE - HOTTEST VANE
TE
LE
SUCTION SIDE
LE
TE
PRESSURE SIDE
A=1120 C
B=1100 C
C=1040 C
D=960 C
E=780 C

Fig 40 - Results of 3D thermal analysis - Tested Hardware Hottest Vane

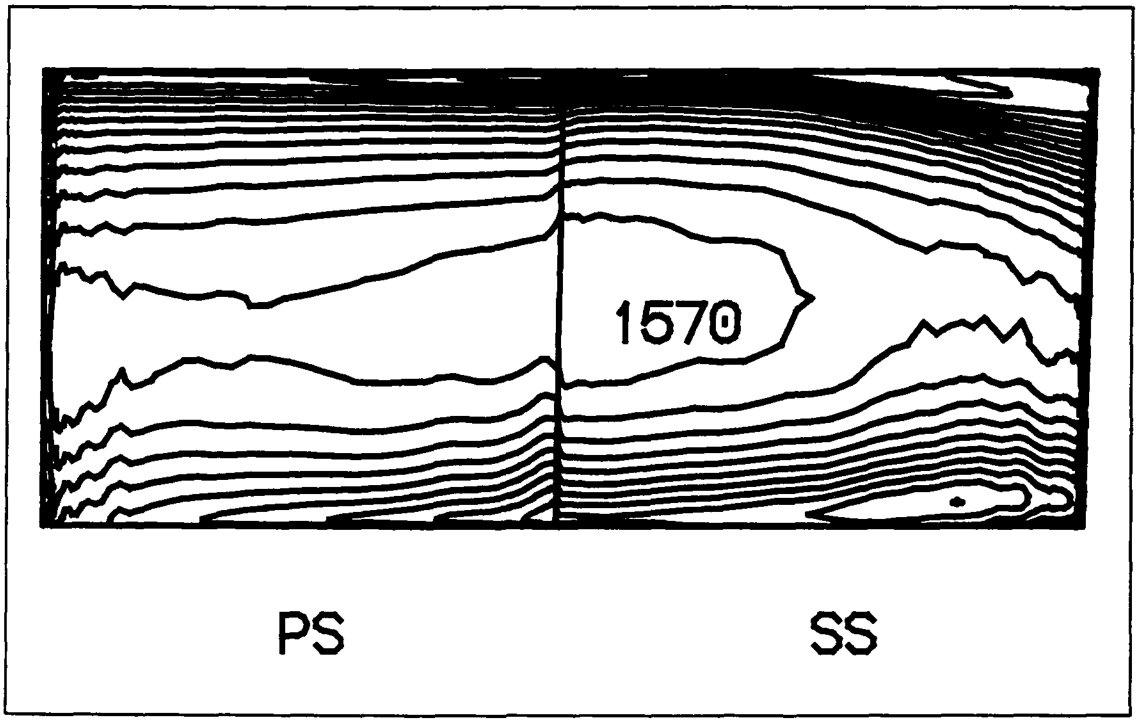

Fig 41-Gas temperature around the blade obtained by 3D Navier-Stokes analysis. ΔT=20 Range=(1250K, 1570K)

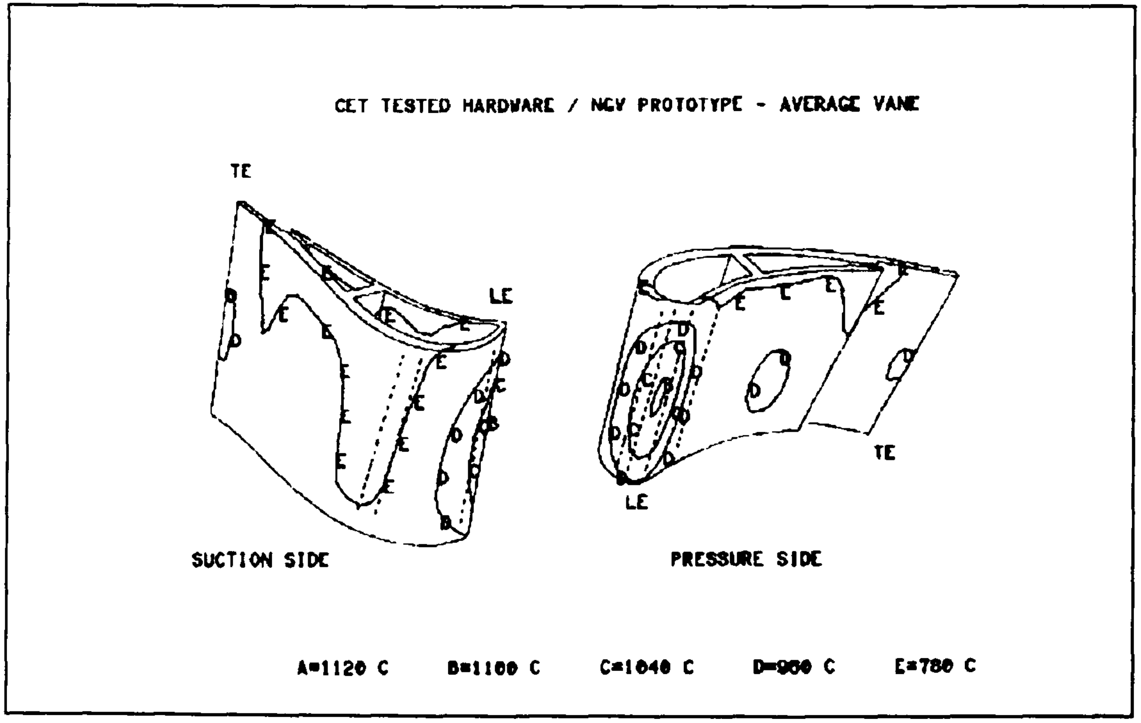
CET TESTED HARDWARE / NGV PROTOTYPE - AVERAGE VANE
TE
LE
SUCTION SIDE
LE
TE
PRESSURE SIDE
A=1120 C
B=1100 C
C=1040 C
D=960 C
E=780 C

Fig 42 - Results of 3D thermal analysis - NGV Prototype Average Vane

Acknowledgement

The authors are indebted to Prof. Claus Sieverding and Prof. Tony Arts of the Von Karman Institute for their assistance in the evaluation of CT2 cascade rig results and to many colleagues of the Alfa Romeo Avio Experimental Center for their work in securing the experimental data on the demonstrator engine.

References

[1] Arts T., Van Den Braembussche-"Program for the time-dependent solution of the transonic blade-to-blade calculation"-
VKI CR 1979-32

[2] Arts T., 1988 - " Three Dimensional inviscid Flow Calculations in Turbomachinery Components".
16th ICAS Congress

[3] Arts T. & Lambert J.-"Aerodynamic and thermal performances of a film cooled 2D nozzle guide vane"-
VKI CR 1989-15/TU Feb. 1989.

[4] S.Colantuoni, P.Di Martino, D.Carbone-"Turbine Blade heat transfer evaluation by modified version of STAN5. Comparison with experimental data"- CMEM 89, 23-26 May 1989-Capri(Italy).

[5] D.K.Hukherdjee,Switzerlandy-"Film Cooling with injection through slots"- VKI, Lecture series 82, Febr.22-26, 1982.

[6] Kerker,D.M., and Tabakoff,W.-"Heat transfer by a square array of round jets impinging perpendicular to a flat plate surface including the effect of spent air"- J.Eng.Power, Vol.92, N.°1, Jan.1970, pp.73-82.

[7] Y.Becke, ACEC Charleroi, Belgium, "Impingement cooling-A Review", VKI Lecture series 83, January 12-16, 1976.

[8] Kreith,F.E.-"Principles of heat transfer"- Second ed. International text book Co.1967.

[9] Arts.T and Lamber de Rouvroit M.-"Aerodynamic testing of the Alfa Romeo HP Turbine nozzle blade"-
VKI CR 1990-09/TU, January 1990.

[10] S.Colantuoni, A.Terlizzi, F. Grasso-"A validation of a Navier-Stokes 2D solver for transonic turbine cascade flows"- AIAA-89-2451

[11] Rolls-Royce plc -"Thermal indicator paint training course itinerary and course notes"

APPENDIX A

- Relationship to calculation of effectiveness η for tangential injection from slot

$$B = (\mu c/\mu\infty \ Reb)^{-0.25} \frac{x}{m\ b}$$

$$\eta = 1 \qquad \text{if } B<1$$

$$\eta = \frac{1.9\ Pr^{2/3}}{1 + 0.525\ B^{0.47} \frac{Cp\infty}{Cpc}} \qquad \text{if } 1<B<4$$

$$\eta = \frac{1.9\ Pr^{2/3}}{1 + 0.329\ B^{0.8} \frac{Cp\infty}{Cpc}} \qquad \text{if } B>4$$

Kercher-Tabakoff [5] Coefficients of the relationship for impingement realized through a square array of circular holes.

For $300<Red<3000$

$$k = -0.00145\ (S/d)^2+0.04284(S/d)+0.51655$$

$$\varphi_1=\exp\{.0126(S/d)^2-0.5106(S/d)-0.2057\}$$

$$\varphi_2=\{1.+0.374\left(\frac{Wc\ Z}{Wj\ d}\right)^{0.906}\}^{-1}$$

if $3000<Red<30000$

$$k = -0.00252\ (S/d)^2+0.06849(S/d)+0.50699$$

$$\varphi_1=\exp\{.0260(S/d)^2-0.8259(S/d)-0.3985\}$$

$$\varphi_2=\{1.+0.4696\left(\frac{Wc\ Z}{Wj\ d}\right)^{0.965}\}^{-1}$$

The Aerodynamic Effect of Coolant Ejection in the Leading Edge Region of a Film-cooled Turbine Blade

A. Beeck
ABB Power Generation Ltd, CH-5401 Baden, Switzerland
L. Fottner
University of the Armed Forces Munich, D-W-8014 Neubiberg, Germany
E. Benz, S. Wittig
University Karlsruhe, D-W-7500 Karlsruhe, Germany

Summary:

Air ejection for film-cooling affects the aerodynamic behavior of the blading by the mixing of the coolant with the mainstream as well as by the interaction between the jet and the boundary layer.

The main objective of this investigation is to receive more information on the flow field in the leading edge region. The focus is the aerodynamic behavior of ejection in the stagnation region.

A Navier-Stokes code was used to evaluate the flow field considering the ejection.The calculated results are compared with experimental investigations. Cold gas experiments were conducted in a cascade wind tunnel on three large scaled turbine blades with slotted leading edges. The mass flux ratio was varied from 0.0 to 2.5 to simulate film-cooling effects. A high resolution of the flow field, especially close to the wall (nearest distance: 50 microns) was achieved by Laser-2-Focus measurements. The pressure distributions on the blade surface and in the wake were measured in order to determine the overall behavior of the blades quantitatively while oil flow patterns and Schlieren pictures provide qualitative results.

The experimental results show, that the strong pressure gradient near the stagnation point affects the velocity distribution of the jets. This non-uniformity produces additional aerodynamic losses. To take these effects into account for the Navier-Stokes calculation a multi-block grid was used to model the flowfield in the ejection holes and in the mainstream. Thus the experimental and numerical results show a good agreement.

List of symbols

b	slot width
e_m	distance for wake traverse measurements
h	blade height = span
l	chord length
$\dot{m}$	mass flow
M	blowing ratio = $(\rho_c w_c)/(\rho_1 w_1)$
Ma	Mach number
p	pressure
P	power
Re	Reynolds number
s	surface coordinate
t	pitch of blade row
T	temperature
Tu	turbulence intensity
u	circumferential coordinate
w	velocity
x,y,z	profile coordinates, bitangential
β	flow angle
γ	slot angle
Γ	circulation
Δ	difference
ζ	loss coefficient
κ	ratio of specific heats
ρ	density

Indices:

1	cascade inlet
2	cascade outlet
c	cooling air
DS	pressure side
is	isentropic
k	tank
kin	kinetic
s	stagger
SS	suction side
t	total
th	theoretic

1. Introduction

The best way to minimize pollution is to minimize the specific fuel consumption of a gas turbine. This leads to a demand for a rise of the thermal efficiency. It can be achieved by increasing the turbine entry temperature (TET). The maximum TET is limited by the capability of materials to withstand high gas temperatures. Currently filmcooling is widely used to maintain blade and vane temperatures at acceptable temperatures. However, the filmcooling influences the aerodynamic loss behaviour of the turbine stage and this in turn affects the thermal efficiency of the gas turbine. Especially in the stagnation region, where the cooling air has a velocity component against the mainstream, because of the relatively high momentum, additional aerodynamic losses occur.

Only a few studies on the effect of coolant ejection in the vicinity of the leading edge (L.E.) on the aerodynamic losses of film cooled turbine blades are available in the literature. This study shows a very detailed investigation of the increased losses due to coolant ejection in the L.E. region, which is described in more detail in Beeck (1992) [1]

The purpose of this study is to get a closer look in the aerodynamic behaviour of the flowfield around a film cooled turbine blade especially in the stagnation region and in the vicinity of the jet location.

The experimental results of this cold air study of a 2D-Cascade are compared to numerical results of a 2D-Navier-Stokes calculation.

2. Experimental Setup

The high pressure turbine cascade was designed for two dimensional turning of 104.7° for an isentropic Mach number of $Ma_{2th} = 0.95$. The Reynolds number was $Re_{2th} = 6.95 \cdot 10^5$. The cascade consists of three large scaled turbine blades (Fig. 1).

Table 1 gives the aerodynamic and geometric data.

Ma_1	=	0.37	l	=	250 mm
Ma_2	=	0.95	t/l	=	0.714
Re_1	=	$3.7 \cdot 10^5$	b_s	=	73°
Re_2	=	$6.95 \cdot 10^5$	s/l_{SS}	=	0.02
β_1	=	133°	s/l_{DS}	=	0.03
β_2	=	28.3°	β_s/l	=	0.01018
$\Delta\beta$	=	104.7°	γ_{SS}	=	55°
			γ_{DS}	=	70°
			h	=	300 mm

Table 1 Design Data of the Turbine Cascade

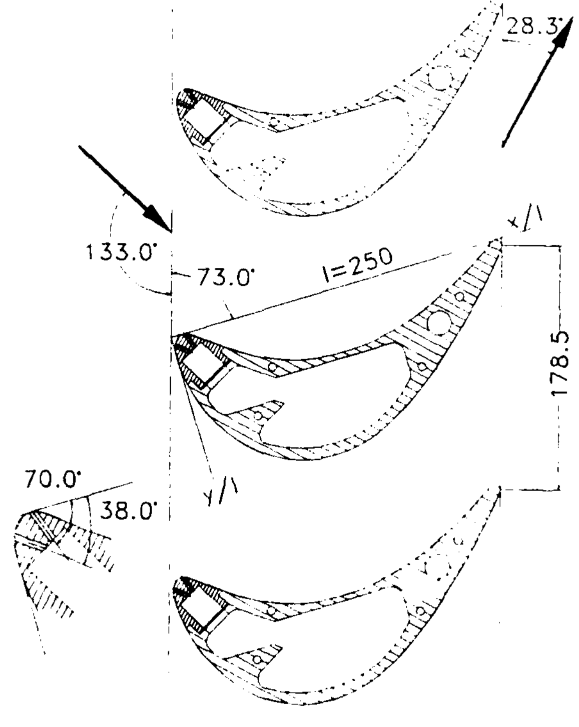

Fig. 1 High pressure turbine cascade

To achieve a constant inlet area pressure distribution, adjustable guide vanes are mounted at the cascade end. Thus an equal flow field coud be assumed for all three blades (Fig. 2). The centre blade was equipped with tappings in the midspan region of the blade. It also had a removable leading edge for a study of different nose geometries and cooling configurations, which will not be discussed here.

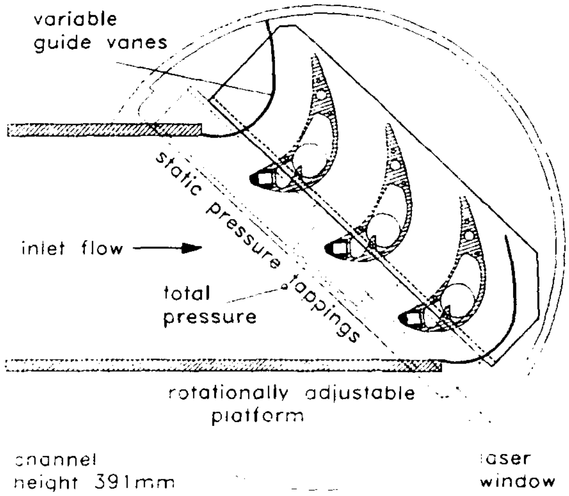

Fig. 2 Test section

Glass windows were installed in the front part of the side walls of the cascade for Schlieren observations and laser anemometry. The cooling air supply was fitted in the rear-part of the side walls. The leading edge region was fitted with slots in spanwise direction close to the stagnation line as a 2D model of ejection holes.

The experiments were carried out in the high speed cascade wind tunnel of the University of the Armed Forces Munich (Fig. 3). This facility operates continuously and allows the independent variation of Mach number and Reynolds number by changing the pressure level of the surrounding tank (Scholz et al. (1959), Sturm et al. (1985), [2,3]) A turbulence grid was installed upstream of the cascade in order to produce a design turbulence level of about 8% (Kiock et al. (1985) [4]).

The mainstream air has a total temperature of 313 K, while the cooling air temperature was about 30 K lower. The cooling air is delivered from a separate screw compresser. The mass flow rate was measured by an orifice plate (DIN). The uniform cooling air distribution over the three blades was controlled by adjustable resistance in the cooling air entry of each blade via total pressure tappings within the hollow blades.

The loss coefficients of the cooling air slots were determined by measuring the velocity profile at the slot outlet with laser anemometry and the comparison with the theoretical average velocity.

For wake traverse measurements, a wedge probe was used (Scholz (1956), Römer et al. (1988), [5,6]) at 32% of the chord axially downstream of the trailing edge plane. From the surface pressure distribution, the surface Mach number

UniBw München
Institut fur Strahlantriebe

High-Speed Cascade Wind Tunnel

1985

test section data:		supply units:		wind tunnel data:	
· Mach number	$0.2 \leq Ma \leq 1.05$	· evacuating unit :	P_1 = 30 kW	· AC electric motor	P = 1300 kW
· Reynolds number :	$0.2 \cdot 10^6 m^{-1} \leq Re/l \leq 16.0 \cdot 10^6 m^{-1}$		P_2 = 20 kW	· axial compressor :	6 stages
· degree of turbulence :	$0.4\% \leq Tu_1 \leq 7.5\%$	· boundary layer suction :	P = 155 kW	air flow rate	V_{max} = 30 m³/s
· upstream flow angle :	$25° \leq \beta_1 \leq 155°$	(centrifugal compressor)		total pressure ratio :	$(p_{t1}/p_K)_{max}$ = 2.14
· blade height	300 mm	· additional air supply	P = 1000 kW	number of revolutions :	n_{max} = 6300 min⁻¹
· test section height :	235 mm - 510 mm	(screw compressor)		tank pressure	p_K = 0.04 - 1.2 bar

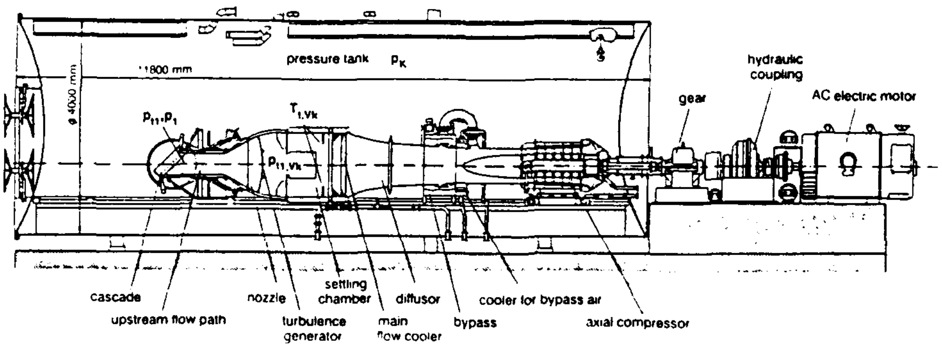

Fig. 3 High speed cascade wind tunnel

distribuiton was evaluated with the assumption of constant total pressure.

The flow field around the leading edge region was measured in detail by use of an Laser Transit Velocimeter (Schodl (1974), [7]). This measuring technique is non intrusive and allows measurements very close to the wall (about 50 microns) as well as in regions with large velocity gradients i.e. in the jet boundary, near the stagnation point or in the region between reverse flow and main stream.

Due to the small probe volume (0.17x0.2x0.008 mm^3) a very high resolution of the flow field within the jets, the stagnation area, the boundary layer, and even in recirculation regions could be achieved.

Schlieren observations helped to determine the path of the cooling air with different blowing ratios. The number of LTV measuring points could thus be concentrated at interesting parts of the flow field.

The surface flow on the blade and the endwalls was observed by means of oil flow patterns. The mentioned measuring techniques together gave a good overview on the aerodynamic behaviour of the film cooled turbine cascade (Beeck (1992), [1]).

3. Test Program

The LTV, Schlieren (S) and oil flow (OF) experiments were carried out at three different blowing ratios and without blowing as reference. The cascade inlet values instead of the outlet values were fixed at the design point, because the L.E. was the investigated region. Pressure distribution (PD) and wake traverse (WT) measurements were conducted at higher Mach numbers as well. Table 2 gives the combination of the experimental data.

4. Experimental Results

The aerodynamic behaviour of the cascade with simulated leading edge film cooling is discussed on the basis of LTV vector field and flow line plots and surface Mach number distributions.

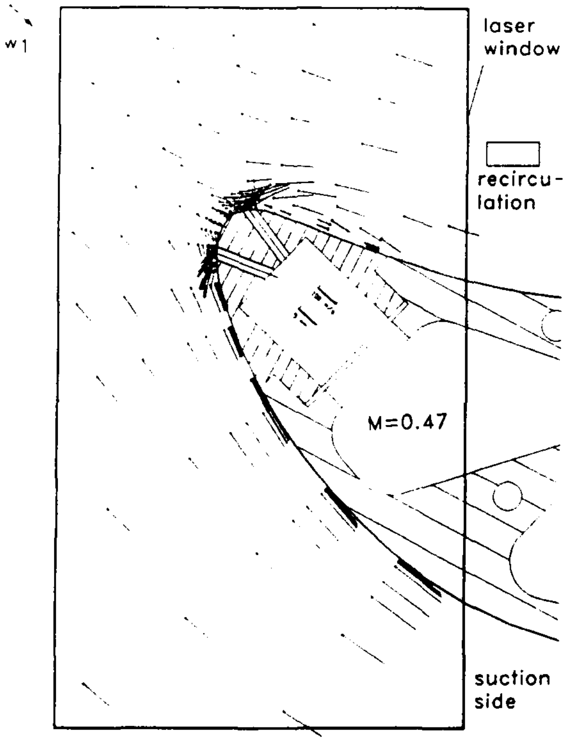

Fig. 4 Flow fiel in the leading edge region at M=0.47

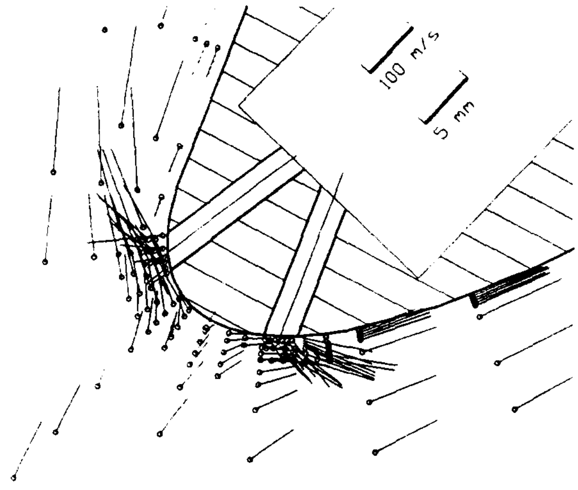

Fig. 5 Zoomed view of the flow field at M=0.47

Ma_1	Ma_2	Re_{2th}	M	PD/WT	LTV/S/OF
0.407	0.712	610000	0	X	X
0.380	0.665	586000	0.47	XX	XX
0.378	0.671	591000	0.76	X	X
0.379	0.694	610000	1.14	XX	XX
0.425	0.934	691000	0.47	X	
0.418	0.923	687000	0.76	X	
0.396	0.901	695000	1.14	X	

X: accomplished XX: discussed herein

Table 2 Test Program

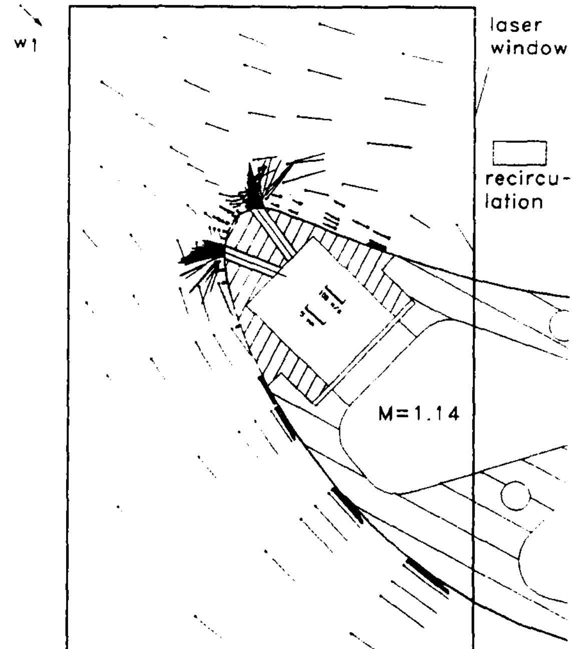

Fig. 6 Flow field in the leading edge region at M=1.14

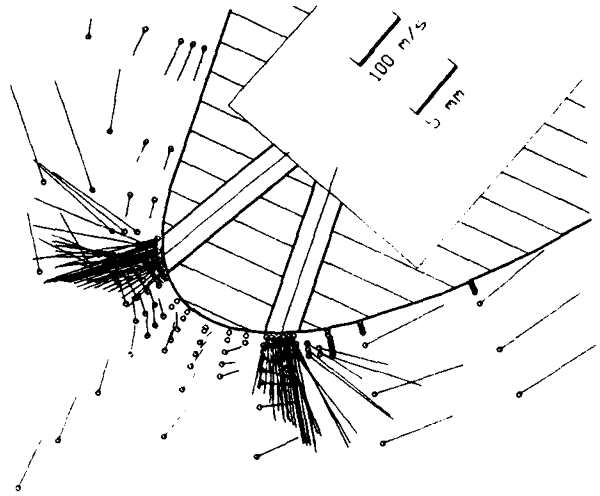

Fig. 7 Zoomed view of the flow field at M=1.14

LTV Results with the small blowing ratio M = 0.47 are shown in Fig. 4. The frame represents the glass window for laser measurements. The vectors are starting at the small dots. Pay attention to the boundary layer profiles with a nearest wall distance of about 50 microns. Even the small blowinig ratio leads to diversion towards the mainstream, so a small stationary recirculation area (dottet region) could be measured behind the pressure side slot. An important result of this high resolution field measurement are the deformed velocity profiles of the jets. This is due to the very strong pressure gradient in the vicinity of the stagnation point. The inboard jet boundary feels a higher back pressure than the outboard jet boundary, because the mainstream is deflected at the stagnation point and then decelerates again as it meets the jet. So the static pressure is increased compared without blowing. On the other hand, the static pressure decreases in the recirculation area in dependance of its extension and thus the outboard jet boundary is exposed to a lower back pressure. The jet orifice with blowing feels a higher pressure gradient than without. A closer look to this phenomena is given in Fig. 5.

The higher blowing ratio M = 1.14 (Fig. 6) leads to a bigger recirculation flow field behind the pressure side slot (dottet area). The reason is the stronger jet penetration due to the augmented jet momentum. The detailed LTV measurements within the jets show a similar behaviour concerning the deformed velocity distributions right at the slot outlets. Behind the suction side slot also a small recirculation appears. This is shown enlarged in Fig. 7. The aerodynamic losses increase by the recirculation areas as clearly can be seen in flow line pictures (Fig. 8). These loss producing fields appear in the surface Mach number distribution as well, because of the diminished blade load which is proportional to the area between the pressure side Mach number distribution and the suction side Mach number distribution at same x/l location. This is represented in Fig. 9 as an increase of local surface Mach number between s/l = -0.07 and s/l = -0.6 with higher blowing ratios.

The loss coefficients are determined with inclusion of the coolant energy in the inlet plane (Kiock et al. (1985), [8]). Here is assumed, that the total temperature of mainstream, coolant and mixed out flow are approximately equal. The kinetic energy loss coefficient ζ_{kin} is defined:

$$\zeta_{kan} = 1 - \frac{\left[1-\left(\frac{p_2}{p_{t2}}\right)^{\frac{\kappa-1}{\kappa}}\right]\cdot\left[1+\frac{\sum\limits_{i=SS,DS}\dot{m}_{c,i}}{\dot{m}_1}\right]}{\left[1-\left(\frac{p_2}{p_{t1}}\right)^{\frac{\kappa-1}{\kappa}}\right]+\sum\limits_{i=SS,DS}\left[1-\left(\frac{p_2}{p_{c,i}}\right)^{\frac{\kappa-1}{\kappa}}\right]\cdot\frac{3\cdot\dot{m}_{c,i}}{\dot{m}_1}}$$

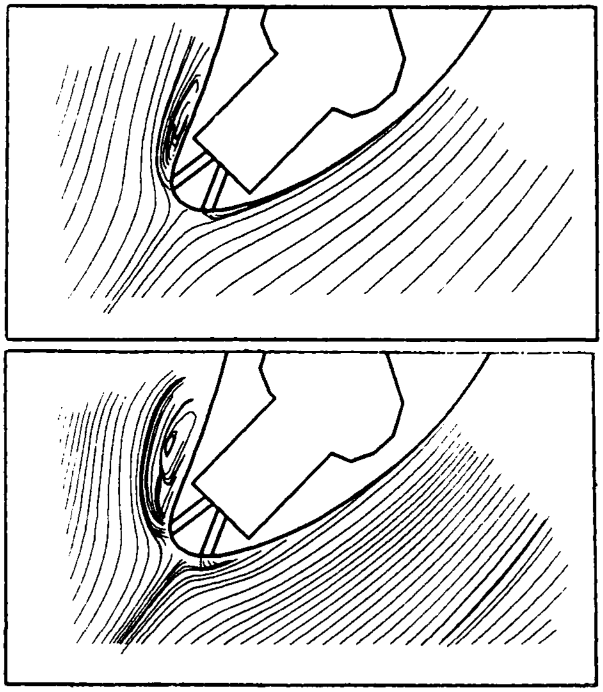

Fig. 8 Flow lines at M=0.47 (top) and M=1.14 (bottom)

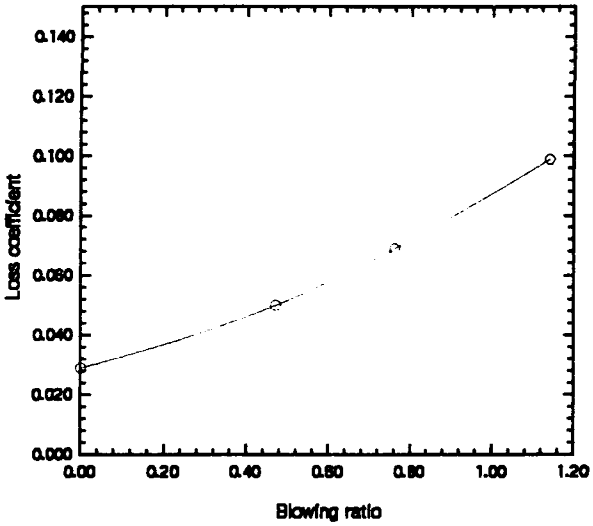

Fig. 10 Loss coefficient vs. blowing ratio

The total pressure of the jets $p_{tc,i}$ is evaluated by means of the velocity distribution of the jets at the outlets, the static pressure evaluated from the pressure distribution for the jet location and the total temperature which is measured within the blade plenum. The average value of the LTV measured velocity vectors is mass weighted. Thus losses within the plenum and within the slots are not includet in the kinetic energy loss coefficient. Fig. 10 shows the loss coefficient vs. blowing ratio. The aerodynamic losses increase with the blowing ratio because of the increase of the jet momentum component against the mainstram direction. Additional losses occur because of the deformed jet velocity distribution which introduces additive rotational flow. The accelerated flow in the turbine augments the stresses in this shear layer and the shear layers of the jet boundaries. These results clearly show, that blowing with high momentum or with a strong velocity component against the incoming flow is to be avoided. Even in modern turbine cooling design often a high cooling jet momentum is provided to ensure a proper convective heat transfer within the blowing holes. The cooling holes are often angled in spanwise direction to minimize the counter flow component of the jets. However the above mentioned high momentum and the strong pressure gradient in the L.E. region raises the aerodynamic losses. The principal mechanism which happens to the jet in such a configuration is shown in fig. 11. Keep in mind, that all occuring velocity gradients introduce loss producing rotational flow.

5. Numerical Method

The numerical method used here is described in detail in Benz et al. (1992), Noll (1992), Noll et al. (1992), [8,9,10], here only a brief overview is given.

The numerical code can be used to solve the two- and three-dimensional Navier-Stokes-transport equations in a body-fitted curvilinear coordinate system. For turbulent flow calculations the Reynolds-averaged equations are solved. The turbulence model used here is the well known k-ε-model in the standard form with the wall-function approach.

By the finite volume discretization method the differential equation is transformed into an algebraic equation. The convective terms are discretized by the Monotonized-Linear-Upwind-scheme

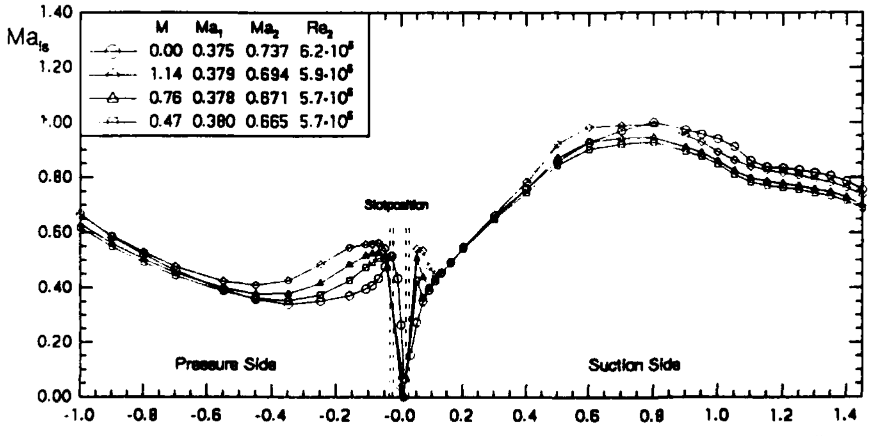

Fig. 9 Surface Mach number distribution

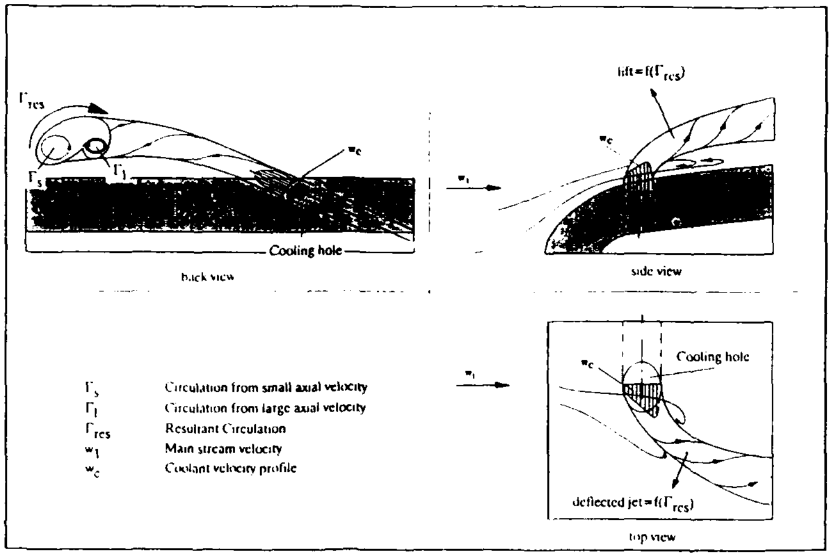
Γ_{res}
Γ_s
Γ_l
w_c
Cooling hole
back view
w_1
lift = $f(\Gamma_{res})$
w_c
side view
Γ_s Circulation from small axial velocity
Γ_l Circulation from large axial velocity
Γ_{res} Resultant Circulation
w_1 Main stream velocity
w_c Coolant velocity profile
w_1
w_c
Cooling hole
deflected jet = $f(\Gamma_{res})$
top view

Fig. 11 Mechanism of jet rotation in a region with large pressure gradient

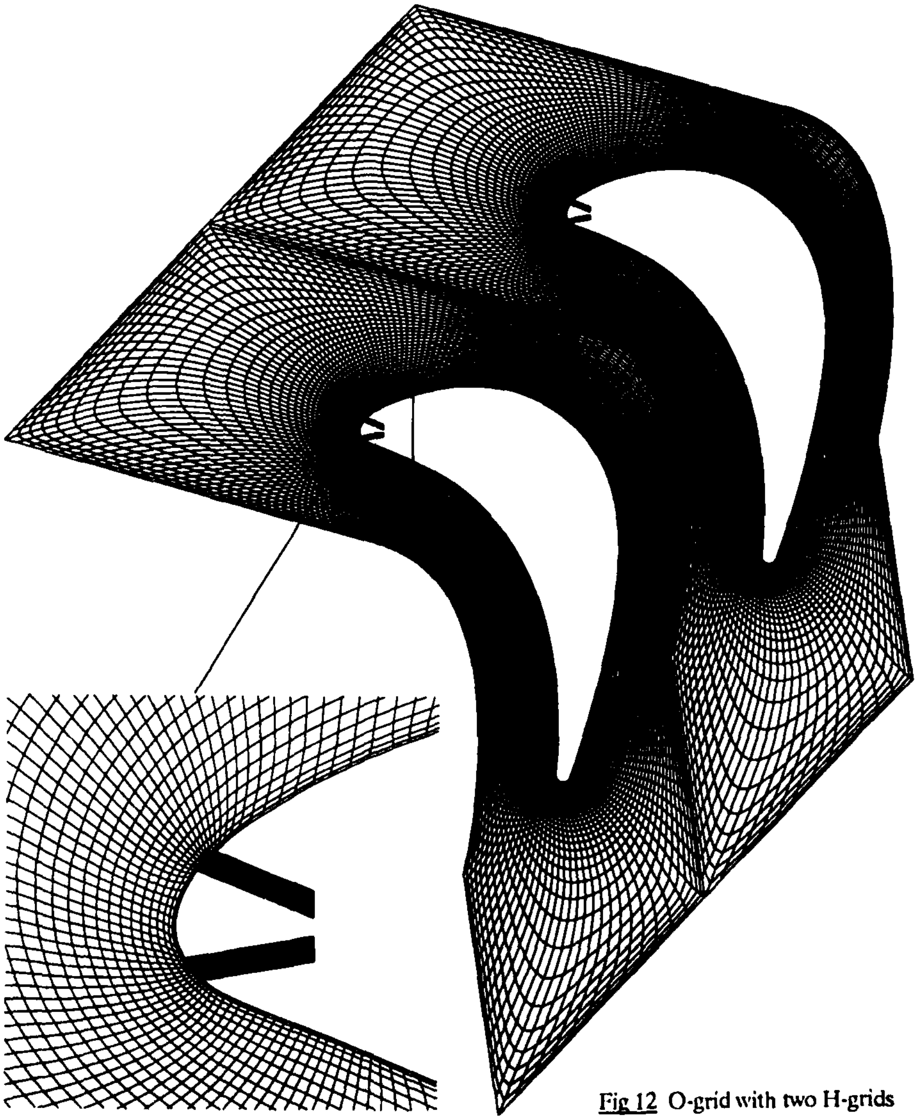

Fig 12 O-grid with two H-grids

(MLU) (Noll (1992), [10]). For the solution of the system of the finite difference equations the generalized conjugate gradient (CG) iterative procedure, decribed in detail by Noll et al. (1992) [11], was employed. Various SIMPLE-like velocity-pressure coupling methods are available. In the present study the one step corrector-predictor SIMPLEC-algorithm (Doormal et al. (1984), Doormal et al. (1987), [12,13]) for compressible flows is used. To prevent decoupling of the velocity and pressure field on co-located grids a flux-correction method similar to the method proposed by Rhie and Chow (1983) [14] is incorporated.

In the code a multiblock technique is applied which allows one to subdivide a complex computational domain into simple blocks. This domain-decomposition or grid-attaching method, which can be incorporated relativly simple in every CFD-code, is discussed in detail by Benz et al. (1992) [9]. For the present study the computational domain includes the film cooling slots. The reason is that for low-mass-flux-ratios the velocity profile at the slot exit is not known a priori. Inside the slot a realistic guess of the boundary condition for the prediction is relatively simple.

Therefore a single O-grid around the blade with two attached H-grids for the discretization of the film cooling slots is used (Fig. 12). The O-grid is generated by solving the Poisson-equations, while the generation of the two H-grids is done by a simple algebraic method. The three grids comprise approximatly 10000 points, while the number of the gridpoints of the O-grids is 211x42. In Fig. 12 the fine discretization of the leading edge is seen.

5.1 Boundary conditions

At the turbine blade inlet a constant velocity of 130 m/s was specified. The static pressure was set to 18650 Pa. In the predictions the inlet Mach-number was 0.37 for all calculation in contrast to the experiments were the inlet Mach-number differs for the different mass-flux-ratios. In the slots a uniform velocity profile according to the mass-flux-ratio M=1.14 and M=0.47 was specified. The turbulence intensity was assumed to be 5 % at the turbine inlet and at the inlet of the slots.

6. Comparison of Experimental and Numerical Data

Flowline patterns at the small blowing ratio show less disturbance of the L.E. flow field in the calculated case (fig. 13). This is due to the difference of the two dimensional calculation and three dimensional effects, which occure even in a two dimensional cascade (see fig. 8 top). The slots do not extend the entire span to the sidewalls. Therefore a small region exists near the wall, where the mainstream bypasses the cooling film and mixes into the recirculation zone. The thickness of the recirculation regions normal to surface are larger in the measurement due to 3D effects as well. The agreement is better at the high blowing ratio of M=1.14 (fig. 14, fig. 8, bottom). The calculated flowlines show recirculation regions at the pressure side slot as well as

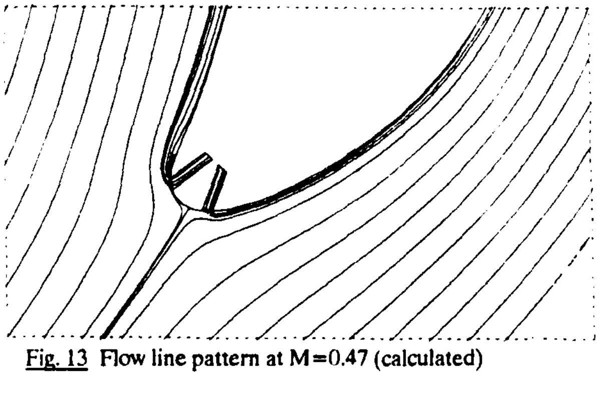

Fig. 13 Flow line pattern at M=0.47 (calculated)

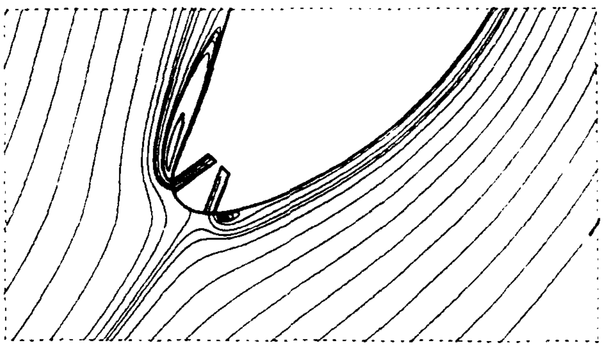

Fig. 14 Flow line pattern at M=1.14 (calculated)

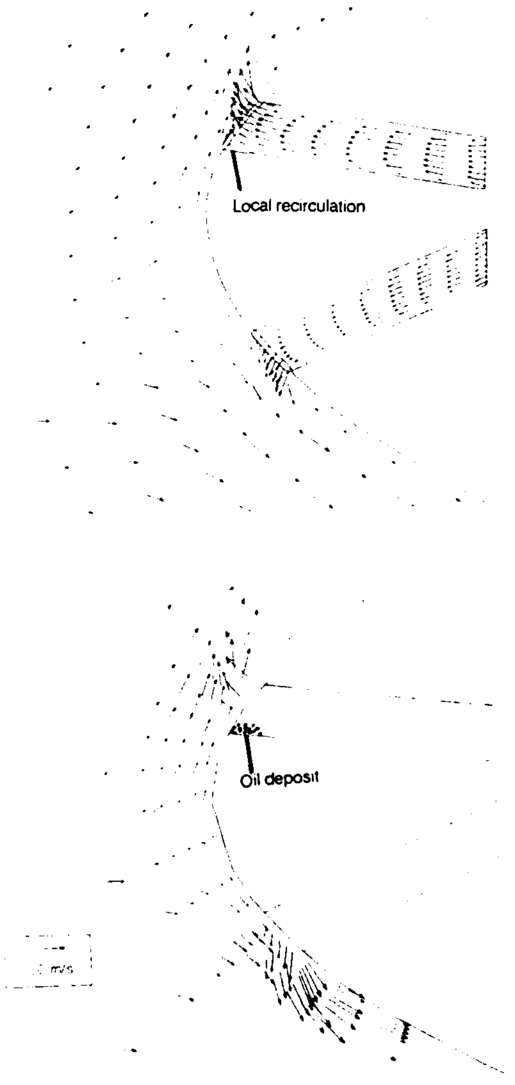

Fig. 15 Vector plot at M=0.47 calculated (top) and measured (bottom)

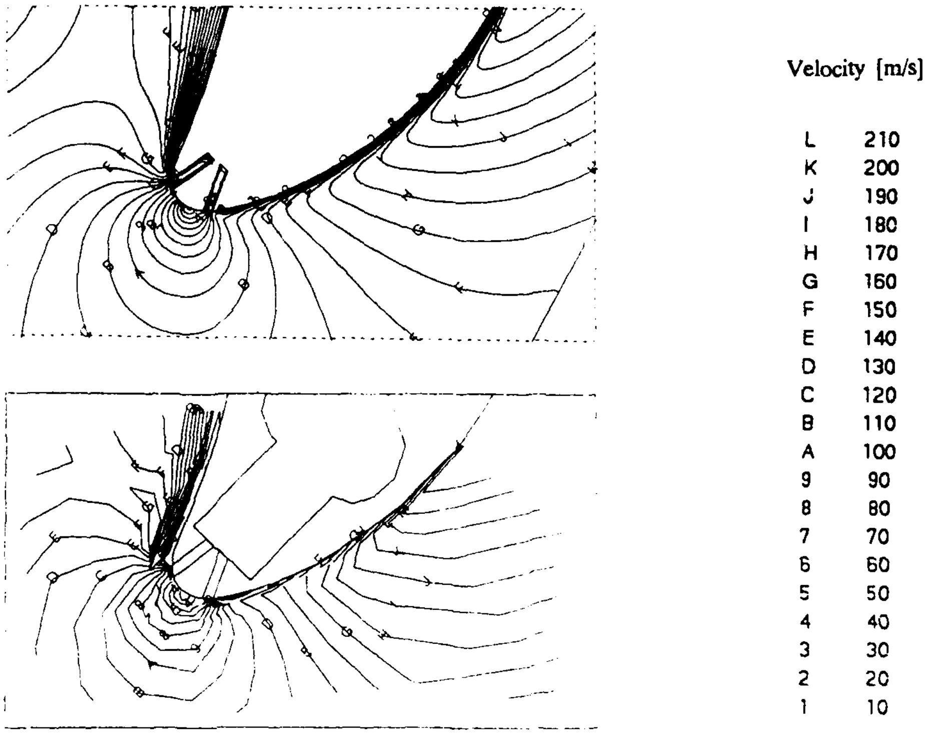

Fig 16 Isolines of the velocity field at M=0.47 calculated (top) and measured (bottom)

at the suction side slot. The extension of these regions in flowline direction is quite well calculated. The LTV measurements (fig. 15, bottom) show a very interesting result. At the small blowing ratio a significant deflection of the jets at the inner rim of the blowing holes occurs. A small recirculation zone within the holes, influenced by the pressure distribution at the blade surface is assumed to be the cause for the jet deflection. This leads to the demand to calculate the flow within the holes to take the occuring effects into account. The comparison of the vector plots (fig. 15) as well as isolines of the velocity (fig. 16) show the good agreement between calculation and measurement. This shows the necessity of a calculation within the slots with help of the mentioned multi block technique. Note the velocity profiles within the slots, especially in the vicinity of the pressure side slot, which results in a realistic (i.e. measured) flow pattern. Benz et al. (1992) [9] showed that a small recirculation zone exists in the hole on the upstream side. This can also be seen with oil flow visualisation, as a small oil concentration occured at the same region. (see fig. 15, bottom).

7. Conclusions

Very detailed measurements of the flow field in the leading edge region of a high pressure turbine cascade with simulation of film cooling ejection in the vicinity of the stagnation area show a strong interaction of the cooling jets with the mainstream. This interaction raises the aerodynamic losses. It is found, that the strong pressure gradient in the stagnation region and a jet component against the mainstream are responsible for the mentioned effects. Navier-Stokes calculations show that for a good agreement between numerical and measured results it is necessary to take the flowfield within the blowing holes into account. It is simply achieved by the multi block method. This is due to the influence of the pressure gradient in the leading edge region, which affects the outcoming flow deep inside the holes.

The following conclusions are drawn from these results. First, the blowing against the mainstream and in the region of very large pressure gradients (i.e. near the leading edge) is to be avoided. Second, numerical calculations need in the leading edge region to consider the inner part of the blowing holes.

8. Acknowledgements

The work reported in this paper was supported within research programs of the German Bundesministerium der Verteidigung. The authors greatly acknowledge the permission to publish the results.

9. References

[1] Beeck A.
Strömungsfelduntersuchungen zum aerodynamischen Verhalten eines hochbelasteten Turbinengitters mit Kühlluftausblasung an der Vorderkante
Dissertation, University of the Federal Armed Forces Munich (1992)

[2] Scholz N., Hopkes U.
Der Hochgeschwindigkeits-Gitterwindkanal der Deutschen Forschungsanstalt für Luftfahrt Braunschweig
Forschung auf dem Gebiet des Ingenieurwesens, Bd. 25, S. 79-93, (1959)

[3] Sturm W., Fottner L.
The High-Speed Cascade Wind Tunnel of the German Armed Forces University Munich
8th Symposium of Measuring Techniques for Transsonic and Supersonic Flows in Cascades and Turbomachines,Genua (1985)

[4] Kiock R., Laskowski G., Hoheisel H.
Die Erzeugung höherer Turbulenzgrade in der Meßstrecke des Hochgeschwindigkeits-Gitterwindkanals Braunschweig zurSimulation turbomaschinenähnlicher Bedingungen
DFVLR FB 82-25, Braunschweig (1982)

[5] Scholz, N.
Über die Durchführung systematischer Messungen an ebenen Schaufelgittern
Zeitschr. Flugw. 4 , Vol. 10 (1956)

[6] Römer N., Ladwig M., Fottner L.
Measuring Techniques at the High Speed Cascade Wind Tunnel of the University of the Fedreal Armed Forces Munich
9th Symposium of Measuring Techniques for Transsonic and Supersonic Flows in Cascades and Turbomachines, Oxford (1988)

[7] Schodl R.
On the Development of a New Optical Method for Flow Measurements in Turbomachines
ASME 74-GT-157 (1974)

[8] Kiock R., Dietrichs H.J., Holmes A.T.
The Boundary Layer Behaviour of an advanced Gas Turbine Rotor Blade under the Influence of Simulated Film Cooling
AGARD CP-390 (1985)

[9] Benz E., Wittig S.
Prediction of the Interaction of Coolant Ejection with the Main Stream at the Leading Edge of a Turbine Blade: Attached Grid Application, Int. Sym. Heat Transfer in Turbomachinery, August 24-28, Athen, Greece (1992)

[10] Noll B.
Evaluation of a bounded high resolution scheme for combustor flow computations
AIAA-Journal, Vol. 30 No. 1 (1992)

[11] Noll B., Wittig S.
A generalized conjugate gradient method for the efficient solution of three dimesional fluid flow problems
Numerical Heat Transfer, Vol. 20 No. 2, pp. 207-221 (1992)

[12] Van Doormaal J.P., Raithby G.D.
Enhancements of the simple method for predicting incompressible fluid flows,
Numerical heat transfer, Vol.7, pp.147-163 (1984)

[13] Van Doormaal J.P., Raithby G.D., McDonald B.H.
The segregated approach to predicting viscous compressible fluid flow,
Transactions of the ASME, Vol.109 (1987)

[14] Rhie C., Chow W.L.
Numerical study of the turbulent flow past an airfoil with trailing edge separation,
AIAA Journal, Vol.21, No.11 (1983)

Discussion

QUESTION 1:

DISCUSSOR: Y. Gogus, Havacilik Muh Bol

The large body forces caused by high revolutions and large temperature differences will cause the injected cooling air to move towards the tip. Have you checked order of magnitude of this effect?

AUTHOR'S REPLY:

No. We used a two-dimensional cascade for the tests and the calculations, so no influence of rotation can be evaluated.

QUESTION 2:

DISCUSSOR: P. Harasgama, ABB

Can the Navier-Stokes code also be used for the three-dimensional flow?

AUTHOR'S REPLY:

Yes. It is a three-dimensional code, but our experience indicates that it is necessary to use half a million points to predict the flow from holes. This takes about 10 hours on a vector computer.

On the Development of a film cooling layer

F. López Peña
T. Arts
von Karman Institute for Fluid Dynamics
Chausseé de Waterloo, 72
B-1640 Rhode Saint Genèse
Belgium

SUMMARY

The aim of this work is to experimentally investigate different aerodynamic aspects of the flow field generated when a single jet or a row of jets are ejected into a mainstream. The similarity parameters are taken such as to match those of the three-dimensional film cooling. The objective of the investigation is to deepen the understanding of the complex phenomena associated with these flows, and to provide a comprehensible and detailed data base for validation of numerical codes. To be able to obtain high resolution measurements, the study is made on large scale models. The scale enlargement obliges to use moderate velocities, so that the Reynolds number can be kept within realistic limits and the similarity preserved. The use of low air speeds prevents the analysis of compressibility effects in this study. This restriction is not as severe as one can think because, according to the related bibliography, these effects start to be noticeable at Mach numbers higher than 0.8, while the designers avoid to inject the coolant in the vicinity of shock waves to avoid boundary layer separation.

The study is made on three different models installed in a low speed wind tunnel. A first model consists of a flat plate with a single inclined circular hole. The isolated jet/mainstream interaction is investigated by means of this first test plate. The other two models present the same configuration as the first but having now a row of holes with different pitch to diameter ratios in each case. These models are useful to understand the interaction between jets and to analyze the formation and development of the coolant layer.

LIST OF SYMBOLS

C	Constant
D	Injection hole diameter
I	Momentum flux ratio ($\rho_i v_i^2/\rho_\infty v_\infty^2$)
M	Mass flux ratio ($\rho_i v_i/\rho_\infty v_\infty$)
p	Pitch (of a row of holes)
R	Density ratio (ρ_i/ρ_∞)
V	Velocity ratio (v_i/v_∞)

Subscripts.

i	At the injection
∞	At the freestream

1 INTRODUCTION

The flow generated by a jet emerging into a stream of a fluid of similar density is important in a wide range of cases of technological interest, such as VSTOL aircraft aerodynamics during take-off or landing, the mixing process taking place in combustors, the dispersal of pollutants in the environment, or the film cooling of gas turbine blades and combustion chambers. These applications among some others made this type of flows the subject of many experimental, computational and theoretical studies. Despite the similarities between the flow fields in all mentioned cases, the variation of some parameters may drastically change the character of this type of flows. This is, for instance, the case of the injection through an orifice in a wall versus the injection through a long pipe. In the former case the presence of the wall and the interaction between the injected flow and the incoming boundary layer strongly characterize the flow while in the latter case both influences simply do not exist. The existence or not of strong compressibility effects or even shock waves may also change the flow configuration. Therefore, the geometry and the flow parameters of any experimental study concerning this type of flow must be chosen in agreement with the case under investigation. Since this experimental work is conceived as a film cooling study, only this type of flow configuration will be considered here.

Thermodynamic considerations about the Joule/Brayton cycle clearly show how gas turbine efficiency and specific power increase for higher flow temperatures after combustion. Any increase in efficiency is directly translated into a reduction on fuel consumption. Increasing the specific power, or the thrust, allows the reduction of the machine size and weight, which are very important factors in aerospace applications. Improvements on blade cooling and high temperature materials are therefore the two major tools given to the designer to improve the performances of gas turbines. Thermal barrier coatings, single crystals and ceramics are some of the improvements on materials technology recently applied to turbine blades. For a given material, the working temperature of a blade is usually limited by life time considerations. Once this limiting parameter has been fixed, the mainstream temperature can be augmented only by improving the blade cooling procedure.

The idea of film cooling was initially developed in the early forties as a anti-icing system for airplane wings by ejecting hot air through slots. Very quickly, research was focused on turbine blade cooling; it is in this field that the largest efforts have been made. Studies on blade cooling and particularly on film cooling are widespread in the literature. Unfortunately, most of these investigations are only devoted to the analysis of heat transfer phenomena.

The very first approach to blade film cooling was to eject the fresh air out of the blade through slots. This provides a two dimensional cold layer giving a very high protection. Two serious drawbacks limit however the use of this method in blade cooling. Firstly, the use of longitudinal slots along the blade strongly reduces its mechanical strength. Secondly, the high thermal efficiency of this method produces a large temperature difference between the two sides of the slot, leading to an intense thermal stress, just where the mechanical weakness is located. These constraints impose rather severe limitations to the practical application of such a system in blade cooling. It is most usually restricted to the trailing edge area. This method is also commonly used in combustion chambers, afterburners, and for end wall film cooling. In all three cases the structural material is not strained as much as in the blades.

The solution commonly adopted to overcome the above mentioned drawbacks has been to replace the slots by rows of discrete holes. The flow field generated under these circumstances is not any more two dimensional but three dimensional until far away from the holes. The mainstream flow bends each jet; this produces a pair of counter rotating vortices which, when the jet separates from the wall, modifies its cross sectional shape in a kidney-like form. Each jet interacts with the wall, with the neighbouring jets, and with the main stream and its boundary layer. The flow topology corresponding to an inclined jet as well as the cold layer formation is shown in Figure 1. In any case, the flowfield becomes much more complex than it is for a two dimensional configuration. The aerodynamic properties of the flow now depend upon many different parameters, some of which are listed in Table 1. Aerodynamic aspects related to the jet-mainstream interaction and the coolant layer formation are not yet completely understood. In particular, the influence of the jet-mainstream density ratio on these phenomena has not been deeply studied yet.

As indicated in Table 1, there are a number of parameters affecting film cooling aerodynamics. It is unfortunately not possible to analyze all of them. The mainstream Reynolds number and the thickness of the upstream boundary layer are selected according to actual turbine blade operating conditions, and are kept constant. The incoming boundary layer is laminar. In a real turbine blade it can be both, laminar or turbulent, but the incoming laminar boundary layer case has been less studied than the turbulent one. The jet is kept turbulent, this being the usual case in a turbine blade. Coolant mass flux and density ratios are varied and , therefore, considered as parameters. It is particularly desired to analyze in the present study the effects of density difference between coolant and mainstream. To obtain density ratios similar to those existing in a real case, mixtures of air with a heavy gas have been considered. The use of hot wire anemometers is prevented when gas mixtures are in use. Therefore, a two dimensional Laser Doppler Velocimeter is used.

The test conditions employed in the present investigation are sumarized in Table 2. The set of selected parameters is large enough to provide a better understanding of the jet/mainstream interaction. The measurements are arranged in a set of graphs providing a data base which can be used to look into the particulars of the flow field or for validation of numerical codes. At design, the temperature of the blade material must be estimated. The accurate prediction of the metal temperature depends on a correct estimation of the external and the internal heat transfer coefficients. This estimation relies on numerical codes solving the flowfield upon the surface. The codes require detailed experimental measurements to be validated and also to verify the correctness of the used turbulence models.

2 LITERATURE SURVEY

2.1 General description of the phenomenon.

Early investigations on film cooling, e.g. Küppers [1], and Arne & Esgard [2], were mostly devoted to the two-dimensional film cooling, produced by ejection through slots. A very good literature survey on this topic was presented by Goldstein [3]. This type of film cooling is, by far, more efficient than the discrete hole coolant ejection (three dimensional in nature) and also much easier to analyze and to describe. However, with the possible exception of the trailing edge region, slots are rarely used on turbine blades due to the mechanical and thermal stress limitations already mentioned in the introduction. On the blade surface, these slots are replaced by rows of discrete holes. The generated flow field then definitely three dimensional until far away from the holes. Studies of a jet ejected normal to the wall were made by Bergeles, et al [4] and Andreopoulos and Rodi [5]. The last authors give a very good description of turbulence characteristics and flow topology. Two different mass flux regimes are shown. At low injection rates, the momentum of the injected flow is not important enough to break into the main stream, and the injected flow remains attached to the wall. If the injection rate is increased, a jet penetrating into the mainstream forms. When the jet separates from the wall, its trajectory is bent by the interaction with the mainstream. This bending produces a pair of contra- rotating vortices inside the jet which modify the jet cross sectional shape to a kidney-like form.

Some other investigations (e.g. Bergeles, et al. [6]) deal with single inclined jets. They show that, like normal jets, the jet remains attached to the wall at small mass flux ratio values. Above a given value of the mass flux ratio, the jet detaches from the wall locally and re-attaches further downstream. In contrast with the normal jet considered in Ref. [4], this type of ejection produces almost no changes in the flow-field upstream of the ejection hole. A sketch of the flow topology for a single inclined jet was given by Kruse [7]. The latter also describes how the interaction between different jets coming from a row of holes decreases their penetration into the free-stream, and how the generated vortices develop into a layer of contra-rotating parallel vortices into the film generated downstream of the emission holes (fig. 1). This layer of vortices is also described by Liess [8].

2.2 Theoretical studies.

Some semi-analytical models have been developed to analyze the vortex pair structure and its behaviour and to predict the jet trajectory. Earlier models, e.g. Durando [9], are inviscid and two dimensional; they are therefore applicable only in the far field. The model of Fearn and Weston [10] assumes the vortices to be locally two dimensional and to have a Gaussian distribution of vorticity; it uses empirical information to obtain the jet trajectory. Le Grives [11] uses this model in combination with a jet penetration model that reduces the amount of empirical data required. However, a pressure-drag empirical coefficient is used to evaluate the jet trajectory. The rate of entrainment is also predicted in this model.

The goal of most of the existing models is to predict, as accurately as possible, the jet trajectory and the entrainment rate. The use of tuneable empirical coefficients is the instrument generally used to reach this goal. As a result, frequently, the achievement of better predictions does not necessarily come from the improvement in the understanding of the phenomena. On the contrary, few works seek to deepen this understanding. Needham, et al [12, 13] and Coelho & Hunt [14] come back to the analysis of the inviscid flows, in an attempt to determine if an inviscid mechanism exists for the deflection of a jet in cross flow. In the study of Needham, the jet is considered to emerge from a pipe inclined to the main flow while in the case of Coelho & Hunt the jet is considered to emerge normally to a plane wall. A small disturbances treatment of an inviscid three dimensional vortex sheet model is applied. An inviscid mechanism for the deflection of the jet is found in this way. Such a mechanism exists only when the cross flow has a velocity component in the jet direction. Therefore, in the case of a jet normal to the cross flow, there is no inviscid mechanism for the jet deflection. These works also show that the jet-crossflow interaction already begins in the interior of the injection pipe. The correct shape and the entrainment of the jet cannot possibly be predicted by inviscid models. In the model of Coelho & Hunt [14] these jet features are restored at the expense of the model simplicity by introducing an entraining vortex sheet.

Higuera & Martinez Sanchez [15] model the initial bending of turbulent or laminar jets into cross flows without the use of any empirical parameter. They use Landau's self-similar solution for a point source of momentum (Batchelor [16]) and, after expanding the solution in series, they introduce the effect of the cross flow as a perturbation. The turbulent viscosity is assumed to be constant in this model.

All of the above mentioned models are valid only for jets which are much stronger than the cross flow. In the opposite case, weak injection into a strong cross flow, it is possible to use the boundary layer equations and introduce the injection as a perturbation. This approach does not consider the strong crossflow-injection interaction taking place inside the injection pipe in such cases. In the case of film cooling and in any other case where the jet-to-mainstream velocity ratio is of order unity, no simplification can be applied. In such cases the full three-dimensional form of the Navier Stokes equations must be solved, at least in the vicinity of the injection site. Such a procedure should rely on numerical calculations involving strong computer requirements.

2.3 Experimental Studies.

Most of the experimental studies related with film cooling are related to the heat transfer analysis. Aerodynamic investigations directly related with the film cooling process rarely appear in the technical literature. Only flow visualizations and partial aerodynamic measurements are often used as illustrations for experimental studies on heat transfer.

The published experimental works on the aerodynamics of jets emerging from a wall into a cross flow are, so far, mainly devoted to the case of injection normal to the cross flow. An early example is the article by Keffer and Baines [17], where the presence of the pair of contra-rotating vortices is already reported. Kamotani and Greber [18] not only confirm the existence of the vortex pair, but also report that these vortices can dominate the flow-field far downstream. Andreopoulos and Rodi [5] made a detailed turbulence study and an aerodynamic description of a jet normal to a wall. They used a triple hot-wire probe to collect their data. Andreopoulos [19] studied the structure and mixing of normal jets by means of spectral analysis, flow visualization and conditional-sampling techniques. Crab, et al [20] also conducted an aerodynamic research programme with a normal jet.

Aerodynamic studies on inclined jets appear less often than those on normal jets, and few of them attempt to measure turbulent characteristics. Yoshida and Goldstein [21], as well as Kadotani and Goldstein [22], measured the mean and RMS longitudinal and transverse velocity components at one streamwise position. Jubran and Brown [23] also performed some measurements of turbulence intensity within this type of jet. Pietrzyk, et al [24] recently conducted a detailed aerodynamic measurement program on inclined jets. This study was made on a flat plate with a single row of holes inclined at 35 degrees. A Laser Doppler Velocimeter system was used to measure two components of the velocity.

3 EXPERIMENTAL APPARATUS.

3.1 The Facility.

The VKI Low Turbulence Wind Tunnel (LT1) has been selected to perform the present experimental investigation. A schematic view of the facility is presented in Figure 2. It is an aspirating open type wind tunnel made of wood. A 10:1 two dimensional contraction is followed by the test section, a 2D diffuser, two settling chambers, and a centrifugal blower driven by a 20 KW variable speed DC motor. The 0.35 m X 0.8 m test section has transparent walls, and is 2 m long. A flat plate model, described in the next section, is mounted 5 cm above the bottom wall, leaving a useful section of about 0.28 m X 0.8 m. The upper wall is adjustable, allowing the regulation of the pressure gradients along the test section. This wall is equiped with several slits allowing to introduce probes for temperature, pressure, and hot wire measurements. The maximum air velocity is approximately 20 m/s with a turbulence intensity of the order of 0.4% in the mainstream.

3.2 The model.

A test plate has been designed, built, instrumented and installed in the facility. It consists of four parts assembled between two T-shaped aluminium beams. The lead part of the test plate presents the cross sectional shape of a Clark-V profile. This profile is of a laminar type with very smooth pressure gradients along both the pressure and suction sides. Its pressure side is put on the upper (measurement) side of the model because it has a flat part allowing a continuous connection with the main test plate. This system guarantees the growth of a laminar boundary layer if the stagnation point is well positioned at the front of the profile nose. To check the stagnation point position, the leading edge is instrumented with static pressure tappings around its mid section perimeter.

The jets are produced by injecting the secondary flow through holes made in an insert placed in the central part of the model. Three different inserts are available. All of them have the same external dimensions and sectional shape. One is equipped with a single inclined injection hole whereas the two others have a row of seven injection holes with two different pitch to diameter ratios. The first piece is used to perform a series of experiments dealing with a single inclined air jet blowing into the freestream. These tests provide information about the near field character of a cooling jet. The two other pieces are used to investigate the phenomena associated with the recovery region and the interaction between jets coming from a row of holes. The use of two different pitch to diameter ratios allows to examine the influence of this parameter upon the coolant film behaviour.

3.3 The secondary flow supply.

To reproduce the jet to mainstream density ratios taking place in real turbine blades, not only jets of air are used, but also mixtures of air with a heavier gas. The gas selected for this purpose is SF_6. This is a non toxic, non flammable, and non corrosive gas commonly use as dielectric in high voltage transformers, it does not smell, and its price is about twice the price of Freon. Freon was rejected as a working gas for environmental reasons.

A schematic of the secondary flow supply is shown in Figure 3. Two valves are used to regulate the air and the heavy gas supplies. Each valve is mounted in series with a heat exchanger and a flowmeter. The heat exchangers were introduced in the circuit to damp the drop in temperature caused by the expansion of the air or the SF_6. Downstream of the flowmeters, the air and foreign gas are mixed in a single pipe connected to an ejection box just below the model. For each tested geometry a different ejection box is used. When Laser Doppler Velocimetry is used, seeding is added just upstream of the ejection box.

3.4 The Laser Doppler Anemometer.

A two-component fiber optic Laser Doppler Anemometer system, provided by DANTEC has been used. The first element of the optical measurement chain is a 4 W Ar-I Laser operated in multi-mode colour and mounted on an optical bench. The Laser beam is sent to a Transmitter Unit mounted on the same optical bench. The Transmitter includes a 40 MHz frequency shifter and four fiber manipulators. Then, the light is sent to a two-component emitting-receiving probe. Two photomultipliers with a colour separator receive the signal from the probe through a single fibre cable. To be able to measure a 3D flow field with a 2 component probe, all points are measured twice: once from one side of the test section, and once again placing the optical probe downstream of the measured point. Therefore, two different sets of traversing mechanism are used. This solution prohibits the measurement of one of the shear Reynolds stresses.

The Doppler signals are processed by two DANTEC Burst Spectrum Analyzers (BSA). These BSA processors do not work directly on the Doppler signal but on its power spectrum after performing a Fast Fourier Transform of the signal. Both BSA's are computer controlled via an IEEE-488 interface. A DANTEC software package is used for data acquisition, and to control and set-up the system.

Two different seeding systems are in use simultaneously, one for the mainstream and the other for the injection. The mainstream is seeded by using condensation of propylene glycol. The jets are seeded by using an incense burner constructed as a cyclone. Both seeding systems produce a similar particle size distribution, with 95% of the particles having diameters of less than one micron.

4 DISCUSSION OF RESULTS

4.1 The jet characteristics.

LDV measurements have been performed in series of vertical traverses contained in planes perpendicular to the freestream direction. These planes are located in the positions downstream of the injection position indicated in Table 3. The test conditions specified in Table 4 have been used for the case of a single jet. When injecting through a row of holes, only the first six conditions in this table have been used. Hence, the test cases in which a large amount of SF_6 would be exhausted in the laboratory have been advoided. The combination of the cases in Table 3 with the conditions in Table 4 results in 82 test planes where measurements were performed. All these measurements have been summarized in a graphical data base where one page is used for each measurement plane. Each one of these pages displays nine graphs with isolines corresponding to: the three velocity components, the three normal Reynolds stresses, the turbulence level, and two shear Reynolds stresses. The used reference coordinate system is represented in Figure 4. An example of the data base sheets is presented in Figure 5. It shows the cross section of a single jet of air of mass flux ratio equal to 2 at 5 diameters downstream of the injection site. Only the half jet where measurements have been performed is represented. The first graph in the figure displays the isolines corresponding to the velocity component in the mainstream direction. These velocity isolines present the kidney shape characteristic of this type of flows. The next two graphs represent the velocity components normal to the mainstream. The vortical motion of the flow can be appreciated in these two graphs. The three components of the normal shear stresses are represented next. All three ranged around the same values, but their actual distribution changes from one to another. They have been combined to obtain the turbulence level distribution represented in the next graph. The remaining graphs represent two of the three shear Reynolds stress. The error on velocities and normal Reynolds stresses is estimated to be less than 5%, while the error on the shear Reynolds stresses can go up to 20%. All the information used for the discussion in the next sections has been extracted from the aforementioned database. Additionally, cross planes taken at different locations for the same flow conditions have been grouped together to obtain 3D representations of the overall flowfield. This is the case of Figure 6 which represents the velocity distribution generated by a single jet of air with mass flux ratio (M) equal to 2. It shows an overall view of the jet features, such as the evolution to its characteristic kidney shape, and the migration of the maximum of velocity from the meridional plane to the vortex core. The streamlines of the averaged flow are plotted in Figure 7. These streamlines provide a good view of the behaviour of the mean flow, but the reader must be aware that they may not correspond to any instantaneous picture of the real flow field.

4.2 The jet trajectory.

There is not a unique way to define the jet trajectory. In general, the jet trajectory can be described as the line in space defined by the position taken by a given point characterizing each jet cross section. As there is more than one characteristic point in a given cross section, it is possible to define more than one jet trajectory. In the present work four points are used to characterize each jet cross section: the point of zero transverse velocity, and the three points corresponding to the maximum normal Reynolds stresses in each direction. The point of maximum velocity is not used because it would not make sense in all cases having velocity ratios less than unity.

Figure 8 shows, for the cases under study, the jet trajectory based on the point having zero transverse velocity. Each graph in this figure displays, in its upper part, the projection of the trajectory on the vertical meridional plane and, in its lower part, the projection of the trajectory on the horizontal plane. The trajectories represented in this figure approximately correspond with the core of one of the vortices generated in the jet. In fact, the vortex core corresponds to a point in the plane normal to the jet trajectory having zero transverse velocity. In general the angle between this later plane and the y-z plane is small. However, this correspondence weakens close to the injection site because, there, the y-z plane is far from being normal to the jet trajectory. This fact partially explains the trend of the contra rotating vortex pair to get closer together at the initial stages of the trajectories displayed in this figure. Nevertheless, a second reason exists for this initial trend of the jet trajectory: the ground effect. This can be easily explained by looking at the simplified scheme of the vortex pair displayed in Figure 7. In this scheme the ground has been replaced by a mirror image of the vortex pair. For each vortex, its mirror image pushes it towards its partner, while each one pushes the other up. Further downstream the distance between the vortices becomes small in comparison to the distance to their mirror images. Thus, the mirror images almost compensate each other effect and the flow field becomes dominated by the interaction between the two vortices. As it was observed by Durando [9] and analytically proven by Broadwell and Breidenthal [25], the distance between two contra-rotating vortices moving in a freestream grows as:

$$d = C * x^{1/3}$$

were, for given flow conditions, C is constant.

By looking at the case of a row of jets represented in Figure 8, it can be seen that the trend towards separation disappears after a while and the vortices begin to move parallel to each other, although they conserve a vertical motion. The trajectories in the vertical plane show to be lower than in the case of a single jet. This effect is produced by the interaction between the jets in the row. In fact, for a given vortex, its partner pushes it up while the closest vortex of the next jet pushes it down. Therefore, the lifting effect induced in the vortex pair is diminished.

Figures 10, 11, and 12 represents the trajectory in a vertical plane of the point having maximum normal Reynolds stresses in x, y, and z directions respectively. With the exception of the low injection rate cases, the maximum Reynolds stress in the y direction is reached closer to the wall than the maximum in the other two directions. This means that the flow close to the wall is dominated by lateral oscillations, while in the jet itself the oscillations are mainly up-down and back-forth.

4.3 The momentum flux ratio effect.

A striking feature, observed in the generated graphical data base, is the correlation between the lateral spreading of turbulence and the momentum flux ratio (I). This can be seen in Figure 13 which shows isolines of the turbulence intensity in a single jet at ten diameters downstream of the injection site. Seven cases are displayed, 3 of them with density ratio equal to 1, 2 with density ratio equal to 1.5, and the last 2 cases with density ratio equal to 2. The used mass flux ratio (M), as well as the corresponding momentum flux ratio, are displayed in each graph. All cases having a momentum flux ratio less than unity present a turbulent spot growing beside the jet itself. This lateral spreading of turbulence disappears for momentum flux ratios greater than unity. This is an indication that the high momentum jets break through the boundary layer and produce a large interaction with the freestream, while low momentum jets get confined in the low levels producing a wide interaction with the boundary layer.

The growth of a lateral turbulent spot has also been observed for the case of a row of jets. Figure 14 represents the turbulence level in a plane at the same position as the one of Figure 13, but in this case two rows of holes of pitch to diameter ratios of 3 and 5 are considered. For simplicity, only the case of air injection is analyzed, and only one low mass flow injection case, and one high mass flow injection case are considered for each row. The row with pitch to diameter ratio equal to 5 does not present major differences with the single jet case already presented in Figure 11. Therefore, it must be correct to assume that the interaction between the jets eventually appears downstream of the considered position. On the contrary, the two cases of the row of pitch to diameter ratio equal to 3 appear to be different than the equivalent single jet cases. The first difference is that the turbulence intensity inside the jet appears to have lower values, and does not extend as high as the single jet case. Additionally, the lateral turbulent spot characteristic of the low momentum case has a higher turbulence level, and appears to be shared by two consecutive jets.

5 CONCLUSIONS

The flowfield generated when an inclined turbulent jet is injected into a laminar cross-flow has been experimentally investigated by means of an LDV system. A single jet and two different rows of jets have been separately studied. Air and a mixture of gases producing density ratios of 1.5 and 2 have been used for injection. All the data have been processed and arranged into a graphical data base. From this data base information is taken about some general features of the jet, as the velocity evolution or the jet trajectory. The vortex pair generated within a single jet appears to have a trend towards separation some diameters after the injection location. The interaction between the jets in a row with pitch to diameter ratio equal to 3 is found to start between 5 and 10 diameters downstream of the injection site, and further downstream when a row of pitch to diameter ratio equal to 5 is studied. This interaction between jets lowers the height of the jet penetration, and makes the vortex core trajectory parallel to the meridional plane. The momentum flux ratio is found to characterize the interaction between the jet and the incoming boundary layer. When the momentum flux ratio is lower than 1 the jet penetration is small, and the jet is essentially confined within the boundary layer. The interaction generated in such conditions, produces a spreading of turbulence in the boundary layer, and a turbulent spot is generated beside the jet itself. By increasing the mass flux ratio, the lateral spreading of turbulence disappears when the momentum flux ratio gets larger than 1. When injecting through a row of holes, the turbulent spot is shared by two consecutive jets further downstream of the injection holes.

ACKNOWLEDGEMENTS

The finantial support provided by the European Economic Community under contract No SC1*296 to the first author is gratefully acknowledged. The authors are also pleased to acknowledge DANTEC Measurement Technology A/S for providing the Laser Doppler Anemometry system.

REFERENCES

1 KÜPPERS,K.H.; "Temperaturmessungen an Zwei Ruhenden Gasturbinen-Schaufelprofilen mit Grenzschichtkühlung". DVL-ST-Bericht Nr 82, 1944.

2 ARNE, V.L. & ESGAR, J.B.; "Experimental Investigation of Air-Cooled Turbine Blades in Turbo Jet Engine". NACA RME51C29, 1951.

3 GOLDSTEIN, R.J.; "Film Cooling", in Advances in Heat Transfer, vol. 7, Academic Press, 1971.

4 BERGELES, G., GOSMAN, A.D. & LAUNDER, B.E.; "The Near-Field Character of a Jet Discharged Normal to a Main Stream". Journal of Heat Transfer, Vol. 98, Aug. 1976.

5 ANDREOPOULOS, J. & RODI, W.; "Experimental investigation of Jets in a Cross Flow". Journal of Fluid Mechanics, Vol. 138, 1984

6 BERGELES, G., GOSMAN, A.D. & LAUNDER, B.E.; "Near-Field Character of a Jet Discharged Through a Wall at 30° to a Mainstream". AIAA Journal, Vol. 15, No. 4, 1977.

7 KRUSE, H.; "Efects of Hole Geometry, Wall Curvature and Pressure Gradient on a Film Cooling Downstream of a Single Row". AGARD Conference Proceedings 390, 1985.

8 LIESS, C.; "Film Cooling with Ejection from a Row of Inclined Circular Holes. An Experimental Study for the Application to Gas Turbine Blades" V.K.I. [illegible] nical Note 97, March 1973

9 DURANDO, N.A.;"Vortices Iduced in a Jet [illegible] a Subsonic Cross Flow". AIAA Journal, Vol. 9, No. 2, pp 325-327, Feb. 1971.

10 FEARN, R. & WESTON, R.P.;"Vorticity Associated with a Jet in a Cross Flow". AIAA Journal, Vol. 12, No.12, pp 1666-1671, Dec 1974.

11 LE GRIVES,E.;"Mixing Process Induced by the Vorticity Associated with the Penetration of a Jet Into a Cross Flow". Journal of Eng. for Power, Vol. 100, pp 465-475, July 1978.

12 NEEDHAM, D.J.; RILEY, N. & SMITH, J.H.B.; "A Jet in a Crossflow". Journal of Fluid Mech., Vol. 188, 1988.

13 NEEDHAM, D.J.; RILEY, N.; LYTTON, C.C. & SMITH, J.H.B.;"A Jet in a Crossflow. Part 2". Journal of Fluid Mech., Vol. 211, 1990.

14 COELHO, S.L.V. & HUNT , J.C.R.; "The Dynamics of the Near Field of Strong Jets in Crossflows". Journal of Fluid mech., Vol. 200, 1989.

15 HIGUERA, F.J. & MARTINEZ SANCHEZ, M.; "Incompressible Jet in a Weak Crossflow". Submitted to the Journal of Fluid Mech., 1992.

16 BATCHELOR, G.K.;"An Introduction to Fluid Dynamics". Cambridge University Press, Cambridge,1967.

17 KEFFER, J.F. & BAINES, W.D."The Round Turbulent Jet in a Cross Wind". Journal of Fluid Mechanics, Vol. 15, NO. 4, pp481-496, 1963.

18 KAMOTANI, Y. & GREBER,I.; "Experiments on a Turbulent Jet in a Cross Flow". AIAA Journal, Vol. 10, No. 11, pp 1425-1429, Nov. 1972.

19 ANDREOPOULOS, J.; "On the Structure of Jets in a Cross Flow". Journal of Fluid Mechanics, Vol. 157, pp 163-197, 1985.

20 CRABB, D.; DURAO, D.F.G. & WHITELAW, J.H.;"A Round Jet Normal to a Cross Flow". Journal of Fluid Eng., Vol. 103, March 1981.

21 YOSHIDA, T. & GOLDSTEIN, R.J.; "On the Nature of Jets Issuing From a Row of Holes Into a Low Reynolds Number Mainstream Flow". Journal of Eng. for Gas Turbines and Power, Vol. 106, 1984.

22 KADOTANI, K. & GOLDSTEIN, R.J.; "On the Nature of Jets Entering a Turbulent Flow" Journal of Eng. for Power, Vol. 101, 1979.

23 JUBRAN, B. & BROWN, A.; "Film Cooling from Two Rows of Holes Inclined in the Streamwise and Spanwise Directions" Journal of Eng. for Gas urbines and Power, Vol. 107, 1985.

24 PIETRZYK, J.R.; BOGARD, D.G. & CRAWFORD, M.E.; "Hydrodinamic Measurements of Jets in Crossflow for Gas Turbine Film Cooling Application". ASME Paper 88-GT-174, 1988.

25 BROADWELL, J.E. & BREIDENTHAL, R.E.; "Structure and Mixing of a Transverse Jet in Incompressible Flow". Journal of Fluid Mechanics, Vol. 148, pp. 405-412, 1984.

FLOW-FIELD PARAMETERS	GEOMETRICAL PARAMETERS
- Blowing Ratio	- Hole Inclination and Shape
- Momentum Flux Ratio	- Distribution of Rows
- Upstream Boundary Layer	- Curvature
- Freestream and Jet Turbulence	- Surface Roughness
- Pressure Gradients	- Injection Duct Length
- Re, Ma & Pr Numbers	

Table 1 Parameters affecting film cooling

Freestream Velocity (V_∞)	5 m/s
Injection Angle (α)	35º
Injection Hole Diameter (D)	12 mm
Incoming Boundary Layer Thickness (δ)	8 mm
Pitch to Diameter Ratio (p/D)	3,5,
Mass Flux Ratio (M)	0.5 ... 2.4
Density Ratio (R)	1.0, 1.5, 2.0

Table 2 Present test conditions

R	Case	p/D	x/D							
			0	0.5	1.0	2.0	3.0	5.0	10.0	20.0
1	Single Hole	-	•	•	•	•	•	•	•	•
	Row of holes	3						•	•	•
		5							•	•
1.5	Single Hole	-				•	•	•	•	
	Row of holes	3						•	•	
		5							•	
2	Single Hole	.				•	•	•	•	

Table 3 Distribution of measurement planes

R	M	I	V
1.0	0.5	0.25	0.5
	1.0	1.0	1.0
	1.5	2.25	1.5
	2.0	4.0	2.0
1.5	0.9	0.54	0.6
	1.5	1.5	1.0
	2.25	3.38	1.5
2.0	1.0	0.5	0.5
	2.0	2.0	1.0
	2.9	4.2	1.46

Table 4 Test cases matrix

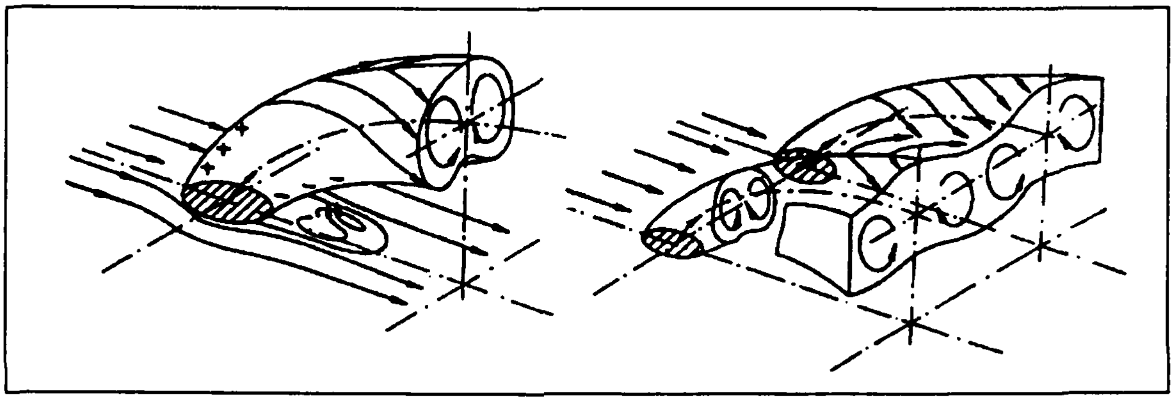

Fig. 1 A single jet and a row of jets into a crossflow [7].

Fig. 2 The LT1 wind tunnel.

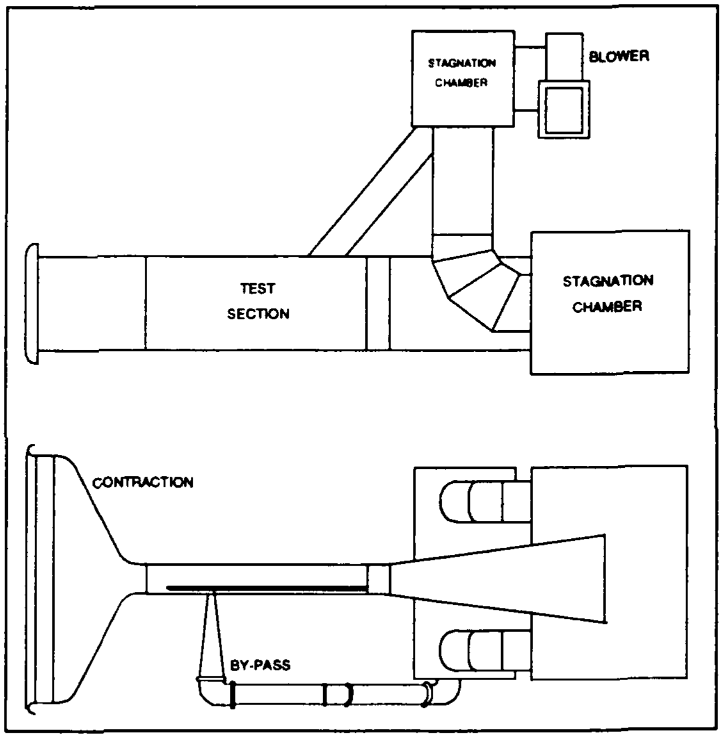
STAGNATION CHAMBER
BLOWER
TEST SECTION
STAGNATION CHAMBER
CONTRACTION
BY-PASS

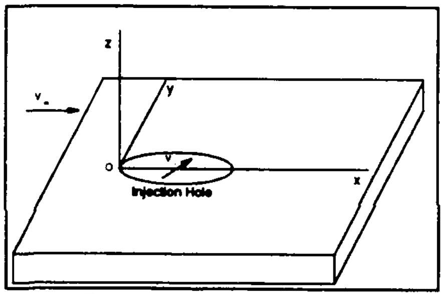
z
y
V∞
o
V
x
Injection Hole

Fig. 4 The coordinate reference system

Fig. 3 The secondary flow suply

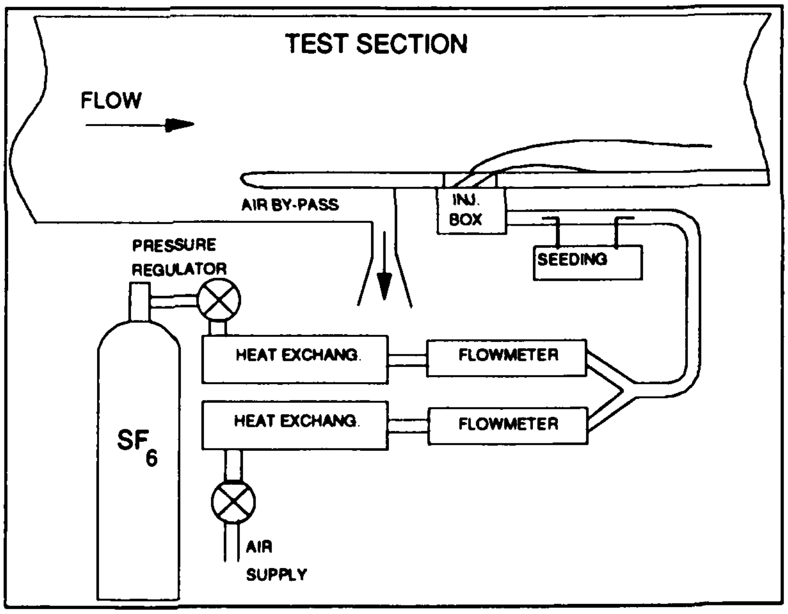
TEST SECTION
FLOW
AIR BY-PASS
INJ. BOX
SEEDING
PRESSURE REGULATOR
HEAT EXCHANG.
FLOWMETER
HEAT EXCHANG.
FLOWMETER
SF6
AIR SUPPLY

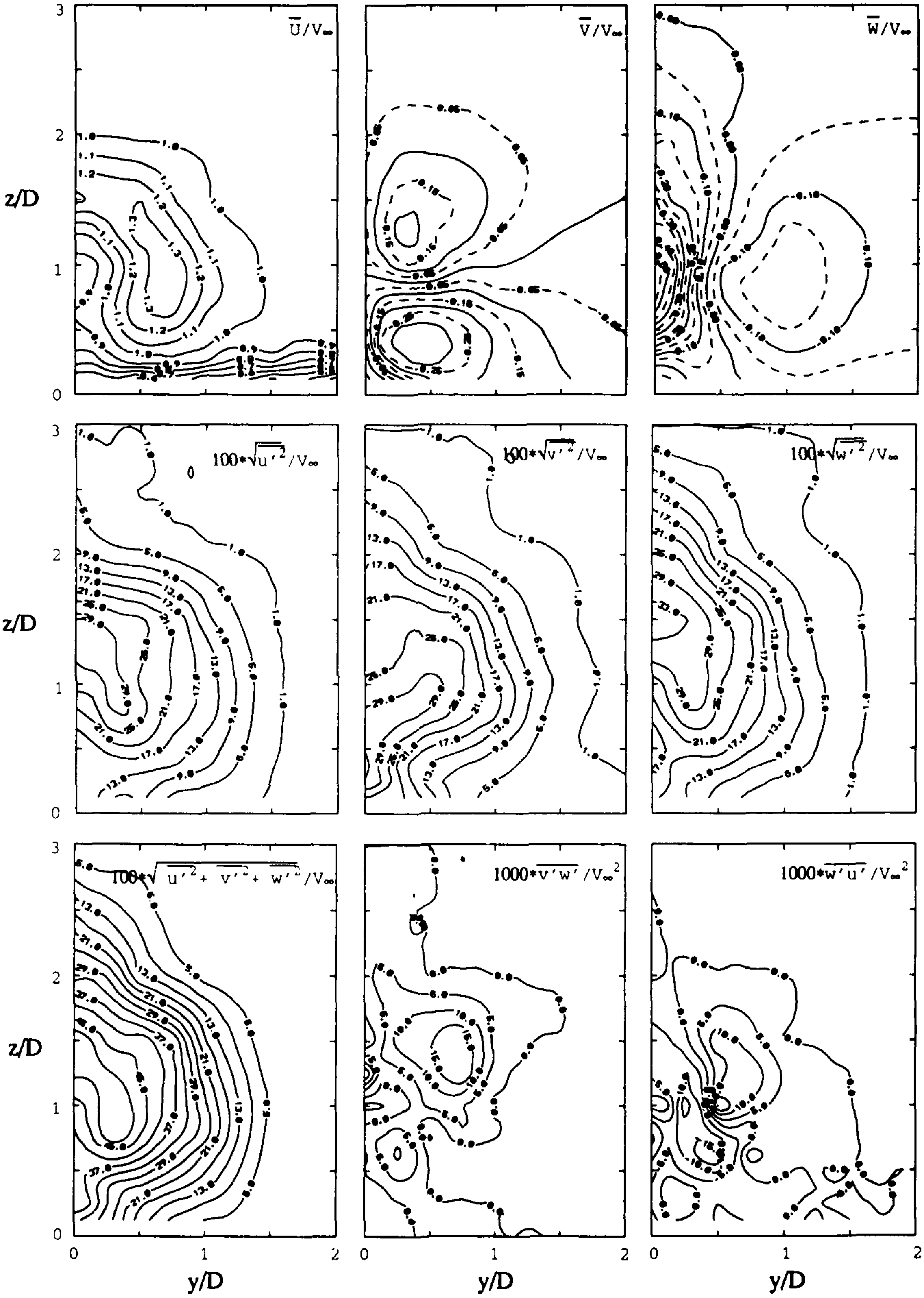

Fig. 5. Cross section at x/D=5.0 of a single jet of air (Density Ratio =1.0), Mass Flow Ratio = 2.0.

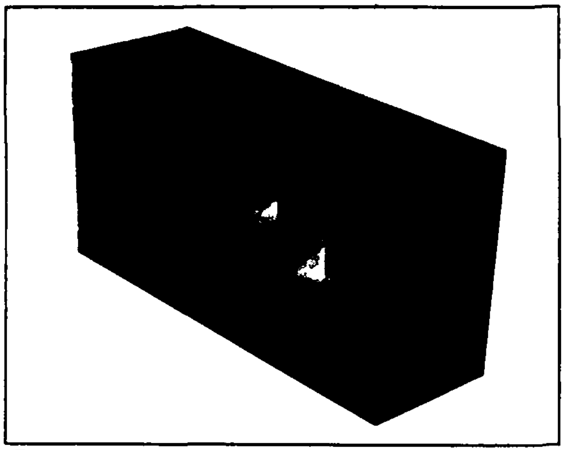

Fig. 6 Velocity distribution in a jet of air (M = 2.0)

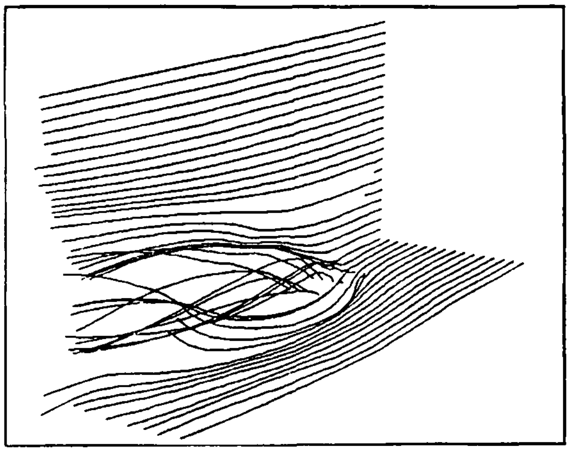

Fig. 7 Streamlines in a single jet of air (M = 2.0)

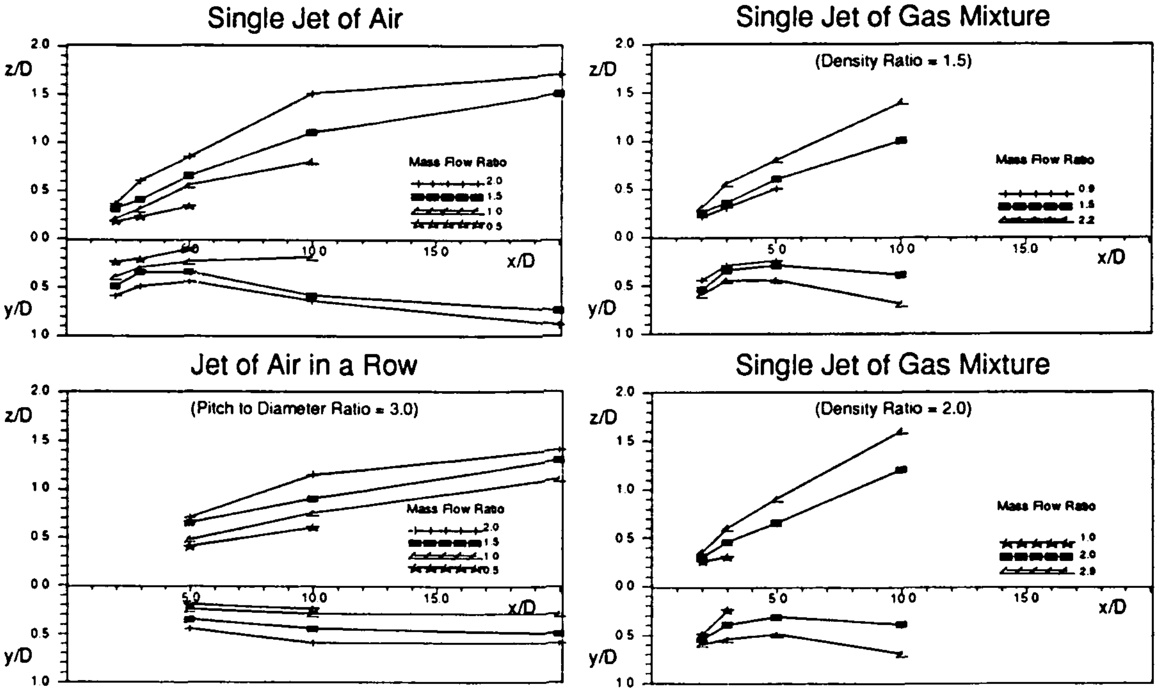

Single Jet of Air

Single Jet of Gas Mixture

(Density Ratio = 1.5)

Jet of Air in a Row

(Pitch to Diameter Ratio = 3.0)

Single Jet of Gas Mixture

(Density Ratio = 2.0)

Fig. 8 Zero transverse velocity point trajectory.

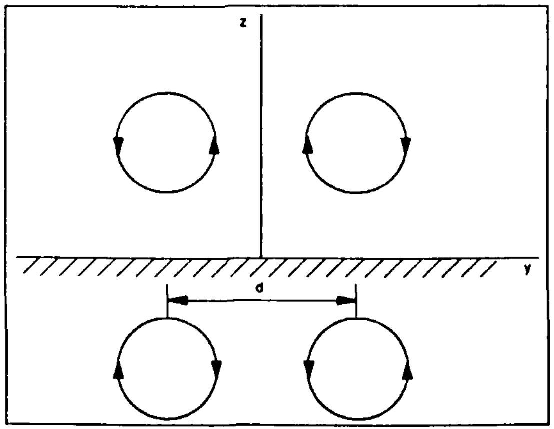

Fig. 9 A vortex pair and its mirror image

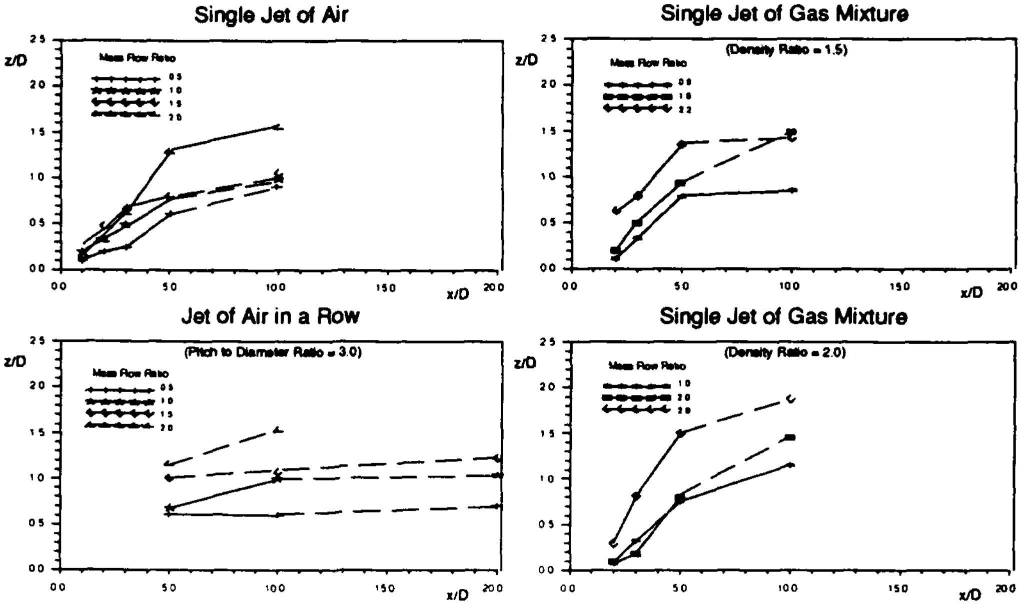

Fig. 10
Jet trajectory based on the point having maximum normal Reynolds stress in x direction.

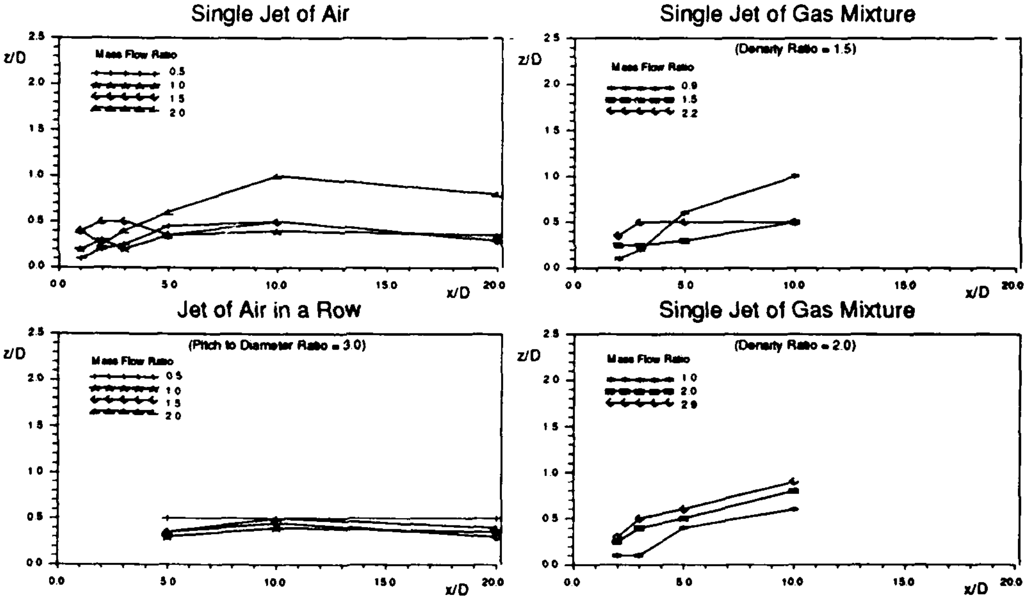

Fig. 11
Jet trajectory based on the point having maximum normal Reynolds stress in y direction.

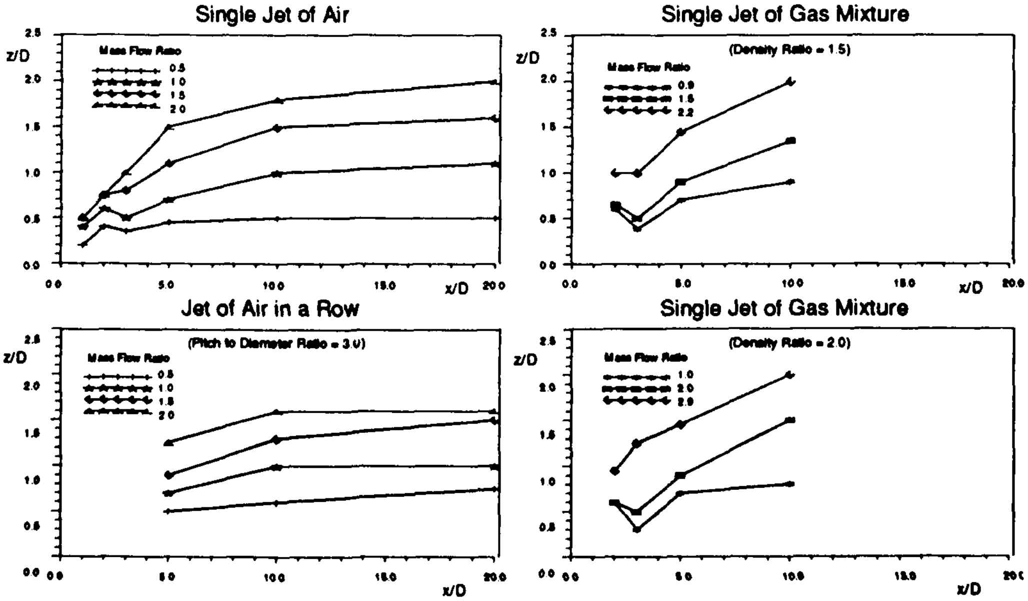

Fig. 12
Jet trajectory based on the point having maximum normal Reynolds stress in z direction.

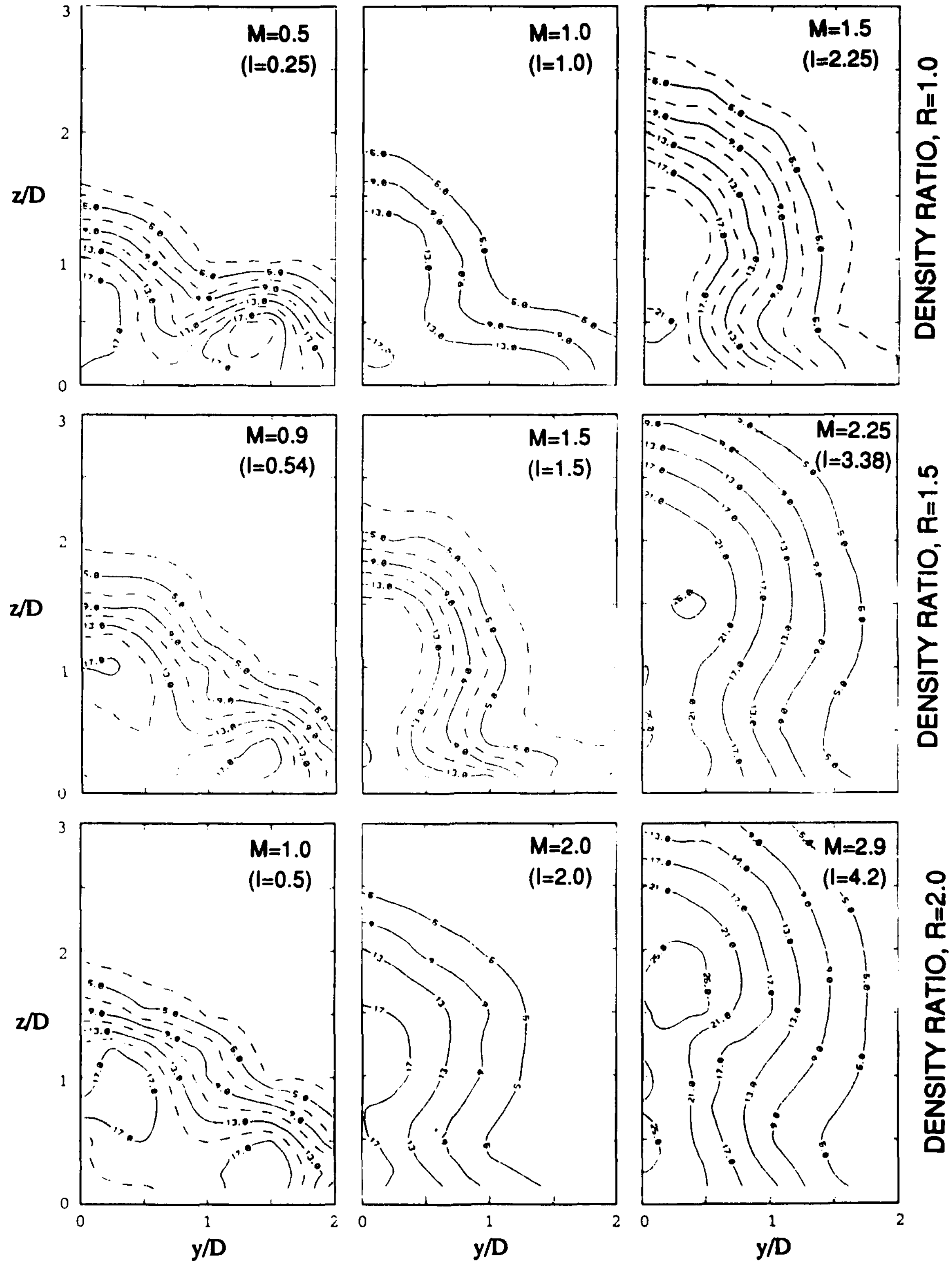

Fig. 13 Turbulence intensity for different jets of gas mixture at x/D = 10.

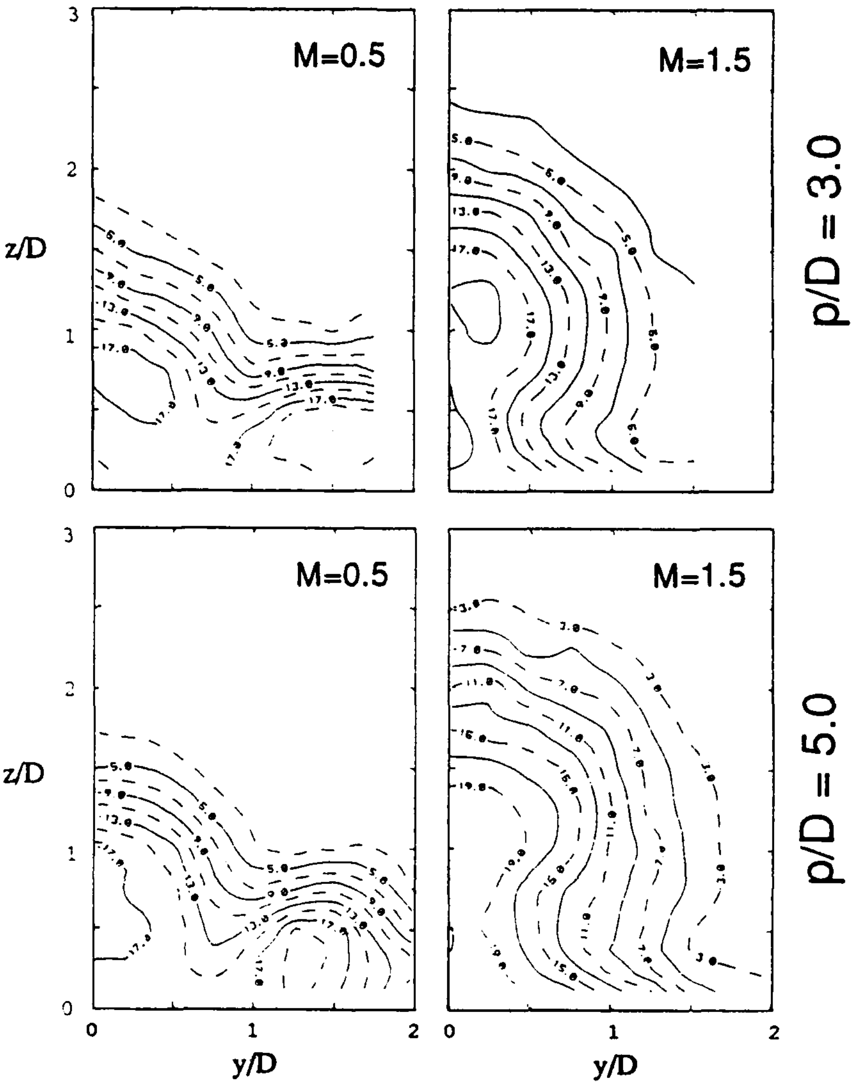

Fig. 14 Turbulence intensity for jets of air in a row at x/D=10.

Discussion

QUESTION 1:

DISCUSSOR: N. Hay, University of Nottingham

There must be a good reason why you used a length-to-diameter ratio for the hole of about one. A larger ratio would have been a lot better for two reasons: firstly, the flow in the hole would have been fully developed, and secondly, from the point of view of modelling this would have decoupled the region upstream of the hole from that downstream. As the rig is designed, one would have to model the plenum chamber, the hole and the jet and crossflow to get a true representation.

AUTHOR'S REPLY:

I agree with the comment. The choice of this model was, among other factors, dictated by the availability of existing hardware. On the other hand, the plenum could be considered as boundary condition for the jet flow.

MODELISATION D'UN ECOULEMENT TURBULENT EN PRESENCE DE JETS PARIETAUX DISCRETS DE REFROIDISSEMENT

J.M. Maurice, F. Leboeuf, P. Kulisa
Laboratoire de Mécanique des Fluides et d'Acoustique
URA CNRS 263
Ecole Centrale de Lyon
36 avenue Guy de Collongue,
BP 163,
69131 Ecully Cedex, France.

1. RESUME

Les températures de plus en plus élevées atteintes dans les premiers étages de turbine nécessitent un refroidissement efficace des aubages. Le refroidissement par film d'air a prouvé sa capacité à protéger la paroi de l'écoulement amont chaud. Toutefois, il perturbe fortement les caractéristiques aérodynamiques de l'écoulement. En conséquence, l'objectif des constructeurs est de réaliser le meilleur compromis entre les pertes aérodynamiques et les contraintes thermiques.

Une modélisation bidimensionnelle aérothermique de l'écoulement visqueux refroidi par jets discrets et basée sur le concept de couche limite, a été développée à l'Ecole Centrale de Lyon. Dans un premier temps, un modèle de fermeture turbulente utilisant une longueur de mélange a été implanté. Un modèle k-ε à bas nombre de Reynolds est ici présenté. Une technique de moyenne en espace dans la direction transversale à l'écoulement principal permet de conserver un caractère bidimensionnel au problème. Par suite, les équations de transport des grandeurs turbulentes contiennent des termes-source qui traduisent la présence des jets.

Des comparaisons avec des résultats expérimentaux sont présentés dans le cas d'une rangée de jets introduits dans une couche limite turbulente se développant sur une plaque plane, à proximité de l'orifice d'injection.

SUMMARY

The high temperature level reached in the first turbine stages requires efficient blade cooling. Film cooling has proved its ability to protect the wall from the hot upstream flow. However, the jets strongly disturb the aerodynamic flow characteristics. As a consequence, the main objective of the designers is to get the best compromise between thermal strains and aerodynamic losses.

A two-dimensional viscous flow model, with discrete jets and based on a boundary layer concept, was developed at Ecole Centrale de Lyon. The turbulence closure was first performed by a mixing length model. A low Reynolds number version of a k-ε model is presented here. We use a space averaging method in the transverse direction; thereby the two-dimensional character of the computation is preserved, while the specific effects of the discrete jets are taking into account in the model.

Comparisons with experimental results are given in the case of a row of jets, as injected through a turbulent boundary layer on a flat plate, near the injection orifice.

2. INTRODUCTION

Le refroidissement par film des aubes de turbine est un mécanisme très employé pour augmenter les performances des turbines à gaz, afin de préserver les parois du fluide chaud issu de la chambre de combustion. Du fluide "froid" peut être ainsi prélevé dans le compresseur pour être réintroduit dans la turbine. Dans ce travail, nous considérons uniquement le refroidissement à l'aide de jets discrets, qui sont introduits dans l'écoulement principal entre les aubages. La priorité affichée par les constructeurs est en général d'assurer une durée de vie suffisante des turbines, ce qui implique une bonne protection thermique des parois. Cependant, la complexité des phénomènes physiques observés à proximité des zones d'injection, ainsi que l'emploi de méthodes de prédiction thermique imparfaites, conduit en général à un sur-dimensionnement des débits d'injection. Il en résulte une pénalisation du compresseur, qui fournit du fluide à haute pression non valorisé dans la chambre de combustion; par ailleurs, la maîtrise de l'aspect cinématique des phénomènes d'injection est encore imparfaite, ce qui agit sur le rendement des turbines.

La physique des phénomènes est très complexe. Fortement accéléré et dévié par les aubes, la structure de l'écoulement entre les aubes de turbine est fortement tridimensionnelle, suite au développement de nombreux tourbillons (Escande, 1991). La transition entre les régimes laminaire et turbulent est très étalée sur la paroi des aubes; elle est influencée à la fois par des mécanismes liés à la paroi (ondes de Tollmien-Schlichting, tourbillons de Görtler, forts gradients de température, décollement local),et par l'écoulement extérieur à la couche visqueuse pariétale (sillages issus des aubes à l'amont, turbulence de l'écoulement extérieur). Introduit dans l'écoulement principal entre les aubes, le jet a un comportement très complexe, dominé par de nombreuses structures tourbillonnaires.

Pour la zone située loin de l'orifice d'injection, il existe deux tourbillons contra-rotatifs, nommés ici Ω_1, et qui confèrent au jet une forme classique en "haricot". Ces deux tourbillons apparaissent en particulier pour des jets issus d'un tube débouchant dans un écoulement transversal, à même température et *masse volumique (Fearn et Weston,1974); leur origine* est liée aux couches visqueuses se développant sur les parois intérieures du tube, dont la vorticité est réorientée lors de la déflexion du jet par l'écoulement transversal . Ces tourbillons apparaissent dans le tube d'injection lui-même, car l'écoulement y est déjà dévié par l'écoulement transversal se développant au niveau de l'orifice (Sykes, Lewellen et Parker,1986, Pinho Brasil, 1992). Pour des nombres de Reynolds assez faibles, la périphérie du jet est influencée par des enroulements toriques Ω_2, rencontrés également dans le cas de jets libres, mais ici déformés par l'écoulement transversal (Figure 2, Bousgarbiès, Brizzi, Foucault, 1991). Un jet débouchant au niveau d'une paroi sur laquelle se développe un écoulement visqueux du type d'une couche limite, est influencé par des structures tourbillonnaires supplémentaires. Une description assez précise de la topologie à la paroi de l'écoulement a été proposée par Charbonnier, (1992). Une paire de *tourbillons en fer à cheval* Ω_3, *induit par le* ralentissement de la couche limite transversale sous l'influence du jet, s'enroule autour de celui-ci; le jet a donc ici un rôle de blocage de l'écoulement transversal, dans lequel il se comporte, au moins pour sa face amont, comme un corps solide souple (Moussa, Trischka et Eskinazi,1977). Ces deux tourbillons Ω_3 tournent en sens opposés par rapport à ceux Ω_1 liés aux couches visqueuses crées dans le tube d'injection. Pour de faibles valeurs du nombre de Reynolds, les deux branches du tourbillon en fer à cheval Ω_3, pourront se rejoindre à l'aval du jet (Bousgarbiès, Brizzi, Foucault, 1991). Enfin, la face aval du jet est le siège d'enroulements tourbillonnaires Ω_4 qui sont liés à l'existence de zones d'accumulation de fluide entre les deux points selles S1 et S2; alimentés en grande partie par la couche visqueuse transversale, ils sont aspirés par le jet lui-même et tournent dans le même sens que Ω_1 (Andreopoulos et Rodi,1984; Andreopoulos, 1985; Fric et Roshko, 1989; Charbonnier et Leblanc, 1990; Pinho Brasil, 1992); il est donc très possible que les mouvements tourbillonnaires Ω_1 et Ω_4 soient conjointement responsables de la mécanique du jet à une certaines distance à l'aval de l'orifice d'injection. Tous ces mécanismes supposent un écoulement dans lequel la masse volumique varie peu. Dans une turbine refroidie, l'existence de forts gradients de température entre les jets, la paroi et l'écoulement extérieur, ainsi que de fortes variations de pression statique liées aux courbures locales des trajectoires fluides, vont être responsables de variations importantes de la masse volumique. Il doit en résulter des sources de tourbillons Ω_5 liés aux interactions entre les gradients de pression et de masse volumique, alors que tous les mécanismes Ω_1 à Ω_4 ne sont que des réorientations de la vorticité existante dans le jet ou la couche limite amont.

Des mesures de quantités turbulentes dans le jet tridimensionnel ont été réalisées par Moussa, Trischka et Eskinazi (1977), Crab, Durao et Whitelaw (1981), Andreopoulos et Rodi,(1984), Charbonnier (1992) pour un jet isolé; de fortes valeurs des contraintes ont été mesurées sur la face aval du jet, et à proximité *immédiate de la paroi.* Dans le cas de rangées de jets, Yavuzkurt, Moffat et Kays (1981), Pietrzyk, Bogard, et Crawford (1989), Vuillerme et alii,(1992) ont montré la forte influence du jet sur les grandeurs turbulentes dans la couche limite de paroi.

Les contraintes imposées sur un calcul du refroidissement par film dans des aubes de turbines sont très fortes. Afin d'assurer une protection thermique suffisante, le constructeur doit employer souvent plusieurs rangées de jets discrets par canal; un nombre d'orifices percés sur les aubes, de l'ordre de la centaine est donc courant; ils sont répartis à la fois sur les aubes ou les plate-formes (Bry, 1989). La détermination des flux de chaleur aux parois nécessite une grande précision de la part du calcul du champ cinématique. Etant donné la taille des structures tourbillonnaires en présence, l'emploi de maillage très fin est nécessaire (Calatano, Chang, Mathis, 1989); *par ailleurs, il n'est pas évident que l'utilisation de* lois de parois soit possible dans les zones d'injections, étant données les recirculations locales de fluides qui perturbent l'équilibre local des transferts turbulents (White, 1980). Pour ces raisons, l'usage de codes résolvant les équations de Navier-Stokes sous une forme tridimensionnelle est encore restreinte au traitement simultané d'un nombre limité de jets. Les conclusions apportées par ces calculs montrent que la prédiction de l'écoulement dans la zone aval du jet est fortement améliorée par l'utilisation de conditions aux limites appropriées au niveau de l'orifice (Khan, Mc Guirk, Whitelaw, 1982). La plupart des auteurs emploient des modèles de turbulence avec équations de transport de l'énergie cinétique turbulente k et du taux de dissipation turbulente ε; notons que Ince et Leschziner (1990), et Demuren (1990) ont employé des équations de transport de tension de Reynolds, sur des maillages cependant trop grossiers pour capter toute la physique des phénomènes.

Entre ces calculs tridimensionnels et l'utilisation de relations analytiques permettant de prédire le flux de chaleur en présence d'injections multiples, il existe des modèles bidimensionnels adaptés au traitement de rangées de jets et basés, plus ou moins explicitement, sur une hypothèse de moyenne spatiale selon la direction de la rangée de jets (Herring, 1975). Ces modèles diffèrent d'une part par le traitement de l'écoulement transversal, en général basé sur un modèle de couche limite, et sur la prise en compte des informations liées aux jets. Herring (1975), Kulisa, Leboeuf et Perrin, (1991) ont utilisé une méthode intégrale de calcul du jet. Miller et Crawford (1984),Yavuzkurt, Moffat et Kays (1980) ont utilisé un modèle d'injection qui respecte essentiellement la conservation de la masse, et utilise une version de la longueur de mélange, corrigée des effets du jet. Schönung et Rodi (1987) ont utilisé un modèle d'injection-dispersion qui relie, à l'aide d'une équation de transport, le flux de chaleur et la quantité de mouvement. L'étalonnage de cette méthode a été réalisé à l'aide d'un grand nombre de calculs tridimensionnels de jets (Demuren, 1983); les résultats sont assez approchés à proximité immédiate de l'orifice d'injection. Des modèles de turbulence du type k-ε ont été employés par Schönung et Rodi (1987), Tafti et Yavuzkurt (1989) avec des résultats améliorés par rapport à l'utilisation d'une longueur de mélange.

Nous ne discuterons pas ici de la validité du modèle à deux équations de transport de k et ε dans le cadre d'un écoulement général en turbine, dans la mesure où seules les applications sur des plaques planes seront considérées ici. Il convient cependant de rappeler que ce modèle prédit difficilement les écoulements présentant de fortes contraintes normales, tels les effets de courbure; de même, il doit être au moins adapté pour un traitement de la transition entre les régimes laminaire et turbulent. L'objectif essentiel de cette étude est la prédiction des flux de chaleur aux parois; compte tenu de la forte influence de l'aspect cinématique du problème sur l'aspect thermique, il semble essentiel d'opter pour un modèle à bas nombre de Reynolds, qui évite l'utilisation de lois de parois trop approximatives dans le cadre d'injections fortes. En effet d'après Launder, (1988), il n'est pas aisé de définir la frontière entre la sous-couche visqueuse et la zone extérieure dans les écoulement complexes; en outre, la zone logarithmique n'existe pas dans les zones décollées. Un modèle à bas nombre de Reynolds doit respecter le comportement de chacun des termes des équations de transport des grandeurs turbulentes à proximité de la paroi, grâce à des fonctions d'amortissement adaptées; de tels modèles ont été développés pour des parois étanches par Nagano et Tagawa, (1990), Shih et Mansour, (1990). Il est également essentiel que la condition à la limite pariétale sur ε traduise l'équilibre entre le taux de dissipation de k et sa diffusion par effet visqueux à la paroi (Lam et Bremhorst, 1981). Il importe enfin de pouvoir calculer des zones décollées sans problèmes numériques; il semble que le modèle de Michelassi et Shih (1991) facilite ce traitement car la distance à la paroi est exprimée directement en fonction de l'échelle de longueur turbulente, plutôt qu'en terme de la vitesse de frottement à la paroi U_τ. Ces artifices pariétaux ne sont pas cependant suffisants pour garantir une validité complète des modèles k-ε dans le cas d'injections pariétales. Il est bien connu en effet que l'hypothèse de Boussinesq est déjà mise en défaut dans le cas d'un jet libre; en outre, une forte déformation est mal traduite par ce modèle.

L'approche choisie dans cette étude suppose l'emploi d'un maillage très fin dans la direction normale à la paroi, avec comme objectif ultime la prédiction précise des flux de chaleur. Par contre, nous acceptons une certaine imprécision sur la prévision de la distribution pariétale du flux, en particulier dans la direction de la rangée de jets. Enfin, le calcul doit être utilisé dans le cadre de dessin de machine, ce qui impose des temps de calculs raisonnables. Le respect de ces contraintes nous a conduit, pour le calcul de l'écoulement transversal au jet, a opter pour un modèle de couche limite; la stabilité de ce calcul est assurée grâce à un couplage fort avec l'écoulement non visqueux extérieur à la zone pariétale (Kulisa, Leboeuf, Klinger et Bernard, 1992). Le calcul de jet tridimensionnel est basé sur une forme intégrale des équations de Navier-Stokes parabolisée selon la trajectoire du jet. La fermeture du modèle est assurée grâce à l'emploi de lois analytiques, et au calcul des composantes de vitesse induites par des singularités tourbillonnaires emportées par le jet (Leboeuf, Huang, Kulisa, Perrin, 1991). Une moyenne de l'écoulement est alors réalisée selon la direction parallèle à la rangée de jets (Kulisa, Leboeuf, Perrin, 1991). Dans le cadre de ce travail, nous présentons l'utilisation d'un modèle de turbulence à bas nombre de Reynolds avec deux équations de transport de k et ε; les modèles de Nagano et Tagawa (1990) et Michelassi et Shih (1991) ont été testés.

Des résultats seront présentés pour deux cas de couches limites turbulentes qui se développent sur une plaque plane, en présence d'injections pariétales (Vuillerme, Foucault, Dorignac, Deniboire et Bousgarbiès,1992).

3. MODELES DE CALCUL

3.1 Moyennes spatiales et moyenne turbulente

Les diverses équations de transport sont tout d'abord moyennées statistiquement au sens turbulent. Nous noterons indifféremment $\tilde{u}$ ou u la valeur moyenne au sens turbulent de la variable u, et u' sa fluctuation au sens turbulent. Puis les équations sont moyennées spatialement selon la direction z de la rangée de jets, supposée ici perpendiculaire à la direction x de l'écoulement transversal à l'infini amont. La moyenne spatiale sera notée $\bar{u}$, et sa fluctuation spatiale (du). Dans tout ce qui suit, il faut en outre noter que toute les moyennes spatiales ou turbulentes sont pondérées par la masse volumique ρ, hormis les moyennes de ρ et de la pression statique P. Par exemple pour la vitesse u, nous aurons pour la moyenne spatiale selon z, sur une distance G:

$$\bar{u} = \frac{\int_{z}^{z+G} \rho u \, dz}{\int_{z}^{z+G} \rho \, dz} \quad , \quad u = \bar{u} + du \qquad (1)$$

3.2 Equations du champ moyen pour la couche limite

Le repère utlisé (x,y,z) est précisé sur la figure 1. Les équations qui gouvernent le champ transversal, au sens des moyennes turbulentes et spatiales, sont celles de la couche limite; elles sont données ci-dessous, en tenant compte d'une périodicité selon z, sur une distance G séparant deux orifices d'injection:

$$\frac{\partial}{\partial x}\overline{\rho u}+\frac{\partial}{\partial y}\overline{\rho v}=0 \tag{2}$$

$$\overline{\rho u}\frac{\partial\overline{u}}{\partial x}+\overline{\rho v}\frac{\partial\overline{u}}{\partial y}+2K_X\overline{\rho u}\,\overline{v}=$$

$$-\frac{\partial\overline{P}}{\partial x}+\frac{\partial\overline{\tau_{XY}}}{\partial y}-\frac{\partial}{\partial x}\overline{d(\rho u)du}-\frac{\partial}{\partial y}\overline{d(\rho v)du} \tag{3}$$

$$\tau_{xy}=\tilde{\mu}\left(\frac{\partial\tilde{u}}{\partial y}+\frac{\partial\tilde{v}}{\partial x}-\frac{2}{3}\left(\frac{\partial\tilde{u}}{\partial x}+\frac{\partial\tilde{v}}{\partial y}\right)\right)-\tilde{\rho}\,\tilde{u}'v' \tag{4}$$

$$\overline{\rho u}\frac{\partial\overline{H_t}}{\partial x}+\overline{\rho v}\frac{\partial\overline{H_t}}{\partial y}=$$

$$\frac{\partial}{\partial y}\left(\overline{\tau_{XY}}-\overline{q_Y}-\overline{\tilde{\rho}\,(\tilde{v}'H_t')}\right)-\frac{\partial}{\partial x}\overline{d(\rho u)\,dH_t}-\frac{\partial}{\partial y}\overline{d(\rho v)\,dH_t} \tag{5}$$

q_y est le flux de chaleur dans la direction y. Les inconnues sont $\overline{u}$, $\overline{v}$, $\overline{H}_t$. La masse volumique est calculée à partir de la loi des gaz parfaits. La pression statique est supposée constante selon y. Quoique cette hypothèse soit classique dans un modèle de couche limite, la présence de valeurs élevées de la composante v, au voisinage de l'injection, infirme cette hypothèse: aussi, le présent calcul doit être vu comme une première étape uniquement.

Quoique la pression statique P soit identifiée avec sa valeur P_e dans la zone non visqueuse en dehors de la couche pariétale, cette valeur n'est pas imposée dans le calcul, comme dans un mode direct. Au contraire, P_e est obtenue à l'aide d'une équation qui traduit le couplage fort entre l'écoulement non visqueux externe et la couche visqueuse refroidie à la paroi. Les principales caractéristiques de ce couplage sont rappelées ici.

Afin de stabiliser le calcul de couche limite, il est nécessaire de réintroduire un effet elliptique à proximité de la paroi, qui a été perdu suite à l'hypothèse de parabolisation. Dans ce but on résout une équation qui simule la réaction de l'écoulement non visqueux externe à la présence de la couche de paroi. Nous utilisons une technique de superposition de domaines, en ce sens que le même domaine est utilisé pour les calculs des écoulements visqueux et non visqueux; en conséquence, l'écoulement non-visqueux à la paroi est totalement fictif. Les deux écoulements échangent de l'information à la paroi; ceci maintien un caractère subcritique au couplage, qui se comporte comme un écoulement subsonique, quel que soit le nombre de Mach de l'écoulement non visqueux externe.

L'interaction visqueuse-non visqueuse est basée sur l'utilisation du déficit de masse δq, entre les deux écoulements, définis par:

$$\delta q=\int_0^h(\rho_e u_e-\rho u)\,dy \tag{6}$$

Ces déficits de masse sont introduits à la paroi dans l'écoulement non visqueux; ils induisent des courbures des lignes de courant, qui s'accompagnent de variation de la pression statique P_e selon y, dont seule la valeur à la paroi est ici prise en compte. Les conditions d'arrêt de l'écoulement non visqueux restant inchangées dans tout le calcul, il est équivalent de déterminer P_e ou u_e. La correction de u_e sous l'effet des injection de débit δq est donnée par l'équation de Poincaré. Après quelques calculs intermédiaires, il vient (Kulisa, Leboeuf, Klinger, Bernard , 1992) :

$$\delta u_e(M)=-\frac{1}{\pi}\int_{x_0}^{x_1}\frac{1}{\rho}\,\frac{\frac{d}{dx}(\delta q)+(\rho v)_{y=0}}{(x-x_M)}\,dx \tag{7}$$

(7) est appelée équation d'interaction. Notons que cette relation tient compte également d'injection réelle de fluide par le terme $(\rho v)_{y=0}$. Cette technique a quelques avantages. Tout d'abord, elle relie la correction de vitesse δu_e au point M situé à la paroi, à la répartition de déficit de masse δq, en amont et en aval, restituant ainsi l'effet elliptique. En outre, la forme simple de l'équation (7) lui permet d'être résolue simultanément avec les équations de la couche limite (1) à (5). Ceci confère une excellente stabilité au calcul, sans utilisation de relaxation, et en évitant un coût de calcul excessif, qui serait lié à la résolution des équations complètes de l'écoulement non visqueux.

3.3 Le modèle de jet tridimensionnel

Le modèle de jet tridimensionnel a été décrit par Kulisa, Leboeuf, Klinger, Bernard, (1992), et Leboeuf, Huang, Kulisa, Perrin, (1991), pour une utilisation simplifiée dans un écoulement extérieur uniforme. Nous redonnons ici les éléments essentiels du modèle, sans préciser cependant en détail les adaptations nécessaires du calcul de jet dans un environnement de couche limite en paroi. Pour un écoulement stationnaire, les équations de conservation de masse, quantité de mouvement et énergie sont écrites dans un repère curviligne orthogonal (s, n, b), lié à la trajectoire du jet; cette ligne particulière est définie ici comme le lieu du maximum de l'excès de vitesse v_s dans le jet, par rapport à l'écoulement transversal au jet. Une hypothèse de parabolisation est ensuite utilisée selon s; en conséquence, le gradient de pression selon s est imposé par l'écoulement transversal au jet. En utilisant la règle limite de Leibnitz pour transformer un bilan réalisé sur une tranche de jet de longueur ds, ces équations sont intégrées sur une section transversale σ du jet.

Cette formulation intégrale a deux conséquences. Elle change la nature des équations précédentes, qui de paraboliques deviennent hyperboliques. Le processus de moyenne ainsi introduit nécessite l'utilisation de fermetures particulières, en particulier sur la frontière du jet. Nous les rappelons ici. Il existe une zone potentielle à proximité de l'orifice, dans laquelle la vitesse du jet reste constante. La section transversale du jet, dans le plan (n,b), a une forme elliptique dont le rapport des axes varie linéairement, depuis l'orifice jusqu'à une valeur fixée entre 2 et 4, à la fin de la zone potentielle. L'entraînement de fluide de l'écoulement transversal dans le jet a deux origines: un effet de diffusion turbulente E_1, simulé comme dans un jet mono-dimensionnel, et un effet tridimensionnel E_2 approché par un apport de masse sur la face aval du jet. Cet apport de masse est traduit par un puits situé sur la face aval du jet. Dans le cadre d'une approximation localement potentielle, il est alors possible de relier la traînée de pression ΔF_p induite par le champ de vitesse lié au puits, à la valeur de l'entraînement E_2. La traînée de pression est finalement déterminée à l'aide d'un coefficient de traînée C_D dont la valeur théorique pour un jet de section circulaire est 2; cette valeur est utilisée dans tous les calculs. Un modèle simplifié de force de frottement est utilisé avec un coefficient de frottement constant. Des lois analytiques décrivant les répartitions de la composante de vitesse v_s et de la température d'arrêt T_t sur σ sont employées. Les composantes de vitesse selon n et b sont déduites de singularités tourbillonnaires localisées sur la face aval du jet; leur intensité est déduite d'une équation de transport de la composante Ω_s du vecteur tourbillon, intégrée sur les deux demi-ellipses incluses dans σ.

Les inconnues du système d'équations précédent sont l'excès de vitesse maximum dans le jet $\Delta v_{s,max}$, la surface de la section transversale σ, l'angle α_n formé entre les directions s et x, et l'excès de la température maximum dans le jet $\Delta T_{t,max}$; dans la zone potentielle, $\Delta v_{s,max}$ est remplacée par le rapport entre la surface du noyau potentiel et σ.

3.4 Equations du modèle de turbulence

Seul l'aspect cinématique du modèle de turbulence sera traité ici. La fermeture turbulente du problème revient à déterminer la composante de cisaillement du tenseur de Reynolds moyennée selon z, qui apparait dans (3), et que nous rappelons ici:

$$\overline{\tilde{u}'\tilde{v}'} = \frac{\overline{\rho\, \tilde{u}'\tilde{v}'}}{\overline{\rho}} = \frac{1}{\overline{\rho}}\int_{z}^{z+G} \rho\, \tilde{u}'\tilde{v}'\, dz \qquad (8)$$

Dans un cas général, la valeur donnée par (8) est très différente de celle trouvée dans une couche limite bidimensionnelle, étant donnée la présence d'une information propre au jet sous l'intégrale.
Pour modéliser cette tension de Reynolds moyennée selon z, certains auteurs ont corrigé la viscosité turbulente de la couche limite par un effet de jet (Miller, Crawford , 1984; Kulisa, Leboeuf, Perrin, 1991):

$$\overline{\tilde{u}'v'} = -\left(\nu_{t,2D} + \nu_{t,\,jet}\right)\left(\frac{\partial \overline{u}}{\partial y} + \frac{\partial \overline{v}}{\partial x}\right) \qquad (9)$$

, où $\nu_{\tau,2D}$ est la valeur donnée par un modèle adapté à un calcul de couche limite bidimensionnelle. Dans le modèle de Kulisa (1991), la part du jet est donné par:

$$\nu_{tjet} = l\, \Delta V_{Smax}\, \gamma \quad ; \; l^2 = \frac{\alpha^2}{V_{Smax}}\iint_{\sigma} \Delta V_s\, d\sigma \qquad (10)$$

γ est la fonction de Van Driest, qui permet de distribuer $\nu_{t,\,jet}$ sur la section σ, α est une constante tenant compte des échelles intégrales dans le jet et ΔV est l'excès de vitesse dans le jet par rapport à l'écoulement transversal. Notons que $\nu_{t,jet}$ est une grandeur tridimensionnelle qui est moyennée selon z.

Cette démarche est cependant très restrictive, car elle ne tient pas compte d'une influence directe du jet sur la valeur bidimensionnelle moyenne $\nu_{t(2D)}$. En outre, la relation (9) ignore les variations (du et dv) du champ de vitesse selon z; en effet la moyenne spatiale de la relation locale de Boussinesq donne:

$$\overline{\tilde{u}'v'} = -\,\overline{\nu_t}\left(\frac{\partial \overline{u}}{\partial y} + \frac{\partial \overline{v}}{\partial x}\right)$$

$$\overline{-\,d(\nu_t)\left(\frac{\partial\, d(u)}{\partial y} + \frac{\partial\, d(v)}{\partial x}\right)} \qquad (11)$$

Le modèle que nous décrivons ici est basé sur les équations de transport de l'énergie cinétique turbulente k et de le taux de dissipation turbulente ε. Les formes locales de ces équations s'écrivent:

$$\frac{Dk}{Dt} - \frac{\partial}{\partial x_j}\left[\left(\nu + \frac{\nu_t}{\sigma_k}\right)\frac{\partial k}{\partial x_j}\right] + \overline{\tilde{u}_i\tilde{u}_j}\frac{\partial \tilde{u}_i}{\partial x_j} + \varepsilon + \Pi = 0 \qquad (12)$$

$$\frac{D\varepsilon}{Dt} - \frac{\partial}{\partial x_j}\left[\left(\nu + \frac{\nu_t}{\sigma_\varepsilon}\right)\frac{\partial \varepsilon}{\partial x_j}\right]$$

$$+\; C_{\varepsilon 1} f_1 \frac{\varepsilon}{k}\overline{\tilde{u}_i\tilde{u}_j}\frac{\partial \tilde{u}_i}{\partial x_j} + C_{\varepsilon 2} f_2 f_\varepsilon \frac{\varepsilon^2}{k} - E = 0 \qquad (13)$$

$$\overline{\tilde{u}_i\tilde{u}_j} = -\nu_t\left(\frac{\partial \tilde{u}_i}{\partial x_j} + \frac{\partial \tilde{u}_j}{\partial x_i}\right) + \frac{2}{3}\delta_{ij}\, k \qquad (14)$$

$$\nu_t = C_\mu f_\mu \frac{k^2}{\varepsilon} \qquad (15)$$

Deux modèles à bas nombre de Reynolds ont été testés. Le modèle de Nagano et Tagawa, (1990), s'écrit:
$\sigma_k = 1.4$, $\sigma_\varepsilon = 1.3$, $C_{\varepsilon 1} = 1.45$, $C_{\varepsilon 2} = 1.9$, $C_\mu = 0.09$

$$f_1 = 1,\; f_2 = \left(1 - 0.3\exp\left[\frac{-R_t}{65}\right]^2\right)\left(1 - \exp\left[\frac{-y^+}{6}\right]\right)^2,\quad f_\varepsilon = 1.$$

$$f_\mu = \left(1 - \exp\left[\frac{-y^+}{26}\right]\right)^2 \left(1 + \frac{4.1}{R_t^{0.75}}\right)$$

$$\Pi = E = 0 \qquad (16)$$

$$R_t = \frac{k^2}{\nu\,\varepsilon}\ ,\ y^+ = \frac{y\,u_\tau}{\nu}\ ,\ u_\tau = \sqrt{\frac{\tau_w}{\rho}}$$

Nous utilisons également le modèle de Michelassi et Shih (1991), qui ne dépend pas explicitement de la distance y^+; cette caractéristique est importante pour le traitement particulier de l'orifice d'injection.

$\sigma_k = 1.3,\ \sigma_\varepsilon = 1.3,\ C_{\varepsilon 1} = 1.45,\ C_{\varepsilon 2} = 2.0,\ C_\mu = 0.09$

$$f_1 = 1,\ f_2 = 1 - 0.22\exp\left[\frac{-R_t}{36}\right]^2\ ,\ f_\varepsilon = 1 - \exp(-\sqrt{R_t})$$

$$f_\mu = 1 - \frac{\exp(-0.4\ 10^{-3}\exp[1.2\,R_L^{0.25}]}{\exp(-0.4\ 10^{-3})}$$

$$\Pi = \frac{\partial}{\partial x_j}\left(\frac{0.004}{f_\mu^2}\frac{\nu_t}{\sigma_k}\frac{\partial k}{\partial x_j}\right)\ ,\ E = -\nu\,\nu_t\left(\frac{\partial^2\tilde{u}}{\partial y^2}\right)^2 \qquad (17)$$

$$R_L = \frac{L}{L_\nu}\ ,\ L = \frac{k^{1.5}}{\varepsilon}\ ,\ L_\nu = \frac{\nu}{|u|}$$

Lors de l'utilisation pratique de ces modèles, nous utiliserons une hypothèse de parabolisation, caractéristique d'une couche limite; les termes de diffusion contenant des dérivées selon x seront donc éliminés.

Ces équations de transport de grandeurs turbulentes (12) et (13) sont ensuite moyennées selon z, selon une démarche similaire à celle employée pour obtenir les équations (2) à (5). Après calcul, nous obtenons:

$$\frac{\overline{D\,k}}{Dt} - \frac{\partial}{\partial x_j}\left[\left(\overline{\nu} + \frac{\overline{\nu_t}}{\sigma_k}\right)\frac{\partial\overline{k}}{\partial x_j}\right] + \overline{\tilde{u}_i'\tilde{u}_j'}\,\frac{\partial\overline{\tilde{u}_i}}{\partial x_j} + \overline{\varepsilon} + \overline{\Pi} = S_k \qquad (18)$$

$$S_k = \underbrace{-\frac{1}{\overline{\rho}}\frac{\partial}{\partial x_j}\left(\overline{\rho}\,\overline{d\tilde{u}_j\,dk}\right)}_{(a)} + \underbrace{\frac{\partial}{\partial x_j}\left(\overline{\frac{d\nu_t}{\sigma_k}\frac{\partial\,dk}{\partial x_j}}\right)}_{(b)} \underbrace{- \overline{d\left(\tilde{u}_i'\tilde{u}_j'\right)\frac{\partial d\tilde{u}_i}{\partial x_j}}}_{(c)} \qquad (19)$$

$$\frac{\overline{D\,\overline{\varepsilon}}}{Dt} - \frac{\partial}{\partial x_j}\left[\left(\overline{\nu} + \frac{\overline{\nu_t}}{\sigma_\varepsilon}\right)\frac{\partial\overline{\varepsilon}}{\partial x_j}\right]$$

$$+ C_{\varepsilon 1} f_1 \frac{\overline{\varepsilon}}{\overline{k}}\,\overline{\tilde{u}_i'\tilde{u}_j'}\,\frac{\partial\overline{\tilde{u}_i}}{\partial x_j} + C_{\varepsilon 2} f_2 f_\varepsilon \frac{\overline{\varepsilon}^2}{\overline{k}} - \overline{E} = S_\varepsilon \qquad (20)$$

$$S_\varepsilon = -\frac{1}{\overline{\rho}}\frac{\partial}{\partial x_j}\left(\overline{\rho}\,\overline{d\tilde{u}_j\,d\varepsilon}\right)$$

$$-\frac{1}{\overline{\rho}\,\overline{k}}\,\overline{dk\,\frac{\partial}{\partial x_j}\left(\overline{\rho}\,\tilde{u}_j\,\overline{\varepsilon}\right)} - \frac{1}{\overline{\rho}\,\overline{k}}\,\overline{dk\,\frac{\partial}{\partial x_j}\left(\overline{\rho}\,\overline{\tilde{u}_j}\,d\varepsilon\right)}$$

$$+\frac{\partial}{\partial x_j}\left(\overline{\frac{d\nu_t}{\sigma_\varepsilon}\frac{\partial\,d\varepsilon}{\partial x_j}}\right)$$

$$+\frac{1}{\overline{k}}\,\overline{dk\,\frac{\partial}{\partial x_j}\left(\frac{d\nu_t}{\sigma_\varepsilon}\frac{\partial\overline{\varepsilon}}{\partial x_j}\right)} + \frac{1}{\overline{k}}\,\overline{dk\,\frac{\partial}{\partial x_j}\left(\frac{\overline{\nu_t}}{\sigma_\varepsilon}\frac{\partial\,d\varepsilon}{\partial x_j}\right)}$$

$$-\frac{C_{\varepsilon 1} f_1}{\overline{k}}\left[\overline{\varepsilon}\,\overline{d\,\tilde{u}_i'\tilde{u}_j'\,\frac{\partial d\tilde{u}_i}{\partial x_j}} + \overline{d\varepsilon\,d\tilde{u}_i'\tilde{u}_j'}\,\frac{\partial\overline{\tilde{u}_i}}{\partial x_j} + \overline{d\varepsilon\,\frac{\partial\,d\tilde{u}_i}{\partial x_j}}\,\overline{\tilde{u}_i'\tilde{u}_j'}\right]$$

$$-C_{\varepsilon 2} f_2 f_\varepsilon \frac{\overline{d\varepsilon^2}}{\overline{k}} + \frac{\overline{dk\,dE}}{\overline{k}} \qquad (21)$$

Les termes sources S_k et S_ε représentent la contribution des jets sur le champ turbulent moyen.

4. METHODE NUMERIQUE

Les équations précédentes ont été résolues à l'aide d'un schéma de différences finies de Keller pour les équations parabolisées; l'équation (7) est écrite à la paroi, et est résolue en même temps que les équations de la couche limite (Kulisa, Leboeuf Klinger, Bernard, 1992). Les équations de transport des grandeurs turbulentes ont été résolues de manière découplée, une fois calculé le champ de vitesse moyen, suite à la solution des équations (2) à (7) et du modèle de jet tridimensionnel. La valeur de ν_t obtenue à l'aide de k et ε n'a pas été réintroduite dans les équations de la couche limite (2) à (5). Pour les résultats présentés dans ce papier, le champ de vitesse moyen est donc uniquement obtenu à l'aide d'un modèle de turbulence de longueur de mélange de Cebeci-Smith. L'emploi d'une méthode de marche de l'amont vers l'aval se traduit par des coûts de calcul particulièrement faibles, qui permet son utlisation sur une station de travail. En outre, le couplage des équations de la couche limite avec la simulation de l'écoulement non-visqueux, donnée par l'équation (7), se traduit par une excellente stabilité du code.

5. VALIDATIONS DU MODELE

Des résultats sont présentés pour deux cas de couches limites turbulentes qui se développent sur une plaque plane, en présence d'injections discrètes (Vuillerme, Foucault, Dorignac, Deniboire et Bousgarbiès,1992). Les conditions d'injections sont les suivantes : diamètre des tubes d'injection D= 0.005 m, distance entre tubes G=0.015 m, épaisseur de la couche limite en amont de l'injection δ =0.010 m, vitesse extérieure à la couche limite U_e= 30 m/s, taux d'injection U_J/ U_e = 2/3 et 5/3; angle d'injection 45°, température des jets = 340°K, température du fluide transversal = 301°K, température de la paroi loin des injections = 310°K. Seule les résultats cinématiques seront analysés ici.

Un exemple de variations selon la direction y normale à la paroi et dans le plan de symétrie z=0, de la composante u de la vitesse, est donnée dans la figure 3 pour les deux taux d'injection U_J/ U_e = 2/3 et 5/3; ces résultats sont présentés après un calcul de couche limite et de jet, sans tenir compte du modèle de turbulence k-ε. Nous remarquons que la perturbation introduite par le jet à taux d'injection élevé est très forte.

Le test du modèle de turbulence k-ε sans termes-source est tout d'abord réalisé dans le plan de symétrie z=0, qui se rapproche le plus d'une configuration bidimensionnelle, et en utilisant les résultats tridimensionnels non moyennés du calcul du calcul de couche limite et de jet. Les deux modèles à bas nombre de Reynolds de Nagano et Tagawa (1990) et Michelassi et Shih (1991) ont été utilisés. Pour le premier, les fonctions d'amortissement ne sont pas utilisées dans l'orifice d'injection puisque le paramètre y^+ n'est pas defini. Les figures 4 et 5 présentent les résultats pour les taux d'injection 2/3 et 5/3 respectivement, dans les sections de mesures x=-1D,- 0.5D, 0D, +0.5D, +1D, +2D. L'axe du jet est situé à x=0; l'orifice d'injection s'étend de x=-0.5D à x=+-0.5D. D'une manière générale, le modèle de Michelassi et Shih donne de meilleurs résultats; le modèle de Nagano et Tagawa a en effet tendance à surestimer les variations de la tension de Reynolds à proximité de la paroi. Ce comportement est lié à l'utilisation de l'échelle locale de turbulence $L=k^{1.5}/\varepsilon$ dans les fonctions d'amortissement du modèle de Michelassi et Shih, alors que ces dernières sont supprimées au niveau de l'orifice pour le modèle de Nagano et Tagawa. La différence entre les deux modèles devient cependant négligeable pour y>0.003 m. Quoique la vitesse $\tilde{u}$ soit assez bien prédite, même dans la zone d'injection (figure 3), en particulier pour la localisation du maximum de vitesse selon y, il existe un net décalage sur la position du maximum de la tension de Reynolds entre les valeurs prédites et mesurées (x=-0.5D à +0.5D); il est probable que l'hypothèse de Boussinesq ne soit pas acceptable dans cette zone. A l'aval de la zone d'injection (x≥+0.005 m), l'accord entre prédictions et mesures est nettement plus satisfaisant. Des comparaisons similaires sont données dans les figures 5 pour le taux d'injection 5/3. Deux pics de tensions de Reynolds apparaissent sur ces figures pour x≥0 m; ces deux pics s'éloignent de la paroi pour les sections aval. Alors que le pic situé dans la zone externe de la couche limite peut être approché par le calcul, le pic situé à proximité de la paroi est totalement ignoré. Enfin les valeurs expérimentales très élevées pour les tensions, en particulier sur la face aval de l'orifice (x=+1D), sont sous-estimés par le calcul.

Il semble que le calcul ne reproduise pas du tout l'allure de l'évolution de la tension turbulente à la paroi sous l'effet du jet; ce comportement est particulièrement flagrant en x=+2D, pour laquelle le calcul inverse complètement l'évolution de la tension de Reynolds à la paroi, alors que la prédiction à l'extérieur de la couche est correcte.

Plusieurs hypothèses peuvent être émises pour expliquer ce phénomène:

a) Tout d'abord, le rôle du modèle de Boussinesq dans le calcul doit être souligné; l'utilisation de celui-ci empêche de déterminer le pic positif de tension près de la paroi; un comportement similaire a été observé par Pinho Brasil (1992), à l'aide d'un code résolvant les équations de Navier-Stokes tridimensionnelles, mais en utilisant un modèle de turbulence du type k-ε avec lois de parois.

b) Il faut noter que notre modèle ignore complétement les structures tourbillonnaires, appelés Ω_2, Ω_3, et Ω_4 au début de ce texte, et qui sont liées à la vorticité propre de la couche limite de paroi. Il serait intéressant de quantifier les diverses grandeurs turbulentes liées à ces structures; cependant, notons que les résultats de Pinho Brasil (1992) qui présentent les tourbillons Ω_2, ne montrent pas clairement un excès de k dans ces zones.

c) Enfin, rappelons que notre calcul ne tient pas compte de la déflexion du jet dans le tube d'injection lui-même, qui est très importante pour les faibles taux d'injection (Bergelés et al, 1976); ceci conduit a de fortes augmentations du taux de turbulence près de la paroi (Bergelés et al, 1976); cependant, les expériences menées avec un conduit d'injection court (l/d ≤ 3.5), telles que celles traitées ici, peuvent être influencées par un décollement à l'entrée du conduit, ce qui modifie fortement les structures turbulentes issues de l'orifice (Pietrzyk, Bogard, Crawford, 1989). Il existe donc une certaine imprécision concernant les informations turbulentes issues de l'orifice, en particulier liée à l'existence possible d'une zone potentielle dans le jet, qui doit réduire le niveau de turbulence dans le jet (Charbonnier,1992), ou d'une zone de mélange turbulent introduite par un décollement dans le conduit, qui pourrait accroître le niveau de turbulence dès l'orifice.

d) Finalement, des phénomènes instationnaires plus ou moins périodiques existent peut-être dans ces mesures et qui pourraient expliquer en partie les fortes valeurs de tensions mesurées à la paroi; de tels phénomènes ont été observés par Charbonnier (1992) pour un jet normal à la paroi, et un taux d'injection de 0.56, suite à l'introduction de fluide extérieur dans la zone amont de l'orifice, qui induit un battement de la frontière externe du jet, mais aussi au comportement du sillage à l'aval.

Les calculs moyennés selon z sont présentées sur les figures 6 et 7, pour les deux taux d'injection 2/3 et 5/3 respectivement, en utilisant cette fois-ci les champs de vitesse en moyenne d'espace. Les grandeurs moyennées selon z ont des évolutions beaucoup plus lisses que celles présentées en z=0 sur les figures 4 et 5. Les résultats obtenus sans termes-source turbulent du jet S_k ou S_ε sont peu éloignés de ceux obtenus dans une couche limite bidimensionnelle. Les termes-source de jet ont été introduits dans le calcul; seuls le terme (c) de S_k (équation 19) et la forme complète de l'équation 11 ont été utilisés; le terme S_ε a été ignoré compte tenu du degré d'approximation du modèle de turbulence employé pour le calcul de jet. Nous constatons une nette amélioration de la prédiction en tenant compte des termes-source de jet. Une analyse détaillée de l'importance des termes des équations (19) et (21) reste cependant à mener pour confirmer ces premiers résultats.

6. CONCLUSIONS

Une résolution des équations de k et ε a été réalisée dans le but de calculer le champ turbulent dans une couche limite en présence d'injection discrètes à la paroi. L'objectif de disposer d'une méthode de calcul, plus légère que la résolution directe des équations tridimensionnelles de Navier-Stokes, nous a conduit à rechercher l'utilisation de méthode bidimensionnelle. Dans ce but, les équations de conservation des grandeurs turbulentes sont moyennées selon la direction spatiale z, parallèle à la rangée d'orifices d'injection. Des termes-source, liés aux jets, apparaissent alors dans les équations moyennées; ces termes sont déduits du calcul d'un jet tridimensionnel. Un modèle de turbulence à bas nombre de Reynolds a été employé; le modèle de Michelassi et Shih semble donner de meilleurs résultats par rapport au modèle de Nagano et Tagawa, essentiellement car les fonctions d'amortissement basées sur des échelles locales de turbulence ont pu être utilisées dans l'orifice d'injection.

Les résultats du modèle ont été comparés avec les mesures réalisées au CEAT de Poitiers, pour une couche limite turbulente, avec deux taux d'injection (2/3 et 5/3). Les résultats de la comparaison, pour le plan médian z=0, sont assez satisfaisants pour le faible taux d'injection 2/3. Cependant, pour le fort taux d'injection 5/3, il apparaît un pic de tension de Reynolds à la paroi, dans la zone d'injection, qui est complètement ignoré par le modèle actuel basé sur l'hypothèse de Boussinesq. Les prédictions sont en général de meilleure qualité dans la zone externe de la couche limite. Il importe maintenant de préciser la contribution au niveau des informations turbulentes, des structures tourbillonaires qui apparaissent dans la couche limite, sous l'influence du jet.

Les informations moyennées selon z présentent des variations beaucoup plus faibles selon la normale y à la paroi. La prédiction est cependant fortement améliorée lorsque les termes sources de jet sont introduits. Cependant, compte tenu de la simplicité du modèle de turbulence retenu jusqu'ici pour le jet, nous n'avons pas ici déterminé tous les termes sources dans les équations de transport de k et de ε. Ce résultat devra donc être confirmé ultérieurement.

Remerciements

Les auteurs sont reconnaissants à SNECMA pour le soutien et l'intérêt constant manifesté au cours de cette étude, ainsi que des discussions fructueuses qui ont permis d'améliorer ce modèle. Le travail de doctorat de J.M. Maurice est financé à l'aide d'une convention Cifre SNECMA, n° 429-89. Les résultats expérimentaux ont été obtenus au CEAT de Poitiers, avec un financement DRET.

Références

1. Andreopoulos J., Rodi W. ,1984, "Experimental Investigation of Jets in a Crossflow", J. Fluid Mech., 138, pp. 93-127.
2. Andreopoulos J., 1985, "On the structure of jets in a crossflow", J. Fluid Mech., 17, pp.163-197.
3. Bergeles G., Gosman A.D., Launder B.E., 1976, "The near field character of a jet discharged normal to a main stream" Asme J. Heat Transfer, vol. 98, p.973.
4. Bergeles G., Gosman A.D., Launder B.E., 1981, "The prediction of the three-dimensional discrete hole cooling processes, part 2: turbulent flow" Asme J. Heat Transfer, vol. 103, p. 141.
5. Bousgarbiès J.L., Brizzi L.E., Foucault E., 1991 "Vorticité au voisinage d'un jet circulaire débouchant perpendiculairement dans une couche limite; cas des petits nombres de Reynolds", AUM, 10ème congrès Français de Mécanique, Paris.
6. Bry P., 1989 "Blading design for cooled high pressure turbines", Agard LS 167, n°7.
7. Calatano G.D., Chang K.S., Mathis J.A., 1989, "Investigation of turbulent jet impingement in a confined crossflow", AIAA J., vol. 27, N° 11, pp. 1487-1493, Nov.
8. Charbonnier J.M., Leblanc R., 1990, "Preliminary Investigations in the Exit Region of a Jet in a Crossflow", First ISAIF, Beijing.
9. Charbonnier J.M., 1992, "Analyse et modélisation de l'interaction d'un jet perpendiculaire de paroi avec un écoulement principal", thèse de doctorat, Université de Poitiers, N° 504, Mai.
10. Crab D., Durao D.F.G., Whitelaw J.H., 1981, " A round jet normal to a cross flow", ASME J. of Fluids Eng. , 103, pp.142-153.
11. Demuren A.O., 1983, "Numerical calculations of steady three dimensional turbulent jets in a crossflow", comp. Meth. in applied Mech. and eng., vol. 27, pp. 309-328.
12. Demuren A.O., 1990, "Calculation of 3D turbulent jets in a crossflow with a multigrid method and second moment closure". International symposium on engineering turbulent modelling and measurements, Dubrovnik, Yougoslavia, pp. 13-23, Elsevier ed., Sept 24-28.
13. Escande B.,Cambier L., 1991, "Validation du code "CANARI" par le calcul de l'écoulement tridimensionnel dans un distributeur de turbine", 77th PEP/AGARD "CFD

Techniques for propulsion applications, San Antonio, USA, May 27-31, N° 14.

14. Fearn A., Weston R.P, 1974, "Vorticity Associated with a jet in a Crossflow", AIAA Journal, 12, pp.1666-1671.

15. Fric T.F., Roshko A., 1989, "Structure in the Near Field of the Transverse Jet", tenth symposium on turbulent shear flows, Oxford University.

16. Herring H. J. 1975, "A method of predicting the behaviour of turbulent boundary layer with discrete transpiration jets", J. Eng. for Power, pp. 214-224.

17. Ince N.Z., Leschziner M.A., 1990, "Computation of three dimensional jets in crossflow with and without impingement using second moment closure", International symposium on engineering turbulent modelling and measurements, Dubrovnik, Yougoslavia, pp. 13-23, Elsevier ed., Sept 24-28.

18. Khan Z.A., Mc Guirk J.J., Whitelaw J.H., 1982 "A row of jets in a crossflow", AGARD CP 308.

19. Kulisa P., Leboeuf F., Perrin G., 1991, "Computation of a Wall Boundary Layer with Discrete Jet Injections ", ASME Paper n° 91-GT-143, 1991, ORLANDO ; to appear in the Journal of Turbomachinery in 1992.

20. Kulisa P., Leboeuf F., Klinger P., Bernard J., 1992 "Computation of a thermal Boundary Layer including strong viscous-inviscid Flow Interaction", Journal de Physique III, numéro spécial Turbomachine, Avril.

21. Lam C.K.G., Bremhorst K., 1981 "A modified form of the k-ε model for predicting wall turbulence", ASME J. Fluids eng., vol. 103, pp. 456-460, sept.

22. Launder B.E., 1988, " On the computation of convective heat transfer in complex turbulent flows", ASME J. Heat Transfer, vol. 110, pp. 1112-1126, nov.

23. Leboeuf F., Huang G.P., Kulisa P., Perrin G., 1991, "Model and Computation of discrete Jets in Crossflow", European Journal of Mechanics, B/fluids, vol. 10 n° 6, pp. 629-650.

24. Michelassi V., Shih T.H.,1991, "Low Reynolds number two equation modelling of turbulent flows", NASA TM 104368, ICOMP-91-06, CMOTT-91-01, may.

25. Miller K.L., Crawford M.E., 1984, " Numerical simulation of single, double and multiple row film cooling effectiveness and heat transfer", ASME paper 84-GT_112, Amsterdam, June 4-7.

26. Moussa Z.M., Trischka J.W., Eskinazi S., 1977, "The near field in the mixing of a round jet with a cross-stream", J. Fluid Mechanics , 80, pp. 48-80.

27. Nagano Y., Tagawa M., 1990 "An improved k-ε model for boundary layer flows", ASME J. Fluid Eng., vol 112, pp. 33-39, March.

28. Pietrzyk J.R., Bogard D.G., Crawford M.E., 1989 "Effects of density ratio on the hydrodynamics of film cooling", ASME paper n° 89-GT 175, Toronto, june 4-8.

29. Pinho Brasil Junior A.C., 1992, " Simulation numérique par éléments finis des écoulements turbulents tridimensionnels avec dispersion : approches eulérienne et lagrangienne", thèse de doctorat Ecole centrale de Lyon, Juillet.

30. Schönung B., Rodi W., 1987, "Prediction of a film cooling by a row of holes with a 2D boundary layer procedure", J. of turbomachinery, vol. 109, pp. 579-587, oct.

31. Shih T.H., Mansour N.N. 1990, " Modelling of near-wall turbulence", International symposium on engineering turbulent modelling and measurements, Dubrovnik, Yougoslavia, pp. 13-23, Elsevier ed., Sept 24-28.

32. Sykes R.I., Lewellen W.S., Parker S.F., 1986, "On The Vorticity Dynamics of a Turbulent Jet in a Crossflow" J. Fluid Mech, 168, pp. 393-413.

33. Tafti D.K., Yavuzkurt S., 1989, "Prediction of heat transfer characteristics for discrete hole film cooling for turbine blade application", Asme paper 89-GT-139, Toronto, June.

34. Vuillerme J.J., Foucault E., Dorignac E., Deniboire P., Bousgarbiès J.J.,1992 "Experimental study of heat transfer near a heated flat wall with multiple injections" , paper n°4, AGARD 80th Symposium on Heat transfer and cooling in gas turbines, Antalya, Turkey, October.

35. White A.J., 1980, "The prediction of the flow and heat transfer in the vicinity of a jet in a crossflow", PNR 90025, Rolls Royce Ltd.

36. Yavuzkurt S., Moffat R.J., Kays W.H., "Full coverage film cooling, part 2: Prediction of the recovery region hydrodynamics", J. Fluid Mech., Vol. 101, pp. 129-158.

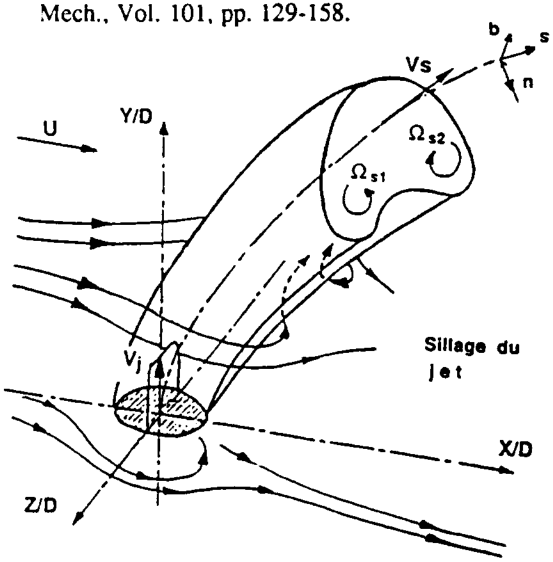

Figure 1. Structure d'un jet à fort taux d'injection. Repère local.

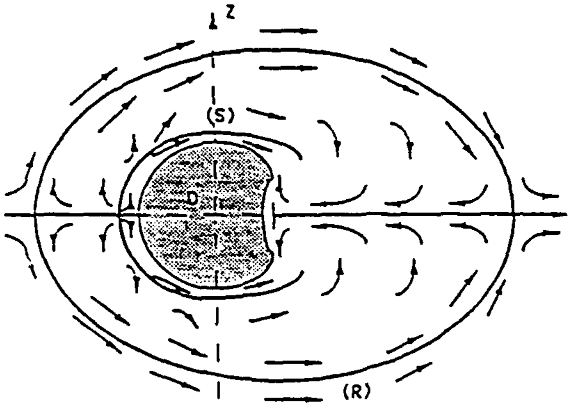

Figure 2. Visualisation des lignes de courant pariétales (Bousgarbiès, Brizzi, Foucault , 1991).

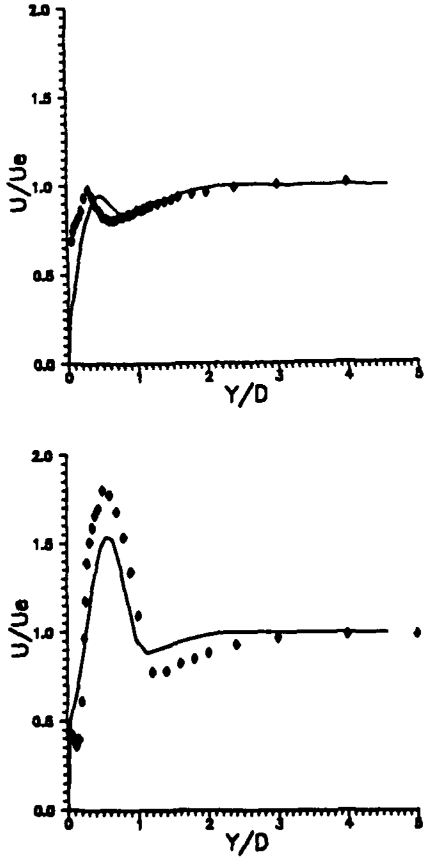

Figure 3. Exemple de variation de la composante U de la vitesse selon la normale à la paroi: (a) taux d'injection $U_J/U_e = 2/3$, (b)$U_J/U_e = 5/3$ (mesures réf. 34 ◊, calcul ___). x=1D, z=0.

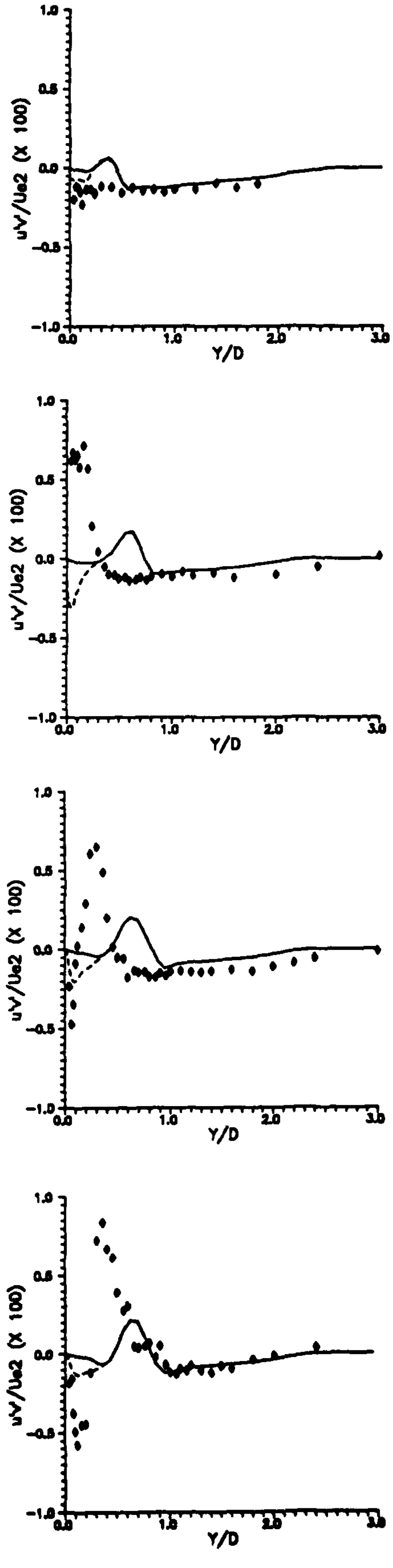

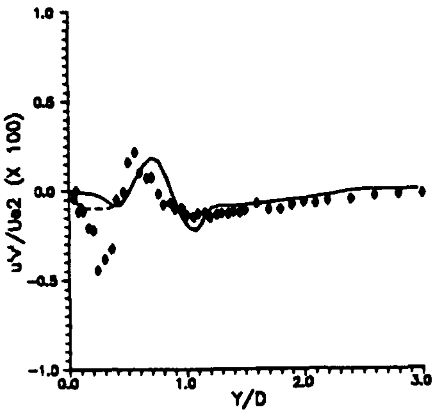

Figure 4. Comparaisons entre les mesures de $\widetilde{u'v'}$ et les calculs dans le plan médian z=0. Taux d'injection $U_J/U_e = 2/3$. ◊ mesures réf. 34, ---- calcul avec le modèle de Nagano et Tagawa , _____ calcul avec le modèle de Michelassi et Shih ; a) x=-1D, b) x=0, c) x=0.5D, d) x=1D, e) x=2D

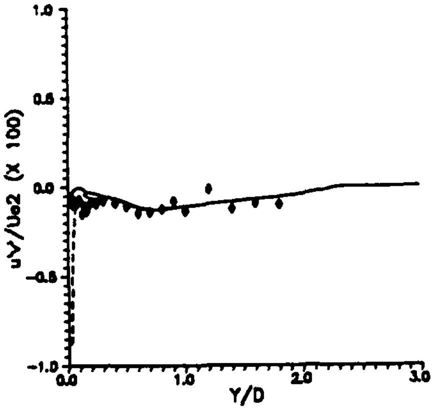

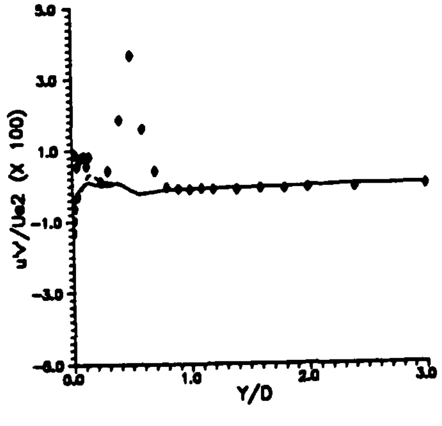

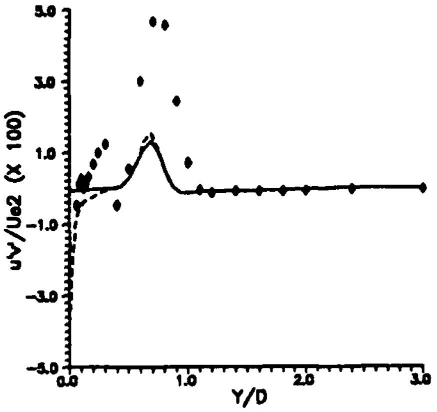

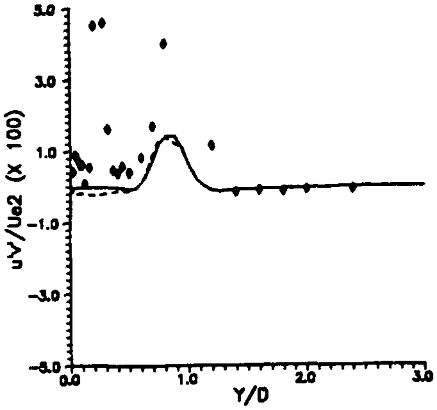

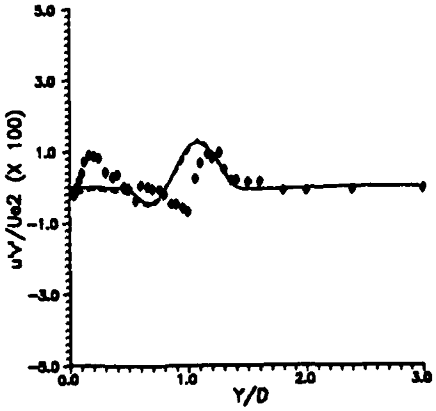

Figure 5. Comparaisons entre les mesures de $\widetilde{u'v'}$ et les calculs dans le plan médian z=0. Taux d'injection $U_J/U_e = 5/3$. ◊ mesures réf. 34,_____ calcul avec le modèle de Nagano et Tagawa; a) x=-1D, b) x=0 ,c) x=0.5D, d) x=1D, e) x=2D

Figure 6. Calculs moyennés selon z de $\overline{\widetilde{u'v'}}$. Taux d'injection $U_J/U_e = 2/3$. ----calculs sans termes-source du jet, et ____avec les termes-source du jet (modèle de Nagano et Tagawa) mesures moyennées réf. 34 ◊ ;
a) x=0 , b) x=0.5D, c) x=1D, d) x=2D.

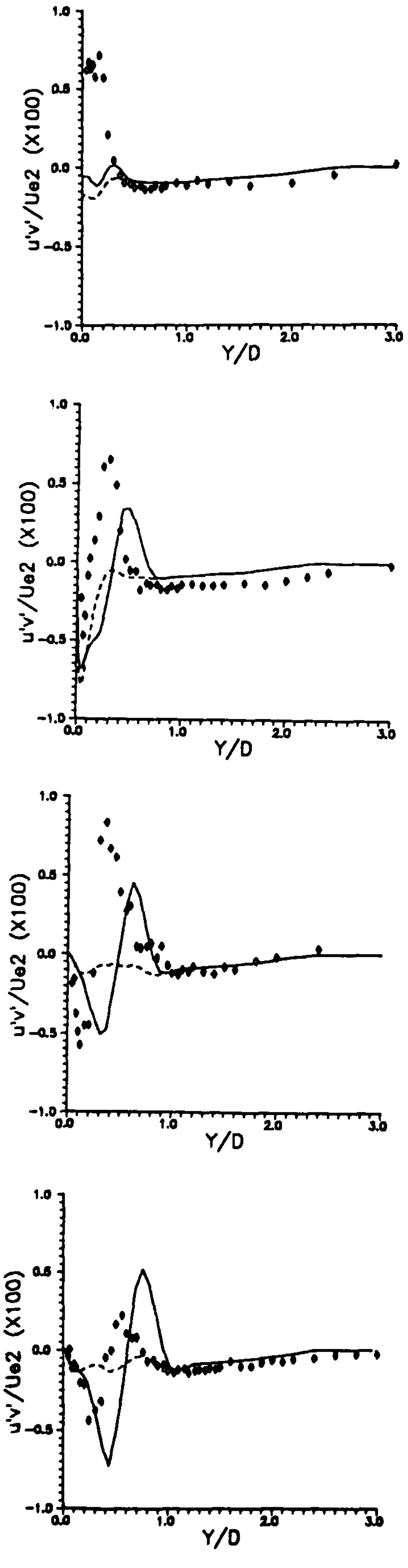

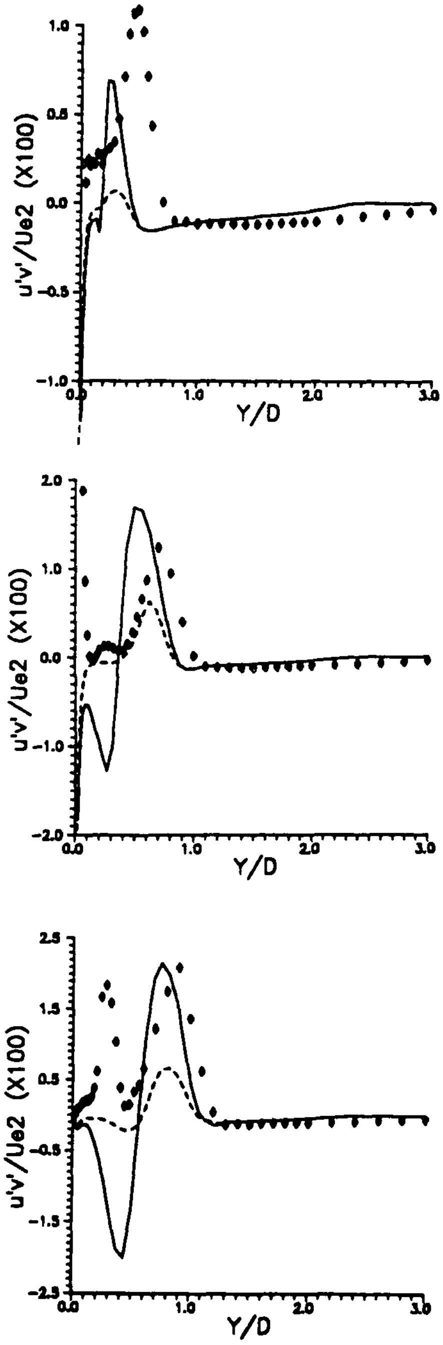

Figure 7. Calculs moyennés selon z de $\overline{\widetilde{u'v'}}$. Taux d'injection $U_J/U_e = 5/3$. ----calculs sans termes-source du jet, et ____avec les termes-source du jet (modèle de Nagano et Tagawa) mesures moyennées réf. 34 ◊ ;
a) x=0, b) x=0.5D, c) x=1D.

Discussion

QUESTION 1:

DISCUSSOR: D.T. Vogel, DLR

What is the difference between your work and the work of Schönung and Rodi?

AUTHOR'S REPLY:

There are three differences. First, our formulation, based on Herring's space averaged method, gives us all the source-terms in Navier-Stokes and k-ε equations. Secondly, the turbulence model takes into account the specific turbulent scales of the jet in the k-ε equations. The third difference is that our computational domain covers the injection region.

QUESTION 2:

DISCUSSOR: D.T. Vogel, DLR

What happens if the jet passes through the boundary layer as for higher blowing rates and blowing angles?

AUTHOR'S REPLY:

For the case with a blowing ratio of five-thirds, the jet does penetrate into the outer part of the boundary layer. Our model accounts for this by considering source terms in the inviscid flow.

QUESTION 3:

DISCUSSOR: F. Baron, EDF/DER Dept. Machines

Which of the two low-Reynolds-number models do you prefer?

AUTHOR'S REPLY:

It is very difficult to draw a conclusion at this time. The two models differ primarily in their damping functions. The Nagano-Tagawa model explicitly involves the distance from the wall which is a problem above a hole. Here, we used a high-Reynolds-number model instead. For the Michelassi-Shih model, even though the local length scales and damping functions are used, the coarse grid yields questionable results. Therefore, we can't tell which model is best and presently keep both for our use.

Coupling of 3D-Navier-Stokes External Flow Calculations and Internal 3D-Heat Conduction Calculations for Cooled Turbine Blades

A. Heselhaus
D.T. Vogel
H. Krain
DLR, Institut für Antriebstechnik
Linder Höhe, D-5000 Köln 90

1 Abstract

The problem of cooled gas turbine blades is theoretically investigated. The presented code solves the 3D–Reynolds averaged–Navier–Stokes equations for the external passage flow and the 3D–heat conduction equation for the interior of the blade. Both calculation schemes are coupled without any modelling of the heat transfer boundary conditions at the blade surface.

In this paper calculations are presented for a thin hollow flat plate and a typical guide vane blade with a simple cooling channel configuration. Both geometries are cooled by prescribing fixed heat transfer boundary conditions at the inner boundaries.

Additionally numerical results are compared to analytical data. The agreement is quite satisfactory.

2 List of symbols

A	cell face surface
c_p	specific heat
D	dissipation
e	energy
f	load vector
K	stiffness matrix
l	axial chord length
n	number of flow-solver timesteps per coupling step
N	shape function
Nu	Nusselt number
Pr	Prandtl number
p	pressure
$\dot{q}$	heat flux density
r	radius
Re	Reynolds number
T	temperature
t	time
u	velocity
V	finite volume
x, y, z	cartesian coordinates
x, φ, r	cylindrical coordinates
y	distance from wall
α	heat transfer coefficient
ϵ	residual
Γ	boundary with spec. heat transf. coeff.
λ	thermal conductivity
μ	viscosity
∇	Nabla Operator
Ω	integration domain
ω	rotational speed
Ψ	weighting factor
ρ	density
τ	shear stress
θ	dimensionless temperature
ξ, η, ζ	local FEM-coordinates

Superscripts

e	element
T	transposed
V	volumetric
$+$	wall coordinate
$*$	virtual

Subscripts

1	center of cell next to the wall
a	ambient
c	cooling fluid
f	friction
i, j	local node number
in	inlet
l	based on the axial chord length
n	normal direction
t	total
w	wall
x, y, z	in direction of cartesian coordiantes
x, φ, r	in direction of cylindrical coordiantes

3 Introduction

The requirement for lower specific fuel consumuption or higher thrust to weight ratios in modern jet engine design generally results in higher turbine inlet temperatures. Nowadays turbine inlet temperatures up to 1750 K and even more are realized, whereas the blade temperatures are limited to a maximum value of approximately 1150 K. This necessitates an effective turbine blade cooling.

Designing a new blade cooling configuration, the design engineers have to take care that the maximum material temperatures and stresses inside the blade are sufficiently small. Therefore temperature-field calculations have to be performed which are usually based on heat transfer boundary conditions obtained by experiments or boundary layer calculations.

Deriving blade surface-heat transfer coefficients from experiments requires test blades and a suitable testrig. Generally, time consuming and expensive runs have to be performed to measure the local heat transfer coefficients for different hot gas inlet conditions.

When deriving the heat transfer coefficients from boundary layer calculations 3D-effects of the real gas flow are not taken into account. The necessary pressure- or velocity-distribution along the surface is usually taken from experiments or CFD-calculations.

Meanwhile there are several publications on 3D-heat transfer calculations with fixed thermal boundary conditions, [1], [4], [9]. A thermal coupling between flow and structure is performed only by a few authors [10], [13], [14], [15]. Most of this work is based on a 2D-approach [10], [13], [15]. Vogel [14] at first coupled a 3D-finite volume Navier-Stokes code with a 3D-finite volume heat conduction program. Resolving of cooling channels was difficult because therefore a complex multiblocking inside the blade would have been necessary. Blade cooling was here simulated by prescribing constant hub and tip temperatures.

In the here presented paper a steady state 3D-Navier-Stokes flow solver is coupled with a steady state 3D-finite element heat conduction solver. The finite element approach for calculating the blade temperature distribution offers excellent possibilities to resolve complex cooling channel geometries. The wanted temperature distribution inside the blade results directly from the passage flow calculation thermally coupled with the blade-heat conduction calculation. Thermal boundary conditions have to be specified at the endwalls and at the cooling channel surfaces. No further thermal boundary conditions are necessary. Heat transfer coefficients at the outer blade surface are here obtained as a result of the calculation.

Furthermore this method offers the possibility to take care of the thermal interactions between flow and blade when calculating the heat fluxes into the blade.

All coupling-calculations were performed in 3D with Reynolds-numbers of 10^4, so that the flow was treated as laminar and the currently implemented Baldwin-Lomax turbulence model was not used. The calculation of the temperature gradients at the wall were made *without* using any model.

4 Program Description

To compute the hot gas flow through a turbine stator or rotor a 5-block finite volume Navier Stokes flow solver was developed (**FLOWNS**, Fig. 1). The flow solver is also able to compute heat transfer problems by simultaneously solving the energy equation.

The computation of the temperature distribution inside the blade is performed with a finite element code (**BLADFE**, Fig. 1), offering the possibility to model complex shapes of internal cooling channels.

A third program (**COUP**, Fig. 1) controls the correct thermal coupling at the common boundaries of the two different and completely independent grids.

The three programs were combined to a program system, where each program acts as a single processor with well defined functions. Every n time steps of the flow solver **COUP** calls the finite element solver and returns the new wall temperatures back to the flow solver, Fig. 1. This cycle is repeated until a choosen maximum number of coupling steps is performed. The value of n can be freely choosen by the user.

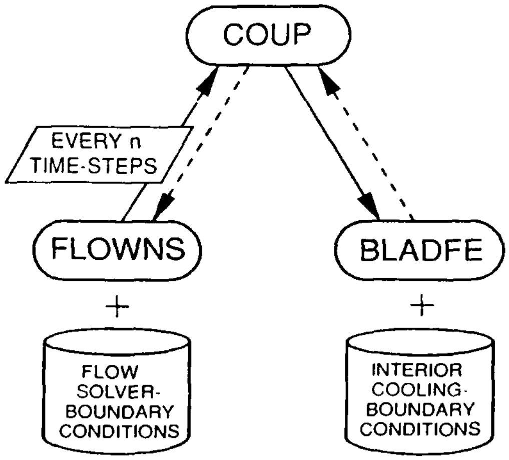
COUP
EVERY n TIME-STEPS
FLOWNS
BLADFE
+
+
FLOW SOLVER-BOUNDARY CONDITIONS
INTERIOR COOLING-BOUNDARY CONDITIONS

Figure 1: Program-system scheme

4.1 Finite Element Program

The used program is based on the Finite Elment Analysis Program FEAP written by R.L. Taylor and extended by J.M. Bettencourt, [3]. The program was extended in such a way that it can be used as a subroutine and that the boundary conditions can be set when the routine is called. Although the program is able to calculate with temperature-dependant heat conductivities the heat conductivity was set constant to save computing time.

Isoparametric, 20-node 3D-heat conduction elements were used to build the blade-mesh, Fig. 2. Geometry and Temperature distribution inside those elements are described in local coordinates ξ, η and ζ, which vary between -1 and $+1$. The six limiting surfaces are defined by $\xi = \pm 1$, $\eta = \pm 1$ and $\zeta = \pm 1$. The temperature and the related spatial coordinates are defined by

$$T = \sum_{i=1}^{20} T_i N_i \left(\vec{\xi}\right)$$

$$\vec{x} = \sum_{i=1}^{20} \vec{X}_i N_i \left(\vec{\xi}\right)$$

where the T_i are the temperatures and the $\vec{X}_i$ are the coordinates of the element nodes. N_i are the *shape functions*, which define the 'influence' of temperature and coordinate of each of the 20 nodes on the point $\vec{\xi} = \xi, \eta, \zeta$, in which temperature and coordinates are to be calculated. These shape functions are of the serendipity type and are defined for the 8 corner nodes by

$$N_i \left(\vec{\xi}\right) = \tfrac{1}{8}(1 + \xi_i\xi)(1 + \eta_i\eta)(1 + \zeta_i\zeta)(\xi_i\xi + \eta_i\eta + \zeta_i\zeta - 2)$$
$$\xi_i = \pm 1,\ \eta_i = \pm 1 \text{ and } \zeta_i = \pm 1,$$

for nodes 9, 11, 13, 15 by

$$N_i \left(\vec{\xi}\right) = \tfrac{1}{4}(1 - \xi^2)(1 + \eta_i\eta)(1 + \zeta_i\zeta)$$
$$\eta_i = \pm 1,\ \zeta_i = \pm 1,$$

for nodes 10, 12, 14, 16 by

$$N_i \left(\vec{\xi}\right) = \tfrac{1}{4}(1 - \eta^2)(1 + \xi_i\xi)(1 + \zeta_i\zeta)$$
$$\xi_i = \pm 1,\ \zeta_i = \pm 1,$$

and for nodes 17, 18, 19, 20 by

$$N_i \left(\vec{\xi}\right) = \tfrac{1}{4}(1 - \zeta^2)(1 + \xi_i\xi)(1 + \eta_i\eta)$$
$$\xi_i = \pm 1,\ \eta_i = \pm 1.$$

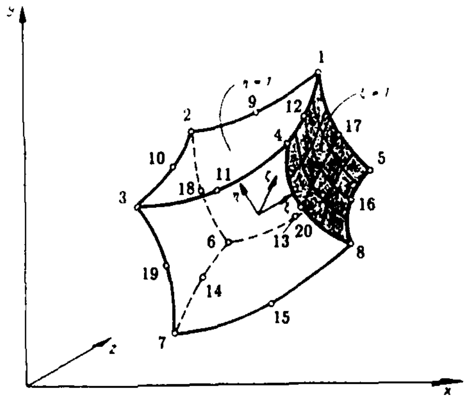

Figure 2: Isoparamteric 20-node finite element, [17]

Generally, the nonlinear heat conduction equation

$$\nabla^T \lambda \nabla T(\vec{x}) + \dot{q}^V = 0 \tag{1}$$

is to be solved. Because solving a discretised differential equation never leads to the exact solution, eq. 1 becomes

$$\nabla^T \lambda \nabla T(\vec{x}) + \dot{q}^V = \epsilon(\vec{x})$$

FEAP uses the method of weighted residuals for the solution. The basic principle of this method is that the residuals $\epsilon(\vec{x})$ multiplied with a weighting factor $\Psi(\vec{x})$ and integrated over the whole computing domain must become zero:

$$\int_\Omega \left(\nabla^T \lambda \nabla T(\vec{x}) + \dot{q}^V\right) \Psi(\vec{x})\, d\Omega = 0$$

The weighting functions are chosen to be the same as the shape functions. This is Galerkins principle:

$$\Psi_i(\vec{x}) = N_i(\vec{x})$$

Adding the boundary conditions and discretizing by elements leads to the equation system

$$\sum_{e=1}^{NEL} (\mathbf{K}^e \mathbf{T}^e - \mathbf{f}^e) = 0$$

with

$$\begin{aligned} \mathbf{K}^e &= \int_{\Omega^e} \nabla^T N_i^e \lambda \nabla N_j^e \, d\Omega - \int_{\Gamma^e} N_i^e \alpha N_j^e \, d\Gamma & (2) \\ \mathbf{f}^e &= -\int_{\Omega^e} \dot{q}^V d\Omega + \int_{\Gamma^e} N_i^e \alpha T_a \, d\Gamma & (3) \\ i,j &= 1,\ldots,20. \end{aligned}$$

NEL is the number of Elements, **K** is the element stiffness matrix, **T** is the solution vector, which contains the temperatures at all element nodes and **f** the load vector of the equation system containing the boundary conditions. Ω is the computational domain and Γ is that part of its boundary on which convective-type boundary conditions are specified. When calculating the element matrices, equations 2 and 3 are transformed into local coordinates ξ, η and ζ. The integration is carried out by Gauss-Legendre integration, which is exact and easy to perform. The value which is to be integrated is taken at exactly defined Gauss-points inside the element and multiplied with special Gauss-weighting factors. The products are summed up and devided by the element volume, which is easily determined in local coordinates. The result is a very good approximation of the exakt integral value.

The calculations presented here were performed with three Gauss points per edge (Fig. 5), which is a good compromise between resulting accuracy and necessary computing time. To minimize the amount of required storage the bandwidth of matrix **K** was reduced by renumbering the nodes of the produced FEM-grids with the Reverse Cuthill-McKee algorithm. Basic principle of the Cuthill-McKee algorithm is to achieve minimum differences between the nodenumbers of each element. Inverting the new numbering can reduce the bandwidth further more, [12].
Further details on the applied skyline technique used to store matrix **K** and the applied equation solver are given in ref. [17].
FEAP results are compared with analytical solutions for a hollow cylinder in ref. [3]. The agreement between calculation and theory is found to be very good.

4.2 Navier-Stokes Solver

The Reynolds-averaged Navier-Stokes equations (eq. 4) are numerically solved using a finite volume technique with a cell centred difference approximation to represent the convection and diffusion terms in space and a three step Runge-Kutta algorithm for the time discretization. Stability is gained by using a residual averaging method which can be run either implicit, or if the user wishes, explicit. The maximal timesteps which lead to a stationary solution are calculated from the CFL-criteria [11].
The algebraic Baldwin-Lomax turbulence model [2] coupled with the Cebecci-Smith model [6] to account for the freestream pressure gradient is used to calculate the turbulent viscosity of the Boussinesq theorem [5]. The turbulent Prandtl number used for the modelling of the turbulent heat fluxes is found from an expression given by Kays and Moffat [8] and [14]. Furthermore it is possible to run the code with and without a wallfunction in the laminar and turbulent case.
The governing equations in conservative form are

$$\int_V \frac{\partial \vec{Q}}{\partial t} dV + \int_{\partial V} \vec{H} \cdot \vec{n} dA = \int_{\partial V} \vec{D} \vec{n} dA + \int_{\partial V} \vec{S} \vec{n} dA \tag{4}$$

where $\vec{Q}$ is the vector of the conservative variables, i.e. density, momentum density and total energy density. $\vec{H}$ represents the flux vector, $\vec{D}$ the diffusion vector, $\vec{S}$ the source vector and $\vec{I}$ the unit vector.

$$\vec{Q} = \begin{pmatrix} \rho \\ \rho u_x \\ \rho u_\varphi r \\ \rho u_r \\ \rho e \end{pmatrix} \quad \text{and} \quad \vec{H} = \begin{pmatrix} \rho \vec{u} \\ u_x \vec{u} \\ u_\varphi r \vec{u} \\ u_r \vec{u} \\ (e+p)\vec{u} \end{pmatrix}$$

and

$$\vec{D} = \begin{pmatrix} 0 \\ \tau_x - p\vec{I} \\ \tau_\varphi - p\vec{I} \\ \tau_r - p\vec{I} \\ \bar{\bar{\tau}} \cdot \vec{u} - \dot{q} \end{pmatrix} \text{ and } \vec{S} = \begin{pmatrix} 0 \\ 0 \\ -2\omega r u_r \\ {u_\varphi}^2/r + r\omega^2 + 2\omega u_\varphi \\ 0 \end{pmatrix}.$$

The stress tensor $\bar{\bar{\tau}}$ is given by Newton's law and the heat flux $\dot{q}$ is expressed by Fourier's law:

$$\dot{q} = -\lambda grad T \tag{5}$$

Due to the central differencing scheme in the spatial discretization odd-even point decoupling will occur and lead to saw tooth waves or wiggles. This difficulty is resolved by adding a certain amount of artificial dissipation to the NS-model to prevent wiggles and to permit shock capture. The artificial dissipation values are additionally stored upon the viscous values ($\vec{D}$) of each equation (with exception of the dissipation quantity of the continuity equation).
Eq. 4 can be written in semidiscrete approximation as:

$$\frac{d\vec{Q}}{dt} = \vec{F}(\vec{Q}) \tag{6}$$

Eq. 6 respresents an ordinary system of linear differential equations. This system is solved by the second order explicit three-stage Runge-Kutta scheme [11]:

$$\begin{aligned} \vec{Q}^{(0)} &= \vec{Q}^n, \\ \vec{Q}^{(1)} &= \vec{Q}^{(0)} + \Delta t \vec{F}(\vec{Q}^{(0)}), \\ \vec{Q}^{(2)} &= \vec{Q}^{(0)} + \Delta t[(1-\theta)\vec{F}(\vec{Q}^{(0)}) + \theta \vec{F}(\vec{Q}^{(1)})], \\ \vec{Q}^{(3)} &= \vec{Q}^{(0)} + \Delta t[(1-\theta)\vec{F}(\vec{Q}^{(0)}) + \theta \vec{F}(\vec{Q}^{(2)})], \\ \vec{Q}^{(n+1)} &= \vec{Q}^{(3)} \end{aligned} \tag{7}$$

4.2.1 Modelling of the wall temperature gradient on coarse grids

Heat transfer calculations on *coarse* grids can only be performed by modelling the wall temperature gradient, or, if the ***Reynolds analogy*** is used, by modelling the wall shear stress.
The Reynolds analogy implies that under certain flow conditions the dimensionless temperature- and velocity-profiles are identical. Therefore the wall-temperature gradient can be calculated from the velocity profile. When using the Reynolds analogy, the modelling of the velocity profile near the wall is generally done with the help of a laminar or turbulent wall function. The velocity in the near wall grid cell is influenced by the variation of the skin friction factor c_f. For laminar flows c_f is exactly determined by:

$$\frac{c_f}{2} = 0.332 Re^{-\frac{1}{2}} \tag{8}$$

For turbulent flows c_f reads as:

$$\frac{c_f}{2} = \left(\frac{u_\tau}{u_\delta}\right)^2 \tag{9}$$

u_τ is calculated from the logarithmic law of the wall.
Although the code is equipped with the feature to perform heat transfer calculations using the Reynolds-analogy, it was not used for the presented calculations.

4.2.2 Numerical approach

As mentioned earlier, the system of equations (eq. 4) is numerically solved by using the finite volume method with (second order) central differences for the convective and diffusive terms. The code uses structured multi block meshes. For turbomachinery geometries a mesh configuration using a five block system consisting of one 'O' and four 'H'-meshes delivers a good resolution of the leading and trailing edge of the blade (Fig. 3). Furthermore the 'O'-mesh around the blade allows a constant orthogonal distance of the first streamwise (ξ-) gridline. This detail is important for the heat transfer calculation.
The heat transfer coefficient is defined as:

$$\alpha \equiv \frac{-\lambda_{fluid} \frac{\partial T}{\partial n}}{T_w - T_a} \tag{10}$$

T_a should be the temperature at the edge of the thermal boundary layer. Due to the difficulty to find this edge T_a is set equal to $T_{t_{in}}$, i.e. α is defined with the known total temperature at turbine inlet.
∂n in eq. 10 can simply be discretized by Δn, with $\Delta n = \frac{1}{2} y_n$. y_n is the normal distance of the first ξ-gridline from the wall.

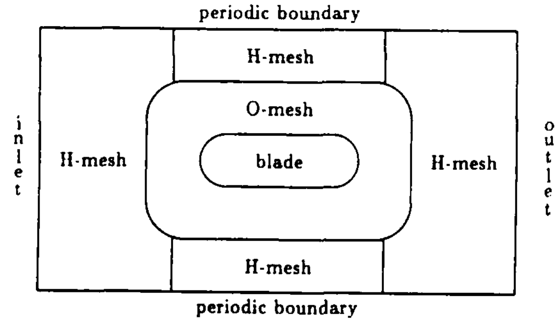

Figure 3: Symbolic block mesh configuration

All calculations discussed in this paper are carried out for small Reynolds numbers, i.e. $Re < 100000$ (based on the axial chord length). That means that the flow is laminar.
The 3D-Navier-Stokes code is completely vectorized for the use on vector computers. Quick information about the blade to blade flowfield and the required Reynolds number for the direct heat transfer calculation were obtained with a 2D-FMG-Multigrid code written in *C-language*, which is able to run on every computer, even on a PC with enough extended memory (RDP = $4.5 \cdot 10^{-4} \frac{sec}{cellstep}$ on PC 486 33Mhz). The 2D-version is also an useful tool for the developement of the 3D-code.

4.3 Coupling Procedure

Neglecting radiation, the heat flux density leaving the flow area at the blade surface is equal to the Fourier-heat flux density

$$\dot{q}_{fluid} = -\lambda_{fluid} \left(\frac{dT}{dn}\right)_w \equiv \lambda_{fluid} \frac{T_1 - T_w}{\Delta n}, \quad Fig. 4. \tag{11}$$

This assumption can be made because the flow velocity in the near wall region is sufficiently small to be neglected. When performing a coupling step the temperature calculation inside the blade is made with fixed boundary conditions α_c and T_c at the cooling channel surfaces and variable α^* and T_a^* at the flow surface, where

$$\begin{aligned} \alpha^* &\equiv \frac{\lambda_{fluid}}{\Delta n} && (12) \\ T_a^* &\equiv T_1. && (13) \end{aligned}$$

With the *resulting* wall temperatures this leads to a Newtonian heat flux density into the blade of

$$\dot{q}_{blade} = \alpha^*(T_a^* - T_w). \tag{14}$$

Inserting eqns. 12 and 13 in eq. 14 and comparing with eq. 11 shows that the wall heat flux balance

$$\dot{q}_{blade} = \alpha^*(T_a^* - T_w) = \frac{\lambda_{fluid}}{\Delta n}(T_1 - T_w) = \dot{q}_{fluid} \tag{15}$$

is automatically satisfied.
The advantage compared to calculating with real heat transfer coefficients is that T_w in eq. 14 does not have to be known when the coupling step is performed. The determination of T_w would require an iterative procedure within each coupling step, which is time consuming especially for blade materials with low thermal conductivity, [15].

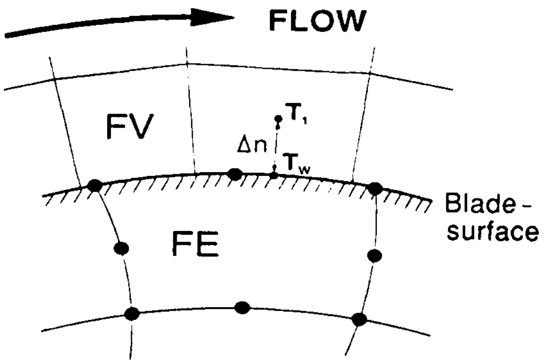

Figure 4: Coupling-principle. FE = finite element, FV = finite volume

The coupling procedure starts when the first n Navier Stokes-time steps are finished, where n is a value which can be choosen by the user. The coupling is performed on plane grids which are generated by unwrapping both the finite element (FE)- and the finite volume (FV)-surface. The cornerpoints of the FV-coupling grid in fig. 5 are the centerpoints of the FV-blade surface cells, because this is the location where the temperature is calculated.

The boundary conditions (eqns. 12 and 13) have to be specified for every surface-Gauss point of all surface-FE. Therefore for every surface-Gauss point the corresponding FV-cell is searched, see Fig. 5. The values of λ_{fluid}, Δn and T_1 are taken at the four cornerpoints of the corresponding cell and are bilinearily interpolated .

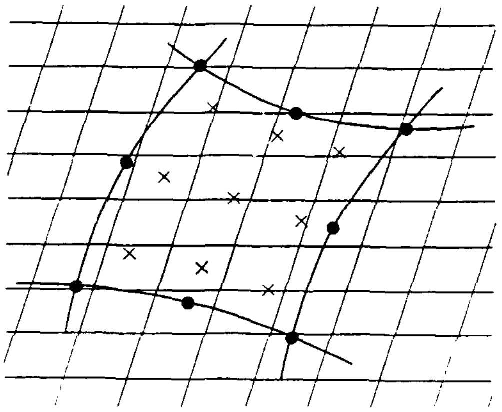

Figure 5: Interpolation of α^* and T_1 for a Gauss point (FV → FE)

With the obtained boundary conditions a FEM-calculation is performed and the resulting new wall temperatures T_w are returned to the flow solver.

The back-interpolation of the T_w at each FV-cornerpoint is done on the FE-grid in the same way as described above. Therefore the FE interpolation grid is build by taking the temperatures at the eight surface nodes and at the point ($\xi = 0, \eta = 0$) 'in the middle' of the element surface, see Fig. 6.

The next n Navier Stokes steps are calculated and the coupling procedure starts again, until a chosen maximum number of couplings has been performed.

The convergence of the blade's surface temperature can be controlled after each coupling step in terms of its average value and location and quantity of the maximum temperature difference to the prior coupling step.

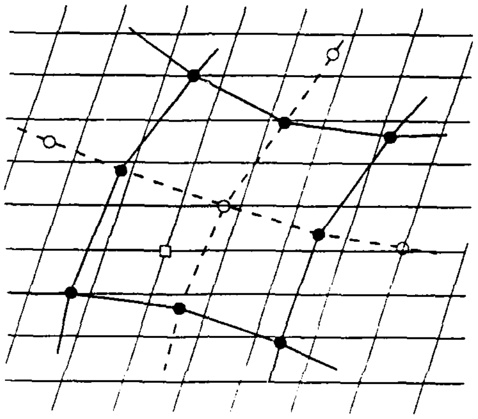

Figure 6: Interpolation of T_w for an FV-cell (FE → FV)

5 Results

Calculations were made on two different geometries. The first was a flat hollow plate cooled on its internal boundary (Figs. 7 and 8), the second was a typical guide vane blade cooled by 27 cylindrical cooling channels, Figs. 11 and 12.

In case I the flow calculation was performed on the 5-block grid shown in Fig. 7. The 3D-grid was generated by stacking the hub-grid shown in Fig. 7 in radial direction. Fig. 8 shows both the FE- and the FV-grid at the leading edge of the plate.

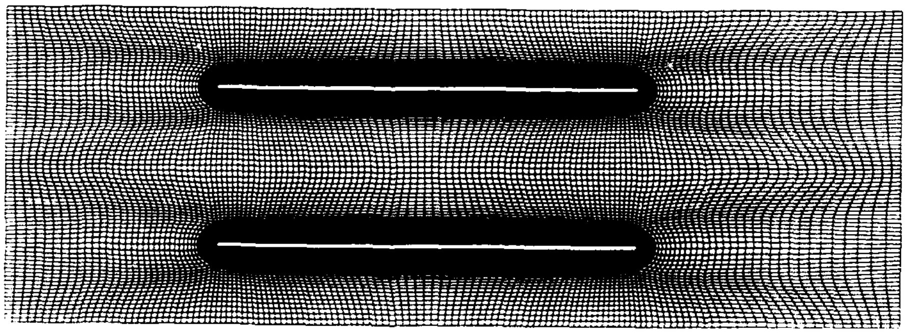

Figure 7: Hub section of the 5-block FV-grid for the flat plate calculation

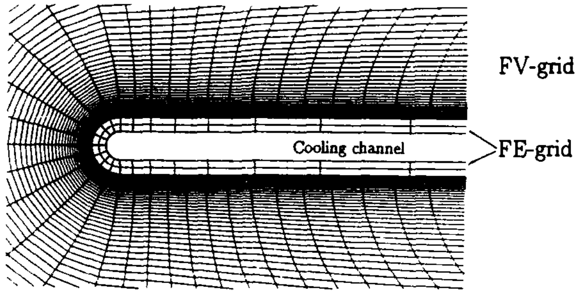

Figure 8: FV- and FE-grid at the leading edge of the hollow flat plate

Setting the internal heat transfer coefficient to a comparatively high value resulted in a nearly constant outer wall temperature close to the inner ambient temperature. Therefore the calculated Nu-numbers

$$Nu_l = \frac{\alpha_x l}{\lambda} \tag{16}$$

(α_x from eq. 10) could be compared with the anlytical values, which are given for a flat plate of thickness zero, constant wall temperature and full cooling length by Eckert [7]:

$$Nu_l = 0.332\ \sqrt[3]{Pr}\ \sqrt{Re_x}\ \frac{l}{x} \tag{17}$$

Both curves are plotted in Fig. 9.

The difference between the calculated and the analytical curve in the region close to the leading edge is believed to be due to the influence of the plate's finite thickness.

The boundary layer of an infintesimal thick plate immediately downstream its leading edge would be very thin, causing strong velocity gradients. Using the Reynolds-analogy, this leads to very high Nusselt numbers.

When calculating the hollow flat plate with finite thickness, the curvature-change between the plate's leading edge and its straight section nearly leads to a flow-separation at the beginning of the straight section. This results in a thick boundary layer and small velocity-gradients in the whole downstream region; the Nusselt numbers are smaller than in the theoretical case.

Because this phenomenon is not taken into account in eq. 17, the calculated curve in Fig. 9 may represent the heat transfer distribution of a *realistic* flat plate with finite thickness better than the analytical curve.

Further downstream the theoretical boundary layer thickness becomes equal to that one of the plate with finite thickness and the values compare very well.

The resulting temperature distribution in the plate's leading edge is shown in Fig. 10.

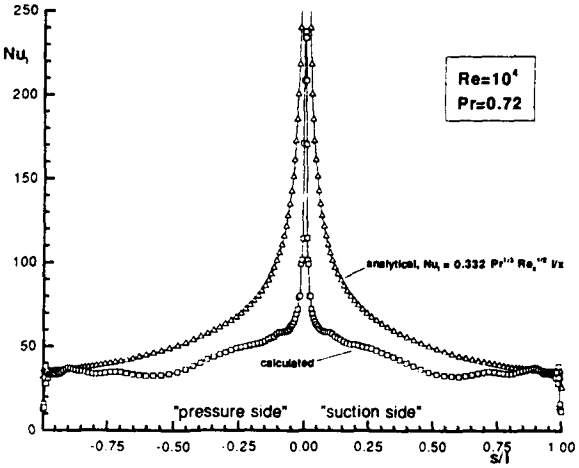

Figure 9: Nu-number of the flat plate

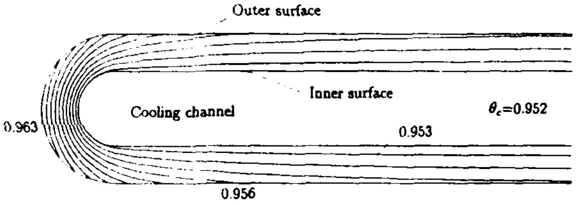

Figure 10: Distribution of dimensionless temperature $\theta = \frac{T}{T_{c,in}}$ in the leading edge region of the hollow flat plate

For case II the FV- and the FE-grid are shown in Fig. 11. A simple cooling geometry was used and discretized as indicated in Fig. 12. Again, the internal thermal boundary conditions were set constant. The cooling temperature was choosen to be close to the free stream temperature to keep temperature gradients small, as recommended in ref. [4]. However, the influence of the temperature gradient on the resulting heat transfer coefficient was not studied in this work.

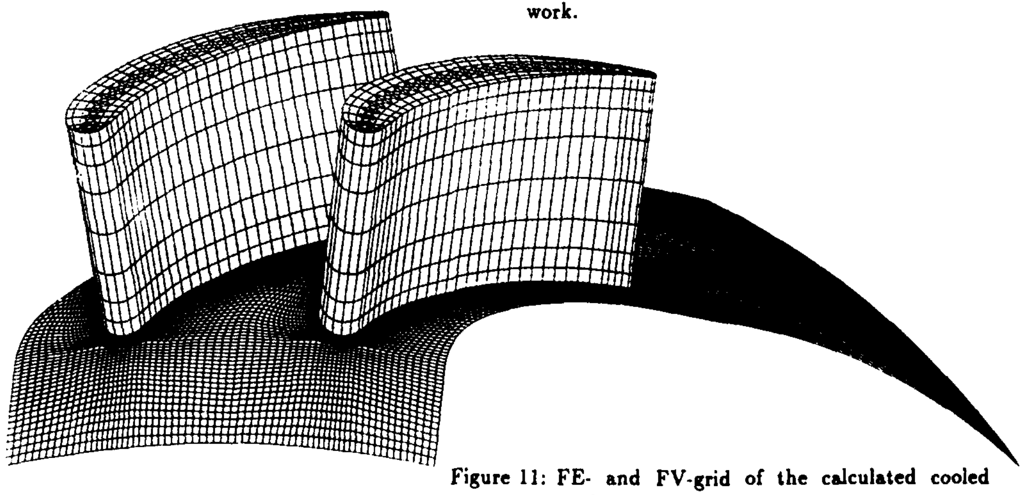

Figure 11: FE- and FV-grid of the calculated cooled guide vane blade

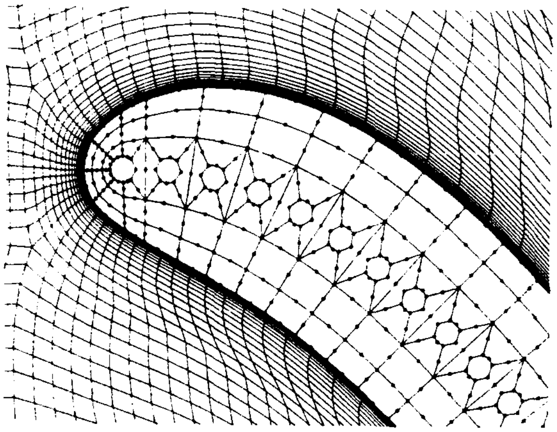

Figure 12: Cross section of FE- and FV-grid at the leading edge of the guide vane blade

Fig. 13 shows the resulting temperature distribution inside the blade. The used cooling geometry just leads to small differences between the temperature distributions of the several cross sections.
The distribution of the wall temperatures and the resulting heat transfer coefficients at the blade surface are plotted in Fig. 14 and Fig. 15. The influence of the passage vortex transporting hot fluid from the adiabatic hub and tip to the suction surface can be seen in the regions of higher temperature and heat transfer coefficient compared to midspan.

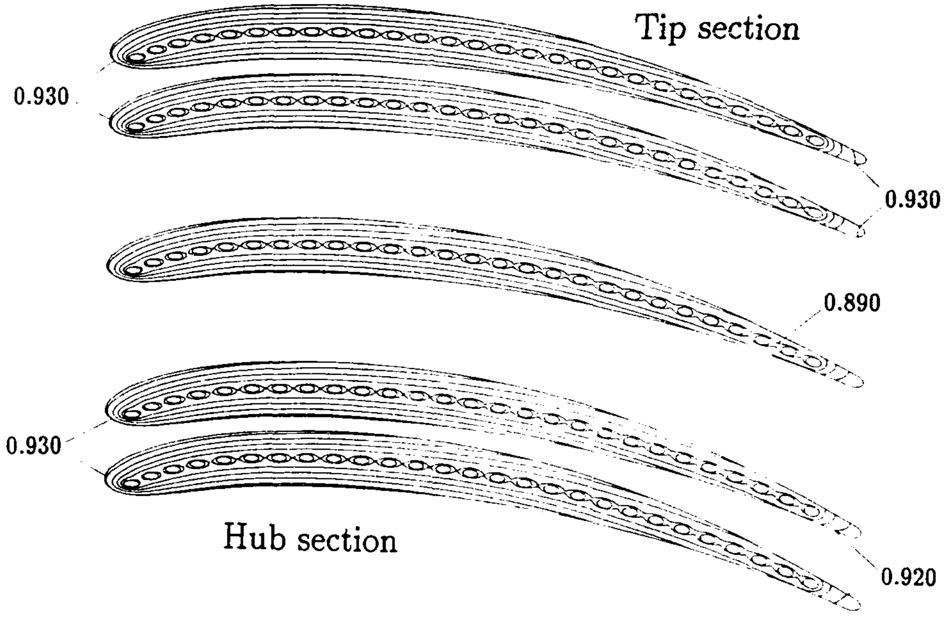

Figure 13: Distribution of dimensionless temperature $\theta = \frac{T}{T_{t,in}}$ inside the blade

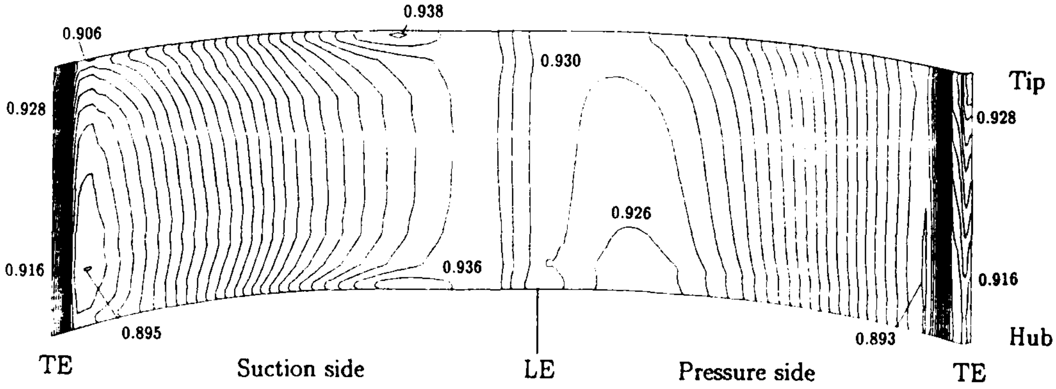

Figure 14: Distribution of dimensionless temperature $\theta = \frac{T}{T_{t,in}}$ at the unwrapped blade surface

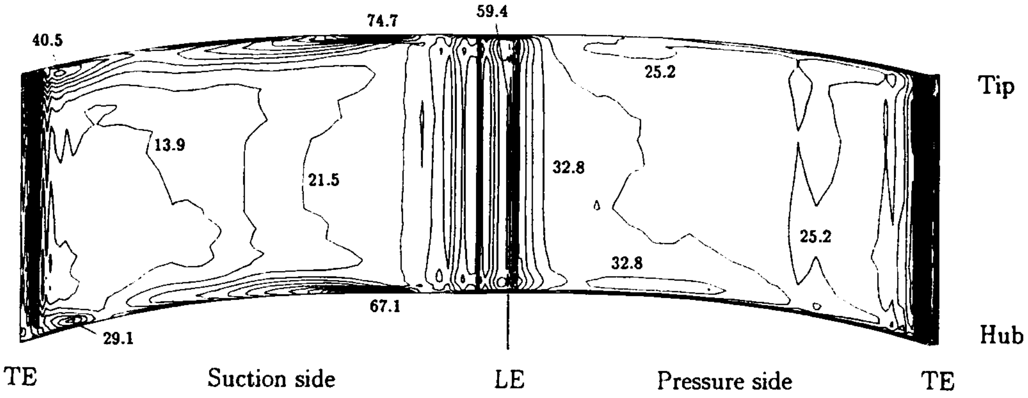

Figure 15: Distribution of Nu-number at the unwrapped blade surface

Fig. 16 shows the heat transfer coefficient at midspan, compared with the anlytical values calculated with eq. 17. Strictly speaking, eq. 17 is valid only for zero-curvature geometries and zero-pressure gradients. Although these conditions are usually not fullfilled for turbine flows, eq. 17 can be used to obtain an estimate of tendencies and of the level the Nusselt-numbers should be. The differences at the *suction side* are believed to be due to the strong curvature of the blade surface and the strong acceleration of the flow, which causes the analytical values to be predicted too high.
At the *pressure side* curvature and acceleration are smaller than at the suction side and this leads to a good agreement between analytical and calculated values.

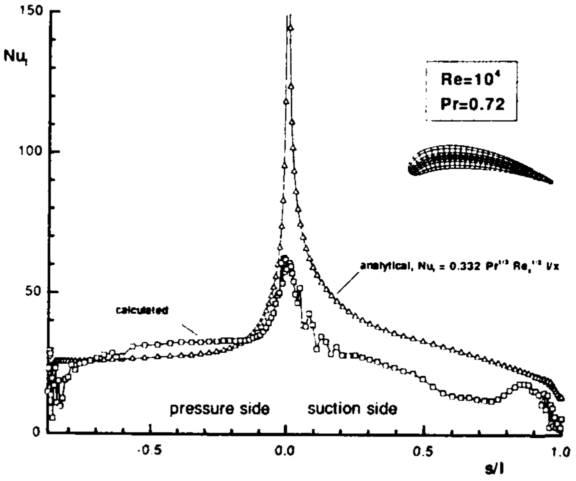

Figure 16: Nu-number of the guide vane blade at midspan

All these calculations are made determining the wall temperature gradients *directly* from the computational grid, see chapter 4.3. No model was used to obtain or to modify these gradients.

The finite volume grid for the flat plate calculation consisted of 132864 cells and the corresponding finite element grid of 544 elements with 3536 nodes. For the flow calculation of the guide vane blade a finite volume grid of 118944 cells was used and the blade was discretised by 2024 elements with 10831 nodes.

The y^+-values calculated by

$$y^+ = \frac{\sqrt{\rho_w \tau_w}}{\mu_w} y$$

differed for the calculation of the flat plate between 0.07 and 0.56 with an average value of 0.21 and for the guide vane blade between 0.07 and 0.84 with an average value of 0.43. The Reynolds number based on axial chord length was in both cases 10^4.
All calculations were performed on an IBM RS-6000 Workstation with 128 MB RAM and 25 MFLOPS (nominal). The computing time per timestep was 35 seconds for the guide vane blade and 40 seconds for the flat plate. These values are averaged and proportional include the computational time of the heat conduction calculation. The calculations were carried out with 10 Navier-Stokes timesteps per couplingstep. No difference was found to the results of runs performed with one coupling step per Navier-Stokes-timestep. For both cases the presented results were obtained after 4000 timesteps; the guide vane blade calculation converged by an order of 2.5 and the flat plate by an order of 3.

6 Conclusions

The thermal coupling of a 3D-flow solver and a 3D-heat conduction solver was sucessfully performed. The resulting heat transfer coefficients compare satisfactory with analytical data. A full thermal interaction between flow and blade can be realized and influences of the 3D-flow on the temperature distribution can be detected.
In this paper calculations were carried out for laminar flows with Reynols numbers of 10^4. For this case the prediction of the blade temperature distribution was possible without modelling the heat transfer conditions at the blade surface. Aspects of future-work will be the implementation of a two-equation turbulence model and a laminar/turbulent transition model. Furtheron the flow solver is planned to be extended to also calculate external flows and to run on any number of blocks.
The influence of higher Reynolds numbers and realistic temperature gradients on heat transfer has to be investigated. The resulting heat transfer coefficients of the guide vane blade are planned to be compared with experimental data that are now under preparation.
Additionally, a coupling with an internal flow-solver for simple cooling geometries is planned.

References

[1] Ameri, A.A., Arnone, A.: *'Three Dimensional Navier-Stokes Analysis of Turbine Passage Heat Transfer'*, AIAA paper 91-2241 (1991)

[2] Baldwin, B. and Lomax, H.: *'Thin layer approximation and algebraic model for seperated turbulent flows'*, AIAA paper 78-257 (1978)

[3] Bettencourt, J.M.: *'Finite Element Analysis Program (FEAP) for Conduction Heat Transfer'*, Master's Thesis, Naval Postgraduate School, Monterey, California 93940 (1979)

[4] Boyle, R., Giel, P.: *'Three Dimensional Navier Stokes Heat Transfer Predictions For Turbine Blade Rows'*, AIAA paper 92-3068 (1992)

[5] Boussinesq, J.: *'Théorie de l'écoulement tourbillant'*, Mem. Pre. par. div. Sav. 23, Paris, (1877)

[6] Cebecci, T. :*'Calculation of unsteady two-dimensional laminar boundary layers with fluctuations in external velocity'* , Mechanical Engineering Department, California State University at Long Beach (1977)

[7] Eckert, E.R.G. :*'Einführung in den Wärme- und Stoffaustausch'*, Springer Verlag, 1966

[8] Crawford, M.E., Kays, W.M. and Moffat, R.J: *'Heat transfer to a full-coverage film-cooled surface with 30 deg. slant-hole injection'* , NASA Contractor Report, NASA CR-2786

[9] Hah, C.: *'Numerical Study of Three-Dimensional Flow and Heat Transfer Near the Endwall of a Turbine Blade Row'*, AIAA paper 89-1689 (1989)

[10] Nitsche,W., Wald, L.: *'Numerical Simulation of Transient Thermal Interaction Between Supersonic Flows and Structures'*, Numerical Methods in Thermal Problems, Vol.VII/1, Pineridge Press LTD (1991)

[11] Müller, B. and Rizzi, A.: *'Navier-Stokes computation of transonic vortices over a round leading edge delta wing'*, Int. J. for Num. Methods in Fluids, Vol. 9, 943-962 (1989)

[12] Schwarz, H.R.: *'Methode der finiten Elemente'*, Teubner Verlag, Stuttgart (1984)

[13] Tietz, T.A., Koschel, W.W.: *'Computer Code For The Calculation of the Temperature Distribution of Cooled Turbine Blades'*, ISABE paper 91-7017 (1991)

[14] Vogel, D.T.: *'Computation of 3D-viscous flow and heat transfer for the application to film cooled gas turbine blades'*, AGARD-paper 7 (1991)

[15] Wald, L.: *'Numerische Bestimmung der instationären Temperaturverteilung in einer thermisch belasteten ebenen Platte in Kopplung mit einem Grenzschichtverfahren'*, DGLR-Jahrbuch '89, Vol.1, pp.397 (1989)

[16] Walz, A.: *'Strömungs- und Temperaturgrenzschichten'*, by G. Braun, Karlsruhe (Germany) (1966)

[17] Zienkiewicz, O.C.: *'Methode der finiten Elemente'*, Carl Hanser Verlag, München, 1984 by G. Braun, Karlsruhe (Germany) (1966)

Discussion

QUESTION 1:

DISCUSSOR: J. Salva Monfort, Escuela Tecnica Superior de Ingenieros Aeronauticos

What boundary conditions have you used?

AUTHOR'S REPLY:

We used the standard boundary conditions. At the inlet we prescribed the total pressure, total temperature and flow angle. At the outlet we prescribed the static pressure.

COOLING PREDICTIONS IN TURBOFAN ENGINE COMPONENTS

A. MATESANZ, R. REBOLO, A. VIEDMA[*] & M. RODRIGUEZ[*]

SENER Ingeniería y Sistemas, S.A.
Parque Tecnológico de Madrid
28760 Tres Cantos, Madrid, Spain

(*) Also in Universidad Politécnica de Madrid
School of Aeronautical Engineering,
Pl. Cardenal Cisneros 3, 28040 Madrid, Spain

SUMMARY

The aim of this work is to show how the metal temperature measured in a convergent-divergent nozzle and in a turbine exhaust diffuser of a turbofan engine, can be predicted with reasonable approximation using the data available in the open literature. It is shown how the simplified fluid dynamic equations with the appropriate experimental correlation allow the prediction of these results in other flight conditions than those tested.

LIST OF SYMBOLS

$C_{p\infty}$= specific heat at main stream temperature.
C_{p2}= specific heat at cooling flow temperature.
D_h= Hydraulic diameter
d = local curvature diameter
h = convective heat flux coefficient
K = thermal conductivity coefficient
L = inner blade passage length

M =blowing factor $\dfrac{\rho_2 V_2}{\rho_\infty V_\infty}$

N_u= Nusselt number
P_r= Prandtl number
q = heat flux
R_{e2}= Reynolds number for the cooling parameters $\dfrac{\rho_2 V_2 .S}{\mu_2}$

$R_{e_{x,s,d}}$ = Reynolds number based on x,s,d.

s = cooling slot height.

T_g= absolute gas temperature.

T_r = recovery temperature = $T_\infty+0,9\left[T_{\infty 0}-T_\infty\right]$
T_w= actual wall temperature
T_{aw} = adiabatic wall temperature

$T_\infty, T_{\infty 0}$ = static and stagnation temperature of the main stream.

$T_*= T_\infty+ 0,72\left[T_{aw}- T_\infty\right]$

T_2= cooling injection temperature.
x = distance from the point of injection.
$\Delta\varepsilon$= correcting factor due to spectral overlapping.
ε_w= inner face wall emissivity.
ε_g= gas emissivity = $\varepsilon_{CO2}\rho_{CO2}+ \varepsilon_{H2O}\rho_{H2o}-\Delta\varepsilon$

η = film cooling effectiveness
μ = gas dynamic viscosity
θ = angle from stagnation point in profile leading edge.
ρ = density
ρ_*, μ_*= density and viscosity at a temperature T_*

σ = Stefan-Boltzman constant.

ξ^* = non dimensional distance

$$= \frac{x}{M.S}\left[\frac{R_{e2}\ \mu_2}{\mu_*}\right]^{-0,25} \frac{\rho_*}{\rho_\infty}$$

Subscripts

g = gas
w = wall
1,2 = cold gas injection

1 INTRODUCTION

The modern engine solid surfaces exposed to internal flow need improved thermal protection because high temperature cycles are used to increase performance. During the past decades, different cooling methods have been used to reduce the metal temperature, therefore minimizing the required amount of cooling air.

The simplest way to cool surfaces is by convective cooling. In this process, heat flows by conduction from exposed metal surfaces to un-exposed ones, which are cooled by air flowing usually parallel to it. Convective cooling is used whenever low levels of cooling effectiveness are required. This limitation exists due to the fact that the air supply is somehow limited. On the other hand, high effectiveness levels tend to increase thermal stress problems [1-3].
A special type of convective cooling is by means of impingement. It is used whenever large heat transfer coefficients are needed on the un-exposed surfaces [4-8]. Another

method to obtain high heat transfer coefficients is to place fins or ribs normal to the coolant flow path [9].

When higher levels of cooling effectiveness are required it is necessary to use more sophisticated alternatives. The most common method is to insert a secondary fluid into the boundary layer on the surface which is to be protected. There are different means of injecting this fluid such as ablation, transpiration and film cooling. In ablation cooling, a heat shield ablates and secondary fluids enter the boundary layer [10] In transpiration cooling the coolant enters the boundary layer through a porous material [11-13]. Both methods are used to protect the region where coolants are added. Unfortunately the application of these systems is difficult because ablation has a limited time span and porous materials are not strong enough to be used in engines. The basic mechanism of film cooling is the introduction of a secondary fluid at several locations along a surface to protect that surface not only in the injection area but also in the downstream region [12-14].

Thermal studies on aircraft engines, particularly modern ones with large flight envelopes, require a great amount of testing and instrumentation. Designers have different tools for obtaining engine component temperature predictions. These tools can be classified as: 1) theoretical, 2) experimental and 3) numerical methods. Theoretical analysis is usually aimed at finding parameters to describe the temperature of an adiabatic wall downstream of the coolant injection [15]. Real and three-dimensional effects are studied on test rigs with controlled conditions [16-18]. Predictive numerical calculations are being widely used nowadays for different cooling applications and configurations, because they help to speed up the design and to reduce the number of experiments [19-20].

In this paper a method to predict full scale engine temperatures is described. This method combines the fluid dynamic equations with semi-empirical data obtained from the open literature.

The result is an easy to use procedure.

2. NOZZLE COOLING PREDICTION

The prediction of the petal temperature of a convergent-divergent nozzle has been performed through a computer code that uses correlation models available in the open literature with actual data obtained from a test program that includes a reduced scale hot test, a full scale rig test and a DVE (Design Verification Engine) program.

The film cooling produced when the relative cold layer is injected at the beginning of the convergent petal of the nozzle, produces a reduction in the metal temperature along the petal.

The heat transfer rate is modelled by:

$$q = \lambda . h \left[T_{aw} - T_{w} \right]$$

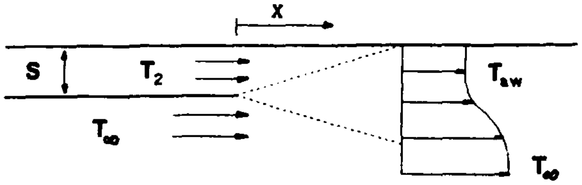

Fig.1. Single slot film cooling configuration.

The convective coefficient h is calculated independently from the adiabatic wall temperature T_{aw}.

This magnitude is related to the concept of effectiveness of the film cooling, figure 1:

$$\eta = \frac{T_r - T_{aw}}{T_r - T_2}$$

The correlation found more suitable for the flow conditions and geometry is the model of Kutatelache & Leanter, in reference [14] because the flow can be considered twodimensional and compressible and the difference of temperature between the wall and the main stream is important.

The effectiveness is given from this reference by the expression:

$$\eta = \frac{1}{1 + \frac{C_{p\infty}}{C_{p2}} \left[0,33\ (4,0 + \xi^{*})^{0,8} - 1 \right]}$$

When the cooling injection is made by two consecutive slots, the total effectiveness can be treated as the combination of two cooling layers where the external temperature for the inner flow is the "adiabatic wall temperature" for the external one [21], figure 2.

$$\eta_1 = \frac{T_\infty - T_{aw1}}{T_\infty - T_1}$$

$$\eta_2 = \frac{T_{aw1} - T_{aw2}}{T_{aw1} - T_2}$$

and the total effectiveness is:

$$\eta = \frac{T_\infty - T_{aw2}}{T_\infty - T_2} = \eta_1 + \eta_2\ (1 - \eta_1)$$

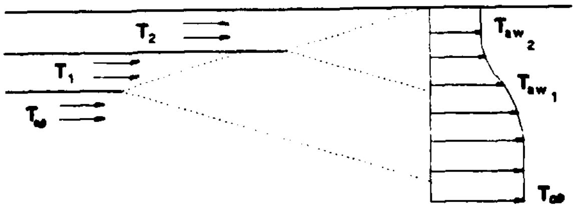

Fig.2. Double slot film cooling configuration.

A Navier-Stokes Solver with Different Turbulence Models Applied to Film-Cooled Turbine Cascades

F. Bassi[1], **S. Rebay**[1] **and M. Savini**[2]
[1]Dipartimento di Energetica
Politecnico di Milano
Piazza Leonardo da Vinci 32, 20133 Milano, Italy
[2]Istituto per Ricerche sulla Propulsione e sull'Energetica, CNPM-CNR
Via Francesco Baracca 69, 20068 Peschiera Borromeo (MI), Italy

S. Colantuoni and G. Santoriello
Alfa Romeo Avio S.p.A.
Viale dell'Aeronautica, 80038 Pomigliano d'Arco (NA), Italy

1. SUMMARY

This paper describes the numerical simulation of transonic flows through film-cooled turbine cascades. The modelization of coolant injection has been implemented in a computational code which solves either the laminar or the Reynolds-averaged Navier-Stokes equations in cascades. Turbulence effects are accounted for by means of the eddy viscosity concept. Two turbulence models have been implemented in the code. The first is the Baldwin-Lomax algebraic model and the second is the two-equation k-ω model proposed by Wilcox. Both models have been coupled with a Navier-Stokes solver in a simple, robust and efficient way. The numerical solution of both the flow and the turbulence model equations is based on a cell centred finite volume scheme and on an explicit Runge-Kutta method for time integration.

The code has been applied to compute the transonic flow in a cascade of nozzle guide vanes (NGVs) developed by Alfa Romeo Avio S.p.A.. The computations have been performed both for a cascade of "solid" vane profiles and for a cascade of "cutted" vane profiles that allow coolant flow ejection through a slot on the pressure side near the trailing edge. The NGV cascade is still under testing and at present only the experimental data for the "solid" NGV cascade are available for code validation.

The computational results presented in the paper show that the proposed coupling of the k-ω model with the explicit Navier-Stokes solver does not seem to suffer from the stiffness problems often characterizing other two-equation turbulence models.

2. INTRODUCTION

To increase the performance of advanced gas turbines it is necessary to rise the turbine inlet gas temperature. Available materials can withstand such high entry temperatures only if some cooling technique such as convection, impingement or film cooling is used. A detailed analysis of the effects of such cooling methods upon the aerodynamic performance and cooling effectiveness is therefore very useful for aerodynamic designers.

Modern computer codes for turbulent flow analysis are thus required to simulate very localized details of the flow. Several factors have helped to reach this goal, such as the availability of turbulence models of rather general validity, fast numerical algorithms, and computers allowing to obtain fine grid solutions at a reasonable cost and in a reasonable time. However, much work is still to be done both to compare the analysis methods among them and to assess the computed predictions with respect to the experimental data.

In this work we have developed a Navier-Stokes solver that can simulate the coolant ejection through holes or slots and that uses optionally one of two types of turbulence models. The first model considered is the Baldwin-Lomax algebraic model, Ref. [1], which is probably the most widely used algebraic model, and the second is the two-equation k-ω model proposed by Wilcox, Ref. [2], which has several physical and numerical interesting features. For comparison purposes we have used the same explicit Navier-Stokes solver in conjunction with the two above mentioned turbulence models. The developed code has been applied to the challenging problem of coolant ejection through a slot placed on a step of the blade pressure side near the trailing edge. In order to obtain an extensive comparison of the two turbulence models, the computations have been perrformed both on the "solid" blade (i.e. the original blade profile without the step for the coolant ejection) and on the "cutted" blade. For the "cutted" blade we considered both the case of no fluid injection and that of 4% of fluid injection.

3. MATHEMATICAL MODEL AND NUMERICAL SOLUTION

3.1 Governing Equations

The governing equations are the Favre mass-averaged Navier-Stokes equations. The averaging process generates the Reynolds stresses as additional unknowns in the equations of conservation of momentum and energy. By making the Boussinesq approximation that the Reynolds stress tensor is proportional to the mean strain-rate tensor and by using a simple algebraic turbulence model, the averaged equations of motion look exactly as the laminar equations, except for the molecular viscosity and heat conduction coefficients that are expressed as sum of a laminar and a "turbulent" part. On the other hand, by using the two-equation k-ω model and still retaining the Boussinesq hypothesis, the complete set of equations of motion and of the turbulence model read as:

$$\frac{\partial \rho}{\partial t} + \frac{\partial}{\partial x_j}(\rho u_j) = 0 \qquad (1)$$

$$\frac{\partial}{\partial t}(\rho u_j) + \frac{\partial}{\partial x_j}(\rho u_j u_i) = -\frac{\partial p}{\partial x_i} + \frac{\partial \hat{\tau}_{ji}}{\partial x_j} \qquad (2)$$

$$\frac{\partial}{\partial t}(\rho E) + \frac{\partial}{\partial x_j}(\rho u_j H) = \frac{\partial}{\partial x_j}\left[u_i \hat{\tau}_{ij} - q_j\right] + \frac{\partial}{\partial x_j}\left[(\mu + \sigma^* \mu_t)\frac{\partial k}{\partial x_j}\right] \qquad (3)$$

$$\frac{\partial}{\partial t}(\rho k) + \frac{\partial}{\partial x_j}(\rho u_j k) = \tau_{ij}\frac{\partial u_i}{\partial xj} - \beta^* \rho \omega k + \frac{\partial}{\partial x_j}\left[(\mu + \sigma^* \mu_t)\frac{\partial k}{\partial x_j}\right] \qquad (4)$$

$$\frac{\partial}{\partial t}(\rho \omega) + \frac{\partial}{\partial x_j}(\rho u_j \omega) = \frac{\gamma \omega}{k}\tau_{ij}\frac{\partial u_i}{\partial xj} - \beta \rho \omega^2 + \frac{\partial}{\partial x_j}\left[(\mu + \sigma \mu_t)\frac{\partial \omega}{\partial x_j}\right] \qquad (5)$$

where t is time, x_i position vector, u_i velocity vector, ρ density,p pressure, μ and μ_t molecular and eddy viscosity coefficients, $\hat{\tau}_{ij}$ the sum of the viscous and Reynolds stress tensors, and q_j the sum of the viscous and turbulent heat flux vectors. The quantities $E = e + u_i u_i/2 + k$ and $H = h + u_i u_i/2 + k$ are total internal energy and enthalpy, respectively; e and h denote internal energy and enthalpy, and $h = e + p/\rho$. The turbulent mixing energy k and the specific dissipation rate ω define the eddy viscosity coefficient:

$$\mu_t = \gamma^* \frac{\rho k}{\omega} \qquad (6)$$

The total stress tensor is given by

$$\hat{\tau}_{ij} = 2\mu\left[S_{ij} - \frac{1}{3}\frac{\partial u_k}{\partial x_k}\delta_{ij}\right] + \tau_{ij} \qquad (7)$$

where the mean strain-rate S_{ij} is

$$S_{ij} = \frac{1}{3}\left[\frac{\partial u_i}{\partial x_j} + \frac{\partial u_j}{\partial x_i}\right] \qquad (8)$$

The Boussinesq hypothesis assumes that the Reynolds stress tensor is proportional to the mean strain-rate tensor, that is

$$\tau_{ij} = 2\mu_t\left[S_{ij} - \frac{1}{3}\frac{\partial u_k}{\partial x_k}\delta_{ij}\right] - \frac{2}{3}\rho k \delta_{ij} \qquad (9)$$

The total heat flux vector is given by

$$q_j = -\left(\frac{\mu}{\mathrm{Pr}} + \frac{\mu_t}{\mathrm{Pr}_t}\right)\frac{\partial h}{\partial x_j} \qquad (10)$$

where Pr and Pr_t are the laminar and turbulent Prandtl numbers and have been assumed equal to 0.72 and to 0.9, respectively. The values of the closure coeficients β, β^*, γ, γ^*, σ, σ^* that appear in the equations have been established by Wilcox, Ref. [2], and are given by:

$$\beta = 3/40, \quad \beta^* = 9/100, \quad \gamma = 5/9, \quad \gamma^* = 1, \quad \sigma = 1/2, \quad \sigma^* = 1/2 \qquad (11)$$

As almost all two-equation turbulence models, also the k-ω model includes an evolution equation for the turbulent kinetic energy. The other equation of the model can be interpreted as the evolution equation for the ratio of the turbulence dissipation rate ϵ to the turbulent mixing energy k. A distinctive feature of the k-ω model is that it does not require damping functions in the viscous sublayer and that the equations are less stiff near the wall; this is very useful because it is possible to extend the model down to the wall without introducing wall functions that could be questionable for general flows and without suffering too much from the stability problems typical of other models near the wall.

3.2 Numerical Solution

We use a finite volume discretization, whereby the computational domain is partitioned into quadrilateral cells and the integral form of Eqs. (1)–(5) is applied to each cell. By taking advantage of the divergence theorem the volume integral of spatial derivatives reduces to the surface integral of fluxes, which need to be evaluated at cell interfaces. The convective fluxes in Eqs. (1)–(3) are evaluated at each face as the arithmetic mean of the fluxes in the cells which share that face. This is equivalent to a centred discretization of first order derivatives that can decouple the solution and induces oscillations near shock waves and stagnation points; following Jameson's approach, Ref. [4], we add a controlled amount of artificial dissipation given by a blend of second and fourth order spatial differences of conservative variables: in this work particular attention was devoted to limit the amount of added artificial viscosity in order to do not alter the computed total pressure losses. The main advantage of Jameson's approach is that it is very efficient, especially if one uses the convergence acceleration techniques that have been proposed in the literature. The convective fluxes in Eqs. (4),(5) are evaluated by an upwind method belonging to the class of the so-called projection-evolution methods or higher order Godunov methods. In this class of methods the numerical approximation of the variables inside each computational cell is reconstructed to the desired order of accuracy by using the average values of the variables in that cell and in the neighbouring ones; considering, for example, the one-dimensional case we can obtain values of the variable w at $i \pm 1/2$ by means of the equation

$$w^{\mp}_{i\pm\frac{1}{2}} = w_i \pm \psi \left(\frac{1 \mp \phi}{4} \Delta^- + \frac{1 \pm \phi}{4} \Delta^+ \right) \tag{12}$$

where $\Delta^+ = w_{i+1} - w_i$, $\Delta^- = w_i - w_{i-1}$ and ψ and ϕ control, respectively, the accuracy and the degree of upwinding of the reconstruction. When using higher order reconstruction ($\psi = 1$) some monotonicity constraint is needed in order to avoid spourious minima and maxima in the reconstructed solution. After the reconstruction process has been completed, we can use one of the so called Riemann solvers that can be found in the literature in order to introduce a proper upwinding in the evaluation of the numerical flux from the couple of variable values that have been reconstructed at cell interfaces. The results presented in this work have been obtained by using a simple constant reconstruction in the k and ω equations and the local Lax-Friedrichs numerical flux, that is:

$$\begin{gathered} f_{i+\frac{1}{2}} = \frac{1}{2}\left[f\left(w^+\right) + f\left(w^-\right) - \lambda\left(w^+ - w^-\right)\right]_{i+\frac{1}{2}} \\ \lambda = \max\left(\left|\lambda^+\right|, \left|\lambda^-\right|\right) \end{gathered} \tag{13}$$

where λ is the maximum absolute eigenvalue of the Jacobian matrices of $f(w^+)$ and $f(w^-)$; on account of the weak coupling between Eqs. (4),(5) and Eqs. (1)–(3) for λ we simply use the convective velocity. It is worth mentioning that the outlined procedure could also be applied to evaluate the convective fluxes in Eqs. (1)–(3), and in fact many existing upwind methods use this approach. However, in this work we wanted to examine the effects of changing only the turbulence model in a code based on the well known Jameson's approach.

To compute the surface integral of diffusive fluxes one needs to know the derivatives of velocity components, temperature, k and ω at cell faces; a mean value of these derivatives is obtained by applying the divergence theorem to an auxiliary control volume placed around each face and having the vertices at the cell centres of the cells sharing that face and at the end points of the face. By doing so one needs the variables at grid points and these are obtained by a simple arithmetic average of the variables in the cells surrounding that grid point.

The time integration of the discretized form of Eqs. (1)–(5) is performed by an explicit multistage Runge-Kutta algorithm; in this work we used both the three and the five stage schemes with the coefficients advised by Jameson, Ref. [5]. The convergence toward steady state is improved by using the local time step to advance the solution of Eqs. (1)–(5) and the variable coefficients implicit residual smoothing, described in Refs. [6],[7], for Eqs. (1)–(3). The source terms in Eqs. (4),(5) are evaluated implicitly at the beginning of the multistage algorithm. As a result of these implementations solutions can be marched with a local CFL number up to 3 for the three stage scheme and up to 6 for the five stage scheme. Each computation takes about 4000 Runge-Kutta multistage cycles to reduce the RMS of the density time derivative of about four orders of magnitude; the convergence of the k-ω model is checked looking at the maximum modulus and at the RMS of the eddy viscosity time derivative. Marching with the k-ω model the code requires 30% more CPU time per cycle than with the algebraic model. In all the computations with the k-ω model we start the turbulent solution from the laminar one, this being not necessarily well converged. The k field is initialized to its freestream value and the initial ω distribution is computed from Eq. (6), assuming the eddy viscosity distribution equal to the laminar one. In our experience this crude initialization has always been sufficient to start the turbulent computations without compromising the stability of the coupled solution.

3.3 Boundary Conditions

The boundary conditions for the Navier-Stokes solver are rather standard. The flow variables at the inflow, assumed subsonic, are computed by using the set values of total enthalpy, entropy, and flow direction and the extrapolated Riemann invariant associated with the characteristic running from inside the domain.

At the outflow the static pressure, corresponding to the prescribed outlet Mach number, is set; the effects of spourious reflections from the downstream boundary are reduced by placing the outlet boundary at a distance from the trailing edge greater than one axial chord. The numerical boundary conditions are computed by extrapolating from the interior the characteristic variables of the flow, assumed locally one-dimensional in the axial direction.

At solid walls the velocity is zero and, by neglecting the pressure gradient in the normal direction, the pressure is set equal to that of the first cell adjacent to the surface; moreover adiabatic wall condition is assumed. The solid wall boundary conditions have been modified in the cells interested by coolant injection; in these cells the boundary condition treatment is exactly the same as for an inflow boundary. Hence, the mass flow rate of injected fluid is not given directly but results from the computation; to obtain a specified value of mass flow rate the entropy must be properly adjusted.

Periodicity conditions are enforced along the periodic boundaries.

When using the k-ω model, boundary conditions must be provided at inflow and solid wall boundaries; at the outflow k and ω are freely convected out. In the present computations, at the inflow boundary k is evaluated from the given inlet turbulence intensity and ω is computed by assuming the eddy viscosity coefficient equal to the laminar one. At solid walls k is zero and ω is computed by following the approach suggested by Wilcox in Ref. [3]. In this paper Wilcox describes a procedure that assigns to ω at a perfectly smooth surface a value sufficiently high to guarantee that the surface is hydraulically smooth. The prescribed value of ω can be deduced from the relation

$$\omega \geq 100 \frac{u_\tau^2}{\nu} \qquad (14)$$

where u_τ is the friction velocity and ν is the kinematic viscosity. This relation is more general than the original analytical formula, Ref. [2], because it does not make any reference to geometrical quantities such as the distance from the wall and can be easily applied also in three-dimensional geometries.

4. APPLICATION TO A NGV CASCADE

The code has been applied to compute the transonic flow trough a NGV cascade for an outlet isentropic Mach number $M_{2is} = 1.07$ and a Reynolds number based on the outlet isentropic conditions $Re_{2is} = 0.55 \cdot 10^6$. In all the computations the inlet boundary value for k was deduced from the experimental value of the inlet turbulence intensity equal to 4%; the inlet boundary value of ω was computed by assuming the inlet eddy viscosity coefficient equal to the laminar one. In the following we present the results of the computed flow through a cascade of "solid" blades (i.e. the original blades without the step for the coolant ejection) and through a cascade of "cutted" blades with coolant mass flow rate equal to 0% and 4% of the inlet mass flow rate. In the computations with coolant ejection the inlet total temperature of the coolant is set to its design value (0.39 times the total temperature at cascade inlet) and the entropy is adjusted in order to obtain the required coolant mass flow rate; on account of the great difference between total temperatures, the coolant density is much higher than that of the main stream. At present we can compare experimental and computational results only for the cascade of "solid" blades; the computational results for the cascade of "cutted" blades with and without coolant ejection will serve to show and to discuss the different predictions of the two turbulence models.

4.1 NGV Cascade: "solid" blades

Fig. 1 shows the C-type computational grid which consists of 320 x 48 with 208 cells on the blade and 56 cells along each side of the wake. The rather generous number of cells along the wake was chosen in order to reduce the numerical diffusion downstream of the trailing edge. The grid cells are properly clustered near the blade surface and the wake cut and the distance of the cell centres nearest to the wall varies between $6 \cdot 10^{-5}$ and $2 \cdot 10^{-4}$ times the blade chord; the resulting non-dimensional distance y^+ varies between 0.4 and 1.3. Particular attention was devoted to obtain a smoothly varying grid in order to preserve the numerical accuracy of the scheme.

Fig. 2 displays the comparison between experimental and computed isentropic Mach number distributions on the blade surface: the predictions from the two turbulence models are quite similar and both display a significant discrepancy with respect to the experimental data in the recompression zone on the suction surface. In this case the discrepancy is neither due to the poor behaviour of turbulence models in the shock-boundary layer interaction nor to pressure reflections from the downstream boundary. Instead it must be ascribed to the procedure used in the experiments to set the downstream pressure, that causes a spourious influence on the suction side blade pressure distribution. This is clearly confirmed by the results displayed in Fig. 3, obtained by halving the distance of the downstream boundary from the trailing edge.

The Mach contours for the two turbulence models, shown in Figg. 4,5, display appreciable differences only in the wake downstream of the trailing edge: it is likely that in this region the k-ω model does a better job in predicting the wake diffusion.
Much more evident is the difference of the eddy viscosity fields predicted by the Baldwin-Lomax and k-ω models. From the contour plots of the ratio μ_t/μ_l, Figg. 4,5, it appears that the algebraic model predicts an eddy viscosity distribution less smooth than the k-ω model; moreover, the μ_τ distribution in the wake seems badly captured by the Baldwin-Lomax model.
As an example of the near-wall resolution used in the computations, Fig. 6 compares the predicted near-wall velocity profiles with the law of the wall (with constants equal to 0.41 and 5.1 for the logarithmic part) on the rear part of the blade suction side. The two velocity profiles are quite similar (this is true all along the blade) and the mesh is fine enough to properly resolve the laminar sublayer and the logarithmic part of the inner portion of the turbulent boundary layer.

Looking at the overall results, reported in Table 1, concerning the mixed out kinetic energy loss coefficient and exit flow angle we can see that both the k-ω and the Baldwin-Lomax predictions are sufficiently close to the experimental data. It is worth to mention that using the grid having the distance from the downstream boundary to the trailing edge halved, the predicted loss coefficient is .0394 for the k-ω and .0409 for the Baldwin-Lomax model. The mixed-out flow angle is -71.7 degrees for both models.

4.2 NGV Cascade: "cutted" blades

The computational grid, shown in Fig. 7, has the same number of cells of the previous case but the greater mesh resolution required in the coolant ejection zone results in a slightly different distribution of grid points.

Looking at the computational results with 0% coolant mass flow rate, Figg. 8-10, we can make almost the same considerations of the previous case about the different results of the two turbulence models. In particular we can notice the exceedingly high eddy viscosities and the higher global loss coefficient predicted by the Baldwin-Lomax model. Figg. 13,14 show a more detailed comparison of density and μ_t/μ contours in the step region. It appears clearly that the algebraic model predicts an eddy viscosity distribution much more random and much higher than the k-ω model. As a consequence, the density distribution is more spreaded in the Baldwin-Lomax prediction. The different eddy viscosity field, product of the two models, is also rensponsible for the large difference in velocity and temperature profiles in the recirculation region, see Figg. 11,12. Looking at these results, we feel that the Baldwin-Lomax model, as crude as it stands, is not well suited for this complex flow situation and probably needs some ad hoc modifications in the outer layer formulation.

The case with 4% coolant mass flow rate required to set the k and ω inlet values of the injected fluid; lacking the experimental data, we tried a couple of choices: in one case we set k and ω equal to the values at the cascade inlet and in the other case we set the same value of k and a much lower value of ω. In the second case the choice of ω was guided by the following reasoning. In Ref. [2] Wilcox suggests a boundary condition for ω that takes into account surface mass injection into a boundary layer; the proposed formula is

$$\omega = \frac{u_\tau^2}{\nu} S_B \tag{15}$$

where u_τ is the friction velocity, ν is the kinematic viscosity and S_B is a function of the non-dimensional normal velocity at the wall $v_w^+ = v_w/u_\tau$. Wilcox gives for S_B a formula that correlates well the computed and the experimental sublayer velocity profiles $u^+ = f(y^+)$ for values of v_w^+ up to about 1. In our application the proposed formula for S_B does not apply directly because v_w^+ is much higher than 1 and because we have a fluid injection into a region of stagnant fluid rather than a surface mass transpiration into a developed boundary layer. However, retaining the functional dependency of ω from the ratio u_τ^2/ν and considering that ω lowers in presence of fluid injection, we tried a boundary value of ω given by $\omega = 2u_\tau^2/\nu$. Obviously, this choice lead to computed eddy viscosity coefficients much higher than in the previous case.

Besides the usual plots of Figg. 15-17, in this case it is interesting to look at the detail of the coolant ejection region, Figg. 20,21. We can observe that the eddy viscosity distributions from the two models are totally different, and even considering the k-ω results obtained with the second choice for the ω inlet boundary value (not reported here), the k-ω model predicts a much lower level of μ_t. As a consequence, the density distribution (hence the temperature distribution) predicted by the Baldwin-Lomax model is much more diffused and this should be very important for the cooling effectiveness predicted by the two models and not considered in the present work. As for the case with 0% coolant mass flow rate, we can observe large disagreements in the velocity and temperature profiles in the step region, as shown in Figg. 18,19. In this case detailed experimental data should be very helpful in providing guidance for the evaluation of the two turbulence models.

5. CONCLUSIONS

A Navier-Stokes code with an algebraic and a two-equation turbulence model has been developed and used to predict the flow in a transonic film-cooled NGV cascade.

The coupling of the two-equation k-ω model with the explicit Navier-Stokes solver has proven very successful and not much affected by the stiffness problems of other two-equation turbulence models.

The application of the code to the difficult problem of coolant ejection through a slot has pointed out remarkable differences in the flow predicted by the two models in the coolant ejection region; this should be extremely important in predicting the film cooling effectiveness.

In the next future we will perform a careful validation of the code predictions with avaliable data of film cooled turbine blades.

ACKNOWLEDGEMENTS

The authors would like to thank Alfa Romeo Avio S.p.A. for permission to publish computational results and experimental data concerning the NGV cascade.

REFERENCES

[1] Baldwin, B.S., Lomax, H., "Thin Layer Approximation and Algebraic Model for Separated Turbulent Flows", AIAA paper no. 78-257, 1978.

[2] Wilcox, D.C., "Reassessment of the Scale-Determining Equation for Advanced Turbulence Models", AIAA Journal, vol. 26, no. 11, 1988.

[3] Wilcox, D.C., "A Half Century Historical Review of the k-ω Model", AIAA paper no. 91-0615, 1991.

[4] Jameson A., Schmidt, W., Turkel, E., "Numerical Solutions of the Euler Equations by Finite-Volume Methods Using Runge-Kutta Time-Stepping Schemes", AIAA paper no. 81-1259, 1981.

[5] Jameson A., "Transonic Flow Calculations", Dept. of Mechanical and Aerospace Engineering, Princeton Univ., Princeton, NJ, MAE Rept. 1651, 1984.

[6] Martinelli, L., "Validation of a Multigrid Method for the Reynolds-Averaged Equations", AIAA paper no. 88-0414, 1988.

[7] Swanson, R.C., Radespiel, R., "Cell Centered and Cell Vertex Multigrid Schemes for the Navier-Stokes Equations", AIAA Journal, vol. 29, no. 5, 1991.

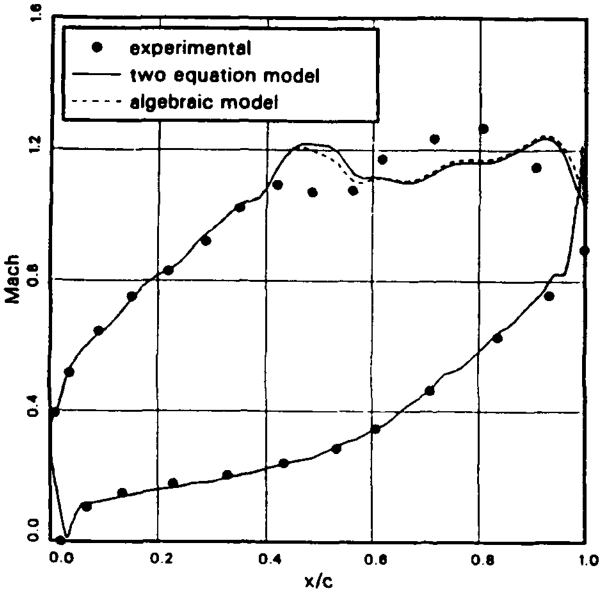

Figure 2: Blade isentropic Mach number distribution, "solid" blades

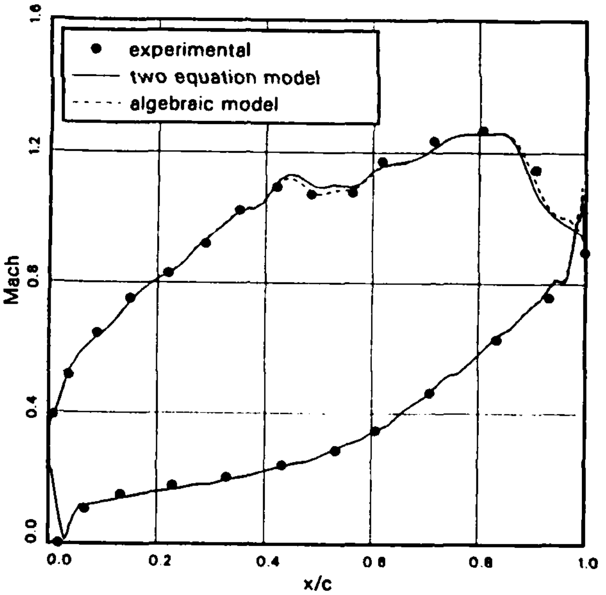

Figure 3: Blade isentropic Mach number distribution, halved grid

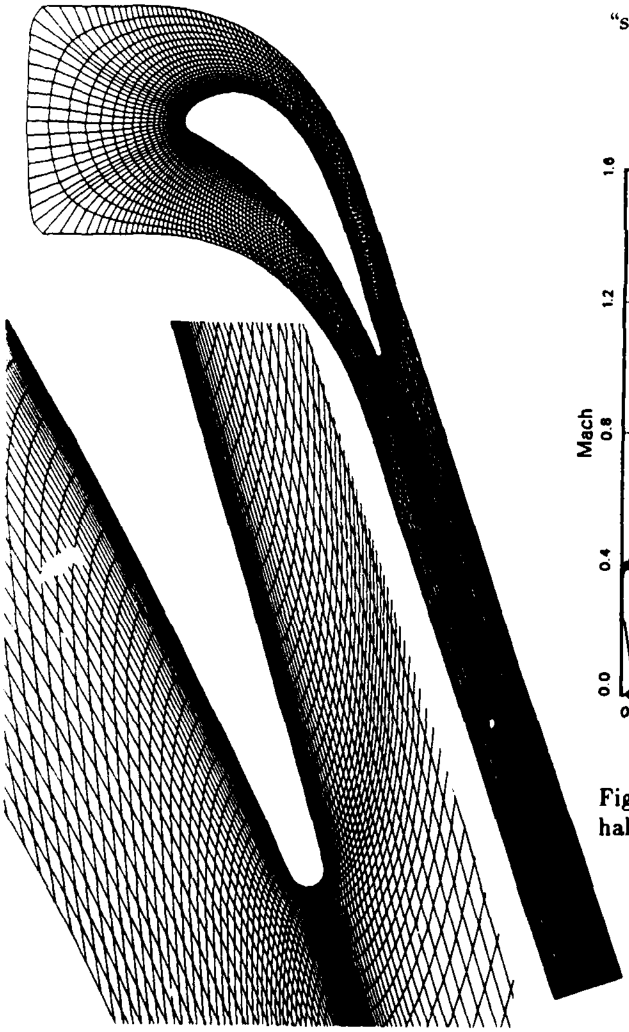

Figure 1: Computational grid, "solid" blades

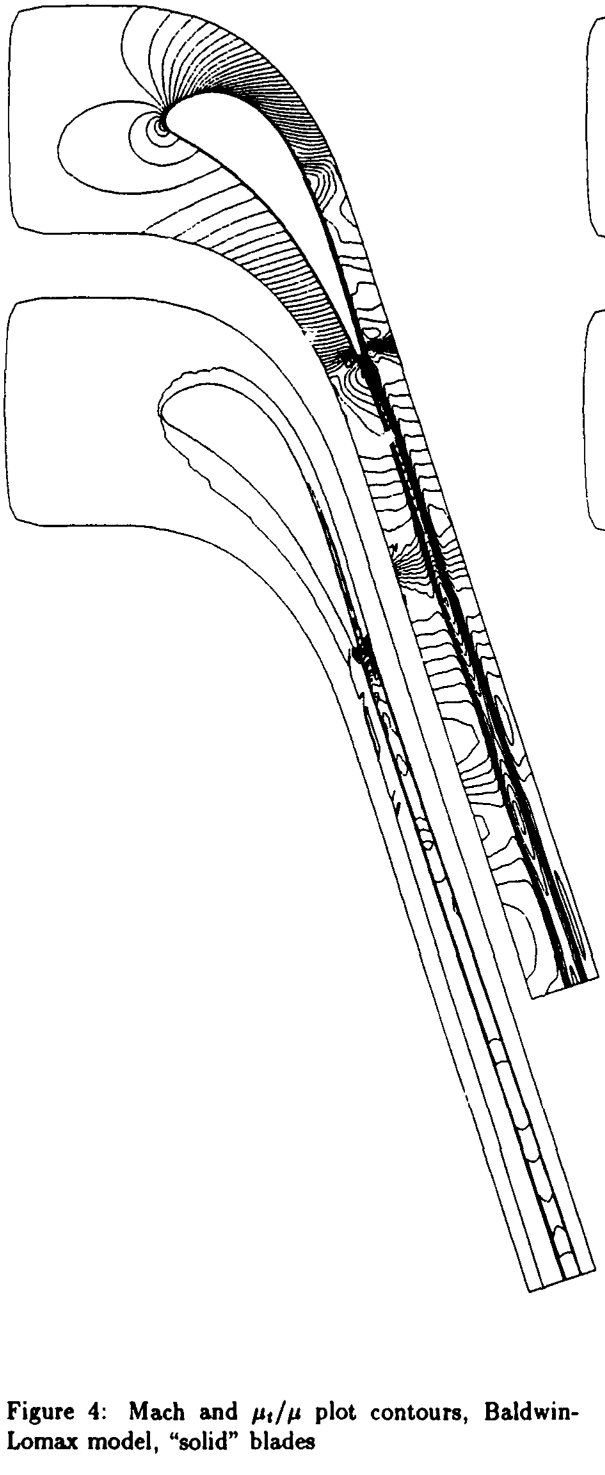

Figure 4: Mach and μ_t/μ plot contours, Baldwin-Lomax model, "solid" blades

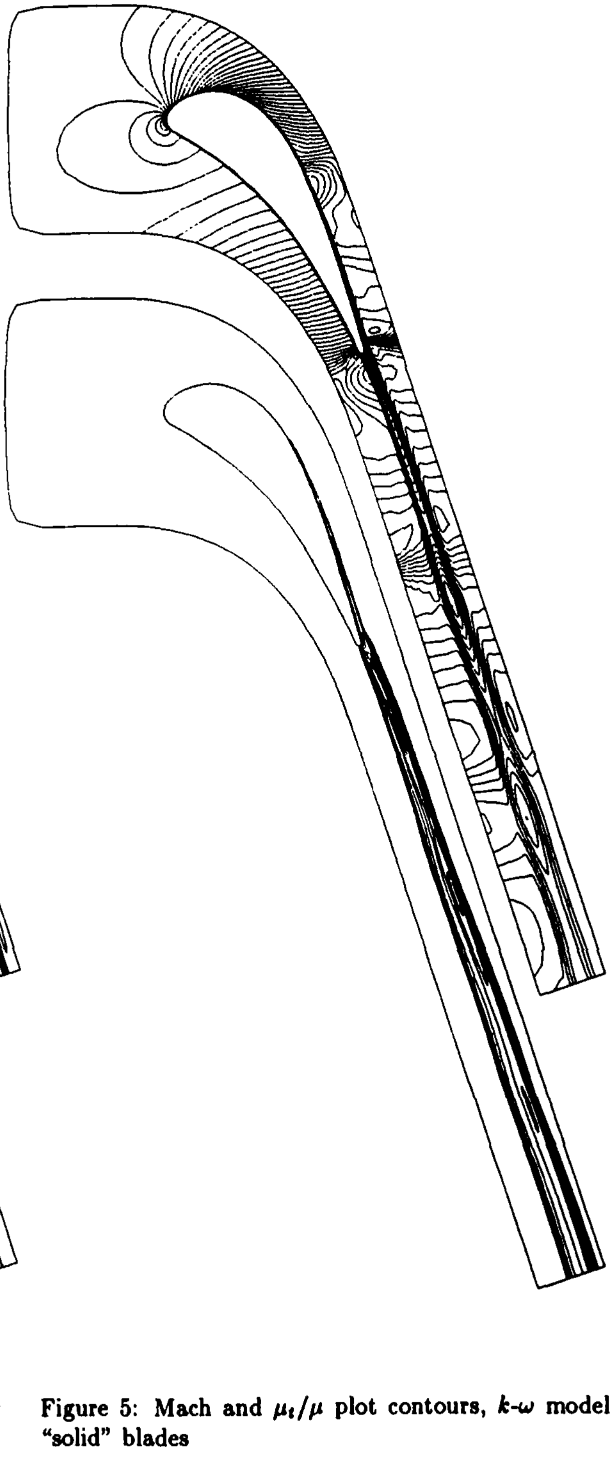

Figure 5: Mach and μ_t/μ plot contours, k-ω model, "solid" blades

Cascade	$\dot{m}_{cool}$	Loss			Flow Angle		
		exp	B-L	*k*-ω	exp	B-L	*k*-ω
"Solid"	-	.0460	.0509	.0466	70.70	71.48	71.55
"Cutted"	0%	-	.0575	.0506	-	71.56	71.62
"Cutted"	4%	-	.0608	.0551	-	71.52	71.51

Table 1: Mixed-out loss and flow angle, $M_{2is} = 1.07$

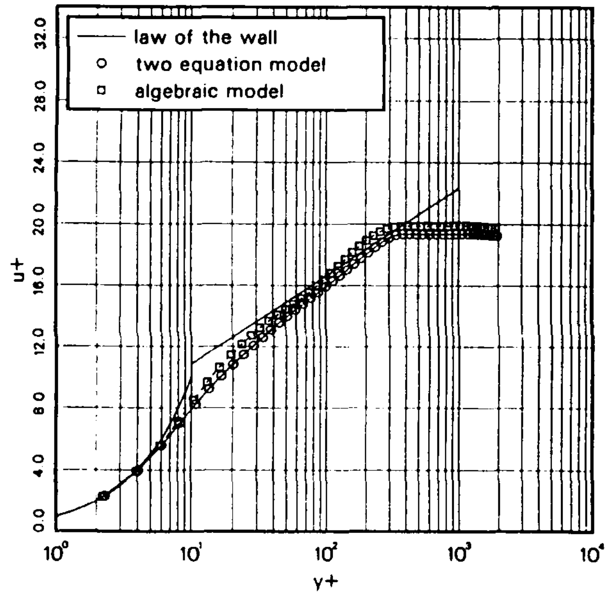

Figure 6: Boundary layer at x/c = 0.80

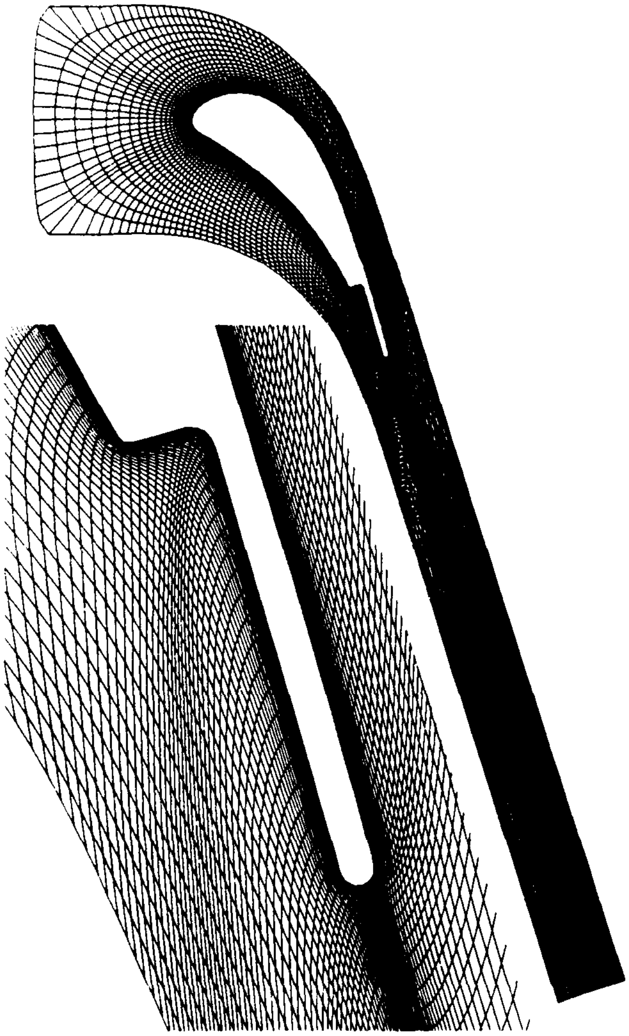

Figure 7: Computational grid, "cutted" blades

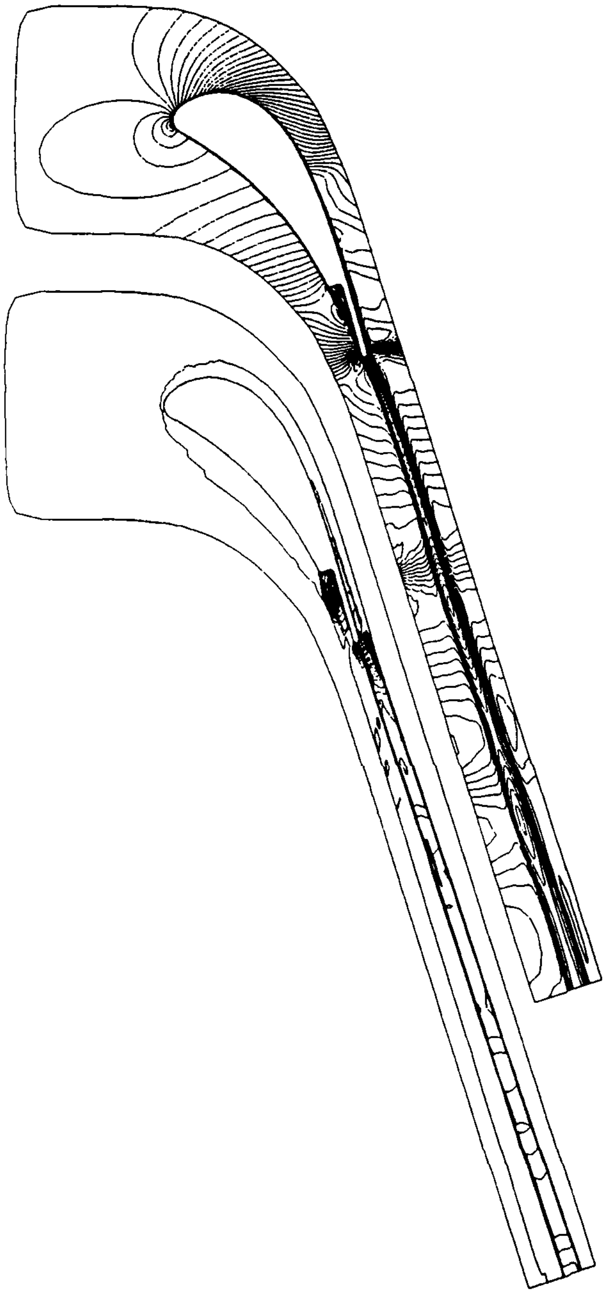

Figure 8: Mach and μ_t/μ plot contours, Baldwin-Lomax model, "cutted" blades, $\dot{m}_{cool} = 0\%$

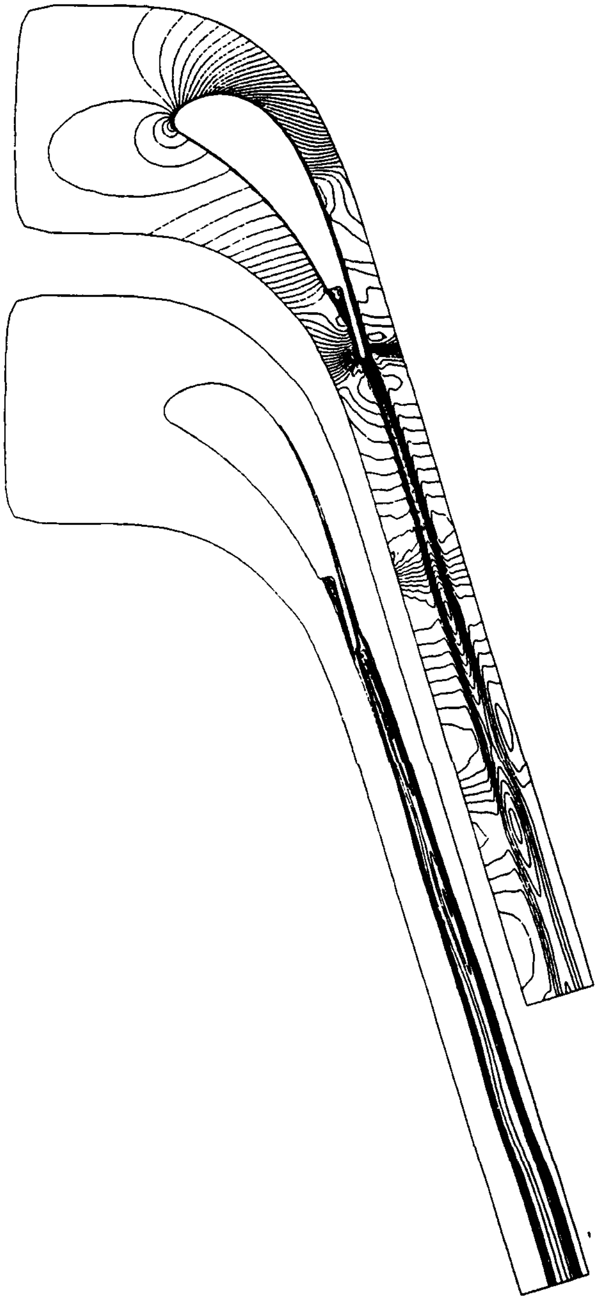

Figure 9: Mach and μ_t/μ plot contours, k-ω model, "cutted" blades, $\dot{m}_{cool} = 0\%$

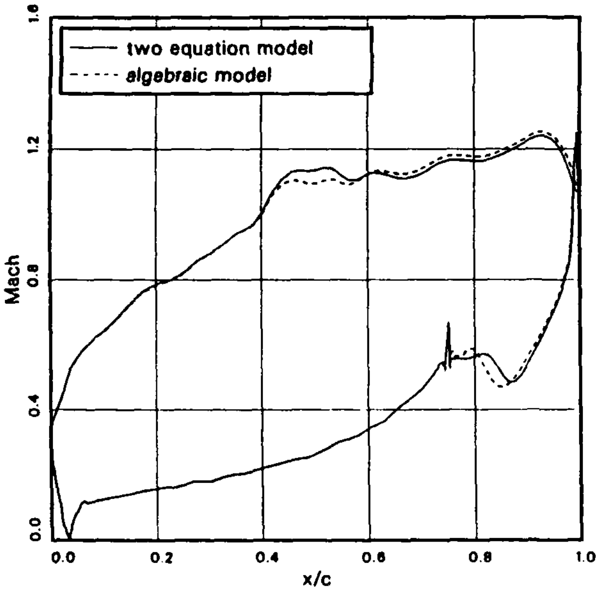

Figure 10: Blade isentropic Mach number distribution, "cutted" blades, $\dot{m}_{cool} = 0\%$

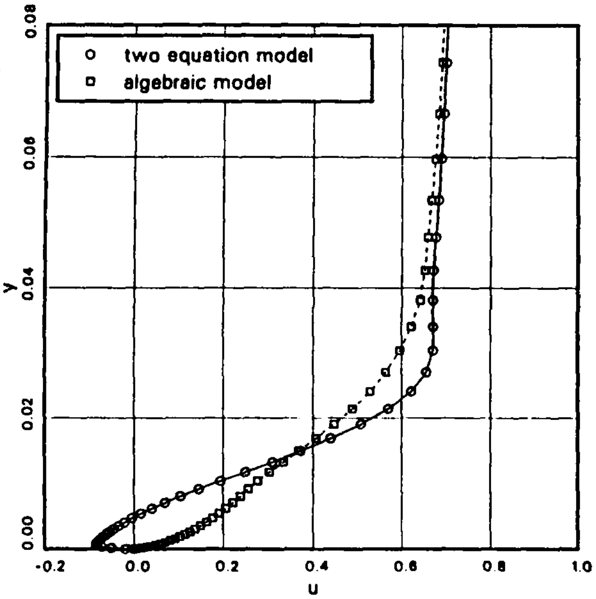

Figure 11: Velocity profile at x/c = 0.85

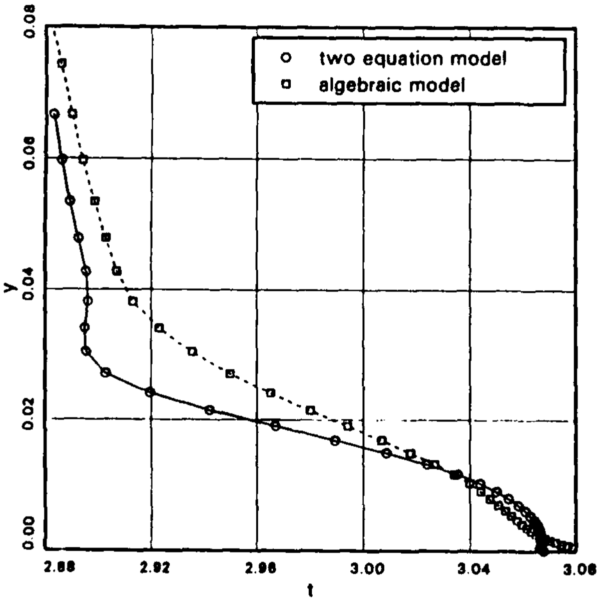

Figure 12: Temperature profile at x/c = 0.85

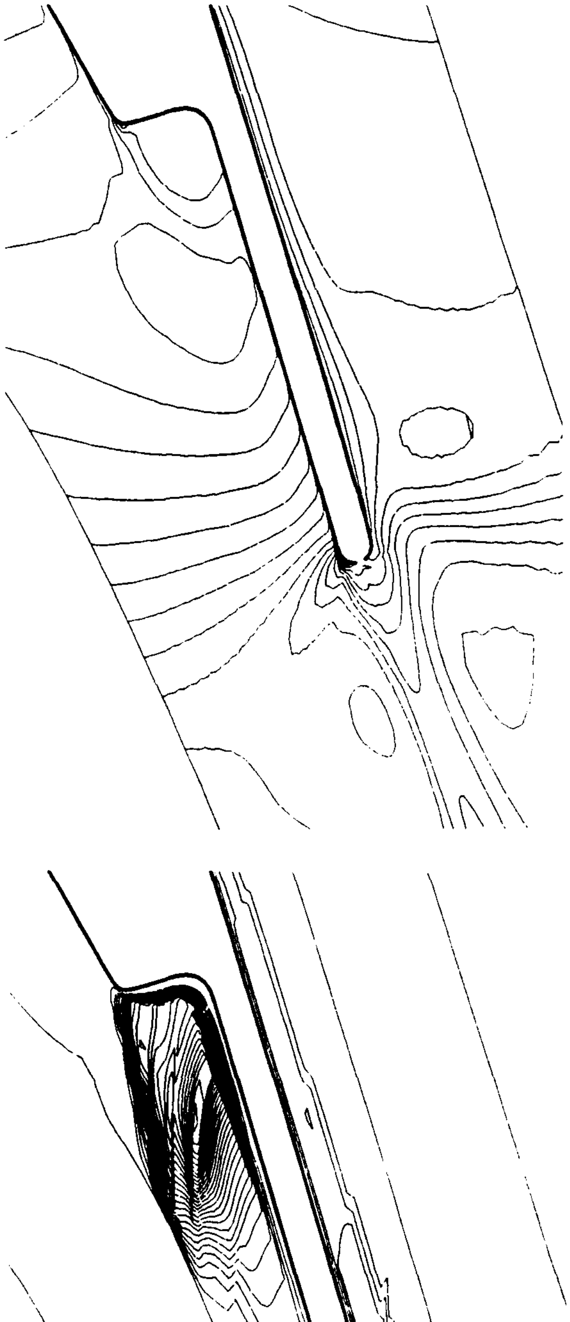

Figure 13: Detail of density and μ_t/μ plot contours, Baldwin-Lomax model, "cutted" blades, $\dot{m}_{cool} = 0\%$

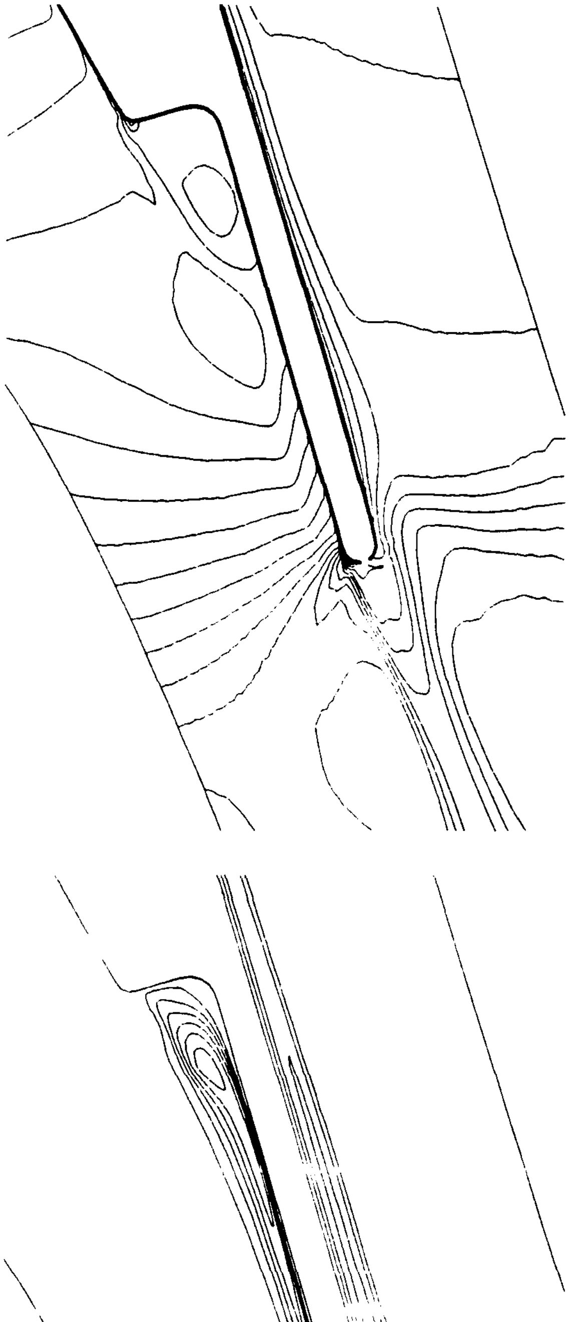

Figure 14: Detail of density and μ_t/μ plot contours, k-ω model, "cutted" blades, $\dot{m}_{cool} = 0\%$

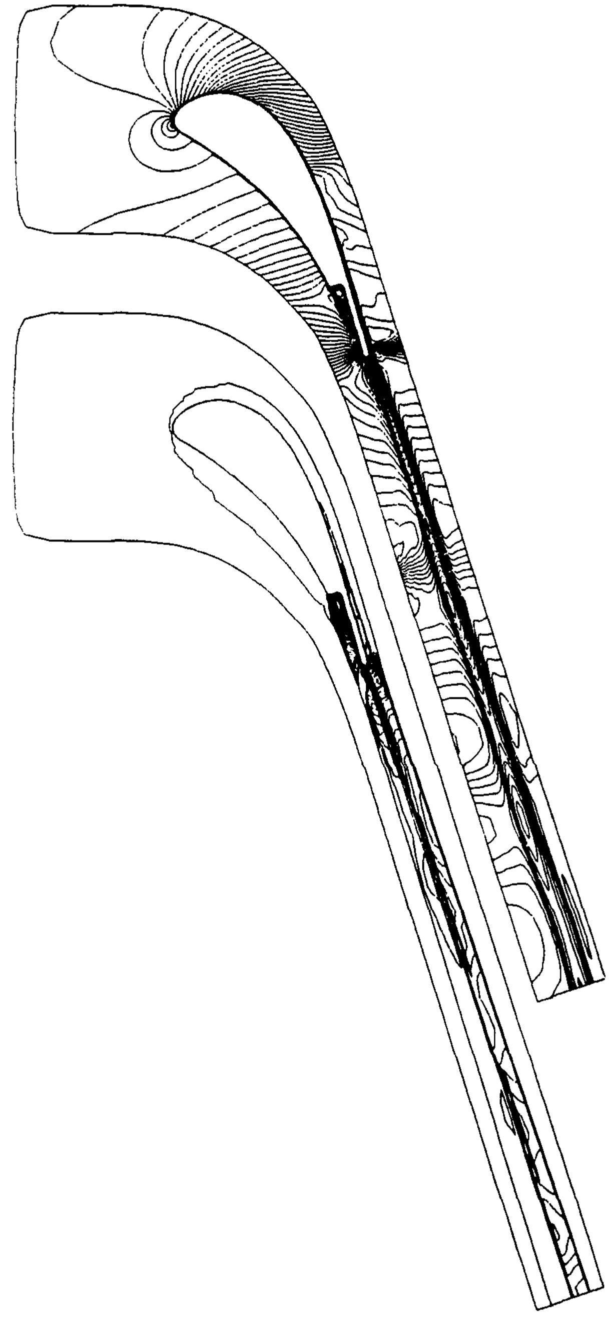

Figure 15: Mach and μ_t/μ plot contours, Baldwin-Lomax model, "cutted" blades, $\dot{m}_{cool} = 4\%$

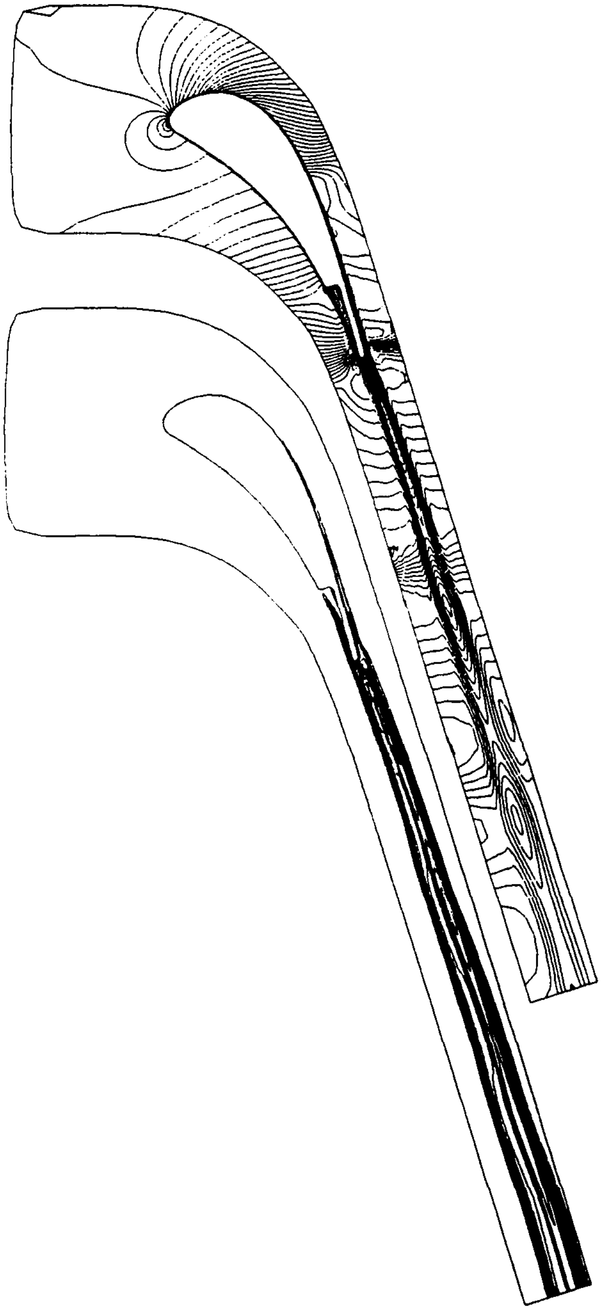

Figure 16: Mach and μ_t/μ plot contours, k-ω model, "cutted" blades, $\dot{m}_{cool} = 4\%$

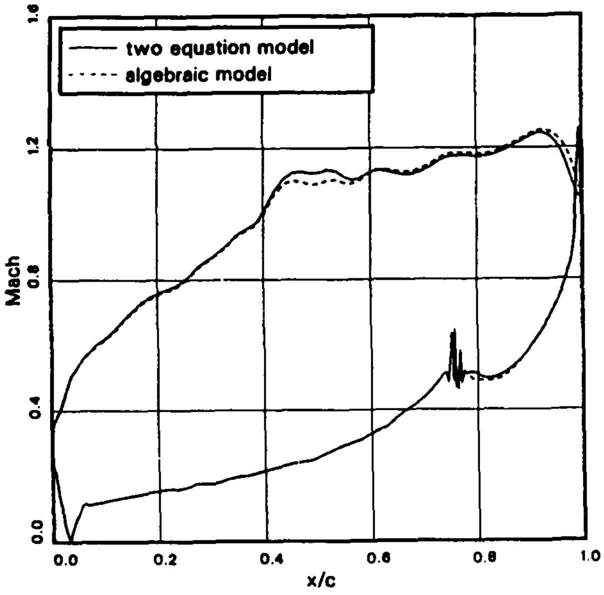

Figure 17: Blade isentropic Mach number distribution, "cutted" blades, $\dot{m}_{cool} = 4\%$

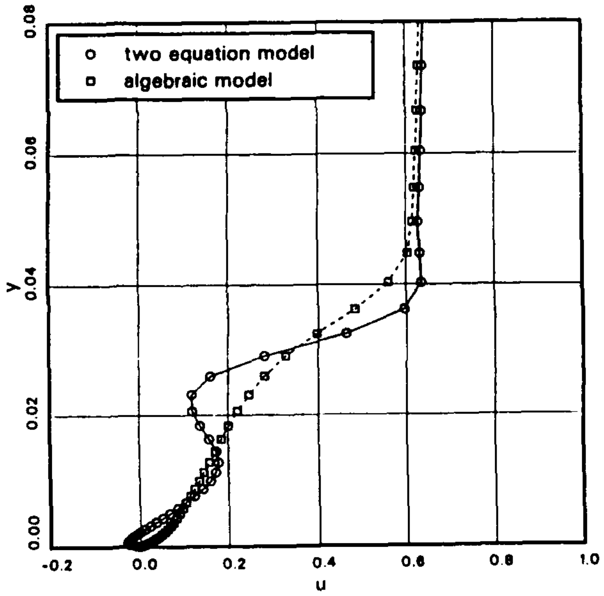

Figure 18: Velocity profile at x/c = 0.81

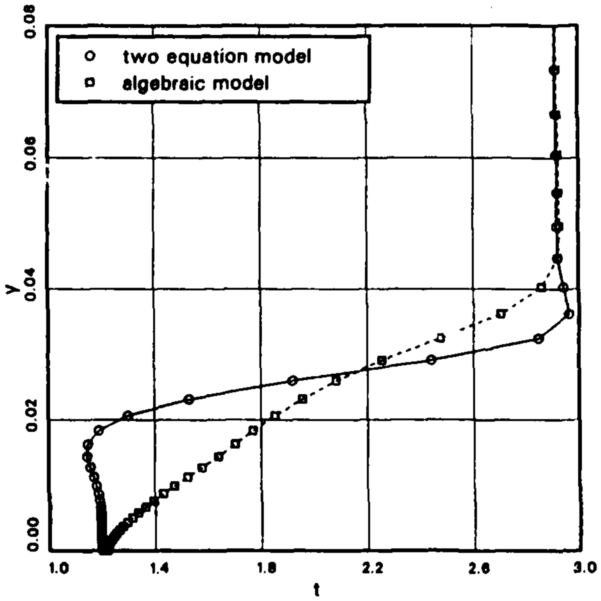

Figure 19: Temperature profile at x/c = 0.81

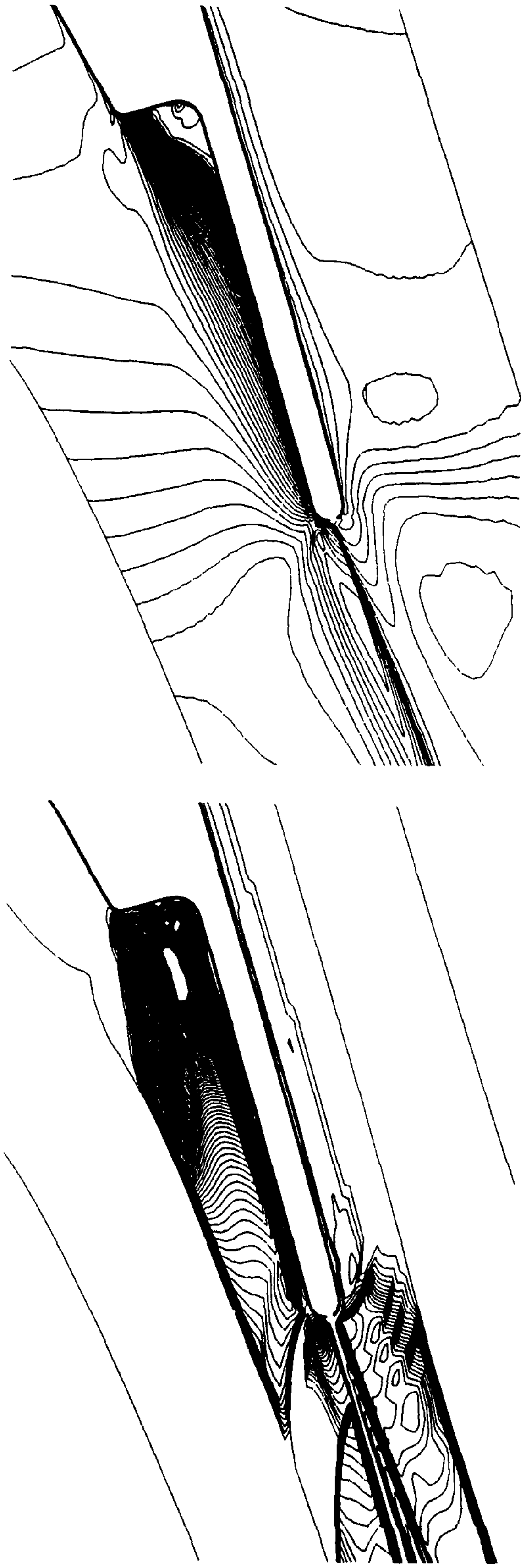

Figure 20: Detail of density and μ_t/μ plot contours, Baldwin-Lomax model, "cutted" blades, $\dot{m}_{cool} = 4\%$

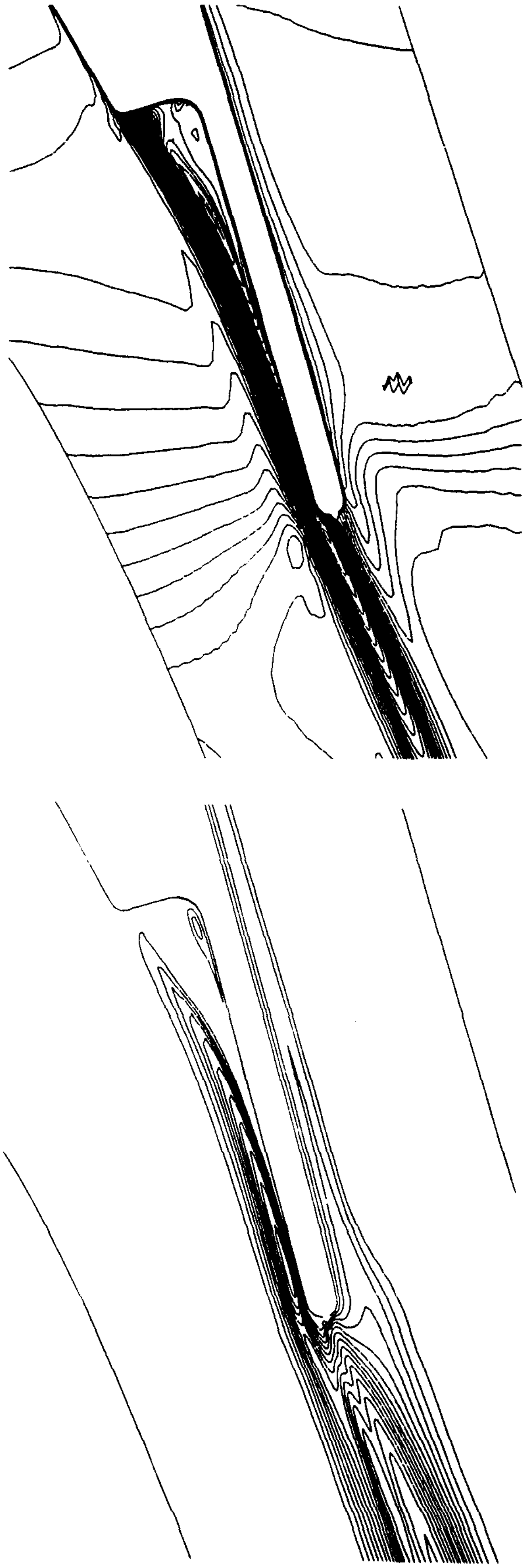

Figure 21: Detail of density and μ_t/μ plot contours, k-ω model, "cutted" blades, $\dot{m}_{cool} = 4\%$

Discussion

QUESTION 1:

DISCUSSOR: P. Harasgama, ABB

You use an adiabatic wall for your calculations. Can you implement different wall boundary conditions in order to predict heat transfer?

AUTHOR'S REPLY:

The code is already suited to impose a temperature distribution at wall and hence predict the heat transfer.

QUESTION 2:

DISCUSSOR: P. Harasgama, ABB

Table 1 shows that the loss predicted by the algebraic model is higher than that by the k-ω model. However, Figure 6 shows that u^+ vs y^+ is almost the same. Could you explain why the predicted losses are quite different?

AUTHOR'S REPLY:

The largest difference between the predictions is only in the rear part of the blade near the trailing edge. This is probably caused by the very different behavior of the two models in the wake regions.

QUESTION 3:

DISCUSSOR: O. Oymak, Middle East Technical University

As can be seen from the governing equations, there is a time dependency. I would like to ask two questions What are the initial conditions for k and ω, and what are the boundary conditions on ω.

AUTHOR'S REPLY:

For steady flow, if the method is correct, the solution is unique. Therefore, the initial conditions are not important. At the inlet, k is prescribed according to the inlet turbulence intensity. In addition, ω is deduced by setting the eddy viscosity equal to the laminar value of viscosity.

QUESTION 4:

DISCUSSOR: K. Broichhausen, MTU

Near the trailing edge region of the "cutted" blades you have a strongly skewed grid coupled with large gradients in the boundary conditions. Do you think, as shown yesterday in the paper by A. Beeck, that the results with the Baldwin-Lomax turbulence model are improved if the ejection hole is also modeled?

AUTHOR'S REPLY:

To my experience the skewedness of the grid does not matter and this can be easily checked. With our boundary conditions one takes the pressure (and hence velocity) variations into account along a line at the exit. If the boundary layer flux inside the channel is adequately resolved, one may impose the conditions inside simply by extending the grid inside.

QUESTION 5:

DISCUSSOR: D.T. Vogel, DLR

Which boundary conditions did you apply for the jet, especially for k? How did you model the eddy viscosity in the jet region using the Baldwin-Lomax model?

AUTHOR'S REPLY:

Lacking any experimental information, k and ω were set equal to the freestream values. Other choices were tested (up to 12% turbulence intensity) but the related differences in the computed solution are much less significant than those due to the turbulence model itself.

QUESTION 6:

DISCUSSOR: C. Hah, NASA Lewis

The numerical results show that the wake does not decay enough even after interaction with the trailing edge shock. Could you comment about this?

AUTHOR'S REPLY:

The trailing edge shocks are in this case quite weak so have little effect on the decay. Wakes are not correctly simulated by any eddy-viscosity model.

QUESTION 7:

DISCUSSOR: E. Benz, University of Karlsruhe

Have you already, or is it planned to test the code by comparing it with simple test cases (e.g., backward facing step, tangential film-cooling experiments) where a lot of experimental and numerical results are available?

AUTHOR'S REPLY:

In the near future it is planned to test both models, including a version of the k-ε model, for the backward facing step.

Navier-Stokes Analysis of Three-Dimensional Flow and Heat Transfer inside Turbine Blade Rows

C. Hah
NASA Lewis Research Center
Cleveland, Ohio
U. S. A.

SUMMARY

This study presents a numerical method for solving the three-dimensional, Navier-Stokes equations for unsteady, viscous flow and heat transfer through multiple turbomachinery blade rows. The method solves the fully three-dimensional Navier-Stokes equations with an implicit scheme which is based on a control volume approach. A two-equation turbulence model with a low Reynolds number modification is employed in the present study. A third-order accurate upwinding scheme is used to approximate convection terms while a second order accurate central difference scheme is used for the discretization of viscous terms. A second-order accurate scheme is employed for the temporal discretization.

The numerical method is applied to study the unsteady flow and heat transfer field of the High Pressure Fuel side Turbo-Pump (HPFTP) of the Space Shuttle Main Engine (SSME). The stage calculation is performed by coupling the stator and the rotor flow fields at each time step through an over-laid grid. Numerical results for the complete geometry with the vane trailing edge cutback are presented and compared with the available experimental data.

INTRODUCTION

Advanced design in rocket propulsion requires increased durability and performance of turbomachinery components. To achieve these very aggressive design goals, accurate prediction of the aero- and thermal- loading and the characteristics of flow unsteadiness and three-dimensional effects is essential.

Significant developments in numerical methods for the analysis of turbomachinery flows have been made over the last decade (Davis et al. [1987], Dawes [1986], Denton [1986], Giles [1988], Hah [1986], Moore and Moore [1985], Rao and Delaney [1990] etc.). Three-dimensional steady flow calculations based on the Reynolds-averaged Navier-Stokes equation are now relatively well established and routinely used to optimize blading and flow-path contours. At the present time, design optimization of multiple blade rows is performed by running isolated blade calculations or a simple steady state multiple-blade-rows calculation (Copenhaver et al. [1992], Dawes [1991], Denton and Singh [1979], Ni [1989], etc.) Although these optimization procedures based on steady flow calculations work relatively well for most turbine designs, unsteady flow and heat transfer analysis might be necessary when unsteady loading and local heat transfer information is required.

Recently, various unsteady flow analysis methods have been developed for the simulation of multiple blade row interactions (for example, Chen [1988], Erdos et al. [1977], Giles [1988], Jorgenson and Chima [1989], Rai [1987], Rao and Delaney [1990], etc.). However, most unsteady flow analysis for turbomachinery blade rows are conducted with two-dimensional or quasi three-dimensional configurations because of the extremely high cost of three-dimensional analysis.

In this study, a three-dimensional, viscous, and unsteady flow and heat transfer calculation procedure for multiple blade rows is developed and applied to analize the flow field of the first stage turbine of the High Pressure Fuel side Turbo-Pump (HPFTP) of the Space Shuttle Main Engine (SSME). The numerical procedure is the direct extension to unsteady flow calculation of a steady Navier-Stokes code which has been tested and applied for a wide range of turbomachinery flows (Hah [1983, 1987], Hah and Wennerstrom [1990], Copenhaver et al. [1992]).

Although several unsteady flow and heat transfer studies for the current SSME flow field have been reported previously (for example, Chen [1988], Griffin and McConnaughy [1989], etc.), the full three-dimensional geometry with the vane trailing edge cutback (figure 1) has not yet been studied. The numerical results are compared with the currently available measured data on the time-averaged and time-dependent flow and heat transfer quantities.

GOVERNING EQUATIONS

The following Reynolds-averaged Navier-Stokes equations are solved for the current problem.

$$\frac{\partial \rho}{\partial t} + \frac{\partial}{\partial x_i}(\rho U_i) = 0 \qquad (1)$$

$$\frac{\partial(\rho U_i)}{\partial t} + \frac{\partial}{\partial x_j}(\rho U_i U_j) + 2\rho\varepsilon_{ijk}\Omega_j U_k = -\frac{\partial p}{\partial x_i} + \frac{\partial}{\partial x_j}\left[\mu\left\{\frac{\partial U_i}{\partial x_j} + \frac{\partial U_j}{\partial x_i} - \frac{2}{3}\frac{\partial U_k}{\partial x_k}\delta_{ij}\right\} - \rho\bar{u}_i\bar{u}_j\right] + F_i \quad (2)$$

$$\frac{\partial(\rho e)}{\partial t} + \frac{\partial}{\partial x_j}(\rho U_j e) = \frac{\partial}{\partial x_j}\left[\frac{\mu}{Pr}|_{eff}\frac{\partial T}{\partial x_j}\right] - \frac{\partial}{\partial x_j}(pU_j) + U_i F_i + \frac{\partial}{\partial x_j}\left[U_i\mu\left\{\frac{\partial U_i}{\partial x_j} + \frac{\partial U_j}{\partial x_i} - \frac{2}{3}\frac{\partial U_k}{\partial x_k}\delta_{ij}\right\}\right] \quad (3)$$

$$p = \rho RT \quad (4)$$

where U_i = mean velocity, u_i = fluctuation velocity, e = total energy, Ω_i = angular velocity,

$$\frac{\mu}{Pr}|_{eff} = \frac{\mu}{Pr}|_{laminar} + \frac{\mu}{Pr}|_{turbulent}$$

and

$$e = C_v T + \frac{1}{2}U_i U_i$$

It is well known that neither the conventional mixing length type turbulence model nor any standard two-equation type turbulence model describes turbulence stresses properly in the region behind a shock wave or in the separated flow regions. Several recent studies indicate that significant improvement can be achieved when the standard two-equation model is modified to include the low Reynolds number effects. For the current study, a standard two-equation model is modified to include the low Reynolds number effects following the studies of Chien [1982]. The following additional transport equations are solved for the turbulent shear stresses.

$$\frac{\partial(\rho k)}{\partial t} + \frac{\partial(\rho U_i k)}{\partial x_i} = \frac{\partial}{\partial x_i}\left[\frac{\mu_{eff}}{\sigma_k}\frac{\partial k}{\partial x_i}\right] - \rho u_i u_j U_{i,j} - \rho\varepsilon - \frac{2\mu k}{\rho^2} \quad (5)$$

$$\frac{\partial(\rho\varepsilon)}{\partial t} + \frac{\partial(\rho U_i\varepsilon)}{\partial x_i} = \frac{\partial}{\partial x_i}\left[\frac{\mu_{eff}}{\sigma_\epsilon}\frac{\partial\varepsilon}{\partial x_i}\right] - C_1\frac{\rho\varepsilon}{k}(\bar{u}_i u_j U_{i,j}) - \frac{\rho\varepsilon}{k}\left[C_2 f\varepsilon + \frac{2\nu k e^{-C_4 u_* l/\nu}}{l^2}\right] \quad (6)$$

where

$$\mu_{eff} = \mu + C_\mu(k^2/\varepsilon)[1 - exp(-C_3 u_* l/\nu)]$$

and

$$f = 1 - \frac{0.4}{1.8}e^{-(k^2/6\nu\epsilon)^2}$$

No attempt was made to optimize constants of the turbulence modeling equations for this study. Therefore, standard values of various constants of the turbulence model are used: the values are

$C_\mu = 0.09, C_1 = 1.35, C_2$ [illegible] $\sigma_k = 1.0,$

$\sigma_e = 1.3, C_3 = 0.00115, C_4 = 0.5$

NUMERICAL METHOD

The unsteady flow effects on the current turbine stage are due to the interactions of the potential flow fields and the stator wake with the rotor flow field. Consequently, any instantaneous flow variable can be split into three components: the time-averaged components, the periodic fluctuation due to the motion of the rotor relative to the stator frame, and the turbulent fluctuation. The sum of the first two parts is the phase-averaged value which is a function of time and space. The present study aims to numerically solve for this ensemble-averaged flow field. The effects of the turbulent fluctuation are included through the turbulence model. The turbulence is represented through the ensemble-averaged turbulence kinetic energy and the turbulence dissipation rate. These two turbulence variables are obtained by solving unsteady semi-empirical transport equations.

The ensemble-averaged flow variables in the current unsteady flow field can be efficiently obtained by coupling the time-dependent stator flow with the time-dependent rotor flow. Therefore, two flow fields are solved with coupled time-dependent interface boundary conditions. As shown in the computational grid (figure 2), an interface is used to transmit flow conditions between two zones. A sliding over-laid grid is used for the present application. A three-dimensional steady Navier-Stokes code which has been successfully tested for a wide range of turbomachinery flows (Hah [1983,1987]) is extended to execute time accurate calculation. During the development, it was found that high-order discretization schemes are necessary for both the space and the time discretization to avoid excessive numerical dissipation. For the time-dependent terms, an implicit second-order scheme is used.

$$\frac{\partial\phi}{\partial t} = \frac{1}{\Delta t}\left(1.5\phi^{n+1} - 2\phi^n + 0.5\phi^{n-1}\right)$$

where $n-1, n, n+1$ denote time levels and Δt the time step.

For unsteady flow calculations, the size of the time step is primarily determined by the requirement for physical accuracy. However, the time step is also restricted by the numerical stability. For the current implicit time integration approach, a sub-iteration is performed at each time step. The number of sub-iterations is determined by the size of the time step and is typically eight to ten for the present application.

At each time step, the governing equations are solved with an implicit relaxation method using a fully conservative control volume approach. A third-order accurate interpolation scheme is used for the discretization of the convection terms and central differencing is used for the diffusion terms. The method is of second-order accuracy with smoothly varying grids. For convenience, the governing equations are transformed to generalized coordinates as follows,

$$\begin{aligned}
&\frac{1}{J}\frac{\partial}{\partial \xi}(G_1\phi) + \frac{1}{J}\frac{\partial}{\partial \eta}(G_2\phi) + \frac{1}{J}\frac{\partial}{\partial \psi}(G_3\phi) \\
&= \frac{1}{J}\frac{\partial}{\partial \xi}\left[\frac{\acute{\Gamma}_\phi}{J}D_{\xi\xi}\phi_\xi + \frac{\acute{\Gamma}_\phi}{J}D_{\xi\eta}\phi_\eta + \frac{\acute{\Gamma}_\phi}{J}D_{\xi\psi}\phi_\psi\right] \\
&+ \frac{1}{J}\frac{\partial}{\partial \eta}\left[\frac{\acute{\Gamma}_\phi}{J}D_{\eta\xi}\phi_\xi + \frac{\acute{\Gamma}_\phi}{J}D_{\eta\eta}\phi_\eta + \frac{\acute{\Gamma}_\phi}{J}D_{\eta\psi}\phi_\psi\right] \\
&+ \frac{1}{J}\frac{\partial}{\partial \psi}\left[\frac{\acute{\Gamma}_\phi}{J}D_{\psi\xi}\phi_\xi + \frac{\acute{\Gamma}_\phi}{J}D_{\psi\eta}\phi_\eta + \frac{\acute{\Gamma}_\phi}{J}D_{\psi\psi}\phi_\psi\right] + \hat{S}_\phi \qquad (7)
\end{aligned}$$

where $\acute{\Gamma}_\phi$ is the diffusion coefficient, G_i is a velocity component along the transformed coordinates (ξ, η, ψ), and $\hat{S}_\phi$ consists of additional body force terms and pressure terms. A 3-point central difference approximation is used for all the diffusion terms and a modified quadratic upwinding scheme is used for convection terms.

Because the coefficients of the finite difference equation (7) are based on the values at the previous step, the resulting ρU_i does not satisfy mass conservation. Two correction steps are needed to satisfy the mass conservation at each iteration.

The two correction steps are as follows:

$$(\rho U_i)^{**} - (\rho U_i)^{*} = \Delta_p^{-1}\Delta_i(P^* - P^n) \qquad (8)$$

$$\begin{aligned}
(\rho U_i)^{n+1} - (\rho U_i)^{**} &= A_p^{-1}\Sigma A_{pm}[(\rho U)^{**} - (\rho U)^{*}] \\
&-\Delta_i(P^{n+1} - P^*) \qquad (9)
\end{aligned}$$

For eqs. (8) and (9), the mass conservation condition is imposed as

$$\Delta_i(\rho U_i)^{**} = \Delta_i(\rho U_i)^{n+1} = \Delta_i(\rho U_i)^{**} = 0 \qquad (10)$$

By combining eq. (10) with eqs. (8) and (9), Poisson-type equations are obtained for $(P^* - P^n)$ and $(P^{**}.- P^*)$ and the value of $(\rho U)_i^{n+1}, P^{n+1}$ is calculated with the corrected pressure. With the correction step in eqs. (8)-(10), density is handled rather implicitly and (ρU_i) and P are updated. A single implicit step is used to calculate k, ε, and e with the corrected values of ρU_i and p.

The first stage turbine of the High Pressure Fuel side Turbo-Pump (HPHTP) of the Space Shuttle Main Engine (SSME) consists of 41 stator vanes and 63 rotor blades. To obtain a solution with all of the unsteady information, the entire flow passage should be calculated. This is not a practical option at the moment because of the required computer resources. Alternatively, two stator passage and three rotor passages can be calculated with a time-lagged boundary condition treatment to account for the uneven number of blades (Erdos et al. [1977]). However, this approach also requires large amounts of computer memory. Previous studies in two-dimension showed that the overall aerodynamic characteristics are predicted very well with a one-to-one flow passage with a rescaled rotor. The main objective of the current study is to predict the unsteady aerodynamic characteristics of the turbine stage with the correct stator geometry which has a significant trailing edge cutback. Therefore, the numerical procedure was applied to a single blade passage for each blade row, with the rotor scaled to the stator pitch. The scaling of the rotor for the single passage calculation was done such that the pitch-to-chord ratio remained unchanged. Six computational nodes are used to describe the tip clearance of the rotor (0.019 inches). The steady multi-blade-row solution was performed first, and this solution was used as an initial condition for the unsteady calculation. Eight cycles of the blade pass were typically required to obtain periodicity of the solution. The current computational grid was generated to give an orthogonal grid near the leading edge and near the blade surface where the most important flow phenomena occur. With this grid, spatial periodicity at the periodic surfaces is not enforced for the grid, so the physical periodicity condition is handled inside the code using an interpolation function. The grid consists of 50 nodes in the blade-to-blade direction, 35 nodes in the spanwise direction, and 204 nodes in the streamwise direction. The standard boundary conditions for the three-dimensional blade row calculation (Hah and Wennerstrom [1990]) are applied for the stage inlet and exit. Approximately five Cray YMP single processor CPU hours are required to advance the solution for each cycle.

RESULTS AND DISCUSSION

The current numerical method has been applied to study the time-dependent flow and heat transfer field of the first turbine stage of the High Pressure Fuel-side Turbo-Pump of the Space Shuttle Main Engine. The main objective of the current study is to investigate the effect of the trailing edge cutback of the stator on the aero- and heat-load of the stage. The results for the flow field are presented first. The results for the heat transfer analysis are presented in the second part of this section.

STEADY AND UNSTEADY FLOW FIELD

Calculated time-averaged static pressure distributions at 10 percent, 50 percent, and 90 percent span of the blades are compared with the measured time-mean static pressure distribution on the stator (Susan et al. [1991]) in figure 3. The calculated pressure field agrees well with the measured time-mean pressure field. For the current SSME turbine stage, the pressure drop across each blade row is relatively small compared to some highly loaded turbine stages. Therefore, the unsteady envelope of the static pressure distribution on the stator blade surface is quite small. Previously reported numerical results for the stator, which did not model the trailing edge cutback, showed almost uniform pressure profiles along the radial direction. However, the present results indicate that the lift forces on the blade change near the hub section due to the trailing edge cutback. The calculated static pressure distribution on the rotor blade surface at five different times during one cycle of the blade passage are shown in figure 4. The blade loading seems to be fluctuating more in the tip region than in the hub region because of the blade interaction.

The calculated Mach number contours across the blade passage at two different times are given in figure 5. Changes in the rotor flow field when the rotor moves through the stator wakes are shown in figure 5. Due to the tip clearance flow and the endwall boundary layers, three-dimensional effects are significant in the endwall regions. At the 90 percent span of the blade, the unsteady effects are more pronounced than at other radial locations. Although the overall effects of the blade interactions (both the potential and the wake interactions) are relatively small, the influence of the stator flow field on the rotor flow field is still evident in figure 5.

Calculated velocity vectors near the blade surface at a given time are shown in figure 6. Small three-dimensional effects due to the cutback in the stator are shown in the stator flow field. For the rotor flow field, typical radially inward and outward fluid movements are observed near the suction and pressure surfaces of the blade. Velocity vectors near the tip of the rotor blade are shown in figure 7. The formation of the tip-clearance vortex near the suction side of the blade is clearly illustrated in this figure. However, this vortex seems relatively weak as shown in figure 8 .

The calculated flow angles at the rotor inlet and the rotor exit are given in figure 9 for different five different times during one cycle of the blade passage. The angles shown in figure 9 are mass-averaged values across the pitch-wise direction. Again, relatively small changes in the flow angles during the cycle are calculated.

HEAT TRANSFER FIELD

Figure 10. shows a comparison between the calculated and the measured heat transfer coefficient of the stator. The experimental data are for the low Reynolds number case (Dunn and Kim [1991]). The Stanton number is defined with the stage inlet density and the stage inlet total velocity. The overall trend in the distribution of the blade surface Stanton number is reasonably well calculated. However, significant disagreements between the data and the calculation are observed near the end wall region. On the pressure side, the numerical analysis underpredicts the heat transfer. On the suction surface, the analysis calculates a shorter laminar flow region than the measured data show. The currently employed turbulence model, which is known to be able to simulate flow transition when the free stream turbulence is relatively high, does not predict the flow transition properly for the present flow which has very low incoming turbulence intensity. The measured Stanton numbers at the 90 percent span are much lower than those at the mid-span. The numerical solution does not predict this large variation in the spanwise direction. Further study is necessary to verify both the experimental and the numerical results.

Comparisons between the calculated and the measured heat transfer at 10, 50, and 90 percent span of the rotor are shown in figure 11. The calculated values are obtained by time-averaging instantaneous values from the present unsteady solution. Figure 11 indicates that the overall agreement is reasonably good especially on the pressure side of the blade. On the suction side, the agreement is good at mid-span and 90 percent span. However, the numerical analysis does not predict lower heat transfer immediately after the leading edge. Overall, the agreement seems better for the rotor than for the stator. This might be due to the nature of the current turbulence model.

CONCLUDING REMARKS

The unsteady three-dimensional flow and heat transfer field inside the first stage turbine of the High Pressure Fuel-side Turbo Pump of the Space Shuttle Main Engine has been numerically studied with the Reynolds-averaged Navier-Stokes equations. The numerical scheme is based on a fully conservative control volume approach. A third-order accurate space discretization and a second-order accurate time discretization are applied to avoid excessive numerical dissipation with a limited computational grid. A two-equation turbulence model is used for turbulence closure. The numerical results agree well with the currently available measured data for the flow field. For the heat transfer field, the overall trend is reasonably well calculated. However, significant disagreements are observed near the hub region. Further study is necessary to verify both the experimental and the numerical results near the endwall of the stage. Further development of transition modeling is essential for improved heat transfer prediction especially for the stator. Some three-dimensional flow and heat transfer effects due to the trailing edge cutback of the stator are also observed in the numerical solution. The current numerical approach seems quite efficient in terms of computer resource requirements for the unsteady analysis of the multiple blade row interactions. Further verification and application of this type of tool to the aero- and thermal-analysis of multi-blade rows will enhance the understanding of multi-stage flow physics.

REFERENCES

Chen, Y. S., 1988, "3-D Stator-Rotor Interaction of the SSME ," AIAA Paper 88-3095.

Chien, K.Y., 1982, "Prediction of Channel and Boundary-Layer Flows With a Low Reynolds Number Turbulence Model," AIAA Journal Vol.20,No.1,pp. 33-38.

Copenhaver, W. W., Hah, C., and Puterbauch, S. L., 1992 " Three-Dimensional Flow Phenomena in a Transonic, High-Through-Flow Compressor Stage ," ASME paper 92-GT-169.

Davis, R.L., Hobbs, D.E., and Weingold, H.D., 1988, "Prediction of Compressor Cascade Performance Using a Navier-Stokes Tchnique," ASME Journal of Turbomachinery, Vol.110,No.4,pp. 520-531.

Dawes, W.N., 1986, "Development of a 3D Navier-Stokes Solver for Application to All Types of Turbomachinery," ASME paper 86-GT-70.

Denton, J.D., 1986, "The Use of a Distributed Body Force to Simulate Viscous Flow in 3D flow Calculations," ASME Paper 86-GT-144.

Denton, J.D. and Singh, U.K., 1979, " Time Marching Methods for Turbomachinery Flow Calculation," VKI Lecture Series, 1979-7.

Dunn, M. G. and Kim, J., 1992, " Time Averaged and Phase-Resolved Heat Transfer and Pressure Measurement for the Turbine of the SSME Fuel Side Turbopump ," CUBRC Report No.6401.

Giles, M.B., 1988, "Stator/Rotor Interaction in a Transonic Turbine," AIAA Paper 88-3093.

Hah, C., 1984, "A Navier-Stokes Analysis of Three-Dimensional Turbine Flows inside Turbine Blade Rows at Design and Off-Design Conditions ," ASME Journal of Engineering for Gas Turbines and Power, Vol.106,No.2,pp.421-429.

Hah, C., 1986, "A Numerical Modeling of Endwall and Tip-Clearance Flow of an Isolated Compressor ," ASME Journal of Engineering for Gas Turbines and Power, Vol.108,No.1,pp.15-21.

Hah, C., 1987, "Calculation of Three-Dimensional Viscous Flows in Turbomachinery With an Implicit Relaxation Method," AIAA Journal of Propulsion and Power, Vol.3,No.5,pp.415-422.

Hah, C., and Wennerstrom, A.J., 1990, "Three-Dimensional Flowfields Inside a Transonic Compressor with Swept Blades," ASME Paper 90-GT-359.

Hudson, S. T., Gaddis, S. W., Jhonson, P. D., and Boynton, J. L., 1991," Cold Flow Testing of the Space Shuttle Main Engine High Pressure Fuel Turbine Model," AIAA Paper 88-3093.

Jorgenson, P. C. E. and Chima, R. V., 1988,"An Explicit Runge-Kutta Method for Unsteady Rotor/Stator Interaction," AIAA Paper 88-0049.

Griffin, L. W. and McConnaughey, H. V., 1989, " Prediction of Aerodynamic Environment and Heat Transfer for Rotor-Stator Configurations ," ASME paper 89-GT-89.

Moore,J., and Moore,J.E., 1981,"Calculations of Three-Dimensional Viscous Flow and Wake Development in a Centrufugal Impeller," ASME Journal of Engineering for Power, Vol.103,No.2,pp.367-372.

Ni, R.H., 1989," Prediction of 3D Multi Stage Turbine Flow Field Using a Multiple Grid Euler Solver," AIAA paper 89-0203.

Rai, M. M., 1985, "Navier-Stokes Simulations of Rotor-Stator Interaction Using Patched and Overlaid Grids ," AIAA Paper 85-1519.

Rao, K. and Delaney, R., 1990, "Investigation of Unsteady Flow Through Transonic Turbine Stage," AIAA Paper 90-2408.

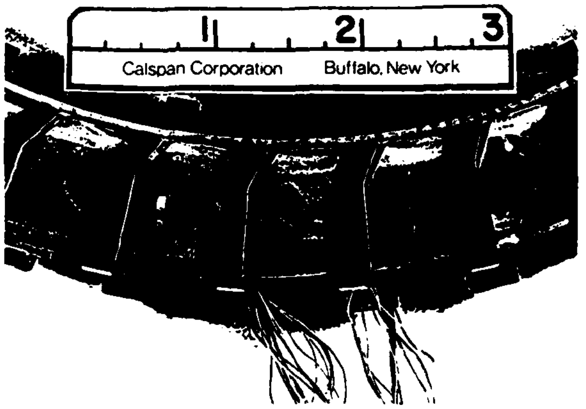

Fig. 1. Stator vane with trailing edge cutback.

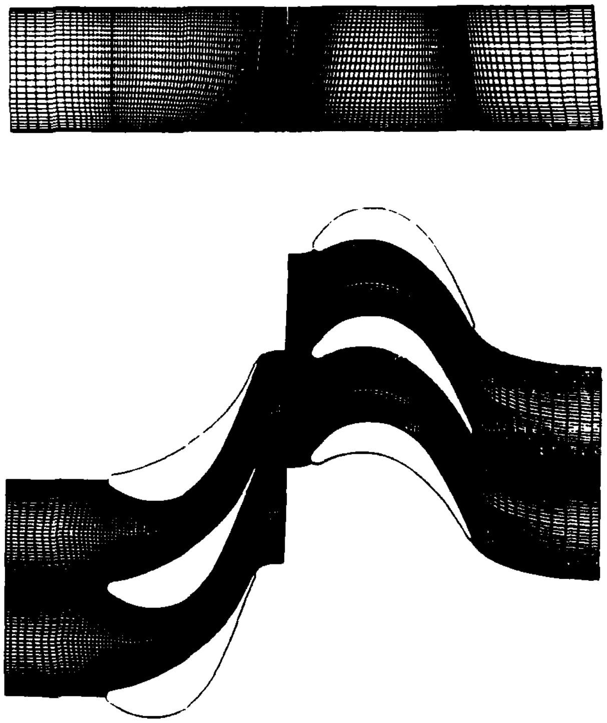

Fig. 2. Computational grid.

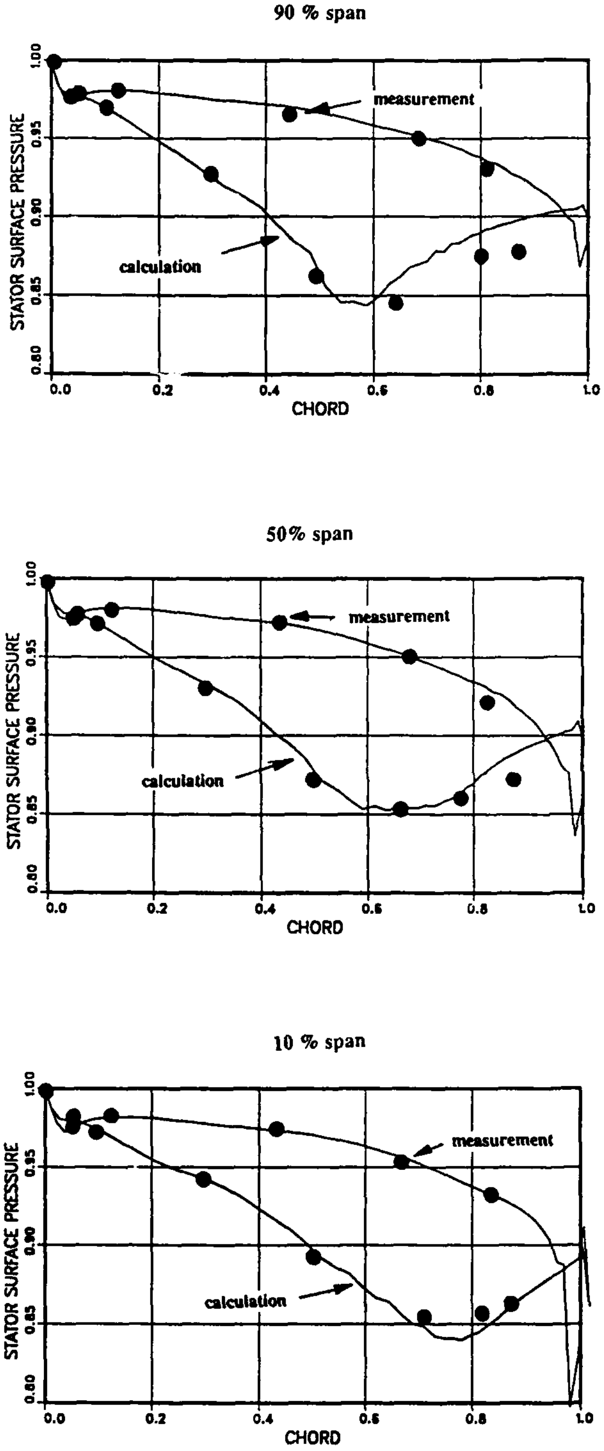

Fig. 3. Time-averaged pressure distribution on vane.

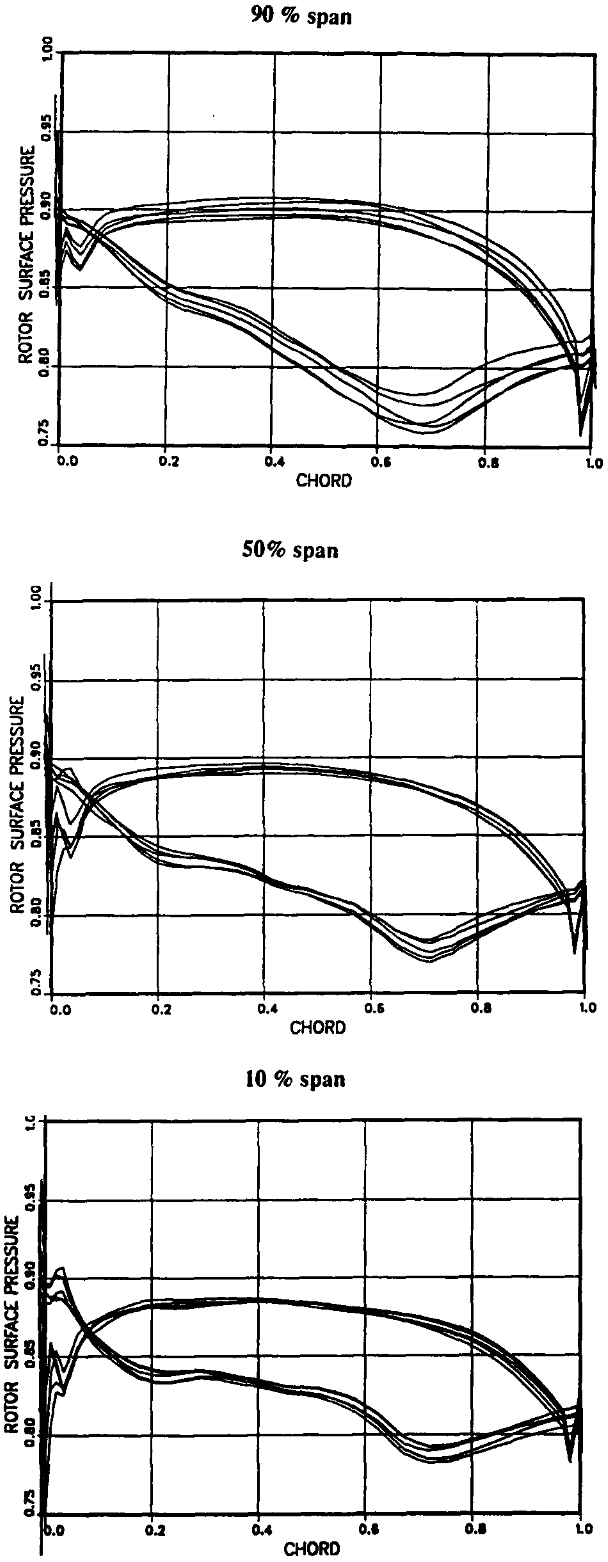

Fig. 4. Unsteady pressure distribution on blade.

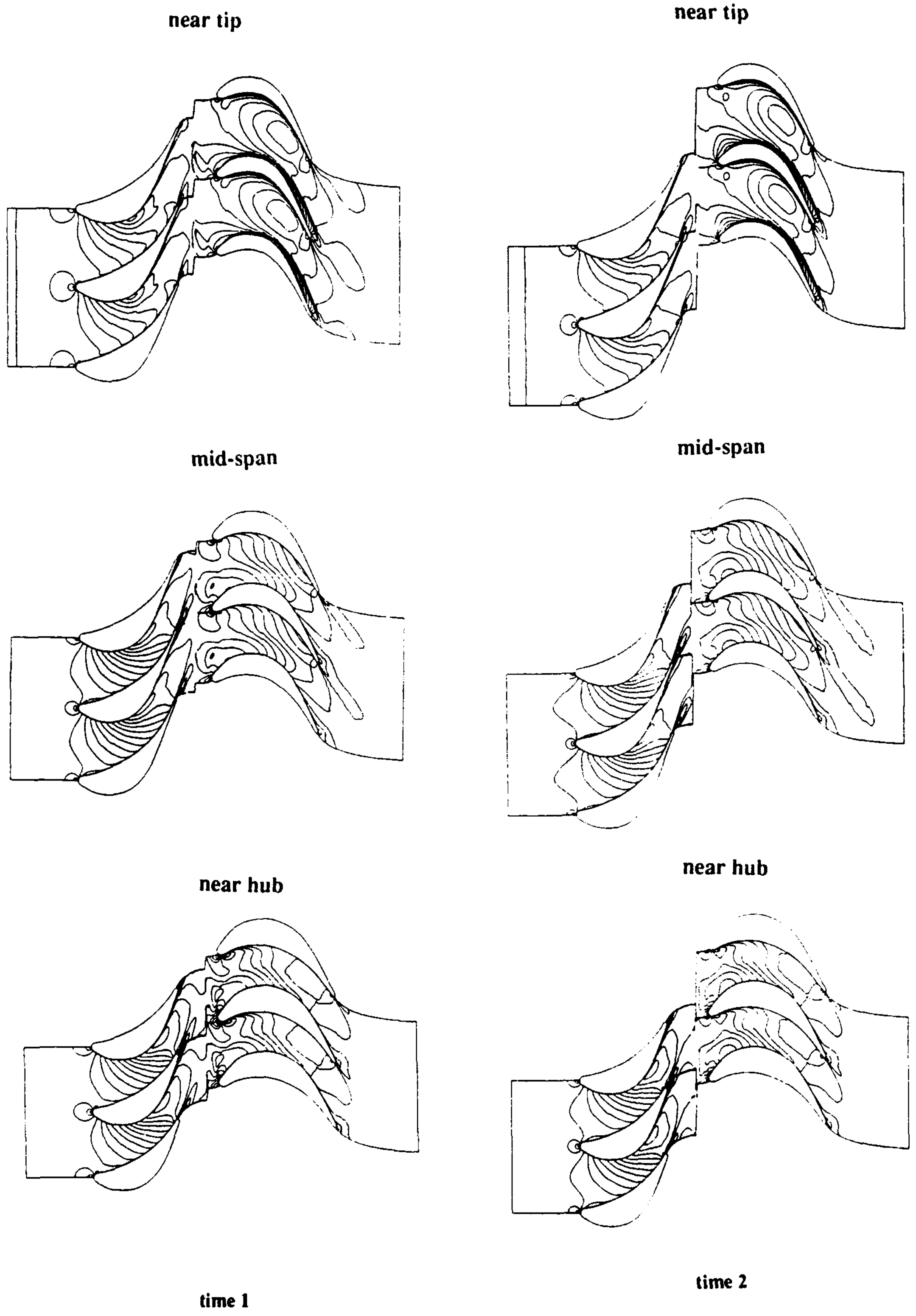

Fig. 5. Calculated Mach number contours.

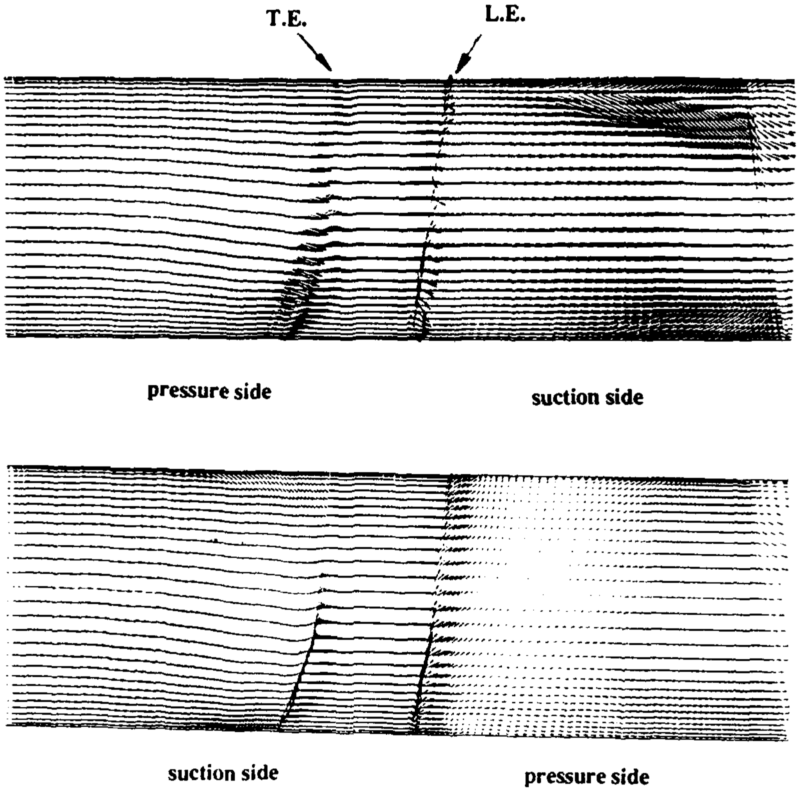

Fig. 6. Velocity vectors near blade surface.

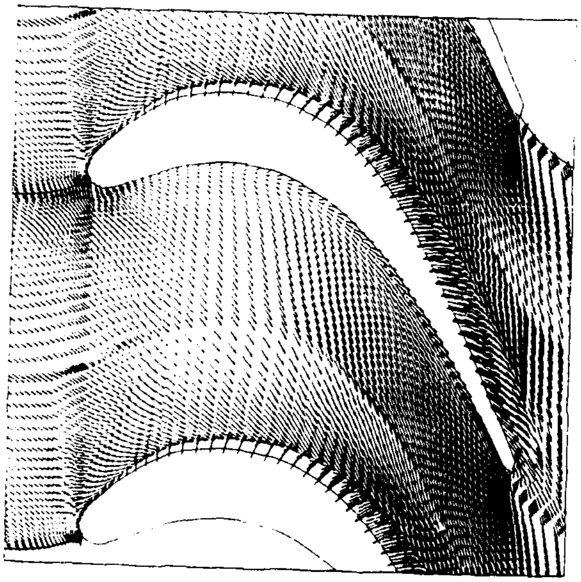

Fig. 7. Velocity vectors near tip.

Fig. 8. Particle traces near the suction side of the tip.

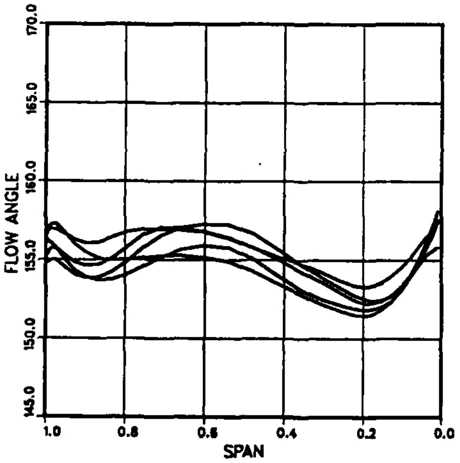

Fig. 9a. Unsteady flow angles at the rotor inlet.

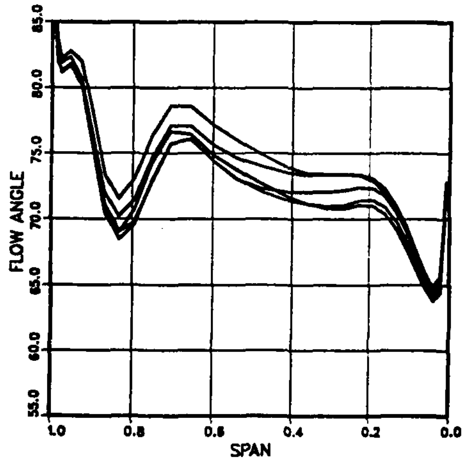

Fig. 9b. Unsteady flow angles at the rotor exit.

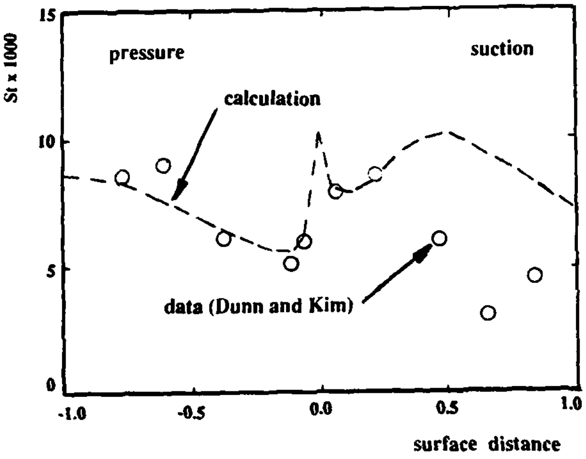

Fig. 10a. Comparison of stator heat transfer at 10 % span.

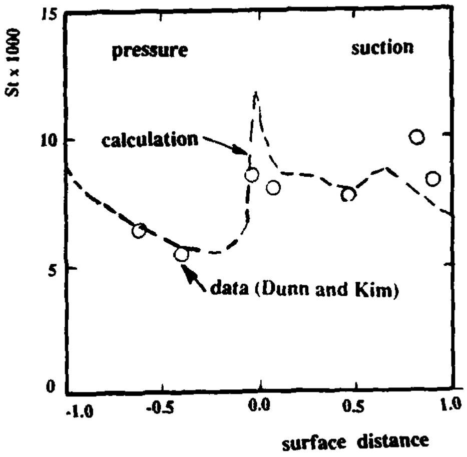

Fig. 11a. Comparison of rotor heat transfer at 10 % span.

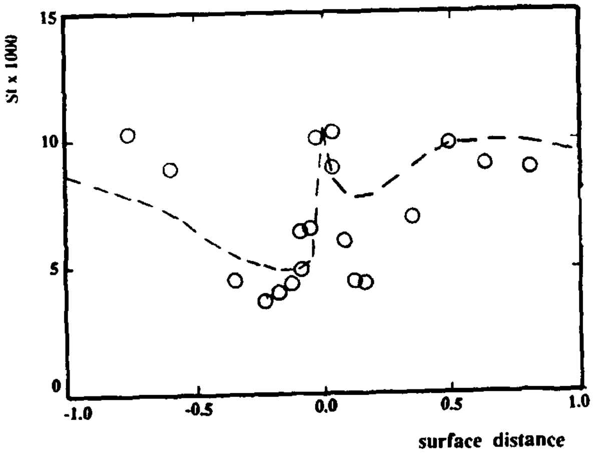

Fig. 10b. Comparison of stator heat transfer at 50 % span.

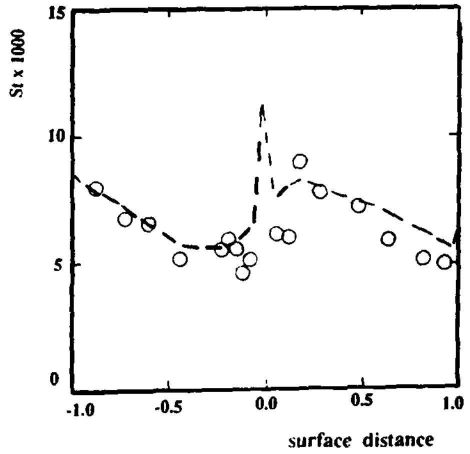

Fig. 11b. Comparison of rotor heat transfer at 50 % span.

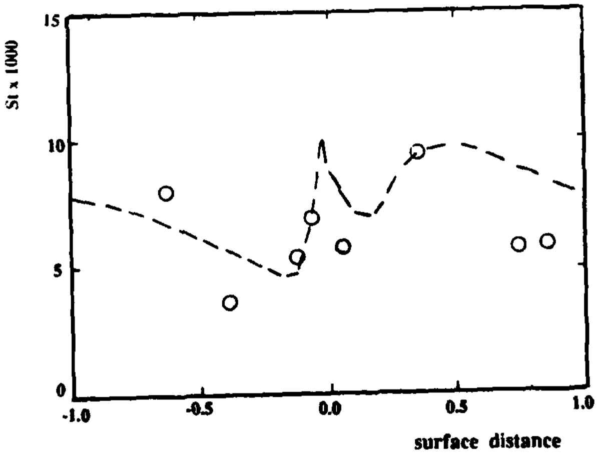

Fig. 10c. Comparison of stator heat transfer at 90 % span.

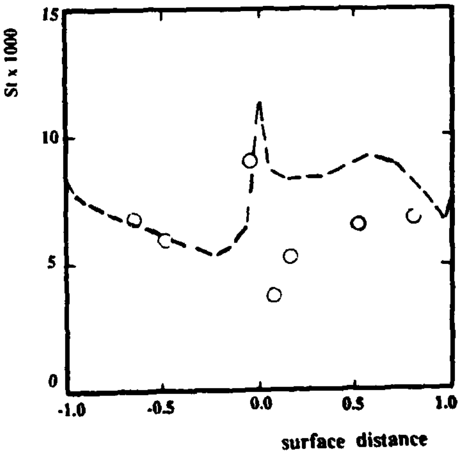

Fig. 11c. Comparison of rotor heat transfer at 90 % span.

Discussion

QUESTION 1:

DISCUSSOR: D.T. Vogel, DLR

Which boundary conditions did you apply for the unsteady calculations at the inlet and outlet?

AUTHOR'S REPLY:

Total temperature and total pressure were specified at the inlet of the stage along with flow angles at the inlet. At the exit, the static pressure is specified. All the boundary conditions were handled using a non-reflecting treatment.

QUESTION 2:

DISCUSSOR: D.T. Vogel, DLR

Is it only possible to calculate stator and rotor with the same pitch?

AUTHOR'S REPLY:

We can calculate any combination of blade numbers in the rotor and the stator with the time-stored boundary condition treatment.

QUESTION 3:

DISCUSSOR: D.T. Vogel, DLR

What about the time step size of you calculations relative to steady state calculations?

AUTHOR'S REPLY:

We are using sub-iteration at each time-step. Therefore, there is no numerical restriction on time-step. Usually it takes about 7-8 blade passes to reach a converged unsteady solution.

QUESTION 4:

DISCUSSOR: J.W. Chew, Rolls Royce

Have you compared your unsteady calculation with steady flow models?

AUTHOR'S REPLY:

Yes. The time-averaged results from the unsteady solution are different from the pure steady solution. We have seen differences both in secondary flow structure and local heat transfer coefficients.

COOLING PREDICTIONS IN TURBOFAN ENGINE COMPONENTS

A. MATESANZ, R. REBOLO, A. VIEDMA[*] & M. RODRIGUEZ[*]

SENER Ingeniería y Sistemas, S.A.
Parque Tecnológico de Madrid
28760 Tres Cantos, Madrid, Spain

(*) Also in Universidad Politécnica de Madrid
School of Aeronautical Engineering,
Pl. Cardenal Cisneros 3, 28040 Madrid, Spain

SUMMARY

The aim of this work is to show how the metal temperature measured in a convergent-divergent nozzle and in a turbine exhaust diffuser of a turbofan engine, can be predicted with reasonable approximation using the data available in the open literature. It is shown how the simplified fluid dynamic equations with the appropriate experimental correlation allow the prediction of these results in other flight conditions than those tested.

LIST OF SYMBOLS

$C_{p\infty}$= specific heat at main stream temperature.
C_{p2}= specific heat at cooling flow temperature.
D_h= Hydraulic diameter
d = local curvature diameter
h = convective heat flux coefficient
K = thermal conductivity coefficient
L = inner blade passage length
M =blowing factor $\frac{\rho_2 V_2}{\rho_\infty V_\infty}$
N_u= Nusselt number
P_r= Prandtl number
q = heat flux
R_{e2}= Reynolds number for the cooling parameters $\frac{\rho_2 V_2 .S}{\mu_2}$
$R_{e_{x,s,d}}$ = Reynolds number based on x,s,d.
s = cooling slot height.
T_g= absolute gas temperature.
T_r = recovery temperature = $T_\infty+0,9\left[T_{\infty 0}-T_\infty\right]$
T_w= actual wall temperature
T_{aw} = adiabatic wall temperature
$T_\infty, T_{\infty 0}$ = static and stagnation temperature of the main stream.
$T_* = T_\infty + 0,72\left[T_{aw} - T_\infty\right]$
T_2= cooling injection temperature.
x = distance from the point of injection.
$\Delta\varepsilon$= correcting factor due to spectral overlapping.
ε_w= inner face wall emissivity.
ε_g= gas emissivity = $\varepsilon_{CO2}\rho_{CO2}+ \varepsilon_{H2O}\rho_{H2O}-\Delta\varepsilon$
η = film cooling effectiveness
μ = gas dynamic viscosity
θ = angle from stagnation point in profile leading edge.
ρ = density
ρ_*, μ_*= density and viscosity at a temperature T_*
σ = Stefan-Boltzman constant.
ξ^* = non dimensional distance

$$= \frac{x}{M.S}\left[\frac{R_{e2}\,\mu_2}{\mu_*}\right]^{-0,25}\frac{\rho_*}{\rho_\infty}$$

Subscripts

g = gas
w = wall
1,2 = cold gas injection

1 INTRODUCTION

The modern engine solid surfaces exposed to internal flow need improved thermal protection because high temperature cycles are used to increase performance. During the past decades, different cooling methods have been used to reduce the metal temperature, therefore minimizing the required amount of cooling air.

The simplest way to cool surfaces is by convective cooling. In this process, heat flows by conduction from exposed metal surfaces to un-exposed ones, which are cooled by air flowing usually parallel to it. Convective cooling is used whenever low levels of cooling effectiveness are required. This limitation exists due to the fact that the air supply is somehow limited. On the other hand, high effectiveness levels tend to increase thermal stress problems [1-3].
A special type of convective cooling is by means of impingement. It is used whenever large heat transfer coefficients are needed on the un-exposed surfaces [4-8]. Another

method to obtain high heat transfer coefficients is to place fins or ribs normal to the coolant flow path [9].

When higher levels of cooling effectiveness are required it is necessary to use more sophisticated alternatives. The most common method is to insert a secondary fluid into the boundary layer on the surface which is to be protected. There are different means of injecting this fluid such as ablation, transpiration and film cooling. In ablation cooling, a heat shield ablates and secondary fluids enter the boundary layer [10] In transpiration cooling the coolant enters the boundary layer through a porous material [11-13]. Both methods are used to protect the region where coolants are added. Unfortunately the application of these systems is difficult because ablation has a limited time span and porous materials are not strong enough to be used in engines. The basic mechanism of film cooling is the introduction of a secondary fluid at several locations along a surface to protect that surface not only in the injection area but also in the downstream region [12-14].

Thermal studies on aircraft engines, particularly modern ones with large flight envelopes, require a great amount of testing and instrumentation. Designers have different tools for obtaining engine component temperature predictions. These tools can be classified as: 1) theoretical, 2) experimental and 3) numerical methods. Theoretical analysis is usually aimed at finding parameters to describe the temperature of an adiabatic wall downstream of the coolant injection [15]. Real and three-dimensional effects are studied on test rigs with controlled conditions [16-18]. Predictive numerical calculations are being widely used nowadays for different cooling applications and configurations, because they help to speed up the design and to reduce the number of experiments [19-20].
In this paper a method to predict full scale engine temperatures is described. This method combines the fluid dynamic equations with semi-empirical data obtained from the open literature.

The result is an easy to use procedure.

2. NOZZLE COOLING PREDICTION

The prediction of the petal temperature of a convergent-divergent nozzle has been performed through a computer code that uses correlation models available in the open literature with actual data obtained from a test program that includes a reduced scale hot test, a full scale rig test and a DVE (Design Verification Engine) program.

The film cooling produced when the relative cold layer is injected at the beginning of the convergent petal of the nozzle, produces a reduction in the metal temperature along the petal.

The heat transfer rate is modelled by:

$$q = A.h \left[T_{aw} - T_w\right]$$

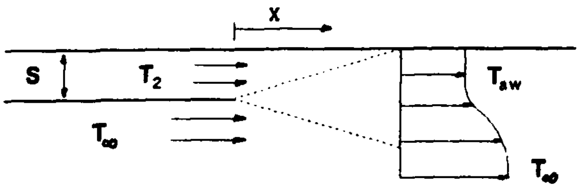

Fig.1. Single slot film cooling configuration.

The convective coefficient h is calculated independently from the adiabatic wall temperature T_{aw}.

This magnitude is related to the concept of effectiveness of the film cooling, figure 1:

$$\eta = \frac{T_r - T_{aw}}{T_r - T_2}$$

The correlation found more suitable for the flow conditions and geometry is the model of Kutatelache & Leanter, in reference [14] because the flow can be considered twodimensional and compressible and the difference of temperature between the wall and the main stream is important.

The effectiveness is given from this reference by the expression:

$$\eta = \frac{1}{1 + \frac{C_{p\infty}}{C_{p2}}\left[0,33\ (4,0 + \xi^*)^{0,8} - 1\right]}$$

When the cooling injection is made by two consecutive slots, the total effectiveness can be treated as the combination of two cooling layers where the external temperature for the inner flow is the "adiabatic wall temperature" for the external one [21], figure 2.

$$\eta_1 = \frac{T_\infty - T_{aw1}}{T_\infty - T_1}$$

$$\eta_2 = \frac{T_{aw1} - T_{aw2}}{T_{aw1} - T_2}$$

and the total effectiveness is:

$$\eta = \frac{T_\infty - T_{aw2}}{T_\infty - T_2} = \eta_1 + \eta_2\ (1 - \eta_1)$$

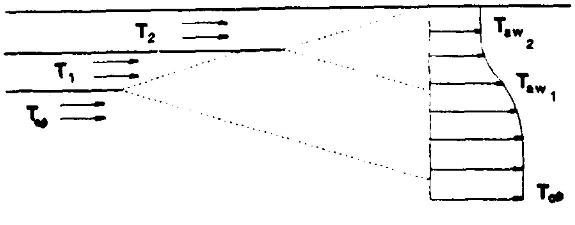

Fig.2. Double slot film cooling configuration.

The convective coefficient h is obtained from semiempirical correlation for film cooling with a high velocity compressible boundary layer.

As the blowing factor $M < 2$ the correlation used is the one proposed by Lefebre [22].

$$x \leq 0{,}01 \ m \qquad h_x = N_{ux} \cdot \frac{K_2}{x}$$

$$N_{ux} = 0{,}057 \ R_{ex}^{0,7}$$

$$R_{ex} = \frac{\rho_2 \ V_2 \ . x}{\mu_2}$$

$$x > 0.01 \ m \qquad h_x = \frac{N_{ux} \ K_2}{x}$$

$$N_{ux} = 0{,}0256 \left[R_{es} \ \frac{x}{M.S}\right]^{0,8}$$

$$R_{es} = \frac{\rho_2 \ V_2 \ . S}{\mu_2}$$

The wall temperature of the petal is obtained for an equilibrium model where the convective and radiative heat transfer with the cavity between the nozzle petals and the fairing flap, and the conduction along the petal are modeled in the classical way.

It may be of interest to note that the radiative heat transfer with the hot gas of the main flow is modeled as [15 & 23].

$$\frac{q}{A} = \frac{1}{2} \ \sigma \ \left(1 + \varepsilon_v\right) \ \varepsilon_g \ T_g^{1,5} \ \left(T_g^{2,5} - T_v^{2,5}\right)$$

3. NOZZLE THERMAL TESTS

The model resulting from this information gave good results for wall temperature estimation always with a conservative margin that the test in the scale model helped to reduce (figure 3). The full scale results with fixed convergent-divergent nozzle tested in a hot rig showed very good agreement between the predictions and the actual values from the thermocouples and thermal paints. (see figures 4 and 5).

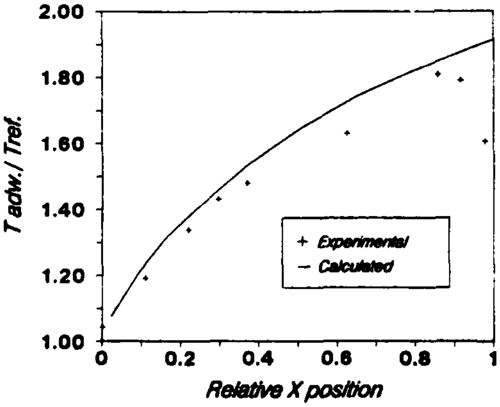

Fig.3. Initial prediction and scaled hot test results along nozzle petal.

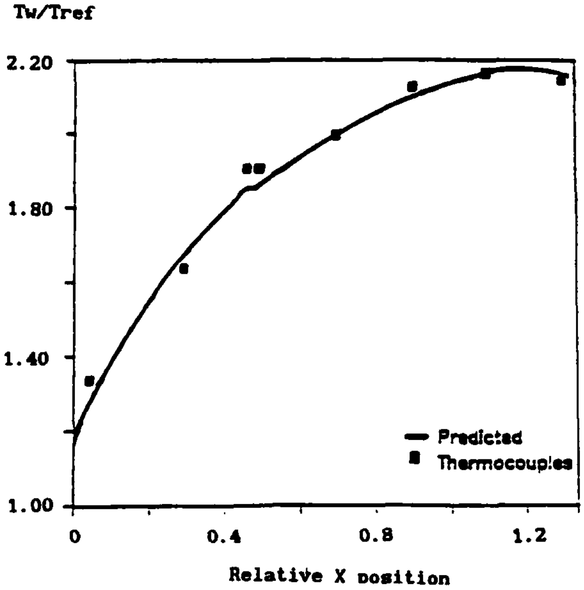

Fig.4. Comparison of predicted temperatures and fixed condi nozzle test results.

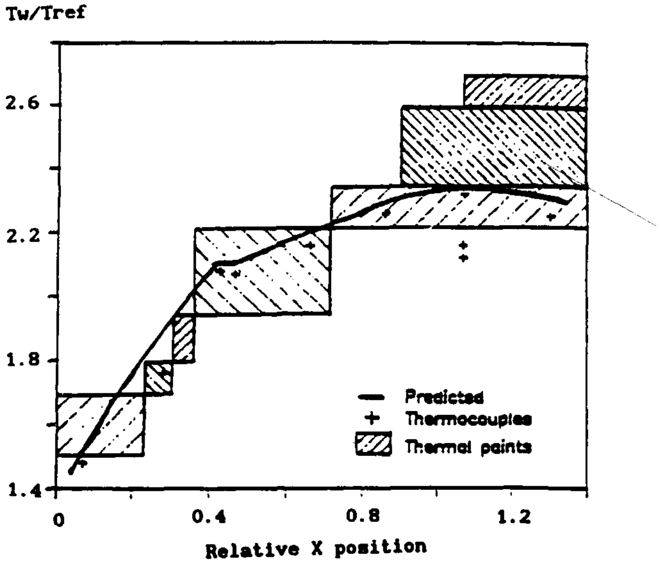

Fig.5. Thermal points, predicted temperature and thermocouples values in fixed condi nozzle.

When the true variable convergent-divergent nozzle was tested in the Design Verification Engine (DVE) the differences between the prediction and the measurement in the beginning of the divergent petal were important. But if a cooling ingestion through the gap in the throat is considered, this disagreement disappears and the model appears to be consistent and to give accurate temperature predictions. (Figure 6).

4. EXHAUST DIFFUSER COOLING CIRCUIT

The cooling circuit of the exhaust diffuser has been designed with a method that modelise the more relevant fluid factors

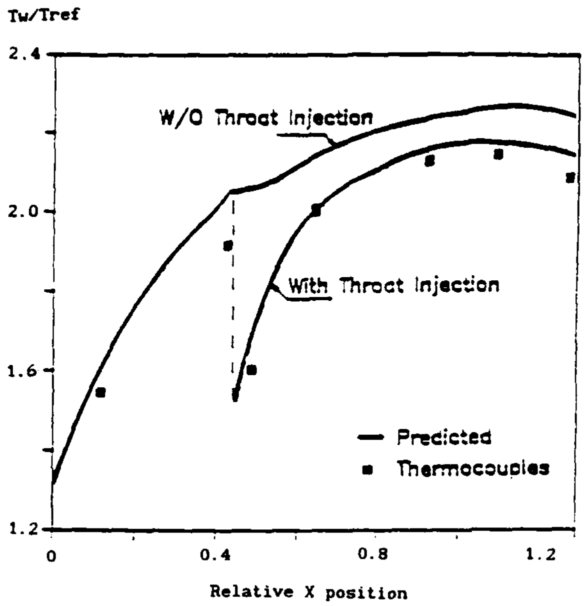

Fig.6. Predicted and measured temperatures with and without throat cold air injection.

around the circuit and use the available data in the open literature. This prediction method includes theoretical analysis and semienpirical correlations coupled to numerical simulation wherever further refinement is required. A more detailed description of this design method has been given elsewhere [24]. Therefore here we will only comment at the aspects related to the general objectives of this paper.

The geometry of the cooling circuit can be seen in figure 7, the fixed blade diffuser cascade has an inner passage with cooling capillaries in the trailing edge. The thermal analysis of the blades requires a detailed numerical process with NASTRAN code for the solid pieces and CFD code for the convective heat transfer in the blade boundary layer. But for the purpose of the circuit flow prediction a simpler model is used estimating the internal friction coefficient using [25] and the inner heat flux with the expression from [2].

$$N_u = \sqrt{\frac{T}{T_w}}\ .0{,}036\ R_e^{0{,}8} P_r^{1/3} \left(\frac{D_h}{L} \right)^{0{,}035}$$

The mean blade temperature is fixed by a heat equilibrium analysis where the external heat transfer is modelled in the leading edge with the correlation

$$N_u = 1{,}14\ R_{ed}^{1/2}\ P_r^{0{,}4} \left(1 - \frac{2\,\theta}{\pi} \right)$$

and in the rest of the blade surface with the standard Nusselt value for turbulent boundary layer.

The remaining heated flow which reaches the plenum is forced to cross the perforated wall to impinge onto the rear wall. This is needed to enhance the cooling of this wall which receives strong radiative heat flux from the afterburner. The dominant feature in this part of the cooling circuit is the combination of cross-flow and impingement cooling. The radial geometry simplifies the mathematical model which follows the scheme of [26].

The calculation of the flow through the holes in each station is also modified to allow for the cross flow. Correlation from [27] is used to take this effect into account. The convective heat coefficient produced by the impingement is modelled following [4 & 28].

To reproduce this correlation here is beyond our limits, so our advice is to consult the original papers.

Wall temperature is obtained by a thermal balance between external and internal radiative heat flux and the impingement as already commented. Upon the reheat luminous flame emissivity and radiative terms of this equilibrium are modelled after references [3 & 15].

The flow behavior inside the lateral double wall is calculated in a similar way with the simplification that no impingement effect is present.

The mass flow and thermal predictions are performed jointly in an iterative mode. It starts with a hypothetical mass flow at the beginning of the circuit. Its` purpose being to match the pressure, at the exit located downstream of the cascade, obtained by the program with the actual value.

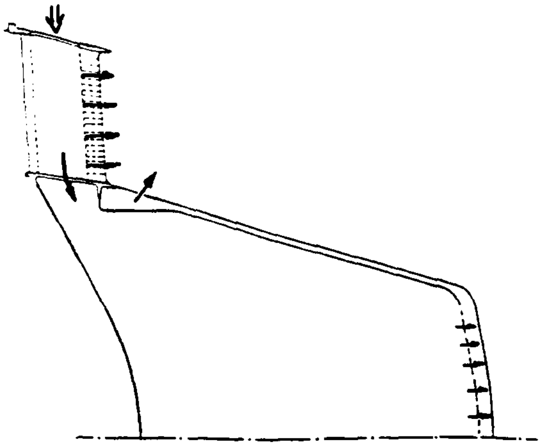

Fig.7. Exhaust diffuser cooling circuit.

5. EXHAUST DIFFUSER TEMPERATURE ASSESSMENT

Calibration tests were carried out to check the mass flow predicted through the cooling circuit. It was performed in a rig that reproduces the geometry and flow conditions, and is divided into two phases to obtain separately the mass flow through out both capillary trailing edge tubes and discharge exit downstream blade trailing edge.

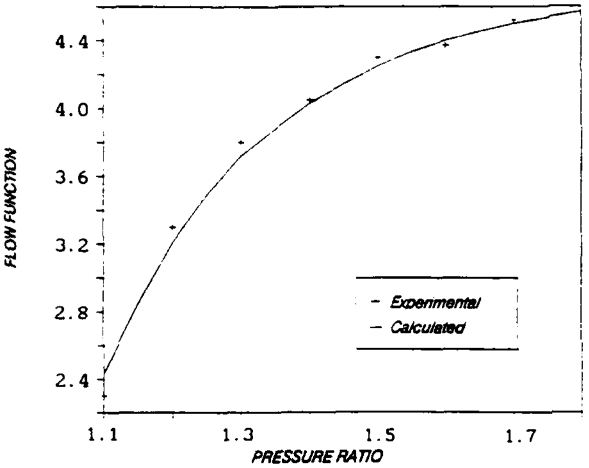

Fig.8. Results of calibration test mass flow through capillary cooling tubes in the blade trailing edge.

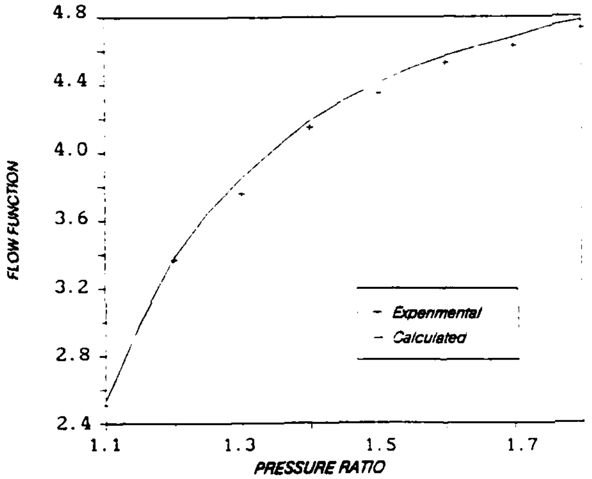

Fig.9. Results of calibration test. Total cooling mass flow in exhaust diffuser cooling circuit.

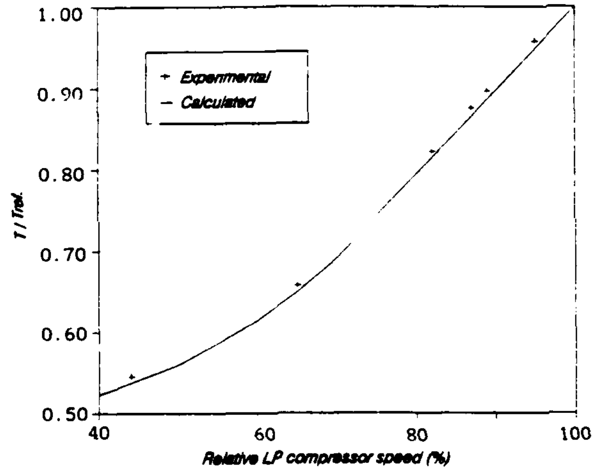

Fig.10. Comparison between predicted and experimental values of temperature at the center of the diffuser rear wall.

Figures [8 and 9] show the comparison between experiments and theoretical predictions for the capillary tubes and the total cooling mass flow.

The engine validation tests were performed to assess the pressure and temperature predictions. We will focus on the cone, lateral and rear walls where no further calculation was performed. The figures [10,11 and 12] show the comparison of predicted and measured temperature in the range of compressor speed, while figure [13] shows the relative error for both temperature and pressure in several circuit locations.

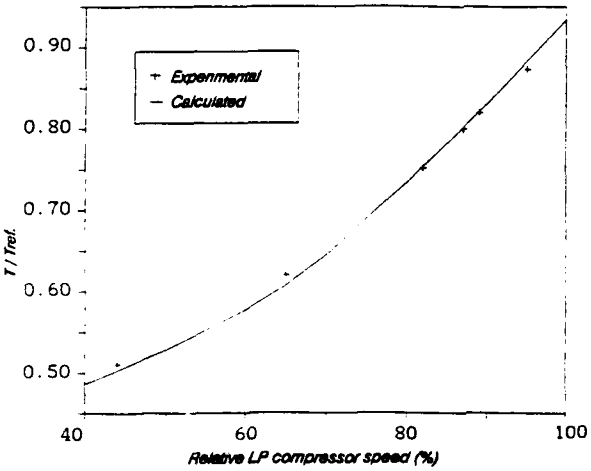

Fig.11. Comparison between predicted and experimental values of temperature at the periphery of the diffuser rear wall.

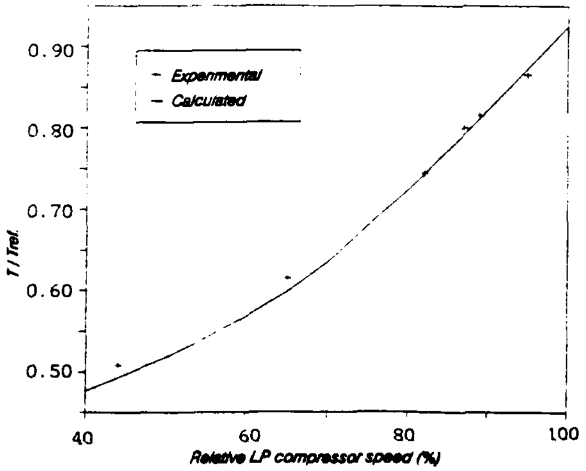

Fig.12. Comparison between predicted and experimental values of temperature at an intermediate section of the lateral wall.

6. CONCLUSIONS

The comparison between predicted and actual test results of calibration rigs and engine test beds shows that for design purposes the accuracy obtained is enough and no other complicated method is needed.

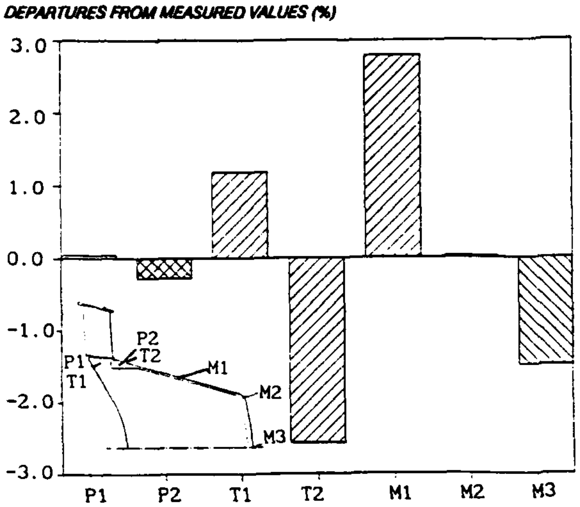

Fig.13. Differences between prediction and measured values. P, T and M are pressure, air temperature and metal temperature respectively.

Relevant engineering design parameters, such as metal temperatures, pressures and mass flow were predicted within 3% of accuracy. It is possible to explore a broad range of flight envelope points using this simple design tool. Further improvements on the modeling of reheat radiative properties would be needed if greater accuracy were required.

REFERENCES

1. ECKERT, E.R.G. and DRAKE, M.M. Jr, "Heat and Mass Transfer", New York, USA, McGraw-Hill, 1959, pp. 167-253.

2. NECATI OZISIK, M. "Heat Transfer. A Basic Approach", New York, USA, McGraw-Hill, pp. 281-415.

3. CHAPMAN, A.J., "Heat Transfer", New York, USA, McMillan, 1984.

4. KERCHER, D.M. and TABAKOFF, W. "Heat Transfer by a Square Array of Round Air Jest Impinging Perpendicular to a Flat Surface Including the Effect of Spent Air". ASME I. of Eng. for Power, Jan 1970.

5. OBOT, N.T. and TRABOLD, T.A. "Impingement Heat Transfer within Arrays of Circular Jets: Parts I and II". Transactions of the ASME, vol. 109, 1987.

6. DABAGH, A.M. et al. "Impingement/Effusion Cooling: The Influence of the Number of Impingement Holes and Pressure Loss on the Heat Transfer Coefficient", Gas Turbine and Aeroengine Congress and Exposition, 1989, 89-GT-188.

7. ABDUL HUSAIN, R.A.A. and ANDREWS, G.E. "Full Coverage Impingement Heat Transfer at High Temperatures". Gas Turbine and Aeroengine Congress and Exposition, 1990, 90-GT-285.

8. ANDREWS, G.E. et al. "Full Coverage Impingement Heat Transfer: The Variation in Pitch to Diameter Ratio at a Constant Gap", University of Leeds, Leeds, U.K.

9. WEBB, R.L., ECKERT, E.R.G. and GOLDSTEIN, R.J. "Heat Transfer and Friction in Tubes with Repeated-Rib Roughness". Int. J Heat Mass Transfer, vol. 14, pp. 601-617, 1971.

10. LAUB, B. "Thermochemical Ablation of Tantalum Carbide Loaded Carbon-Carbons. Paper 80-0290 AIAA 18+h Aerospace Sciences Meeting. 1980.

11. LIBRIZZI, J. and CRESCI, R.J. "Transpiration Cooling of a Turbulent Boundary Layer in a Axisymmetric Nozzle". AIAA Journal, vol. 2, April 1964, pp. 617-624.

12. MOFFAT, R.J. and KAYS, W.M. "A Review of Turbulent-Boundary-Layer Heat Transfer Research at Stanford, 1958-1983". Advances in Heat Transfer, vol. 16, Academic Press, Orlando 1984, p. 241.

13. HARTNETT, J.P. "Mass Transfer Cooling", Handbook of Heat Transfer Applications, pp. 1-1, 1-111.

14. GOLDSTEIN, R.J. "Fluid Cooling". Advances in Heat Transfer, Academic Press, 1971.

15. LEFEBVRE, A.H. "Gas Turbine Combustion", McGraw-Hill, New York, pp. 287-295.

16. LUCAS, G.J. and GOLLADAY, R.L. "Gaseous-Film Cooling of a Rocket Motor with Injection Near the Throat". NASA TN D-3836, 1967.

17. STEPHEN DAPELL, S. "Effect on Gaseous Film Cooling of Coolant Injection through Angled slots and Normal Holes". NASA TN D-299, 1960.

18. SHAO-YEN KO and DENG-YING LIU, "Experimental Investigations on Effectiveness, Heat Transfer Coefficient, and Turbulence of Film Cooling", AIAA Journal, vol. 18, August 1980, pp. 907-913.

19. DIBELIOS, G.H. et al. "Numerical Predictions of Film Cooling Effectiveness and the Associated Aerodynamics Losses with a Three-Dimensional Calculation Procedure". ASME 90-GT-226.

20. STOLL, J. and STRAUB, J. "Film Cooling and Heat Transfer in Nozzles". Journal of Turbomachinery, January 1988, vol. 110.

21. SELLORS, J.P., "Gaseous film cooling with multiple injection stations", AIAA J., vol. 1, Sept. 1963, pp. 2154-2156.

22. LEFEBVRE, , "A proposed method for calculating film cooled wall temperatures in gas turbine combustion chambers". A.H., ASME 72-WA/HT-24

23. HOLMAN, J.P., "Heat Transfer", McGraw-Hill.

24. MATESANZ, A., VIEDMA, A., VELAZQUEZ, A. & RODRIGUEZ, M., "Cooling study in the exhaust diffuser of a reheat turbofan", International Symposium on Heat Transfer in Turbomachinery, Athens, 24-28 August 1992.

25. HACLAND, S.E., "Simple and explicit formulas for the friction factor in turbulent pipe flow", J. Fluid Eng., vol. 105, pp. 89-90, 1983.

26. SHAPIRO, A.H., "The dynamics and thermodynamics of compressible fluid flow". Ronald Press. Co., New York, 1953, vol. I, p. 228.

27. FLORSCHUETZ, C.W. & ISODA, Y., "Flow distribution and discharge coefficient effects for jet away impingement with initial cross flow", J. Eng. for Power, vol. 105, pp. 296-304, 1983.

28. FLORSCHUETZ, L.W. & S.U, C.C., "Effects of cross flow temperature on heat transfer within an array of impinging jets", Trans. ASME, vol. 109, Feb. 1987.

Discussion

QUESTION 1:

DISCUSSOR: J. Salva Monfort, Escuela Tecnica Superior de Ingenieros Aeronauticos

Can you explain in more detail how you have calculated the cooling flux through the capillary tubes in the trailing edges of the blades?

AUTHOR'S REPLY:

The flow through the cooling capillary tubes in the trailing edge of the blades is calculated using the same turbulent one-dimensional equations as for the main passages of the blade. Some problems of choking due to the high heat transfer can arise. In this case, it is necessary to detect the Mach number increase and to reduce the mass flow for that capillary tube accordingly.

QUESTION 2:

DISCUSSOR: D.T. Vogel, DLR

You used many of empirical constants in your calculations. Are these constants related to your special problem, or is it possible to calculate other cooling configurations?

AUTHOR'S REPLY:

The correlations used are all chosen from open literature taking into account the geometry and dimensionless parameters of the problem. Please refer to the original paper to find out if it can be applied to other configurations.

REPORT DOCUMENTATION PAGE

1. Recipient's Reference	**2. Originator's Reference**	**3. Further Reference**	**4. Security Classification of Document**
	AGARD-CP-527	ISBN 92-835-0701-0	UNCLASSIFIED/ UNLIMITED

5. Originator
Advisory Group for Aerospace Research and Development
North Atlantic Treaty Organization
7 Rue Ancelle, 92200 Neuilly sur Seine, France

6. Title
HEAT TRANSFER AND COOLING IN GAS TURBINES

7. Presented at
the Propulsion and Energetics Panel 80th Symposium held in Antalya, Turkey, 12th—16th October 1992.

8. Author(s)/Editor(s)	**9. Date**
Various	February 1993
10. Author's/Editor's Address	**11. Pages**
Various	510

12. Distribution Statement
There are no restrictions on the distribution of this document. Information about the availability of this and other AGARD unclassified publications is given on the back cover.

13. Keywords/Descriptors

Combustors
Convective heat transfer
Cooling
Film cooling
Gas turbines
Heat transfer
Impingement cooling
Rotating discs
Seals technology
Turbine blades
Turbulent flow
Wake flow

14. Abstract

The Conference Proceedings contains the 38 papers presented at the Propulsion and Energetics Panel 80th Symposium on "Heat Transfer and Cooling in Gas Turbines" which was held from 12th—16th October 1992 in Antalya, Turkey. The Technical Evaluation Report and the Keynote Address are included at the beginning, and discussions follow most papers.

The Symposium was arranged in the following Sessions: Turbine Blades: External Heat Transfer (9); Turbine Blades: Internal Heat Transfer (6); Measurement Techniques (4); Rotating Disks, Labyrinth Seals and Shafts (7); Combustors (4); Design, Interactions (3); and Prediction Methods (5).

Heat transfer and cooling in gas turbines are still key factors for achieving high performance, increased life and improved reliability. Any progress in this field will lead to a reduction of maintenance cost and fuel consumption. The purpose of the Symposium was to bring together experts from industry, research establishments and universities to discuss fundamental and applied heat transfer problems relevant to gas turbines, to exchange practical experience gained and to review the state of the art.

AGARD Conference Proceedings 527
Advisory Group for Aerospace Research and Development, NATO
HEAT TRANSFER AND COOLING IN GAS TURBINES
Published February 1993
510 pages

The Conference Proceedings contains the 38 papers presented at the Propulsion and Energetics Panel 80th Symposium on "Heat Transfer and Cooling in Gas Turbines" which was held from 12th—16th October 1992 in Antalya, Turkey. The Technical Evaluation Report and the Keynote Address are included at the beginning, and discussions follow most papers.

The Symposium was arranged in the following Sessions: Turbine Blades: External Heat Transfer (9); Turbine

P.T.O.

AGARD-CP-527

Combustors
Convective heat transfer
Cooling
Film cooling
Gas turbines
Heat transfer
Impingement cooling
Rotating discs
Seals technology
Turbine blades
Turbulent flow
Wake flow

AGARD Conference Proceedings 527
Advisory Group for Aerospace Research and Development, NATO
HEAT TRANSFER AND COOLING IN GAS TURBINES
Published February 1993
510 pages

The Conference Proceedings contains the 38 papers presented at the Propulsion and Energetics Panel 80th Symposium on "Heat Transfer and Cooling in Gas Turbines" which was held from 12th—16th October 1992 in Antalya, Turkey. The Technical Evaluation Report and the Keynote Address are included at the beginning, and discussions follow most papers.

The Symposium was arranged in the following Sessions: Turbine Blades: External Heat Transfer (9); Turbine

P.T.O.

AGARD-CP-527

Combustors
Convective heat transfer
Cooling
Film cooling
Gas turbines
Heat transfer
Impingement cooling
Rotating discs
Seals technology
Turbine blades
Turbulent flow
Wake flow

AGARD Conference Proceedings 527
Advisory Group for Aerospace Research and Development, NATO
HEAT TRANSFER AND COOLING IN GAS TURBINES
Published February 1993
510 pages

The Conference Proceedings contains the 38 papers presented at the Propulsion and Energetics Panel 80th Symposium on "Heat Transfer and Cooling in Gas Turbines" which was held from 12th—16th October 1992 in Antalya, Turkey. The Technical Evaluation Report and the Keynote Address are included at the beginning, and discussions follow most papers.

The Symposium was arranged in the following Sessions: Turbine Blades: External Heat Transfer (9); Turbine

P.T.O.

AGARD-CP-527

Combustors
Convective heat transfer
Cooling
Film cooling
Gas turbines
Heat transfer
Impingement cooling
Rotating discs
Seals technology
Turbine blades
Turbulent flow
Wake flow

AGARD Conference Proceedings 527
Advisory Group for Aerospace Research and Development, NATO
HEAT TRANSFER AND COOLING IN GAS TURBINES
Published February 1993
510 pages

The Conference Proceedings contains the 38 papers presented at the Propulsion and Energetics Panel 80th Symposium on "Heat Transfer and Cooling in Gas Turbines" which was held from 12th—16th October 1992 in Antalya, Turkey. The Technical Evaluation Report and the Keynote Address are included at the beginning, and discussions follow most papers.

The Symposium was arranged in the following Sessions: Turbine Blades: External Heat Transfer (9); Turbine

P.T.O.

AGARD-CP-527

Combustors
Convective heat transfer
Cooling
Film cooling
Gas turbines
Heat transfer
Impingement cooling
Rotating discs
Seals technology
Turbine blades
Turbulent flow
Wake flow

Blades: Internal Heat Transfer (6); Measurement Techniques (4); Rotating Disks, Labyrinth Seals and Shafts (7); Combustors (4); Design, Interactions (3); and Prediction Methods (5).

Heat transfer and cooling in gas turbines are still key factors for achieving high performance, *increased life and improved reliability*. Any progress in this field will lead to a reduction of maintenance cost and fuel consumption. The purpose of the Symposium was to bring together experts from industry, research establishments and universities to discuss fundamental and applied heat transfer problems relevant to gas turbines, to exchange practical experience gained and to review the state of the art.

ISBN 92-835-0701-0

Blades: Internal Heat Transfer (6); Measurement Techniques (4); Rotating Disks, Labyrinth Seals and Shafts (7); Combustors (4); Design, Interactions (3); and Prediction Methods (5).

Heat transfer and cooling in gas turbines are still key factors for achieving high performance, increased life and improved reliability. Any progress in this field will lead to a reduction of maintenance cost and fuel consumption. The purpose of the Symposium was to bring together experts from industry, research establishments and universities to discuss fundamental and applied heat transfer problems relevant to gas turbines, to exchange practical experience gained and to review the state of the art.

ISBN 92-835-0701-0

Blades: Internal Heat Transfer (6); Measurement Techniques (4); Rotating Disks, Labyrinth Seals and Shafts (7); Combustors (4); Design, Interactions (3); and Prediction Methods (5).

Heat transfer and cooling in gas turbines are still key factors for achieving high performance, increased life and improved reliability. Any progress in this field will lead to a reduction of maintenance cost and fuel consumption. The purpose of the Symposium was to bring together experts from industry, research establishments and universities to discuss fundamental and applied heat transfer problems relevant to gas turbines, to exchange practical experience gained and to review the state of the art.

ISBN 92-835-0701-0

Blades: Internal Heat Transfer (6); Measurement Techniques (4); Rotating Disks, Labyrinth Seals and Shafts (7); Combustors (4); Design, Interactions (3); and Prediction Methods (5).

Heat transfer and cooling in gas turbines are still key factors for achieving high performance, increased life and improved reliability. Any progress in this field will lead to a reduction of maintenance cost and fuel consumption. The purpose of the Symposium was to bring together experts from industry, research establishments and universities to discuss fundamental and applied heat transfer problems relevant to gas turbines, to exchange practical experience gained and to review the state of the art.

ISBN 92-835-0701-0